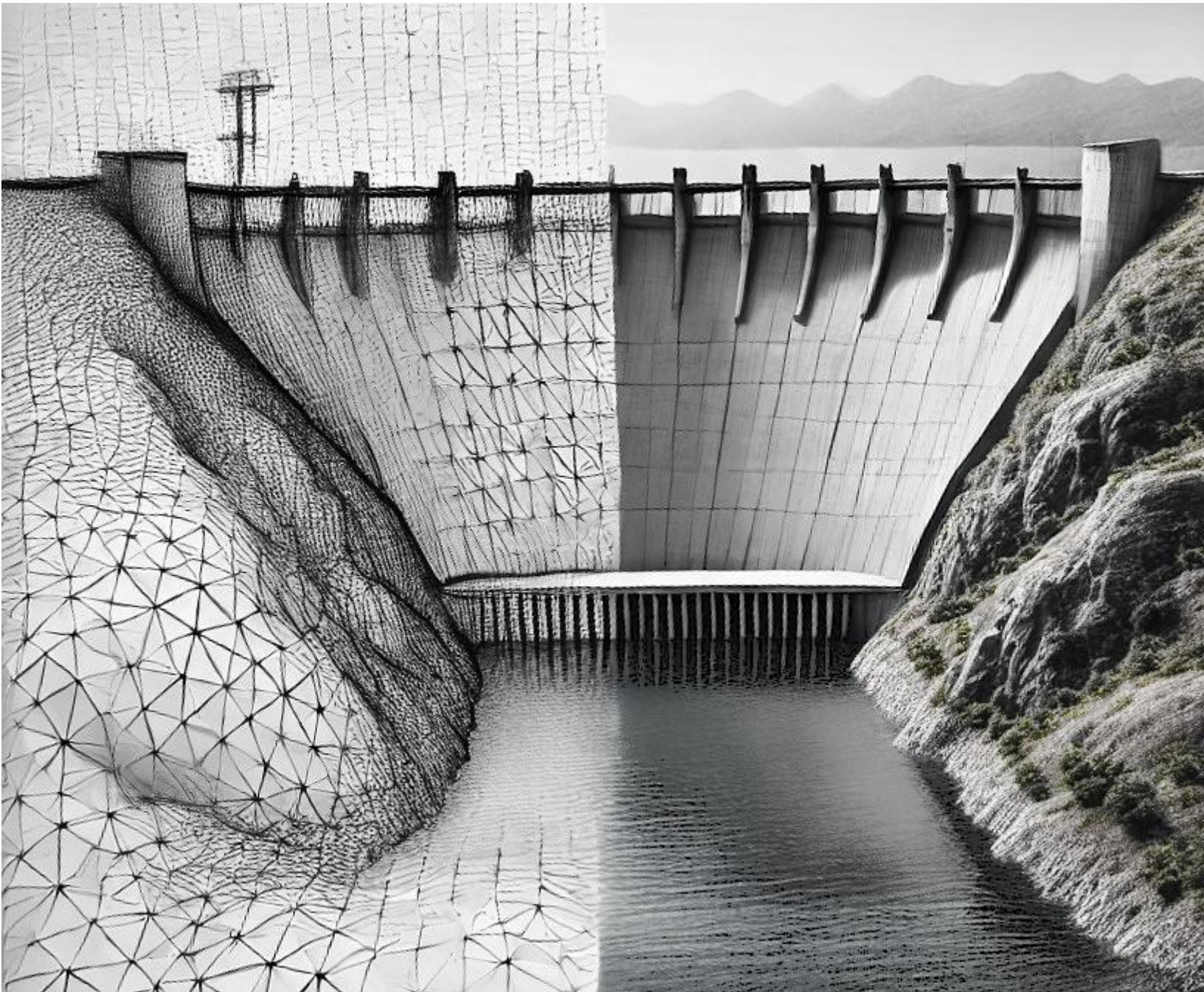


Seismic Analysis of Dams and Levees

Papers and Presentations at the 18th World Conference on
Earthquake Engineering (WCEE 2024), Milan, Italy

Editors and Session Organizers:

M. Amin Hariri-Ardebili (University of Maryland, College Park, USA)
Anna De Falco (University of Pisa, Italy)
Guido Mazzà (ITCOLD - Italian Committee on Large Dams, Italy)



Preface

Dams and levees play a crucial role in ensuring water security, providing essential resources for irrigation, drinking water, and hydropower generation. However, the potential consequences of dam failure are severe, posing significant risks to downstream communities, properties, and ecosystems. The engineering, maintenance, and monitoring of these structures are of paramount importance to mitigate such risks and ensure their safe operation.

The World Conference on Earthquake Engineering (WCEE), held every four years, is one of the most prestigious events in the field of earthquake engineering. It attracts experts, researchers, and practitioners from around the globe, fostering the exchange of knowledge and advancements in earthquake resilience. The 18th WCEE, held in Milan, Italy, continued this tradition, providing a platform for the presentation and discussion of cutting-edge research and innovative solutions.

As part of this esteemed conference, we organized a session focused on dams and levees. This session drew significant interest, with approximately 70 abstracts submitted. Through a rigorous review process, 44 papers were selected for final presentation. These papers, which were presented over six sessions, encompass a diverse range of themes, including seismic fragility, numerical simulations, experimental studies, concrete dams, embankments, and risk analysis.

Each session featured 7-8 papers, with presentations delivered by a diverse group of attendees from academia, industry, research laboratories, and governmental agencies. This multidisciplinary participation highlighted the collaborative efforts needed to advance our understanding and enhance the safety of dam and levee structures.

In this edited book, we have compiled all 44 papers and the associated presentations from our sessions. This comprehensive collection showcases the latest research and practical insights into the seismic analysis of dams and levees. It serves as a valuable resource for engineers, researchers, policymakers, and anyone involved in the field of earthquake engineering and dam safety.

We hope this edited book will contribute to the ongoing efforts to improve the resilience and safety of dams and levees worldwide. By sharing these findings, we aim to promote further research, foster collaboration, and ultimately enhance the protection of communities and the environment.

Editors and Session Organizers:

M. Amin Hariri-Ardebili (University of Maryland, College Park, USA)

Anna De Falco (University of Pisa, Italy)

Guido Mazzà (ITCOLD - Italian Committee on Large Dams, Italy)

Table of Contents

Title	Authors	Presenter's country
Analysis of the behavior of a gravity dam in Central America subject to high seismic forces	A. De Paola, E. Baldovin, S. Pavone	ITALY
Assessment of the seismic behavior of concrete dams: from simplified to advanced methods	G. Faggiani, P. Masarati	ITALY
Monitoring and simulated response of dams to the February 2023 Turkey earthquake sequence	M.A. Hariri-Ardebili, H. Tosun	USA/TURKEY
The role of modeling uncertainties in seismic analysis of concrete dams	M.A. Hariri-Ardebili, J. Salamon	USA
Understanding the role of stress-dependent material damping in seismic analysis of concrete dams	M.A. Hariri-Ardebili, M. Noorbakhsh-Saleh, S.M. Seyed-Kolbadi, F. Pourkamali-Anaraki	USA
BEM-FEM solution of arch dam-fluid interaction using ADAD-IZIIS software	V. Mircevska, A. Nanevska	REPUBLIC OF MACEDONIA – FYROM
Non-linear seismic analysis of concrete gravity dam using time domain spectral finite element method	A. Sarkar, A. Bagchi	CANADA
Non-linear seismic response of an ultra-high arch dam. ETA-based safety assessment	A. Alegre, S. Oliveira, P. Mendes, J. Proença, R. Ramos	PORTUGAL
Comparison of damage prediction for concrete dams, finite element with smeared crack vs. Discrete element models	B.F. Soysal, Y. Arici	TURKEY
Dam portfolio assessment for risk-informed decision-making	T. Elkhoraibi, A. Hashemi, A. Kottke, Y. Arici	TURKEY
Influence of non-linearity of dynamic shear modulus on the seismic safety evaluation of arch dam	Y. Ariga	JAPAN
Seismic slope stability of hybrid tailings dams: a probabilistic approach	T.S. Aswathi, S. Kuili, R.S. Jakka	INDIA
New efficient methods for the seismic analysis of dams and their appurtenant structures	N. Bouaanani, R. Kouhdasti	CANADA
The seismic safety assessment of a multiple arch dam	M. Colombo, A. Frigerio	ITALY
Implementation and validation of the direct method for simulating dynamic dam-foundation interaction	D. Froio, F. Carnevale	ITALY

Non-linear seismic response of concrete dams	L. Furgani	ITALY
A validation framework for linear and nonlinear dam safety analysis techniques	Y. Ghanaat, Z. Harper, Z. Han	USA
Nonlinear seismic analysis of gravity dams including lift and base joints	S. Guo, H. Liang, D. Li, H. Wang	CHINA
Centrifuge shake table tests and numerical simulations on seismic damage process of embankments	R. Ibuki, K. Uemura, T. Doi, J. Izawa, S. Sreng	JAPAN
Seismic fracture modeling of 3D gravity dam monoliths using the scaled boundary finite element method	X. Jiang, H. Zhong, D. Li, J. Niu, B. Wu	CHINA
Performance evaluation of concrete gravity dam in the event of seismic aftershocks	S.S. K P, M.K. Shrimali, S.D. Bharti, C.V.R. Murty, N. Roy	INDIA
Use of three-dimensional numerical analyses in seismic design of earth embankments	M. Kafash, Z. Karimi, L. Yenne	USA
3D seismic analysis of arch dam for random ground motion	D. Khandelwal, S.D. Bharti, M.K. Shrimali, J.N. Arlekar, N. Roy	INDIA
Challenges in developing vertical hazard for seismic analysis of concrete dams	N. Kwong, S. Rezaeian, A. Makdisi, N. Luco	USA
Seismic damage analysis of high concrete arch dam-foundation systems: a comprehensive study	h. Liang, s. Guo, c. Yan, j. Tu	CHINA
Intensifying dynamic response of a concrete dam affected by alkali-aggregate reaction	G. Mahdavi, V.E. Saouma	USA
3D seismic stability analysis of a concrete spillway pier affected by AAR	A. Nour, A. Cherfaoui	CANADA
Impact of uncertainty associated with ground motion selection on fragility assessment of dams	B.K. Patra, R. Segura, A. Bagchi	CANADA
Deconvolution of real and artificial accelerations for dynamic analysis of dams	M. Poul, M.A. Hariri-Ardebili	USA
Dynamic analyses of an earth dam with different initial stress state	R. Previtali, R. Pellegrini, F. Carnevale, P. Chemello	ITALY
Effect on non-vertical propagation seismic waves on the behavior of gravity and arch dams	E. Robbe, N. Humbert, S. Cherubini	FRANCE
Implications of seismic risk analysis for dams and decision making in a risk informed framework	M. Rocha, K.Z.Z. Lee, P. Mott	USA
Low-to-high fidelity transformation function for the seismic fragility assessment of gravity dams	R.J. de Almeida Torres Filho, R.L. Segura, P. Paultre	USA
Application of ground motion-compatible intensifying artificial acceleration in dams	G. Sevieri, M.A. Hariri-Ardebili, C. Resta, A. De Falco	ITALY

Centrifuge model tests and numerical simulations of irrigation dams during earthquake	S.S. Suzuki, K. Fukuda, H. Ishikawa, N. Takahashi	JAPAN
Impacts of the February 06, 2023, turkey earthquake sequences on risk assessment of embankment dams	H. Tosun, M.A. Hariri-Ardebili	USA/TURKEY
Seismic performance of an earth dam with strong motion input signals selected with different criteria	M. Tretola, G. Fiorentino, F. Sabetta, S. Sica	ITALY
Effect of internal structure of levees on the seismic and seepage behavior	R. Uzuoka, S. Yamada, K. Ueda	JAPAN
Seismic analysis of the Garcia Dam located in the Belice Valley of Sicily	R. Vincifora, G. Amato, M. Ferrotto, S. Pagnotta, A. Cusmano, S. Volo	ITALY
Comparisons between ground improvement methods for a high embankment dam on thick alluvial deposit	Z. Wang, R. Wang, J. Zhang	CHINA
Predictive model for seismic displacements of a general flexible sliding block in near-fault region	C. Xiang, D. Huang, Y. Zhang, L. Zhao	CHINA
Dynamic response of the Punta Negra Dam under the 2021 San Juan earthquake	F. Zabala, N.G. Sanchez, G.S. Zabala	ARGENTINA
Seismic response analysis of water-sediment-foundation-arch dam system	J. Zhang, S.L. Chen	CHINA
Impacts of constitutive model and input ground motion selection on the seismic response of an earth dam	A.G. Ozcebe, D. Gioffre, A. Famà, E. Zuccolo, F. Bozzoni, C.G. Lai	ITALY

NON-LINEAR SEISMIC RESPONSE OF AN ULTRA-HIGH ARCH DAM. ETA-BASED SAFETY ASSESSMENT

A. Alegre^{1,2}, S. Oliveira², P. Mendes¹, J. Proença³ & R. Ramos^{2,3}

¹ Instituto Superior de Engenharia de Lisboa (ISEL-IPL), Lisbon, Portugal, andrefalegre92@gmail.com

² Concrete Dams Department - National Laboratory for Civil Engineering (LNCEC), Lisbon, Portugal

³ CERIS – Instituto Superior Técnico, Lisbon, Portugal

Abstract: This paper presents a complete study on the seismic behaviour of an ultra-high arch dam, with a focus on non-linear seismic response analysis and seismic safety assessment. The calculations are performed using the finite element program DamDySSA, developed for linear and non-linear dynamics analysis of dam-reservoir-foundation systems. The case study is a 300 m-high double curvature arch dam, using a finite element mesh that incorporates the vertical contraction joints. The structural model includes a constitutive joint model, to simulate opening/closing and sliding movements between blocks, and an isotropic constitutive damage model with softening and two independent damage variables, to simulate tensile and compressive damage. Initially, the paper provides a comparison between linear and non-linear seismic response results for a seismic input with a peak ground acceleration of 0.6g, assessing the influence of joint movements on the structural response (analysis of displacements and stresses). Overall, the opening of the vertical joints originates a release of arch tensile stresses along the top of the dam, which in turn causes an increase of the vertical stresses, resulting in concrete tensile damage, while compressive damage is not significant. Then, a method based on Endurance Time Analysis (ETA) is used to conduct the seismic safety assessment of the dam for the Operating Basis Earthquake (OBE) and the Safety Evaluation Earthquake (SEE). This method resorts to a procedure for controlling the evolution of both tensile and compressive damage under accelerations of increasing intensity (in this case, up to 1.5g in 15 s). The results emphasize the good seismic performance of the dam, which can withstand considerable seismic excitation with acceptable damage levels.

1. Introduction

Large arch dams are structures of high potential risk, making it essential to ensure their structural safety in normal operating conditions and during/after exceptional events, such as earthquakes. This is particularly important since there are many major dams (some of which ultra-high dams, over 250 m) in operation or under construction in seismic zones (IJHD, 2023), and it is recognized that strong earthquakes can cause unacceptable joint openings and significant damages that may require service interruption or even compromise structural integrity, among other incidents (Wieland, 2010). Therefore, it is fundamental to conduct reliable behavior prediction studies, not only for seismic design and performance assessment of new dams (Wang, 2016) but also for safety reassessment of older dams (Darbre et al., 2019), possibly to propose seismic strengthening measures. To achieve this goal, dam engineers should adopt suitable and efficient methods of analysis, considering modern performance criteria, and use advanced computational models that allow the simulation of non-linear structural behavior (ICOLD, 2016).

The numerical modelling of the seismic response of arch dams continues to be a relevant and challenging topic in dam engineering, especially considering the singular design of arch dams, which are usually thin curved structures, with reduced thickness at the top and vertical joints between adjacent blocks, as well as the structural effects that may occur under seismic loads. For example, under low intensity earthquakes, vibrations of reduced amplitude are expected and hence the numerical simulations can be performed based on linear models, assuming linear-elastic concrete behaviour and that joints in the dam body remain closed (Proulx et al., 2004; Alegre et al. 2019). However, under strong earthquakes the movements of the dam may result in opening/closing joint movements (Fenves et al. 1992; Niwa and Clough, 1982), and, simultaneously, in high stresses that cause tensile cracking and/or compressive crushing of concrete (Cervera et al., 1995; Valliappan et al., 1999). Thus, for non-linear seismic analysis, appropriate constitutive models should be used to simulate both the structural effects due to joint movements and the concrete damage under tension and compression (Chopra, 2012; Chen, 2014).

In this context, the paper will focus on the use of advanced finite element models for non-linear seismic analysis and seismic safety assessment of arch dams. The numerical simulations are conducted using the finite element program *DamDySSA* (section 2), and the case study is a computational model of a 300 m-high double curvature arch dam (section 3). First, results from both linear and non-linear seismic analyses are compared in order to assess the influence of joint movements on the structural response under a strong earthquake, including the displacements and stresses in the dam body (section 4). After that, a method based on the Endurance Time Analysis (ETA) concept (Estekanchi et al., 2004) is used to conduct a seismic safety assessment study for the dam (section 5), considering the evolution of both tensile and compressive damage under seismic excitation of increasing intensity (with accelerations increasing up to 1.5g in 15 s).

2. Used software: *DamDySSA5.0*

DamDySSA is a 3D finite element program developed by the authors for dynamic analysis of concrete dam-reservoir-foundation systems. In the latest version of the program, the reservoir can be simulated (a) using pressure-based fluid finite elements, enabling to consider the dam-water dynamic interaction effects and the pressure waves' propagation in water (Zienkiewicz and Bettess, 1978), or (b) using the classic added water mass approach based on Westergaard's (1933) solution, considering an added mass correction factor (Chen, 2014). The foundation is computed as an elastic and massless substructure, with equivalent stiffness and damping at the dam-rock interface; therefore, the seismic input is applied directly at the dam base, assuming uniform ground motion. *DamDySSA* (Figure 1) is a complete program that allows users to carry out different types of dynamic calculations, including modal analysis and linear or non-linear seismic response analysis (Alegre, 2021). For seismic response simulation, a Newmark-based time-stepping method is applied to solve the dynamic equation of the dam-reservoir-foundation system in time domain, enabling to compute the structural response. To simulate non-linear behavior, the time-stepping algorithm is combined with a stress-transfer iterative method (Alegre et al., 2022), using (a) a joint constitutive model, based on the Mohr-Coulomb failure criterion and using normal and shear stress-displacement laws (Fenves et al. 92), to consider the effects due to opening/closing/sliding joint movements, and (b) a constitutive damage model with strain-softening and two independent damage variables (Oliveira and Faria, 2006), to reproduce the concrete behavior up to failure under both tension and under compression.

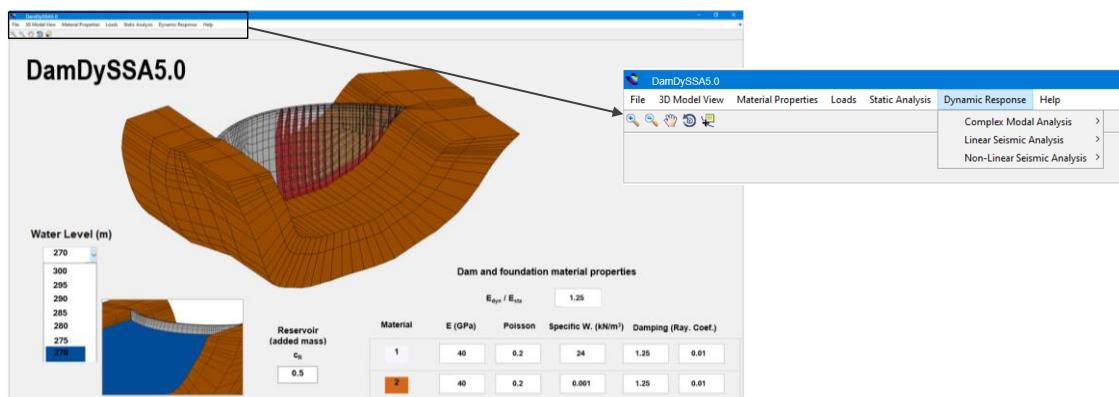


Figure 1. *DamDySSA5.0*: finite element program for dynamic analysis of dam-reservoir-foundation systems.

3. Case study: 300 m ultra-high arch dam

The case study of this work is a non-symmetric double curvature arch dam, with a maximum height of 300 m and a crest length of around 700 m. Figure 2 presents the finite element mesh of the dam-reservoir-foundation system and the main material properties of the model. The mesh includes 1047 elements in the dam body, with cantilevers comprised of 3 elements along the thickness, and 602 elements in the foundation, to represent the rock mass around the structure. Furthermore, a total of 813 interface elements were incorporated into the dam mesh, in order to represent the vertical contraction joints. The discretization of the system is achieved using hexahedral isoparametric elements with 20 nodes and 27 Gauss points, while the joint elements are compatible interface elements with 16 nodes and 9 Gauss points (in *DamDySSA*, numerical integration is carried out considering 2nd degree interpolation functions).

Regarding the material properties, the dam concrete and foundation rock are assumed as isotropic materials with Young's modulus $E = 25$ GPa and Poisson ratio $\nu = 0.2$. Since the foundation is computed as a massless and elastic substructure in *DamDySSA*, the rock mass effect is neglected for dynamic analyses. Moreover, an added water mass model based on Westergaard's hydrodynamic pressures distribution is used to simulate the reservoir, considering an added mass reduction factor (c_R) of 0.5, as recommended in the literature for dynamic analysis of arch dams (Chen, 2014).

For linear seismic response simulation, a dam model with closed joints and linear-elastic concrete behaviour is used. As for the non-linear structural model, the joint properties are normal and shear stiffness $K_N = 5 \times 10^7$ kN/m and $K_T = 2.5 \times 10^7$ kN/m, null cohesion $c = 0$, and friction angle $\phi = 30^\circ$; in addition, a concrete constitutive damage law with two independent damage variables (d^+ and d^- , for damage under tension and compression) is adopted for all dam elements, with tensile strength $f_t = 3$ MPa and compressive strength $f_c = -30$ MPa. In this work, damping ratios of 5% in the dam and 10% in the foundation are considered, for the frequency band around the fundamental frequency. Finally,

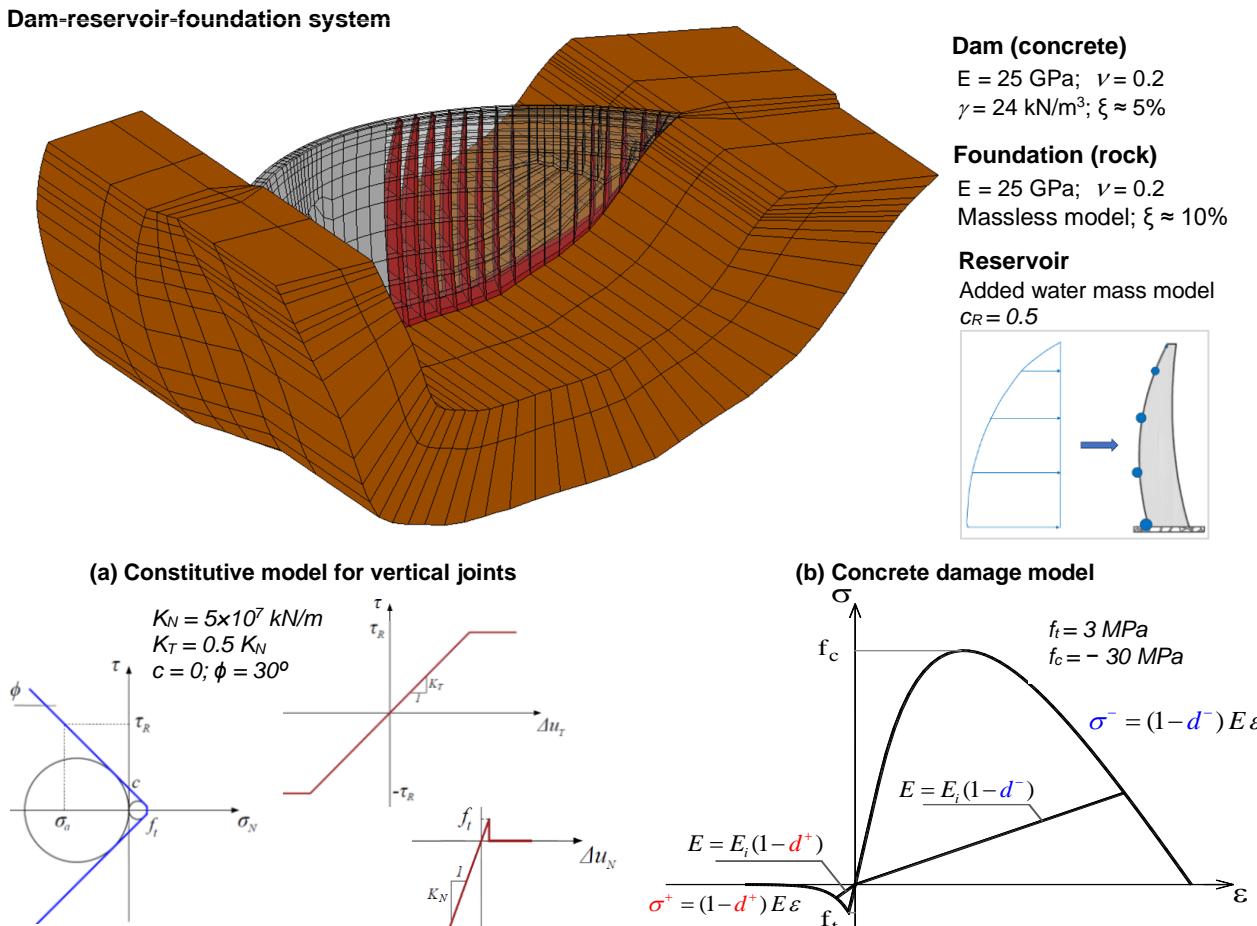


Figure 2. Arch dam model: finite element mesh and dam-reservoir-foundation system material properties. Non-linear models: (a) constitutive model for vertical joints and (b) constitutive damage model for concrete.

4. Seismic response analysis

This section presents an analysis of the seismic behavior of the 300 m ultra-high arch dam. The structural response predicted in a non-linear seismic simulation, using the model with joints and concrete damage, is compared with the response from a linear seismic analysis, using a simplified version of the model without joints and assuming linear-elastic material behavior. The aim is to study the effects of the vertical contraction joint opening/closing movements on the dam's seismic response and to evaluate the resulting damage.

The seismic analyses were carried out for a load combination (Figure 3) including (a) the dam's self-weight (W), the hydrostatic pressure for full reservoir (HP_{300}), and the seismic action ($S_{0.6g}$); in this case, the seismic input (uniform ground motion, applied at the dam base) is a generated 10 s acceleration time history with a peak acceleration of 0.6g.

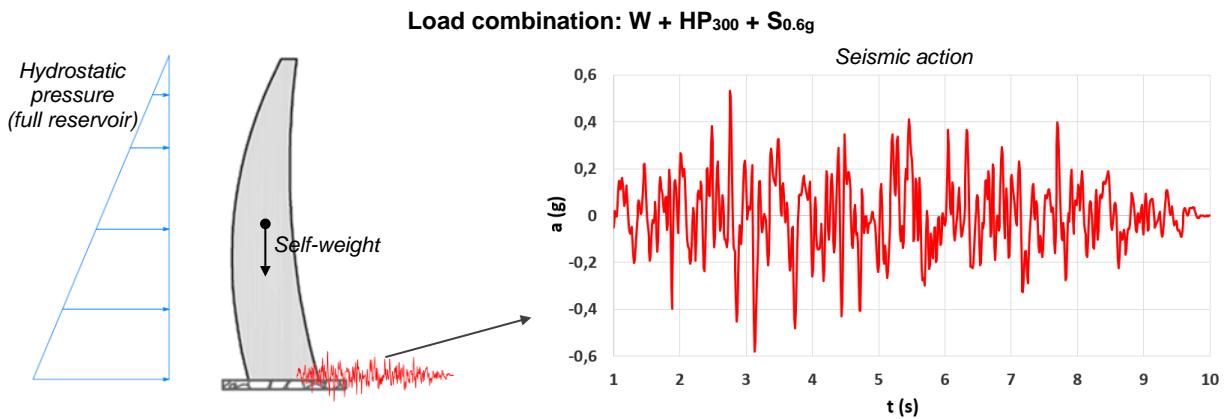


Figure 3. Load combination and seismic input used for seismic response analysis.

First, the comparative study between linear and non-linear seismic response focuses on the results of the deformed shapes and the corresponding stress fields (Figure 4). Specifically, these results are presented at two instants of interest for a more detailed analysis: the instants of maximum displacements in both the upstream and downstream directions.

Starting with the linear seismic response, the maximum upstream (≈ 210 mm) and downstream (≈ 479 mm) displacement values are calculated at the crest, in the central part of the dam; however, since the dam is not symmetrical, the maximum displacements do not occur exactly midway through the arch span. Regarding the stress fields computed at the captured instants, high arch tensions arise when the dam moves in the upstream direction, namely at the upper blocks of the upstream face of the central cantilevers (up to 9.5 MPa), and in the lateral zones of the downstream surface (around 7.9 MPa); the maximum tensions appear at the upstream base of the dam (12.1 MPa), in the normal direction to the insertion line, when the dam moves towards downstream. It is also worth highlighting the significant compressions that arise (with values close to the concrete compressive strength), particularly at the top of the upstream surface (-22.3 MPa), in the arch direction, and along the downstream base (maximum of -23 MPa), oriented normally to the insertion.

As for the non-linear seismic response, the results show that when the seismic forces push the dam towards upstream then the vertical contraction joints open – in the figure it is possible to see the relative movements between the lateral surfaces of the cantilevers. On the other hand, when the dam moves towards downstream, it becomes mainly under compressions, resulting in the closing of the vertical joints. Overall, due to the global non-linear behavior, there is an increase the maximum upstream (263 mm) and downstream displacements (547 mm), which occur in the same zone at the crest. In what concerns the non-linear stress fields, the opening of the vertical contraction joints caused a release of the arch tensions at the top of the dam. However, the subsequent stress redistribution process led to the appearance and gradual increase of vertical stresses along the height of the cantilevers; in the provided 3D figures the maximum tensions never exceed the concrete tensile strength (3 MPa), since stresses above this value end up being released either due to the joint movements or due to the occurrence of concrete damage (as will be shown below). Furthermore, there is an overall increase in the compressions when the dam moves towards upstream, specifically near the downstream base and along the upstream face of the cantilevers, as well as on the upper central blocks when the dam moves towards downstream.

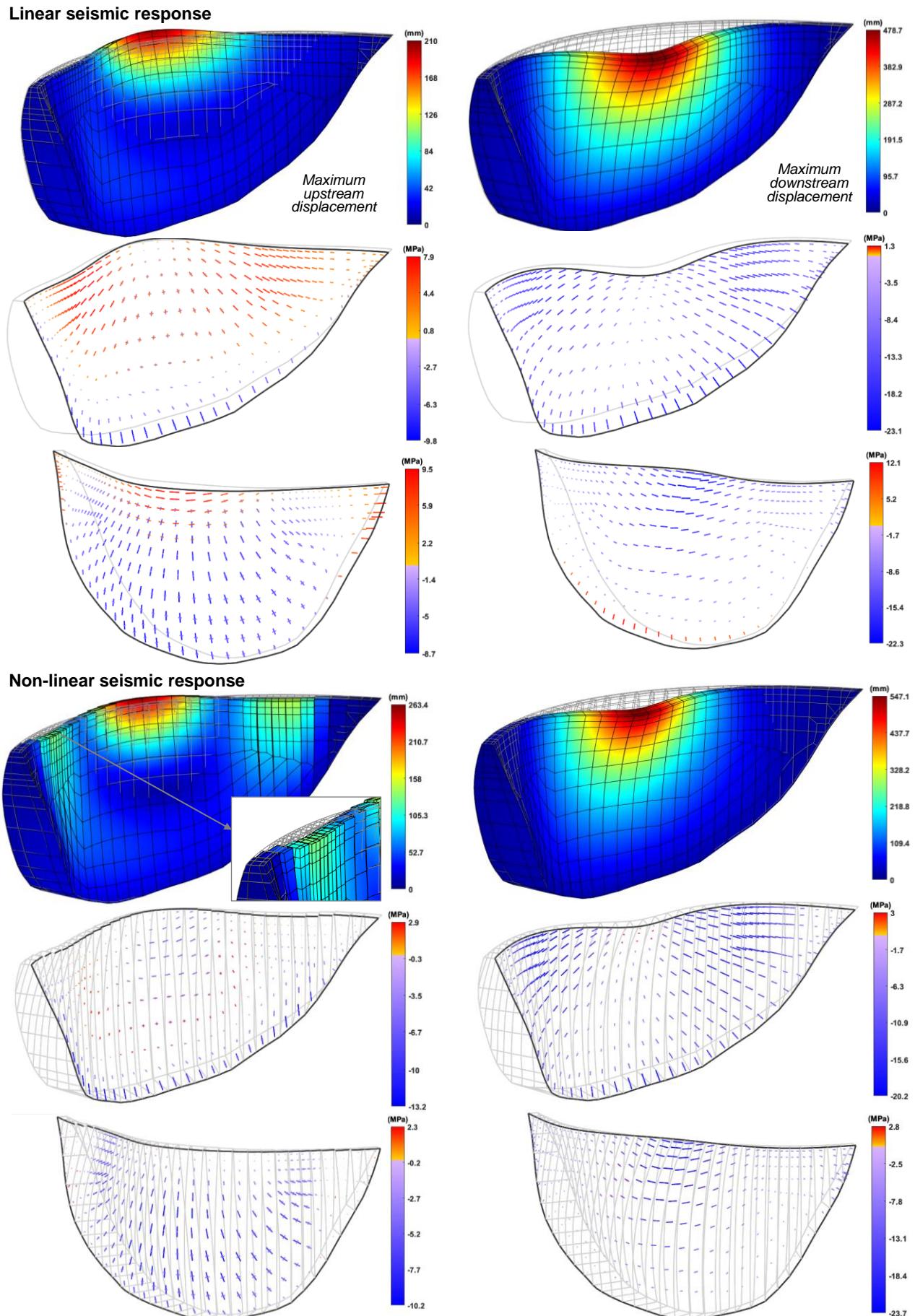


Figure 4. Linear and non-linear seismic response ($W+HP_{300}+S_{0.6g}$). Deformed shapes and stress fields.

Next are the arch and cantilever stresses envelopes, representing the global maximum and minimum stress values, computed both on the upstream and downstream surfaces of the dam; the envelopes obtained in the linear seismic analysis are presented in Figure 5 and those calculated in the non-linear seismic simulation are shown in Figure 6. Finally, the tensile and compressive damages computed in the non-linear seismic simulation are presented in Figure 7. The goal is to provide a global perspective of the dam's non-linear seismic behavior.

The stress envelopes calculated assuming linear elastic-behavior show that important arch tensions arise at the upper central blocks and close to the abutments (≈ 10 MPa), on the upstream face of the dam, as well as in the lateral upper part of the downstream surface; the global maximum tensions (15.3 MPa) are calculated in the cantilever direction at the upstream base of the dam. Furthermore, considerable compressions (≈ -27 MPa) occur at the central upper part of the upstream face, in the arch direction, and along the insertion at the downstream base, in the cantilever direction; high arch compressions also arise in the lateral zones of the downstream surface, along the upper half of the cantilevers (≈ -20 MPa).

Linear seismic response: stress envelopes

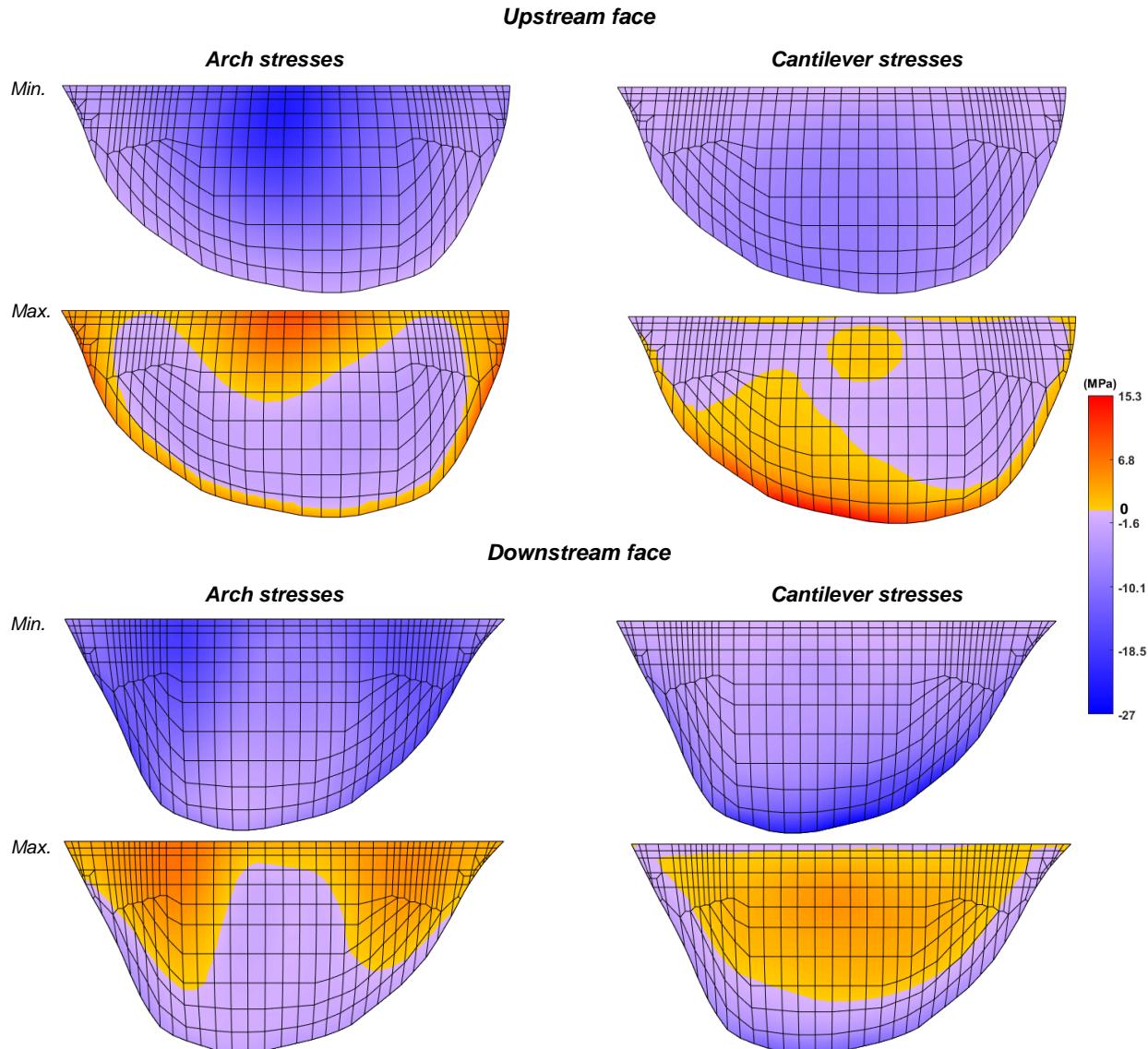


Figure 5. Linear seismic response ($W+HP_{300}+S_{0.6g}$). Arch and cantilever stress envelopes.

As for the stress envelopes computed in the non-linear seismic simulation, the results show once again the overall release of the arch tensions due to the opening of the vertical contraction joints, namely in the central upper part of the upstream surface and along the lateral upper half of the downstream face of the dam. However, the arch tensions close to the abutments and the cantilever tensions at the downstream base cause

concrete tensile failure ($d^+ = 100\%$). Furthermore, as mentioned previously, the release of arch stresses leads to a stress redistribution process that causes an overall increase of the cantilever stresses, particularly along the upper half of the downstream surface of the dam and, in a less severe way, in the central upper part of the upstream face; as a result, concrete tensile failure occurs in these areas. Finally, the results show that the maximum arch compressions ($\approx -29 \text{ MPa}$), arising in the upper part of the upstream wall, cause compressive damage (d') around 30%, and that the maximum cantilever compressions ($\approx -27 \text{ MPa}$) along the insertion cause very low damage values, thus showing the resistant capacity of such a high arch dam.

Non-linear seismic response: stress envelopes

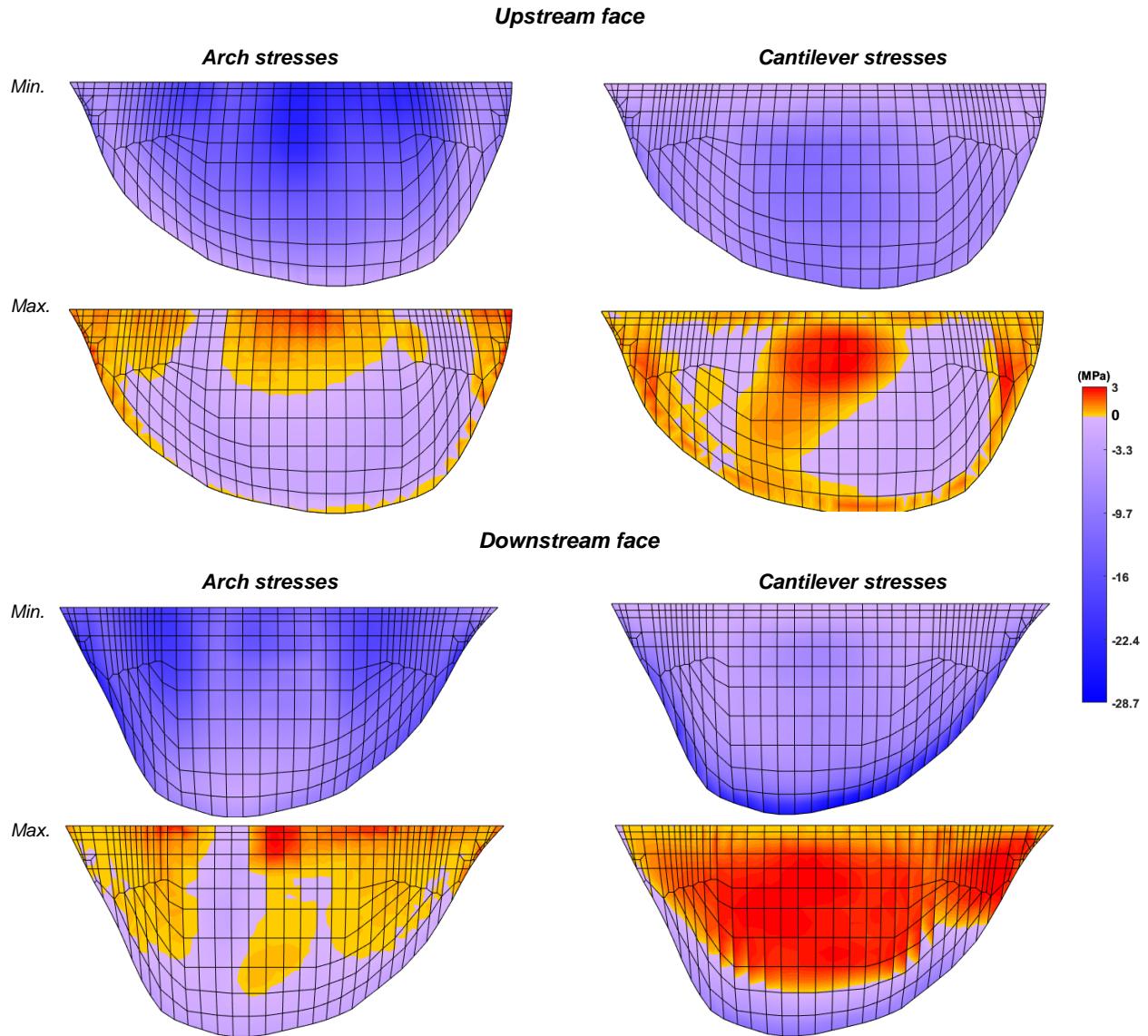


Figure 6. Non-linear seismic response ($W+HP_{300}+S_{0.6g}$). Arch and cantilever stress envelopes.

5. ETA-based seismic safety assessment

This section presents the study conducted for seismic safety assessment of the 300 m ultra-high arch dam, using an efficient ETA-based method proposed by the authors (Alegre et al. 2022). Essentially, with this method the seismic performance of a dam is evaluated by controlling the evolution of the tensile and compressive damage states under seismic excitation of increasing intensity. The goal is to determine two endurance limits, one associated with tensile damage (a_{d^+}) and another with compressive damage ($a_{d'}$), which give the maximum accelerations that the dam can withstand without presenting unacceptable damage levels. Specific performance criteria are considered in order to meet the requirements defined for large concrete dams

Non-linear seismic response: concrete damage

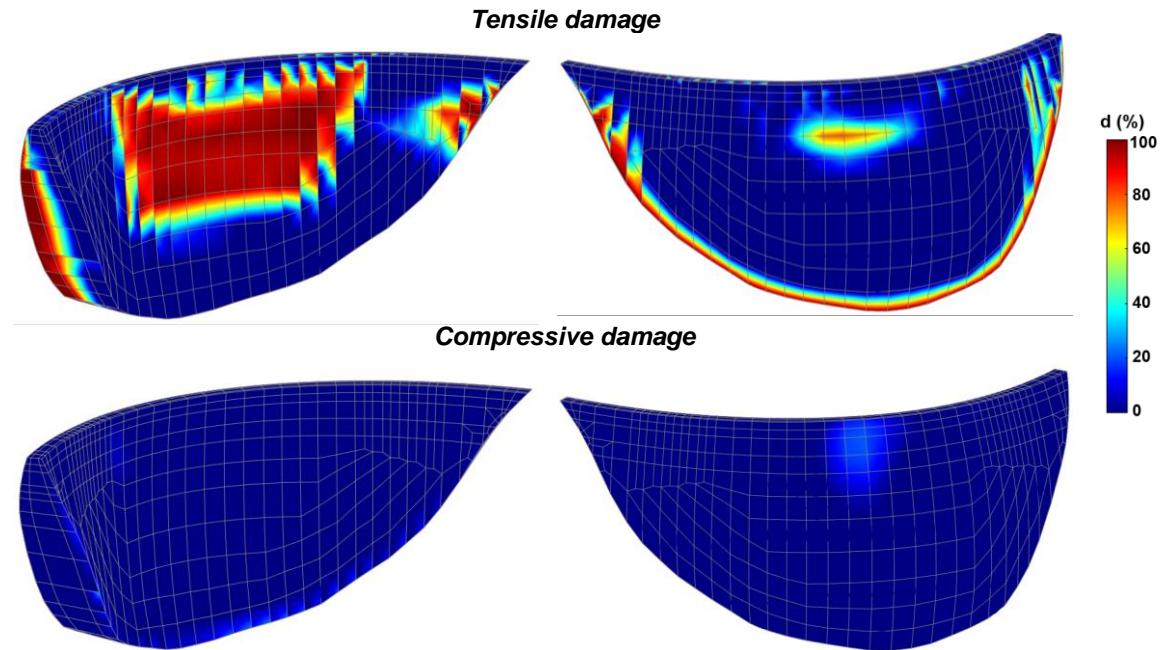


Figure 7. Non-linear seismic response ($W+HP_{300}+S_{0.6g}$). Tensile and compressive damage.

under both the Operating Basis Earthquake (OBE) and the Safety Evaluation Earthquake (SEE) in the current seismic design and safety guidelines (ICOLD, 2016; Wieland 2016): (i) under the OBE, an unacceptable damage state would be that involving the occurrence of concrete cracking in significant areas of the dam surfaces, particularly with cracking propagation across the thickness of the blocks, as this scenario could affect the structural integrity and require repair interventions; (ii) under SEE excitation levels, it is considered unacceptable the occurrence of concrete crushing caused by compressions in key areas, e.g., in the upper blocks of the main cantilevers, as this damage state could ultimately result in collapse and hence in the uncontrolled release of water from the reservoir.

The seismic safety assessment study was conducted for a dynamic load combination (Figure 8) including the self-weight of the dam (W), the hydrostatic pressure for full reservoir (HP_{300}), and a seismic action given by an acceleration time history designed for ETA (S_{ETA}), with accelerations increasing to about 1.5 g in 15 s.

The results obtained in the non-linear simulations under the intensifying seismic accelerations are presented next, with focus on the evolution of both tensile damage (Figure 9) and compressive damage (Figure 10). The aim is to enable an overall assessment of the seismic performance of the 300 m-high arch dam and thus estimate the endurance limits according to the adopted performance criteria.

Load combination: $W + HP_{300} + S_{ETA}$

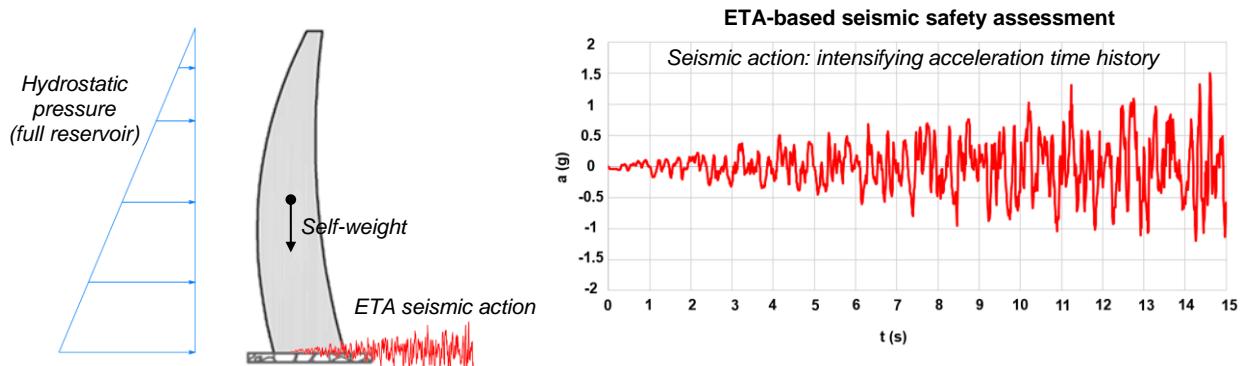


Figure 8. Load combination for seismic safety assessment. Seismic input used for the ETA-based method.

In what concerns the tensile damage evolution, the results show that the first areas exhibiting concrete failure ($d = 100\%$) appear, as expected, along the upstream base of the dam, due to the high cantilever tensions that arise along the insertion. Afterwards, until $t = 6$ s, there is a gradual progression of damage as cantilever tensions also increase due to the non-linear stress redistribution process, eventually causing concrete failure, initially in the blocks along the upper part of the downstream surface of the dam, and subsequently in several blocks at the central upper part of the upstream face. Even so, up to this point the concrete failure is mostly superficial and hence this damage state is considered acceptable. However, under higher excitation levels, around 0.7g, concrete cracking has already started to propagate from upstream to downstream in some of the blocks; this is a scenario that could affect the structural integrity of the dam and thus require the interruption of normal operating conditions for repairs, hence failing to meet the performance criterion defined in the proposed method for the OBE excitation level. Therefore, the endurance limit associated with tensile damage corresponds to an acceleration of around 0.6g.

With respect to the compressive damage results, it should be emphasized that there is no significant damage until $t = 8$ s; only under excitation levels around 0.9g the dam starts evidencing damage values of about 50% at the downstream base, caused by cantilever compressions, and in the central and lateral upper parts of the upstream and downstream surfaces, with damage values between 20 and 40%, due to arch compressions. Afterwards, there is a gradual increase in the compressive stresses and thus in the damage occurring in the mentioned zones. Nevertheless, even for the maximum excitation level considered in this study (1.5g), the higher compressive damage values do not exceed 70-75%, in the upper lateral zones of the upstream face, and near the abutments, on the downstream base. This means that the compressive damage computed during the performed seismic safety assessment study is acceptable. Thus, further studies considering ETA accelerograms with higher excitation levels will be required in the future, with the purpose of determining the endurance limit associated with compressive damage for this dam.

In summary, the conducted seismic safety assessment demonstrated the impressive resistant capacity of the 300 m-high arch dam under strong seismic loads. In particular, the compressive damage evolution showed that the dam under analysis can withstand considerable seismic forces without being subject to excessive compressions (which, as mentioned before, can be a determining factor for structural safety). Finally, the achieved results evidenced that, when designed properly, ultra-high arch dams can present a very good seismic performance.

6. Conclusions

This paper presented important numerical results on the non-linear seismic behavior of a 300 m ultra-high arch dam. These results were obtained using the team's own finite element program (*DamDySSA5.0*), which includes modules for linear and non-linear dynamic analysis of dam-reservoir-foundation foundation systems. In this program the non-linear simulations are performed using a dam structural model that includes (a) a joint constitutive model to simulate the opening/closing and sliding joint movements, and (b) a strain-softening constitutive damage model to simulate the concrete behavior up to failure both under tension and compression.

First, the comparison was made between the response calculated using linear and non-linear dam models, enabling to assess the structural effects due to both joint and material non-linear behavior. Essentially, the opening of the vertical contraction joints caused a release of arch tensions along the upper blocks of the dam, and the subsequent stress redistribution process originated an overall increase of cantilever stresses along the height of the dam's cantilevers, resulting in concrete tensile damage in the expected locations.

After that, an efficient ETA-based method was used to perform a seismic safety assessment of the dam. The seismic performance was evaluated by controlling the evolution of both tensile and compressive damage under accelerations of increasing intensity up to 1.5g. The determined endurance limit for tensile damage (0.6g) showed that the dam can withstand considerable seismic excitation levels without presenting unacceptable damage levels, emphasizing the good seismic performance of this ultra-high arch dam. In addition, the fact that the dam did not present an unacceptable compressive damage state during the entire simulation was particularly relevant, since the occurrence of compressive crushing in key areas of the dam may ultimately result in collapse and hence in the uncontrolled release of water from the reservoir. In the future it may be interesting to conduct a sensitivity analysis on the values adopted for the material parameters and the constitutive laws employed, in order to evaluate their influence on the seismic endurance limits.

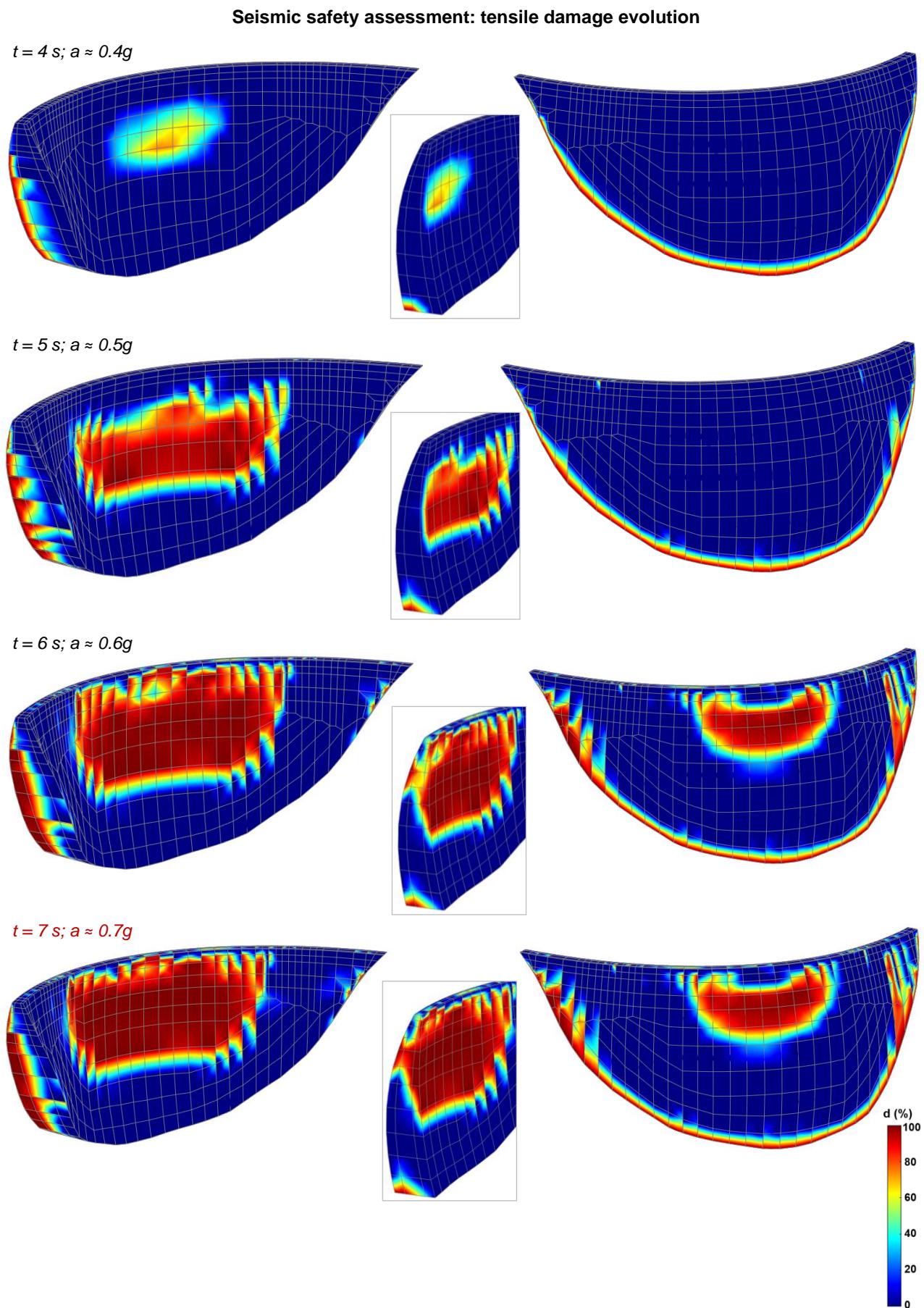


Figure 9. Seismic safety assessment results: evolution of tensile damage.

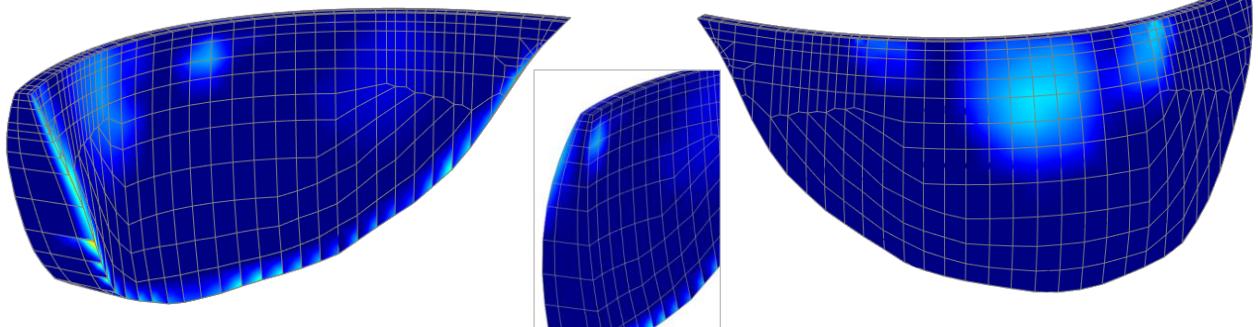
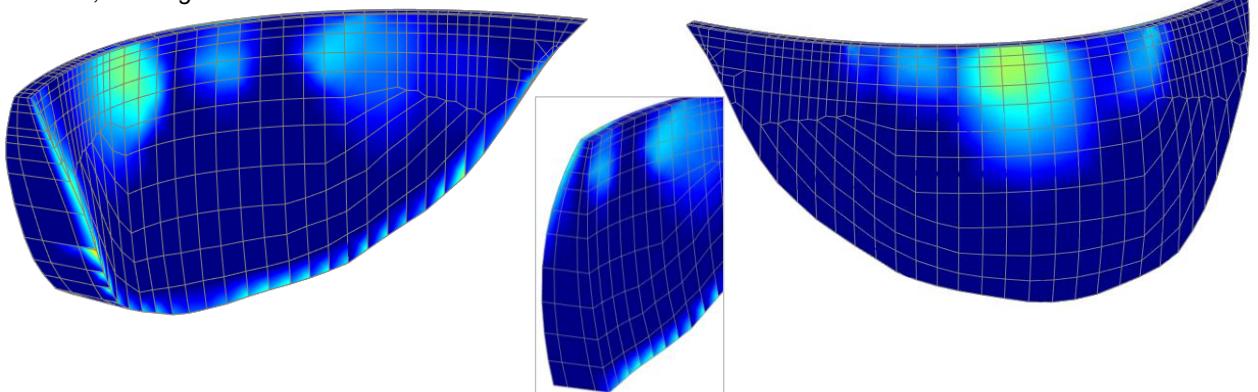
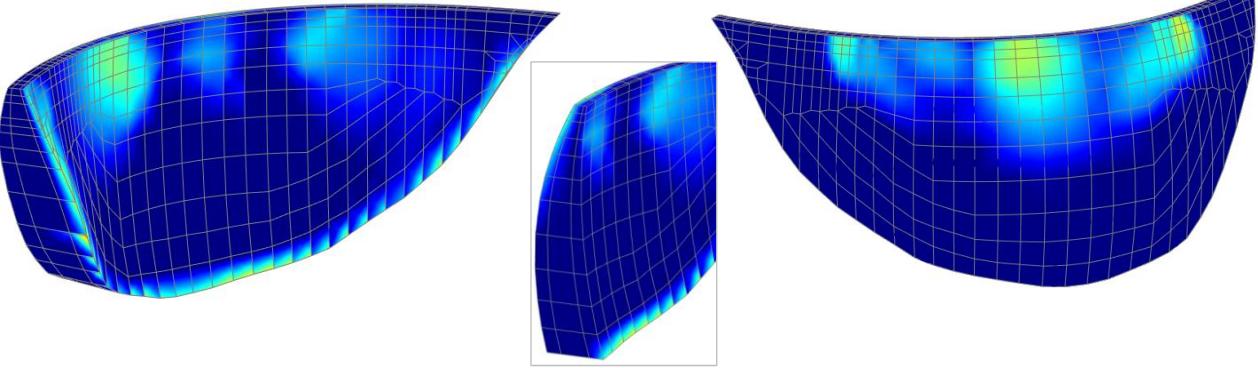
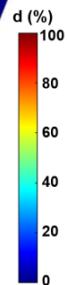
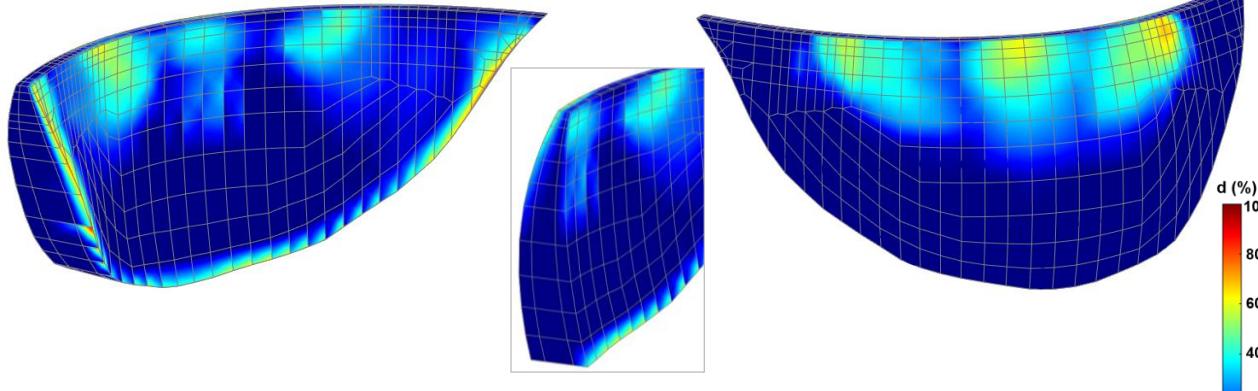
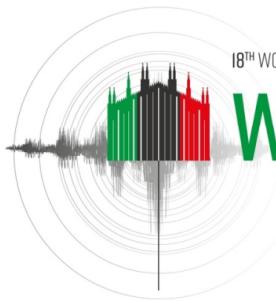
Seismic safety assessment: compressive damage evolution $t = 9 \text{ s}; a \approx 0.9g$  $t = 11 \text{ s}; a \approx 1.1g$  $t = 13 \text{ s}; a \approx 1.3g$  $t = 15 \text{ s}; a \approx 1.5g$ 

Figure 10. Seismic safety assessment results: evolution of compressive damage.

Finally, this work showed the potential of the finite element program *DamDySSA* to properly simulate the seismic response of arch dams, considering either linear or non-linear structural behavior, in a relatively efficient way (the calculations for both studies presented in this paper were completed in about a work week). Therefore, this program can be a very useful tool to perform seismic behavior prediction studies, enabling to support the seismic design of new dams or the seismic safety reassessment of older dams.

7. References

- Alegre, A. (2021). *Modelling and monitoring the dynamic behaviour of concrete dams. Modal analysis and seismic response*, PhD Thesis, Instituto Superior Técnico, University of Lisbon, Portugal.
- Alegre A., Oliveira S., Mendes P., Proença J., Ramos R., Carvalho E. (2022). Seismic Safety Assessment of Arch Dams Using an ETA-Based Method with Control of Tensile and Compressive Damage, *Water*, 14(23): 3835.
- Alegre, A., Oliveira, S., Mendes, P., Proença, J., Carvalho, E., Matsinhe, B. (2022). Numerical models for seismic analysis of arch dams, *Congreso de Métodos Numéricos en Ingeniería*, Las Palmas de Gran Canaria, Spain.
- Cervera M., Oliver J., Faria R. (1995). Seismic Evaluation of Concrete Dams via Continuum Damage Models, *Earthquake Engineering and Structural Dynamics*, 24: 1225-1245.
- Chen H. (2014). Seismic safety of high concrete dams, *Earthquake Engineering and Engineering Vibration*, 13(1): 1–16.
- Chopra A.K. (2012). Earthquake Analysis of Arch Dams: Factors to Be Considered, *Journal of Structural Engineering*, 138(2): 205-214.
- Dabre G.R., Schwager M.V., Panduri R. (2019). Seismic Safety Evaluation of Large Dams in Switzerland: Lessons Learned, *International Water Power & Dam Construction*, 70(5): 22-27.
- Estekanchi H.E., Vafai H., Sadeghazar M. (2004). Endurance Time Method for Seismic Analysis and Design of Structures, *Scientia Iranica*, 11: 361–370.
- Fenes G.L., Mojtabaei S., Reimer R.B. (1992). Effect of Contraction Joints on Earthquake Response of an Arch Dam, *Journal of Structural Engineering*, 118: 1039-1055.
- ICOLD (2016). *Bulletin 148: Selecting Seismic Parameters for Large Dams - Guidelines (revision of Bulletin 72)*, Committee on Seismic Aspects of Dam Design, International Commission on Large Dams, Paris.
- IJHD (2022). *World Atlas & Industry Guide*, International Journal of Hydropower and Dams, Aqua Media Int.
- Niwa A., Clough R.W. (1982). Non-Linear Seismic Response of Arch Dams, *Earthquake Engineering and Structural Dynamics*, 10: 267-281.
- Oliveira S., Faria, R. (2006). Numerical Simulation of Collapse Scenarios in Reduced Scale Tests of Arch Dams, *Engineering Structures*, 28: 1430–1439.
- Proulx J., Dabre G. R., Kamileris, N. (2004). Analytical and experimental investigation of damping in arch dams based on recorded earthquakes. *13th World Conference on Earthquake Engineering*, Vancouver, Canada.
- Valliappan S., Yazdchi M., Khalili N. (1999). Seismic Analysis of Arch Dams - a Continuum Damage Mechanics Approach, *International Journal of Numerical Methods*, 45: 1695-1724.
- Wang R. (2016). Key Technologies in the Design and Construction of 300 M Ultra-High Arch Dams. *Engineering*, 2: 350–359.
- Westergaard H. M. (1933). Water pressures on dams during earthquakes, *Transactions (ASCE)*, 98: 418–472.
- Wieland M. (2016). Safety Aspects of Sustainable Storage Dams and Earthquake Safety of Existing Dams, *Engineering*, 2: 325–331.
- Zienkiewicz O. C., Bettess P. (1978). Fluid-structure dynamic interaction and wave forces. An introduction to numerical treatment, *International Journal on Numerical Methods in Engineering*, 13: 1–16.



INFLUENCE OF NONLINEARITY OF DYNAMIC SHEAR MODULUS ON THE SEISMIC SAFETY EVALUATION OF ARCH DAMS

Y. Ariga¹

¹ Hirosaki University, aomori city, japan, y-a-arig@hirosaki-u.ac.jp

Abstract: When evaluating the safety of dams against strong earthquake motions, consideration of nonlinearity of dynamic deformation property of dam material becomes an important issue. Therefore, we investigated the influence of dynamic shear modulus of dam body on the seismic tensile stresses by executing three-dimensional dynamic analysis for arch dam. As a result, the seismic tensile stresses decreased in many parts of dam body as the dynamic shear modulus decreased, but increased in some parts of dam crest and foundation rock. The safety of arch dam is highly dependent on the soundness of foundation rock. Therefore, if the seismic tensile stresses increase around the foundation rock and the abutment as the dynamic shear modulus decreases, the seismic safety must be carefully verified.

1. Introduction

In regard to the dynamic deformation property of dam material, nonlinearity depending on the strain caused by earthquake motion, that is the strain dependence of dynamic deformation property, is known. And consideration of nonlinearity of dynamic deformation becomes an issue when evaluating the safety of dam against strong earthquake motion. However, there are few studies that have investigated how the strain dependence of dynamic deformation property affects the seismic tensile stresses caused by strong earthquake motion. So, we investigated the influence of decrease in dynamic shear modulus on the seismic tensile stresses by 3-D dynamic analysis. As for the strain dependence of dynamic shear modulus of dam body, we utilized the results of previous research for the reproduction analysis of actual earthquake behaviour of existing arch dam during the 2011 off the Pacific Coast of Tohoku Earthquake, Ariga (2022).

2. Background and purpose of study

In verifying the seismic performance of concrete dam, it is required to quantitatively evaluate that the tensile stress does not exceed the tensile strength, and that compressive failure, shear failure or tensile failure does not occur, MILIM (2005). In the seismic performance verification of arch dam, as stated in the Technical Criteria for River Works, MILT (2009), it is important to properly consider the behaviour of joints due to the structure of arch dam, and it is necessary to confirm the safety of dam regarding the tensile failure, since the tensile failure is the most severe condition due to the material property and the response characteristics of dam, MILT (2009).

When verifying the seismic performance against strong earthquake motion, the issue is whether to consider nonlinearity or not. With regard to nonlinearity, it is necessary to distinguish between structural and material nonlinearity. The former is the nonlinearity associated with the discontinuous behaviour of opening and sliding at the joints and so forth. In this regard, the research cases such as the study based on the earthquake observation records, Ueda et al. (2000), the study based on the crack propagation analysis, Kimata et al.

(2013), etc. were reported. Thus far, we developed the three-dimensional dynamic analysis method for the coupled dam-joint-foundation-reservoir system, Ariga et al. (2004), and executed the three-dimensional dynamic analyses considering the discontinuous behaviour at the contraction joints and the peripheral joints placed in the arch dam, Ariga et al. (2003, 2004).

The latter is the nonlinearity of dynamic deformation property of dam body due to the response history caused by strong earthquake motion, which is so-called the strain dependence of dynamic deformation property of dam material. In regard to this, there are research cases such as the study based on laboratory tests using specimens, Hatano (1968), the study based on seismic observation data, Okuma et al. (2012), the study based on the reproduction analysis for the actual seismic behaviour of arch dam during the 1995 Hyogo-ken Nanbu Earthquake, Ariga et al. (2004), the study based on the reproduced analysis for the actual behaviour of dual arch dam during the 2011 off the Pacific coast of Tohoku Earthquake, Ariga et al (2014). Regarding the influence of the strain dependence of dynamic deformation on the seismic safety stress evaluation, there are research cases such as the study focusing on the changes in dynamic stiffness, Watanabe et al. (2002), the study focusing on the changes in damping constants, Hiramatsu et al. (2017), etc.

As described above, the mechanisms and phenomena of material nonlinearity and structural nonlinearity are different, and the analytical evaluation methods are also different. Taking these matters into account, in this study, we focused on the material nonlinearity and examined the influence of the strain dependence of dynamic shear modulus on the stresses generated in the arch dam caused by strong earthquake motion. The value of dynamic shear modulus of dam body has a direct effect on the displacement and deformation of the dam. However, it is still unclear how the value of dynamic shear modulus affects the stresses occurring in the dam. Therefore, in order to improve the accuracy and reliability of seismic performance evaluation of dams, a three-dimensional dynamic analysis was conducted to investigate how the decrease in the dynamic shear modulus affects the tensile stresses caused by strong earthquake motion.

3. 3-D dynamic analysis method

3.1. Overview

In order to examine the influence of nonlinearity of dynamic shear modulus on the seismic safety evaluation, 3-D dynamic analysis was executed by setting a simplified arch dam with a height of 100 m as the analysis object. Regarding the dam shape, we executed a comparative analysis using two analysis models, and considered the influence of geometry and structure of dam.

3.2. 3-D FEM analysis model

As shown in Figure 1, two types of 3-D FEM model were set, or a single dam model and a dual dam model. In order to examine the influence of nonlinearity of dynamic shear modulus on the seismic safety evaluation, 3-D dynamic analysis was executed by setting a simplified arch dam with a height of 100 m as the analysis object. Regarding the dam shape, we executed a comparative analysis using two analysis models, and considered the influence of geometry and structure of dam.

The dimensions of the single dam were 100 m in height, 310 m in crest length, and 166 m in base length, and the dam shape was set asymmetrically. A dual dam consists of a left dam and a right dam. The dimensions of the right dam are 100 m in height, 310 m in crest length, and 166 m in base length, and the left dam has 100 m in height, 246 m in crest length, and 100 m in base length. The thrust block was made of concrete, with a downstream crest width of 50 m and a bottom width of 143 m. The dimensions and shapes of the right dam of the dual dam and the single dam are the same.

The dam body and the foundation rock were modelled using solid elements. The lateral boundary of the analytical model is a viscous boundary, and the bottom boundary is a rigid base. The dam body was divided into five layers in the depth direction so that the stress within the dam body could be output. The dual dam model was set with reference to existing dams such as the Hongrin Dam (dam height: 123 m, total crest length: 600 m), the Okura Dam (dam height: 82 m, total crest length: 323 m). Regarding reservoir water, empty conditions were assumed because the tensile stress is more likely to occur when the reservoir is empty than full.

Seismic performance verification of arch dam is normally performed by the three-dimensional linear dynamic analysis, in which the dam body is treated as a linear elastic body. And, if the results of the linear analysis

indicate a risk of damage (especially tensile fracture), nonlinear dynamic analysis is to be performed as the next step. With these procedures in mind, and in order to simply study the effects of the reduction in dynamic shear modulus, the analysis here was performed as a linear dynamic analysis by the time history response analysis based on the direct integration method. The analysis program ISCEF (Integrated Software for Civil Engineering Fluid-structure interaction system), Century-techno (2023) was used.

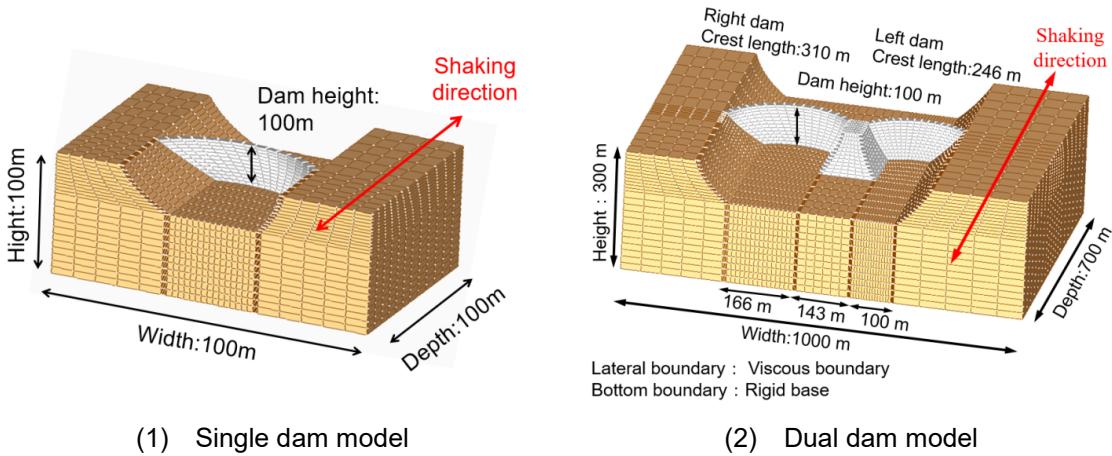


Figure 1. 3-D dynamic analysis model.

3.3. Dynamic property values for analysis

Table 1 shows the dynamic property values of the dam and the thrust block. Two cases were set for the values of dynamic shear modulus, assuming weak earthquake motion ($G_d/G_0 = 1.0$) and strong earthquake motion ($G_d/G_0 = 0.65$). The dynamic property values of the foundation rock are shown in Table 2. The nonlinear property, or the strain dependence, of the dam body was set as shown in Figure 2. The black square marks in Figure 2 are the results of laboratory tensile tests of dam concrete, Hatano (1968), and the three red circle marks are the results evaluated by the reproduction analysis of actual behaviour of existing dam during the 2011 off the Pacific coast of Tohoku Earthquake, Ariga (2022).

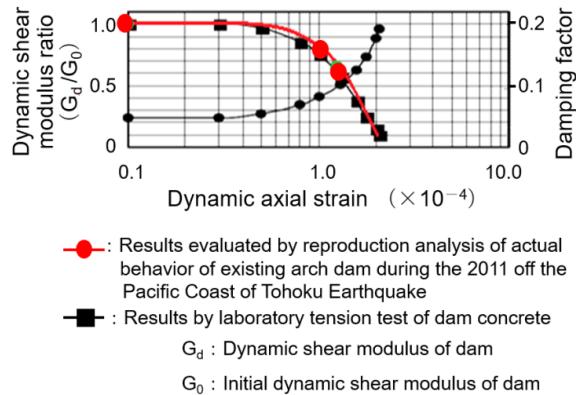


Figure 2. Nonlinear property of dynamic shear modulus and damping factor of dam concrete.

Table 1. Dynamic property values of dam and thrust block.

Case	G_d	Density	Poisson's ratio	Damping factor	G_d/G_0	Notes
Case-1	9250 N/mm ²	2.40 t/m ³	0.20	0.05	1.0	Weak motion
Case-2	6000 N/mm ²	2.40 t/m ³	0.20	0.05	0.65	Strong motion

(Note) G_d : Dynamic shear modulus, G_0 : Initial dynamic shear modulus , G_d/G_0 : Reduction rate

The damping constant was set to 0.05 based on the reproduction analyses of the behaviour of existing dams during the actual earthquakes, Ariga (2007).

Table 2. Dynamic property values of foundation rock.

Dynamic shear modulus	S-wave velocity	Density	Poisson's ratio	Damping factor
4500 N/mm ²	1315 m/s	2.60 t/m ³	0.25	0.05

3.4 Input earthquake motion

The earthquake motion shown in Figure 3, JSCE (2002), was used for the analysis, and input in the upstream-downstream direction from the bottom rigid base.

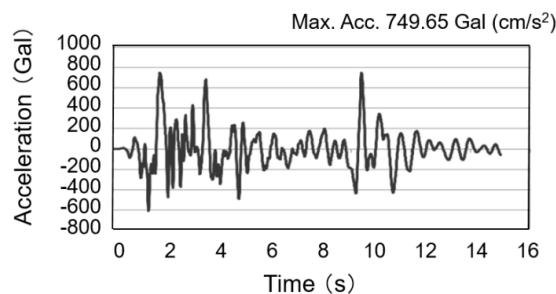
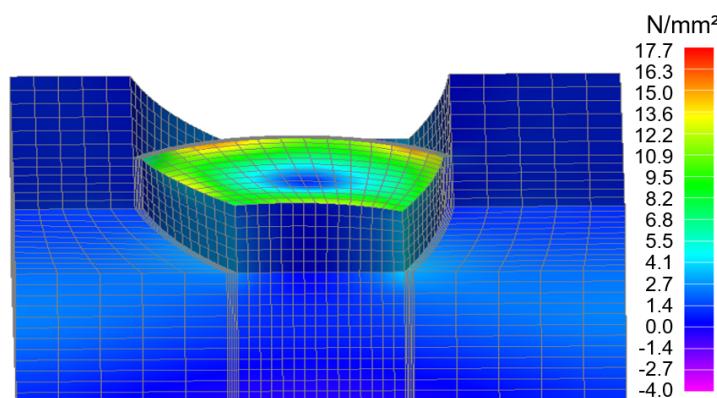


Figure 3. Input earthquake motion, JSCE (2002).

4. 3-D analysis results for seismic tensile stress

4.1. Analysis results in the case of single dam

Figure 4 shows the distribution of seismic tensile stress in the case of the single dam. Table 3 shows the maximum values of the seismic tensile stress at the representative output positions shown in Figure 5. The seismic tensile stress shown in Table 3 is not the stress added to normal tensile stress, but the tensile stress generated by earthquake motion. At position 5 (Dam crest of left abutment), the value of the seismic tensile stress was 13.21 N/mm² when $G_d = 9250$ N/mm², and decreased to 11.94 N/mm² when $G_d = 6000$ N/mm². At position 2 (Dam crest near right abutment), the value was 15.18 N/mm² when $G_d = 9250$ N/mm², but it slightly increased to 15.72 N/mm² when $G_d = 6000$ N/mm². Thus, as the dynamic shear modulus of dam body decreased, the seismic tensile stresses decreased at most positions, but increased at some positions.



(1) $G_d = 9250$ N/mm²

Figure 4 (1). Distribution of seismic tensile stress in the case of single dam.

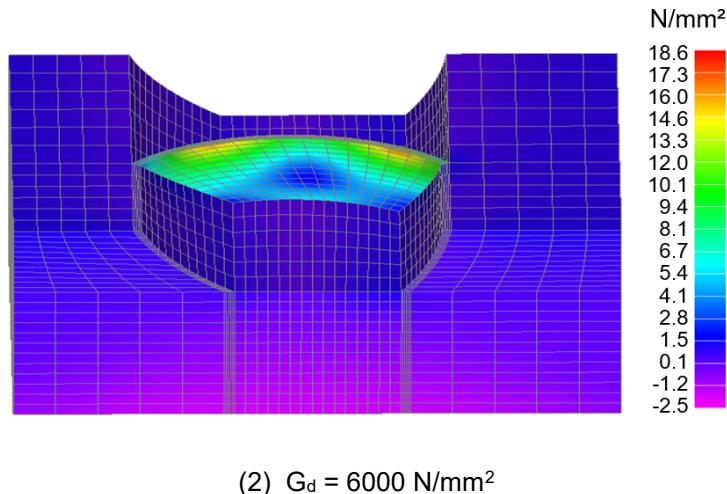


Figure 4 (2). Distribution of seismic tensile stress in the case of single dam.

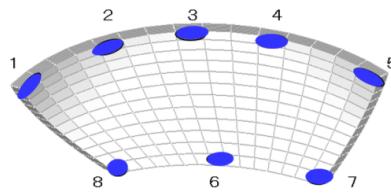


Figure 5. Representative output positions for single dam.

Table 3. Seismic tensile stress at representative positions for single dam.

(Unit : N/mm²)

Positions		$G_d : 9250 \text{ N/mm}^2$	$G_d : 6000 \text{ N/mm}^2$
Dam crest	1	Right abutment	7.10
	2	Near right abutment	15.18
	3	Centre	13.14
	4	Near left abutment	11.58
Dam base	5	Left abutment	13.21
	6	Centre	12.81
	7	Left abutment	10.47
	8	Right abutment	8.18

(Note) G_d : Dynamic shear modulus of dam.

4.2. Analysis results in the case of dual dam

Figure 6 shows the distribution of seismic tensile stress in the case of the dual dam. Table 4 shows the maximum values of the seismic tensile stress at the representative output positions shown in Figure 7. At position 5 (Dam crest of right dam, thrust block connection), the value was 29.75 N/mm² when $G_d = 9250 \text{ N/mm}^2$, and decreased to 19.27 N/mm² when $G_d = 6000 \text{ N/mm}^2$. At position 9 (Dam crest of left dam, thrust block connection), the value was 32.59 N/mm² when $G_d = 9250 \text{ N/mm}^2$, and decreased to 29.66 N/mm² when $G_d = 6000 \text{ N/mm}^2$. On the other hand, at position 10 (Dam crest of left dam, near right abutment), the value was 18.78 N/mm² when $G_d = 9250 \text{ N/mm}^2$, but increased to 23.97 N/mm² when $G_d = 6000 \text{ N/mm}^2$. At position 17 (Right dam, middle level, right abutment), the value increased from 10.53 N/mm² when $G_d = 9250 \text{ N/mm}^2$ to 11.42 N/mm² when $G_d = 6000 \text{ N/mm}^2$. Thus, as the dynamic shear modulus of dam body decreased, the seismic tensile stress decreased at many positions, but increased at some locations. It is thought that the increase or decrease in tensile stress occurred at positions where the seismic response changed due to the dynamic interaction between dam and foundation rock.

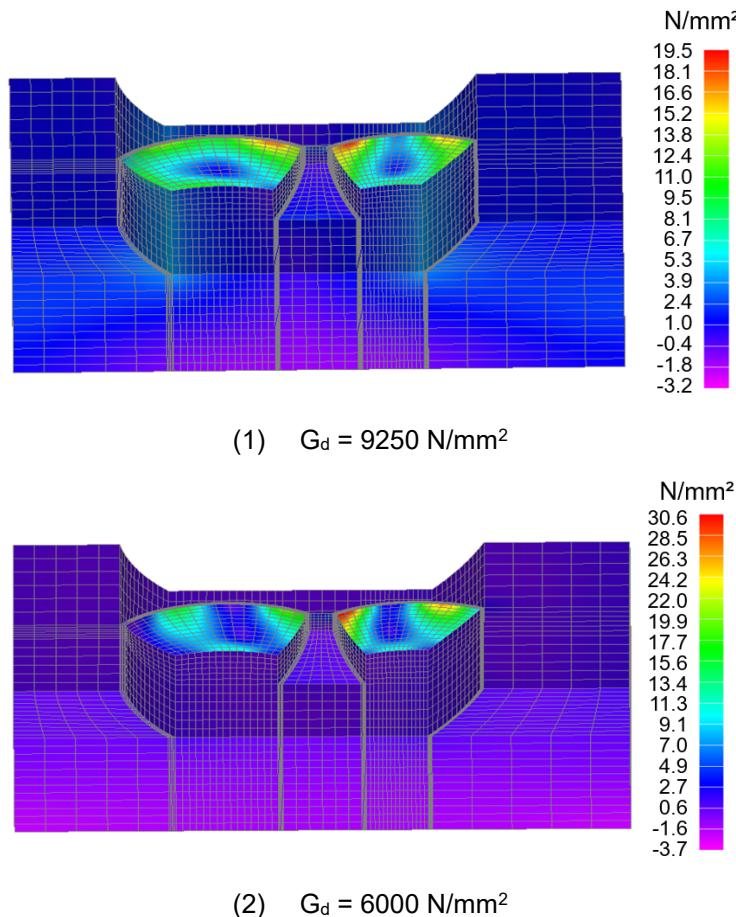


Figure 6. Distribution of seismic tensile stress in the case of dual dam.

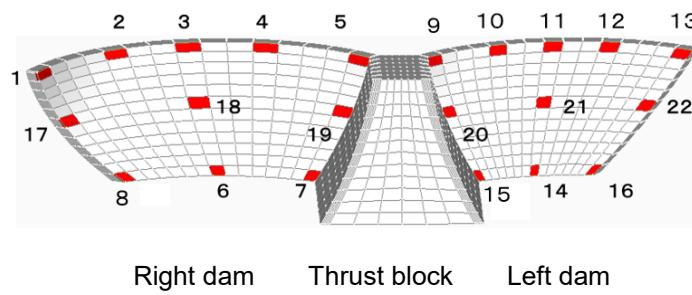


Figure 7. Representative output positions for dual dam.

4.3. Comparison of single dam and dual dam

4.3.1. Consideration on seismic safety evaluation method for dual dam

Figure 8 shows the distribution of seismic tensile stress in the case of the single dam and the dual dam. Table 5 shows the maximum values of seismic tensile stress at the representative positions shown in Figure 9. The dimensions and shape of the right dam of dual dam and the single dam are the same. However, from Figure 8 and Table 5, it is clear that the distribution of seismic tensile stress is different between the single dam and the dual dam, and their values are also different. At position 1 (Dam crest of right abutment), the value for the single dam was 5.96 N/mm², but 11.20 N/mm² for the dual dam. At position 2 (Dam crest of near right abutment), the value for the single dam was 15.72 N/mm², but 22.38 N/mm² for the dual dam.

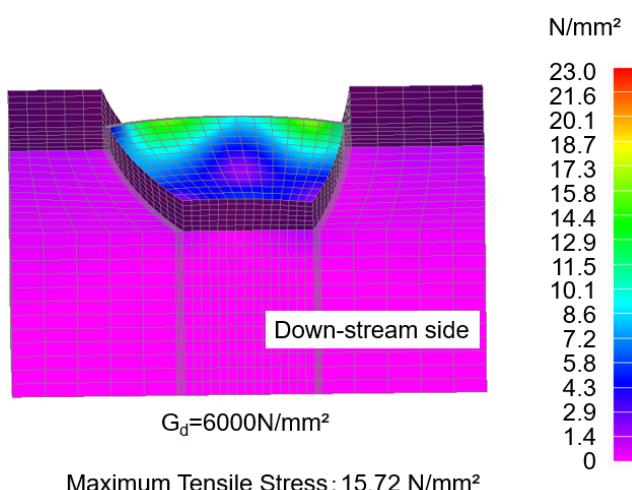
Table 4. Seismic tensile stress at representative positions for dual dam.

(Unit : N/mm²)

		Position	$G_d : 9250 \text{ N/mm}^2$	$G_d : 6000 \text{ N/mm}^2$
1 2 3 4 5 6	Right dam	Right abutment	11.35	11.20
		Near right abutment	24.79	22.38
		Centre	20.13	14.65
	Dam base	Near left abutment	13.68	13.32
		Thrust block connection	29.75	19.27
		Centre	15.46	12.80
7 8 9 10 11 12	Left dam	Thrust block connection	6.31	5.38
		Right abutment	8.85	7.59
		Thrust block connection	32.60	29.66
	Dam crest	Near right abutment	18.78	23.97
		Centre	7.23	7.07
		Near left abutment	32.07	26.62
13 14 15 16 17 18	Middle level	Let abutment	19.58	17.71
		Centre	14.61	11.42
		Thrust block connection	7.59	5.79
	Right dam	Left abutment	8.24	6.42
		Right abutment	10.53	11.42
		Centre	10.24	6.61
19 20 21 22	Left dam	Thrust block connection	22.48	13.68
		Thrust block connection	25.44	22.85
	Middle level	Centre	4.27	4.81
		Left abutment	21.16	19.98

(Note) G_d : Dynamic shear modulus of dam.

When evaluating the seismic safety for the single dam, since there is only one dam, the object of safety evaluation is uniquely determined. On the other hand, for the dual dam, two methods can be thought. One is the individual evaluation method to evaluate each dam individually by treating the left dam and the right dam as independent individual dams. The other is whole evaluation method by treating as one dam consist of the right and left dam. From the results of this analysis, it is thought that there is a risk of underestimating the seismic tensile stress by the individual evaluation method. Therefore, in the case of a multiple dam consisting of plural dams, the whole evaluation method is to be required.



(1) Single dam

Figure 8 (1). Comparison between single dam and dual dam.

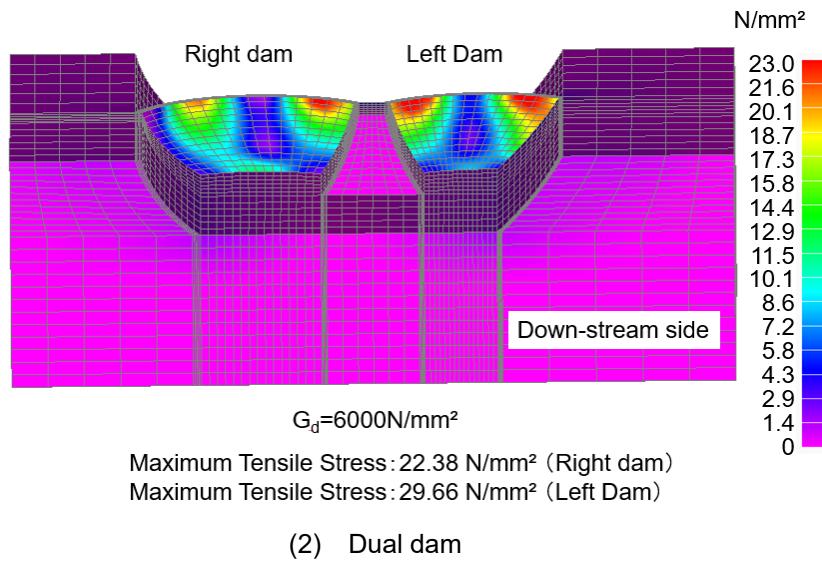


Figure 8 (2). Comparison between single dam and dual dam.

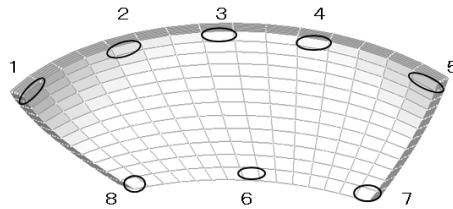


Figure 9. Representative positions at single dam and right dam of dual dam.

Table 5. Comparison of seismic tensile stress between single dam and dual dam.

(Unit : N/mm²)

	Position	Dynamic shear modulus of dam (G_d) : 6000 N/mm ²	
		Single dam	Right dam of dual dam
1	Dam crest	Right abutment	5.96
2		Near right abutment	15.72
3		Centre	10.40
4		Near left abutment	12.49
5	Dam base	Thrust block connection	11.94
6		Centre	12.72
7		Thrust block connection	8.23
8		Right abutment	6.96

4.3.2. Influence on the stability of foundation rock

Table 6 shows the maximum seismic tensile stresses at the foundation rock for the single dam and the dual dam. The representative positions are shown in Figure 10. Table 6 shows that the seismic tensile stresses at the foundation rock were generally larger in the dual dam than in the single dam, except for position 5. At

position 1 (Upper part of right bank), the value increased from 3.20 N/mm² for the single dam to 5.33 N/mm² for the dual dam.

The seismic tensile stresses in the foundation rock became larger in the dual dam than in the single dam. It can be thought that if the shape and structure of dam is complex, the dynamic interaction between dam and foundation rock becomes complex, and the tensile stresses in the foundation rock increase accordingly. From the viewpoint of seismic tensile stress in the foundation rock, the overall evaluation is needed for the dual dam. The seismic safety of arch dam is highly dependent on the soundness of the foundation rock. If tensile stresses increase in the foundation rock, the integrity of the foundation rock must be carefully evaluated.

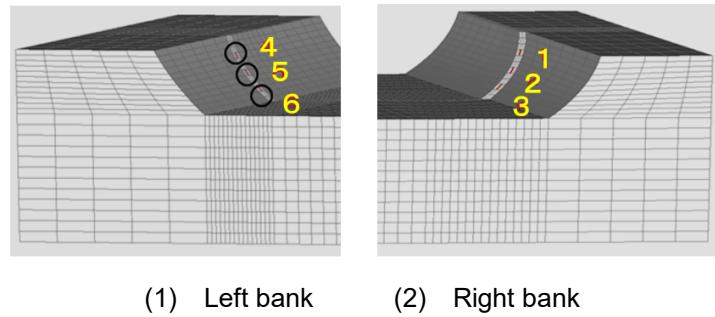


Figure 10. Representative positions at foundation rock.

Table 6. Comparison of seismic tensile stress at foundation rock between single dam and dual dam.

Position	Dynamic shear modulus of dam (G_d) : 6000 N/mm ²		
	Single dam	Right dam of dual dam	
1 Foundation rock	Upper	3.20	5.33
2 Right bank	Middle	3.77	5.20
3	Lower	3.58	4.59
4 Foundation rock	Upper	3.53	4.39
5 Left bank	Middle	4.04	3.53
6	Lower	4.23	3.60

(Unit : N/mm²)

5. Conclusion

In our previous study, we conducted a reproduction analysis of the actual seismic behaviour of an existing arch dam during the 2011 off the Pacific Coast of Tohoku Earthquake, and evaluated the strain dependence of dynamic shear modulus. Utilizing the results of that study, the effect of reduced dynamic shear modulus on seismic tensile stresses in the dam body and foundation rock mass was investigated by three-dimensional dynamic analysis.

The seismic tensile stresses in the dam body decreased in many locations as the dynamic shear modulus decreased. However, the seismic tensile stresses increased at some parts of the dam crest and the foundation rock as the dynamic shear modulus decreased.

Since the seismic safety of an arch dam is highly dependent on the soundness of the foundation rock, careful safety verification is necessary when tensile stresses increase in the foundation rock and the abutments.

A multiple arch dam is a dam consisting of two or more arch dams connected together. With regard to the seismic safety evaluation of dams with such composite structures, two methods can be considered, or individual evaluation and overall evaluation. The former is a method in which each dam is considered to be an independent structure and is evaluated individually. The latter is a method in which multiple dams are considered to be a single structure and the entire system is evaluated. The results of this study suggest that

the seismic safety evaluation of multiple arch dams should be conducted not by individual evaluation but by overall evaluation.

6. Afterword

The increase or decrease in seismic tensile stress due to a decrease in dynamic shear modulus is considered to vary depending on the mutual effects of the dam, foundation rock, and earthquake motion.

Since dams are large-scale structures with strong site-dependence, seismic safety evaluation must accurately reflect the characteristics of each individual site. The effect of changes in dynamic shear modulus on seismic stresses is expected to be greater for structures with more complex seismic behaviour. So, it is considered that the effect of changes in dynamic shear modulus should be taken into account for larger structures with more complex geometry.

As future issues, it is important to study the mutual influence of the stiffness of the dam body and the foundation rock, and the influence on the seismic safety of the foundation rock.

7. Acknowledgment

The author would like to thank Mr. Hiroaki Nakagawa, Dr. Yoshiaki Ozawa and Mr. Taku Yasue (Century Techno Inc.) for their great consideration and cooperation in using the analysis program ISCEF.

8. References

- Ariga Y., Cao Z., Watanabe H. (2003) : Seismic stability assessment of an existing arch dam considering the effects of joints, *Proceedings of the 21th International Congress on Large Dams (21st ICOLD)*, Q.83-R.33, 553-576, (in English).
- Ariga Y., Cao Z., Watanabe H. (2004). Study on 3-D dynamic analysis of arch dam against strong earthquake motion considering discontinuous behaviour of Joints, *Journal of Japan Society of Civil Engineers*, No. 759, I-67, 53-67, (in Japanese).
- Ariga Y., Watanabe H. (2004) : Reproduction analysis of real behaviour of existing arch dam during the 1995 Hyogoken-Nanbu Earthquake, *Proceedings of the 13th World Conference on Earthquake Engineering (13th WCEE)* , No.405, 1-10, (in English).
- Ariga Y., Cao Z., Watanabe H. (2004) : Development of 3-D dynamic analysis method for coupled dam-joints-foundation-reservoir system, *Proceedings of the 13th World Conference on Earthquake Engineering (13th WCEE)* , No.412, 1-13, (in English).
- Ariga Y. (2006) : Verification of 3-D seismic safety evaluation method for existing dams by reproduction analysis for actual earthquake behaviour, *Proceedings of the 1st European Conference on Earthquake Engineering and Seismology (1st ECEES)*, No.1214, 409-416, (in English).
- Ariga Y. (2007) : 3-D reproduction analyses for actual earthquake behaviours and quantitative evaluation of dynamic property values of existing concrete dams, *Proceedings of the 9th Canadian Conference on Earthquake Engineering*, No.1043, 1-10, (in English)
- Ariga Y., Ueshima T., Nakamura, S., Shiojiri H. (2014). Seismic safety evaluation for double arch dam during the 2011 off the Pacific Coast of Tohoku Earthquake by three-dimensional dynamic analysis, *Journal of Japan Society of Civil Engineers*, SER. A1 (Structural Engineering & Earthquake Engineering), Vol. 70, No. 4, I_121-I_129, (in Japanese).
- Ariga Y. (2022). Influence of reduction of dynamic shear modulus on seismic tensile stress of arch dam, *Journal of Japan Association for Earthquake Engineering*, Vol.22, No.3, 3_16-3_29, (in English).
- Century-techno. (2023), ISCEF (Integrated software for civil engineering fluid-structure interaction system), (in Japanese), <http://www.century-techno.co.jp>.
- Hatano T. (1968). Theory of failure of concrete and similar brittle solid on the basis of strain, *Journal of Japan Society of Civil Engineers*, 153, 31-39, (in Japanese).

- Hiramatsu T., Sato H., Kondo, M. (2017). Influence of damping factor on earthquake response of arch dam, *the 72th Annual Meeting Proceedings of Japan Society of Civil Engineers*, I-547, 1093-1094, (in Japanese).
- Japanese Ministry of Land, Infrastructure, Transport and Tourism (MLIT). (2009), Technical criteria for river works, Practical guide for planning, Chapter 2, Section 12, 15-21, (in Japanese).
- Japan Society of Civil Engineers. (2002). Standard specifications for concrete structures—2002 (Seismic performance verification), pp. 47, (in Japanese).
- Kimata H., Horii H., Yazdani M. (2013). Seismic safety evaluation of concrete arch dam against earthquake-induced failure of joint rock foundations, *Journal of Japan Society of Civil Engineers*, SER. A1 (Structural Engineering & Earthquake Engineering), Vol. 69, No. 4, I_9-I_19, (in Japanese).
- National Institute for Land and Infrastructure Management (NILIM). (2005). Technical note on seismic performance evaluation of dams against large earthquake, *Technical note of NILIM*, No.244, ISNN1346-7328, 17-19, (in Japanese).
- Okuma N., Mazda T., Kanazawa K., Ikeda, K. (2012). Seasonal changes in dynamic properties of two large arch dams on ambient vibration measurements, *Journal of Japan Society of Civil Engineers*, SER. A1 (Structural engineering & earthquake engineering), Vol. 68, No. 4, I_883-I_890, (in Japanese).
- Ueda M., Toyoda Y., Shiojiri H., Sato, M. (2000). Resonant frequency of concrete arch dam evaluated from observational in-situ records and effects of contraction joints on these features, *Journal of Japan Society of Civil Engineers*, No. 654, I-52, 207-221, (in Japanese).
- Watanabe H., Ariga Y., Cao, Z. (2002). Earthquake resistance of a concrete gravity dam reevaluated with 3-D nonlinear analyses, *Journal of Japan Society of Civil Engineers*, No. 696, I-58, 99-110, (in Japanese).

SEISMIC SLOPE STABILITY OF HYBRID TAILINGS DAMS: A PROBABILISTIC APPROACH

T. S. Aswathi¹, S. Kuili² & R. S. Jakka³

¹ Research Scholar, Indian Institute of Technology Roorkee, Uttarakhand 247667 India, as@eq.iitr.ac.in

² Research Scholar, Indian Institute of Technology Roorkee, Uttarakhand 247667 India

³ Professor, Indian Institute of Technology Roorkee, Uttarakhand 247667 India

Abstract: Tailings dams are earth structures used to store mining waste and upstream construction method has been a popular choice among the three conventional methods. However, upstream tailings dams forecasted major failures, leading to a worldwide ban. Examples of such disasters includes failure of Fundao tailings dam on 5th November 2015 and B1 tailings dam on 25th January, 2019, Brazil. To address the challenge of limited disposal areas and large tailings production, old tailings dams can be converted to hybrid methods such as downstream on upstream and centreline on upstream. This study presents a probabilistic seismic slope stability analysis of four different hybrid tailings dams having two different sloping configurations, using GeoStudio software. Monte Carlo simulations were performed to account for the variabilities of input parameters, such as the frictional angle of tailings sand and slimes as well as phreatic line. The study highlights the importance of variability considerations in geotechnical modelling for critical structures like tailings dams and demonstrates the effectiveness of probabilistic seismic slope stability analysis in evaluating the risk under different loading conditions.

1. Introduction

Tailings dams serve as engineered embankment structures designed to confine the waste materials produced by the mining industry, which generates a substantial volume of waste, necessitating adequate disposal solutions. These dams are typically constructed using three conventional methods: upstream, downstream, and centerline. These methods differ based on the movement of the dike crest with respect to the initial dike position during the construction process. (Vick, 1990). Historically, upstream tailings dams were widely favoured for their cost-effectiveness, reduced material requirements, and smaller spatial footprints. Nevertheless, their global performance record has been tarnished by major failures, which led to their prohibition and abandonment in accordance with new regulations (Lyu et al., 2019). In recent decades, the occurrence of significant disasters stemming from the failure of expansive tailing ponds has garnered substantial public concern regarding the safety of tailings dams (Rico et al., 2008). Key factors leading to the failure of tailings dams include slope instability, seepage, insufficient freeboard, elevated phreatic levels, foundation issues, intense rainfall, and seismic liquefaction, among various others.

Researchers have conducted deterministic studies on the responses of conventional tailings dams under both static and dynamic loading. Dynamic analyses included pseudo-static, pseudo-dynamic, and time history approaches (Psarropoulos and Tsompanakis, 2008; Jakka et al., 2011; Liu et al., 2012; Özer and Bromwell, 2012; Ferdosi et al., 2015). Despite an abundance of research on traditional tailings dams constructed with

downstream, upstream, and centerline methods, studies exploring the combination of these construction techniques are limited. The challenge of land scarcity has made raising existing tailings dams using conventional methods increasingly difficult, leading to a shift towards mixed construction approaches. Recognizing that upstream areas are often abundant and abandoned, a practical solution involves converting these abandoned upstream tailings dams into hybrid structures. Sitharam and Hegde (2017) and Chen and Wei (2023) have deterministically investigated the elevation of dam height through mixed construction method resulting in the development of hybrid tailings dams. The adoption of a hybrid approach aims to enhance the capacity of existing dams, particularly when facing limitations in extension areas or instability using the same raising method. In a feasibility study, Sitharam and Hegde (2017) raised the height of a rock-fill tailings dam at RA mines in Rajasthan, India, using static and pseudo-static loading conditions and incorporating both upstream and downstream raising methods. In a numerical analysis of the Dahongshan Longdu tailings pond, Chen and Wei (2023) demonstrated that employing a mixed construction method, which combines upstream and centerline techniques, led to improved control of seepage, reduced displacement, enhanced stability, and increased storage capacity compared to relying solely on the upstream method.

Evaluating stability stands as a pivotal consideration in averting catastrophic disasters and ensuring safety. Contemporary practices for assessing soil strength often assume uniform material properties. However, the introduction of slimes into the impoundment created by dikes introduces variability in soil properties. Typically, dikes are constructed in thin layers with subsequent compaction. Neglecting the recognition of a homogeneous dam condition dismisses the impact of soil property variations, which can have adverse effects on design integrity. These variations can be attributed to multiple factors, one of which is the amalgamation of distinct soil properties within the slimes and tailings sand. Geotechnical dam designs prioritize comprehensive safety margins, but they must contend with substantial uncertainties that yield varying outcomes. The fluctuations in soil properties play a significant role in influencing dam stability. Additionally, variability arises from both field and laboratory testing of the soil (Elkateb et al., 2003; Baecher and Christian, 2005). Typically, stability analyses are conducted using traditional deterministic techniques employing a sole Factor of Safety (FoS). Regrettably, deterministic approaches do not explicitly address the uncertainty associated with soil properties. A slope is deemed secure when the deterministic FoS surpasses 1. However, Duncan (2000) suggests that applying a consistent factor of safety to situations characterized by significantly differing levels of uncertainty is not a logical approach. This is because slopes with an identical safety factor may present varying risk levels due to the variability in soil properties, as pointed out by Li and Lumb (1987).

The FoS is a widely employed metric in the evaluation of slope stability, offering an index that reflects the relative stability of a given structure. However, it is important to recognize that the FoS alone does not provide a complete understanding of the actual risk level. This limitation arises from the inherent variability in input parameters that can significantly affect stability outcomes. To gain a more comprehensive perspective on slope stability and its associated risk, probabilistic analysis introduces two critical indices: the probability of failure (P_f) and the reliability index (β). Lade (1992) emphasized the reality that conventional stability assessments may not capture the full spectrum of risks. In fact, even a tailings dam that appears secure within the confines of traditional standards can be rendered vulnerable to instability by seemingly minor disturbances, potentially resulting in a catastrophic failure. It is worth noting that there have been limited instances of probabilistic analyses focused on the static and seismic stability of slopes. Hamade et al. (2011) highlights the significance of probabilistic analysis, particularly in the context of the upstream method of construction. Their findings reveal that the FoS tends to be lower, while the P_f is higher, and β is lower, indicating a more precarious stability situation. Additionally, Hegde and Das (2019), Sitharam and Hegde (2019), and Das and Hegde (2020) extended the scope of their studies to encompass probabilistic assessments of tailings dam heightening. Their research investigated the probabilistic aspects of the study primarily done on tailings heightening by Sitharam and Hegde (2017). Their major conclusion being spatial variability of soil properties plays a significant role in influencing FoS values, demonstrating the critical importance of these probabilistic approaches in providing a more realistic and comprehensive view of slope stability and associated risks. These studies were done a particular tailings dam heightening considering upstream and downstream as the raising method options of the existing dam.

While the mixed construction methods of tailings dam present advantages, it is crucial to emphasize the scarcity of research dedicated to evaluating the safety of hybrid tailings. Only a handful of studies have delved into hybrid tailings dams, typically focusing on one or two configurations at most, leaving a noticeable gap in

research on the probabilistic slope stability of such dams. The present study aims to address this need by assessing the probabilistic aspects of slope stability in hybrid tailings dams under both static and seismic loading conditions. It considers the influence of random variables, such as the friction angle of tailings and the position of the phreatic line, while also investigating the impact of the upstream construction method on hybrid tailings dam stability. Additionally, the study explores the potential repurposing of abandoned upstream tailings dams into hybrid structures, offering a comprehensive perspective on the dynamic field of tailings dam stability research considering the uncertainties associated with material properties and the phreatic line.

2. Methodology

The research is dedicated to the assessment of the probabilistic aspects of slope stability in hybrid tailings dams, considering the impact of random variables in both static and seismic loading conditions. These variables include the friction angle of tailings, which extends to encompass slimes and tailings sand, and the position of the phreatic line. While the former focuses on material variability, maintaining a constant unit weight, the latter delves into the variability within the saturation zone, where material properties remain constant. The study explores four distinct configurations of hybrid tailings dams, possessing an upstream method for raising either the lower or upper segment of the hybrid tailings dam to explore the possibility of repurposing of abandoned upstream tailings dams into hybrid structures to alleviate the shortage of tailings disposal sites. The four categories of hybrid tailings dams considered are: Hybrid Downstream over Upstream (HDU), Hybrid Centreline over Upstream (HCU), Hybrid Upstream over Centreline (HUC), and Hybrid Upstream over Downstream (HUD), all sharing a total height of 60m. These dams are constructed with dikes that feature uniform height, crest, and slopes on both sides, with 5m of height and crest measurement. Furthermore, two different slope configurations, steeper (1V:3H) and flatter (1V:5H), are examined for the individual dikes, enabling the assessment on the effect of slope. Figure 1 displays the cross-section of all four hybrid tailings dams, each with a slope of 1V:5H. Seismic slope stability analysis is executed using the pseudo-static method to assess the impact of seismic loading on the FoS of the tailings dam impoundment. Pseudo-static method for seismic assessment is ideal in the absence of dynamic soil properties. Peak Ground Acceleration (PGA) values, ranging from 0.1g to 0.4g, are converted into seismic coefficients to act as horizontal inertial forces on all slices of potential slip surfaces. The research consistently applies the Limit Equilibrium Method (LEM), specifically the Morgenstern-Price (M-P) method, renowned for ensuring both force and moment equilibrium, thereby providing a robust FoS.

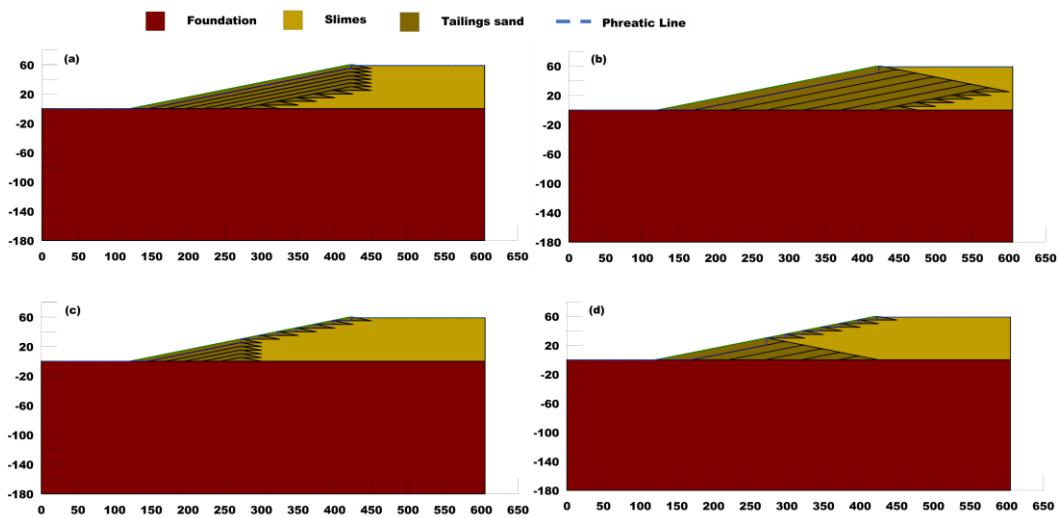


Figure 1. Cross section of different hybrid tailings dam with 1V:5H slope (a) HCU, (b) HDU, (c) HUC and (d) HUD.

Deterministic slope stability analysis employs mean values for all materials, while probabilistic analysis adopts the variabilities using Monte Carlo simulation (MCS). In this study, 10,000 iterations have been performed for the attainment of probabilistic outcomes via MCS. Normal distributions pertaining to the parameters with variability have been utilized and through MCS, the probability distribution of computed FoS for all the analysed slip surfaces is performed. Through the assertion of this probabilistic distribution, assessment of failure

probability and reliability index becomes feasible. The computation of cumulative distribution function is performed by computing the area under the probability distribution function. The attainment of sampling function is done by inverting the cumulative distribution function. Thus, employing normal distribution for different input parameters for performing probabilistic assessments in SLOPE/W results in increase in likelihood for sampling parameters around the mean value as compared to values present at the extreme ends. MCS is a commonly employed technique in the field of geotechnical engineering, particularly in addressing challenges related to slope stability, where uncertainties significantly influence the outcomes (El-Ramly et al. 2002). The FoS pertaining to the critical slip surface has been evaluated deterministically i.e., by accounting homogenous conditions for both static and pseudo-static loadings. The attained critical slip surfaces from deterministic analysis corresponding to individual loading conditions have been utilized by accounting different aspects of variability. The failure risk along with the confidence level attained on the final outcome have been delineated in this study for different hybrid dam configurations having various extents of variabilities. Through probabilistic analysis, another important parameter i.e., reliability index is attained which forecasts the reliance of the final probabilistic outcome (Phoon, 2002). The P_f is computed by tallying the count of safety factors falling below 1.0, and this count is then expressed as a percentage of the total number of successfully converged Monte Carlo trials. The reliability index quantifies stability based on the number of standard deviations that separate the mean factor of safety from the defined failure threshold of 1.0. This measure also serves as a means of standardizing the factor of safety in relation to its associated uncertainty.

Table 1 furnishes an extensive overview of the materials utilized in the analysis, presenting their properties in both deterministic and probabilistic contexts. Mohr Coulomb material model is incorporated in this study. Variations in material properties primarily revolve around the friction angle of tailings, expressed as a coefficient of variation (CoV) with a maximum permissible variation of 25% (Baecher and Christian, 2005; Hamade et al., 2011) as the tailings material are cohesionless soil. To ensure consistency, the study maintains the same level of friction angle variation for both tailings sand and slimes simultaneously. FoS calculations are not influenced by change in unit weight. Additionally, the study explores variations in the phreatic line by adjusting its height from the mean by three different standard deviations (std.), i.e., 0.5, 1, and 2, as depicted in Figure 2. Notably, the illustration does not accurately portray variations to scale for the presented phreatic lines. Additionally, the upper limit of phreatic line variation with 1 std. and 2 std. is aligned with both surface of the dam and ground surface during analysis, as this negates the unrealistic scenarios of the phreatic line existing above the surface of the tailings dam.

Table 1. Material properties along with their probability characteristics (Mabes et al., 1977 and McKee et al., 1978).

Material	Unit weight (kN/m ³)	Angle of friction (°)	Friction angle CoV (%)	Probability distribution
Slimes	14	31	5, 10, 15, 25	Normal
Tailings sand	17.5	35	5, 10, 15, 25	Normal
Foundation	20	40	-	-

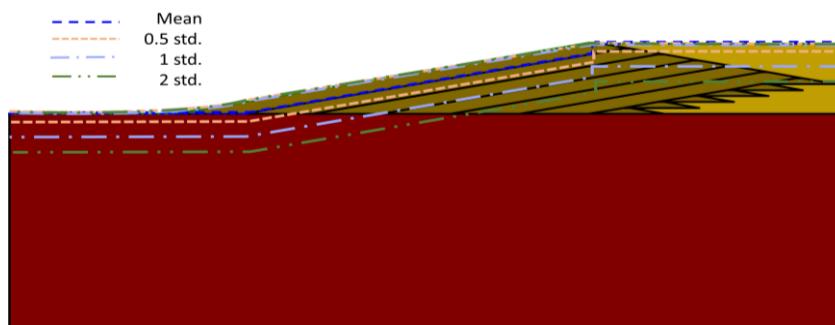


Figure 2. Typical illustration of phreatic line variation with 0.5 std., 1 std. and 2 std. along with mean phreatic line.

3. Results and Discussions

The ensuing section delves into the outcomes derived from examining the stability of a hybrid tailings dam through both deterministic and probabilistic analyses. These evaluations encompass static and seismic loading conditions. The probabilistic slope stability analysis is conducted to evaluate the impact of fluctuations in the friction angle of tailings, considering that variations in slimes and tailings sand are the same. Additionally, the study assesses the outcomes of phreatic line fluctuations.

3.1 Deterministic slope stability

The results of deterministic slope stability assessments for four hybrid tailings dams, conducted under both static and seismic loading conditions using the pseudo-static approach for two different sloping configurations (1V:3H and 1V:5H), are presented in Figure 3. For a deterministic approach, prescribed minimum FoS for stability is 1.5 for static conditions and 1.0 for seismic loading, according to ANCOLD guidelines. Among the hybrid tailings dams considered, the hybrid HDU demonstrated the highest stability, followed by HCU, HUD, and HUC. Under static loading and pseudo-static load of $k_h = 0.1$, all flatter slope hybrid tailings dams have FoS greater than the prescribed minimum FoS indicating they are safe. HDU with a steeper slope also exhibits a similar trend. Moreover, HDU with a flatter slope remains stable under an elevated pseudo-static load of $k_h = 0.2$. However, upon further increase of seismicity, the hybrid tailings dams are regarded as unstable, as their FoS falls below the specified threshold. To compare deterministic and probabilistic slope stability outcomes, a FoS threshold of 1 is employed to determine safety. According to this criterion, all four hybrid tailings dams, regardless of their slopes, exhibit stability under static loading conditions. It can also be concluded that hybrid tailings dams with upstream in their lower segments outperform those hybrid tailings dams with upstream on their upper segment.

Figure 4 and 5 illustrates the critical slip surfaces of hybrid tailings dams with 1V:3H and 1V:5H under static loading respectively. It is evident that the steeper slope results in a deeper slip surface. In the case of a hybrid tailings dam having upstream method in the upper segment, the critical slip surface traverses through both the slimes and the dike portion and primarily within the upstream segment of the hybrid tailings dam. However, when the upstream section is positioned in the lower segment of the hybrid tailings dam, the slip surface extends through the dike and spans through entire height of the hybrid tailings dam.

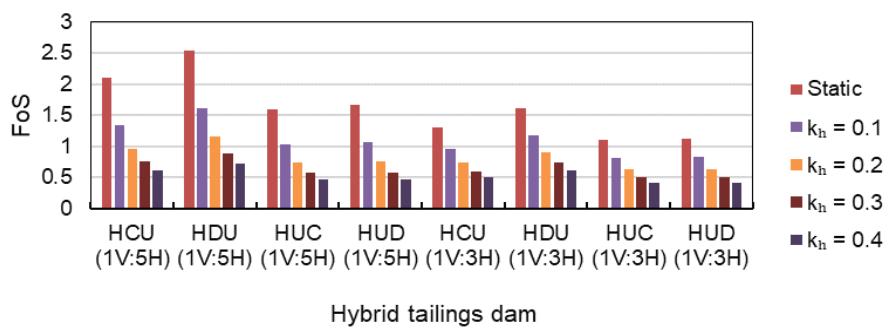


Figure 3. Deterministic FoS of different hybrid tailings dam for different loading cases.

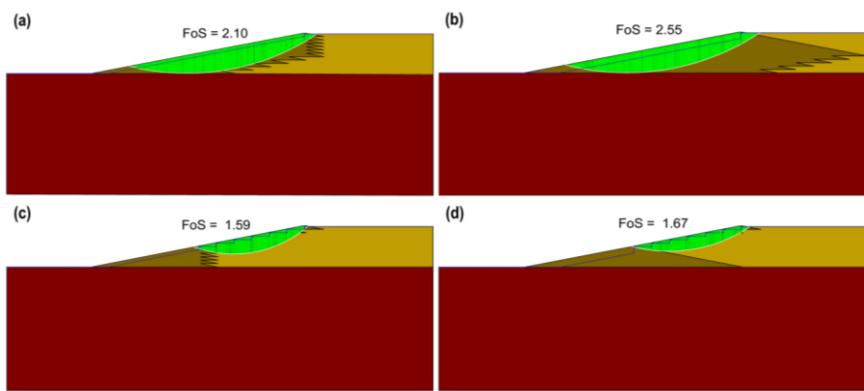


Figure 4. Critical slip surface of different hybrid tailings dam with slope (1V:5H) under deterministic static stability analysis (a) HCU, (b) HDU, (c) HUC and (d) HUD.

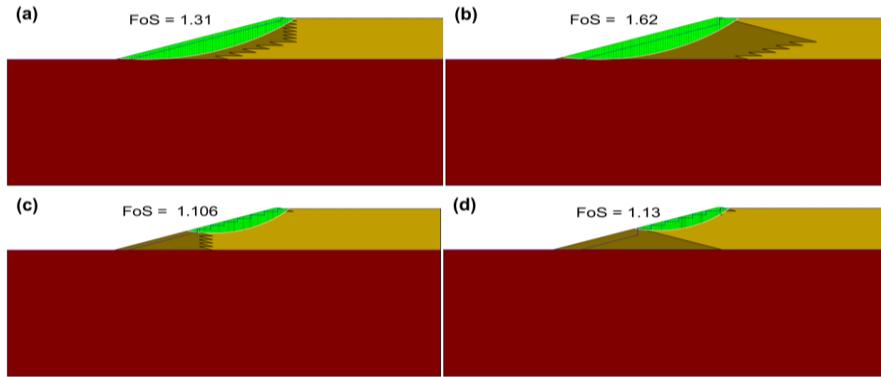


Figure 5. Critical slip surface of different hybrid tailings dam with slope (1V:3H) under deterministic static stability analysis (a) HCU, (b) HDU, (c) HUC and (d) HUD.

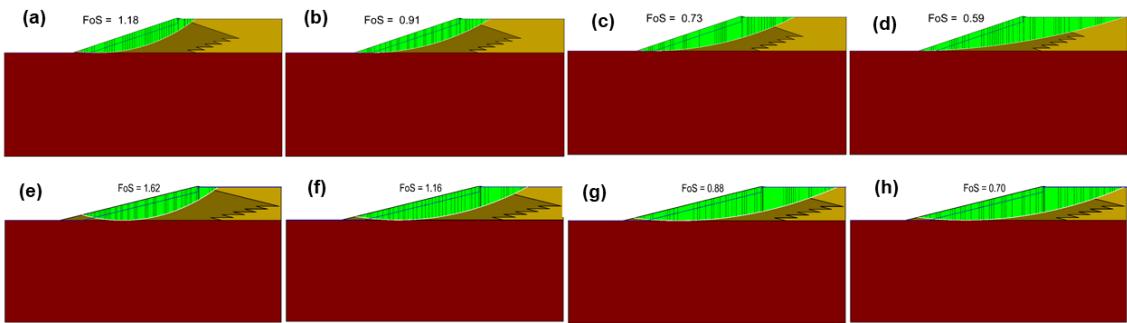


Figure 6. Critical slip surface pertaining to different pseudo-static loads of (a) $k_h = 0.1$, (b) $k_h = 0.2$, (c) $k_h = 0.3$ and (d) $k_h = 0.4$ for HDU(1V:3H) and correspondingly (e) $k_h = 0.1$, (f) $k_h = 0.2$, (g) $k_h = 0.3$ and (h) $k_h = 0.4$ for HDU(1V:5H).

The critical slip surfaces under different pseudo-static loadings varying from $k_h = 0.1$ to 0.4 for HDU(1V:3H) and HDU(1V:5H) are visually represented in Figure 6. It becomes apparent that, regardless of the slope configuration, HDU experiences an expansion of the slip surface extent with increase in seismic loading. This is due to the increase in driving forces due to seismic loading. In the deterministic analysis, FoS are employed but do not account for material property variations. Consequently, they fall short in offering insights into the likelihood of failure risk. In contrast, the probabilistic method takes into consideration a spectrum of potential outcomes, factoring in uncertainties related to various parameters. This approach, therefore, provides a more comprehensive and holistic understanding of the associated risks of potential scenarios along with their confidence level.

3.2 Probabilistic slope stability

This section discusses the results of the probabilistic slope stability analysis, with a focus on the impact of uncertainties in material properties and phreatic line variation on the FoS in terms of P_f and β . The study explores the impact of uncertainty on material properties by altering the friction angle of both slimes and tailings sand, while ensuring that the variation remains consistent. The four hybrid tailings dams are divided into two groups: hybrid tailings dams with upstream construction in the lower segment and hybrid tailings dams with upstream construction in the upper segment, to assess the risk of failure and confidence of the results under the considered uncertainties.

Hybrid tailings dams with upstream construction in lower segment

HDU and HCU comes under the classification hybrid tailings dam with upstream in lower segment. The P_f and β for HCU concerning variations in tailings friction angle under both static and seismic loading are displayed in Figure 7 (a) and (b). Under static loading conditions with a slope of 1V:3H, an increase in the variability of the friction angle leads to an escalation in P_f . This indicates that due to the variation in the friction angle, there is a potential for the FoS to drop below 1, even when the deterministic FoS exceeds 1. A similar response is observed with the flatter slope configuration at the highest considered variation. Under pseudo-static loading for angle variations, as the intensity increases, P_f also increases, signifying an increased susceptibility of the

dam to failure. However, when the variability of friction angle increases, P_f decreases under specific seismic loading conditions for both slopes, except for the flatter slope subjected to lower seismic loading. However, the behaviour of the flatter slope under low seismic loading is akin to that of the steeper slope under static loading. This decrease in P_f is due to an increase in the attainment of outcomes representing FoS exceeding 1. Under static and low-intensity seismic loading, the risk of failure increases with an increase in the variation of the friction angle while comprehending constant unit weight. Conversely, a reverse trend is observed at higher intensity seismic loading. It is important to note that as the variation in friction angle increases, the reliability index decreases thus emphasising lower confidence on the probabilistic outcomes. The presence of higher variation in friction angle of the tailings implies greater uncertainty regarding the strength of the tailings dam, which leads to reduced confidence as indicated by reliability index. The highest level of confidence is observed for seismic loading with $k_h = 0.4$ when CoV for the friction angle is 5%. In terms of slope configurations, confidence is higher for 1V:5H than for 1V:3H under static and seismic loading conditions with $k_h = 0.1$, but this trend reverses for k_h values greater than or equal to 0.2. A similar behaviour is noted for HCU with 1V:5H slope subjected to seismic loading of $k_h = 0.2$.

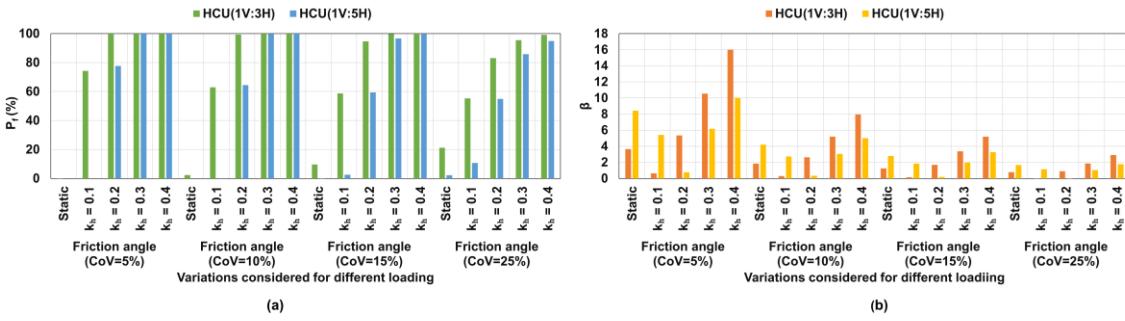


Figure 7. Probabilistic analysis outcomes of HCU with varying slopes and friction angle variations, depicting (a) probability of failure and (b) reliability index.

Figure 8 (a) and (b) portrays the P_f and β of HCU with two different slope configurations, 1V:3H and 1V:5H, pertaining to phreatic line variations with std. of 0.5, 1, and 2. Under static loading conditions, the risk of failure is negligible for both slope configurations, except for the steeper slope with the highest phreatic line variation, where slight increase in risk was observed. Subjecting a seismic load of $k_h = 0.1$ for the steeper slope resulted in decreased P_f pertaining to higher extend of phreatic line variations. A similar trend is observed for the flatter slope under seismic loading at $k_h = 0.2$. As the variability in phreatic line increases, there is an increased likelihood for the phreatic line to move way below the mean phreatic line. Consequently, this leads to an improvement in the FoS, suggesting an increased chance of attaining FoS exceeding 1, thus resulting in decreased risk of failure. However, impartation of higher intensity of seismic loading, P_f remains at 100% for both slopes. This indicates that adjusting the phreatic line does not elevate the FoS beyond 1 under high-intensity seismic loading. The confidence levels was observed to be higher for HCU(1V:5H) under static and pseudo-static loading of $k_h = 0.4$ for lower extent of phreatic line variations, however, HCU(1V:3H) delineated highest reliability index for seismic loading of $k_h = 0.4$.

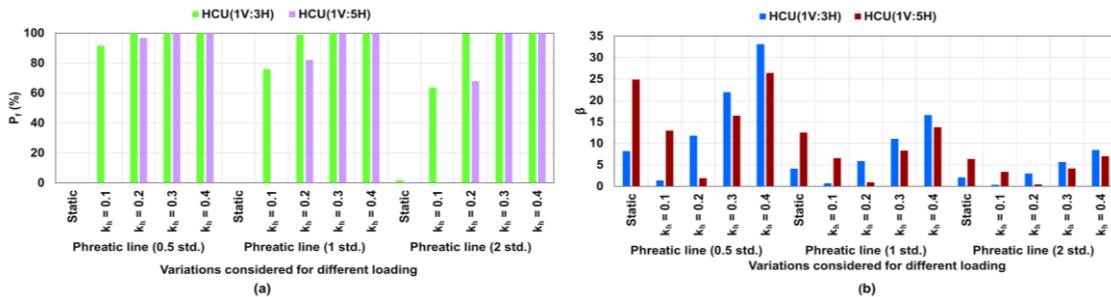


Figure 8. Probabilistic analysis outcomes of HCU with varying slopes and phreatic line variations, depicting (a) probability of failure and (b) reliability index.

Figure 9 (a) and (b) depicts the plot of P_f and β for HDU configuration having two different slopes under static and seismic loading conditions, accounting for variability in the friction angle of tailings material. As the

variability of the soil's friction angle changes, noticeable fluctuations in P_f and β become evident under different loading scenarios for both slope configurations. In static and low-intensity seismic loadings, the probabilistic outcomes indicate that the risk of failure increases with increase of variability of friction angle. However, when seismic intensity increases, the risk of failure decreases from 100% for higher extent of variability. The steeper slope exhibits an increase in P_f for static and seismic loading of $k_h = 0.1$ with increase in variability. Similar behaviour was procured for flatter slope subjected to a seismic loading of $k_h = 0.2$. For a given CoV of the frictional angle, there is a reduction in β as the loading increases up to a certain point, followed by an increase in β . The lowest β value is observed for 1V:3H and 1V:5H sloping configurations at seismic loads of $k_h = 0.2$ and 0.3 respectively. Furthermore, at seismic loadings of 0.3 and 0.4, the confidence in the probabilistic outcomes for 1V:3H slope exceeds than the values obtained for 1V:5H slope. However, the confidence is higher for flatter slopes for static and seismic loading with $k_h = 0.1$ and 0.2.

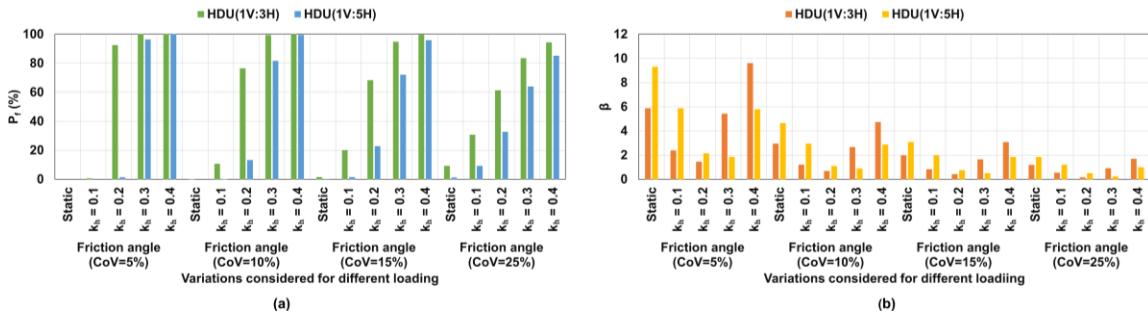


Figure 9. Probabilistic analysis outcomes of HDU with varying slopes and friction angle variations, depicting (a) probability of failure and (b) reliability index.

Figure 10 (a) and (b) display the probabilistic outcomes for HDU configuration with varying slopes considering phreatic line variations. Both sloping configurations exhibited negligible failure risk under static and seismic loading of $k_h = 0.1$ and flatter slope depicted the same at seismic load of $k_h = 0.2$. Further at higher seismic loading both the sloping configurations exhibited P_f of 100% for 0.5 and 1 std. However, there is a slight decrease in P_f from 100% for phreatic line variation of 2 std. This is due to increased outcomes of FoS greater than 1 due to consideration of water table locations at deeper depths. The confidence level for a flatter slope was observed to be higher than that of a steeper slope under static and seismic loadings having k_h of 0.1 and 0.2. Nevertheless, a reverse trend is observed at higher seismicity.

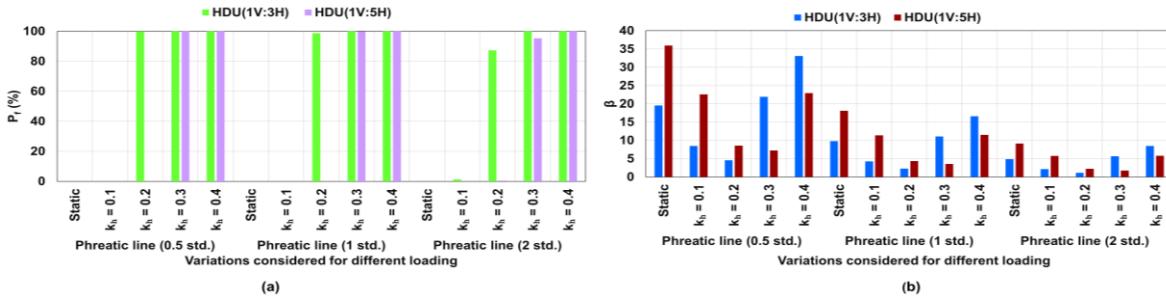


Figure 10. Probabilistic analysis outcomes of HDU with varying slopes and phreatic line variations, depicting (a) probability of failure and (b) reliability index.

Probabilistic analysis of HCU and HDU shows that the risk of failure corresponding to HDU configuration is lower for static and low intensity seismic loading for both material variation and phreatic line fluctuations. However, both hybrid tailings dams exhibit high failure risks at increased seismic intensities. This establishes that HDU is the safer choice when compared to HCU configuration. The variation in failure risk on account of tailings friction angle variability is considerably higher in comparison to phreatic line fluctuation. This aspect indicates that the impact of material variability outweighs that of phreatic line variability.

Hybrid tailings dams with upstream construction in upper segments

HUC and HUD comes under the classification hybrid tailings dam with upstream in upper segment. Figure 11 (a) and (b) presents the plot of P_f and β for HUC having different slopes (1V:3H and 1V:5H), subjected to different loadings while considering variation in friction angle. Under static loading the steeper slope depicted

an increase in P_f with increase in CoV of the frictional angle. Similar trend is observed for flatter slope configuration under static as well as seismic load of $k_h = 0.1$. Under seismic loading of $k_h = 0.2$ and 0.3, a decrease in failure risk is observed at higher variability of friction angle particularly evident for extensive variations i.e., CoV of 25%. The confidence level attained for flatter slope is higher than that of steeper slope under static loading for all the friction angle variations considered. The reverse trend is observed for all the seismic loadings pertaining to the accounted variabilities as per this study.

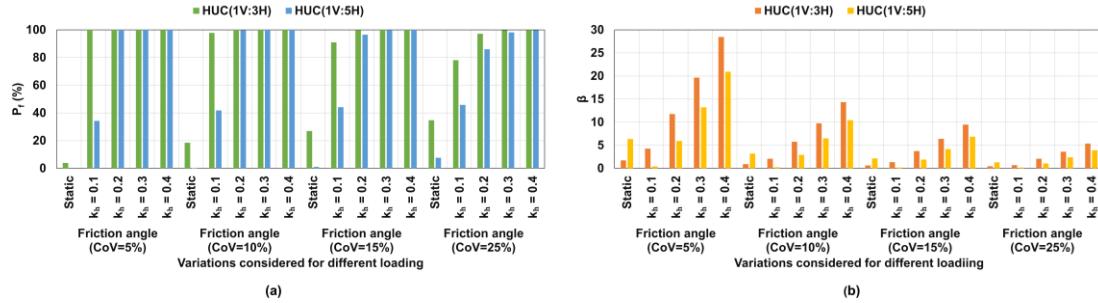


Figure 11. Probabilistic analysis outcomes of HUC with varying slopes and friction angle variations, depicting (a) probability of failure and (b) reliability index.

Figure 12 (a) and (b) illustrates the P_f and β of HUC with two different slopes for phreatic line variations at std. of 0.5, 1, and 2. Under static loading, the failure probability is zero for the flatter slope at all the variability of phreatic line considered in this study. However, for 1V:3H slope pertaining to static loading and 1V:5H slope under seismic load of $k_h = 0.1$, the P_f increases as the phreatic line's variation increases. The opposite trend is observed for the 1V:3H slope under seismic loading with $k_h = 0.1$. In all other extents of variability comprehended in this study, the risk of failure is 100%. Under seismic loading of $k_h = 0.3$ and 0.4, the confidence level acquired for all the extents of variability were observed to be similar. In case of static loading, HUC with flatter slope depicted increase confidence levels over steeper slopes for all extents of variability. A reverse trend was observed for seismic loadings of $k_h = 0.1$ and 0.2.

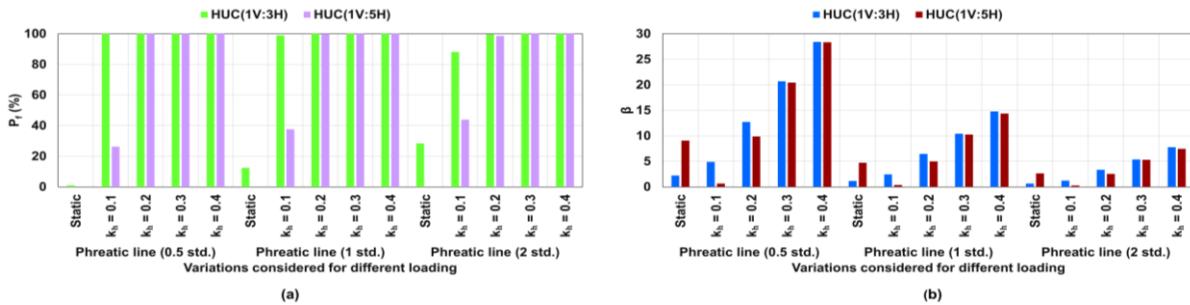


Figure 12. Probabilistic analysis outcomes of HUC with varying slopes and phreatic line variations, depicting (a) probability of failure and (b) reliability index.

Figure 13 (a) and (b) displays the plot of probabilistic outcomes along with acquired confidence levels for HUC configurations while comprehending different variation of friction angle. The plot of P_f exhibits an increasing trend with increase in the friction angle variability under static loading for steeper slope whereas, flatter slope depicted a negligible failure probability pertaining to friction angle variability of CoV = 25%. Under a seismic load of $k_h = 0.1$, 1V:5H sloping configuration depicted an increase in failure risk with increase in variability. For $k_h = 0.3$ and 0.4, the probability of failure was observed to be 100% for both sloping configurations. The reliability index was observed to be higher for steeper sloping configurations subjected to seismic loading. However, flatter slope depicted increased confidence levels under static loading for all extents of variability adhered in this study.

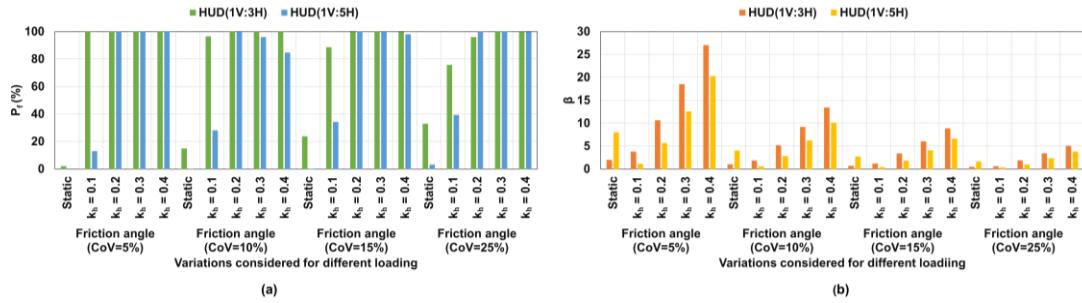


Figure 13. Probabilistic analysis outcomes of HUD with varying slopes and friction angle variations, depicting (a) probability of failure and (b) reliability index.

Figure 14 (a) and (b) depicts plot of P_f and β for HUD configurations having two different slopes for fluctuations in phreatic line locations. Under static loading, the steeper slope depicted an increase in failure risk with increase in phreatic line variability. Under seismic load of $k_h = 0.1$, a similar trend was observed by the flatter slope however steeper slope exhibited a reverse trend. Under seismic load of $k_h = 0.3$ and 0.4, both slopes exhibited failure risk of 100% for all the extents of variability considered in this study. The reliability index under seismic loading was observed to lower for flatter slope. However, a reverse trend was observed under static loading. Figure 14 (b) presents the fact that the reliability index also increased with increase in pseudo-static loading for all the sloping configurations of HUD tailings dam.

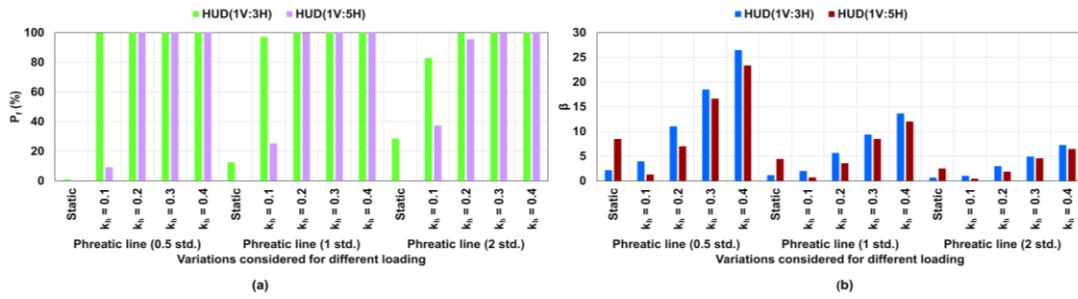


Figure 14. Probabilistic analysis outcomes of HUD with varying slopes and phreatic line variations, depicting (a) probability of failure and (b) reliability index.

HUD exhibited a higher performance than HUC in terms of probability of failure for both friction angle variations and phreatic line fluctuations. The outcomes of probabilistic analysis of hybrid tailings dam comprising upstream method on their upper segment depicts that failure risk is higher than that of hybrid dams having upstream method on their lower segment. The impartment of deterministic approaches to ascertain the stability of tailings dam slopes yields in the attainment of FoS by accounting homogenous conditions. The accountancy of homogeneity aids in the ease of stability assessment but negates the implications of the uncertainties invoked deviations due to existence of variabilities. Comprehensive insights have been depicted in this study highlighting the implications of two different aspects of variabilities on the risk of slope failure associated with hybrid tailings dam configurations.

4. Conclusions

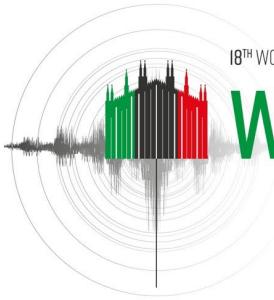
This study has undertaken stability evaluations of four distinct hybrid configurations of tailings dams, subjected to both static and pseudo-static loadings. The stability assessments have been performed via limit equilibrium approach to ascertain the FoS deterministically and consequently, implications due to the presence of variability in material properties and fluctuations in the water table within the tailings dams has been undergone via probabilistic analysis. Among the evaluated dam configurations, the HDU configuration consistently emerged as the most stable, followed by HCU configuration. Notably, configurations utilizing the upstream construction method in the lower segment consistently outperformed those with the upstream method in the upper segment. Construction of upstream method on upper segment of hybrid tailings dam resulted in the formation of the failure surface restricted to upper segment resulting lower stability, whereas, in contrary, presence of upstream method on the lower segment imposed by some other configuration on top results in higher stability. This held true both for deterministic and probabilistic slope stability evaluations. The

deterministic FoS of the hybrid tailings dams exhibited a decreasing trend with an increase in seismic loading. The increase in seismic loading also depicted a huge extent of soil mass attributed to slope failure, thus leading to the formation of an enlarged critical slip surface. The probabilistic seismic slope stability analysis offered detailed insights into the risk of failure associated with hybrid tailings dams for both loading conditions, via probability of failure and reliability index. The latter parameter underlined the confidence in the probabilistic outcomes while accounting for different extents of variability. This study evidently depicted that the variations in friction angle of the tailings exerted a more significant impact on stability than fluctuations in the phreatic line across all scenarios. The risk of failure proved highly dependent on the loading intensity, with static and low-intensity seismic loading resulting in negligible failure risks. However, increased material property variability led to an increase in probability of failure. Conversely, at higher seismic loading, the risk of failure reached 100% at lower variability and with increase in extents of variability, a gradual decline in the failure probability was observed. The confidence levels in the obtained probabilistic outcomes decreased as uncertainty increased. Comparison of the P_f values between HCU and HDU revealed distinct trends. For steeper slopes, HCU exhibited a P_f of 23% under static loading, while HDU had a lower P_f of 9.71%. In case of seismic loading corresponding to PGA of 0.4g, P_f of HCU increased to 98.5%, while HDU's P_f was observed to be 94% for the same sloping configuration. However, for flatter slopes, the P_f values decreased significantly, with HCU showing a P_f of 2.5% under static loading, while HDU demonstrated a lower P_f of 1.4%. Similarly, under the highest seismic loading, HCU depicted a P_f of 94%, whereas HDU exhibited a lower P_f i.e., 84%. Regarding variations in the phreatic line, HDU demonstrated a minimal failure risk under static and low seismic intensity conditions for both slope configurations. However, at elevated seismic loading, HDU (both configurations) depicted a P_f of 100% for low fluctuations of phreatic line. In case of higher extent of phreatic line fluctuations, HDU having a steeper slope depicts a decrease in P_f at seismic loading of 0.2g whereas, HDU with flatter slope depicts decrease in P_f when subjected to PGA of 0.3g. In case of HUC and HUD, the P_f is 100% under all seismic loading for lower extents of phreatic line variations whereas, phreatic line variations with 2 std. resulted in slightly decreased P_f for seismic loading of PGA 0.1g and 0.2g for both sloping configurations. These findings emphasize the critical importance of conducting probabilistic analyses in assessing the risk of slope failures associated while comprehending variabilities, as they reveal significant insights on different scenarios of variability for different slope configurations and loading conditions. Moreover, they highlight the consistent advantage of HDU in terms of lower failure risk compared to HCU. This accentuates the necessity for a comprehensive understanding of these factors in slope engineering and risk mitigation, ensuring safer and more robust tailings dam designs in the future.

5. References

- ANCOLD (2019). *Guidelines on Tailings Dams Planning, Design, Construction, Operation and Closure - Addendum*.
- Baecher G. B., Christian J. T. (2005). *Reliability and Statistics in Geotechnical Engineering*, John Wiley & Sons.
- Chen Y., Wei Z. (2023). Stability of Tailings Dam Constructed by both Upstream and Centerline Methods, *Geotechnical and Geological Engineering*, 1-12.
- Das T., Hegde A. M. (2020). "A comparative deterministic and probabilistic stability analysis of rock-fill tailing dam", *Proceedings of the IACMAG Symposium 2019*, 607-617.
- Duncan M. (2000). Factors of safety and reliability in geotechnical engineering, *Journal of Geotechnical and Geoenvironmental Engineering*, 126(4): 307-316.
- EI-Ramly H., Morgenstern N. R., Cruden D. M. (2002). Probabilistic slope stability analysis for practice, *Canadian Geotechnical Journal*, 39(3): 665-683.
- Elkateeb T., Chalaturnyk R., Robertson P. K. (2003). An overview of soil heterogeneity: quantification and implications on geotechnical field problems, *Canadian Geotechnical Journal*, 40(1): 1-15.
- Ferdosi B., James M., Aubertin M. (2015). Investigation of the effect of waste rock inclusions configuration on the seismic performance of a tailings impoundment, *Geotechnical and Geological Engineering*, 33: 1519-1537
- Hamade T., Mitri H., Saad B., Pouliot S. (2011). "Stochastic analysis of tailing dams stability using numerical modelling", *Proceedings of the 14th Pan-American Conference on Soil Mechanics and Geotechnical Engineering 64th Canadian Geotechnical Conference*, Toronto, Canada, 1-8.

- Hegde A. M., Das T. (2019). Finite element-based probabilistic stability analysis of rock-fill tailing dam considering regional seismicity, *Innovative Infrastructure Solutions*, 4: 1-14.
- Jakka R. S., Ramana G. V., Datta M. (2011). Seismic slope stability of embankments constructed with pond ash, *Geotechnical and Geological Engineering*, 29: 821-835.
- Lade P. V. (1992). Static instability and liquefaction of loose fine sandy slopes, *Journal of Geotechnical Engineering*, 118(1): 51-71.
- Li K. S., Lumb P. (1987). Probabilistic design of slopes, *Canadian Geotechnical Journal*, 24(4): 520-535.
- Liu H., Yang C., Zhang C., Mao H. (2012). Study on static and dynamic strength characteristics of tailings silty sand and its engineering application, *Safety Science*, 50(4): 828-834.
- Lyu Z., Chai J., Xu Z., Qin Y., Cao J. (2019). A comprehensive review on reasons for tailings dam failures based on case history, *Advances in Civil Engineering*, 2019: 1-18.
- Mabes D. L., Hardcastle J. H., Williams R. E. (1977). "Physical properties of Pb-Zn mine-process wastes", *Proceedings of the Conference on Geotechnical Practice for Disposal of Solid Waste Materials*, ASCE, 103-117.
- McKee B. E., Robinson K. E., Urlich C. M. (1978). "Upstream design for extension of an abandoned tailings pond", *Proceedings of the 2nd International Tailings Symposium*, Denver, Colo, 2: 210-233.
- Özer A. T., Bromwell L. G. (2012). Stability assessment of an earth dam on silt/clay tailings foundation: A case study, *Engineering Geology*, 151: 89-99.
- Phoon K. K. (2002). "Potential application of reliability-based design to geotechnical engineering", *Proceedings of the 4th Colombia Geotechnical Seminar*, Medellin, 1-24.
- Psarropoulos P. N., Tsompanakis Y. (2008). Stability of tailings dams under static and seismic loading, *Canadian Geotechnical Journal*, 45(5): 663-675.
- Rico M., Benito G., Salgueiro A. R., Díez-Herrero A., Pereira H. G. (2008). Reported tailings dam failures: a review of the European incidents in the worldwide context, *Journal of Hazardous Material*, 152(2): 846-852.
- Sitharam T. G., Hegde A. M. (2017). Stability analysis of rock-fill tailing dam: an Indian case study, *International Journal of Geotechnical Engineering*, 11(4): 332-342.
- Sitharam T. G., Hegde A. M. (2019). A case study of probabilistic seismic slope stability analysis of rock fill tailing dam, *International Journal of Geotechnical Earthquake Engineering*, 10(1): 43-60.
- Vick S. G. (1990). *Planning, design, and analysis of tailings dams*, BiTech Publishers Ltd



NEW EFFICIENT METHODS FOR THE SEISMIC ANALYSIS OF DAMS AND THEIR APPURTENANT STRUCTURES

N. Bouaanani¹, R. Kouhdasti²

¹ Polytechnique Montréal, Montréal, Canada, najib.bouaanani@polymtl.ca

² Polytechnique Montréal, Montréal, Canada

Abstract: The literature abounds with various methods for the seismic analysis of dams and their appurtenant structures or equipment. However, practicing dam engineers still often struggle with several issues when modeling the response of dam-reservoir-foundation systems under earthquake effects. They are generally required to select most appropriate assumptions underlying the appropriate numerical modelling of such systems without necessarily having a sense or clear understanding of the relative impact on such selection on the seismic response of the studied structures. Therefore, practical approaches are still in high demand due to their simplicity, ease of application and rapid implementation, particularly for verification purposes and routine engineering tasks. Although semi-analytical techniques are generally limited by the simple geometry of the reservoir, and water modeling assumptions (e.g. added-masses vs water compressibility), they can provide a wealth of useful information about the seismic behaviour of gravity dams, especially in the preliminary stages of design or safety evaluation of such critical structures. This paper will focus on the state-of-the art of simplified methods for the time-history and modal seismic analyses of gravity dams and their appurtenant structures. The proposed methods waive the need for specialized fluid-structure interaction software and allow more accurate assessment of coupled structural flexibility and hydrodynamic effects due to each vibration mode. It is proposed to conduct time-history modal superposition and response spectrum analyses while directly accounting for higher mode effects in lieu of static correction. A developed approach is based on the inclusion of earthquake-induced reservoir effects into modified versions of the original ground acceleration and its response spectrum that can be applied directly to the dam with empty reservoir (i.e. without water). The proposed approach is also used to illustrate the sensitivity of seismic demands on dam appurtenant structures and equipment to reservoir modelling assumptions and dam size.

1 Introduction

Major research and engineering concerns for the last several decades have been related to the investigation of the dynamic behaviour of dam-reservoir systems and evaluating their seismic safety. These systems have the particularity of being subjected to hydrodynamic effects induced by the impounded reservoir during earthquakes (e.g. Chopra 1967; Bouaanani and Perrault 2010). Appropriate modeling of such effects can be performed through several available analytical and numerical methods (e.g. Westergaard 1933; Fenves and Chopra 1984; Bouaanani and Lu 2009; Miquel and Bouaanani 2013; Bernier et al. 2016; Hariri-Ardebili et al. 2018). Although several sophisticated methods have been successfully applied to the seismic assessment of dam-reservoir systems, practical approaches are still in high demand due to their simplicity, ease of application and rapid implementation, particularly for routine engineering tasks. In this regard, dynamic modal superposition and response spectrum analyses (RSA) are popular among the broad range of available numerical tools, as they allow the dissection of a structure's response into the contributions of multiple vibration

modes, thus enabling a comprehensive understanding of each mode's impact on the total seismic response (e.g. Clough and Penzien 1975). For a dam-reservoir system, such analyses can be conducted using finite element formulations coupling solid and fluid elements to model earthquake-induced responses of the dam and the reservoir, respectively (e.g. Maity and Bhattacharyya 1999; Bouaanani and Lu 2009; Hariri-Ardebili et al. 2018). However, such solutions still generally require specialized software and a high-level of expertise to obtain valid results. Fenves and Chopra (1985) proposed a simplified method that can be used to estimate a gravity dam's peak seismic response directly from an earthquake design spectrum. This technique consists of modeling a gravity dam as an equivalent single degree of freedom (ESDOF) system used to evaluate the fundamental mode response of the dam through equivalent lateral static forces and response spectrum analysis. The effects of higher vibration modes are accounted for approximately through a static correction method (Clough and Penzien 1975). In this paper, an alternative simplified approach is proposed to conduct time-history modal superposition and response spectrum analyses of a dam-reservoir system while directly accounting for higher mode effects in lieu of static correction. The proposed technique is based on the inclusion of earthquake-induced reservoir effects into modified versions of the original ground acceleration and its response spectrum that can be applied directly to the dam with empty reservoir (i.e. without water). Therefore, specialized software accounting for fluid-structure dynamic interaction is not required. A similar approach was developed by Miquel and Bouaanani (2013) but their focus was on direct integration time-history dynamic analysis of dam-reservoir systems rather than response spectrum and modal superposition analyses.

2 Theoretical background and proposed methods

2.1 Basic assumptions

We consider a typical dam-reservoir system as the one shown in Figure 1. The dam monolith and the impounded rectangular reservoir have heights of H_s and H_w , respectively. A Cartesian coordinate system with axes x and z with origin at the heel of the dam is adopted and the following main assumptions are made : (i) the dam has a vertical upstream face and a linear elastic behaviour (i.e. no concrete cracking, degradation or sliding at the joints are considered); (ii) the dam foundation is rigid, massless and foundation radiation damping is neglected; (iii) the water in the reservoir is assumed inviscid, with its motion irrotational and limited to small amplitudes; (iv) gravity surface waves and compulsive effects are neglected; (v) effects of sediments that may be deposited at reservoir bottom can be considered; (vi) the applied ground motion acceleration is horizontal (i.e. no vertical earthquake component is applied).

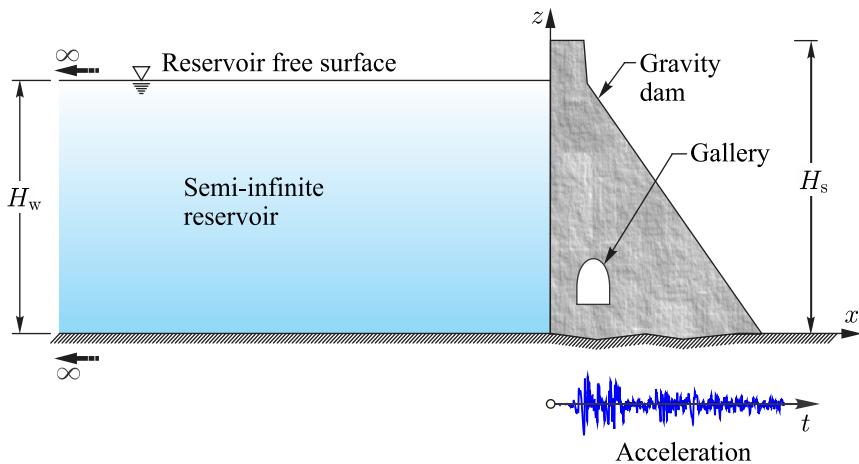


Figure 1. Typical dam-reservoir system studied.

2.2 Review of main governing equations for earthquake-excited dam-reservoir system

The equations of motion of the dam-reservoir system subjected to horizontal ground acceleration $\ddot{x}_g(t)$ can be expressed as (Fenves and Chopra 1984; Bouaanani and Lu 2009)

$$\mathbf{M} \ddot{\mathbf{U}}(t) + \mathbf{C} \dot{\mathbf{U}}(t) + \mathbf{K} \mathbf{\hat{U}}(t) = -\mathbf{M} \mathbf{1}^{(x)} \ddot{x}_g(t) + \mathbf{F}_h(t) \quad (1)$$

where $\hat{\mathbf{U}}(t)$, $\dot{\hat{\mathbf{U}}}(t)$ and $\ddot{\hat{\mathbf{U}}}(t)$ are column-vectors containing the time-history nodal displacements, velocities and accelerations of the finite element nodes of the dam relative to the ground, respectively, \mathbf{M} , \mathbf{C} and \mathbf{K} are the structure's mass, damping and stiffness matrices, respectively, $\mathbf{1}^{(x)}$ is a column-vector containing zeros except along horizontal degrees of freedom corresponding to earthquake direction, and $\mathbf{F}_h(t)$ is a column-vector representing earthquake-induced hydrodynamic forces on the upstream face of the dam.

An analytical approach consists of modeling the dam monolith as an Equivalent Single Degree of Freedom (ESDOF) system and expressing the horizontal and vertical displacements at a given point of coordinates (x, z) , i.e. $\hat{u}(x, z, t)$ and $\hat{v}(x, z, t)$, respectively, as

$$\hat{u}(x, z, t) = \sum_{j=1}^{N_s} \hat{Z}_j(t) \psi_j^{(x)}(x, z); \quad \hat{v}(x, z, t) = \sum_{j=1}^{N_s} \hat{Z}_j(t) \psi_j^{(y)}(x, z) \quad (2)$$

in which $\psi_j^{(x)}(x, z)$ and $\psi_j^{(y)}(x, z)$ denote the x - and z -components of structural mode shape ψ_j at point of coordinates (x, z) and \hat{Z}_j the associated generalized modal coordinate. It can be shown that the vector $\hat{\mathbf{Z}}(\omega)$ of the frequency-response functions of generalized modal coordinates $\hat{Z}_j(\omega)$ can be obtained by solving the system of equations (Fenves and Chopra 1984; Bouaanani and Perrault 2010)

$$\hat{\mathbf{S}}(\omega) \hat{\mathbf{Z}}(\omega) = \hat{\mathbf{Q}}(\omega) \quad (3)$$

in which the elements of the matrix $\hat{\mathbf{S}}$ and vector $\hat{\mathbf{Q}}$ are given for $m = 1 \dots N_s$ and $j = 1 \dots N_s$ as

$$\hat{S}_{j,m}(\omega) = (-\omega^2 + 2i\xi_j \omega \omega_j + \omega_j^2) M_j \delta_{j,m} + \omega^2 \vartheta_{j,m}(\omega) \quad (4)$$

$$\hat{Q}_m(\omega) = -L_m + \vartheta_{0,m}(\omega) \quad (5)$$

where ξ_j denotes the fraction of critical modal damping corresponding to mode j of the dam with empty reservoir, ω_j the natural vibration frequency at mode j . The generalized modal mass M_j and modal participation factor L_j of the dam with empty reservoir are given by (Fenves and Chopra 1984; Miquel and Bouaanani 2010)

$$M_j = \psi^T \mathbf{M} \psi; \quad L_j = \psi^T \mathbf{M} \mathbf{1}^{(x)} \quad (6)$$

and $\delta_{j,m}$ is the Kronecker symbol and where $\vartheta_{0,m}$, and $\vartheta_{j,m}$ are integral terms of analytical formulation of hydrodynamic pressure that can be expressed as

$$\vartheta_{0,m}(\omega) = \int_0^{H_w} p_0(y, \omega) \psi_m^{(x)}(z) dz; \quad \vartheta_{j,m}(\omega) = \int_0^{H_w} p_j(y, \omega) \psi_m^{(x)}(z) dz \quad (7)$$

with p_0 denoting the hydrodynamic pressure FRF at rigid dam-reservoir interface due to horizontal ground motion \ddot{x}_g and p_j the hydrodynamic pressure FRF at flexible dam-reservoir interface due to horizontal acceleration $\psi_1^{(x)}(0, z)$ of the structure (Fenves and Chopra 1984; Bouanaani and Perrault 2010). The FRFs p_0 and p_1 can be evaluated as

$$p_0(z, \omega) = -2\rho_w H_w \sum_{n=1}^{N_w} \frac{\lambda_n(\omega)^2 I_{0,n}(\omega)}{\beta_n(\omega) \kappa_n(\omega)} Y_n(z, \omega); \quad p_j(z, \omega) = -2\rho_w H_w \sum_{n=1}^{N_w} \frac{\lambda_n(\omega)^2 I_{j,n}(\omega)}{\beta_n(\omega) \kappa_n(\omega)} Y_n(z, \omega) \quad (8)$$

where N_w is the number of water (i.e. acoustical) modes included in the analysis, and λ_n and Y_n are complex-valued frequency-dependent eigenvalues and orthogonal eigenfunctions satisfying for each reservoir acoustical mode n

$$e^{2i\lambda_n(\omega)H_w} = -\frac{\lambda_n(\omega) - \omega q}{\lambda_n(\omega) + \omega q} \quad (9)$$

$$Y_n(z, \omega) = \frac{[\lambda_n(\omega) - \omega q]e^{-i\lambda_n(\omega)z} + [\lambda_n(\omega) + \omega q]e^{i\lambda_n(\omega)z}}{2\lambda_n(\omega)} \quad (10)$$

in which q is a damping coefficient defined at reservoir bottom as

$$q = \frac{\rho_w}{\rho_f C_f} = \frac{1}{C_w} \frac{1-\alpha}{1+\alpha} \quad (11)$$

where ρ_f and C_f denote the mass density and the compression wave velocity within the reservoir bottom foundation, respectively, C_w is compression wave velocity within the reservoir, and α is the wave reflection coefficient representing the portion of the wave amplitude reflected back to the reservoir. Instead of solving the transcendental equation (9) the eigenvalues λ_n can be approximated using the closed-form expression developed by Bouaanani and Perrault (2010) for moderately to highly reflective reservoir bottoms, i.e. $\alpha \geq 0.65$

$$\lambda_n(\omega) = \frac{(2n-1)\pi}{4H_w} + \sqrt{\frac{(2n-1)^2\pi^2}{(4H_w)^2} + i \frac{\omega q}{H_w}} \quad (12)$$

If full wave reflection at reservoir bottom is assumed (i.e. $\alpha = 1$), the reservoir eigenvalues λ_n are frequency-independent, simplifying to

$$\lambda_n = \frac{(2n-1)\pi}{2H_w} \quad (13)$$

In this case, hydrodynamic pressure FRFs p_0 and p_j are expressed as

$$p_0(z, \omega) = \frac{-4\rho_w}{\pi} \sum_{n=1}^{N_w} \frac{(-1)^n}{(2n-1)} \frac{\cos(\lambda_n z)}{\sqrt{\lambda_n^2 - \frac{\omega^2}{C_w^2}}}; \quad p_j(z, \omega) = 2\rho_w \sum_{n=1}^{N_w} \frac{I_{j,n}(\omega)}{\sqrt{\lambda_n^2 - \frac{\omega^2}{C_w^2}}} \cos(\lambda_n z) \quad (14)$$

The parameters β_n , κ_n , $I_{0,n}$, and $I_{j,n}$ are given by

$$\beta_n(\omega) = H_w[\lambda_n(\omega)^2 - \omega^2 q^2] + i\omega q; \quad \kappa_n(\omega) = \sqrt{\lambda_n(\omega)^2 - \frac{\omega^2}{C_w^2}} \quad (15)$$

$$I_{0,n}(\omega) = \frac{i e^{-i\lambda_n(\omega)H_w}}{\lambda_n(\omega)^2 H_w} [\lambda_n(\omega) - \omega q + \omega q e^{i\lambda_n(\omega)H_w}]; \quad I_{j,n}(\omega) = \frac{1}{H_w} \int_0^{H_w} \psi_j^{(x)}(y) Y_n(z, \omega) dy \quad (16)$$

For practical computations, the x -component of mode shape $\psi_j^{(x)}$, $j = 1 \dots N_s$, of the dry structure can be approximated by a polynomial function of order N_{ψ_j} and coefficients $a_{j,k}$ as proposed by Bouaanani and Perrault (2010). The generalized coordinates, solutions of the system of equations in equation (3), can also be obtained as proposed by Miquel and Bouaanani (2010)

$$\hat{Z}_1(\omega) = \frac{\tilde{S}_{2,2}(\omega) \tilde{Q}_1(\omega) - \tilde{S}_{1,2}(\omega) \tilde{Q}_2(\omega)}{\tilde{S}_{1,1}(\omega) \tilde{S}_{2,2}(\omega) - \tilde{S}_{1,2}^2(\omega)} \quad (17)$$

$$\hat{Z}_j(\omega) = \frac{\tilde{S}_{j-1,j-1}(\omega) \tilde{Q}_j(\omega) - \tilde{S}_{j-1,j}(\omega) \tilde{Q}_{j-1}(\omega)}{\tilde{S}_{j-1,j-1}(\omega) \tilde{S}_{j,j}(\omega) - \tilde{S}_{j-1,j}^2(\omega)} \quad \text{for } j = 2 \dots N_s \quad (18)$$

We note that equations (17) and (18) are exact when only two modes are included in the analysis and approximations otherwise.

The generalized coordinates $Z_j(\omega)$ corresponding to the dam with empty reservoir can be obtained as

$$Z_j(\omega) = \frac{L_j}{M_j} \times \frac{1}{(-\omega^2 + 2i\xi_j \omega \omega_j + \omega_j^2)} \quad (19)$$

A new accelerogram $a_g^{(j)}(t)$ is defined for each mode j as

$$a_g^{(j)}(t) = \frac{1}{2\pi} \int_{-\infty}^{\infty} a_g^{(j)}(\omega) e^{i\omega t} d\omega, \quad j = 1 \dots N_s \quad (20)$$

where $a_g^{(j)}(\omega)$ is obtained from the original ground motion acceleration $\ddot{x}_g(\omega)$ as

$$a_g^{(j)}(\omega) = \ddot{x}_g(\omega) \frac{\hat{Z}_j(\omega)}{Z_j(\omega)}, \quad j = 1 \dots N_s \quad (21)$$

We show that the generalized coordinates $\hat{Z}_j(t)$ can also be obtained by solving the decoupled equations

$$\ddot{\hat{Z}}_j(t) + \frac{4\pi}{T_j} \xi_j \dot{\hat{Z}}_j(t) + \frac{4\pi^2}{T_j^2} \hat{Z}_j(t) = -\frac{L_j}{M_j} a_g^{(j)}(t), \quad j = 1 \dots N_s \quad (22)$$

In other terms, the solutions $\tilde{Z}_j(t)$ can be obtained for each mode $j = 1 \dots N_s$ as the time-history relative displacements of Single Degree of Freedom (SDOF) systems with mass M_j given by equation (6), stiffness $K_j = 4\pi^2 M_j / T_j^2$ and viscous damping $C_j = 4\pi \xi_j M_j / T_j$ subjected to ground motion acceleration $L_j a_g^{(j)}(t)$. This approach is illustrated in Figure 2.

The maximum absolute seismic relative displacement of the dam-reservoir corresponding to a given vibration mode $j = 1 \dots N_s$ can then be evaluated as

$$|\hat{u}_j(x, z, t)|^{(\max)} = \frac{L_j}{M_j} \frac{T_j^2}{4\pi^2} S_A^{[a_g^{(j)}]}(T_j, \xi_j) \psi_j^{(x)}(x, z) \quad (23)$$

in which $S_A^{[a_g^{(j)}]}(T_j, \xi_j)$ denote pseudo-acceleration of ground motion $a_g^{(j)}(t)$ at the period T_j of the dam with empty reservoir, considering a modal viscous damping ξ_j .

The heightwise distribution of the equivalent lateral static forces including hydrodynamic effects corresponding to each higher mode j of the dam can then be obtained as

$$\hat{f}_j(z) = \frac{L_j}{M_j} \mu_s(z) S_A^{[a_g^{(j)}]}(T_j, \xi_j) \psi_j^{(x)}(z) \quad (24)$$

with $\mu_s(z)$ denoting the mass per unit height of the structure. These equivalent static forces can be applied to the finite element model of a dry dam to approximate the maximum contribution $\tilde{r}_j^{(\max)}$ of each mode j to a given key response indicator \tilde{r} . When applicable, the absolute maximum total seismic response can then be obtained using a combination rule such as the Square Root of the Sum of the Squares (SRSS)

$$|\tilde{r}|^{(\max)} = \sqrt{\sum_{j=1}^{N_s} [|\tilde{r}_j|^{(\max)}]^2} \quad (25)$$

The maximum absolute seismic relative displacement and heightwise distribution of the equivalent lateral static forces corresponding to the dam with empty reservoir subjected to original ground motion acceleration, can be expressed for each higher mode j of the dam as

$$|u_j(z, t)|^{(\max)} = \frac{L_j}{M_j} \frac{T_j^2}{4\pi^2} S_A^{[\ddot{x}_g]}(T_j, \xi_j) \psi_j^{(x)}(z) \quad (26)$$

$$f_j(y) = \frac{L_j}{M_j} \mu_s(z) S_A^{[\ddot{x}_g]}(T_j, \xi_j) \psi_j^{(x)}(z) \quad (27)$$

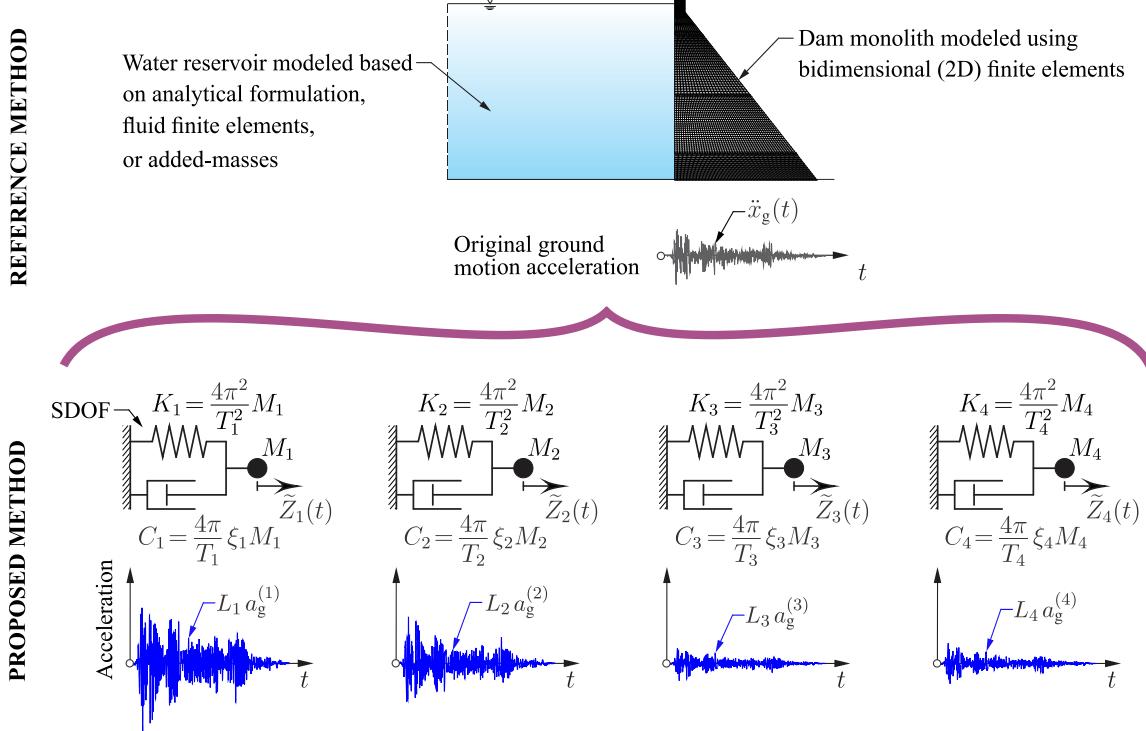


Figure 2. Reference and proposed methods

2.3 Review of main governing equations for an earthquake-excited structure appurtenant to the dam

Seismic demands at a given point P of coordinates (x, z) of the dam can be evaluated by studying the dynamic response of SDOF systems with various vibration frequencies f_s attached to point P, while the dam is excited by ground acceleration applied at its base. As illustrated in Figure 3, the SDOF systems, can represent dam-supported appurtenant structures or equipment, with mass m_s , stiffness k_s and viscous damping c_s .

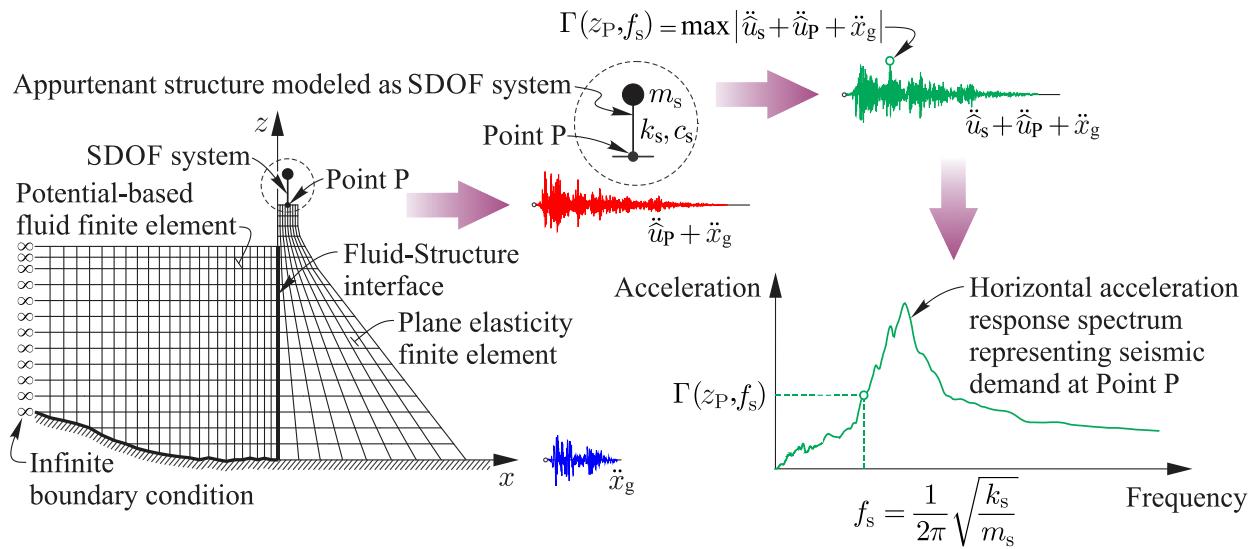


Figure 3. Illustration of the computation of floor acceleration spectra at a given point P of a gravity dam

The mass of the appurtenant SDOF system is assumed to be too light so that its dynamic response does not affect that of the dam monolith. The equation of motion of the appurtenant SDOF can be written as

$$m_s \ddot{u}_s + c_s \dot{u}_s + k_s u_s = -m_s (\ddot{u}_P + \ddot{x}_g) \quad (28)$$

where \ddot{u}_P denotes the horizontal acceleration at point P of the dam relative to dam base, and \hat{u}_s , \dot{u}_s and \ddot{u}_s the horizontal displacement, horizontal velocity and horizontal acceleration of the secondary SDOF system relative to point P, respectively. The seismic acceleration demand $\Gamma(z_P)$, at a point P of coordinate z_P , is defined hereafter as the maximum absolute acceleration response $|\ddot{u}_s + \ddot{u}_P + \ddot{x}_g|$ of the secondary SDOF system for a given vibration frequency $f_s = 1/(2\pi)\sqrt{k_s/m_s}$ and damping coefficient c_s or equivalent damping ratio $\xi_s = c_s/(4\pi m_s f_s)$. We denote by $\Gamma^*(z_P)$ the maximum acceleration at a point P of coordinate z_P over the whole range of frequencies f_s considered, i.e. from 0 to 50 Hz in this paper. The acceleration \ddot{u}_P at point P relative to the dam base required in equation (28) can be obtained using the methods proposed above in previous section.

3 Numerical examples

3.1 Studied dam-reservoir systems and selected ground motions

Two gravity dam monoliths differing by their size are used next to illustrate the application of the methods proposed above. The two dams, referred to hereafter as D35 and D90, have heights H_s of 35 m, and 90 m, respectively, to assess flexibility effects. They impound reservoirs with heights H_w of 32 m and 86 m, respectively. Figure 4 illustrates the dimensions of both dam-reservoir systems. A mass density $\rho_s = 2400 \text{ kg/m}^3$, a Poisson's ratio $\nu = 0.2$ and a modulus of elasticity $E_s = 25 \text{ GPa}$ are assumed as concrete material properties for each dam. A water mass density of $\rho_w = 1000 \text{ kg/m}^3$ is considered with pressure wave velocity of $C_w = 1440 \text{ m/s}$ when water compressibility effects are included in the analysis.

The dam monoliths are discretized into 4-node plane strain finite elements using the software ADINA (2022) as shown in Figure 4. Figures 5 and 6 illustrate the first five modes as well as the corresponding vibration periods, i.e. T_1 to T_5 of the two dams with empty reservoirs, respectively. Figures 5 and 6 also show the horizontal and vertical effective modal masses, i.e. $\Lambda_j^{(x)}$ and $\Lambda_j^{(z)}$, respectively, reflecting the relative importance of the contribution of each mode $j = 1 \dots 5$ to the global seismic response of the dam monoliths. For both dams, it is observed that the fundamental and second modes predominate the seismic response and that the third mode is essentially vertical.

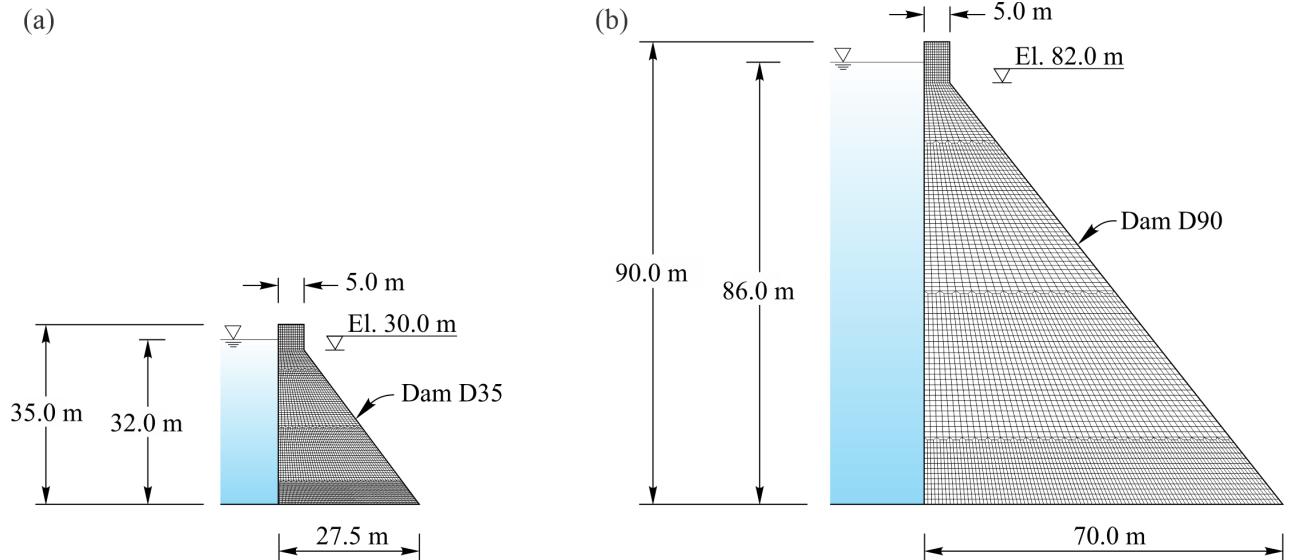


Figure 4. Dimensions and solid finite element meshes of the studied dam-reservoir systems: (a) 35 m height gravity dam monolith (D35), (b) 90 m height gravity dam monolith (D90).

The dam monoliths are subjected to the horizontal components of ground motions recorded during the Imperial Valley earthquake (1940) at station El Centro and Nahanni earthquake (1985) at station Iverson. These ground motions are selected to illustrate the influence of differences in time-history signature and frequency content, as shown in Figure 7. A constant 5 % modal viscous damping ratio is considered for all the vibration modes of the dam with empty reservoir, i.e. $\xi_j = 0.05$ for $j = 1$ to 5.

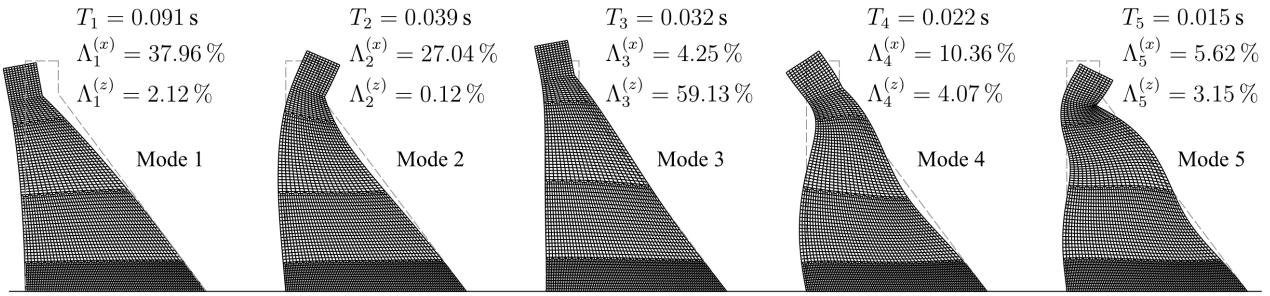


Figure 5. Five first mode shapes and corresponding vibration periods and effective modal masses of the 35 m high gravity dam monolith (D35).

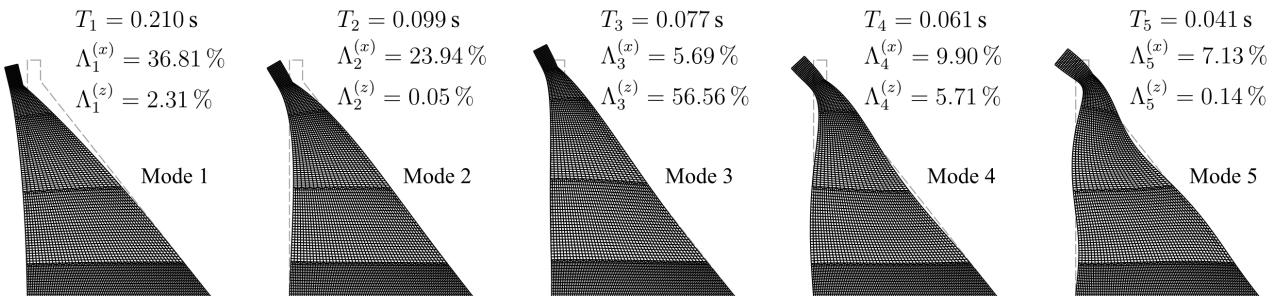


Figure 6. Five first mode shapes and corresponding vibration periods and effective modal masses of the 90 m high gravity dam monolith (D90).

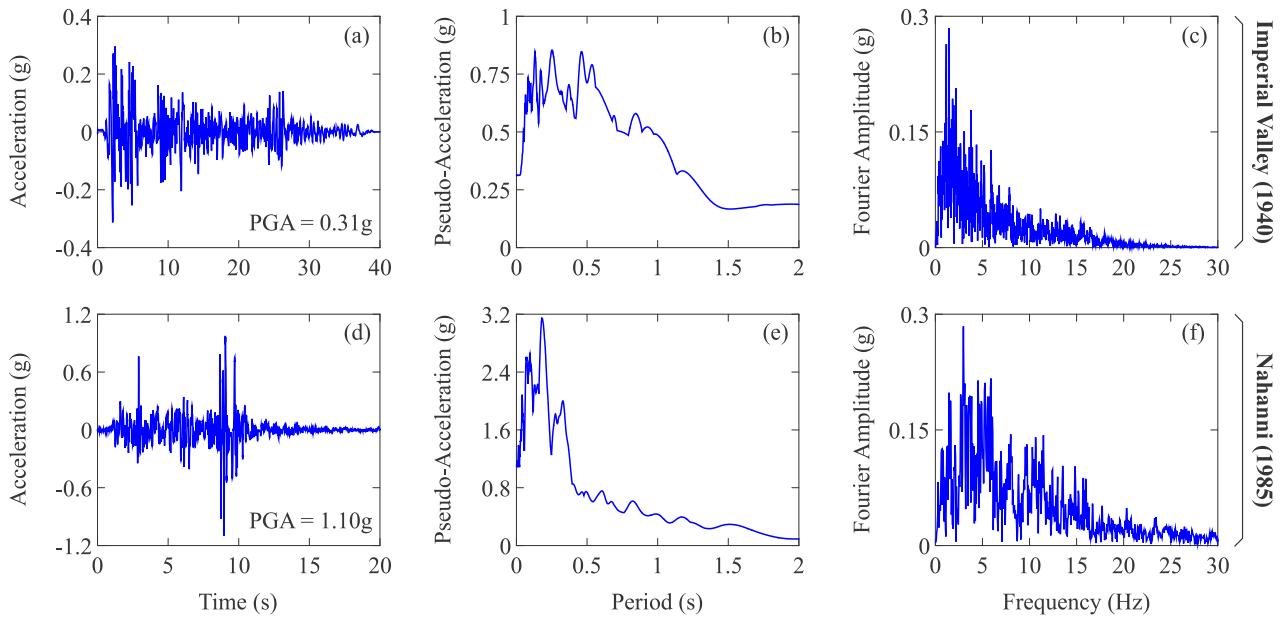


Figure 7. Time-history accelerations, pseudo-acceleration response spectra and Fourier amplitudes of the ground motions selected for this study: (a) to (c) Imperial Valley (1940) earthquake; (d) to (f) Nahanni (1985) earthquake.

The modified accelerograms corresponding to the two earthquake components mentioned earlier are displayed in Figure 8 for both dams D35 and D90. In the same figure, the original ground accelerations are also presented for comparison. Notably, the amplitudes of the modified accelerations are consistently greater than those of the original accelerograms for both dams. It also illustrates that the amplification of modified

ground motions becomes more obvious as the dam's flexibility increases. Additionally, it can be deduced, as anticipated, that the frequency content of the modified accelerations differs from that of the original accelerograms and that such alterations depend on the specific dam being studied, reservoir water level as well as the characteristics of the original ground motion.

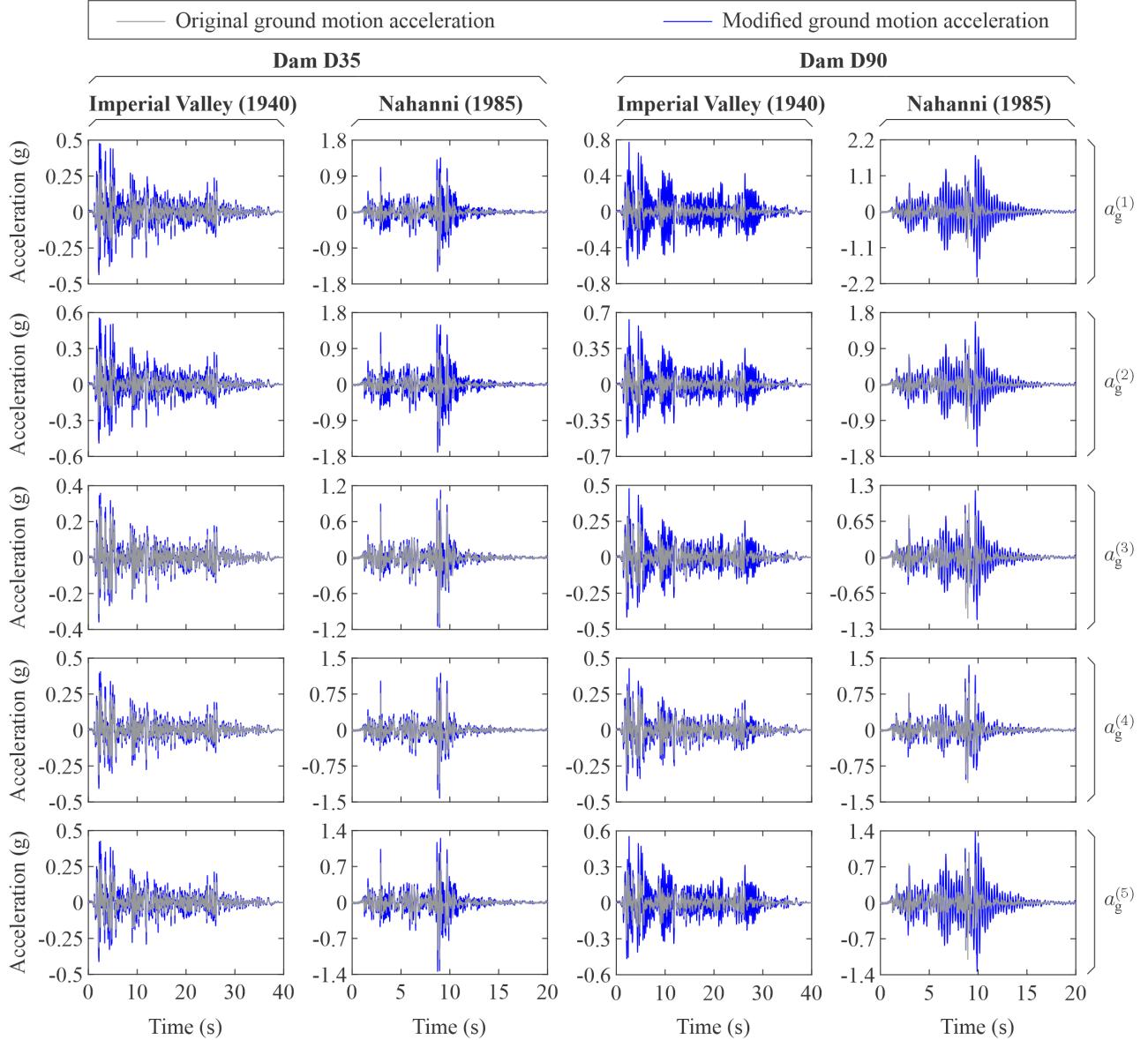


Figure 8. Original and modified Imperial Valley (1940) and Nahanni (1985) ground motion accelerations corresponding to dams D35 and D90 and to vibration modes 1 to 5 assuming water to be compressible.

The 5%-damped pseudo-acceleration response for the modified ground accelerations are then obtained for the first five vibration periods T_1 to T_5 , i.e. $S_A^{[a_g^{(j)}]}(T_j, 5\%)$, $j = 1 \dots 5$. In Figure 9, these results are presented with values highlighted in blue. The pseudo-spectral accelerations of the original ground motions for the corresponding vibration periods are also shown, with values marked in black. It is seen that the acceleration demands for the fundamental modes of dams D35 and D90 with empty reservoirs are approximately equal when subjected to the Imperial Valley ground motion, specifically 0.67 and 0.66, respectively. These acceleration demands significantly increase by 46 %, i.e. $(0.98 - 0.67)/0.67 \times 100$ for dam D35 and 115 %, i.e. $(1.42 - 0.66)/0.66 \times 100$ for dam D90 when hydrodynamic effects are included. The larger amplification associated with Dam D90 is mainly due to its higher flexibility and associated hydrodynamic pressures in the reservoir compared to dam D35.

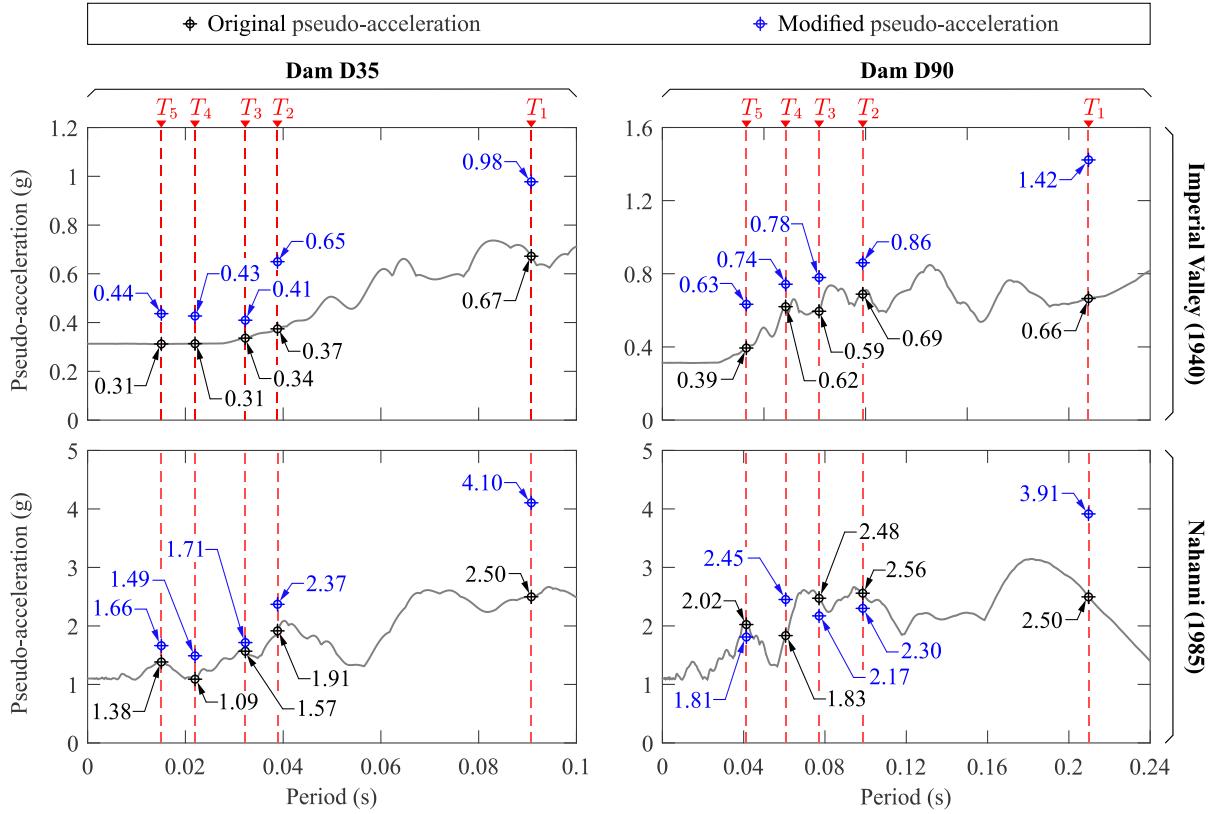


Figure 9. 5%-damped pseudo-acceleration response spectra of the original ground motion and the modified ground motions of dams D35 and D90 obtained assuming compressible water in the reservoir.

Figure 10 present results of the maximum absolute horizontal displacements obtained along the height of the upstream faces of dam monolith D90 under the effects of the considered ground motions. It illustrates the horizontal displacement for each vibration mode of the dam using proposed response spectrum analysis (RSA). The total maximum absolute horizontal relative displacements are also shown in the last columns titled *Total*. These total responses are obtained using two approaches: (i) a direct method consisting of the summation of the modal responses of horizontal relative displacements (i.e. algebraic values with signs) and then the computation of the maximum value of the resulting summed response, and (ii) the SRSS method consisting of summing the absolute values of the maximum horizontal relative displacements obtained for each mode. As expected, the results provided by the direct method are found to be identical to those of the reference solution. For the two earthquakes considered, it is seen that the SRSS method yields larger values than the direct method at the dam crest and slightly below (i.e. $y/H_s > \approx 0.75$). At lower heights, the total maximum responses obtained using the SRSS method are practically the same as the direct method or slightly smaller. The maximum absolute horizontal displacements of the dam with empty reservoir, also shown in Figure 10 for comparison purposes, are found to be generally lower than those with the reservoir. The time-history relative displacements at any location of the dams can be obtained using the proposed method as described previously. Figure 11 shows the time-history relative displacements at the crest of dam D35 and D90 subjected Imperial Valley (1940) and Nahanni (1985) ground motion accelerations. For comparison purposes, the results are shown for the dams without reservoirs and including compressible water effects. These results are identical to those obtained using the reference solution. The proposed approach can also be used efficiently to evaluate the seismic response of dam appurtenant structures. As an example, Figure 12 compares the “floor” response spectra obtained at the crest of both dams considering an added mass formulation to those corresponding to a fully reflective reservoir containing compressible water. In this figure, the seismic demands are normalized by the peak horizontal ground acceleration (PHGA). The acceleration demands in the dry dams are also shown for comparison purposes. These results demonstrate the sensitivity of acceleration demands on appurtenant structures to reservoir modelling assumptions and dam size.

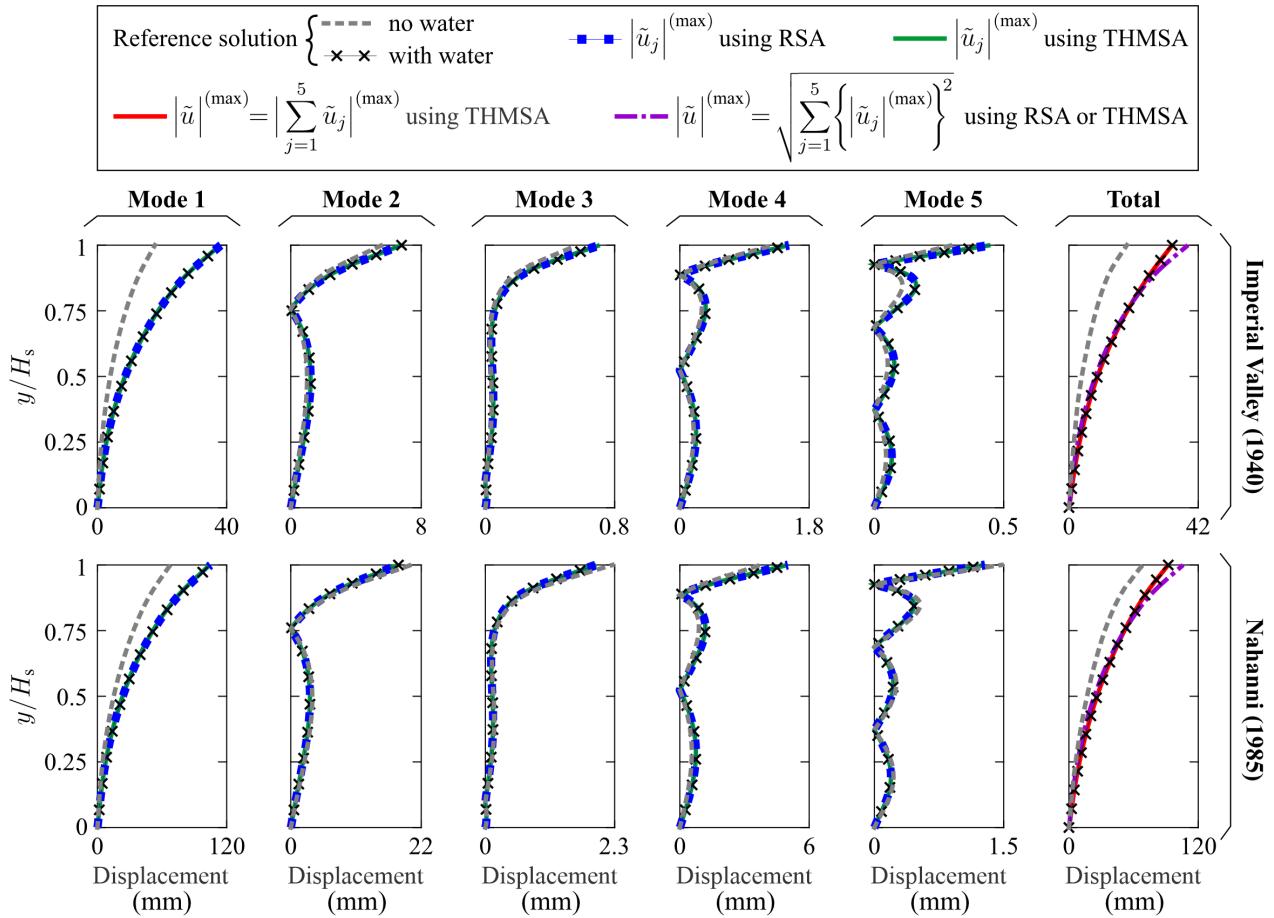


Figure 10. Absolute maximum displacements along the height of the upstream face of the 90 m high dam (D90) determined for each vibration mode using modified ground motion accelerations.

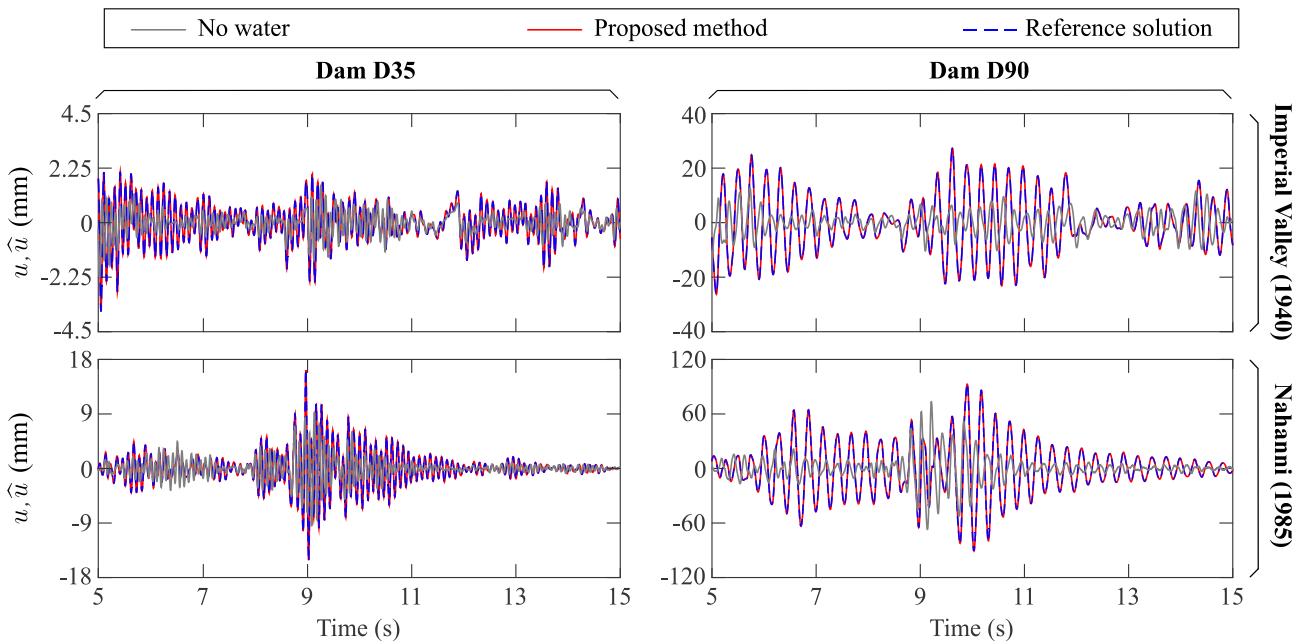


Figure 11. Time-history horizontal relative displacements at the crest of dams D35 and D90 with impounded reservoir obtained for each vibration mode using the proposed method assuming water to be compressible.

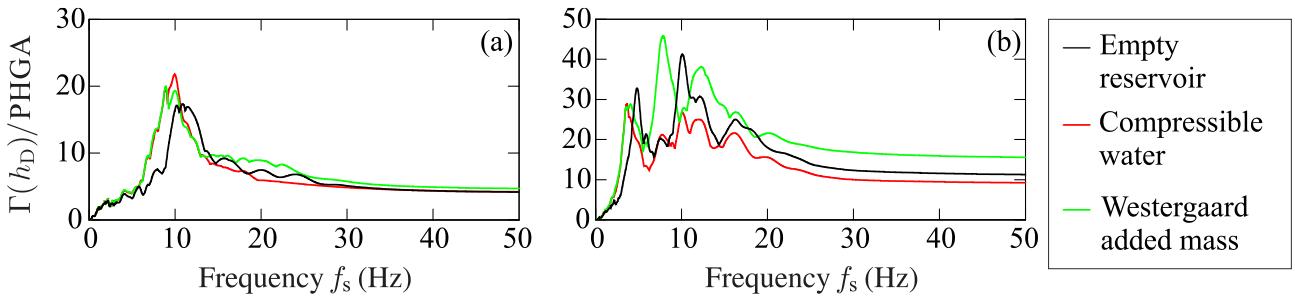


Figure 12. Effects of water modelling assumptions and dam size on “floor” response spectra at the crest of dams D35 and D90 subjected to Imperial Valley (1940) earthquake: (a) Dam D35; and (d) Dam D90.

4 Conclusions

This paper proposed new methods to evaluate the seismic response of gravity dam-reservoir systems through dynamic modal superposition and response spectrum analyses. The main originality of the developed techniques is the inclusion of earthquake-induced reservoir effects into modified versions of the original ground motion acceleration and its response spectrum. The modified ground motion time-history and spectral accelerations can then be applied directly to the dam with empty reservoir, thus eliminating the need for specialized software accounting for fluid-structure interaction dynamic effects. In addition to this practical aspect, the proposed approach allows the evaluation and analysis of the impact of any specific vibration mode on the total seismic response of the gravity dam studied. For example, coupled structural flexibility and hydrodynamic effects due to each vibration mode can be accurately assessed in lieu of the approximate results generally given by the conventional static correction method. The application of the proposed approach was illustrated through examples of two typical gravity dam-reservoir systems subjected to two earthquakes. The obtained results were shown to be in excellent agreement with the classical reference solutions.

Acknowledgements

The authors would like to acknowledge the financial support of the Canada Research Chairs and the Natural Sciences and Engineering Research Council of Canada (NSERC).

5 References

- Bouaanani, N. and Lu, F. Y., (2009). Assessment of potential-based fluid finite elements for seismic analysis of dam–reservoir systems. *Computers & Structures* 87, 206–224.
- Bouaanani, N. and Perrault, C., (2010). Practical formulas for frequency domain analysis of earthquake induced dam-reservoir interaction. *Journal of Engineering Mechanics* 136, 107–119.
- Chopra, A. K., (1967). Hydrodynamic pressures on dams during earthquakes. *Journal of the Engineering Mechanics Division* 93, 205–223.
- Clough Ray W, P. J., (1975). Dynamics of Structures. McGraw-Hill Book Company, New York, 584-588 pp.
- Fenves, G. L. and Chopra, A. K., (1984). Earthquake analysis and response of concrete gravity dams. University of California, Earthquake Engineering Research Center.
- Fenves, G. L. and Chopra, A. K., (1985). Simplified analysis for earthquake resistant design of concrete gravity dams. University of California, Earthquake Engineering Research Center.
- Hariri-Ardebili, M. A. and Saouma, V. E., (2018). Random response spectrum analysis of gravity dam classes: simplified, practical, and fast approach. *Earthquake Spectra* 34, 941–975.
- Maity, D. and Bhattacharyya, S., (1999). Time-domain analysis of infinite reservoir by finite element method using a novel far-boundary condition. *Finite Elements in Analysis and Design* 32, 85–96.
- Miquel, B. and Bouaanani, N., (2010). Simplified evaluation of the vibration period and seismic response of gravity dam–water systems. *Engineering structures* 32, 2488–2502.
- Miquel, B. and Bouaanani, N., (2013). Accounting for earthquake-induced dam-reservoir interaction using modified accelerograms. *Journal of Structural Engineering* 139, 1608–1617.
- Westergaard, H. M., (1933). Water pressures on dams during earthquakes. *Transactions of the American society of Civil Engineers* 98, 418–433.

THE SEISMIC SAFETY ASSESSMENT OF A MULTIPLE ARCH DAM

M. Colombo¹ & A. Frigerio²

¹ Researcher, Ricerca sul Sistema Energetico - RSE S.p.A., Milan, Italy, martina.colombo@rse-web.it

² Deputy Director, Ricerca sul Sistema Energetico - RSE S.p.A., Milan, Italy

Colombo Martina - Ricerca sul Sistema Energetico - RSE S.p.A., Milan, Italy

Frigerio Antonella - Ricerca sul Sistema Energetico - RSE S.p.A., Milan, Italy

Corresponding author: martina.colombo@rse-web.it

Abstract: As in many European countries, today in Italy there are few possibilities to design and build new dams. In particular, the construction of buttress (both solid or hollow) or multiple arch/slab dams is practically abandoned because they have shown in time several problems, namely cracks. On the other hand, there is a strong need to keep existing dams in safe service conditions, considering also the effects of seismic loadings, not foreseen during the design.

In order to evaluate the health of an existing infrastructure, it is necessary to define the external acting forces and to analyse the structural response towards these loads by means of mathematical models of the dam-rock-reservoir system.

The Italian standard (D.M. 26 June 2014) is indeed focused into this aspect by suggesting the development of a reference dam model (e.g., based on the finite element method), able to analyse the response of these hydraulic structures under static and seismic actions, higher than those applied in the design phase, thus leading to more stringent conditions.

Therefore, the finite element models are used to evaluate and predict possible structural deterioration, which can imply abnormal behaviour and consequences, such as, for example, cracks and displacements due to environmental conditions (thermal or chemical phenomena) and aging.

First, this article presents an overview of the problems concerning buttress or multiple arch/slab dams and highlights the importance of the numerical models, which allow to study their safety under seismic loadings. Then, finite element analysis of an Italian multiple arch dam, subject to static and seismic loads, is presented. The response of this hydraulic structure is studied considering different results: principal stresses, compared with standard limits; sliding coefficient of horizontal sections (defined as the ratio between horizontal and vertical forces), which must both be less than one; eccentric axial force analysis.

1. Introduction

In Europe the need to guarantee the safety of existing dams is strongly felt. Indeed, a service life that often reaches or exceeds 5/6 decades can lead to possible problems of aging.

The design, construction and supervision of dams are regulated by current national and regional regulations, considering the hydraulic structure dimension (Evangelisti, 1982).

In ancient times dams were mainly built for the storage of water intended for irrigation and water supply. With the civilization development, these needs also extended to flood and sediments control, navigation, aqueduct support and, above all, hydropower generation (e.g., in Italy hydropower is still the main renewable source and accounts for 15-17% of the national electricity production, Figure 1). The multiple use of water of dam reservoirs represents a necessity, but also an opportunity, for countries development, as the population would be able to obtain both domestic and economic benefits from a single investment. The need to exploit the water resources for the energy production accelerated the construction of increasingly large dams (Figure 2). Italy, for instance, went from a dozen of dams at the end of the nineteenth century to almost 400 large dams in the first half of the twentieth century. At present, the large dams in operation are 531.

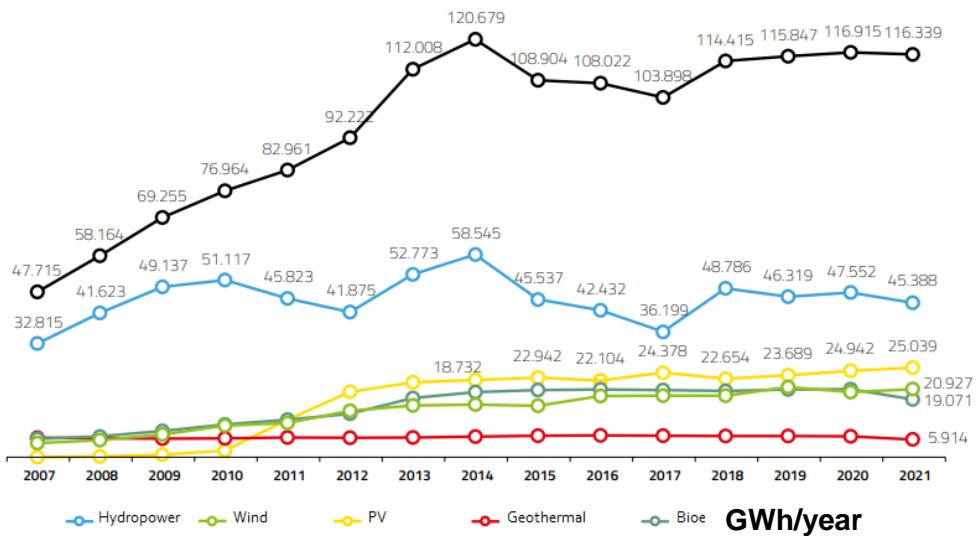


Figure 1. Annual hydroelectric power production in Italy.



Legend

The small green point means 1 dam; the number reported in all the other points stands for the number of dams in that area.

NORTH = 46 %

CENTER = 32 %

SOUTH = 32 %

Total 531 dams

Figure 2. Location of dams in Italy.

Existing dams are controlled through monitoring systems and periodic inspections, with the aim of promptly identifying any anomalous behaviour, which must subsequently be interpreted to evaluate the causes (Brownjohn, 2007; Ardito et al., 2008; Bukenya et al., 2014). The physical-mathematical modelling of a dam-rock-reservoir system is also part of the investigations. Under known external actions, the comparison between the structural response of the finite element model (which predicts the expected effects) and the actual dam response described in terms of monitoring data represents a fundamental interpretation of real phenomena (Mirzabozorg et al., 2014; Colombo et al., 2015; Colombo et al., 2016).

There are several types of dams, defined according to the Italian regulation (DM2014): gravity, arch, slab/arch, earth fill, mixed. The first slab/arch dams were built in the first twenty-five years of the 1900. The collapse a mixed gravity and multiple arches dam (Gleno dam, Figure 3) in 1923 led to build more massive hydraulic structures (e.g., gravity dams).

In this article an overview of the problems concerning buttress or multiple arch/slab dams is reported. Furthermore, the importance of the numerical models to evaluate their safety under seismic loadings is shown. Finally, finite element analysis of an Italian multiple arch dam, subject to static and seismic loads, is presented.



Figure 3. Gleno dam (Italy): downstream face view after construction (left) [Source: Gleno Archive] and upstream face view after collapse (right).

2. The main problems affecting buttress and slab/arch dams

Generally, the crack pattern of dams is related to thermal phenomena that could occur already during the phase construction, particularly in the case of buttress and slab/arch structures.

The aging of materials, due to environmental conditions or chemical phenomena, such as the alkali-silica reaction (Ingraffea, 1990; Thomas et al., 2013), shown in Figure 4, and the corrosion of steel rebars in slabs and multiple arches represent other issues. In addition, also the quality and the porosity of the material (concrete) contribute to aggravate its deterioration condition. Finally, other problems are related to possible loss of resistance to sliding (caused by the development of high uplift pressures), leakage through the upstream face and low resilience to seismic actions.

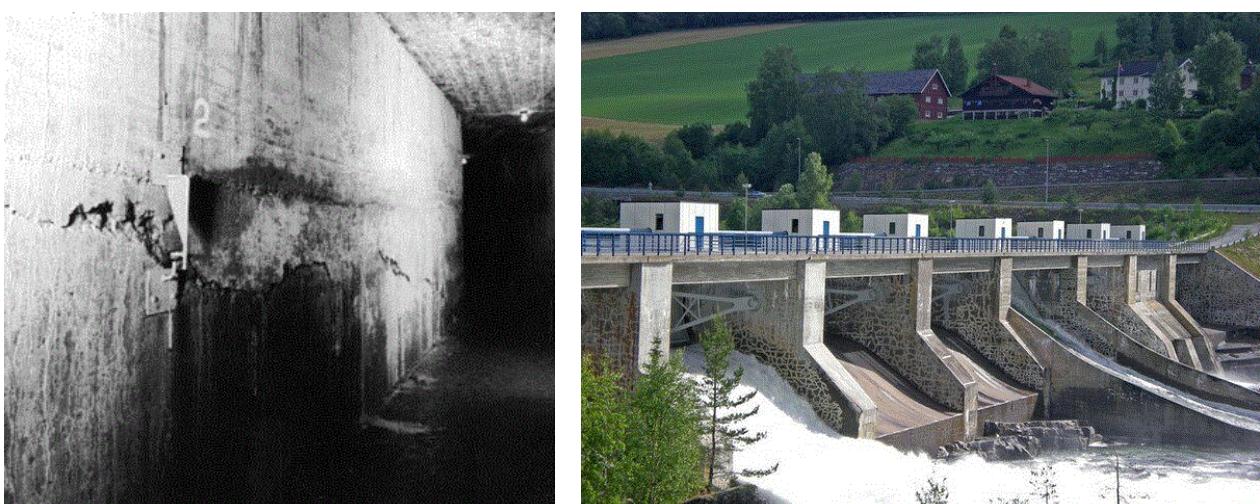


Figure 4. Example of crack pattern due to alkali-silica reaction: Fontana dam (inspection gallery by Ingraffea, 1990); dam in Norway by Thomas et al., 2013.

About buttress and slab/arch dams, in Italy there are 1 slab dam, 8 multiple arch dams, 13 buttress dams and 15 hollow gravity dams, all of them built in the last century (Figure 5). For this reason, some rehabilitation works have been required to respect the new regulations and guarantee their safe operation over time.

The Italian Committee on Large Dams (ITCOLD) has set up the Working Group "Behaviour, problems, rehabilitation of hollow gravity, buttress and multiple arch/slab dams", whose main topics refers to control and monitoring systems, criteria for safety assessment, rehabilitation works. Several case histories have been analysed by this Working Group: e.g., Ancipa dam (a hollow gravity infrastructure, located in Sicily and operated by ENEL Green Power), in which a steel insulating shield was built on the downstream face to reduce the seasonal thermal gradients and slow down the propagation of cracks in the buttresses; San Giacomo di Fraele dam (a buttress infrastructure, located in Lombardy and operated by A2A), for which the partial closure of the buttresses with a sloped slab was created to reduce the effects of a reservoir located downstream the dam, thus prevent sliding (Figure 6).

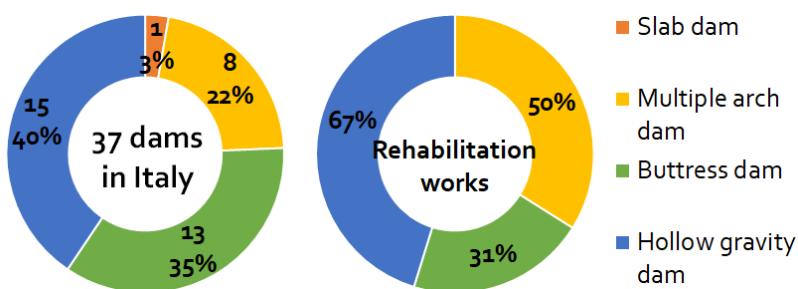


Figure 5. Number of dams belonging to slab/multiple arch, buttress and hollow gravity dams in Italy and percentage of structures that underwent rehabilitation works according to their type.



Figure 6. Ancipa dam: construction of the steel insulating shield on the downstream face (left). San Giacomo di Fraele dam: weighting of the downstream lower part (right).

3. The importance of numerical modeling

For assessing the safety of strategic hydraulic structures (e.g., dams) and understanding the influence of several impact phenomena (temperature, humidity, degradation of materials), numerical modelling, in which different loading conditions and possible crack patterns are implemented, plays a fundamental role.

Advanced numerical modelling (e.g., finite element models, FEM) can help to remove the conservative assumptions of simple approaches and to describe with greater accuracy the real behaviour of dams. Thus, operating restrictions that directly impact on the clean energy production of these power plants and their storage capacity can be prevented, in such a way to respect the European Union energy and climate targets.

Indeed, hydroelectric power plants are essential in the transition towards a decarbonized energy system, thanks to their capacity for delivering balancing services to the power network. Furthermore, the effects of long periods of drought or flooding can be mitigated thanks to the storage capacity of dams preventing catastrophes for agriculture and society at large. Finally, numerical modelling can be used for diagnosis of possible damage in aged structures as well as to support design engineers in the choice of the most effective rehabilitation solution for keeping the structures in safety conditions over time.

4. Case history of Molato dam (Italy)

Molato dam, operated by the *Consorzio di Bonifica di Piacenza*, blocks Tidone River in Emilia-Romagna (Italy) and provides water for irrigation with its total storage capacity of 13 Mm³. It is a reinforced concrete multiple arch and buttress dam (Figure 7), built between 1921 and 1928, with two gravity lateral abutments, 55 m high and a crest length of 335 m.

The dam consists in 17 reinforced concrete arches, inclined 45° to the horizontal plane, resting upon intermediate buttresses, which are 10 m apart (connected by reinforced concrete T-shape beams in the transversal direction, Figure 8) and have a variable thickness from 2.40 m at the base to 0.90 m at the top (ANIDEL, 1953). The arches have a circular section with a constant extrados radius of 5 m and a thickness which originally varied from 1.20 m at the base to 0.45 m at the top. In the 80s all the arches were thickened up to 2.40 m at the base e 0.90 m at the top.

At the base of the arches and the buttresses a concrete slab which covers and protects the rock foundation has been built in the period 2002-2005.

In the central part of the dam, there is a concrete spillway consisting of three sluices 8.80 m wide, controlled by automatic balance sector gates.

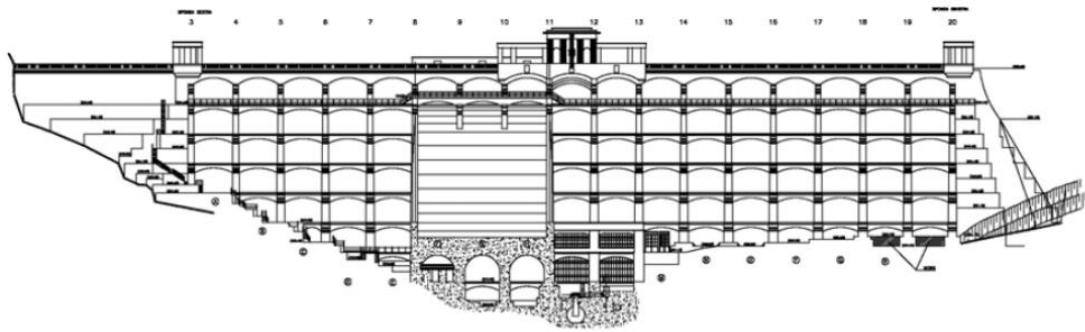


Figure 7. Downstream face views of Molato dam.

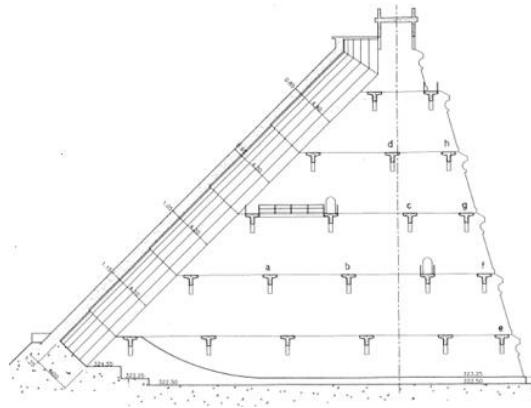


Figure 8. Reinforced concrete T-shape beams, connecting dam buttresses.

4.1. Finite element model

The seismic response of Molato dam was evaluated, according to Italian standard (DM2014; DM2018), by means of a numerical model capable of taking into account both the non-linear behaviour of the concrete and the dam-rock foundation interface.

The finite element model (Figure 9), used in the seismic reassessment of Molato dam, consists of solid elements for buttresses, slabs, concrete weightings among spans, gravity shoulders and rock foundation; beam elements for the T-shaped beams; shell elements for the multiple arches; acoustic elements for the reservoir (the mesh of the reservoir domain was obtained by extruding the dam upstream face over a length three times the dam height and was connected only with the upstream dam elements).

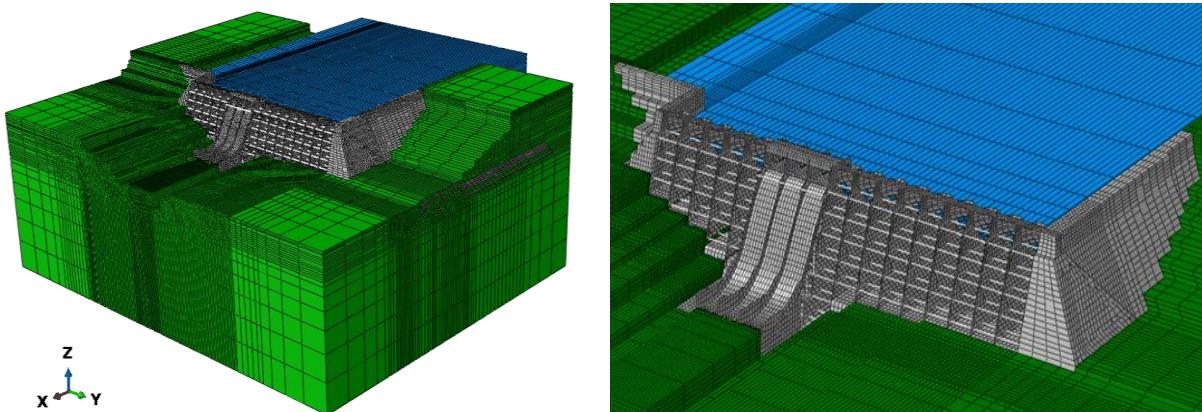


Figure 9. Finite element model of the dam-rock-reservoir system.

A Mohr-Coulomb frictional model was assigned to the dam-rock foundation interface. A shell to solid coupling interaction was adopted to join shell elements to solid.

The nonlinear concrete behaviour was simulated using an elasto-plastic damage constitutive model (Lee & Fenves, 1988), while for the rock foundation a linear elastic behaviour was assumed.

The dynamic fluid-structure interaction was modelled according to the classic approach of the mechanical-acoustic coupling suggested by Zienkiewicz, 1977. The acoustic approach allows to consider both the compressibility of water and the damping effects at the boundary of the fluid domain.

The traditional massless approach (Clough, 1980), in which rock foundation is assumed without mass, was adopted. This method is somewhat conservative because it does not take into account the energy dissipated in the rock foundation during the seismic motion.

4.2. Seismic analyses

The seismic structural response of Molato dam was evaluated performing time history analyses and applying the following forces: gravity load, hydrostatic pressure and corresponding uplift (for three different water level conditions: maximum level of regulation, intermediate level and empty reservoir), winter thermal load (which represents the worst condition) and seismic forces.

The seismic actions for the various limit states (serviceability and the ultimate limit states, according to DM2014) were defined starting from the "basic seismic hazard" of the site where the dam is located. Natural accelerogram terns were chosen: in Figure 10 the upstream-downstream (X), shoulder-to-shoulder (Y) and vertical direction (Z) of the accelerogram tern called SADR is shown.

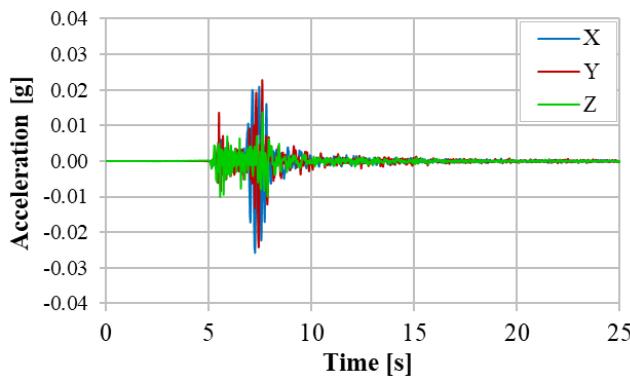


Figure 10. The accelerogram tern called SADR.

According to the analysis type and the structural elements, different criterions were followed.

Referring to the stress state, according to US Army Corps of Engineers (USACE, 2007), in arch structures the following parameters have to be controlled: the maximum principal stresses can be up to twice the tensile strength of concrete (equal to 1.8 MPa), but only up to a fifth of the total area of the upstream and downstream face and for a cumulative duration not exceeding 0.4 s (Figure 11).

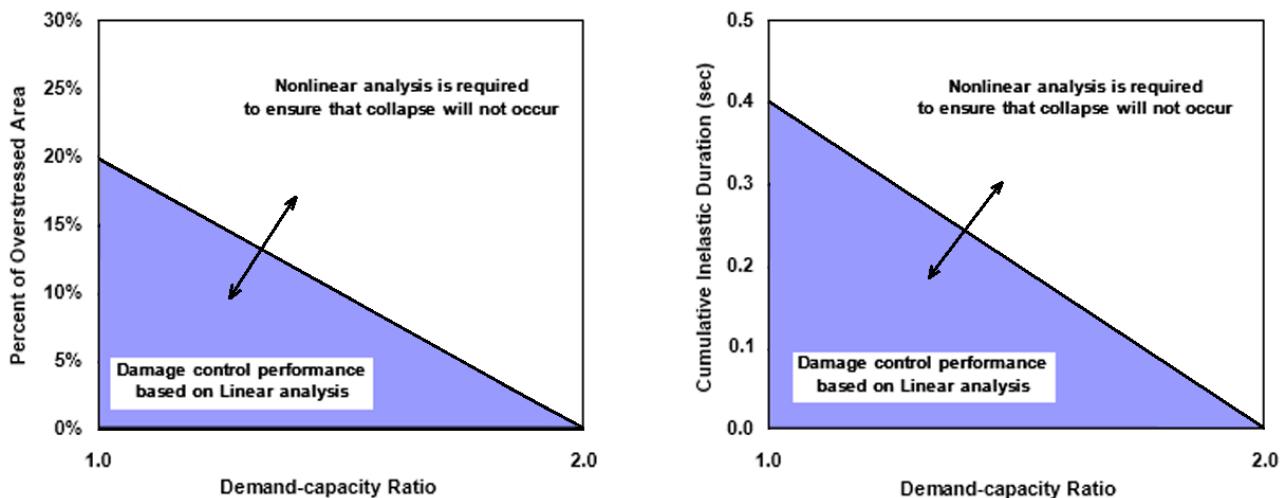


Figure 11. Prescription about seismic analyses in arch dam, according to USACE, 2007.

Considering the accelerogram tern called SADR (Fig. 10), in Figure 12 the maximum principal stresses envelop on the upstream face, obtained considering the maximum level of reservoir, is shown. This parameter does not overcome the tensile limit defined according to USACE (3.6 MPa) in all the multiple arches.

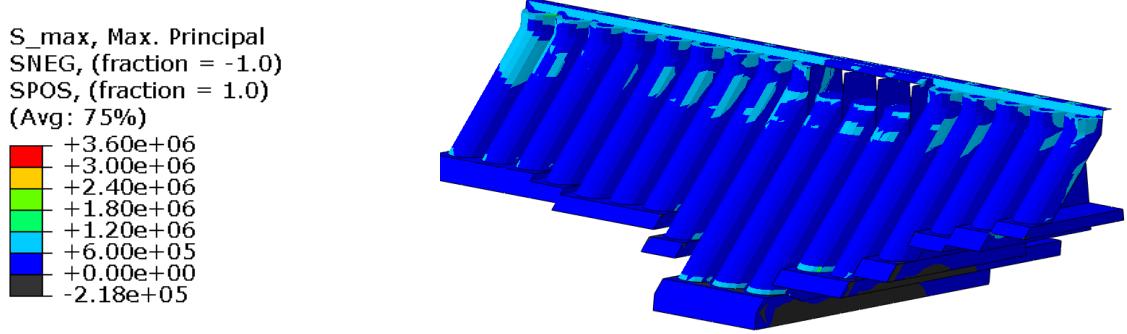


Figure 12. Maximum principal stresses envelop on the upstream face with the maximum level of reservoir.

For the buttresses and the shoulders, considered equivalent to gravity dams, sliding stability must be checked in all the horizontal sections (joints and dam-rock foundation interface, Figure 13 left). The verification is satisfied if for each section the ratio between the sum of horizontal forces (F_x) and the sum of vertical forces (F_y) is less than one. The most stressed buttress was considered (Figure 13, right) and the forces acting, when the maximum seismic acceleration is present, were evaluated.

Table 1 shows that the safety against sliding is satisfied in all horizontal sections for the acceleration term SADR with the maximum level of reservoir.

Table 1. Sliding safety verification for the acceleration term SADR with the maximum level of reservoir.

Section	F_x [kN]	F_y [kN]	$F_x / F_y [-]$
A	47	4660	0.010
B	1540	9050	0.170
C	11300	35700	0.317
D	18000	46900	0.384

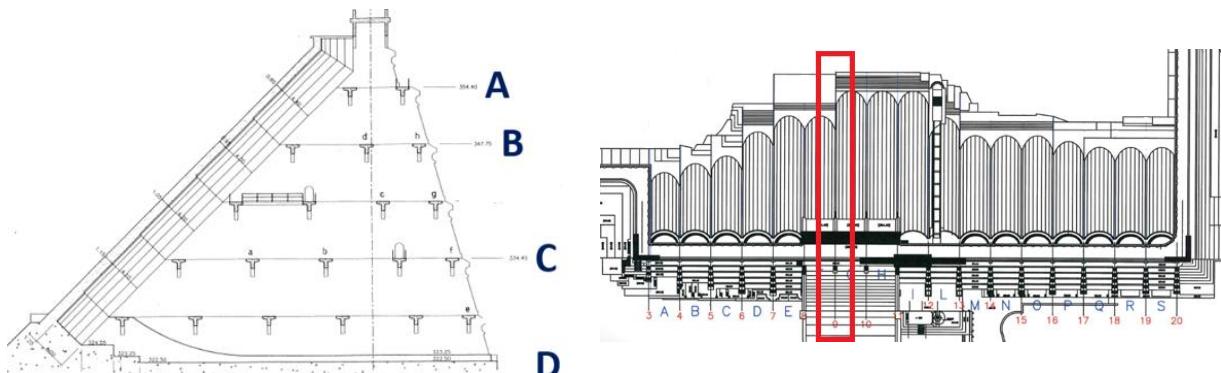


Figure 13. Horizontal sections and the most stressed buttress considered for the sliding safety.

For the reinforced concrete T-shaped beams and arches, starting from the geometrical and mechanical parameters of the section, a bending moment versus axial force diagram was computed to define the strength domain. A reinforced cross-section is verified if the acting bending moments and axial forces are inside this domain at any time step of the analysis. Results for the acceleration term SADR and the maximum level of reservoir are reported in Figure 14: the comparison between the strength domain and the acting force couples (bending moment versus axial force) for the most stressed T-shaped beam (above) and arch (below) is shown. Four different acting force couples are reported: static loading condition in purple; maximum tension and compression over the seismic analysis, respectively in light blue (only for the T-shaped beam) and pink; final condition in yellow. The analyses are satisfied since the acting forces are inside the strength domains.

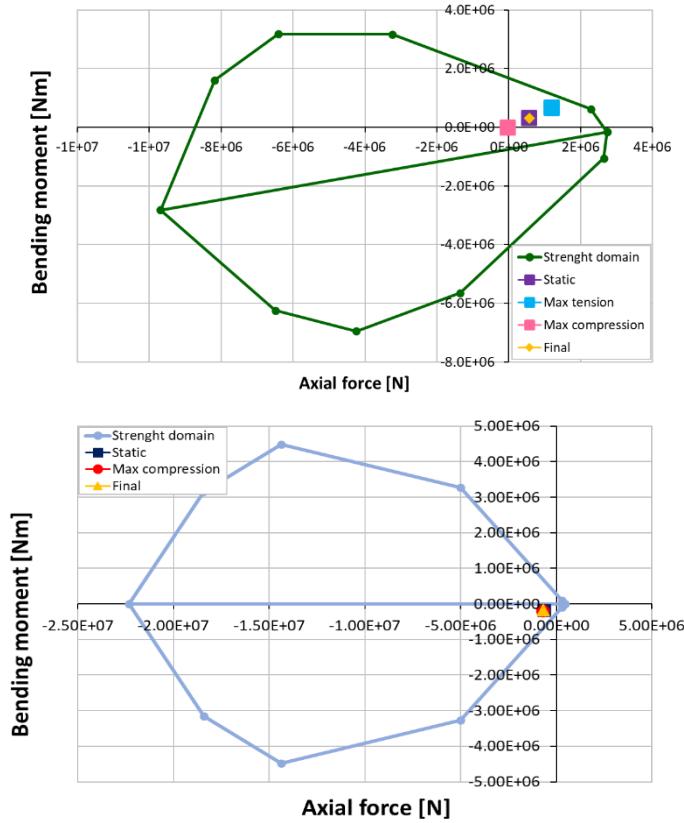


Figure 14. Bending moment versus axial force diagram for the most stressed T-shape beam (above) and arch (below) for SADR tern and maximum level of reservoir.

5. Conclusion

In this paper an overview of the typical problems concerning buttress, hollow gravity and multiple arch/slab dams has been provided.

Then, the role of numerical modeling has been highlighted for the evaluation of dam safety, for diagnostic investigation and for identifying the most effective rehabilitation works to guarantee long-term safety conditions.

Finally, the seismic analyses of Molato dam, operated by the *Consorzio di Bonifica di Piacenza*, is presented. This case study demonstrates how numerical analysis allows evaluating the real response of all the structural elements of a strategic dam. In conclusion, it is extremely evident that the properties of the materials, the constitutive laws, the geometric characteristics and the acting loads play a fundamental role in the evaluation of the seismic behavior of dams.

6. Acknowledgement

The work done by Colombo and Frigerio, except that related to the seismic assessment of Molato dam commissioned by *Consorzio di Bonifica di Piacenza*, has been financed by the Research Fund for the Italian Electrical System under the Three-Year Research Plan 2022-2024 (DM MITE n. 337, 15.09.2022), in compliance with the Decree of April 16th, 2018.

7. References

- ANIDEL (1953). *Dams for hydroelectric power in Italy*, Vol. 7.
- Ardito R., Maier G., Massalongo G. (2008). Diagnostic analysis of concrete dams based on seasonal hydrostatic loading, *Engineering Structures*, Vol. 30: 3176-3185.
- Brownjohn J.M.W. (2007). Structural health monitoring of civil infrastructure, *Philosophical Transactions of the Royal Society A*, Vol. 365: 589–622.

- Bukenya P., Moyo P., Beushausen H., Oosthuizen C. (2014). Health monitoring of concrete dams: a literature review, *Journal of Civil Structural Health Monitoring*, Vol. 4: 235–244.
- Clough R.W. (1980). Non-linear mechanisms in the seismic response of arch dams, *Proceedings of the International Research Conference Earthquake Engineering*, Skopje, Yugoslavia.
- Colombo M., Domaneschi M., Ghisi A. (2016). Existing concrete dams: loads definition and finite element models validation, *Structural Monitoring and Maintenance*, Vol. 3: 129-144.
- Colombo M., Domaneschi M., Ghisi A. (2015). Validation of Finite Element Models of concrete dams through monitoring data, *Proceedings of the 10th International Workshop on Structural Health Monitoring*, Stanford University, USA, Vol. 2: 473-480.
- Evangelisti G. (1982). *Impianti idroelettrici*, Vol. I, Patron, Bologna.
- Ingraffea A.R. (1990). Case studies of simulation of fracture in concrete dams, *Engineering Fracture Mechanics*, Vol. 35: 553-564.
- Lee J., Fenves G.L. (1998). A plastic-damage concrete model for earthquake analysis of dams, *Earthquake Engineering and Structural Dynamics*, Vol. 27: 937-956.
- Ministero delle Infrastrutture e dei Trasporti (DM2014). *Decreto Ministeriale 26 Giugno 2014. Norme tecniche per la progettazione e la costruzione degli sbarramenti di ritenuta (dighe e traverse)*.
- Ministero delle Infrastrutture e dei Trasporti (DM2018). *Decreto Ministeriale 17 gennaio 2018. Norme tecniche per le costruzioni*.
- Mirzabozorg H., Hariri-Ardebili M.A., Heshmati M., Seyed-Kolbadi S.M. (2014). Structural safety evaluation of Karun III Dam and calibration of its finite element model using instrumentation and site observation, *Case Studies in Structural Engineering*, Vol. 1: 6–12.
- Thomas M., Folliard K.J., Fournier B., Rivard P., Drimalas T. (2013). *Methods for Evaluating and Treating ASR-Affected Structures: Results of Field Application and Demonstration Projects*, U.S. Department of Transportation.
- USACE (2007). *Engineering and Design - Earthquake Design and Evaluation of Concrete Hydraulic Structures*, EM 1110-2-6053.
- Zienkiewicz O.C. (1977). *The Finite Element Method*, 3rd Edition, McGraw-Hill.

LOW-TO-HIGH FIDELITY TRANSFORMATION FUNCTION FOR THE SEISMIC FRAGILITY ASSESSMENT OF GRAVITY DAMS

R. J. A. Torres Filho¹, R. L. Segura² & P. Paultre³

¹ Dept. of Civil and Building Engineering, University of Sherbrooke, Sherbrooke, Canada

² Dept. of Civil, Environmental, and Sustainable Engineering, Santa Clara University, Santa Clara, U.S.A,
rsegura@scu.edu

³ Dept. of Civil and Building Engineering, University of Sherbrooke, Sherbrooke, Canada

Abstract: Precise representation of dam-foundation-reservoir systems is essential to accurately represent the behavior of the structure. Furthermore, dams exposed to extreme loads may behave non-linearly, requiring highly complex and time-consuming models. Consequently, probabilistic seismic evaluation of dams becomes challenging, given the number of analyses required to consider an adequate number of possible scenarios. The trade-off between accuracy and computational resources often leads to a choice between a set of a few but high-quality samples and lower-fidelity analyses that can produce adequate number of observations at a lower cost. However, neither option is ideal, and hence, machine learning techniques are being employed to reduce the computational burden while preserving the accuracy of high-fidelity models. In this paper, a machine learning-based transformation function is used to convert lower-fidelity observations into its high-fidelity equivalent to perform seismic fragility assessment of concrete gravity dams. The transformation function takes sliding factor of safety, resulting from a pseudo-static analysis, as well as geometric, material and seismic parameters as input, and outputs sliding displacement, with accuracy levels comparable to those that would be obtained with a non-linear finite element model, but at a much lower cost. The training dataset was generated using Latin hypercube sampling to obtain 2,500 samples that reflect the entire range parameters' uncertainty. The scenarios defined by the samples are then analysed using both high and low-fidelity methods and the results are used in the training procedure. The accuracy of the model is controlled by goodness-of-fit parameters estimated from 10-fold cross-validation. The transformation function is assessed by applying it to replicate the seismic fragility analysis of three established references in the literature. It yields promising outcomes for studies conducted in settings akin to those used in developing the function. Ultimately, the function's efficacy is showcased through a comparison of dam fragility across varying heights, all achieved with a significantly reduced computational workload.

1 Introduction

Due to the risks and costs associated with constructing and maintaining a gravity dam, their safety assessment must be a priority, especially if the structure is in a seismic-active region (Bilici et al., 2009). Loads resulting from seismic activity are among the most important actions to be considered in concrete dam design as they are associated with the appearance and propagation of cracks. The nonlinearity, characteristic of this phenomenon, requires the correspondence of the analysis model with the real-world structure to be maximized through appropriate numerical representation.

Probabilistic methods, such as fragility analysis and optimization, have emerged as a reliable tool for the seismic assessment of dam-type structures. Nevertheless, these methods require a large number of analyses to capture the uncertainties inherent in the system. In addition, a large set of uncertain parameters and/or highly non-linear problems require larger datasets to capture the behavior of the system (Jeong and Elnashai, 2007). The probabilistic seismic analysis of concrete gravity dams has been widely studied in the literature (Tekie and Ellingwood, 2003; Lupoi and Callari, 2012; Hariri-Ardebili, 2016; Sevieri et al., 2021; Segura et al., 2023), with the majority of studies focusing on a single monolith and considering material and seismic uncertainties. Although there are recent studies assessing the dam response considering geometry variation (Ansari, Saqib and Agarwal, 2018; Hariri-Ardebili and Nuss, 2018; Sevim, 2018), studies that consider fragility with geometric uncertainty are fairly rare (Gavabar and Alembagheri, 2020).

A model considering the dam-reservoir-foundation interaction with the dynamic response driven to the nonlinear domain due to seismic load can be very challenging in terms of processing time and require high expertise to be properly prepared (Ribeiro and Léger, 2023). Simplified methods can be used for this analysis (USBR, 1987; FERC, 2016), but they tend to result in over-conservative designs (Renaud et al., 2016). Therefore, using more refined methods is strongly recommended (Léger and Katsouli, 1989). In recent years, the potential of machine learning to address the computational demands from high-fidelity (HF) analyses has been explored. Within this framework, the prediction of dam response, often incorporating seismic loading, is drawing attention (Chen et al., 2010; Fan et al., 2010; Karimi et al., 2010; Su et al., 2016; Hariri-Ardebili, 2018; Hariri-Ardebili and Pourkamali-Anaraki, 2018). Material uncertainty (Hariri-Ardebili and Sudret, 2019), or a combination of material and seismic uncertainty (Segura et al., 2020), are typical considerations. Although literature does contain studies involving variations in dam geometry (Segura et al., 2022; Abdollahi et al., 2022, Torres Filho et al., 2023), such instances are rare and infrequently encompass both material and geometric uncertainties. Furthermore, many of these studies rely on simplified models to reduce the computational expenses associated with data generation for machine learning model training. The cost can vary significantly depending on the study's scope. This complexity presents a challenge in assessing the fragility of sliding in concrete gravity dams, as these are nonlinear problems greatly influenced by the material, seismic, and geometric characteristics of the system.

To address these issues, in this study the precision of HF methods is combined with the practicality and low cost of lower-fidelity (LF) methods through machine learning to allow the generation of accurate and inexpensive data. To this end, a regression-based transformation function (TF) that translates pseudostatic sliding factor of safety into sliding displacement with precision levels comparable to data obtained from nonlinear time-history analyses is developed. In addition, given the consideration of geometry variation alongside material and geometry uncertainty, the presented function is robust enough to be applied to a variety of dams without requiring the generation of a transformation function for each structure. Additionally, including the LF response among the function inputs greatly boosts the prediction of the model without requiring the user to perform any further complex or time-consuming calculations. As presented later in the text, the proposed transformation function stands out for its ability to conduct thorough fragility analysis with good precision while demanding minimal computational resources. This efficiency significantly cuts down the time required to generate observations, reducing a process that could take weeks to mere seconds.

2 Methodology

The transformation function's applicability and performance hinge on several key factors: the correlation between HF and LF methods, the choice of uncertain parameters, the sampling strategy for constructing the experimental design matrix, and the regression methodology employed during function training. The subsequent subsections provide detailed explanations of each of these aspects.

2.1 High- and low-fidelity methods

As a non-linear phenomenon, the accurate representation of the sliding of a dam under seismic loading requires the use of a nonlinear time-history analysis. However, being a demanding analysis, many LF methods with different simplification hypotheses are available to evaluate the sliding stability of dams (Chávez and Fenves, 1995). For this work, the pseudostatic method is selected as the LF method.

HF method: Time-history analysis

To accurately capture the behavior of a gravity dam under seismic loading, a nonlinear time-history analysis was performed using a finite element model of the system. The modeling and the analysis follow a procedure validated in the literature (Mills-Bria, Anastasia and Percell, 2008). The dam and the foundation are modeled using a linear elastic material, whereas the reservoir is modeled with compressible fluid elements. The dam-reservoir interface is modeled through a sliding contact with zero friction while the contact between the foundation and the reservoir is considered tied. Tiebreak contact elements with a tension-shear failure criterion are used at the dam-foundation interface to model the potential non-linear sliding behavior. Non-reflective boundaries are added to the extremities of the reservoir and foundation to eliminate the effect of energy reflection due to their finite length and to account for the radiation damping. Detailed information concerning the modeling and analysis procedure can be found in Segura et al. (2019a) and Proulx and Paultre (1997).

LF method: Pseudostatic analysis

The sliding factor of safety was obtained considering a non-linear pseudostatic analysis with the software CADAM3D (Leclerc, 2020). The software evaluates the stability of concrete gravity dams via the gravity method and considers the dam as a cantilevered structure. The pseudo-static method was chosen for generating LF data due to its speed, accessibility to a broad range of practitioners, and widespread acceptance in numerous guidelines (USBR, 1987; FERC, 2016).

Correlation between HF and LF methods

The performance of the transformation function is affected by the correlation between the HF and the LF data. Both don't need to have the same outputs, however, the LF method should be capable of capturing the trend of changes in the response due to changes in the input variables (Balabanov and Venter, 2014). Preliminary analyses indicate a correlation coefficient of $R^2 = -0.74$ between the sliding displacement of the HF method and the sliding factor of safety of the LF method, which validates the selection. Table 1 presents the most prominent distinctions between the selected methods.

Table 1. HF and LF methods main differences

Analysis method	Pseudo-static	Time-history
Seismic input	Peak ground acceleration	Ground motion time history
Water compressibility	Incompressible	Compressible
Foundation	Rigid	Flexible
Numerical representation	Cantilever	Finite elements
Output	Sliding factor of safety	Sliding displacement

2.2 Design of experiments

The selection of parameters is a key step in the generation of the transformation function. Considering a large number of parameters leads to a broad uncertain domain and requires a higher number of samples for the regression phase. However, it produces a more robust function that can be applied to a broad range of scenarios. That is why material, seismic, and geometric parameters were considered. For this, four uniformly distributed material parameters sampled using the Latin hypercube sampling (LHS) technique were randomly paired with 250 earthquakes and 40 geometries to generate 2,500 scenarios. More details about the varying parameters are given in Table 2.

2.3 Regression method and fitting process

The polynomial response surface method, a commonly employed technique in machine learning for predicting dam sliding displacement (Hariri-Ardebili, 2018; Segura et al. 2019; Segura et al., 2022), was chosen for this study due to its suitability for the problem at hand. Additionally, it yields a straightforward polynomial function that can be readily implemented in any calculation software.

Table 2. Variable parameters

Material Parameter	Minimum – maximum	Unit
Dam-foundation tensile strength	0.2 – 1.5	MPa
Dam-foundation cohesion	0.3 – 2.0	MPa
Dam-foundation angle of friction	42 – 55	degree
Drain efficiency	0 – 66	%
Seismic Parameter	Minimum – maximum	Unit
Horizontal peak ground acceleration	0.023 – 1.115	g
Vertical peak ground acceleration	0.013 – 0.429	g
Horizontal peak ground velocity	0.820 – 94.966	cm/s
Vertical peak ground velocity	0.302 – 28.191	cm/s
Horizontal Arias intensity	0.004 – 9.032	m/s
Vertical Arias intensity	0.001 – 1.936	m/s
Horizontal spectral acceleration	0.006 – 4.598	g
Vertical spectral acceleration	0.003 – 1.200	g
Geometry Parameter	Minimum – maximum	Unit
Height	30 – 210	m
Base-to-height ratio	0.65 – 1.10	–

The readily available material, seismic, and geometric data can be incorporated into the function as inputs to enhance its performance. Furthermore, this list of features was expanded by calculating parameters unique to each scenario, which were initially omitted during the sampling phase. These included metrics like the horizontal and vertical center of gravity, as well as the volume of the monolith. To further enrich this feature set, higher-order versions were generated using mathematical functions such as square, cube, fourth power, exponential, square root, logarithmic, natural logarithmic, pairwise summation, and product.

Next, to prevent model overfitting and minimize the learning algorithm's error rate, the unwanted features were removed by using a hybrid feature selection approach. This method combines the correlation filter (Hall and Smith, 1998) with the stepwise wrapper (Kohavi and John, 1997) to identify the most relevant features for optimizing the regression model's predictive performance. In addition, the entire feature selection and regression process was executed while adhering to a 10-fold cross-validation procedure.

3 Results

The resulting transformation function is a 4th-order polynomial composed of 10 parameters. Stepwise regression was used to eliminate terms with low contribution ($p\text{-value} < 0.05$) to ensure that the terms were not chosen randomly. The performance of the function is depicted in Figure 1, where the simulations calculated with the HF method are compared with the predictions achieving a coefficient of determination $R^2 = 0.84$ (Figure 1a). From Figure 1b it can be observed that the model satisfies the normal error distribution hypothesis assumed by the polynomial response surface.

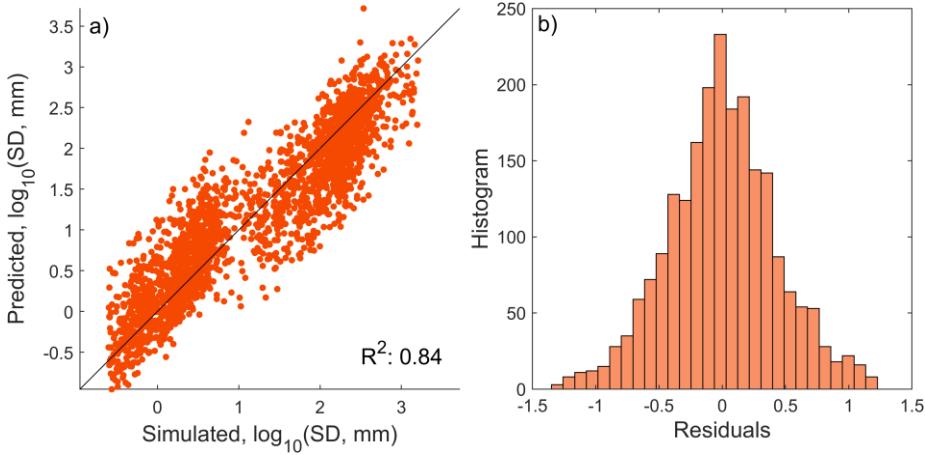


Figure 1. Transformation function performance: (a) predicted vs. simulated values and (b) residual frequency.

The lack of fit with the HF simulations is represented in the TF with the addition of a normally distributed error (v) term as shown in Eqs. 1 and 2,

$$SD_{predicted} = SD_{TF} + v \quad (1)$$

$$v = N(0, 0.43) \quad (2)$$

where SD_{TF} is the sliding displacement obtained with the TF before the addition of the error and $SD_{predicted}$ is the final prediction. The complete function is presented in Table 3. Next, the applicability of the function is tested and discussed by reproducing three sliding fragility studies from the literature.

3.1 Case studies

To assess the robustness of the above-presented transformation function, it was intended to replicate the seismic fragility analysis of three established references in the literature. The proposed transformation function underwent training with a specific set of variables and modeling considerations. When comparing its results with studies that adopt different considerations, further disparities emerge in the outcomes. To mitigate the introduction of uncertainty stemming from using distinct analysis methodologies, three case studies employing modeling and analysis procedures similar to the HF methodology applied in this study, were selected.

Case study 1 (Segura et al., 2019) and 2 (Bernier et al., 2016) studied the fragility of a concrete gravity dam located in eastern Canada. The dam has a vertical upstream and both studies considered a full reservoir, which is in accordance with the premises used during the transformation function generation. Case study 1 and 2 selected records consistent with the 2015 and 2010 National Building Code of Canada (NBCC, 2010 and 2015) hazard model, respectively. Case study 3 (Ghanaat et al., 2012) differs the most from the transformation function's development conditions. Folsom dam, which is studied in this work, has an inclined upstream, the concrete elastic modulus, the rock elastic modulus and the concrete damping are included as uncertain parameters, and the dam is located in western United States, presenting different foundation and seismic characteristics. Additionally, details about the probability density function (PDF) parameters are not available for all the uncertain parameters which caused the present study to assume the values. The design of experiments parameters' set for the three case study dams are presented in Table 4.

3.2 Fragility analysis

The process for generating the sliding fragility curves using the transformation function involves producing an experimental design matrix that emulates the original study. To this end, material parameters were sampled from Table 4 using LHS technique. The geometric parameters were fixed to the values of each case study dam, and the seismic parameters were sampled from a multi-lognormal distribution consistent with the seismic scenario used in the original study. Pseudostatic analyses are then performed for each sample to obtain the sliding factor of safety. Finally, the sliding displacement is calculated using the transformation function, and the fragility curves are obtained following the multiple stripes methodology (Baker, 2015).

Table 3. Eq. 1 terms and coefficients

Term	Coefficient	Term	Coefficient
Intercept	7.18E+00	$\log x_9 x_1 x_3$	-2.88E-03
$\log^3 x_1 \log x_9$	-1.57E+00	$\log x_9 (x_4 + x_8)(x_6 + x_7)$	-1.26E-02
$\log^3 x_1$	-4.82E+01	$x_{10} x_2 x_5 (x_1 + x_4)$	1.77E-01
$\log^2 x_1 \sqrt{x_{10}} x_1 x_3$	-3.72E-02	$\sqrt{x_{10}} (x_4 + x_8)^3$	-9.43E-02
$\log^2 x_1 (x_1 + x_4)$	7.78E+00	$(x_1 x_3)^2 (x_1 + x_4)(x_6 + x_7)$	2.01E-07
$\log x_1 \log^2 x_9 \sqrt{x_{10}}$	-6.17E+00	$x_1 x_3 (x_1 + x_4)^2 (x_4 + x_8)$	2.64E-04
$\log x_1 \log x_9 x_{10}$	6.79E+00	$x_1 x_3 (x_4 + x_8)$	-6.06E-03
$\log x_1 \log x_9 \sqrt{x_{10}} (x_6 + x_7)$	-1.05E-01	$(x_2 x_5)^2 (x_1 + x_4)^2$	-3.04E-02
$\log x_1 \log x_9 \sqrt{x_{10}}$	-1.29E+01	$(x_2 x_5)^2$	1.46E+00
$\log x_1 \log x_9 (x_6 + x_7)^2$	1.08E-03	$x_2 x_5 (x_1 + x_4)^2 (x_6 + x_7)$	-3.11E-04
$\log x_1 \sqrt{x_{10}}$	2.43E+00	$x_2 x_5 (x_1 + x_4)$	9.43E-01
$\log x_1 (x_1 + x_4)^3$	-5.93E-02	$x_2 x_5$	-6.33E+00
$\log x_1 (x_4 + x_8)$	-3.09E+00	$(x_1 + x_4)^4$	3.18E-03
$\log x_9 (\sqrt{x_{10}})^3$	7.05E-02	$(x_1 + x_4)$	-1.51E+00

x_1 : factor of safety
 x_2 : base to height ratio
 x_3 : vertical center of gravity, m
 x_4 : drain efficiency
 x_5 : $\text{tg}(\text{angle of friction})$

x_6 : horizontal peak ground velocity, cm/s
 x_7 : vertical peak ground velocity, cm/s
 x_8 : horizontal peak ground acceleration, g
 x_9 : vertical peak ground acceleration, g
 x_{10} : horizontal arias intensity, m/s

Table 4. Case studies experimental design matrix basis

Parameters	Case study 1	Case study 2	Case study 3
Height	78	78	80
Base-to-height ratio	0.79	0.79	0.75
Dam-foundation tensile strength	Uniform	Uniform	Uniform
Dam-foundation cohesion	Uniform	Uniform	Uniform
Dam-foundation angle of friction	Uniform	Uniform	Uniform
Drain efficiency	Uniform	Uniform	Uniform
Horizontal spectral acceleration	0.1 to 0.9 g	0.1 to 0.9 g	-
Horizontal peak ground acceleration	-	-	0.1 to 1.2 g

Figure 2 presents the comparison of the fragility curves obtained with the transformation function with the traditional fragility curves for each case study. Fragility point estimates are calculated from probability density functions fitted for the sliding displacement at each intensity measure, namely spectral acceleration (Figure 2(a) and (b)) and peak ground acceleration (Figure 2(c)). Similarly, to case studies 1 and 2, the fragility analysis performed with the TF adopted as limit states (LS) the four levels of damage proposed by (Tekie and Ellingwood, 2003). Case study 3 considered insipient sliding as the single level of damage, as depicted by the

single dashed line in Figure 2(c). It can be seen that the transformation function is capable of capturing the overall sliding response trend in all presented cases. This is particularly notable in Figure 2(a) and 2(b), especially for more critical limit states at 50 and 150 mm. Concerning Figure 2(c), it is observed that 5 mm is the best correspondent to case 3 insipient sliding limit state. The original work uses the lognormal PDF for many of the uncertain parameters, which reduces variation when compared to the uniform PDF used for the transformation function. This means that if the mean is prone to stability, then the overall results would be more stable, thus reducing fragility.

3.3 Geometry and NBCC edition impact on dam seismic fragility

The transformation function's primary advantage lies in its ability to generate a large number of observations at an extremely low cost. Leveraging this capability, we examine the impact of varying dam heights on fragility. The case study 1 dam and the parameters presented in Table 4 were selected. While maintaining a constant base-to-height ratio, dam heights of 90 m, 70 m, and 50 m were compared to the actual dam height. The resulting fragility curves presented in Figure 3 depict the probability of exceedance of the four LS's given the selected intensity measure. Additionally, the PGA values for different editions of the NBCC considered for a return period of 2475 years at the dam location (Segura et al., 2023) were included to show the impact of the evolution of the hazard model in safety interpretation. As expected, the findings indicate that reducing dam height significantly influences the probability of failure, and when height is the sole variable, employing the tallest monolith as a representation of the worst-case scenario is a reasonable choice. Moreover, it becomes apparent that employing various monoliths height for the analysis in conjunction with an outdated hazard model can result in significantly divergent exceedance probabilities.

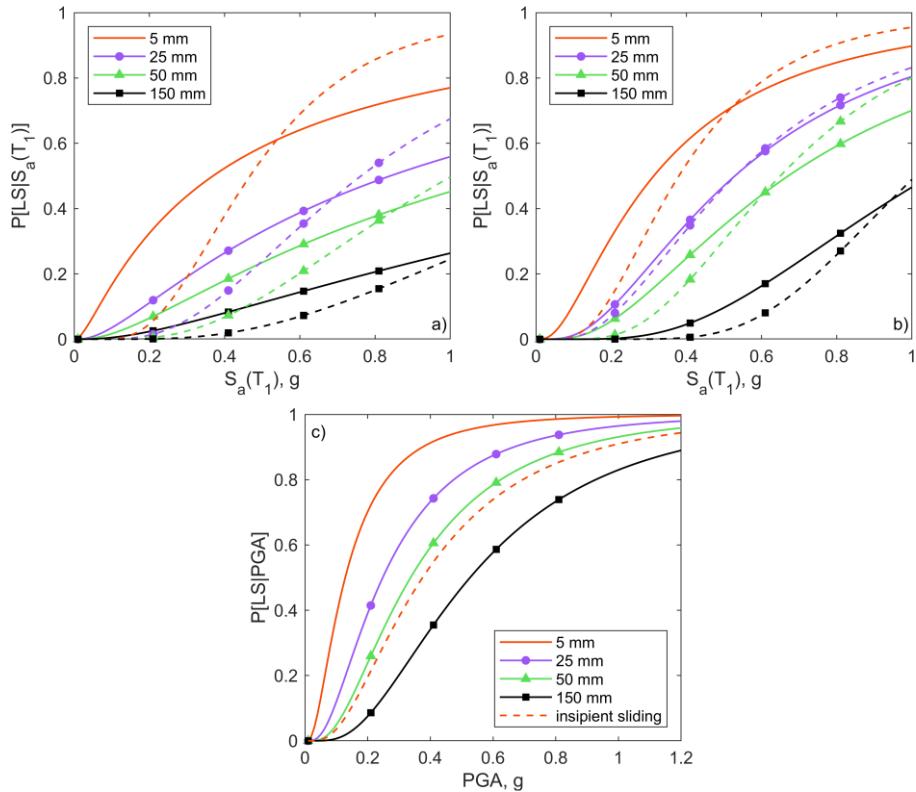


Figure 2. Comparison of fragility curves obtained from the transformation function (solid line) and the literature (dashed line) for (a) case study 1, (b) case study 2 and (c) case study 3

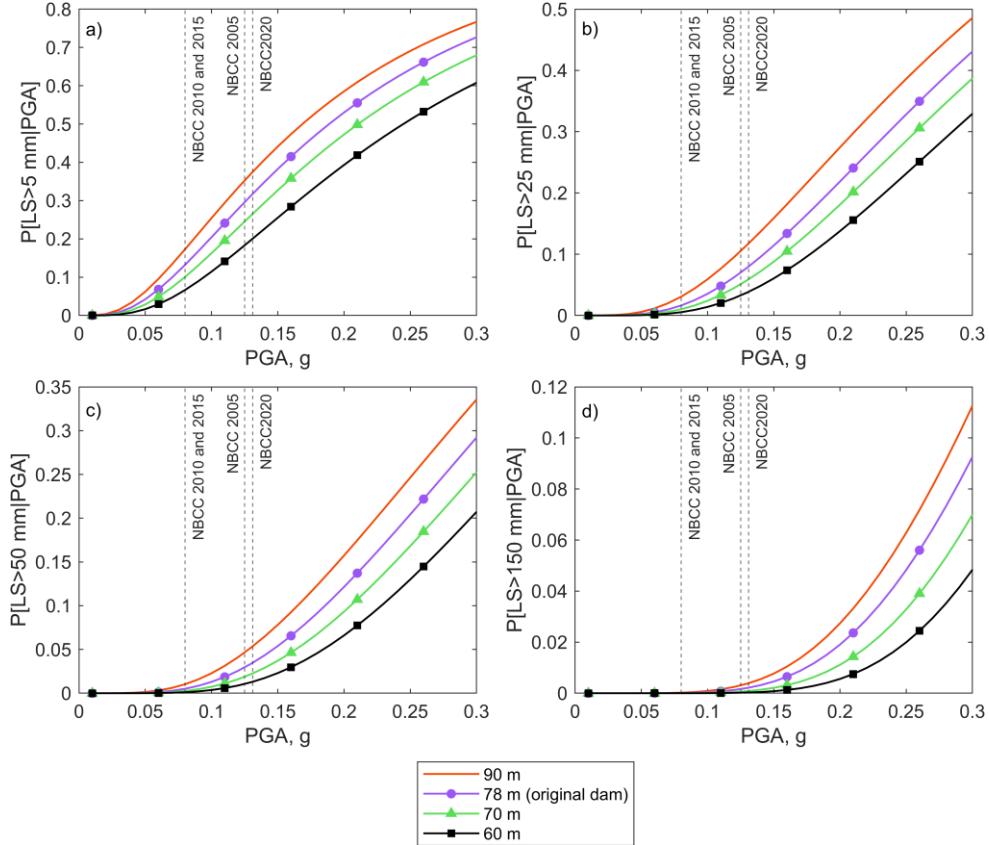


Figure 3. Geometry-dependent fragility comparison for different levels of damage: (a) 5 mm, (b) 25 mm, (c) 50 mm and (d) 150 mm

4 Conclusion

Proper numerical representation is essential for accurately depicting the dynamic behavior of dams. However, the non-linear seismic analysis of dam-reservoir-foundation systems is time-consuming, and consequently, can make unfeasible studies that require a great number of analyses. This study presents a machine learning based transformation function that improves the sliding factor of safety obtained with a pseudostatic analysis into sliding displacement with accuracy comparable to nonlinear finite element time-history analysis results. Material, seismic, and geometric parameters readily available are considered variables to increase the applicability range and to boost the performance of the function through feature selection. The polynomial response surface is selected as the regression method to generate a 4th-order polynomial function that can be easily implemented in spreadsheets or other calculation software. The performance of the transformation function is evaluated by replicating three seismic fragility studies from the literature. For case studies 1 and 2, the fragility curves generated using the transformation function closely align with those from the original studies. However, in case study 3, the hypothesis substantially deviated from the conditions used to develop the transformation function, resulting in an overestimation of fragility. This indicates that the function remains valuable for preliminary assessments, providing conservative safety-oriented results. It's worth noting that the methodology is most suitable for studies aligned with the variable parameters and hypothesis used during the transformation function's development. Furthermore, the method's potential is demonstrated by examining the fragility of a set of dams with varying heights, significantly reducing the computational workload of the study. The transformation function introduced in this work offers a cost-effective and precise means of generating sliding displacement observations. Its performance is optimized when study conditions align with those of its development, but the incorporation of material, seismic, and geometric parameters expands its applicability across a wide range of scenarios.

5 References

- Abdollahi, A., Amini, A. and Hariri-Ardebili, M.A. (2022) 'An uncertainty-aware dynamic shape optimization framework: Gravity dam design', *Reliability Engineering and System Safety*, 222(November 2021), p. 108402. Available at: <https://doi.org/10.1016/j.ress.2022.108402>.
- Aldemir, A., Binici, B., Canbay, E., Kurc, O. and Arici, Y. (2014) 'Pseudo dynamic test results of a concrete gravity dam', *NCEE 2014 - 10th U.S. National Conference on Earthquake Engineering: Frontiers of Earthquake Engineering* [Preprint]. Available at: <https://doi.org/10.4231/D3DJ58H28>.
- Ansari, M.I., Saqib, M. and Agarwal, P. (2018) 'Geometric Configuration Effects on Nonlinear Seismic Behavior of Concrete Gravity Dam', *Journal of Earthquake and Tsunami*, 12(1), pp. 1–25. Available at: <https://doi.org/10.1142/S1793431118500033>.
- Baker, J.W. (2015) 'Efficient analytical fragility function fitting using dynamic structural analysis', *Earthquake Spectra*, 31(1), pp. 579–599. Available at: <https://doi.org/10.1193/021113EQS025M>.
- Balabanov, V.O. and Venter, G. (2014) 'Multi-fidelity optimization with high-fidelity analysis and low-fidelity gradients', *American Institute of Aeronautics and Astronautics* [Preprint].
- Bernier, C., Monteiro, R. and Paultre, P. (2016) 'Using the conditional spectrum method for improved fragility assessment of concrete gravity dams in Eastern Canada', *Earthquake Spectra*, 32(3), pp. 1449–1468. Available at: <https://doi.org/10.1193/072015EQS116M>.
- Bernier, C., Paultre, P. and Proulx, J. (2014) *Développement de courbes de fragilité pour le barrage-poids aux Outardes-3*. Université de Sherbrooke.
- Chávez, J.W. and Fenves, G.L. (1995) 'Earthquake response of concrete gravity dams including base sliding', *Journal of Structural Engineering*, 121(5), pp. 865–875. Available at: [https://doi.org/10.1061/\(ASCE\)0733-9445\(1995\)121:5\(865\)](https://doi.org/10.1061/(ASCE)0733-9445(1995)121:5(865)).
- Chen, J.Y., Xu, Q., Li, J. and Fan, S.L. (2010) 'Improved response surface method for anti-slide reliability analysis of gravity dam based on weighted regression', *Journal of Zhejiang University: Science A*, 11(6), pp. 432–439. Available at: <https://doi.org/10.1631/jzus.A0900709>.
- Fan, S.L., Chen, J.Y., Li, J. and Wu-Qiang, F. (2010) 'Roller compacted concrete gravity dams reliability analysis based on response surface approach', *Proceedings of the 12th International Conference on Engineering, Science, Construction, and Operations in Challenging Environments - Earth and Space 2010*, pp. 3355–3367. Available at: [https://doi.org/10.1061/41096\(366\)320](https://doi.org/10.1061/41096(366)320).
- FERC (2016) *Engineering guidelines for the evaluation of hydropower projects. Chapter III: gravity dams, Engineering Guidelines for the Evaluation of hydropower Projects*. Washington, DC.
- Gavabar, S.G. and Alembagheri, M. (2020) 'A study on seismic performance and fragility of gravity dams with various monolith shapes using nonlinear IDA', *Geotechnical and Geological Engineering*, 38(2), pp. 1133–1150. Available at: <https://doi.org/10.1007/s10706-019-01077-8>.
- Ghanaat, Y., Patev, R.C. and Chudgar, A.K. (2012) 'Seismic fragility analysis of concrete gravity dams', *Proceedings of the 15th world conference on earthquake engineering*, pp. 24–28.
- Hall, M. and Smith, L. (1998) 'Feature subset selection: a correlation based filter approach', in *Proceedings of International Conference on Neural Information Processing and Intelligent Information Systems*, pp. 855–858.
- Hariri-Ardebili, M.A. (2016) 'Concrete dams: from failure modes to seismic fragility', in *Encyclopedia of Earthquake Engineering*. Berlin, Heidelberg: Springer Berlin Heidelberg, pp. 1–26. Available at: https://doi.org/10.1007/978-3-642-36197-5_409-1.
- Hariri-Ardebili, M.A. (2018) 'MCS-based response surface metamodels and optimal design of experiments for gravity dams', *Structure and Infrastructure Engineering*, 14(12), pp. 1641–1663. Available at: <https://doi.org/10.1080/15732479.2018.1469650>.
- Hariri-Ardebili, M.A. and Nuss, L.K. (2018) 'Seismic risk prioritization of a large portfolio of dams: Revisited', *Advances in Mechanical Engineering*, 10(9), pp. 1–20. Available at: <https://doi.org/10.1177/1687814018802531>.

- Hariri-Ardebili, M.A. and Pourkamali-Anaraki, F. (2018) 'Simplified reliability analysis of multi hazard risk in gravity dams via machine learning techniques', *Archives of Civil and Mechanical Engineering*, 18(2), pp. 592–610. Available at: <https://doi.org/10.1016/j.acme.2017.09.003>.
- Karimi, I., Khaji, N., Ahmadi, M.T. and Mirzayee, M. (2010) 'System identification of concrete gravity dams using artificial neural networks based on a hybrid finite element-boundary element approach', *Engineering Structures*, 32(11), pp. 3583–3591. Available at: <https://doi.org/10.1016/j.engstruct.2010.08.002>.
- Kohavi, R. and John, H. (1997) 'Wrappers for feature subset selection', *Artificial Intelligence* [Preprint].
- Leclerc, M. (2020) 'CADAM3D User's Manual', *MLT TECHNOLOGY INC. Polytechnique Montreal* [Preprint], (April).
- Lupoi, A. and Callari, C. (2012) 'A probabilistic method for the seismic assessment of existing concrete gravity dams.', *Structure and Infrastructure Engineering* [Preprint].
- Mills-Bria, B., Anastasia, J. and Percell, P. (2008) 'Nonlinear analysis research', *Technical Report, DSO-08-02* [Preprint].
- Murphy, K.P. (2012) *Machine learning : A probabilistic perspective*. Cambridge: The MIT Press.
- Nicholson, G.A. (1983) 'Design of gravity dams on rock foundations : sliding stability assessment by limit equilibrium and selection of shear strength', *U.S. Army Corps of Engineers, Technical Report, GL-83-13* [Preprint].
- Ribeiro, P.M.V. and Léger, P. (2023) 'On a Benchmark Problem for Modeling and Simulation of Concrete Dams Cracking Response', *Infrastructures*, 8(3), p. 50. Available at: <https://doi.org/10.3390/infrastructures8030050>.
- Ruggeri, G. (2004) 'Sliding safety of existing gravity dams - Final report', *International Commission on Large Dams* [Preprint].
- Segura, R., Padgett, J.E. and Paultre, P. (2020) 'Metamodel-based seismic fragility analysis of concrete gravity dams', *Journal of Structural Engineering*, 146(7), p. 04020121. Available at: [https://doi.org/10.1061/\(asce\)st.1943-541x.0002629](https://doi.org/10.1061/(asce)st.1943-541x.0002629).
- Segura, R.L., Bernier, C., Monteiro, R. and Paultre, P. (2019) 'On the seismic fragility assessment of concrete gravity dams in eastern Canada', *Earthquake Spectra*, 55(1), pp. 211–231. Available at: <https://doi.org/10.1193/012418EQS024M>.
- Segura, R.L., Fréchette, V., Miquel, B. and Paultre, P. (2022) 'Dual layer metamodel-based safety assessment for rock wedge stability of a free-crested weir', *Engineering Structures*, 268(February), p. 114691. Available at: <https://doi.org/10.1016/j.engstruct.2022.114691>.
- Segura, R.L., Miquel, B. and Paultre, P. (2023) 'Parameterized seismic fragility functions for gravity dams: An approach including the effect of updated model parameter knowledge', *Canadian Conference - Pacific Conference on Earthquake Engineering* [Preprint].
- Segura, R.L., Padgett, J.E. and Paultre, P. (2019) 'Polynomial response surface-based seismic fragility assessment of concrete gravity dams', *12th Canadian Conference on Earthquake Engineering* [Preprint].
- Segura, R.L., Padgett, J.E. and Paultre, P. (2021) 'Expected seismic performance of gravity dams using machine learning techniques', *Bulletin of the New Zealand Society for Earthquake Engineering*, 54(2), pp. 58–68. Available at: <https://doi.org/10.5459/bnzsee.54.2.58-68>.
- Sevieri, G., De Falco, A., Andreini, M. and Matthies, H.G. (2021) 'Hierarchical Bayesian framework for uncertainty reduction in the seismic fragility analysis of concrete gravity dams', *Engineering Structures*, 246(June), p. 113001. Available at: <https://doi.org/10.1016/j.engstruct.2021.113001>.
- Sevim, B. (2018) 'Geometrical dimensions effects on the seismic response of concrete gravity dams', *Advances in Concrete Construction*, 6(3), pp. 269–283. Available at: <https://doi.org/10.12989/acc.2018.6.3.269>.
- Su, H., Wen, Z., Zhang, S. and Tian, S. (2016) 'Method for choosing the optimal resource in back-analysis for multiple material parameters of a dam and its foundation', *Journal of Computing in Civil Engineering*, 30(4), pp. 1–9. Available at: [https://doi.org/10.1061/\(ASCE\)CP.1943-5487.0000537](https://doi.org/10.1061/(ASCE)CP.1943-5487.0000537).

- Tekie, P.B. and Ellingwood, B.R. (2003) 'Seismic fragility assessment of concrete gravity dams', *Earthquake Engineering and Structural Dynamics*, 32(14), pp. 2221–2240. Available at: <https://doi.org/10.1002/eqe.325>.
- Torres Filho, R.J. de A., Segura, R.L. and Paultre, P. (2023) 'Polynomial response surface-based transformation function for the performance improvement of low-fidelity models for concrete gravity dams', *Probabilistic Engineering Mechanics*, 74, p. 103544. Available at: <https://doi.org/10.1016/j.probengmech.2023.103544>.
- U.S. Army Corps of Engineers (1995) 'Gravity dam design', *Technical Report, EM-1110-2-2200* [Preprint].

ANALYSIS OF THE BEHAVIOUR OF A GRAVITY DAM IN CENTRAL AMERICA SUBJECT TO HIGH SEISMIC FORCES

A. De Paola¹, E. Baldovin² & S. Pavone³

¹ Geotecna Progetti, Milan, Italy, a.depaola@geotecnaprogetti.com

² Geotecna Progetti, Milan, Italy

³ Geotecna Progetti, Milan, Italy

Abstract: Dams fall into the category of strategic or relevant works due to the important economic value they represent and the dreadful consequences of anomalous functioning or hypothetical collapse. Taking into account the verification criteria of the dams of the U.S. Army Corps of Engineers (USACE) recommendations, the paper illustrates some aspects concerning the evaluation of the safety in seismic conditions of a gravity dam located in Central America in a context of high seismicity. In particular, the results of the analyses developed using various numerical methods and methodologies of increasing complexity are presented, starting from a traditional calculation approach, based on the classic formulations of science of construction (called Theoretical Method), up to FEM analyses both in the linear and nonlinear field. The analyses were performed in Safety Evaluation Earthquake (SEE) and Operating Basis Earthquake (OBE) conditions. The pseudo-static analyses with the Theoretical Method have made it possible to evaluate the safety coefficients of the structure in terms of general stability (sliding, overturning and uplift), as well as to provide the first elements on the state of stresses in the body of the dam and at the contact with the foundation massif. To evaluate the influence of the geotechnical characteristics of the foundation mass, in particular in terms of safety coefficients against sliding open parameter analyses were carried out by varying the characteristic values. Subsequent linear and nonlinear dynamic FEM time history analyses, performed using suitably selected accelerograms scaled to the site-specific response spectra values, were used to calculate step by step during the seismic event the stress and strain response of the dam body and of the foundation mass. The calculation models used in the analyses were validated by comparing the results obtained with the Theoretical Method and with the FEM Model. The acceptability of the results of the dynamic analyses was also verified using the assessment method suggested by USACE.

1. Introduction

In the present paper a progressive analysis process used to evaluate the seismic behaviour of a gravity dam in a high seismicity region of the Central America is exposed. After a summary of the parameters to be evaluated and the dam safety verifications to be performed according to USACE recommendations, a brief presentation of the examined case study is reported. The seismic analysis of the dam started in the feasibility project stage with the evaluation of the dam rigid body stability performed with a traditional method of analysis. Afterwards, the analyses continued in the pre-construction engineering and design (PED) project stage with different applications of the FEM method, which made it possible to estimate the trend of the stress-strain state in the body of the dam and in the foundation rock mass during possible seismic events. The method of analysis to be used to evaluate the seismic behaviour of a gravity dam essentially depends on the seismic hazard of the region in which the work has been or will be built and on the project stage [6]. Connected to these conditions are the level of knowledge of the materials constituting the dam and the

ground and the performance required for the examined structure. Therefore, the analysis depends on the specific characteristics of the structure and on the related boundary conditions, which inevitably vary from a case to another and influence the design choices and the numerical verifications. In this context, the preparatory activities for the definition of the boundary conditions of the structure are very important, especially in areas of high seismicity such as that in which the dam discussed in the present paper falls. For this purpose, it is necessary to carry out a geognostic and geotechnical survey on site to obtain a reliable geomechanical characterization of the foundation rock mass and the execution of a seismotectonic study of the site to define adequate design seismic actions. The following figure reports the flow chart of the analysis process adopted for the dam examined in the present case study.

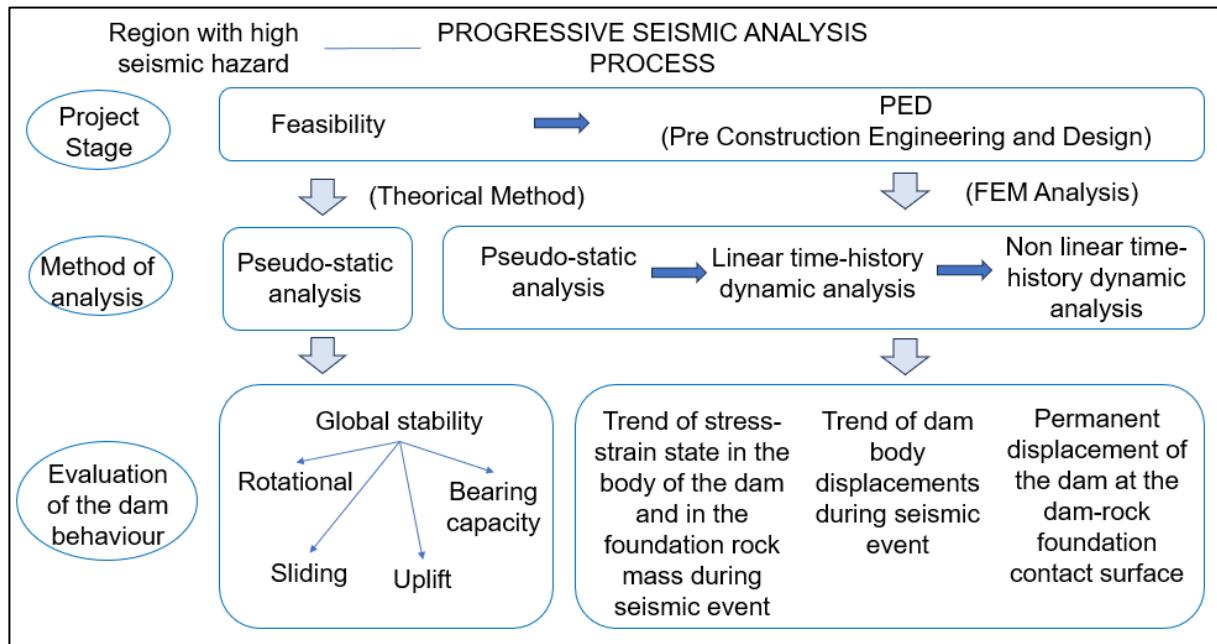


Figure 1. Progressive seismic analysis process – Flow chart.

2. Evaluation of gravity dam seismic behaviour

In the following paragraphs the main parameters to be evaluated and the dam verifications to be performed when carrying out seismic analyses of a gravity dam according to USACE recommendations are reported.

2.1. Rigid body stability

Gravity dam must be checked against rigid body motion. The dam stability against dam sliding, overturning and uplift potential phenomena is expressed by a Safety Factor (SF) obtained comparing the resultants of the stabilizing and un-stabilizing actions acting on the dam body. The dam sliding stability is checked comparing the resultant of the acting forces with the material shear strength resultant on a potential sliding plane. Sliding planes could occur inside the foundation rock mass, along contact surface between dam concrete base and rock foundation and inside the dam concrete body, with particular reference to the concrete lifts position. The dam overturning stability is evaluated comparing the resultant of the stabilizing and un-stabilizing moments acting on the dam body. The equilibrium against overturning phenomena is ensured if the resultant of the actions is located inside the dam base section. A different stresses trend is expected in the foundation rock mass based on the position of the mentioned resultant respect to the middle third of the dam base section. The dam uplift stability is estimated comparing the resultant in the vertical direction of the actions acting on the dam body with the resultant of the water pressure at the dam-foundation contact surface. The evaluation of the dam rigid body stability in seismic conditions must refer to the SEE load combinations.

2.2. Bearing capacity

The bearing capacity of the dam-foundation system is checked by ensuring that the maximum value of the stresses transferred from the dam to the ground is lower than the value at which failure phenomena occur in the foundation rock mass.

2.3. Stress state in the dam body

The stress state must be evaluated in the dam body, with particular reference to the upstream and downstream faces, at the change of slope in the upper part of the dam, in correspondence of cavities inside the dam body (drainage gallery, internal control rooms, shaft etc), in the spillway and in the dam thinner portions (crest, possible bridge piers in the dam crest), where stress concentration are expected to occur. Evaluated stresses must result lower than tensile and compression concrete strength values in order to avoid damage and crack phenomena in the dam for the OBE seismic conditions. The performance of dams for the SEE conditions is considered satisfactory if the cracks that develop during intense ground shaking do not open to the extent that significant leakage through the dam can occur, or to the extent that significant permanent irrecoverable displacements within the dam or foundation occur.

2.4. Displacements

The evaluation of concrete gravity dam behaviour regards differential and absolute displacements that could occur respectively in the dam body and at the dam-foundation contact surface. The displacements of the dam should be contained in order to ensure the operability of electromechanical equipment and utilities (gates, outlets, bridge etc..) for the OBE seismic conditions. For the SEE seismic condition, differential displacements among the dam independent concrete blocks have to be limited to low values, in order to ensure the operability of the water stop elements; similarly absolute displacements at the dam base have to ensure the operability of the possible drainage system and grout curtain realized in the t dam foundations.

3. The case study

3.1. Principal characteristics of the analyzed dam

The analysed structure is a 39.65 m high conventional concrete gravity dam (top elevation at 94.60 m a.s.l. and minimum foundation elevation at 54.95 m a.s.l.) divided into 9 independent blocks of width ranging from 11.30 m to 25.20 m, for a total longitudinal extension equal to 153.50 m. The dam upstream and downstream faces are inclined respectively 1v/0.4h and 1v/0.7h. The foundation plane has an inclination respect to the horizontal equal to 3° degree, rising from upstream to downstream. The central part of the dam includes five spillways with a discharge threshold at an elevation of +87.70 m and width ranging from 8.40 m to 14.40 m, separated by piers and topped by 3.00 m high flap gates. A drainage system and a grout curtain executed from the dam drainage gallery intercept the foundation rock mass.

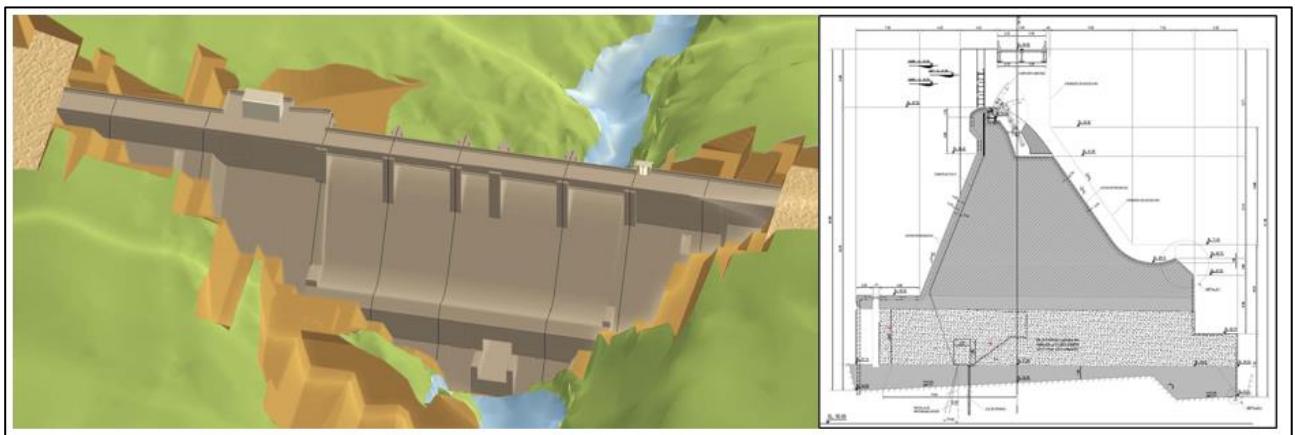


Figure 2. A 3D dam view (Revit software) and a dam typical cross section.

Concretes with values of strength f_c' ranging from 21 to 30 MPa have been chosen to realize the dam: $f_c'=21$ MPa for the dam body above elevation 66 m a.s.l., $f_c'=25$ MPa for the dam body under the elevation of 66 m a.s.l. and the dam upstream face and $f_c'=30$ MPa for the superficial layer of the spillway. The Maximum Operating Water Level (NAMO) of the dam was fixed at +90.50 m a.s.l..

3.2. The foundation rock mass

The dam foundation rock mass is composed by grey to light green-brown foliated metavolcanic rocks, classifiable as Type III-II Metandesite in the characterization of the International Society of Rock Mechanics (ISRM). According to the results of geological and geomechanical surveys, the massif has a compact

structure and, in general, a low degree of fracturing and alteration, with RQD values typically greater than 70%. It is characterized by the following geomechanical properties: Unit weight $\gamma=26-27 \text{ kN/m}^3$, Compression strength of the intact rock $\sigma_{ci}= 10-50 \text{ MPa}$, Geological Strength Index $GSI= 35-70$, Static Young Modulus $E_m= 5-30 \text{ GPa}$, Dynamic Young Modulus $E_d= 10-70 \text{ GPa}$. The dam-foundation contact surface is characterized by the following strength parameters: friction angle $\phi=32^\circ$, cohesion $c_k=300 \text{ kPa}$.

3.3. Seismic loading conditions

The following loads have been taken into account in the seismic analyses of the dam: weight of the dam, weight and pressure of the water on the dam upstream face, water uplift pressure at the dam base, weight and pressure of the sediment acting on the dam upstream face, seismic actions. Different load combinations have been considered by varying the design earthquake condition (Operating Basis Earthquake (OBE) or Safety Evaluation Earthquake (SEE), coincident with the Maximum Design Earthquake (MDE)) and the reservoir conditions (empty or full with the “*coincident pool*” water level assumed at an elevation equal to 86.02 m a.s.l.) according to USACE prescriptions reported in Annex B of [4]. In the following table the very high values of the Peak Ground Acceleration (PGA) associated with the OBE and SEE design earthquake for the dam site are reported.

Table 1. Peak ground acceleration for OBE and SEE design earthquake.

Design Earthquake	Return period T (years)	PGA _h (g)	PGA _v (g)
OBE	144.3	0.179	0.099
SEE	5750	0.776	0.484

4. Analysis of the dam with the Theoretical Method

4.1. Calculation hypotheses

In the feasibility project stage, the dam behavior has been evaluated by means of a method of analysis called “*Theoretical Method*”. The dam has been analyzed through the calculation program “*Gravity Dams Analyses*” (G.D.A.) developed over the years by Geotecna Progetti and fully validated, implemented for the specific case study with the coefficients required by the USACE recommendations. The program analyzes the 2D behavior of the dam cross section with reference to rigid body motions and stresses values at dam faces. Through equilibrium equations and science of construction formulations it allows to evaluate the stability conditions of every single strip in which the dam cross section has been subdivided by the user and to carry out for each load combinations the following outputs: the resultant of acting vertical actions, horizontal actions and bending moments, the eccentricities of the loads, the pressure line along dam height. The program generates graphs with the geometry of the dam in which the central core of inertia and the position of the center of pressure along the dam height for each analyzed load combination (Figure 3) are represented.

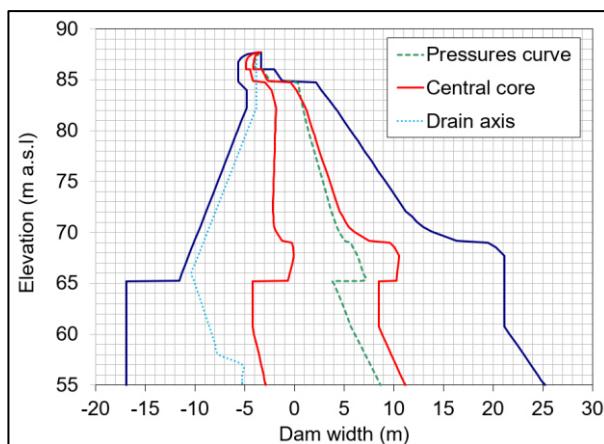


Figure 3. Example of an output of the analyses with “*Theoretical Method*” - Position of the centre of pressure along the dam height.

In the dam seismic analyses performed with the Theoretical Method, the earthquake input has been considered according to a pseudo static approach. Inertial actions have been evaluated taking into account the values of PGA above mentioned and the seismic method coefficients k_h and k_v suggested by USACE [4].

4.2. Interpretation of the analysis results

The results of the performed analysis provided dam safety factors against dam sliding, overturning and uplift potential phenomena greater than the minimum values suggested by USACE recommendations.

It has to be considered that sliding stability checks are of fundamental importance in the analysis of a gravity dam and require correct evaluation of the shear resistance parameters of the concrete along the casting joints and the contact surface between dam and foundation rock mass.

The calculation program used for the “Theoretical Method” requires an easy set up and very low calculation time if compared with the complex FEM method later mentioned. Those qualities have allowed to study the sliding stability of the dam changing the geomechanical parameters of the contact surface between the dam base and the foundation rock mass (friction angle and cohesion) and imposing the minimal required values of the safety factor against sliding phenomena for all the analyzed load combinations. As a result of the performed analysis a domain with the minimal values of the geotechnical parameters necessary to ensure dam sliding stability has been obtained (Figure 4).

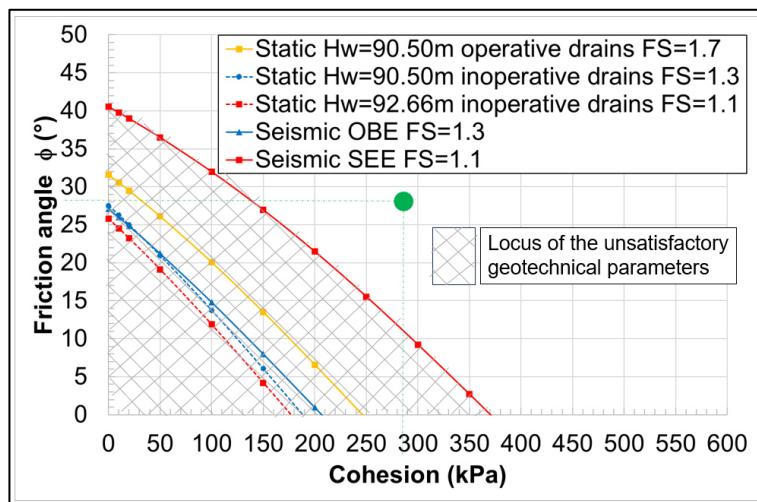


Figure 4. Example of an output of the analyses with “Theoretical Method – Locus of the unsatisfactory geotechnical parameters

Based on the results of the sliding verifications on potential planes inside the foundation rock mass performed according documents [1] and [2], it was possible to evaluate f the consolidation measures to adopt in the dam foundation rock mass.

In a preliminary calculation stress values resulted lower than the materials strength limits. In particular, in SEE condition, a maximum value of compression in the dam downstream toe of about 1.85 MPa and a maximum tension stress in the dam upstream toe of about 0.45 MPa have been obtained.

The additional in situ geotechnical surveys carried out returned shear strength characteristics of the rock mass sufficient to verify the dam for sliding phenomena (green point in figure 4). The geometries of the dam adopted in the feasibility project stage were therefore confirmed and used as a starting point for the FEM analyses method.

5. Analysis of the dam with the FEM Method

The behaviour of the dam was more deeply studied in the PED project stage by means of numerical analyses performed with the FEM Method. Several types of analyses with increasing complexity have been executed changing the characteristics of the used numerical model and the way to assign to it the earthquake loads. In the following figure the flow chart of the FEM analyses performed for the dam analysed in the present case study is reported.

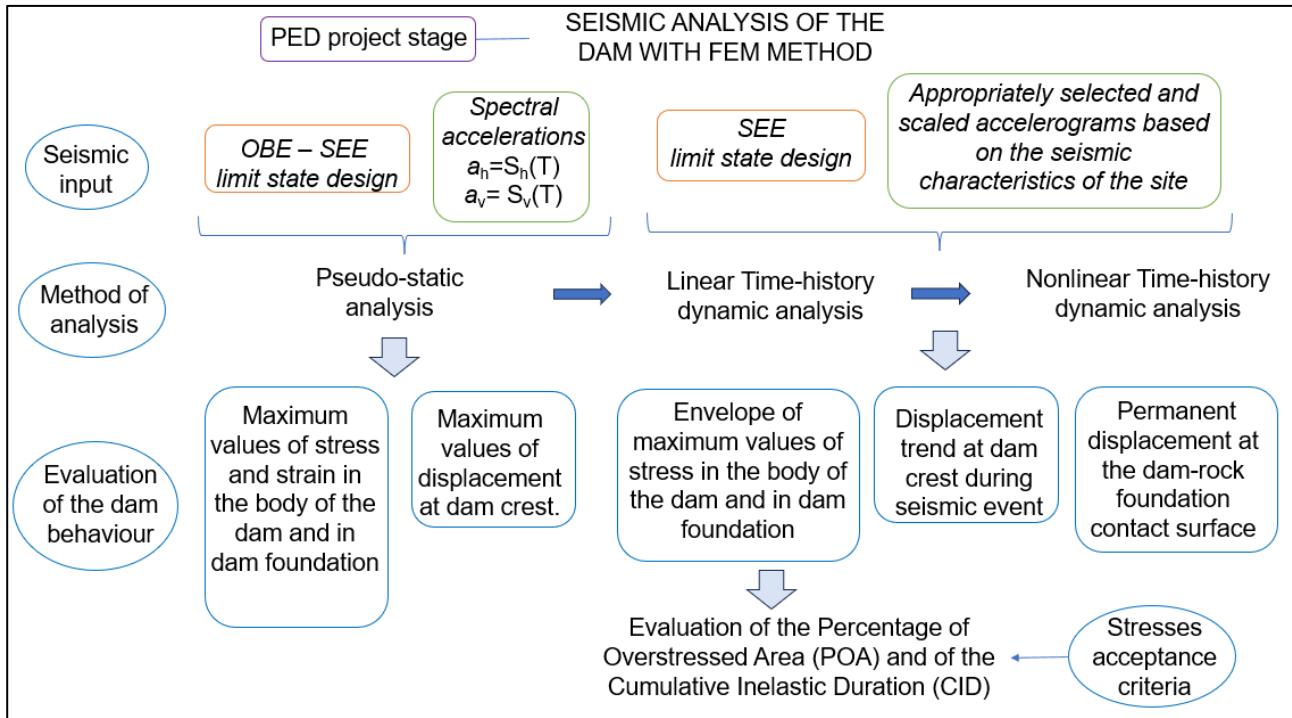


Figure 5. FEM Method analysis – Flow Chart

5.1. Numerical model description

The FEM numerical models of the dam analyzed typical cross sections have been realized with Straus7 calculation software using 3D brick type elements (8 nodes) 1 m in thickness.

The rock mass foundation has been modeled with a lateral extension and depth equal respectively to about three and two times the base width of the dam. The boundary nodes of the foundation rock mass have been restrained in all the directions.

FEM model peculiarities, loads and material properties (dam concrete and foundation rock mass) have been assumed in calculations according to the USACE prescriptions and depending on the type of the performed analysis (pseudo-static or dynamic time-history analysis).

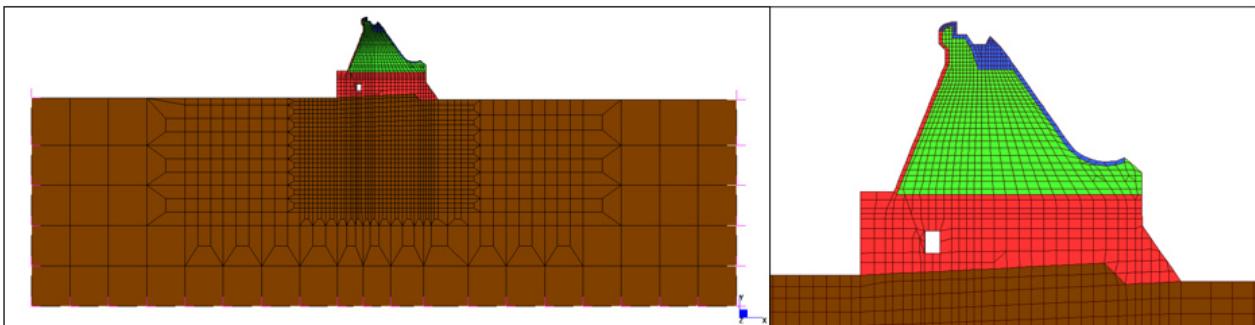


Figure 6.Example of a FEM numerical model of a dam analysed typical cross section.

6. Pseudo-static analysis

6.1. Calculation hypotheses

The FEM model was firstly validated comparing the analyses results obtained assuming the same pseudo static seismic action with those of the Theoretical Method based on the PGA values evaluated for the site. Afterward, the pseudo static analyses were performed considering the spectral accelerations values evaluated in correspondence of the fundamental periods that characterize the dam. For this purpose, a modal analysis was executed, considering the weight of the dam and the added masses due to the water

and the sediment in the reservoir. In the following figure the first three fundamental vibrational modes of the dam with the relative vibrational periods and percentage of involved mass are illustrated.

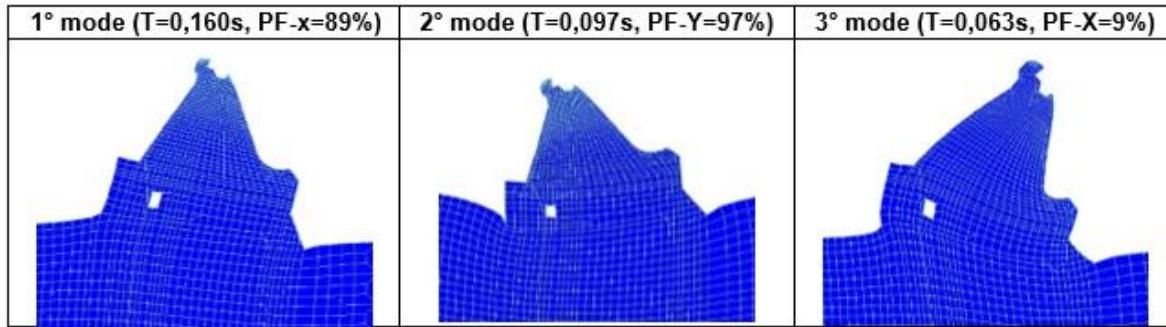


Figure 7. FEM Method – Pseudo-static analysis – First three natural vibration modes of the dam.

According to the horizontal and vertical spectral response of the site and to the first vibration mode of the analysed dam the following values of seismic acceleration have been adopted in the pseudo static analysis executed with the FEM method: for OBE seismic condition: $S_h=0.357$ g and $S_v= 0.238$ g; for SEE $S_h=1.612$ g and $S_v=1.161$ g.

The hydrodynamic pressure acting on the dam upstream face has been calculated according to the Westergaard formulation as suggested in paragraph 4-7 of [4]. The action due to the silt accumulation upstream of the dam has been evaluated according to paragraph 4-8 of [4].

6.2. Interpretation of the analysis results

In the following figure the trends of the maximum and minimum stress values resulting in the body of the dam and in the rock mass from the most severe analyses performed for the SEE seismic condition in full reservoir combination are reported.

For a correct interpretation it is necessary to consider the following aspects. In the adopted mesh, the rock mass foundation and the dam concrete base surface are physically connected (the dam and the rock share the same finite element nodes), therefore, according to the model, rock finite elements are capable of developing tensile stresses, which could also be transferred from the above dam finite elements.

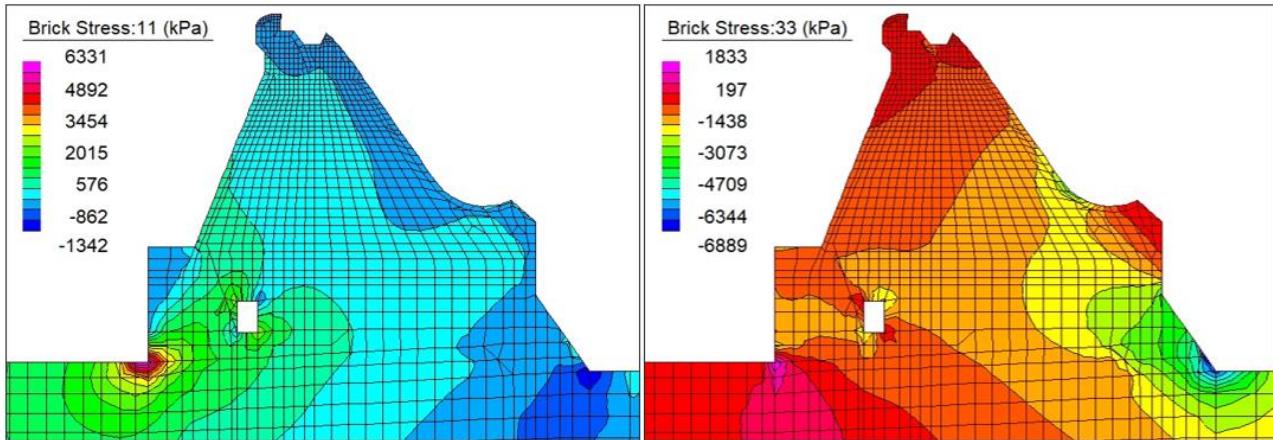


Figure 8. FEM Model – Pseudo static analysis – Trend of maximum and minimum stress values in the body of the dam and in the rock mass in SEE seismic condition.

The stresses trend obtained at the dam upstream and downstream toes (with very high values of the maximum tensile stress equal to about 6.3 MPa), appears different from the stresses distribution expected in the reality, with no peak values of tensile stress in correspondence of the dam-foundation contact elements. Furthermore, the stresses trend obtained in the ground, even if generally complies with the theory of the indefinite half-space at Boussinesq, provides an unrealistic asymptotic trend near the edge of the dam foundation due to the above-mentioned FEM model peculiarity. Although FEM modelling introduces

deformability to the analysed dam-foundation system unlike the Theoretical Method previously discussed (rigid body hypothesis), the high values of the spectral accelerations assumed as seismic input and the numerical limits of the FEM model above exposed lead to unrealistic tensile stress values greater than the limit suggest by USACE for the adopted concrete. As a consequence, it is necessary to analyse the seismic behaviour of the dam through more evolved numerical models with time history dynamic analyses presented further on. Therefore, first dynamic analyses have been performed by means of numerical linear model (Chapter 7), then more complex nonlinear models have been implemented (Chapter 8) in order to simulate the nonlinear behaviour of the contact surface between the dam and the foundation rock mass.

7. Linear time history dynamic analysis

7.1. Calculation hypotheses

The FEM model previously described for the pseudo-static analysis was implemented according to the recommendations reported in paragraph 2-12 of [3], in order to perform the dynamic time-history analyses. The damping effects induced by the motion of the dam during the seismic event were considered in FEM analyses by adopting a Rayleigh model. The inertial action of the reservoir water for the dynamic time-history analyzes was modeled by means of a distribution of equivalent concentrated masses, positioned on the nodes of the upstream face of the dam. The masses were evaluated using Westergaard's formulation reported in paragraph 2-19 of [3]. The stiffness values attributed to the FEM brick elements that constitute the dam and the foundation have been assumed based on specific tests executed on site rock mass. Time-history dynamic analyses have been performed using suitably selected accelerograms scaled to the site-specific response spectra values. In each analysis, the seismic action was simulated through a couple of natural accelerometers recordings (X, Z components) associated with a specific seismic event. Eleven couples of accelerograms were selected, which respect the compatibility criteria defined according to the regional seismotectonic model of the area of interest, appropriately scaled in such a way that the related response spectra approximate the reference elastic response spectrum in the field of proper periods of vibration of interest for the dam, as showed in the following figure.

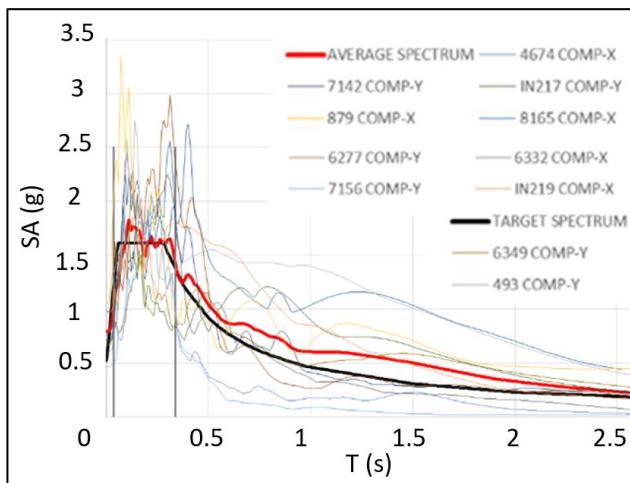


Figure 9. Comparison between the average horizontal spectral shape and the target spectral shape for the dam site.

7.2. Interpretation of the analysis results

The following figure shows the envelope of the maximum and minimum stress values in the body of the dam and in the rock mass, resulting from the most severe seismic event analyzed in the SEE condition in full reservoir combination. From a first analysis of the results, it could be noted that the highest stress values are located in correspondence of the upstream and downstream toes of the dam (red circle in the following figure). The maximum tensile stresses obtained are of the order of 4.5-5 MPa and exceed the static tensile strength of concrete assumed equal to 2.17 MPa for concrete class C21 and 2.44 MPa for concrete class C25. The exceeding of the tensile strength values seems to be limited only to the upstream and downstream toes of the dam; therefore, it is possible to exclude the formation of continuous fracture surfaces, which could generate general instability effects on the structure, between the upstream and downstream faces.

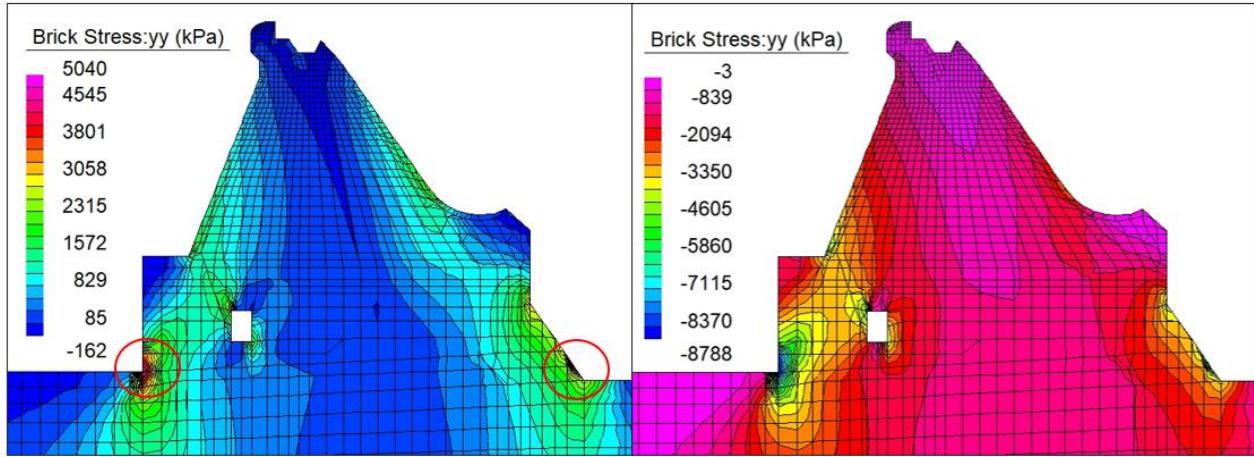


Figure 10. Linear dynamic time history analysis - Envelope of maximum and minimum stresses values in the body of the dam and of the foundation rock mass.

For a correct interpretation of the obtained results, it has to be remembered that the FEM model used in the linear dynamic analyses in correspondence of the dam base has the same peculiarity of the model used in the pseudo static calculations (the concrete and the rock share the same finite element nodes). Therefore, the aforementioned high stress values could be caused by the same limits of the numerical model. Despite that, the acceptability of their values has been checked, according to USACE recommendations by means of the assessment method reported in paragraph 6-3 of the [5], in terms of transient exceedance during the seismic event of the admissible tensile stresses. The maximum value obtained for the percentage of the overstressed area (POA), equal to about 3%, resulted widely below the limit imposed by the method, equal to 15% for a demand-capacity ratio DCR equal to 1 (see the following figure on the left). Similarly, the highest value obtained for the cumulative inelastic duration (CID), equal to 0.262 seconds, was below the imposed limit of 0.3 seconds for a DCR=1 (see the following figure on the right).

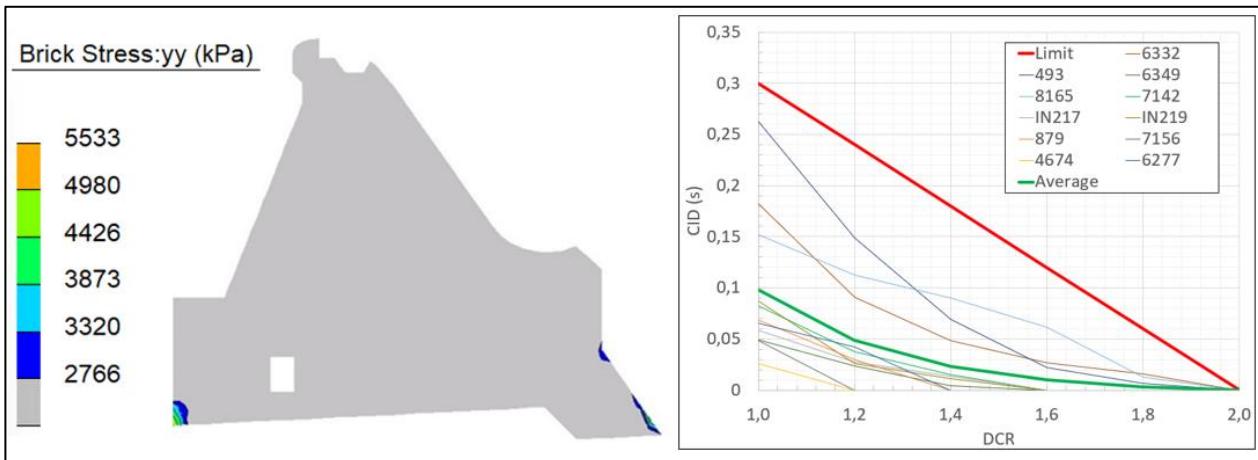


Figure 11. Linear time-history dynamic analysis – Acceptance criteria – Example of Overstressed Area (left side) and CIR calculation (right side)

The maximum compression stresses in the foundation rock mass resulted equal to about 3 MPa in SEE seismic condition and, except for some singular edge points (due to the limits of the numerical model), they resulted compatible with the admissible stress values of the rock mass (equal to about 4.16 MPa). As showed in the following figures, the maximum values of displacement "Sc" at the dam crest were of the order of 2 cm, such as the ratio between Sc and the dam height H resulted of the order of 0.061%. The obtained ratio Sc/H is widely lower than the interval 0.08 ÷ 0.1% to which in the literature (for example see document [8]) partial or global collapse phenomena in gravity dams are associated.

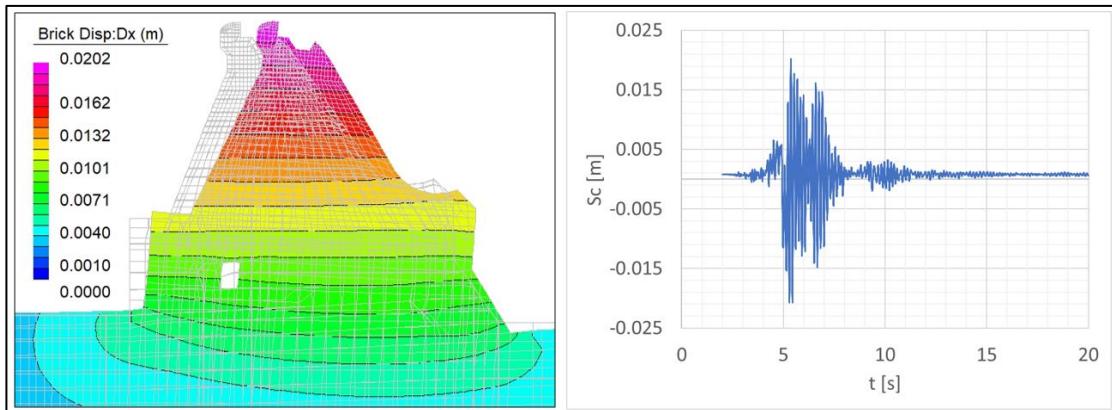


Figure 12. Linear time-history dynamic analysis – Displacement trend at the dam crest during the most severe analysed seismic event (right side) and displacement trend in the dam and in the foundation at the instant of time in which the maximum horizontal displacement was recorded (left side).

The good results obtained in the analyses performed in SEE seismic conditions, in terms of both displacements and stress state, show that the level of damage in the body of the dam remains below the acceptance limit, except for some singular edge points due to the limits of the numerical model. Therefore, the performed linear time-history dynamic analysis could be considered sufficient for the interpretation of the dam behavior in seismic conditions. Despite that, it was decided to perform non-linear time-history dynamic analyses in order to evaluate in an even more precise and reliable way the tensile stress values that occur at the dam toes of the dam and the possible permanent displacements in the foundation.

8. Nonlinear time history dynamic analysis

8.1. Calculation hypotheses

Specific beam type finite elements called "contact points" have been introduced in the FEM mesh between the nodes of the concrete dam brick type element and those of the foundation rock mass, in order to simulate the frictional behaviour between the dam and the foundation rock mass and the possibility that part of the foundation does not react when subjected to tensile stress. Therefore, the elements in question are "activated" exclusively when subjected to compression, providing a stiffness contribution both in the axial direction and in the horizontal plane. The following figure represents the FEM mesh used, in which the absence of solid finite elements "brick" between the material constituting the rock mass in the foundation (represented in brown) and those constituting the dam (represented in red) is showed.

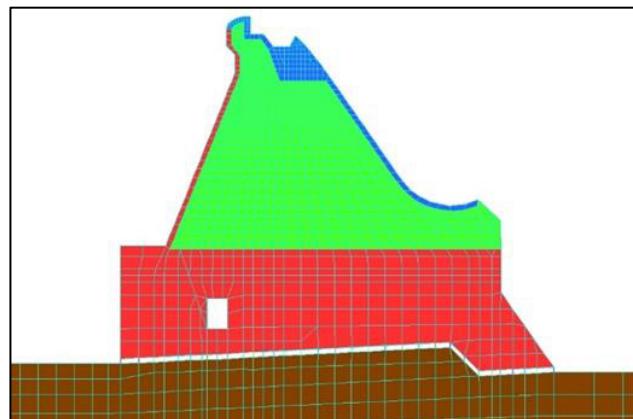


Figure 13. Nonlinear time-history dynamic analysis – Detail of the FEM mesh showing "contact point" elements at the dam base.

The nonlinear time history dynamic analyses have been executed considering the couple of accelerograms (horizontal and vertical direction) of the seismic event selected in the SEE condition, that resulted with most severe consequence for the dam in the linear time history dynamic analyses previously performed.

8.1. Interpretation of the analysis results

In the following figures the envelope of the maximum and minimal stresses obtained in the body of the dam and in the foundation rock mass have been reported. From a first interpretation of the results, it can be noted that the highest values of the tensile stresses are not located in the dam toes, as it was recorded in the linear dynamic time history analyses previously discussed, but in the upstream and downstream faces of the dam (red circle in the following figure). Relevant stresses concentrations have been obtained also in correspondence of the drainage gallery and as usual where face slope changes. The maximum stress value was equal to about 1.7 MPa, lower than the tensile strength of the several concrete types adopted for the dam; damage and crack phenomena in the dam for both SEE and OBE seismic conditions were then avoided.

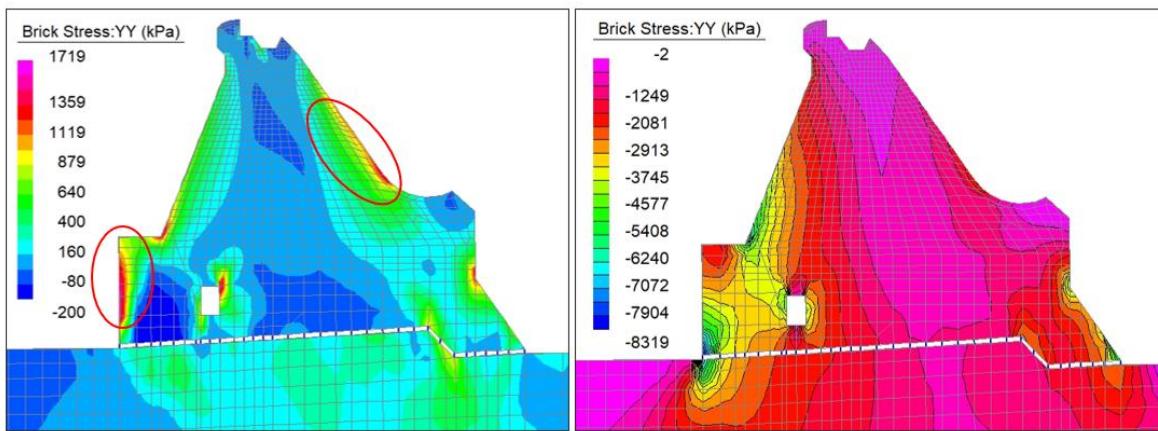


Figure 14. Nonlinear time history dynamic analyses - Envelope of maximum and minimum stresses values in the body of the dam and in the foundation rock mass.

As showed in the following figure, the maximum value of the absolute displacement "Sc" at the dam crest was of the order of 2 cm, while the residual displacement at the dam base "Sb" was equal to about 7 mm ($Sb/H=0.035\%$).

The maximum relative displacement at the dam crest, of about 1.3 cm, resulted lower than that recorded in the linear dynamic time history analyses discussed at chapter 7 (about 2 cm). This result can be related to the joint with frictional behaviour introduced in the nonlinear model to simulate the contact surface between the dam and the foundation rock mass, which contributes to a greater earthquake energy dissipation.

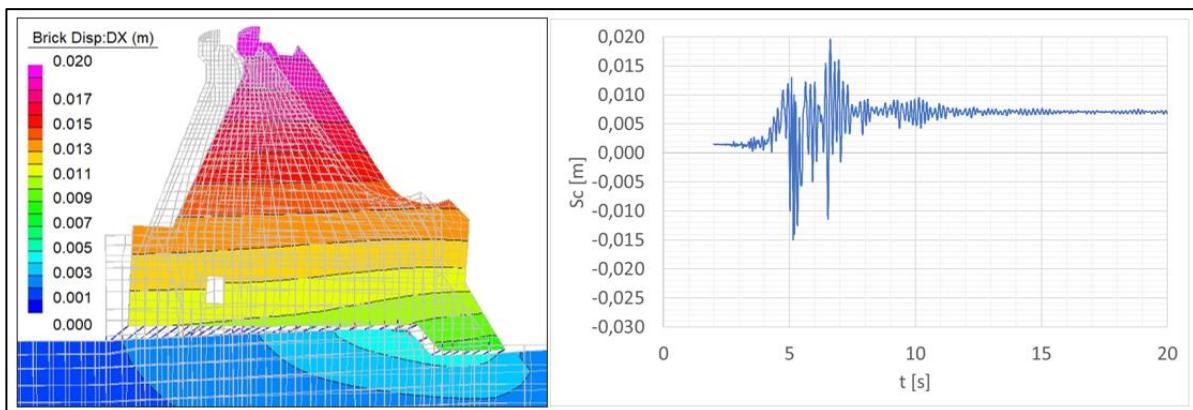


Figure 15. Nonlinear time-history dynamic analysis - Displacement trend at the dam crest during the most severe analysed seismic event (right side) and displacement trend in the dam and in the foundation at the instant of time in which the maximum horizontal displacement was recorded (left side).

The values of displacements, equal to few millimeters in OBE and about 2 cm in SEE, obtained at the dam crest in all the performed FEM analyses ensure the operability of the dam electromechanical equipment and utilities (gates, outlets, bridge etc.). Likewise the residual displacements resulted at the dam base warranty

the safe operation of the water stop elements and of the drainage system and grout curtain in dam foundations in both OBE and SEE seismic conditions.

The result confirms the satisfactory values of the safety factor obtained in the sliding stability analyses performed in the feasibility project stage and underlines that nonlinear time history dynamic analyses exclude any partial or global collapse phenomena in the dam.

9. Conclusions

A case study concerning the evaluation of a gravity dam safety in seismic conditions in a context of high seismicity is presented considering the USACE verification criteria for dams. The results of the analyses, developed using various numerical methods of increasing complexity, are reported and commented in the paper. In the feasibility project stage, the safety of the dam against sliding, overturning and uplift phenomena has been checked and preliminary values of stresses in the dam faces and foundation have been evaluated with the "Theoretical Method". During this project stage an open parameter analysis of the minimum shear resistance characteristics that the foundation plan has to guarantee was developed. As the abovementioned characteristics have been defined through in situ specific geotechnical surveys, in the next design stages it has been possible to proceed with a targeted design of the structure, confirming the geometries defined in the feasibility project stage. In the PED project stage, the seismic behaviour of the dam has been investigated with more complex numerical analyses. A 3D FEM model has been realized with specific characteristics based on the type of seismic analysis to be performed (based on an adequate seismotectonic study and a reliable geomechanical characterization of the foundation rock mass). The results obtained with the numerical FEM analyses allowed to evaluate the stress-strain state in the dam body and its displacements under the defined design earthquakes. As confirmed by the present case study, in the design of a complex structure, such as a dam, it is absolutely important to adopt a numerical approach of increasing complexity during the several project stages. A basic numerical analysis (methods based on the classical formulations of construction science), which allows to acquire a good sensitivity of the general behaviour of the dam, has to be followed by more advanced modelling (e.g. pseudo static, dynamic, linear and non-linear analyses) which guarantees an extensive study of the stress-strain state and of the dam general behaviour. This approach appears fundamental to develop solid numerical models and consequent reliable results representative of the real behaviour of the dam. Therefore, the seismic analysis process cannot be completely standardized and acritically applied to every gravity dam. It depends, in fact, on the specific characteristics of the analysed structure and on the related boundary conditions, which inevitably vary from a case to another, and influence the design choices and the numerical verifications.

10. References

- [1] U.S. Army Corps of Engineers USACE (1994). Engineering Manual EM 1110-1-2908: *Rock Foundations*.
- [2] U.S. Army Corps of Engineers USACE (1995). Engineering Manual EM 1110-2-2200: *Gravity Dam Design*.
- [3] U.S. Army Corps of Engineers USACE (2003). Engineering Manual EM 1110-2-6051: *Time-History Dynamic Analysis of Concrete Hydraulic Structures*.
- [4] U.S. Army Corps of Engineers USACE (2005). Engineering Manual EM 1110-2-2100: *Stability analysis of concrete structures*.
- [5] U.S. Army Corps of Engineers USACE (2007). Engineering Manual EM 1110-2-6053: *Earthquake Design and Evaluation of Concrete Hydraulic Structures*.
- [6] U.S. Army Corps of Engineers USACE (2016). Engineering Regulation ER 1110-2-1806: *Earthquake design and evaluation for civil works projects*.
- [7] American Society of Civil Engineers ASCE (2010). ASCE/SEI 7-10: *Minimum Design Loads for Building and Other Structures*.
- [8] M. A. Hariri-Ardebili and V. Saouma. (2014). "Quantitative failure metric for gravity dams". The Journal of the International Association for Earthquake Engineering.

DAM PORTFOLIO ASSESSMENT FOR RISK INFORMED DECISION MAKING

T.Elkhoraibi¹, A. Hashemi¹, A.Kottke² & Y. Arici³

¹ Hashemi & Elkhoraibi Earthquake Engineering Inc., Berkeley, CA, USA

² Pacific Gas and Electric Company, San Francisco, CA, USA

³ Middle East Technical University, Ankara, Turkey, yarici@metu.edu.tr

Abstract: There is a large inventory of older gravity dams in North America which are used for energy generation and control of river regimes. The performance of these systems under seismic hazard is a significant concern as the understanding of seismic hazard has changed significantly, with most systems subject to significantly higher hazard compared to the original design specifications. The management decisions on these systems, such as possible strengthening, are a substantial challenge requiring collection and evaluation of site data, in-situ dam conditions, and analysis and hazard assessment for a large number of systems. Correspondingly, techniques for rapid screening and selecting systems with higher risk are required for optimal allocation of resources on more fragile systems. The evaluation of the seismic risk for gravity dams, in connection with this decision making for dam portfolio management, is already a difficult task. Rigorous consideration of soil-structure-reservoir interaction is required while also considering epistemic and aleatory uncertainties. The effects of uncertainties on assessment need also be quantified so that further investigative work could be scheduled where appropriate.

In accordance with the needs mentioned above, a methodology for comparative evaluation of the seismic risk for dam stock is proposed in this study with the goal of informing decision making related to risk mitigation measures. As the first level of a multi-level screening approach, the seismic risk is quantified in terms of fragility functions and Annual Probability of Exceedance (APE) of a damage state. Two damage states, incipient and severe damage, were defined. The Simplified Response Spectrum Analysis (SRSA) method, with modifications for incorporation of drain damage potential and post-seismic sliding evaluations, is chosen as the analysis method for constructing fragility functions, allowing for explicit evaluation of epistemic uncertainty using Latin Hypercube simulations. Cracking, sliding and bearing limits were considered and the aggregate comparative risk of exceeding the damage states, along with the associated effect of uncertainties, are determined. The APE values can be incorporated into the larger database for multi-hazard assessment. The proposed method allows screening of systems for the next level of assessment, ranking in a portfolio and provides directions for investigative work for better decision making.

1 Introduction

There is a significant inventory of older gravity dams in North America and Europe which are used for energy generation, irrigation, as well as control of river regimes. Of the estimated 4500 dams in North America, 40% are concrete gravity/arch or buttress dams. A fundamental difficulty faced by the owners or the regulators of these systems is the comparison of the fragility of these systems to seismic hazard to inform decision making related to risk mitigation procedures. Part of this difficulty is due to the fact that dams, one of a kind large

structures, have generally been assessed through deterministic approach (Carvajal et al., 2009). Uncertainty included first by fragility curves (Ellingwood and Tekie, 2001), leading to the adoption of PEER methodology in the last decade to this end (Hariri-Ardebili (2016)). In contrast to buildings, however, the inclusion of variabilities to decision making is challenging, given the large size of these systems along with the difficulties in seismic demand analysis. Correspondingly, there are no techniques to compare the risk associated with seismicity in a large dam portfolio with the particular goal of prioritizing further assessment, especially with regard to relevant information for sites, seismic hazard or foundation conditions.

In accordance with this need for providing information to decision making frameworks, a methodology for comparative evaluation of the seismic risk for dam stock is proposed. The goal of this methodology is twofold: 1) quantifying the seismic risk in terms of fragility functions and Annual Probability of Exceedance (APE) for incorporation into a larger database of facilities and 2) ranking the systems in terms of their fragility to seismic hazard to inform decision making. After the presentation of the framework for obtaining fragility functions, the considered uncertainties, the selected damage states and the associated analysis framework, a case study is presented. The quantification of the epistemic and aleatory variability for different failure modes in obtaining the final APE distribution is shown.

2 Fragility for gravity dams

A consistent estimate of seismic risk for concrete gravity dams can be expressed as the annual probability of exceeding a specific damage state. For the dam portfolio, fragility functions should be constructed for damage states considering uncertainties.

2.1 Dam portfolio categorization

In contrast to moment frames, seismic assessment of dams derives largely on system types or particular design aspect. Consequently, use of three tiers of analyses is proposed.

Tier 1: employs SRSA procedure suitable for sections with standard geometry, the main focus of this study.

Tier 2: employs 2D FEM analysis for non-standard sections where SRSA is not applicable.

Tier 3: employs more sophisticated analysis for systems with special issues or 3D features like arches.

2.2 Fragility functions

Fragility functions are defined as the conditional probability of exceeding a damage state as a function of an intensity measure of the earthquake ground motion, $P_E(a)$. Given the seismic hazard information as a function of ground motion intensity, $H(a)$, the APE is estimated by convolving the fragility function with the seismic hazard for the damage state, as a measure of seismic risk (Eq. 1). The fragility function is commonly assumed to follow a lognormal distribution (EPRI, 2018) where, $a_{x\%}$ is the ground motion intensity parameter (e.g. PGA) corresponding to $x\%$ probability of exceedance, Φ is the standard normal cumulative distribution function, and β^2 is the variance. as described by Eq. 2:

$$APE = \int_0^\infty -P_E(a) \frac{dH(a)}{da} \times da \quad (1)$$

$$a_{x\%} = a_{Ref} \times e^{\beta(\Phi^{-1}(x\%) - \Phi^{-1}(X_{Ref}))} \quad (2)$$

In Eq. 2, a_{Ref} is the ground motion intensity for a reference point on the fragility function, and X_{Ref} is the corresponding probability of exceedance. Given one point on the curve and its standard deviation, β , Equation 2 is used to compute the value of a as a function of the probability of exceedance. In the specific case where X_{Ref} is 0.5 (or 50%), Eq. 2 is reduced to Equation 3 below.

$$a_{x\%} = a_{50\%} \times e^{\beta\Phi^{-1}(x\%)} \quad (3)$$

In the case of the mean fragility curve, the applicable variance is composite, β_c^2 , and is comprised of the sum of the variances due to aleatory variability, β_r^2 , epistemic uncertainty due to the uncertainty about the input parameters, $\beta_{u,P}^2$, as well as the epistemic uncertainty due to modeling, $\beta_{u,M}^2$. The sources of uncertainty are presented in Table 1.

$$\beta_c^2 = \beta_r^2 + \beta_{u,P}^2 + \beta_{u,M}^2 \quad (4)$$

Table 1. Values and range of variable input parameters for Dam 1

Symbol	Source	Aleatory/Epistemic
β_r	Record-to-record variability	Aleatory
Input parameters including:		
$\beta_{u,P}$	<ul style="list-style-type: none"> Concrete compressive and tensile strength Structural damping ratio Concrete elastic modulus Foundation elastic modulus Foundation hysteretic damping Wave reflection coefficient Friction angle Cohesion Foundation bearing capacity Vertical drain effectiveness Height of reservoir water Height and density of sedimentation 	Epistemic
$\beta_{u,M}$	Modeling of analyzed system	Epistemic
β_c	Total (composite) aleatory and epistemic uncertainty with contributions from β_r , $\beta_{u,P}$ and $\beta_{u,M}$	Composite
$\beta_{u,H}$	Estimation of seismic hazard	Epistemic

In the case of the median fragility curve, the variance is defined only by β_r^2 (EPRI, 2018). As illustrated in Figure 1 and discussed in the next section, the fragility function for the dam is defined by defining the “anchor point” which represents one point on the fragility curve, in addition to the standard deviation β .

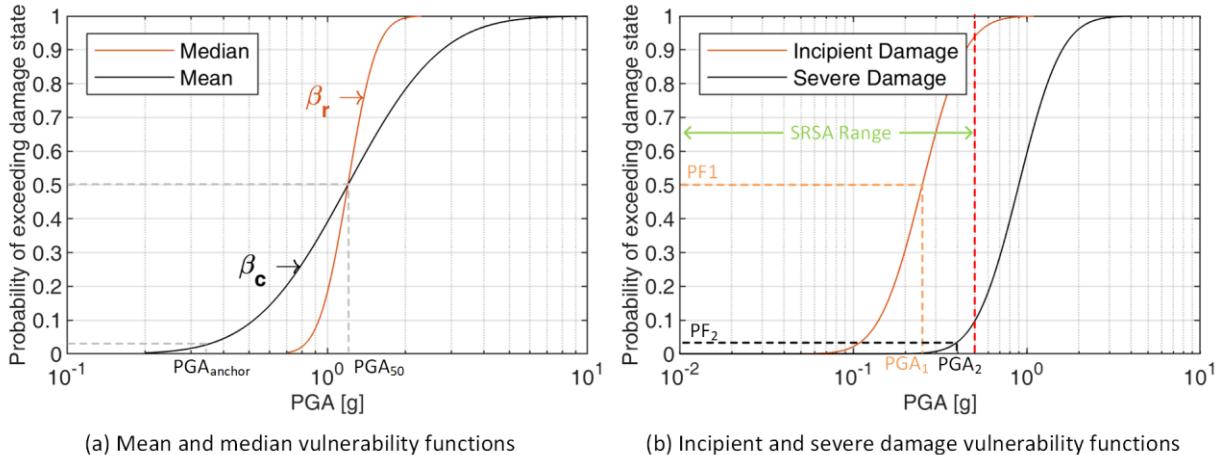


Figure 1. Fragility Functions.

2.3 Damage states

In the scope of this study, two distinct damage states are defined: 1) Incipient and 2) Severe damage state, as well as the associated modes of failure (Ghanaat, 2012, Soysal *et al.*, 2016). The incipient damage state was defined to coincide with one or both of the following conditions: a) The onset of separation at the dam-foundation interface during the shaking due to sliding or overturning and b) The onset of a tensile crack in the body of the dam. The severe damage state, on the other hand, was defined to coincide with three failure modes, seismic stress, post-seismic instability and bearing failure. These are defined in line with the FERC guidelines (FERC, 2016) setting no failure criteria for performance during shaking, but state “stability under post-earthquake conditions, which include whatever damage results from the earthquake, must be verified”. Damage states associated with appurtenant structures was not considered in this work.

For the incipient damage state, coinciding with the onset of nonlinear behavior, fragility function is determined without introduction of factors of safety for defining the median ground motion capacity corresponding to PGA1. The probability of exceeding the moderate damage state at PGA1 is estimated as 50% provided that median (best estimate) values are used for all input parameters (e.g. damping, concrete tensile strength, etc.).

For the severe damage state, the maximum level of ground motion for which the dam meets the seismic design criteria was targeted. Using conservative design assumptions (e.g. specified 28-day compressive strength of concrete), input parameters as well as factors of safety greater than 1, the ground motion intensity (e.g. PGA) associated with low probability of exceeding the severe damage state (PGA2) is determined for the aforementioned three damage states in accordance with the FERC guidelines (FERC, 2016).

2.4 Damage state prediction

The primary purpose of the suggested methodology is to provide consistent, comparable risk estimates considering the available knowledge and the associated variability in the assessment. For this reason, the linear analysis technique SRSA, validated extensively for predicting demands on gravity dam systems soundly considering soil-structure-reservoir interaction, was used. A schematic representation of the evaluation approach and the corresponding limit states for post-seismic assessment of the system are presented in Figure 2.

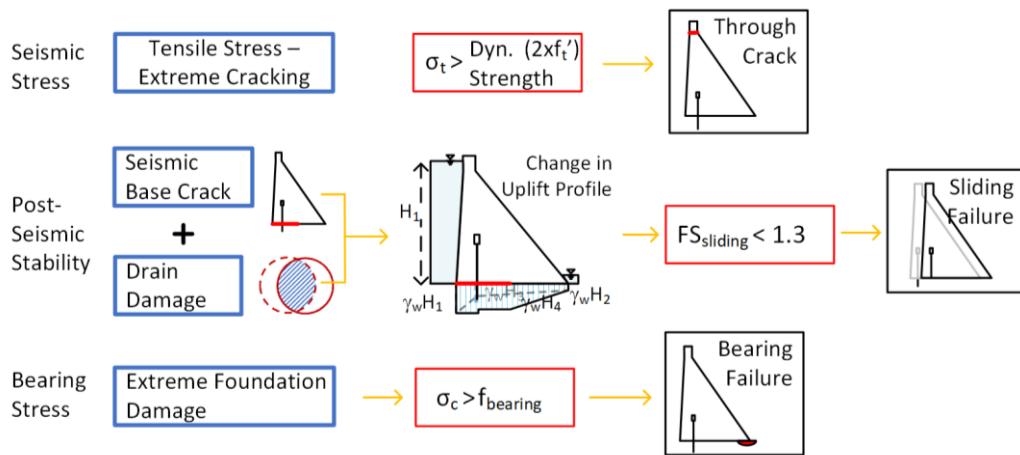


Figure 2. Simplified evaluation approach for severe damage state using linear analysis

2.5 Anchor point for severe damage fragility functions

For severe damage fragility functions, the definition of an anchor point is required. A clearly stated target performance objective or APE is not available for the design of concrete gravity dams. For reference, the performance objective is defined by a conditional probability of failure of 1% for a 10000 year return period motion for nuclear structures (ASCE 43-05, 2019) and 2.5% for the 2475 year motion (ASCE 7-16, 2016) for essential new buildings, corresponding to APE of 1E-5 and 5E-5, respectively.

Considering the 2,475 year return period motion as the reference level earthquake and the two conditional probabilities of exceedance of 1% and 2.5%, the APE values for a β_c value of 0.6 (similar to what is used for buildings and expected for gravity dams) were calculated. For the seismic hazard for the site, the annual probabilities of exceedance were estimated to be 2.3E-5 and 4.9E-5 for the 1% and 2.5% conditional probabilities of failure, respectively. The former P_F is chosen as the anchor point in this study considering the critical nature of dam structures. Note that this also implies a new concrete gravity dam designed using current standards achieves a performance level of around 2.3E-5 APE.

Unlike the building and nuclear power plant design standards, current design standards for gravity dams were not developed with an explicit performance goal in mind. Thus, in view of the range of possible values for P_F , the uncertainty associated with the estimated seismic risk estimates is large. However, with the adoption of the 1% P_F for all considered systems, paired with identical analysis framework, the risk estimates obtained are consistent for the purpose of ranking and prioritizing the dams, where the ratio of seismic risk estimates between dams is more important than the individual values.

The evaluation of uncertainty around the estimates are presented below:

2.6 Uncertainty evaluation

The ground motion record-to-record variability is treated as the major source of aleatory variability in this work. The uncertainty around the modelling parameters, concrete strength, damping, soil stiffness and other model parameters was considered to be more specific and were treated as epistemic in nature as discussed below. Record to record variability was considered in terms of the first mode response as validated in Section 3.

The portfolio includes a range of systems with differing details of accumulated information about the state of the system. Epistemic uncertainty due to the input parameters is significant due to the scarcity of test data for some systems, as well as the lack of knowledge in evaluating other parameters such as the effective damping ratio for the dam-reservoir-foundation system. To quantify the effects of epistemic uncertainty, a Latin Hypercube Sampling (LHS) simulation (McKay *et al.*, 1979) was conducted randomizing each of the input parameter variables according to its appropriate statistical distribution.

3 Application example, Dam 1

The implementation of the methodology to a case study to develop the fragility function for the severe damage state is presented below. The case study is a concrete gravity dam built in 1960's, comprised of 18 gravity blocks with a maximum height of approximately 195 ft and is built in a relatively narrow canyon 900 ft wide. Vertical drainage for the dam is provided through drainage and grouting gallery. Most of the information necessary for the seismic performance evaluation was available from the owner. In cases where data were not available or not sufficient to develop best estimate values and ranges with great reliability, we relied on information from the literature and exercised professional judgment to develop the required input data.

3.1 Input parameters

Two sets of values for the input parameters as well as their range is presented in Table 1. The conservative set of values were used to evaluate the anchor point for the fragility function, while the median and range was used to generate a sample set of realizations for uncertainty quantification.

Table 2. Values and range of variable input parameters for Dam 1

Input Parameter	Conservative	Median	Range (5 th ,95 th)	β
Height of reservoir water, H_W [ft]	191	185	178, 188	0.02
Concrete compressive strength, f'_c [psi]	3,500	5,250	3500, 7875	0.25
Concrete elastic modulus, E_s [ksi]	3,370	4,130	3372, 5058	0.12
Static tensile strength, f'_t [psi]	392	514	342, 770	0.25
Damping ratio for Concrete, ζ_s [%]	2	3	2, 4	0.21
Foundation elastic modulus, E_f [ksi]	3,587	3,587	1,509 to 8,513	0.58
E_f/E_s	1.06	0.86	0.37, 2.06	0.52
Hysteretic damping ratio for foundation, η_f [%]	2x0.99	2x0.99	2x0.38, 2x2.58	0.58
Wave reflection coefficient, α	0.9	0.75	0.5 to 0.9	0.21
Effective friction Angle, ϕ [deg]	45	45	35, 55	0.14
Coefficient of friction at foun. interface, μ_f	1	1	0.7, 1.43	0.22
Cohesion, C [psi]	30	30	13, 68	0.5
Drain Effectiveness, E	0.65	0.65	0.43, 0.79	0.18
$K (=1-E)$	0.35	0.35	0.21, 0.57	0.30
Height of Sedimentation upstream, H_{sed} [ft]	20	32	20, 50	0.29

3.2 Seismic input

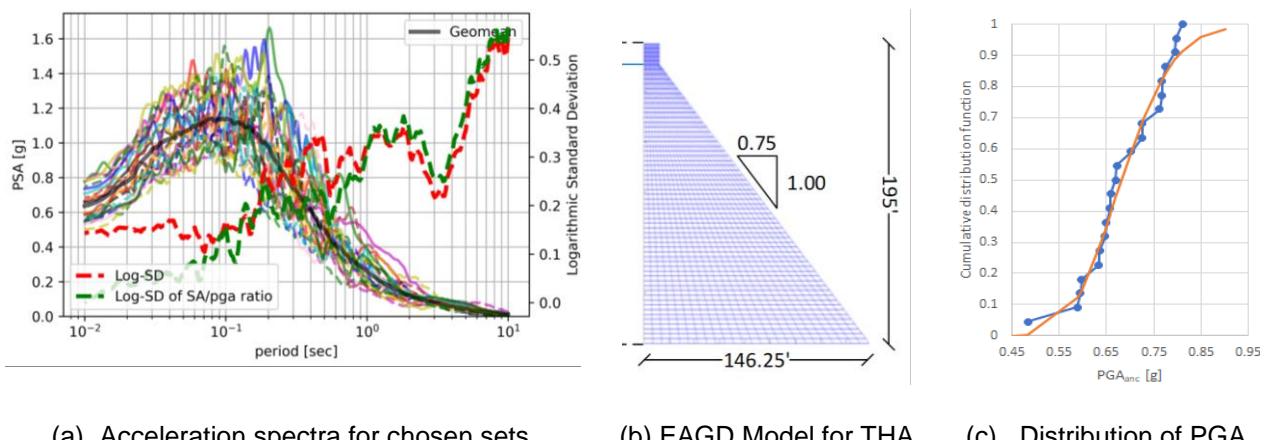
The record-to-record variability is considered to be the main source of aleatory variability. For the purpose of estimating β_r , 11 sets of two ground motion acceleration records were spectrally matched to the 10,000-year return period motion at the site with the spectral matching preserving the expected spectral amplitude variation as a function of the period of vibration. Figure 3a presents the 5% damped acceleration response spectra for the 11 pairs (a total of 22) motions generated to reflect record to record variability at Dam 1 site. The figure also illustrates the logarithmic standard deviation as a function of period.

3.3 Anchor point evaluation for the severe damage state

Using the conservative set of values for the input parameters in Table 1, the SRSA Procedure was implemented for the case study. The first mode of vibration for the structure, T_1 , was 0.149 seconds, elongated to $\tilde{T}_1 = 0.228 \text{ sec}$ for the equivalent dam-reservoir-foundation system. The damping ratio used in the procedure is determined for ideal, infinitely long 2D systems, not supported by the measured damping ratios for existing dams (Chopra, 2020) based on forced vibration and tests and ambient vibration data. Part of the overestimation may be attributed to the discrepancy between 2 and 3D models. Damping ratio was adjusted by a factor of 0.58 for the canyon width-dam height ratio of 4.6 and foundation/structure moduli ratio of 1 in accordance with Bybordiani and Arici (2016). For the 1st mode of vibration and higher modes, base shear and the stresses along the height of the dam were computed and combined with those due to the static forces such as gravity loads, hydrostatic loads, and uplift pressure. For the conservative set of values, the PGA levels for meeting the tensile stress and post-seismic sliding were determined to correspond to 0.71 and 0.50g's.

3.4 Evaluation of aleatory variability β_r

For the purpose of estimating β_r , the ground motion set were used in time history analysis in the 2D FEM code EAGD84 (Fenes and Chopra, 1984), a well-established code rigorously considering soil-structure-reservoir interaction for gravity dams. Stresses throughout the body of the dam, forces acting at the dam-foundation interface in the form of axial, shear forces and overturning moment were determined using the EAGD model (Figure 3b). The corresponding record-record variability was obtained and compared to counterparts from SRSA. The scale factors for each motion were computed for modes of failure; the distribution of scale factors for the tensile stress failure is shown in Figure 3c comparing well with an idealized log-normal distribution with β_r of 0.13. A similar distribution was obtained for the other failure mode.



(a) Acceleration spectra for chosen sets (b) EAGD Model for THA (c) Distribution of PGA

Figure 3. Evaluation of record-record variability with THA and SRSA

The log standard deviation as a function of period for the chosen set, presented in Figure 3c, compares well to the log-SD value of 0.13 in the period range of 0.1 to 0.23 seconds. The favorable comparison enables the use of period dependent log-SD in the procedure directly for accounting for record-to-record variability, in lieu of the use of THA for determining the appropriate β_r without any significant loss of accuracy.

3.5 Evaluation of epistemic uncertainty

The epistemic uncertainty, β_u , due to the input parameters is evaluated in this section using the Latin Hypercube Sampling (LHS) approach to produce a set of realizations for the input parameters representative of their uncertainty.

Latin Hypercube sampling

120 sets of randomly generated realizations are developed for the input parameters following a log-normal distribution with the log-mean (median) and log-SD specified in Table 2. The compressive and tensile strengths of concrete were assumed to be perfectly correlated. Realizations further than twice the standard deviation from the median was not allowed to avoid unrealistic cases. The correlation between all 10 randomized variables are presented in Figure 4a in their standard normal space. For each variable, it is verified that the sample size of 120 results in the desired log-normal distribution and the correlation between different variables is not significant (a maximum correlation coefficient of ± 0.16 to be acceptable). The corresponding distributions of the effective natural period and damping ratio are shown in Figure 4b.

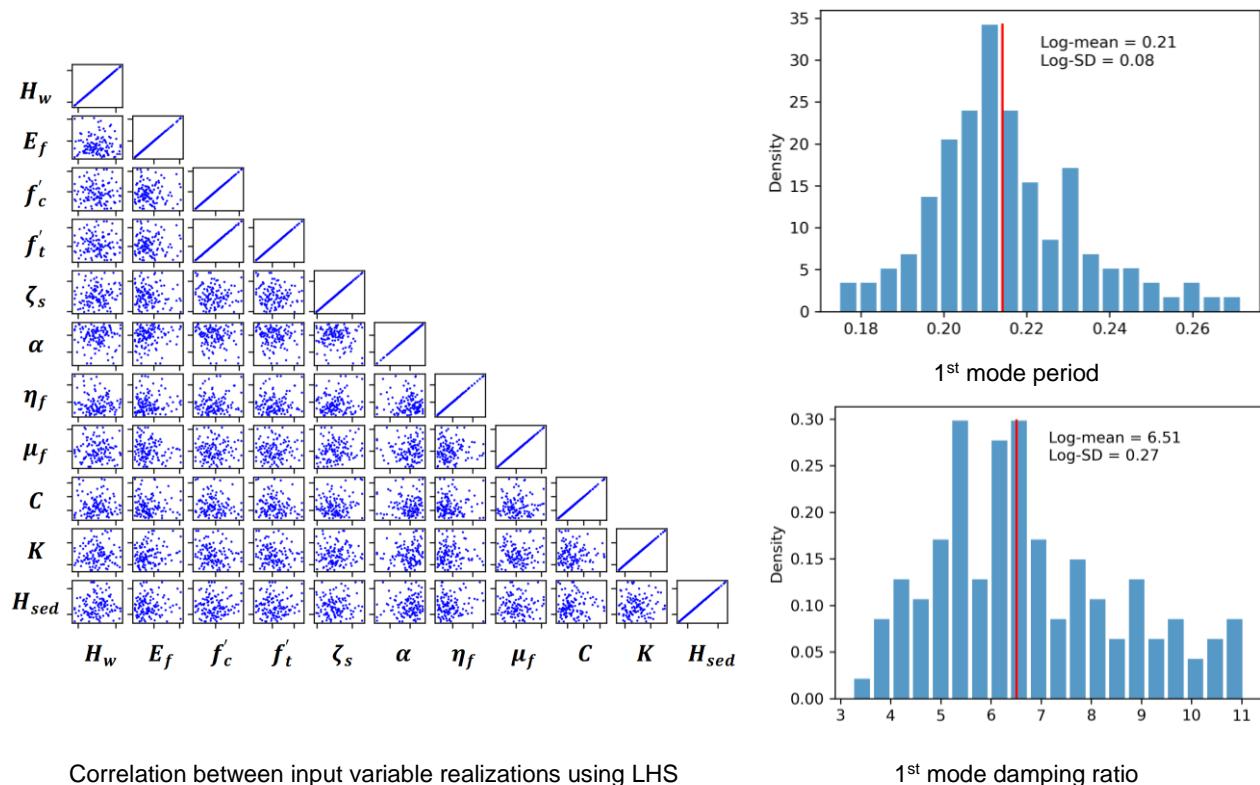


Figure 4. LHS realizations for the system

The 120 sets of realizations were then analyzed with SRSA. The distribution of the PGA for the 120 LHS cases, differentiated by the governing mode of failure, is presented in Figure 5. While the entire set of 120 LHS cases do not comply with the log-normal distribution reflecting the bi-modal mode of failure, separating the cases into two subsets based on the governing mode of failure yields two sample sets conforming each to the log-normal distribution assumption (Figure 6a and 6b). The median PGA capacity values for both modes of failure are larger than that of the anchor point evaluation, as LHS realizations were centered around the best estimate values for the input parameters, as opposed to the conservative values.

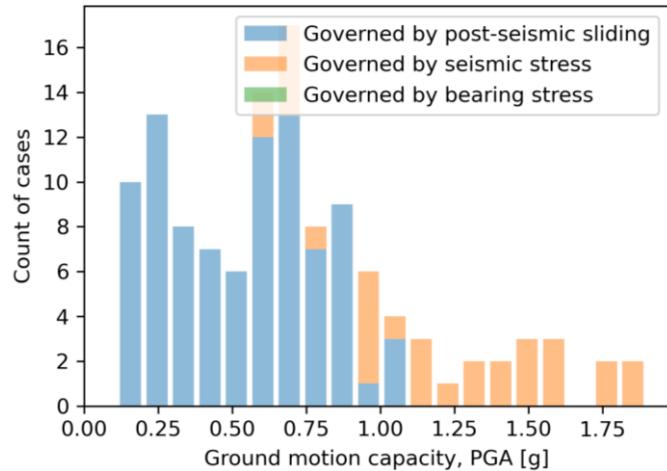
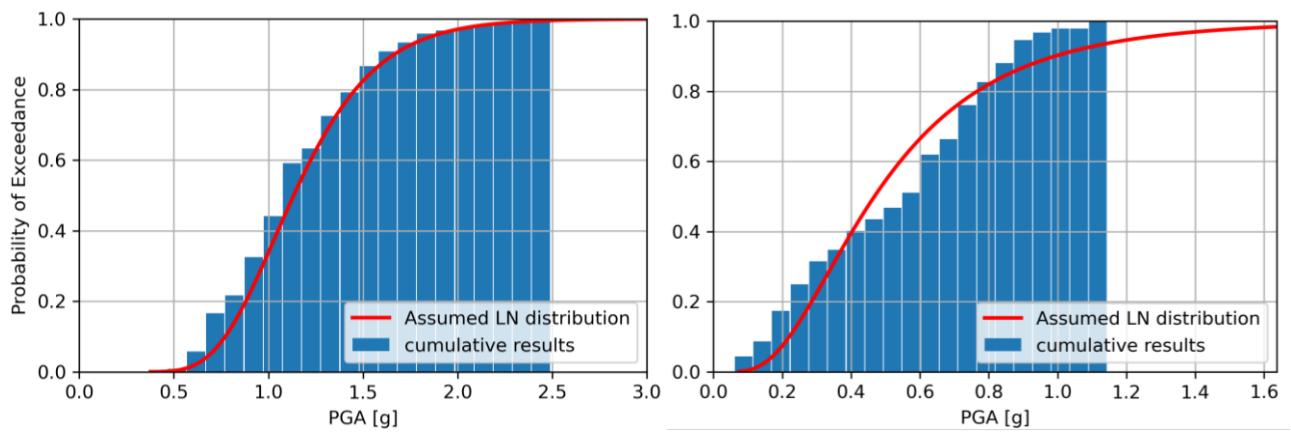


Figure 5. Failure modes for LHS samples and corresponding distributions



(a) Tensile stress mode of failure

(b) Post-seismic sliding mode of failure

Figure 6. Cumulative distribution of PGA at the severe damage state

Individual parameter contribution

Identifying the largest contributors allows for better understanding of the most important parameters and for the potential reduction of epistemic uncertainty by allocating resources to better characterize the input parameters. To that end, the same set of 120 analyses were repeated 10 times – corresponding to the number of input parameters –that for each set of these analyses, the best estimate value was assigned to all input parameters except for the one under consideration. The resulting variance β^2 for each set of analyses represents the contribution of the varied parameter to the overall epistemic uncertainty calculated for each of the two modes of failure separately. The relative variance contributions of the two modes of failure are presented in pie charts in Figure 7a and b. Tensile strength is the largest contributor for the tensile stress mode of failure, and the effective friction angle at the interface is the largest contributor for post-seismic sliding instability. The results suggest that some parameters such as the damping ratio for concrete and the foundation do not contribute significantly to the overall epistemic uncertainty.

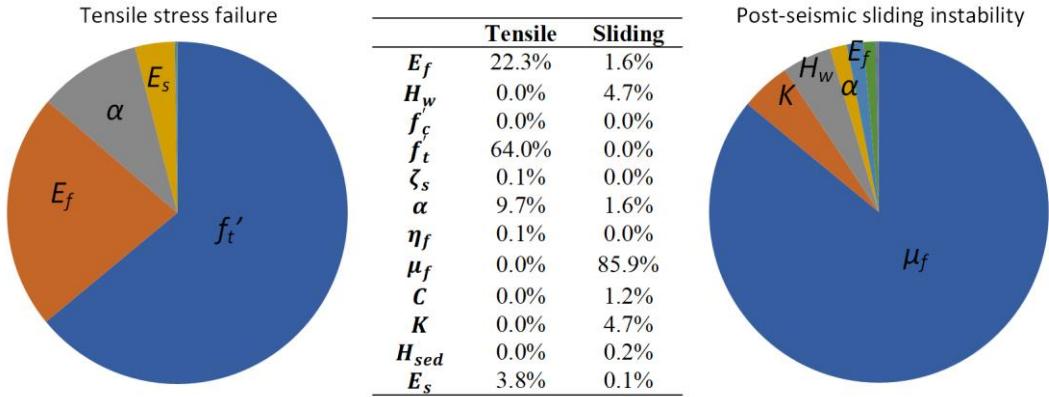


Figure 7. Contribution of individual input parameters to variance due to epistemic uncertainty

3.6 Fragility functions

The fragility function is constructed for each of the two modes of failure using Eq. 3. The severe damage state was defined using the PGA at the anchor point with an associated probability of exceedance of 1%. Accordingly, PGA_{median} was estimated using the combined standard deviation due to epistemic uncertainty uncertainty β_u and β_r ($\beta_{r,u}$), before constructing the fragility function using the calculated PGA_{median} and the full composite standard deviation, β_C . The resulting fragility functions for the tensile stress and sliding mode of failures are presented in Figure 7a and b, respectively. The lower level (and more frequent) motions, coinciding with the anchor point location, are the dominant contributors to the seismic risk. It should be noted that the final fragility functions pass above the anchor point (indicated in these figures by a black dot) implying a higher probability of failure than 1% at the PGA_{anc} , which reflects the added modelling and drain effectiveness uncertainties. The fragility functions determined for the incipient damage state is not shown here for brevity.

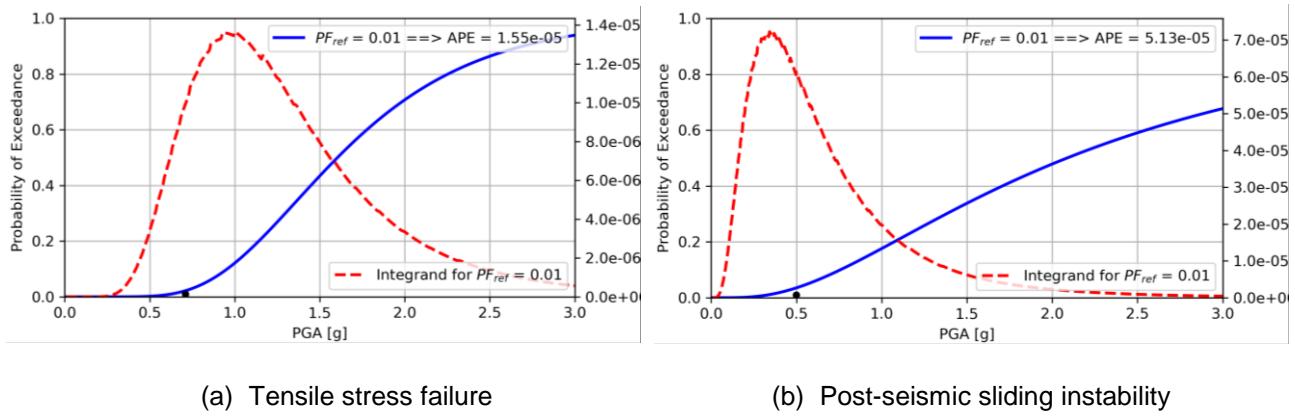
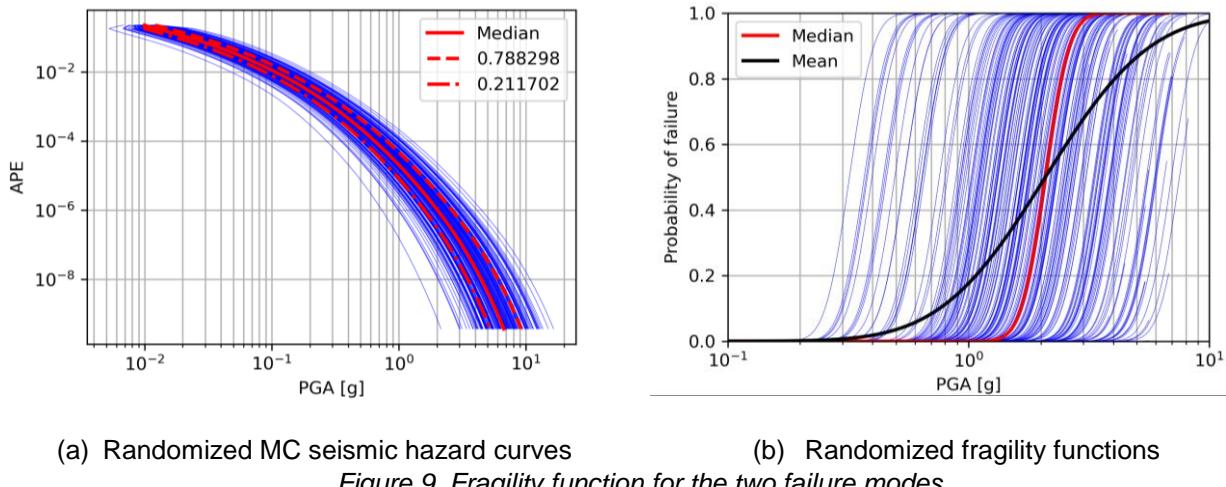


Figure 8. Fragility function for the two failure modes

3.7 Estimates of annual probability of exceedance

In addition to the uncertainty estimated in the fragility function, the uncertainty in the seismic hazard is a major contributor to the uncertainty in the APE estimates. To consider this issue, a set of randomized hazard curves were generated. To estimate the APE and associated uncertainty for a given mode of failure, the Monte Carlo (MC) simulation approach was applied with a sample size of 100,000, where each realization of the fragility function was convolved with a realization of the seismic hazard curve, resulting in 100,000 values of APE representing its distribution. For example, the 100000 randomized fragility functions for the tensile stress failure at severe damage state is given in Figure 9b. The resulting distribution of APE for failure has a mean value of 1.52E-5, a median value of 0.38E-5 and associated log-SD of 2.09, highlighting the large uncertainty around the APE estimates.



(a) Randomized MC seismic hazard curves

(b) Randomized fragility functions

Figure 9. Fragility function for the two failure modes

The main seismic risk was evaluated considering both failure modes (note that bearing failure is not an issue in this case). The aggregate mean APE for two modes of behaviour, for the incipient and severe damage states are presented in Table 3. The aggregate mean APE was obtained as 5.4E-5. This value is similar to target APE for new buildings in highest seismic risk category, corresponding to essential facilities such as hospital and fire stations, but about twice that of estimated APE for a new gravity dam designed using the current standards (as provided in Section 2.5).

Table 3. Summary of APE estimates for Dam 1

Damage state	Incipient damage	Severe damage
Mean	3.58E-3	5.35E-5
Log-Mean	1.92E-3	0.46E-5
Log-SD	1.22	2.42
50 th Percentile	2.12E-3	0.51E-5

4 Conclusions and recommendations

A multi-level screening is proposed for evaluating and comparing the seismic risks in a dam portfolio. Tier 1 of this framework, developed for consistent risk estimation across a portfolio using simplified analysis techniques, is presented with a case example in this study. The development of fragility functions, including the estimation of associated uncertainty, is demonstrated, with the final goal of obtaining consistent, comparable risk estimates for systems within the portfolio. The results and conclusions from this study are presented as follows:

- In the absence of a target performance objective for classical gravity dams, risk values for nuclear structures (very low) and (low) essential new buildings were adopted for determining APE values for seismic hazards at multiple sites. Both approaches yield consistent, comparable APEs with little effect of the hazard curve. The former one was chosen in this study.
- Three different failure modes were included in the framework with the cracking and sliding limit states governing for the case study. For the case of Dam 1, post-seismic sliding instability was determined to be more critical than the tensile stress mode of failure.
- For classical gravity dam sections, the aleatory variability β_r due to record-to-record variability, can be used as the log-SD for the spectral acceleration at the equivalent 1st vibration mode and damping ratio of the dam-foundation-reservoir system without any significant loss of accuracy.
- Among contributors to the epistemic uncertainty, the effective friction angle at the dam-foundation interface is the most dominant contributor to the risk. This parameter is then a prime candidate for

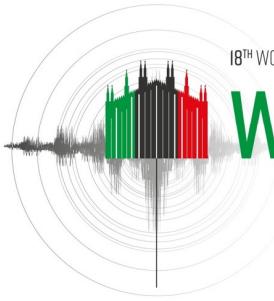
investigation to reduce epistemic uncertainty and obtain a more reliable seismic risk estimate for given system.

- The overall seismic risk for Dam 1, in terms of APE, was determined to be 5.35E-5.

This suggested methodology is subject to certain limitations. The framework is limited to the evaluation of the seismic risk in terms of damage states for the dams such as the uncontrolled release of reservoir water but does not extend to estimating ensuing consequences such as economic loss or casualties. The results and assumptions presented are in generic terms so as to present the methodology while assuring confidentiality.

5 References

- ASCE 43-05 (2005). *Seismic Design Criteria for Structures, Systems and Components in Nuclear Facilities*, American Society of Civil Engineers, Reston, Virginia, United States.
- ASCE 7-16 (2016). *Minimum Design Loads and Associated Criteria for Buildings and Other Structures*, American Society of Civil Engineers, Reston, Virginia, United States.
- Bybordiani M., Arici Y. (2017). 2D versus 3D modeling for the seismic analysis of gravity dams, *Earthquake Engineering and Structural Dynamics*; 46:1769-1789.
- Carjaval C., Peyras L., Bacconnet C., Bécue J-P. (2009). Probability modelling of shear strength parameters of RCC gravity dams for reliability analysis of structural safety, *European Journal of Environmental and Civil Engineering*, 13(1), 91-119.
- Chopra A.K. (2020). *Earthquake Engineering for Concrete Dams Analysis, Design, and Evaluation*, 1st Ed.. Hoboken, NJ: John Wiley & Sons, Inc.
- DeNeale S., Baecher G., Stewart K.M., Smith E., Watson D. (2019). *Current state-of-practice in dam safety risk assessment*, Oak Ridge National Laboratory, ORNL/TM-2019/1069.
- EPRI (2018). *Seismic Fragility and Seismic Margin Guidance for Seismic Probabilistic Risk Assessments*, Electric Power Research Institute, Report No. 3002012994.
- Fenves G., Chopra A.K. (1984). *EAGD-84: A computer program for earthquake response analysis of concrete gravity dams*, Report No. UCB/EERC-84/11, Earthquake Engineering Research Center, University of California, Berkeley, CA, United States.
- FERC (2016). *Engineering Guidelines for the Evaluation of Hydropower Projects, Chapter 3 Gravity Dams*, Washington, D.C., United States.
- Ghanaat Y. (2012). Seismic fragility analysis of concrete gravity dams, *Proc. of the 15th World Conference on Earthquake Engineering*, Lisbon, Portugal.
- Hariri-Ardebili M.A., Seyed-Kolbadi S.M., Kianoush M.R. (2016). FEM-based parametric analysis of a typical gravity dam considering input excitation mechanism, *Soil Dynamics and Earthquake Engineering*, 84, 22-43.
- McKay M.D., Beckman R.J., Conover W.J. (1979). A Comparison of Three Methods for Selecting Values of Input Variables in the Analysis of Output from a Computer Code, *Technometrics*, 21(2): 239-245.
- Soysal B.F., Binici B., Arici Y. (2016). Investigation of the relationship of seismic intensity measures and the accumulation of damage on concrete gravity dams using incremental dynamic analysis, *Earthquake Engineering and Structural Dynamics*, 45(5), 719-737.
- Tekie P.B., Ellingwood B.R. (2003). Seismic fragility assessment of concrete gravity dams, *Earthquake Engineering and Structural Dynamics*, 32(14), 2221-2240.



ASSESSMENT OF THE SEISMIC BEHAVIOUR OF CONCRETE DAMS: FROM SIMPLIFIED TO ADVANCED METHODS

G. Faggiani¹ & P. Masarati²

¹ Ricerca sul Sistema Energetico – RSE S.p.A., Milan, Italy, giorgia.faggiani@rse-web.it

² Ricerca sul Sistema Energetico – RSE S.p.A., Milan, Italy

Abstract: The evaluation of the structural response of concrete dams to earthquake is carried out by means of numerical simulations generally with the finite element method (FEM), which allow to reproduce with good accuracy the real dynamic behaviour of the system consisting of the dam, the reservoir and the foundation. Different methods of analysis can be adopted, characterized by increasing complexity: the simplest methods, based on some simplifying physical assumptions, generally provide a faster, conservative and more comprehensible response; on the other hand, the most complex methods, although computationally expensive, allow to successfully deal with physical situations that often the simplest methods are not able to represent, providing a more accurate and realistic description of the structural behaviour and reducing the excessive conservativeness of the results. An accurate method for the seismic analysis of dam-foundation-reservoir systems should be able to consider the three-dimensionality of the problem, the semi-unbounded size of the foundation, the non-linear behaviour of the system and the dynamic interactions of the dam with the foundation and the reservoir. An advanced approach, to be adopted in the frame of time-history linear or non-linear analyses and able to face all the aforementioned complexities, was recently implemented and tested by RSE: the approach, indicated by the acronym SAM-4D (Seismic Advanced Model for Dams), allows to appropriately simulate the propagation of seismic waves in a realistic massed foundation, considering its semi-unbounded extent. Artificial non-reflecting (or absorbing) boundaries are used to delimit the semi-unbounded foundation and effective earthquake forces (computed with reference to the elastic wave vertical propagation theory) provide the seismic motion. The Pine Flat Dam, used in the frame of the ICOLD 15th International Benchmark Workshop on Numerical Analysis of Dams, is considered as a case study to perform analyses of increasing complexity, starting from the pseudo-static analysis up to the non-linear time-history analysis using the SAM-4D model.

1. Introduction

Numerical simulations, generally carried out by means of the finite element method (FEM), are nowadays the most widely used and effective tool for assessing the structural safety of complex structures such as concrete dams. The analysis methods have been developed hand in hand with the progressive increase of the computing power and today several methods, characterized by increasing complexity, are available. In the frame of seismic analyses, the time-history analysis based on the direct integration of the equations of motion is now the most powerful method available for evaluating the response of the dams to earthquakes: the advantages of this method are that it can be used for both linear and non-linear analyses and can properly consider the dynamic interactions of the dam with the reservoir and the foundation, providing an accurate and reliable description of the seismic response of the structure. An advanced approach in the context of time-

history analyses, that allows to appropriately simulate the propagation of seismic waves considering the dissipation effects through the boundaries of the artificially truncated massed foundation, indicated by the acronym SAM-4D (Seismic Advanced Model for Dams), was recently implemented and tested by RSE (Faggiani et al. 2019, 2020, 2021, 2022). Although the advanced methods can properly simulate important features of the real behaviour of structures, they are complex to use, computationally demanding and require experience and competence for the evaluation of the results and confidence for their comprehension. It could be therefore convenient to adopt a progressive analysis methodology (US Army Corps of Engineers – USACE 2007): this progressive approach is applied to the case study of Pine Flat Dam, already considered in the frame of the ICOLD 15th International Benchmark Workshop on Numerical Analysis of Dams (Salamon et al. 2020).

Section 2 briefly summarizes the progressive analysis methodology with a focus on the methods applied for the case study: the pseudo-static analysis (§ 2.1), the time-history analysis with the massless approach (§ 2.2), the time-history analysis with the SAM-4D model (§ 2.3). Section 3 describes the case study, detailing the numerical model (§ 3.1), the loadings (§ 3.2) and the results (§ 3.3). The main overcomes are summed up in Section 4.

2. Progressive analysis methodology for the seismic safety assessment of concrete dams

The progressive analysis methodology, used to assess the effect of the seismic action, consists in subsequent phases of increasing complexity, starting from the simplest method appropriate to the problem, that provides faster and more easily comprehensible results, and progressing to the more complex methods, that are supposed to provide more accurate and realistic results. The three analysis methods adopted for the case study of Pine Flat Dam, used to show an application of the methodology to the seismic safety assessment of concrete dams, are outlined in this Section: the historical pseudo-static analysis method and two different approaches within the time-history analysis method, based on the direct integration of the equations of motion. The time-history analysis method consists in simulating the entire time history of the behaviour of the structure subject to the ground motion and represents the most robust available method to study the response of structural systems to earthquakes nowadays. One of the main advantages of the method is that it can be used for both linear and non-linear dynamic analyses: it is therefore possible to study the dynamic behaviour of the dam including opening and sliding of the joints and cracking of the concrete. Both the adopted time-history approaches are able to simulate the dynamic interaction between the dam and the reservoir through the classic structural-acoustic coupling on the upstream face of the dam, where the normal component of the dam acceleration is related to the normal gradient of the water hydrodynamic pressure (Zienkiewicz 1977), that allows to consider the compressibility of the water; on the contrary, the two approaches greatly differ in the simulation philosophy of the dynamic interaction between the dam and the foundation.

2.1. Pseudo-static analysis

The pseudo-static analysis method (also referred to as seismic coefficient method), widely used in the past, is considered to be outdated today and should no longer be used for the seismic safety assessment of large dams (Wieland 2008, 2012): nevertheless, it can be useful to get a preliminary estimate of the response of a dam to the seismic action. The method calculates the seismic response with a static analysis, using additional static loads: the inertia forces of the structural mass and the hydrodynamic pressure on the upstream face of the dam. The additional static loads are evaluated considering the whole structure subjected to uniform acceleration (rigid body hypothesis), equal to a fraction of the peak ground acceleration. To better account both for the dynamic characteristics of the dam-foundation-reservoir system and for the characteristics of the ground motion, the spectral ground acceleration corresponding to the fundamental natural frequency of the system can be used.

2.2. Time-history analysis with the massless approach

For a long time, the most used procedure to simulate the dynamic interaction between the dam and the foundation (within the issue of seismic safety assessment of dam-foundation-reservoir systems) was the traditional and consolidated massless approach (Clough 1980) based on the simplifying hypothesis of considering the foundation with zero mass: the input motion is uniformly imposed at its truncated boundaries

and reaches instantaneously the dam-foundation interface since the wave velocity tends to infinity. The main deficiency of the approach is that, considering only the flexibility of the foundation, both inertial and radiation damping effects are neglected: consequently, the seismic response of dams results significantly overestimated (Chopra 2014, Hansen and Nuss 2013, Zhang and Jin 2008).

2.3. Time-history analysis with the SAM-4D model

As the massless approach is proved to significantly overestimate the seismic response of dams, it may be important to reduce its excessive conservativeness, that sometimes leads to the wrong conclusion that an existing dam is unsafe according to the current regulations: this purpose can be achieved by adopting advanced structure-foundation dynamic interaction models, able to correctly reproduce the propagation of seismic waves. The dam-foundation seismic interaction model SAM-4D, recently implemented and tested by RSE (Faggiani et al. 2019, 2020, 2021, 2022), allows to ideally reproduce the behaviour of the real semi-unbounded foundation representing the wave propagation in a computation domain delimited by appropriate artificial boundaries and realistically provided with mass: the main properties of the model are deduced from Chen et al. 2012, Liu et al. 2006, Liu and Chen 2013, Zhang et al. 2009; Løkke and Chopra 2019 was considered as important reference too. The semi-unbounded extension of the foundation is achieved using artificial non-reflecting (or absorbing) boundaries at the truncations of the computational domain: one horizontal (the bottom boundary) and four vertical (the side boundaries) planes. The artificial boundaries consist in a layer of normal and tangential dampers and springs; if only dampers are used, the classic non-reflecting boundaries are obtained (Lysmer and Kuhlemeyer 1969). The incoming seismic waves are specified by means of effective earthquake forces, applied at both the bottom and the side boundaries of the foundation and computed, starting from the free-field ground motion, using the theoretical solution of the vertically propagating elastic wave problem in a half-space; the non-reflectivity of the boundaries allows the exit from the foundation of the outgoing waves, scattered by the dam-reservoir system, that propagate towards infinity. In case the half-space is homogeneous and undamped, the incident motion at the bottom boundary is equal to one-half the free surface motion: this simplification may be appropriate if the rock is assumed homogeneous and with no or little (up to 2%) material damping (Løkke and Chopra 2019).

3. The case study of Pine Flat Dam

The seismic analysis of Pine Flat Dam (Fresno, California, USA), a large concrete gravity dam consisting of thirty-six 15.25 m wide monoliths and one 12.2 m wide monolith, was recently proposed in the frame of the ICOLD 15th International Benchmark Workshop on Numerical Analysis of Dams (Salamon et al. 2020) and before in the USSD Workshop Evaluation of Numerical Models and Input Parameters in the Analysis of Concrete Dams (Salamon 2018). The case study only concerns the tallest 15.25 m-wide dam monolith no. 16 (about 122 m hight).

In this paper, Pine Flat Dam is considered to perform an application of the progressive analysis methodology. Several analyses of increasing complexity are carried out: the linear elastic pseudo-static analysis, the linear elastic time-history analysis with the massless approach, the linear elastic time-history analysis with the SAM-4D model, and the non-linear time-history analysis with the SAM-4D model.

3.1. Geometrical and physical model

The 3D FEM model, reported in Figure 1, includes the dam monolith and the relevant portions of the foundation and of the reservoir. The structural problem is schematized as a 2D (plane strain) problem applying appropriate symmetry conditions at side boundaries of the model. The different parts of the mesh (dam, foundation and reservoir) are discretized quite uniformly, with element size ranging from 3 m to 6 m. The fluid domain is obtained by extruding the upstream face of the dam mesh up to the upstream boundary of the foundation. The model of the foundation is characterized by elements of uniform height equal to about 6 m, that allows to describe with good accuracy frequencies up to about 15 Hz (for the time-history analyses with the SAM-4D model). For the non-linear analysis a more refined mesh only for the dam is considered, with element size of about 1.5 m. The case study was approached with the commercial FEM code Abaqus (Dassault Systèmes 2021).

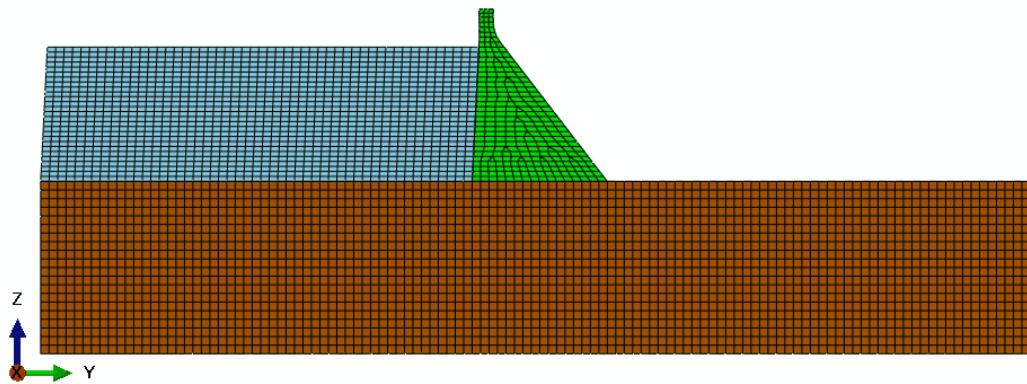


Figure 1. FEM model of the dam monolith, the foundation and the reservoir.

Foundation rock is assumed to behave linear-elastically; depending on the type of analysis (linear or non-linear) dam concrete may behave linear-elastically or according to the Concrete Damaged Plasticity model proposed by Lee and Fenves (1998) and available in Abaqus. According to this model, under uniaxial tensile loading the stress-strain response of concrete is linear-elastic until the tensile strength is attained; subsequent increases of strain cause the progressive damage of the material, characterized by the loss of stress for increasing deformation (softening) and by the reduction of stiffness in the unloading phase. The loss of stress and the growth of damage are assigned as functions of the progressive opening of the crack (Figure 2). The damage variable can take values from zero, representing the undamaged material, to one, which represents total loss of strength.

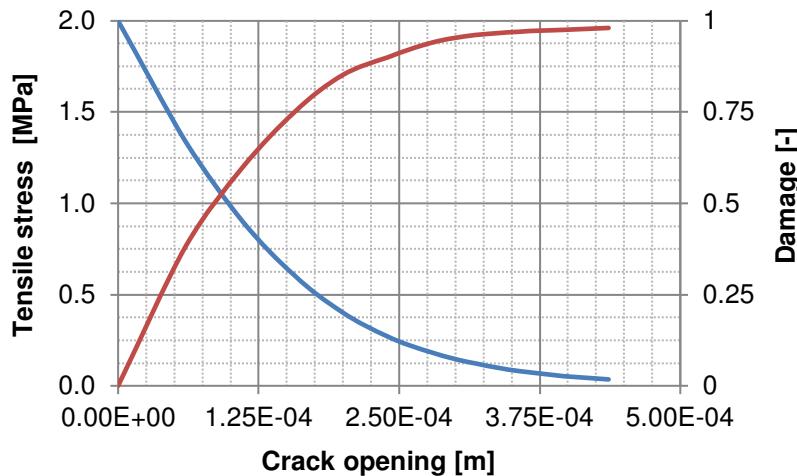


Figure 2. Concrete Damaged Plasticity model. Tensile stress (blue line) and damage variable (red line) versus crack opening.

The dynamic interaction between the dam and the reservoir (for the time-history analyses) is achieved through the classic structural-acoustic coupling (Zienkiewicz 1977); no dynamic interaction is considered between the foundation and the reservoir, while the upstream truncation of the reservoir is provided with non-reflecting acoustic condition.

The dynamic interaction between the dam and the foundation (for the time-history analyses) is approached either with the massless approach or with the SAM-4D model, depending on the type of analysis (foundation without or with mass).

The principal physical-mechanical properties of the materials are summarized in Table 1. The viscous damping, assumed equal to 2% for both the dam and the foundation, is defined using the classic Rayleigh modelling.

Table 1. Material properties.

Parameter	Concrete	Rock	Water
Density [kg/m ³]	2483	2483 (0)	1000
Elastic modulus [MPa]	22410	22410	
Poisson's ratio [-]	0.2	0.2	
Compressive strength [MPa]	28.0		
Tensile strength [MPa]	2.0		
Fracture Energy [N/m]	250		
Shear wave velocity [m/s]		1939	
Compressional wave velocity [m/s]		3167	
Sound velocity [m/s]			1439

3.2. Loadings

The static loads are the self-weight of the dam and the hydrostatic pressure at winter reservoir water level (268.21 m a.s.l.), applied both on the upstream face of the dam and on the surface of the foundation.

The seismic action is the Taft horizontal acceleration time-history record of the M 7.3 Kern County, California, earthquake (peak ground acceleration of 1.77 m/s²), showed in Figure 3 and considered as a free field ground motion at the surface of the foundation.

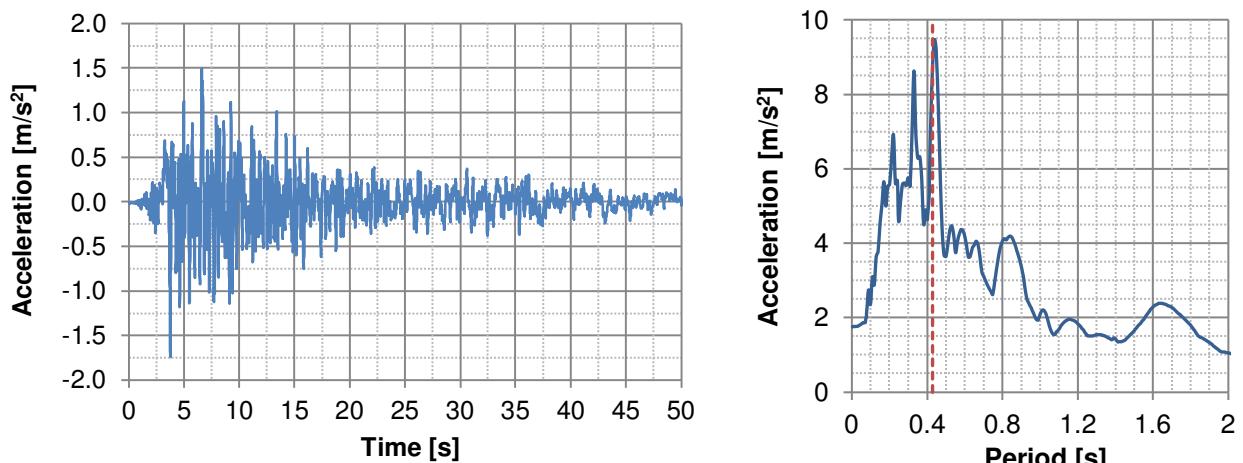


Figure 3. Taft horizontal record: acceleration time-history (left) and response spectrum 2% damping (right).

In the pseudo-static simulations the seismic acceleration (8.77 m/s²), calculated on the response spectrum at the period 0.43 s (frequency 2.33 Hz) relevant to the first resonant mode of the system (modal participation mass 68%) and evaluated with a modal analysis of the coupled dam-foundation-reservoir system, was applied as inertia load towards either downstream or upstream; the hydrodynamic pressure was calculated according to the Zangar formulation (Zangar 1952), using the same seismic acceleration (8.77 m/s²), and applied towards either downstream or upstream according to the inertia load.

In the time-history analyses with the massless approach, the acceleration was uniformly applied at the base and side boundaries of the foundation.

In the time-history analyses with the SAM-4D model, seismic action was applied at the base and at the side boundaries of the foundation, provided with damper and spring elements to model the semi-unbounded extent of the foundation, by means of effective earthquake forces computed using the theoretical solution of the

vertically propagating elastic wave problem in a half-space, considering the incident motion at the bottom foundation boundary ½ the surface motion.

The transient dynamic coupled problem (for the time-history analyses) is solved using the implicit direct time integration method HHT (Hilber et al. 1977), with integration time step of 0.005 s that well represents frequencies up to 10 Hz.

3.3. Results

The results of the analyses are reported in terms of maximum principal stress (envelope in case of time-history analyses) and maximum and minimum horizontal seismic relative (with respect to dam heel) displacements at dam crest. For the non-linear time-history analysis with the SAM-4D model, also the damage variable is reported.

Figure 4 shows the tensile stress state resulting from the two pseudo-static analyses with the seismic inertia load and the hydrodynamic pressure towards downstream (left) and upstream (right) respectively: in the first case tensile stresses occur mainly on the upstream lower part of the dam, varying from about 1.0 MPa to about 12.5 MPa at dam heel; in the second case tensile stresses state involve mainly the downstream part of the dam, varying from about 1.0 MPa to about 6.4 MPa at dam toe.

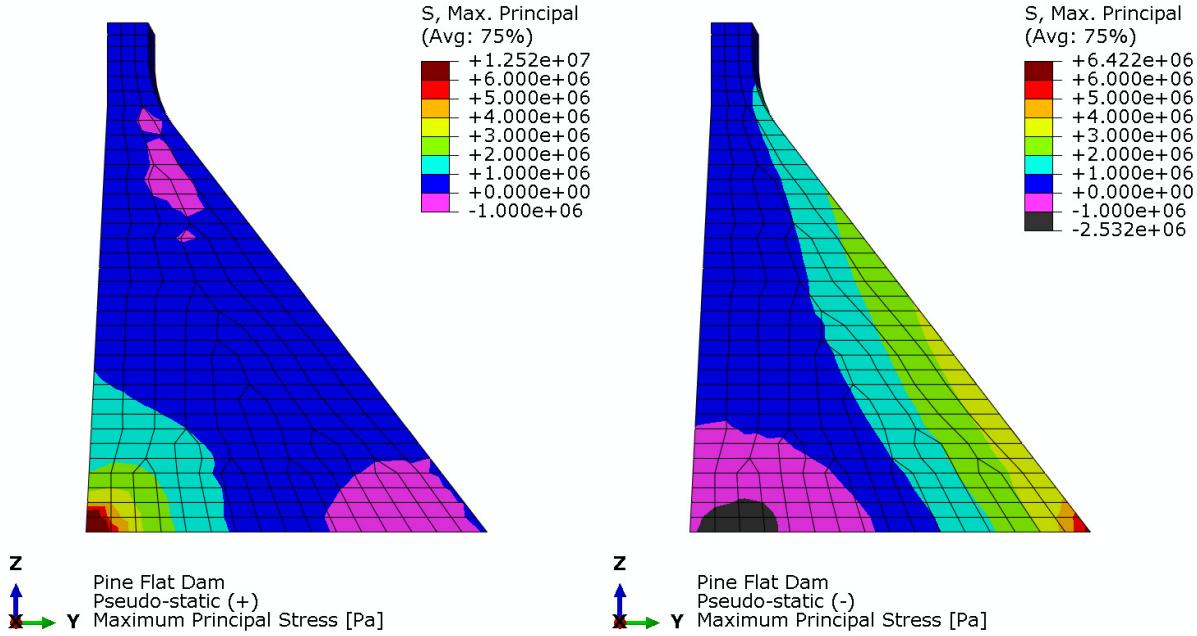


Figure 4. Linear elastic pseudo-static analysis with inertia load towards downstream (left) and upstream (right): maximum principal stress (contour plot).

Figure 5 reports the maximum principal stress envelope resulting from the linear elastic time-history analyses either with the massless approach (left) or with the SAM-4D model (right). In the case with the massless approach a very extensive tensile stress state (higher than the concrete tensile strength) occurs both on the upstream and the downstream face of the dam, also involving a significant depth in the section: the maximum, 11.6 MPa, occurs at dam heel, while at dam toe the tensile stress is a bit lower than 5 MPa. In the case with the SAM-4D model, a quite less severe stress state is observed: tensile stress slightly exceeds the concrete tensile strength only at dam heel, reaching about 3 MPa.

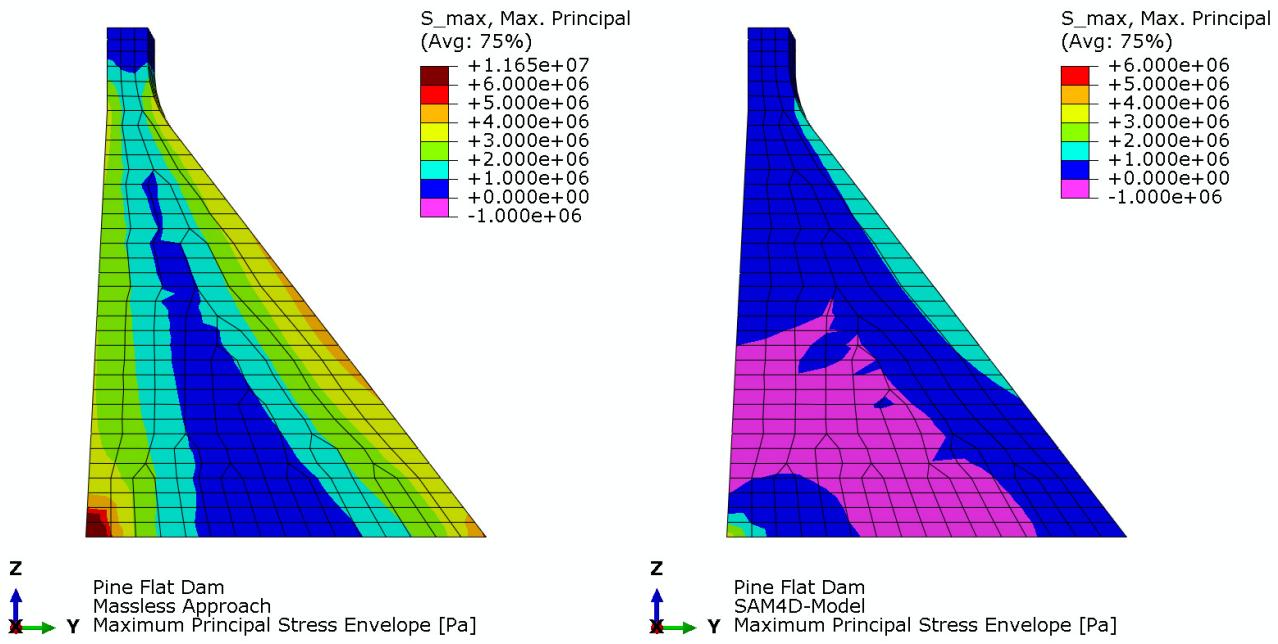


Figure 5. Linear elastic time-history analysis with the massless approach (left) and the SAM-4D model (right): maximum principal stress envelope (contour plot).

In Figure 6 the results of the non-linear time-history analysis with the SAM-4D model are depicted in terms of maximum principal stress envelope (left) and damage variable (right). When the non-linear behaviour of the concrete is considered, a small damaged area occurs at dam-foundation interface in the nearby of dam heel, but the overall structural response of the dam (in terms of stress state) is essentially the same of the linear case as Taft earthquake is not severe enough to highlight significant non-linear effects.

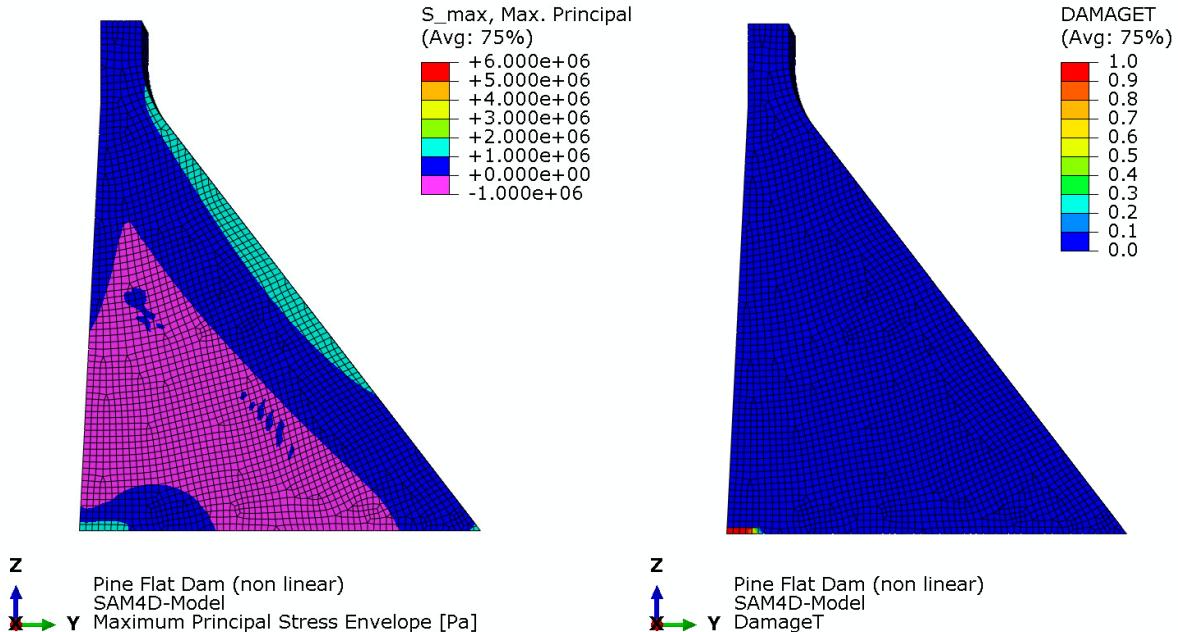


Figure 6. Non-linear time-history analysis with the SAM-4D model: maximum principal stress envelope (contour plot, left) and damage variable (contour plot, right).

Figure 7 summarizes the maximum and minimum horizontal seismic relative (with respect to dam heel) displacements of dam crest resulting from all the performed analyses. As just observed, no difference comes up between linear and non-linear analyses (time-history analyses with the SAM-4D model): displacements are about 0.04 m either downstream or upstream. Using the massless approach, the seismic response of the dam is quite greater than that obtained with the SAM-4D model, as displacements are more than double (0.1 m). The pseudo-static analysis provides displacements of about 0.075 m.

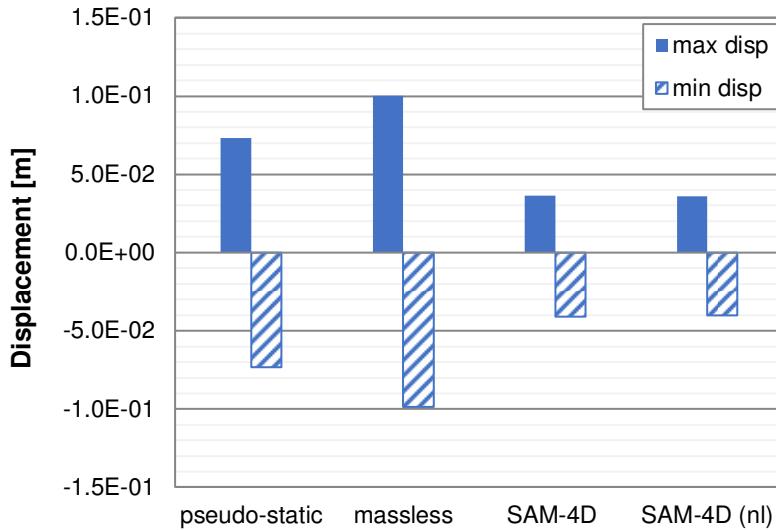


Figure 7. Linear elastic pseudo-static analysis, linear elastic time-history analysis with the massless approach, linear elastic and non-linear time-history analyses with the SAM-4D model: maximum and minimum horizontal seismic relative (with respect to dam heel) displacements of dam crest.

4. Conclusions

The case study of Pine Flat Dam (considered in the frame of the ICOLD 15th International Benchmark Workshop on Numerical Analysis of Dams) was used to apply the progressive analysis methodology, performing analyses of increasing complexity: the linear elastic pseudo-static analysis, the linear elastic time-history analysis with the massless approach, the linear elastic time-history analysis with the SAM-4D (Seismic Advanced Model for Dams) model and the non-linear time-history analysis with the SAM-4D model.

The SAM-4D model was recently implemented by RSE in the frame of the FEM codes used to model the structural behaviour of concrete dams, with the main purpose to reduce the excessive conservativeness of traditional and simplified methods for the seismic safety assessment of dams. It is an advanced structure-foundation dynamic interaction model, in the context of time-history analyses, able to simulate the propagation of seismic waves in a realistic massed foundation, considering its semi-unbounded extent.

The case study of Pine Flat Dam was approached by using the commercial FEM code Abaqus, able to suitably consider both the seismic dam-reservoir and dam-foundation interactions as well as the non-linear behaviour of concrete.

The results of the performed linear elastic analyses show that the seismic response obtained using the SAM-4D model is significantly less severe than that obtained with the traditional approaches. The stress state and the displacements resulting from the SAM-4D analysis are in fact basically consistent with a safe behaviour of the dam under the effect of Taft earthquake: the only exceeding stress, occurring at dam heel, can furthermore be ascribed to the assumption of a monolithic dam-foundation system, without any interface.

The results of the non-linear time-history analysis with the SAM-4D model show that no significant non-linear effect arises: the structural behaviour is pretty unchanged with respect to the corresponding linear case.

The linear elastic time-history analysis with the massless approach provides a structural response, in terms as of stress as of displacement, more than two times greater than that obtained with the SAM-4D model: the tensile strength of the concrete is in this case overcome on both the upstream and downstream entire faces.

The stress state and the displacements calculated with the pseudo-static analysis, although comparable to those resulting from the time-history analysis with the massless approach, are however slightly less demanding: in this regard, it's worth noting that the pseudo-static analysis is able to account only for the fundamental mode of vibration of the system, while also some subsequent modes, instead properly considered in the time-history analysis, could significantly influence the response of the dam to the earthquake.

Anyway, this simplified (pseudo-static) analysis can supply useful hints about the response of the dam, provided that the inertia load is correctly applied in both downstream and upstream directions and that the participating mass of the first resonant mode of the system (used to calculate the seismic action) is significant enough.

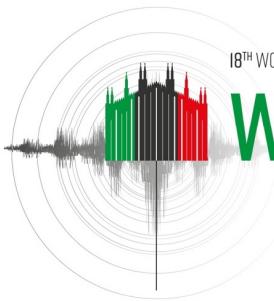
5. Acknowledgments

This work has been financed by the Research Fund for the Italian Electrical System under the Three-Year Research Plan 2022-2024 (DM MITE n. 337, 15.09.2022), in compliance with the Decree of April 16th, 2018.

6. References

- Chen D.H., Du C.B., Yuan J.W., Hong Y.W. (2012). An investigation into the Influence of Damping on the Earthquake Response Analysis of a High Arch Dam, *Journal of Earthquake Engineering*, 16(3): 329-349.
- Chopra A.K. (2014). Earthquake Analysis of Concrete Dams: Factors To Be Considered, *Proceedings of the 10th U.S. National Conference in Earthquake Engineering*, Anchorage, Alaska.
- Clough R.W. (1980). Non-linear mechanisms in the seismic response of arch dams, *Proceedings of the International Research Conference Earthquake Engineering*, Skopje, Yugoslavia.
- Dassault Systèmes S.A. (2021). *SIMULIA Abaqus Unified FEA*.
- Faggiani G., Masarati P., Polidoro F., Bruno G. (2019). Modellazione dell'interazione diga - fondazione nell'analisi sismica delle dighe. Applicazione a casi bi-dimensionali. *Ricerca di Sistema*, RSE, n. 19012845, Milano.
- Faggiani G., Masarati P., Polidoro F., Bruno G. (2020). Analisi sismica dei sistemi tridimensionali diga-bacino-fondazione con modelli di interazione avanzata. *Ricerca di Sistema*, RSE, n. 20010749. Milano.
- Faggiani G., Masarati P., Polidoro F., Bruno G. (2021). Analisi sismica dei sistemi tridimensionali diga-bacino-fondazione, con modelli di interazione avanzata: applicazioni e confronti numerico-sperimentali. *Ricerca di Sistema*, RSE, n. 21010320, Milano.
- Faggiani G., Masarati P., Bruno G. (2022). Metodi avanzati per la modellazione dell'interazione struttura-fondazione nell'analisi sismica delle dighe: implementazione del modello di propagazione delle onde SAM-4D nel codice proprietario CANT-SD. *Ricerca di Sistema*, RSE, n. 22014055, Milano.
- Hansen K.D., Nuss L.K. (2013). Seismic Upgrades for Concrete Dams - Then and Now, *The Journal of Dam Safety*, 11(4): 21-35.
- Hilber H.M., Hughes T.J.R., Taylor R.L (1977). Improved numerical dissipation for time integration algorithms in structural dynamics. *Earthquake Engineering and Structural Dynamics*, 5: 283-292.
- Lee J., Fenves G.L. (1998). A plastic-damage concrete model for earthquake analysis of dams. *Earthquake Engineering and Structural Dynamics*, 27(9): 937-956.
- Liu J., Du Y., Du X., Wang Z., Wu J. (2006). 3D viscous-spring artificial boundary in time domain, *Earthquake Engineering and Engineering Vibration*, 5(1): 93-102.
- Liu Y.S., Chen D.H. (2013). Earthquake Response Analysis of a Gravity Dam Considering the Radiation Damping of Infinite Foundation, *APCOM & ISCM*, Singapore.

- Løkke A., Chopra A.K. (2019). *Direct-Finite-Element Method for Nonlinear Earthquake Analysis of Concrete Dams Including Dam–Water–Foundation Rock Interaction*, PEER Report No. 2019/02, Pacific Earthquake Engineering Research Center, Headquarters at the University of California, Berkeley.
- Lysmer J., Kuhlemeyer R.L. (1969). Finite dynamic model for infinite media, *Journal of the Engineering Mechanics Division*, 95(4): 859-878.
- Salamon J.W., Wood C., Hariri-Ardebili M.A., Malm R., Faggiani G. (2020). Seismic analysis of Pine Flat concrete dam. Theme A – Formulation and Synthesis of Results, *Proceedings of the 15th ICOLD International Benchmark Workshop, Milano, 9–11 September 2019*. Cham: Springer.
- Salamon J.W. (2018). *Evaluation of Numerical Models and Input Parameters in the Analysis of Concrete Dams – A Summary Report of the USSD Workshop, Miami, May 3, 2018*, Report DSO-19-13, USBR.
- US Army Corps of Engineers – USACE (2007). Earthquake design and evaluation of concrete hydraulic structures. EM 1110-2-6053.
- Zangar C.N. (1952). Hydrodynamic pressures on dams due to horizontal earthquake effects. *Engineering Monographs, No. 11, Bureau of Reclamation, United States Department of the Interior*.
- Zhang C., Jin F. (2008). Seismic Safety Evaluation Of High Concrete Dams Part I: State Of The Art Design And Research, *The 14th World Conference on Earthquake Engineering*, Beijing, China.
- Zhang C., Pan J., Wang J. (2009). Influence of seismic input mechanisms and radiation damping on arch dam response, *Soil Dynamics and Earthquake Engineering*, 29(9): 1282-1293.
- Zienkiewicz O.C. (1977). *The Finite Element Method*, 3rd Ed., McGraw-Hill.



IMPLEMENTATION AND VALIDATION OF THE DIRECT METHOD FOR EFFECTIVE SIMULATION OF DYNAMIC DAM-FOUNDATION INTERACTION

D. Froio¹ & F. Carnevale²

¹ ISMES S.p.a., Bergamo, Italy, diego.froio@ismes.it

² ISMES S.p.a., Bergamo, Italy

Abstract: For the seismic analysis of dams, the spatial variation of the ground motion around the underlying canyon, generated by Dynamic Soil-Structure Interaction (DSSI), may introduce differential displacements, possibly detrimental for the stability of high dams. The Direct Method (DM) is the most general procedure to numerically simulate the local spatial variation of the ground motion, when performing both linear and nonlinear seismic DSSI analyses. This method relies on the availability of special Free-Field Boundaries (FFBs), which shall input the seismic wave train and simultaneously absorb outgoing waves at the artificial boundary of the adopted FEM model. However, FFBs are seldom implemented by default in most commercial FEM codes. An original implementation of the DM in Comsol Multiphysics is here presented and validated against available analytical solutions. The present work demonstrates that rigorous DSSI analyses can be correctly performed in the above-mentioned mechanical context, even by using standard FEM programs, once the FFBs are correctly implemented and handled.

1. Introduction

A detailed study of the seismic risk is mandatory for large dam plants located in seismically active regions. One of the crucial aspects for a realistic seismic analysis of a dam is the simulation of the complex wave mechanism induced by Dynamic Soil-Structure Interaction (DSSI). When an incident seismic wave front impinges the dam-foundation interface, wave diffraction occurs due to the inability of such interface to conform to the wave field. Scattered (reflected and diffracted) waves are spread into the surrounding soil without coming back. Seismic waves setting the dam into vibration, once reflected, are also radiated into the soil, thus introducing additional waves within the foundation. Since the motion of the dam depends on that of the foundation and vice versa, the DSSI phenomenon is fully coupled.

The numerical simulation, e.g. by the Finite Element Method (FEM), of DSSI phenomena poses several complications due to the need of materializing an artificial border, so called interaction horizon (Wolf, 1988), where truncating the spatial extension of the model. The computational strategy for handling the unbounded domain not included into the FEM model (far-field) is the main and unique difference among the two main families of methods for simulating DSSI: the Substructure Method (SM) and the Direct Method (DM).

The application of the DM and of its variants has been gradually spreading in dam engineering practice since the last decade. The main practical advantages of the DM as compared to the SM are the following. In the DM the effect of the omitted far-field is reproduced by imposing local Absorbing Boundary Conditions (ABCs) along the artificial boundary of the numerical model. Such transmitting boundaries are devised to approximate the radiation condition, i.e. to limit the wave reflection at the artificial boundary. The simplest of such ABCs is the

well-known viscous boundary of Lysmer and Kuhlemeyer (1969), which is available in the most of commercial FEM computer program. Instead, the SM needs boundary integral techniques to calculate the dynamic stiffness matrix of the unbounded far-field (Wolf, 1985; Chopra, 2020), such as the Boundary Element Method (BEM), which are seldom available in commercial software for structural analysis. Moreover, the DM also allows to simulate the nonlinear behavior of the dam and of the neighboring foundation (near-field) in the time domain, as opposed to the SM, being usually formulated in frequency domain and, thus, requiring a linear behavior of the dam, the reservoir and the foundation.

When the dynamic loading is directly applied within the computational domain, the only scope of an ABC is to transmit outgoing waves out from the numerical model. Froio et al. (2019) showed that the latter case occurs when implementing the DM under the condition of a spatially uniform Ground Motion (GM) in the absence of the structure, as traditionally assumed in the seismic assessment of dams. Nevertheless, the matter becomes more intricate when the spatial variation of the GM caused by the seismic wave passage must be accounted for, as the truncation boundary should allow the incoming seismic wave to enter the model without any modification as well as to ensure that scattered waves are absorbed. Standard ABCs are not able to accomplish this task. Thus, when the excitation originates from outside of the model in the form of incoming seismic waves, the formulation of the ABCs needs to be modified.

Since the shear wave velocities of the earth's surface lie in the range from about 0.1 km/s to about 3 km/s and the strong earthquake shaking of interest falls in the frequency range from about 0.1 Hz to about 20 Hz, the corresponding wavelengths are from tens of meters to tens of kilometres (Sánchez-Sesma, 1987). Then, for a dam footprint having dimensions near to the wavelengths associated with the most important periods of the GM, appreciable variations of GM amplitudes and phases occur along the dam-foundation interface even in the absence of the dam. The spatial variation (incoherence) of the GM caused by local site topography and geology may have significant effects on the seismic GM and, thus, are of particular significance for either the assessment of the seismic risk of existing dams or the planning and seismic design of new important hydroelectric facilities.

The seismic amplification conveyed by ridges and canyons, so-called site effect, has long been recognized as significant. The observations based on available strong motion records near the dam footprint during earthquakes have shown the GM is far from being uniform, especially at its higher frequency components, as reported by Hall (1988), Alves and Hall (2006), Chopra (2012) and more recently by Koufoudi et al. (2018). The outcomes of numerical models implementing either the SM (Szczesiak et al., 1999; Maeso et al., 2002; Chopra and Wang, 2010; Wang and Chopra, 2010) or the DM (Løkke and Chopra, 2017-2019; Jin et al., 2019; Sotoudeh et al., 2019; Varmazyari and Sabbagh-Yazdi, 2021) have confirmed that the spatial nonuniformity of the GM produced by vertically propagating incoming seismic waves has an appreciable influence on the structural response of dams.

A forthright application of the DM in the realm of finite elements under the assumption of a vertical propagation of the seismic waves was possible by the introduction of the Free-Field Boundary (FFB) devised by Zienkiewicz et al. (1989). The basic idea of the FFB is to augment the numerical model with free-field columns and planes to separately calculate the vertically propagating incident seismic wave field, so that its absorption by any ABC acting on different elevations of the artificial boundary can be prevented, as explained in the following Section 2. However, at present FFBs are not available by default in most of the commercial FEM codes commonly used for the seismic analysis of dams. To fill this gap, this paper illustrates an original and convenient computational strategy to model the FFB into COMSOL Multiphysics®. To the authors' best knowledge, no similar approach has been accomplished before by this FEM software. The robustness and accuracy of the present implementation are confirmed through a consistent validation process based on two benchmark problems whose analytical solution is well-known. Hence, the present work demonstrates that the spatial variability of the GM caused by vertically propagating seismic waves can be rigorously simulated using standard FEM programs once the FFBs are correctly implemented and handled.

The present paper is organized as follows. The formulation of the DM for linear DSSI analysis is the subject of Section 2, whereas its implementation in COMSOL Multiphysics® is presented in Section 3. The validation analyses are discussed in Section 4. Conclusive considerations of this work are summarized in final Section 5.

2. General formulation of the Direct Method

In the present section, the formulation of DSSI is discussed with reference to an arbitrary three-dimensional linear soil-structure system. The extension of the explained formulation to nonlinear problems entails minor modifications (see e.g. Aydinoğlu, 1993).

Let consider the general scheme portrayed in Figure 1. The generalized structure, denoted by capital letter \hat{S} , includes the structure (S) and the near-field (N), that is the neighboring foundation enclosing all the material inhomogeneities of the soil, possibly exhibiting a nonlinear behavior. The far-field (F), i.e. the soil-structure system deprived by the generalized structure, is conceived as a semi-unbounded domain possibly having a countable set of layers. The geometry of the far-field, i.e. the shape of the free-surface and of the interfaces between the layers, if any, is assumed to extend towards infinity along the normal direction to the so-called *interaction horizon* Γ_h (Wolf, 1988), the latter being the ideal interface between the generalized structure and the far-field. The mechanical properties of the far-field may vary with depth, but they are assumed to be uniform within each individual layer. The layers are made of isotropic linear viscoelastic materials, except for the bottom homogeneous linear elastic half-space (seismic bedrock), which is traditionally assumed to be undamped.

The location of the interaction horizon is in charge to the analyst, depending on the characteristics of the DSSI problem at hand and on the adopted methodology to solve it. Since part of the scattered wave field is quite always reflected at Γ_h due to the faulty absorption abilities of any local ABC, the generalized structure must always include an adequate volume of the neighbouring soil. Moreover, a reliable simulation of the nonlinear response of the generalized structure can be only attained by placing the interaction horizon sufficiently far away from the structure, so that the linear elastic behaviour of the far-field can be justified.

Although any numerical method apt to spatially discretize the governing equations of motion of the dam-foundation system may be considered, the FEM is usually adopted by virtue of its capabilities to deal with embedment effects as well as any other geometrical or mechanical inhomogeneity quite easily. Thus, the generalized structure is here discretized as an assembly of finite elements.

Let \mathbf{u}^t be the total displacements vector obtained from a FEM discretization of the system, where the adjective "total" means that displacements are evaluated with respect to a fixed coordinate system. The displacements of the generalized structure are included into $\mathbf{u}_u^t = \{\mathbf{u}_s^t, \mathbf{u}_i^t, \mathbf{u}_g^t\}^T$, the nodal displacements of the interaction horizon are identified by \mathbf{u}_h^t , whereas the far-field displacements are pointed out by \mathbf{u}_f^t . Clearly, all previously introduced displacement vectors depends on time variable t .

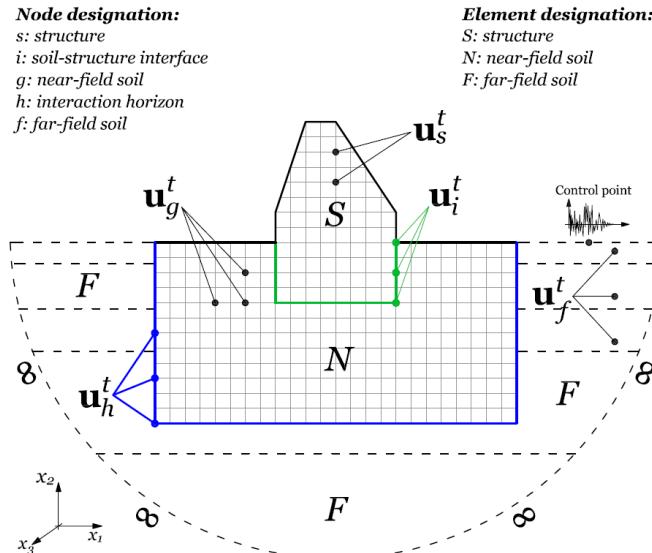


Figure 1. General scheme and notation of the DSSI problem.

By performing a dynamic condensation of the contribution of far-field degrees of freedom (f), the linear equations of motion of a viscously damped soil-structure system in the frequency domain read (Wolf, 1985):

$$\begin{bmatrix} \bar{\mathbf{K}}_{uu} & \bar{\mathbf{K}}_{uh} \\ \bar{\mathbf{K}}_{hu} & \bar{\mathbf{K}}_{hh}^S + \bar{\mathbf{S}}_{hh}^F \end{bmatrix} \begin{Bmatrix} \bar{\mathbf{u}}_u^t \\ \bar{\mathbf{u}}_h^t \end{Bmatrix} = \begin{Bmatrix} \mathbf{0} \\ \bar{\mathbf{S}}_{hh}^F \bar{\mathbf{u}}_h^g \end{Bmatrix}; \quad (1)$$

where $\bar{\mathbf{u}}^t = \{\bar{\mathbf{u}}_u^t, \bar{\mathbf{u}}_h^t\}^T$ is the Fourier transform of $\mathbf{u}^t = \{\mathbf{u}_u^t, \mathbf{u}_h^t\}^T$, $\bar{\mathbf{K}}_{kl} = \mathbf{K}_{kl} + i\omega \mathbf{C}_{kl} - \omega^2 \mathbf{M}_{kl}$ is the dynamic stiffness (impedance) submatrix relating the degrees of freedom (dofs) k and l , \mathbf{K}_{kl} , \mathbf{C}_{kl} and \mathbf{M}_{kl} are the stiffness, damping and mass submatrices, respectively, ω is the angular frequency and

$$\bar{\mathbf{S}}_{hh}^F = \bar{\mathbf{K}}_{hh}^F + \bar{\mathbf{K}}_{hf} \bar{\mathbf{K}}_{ff}^{-1} \bar{\mathbf{K}}_{fh}; \quad (2)$$

is the condensed dynamic stiffness matrix of the far-field, expressing the radiation condition enforced by such unbounded linear viscoelastic domain at the dofs ensuing from the FEM discretization of Γ_h . Vector $\bar{\mathbf{u}}_h^g$ in Eq. (1) is the response of the far-field evaluated at the interaction horizon that would occur in the absence of the generalized structure (Wolf, 1985).

The seismic loading of the soil-structure system on the rhs of Eq. (1) can be evaluated once $\bar{\mathbf{u}}_h^g$ is available. Following a well-established practice in seismic engineering, far-field response $\bar{\mathbf{u}}_h^g$ is usually replaced by so-called Free-Field Motion $\bar{\mathbf{u}}_h^f$ (FFM), i.e. the response of a viscoelastic layered half-space obtained by projecting towards infinity the geometry of the interaction horizon. The main advantage of using $\bar{\mathbf{u}}_h^f$ in place of $\bar{\mathbf{u}}_h^g$ is that the first response can be calculated from simpler analytical/numerical approaches than those required to calculate $\bar{\mathbf{u}}_h^g$, especially under the usual assumption of vertical propagation of the seismic waves. The impedance of the FF half-space is here denoted by $\bar{\mathbf{S}}_{hh}^H$.

Substituting the relationships existing between $\bar{\mathbf{u}}_h^g$ and $\bar{\mathbf{u}}_h^f$ (Wolf, 1985):

$$\bar{\mathbf{S}}_{hh}^H \bar{\mathbf{u}}_h^f = \bar{\mathbf{S}}_{hh}^F \bar{\mathbf{u}}_h^g; \quad (3)$$

into Eq. (1), the following system is obtained

$$\begin{bmatrix} \bar{\mathbf{K}}_{uu} & \bar{\mathbf{K}}_{uh} \\ \bar{\mathbf{K}}_{hu} & \bar{\mathbf{K}}_{hh}^S + \bar{\mathbf{S}}_{hh}^F \end{bmatrix} \begin{Bmatrix} \bar{\mathbf{u}}_u^t \\ \bar{\mathbf{u}}_h^t \end{Bmatrix} = \begin{Bmatrix} \mathbf{0} \\ \bar{\mathbf{S}}_{hh}^H \bar{\mathbf{u}}_h^f \end{Bmatrix}; \quad (4)$$

expressing the equations of motion of DSSI with the FFM determining the load vector. According to the previous equation, the load vector is expressed as the product between the dynamic stiffness matrix of the FF, condensed at the nodes belonging to the interaction horizon where the generalized structure is assembled, and the FFM of the same nodes.

Finally, let $\bar{\mathbf{F}}_h^f$ be the integral of free-field stresses $\bar{\boldsymbol{\sigma}}^f$ over the finite element discretization of Γ_h :

$$\bar{\mathbf{F}}_h^f = \int_{\Gamma_h} \mathbf{N}_h^T \bar{\boldsymbol{\sigma}}^f(\mathbf{u}_h^f) \cdot \mathbf{n} \, dS; \quad (5)$$

where \mathbf{N}_h is the $3 \times 3N_h$ matrix of global shape functions restricted to Γ_h (N_h is the total number of nodes belonging to the mesh of Γ_h) and \mathbf{n} is its normal vector. Then, by equilibrium one has (Wolf, 1988)

$$\bar{\mathbf{F}}_h^f + \bar{\mathbf{S}}_{hh}^F \mathbf{u}_h^f = \bar{\mathbf{S}}_{hh}^H \mathbf{u}_h^f; \quad (6)$$

which, once substituted into Eq. (4), determines the following final system of equations:

$$\begin{bmatrix} \bar{\mathbf{K}}_{uu} & \bar{\mathbf{K}}_{uh} \\ \bar{\mathbf{K}}_{hu} & \bar{\mathbf{K}}_{hh}^S + \bar{\mathbf{S}}_{hh}^F \end{bmatrix} \begin{Bmatrix} \bar{\mathbf{u}}_u^t \\ \bar{\mathbf{u}}_h^t \end{Bmatrix} = \begin{Bmatrix} \mathbf{0} \\ \bar{\mathbf{S}}_{hh}^F \bar{\mathbf{u}}_h^f + \bar{\mathbf{F}}_h^f \end{Bmatrix}. \quad (7)$$

A schematic representation of Eq. (7) and its physical interpretation is given in Figure 2. Notice that the radiation condition of the far-field, transposed in numerical terms by matrix $\bar{\mathbf{S}}_{hh}^F$, applies to motion $\bar{\mathbf{u}}_h^t - \bar{\mathbf{u}}_h^f$ arising from the waves scattered by the generalized structure. As compared to Eq. (4), Eq. (7) has the advantage of not requiring the assembly of matrix $\bar{\mathbf{S}}_{hh}^H$, but on the other hand it requires the computation of both FF displacements and boundary tractions.

The time domain version of Eq. (7) is obtained owing to the Convolution Theorem:

$$\begin{bmatrix} \mathbf{M}_{uu} & \mathbf{M}_{uh} \\ \mathbf{M}_{hu} & \mathbf{M}_{hh}^S \end{bmatrix} \begin{Bmatrix} \ddot{\mathbf{u}}_u^t \\ \dot{\mathbf{u}}_h^t \end{Bmatrix} + \begin{bmatrix} \mathbf{C}_{uu} & \mathbf{C}_{uh} \\ \mathbf{C}_{hu} & \mathbf{C}_{hh}^S \end{bmatrix} \begin{Bmatrix} \dot{\mathbf{u}}_u^t \\ \dot{\mathbf{u}}_h^t \end{Bmatrix} + \begin{bmatrix} \mathbf{K}_{uu} & \mathbf{K}_{uh} \\ \mathbf{K}_{hu} & \mathbf{K}_{hh}^S \end{bmatrix} \begin{Bmatrix} \mathbf{u}_u^t \\ \mathbf{u}_h^t \end{Bmatrix} + \left\{ \int_0^t \mathbf{S}_{hh}^F(t-\tau) (\mathbf{u}_h^t - \mathbf{u}_h^f) d\tau \right\} = \begin{Bmatrix} \mathbf{0} \\ \mathbf{F}_h^f \end{Bmatrix}; \quad (8)$$

where $\mathbf{S}_{hh}^F(t)$ is the Inverse Fourier Transform of impedance matrix $\bar{\mathbf{S}}_{hh}^F(\omega)$ and the overdot is the adopted notation for a time derivative. Eq. (8) forms the reference formulation of the DM in the time domain.

In the DM the radiation condition is approximated by imposing local ABCs along the interaction horizon. The local property of an ABCs means that the enforced boundary condition involves the responses of at most few points in the neighbourhood of the boundary point under consideration within a relatively small time-window. This is opposed to the exact radiation condition of Eq. (8), where the reaction-displacement relation along Γ_h is given by a convolution integral (nonlocal in time) of a dense matrix-vector product (nonlocal in space). Numerous ABCs have been proposed in the literature, such as the viscous boundary, the paraxial boundary, the DtN map, the Perfectly Matched Layer, etc.. For the DSSI analysis procedure described in the following section the viscous boundary is selected owing to its availability in almost any commercial FEM code, acceptable accuracy and ease of implementation.

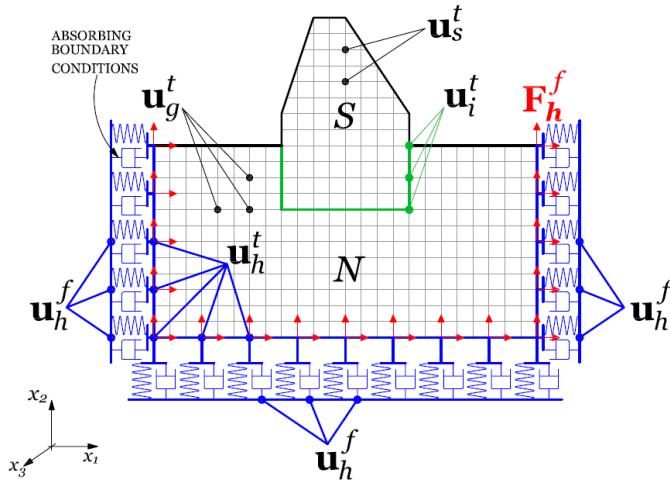


Figure 2. Schematic model, notation and physical interpretation of the DM.

3. Implementation of the DM in Comsol Multiphysics®

Let consider the scheme of a three-dimensional dam-foundation system shown in Figure 3. The unbounded foundation domain is truncated by a box-shaped artificial boundary (interaction horizon) having its faces oriented as the fixed cartesian axes x, y, z . Only the upper free surface of the model tracing the real topography of the valley may depart from flat geometry.

Let Γ_{hk} be the subset of Γ_h having normal parallel to the k -axis. By applying the viscous boundary of Lysmer and Kuhlemeyer (1969), the exact radiation condition in Eq. (8) is approximated as follows:

$$\int_0^t \mathbf{S}_{hh}^F(t-\tau) (\mathbf{u}_h^t - \mathbf{u}_h^f) d\tau \approx (\mathbf{C}_{hh}^{F,x} + \mathbf{C}_{hh}^{F,y} + \mathbf{C}_{hh}^{F,z}) (\dot{\mathbf{u}}_h^t - \dot{\mathbf{u}}_h^f) = \mathbf{C}_{hh}^F (\dot{\mathbf{u}}_h^t - \dot{\mathbf{u}}_h^f); \quad (9)$$

where

$$\begin{aligned} \mathbf{C}_{hh}^{F,x} &= \int_{\Gamma_{hx}} \mathbf{N}_h^T \rho \operatorname{diag}(\{c_{(P)}, c_{(S)}, c_{(S)}\}) \mathbf{N}_h dS, & \mathbf{C}_{hh}^{F,y} &= \int_{\Gamma_{hy}} \mathbf{N}_h^T \rho \operatorname{diag}(\{c_{(S)}, c_{(P)}, c_{(S)}\}) \mathbf{N}_h dS, \\ \mathbf{C}_{hh}^{F,z} &= \int_{\Gamma_{hz}} \mathbf{N}_h^T \rho \operatorname{diag}(\{c_{(S)}, c_{(S)}, c_{(P)}\}) \mathbf{N}_h dS; \end{aligned} \quad (10)$$

are the damping matrices ensuing from the distributed viscous dashpots placed on the vertical faces and on the horizontal bottom face of the interaction horizon, ρ is the far-field mass density, $c_{(S)}$ and $c_{(P)}$ are its shear wave and pressure wave velocities, respectively, and $\operatorname{diag}(\mathbf{d})$ denotes a diagonal matrix having vector \mathbf{d} on its main diagonal.

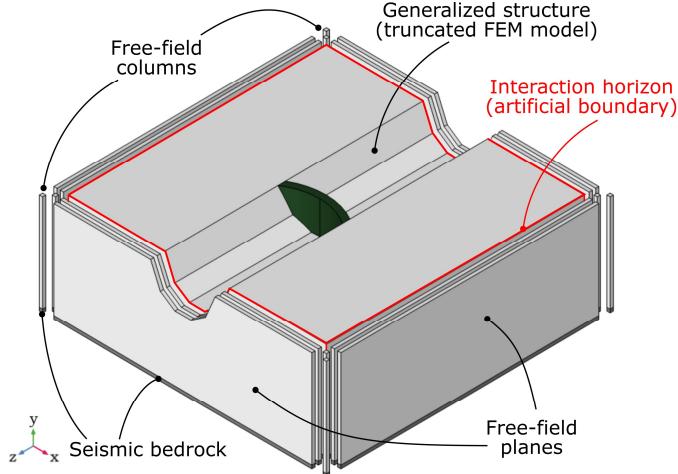


Figure 3. General arrangement of the computational model implementing the DM in Comsol Multiphysics®.

The viscous boundary given by Eq. (9) should be interpreted as an approximation of the exact radiation condition, which is usually accurate for practical engineering purposes provided that the extension of the near-field is sufficiently large. Since the wave absorption capabilities of viscous boundaries downgrade for oblique angles of incidence, it is advisable to leave a relatively large margin between the interaction horizon and the portion of the generalized structure whose response is of interest.

Substitution of Eq. (9) into Eq. (7) and Eq. (8) yields the final equations of motion of the DM including the viscous boundary as the adopted ABC:

$$\begin{bmatrix} \bar{\mathbf{K}}_{uu} & \bar{\mathbf{K}}_{uh} \\ \bar{\mathbf{K}}_{hu} & \bar{\mathbf{K}}_{hh}^S + i\omega \mathbf{C}_{hh}^F \end{bmatrix} \begin{bmatrix} \bar{\mathbf{u}}_u^t \\ \bar{\mathbf{u}}_h^t \end{bmatrix} = \begin{bmatrix} \mathbf{0} \\ \mathbf{P}_h^f \end{bmatrix}. \quad (11a)$$

$$\begin{bmatrix} \mathbf{M}_{uu} & \mathbf{M}_{uh} \\ \mathbf{M}_{hu} & \mathbf{M}_{hh}^S \end{bmatrix} \begin{bmatrix} \ddot{\mathbf{u}}_u^t \\ \ddot{\mathbf{u}}_h^t \end{bmatrix} + \begin{bmatrix} \mathbf{C}_{uu} & \mathbf{C}_{uh} \\ \mathbf{C}_{hu} & \mathbf{C}_{hh}^S + \mathbf{C}_{hh}^F \end{bmatrix} \begin{bmatrix} \dot{\mathbf{u}}_u^t \\ \dot{\mathbf{u}}_h^t \end{bmatrix} + \begin{bmatrix} \mathbf{K}_{uu} & \mathbf{K}_{uh} \\ \mathbf{K}_{hu} & \mathbf{K}_{hh}^S \end{bmatrix} \begin{bmatrix} \mathbf{u}_u^t \\ \mathbf{u}_h^t \end{bmatrix} = \begin{bmatrix} \mathbf{0} \\ \mathbf{P}_h^f \end{bmatrix}; \quad (11b)$$

in the frequency domain and in the time domain, respectively, where

$$\mathbf{P}_h^f = \mathbf{C}_{hh}^F \dot{\mathbf{u}}_h^f + \mathbf{F}_h^f; \quad (12)$$

are the so-called effective earthquake forces (Løkke and Chopra, 2017 and 2018).

Hence, the boundary tractions acting on the interaction horizon are made of two contributions. The first contribution are boundary reactions $-\mathbf{C}_{hh}^F(\dot{\mathbf{u}}_h^t - \dot{\mathbf{u}}_h^f)$ of the viscous dashpots to the scattered motion only, thus leaving the FFM unaffected. The second contribution originates from traction resultants \mathbf{P}_h^f of the FFM. The latter term may also include the reaction forces ensuing from any pre-existing static loads acting on the generalized structure. A FFB is any boundary condition capable of providing both actions on Γ_h .

The calculation of FF velocities $\dot{\mathbf{u}}_h^f$ and traction resultants \mathbf{P}_h^f must rely on the definition of a suitable numerical model of the FF problem. Under the usual and pragmatic hypothesis of a seismic wave field consisting of plane SH-, SV-, and P-waves vertically propagating upwards from the underlying semi-unbounded foundation (Chopra, 2020), the FF system can be modelled by at most eight planar layers and eight FF columns added to the computational model of the generalized structure, as shown in Figure 3. Both FF layers and columns are also discretized by finite elements with the same mesh density of the generalized structure.

Twin FF layers (or planes) are introduced for each vertical face of the interaction horizon, sharing the same in-plane geometry and stratigraphy of Γ_h . Each layer simulates the FF response of the half-space obtained by projecting towards infinity the geometry of the corresponding vertical face of Γ_h along its normal direction. Two layers are needed for each vertical face of Γ_h because two different sets of boundary conditions must be enforced to reproduce the out-of-plane (SH-wave field) and the in-plane (SV- and P-wave fields) half-space motion. In particular, the following BCs must be prescribed at any FF layer with outer normal \mathbf{n}_k ($k = x, z$):

$$\mathbf{u}^f - (\mathbf{u}^f \cdot \mathbf{n}_k) \mathbf{n}_k = 0, \quad \text{for out-of-plane motion;} \quad (13a)$$

$$\mathbf{u}^f \cdot \mathbf{n}_k = 0, \quad \text{for in-plane motion;} \quad (13b)$$

where $\mathbf{u}^f = \{u_x^f, u_y^f, u_z^f\}^T$ is the three-dimensional FF displacement vector.

Since any FF layer is a truncated model of a semi-infinite half-space, its vertical boundaries must be also endowed with FFBs. Towards this scope, twin FF columns are located at each corners of the FEM model to reproduce the FF response of a flat half-space sharing the same stratigraphy of the adjacent FF layers, which is assumed to indefinitely extend in both horizontal directions. Then, two FF columns must be added at each model corner to impose the following two distinct sets of BCs at all nodes of a FF column:

$$u_y^f = 0, \quad \text{for S-wave vertical propagation;} \quad (14a)$$

$$u_x^f = u_z^f = 0, \quad \text{for P-wave vertical propagation;} \quad (14b)$$

when simulating vertical wave propagation by finite elements. The first of Eqs. (14) prevents any bending effect of the FF column, so that its dynamic response is compelled to display a pure shear deformation; the second of Eqs. (14) inhibits any unwanted Poisson's effect associated with the column axial vibration.

The parts of the FF model are highlighted in the Figure 4. The seismic response of the FF model is processed in parallel with that of the generalized structure as the dynamic analysis advances either in the time or in the frequency domains. The FF response must be independent from that of the generalized structure. In fact, the FF system is, by definition, a regular half-space located at an unbounded distance from the generalized structure and, thus, it cannot be reached by the waves scattered by the generalized structure. On the contrary, the FF response ($\dot{\mathbf{u}}_h^f$ and \mathbf{F}_h^f) calculated by each FF column are mapped to the lateral boundaries of the adjacent FF planes by using the *General Extrusion ("genext")* nonlocal coupling function available in Comsol Multiphysics®. Likewise, $\dot{\mathbf{u}}_h^f$ and \mathbf{F}_h^f calculated within the domain of each FF layer are mapped to the corresponding lateral face of the interaction horizon by means of the same coupling function. Hence, the information travels from the FF columns to the FF layers, and from the FF layers to the generalized structure, but never in the opposite way.

Finally, the effective earthquake forces applied at the bottom boundary of the model must be calculated. Currently, the standard approach in dam engineering is to define the earthquake as a suite of three orthogonal acceleration components $a_x^{oc}(t), a_y^{oc}(t), a_z^{oc}(t)$ describing the motion of an outcrop point, i.e. a control point located at the rock surface (Figure 1) where strong-motion earthquakes are normally recorded (Wolf, 1985). The spectra of such acceleration components should, in some sense not examined here, be consistent with a target spectrum representing the seismic hazard of the site, which is usually derived according to either a deterministic or a probabilistic seismic hazard analysis (Kramer, 1996).

Since seismic hazard analysis typically does not consider local site effects, such as topography and stratigraphy, an outcrop signal is intended as the surface motion of a reference flat half-space. Displacement field \mathbf{u}^h of a flat half-space excited by solely plane SH-, SV- and P-waves propagating in the vertical direction (y), is given by the solution of the well-known one-dimensional wave equation (Wolf, 1985; Kramer, 1996):

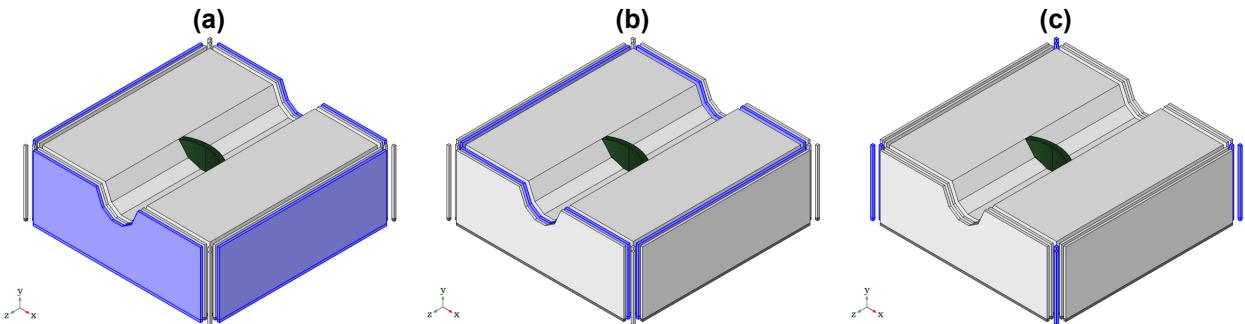


Figure 4. Components of the model required for computing FF displacements and traction resultants: vertical layers for computing the out-of-plane (a) and the in-plane (b) components of the FFM at the lateral artificial boundary of the generalized structure; corner columns for computing the FFM at the lateral artificial boundaries of the vertical layers (c).

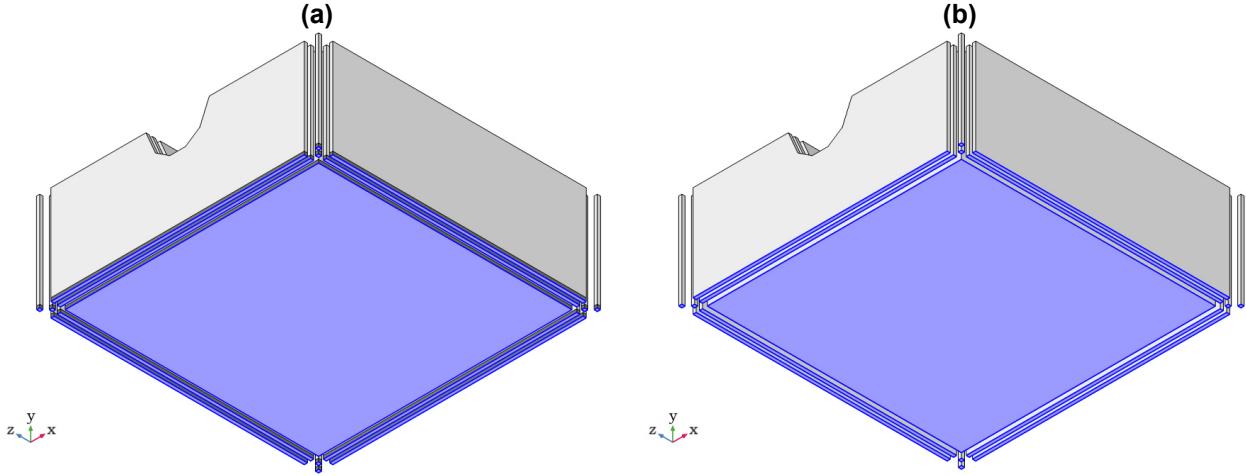


Figure 5. Bottom horizontal face of the interaction horizon where the ABC is enforced (a) and reference plane where effective earthquake forces are applied (b).

$$u_k^h(y, t) = u_k^{hI}(ct - y) + u_k^{hO}(ct + y); \quad (15)$$

where u_k^{hI} and u_k^{hO} denotes the incoming (incident) and outgoing (reflected) wave fields, and $c = c_{(P)}$ in the case of pressure waves ($k = y$) or $c = c_{(S)}$ in the case of shear waves ($k = x, z$).

Within the assumed reference frame ($y > 0$ if upward), the radiation condition at any depth y provides the following expression of the boundary traction for a unit normal \mathbf{n} pointing in the negative y -direction:

$$f_k^{hI} = \sigma_{kl}^{hI}(\mathbf{u}^{hI})n_l = c\rho\dot{u}_k^{hI}, \quad f_k^{hO} = \sigma_{kl}^{hO}(\mathbf{u}^{hO})n_l = -c\rho\dot{u}_k^{hO}. \quad (16)$$

whose resultants over the FEM discretization of the horizontal boundary $y = y_0$ is

$$\mathbf{F}_h^{h,y} = \int_{\Gamma_{hy}} \mathbf{N}_h^T \mathbf{f}^{h0} dS = \int_{\Gamma_{hy}} \mathbf{N}_h^T \rho \text{diag}(\{c_{(S)}, c_{(P)}, c_{(S)}\})(2\dot{\mathbf{u}}^{hI0} - \dot{\mathbf{u}}^{h0}) dS = \mathbf{C}_{hh}^{F,y} (2\dot{\mathbf{u}}^{hI0} - \dot{\mathbf{u}}^{h0}); \quad (17)$$

where $\dot{\mathbf{u}}^{h0} = \dot{\mathbf{u}}^h(y_0, t)$. Thus, by imposing that FF stress resultants at the bottom boundary $\mathbf{F}_h^{h,y}$ is equal to $\mathbf{F}_h^{h,y}$, i.e. $\mathbf{u}^{f0} = \mathbf{u}^{h0}$, the outcrop motion would be recovered at the free surface of the generalized structure when the latter coincides with the reference flat half-space. Recalling Eq. (12), this in turn implies that the effective earthquake forces to be applied at the bottom boundary are

$$\mathbf{P}_h^{f,y} = 2\mathbf{C}_{hh}^{F,y} \dot{\mathbf{u}}^{fI0}. \quad (18)$$

The FF incoming wave velocities $\dot{\mathbf{u}}^{fI0}$ at a given depth must be consistently defined to obtain the surface control motion $\mathbf{a}^{oc}(t)$ at the surface of a one-dimensional column representing the reference half-space. This task can be accomplished by performing a one-dimensional deconvolution analysis of the outcrop motion (Løkke and Chopra, 2017). When specifying the earthquake excitation in this way, the spatial variation of the GM is automatically considered in the numerical analysis, albeit predominantly in the vertical direction.

Effective earthquake forces $\mathbf{P}_h^{f,y}$ do not need to act at the bottom boundary, where ABCs are enforced. Instead, they can be theoretically applied along any horizontal plane in between the bottom artificial boundary of the model and the highest depth below which the near-field can be guaranteed being regular, i.e. constituted by horizontal layers made of linear viscoelastic materials. In fact, it may happen sometimes that the application of external forces badly interacts with the behaviour of the adopted ABC. If this is the case, the effective earthquake forces may be applied to a horizontal surface just above the bottom face of the artificial boundary, as illustrated in Figure 5. Although this paper illustrates a Comsol Multiphysics® realisation, the procedure herein presented is equally valid and adaptable to other commercial FEM codes if a coupling functionality analogous to the *General Extrusion* are made available.

4. Validation of the numerical results

This section illustrates the results of several numerical experiments carried out to verify the correct functioning of the present implementation of the DM. The evaluation of the consistency and accuracy of the proposed methodology is based on the comparison between the computed displacement at the foundation surface for two benchmark problems, whose exact analytical solutions are available in the literature. The analytical solutions of both benchmark problems have been implemented in the MatLab environment.

The first benchmark problem, discussed in Section 4.1, consist in calculating the surface amplification of a planar wave vertically propagating into a homogeneous viscously damped elastic layer resting on a viscoelastic half-space. The second benchmark problem, presented in the subsequent Section 4.2 pertains the scattering of a train of SH harmonic waves propagating in the vertical direction carried out by a semi-cylindrical canyon located at the free surface of a half-space.

4.1. Vertical propagation of a harmonic plane S-wave in a viscoelastic layer on an elastic half-space

Let consider a homogeneous soil/rock deposit of depth H made of an isotropic, linear viscoelastic material behaving according to the following Kelvin-Voigt (KV) model:

$$\tau = G_s \gamma + \eta_s \dot{\gamma}, \quad \tau_{(KV)s} = \frac{\eta_s}{G_s}; \quad (19)$$

where $\tau = \sigma_{12}$ is the shear stress, $\gamma = 2\varepsilon_{12} = u_{1,2}$ is the shear strain, G_s and η_s are the material shear modulus and viscosity of the layer, respectively, and $\tau_{(KV)s}$ is the characteristic time scale governing the behaviour of the KV unit. Thus, the shear stress is given by the sum of an elastic part, proportional to the shear strain, and a viscous part, proportional to the shear strain rate. The shear wave velocity of the soil layer is denoted by $c_{(S)s}$, whereas its mass density is ρ_s . The soil layer rests on an elastic bedrock having a shear wave velocity of $c_{(S)b}$ and a mass density of ρ_b .

The soil layer is subjected to vertically propagating harmonic plane S-waves coming from the bedrock, with unitary amplitude at the surface and circular frequency ω . The S-waves are polarized along the x -axis.

The complex-valued transfer function of the system, i.e. the ratio between free surface motion of the soil layer and the bedrock outcropping motion, is given by the following formula:

$$F(\hat{\omega}_s^*, \alpha^*) = \frac{1}{\cos(\hat{\omega}_s^*) + i\alpha^* \sin(\hat{\omega}_s^*)}; \quad (20)$$

where

$$\hat{\omega}_s^* = \frac{\omega H}{c_{(S)s} \sqrt{1 + i\omega \tau_{(KV)s}}} = \frac{\hat{\omega}_s}{\sqrt{1 + i\hat{\omega}_s \hat{\tau}_{(KV)s}}}; \quad (21a)$$

$$\alpha^* = \frac{\rho_s c_{(S)s}}{\rho_b c_{(S)b}} \sqrt{1 + i\omega \tau_{(KV)s}} = \alpha \sqrt{1 + i\hat{\omega}_s \hat{\tau}_{(KV)s}}; \quad (21b)$$

are the complex nondimensional frequency and the complex impedance ratio, respectively. Transfer function F depends on real impedance ratio $\alpha = \rho_s c_{(S)s} / \rho_b c_{(S)b}$ of the undamped system ($\tau_{(KV)s} = 0$), on the nondimensional frequency of the layer $\hat{\omega}_s = \omega H / c_{(S)s}$ and on the nondimensional characteristic time $\hat{\tau}_{(KV)s} = \tau_{(KV)s} c_{(S)s} / H$. Eq. (20) also holds for the case of harmonic plane P-waves by substituting $c_{(S)s}$ with $c_{(P)s}$ into Eqs. (21).

In the present analysis, the amount of viscous dissipation is expressed in terms of the damping factor of the fundamental mode of the viscoelastic layer resting on a rigid bedrock:

$$\zeta = \zeta_1 = \frac{\tau_{(KV)} \omega_{s1}}{2} = \frac{\hat{\tau}_{(KV)s} \hat{\omega}_{s1}}{2} = \frac{\pi}{4} \hat{\tau}_{(KV)s}. \quad (22)$$

To validate the procedure described in Section 3, the transfer function of Eq. (20) has been numerically evaluated by finite elements. The FEM model of the viscoelastic layer on an elastic half-space is shown in Figure 6a. The horizontal size of the FEM model of the layer is twice its depth. The vertical FEM discretization of the layer comprises 32 elements to reproduce the shortest wavelengths ($\hat{\omega}_s = 4$) with sufficient accuracy.

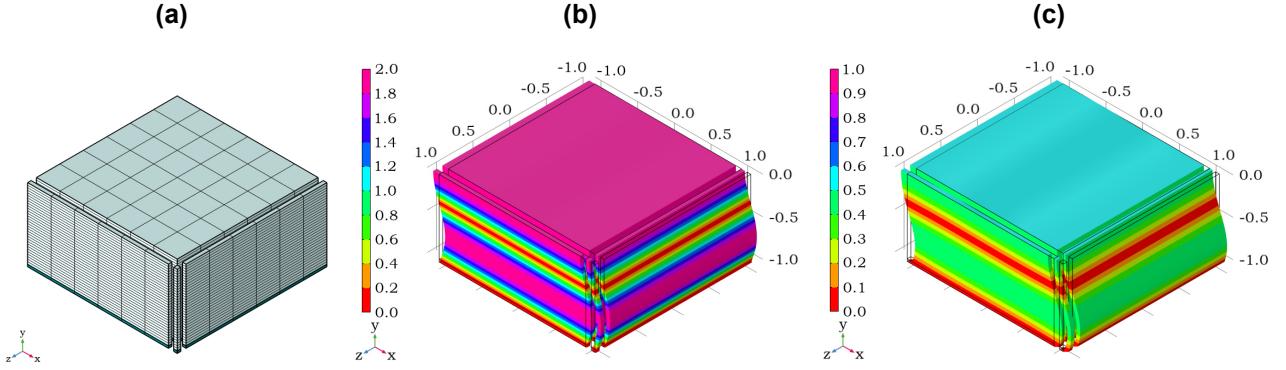


Figure 6. FEM model of a homogeneous linear viscoelastic layer lying on a linear elastic half-space (a) and displacement amplitude distribution for $\hat{\omega}_s = 1.5\pi$, $\zeta = 10^{-4}$ and $\alpha = 0.5$ (b) and $\alpha = 2.0$ (c).

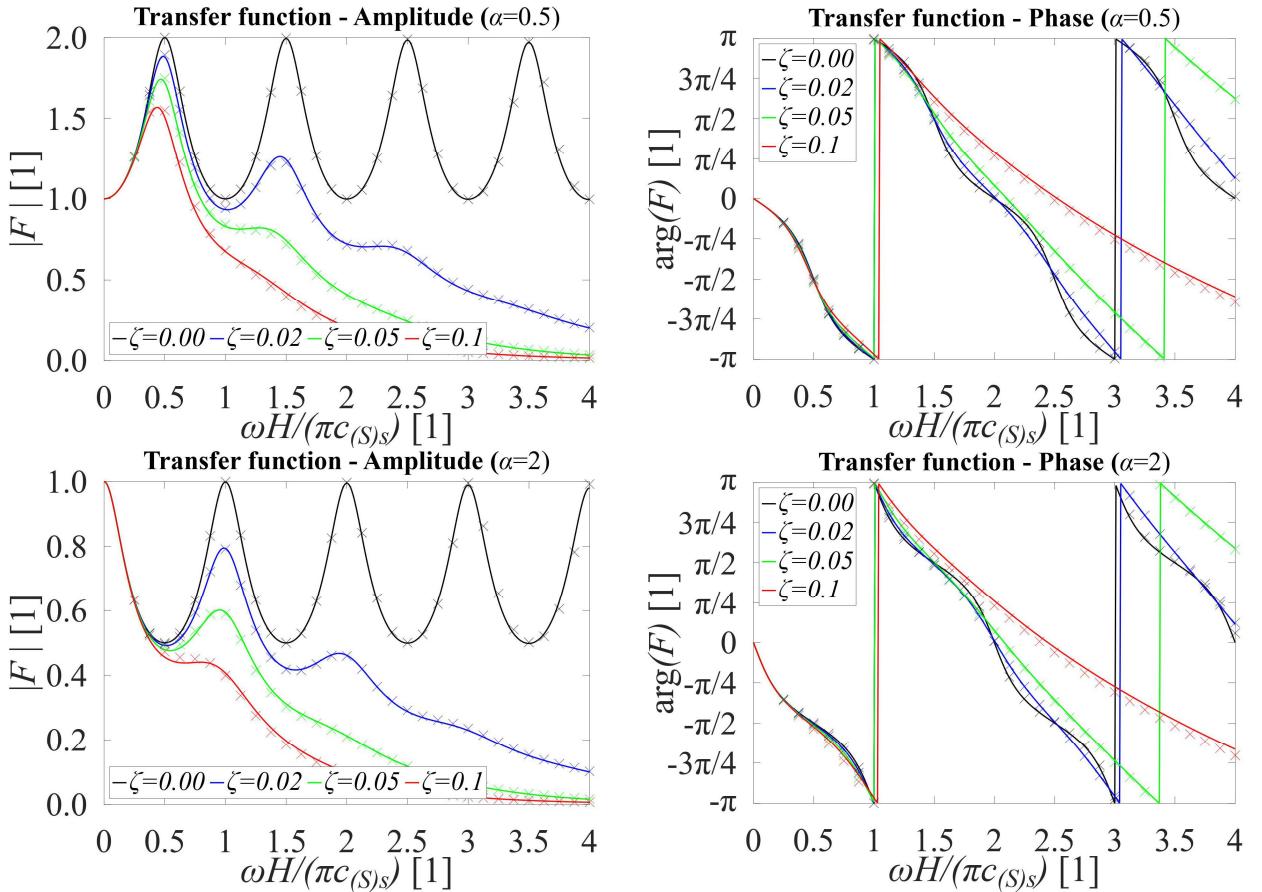


Figure 7. Amplitude and phase of transfer function of Eq. (20) and numerical results (marked by crosses) obtained by the FEM model of Figure 6a for various values of α , $\hat{\omega}_s$ and ζ .

Owing to the S-wave polarization of the seismic waves, a single FF layer only needs to be introduced for each vertical face of the interaction horizon. Moreover, since the opposite vertical faces of the artificial boundary share the same geometry, one FF layer is sufficient for modelling the FFB for each couple of opposite faces. As a result, a single vertical column is only required to reproduce the FFBs of both layers. Hence, by exploiting the symmetry of the interaction horizon and/or the directionality of the seismic input, the implementation of the DM may be much simplified as compared to the general case discussed in Section 3.

A parametric study has been carried out to validate the numerical outcomes for the following values of the characteristic parameters:

$$\alpha = \{0.5, 2\}, \quad \zeta = \{10^{-4}, 0.02, 0.05, 0.10\}, \quad 0.25\pi \leq \hat{\omega}_s \leq 4\pi; \quad (23)$$

encompassing about all practical circumstances encountered in site response analysis.

For each assigned set of parameters $\alpha, \zeta, \hat{\omega}_s$, the x -displacement amplitude and phase of the central node of the surface has been evaluated by performing a steady-state analysis in the frequency domain. Since the seismic input has unitary amplitude at the outcrop point, such x -displacement coincides with transfer function $F(\hat{\omega}_s^*, \alpha^*)$ in Eq. (20). The amplitude and phase of F versus $\hat{\omega}_s$ for various values of α and ζ are displayed in the sequence of graphs in Figure 7. The correspondence between the numerical results, drawn with crosses, and the analytical solution (continuous lines) is remarkable in the whole considered range of the characteristic parameters, thus demonstrating the excellent performances of the FFBs.

The effect of impedance ratio α in amplifying or deamplifying displacement amplitudes along the depth of the layer is depicted in Figure 6b and in Figure 6c, respectively.

4.2. Scattering of vertically propagating plane SH-waves by a semi-cylindrical canyon

Let consider a half-space having a semicylindrical indentation of radius a at its free surface. The half-space is assumed to be homogeneous, isotropic and linear elastic with shear wave velocity $c_{(S)b}$ and mass density ρ_b . The excitation of the half-space consists of vertically propagating harmonic plane SH-waves with circular frequency ω and particle motion in the z -direction with unitary amplitude at the surface.

The complex-valued transfer function of the system, i.e. the ratio between the free surface motion and the bedrock outcropping motion, as derived by Trifunac (1972), assumes this expression:

$$F(r, \theta, ka) = \begin{cases} J_0(ka) - \frac{-J_1(ka)H_0^{(2)}(ka)}{H_1^{(2)}(ka)} + 2 \sum_{n=1}^{\infty} (-1)^n \left(J_{2n}(ka) - \frac{kaJ_{2n+1}(ka) - 2nJ_{2n}(ka)}{kaH_{2n+1}^{(2)}(ka) - 2nH_{2n}^{(2)}(ka)} H_{2n}^{(2)}(ka) \right) \cos(2n\theta) & |\theta| < \frac{\pi}{2} \\ J_0(kr) - \frac{J_1(ka)H_0^{(2)}(kr)}{H_1^{(2)}(ka)} + 2 \sum_{n=1}^{\infty} J_{2n}(kr) - \frac{kaJ_{2n+1}(ka) - 2nJ_{2n}(ka)}{kaH_{2n+1}^{(2)}(ka) - 2nH_{2n}^{(2)}(ka)} H_{2n}^{(2)}(kr) & |\theta| = \frac{\pi}{2} \end{cases}; \quad (24)$$

where $k = \omega/c_{(S)}$ is the (angular) wave number, r e θ the coordinates of the cylindrical system centred at the canyon longitudinal axis, θ being zero along the negative y -axis and positive counter-clockwise, $J_p(\xi)$, $H_p^{(1)}(\xi)$ and $H_p^{(2)}(\xi)$ are the Bessel function of the first kind, the Hankel function of first kind and the Hankel function of second kind, respectively, with argument ξ and order p .

The above transfer function depends on the surface position (r, θ) and on the product

$$ka = \frac{\omega}{c_{(S)}} a = \pi \frac{2a}{\lambda} = \pi\xi; \quad (25)$$

expressing π times the ratio (ξ) between the canyon diameter ($2a$) and the incident SH-wavelengths (λ).

The transfer function of Eq. (24) has been numerically evaluated by applying the DM. The FEM model of the half-space with a semi-cylindrical canyon is shown in Figure 8a. The depth and the lateral extent of the mesh, assumed equal to $3a$ and $4a$, respectively, were selected by trial runs to minimize boundary reflection effects. The vertical FEM discretization of the layer comprises 36 elements to accurately approximate even the shortest wavelengths ($\xi = 2$). As for the benchmark problem discussed in the previous section, only two FF layers and a FF column are needed to appropriately enforce FFBs at all the lateral boundaries of the generalized structure.

The consistency of the numerical results has been again checked by performing a parametric analysis ($0.25\pi \leq \xi \leq 2\pi$). The computed values of the amplitude of $F(r, \theta, ka)$ are plotted along the x -axis in Figure 9. In the same figure the exact curves provided by Eq. (24) are also shown for comparison purposes. Since displacement amplitudes are symmetric with respect to the y -axis, amplification curves evaluated for $\xi \leq \pi$ are plotted only for $x \geq 0$; the remaining amplification curves ($\pi < \xi \leq 2\pi$) are plotted only for $x \leq 0$.

The numerical amplification curves satisfactorily match the target analytical ones within the whole considered range of ξ . Hence, FFBs prove to correctly work even for this more demanding benchmark problem. The spatial distribution of scattered displacement amplitudes within the half-space volume is illustrated in Figure 8b,c for two distinct values of ξ . These maps depict the increasing complexity of the scattered wave patterns as the frequency of the incident wave field increases.

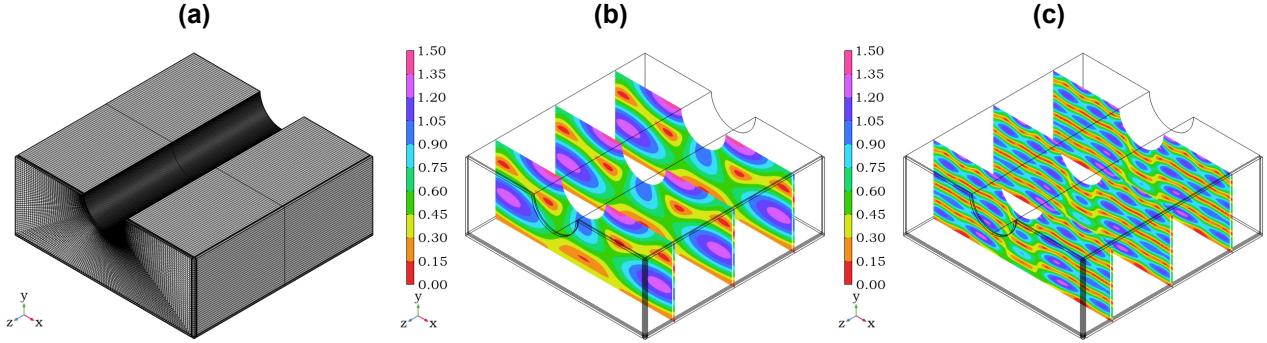


Figure 8. FEM model of a homogeneous linear elastic half-space with a semicylindrical canyon (a) and displacement amplitude distribution for $\xi = 0.25\pi$ (b) and $\xi = 0.75\pi$ (c).

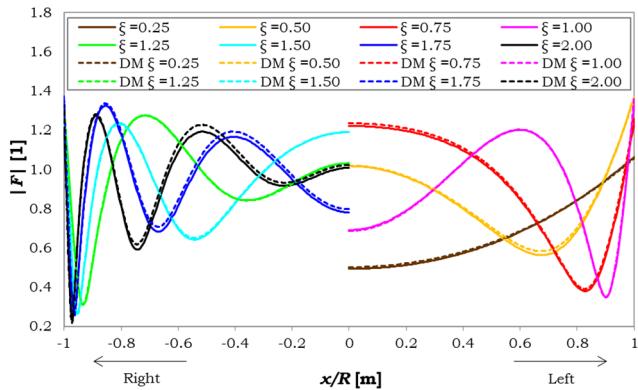


Figure 9. Transfer function amplitude of the points lying on the surface of the cylindrical canyon under vertically propagating harmonic plane SH waves for various values of $\xi = 2a/\lambda$.

5. Conclusions

In this paper, the general formulation of the DM and its implementation in COMSOL Multiphysics® commercial FEM software have been presented. The key steps needed to simulate a FFB, as required by the DM, in COMSOL Multiphysics® have been discussed in detail in Section 3. By the proposed methodology, any linear and nonlinear DSSI analysis of a dam-foundation system can be numerically solved by finite elements under the standard assumption of vertical propagation of the seismic waves from the bedrock towards the structure.

To verify the rigor of the proposed implementation of the DM, the calculated displacements have been compared against those provided by the analytical solutions of two benchmark problems. The numerical results have shown a perfect match with the analytical solution of both benchmark problems, confirming the robustness and accuracy of the present implementation of the DM. Hence, the present analysis demonstrates that rigorous DSSI analyses based on the DM can be correctly executed, even within modern commercial FEM codes, once the FFBs are correctly set up and handled. In particular, the present methodology constitutes a viable and effective tool to be used for the seismic assessment of dams, as testified by the considered examples and derived results.

Acknowledgements

The present Research & Development project on DSSI was partially supported by Enel Green Power S.r.l..

6. References

- Aydinoğlu M.N. (1993). Consistent formulation of direct and substructure methods in nonlinear soil-structure interaction, *Soil Dynamics & Earthquake Engineering*, 12(7): 403-410.
- Alves S.W., Hall J.F. (2006). Generation of spatially non-uniform ground motion for nonlinear analysis of a concrete arch dam, *Earthquake Engineering & Structural Dynamics*, 35(11): 1339-1357.
- Chopra A.K., Wang J.-T. (2010). Earthquake response of arch dams to spatially varying ground motion, *Earthquake Engineering & Structural Dynamics*, 39: 887-906.

- Chopra A.K. (2012). Earthquake Analysis of Arch Dams: Factors to Be Considered, *ASCE Journal of Structural Engineering*, 138: 205-214.
- Chopra A.K. (2020). *Earthquake Engineering for Concrete Dams - Analysis, Design, and Evaluation*, Hoboken, NJ (USA): John Wiley & Sons Ltd.
- COMSOL Multiphysics® (2023). Version 6.1, COMSOL AB, Stockholm, Sweden.
- Froio D., Eusebio M., Bariletti A., Previtali R., Rizzi E. (2019). Direct method for dynamic soil-structure interaction based on seismic inertia forces, *Proceedings of the XV ICOLD International Benchmark Workshop on Numerical Analysis of Dams*, Milan, Italy.
- Hall J.F. (1988). The dynamic and earthquake behaviour of concrete dams: review of experimental behaviour and observational evidence, *Soil Dynamics & Earthquake Engineering*, 7(2): 58-121.
- Jin A.-Y., Pan J.-W., Wang J.-T., Zhang C. (2019). Effect of foundation models on seismic response of arch dams, *Engineering Structures*, 188: 578-590.
- Koufoudi E., Chaljub E., Dufour F., Bard P.Y., Humbert N., Robbe E. (2018). Spatial variability of earthquake ground motions at the dam-foundation rock interface of Saint Guérin: experimental and numerical investigations, *Bulletin of Earthquake Engineering*, 16: 1751-1777.
- Kramer S.L. (1996), Geotechnical Earthquake Engineering, Upper Saddle River, NJ (USA): Prentice Hall.
- Løkke A., Chopra A.K. (2017). Direct finite element method for nonlinear analysis of semi-unbounded dam-water-foundation rock systems, *Earthquake Engineering & Structural Dynamics*, 46(8): 1267-1285.
- Løkke A., Chopra A.K. (2018). Direct finite element method for nonlinear earthquake analysis of 3-dimensional semi-unbounded dam-water-foundation rock systems, *Earthquake Engineering & Structural Dynamics*, 47(5): 1309-1328.
- Løkke A., Chopra A.K. (2019). Direct finite element method for nonlinear earthquake analysis of concrete dams: simplification, modelling, and practical applications, *Earthquake Engineering & Structural Dynamics*, 48(7): 812-842.
- Lysmer J., Kuhlemeyer R.L. (1969). Finite dynamic model for infinite media, *Journal of Engineering Mechanics Division (ASCE)*, 95(EM4): 859-877.
- Maeso O., Aznárez J.J., Dominguez J. (2002). Effects of space distribution of excitation on seismic response of arch dams, *ASCE Journal of Engineering Mechanics*, 128(7): 759-768.
- MatLab (2022) Version R2022b. Natick, Massachusetts.
- Sánchez-Sesma F.J. (1987). Site effects on strong ground motion, *Soil Dynamics & Earthquake Engineering*, 6(2): 124-132.
- Sotoudeh P., Ghaemian M., Mohammadnezhad H. (2019). Seismic analysis of reservoir-gravity dam massed layered foundation system due to vertically propagating earthquake, *Soil Dynamics & Earthquake Engineering*, 116: 174-184.
- Szczesiak T., Weber B., Bachmann H. (1999). Nonuniform earthquake input for arch dam foundation interaction, *Soil Dynamics and Earthquake Engineering*, 18(7): 487-493.
- Trifunac M.D. (1972). Scattering of plane SH waves by a semi-cylindrical canyon, *Earthquake Engineering & Structural Dynamics*, 1(3): 267-281.
- Varmazyari M., Sabbagh-Yazdi S.-R. (2021). Modification of direct-FE method for nonlinear seismic analysis of arch dam-reservoir-foundation system considering spatially varying ground motion, *Soil Dynamics & Earthquake Engineering*, 140: 106477.
- Wang J.-T., Chopra A.K. (2010). Linear analysis of concrete arch dams including dam-water-foundation rock interaction considering spatially varying ground motions, *Earthquake Engineering & Structural Dynamics*, 39(7): 731-750.
- Wolf J.P. (1985). Dynamic soil-structure-interaction, Englewood Cliffs, NJ (USA): Prentice Hall.
- Wolf J.P. (1988). Soil-structure-interaction analysis in time domain, Englewood Cliffs, NJ (USA): Prentice Hall.
- Zienkiewicz O.C., Bicanic N., Shen F.Q. (1989). Earthquake input definition and the transmitting boundary conditions, In: *Advances in Computational Nonlinear Mechanics*, Ed. Doltsinis I. St., 109-138, Vienna, Austria: Springer-Verlag Wien.

NONLINEAR SEISMIC RESPONSE OF CONCRETE DAMS

L. Furgani¹

Mott MacDonald, Genoa, Italy, luca.furgani@mottmac.com

Abstract: *The purpose of this paper is to provide a holistic overview of nonlinear analysis procedures for the seismic response of concrete dams. A review of recent works and typical case studies will be presented to explain the pros and cons of these methods. Different strategies will be discussed to deliver nonlinear outcomes and to meet the expectations of checkers, clients and authorities.*

1 Introduction

Nonlinear analyses are starting to be more and more common for most of the civil engineering problems. For some specific methods such as pushover analyses of buildings, there is clear guidance on procedures to follow while in cases such as the nonlinear procedures for dams details are left to the experience of engineers. Some authors have already attempted to use well-known building methods for dams (Andonov A., Iliev A. and Stoev K.S. (2013)). Truly convinced the development of these procedures is the direction to take for the seismic safety of dams, I have worked with other authors on nonlinear analyses of concrete dams (see references). Over the years I gathered some lessons learned worth sharing in this contribution to the 18th WCEE.

In the dams sector, considering the high risk associated with the outcomes of the nonlinear analyses there is a reasonable resistance against nonlinear procedures or more in general complex studies. This makes the application of new procedures even more challenging compared to other sectors. In the past ten years, I have been involved in large and complex multidisciplinary infrastructure projects and I can still recognize the unique condition of existing dams located in high seismicity regions.

It's worth noting that structural and geotechnical assessments for dams and appurtenant structures can be affected by several aspects including non-technical ones not limited to project budget. The most advanced technical solution may not be cost effective if stakeholders may disagree with the approach taken. At the same time, technical standards and local legislations are introducing new requirements to be met and some of them are particularly challenging for existing dams. In this scenario, engineers' only option is to look for holistic approaches. The decision of the assessment strategy is sometimes constrained by particular requests from the client and legislators, in other cases is up to the engineers to propose the right approach for the specific dam.

During my early studies on this topic, I applied 48 different methods for the seismic assessment of the same concrete gravity dam to appreciate the pain gain balance associated with this selection process. I have been able to evaluate the accuracy gained for each level of complexity added. Figure 1 gives an appreciation of the effects of the approach used for the seismic assessment of the 87m high concrete gravity dam case study. As shown in this example, the crest displacement varies based on the level of complexity considered. Despite the displacement may increase with an additional numerical effort some of the other key outputs may reduce and help with the fulfilment of the key requirements. This is the case of stress exceeding predefined limits defined for linear analyses reduced introducing the nonlinear behaviour of concrete and resulting typically in minor cracks.

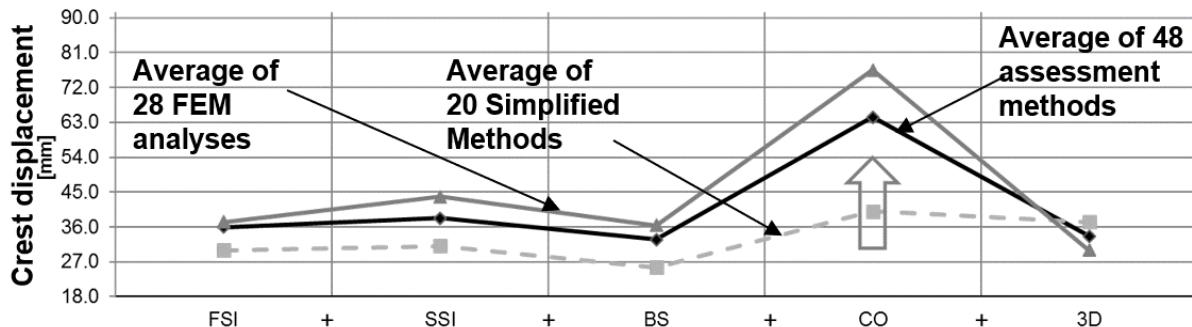


Figure 1 Effects of increasing level of complexity on the seismic response (crest displacement) of an 87m high gravity dam (FSI: Fluid Structure Interaction, SSI: Soil Structure Interaction, BS: Base Sliding, CO: Crack Opening, 3D: Three Dimensional Effects).

Even if engineers have a wide range of tools, there is still a certain reluctance for new assessment methods selection. The aforementioned potential rejection from authorities brings engineers back to simplified methods with additional assessment costs and more importantly, as a consequence of this simplified approach, the dam under assessment may fail safety criteria and some retrofitting actions, limit in operation or decommission will be required. In general terms, to balance between seismic safety, environmental impacts and cost-effective solutions, it is necessary to develop strategies to use these advanced methodologies more frequently for the dam's seismic design and assessments.

In the following sections nonlinear procedures will be introduced first followed by few examples and considerations on the outcomes.

2 Non Linear Procedures for Concrete Dams

2.1 General considerations

Before starting the dissemination of some of the methods available, it is worth saying that the real behaviour of a dam under seismic actions may be quite different from the results of a nonlinear numerical analysis. This is particularly true if we do not have any monitoring data to be used to calibrate our models. Worth noting that trying to model the behaviour of the dam for extreme events means trying to forecast something that did not happen during the entire life of this structure. Some authors are focused on the study of the dams' behaviour using monitoring data (refer to Robbe E., Humbert N. (2019)). These studies will be important to understand the effects produced by short return period events but they cannot replace the information provided by nonlinear analyses for Ultimate Limit State (ULS) return periods having the order of magnitude of thousand years.

It is also important to remember the importance of a step-by-step procedure as mentioned in several ICOLD guidelines. It is not recommended to start a nonlinear assessment without a full understanding of the existing or preliminary results gathered through linear or simplified analysis. For this reason, every nonlinear analysis should be supported by simplified approaches planned from the very beginning as part of the assessment procedure proposal.

Nonlinear features of the assessments imply an additional stage dealing with the characterization of the nonlinear properties of the materials. By experience, we can say that with the right selection of the parameters the numerical modeller can achieve the results he was looking for. For this reason, it is vital that the whole team behind the assessment understand fully the typical behaviour of concrete dams under seismic conditions before any numerical model is prepared. The development of nonlinear analyses should be an intensification of the numerical effort to extract the expected results and confirm if actions are required.

It is also suggested not to change the numerical model geometry and FE models along the assessment process, there should be a mesh strategy from the very beginning. If the concrete dam typology under study is an extreme or high consequence dam (refer to ICOLD Bulletin 148), it is highly probable that the nonlinear behaviour of the concrete or of the joints will be necessary along the assessment process. In this case, the mesh of the dam has to be prepared to receive the nonlinear joint features. One typical example is the location

of the vertical (block interfaces) and horizontal (foundation interfaces) joints in arch dams, the mesh should follow them and there should be a study to define the right way to model them.

To have an idea of the impact of parameters and method selection, it is suggested to refer to the benchmarks organised over the years by the ICOLD committee on “Computational Aspects of Dam Analysis and Design”. In several cases the topic analysed was the seismic response of concrete gravity and arch dams. Figure 2 and Figure 3 show the results of one of the few benchmarks considering the nonlinear response of concrete dams. The first figure indicates the different levels of complexity given to the participants, some of them mandatory. It is worth observing the number of different paths available. The second figure gives an idea of the variability expected when nonlinear dynamic analyses are performed even if the same model approach has been used. For more details refer to the 14th ICOLD Benchmark proceedings.

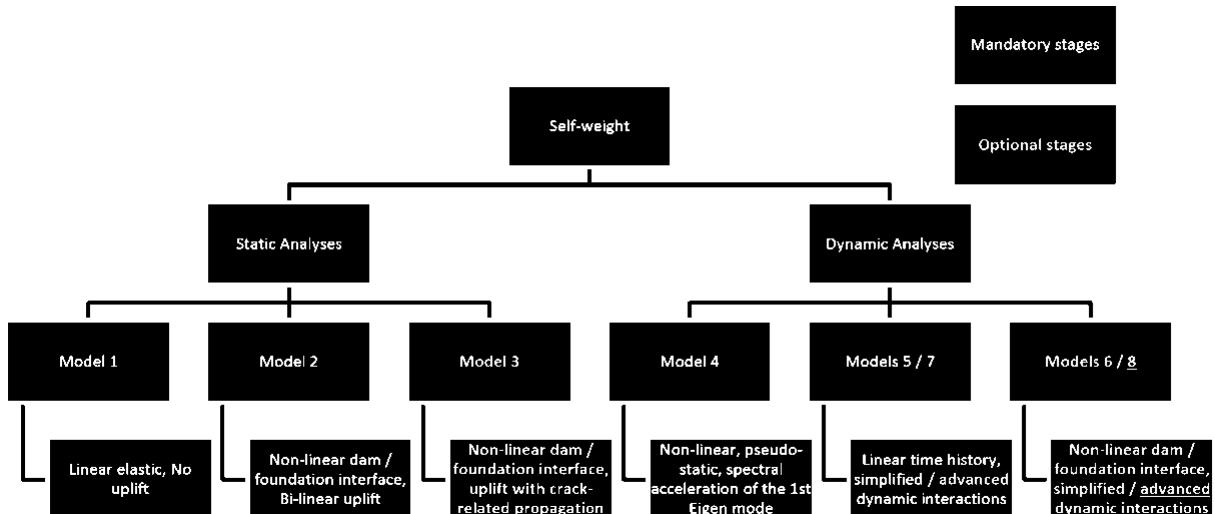


Figure 2 Progressing model complexity from 14th ICOLD Benchmark Theme B dealing with the seismic response of an arch gravity dam

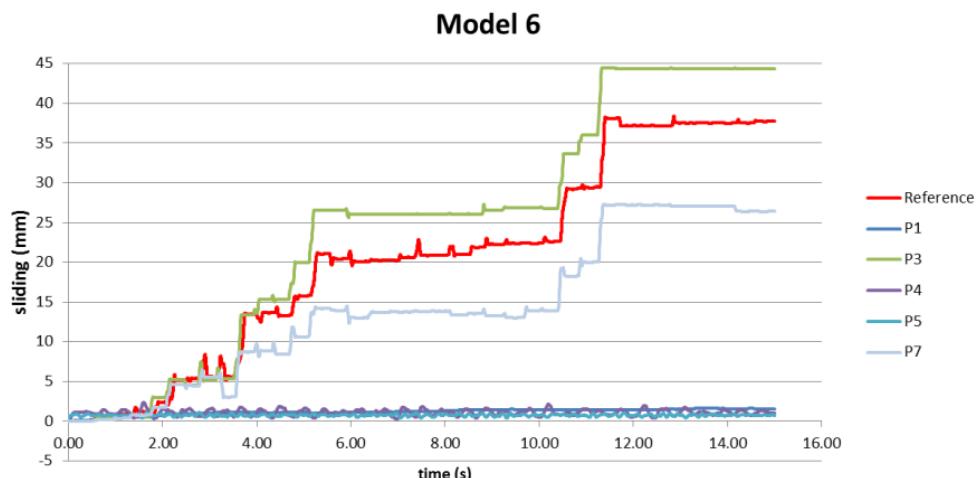


Figure 3 Sliding at the upstream toe of one of the blocks of the arch dam analysed by several participants (P1 to P7) during the 14th ICOLD Benchmark Theme B.

This example has been proposed to remark the importance of the overall strategy, this may include the calibration of the model with monitoring data, sensitivity analyses, comparisons with other technical papers where a similar dam has been analysed and so on. Using the above example, sliding of the arch dam block may happen or not happen based on the outcomes shown, it will be then difficult for stakeholders to make a decision.

Different will be the case where the assessment process is focused on a series of key parameters representing the behaviour of the dam, a process where the localised sliding is not critical for the overall response of the dam. Moving from the local difference between the analyses to the global response of the dams is the key change in the assessment process.

It is suggested to read the open-access publication Hariri-Ardebili, M. A. (2024) dealing with “Quantifying modeling uncertainties in seismic analysis of dams: Insights from an international benchmark study” where the uncertainties mentioned above have been treated statistically. For the development of these assessment procedures will be fundamental to introduce factors of safety based on the expected uncertainties embedded in these advanced processes.

2.2 Nonlinear joints

Contact elements in Finite Element Analysis (FEA) applications are fundamental components that simulate interactions between different parts of a structure. These elements play a crucial role in modelling scenarios where components may come into contact, separate, or slide against each other. There are several ways to model joints in the nonlinear field, some of them are listed below:

- Finite Element Modelling (FEM) such as node to node contact, tied interface, node to surface contact and surface to surface contact;
- Discrete Element Modelling (DEM) approaches or a combination of this approach with the FEM approach (FDEM);
- Simplified approaches based on rigid body dynamic equilibrium approaches (e.g. RS-DAM);
- Simplified methods using closed formulas (e.g. Chopra-Zhang 1991, Danay-Adeghe 1993).

For nonlinear analyses of concrete dams under seismic actions the FEM modelling is the most common and suggested approach. Within the FEM modelling, the selection of the algorithm used is typically constrained by the software, each developer provides their own selection with several parameters to be defined. In this paper, I do not intend to dive into the details of these tools, I just want to share some key aspects for modelling, analysing and assess the behaviour of such joints.

Before modelling the joints it is necessary to study the geometry of the dam in detail and look not only at the as-built drawings but also at the existing conditions. It may be possible to have the vertical and horizontal joints in different locations (as-built different from construction drawings). It is also possible that the dam developed joints on its own over time due to various reasons including but not limited to thermal actions and Alkali Aggregate Reaction (AAR) effects.

To capture the seismic response of concrete dams it is crucial to establish what's the effect of the joints on the behaviour of the dam. In some cases, it is possible to anticipate a mechanism of failure under seismic conditions just by looking at the joint geometry. One typical example coming to mind is those cases where the joint between the base of the concrete blocks and the foundation element (typically the bedrock or a pulvino) is too steep or flat. In this case, it will be necessary to pay extra attention to the assumed geometry and the parameters used to avoid some of the concrete blocks sliding in the upstream directions. This is typical for empty condition combinations and the numerical challenges may start even before the seismic loads are applied. Similar conditions can be experienced at the lateral abutments of arch dams. It is worth noting that the distribution of stresses on the joint under the self-weight it's not something trivial, that is the result of the pours stages during the construction of the dam, the following cycles of summer and winter conditions and more generally the loading history of the dam. Knowing that, it is necessary to find a compromise between real conditions and the assumed conditions at the joints before and during the seismic analysis.

A contentious topic on the nonlinear joint topic it's always the presence of water in these joints and their behaviour under seismic conditions. This is surely one of the current challenges and uncertainties in modelling dams in the nonlinear field. Despite the many enhancements expected in the future, it is suggested not to get into this extra level of complexity. It is preferred to use some conservative approaches on the water pressures within the joints and cracks.

Last but not least, it is important to consider the development of new joints during the earthquake. This means that the initial arrangement of the nonlinear joints should change during the analysis to capture the opening of

a new joint. Because it will be challenging to consider this ahead of results, it is suggested to evaluate it after the completion of the nonlinear analysis where the concrete nonlinearity is considered. In this case, the new block surrounded by horizontal cracks can be considered as one new isolated block shaken by a deconvoluted signal. It is also important to mention that the new joint may be important if the dam suffers aftershocks. If required, a new model of the entire dam with the new arrangement of the joints should be developed to assess the residual capacity of the dam against aftershocks.

Figure 4 shows some examples of how to model nonlinear joints for concrete gravity dams and arch dams. In the gravity dam it is interesting to consider the effect produced by the connection between the short and tall blocks, the three dimensional effect (Furgani L., Imperatore s., Nuti C. (2012)). The example provided for the arch dam shows the challenge behind the definition of the mesh. The purpose is to limit the number of mesh elements without compromising the quality of the results. This challenge has been resolved by some software where there are automatic mesh tools but this significantly impacts the numerical effort and time required to perform a nonlinear analysis in the time domain.

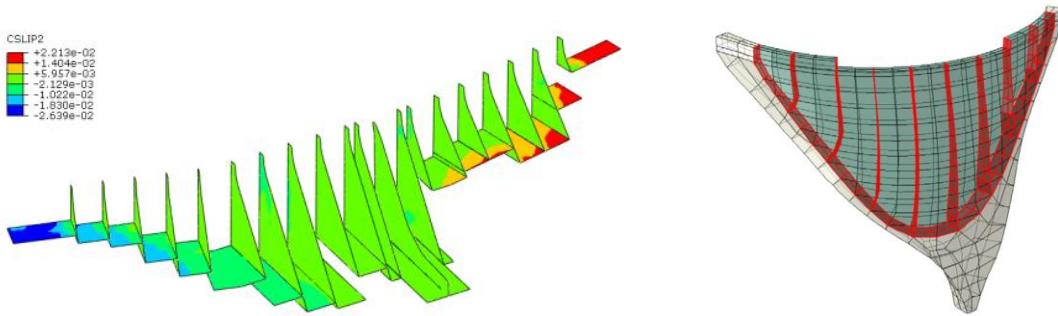


Figure 4 Example of joint modelling for a gravity and arch dam

2.3 Nonlinear material

The behaviour of the concrete is almost the same since the introduction of this material in the sector. Despite additives, aggregates types or small quantities of rebars these structures can be classified as massive concrete structures where the main parameters come from the matrix of the cement and the aggregates used. Concrete nonlinear behaviour can be distinguished by three levels of detail: micro (μm), meso (mm) and macro (m) levels. Considering the size of concrete dams, it is suggested to use a meso or macro level to approach the topic. It is important to consider the scale of such structures compared to the dimensions of damages such as cracks observed in other structures. It is not efficient to concentrate too much of our attention on the way minor damages are modelled. The risk is to make numerical analyses too long and difficult to manage.

The modeller and engineer's attention should be focused on the overall nonlinear behaviour represented by the way we expect the dam to behave when it is going beyond its elastic behaviour. For concrete gravity dams, we should be looking at the representation of damages in the upstream and downstream faces, potentially joining and forming a through crack.

For arch dams, one of the most common damages to look for is the cyclic exceedance of the tensile capacity on the downstream face of the blocks. This particular type of damage appears when the blocks behave as separated or partially separated cantilevers. A special behaviour is particularly expected from old dams, designed with outdated methods and not considering the latest loading requirements. If a dam present already some cracks it is necessary to study them before performing the seismic assessment and define a strategy on the way these will be considered.

In one of his lectures, Prof. Joško Ožbolt provides a comprehensive list of the constitutive frameworks for material models for continua such as concrete: elasticity theory, fracture mechanics, plasticity, damage mechanics, smeared crack models, microplane theory and a combination of the previous ones.

Following this overall introduction to the theme and models, let's focus on the methods available in the most common FE numerical model software. They can be distinguished between discrete crack models and

continuous crack models. The latter is suggested for the numerical effort required by the seismic response of dams.

Two of the most popular models are the smeared crack models such as rotating crack models (refer to Hariri-Ardebili M.A., Kolbadi S.M., Mahdi & Mirzabozorg (2013) for some applications) and the damage plasticity models by Lee and Fenves (1998) (refer to Furgani L., Meghella M. (2014) for an application).

Despite the differences in terms of formulation of strain, crack and damage variables, both models establish the level of damage and a measure of the plastic deformation of the structure. The damage plasticity model is giving two separate nonlinear outputs, the damage index and the plastic deformation while the smeared crack models main outcomes is the crack surface.

It is worth noting that some of these models have been developed for dams and tested against real dam case studies. This is an added value to bring more reliability on the particular model selected for the assessment.

The input parameters used by these concrete models may be different. Every input can be linked back to a few basic concepts such as the confinement aspect, the yielding point, the softening behaviour and the fracture energy. It will be important to understand the representative values to be used for the parameters above and then to set some ranges of these parameters to do some sensitivity studies. The acceptable range of parameters will be useful when the analyses will stop for convergence issues. Changing the parameters within the acceptance criteria will help complete the analyses and represent the expected behaviour. For the most critical case studies, it is suggested to calibrate these models using in-situ (non-destructive) or laboratory structural tests.

There is an additional topic to be considered: the damping assigned to the concrete for the numerical models. It is important to calibrate the damping in relation to the nonlinear behaviour we are already modelling to avoid double-counting the damping mechanisms of the structure. It is not excluded that in the future, the dam body damping parameter could be calibrated and used in linear analyses to resemble the nonlinear behaviour under seismic actions. This can be done then the nonlinear response of dams will be known better at least for the most typical shapes.

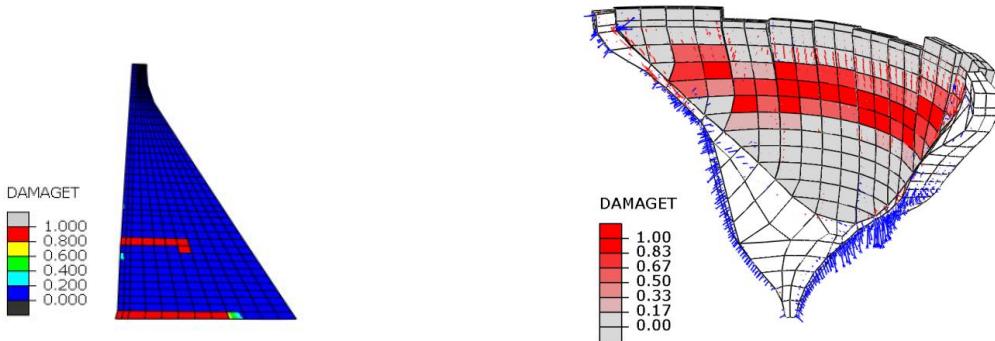


Figure 5 Typical damage patterns for gravity and arch dams

Figure 5 shows two examples of damage patterns obtained with the damage plasticity model. The gravity dam example shows the typical damage expected within the section. Even if it represents just a qualitative measure of the damage may show, as in this case that the dam did not develop a through crack following the cycle of loads applied during the analysis. For the arch dam, the example shows a typical behaviour for arch dams where the arch effect is lost for upstream phases of the seismic action. This mechanism changes the behaviour of the dam from an arch dam to a series of vertical blocks. As a consequence of this, damages are expected to the downstream in the upper portion of the dam. Both these examples have associated measures of plastic deformation but this has not been reported as the main goal of the analyses will be to establish global failure mechanisms rather than local plastic deformation or cracks.

2.4 Nonlinear procedures

Differently from the building sector where nonlinear static analysis procedure can be used to represent the behaviour of the structures exceeding their elastic behaviour, for concrete dams it is suggested to focus directly on nonlinear dynamic procedures. This means it will be necessary to select the seismic signals to be used.

Three main techniques for nonlinear analysis methods are discussed in this section: Time History Analyses (THA), Incremental Dynamic Analyses (IDA) and Endurance Time Analysis (ETA). These are different ways of defining signals used in the analyses, typically three components for each set considered.

It's worth having some general considerations on the THA analyses. Even if there are different techniques to resolve the equation of motion in the time domain, the most critical aspect for these analyses is the selection of the ground motion signals. In nonlinear analyses this is even more important, selecting a signal with few spikes over a certain threshold can significantly reduce the final damage level of the structure. For this reason, it is suggested to agree signals at the very beginning of the assessment, with awareness of the relation between the shape of the signal and the nonlinear behaviour of the dam.

The IDA is a technique to estimate the seismic capacity of dams using a large set of ground motions. The "as-recorded" (unscaled) ground motion time history is selected first. To consider both the stronger and weaker scenarios, this is scaled uniformly using a scale factor generating a certain set of signals. Several nonlinear analyses are then performed with the scaled ground motions. There are several ways to scale the original signal and more details that are not discussed in this paper. The key aspect to be considered is the pros and cons of this approach. On one side we are using scaled ground motion signals that are natural contributing to the reliability of the method, on the other hand, there is the numerical effort required to perform a large number of nonlinear dynamic analyses. For this reason, it is suggested to use this approach for numerical models not having a large number of nodes.

The ETA method is a dynamic pushover procedure used to estimate the seismic performance of structures when subjected to pre-designed intensifying excitation. The simulated acceleration functions are intended to shake the structure from a low excitation level (with a structural response in the elastic range) to a medium excitation level (where the structure experiences some nonlinearity) and ultimately to a high excitation level causing failure (see Figure 6). All these response ranges are experienced in a single time history analysis (see Figure 8 for an application example). The advantage of this method is the significant reduction of the numerical effort compared to the THA and the IDA. The key disadvantage of this method is the synthetic nature of the signal, no signal in nature intensifies regularly in time. Despite this, this method with the appropriate generation of these signals can be used to compare the nonlinear response of different dams without being affected by the signal selection subjectivity.

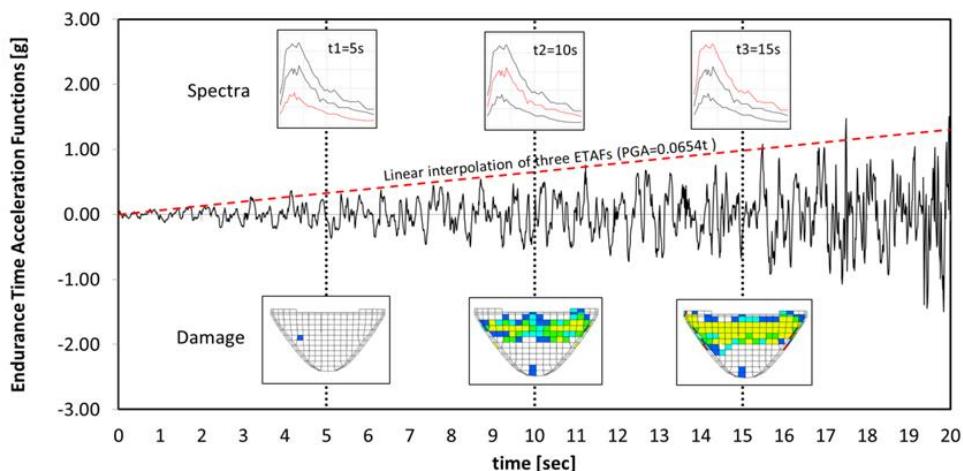


Figure 6 Endurance Time Analysis (ETA) typical function where seismic demand increases over time matching key spectra at different instants resulting in an increased level of damage.

Examples of IDA and ETA method analyses are provided in Furgani L., Hariri-Ardebili M. A., Meghella M., and Seyed-Kolbadi S.M. (2019) where the cloud analyses technique is also discussed.

Considering the main purpose of the nonlinear analyses, evaluate the behaviour of the dam toward collapse, it is reasonable to lose part of the real behaviour conditions. Signal selection is where the dam community can use a pragmatic approach to standardise the seismic assessment procedures. I like to mention that for very old case studies, dam scale tests have been developed using incremental static forces to evaluate the point of failure. This is not far from what we need to achieve today using new numerical tools and procedures. In this paper references there are several publications dealing with the ETA method theory and applications, one of the most effective procedure available at the moment.

3 Case studies and associated assessment or retrofitting strategies

In this section, we will reconsider what has been described before under a holistic approach describing typical cases and different seismic assessment approaches, including nonlinear ones. Dam owners have to guarantee the overall safety of these structures, not just against earthquakes. There are some other challenging requirements to be fulfilled over the lifespan of this strategic infrastructure such as water level control, hydropower production, and usual and extraordinary maintenance needs.

In many cases, dams are already affected by damages under static conditions. For this reason, it is crucial to understand at the very start of the seismic assessment the main requirement undermining the operation of the dam in the near future. If the dam is affected already by a static problem, it is suggested to focus efforts on this, the seismic assessment can be performed with simplified methods and some of the cost savings will be used for more field investigations. It's not reasonable to plan detailed nonlinear analyses about something affected already by other uncertainties. In this sense, it is important to adapt the seismic assessment strategy on the basis of the specific case. In some cases the seismic assessment process can be developed and delivered in stages in agreement with the authority. Simplified analyses are provided first with mitigations in places such as the temporary lowering of the water level. The other assessments will be delivered at a later stage and the operation limits removed if all checks pass.

There are dams where the geometry is very standard and the dam body can be assigned to a specific behaviour in terms of static and seismic response. In Furgani L., Hariri-Ardebili M. A. and Meghella M. (2019) a series of arch dam case studies have been used (see Figure 7 a) to evaluate the seismic capacity of arch dams and to show the typical differences between seismic responses. If the dam under assessment is very close to the case already analysed by other authors, it is worth considering it in the assessment process as a reference.

Considering the challenges introduced by nonlinear procedures, a dam with a simple shape is more suitable for complex nonlinear analyses. If the dam to be assessed has a bespoke shape and it is not easy to identify a typical seismic behaviour, it is suggested to carefully plan the implementation of nonlinear analyses. It is worth considering some retrofitting measures within the available solution to avoid complex studies, this is particularly relevant where the dam presents problems against non-seismic forces (see Figure 7b).

Worth mentioning that the seismic safety of dams is sometimes affected by other hazards such as rockfalls and landslides. It is suggested to read the contributions provided by Martin Wieland on the multi-hazard nature of the seismic response of dams and the typical behaviour of existing dams (Wieland M. (2010)). Even if this is not the main subject of this paper, this "priority of action" principle can be extended to appurtenant structures as well.



Figure 7 Typical concrete arch dams where dynamic nonlinear analyses can be used (a) and an unusual multi-arch dam where the level of complexity may limit their use (b)

If the main purpose of the assessment is to demonstrate the seismic safety of concrete dams, not the overall safety, it is possible to distinguish the real seismic behaviour of the dam from its intrinsic capacity to withstand cyclic actions produced by earthquakes. Its specific surrounding conditions such as the foundation properties will be considered but the history of the dam over the years or existing damages will be ignored to focus just on its intrinsic capacity. This approach is applicable for new projects of dams but also for existing dams if the dam's owner wants an appreciation of the capacity of the dam based on its shape without spending resources trying to understand the behaviour of the dam based on the existing conditions. This approach is particularly useful if the owner or the dams community needs to compare the seismic capacity of different dams, existing or new to better drive resource allocation or research studies. Examples of the derivation of capacity curves for dams are provided in the references.

Capacity curves or in general methods testing the dam for varying seismic level intensities are also suggested where based on seismological studies, it is not easy to define the target spectra or design ground motions. In this sense, the assessment is focused on the capacity and not on the demand.

4 Considerations on outcomes and stakeholders

Results given by numerical analyses on concrete dams especially if performed on large three dimensional models and in the nonlinear field may be difficult to manage for several reasons. Where these results are used to demonstrate the seismic safety of the dam, it is highly probable that stakeholders may feel disoriented and not happy to take a decision based on that. For this reason, the procedure used for the nonlinear analyses, the backbone of the assessment, must be considered reliable by all parties involved. In this section key outcomes of nonlinear analyses will be introduced with the aim to give the decision makers an overview of the state of safety of the dam under seismic conditions.

For linear analyses the aforementioned problems are not so difficult to solve and there are some criteria to evaluate if the linear response of the dam is fulfilling or not the design or assessment requirements. In most of the cases this is done limiting stresses on a certain proportion of the dam (refer to Ghanaat method used in the USACE codes). For nonlinear analyses, typically used when these linear criteria are exceeded, engineers are to assign limiting values for damages and plastic deformations. Unfortunately these limits have not been defined yet and engineering judgment have to be used. This introduce a certain subjectivity into the assessment process. For this reason, until such criteria will be defined by each country or internationally, it is crucial to associate damages to a failure mechanism and give the measure of how far the dam is from this failure mechanism. Acting mainly as unreinforced structures, dams' failure mechanisms are typically associated to the isolation of a concrete block. For arch dam this condition indicate a loss or reduction of the arch effect while for a gravity dam can be associated to the reduction of the friction from peak to residual.

The narrative along the entire assessment should be focused on these overall mechanisms and the results will be used to evaluate the factor of safety. This approach compared to the use of acceptance criteria (limiting values for damages of a single element or group of elements) suit better for dams, especially for those cases where there is a characteristic behaviour of the dam due to existing conditions or problems. Similarly to the approach used for masonry buildings, the dam's community should start developing a list of failure mechanisms for concrete dams under seismic conditions. Even if some of them have not been observed historically they will be useful to define some overall assessment criteria for engineers and stakeholders. The final outcome in such assessment will be how close the dam will be from the activation of the failure mechanism that will produce an uncontrolled release of water.

An interesting approach presented in one of the paper I prepared in the past is the development of capacity curves (see Figure 8), a simple chart showing the displacement of key points (typically the crest of the blocks) in the horizontal axis and the seismic force in the vertical axis. In this case the judgement of the response is similar to the criteria used for concrete buildings within the so called pushover analyses method. The capacity curves have the advantage of giving a clear answer to the question: what's the seismic force producing the collapse of the dam? It is important to mention that the collapse indicated by the analyses is most of the time a numerical failure, an interruption of the analysis for convergence issues. This interruption can be associated to the failure mechanisms discussed before.

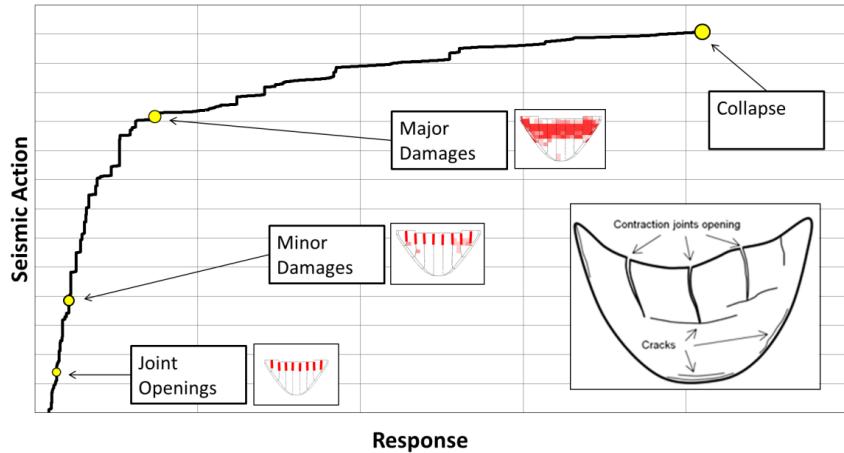


Figure 8 Example of the development of a failure mechanism in an arch dam using a capacity curve obtained with the ETA method.

It is worth mentioning that the numerical effort to achieve a capacity curve is not too different from other procedures if methods such as the ETA method is used. This is not true if we need to perform many nonlinear dynamic analyses. Based on this, it is important to know stakeholders' preferences on assessing the level of safety of the dam. In some cases, national standards leave the decision on the procedure to the engineers and this is producing a variety of approaches that are difficult to reconcile in terms of acceptance principles and final decision making.

Based on my experience on other heavy civil sectors, I think it's worth mentioning an additional measure to control uncertainties affecting the safety assessments of dams. This is called "independent checking procedure" and is the assessment done by a separate engineering company called checking team that perform a separate assessment using the same input parameters. These parameters have to be agreed at the beginning of the checking procedure. At the end of the first assessments, results will be compared, comments raised by the checkers and responded by the design team. If this checking strategy is used, the final stakeholders such as authorities or dam owners have just to take decisions based on an agreed outcome. Once all the parties are in agreement, certificates are produced by the design team and the checker team indicating the agreed conclusions and the potential actions required. Worth mentioning that in most of the cases, the checking team will use different and more simplified procedures. This means the design team has to justify all checks that appear to fail in the checking team analyses. This is the opportunity for the checker to establish if the level of complexity added by the original designer is acceptable or not.

Even in this checking procedure proposal there is a hidden and important consideration dealing with risk management. It is obvious that the simplest decision is to dismiss the dam at the first sign of local failure but this extremely pragmatic approach is not acceptable. Similarly to the decision making process required for the construction of dams, a similar or higher effort is required to maintain the use of it. Large construction works for the seismic retrofitting of the dam may impact severely on the environment and they are not aligned with the goal agreed worldwide to face climate changes. Similarly, lowering levels may impact on the flood scenario management of the area, linked as well with the climate change effects. In this scenario the use and, more importantly, the acceptance of advanced analyses that justify the seismic safety of dams should be ranked as first option.

In Hariri-Ardebili M.A. and Saouma V.E. (2015) there is a comprehensive definition of failure modes for concrete gravity dams and methods to deal with outcomes from nonlinear analysis methods. Similarly in Hariri-Ardebili M.A. , Furgani L., Meghella M. and Saouma V.E. (2016) a new class of seismic damage and performance indices for arch dams have been provided. It is suggested to refer to these contributions to understand in detail how outcomes can be used in the assessment process. There are already technical references providing all the tools required for the definition of standardised procedures, the missing step is to put all of them together to agree with those institutions taking care of the dam safety.

Despite this is not a simple task, I am sure the seismic engineering and dam communities will work together to achieve this goal and produce new guidelines for those engineers and dam owners who are convinced that nonlinear analyses are the most efficient tool to guarantee the dam's safety without impacting negatively on the environment and our lives.

5 Conclusions

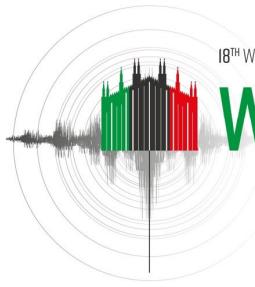
An overview of nonlinear analysis procedures has been provided to explain some of the most important aspects underlying the use of these methods. Some key stages during the assessment process have been pointed out with personal suggestions. One of the key messages is to carefully plan the overall assessment strategy based on the specific condition of the dam and in agreement with all the stakeholders.

As shown using a few examples, modelling choices are so many that results may be highly dependent on the approach used by engineers. It's the author's opinion that we need to move towards procedures that standardise the ground motion signals used for the analyses and focus on tools such as capacity curves to check factors of safety against global failure mechanisms rather than localised damages.

Despite the advancements in our numerical capabilities, nonlinear analysis assessment procedures are still lacking in acceptance criteria. With standard procedures including signals, failure mechanisms and criteria, it will be easier to establish the seismic safety of the dams and to compare them. This will help drive important decisions and fulfil the wider society's goals.

6 References

- Andonov A., Iliev A. and Stoev K.S. (2013). "Towards Displacement-Based Seismic Assessment of Concrete Dams Using Nonlinear Static and Dynamic Procedures", Structural Engineering International.
- Furgani L., Imperatore S., Nuti C. (2012). "Seismic assessment methods for concrete gravity dams". 15th World Conference of Earthquake Engineering, Lisboa.
- Furgani L., Hariri-Ardebili M.A. and Meghella M. (2019). "Towards the seismic capacity assessment of concrete dams", EWG Dams & Earthquakes International Symposium, Lisbon.
- Furgani L., Hariri-Ardebili M.A., Meghella M., and Seyed-Kolbadi S.M. (2019). "On the Dynamic Capacity of Concrete Dams" Infrastructures 4, no. 3: 57.
- Furgani L., Meghella M. (2014). Application of Endurance Time Analysis Method to the Non Linear Seismic Analysis of dams: Potentialities and Limitations, 82nd ICOLD Annual Meeting proceedings.
- Hariri-Ardebili M.A. (2024). "Quantifying modeling uncertainties in seismic analysis of dams: Insights from an international benchmark study". Earthquake Engineering & Structural Dynamics, 53(3), 1168-1194.
- Hariri-Ardebili M.A. , Furgani L., Meghella M. and Saouma V.E. (2016). "A new class of seismic damage and performance indices for arch dams via ETA method", Engineering Structures, Volume 110, Pages 145-160.
- Hariri-Ardebili M.A. and Saouma V.E. (2015). "Quantitative failure metric for gravity dams", Earthquake Engineering & Structural Dynamics, 44(3), 461-480.
- Hariri-Ardebili M.A., Kolbadi S.M., Mahdi & Mirzabozorg (2013). A smeared crack model for seismic failure analysis of concrete gravity dams considering fracture energy effects. Structural engineering & mechanics. 48. 17-39.
- Hariri-Ardebili M.A., Saouma V.E. and Porter K.A. (2016). "Quantification of seismic potential failure modes in concrete dams", Earthquake Engineering & Structural Dynamics, 45(6), 979-997.
- Meghella M., Furgani L., (2015). "Endurance Time Analysis for the Seismic Vulnerability of Arch Dams", 13th International Benchmark on the Numerical Analysis of Dams 9-11 , pp. 251-258, Lausanne.
- Robbe E., Humbert N. (2019). "DamQuake: More than just a database, a powerful tool to analyze and compare earthquake records on dams", Sustainable and Safe Dams Around the World (1st Edition).
- Wieland M. (2010). Features of seismic hazard in large dam projects and strong motion monitoring of large dams. Frontiers of Architecture and Civil Engineering in China. 4. 56-64.



A VALIDATION FRAMEWORK FOR LINEAR AND NONLINEAR DAM SAFETY ANALYSIS TECHNIQUES

Y. Ghanaat¹, Z. Harper¹ & Z. Han¹

¹ Quest Structures, Orinda, USA, yghanaa@QuestStructures.com

Abstract: Design and safety evaluation of dams are critical tasks that rely heavily on numerical computer analyses to model the dam's behavior under different loading conditions. The accuracy of these computer analyses is highly dependent on the assumptions built into the numerical models and the degree to which in-situ material properties, geologic conditions, and site topography are incorporated. Any inaccuracies or oversights in these areas can significantly impact the results, affecting the dam's overall design and safety evaluation.

A well-defined and thoroughly evaluated numerical model is essential to ensure accurate and reliable design and evaluation of dams. Engineers and analysts must understand these models' assumptions, limitations, and applications to use them effectively. Additionally, using measured dam responses and representative dam and foundation conditions can produce more realistic and reliable results, instilling confidence in the design and evaluation process.

The paper presents a comprehensive framework for validating a linear model of a 196-m-high arch dam. The validation process involves calibrating the dam's responses to different measurements, including static dam monitoring, ambient vibration, and seismic responses recorded during an earthquake. Once the linear model is validated, it is converted into a nonlinear model to investigate potential failure modes under static and maximum credible earthquake (MCE) loading. The nonlinear model considers primary nonlinear mechanisms such as contraction joint opening, foundation contact and lift joints cracking, and sliding along cracked sections that may occur in a concrete dam during the MCE. The nonlinear elements representing these mechanisms are thoroughly tested in separate validation studies to ensure their proper application and intended response behavior. The developed model is also used to assess the global post-earthquake stability of the dam using a three-dimensional shear strength reduction method.

The presented instrument monitoring and field-testing framework provides a reliable approach to validate linear models and develop nonlinear models that enable more accurate analysis of potential failure modes and post-earthquake stability. Thus, enhancing the accuracy of assessing dam safety and design ensures the safety and well-being of those relying on the dam for various purposes.

1 Introduction

Dam design and evaluation are critical tasks, necessitating an accurate approach founded on advanced numerical computer analyses. Dam safety assessment is paramount among these tasks, requiring a thorough evaluation of potential failure modes (PFMs). Such was the case with the New Bullards Bar Dam, where a

comprehensive dam safety evaluation was undertaken (Quest, 2021). Central to this evaluation was using numerical analysis to assess the credibility of identified PFM.

A robust validation framework was developed to leverage existing data from dam safety surveillance monitoring (DSSM) and strong motion arrays (SMAs) to enhance the reliability of this analysis. This framework served a dual purpose: not only did it facilitate the validation of the numerical model, but it also instilled confidence in the results obtained. The process was tailored to encompass three key aspects: validation of static responses, validation of modal properties of the dam, and validation of recorded dam responses to an earthquake event.

The study proceeded with the validated numerical model, subjecting the dam to analysis under extreme conditions, such as the MCE and post-earthquake scenarios. This in-depth analysis was paramount in appraising dam safety and the credibility of PFM. This paper elucidates a systematic approach, outlining the steps to ensure the dam's safety and structural integrity in the face of various challenges and seismic events.

2 Project Description

2.1 Dam

The New Bullards Bar Dam, built in 1970 on the North Yuba River, is the tallest arch dam in the US, located 35 miles northeast of Marysville, California. This 645-foot-high double-curvature arch structure stands tall on Smartville ophiolite bedrock. It features twenty-four 80-foot-wide cantilever monoliths separated by contraction joints. The dam's crest is at an elevation of 1,965 feet and spans 2,323 feet, including the spillway and thrust blocks (Figure 1).

The arch structure securely abuts against gravity thrust blocks, rising 165 feet high on the left and 145 feet tall on the right abutment. A chute-type spillway with three 30-foot-wide, 53-foot-high radial gates is situated on the left abutment. Furthermore, the dam accommodates a two-lane county road and features parapet walls along its crest edges.

2.2 Instrumentation

The New Bullards Bar Dam has diverse instruments for comprehensive safety monitoring (YCWA, 2019). Electrical resistance thermometers assess internal and surface temperatures, crucial for understanding thermal impacts. Pore pressure pipe gauges below the dam gauge uplift pressures exerted on the dam. Four plumblines track deflections at central and abutment monoliths, while triangulation methods measure total displacements at the crest and lower levels. Multi-point extensometers monitor movements at and below the dam-foundation interface, and crack meters are deployed to observe crack openings.

Furthermore, the dam includes strategically positioned strong motion accelerometers at the crest, base, and left abutment. These accelerometers detect seismic activity in real-time, providing crucial data on the dam's dynamic response. This integrated system of instruments forms a robust monitoring framework, ensuring the New Bullards Bar Dam's safety and structural stability.

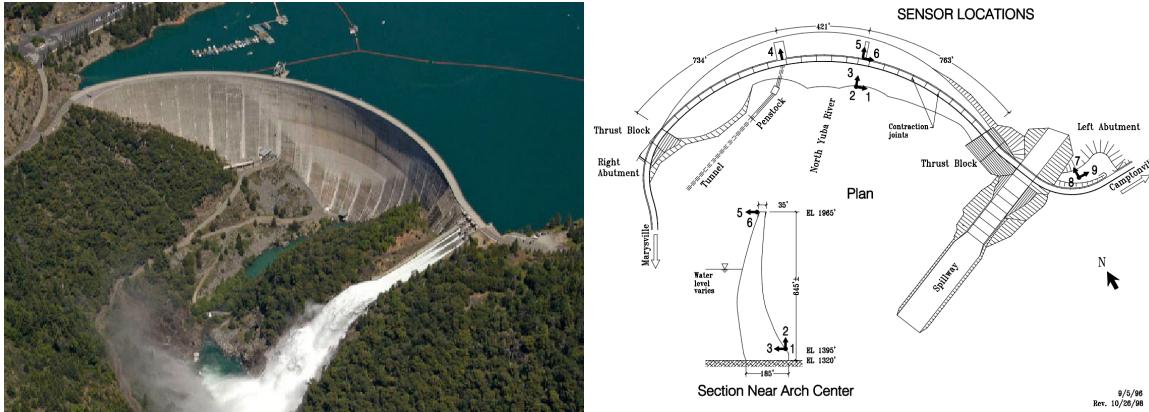


Figure 1. Downstream view of dam and spillway. Figure 2. Location of strong motion accelerometers.

3 Finite Element Model

The linear and nonlinear finite-element model of New Bullards Bar Dam (Figure 3) was developed and analysed using the LS-DYNA software program. The dam structure was modelled to include all 24 arch monoliths (numbered 1-24), three right thrust blocks, two left thrust blocks, and the spillway structure on the left abutment, all represented by solid elements. Nonlinear contact surfaces were incorporated for modelling contraction joints, which is crucial for the final dam safety analyses. However, during intermediate validation steps, it was determined that an entirely linear model without discontinuities was adequate. The contact surfaces were removed in such cases, and the monoliths were connected using tied constraints or nodal merging techniques.

Since each arch and thrust block monolith was modelled as separate structural units, interactions between these monoliths and the foundation were mediated by nonlinear contact surfaces placed between them. Figure 4 illustrates the use of gap-friction contact surfaces for modelling all contraction joints and tiebreak contact surfaces, allowing for cracking behavior and sliding across a selected lift joint and beneath the arch and thrust blocks.

The foundation model incorporated the downstream rock surface topography, measured by a ground-based LiDAR survey of the site, and accounted for passive resistance offered by these features. The foundation model included flexibility, inertia, and damping effects and utilized non-reflecting boundaries and traction time histories at the bottom and sides to simulate seismic input.

The impounded water was explicitly modelled using fluid elements and included a non-reflecting boundary at its upstream section to consider radiation damping and absorption of outgoing pressure waves.

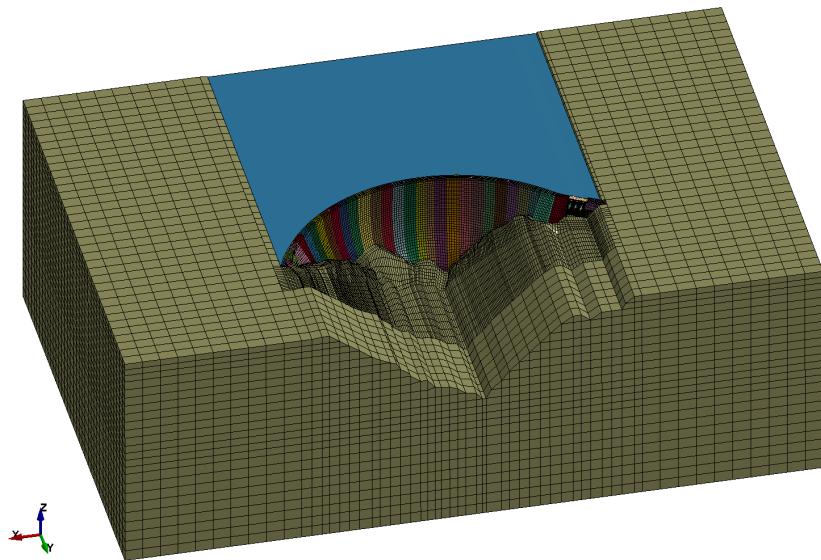


Figure 3. Finite element model with impounded water foundation block.

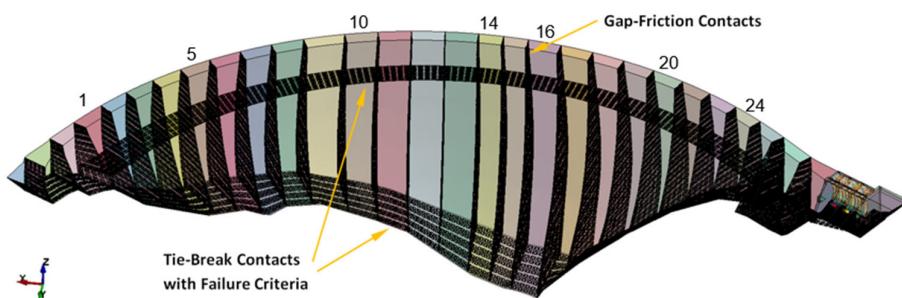


Figure 4. Contact surfaces used to model contraction joints, lift joints, and dam-foundation interface.

4 Validation Framework

4.1 Validation for Static Loads

Aggregated measurements of water pool elevations, concrete temperatures, and uplift pressures beneath selected monoliths provided sufficient detail to reconstruct a reasonable approximation of the overall static operating loads on the dam for four quarterly dates. Electrical resistance thermometers installed in Block 16 provided concrete temperature readings near the faces and interior of the dam, with readings of each thermometer made quarterly. These readings showed the highest average temperature in October and the lowest in April on the downstream face of Block 16. Measured temperatures were applied as nodal temperature boundary conditions to obtain nodal temperatures at all finite-element nodes by running a 2D steady-state thermal analysis. This was then mapped to the other dam blocks for the entire dam. Measurements from pressure pipe gauges installed at various locations in the dam gallery were used to develop uplift pressure distributions under eight blocks. A simple bilinear uplift pressure distribution with an average 58% drain efficiency was assumed for the remaining 16 dam blocks.

Deflections of the dam on specific dates were determined through plumbline observations and triangulation surveys. This data was crucial for validating the static response characteristics of the NBB finite element model. The observed static loads were applied to the model, and the resulting deflections were compared with actual measured values. Four plumblines in Blocks 8, 14, 16, and 18 monitored dam deflections relative to the lowest points. Additionally, triangulation surveys at 13 targets mounted on the dam's downstream face provided the overall deflection of the combined dam and foundation. Initial plumbline readings and triangulation survey data were unavailable, so a reference point was established at a later time using accessible data. Relative deflections were then calculated with respect to this reference point. January 1981 was chosen as the reference point. Plumbline data recorded in April, June, and October 2019 and triangulation surveys from October 2018 were used for correlation. The water level and temperature readings varied for each of these dates, enhancing the robustness of the correlation analysis.

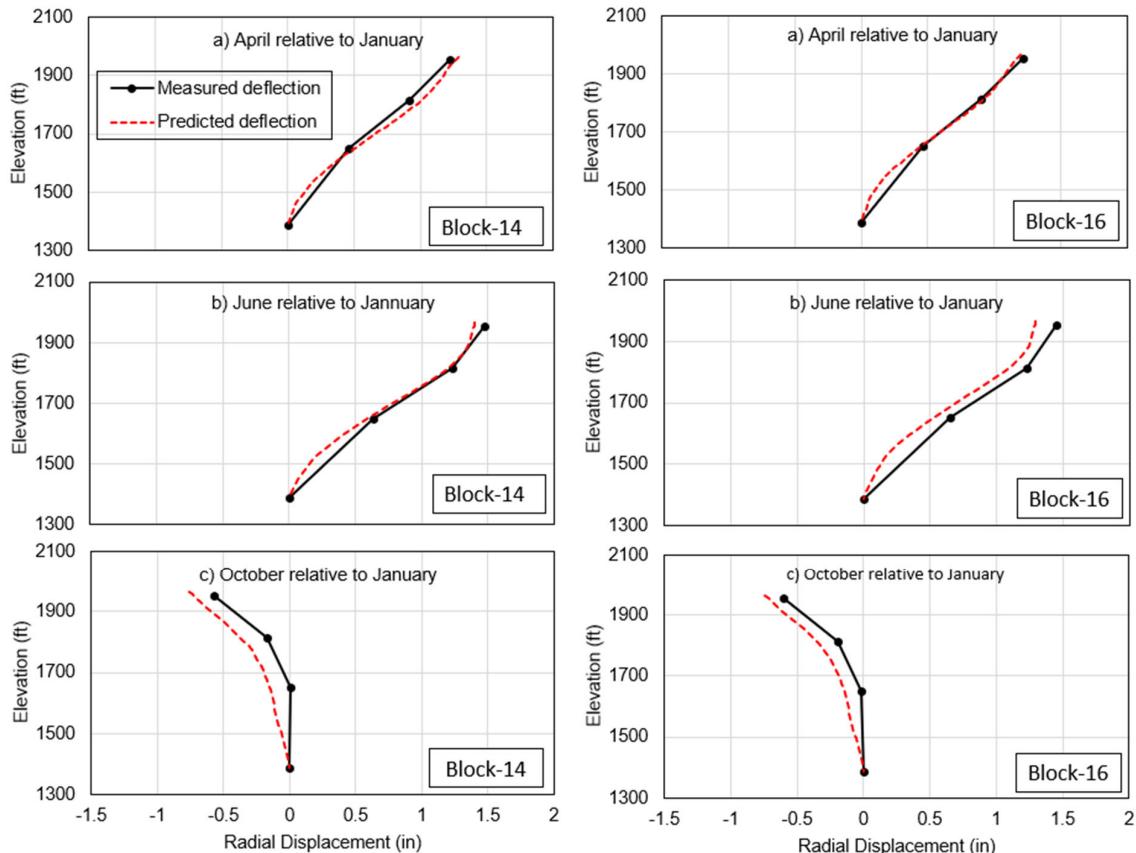


Figure 5. Comparison of measured and predicted plumbline relative deflections.

In addition to applying usual static loads based on water level and temperature measurements, another critical correlation parameter involved using the sustained modulus of concrete and a representative deformation modulus of the foundation rock instead of elastic moduli. Figure 5 displays the predicted and measured plumbline radial deflections for April, June, and October relative to January radial deflections. The results demonstrate an excellent agreement between measured and predicted deflections for all three dates, with minimal differences. Figure 6 compares predicted displacements along two horizontal sections at El. 1950 ft and El. 1815, showing excellent agreement with measured triangulation displacements. Following this successful validation of the model for static loads, the study shifted to validating the dynamic characteristics of the model, as discussed next.

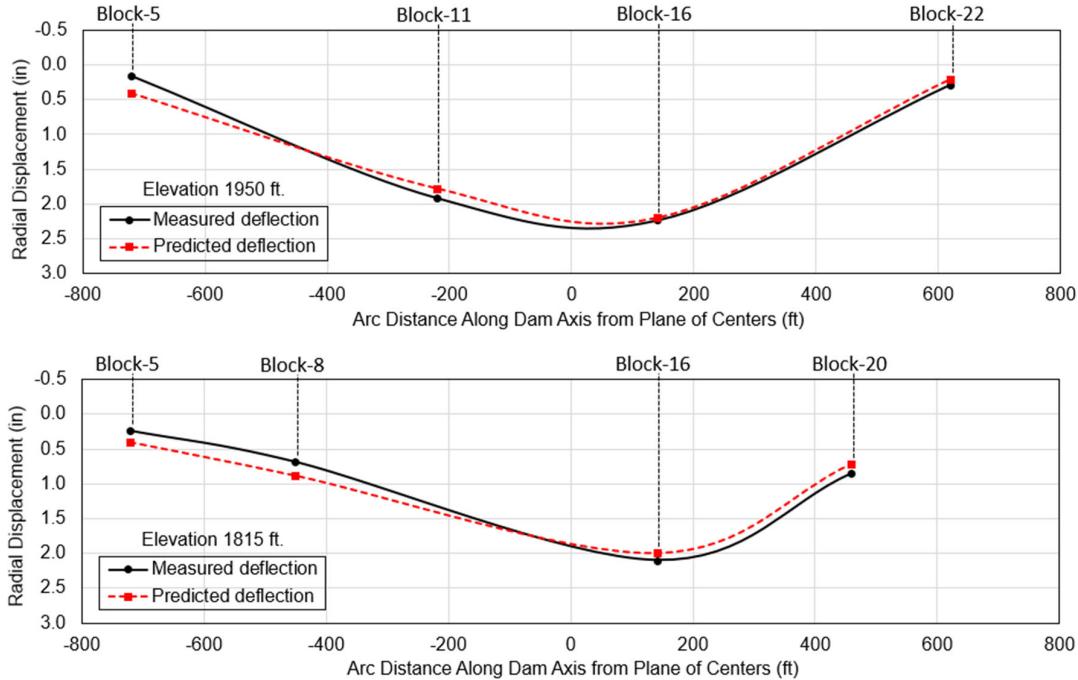


Figure 6. Comparison of measured triangulation and predicted displacements.

4.2 Validation for Dynamic Characteristics

4.2.1 Ambient Vibration Measurements

Ambient vibration measurements were conducted at New Bullards Bar Dam between June 30 and July 2, 2020, to passively record micro-tremors using seismographic sensors (GEOVision, 2019). The measurements aimed to identify mode shapes and frequencies to characterize the dam's dynamic response. Eight one-directional Kinematics SS-1 seismometers were used, connected to synchronized data loggers. The sensors were placed at 12 locations on the dam crest and other areas, recording data simultaneously with a sampling rate of 200 Hz. The most extensive data was collected at Station D (Block 9), where a reference seismometer operated continuously throughout the testing period. Station F at Block 14 also recorded significant data during daytime sessions, while other stations were instrumented selectively for shorter periods of 1 to 4 hours. This measurement approach, called Operational Modal Analysis, helped allow long data records without disrupting the dam's regular operation.

4.2.2 Spectral Analysis of Ambient Vibration Data

Identifying dam resonance frequencies involves analysing peaks in the Power Spectral Density (PSD) of the measured time series data within the specific frequency range of interest (approximately 1-5 Hz for this dam). However, directly computing PSD using the Fast Fourier Transform (FFT) coefficients, known as *periodogram*, is often ineffective. This approach tends to compound minor measurement errors and irregularities, leading to a periodogram curve obscured by high-frequency noise, as shown in Figure 7. This challenge has been extensively studied, resulting in various techniques designed to address these issues, as documented in the literature.

Initially, Welch's Method, a more advanced spectral analysis technique, was applied to one hour of velocity time series collected at three stations, identifying six primary dam resonances at 1.9, 2.1, 2.7, 3.3, 3.9, and 4.7 Hz. Following this, additional spectral analyses were conducted to further reduce noise beyond the capabilities of Welch's Method. These methods included Barlett's Method and the Yule-Walker MEM Method. The primary objective of these advanced techniques is to discern the spectral characteristics of the underlying processes that generate the time series by minimizing noise interference. Many of these methods make no assumptions about the underlying process and focus on noise reduction through various forms of averaging. Barlett's Method is particularly effective for very long signals. At the same time, the Yule-Walker MEM Method is a parametric spectral technique assuming the time series is generated by an underlying parametric mathematical model inclusive of a noise term. Estimating the spectrum then involves determining the model parameters best fitting the time series. This method is especially valuable for analysing signals dominated by sharp peaks in their power spectra, making it ideal for studying dynamic structural systems vibrating at discrete natural frequencies.

Figure 8 compares a Yule-Walker MEM analysis of just 1-hour signal from Station F (Block 14) to the averaged periodogram of Station F computed with Barlett's Method. The MEM method effectively identifies primary resonance frequencies and generates a much cleaner PSD curve, all with significantly less data. It is worth noting that because the MEM method analysed a smaller dataset, the y-values of the PSD curve are lower in magnitude.

Figure 9 displays PSD estimates based on 1 hour of data recorded simultaneously at Stations C, D, E, F, and G. When these PSD curves are plotted together, the six primary resonance peaks become distinctly visible. The frequencies of each spectral peak are listed in Table 1 and averaged to derive a single canonical frequency value. (Station D was excluded from the average due to the potential local influence of the penstock water flow, affecting only the average of the lowest frequency).

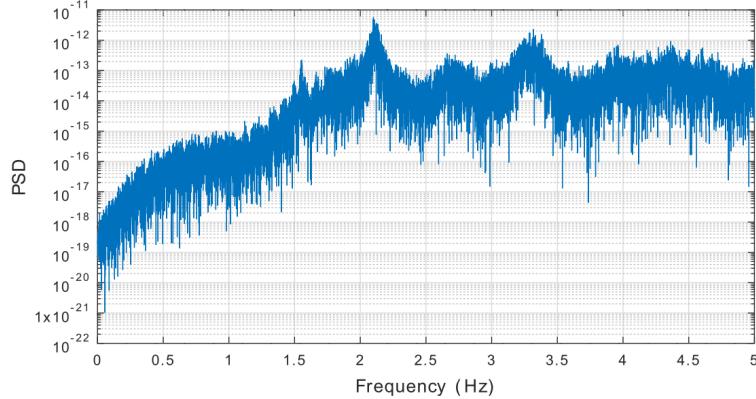


Figure 7. FFT-based periodogram of one hour of data exhibiting significant noise.

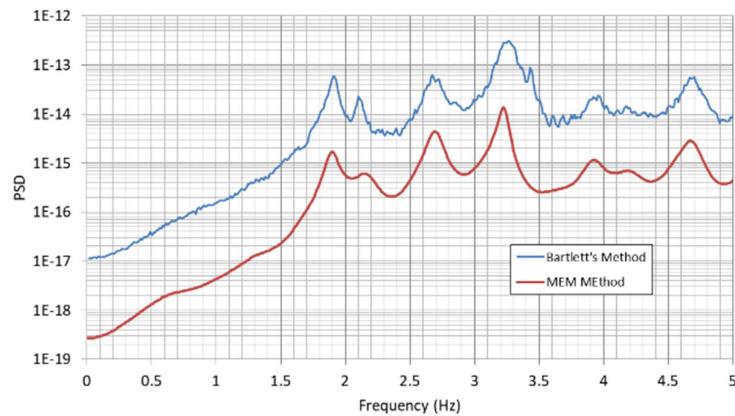


Figure 8. Comparison of Barlett's Method vs. Yule-Walker MEM Method for Station F.

4.2.3 Calibration of Modal Properties

Figure 9 displays PSD estimates based on 1 hour of data recorded simultaneously at Stations C, D, E, F, and G. When these PSD curves are plotted together, the six primary resonance peaks become distinctly visible. The frequencies at each station were averaged to derive a single canonical frequency value for correlation with the model eigenfrequencies, as listed in Table 1.

An eigenanalysis was performed using concrete material properties from a previous study and removing all nonlinear contact surfaces to establish a set of baseline frequencies for subsequent calibration. Additionally, the foundation was assumed to be massless since ambient vibration was determined not to mobilize the foundation's inertia. The predicted fundamental vibration mode was the first order bending of the crest with a frequency of 1.71 Hz. This closely matched the fundamental mode shapes identified in ambient vibration surveys at 1.88 Hz.

Beyond the fundamental mode, the calculated eigenmodes showed increasing higher-order horizontal bending of the crest, resembling the mode shapes observed in ambient vibration surveys. The key parameters for frequency calibration were found to be hydrodynamic effects and the elastic modulus of concrete. Accurate hydrodynamic effects were obtained by direct modelling of the impounded water and were also possible by using generalized Westergaard added mass (with off-diagonal terms) scaled to fluid element solutions. A stiffness increase by a factor of $(1.88 \text{ Hz}/1.71 \text{ Hz})^2 = 1.25$ was required to increase the predicted fundamental frequency from 1.71 Hz to the measured value of 1.88 Hz. Therefore, the calibration involved increasing the concrete modulus by 25%. It is noted that this amount of increase is consistent with the factor usually considered to obtain dynamic modulus from static modulus.

An additional eigenanalysis was performed with the newly calibrated concrete properties. As expected, the resulting vibration modes did not change shape, but the frequencies all shifted by the same factor, as summarized in Table 1. The fundamental frequency of the dam is now almost perfectly matches the ambient vibrations, and the higher-order modes closely match their corresponding measured frequencies to within 5%.

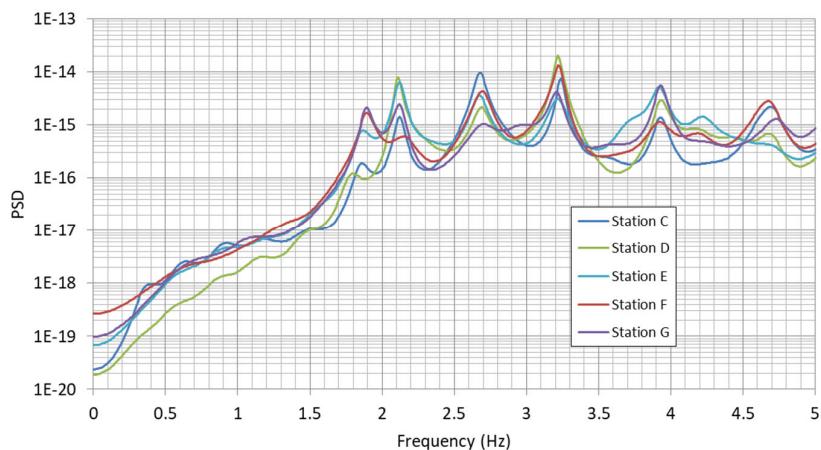


Figure 9. PSD estimated for Stations C to G using Yule-Walker MEM.

Table 1. Comparison of validated model eigenfrequencies and ambient vibration measurements.

Mode	Mode Shape Description	Frequencies (Hz)	
		Calibrated Eigen Model	Ambient Vibration Measurements
1	1 st order bending	1.89	1.88
2	2 nd order bending	2.03	2.12
3	3 rd order bending	2.67	2.69
4	4 th order bending	3.15	3.22
5	5 th order bending	3.80	3.93
6	Vertical 2 nd order bending	3.94	-
7	6 th order bending	4.56	4.70

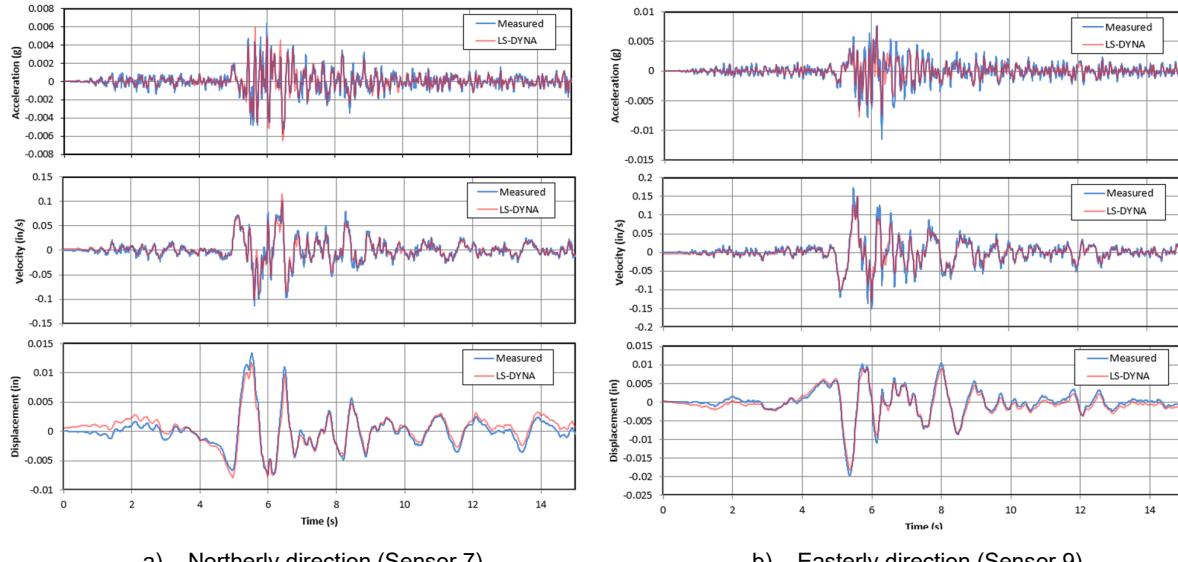
4.3 Validation for Recorded Seismic Response

On August 10, 2001, a magnitude Mw5.2 earthquake, located forty miles from the dam, triggered Strong Motion Arrays (SMAs) installed at the dam site by the Strong Motion Instrumentation Program of the California Department of Geology, providing nine channels of recorded signals (Figure 2). The left abutment records, experiencing less influence from the dam, were considered the closest to the free-field ground motion suitable for dam analysis input. Consequently, they were deconvolved to obtain seismic input at the bottom of the foundation and then propagated upward to generate free-field input for the sides of the foundation model. For the seismic validation analysis, it was necessary to replicate the conditions of the 2001 earthquake, including factors such as the water level at the time of the quake. Due to the low magnitude of ground shaking at the dam site, a linear seismic analysis was deemed sufficient.

The earthquake ground motions recorded at the left abutment in the northern and easterly directions (Sensors 7 and 9) are compared to the output of the LS-DYNA model at the exact location in Figure 10. The LS-DYNA output matches the accelerometer recording, validating that the interaction of the left abutment motions with the dam was insignificant. Therefore, using the left abutment records as the "free field" ground motion was deemed an acceptable choice.

The Sensor 1 recording near the dam base is compared to the LS-DYNA output at the same location in Figure 11. The measured signal shows relatively close agreement with the LS-DYNA output with slightly larger accelerations. This indicates that the seismic waves propagate correctly through the canyon topography and interact well with the dam and reservoir, demonstrating an acceptable degree of accuracy.

Finally, the dam seismic response at crest level (Sensor 5) is compared to the LS-DYNA output, as shown in Figure 11. While an exact replication of the seismic event was not attempted due to numerous unknowns, the results demonstrate reasonable agreement regarding response magnitude and overall frequency content. Based on these results, it was determined that no further calibration of the model was required if the seismic input had been simulated adequately.



a) Northerly direction (Sensor 7)

b) Easterly direction (Sensor 9)

Figure 10. Comparison of left abutment recorded motions with LS-DYNA predictions.

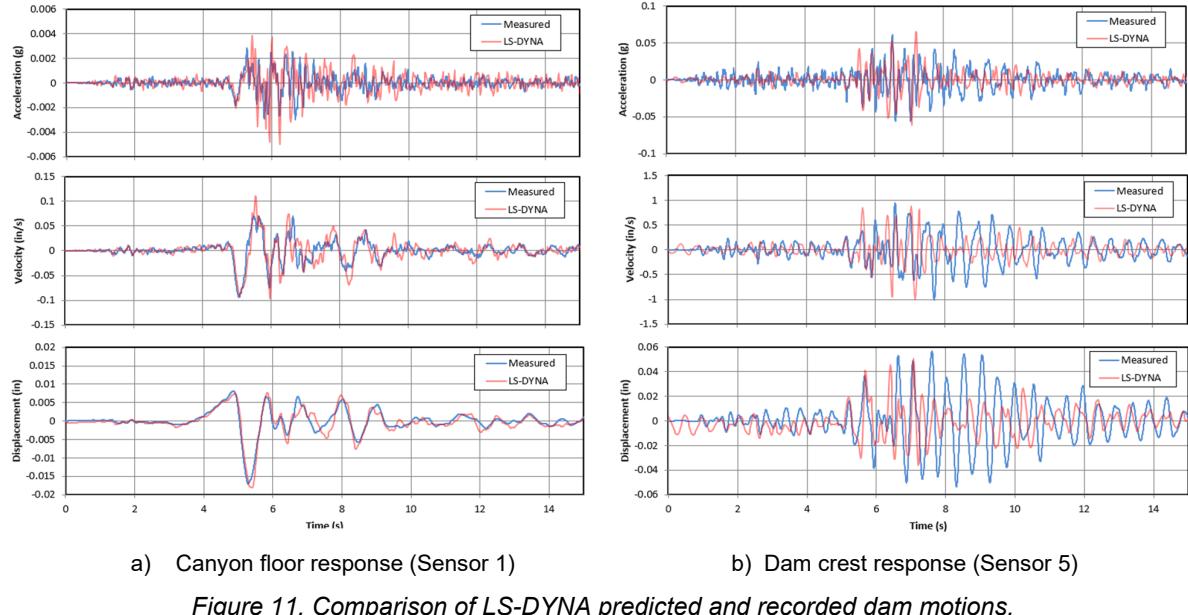


Figure 11. Comparison of LS-DYNA predicted and recorded dam motions.

5 Dam Nonlinear Static and Seismic Responses

The validated FE model assessed several potential failure modes (PFMs) involving the dam's static, seismic loading, and post-earthquake stability. These included structural instability that may develop under the normal water pool, probable maximum flood (PMF), and seismic loading scenarios. It was postulated that the concrete arch and thrust blocks might be overstressed under normal and PMF hydraulic loads, leading to cracking and increased uplift pressure at the dam-foundation interface. This could increase compressive stresses at the dam's downstream toe, potentially causing concrete crushing and loss of support, which could lead to overturning of the arch structure and uncontrolled release of reservoir water.

Similarly, under the MCE loading, it was presumed that the dam could be overstressed, leading to contraction joint opening and lift joint cracking. This might result in the formation of isolated blocks that could topple, causing an uncontrolled discharge. Alternatively, the dam could fail due to cracking at the dam-foundation interface, excessive permanent movement, overturning, concrete crushing, and loss of foundation support.

5.1 Static Response

Under normal loading conditions, the arch dam exhibits mainly compressive stresses with minor tensile stresses and no significant contraction-joint opening or lift-joint cracking. Cracking is limited to the dam's heel (blue triangles in Figure 12) but doesn't compromise stability, as compressive stresses at the downstream toe remain well below the concrete's capacity. Overall, the structure is stable, with no significant cracking to initiate sliding. Hence, the postulated failure scenario was reclassified to a less critical category.

Under PMF conditions, the dam shows mainly compressive stresses within safe limits, with no significant joint opening or cracking. Cracks are limited to the dam's heel but don't affect its stability. Compared to normal loading conditions, the increased PMF hydrostatic load caused the final extent of the cracking to increase from 40% to 60% through the thickness beneath the central monoliths. This indicated satisfactory performance under PMF conditions, justifying the reclassification of the failure scenario to a less critical category.

5.2 Seismic Response

The dam's performance revealed several key points when subjected to extreme seismic load combinations. The contraction joints between Monoliths 11 to 19 were the only ones observed to open, and even then, the openings were brief and minor, with a maximum of 0.07 inches, well below the shear keys' depth. Regarding lift-joint cracking, it was almost negligible, occurring briefly in just one of the six seismic load cases, affecting Monoliths 12 and 13 to a minor extent. As for the thrust blocks, no cracking was observed under the right blocks, and only minor, non-structural cracking occurred under the left blocks in one out of six seismic cases.

The arch monoliths did show additional cracking in the worst seismic scenario (yellow triangles in Figure 12). The maximum crack width at the dam heel was 1.35 inches, with a residual permanent separation of 0.1 inches. Still, these cracks were inconsequential and did not lead to sliding since they only affected up to 80% of the dam thickness under a couple of blocks while extended longitudinally across a broader range of monoliths.

A contour plot of the envelope of the maximum principal tensile stresses over the entire response history for one of the earthquake records, as shown in Figure 13, reveals that the largest tensile stresses are concentrated in a small region on the dam's upstream face. The stress history plot in Figure 13 indicates that the peak principal tensile stress, occurring in a single spike, remains below the dynamic tensile strength of the parent concrete and lift joints. Furthermore, a vector plot of these principal tensile stresses at the time of peak stress, also depicted in Figure 13, demonstrates a vertical orientation. This suggests that the stresses primarily result from cantilever bending, which may lead to minor and localized lift joint cracking at most. Consequently, these results indicate vertical cracking within the blocks, away from the contraction joints, is unlikely.

The seismic-induced cracking at the dam's base also transferred load from the central arch monoliths to the toe, increasing compressive stresses there. However, these stresses were well within the concrete's compressive strength and bearing capacity of foundation rock, eliminating concerns of concrete crushing. Overall, the dam demonstrated stability and capability to retain water under Maximum Credible Earthquake conditions, meeting all set criteria for the nonlinear analysis. This stability is attributed partly to the foundation model's realistic incorporation of local topography, indicating that the dam is effectively keyed into its foundation.

The results indicated that none of the identified seismic failure scenarios are expected to materialize for the MCE. The contraction-joint opening and lift joint cracking are too minor and negligible to create isolated blocks that could topple and lead to uncontrolled release of water. Additionally, concrete crushing and loss of toe support are unlikely to occur, thus preventing the overturning of the arch dam.

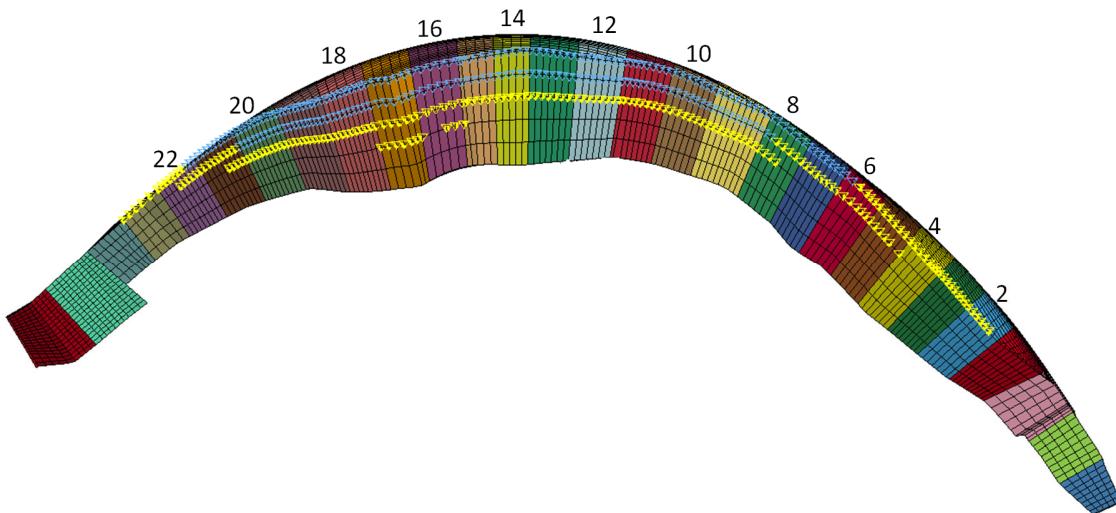


Figure 12. Static and seismic-induced cracking beneath arch dam in winter. (Shown from below. Blue triangles indicate static cracking, and yellow triangles indicate seismic cracking).

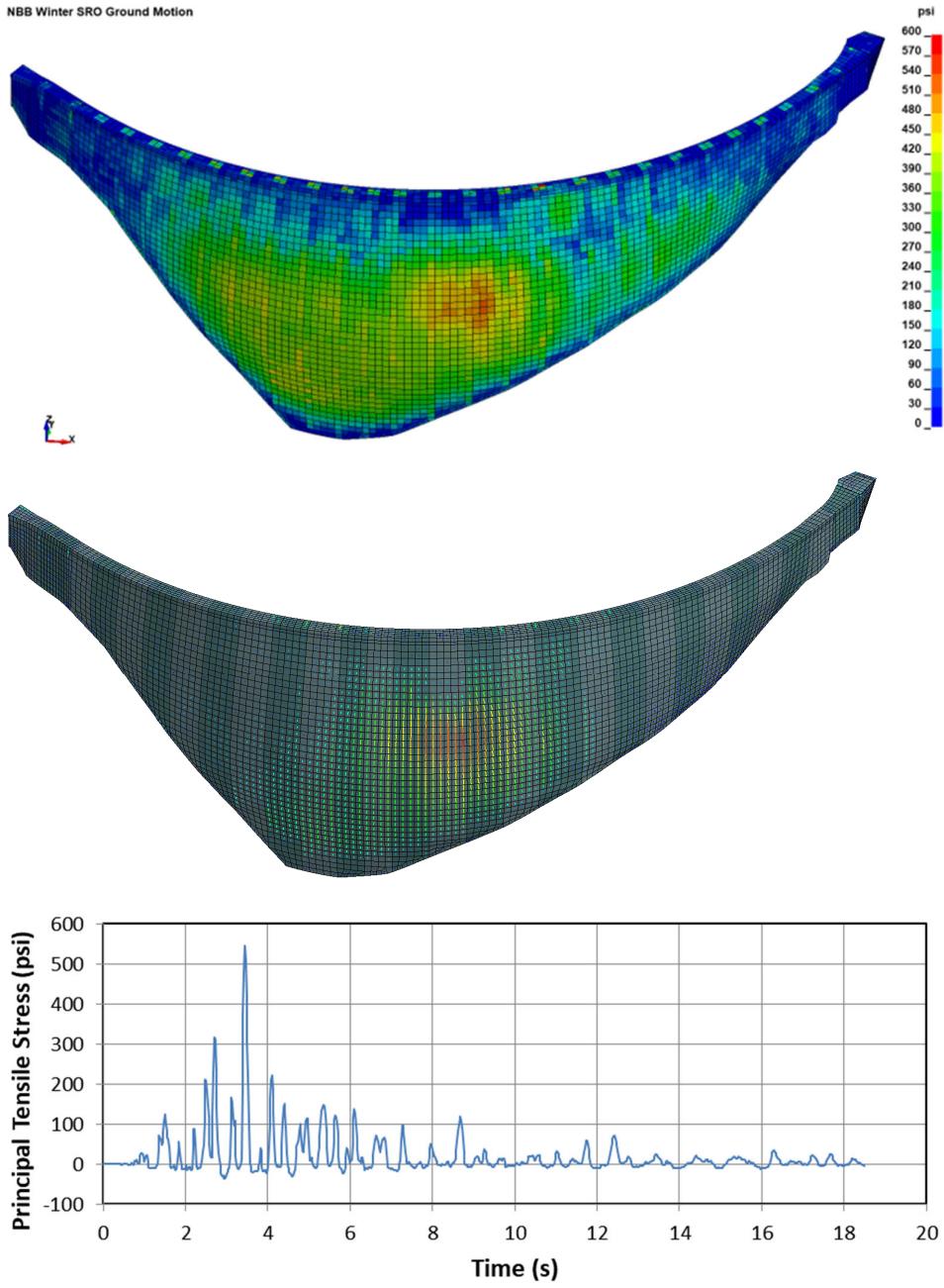


Figure 13. Envelope of principal tensile stress (top), vector plot of principal tensile stress directions (middle) at the time of maximum principal tension (bottom).

6 Dam Post-Earthquake Stability

We utilized the validated finite element model to investigate the dam's stability in the post-earthquake state and develop a post-earthquake factor of safety (FoS). This investigation employed the shear strength reduction technique to assess post-earthquake stability and determine the corresponding FoS. Within the framework of stability analysis, this technique involves incrementally reducing the shear strength parameters—defined by cohesion and friction—beneath the dam. This incremental reduction process aids in pinpointing the critical point at which the dam undergoes incipient sliding or overturning.

The sliding factor of safety, representing both shear strength reduction and the arch's ability to redistribute shear along the interface, can be determined from this formula:

$$FoS = \frac{\tan(\theta_{actual})}{\tan(\theta_{limit})}$$

Where: θ_{actual} = actual interface friction angle

θ_{limit} = limiting value determined by analysis

To induce a sliding or overturning failure, the shear resistance was systematically reduced to its lowest limit state, surpassing any observed damage during the Extreme MCE load cases. In this extreme scenario, we assumed complete cracking beneath the arch dam and thrust blocks, reducing cohesion to zero and friction between the dam and foundation to a residual value of 30°. We also considered the failure of internal drains, resulting in an uplift equivalent to the full headwater pressure beneath the dam, with no mitigation at the drains.

Subsequently, we applied the standard operating loads to provoke sliding or overturning failure under these exceedingly adverse conditions. Despite these implausibly severe circumstances, the dam, firmly keyed into the foundation and surrounded by steep canyon walls, exhibited no instability. Consequently, the post-earthquake FoS met the criteria, affirming the dam's stability in the post-earthquake state.

7 Conclusions

The instrument monitoring and field-testing framework presented here offers a robust method for validating linear models and developing nonlinear models with verified initial stiffness. This approach enhances the accuracy of analyzing potential failure modes and post-earthquake stability, thereby significantly improving dam safety assessment. Such improved evaluations are crucial for ensuring the safety and well-being of those dependent on the dam.

In conclusion, the analysis incorporating this approach for the New Bullards Bar Dam confirms that joint openings, lift joint cracking, tensile stresses, and compressive stresses all remain within the acceptable thresholds for nonlinear response. The inclusion of realistic local topography in the foundation model effectively addressed the issue of widespread cracking and sliding observed in previous analyses, which employed an idealized flat dam-foundation contact surface. This adjustment demonstrates the dam's stability and its effective integration within the foundation. As a result, the dam is expected to maintain stability and water retention capabilities during the MCE event without any anticipated seismic failure scenarios.

8 References

- GEOVision (2019). *New Bullards Bar Dam Ambient Vibration Measurements*. Report prepared by GEOVision Geophysical Service for Yuba County Water Agency, September 2020.
- Quest (2021). *Validated Finite-Element Analyses of New Bullards Bar Dam*. Final Project Report prepared by Quest Structures for Yuba Water Agency, Marysville, California, October 7, 2021.
- YCWA (2019). *Dam Safety Surveillance and Monitoring Report – Annual Cycle Ending 30, 2019*. Report prepared by Christensen Associates for Yuba County Water Agency, August 2019.

NONLINEAR SEISMIC ANALYSIS OF GRAVITY DAMS INCLUDING LIFT AND BASE JOINTS

S. S. Guo, H. Liang, D.Y. Li, & H. B. Wang

China Institute of Water Resources and Hydropower Research, Beijing, China, 305265331@qq.com

Abstract: Gravity dams are considered to have two typical failure modes including tensile cracking at the changing position of the dam geometry and sliding along the weak layer under earthquake. In order to investigate the whole process from crack initiation and crack propagation to overall sliding of blocks caused by penetrated crack, a contact model considering the initial tension strength and shear strength of joints is presented based on the framework of Lagrange multiplier method. A dam-foundation-reservoir comprehensive model is established. Taking a roller compacted concrete (RCC) gravity dam as an example, nonlinear dynamic analysis is performed to investigate the propagation of cracks and the overall sliding of blocks along lift and base joints under different earthquake intensity levels. The results show that the partial cracking failure of the joints occurs under MDE and the upper lift joint appears penetrated crack leading to the occurrence of the block above the joint under MCE. Under overload factor of 1.5, the excessive overall slippage of the block above the lift joint happens which may lead to the ineffectiveness of the drainage hole. According to the cumulative sliding displacement of blocks, the post-earthquake static stability method is employed to evaluate the seismic capacity of the dams for the penetrated blocks. The analysis model and evaluation method provided can be used to evaluate the seismic safety of gravity dams.

1 Introduction

Gravity dams are considered to have two typical failure modes including tensile cracking at the changing position of the dam geometry and sliding along the weak layer under earthquake (Ghanaat, 2004). The seismic cracking of gravity dams has been studied widely by several nonlinear models. These models can be classified into two categories: smeared crack model and discrete crack model.

Linear elastic fracture mechanics (Ayari and Saouma, 1990, Pekau et. al, 1991) and nonlinear fracture mechanics (El-Aidi and Hall, 1989, Bhattacharjee and Leger, 1993, Wang et. al, 2000) were developed to model the seismic fracture of concrete gravity dams. Hariri-Ardebili and Seyed-Kolbadi (2015) used a new co-axial rotating smeared crack model to study the seismic cracking of concrete gravity dams. Zhang et. al (2013) studied the seismic crack process of Koyna gravity dam with initial cracks employing the extended finite element method (XFEM). Lee and Fenves (1998) developed a plastic-damage model to study the seismic cracking process of Koyna dam and the model has been used widely to model the concrete cracking of concrete gravity dams (Long et. al, 2009, Omidi et. al, 2013, Wang et. al, 2017). Zhang et al. (2014) studied the cracking process of a concrete gravity dam with concrete smeared crack model by using ADINA. Pan et al. (2014) investigated the seismic crack propagation of a gravity dam with different modeling including XFEM, the plastic-damage model, and Drucker-Prager model. Chen et al. (2014) established a new damage model to study the damage rupture of Koyna gravity dam. Oudni and Bouafia (2015) developed a damage model considering tension and compression to model the seismic cracking of Koyna gravity dam.

The above studies investigated the process of crack initiation and crack propagation of gravity dams in view of the opening and closing of the cracks. However, once the crack penetrates the upstream and downstream of the dam, great attention should be paid to the overall sliding of the independent block for the prevention of uncontrolled flooding discharge. Then there needs a thorough investigation on the seismic sliding displacement of blocks. Another aspect needs attention is that most models which were presented to investigate the crack propagation of gravity dams (Ayari et. al, 1990, Long et. al, 2009, Oudni et. al, 2015) can't simulate the overall sliding behaviour of the independent blocks caused by penetrated cracks in the framework of continuum mechanics.

To fill this research gap, based in the framework of discrete model, this study is devoted to proposing a method which can also simulate the tensile and shear resistance of concrete before cracking. A contact model based on the Lagrange multiplier method has been given which avoids the introduction of normal and tangential penalty function, and it can only model the opening of the vertical joints of arch dams (Guo et. al, 2019). To reflect the actual situation of gravity dams under earthquake practically, the model considering the opening and sliding of joints and advanced failure criteria with initial tensile and shear strength is presented in this paper based on the framework of the above model. It can model the whole process from crack initiation and crack propagation to overall sliding of blocks caused by penetrated crack.

2 Analysis model

In this part, the contact model based on the Lagrange multiplier method were given. In this contact model, the introduction of normal and tangential penalty function does not need, and it can only model the opening of the vertical joints of arch dams. The detailed derivation can be found in Guo et al. (2019).

The framework of the Lagrange multiplier method is as follows:

$$\begin{cases} \mathbf{AU} = \mathbf{F} - \mathbf{B}\lambda \\ \mathbf{B}^T \mathbf{U} = \gamma \end{cases} \quad (1)$$

From Equation (1), the following contact force equation can be obtained:

$$\begin{cases} \mathbf{AU} = \mathbf{F} - \mathbf{B}\lambda \\ \mathbf{B}^T \mathbf{U} = \gamma \end{cases} \quad (2)$$

Where, \mathbf{A} and \mathbf{B} represent the coefficient and the constraint matrix ; \mathbf{F} and \mathbf{U} are the load and displacement vector; λ and γ are the Lagrange multiplier representing contact force vector and displacement constraint vector; λ^1 and γ^1 are the corresponding vectors in the local coordinate system; $\mathbf{C} = \mathbf{T}\mathbf{B}^T \mathbf{A}^{-1} \mathbf{B}^T \mathbf{T}^T$ and $\mathbf{D} = \mathbf{T}\mathbf{B}^T \mathbf{A}^{-1} \mathbf{F} - \gamma^1$; \mathbf{T} is the transformation matrix between different coordinate systems.

The normal and tangential force of Equation (2) can be obtained by iterative method (Guo et. al, 2019). During the solution, the initial tension and shear strength of joints are introduced to model the propagation of cracks. The Mohr-Coulomb failure criterion defined by the friction coefficient and cohesion is employed for shear sliding in the absence of initial shear strength. The solution of each iterative step is as follows.

Firstly, the normal contact force is obtained as follows:

$$\lambda_n^{k+1} = (D_1 - C_{12}\lambda_s^k - C_{13}\lambda_s^k) / C_{11} \quad (3)$$

λ_n^{k+1} is positive and minus corresponding to compression and tension state of the joints.

If $-\lambda_n^{k+1} \leq \sigma_t A$, then no tensile crack propagation occurs and there is no need for a correction.

If $-\lambda_n^{k+1} > \sigma_t A$, then tensile crack propagation occurs, and the corresponding normal and tangential contact forces vanish. The correction is applied as $\lambda_n^{k+1} = 0$, $\lambda_{s1}^{k+1} = 0$, $\lambda_{s2}^{k+1} = 0$, and owing to the disconnection of bond, the initial tension and shear strength vanish $\sigma_t = 0$, $\sigma_s = 0$.

Where, σ_t and σ_s is the initial tension and shear strength of the joint respectively, and A is the tributary area of the node.

Secondly, the tangential contact forces are obtained as follows:

$$\lambda_{s1}^{k+1} = \left(D_2 - C_{21}\lambda_n^{k+1} - C_{23}\lambda_{s2}^k \right) / C_{22} \quad (4)$$

$$\lambda_{s2}^{k+1} = \left(D_3 - C_{31}\lambda_n^{k+1} - C_{32}\lambda_{s1}^k \right) / C_{33} \quad (5)$$

If $-\lambda_n^{k+1} > \sigma_t A$, then tensile crack propagation occurs and the corresponding normal and tangential contact forces vanish. The correction is applied as $\lambda_n^{k+1} = 0$, $\lambda_{s1}^{k+1} = 0$, $\lambda_{s2}^{k+1} = 0$, and owing to the disconnection of bond, the initial tension and shear strength vanish $\sigma_t = 0$, $\sigma_s = 0$.

Then, $\lambda_s^{k+1} = \sqrt{(\lambda_{s1}^{k+1})^2 + (\lambda_{s2}^{k+1})^2}$.

If $\lambda_s^{k+1} \leq \sigma_s A$, no shear crack propagation occurs and there is no need for a correction.

If $\lambda_s^{k+1} > \sigma_s A$, then shearing crack propagation occurs and owing to the disconnection of bond, the initial shear and tension strength vanish $\sigma_t = 0$, $\sigma_s = 0$.

If $\sigma_s = 0$ and $\lambda_s^{k+1} \leq \mu\lambda_n^{k+1} + cA$, then the joint is in the stick state and there is no need for a correction.

If $c = \frac{\sigma_s}{\lambda_s^{k+1}} - \frac{\mu\lambda_n^{k+1}}{\lambda_s^{k+1}} > \mu\lambda_n^{k+1}$, then the joint is in the sliding state and the scaled tangential force are defined as $\lambda_{s1}^{k+1} = \lambda_{s1}^{k+1} \frac{\mu\lambda_n^{k+1}}{\lambda_s^{k+1}}$ and $\lambda_{s2}^{k+1} = \lambda_{s2}^{k+1} \frac{\mu\lambda_n^{k+1}}{\lambda_s^{k+1}}$. The cohesion strength is assumed to vanish and $c = 0$.

Where, μ is friction coefficient, and c is cohesion strength.

3 Dynamic analysis

3.1 Model construction

The planned gravity dam is located in the strong earthquake area of China. A typical non-overflow section model of the dam-foundation considering the geometry of gate groove is established. The main parameters of the dam are shown in Table 1.

Table 1. Basic parameters of the non-overflow section of the dam (m)

dam monolith width	21.00
dam crest elevation	1740.0
dam base elevation	1582.0
elevation of the upstream change of slope	1640.0
elevation of the downstream change of slope	1707.3
maximum dam height	158.0
dam crest width	21.0
dam base width	131.6

The 3D finite element model of the dam-foundation considering the geometry of gate groove is established. The element size of the dam is approximately 2 m. There are 18692, 14604, and 56076 nodes, elements, and degrees of freedom (DOFs), respectively. Figure 1 shows the 3D finite element model of the dam-foundation. Figure 2 shows the finite element model of the dam. Figure 3 shows the location of joints. For simplification the hydrodynamic effect is accounted for by the Westergaard added mass (Westergaard, 1933). A massed foundation model with viscoelastic boundary conditions is adopted to consider the effect of dam-foundation dynamic interaction and radiation damping of far-field foundation (Lysmer and Kuhlemeyer, 1969, Deeks and Randolph, 1994, Liu and Lv, 1998). The equivalent force time histories at the boundaries can be computed using the free-field response (Chen et. al, 2014).

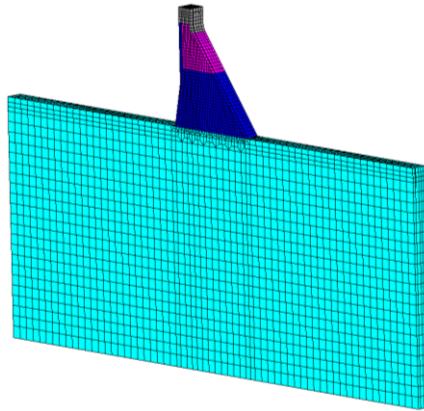


Figure 1. The 3D finite element model of the dam-foundation

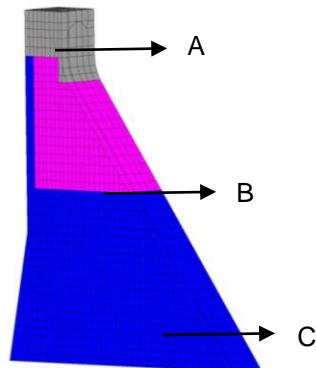


Figure 2. The Finite element model of the dam (different colors represent different material partitions, named A, B, and C)

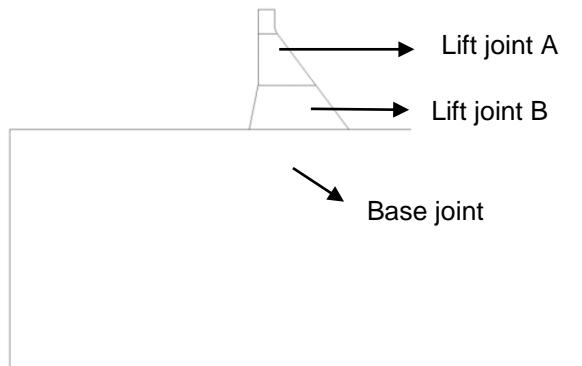


Figure 3. The location of joints

3.2 Material parameters

The concrete material parameters are shown in

Table 2. The foundation rock material parameters are taken as follows: density $\rho = 2600 \text{ kg/m}^3$, static and dynamic elastic modulus $E = 10 \text{ GPa}$, Poisson's ratio $\nu = 0.26$. The strength parameters of joints are shown in Table 3. The Rayleigh type damping is employed with the damping ratio of 10% according to Chinese code.

Table 2. Mechanical parameters of concrete

Location	Density(kg/m ³)	Static elastic modulus (GPa)	Dynamic elastic modulus (GPa)	Poisson ratio
A	24.0	22.4	33.6	0.167
B	24.0	15.4	23.1	0.167
C	24.0	17.9	26.8	0.167

Table 3. Strength parameters of joints

Location	Lift joint A	Lift joint B	Base joint
Tensile strength (MPa)	1.61	1.61	2.00
Shear strength (MPa)	3.22	3.22	4.00
Friction coefficient	1.05	1.05	1.09
Cohesion strength (MPa)	1.50	1.50	1.09

3.3 Load

The main load applied includes up and down water pressure, sediment pressure, uplift pressure, weight load, and earthquake load. The elevations of the upstream normal water level, downstream normal water level and sediment are 1735.0 m, 1620.0 m and 1668.0 m, respectively. The horizontal PGAs of MDE and MCE are 338gal and 397gal respectively, and the vertical PGA is taken as 2/3 of the horizontal PGA. The earthquake wave is shown in Figure 4, and the maximum values of accelerations are normalized to 1.0.

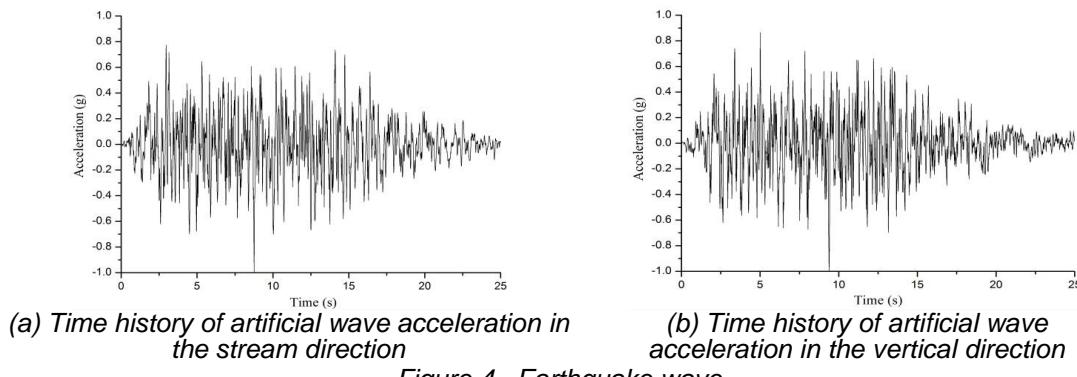


Figure 4. Earthquake wave

3.4 Calculation scheme

The propagation of cracks and sliding of blocks for joints are investigated under several earthquake intensity levels including MDE, MCE and overloading conditions.

3.5 Discussion of results

3.5.1 MDE condition

Figure 5 shows the distribution of the crack propagation under MDE. Partial cracking occurs in all three joints, but there is no penetrated crack. Figure 6, Figure 7 and Figure 8 show the time history of the opening width of the three joints. The maximum opening width of lift joints A, lift joint B and base joint are 0.76 cm, 0.67 cm and 0.48 cm. It can be seen that all the three joints are closed after earthquake. It's concluded that although the local cracking failure of the dam happens under MDE, it can still operate normally after repairing under the earthquake.

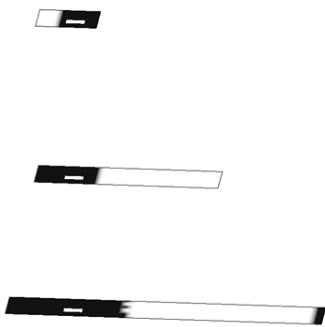


Figure 5. The distribution of the crack propagation under MDE (black for damage, white for undamaged)

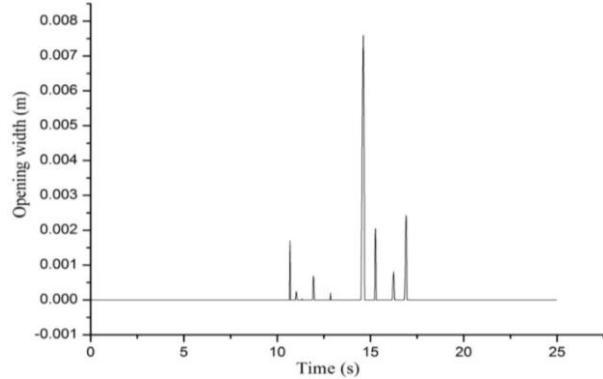


Figure 6. Opening width time history of lift joint A under MDE

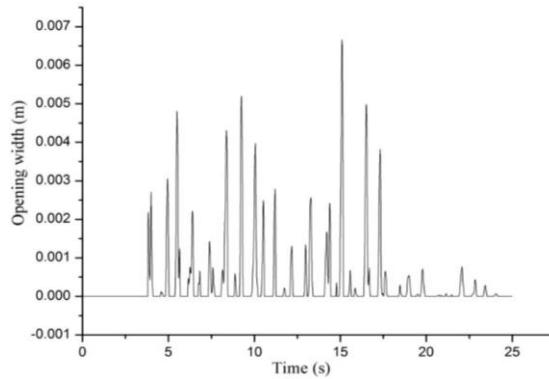


Figure 7. Opening width time history of lift joint B under MDE

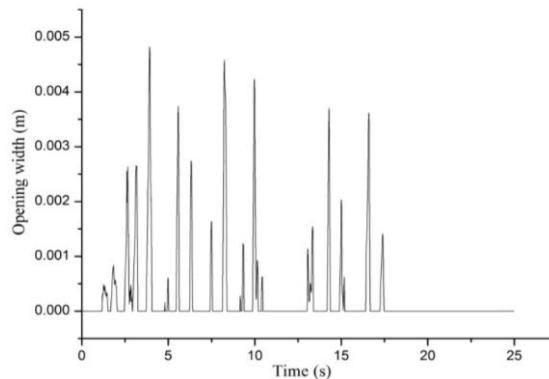


Figure 8. Opening width time history of base joint under MDE

3.5.2 MCE condition

Figure 9 shows the distribution of the crack propagation under MCE. The lift joint A appears penetrated crack leading to the occurrence of the block above the joint, while the other two joints are still in partial cracking state. Figure 10, Figure 11 and Figure 12 show the opening width time history of the three joints. It shows that the maximum opening width of lift joint A, lift joint B and base joint are 2.32 cm, 0.91 cm and 0.70 cm respectively. After the earthquake, all the three joints are closed. Attention should be paid to the overall sliding stability of the independent block above the lift joint A. Figure 13 shows the sliding time history along lift joint A. The maximum overall slippage along lift joint A is 0.70 cm. After the earthquake, it remains stable and the residual slippage is 0.59 cm. The static anti-sliding stability of the block above the lift joint A after earthquake is evaluated according to the post-earthquake static stability evaluation method. Because of slight overall sliding of the block above the lift joint A, the shear mechanical parameters of the joints should be taken as the residual strength, that is, the friction coefficient is taken as 0.9 times of the peak strength, and the cohesion strength is assumed to be 0 MPa. The slippage is far less than the drainage hole diameter, and the drainage hole remains effective. Considering that the overall sliding along the joint A happens, the lifting pressure of the joint can be

calculated as follows: the lifting pressure in front of the drainage hole is taken as the upstream water head, and the lifting pressure behind the drainage hole is taken as 20% of the upstream water head. According to results obtained by the rigid limit equilibrium method, the safety factor of the static anti-sliding stability of the independent block after the earthquake is 3.46. In summary, although slight overall sliding occurs at the lift joint A of the dam under MCE, the uncontrolled flooding discharge will not happen.

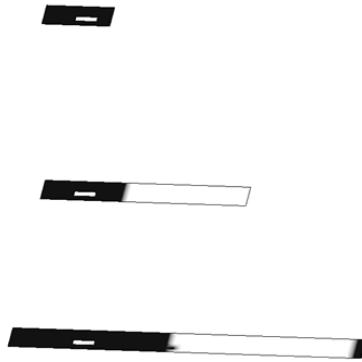


Figure 9. The distribution of the crack propagation under MCE (black for damage, white for undamaged)

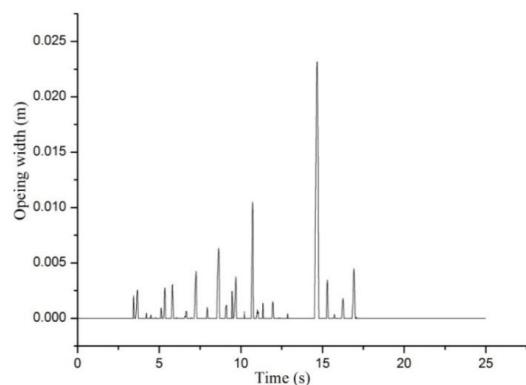


Figure 4. Opening time history of lift joint A under MCE

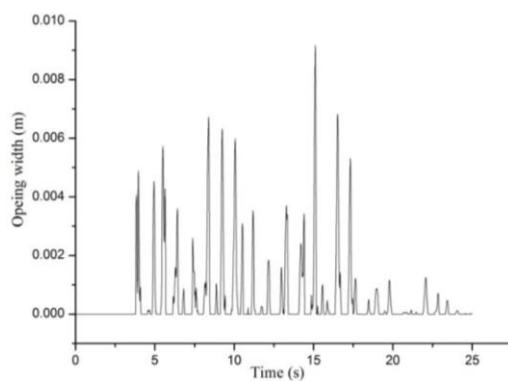


Figure 5. Opening time history of lift joint B under MCE

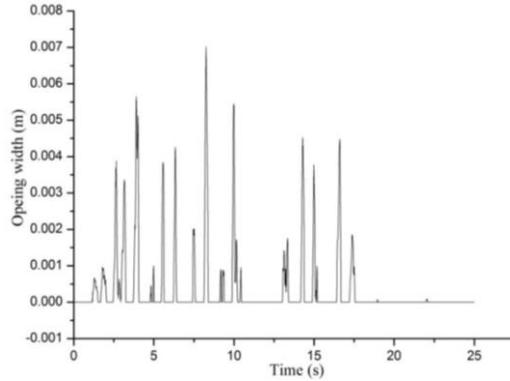


Figure 6. Opening time history of base joint under MCE

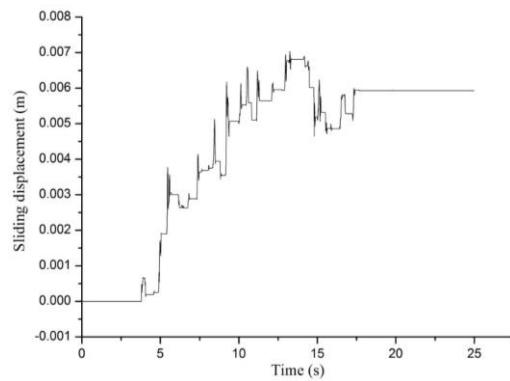


Figure 7. Sliding time history along lift joint A under MCE

3.5.3 Overload analysis condition

The overload analysis is adopted to comprehensively investigate the propagation of cracks and the overall sliding of blocks along lift and base joints based on the overloading of MDE.

Figure 14 shows the distribution of the crack propagation of the joints under 1.3 times the MDE with the corresponding overload factor of 1.3. The lift joint A shows penetrated crack, while the other two joints are in partial cracking state. Figure 15 shows the sliding time history along the lift joint A under overload factor of 1.3. The maximum slippage is 1.22 cm, and the residual slippage is 1.15 cm after the earthquake.

Figure 16 shows the distribution of the crack propagation of the joints under 1.4 times the MDE. It is clear that both the lift joint A and B show penetrated crack. Figure 17 shows the sliding time history along the lift joint A under overload factor of 1.4. The maximum slippage is 2.19 cm, and the residual slippage is 2.12 cm after the earthquake. Figure 18 shows the sliding time history along the lift joint B under overload factor of 1.4. The maximum slippage is 4.10 cm, and the residual slippage is 4.08 cm after the earthquake. Though the residual slippage of the lift joint B is 4.08 cm, the drainage hole can still maintain normal operation under the assumption that the slippage is less than 30% of the drainage hole diameter.

Figure 19 shows the distribution of the crack propagation of the joints under 1.5 times the MDE. It is obvious that both the lift joint A and B show penetrated crack. Figure 20 shows the sliding time history along the lift joint A under overload factor of 1.5. The maximum slippage is 4.07 cm, and the residual slippage is 3.84 cm after the earthquake. Figure 21 shows the sliding time history along the lift joint B under overload factor of 1.5. The maximum slippage is 5.42 cm and the residual slippage is 5.39 cm after the earthquake, which exceed the 30% of the drainage hole diameter. Hence, it can be obtained that the drainage hole may lose effectiveness. According to results obtained by the rigid limit equilibrium method, the safety factor of the static anti-sliding stability of the independent block above the lift joint B after the earthquake is only 0.47.

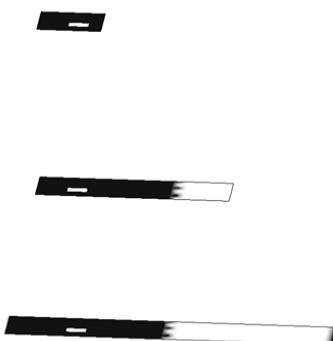


Figure 8. The distribution of the crack propagation under overload factor of 1.3 (black for damage, white for undamaged)

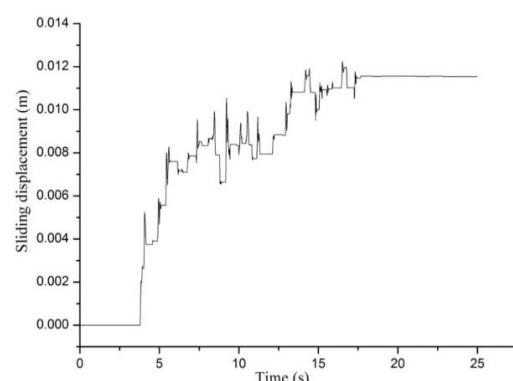


Figure 9. Sliding time history along lift joint A under overload factor of 1.3



Figure 10. The distribution of the crack propagation under overload factor of 1.4 (black for damage, white for undamaged)

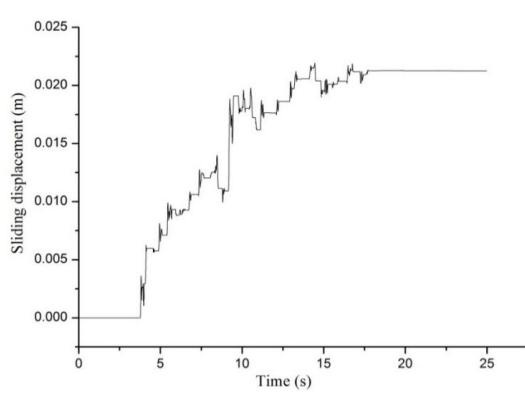


Figure 11. Sliding time history along lift joint A under overload factor of 1.4

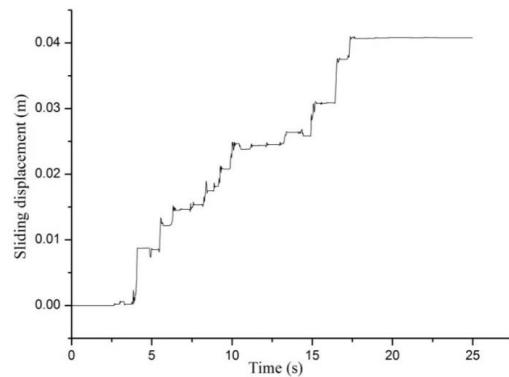


Figure 12. Sliding time history along lift joint B under overload factor of 1.4



Figure 13. The distribution of the crack propagation under overload factor of 1.5 (black for damage, white for undamaged)

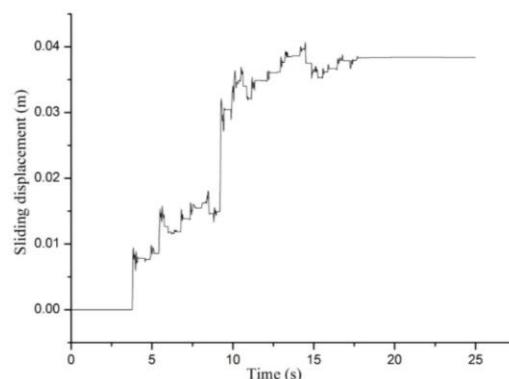


Figure 14. Sliding time history along lift joint A under overload factor of 1.5

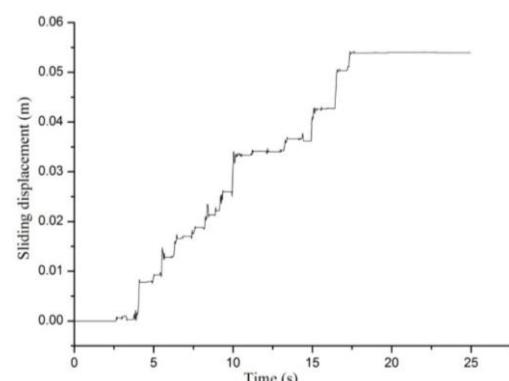


Figure 15. Sliding time history along lift joint B under overload factor of 1.5

4 Conclusions

1. A method is proposed to model the crack propagation and the overall sliding of blocks caused by penetrated cracks in the framework of discrete model, and it can also simulate the tensile and shear resistance of concrete before cracking. A contact model considering the initial tension strength and shear strength of lift and base joints is presented based on the framework of Lagrange multiplier method, which can model the whole process from crack initiation and crack propagation to overall sliding of blocks in the case of penetrated crack.
2. Nonlinear time history analysis of a gravity dam with lift and base joints in China is performed. The propagation of cracks and the overall sliding of blocks along lift and base joints are investigated under different earthquake intensity levels to evaluate the seismic behaviour of the dam.
3. It's concluded that the dam can still operate normally after repairing under MDE owing to the occurrence of the partial cracking failure of the joints under MDE. Under MCE, the lift joint A appears penetrated crack leading to the occurrence of the block above the joint, while the other two joints are still in partial cracking state. Although slight overall sliding occurs at the lift joint A of the dam, the uncontrolled flooding discharge will not happen. Under overload factor of 1.4, besides the lift joint A, the lift joint B appears penetrated crack leading to the occurrence of the block above the joint. Under overload factor of 1.5, the excessive overall slippage of the block above the lift joint B happens which may lead to the ineffectiveness of the drainage hole diameter. The post-earthquake static stability analysis indicates that the independent block may lose stability.
4. The analysis model and evaluation method provided in this paper can be used to evaluate the seismic safety of gravity dams.

5 References

- Alembagheri M., Ghaemian M. (2013). Incremental dynamic analysis of concrete gravity dams including base and lift joints, *Earthquake Engineering and Engineering Vibration*, 12(1): 119-134.
- Ayari M.L., Saouma V.E. (1990). A fracture mechanics based seismic analysis of concrete gravity dams using discrete cracks, *Engineering Fracture Mechanics*, 35(1): 587-598.
- Bhattacharjee S.S., Leger P. (1993). Seismic cracking and energy dissipation in concrete gravity dams, *Earthquake Engineering and Structural Dynamics*, 22:991–1007.
- Chen H.Q., Li D.Y., Guo S.S. (2014). Damage-rupture process of concrete dams under strong earthquakes, *International Journal of Structural Stability and Dynamics*, 14(07):1450021.
- Deeks, A. J., Randolph, M. F. (1994). Axisymmetric time-domain transmitting boundaries. *Journal of Engineering Mechanics*, 120(1), 25-42.
- EI-Aidi B., Hall J.F. (1989). Nonlinear earthquake response of concrete gravity dams, part I: modeling, *Earthquake Engineering and Structural Dynamics*, 18:837–51.
- Ghanaat Y. (2004). Failure modes approach to safety evaluation of dams, *Proc. of the 13th World Conference on Earthquake Engineering*, Vancouver, Canada.
- Guo S.S., Liang H., Li D.Y., Chen H.Q., Liao J.X. (2019). A comparative study of cantilever- and integral-type dead loads on the seismic responses of high arch dams, *International Journal of Structural Stability and Dynamics*, 19(3):1950021.
- Hariri-Ardebili M.A., Seyed-Kolbadi S.M. (2015). Seismic cracking and instability of concrete dams: Smeared crack approach, *Engineering Failure Analysis*, 52: 45-60.
- Jiang S., Du C., Hong Y. (2013). Failure analysis of a cracked concrete gravity dam under earthquake, *Engineering Failure Analysis*, 33(5): 265-280.
- Lee J., Fenves G L. (1998). A plastic-damage concrete model for earthquake analysis of dams, *Earthquake Engineering and Structural Dynamics*, 27: 937-956.
- Liu, J. B., Lv, Y. D. (1998). A direct method for analysis of structural foundation dynamic interaction. *Journal of civil engineering*, 31(3), 55-64.
- Long Y., Zhang C., Xu Y. (2009). Nonlinear seismic analyses of a high gravity dam with and without the presence of reinforcement, *Engineering Structures*, 31(10):2486-2494.

- Lysmer, J., Kuhlemeyer, R. L. (1969). Finite dynamic model for infinite media. *Journal of the engineering mechanics division*, 95(4), 859-877.
- Omidi O., Valliappan S., Lotfi V. (2013). Seismic cracking of concrete gravity dams by plastic-damage model using different damping mechanisms," *Finite Elements in Analysis and Design* 63(1):80–97.
- Oudni N., Bouafia Y. (2015). Response of concrete gravity dam by damage model under seismic excitation, *Engineering Failure Analysis*, 58: 417-428.
- Pan J., Feng Y., Jin F., Zhang C.H., Owen D.R.J. (2014), Comparison of different fracture modelling approaches to gravity dam failure, *Engineering Computations*, 31(1): 18-32.
- Pekau O.A., Zhang C.H., Feng L.M. (1991). Seismic fracture analysis of concrete gravity dams, *Earthquake Engineering and Structural Dynamics*, 20:335–54.
- Wang G.H., Wang Y.X., Lu W.B., Yu M., Wang C. (2017). Deterministic 3D seismic damage analysis of Guandi concrete gravity dam: A case study, *Engineering Structure*, 148:263-276.
- Wang G.L., Pekau O.A., Zhang C.H., Wang S.M. (2000). Seismic fracture analysis of concrete gravity dams based on nonlinear fracture mechanics, *Engineering Fracture Mechanics*, 65(1):67-87.
- Westergaard, H. M. (1933). Water pressures on dams during earthquakes. *Transactions of the American society of Civil Engineers*, 98(2), 418-433.
- Zhang L., Zhang H., Shaowei H.U. (2014). Failure patterns of shear keys and seismic resistance of a gravity dam with longitudinal joints, *Journal of Earthquake and Tsunami*, 08(01):1450004.
- Zhang S., Wang G., Yu X. (2013). Seismic cracking analysis of concrete gravity dams with initial cracks using the extended finite element method, *Engineering Structures*, 56:528-543.



THE ROLE OF MODELING UNCERTAINTIES IN SEISMIC ANALYSIS OF CONCRETE DAMS

M.A. Hariri-Ardebili¹ & J.W. Salamon²

¹ University of Maryland, College Park, USA, hariri@umd.edu

² US Bureau of Reclamation, Denver, USA

Abstract: Despite the significant advances in nonlinear dynamic analysis of engineering structures, concerns still exist regarding the level of confidence in modeling and the accuracy of analysis outcomes. While verification and validation of computational processes are primary tools used to quantify the accuracy of solutions and to build confidence in the analysis results, they cannot fully eliminate sources of uncertainties during performance evaluation. In particular, uncertainties in the dynamic analysis of dam-water-rock coupled systems can be attributed to both epistemic and aleatory sources of uncertainties. This paper focuses on the importance of addressing epistemic uncertainties in the seismic analysis of a gravity dam through careful data collection from the 15th ICOLD's Benchmark Workshop organized in Milan, Italy in 2019. In the case study formulation, the geometry of the model, mechanical properties of materials, and loads were precisely defined, and participants were asked to analyze the defined cases selecting the best practice in modeling and simulation of concrete dams. Significant variability was observed in contributions, particularly in the application of the far-field boundary conditions and the non-linear material models selected for concrete damage modeling. This paper elaborates further on the sources of various variabilities and attempts to quantify the amount of uncertainty in modeling and simulation for such well-defined benchmark problems. The results of this study emphasize the need for establishing a systematic approach to modeling and analyzing seismic hazards in dam engineering to improve the accuracy and consistency of predictions. A better understanding of the sources and magnitudes of modeling uncertainties can help improve the reliability of dam analyses, contribute to the development of more effective risk assessment and mitigation strategies, and build confidence in the analysis results.

1. Introduction

The structural analysis of engineered structures has always posed challenges due to inherent uncertainties in the modeling and simulation process, encompassing modeling techniques, accuracy, solution algorithms, loading definitions, and material parameters. Concrete dams stand out due to their complex response, influenced by interactions with foundation rock and reservoir dynamics, presenting mathematically a coupled system problem. Verification, validation, and uncertainty quantification are fundamental procedures used in modern analysis and design of civil structures that allow quantification of the analysis results. Verification checks mathematical accuracy, validation tests models against real-world systems, while uncertainty quantification integrates variability for comprehensive predictive uncertainty.

The widely used uncertainty classification by Ayyub and Chao (1997) categorizes uncertainties into abstracted and cognitive forms, offering a framework for classifying non-abstracted sources like physical randomness, vagueness, human errors, and information conflicts. This classification is applicable to Civil Engineering, while notable works in Structural Engineering's uncertainty quantification, like Melchers and Beck (2018) and Bulleit (2008), will be detailed later in the paper.

Historical challenges have focused on validating and verifying computational models in simulations of concrete dams, with limited emphasis on uncertainty quantification until recently. Computational model validation and verification have been explored in structural health monitoring (Bukenya et al., 2014) and system identification (Alves and Hall, 2006) for static and transient scenarios. However, fully validating a computational model against an actual dam's behavior under earthquake ground motion remains a challenging process. Some previous efforts involved shake table tests (Harris, 2000) and centrifuge tests (Uchita et al., 2005) on small-scale dam models. These efforts provide insights into dam seismic response, yet challenges remain in fully replicating the complex behaviors of actual dams under earthquake conditions.

To ensure the accuracy of a conceptual model's representation of real-world behavior, cross-validation against published research, benchmark workshops, and blind prediction contests becomes crucial. Several instances of such cross-validation are available, including those organized by ICOLD and national organizations like USSD. Notably, the 15th ICOLD International Benchmark Workshop (Bolzon et al., 2020) and the 2018 USSD benchmark workshop (Salamon, 2018) stand out. The authors of this paper played a role in formulating both workshops and summarized their outcomes (Hariri-Ardebili, 2024). This paper emphasizes the importance of addressing uncertainties in the seismic analysis of gravity dams, using data collected from the 2019 ICOLD benchmark study in Italy.

2. Uncertainty Quantification

The significance of uncertainty quantification is particularly pronounced within the framework of probabilistic risk assessment, an importance that is further highlighted when dealing with crucial structures and complex systems such as dams (Hariri-Ardebili, 2024). There are various classifications of sources of uncertainty, each offering unique perspectives. In this context, we will briefly discuss these classifications.

The classification of uncertainties divides variables into two fundamental categories: epistemic uncertainties and aleatory uncertainties. Aleatory uncertainty, also known as objective uncertainty (Ang, 1997), encompasses the intrinsic randomness of phenomena. Within the context of seismic analysis for concrete dams, uncertainties associated with earthquake events (such as earthquake intensity, timing, and recurrence) are of paramount importance, constituting significant uncertain parameters (Der-Kiureghian and Ditlevsen, 2009). Aleatory uncertainty is typically measured using random variables (RVs) within the mathematical framework of probability theory (Ang and Tang, 2007). On the other hand, epistemic uncertainty, or subjective uncertainty, emerges from gaps in knowledge and can be divided into two types: recognized and blind uncertainties. Examples of the recognized uncertainties pertaining to material properties, such as concrete fracture energy. This category encompasses various sources, including model and statistical uncertainty. Epistemic uncertainty associated with continuous random variables can be quantified using probability density functions.

In the structural analysis of dams, uncertainty sources can be categorized into three groups related to loading uncertainty, randomness in material properties, and modeling uncertainties. Given the focus of this paper on the seismic assessment of concrete dams, the term "loading uncertainty" pertains specifically to the variability in ground motion records from one seismic event to another, commonly known as record-to-record (RTR) variability (Hariri-Ardebili and Saouma, 2016). Material property uncertainties play a significant role in seismic analysis, affecting structural components and systems¹. Variability in material attributes is often represented using statistical distributions, including mean, and standard deviation, and can appear in the form of multivariate correlation (Sevieri, 2021) and spatial correlation (Hariri-Ardebili et al., 2019).

¹ In the context of structural engineering problems, it's essential to note that 'systems' refer to the interconnected network of structural components, whereas 'components' pertain to individual elements.

The primary focus of this paper, however, centers solely on modeling uncertainty quantification. In seismic analysis of dams, modeling uncertainty predominantly arises from the limitations of an idealized computational model to accurately forecast the actual behavior of dam structures subjected to ground motions. Bradley's (2011 and 2013) framework outlines four levels of modeling uncertainties, as illustrated in Figure 1:

- Level 1 Uncertainty: This category encompasses uncertainties in the measurement of physical quantities, such as the mechanical properties of concrete or the estimation of soil shear stiffness. Level 1 uncertainty hinges solely on the quality of physical experiments and doesn't directly affect conceptual model preparation. Nonetheless, since these measurements serve as input parameters in the modeling, they exert influence on the final response quantities.
- Level 2 Uncertainty: At this level, uncertainty arises from the correlation between measurable physical quantities and the constitutive model parameters. For instance, while concrete compressive strength is commonly measured from core samplings, several constitutive models may necessitate knowledge of the tensile strength directly. As evident, the level 2 modeling uncertainty is similar to material randomness.
- Level 3 Uncertainty: This level encapsulates the uncertainty inherent in selecting a constitutive model, involving project-specific assumptions and simplifications. Constitutive models are often crafted either empirically based on observations or theoretically derived via specific assumptions. In the context of concrete dams, a variety of options exist in simulation material behavior, such as smeared crack models, plasticity models, and damage mechanics models to address concrete cracking and crushing during seismic loads.
- Level 4 Uncertainty: This category involves uncertainty in the overall methodology of the idealized model. For instance, it encompasses decisions such as employing 3D models for dams with narrow valleys versus using 2D plane strain models. Other examples include considerations like accounting for dam-foundation or dam-reservoir interactions. For dam-reservoir interaction, hydrodynamic pressure could be determined using fluid-structure interaction or using a simplified Westergaard approach. In the simulation of the seismic wave propagation in the mass foundation, assumptions regarding boundary conditions, damping properties, and ground motion input, also contribute to this category.

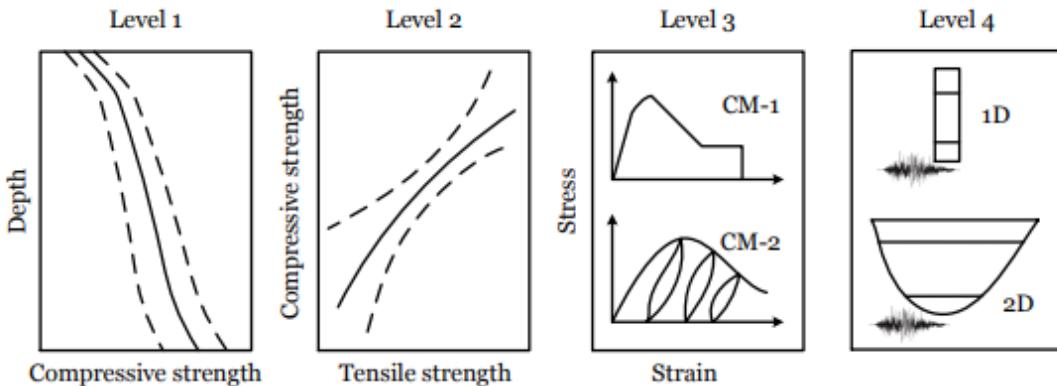


Figure 1. Examples of the four different types of uncertainties in the case of a seismic response analysis of concrete dams; CM: constitutive model; adapted from Bradley (2011)

The integration of uncertainty sources offers a more comprehensive representation of systems, circumventing unwarranted assumptions in their amalgamation. Presently, a notable portion of combined uncertainty studies in dam engineering merges material randomness and RTR variability (Sevieri et al., 2020) or addresses lower-level modeling uncertainties (levels 1 and 2) alongside RTR variability. However, relying solely on these simplified approaches, rather than considering more intricate ones like higher-level modeling uncertainties (levels 3 and 4), can be problematic. These simplified approaches confine uncertainties to material and model

parameters within the constitutive model, disregarding more complex uncertainties such as varying constitutive models and modeling strategies.

3. Illustration of Level of Uncertainties using a Benchmark Problem

Given the emphasis on modeling uncertainty, a crucial question arises: "Does employing a modeling technique that disregards essential physics align with robust uncertainty analysis principles?" To address this query, this paper conducts an inaugural investigation of outcomes from a meticulously structured benchmark workshop. For illustration of the level of uncertainties, a case study of Pine Flat Dam is presented. The dam was the subject of extensive study during the 1970s and 1980s at the University of California at Berkeley (Rea et al., 1972), Chopra et al., 1980, Chavez and Fenes, 1993) and was selected as a theme of the 15th ICOLD Benchmark Workshop (Salamon et al., 2021).

This workshop design strategically isolates Level 3 and Level 4 modeling uncertainties by offering participants comprehensive data. The benchmark includes dam geometry, corresponding finite element mesh, essential material properties, and various reservoir water levels. Required loading scenarios encompass seismic loads, with both surface and foundation-based excitation provided, alongside damping value recommendations.

This extensive dataset provided to participants eliminates ground motion RTR variability, material randomness, and Level 1 and Level 2 modeling uncertainties within the benchmark. Participants are granted the freedom to select any finite element software for analysis, explore diverse approaches for modeling the foundation and reservoir sections and their interactions with the dam, consider wave propagation complexities, implement various boundary conditions, opt for different numerical solvers (such as implicit or explicit methods), and decide on concrete constitutive models and damage behaviors, among other factors. These considerations collectively fall under the umbrella of level 3 and 4 modeling uncertainties.

Pine Flat Dam is a gravity dam constructed by the US Army Corps of Engineers in 1954 in California, and it comprises thirty-six monoliths, of which thirty-six are 15.25 m-wide and one measures 12.2 m-wide. The dam is about 561 m wide and its structural height is about 122 m as shown in Figure 2.

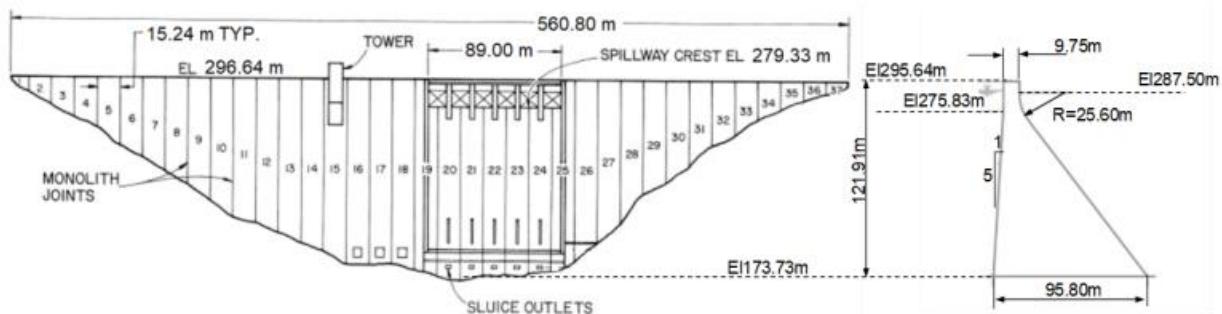


Figure 2. Downstream view and cross-section geometry of monolith No. 16 of Pine Flat Dam; adapted from Salomon et al. (2021).

In the formulation of the benchmark Pine Flat Dam model, the tallest non-overflow monolith was selected, and the foundation block dimensions were specified as 700 m by 122 m. Material properties, as outlined in Table 1, were presumed homogeneous and isotropic for both the concrete and rock components. Static load considerations encompass solely the weight of concrete and water. The benchmark contributors were directed to incorporate viscous damping based on their prevailing comprehension, modeling conventions, and chosen analytical methods, with an expectation for thorough documentation. For nonlinear simulations, contributors were encouraged to explore the utilization of Rayleigh viscous damping, with a recommended value of 2% applied to both the dam and foundation. The dam-foundation interface was fully connected, thereby precluding any potential sliding.

A real ground motion record (the M 7.3 Kern County, California earthquake on July 21, 1952, recorded at the Lincoln School in Taft) was provided to be used for seismic simulations. Given the assumption that this signal

represents free surface conditions, its deconvolved counterpart is also included. The deconvolution procedure assumes a vertically propagating shear wave (SH) within a uniform half-space characterized by the same material properties as the foundation. The free-surface motions are suitable for input in massless foundation models, whereas the deconvolved signals are intended for employment in massed foundation models. Figure 3 illustrates the acceleration, velocity, displacement, and force time histories of the Taft ground motion, accompanied by the 2% acceleration response spectrum.

Table 1. Materials properties in the Pine Flat Dam model (Salamon et al., 2021)

	Parameter	Symbol	Unit	Quantity
Concrete	Modulus of elasticity	E_c	MPa	22,410
	Poisson's ratio	ν_c	—	0.2
	Mass density	ρ_c	Kg/m ³	2,483
	Compressive strength	f_c	MPa	28.0
	Tensile strength	f_t	MPa	2.0
	Fracture energy	G_f	N/m	250
	Compressive strain at peak load	ϵ_c	—	0.0025
Rock	Tensile strain at peak load	ϵ_t	—	0.00012
	Modulus of elasticity	E_f	MPa	22,410
	Poisson's ratio	ν_f	—	0.33
	Mass density	ρ_f	Kg/m ³	2,483
	Shear wave velocity	V_S	m/s	1,939
Water	Compressional wave velocity	V_P	m/s	3,167
	Mass density	ρ_w	Kg/m ³	1,000
	compression wave velocity	C_w	m/s	1,439
	Winter water height	L_W	m	El. 268.21
	Summer water height	L_S	m	El. 278.57
	Normal water height	L_N	m	El. 290.00

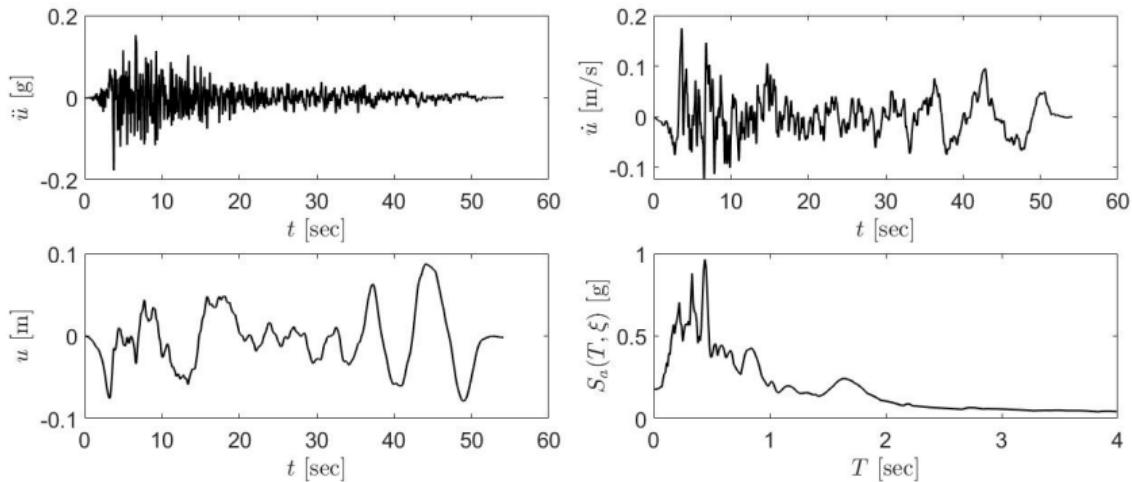
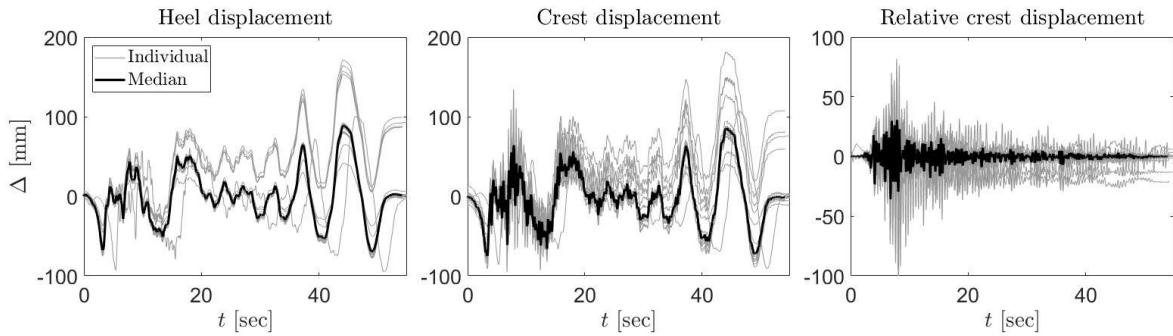


Figure 3. Acceleration, velocity, displacement free-surface records, and the response spectrum of the TAFT ground motion

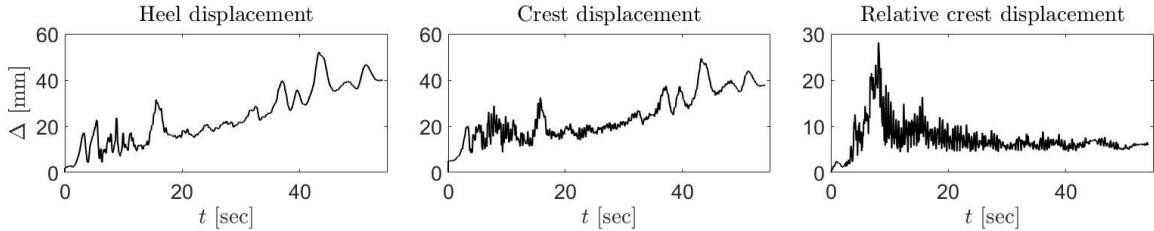
4. Analysis and Synthesis of Benchmark Results

The benchmark studies in their original form covered a wide range of assessments including the frequency analysis of the dam, wave propagation in the foundation model, and linear and nonlinear analysis of the dam-foundation-water system with different pool elevations. This section presents a concise overview of the outcomes obtained from nonlinear seismic analysis subjected to Taft ground motion record. The following scalar and vector quantities were analyzed: dam crest and heel displacements, relative crest displacement

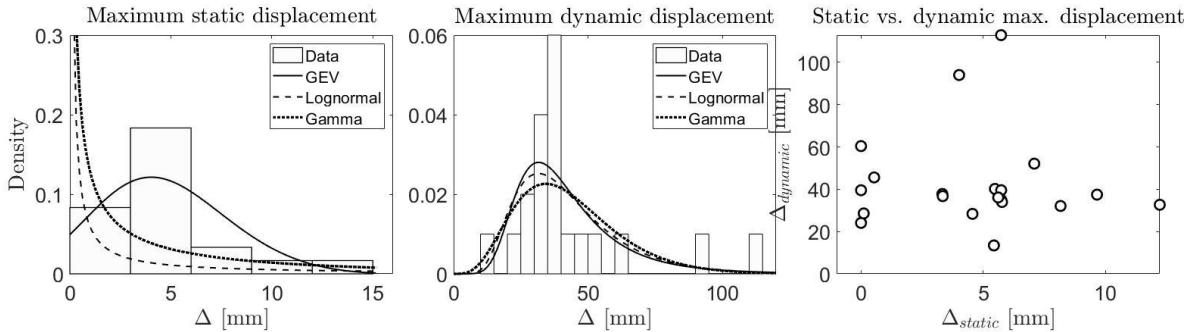
compared to heel, net hydrodynamic pressure at the dam's heel, ratio of crest-to-heel amplitude acceleration spectrum, crack profile, and damage index (DI). The data analyzed in this paper is derived from the findings presented in the individual publications, as well as the summary report (Salamon et al., 2021). The key modeling variations observed across each study include mesh type (2D, 3D slice, full 3D), mesh size (which holds significance for damage index assessment), time step utilized in the numerical simulation, criteria for convergence, the specific foundation model and its associated boundary conditions for wave propagation and absorption (including considerations for the free-field), choice of fluid element and approach for fluid-structure interaction (FSI), the selected concrete constitutive model and its response to dynamic loading-induced damage, the time integration scheme employed for stability control, and finally, the software package employed for analysis.



(a) *Detailed displacement time history at different locations and the median response.*



(b) *Standard deviation of displacement response at different locations.*



(c) *Distribution of different displacement quantities and their relationship.*

Figure 4. Processing displacement response under real ground motion record.

Figure 4 presents a summary of the results collected from 20 contributors, illustrating the displacement response. Before statistical analysis, all results underwent initial data filtering, and any outliers were subsequently removed. Individual displacement time histories for both the heel and crest, along with the relative crest displacement, are shown in Figure 4(a). This figure also highlights the median values. The heel and crest displacements exhibit large oscillations, while the relative displacement demonstrates a high-frequency nature. Four models exhibit residual displacements at both the heel and crest points, which can

indicate either relative sliding between the dam and the foundation block or a rigid body motion of the entire finite element model due to inadequate boundary conditions. This issue can often be resolved by introducing a self-equilibrium loading condition, such as elastic boundary conditions, to one side of the foundation (Saouma and Hariri-Ardebili, 2021). Among these four models, three employ viscous boundary conditions for the foundation, with one of them utilizing infinite elements. Additionally, one simulation exhibits a temporal shift and employs infinite elements for the foundation, including the rock column and direct free field forces. In terms of the relative crest displacement history, two models exhibit residual displacement, both of which involve infinite elements. Notably, the most substantial relative crest displacement arises in a model utilizing a massless foundation approach with fixed boundary conditions. This case yields a maximum relative crest displacement approximately 2.5 times higher than the median value. This observation aligns with prior findings that distinguish between massed and massless foundation models (Saouma and Hariri-Ardebili, 2021).

Figure 4(b) illustrates the standard deviation of displacement histories for both absolute and relative measurements. The absolute displacements at both the heel and crest locations exhibit a nearly linear increasing pattern, punctuated by intermittent spikes along this trajectory. Within the strong motion interval of the analysis (5-15 seconds), these displacements demonstrate standard deviations ranging from 10 to 30 mm. The highest standard deviation is approximately 50 mm, which can be compared to the previously mentioned median displacement of around 100 mm. In contrast, the pattern for the standard deviation of the relative crest displacement differs. Here, the maximum standard deviation occurs around 10 seconds (coinciding with the peak ground motion), followed by a decrease to a smaller and relatively stable value for the rest of the simulation.

All the previous comparisons have been conducted exclusively on ``dynamic only'' results, excluding the static response. Figure 4(c) provides a comprehensive overview of the maximum static and maximum dynamic displacement responses separately, along with three distributional models fitted to the data. The choice of using the generalized extreme value (GEV), lognormal, and gamma distributions is arbitrary, as the goal here is not to determine the most suitable fit based on goodness-of-fit metrics. Given the limited scope of the database used in this study, any conclusion drawn from these models should not be regarded as definitive. As we will explore later in this section, except for static displacement, these three models yield similar outcomes for all other cases. For maximum static displacement, the GEV model appears more reasonable, since the other two models result in very small mean or median values. Additionally, it is worth noting that the lognormal distribution is commonly employed in the fields of structural and earthquake engineering to describe the distribution of engineering demand parameters (Jalayer and Cornell, 2009).

For the maximum static (relative) displacement, the values vary from 0.2 mm to over 12 mm. The GEV model has a location value of 3.4 mm, which is close to the crude mean of 4.6 mm. Concerning the maximum dynamic displacement, values range from 13 mm to 112 mm, with a crude mean of 43 mm. All three distribution models exhibit striking similarities. The GEV model's μ (location) value is 33 mm, while the lognormal model's median is 39 mm, and the logarithmic standard deviation is 0.45. This value coincides with the recommendations from FEMA P695 (2010) regarding modeling uncertainty. EMA P695 characterizes modeling uncertainty through a matrix with two dimensions: (1) Representation of collapse characteristics and (2) Accuracy and robustness of models. Each dimension encompasses three levels: high, medium, and low. For scenarios with a low representation of collapse and medium model accuracy (a condition that can be argued to apply in this study), a dispersion of 0.5 is recommended, which is analogous to the logarithmic standard deviation in the lognormal distribution. It's important to note that while this comparison is approximate, as FEMA P695 pertains directly to buildings and not concrete dams, there are similarities between them, as a concrete gravity dam functions as a cantilever-type short-period multi-degree-of-freedom system.

Lastly, Figure 4(c) (left) depicts the correlation between the maximum static and dynamic displacements. As seen, there is minimal correlation observed across different models. The static displacement is primarily influenced by hydrostatic pressure and the dam's self-weight, along with the stiffness of the foundation. It's worth mentioning that in certain instances, the hydrostatic pressure is applied solely to the dam, while in others, it is also applied to the upper face of the foundation.

Figure 5(a) employs a similar approach to the acceleration response analysis as discussed for displacement in Figure 4. Acceleration at the heel and crest points is depicted in Figure 5(a) (left and middle). Ideally, the acceleration at the heel should be similar to or close to the free-surface Taft record displayed in Figure 3.

However, the median of the recorded heel acceleration exhibits a smaller value. This discrepancy can be attributed to the modeling uncertainty in the foundation and its boundary conditions, including the free-field assumptions. As anticipated, the acceleration at the crest is amplified by approximately 10 times. To better represent the heel and crest acceleration time histories, they are presented as amplitude spectra in Figure 5(a) (right), showing the ratio of the acceleration amplitude spectrum. This ratio is obtained by computing the Fourier spectrum of the acceleration time series.

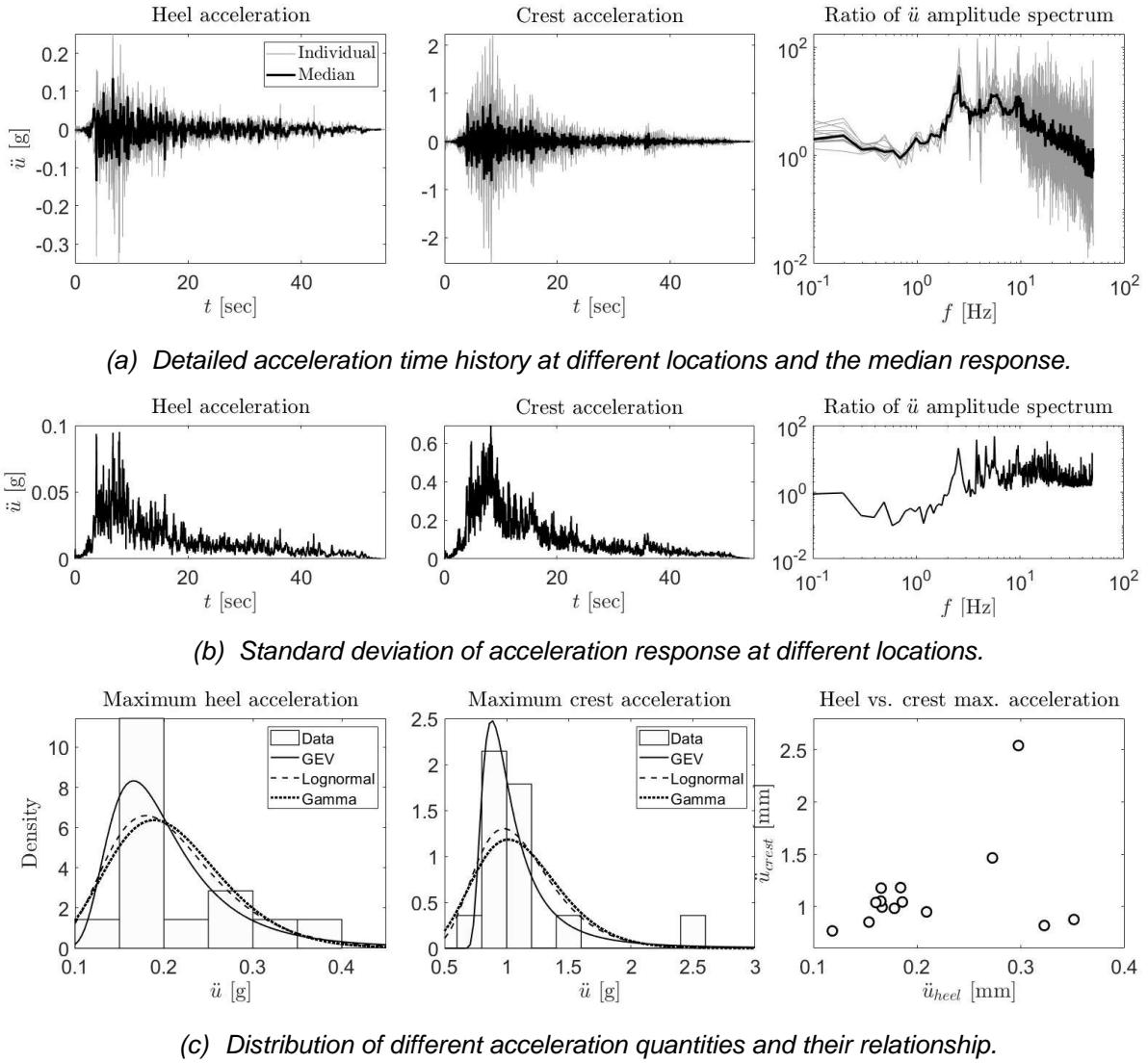


Figure 5. Processing acceleration response under real ground motion record.

For frequencies below 1 Hz, the median response ratio is around 2. Between the frequency range of 5 to 10 Hz, the ratio fluctuates between 3 and 30, with an average value of 10. Beyond 10 Hz (up to about 50 Hz), the ratio gradually decays linearly to 0.5. Among the individual models, three show significant spikes, such as 170, in the amplitude spectrum ratio. Notably, all three models lack free-field boundary conditions.

The standard deviation of the heel and crest acceleration time series follows a similar trend as displacement, peaking at the heel with a value of 0.1 g, equal to the median acceleration. The standard deviation of acceleration spectrum amplitude averages around 0.8 for frequencies below 2 Hz, and then increases to an average value of 5 for $f > 2$ Hz, accompanied by fluctuations.

The fitted distributions for maximum (absolute) heel and crest accelerations are shown in Figure 5(c) (left and middle). The lognormal and gamma models show close agreement, while the GEV model exhibits a minor difference. Based on the lognormal distribution, the median values for maximum heel and crest accelerations are 0.2 g and 1.07 g, respectively. The logarithmic standard deviation (dispersion) in both cases is approximately 0.3, which is lower than the displacement-based dispersion. Finally, Figure 5(c) (right) illustrates the relationship between maximum acceleration at the heel and crest. Except for two outliers, a positive correlation is evident. Further analysis of these two outliers indicates that both suffer from spikes in their heel acceleration responses, which can be attributed to numerical integration issues or the presence of superstructure (i.e., the dam) at the recording location.

Figure 6 employs a similar approach to analyze the hydrodynamic pressure, P_{hyd} , at the heel of the dam. Unlike the displacement response, no instances of residual or shifted values are observed for this parameter. The ratio of the maximum P_{hyd} to the median value is approximately 2. The trend in standard deviation is comparable to that observed for the relative crest displacement, with a peak value of around 0.15 MPa. It is noteworthy that the maximum P_{hyd} in the median response is even lower than 0.15 MPa. Lastly, Figure 6 (right) presents the distribution of the maximum P_{hyd} , which is consistent across the three distribution models. The lognormal model yields a median value of 0.16 MPa and a logarithmic standard deviation of 0.3, indicating less variation compared to the displacement response.

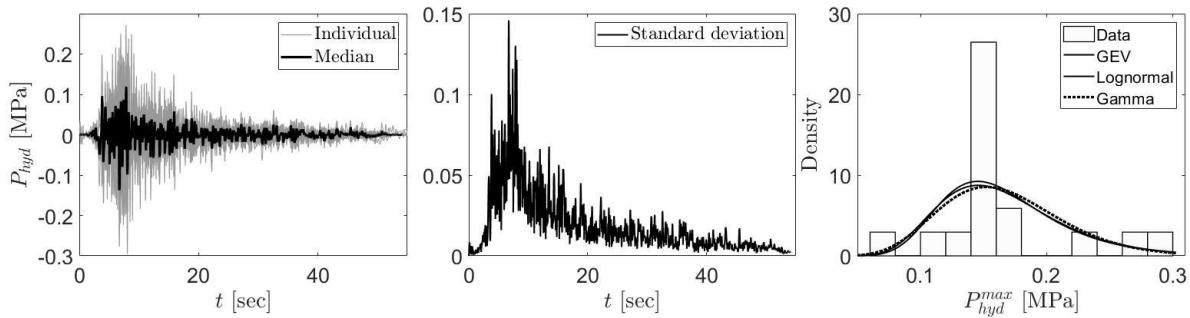


Figure 6. Processing hydrodynamic pressure response under real ground motion record.

Figure 7 provides the damage index for different simulations. Damage at the dam base (i.e., dam-foundation interface) is quantified as the ratio of cracked length to the total base length (Hariri-Ardebili and Saouma, 2014), $DI_{length} = L_{cr} / L_{tot}$. As seen in this figure, some simulations do not report any damage while some others report as large as 18%. The median value from all simulations is about 4.5%.

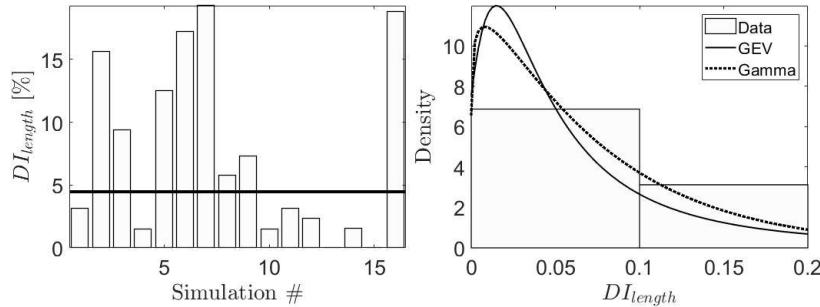


Figure 7. Processing damage index under real ground motion record.

Figure 8 illustrates the potential damage profiles of the dams under the influence of the Taft ground motion record. A range of techniques has been employed to assess the damage, including concrete damage plasticity, Drucker-Prager model, strain-based crack model, anisotropic damage model with Rankine criteria, a discrete crack model with bilinear softening, equivalent linearization technique, micro-plane-based coupled damage plasticity, and concrete plasticity with Menetrey-Willam criterion, among others. While some models indicate no damage, the majority predict damage at the heel and occasionally at the downstream neck.

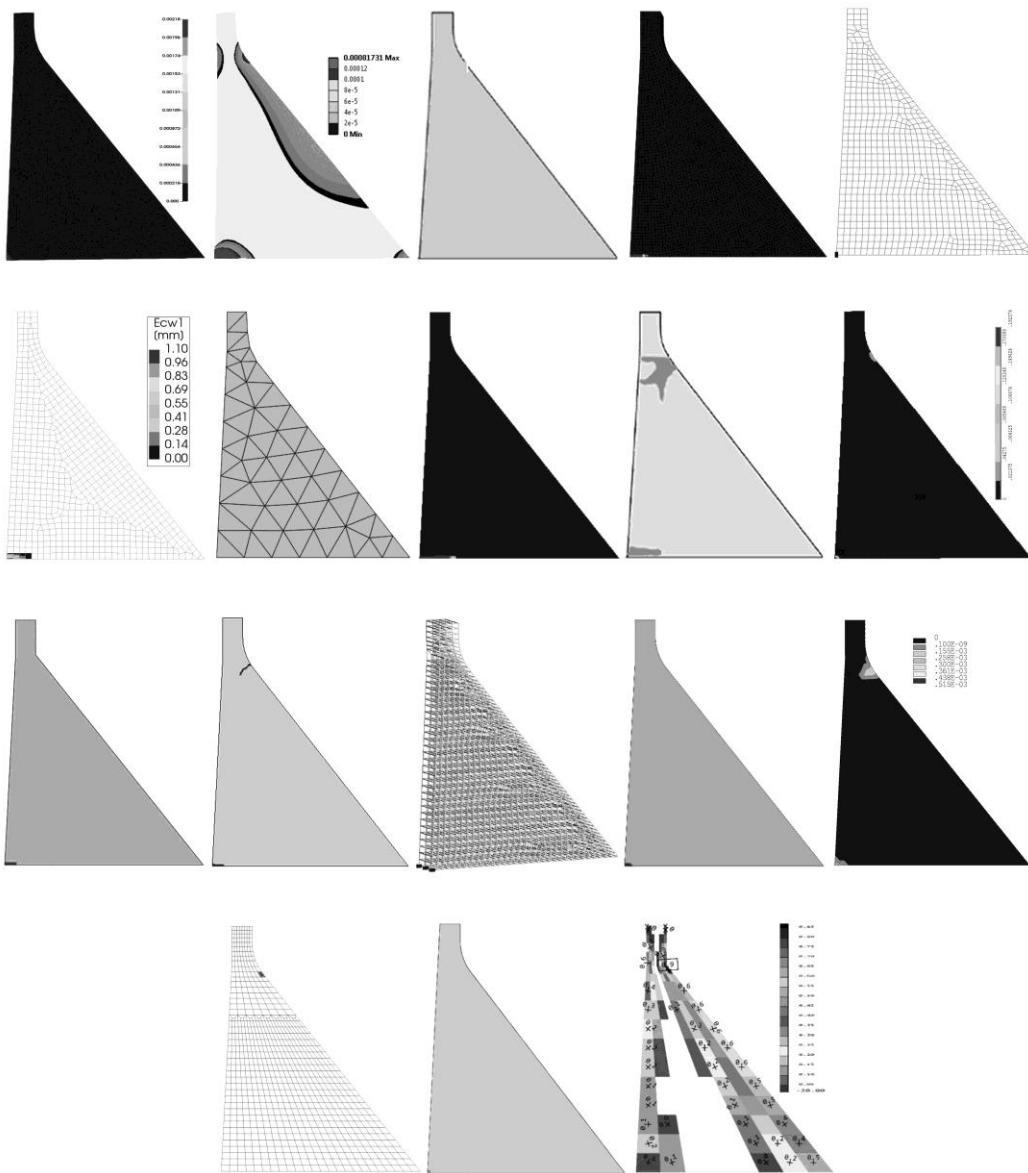


Figure 8. Potential damage profile of dam subjected to Taft ground motion record (Salamon et al., 2021)

5. Conclusions

Static or dynamic analysis with non-linearities plays an important role in structural assessments of concrete dams. Over the past two decades, time history simulations incorporating material and geometric non-linearities, as well as far-field boundary conditions, have gained increasing prominence in engineering practice for concrete dams. However, the paramount concern remains the level of confidence in these modeling approaches, contingent upon the estimation of accuracy and the quantification of uncertainties in analysis results.

In this paper, we have investigated the multifaceted realm of uncertainties associated with the analysis of concrete dams. Our investigation, with a particular focus on the Pine Flat Dam benchmark and real ground motion analysis, provides an engineering perspective on the subject. While this paper may not comprehensively encompass all aspects of uncertainties, it serves as a catalyst for the ongoing discourse aimed at formulating a unified approach for characterizing uncertainties in the analysis of concrete dams.

Within the computational models utilized for structural analyses of concrete dams, the principal uncertainties revolve around the selection of appropriate input parameters, the adoption of suitable analysis methods, the precision of the solution, and the interpretation of analysis outcomes. The presentation of varying levels of uncertainties in dynamic non-linear analyses of concrete dams serves as a primary avenue for assessing accuracy, thereby bolstering confidence and credibility in modeling and computational simulations.

To enhance confidence in modeling and computational simulations for concrete dams, key recommendations are: (1) Fluid-Structure Interaction (FSI): Prioritize accurate hydrodynamic pressure representation on the dam's upstream face using compressible fluid elements in advanced analyses. (2) Foundation-Dam Interaction: Use appropriate non-reflecting boundary conditions, with a preference for free-field boundaries, to address foundation-dam dynamics, crucial for dam safety assessment. (3) Incorporate Nonlinearity: For intense seismic scenarios, introduce nonlinearity. Apply cohesive crack models at known crack/joint locations or use continuum damage models for the entire dam. (4) Meshing and Time Integration: Pay attention to mesh type/size (finer near potential crack sites), time step, convergence criteria, time integration schemes, and damping models, especially in nonlinear analyses. (5) Detailed Considerations: Account for factors like stage construction, reservoir impounding, thermal stresses, and reservoir bottom wave reflection coefficient.

6. References

- Ayyub, B.M. and Chao, R.U., 1997. Uncertainty modeling in civil engineering with structural and reliability applications. *Uncertainty modeling and analysis in civil engineering*, pp.1-8.
- Ang, A.H.S., 1970. Extended reliability basis of structural design under uncertainties (No. 700656). SAE Technical Paper.
- Ang, A.H.S. and Tang, W.H., 2007. Probability concepts in engineering: emphasis on applications in civil and environmental engineering. Wiley.
- Alves, S.W. and Hall, J.F., 2006. System identification of a concrete arch dam and calibration of its finite element model. *Earthquake engineering & structural dynamics*, 35(11), pp.1321-1337.
- Applied Technology Council, 2009. Quantification of building seismic performance factors. US Department of Homeland Security, FEMA.
- Bradley, B.A., 2011. A framework for validation of seismic response analyses using seismometer array recordings. *Soil Dynamics and Earthquake Engineering*, 31(3), pp.512-520.
- Bradley, B.A., 2013. A critical examination of seismic response uncertainty analysis in earthquake engineering. *Earthquake engineering & structural dynamics*, 42(11), pp.1717-1729.
- Bukanya, P., Moyo, P., Beushausen, H. and Oosthuizen, C., 2014. Health monitoring of concrete dams: a literature review. *Journal of Civil Structural Health Monitoring*, 4, pp.235-244.
- Bulleit, W.M., 2008. Uncertainty in structural engineering. *Practice Periodical on Structural Design and Construction*, 13(1), pp.24-30.
- Bolzon, G., Sterpi, D., Mazzà, G. and Frigerio, A. eds., 2020. Numerical Analysis of Dams: Proceedings of the 15th ICOLD International Benchmark Workshop (Vol. 91). Springer Nature.
- Chopra, A.K., Chakrabarti, P. and Gupta, S., 1980. Earthquake response of concrete gravity dams including hydrodynamic and foundation interaction effects (p. 0202). Earthquake Engineering Research Center, College of Engineering, University of California.
- Chavez, J.W. and Fenves, G.L., 1993. Earthquake analysis and response of concrete gravity dams including base sliding. Earthquake Engineering Research Center, University of California.
- Der Kiureghian, A. and Ditlevsen, O., 2009. Aleatory or epistemic? Does it matter?. *Structural safety*, 31(2), pp.105-112.

- Harris, D.W., Snorteland, N., Dolen, T. and Travers, F., 2000. Shaking table 2-D models of a concrete gravity dam. *Earthquake Engineering & Structural Dynamics*, 29(6), pp.769-787.
- Hariri-Ardebili, M.A. (2024). Quantifying modeling uncertainties in seismic analysis of dams: Insights from an international benchmark study. *Earthquake Engineering & Structural Dynamics*.
- Hariri-Ardebili, M.A. and Saouma, V.E., 2016. Probabilistic seismic demand model and optimal intensity measure for concrete dams. *Structural Safety*, 59, pp.67-85.
- Hariri-Ardebili, M.A., Seyed-Kolbadi, S.M., Saouma, V.E., Salamon, J.W. and Nuss, L.K., 2019. Anatomy of the vibration characteristics in old arch dams by random field theory. *Engineering Structures*, 179, pp.460-475.
- Hariri-Ardebili, M.A. and Saouma, V., 2015. Quantitative failure metric for gravity dams. *Earthquake Engineering & Structural Dynamics*, 44(3), pp.461-480.
- Jalayer, F. and Cornell, C.A., 2009. Alternative non-linear demand estimation methods for probability-based seismic assessments. *Earthquake Engineering & Structural Dynamics*, 38(8), pp.951-972.
- Melchers, R.E. and Beck, A.T., 2018. Structural reliability analysis and prediction. John Wiley & Sons.
- Rea, D., Liaw, C.Y. and Chopra, A.K., 1972. Dynamic properties of pine flat dam (p. 0083). Earthquake Engineering Research Center, University of California.
- Salamon, J.W., Wood, C., Hariri-Ardebili, M.A., Malm, R. and Faggiani, G., 2021. Seismic analysis of pine flat concrete dam: formulation and synthesis of results. In Numerical Analysis of Dams: Proceedings of the 15th ICOLD International Benchmark Workshop 15 (pp. 3-97). Springer International Publishing.
- Salamon, J., 2018. Evaluation of Numerical Models and Input Parameters in the Analysis of Concrete Dams, Technical Report DSO-19-13, U.S. Bureau of Reclamation, Denver, Colorado.
- Saouma, V.E. and Hariri-Ardebili, M.A., 2021. Aging, Shaking, and Cracking of Infrastructures: From Mechanics to Concrete Dams and Nuclear Structures. Springer Nature.
- Sevieri, G., De Falco, A., Andreini, M. and Matthies, H.G., 2021. Hierarchical Bayesian framework for uncertainty reduction in the seismic fragility analysis of concrete gravity dams. *Engineering Structures*, 246, p.113001.
- Sevieri, G., De Falco, A. and Marmo, G., 2020. Shedding light on the effect of uncertainties in the seismic fragility analysis of existing concrete dams. *Infrastructures*, 5(3), p.22.
- Uchita, Y., Shimpo, T. and Saouma, V., 2005. Dynamic centrifuge tests of concrete dam. *Earthquake Engineering & Structural Dynamics*, 34(12), pp.1467-1487.

UNDERSTANDING THE ROLE OF STRESS-DEPENDENT MATERIAL DAMPING IN SEISMIC ANALYSIS OF CONCRETE DAMS

M.A. Hariri-Ardebili¹, M. Noorbakhsh-Saleh², S.M. Seyed-Kolbadi³ & F. Pourkamali-Anaraki⁴

¹ University of Maryland, College Park, MD, USA, hariri@umd.edu

² University of Hawaii, Manoa, USA

³ X-Elastica LLC, Boulder, CO, USA

⁴ University of Colorado, Denver, CO, USA

Abstract: Seismic analysis of concrete dams involves numerous parameters and assumptions that can significantly impact both the local and damage responses. One such parameter is structural damping, which is challenging to quantify accurately in large-scale structures and is typically assumed in dynamic analyses. The damping model, including its formulation and value, remains unknown during numerical modeling. This paper presents the implementation of a variable material damping model in the dynamic analysis of concrete dams. In this model, the damping ratio is determined as a function of the maximum principal stress at the structural and elemental levels and is iteratively updated at different time increments. The Koyna Dam is utilized as a case study to illustrate the effects of damping redistribution and various factors associated with the formulation on damage response and crest displacement variability. The research emphasizes the significance of stress-dependent material damping and the resultant response uncertainty for large-scale structures. By addressing these aspects, the study contributes to enhancing our understanding of seismic behavior in concrete dams and improving their seismic design and analysis methodologies.

1. Introduction

Understanding and accurately modeling the seismic response of concrete dams is paramount for ensuring their safety and resilience during earthquake events. Seismic analysis of concrete dams involves the consideration of various parameters, each contributing to the complex interplay of forces and responses. Those factors include fluid-dam-rock interaction, wave propagation, concrete damage model, etc. Among these parameters, the damping mechanism stands out as a critical factor that significantly influences the dynamic behavior of the dam under seismic loading.

Damping in concrete dams is particularly challenging to model due to its stress-dependent nature. The accurate quantification of damping is essential for dynamic analyses, where it directly impacts the amplitude and duration of structural vibrations. In seismic analysis, damping is often assumed rather than precisely determined, introducing uncertainties into the predictions of structural response. This paper focuses on unraveling the intricate relationship between stress-dependent material damping and the seismic behavior of concrete dams. Specifically, it introduces a variable material damping model, wherein the damping ratio is iteratively updated as a function of the maximum principal stress at both the structural and elemental levels.

The significance of stress-dependent material damping becomes apparent as it contributes to the overall uncertainty in seismic response predictions for large-scale structures. By exploring the effects of damping redistribution and considering various factors associated with its formulation, this study aims to shed light on the nuanced dynamics of concrete dams during seismic events.

2. Damping Modeling

Damping is a mechanism causing energy loss in structures from earthquakes, wind, or other sources (Jeary, 1997). Various models exist, each associated with uncertainties in their applications. This section addresses the modeling and uncertainties in damping mechanisms.

1.1. Damping Sources and Mechanisms

While different classifications exist for damping, Kareem (1996) identified three main types: structural, aerodynamic, and hydrodynamic damping. Structural damping measures the energy dissipation in a vibrating structure, bringing it to a quiescent state. Aerodynamic or hydrodynamic damping is experienced by structures vibrating in air or water, with both sources potentially contributing simultaneously to marine structures. Among various structural damping mechanisms, the most significant ones include material damping, interfacial (or frictional) damping, and hysteretic damping (Nashif et al., 1985).

- Material damping: This contribution arises from complex molecular interactions within the material and depends on the type of material, manufacturing methods, and finishing processes (Kareem, 1996; Alipour et al., 2008). The model is generally applicable for low strain rates of loading and linear behavior of structures (Jayamon et al., 2018). Estimating material damping is complicated due to variations in microscopic properties among samples.
- Interfacial damping: Developed through sliding contact between different connected components, interfacial structural damping contributes more than material damping and is highly nonlinear. Energy dissipation mechanisms through the structure are primarily displacement-dependent, making friction damping the most appropriate formulation.
- Hysteretic damping: Sometimes modeled separately by capturing energy dissipation in a cycle independent of frequency.

1.2. Generic Damping Models

One of the most general forms used for damping is $f_d(x, \dot{x}) = \alpha \dot{x} |\dot{x}|^{\theta-1}$, where f_d is the damping force, α is the damping coefficient, θ determines the damping model, and x, \dot{x} are displacement and velocity terms, respectively. Three main forms can be obtained as follows (the equivalent viscous damping - EVD - is also given):

$$f_d(x, \dot{x}) = \begin{cases} \mu \text{sign}(\dot{x}) & \theta = 0 \quad (\text{coulomb damping}) \xrightarrow{\text{EVD}} \frac{2\mu}{\pi m \omega^2 A} \\ c \dot{x} & \theta = 1 \quad (\text{viscous damping}) \xrightarrow{\text{EVD}} \frac{c}{\pi m \omega} \\ q \dot{x} |\dot{x}| & \theta = 2 \quad (\text{quadratic damping}) \xrightarrow{\text{EVD}} \frac{4qA}{3\pi m} \end{cases} \quad (1)$$

where μ and c are the Coulomb and viscous damping coefficients, and A the amplitude of motion.

1.3. Viscous Damping

Viscous damping assumes that the global energy-dissipating characteristics of a structure are only proportional to its dynamic degrees of freedom velocities (Alipour et al., 2008). While mathematically convenient, this model's mechanism cannot be observed in real structures (Jeary, 1997). Therefore, the determination of viscous damping coefficients is not derivable; instead, it relies on a combination of empirical data from building measurements, tests, and analyses, along with judgment (ATC, 2017). Two main types of viscous damping exist Rayleigh and modal damping. Due to the empirical nature of assumed damping (sometimes referred to as equivalent viscous damping), the differences between these types are also a matter of judgment.

Rayleigh damping: This is the most common form in structural engineering but not without drawbacks (Hall, 2006), to account for energy dissipation characteristics of the structure. Considering the general form of $C = \alpha M + \beta K$, various options to use Rayleigh damping are:

- Initial stiffness-proportional damping (K_0)
- Tangent stiffness-proportional damping (K_T)
- Mass-proportional damping (M)
- Mass-stiffness with initial stiffness-proportional damping ($M + K_0$)
- Mass stiffness with tangent stiffness-proportional damping ($M + K_T$)

The original Rayleigh damping model produces unrealistically large damping forces which lead to non-conservative force/displacement demands and overestimation of structural collapse capacities. Salehi (2020) classified those forces into three categories:

- Damping forces resulting from an increase in the damping ratios of the lower modes after yielding,
- Damping reactions at massless degrees of freedom, usually rotations,
- Large damping reactions due to the generation of large velocities at the onset of yielding

Caughey damping (Caughey and O'Kelly, 1965) is an n -parameter model allowing the selection of damping ratios at any n number of modes and predicting the damping ratios at all remaining modes.

Wilson-Penzien damping (Wilson and Penzien, 1972) addressed the numerical instabilities in the calculation of the coefficients in the Caughey model.

Modal damping: This is equivalent to that used in linear modal time-history analysis. With the general form of $C = M^T \left(\sum_{n=1}^N \frac{2\zeta_n \omega_n}{M_n} \phi_n \phi_n^T \right) M$, different modal damping ratios, ζ_n , can be assigned to each mode independently.

1.4. Structural vs. Elemental Level

While classical applications of damping models primarily operate at the structural level (applying the same damping value to all components in the numerical model), an alternative approach considers varying damping at the elemental level. Puthanpurayil et al. (2016) introduced two elemental level discrete damping models, adapted from their global counterparts, for nonlinear analysis of frame structures. They further extended this method based on local and non-local elasticity approaches (Puthanpurayil et al., 2018). In these models, the damping stress at a point in space is a function of the strain history at that point.

1.5. Damping Uncertainties

Various sources of uncertainties are associated with damping in structural engineering. Concerning Rayleigh damping, a widely used model in practical problems, several solutions have been proposed to address inherent uncertainties:

- Bernal (1994) advocates for using initial stiffness-proportional damping for inelastic systems, relating the spurious behavior of damping mechanisms to the appearance of large damping forces at degrees of freedom (DOFs) with small inertias.
- Hall (2006) proposes eliminating the mass-proportional part and using bounded stiffness-proportional damping.
- Charney (2005, 2008) offers multiple solutions:
 - Using the stiffness-proportional part based on the diagonal terms of the initial stiffness matrix,
 - Eliminating viscous damping entirely and using nonlinear frictional or hysteretic damping,
 - Using tangent stiffness with proportionality coefficients from the elastic stiffness part ($K_T(t)$),
 - Updating both the proportionality coefficients with tangent stiffness $\alpha_t M + \beta_t K_T(t)$.
- Ibarra (2005) suggests using a combination of an elastic beam with rotational end springs with zero damping, resolving the stiffness-proportional damping based only on the stiffness of the elastic beam for nonlinear analyses.

- Zareian (2006) extends the previous method by changing the stiffness matrix of the elastic internal beam to compensate for the effect of fixed stiffness of the springs.
- Hall (2018) proposes modified Rayleigh damping in which massless rotational degrees of freedom are condensed out.
- Salehi (2020) addresses concerns related to tangent stiffness-proportional damping: (1) negative definite damping matrices during softening and (2) instantaneous jumps (temporal discontinuities) in the damping reactions.

3. Stress-Dependent Material Damping

Material damping has been studied by Lazan (1954, 1968), Kume et al. (1982), Wang et al. (2014), Mei et al. (2018). Consider the dynamic equilibrium equation of motion for a single-degree-of-freedom structure. In the case of harmonic loading under general conditions and with motion in steady-state resonance, the damping ratio, characterizing the energy dissipated by viscous damping in one cycle of harmonic vibration, E_D , is expressed as follows:

$$\xi = \frac{1}{4\pi} \frac{E_D}{E_S} \quad (2)$$

where E_S represents the strain energy. The loss factor γ is 2ξ .

Lazan [7] conducted a comprehensive study synthesizing various research findings on structures and proposed the unit volume dissipation energy as a function of the stress amplitude:

$$E_D = \int_V f(\sigma_r) dV, \quad E_S = \frac{1}{2} \int_V \frac{\sigma_r^2}{E} dV, \quad f(\sigma_r) = J \sigma_r^n \quad (3)$$

where $f(\sigma_r)$ represents the unit dissipation energy and is linked to the stress amplitude, σ_r denotes the maximum principal stress of the element (Gounaris and Anifantis, 1999), E is the modulus of elasticity, while n and J are material constants determined through experimental tests. Developing the relation for unit dissipation energy is an intricate experimental task that demands significant effort. In this study, the equation proposed by Lazan, derived from experimental results, is employed for unit dissipation energy:

$$f(\sigma_r) = 6895 \left(\frac{\sigma_r}{\sigma_f} \right)^{2.3} + 41360 \left(\frac{\sigma_r}{\sigma_f} \right)^{8.0} \quad (4)$$

where σ_f represents the fatigue limit stress of concrete. It is assumed that σ_f is 65% of the static strength.

Combining Equations 2, 3, and 4, the stress-dependent damping ratio at the elemental level is derived as:

$$\xi_{elem} = \frac{3E}{2\pi} \frac{2089.5 \left(\frac{\sigma_r^{elem}}{\sigma_f} \right)^{2.3} + 4595.5 \left(\frac{\sigma_r^{elem}}{\sigma_f} \right)^{8.0}}{\left(\sigma_r^{elem} \right)^{2.0}} \quad (5)$$

where σ_r^{elem} is the maximum principal stress of the element. This relation provides the damping ratio of each element as a function of its maximum principal stress.

The system level damping is also computed as a summation of all elemental level values:

$$\xi_{sys} = \frac{3E}{2\pi} \frac{\sum_{i=1}^N \left[2089.5 \left(\frac{\sigma_r^{elem}}{\sigma_f} \right)^{2.3} + 4595.5 \left(\frac{\sigma_r^{elem}}{\sigma_f} \right)^{8.0} \right]}{\sum_{i=1}^N \left(\sigma_r^{elem} \right)^{2.0}} \quad (6)$$

4. Finite Element Implementation

The stress-dependent material damping can be implemented in any open source, Commercial, or academic software by defining several for/if loops within the increments and iterations. The following algorithm illustrates the procedure.

```

Input: Finite element model, dynamic excitation, initial guess for damping value
Output: Stress and displacement response, elemental or system level damping values
Perform an initial finite element simulation and compute the stress/strain in all elements
For all time increments
    For all elements
        Compute the elemental level (or system level) damping value.
        Compute the mass and stiffness proportional Rayleigh damping coefficients.
    Check the convergence at the current increment and update the damping for the next increment

```

5. Example 1: Cantilever Column

In this example, we analyze a cantilever column subjected to an intensifying artificial acceleration (IAA) as discussed by Hariri-Ardebili and Sattar (2023). The model employs OpenSees' fiber elements with a linear elastic and nonlinear material. Using elastic models allows for stresses to grow without restrictions on yielding (of steel) or cracking (of concrete). In the case of nonlinear models, the model is collapsed upon reaching the failure criteria. The column consists of only five elements, with a square cross-section of 0.5 m by 0.5 m, and a height of 1.0 m. The total height of the column is 5.0 m. The failure limit stress is assumed to be 27 MPa. The following parametric simulations are conducted on this structural component:

- Transient analysis with constant damping at 1%, 5%, 10%, and 20%.
- Initial and reduced mass assessment.
- Elemental-level updating damping.
- System-level updating damping.
- Unrestrained and restrained updating damping.

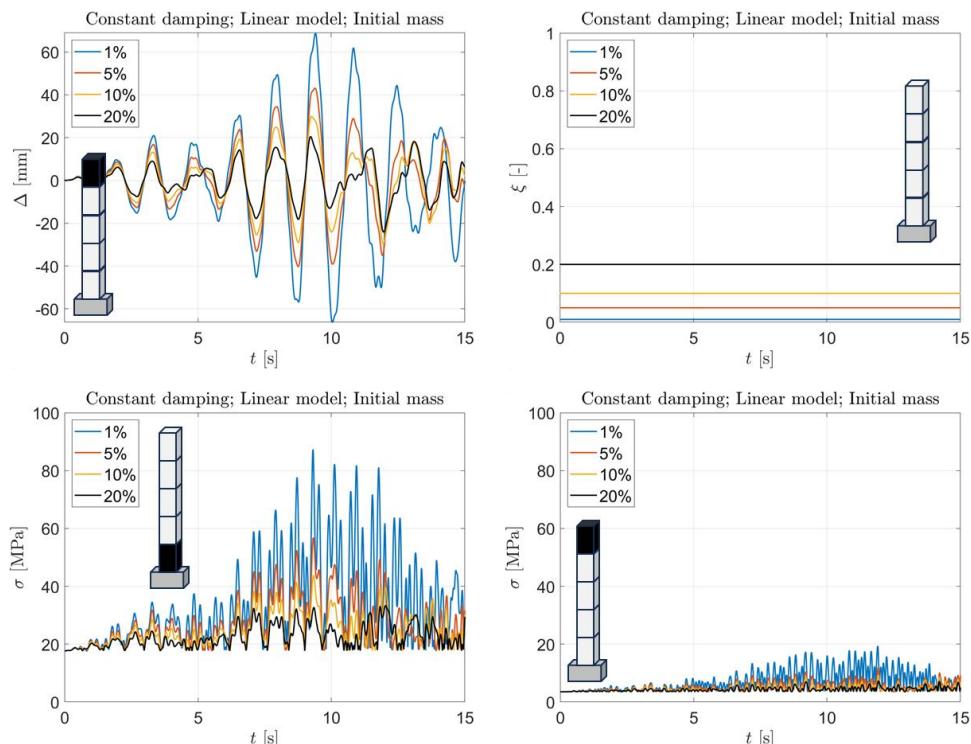


Figure 1. Cantilever column. Comparing the classic constant damping model with different ξ values.

Figure 1 compares different damping values from 1% to 20% in the linear elastic model to provide a baseline for the subsequent comparisons. As intuitive, imposing a higher damping value reduces the displacement and stresses.

Figure 2 compares three damping models, all incorporating a linear elastic model. As observed, the elemental-level updating damping model results in higher displacement compared to the system-level updating damping. Interestingly, the constant damping of 5% falls in the middle of these two updating models. However, this seems more like a coincidence, lacking a solid basis.

Nevertheless, it highlights that, for this specific case study, adopting a 5% constant damping is a suitable choice to replicate results comparable to those from updating models. The damping values in both system-level and elemental-level updating damping models are stress-dependent. Consequently, higher stresses lead to increased damping.

The final segment of this figure depicts the generated stress in different elements along the height for the elemental-level damping updating model and their corresponding damping values. It is evident that the damping value significantly increases for elements located at the base, as they endure the majority of bending and axial stresses. Conversely, the top element experiences very low stress, resulting in negligible damping.

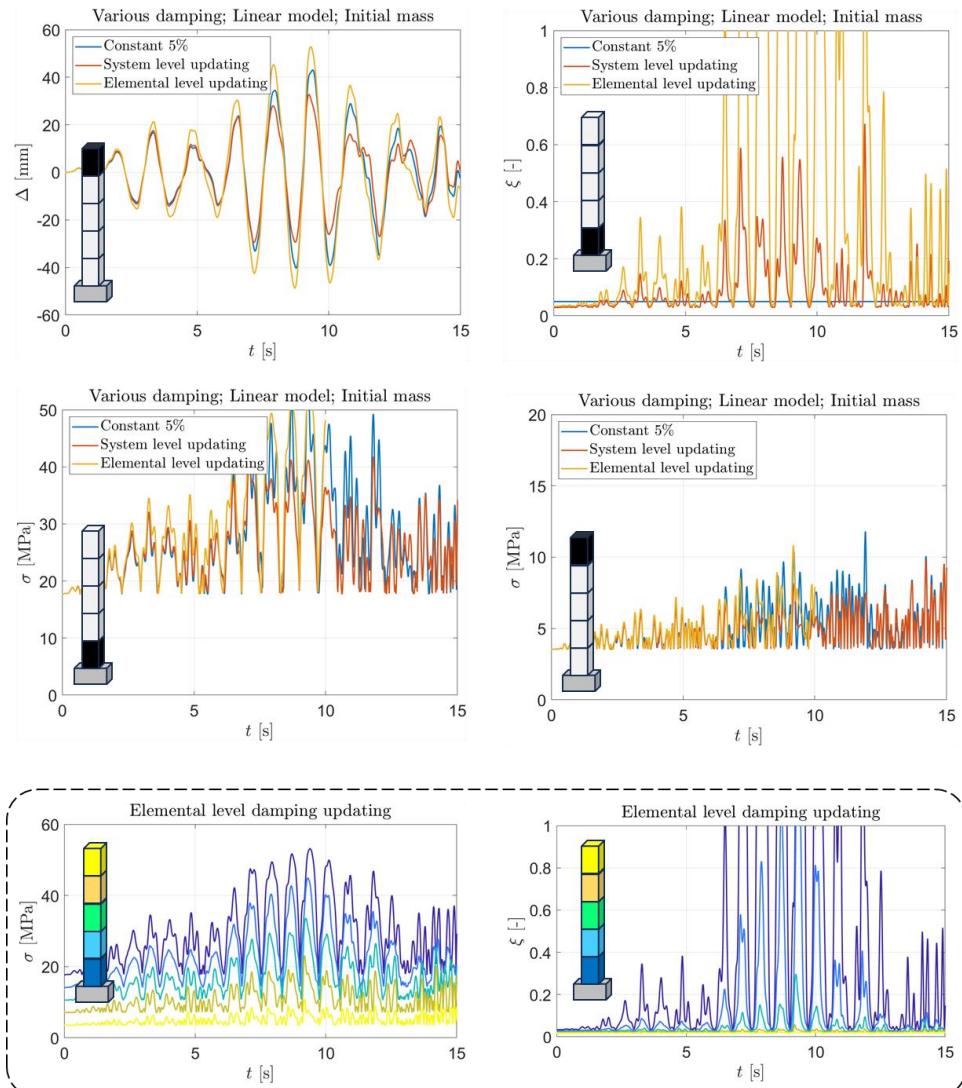


Figure 2. Cantilever column. Comparing linear elastic models with different damping models.

Figure 3 closely resembles Figure 2, but with the introduction of a cap on the stress values used to compute damping through equations 5 or 6. Consequently, these simulations operate under the assumption that σ_r^{elem}/σ_f ratio does not exceed one during damping calculation. This assumption amplifies the displacement response in both damping updating models. The damping values are constrained to a maximum of 10%.

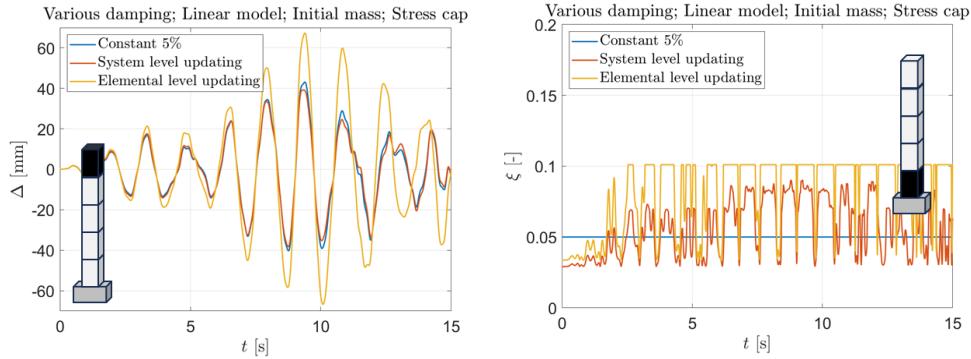


Figure 3. Cantilever column. Comparing linear elastic models with different damping models and capping the stress value.

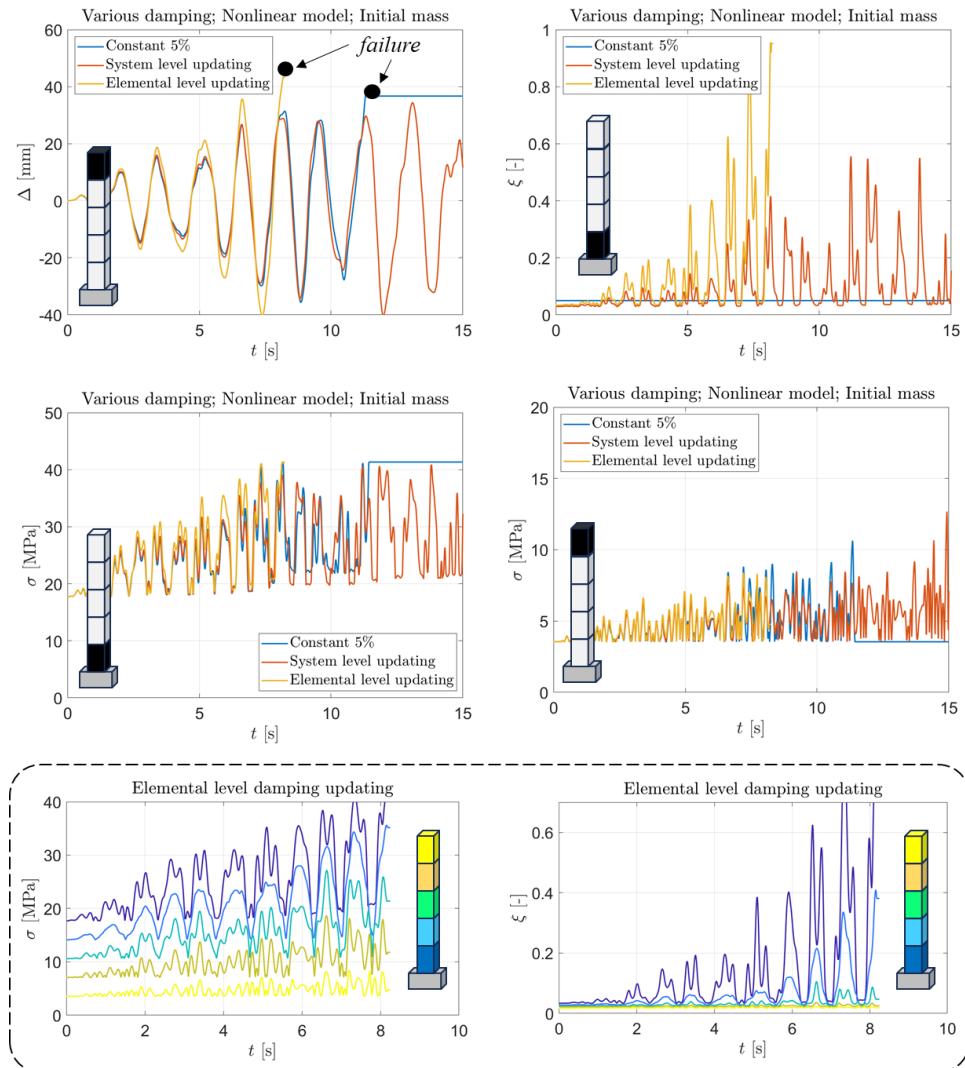


Figure 4. Cantilever column. Comparing nonlinear models with different damping models.

Figure 4 replicates the simulations conducted in Figure 2, but with the incorporation of nonlinear models featuring failure capability. This adjustment inherently addresses situations where the demand stress may surpass the capacity. In the nonlinear models, an element automatically sustains damage, causing its stress values to plummet to zero. Given that this column comprises only one element at the base, its damage signifies the failure of the entire column.

The displacement time history of the three models illustrates this scenario. The elemental-level updating damping model fails early, around 7.5 seconds, followed by the 5% constant damping model at approximately 11 seconds. Meanwhile, the system-level updating damping model continues its vibration throughout the entire 15 seconds of the simulation.

A comparison of damping time histories across Figures 4, 3, and 2 reveals that employing actual nonlinear models results in higher damping compared to artificially capping the capacity stress. Notably, the last segment of this figure demonstrates a direct correlation between stress and damping time histories for the elemental-level updating damping model.

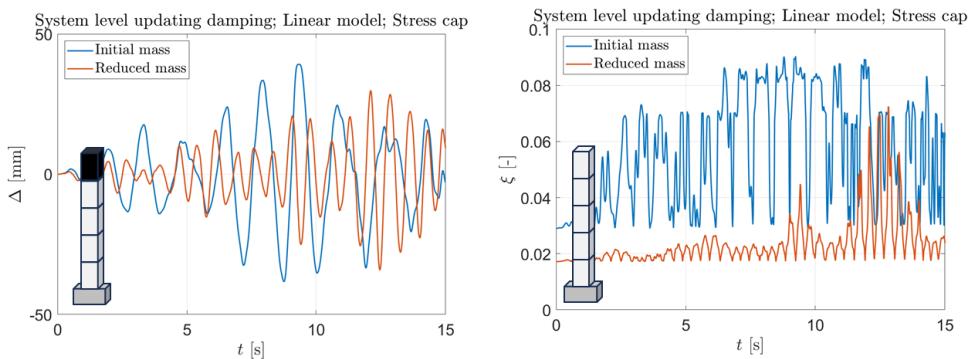


Figure 5. Cantilever column. Comparing linear elastic models using system-level updating damping with initial and reduced masses.

Equations 5 and 6 calculate damping values based on the element stress, which is a combination of static loads (such as self-weight causing axial stress) and dynamic stresses (mainly bending and shear). A very high axial stress can significantly influence the total stress, and if it's substantial enough, it may overshadow stress variations.

Hence, Figure 5 explores a scenario where the structural mass of the column is reduced to only 25% of the original mass. Consequently, the total element stress is reduced at different increments during seismic simulation. The results from the system-level updating damping model indicate a 10-20% reduction in peak displacement, while damping is drastically reduced for the entire simulation duration.

6. Example 2: Gravity Dam

For our second example, we use Koyna Dam as a case study. This concrete gravity dam spans 853 m in length and has a height of 103 m. The thickness at the base and crest measures 70.2 m and 12.1 m, respectively, for the central non-overflow monoliths. Given the substantial dimensions of gravity dams in the cross-stream direction, the assumption of plane strain is generally acceptable, allowing us to analyze gravity dams as 2D structures. However, in this study, we aim for precision in understanding stresses and crack profiles. To achieve this, we employ a sliced 3D model. The finite element model of the coupled dam–reservoir–foundation system closely follows the methodology reported in previous works (Hariri-Ardebili et al., 2016). The numerical model intricately captures the interaction between fluid and solid elements at the interfaces of the dam and reservoir, as well as the reservoir and foundation. To simulate real-world conditions, the model is excited using the horizontal component of the Koyna ground motion record—a 10-second sequence.

In contrast to the cantilever column example, this gravity dam comprises 20 elements along the upstream-downstream direction. Figure 6 presents the relative crest displacement for three main models: 5% constant damping, and elemental-/system-level updating damping. The concrete is modeled using the smeared crack model, enabling solid elements to crack in three orthogonal directions along principal stresses. Similar to the column example, elemental-level updating damping results in slightly higher displacement compared to the system-level assumption. In this specific example, the 5% constant damping leads to smaller displacements. It appears that a constant damping of about 3-4% is needed to align with all three modeling options.

The figure also depicts stress variations at two locations along the upstream face of the dam. The time history of the first principal stress is nearly identical for the first 4 seconds at the heel point. As the intensity of the applied ground motion increases, damage occurs in the element located at the heel for the system-level updating model. Consequently, the stress immediately drops to zero, and the damping value associated with this specific element is also reduced. However, it's crucial to note that the damping value doesn't drop to zero. Upon cracking of the element in the first principal direction (becoming zero), the principal direction changes, and the former second principal stress assumes the role of the new first principal stress, which is used in Equations 5 and 6.

Finally, tracking the stress time history at higher elevations (in the vicinity of the crest) reveals very low stresses. Therefore, observations from all three models are very similar.

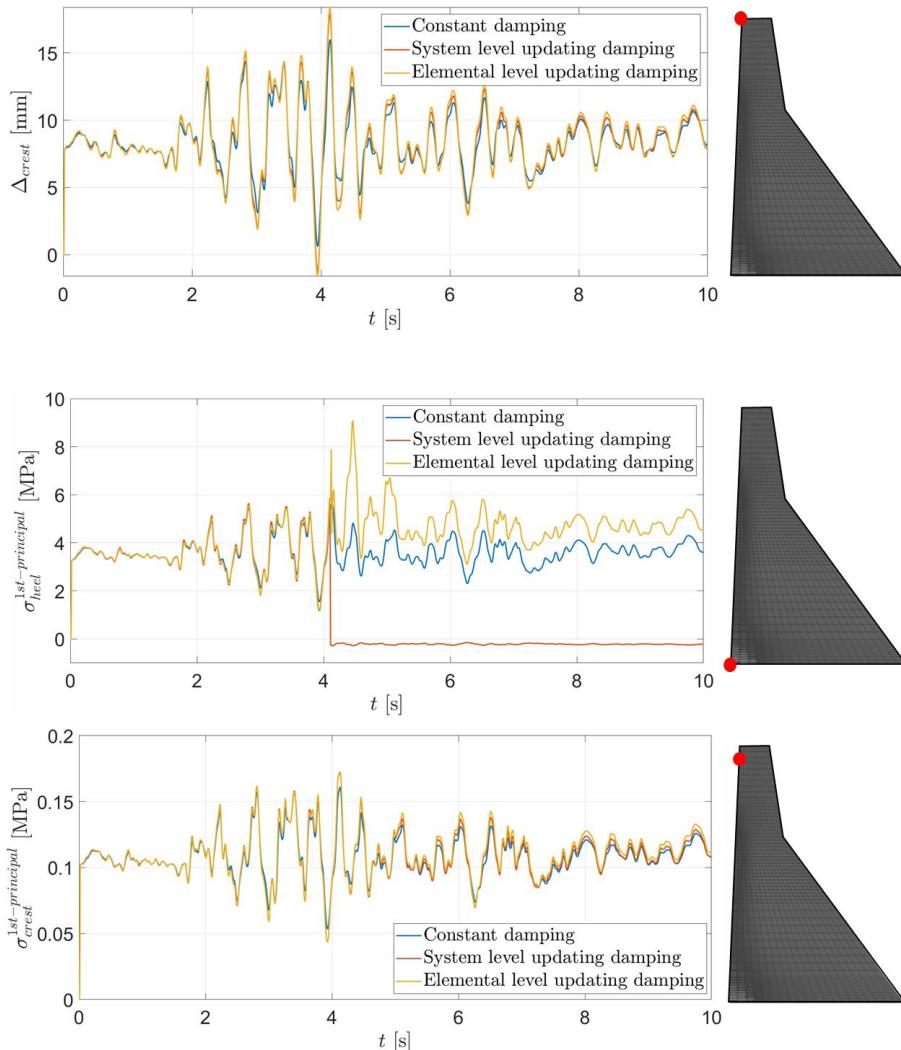


Figure 6. Gravity dam. Comparing nonlinear models with different damping models. Displacement response at the crest; first principal stress variation at the bottom and top.

Figure 7 provides damping time histories along 30 elements in the dam height. Towards the higher elevations, stress values decrease, subsequently reducing damping. For the first two elements at the base, the capacity stress exceeds the threshold, resulting in element damage and, consequently, a drop in damping. The figure also illustrates variations in system-level damping, ranging from 0.03 to 0.04 with a median of 0.035. Additionally, a straight line is depicted, representing the 5% constant damping.

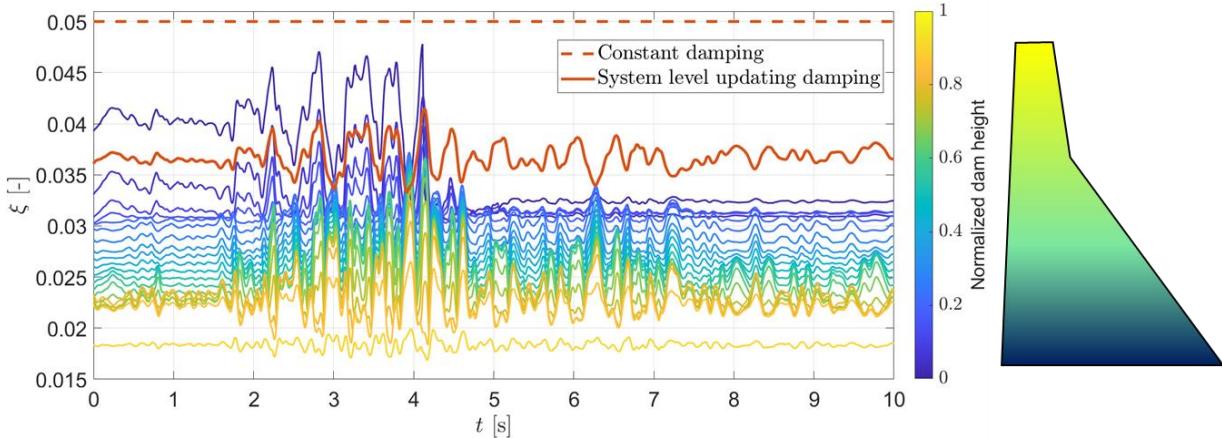


Figure 7. Gravity dam. Damping variation at upstream elements of the dam along the height. Two red curves are associated with constant and system-level updating damping models. The color contour presents the element-level updating damping at the locations normalized to the total height.

7. Conclusions

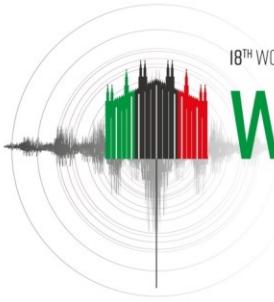
In the exploration of seismic analysis for concrete dams, this study has illuminated the role of structural damping and the challenges associated with its accurate quantification in large-scale structures. The implementation of a variable material damping model, intricately linked to the stress capacity at both structural and elemental levels, provides a unique perspective on stress-dependent material damping.

The case study involving the Koyna Dam serves as a practical illustration, revealing the tangible impacts of damping redistribution and formulation factors on damage response and crest displacement variability. This research underscores the significance of acknowledging stress-dependent material damping in seismic analyses, offering insights into the uncertainties inherent in predicting responses for structures of considerable magnitude. By addressing these complexities, this study not only advances our comprehension of seismic behavior in concrete dams but also contributes practical insights to refine seismic design and analysis methodologies. The introduced approach emerges as a valuable tool for dynamic analyses, enhancing the overall resilience and safety of concrete dams in seismic scenarios.

8. References

- Alipour, A., & Zareian, F. (2008). Study Rayleigh damping in structures; uncertainties and treatments. *In the 14th World Conference on Earthquake Engineering*, pp. 12-17.
- Bernal, D. (1994). Viscous damping in inelastic structural response. *Journal of Structural Engineering*, 120(4), pp. 1240-1254.
- Charney, F. A. (2005). Consequences of using Rayleigh damping in inelastic response history analysis. *In Congreso Chileno de Sismología e Ingeniería Antisísmica IX Jornadas*, Concepción, CL.
- Charney, F. A. (2008). Unintended consequences of modeling damping in structures. *Journal of Structural Engineering*, 134(4), pp. 581-592.
- Caughey, T. K., & O'Kelly, M. E. (1965). Classical normal modes in damped linear dynamic systems. *Journal of Applied Mechanics*, 32(3), pp. 583-588.

- Gounaris, G. D., & Anifantis, N. K. (1999). Structural damping determination by finite element approach. *Computers & structures*, 73(1-5), pp. 445-452.
- Hall, J. F. (2006). Problems encountered from the use (or misuse) of Rayleigh damping. *Earthquake Engineering & Structural Dynamics*, 35(5), pp. 525-545.
- Hall, J. F. (2018). Performance of viscous damping in inelastic seismic analysis of moment - frame buildings. *Earthquake Engineering & Structural Dynamics*, 47(14), pp. 2756-2776.
- Hariri-Ardebili, M. A., & Sattar, S. (2023). Uncertainty and bias in fragility estimates by intensifying artificial accelerations. *Probabilistic Engineering Mechanics*, ID. 103545.
- Hariri-Ardebili, M. A., Seyed-Kolbadi, S. M., & Kianoush, M. R. (2016). FEM-based parametric analysis of a typical gravity dam considering input excitation mechanism. *Soil Dynamics and Earthquake Engineering*, 84, pp. 22-43.
- Ibarra, L. F., Medina, R. A., & Krawinkler, H. (2005). Hysteretic models that incorporate strength and stiffness deterioration. *Earthquake Engineering & Structural Dynamics*, 34(12), pp. 1489-1511.
- Jayamon, J. R., Line, P., & Charney, F. A. (2018). State-of-the-art review on damping in wood-frame shear wall structures. *Journal of Structural Engineering*, 144(12), ID. 03118003.
- Jeary, A. P. (1997). Damping in structures. *Journal of Wind Engineering and Industrial Aerodynamics*, 72, pp. 345-355.
- Kareem, A., & Gurley, K. (1996). Damping in structures: its evaluation and treatment of uncertainty. *Journal of Wind Engineering and Industrial Aerodynamics*, 59(2-3), pp. 131-157.
- Kume, Y., Hashimoto, F., & Maeda, S. (1982). Material damping of cantilever beams. *Journal of Sound and Vibration*, 80(1), pp. 1-10.
- Lazan, B. J. (1954). Effect of damping constants and stress distribution on the resonance of members. *Journal of Applied Mechanics*, 22(3), pp. 201-209.
- Lazan, B. J. (1968). Damping of materials and members in structural mechanics.
- Mei, S., Su, L., Li, P., & Wang, Y. (2018). Material damping of concrete under cyclic axial compression. *Journal of Materials in Civil Engineering*, 30(3), ID. 04017295.
- Nashif, A. D., Jones, D. I., & Henderson, J. P. (1991). *Vibration damping*. John Wiley & Sons.
- NIST. (2017). Guidelines for Nonlinear Structural Analysis and Design of Buildings. Part I-General.
- Puthanpurayil, A. M., Lavan, O., Carr, A. J., & Dhakal, R. P. (2016). Elemental damping formulation: An alternative modelling of inherent damping in nonlinear dynamic analysis. *Bulletin of Earthquake Engineering*, 14, pp. 2405-2434.
- Puthanpurayil, A. M., Carr, A. J., & Dhakal, R. P. (2018). Application of nonlocal elasticity continuum damping models in nonlinear dynamic analysis. *Bulletin of Earthquake Engineering*, 16, pp. 6269-6297.
- Salehi, M., & Sideris, P. (2020). Enhanced Rayleigh damping model for dynamic analysis of inelastic structures. *Journal of Structural Engineering*, 146(10), ID. 04020216.
- Wang, Y., Pan, Y., Wen, J., & Su, L. (2014). Material damping evaluation of frames made of different materials. *Materials Research Innovations*, 18, S3-53.
- Wilson, E. L., & Penzien, J. (1972). Evaluation of orthogonal damping matrices. *International Journal for Numerical Methods in Engineering*, 4(1), pp. 5-10.
- Zareian, F. (2006). Simplified performance-based earthquake engineering. PhD Thesis, Stanford University.



CENTRIFUGE SHAKE TABLE TESTS AND NUMERICAL SIMULATIONS ON SEISMIC DAMAGE PROCESS OF EMBANKMENTS

R. Ibuki¹, K. Uemura², T. Doi³, J. Izawa³ & S. Sreng²

¹ Railway Technical Research Institute, Tokyo, JAPAN, ibuki.ryuichi.85@rtri.or.jp

² Nippon Koei, Ibaraki, JAPAN

³ Railway Technical Research Institute, Tokyo, JAPAN

Abstract: A series of shake table tests were carried out in a centrifugal acceleration of 50G. In particular, slope gradients of model embankments were set to 1:1.5, 1:1.25 and 1:1.0 for slope height: slope width focusing on the effect of a slope gradient on the damage process. The 1:1.5 slope embankment did not lead to sliding failure, and only small displacement occurred even some large earthquakes were input. On the other hand, the other embankments with slope gradient steeper than 1:1.5 led to sliding failure after relatively large deformation occurred especially at the toe of embankments. Furthermore, high-speed and high-resolution digital images were obtained from a camera fixed to the shake table in order to observe strain state of embankments at intervals of 0.5 seconds in prototype scale. The results of the image analysis clearly revealed the seismic damage process of embankments. In other words, shear strain tended to be concentrated at the toe of a slope and progressed into deeper in the embankment, and finally resulted in collapse as soon as a sliding plane was formed. In the numerical analysis, Newmark's sliding block method and Finite Element Method (FEM) were used to simulate the test result, and accuracy of them were compared. As a result, Newmark's sliding block method could give a relatively reasonable settlement of the 1:1.5 slope embankment, although the settlement was slightly overestimated. On the other hand, for the 1:1.0 slope embankment which showed sliding failure, Newmark's sliding block method calculated excessively large settlement whereas FEM can calculate settlement more accurately and reproduce the damage process up to sliding failure observed in the test.

1. Introduction

In the seismic design of embankments in Japanese railway field, a settlement of an embankment calculated using Newmark's sliding block method (Newmark (1965)) (hereinafter referred to as "Newmark method"), which assumes arc slip failure, is often used as a verification index for recoverability (Railway Technical Research Institute (2007), (2012)) (hereinafter referred to as "the earth structure design standard" and "the seismic design standard"). This is because Newmark method can easily calculate some reasonable sliding displacement. In general, it is supposed to verify recoverability instead of safety because recoverability verification is stricter than safety. Furthermore, many studies have been conducted to improve an accuracy of Newmark method, for example, Sarma (1975).

On the other hand, because Newmark method assumes rigid-plastic arc slip failure, it does not always accurately reproduce the damage process of embankments up to the point of sliding failure. This makes it difficult to properly evaluate seismic performance. For instance, Fujiwara et al. (2015) compared the observed

seismic displacement of railway embankments during the 2011 Tohoku Earthquake off the Pacific coast with the settlement calculated using Newmark method. As a result, among the thirteen undamaged embankments, five showed settlements greater than 200mm, which serves as an indicator of minor damage in Japanese railway field. Fujiwara et al. (2015) also cited following factors as contributing to this difference: errors in setting of geotechnical material properties and input seismic acceleration, the influence of soft supporting ground, and the difference in failure modes. In particular, the difference in failure mode is that Newmark method assumes sliding failure, whereas the actual phenomenon is often limited to damage that does not lead to sliding failure, such as settlement, slope bulging, and cracking. In other words, a safety factor of the extreme balance method based on arc slip failure, which is assumed in Newmark method, cannot evaluate these damage process leading up to sliding failure.

Based on the above background, we carried out centrifuge shaking table tests to clarify the seismic damage process of embankments (e.g., Izawa (2022a)). As a result, from digital images captured after each shaking, it was clarified that shear strain was concentrated at the toe of a slope and a sliding plane was formed from there as the damage process leading to sliding failure. It was also confirmed that the strain level at which sliding failure occurs could be explained by the damage level specified by the deformation characteristics of the embankment material, as shown in Figure 1. In addition, a seismic safety performance verification method using shear strain at the toe of a slope was proposed that can take into account the damage process (hereinafter referred to as "proposed verification method") (Izawa (2022b)). However, in the test, sinusoidal waves input and a slope of the embankment was set 1:0.5 to make it easier to failure. Thus, it has not been confirmed whether this proposed verification method can be applied when a slope gradient is closer to actual embankments or when actual seismic waves was input.

In this study, a series of centrifuge shaking table tests were conducted on embankments with different slope gradient to confirm the validity of proposed verification method. The input acceleration waves were the Spectrum I and II that is described in the seismic design standard. In addition, it was also discussed a seismic response value calculation method using Finite Element Method (FEM) analysis to estimate shear strain necessary for a safety verification in proposed verification method. At this time, we combined multiple shear spring model with GHE-S model, which is often used in ground response analysis in Japanese railway field, in order to keep the calculations from becoming too complicated for practical seismic design. Finally, the results of the tests, FEM analysis, and Newmark method were compared to validate proposed verification method and a seismic response value calculation method using FEM analysis.

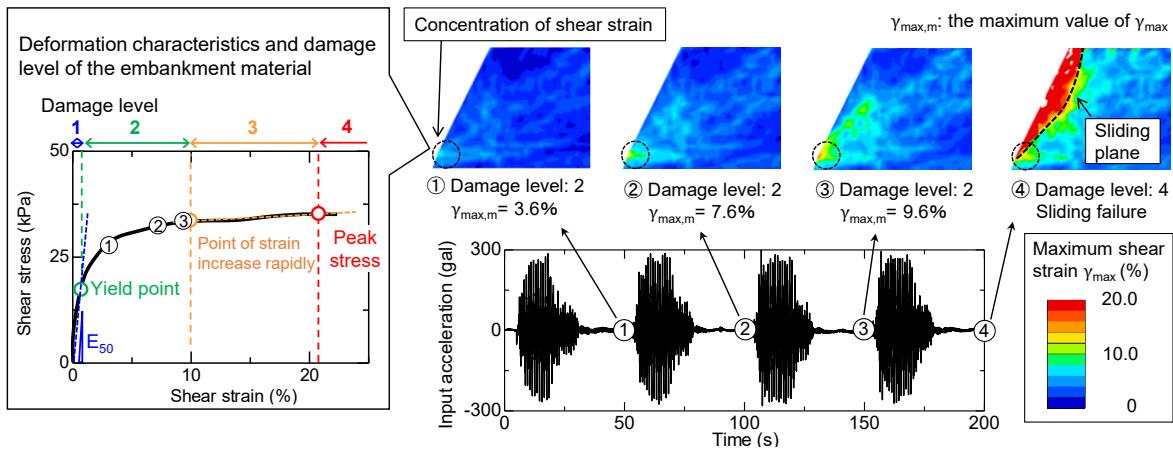


Figure 1. The seismic damage process leading to sliding failure in previous study Izawa (2022a).

2. Centrifuge Shake table tests

Centrifuge shaking table tests were conducted to clarify the damage process of embankment with different slope gradients during earthquakes. A beam type centrifuge with a diameter of 5.2m and a shake table of the Nippon Koei Co. LTD. (Sreng et al., 2015) were used in this study. In particular, the damage process was observed in detail by capturing high-speed, high-resolution digital images of the embankment not only before and after shaking, but also during shaking. All tests were conducted at a centrifugal acceleration field of 50G. All values are shown below in prototype scale.

2.1. Outline of test

Model embankment

The test cases with different slope gradients are shown in Table 1. The embankment material used was *Edosaki* sand with a degree of compaction (D_c) of 95%. The physical and mechanical properties of the embankment material are shown in Tables 2 and 3. In Case3, the slope gradient was set to 1:1.5, which is the standard slope in Japanese railway field. In contrast, the slopes were steeper than 1:1.5 in Cases1 and 2. The embankment height is uniformly set 5m in all cases. An example schematic view of a model embankment, along with an arrangement of sensors, is shown in Figure 2. The left slope was set to the above slope gradient so that deformation would be concentrated on this side, and the right slope was set to gentler than 1:2.0 so that this side would be stable. Since the energy of the seismic acceleration input to an embankment was equal in each case, the bottom of the embankment was uniform in all cases. Additionally, the natural periods obtained from inputting a small white noise wave before main shakings are also shown in Table 1.

Table 1. Test conditions.

	Slope gradient (left side)	Height of embankment (m)	Natural period (s)
Case1	1:1.0	5.0	0.088
Case2	1:1.25	5.0	0.103
Case3	1:1.5	5.0	0.101

Table 2. Physical properties of *Edosaki* sand.

Soil particle density : G_s	2.68
Mean grain size : D_{50}	0.34 mm
Effective grain size : D_{10}	0.15 mm
Uniformity coefficient : U_c	2.6
Coefficient of curvature : U'_c	1.00
Fine content : F_c	4.4 %
Optimum water content : w_{opt}	14.6 %
Maximum dry density : ρ_{dmax}	1.707 g/cm ³

Table 3. Physical and Mechanical properties of *Edosaki* sand ($D_c = 95\%$).

Dry density : ρ_d	1.622 g/cm ³
Degree of compaction : D_c	95 %
Compression index : C_c	0.055
Consolidation yield stress : P_c	318.1 kPa
Cohesion : c	9.5 kPa
Internal friction angle : φ	32.5 deg.

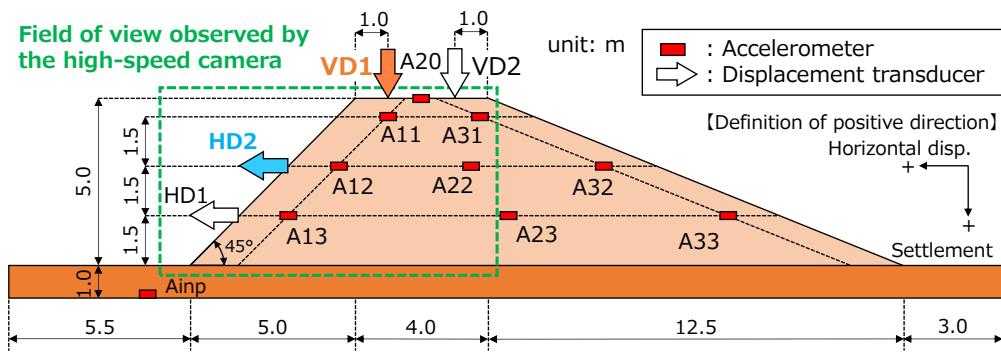


Figure 2. Schematic view of model embankment (Case 1).

Figure 3 shows the shear stress-shear strain relationship obtained from a monotonic loading test performed on the embankment material. This test was carried out using a hollow torsional shear testing machine under a confining pressure of 50 kPa. Additionally, a proposed definition of damage levels and limit value are showed. The shear strain at the point of the maximum shear stress ($\tau_{max} = 48$ kPa), which can be defined as the failure of the embankment material, is 7.5% (hereinafter referred to as " γ_{fail} "). This value is equivalent to the limit value γ_{cr3} of damage level 3. Damage level 2, associated with γ_{cr2} , can be also defined as the point where the shear stress begins to increase linearly toward the failure point ($\gamma_{fail}, \tau_{max}$). For the sake of convenience, it's defined as the point at which shear strain reaches approximately half of γ_{fail} . The limit value γ_{cr1} , associated with damage level 1, shows undamaged region, and is set at the point where shear stress reaches half of τ_{max} .

(24kPa), which corresponds to the elastic region E_{50} . In this scheme, damage level 1 signifies no damage, damage level 2 denotes minor damage, damage level 3 suggests relatively severe damage, and damage level 4 is equivalent to failure. Since these limit values are defined in terms of strain, they can be considered as valid for both at a centrifugal acceleration field and 1G field. Furthermore, these limit values were also examined under higher confining pressures of 100 kPa and 150 kPa. In the embankment material used, it was confirmed that the limit values could be set at approximately the same strain level without being affected by a confining pressure.

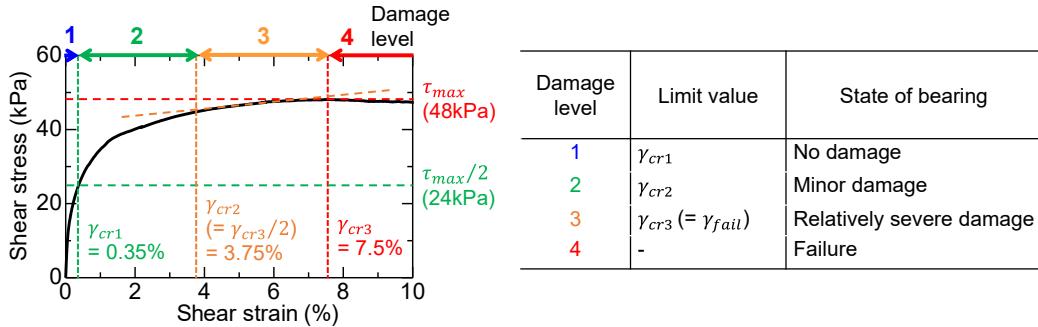


Figure 3. Shear stress-strain relationship of Edosaki sand and proposed damage level.

Camera setup

In capturing digital images during shaking at a centrifugal acceleration field of 50G, it is necessary that a camera possesses an ability to withstand forces equivalent to 50 times its own weight. Furthermore, high frame rate is also necessary since an elapsed time is 1/50 during the tests. There are several constraints, such as lens selection to ensure an adequate field of view within confined spaces, as well as appropriate lighting arrangements. In addition, when capturing images at high-speed, it is desirable to fix a camera on a shake table to maintain a constant positional relationship between a model embankment and a camera. Hence, as in previous study (Ibuki (2022)), a high-speed camera was fixed to the shake table as shown in Figure 4 to capture digital images of an embankment during shaking. A shooting speed of the camera was set to 100 frames per second, allowing for the acquisition of images at intervals of 0.5 seconds (equivalent to 0.01 second intervals in the prototype scale) at a 50G centrifugal acceleration field. An image analysis technique was applied to these images to calculate displacements and strain distribution of embankment during shaking, thereby a seismic damage process of an embankment was observed in detail. In the image analysis, the mesh was approximately 250mm by 250mm (equivalent to 5mm by 5mm in the prototype scale). In addition, it was confirmed that a calculated displacement and a displacement measured with a sensor were generally in agreement.

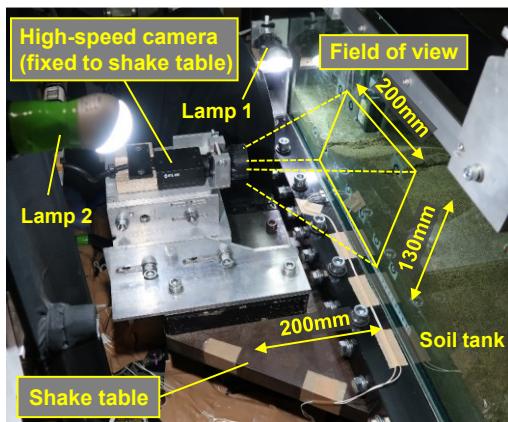


Figure 4. Location of high-speed camera (Ibuki (2022)).

Input acceleration

Input acceleration waves were the standard design earthquake ground motions as indicated in the seismic standard. The Spectrum I and II ground motions were applied in the order of I, II, and I. In addition, when a model embankment didn't lead to sliding failure by above shakings, a sinusoidal wave (600Gal, 1.2Hz, 20 waves) was input several times. Figure 5 shows an example of input acceleration waves (A_{inp}). Although the acceleration amplitude was not accurately reproduced, the characteristics of Spectra I and II were generally reproduced. In addition, it was confirmed that the input seismic motions were equivalent in all cases.

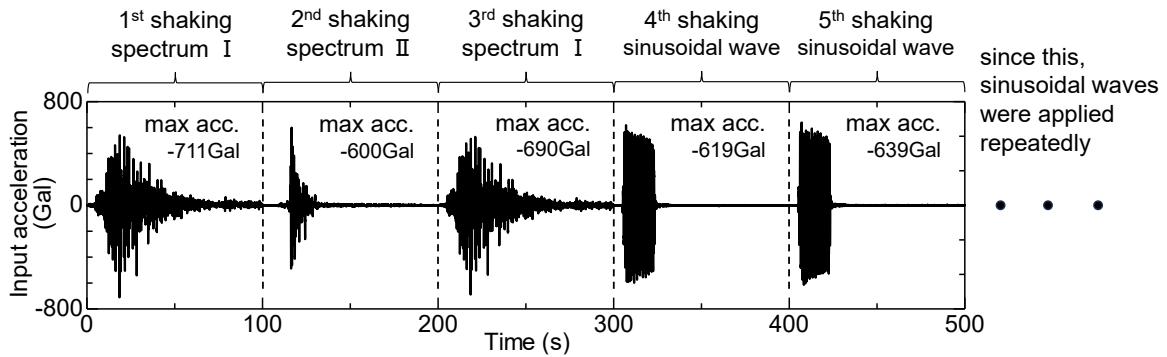


Figure 5. Example of input acceleration waves (Case3).

2.2. Test results

For the steeper slopes of Cases1 and 2, sliding failure occurred during the first shaking (Spectral I) in Case1 and during the sixth shaking (third 600Gal sinusoidal wave) in Case2. In contrast, in Case3 with a standard slope, a series of shakings did not cause sliding failure, but only deformations such as a settlement and a horizontal displacement. In the following sections, the test results of Cases1 and 3 with different failure modes were described in detail.

Case1 (1:1.0 slope gradient embankments)

The time histories of the input acceleration and the settlement VD1 and horizontal displacement HD2 measured in Case1 are shown in Figure 6. The solid line shows the displacement measured by the sensor and the dotted line shows the displacement obtained from the image analysis results. HD2 increase rapidly around 19 seconds since the displacement sensor was not completely fixed due to a defect of the jig. Thus, the sensor of HD2 could not measure the displacement properly after 19 seconds. On the other hand, the image analysis result shows that horizontal displacement began to increase rapidly around 29 seconds. Here, the sliding failure occurred around 30 seconds as shown in Figure 7, and the trend is consistent with the rapid increase in the horizontal displacement obtained from the image analysis. Therefore, the displacements obtained from the image analysis shown by the dotted line in Figure 6 are used hereafter.

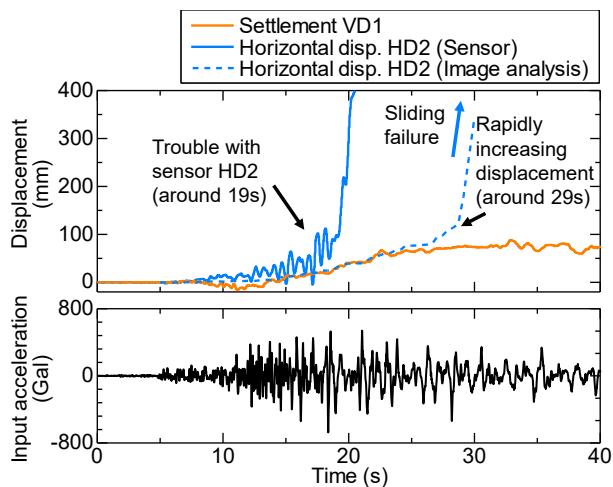


Figure 6. Time histories of displacement in Case1 (1:1.0 slope gradient).

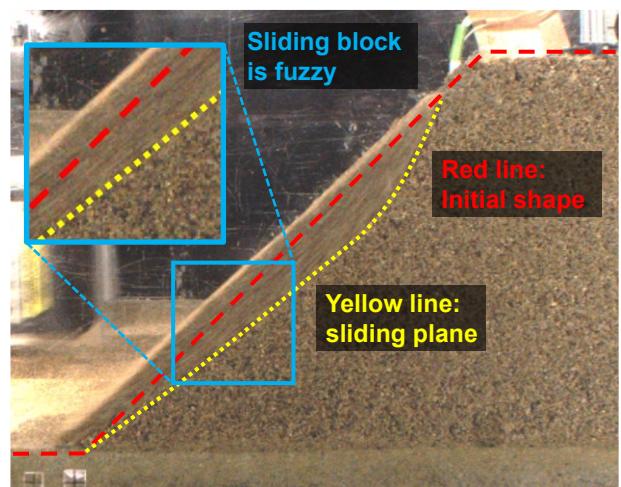


Figure 7. The moment at sliding failure in Case1 (1:1.0 slope gradient).

Figure 8 shows the time history of maximum shear strain at the toe of the slope calculated from the image analysis using images captured between 5 and 30 seconds, together with the input acceleration and horizontal displacement HD2. The timing of shooting is plotted in the time history of the input acceleration. It was confirmed that the horizontal displacement increased rapidly at around 29 seconds and the model embankment led to sliding failure after maximum shear strain at the toe of the slope increased rapidly at around 27 seconds. Furthermore, the digital images captured at ① ~ ④ in Figure 8 and the strain distributions obtained from image analysis as shown in Figure 9. From Figure 9(c), the shear strain is concentrated at the toe of the slope during shaking. In particular, around 19 seconds, the strain is concentrated near the sliding plane showed in Figure 7, which is a so-called potential sliding plane. The red dotted line in Figure 8 is the limit value of Damage level 3 (7.5%), defined from the deformation characteristics of the embankment material shown in Figure 3. Similar to the damage process observed in the previous study (Izawa (2022a)), when the maximum shear strain at the toe of a slope exceeds the limit value of Damage level 3 and reaches Damage level 4, the

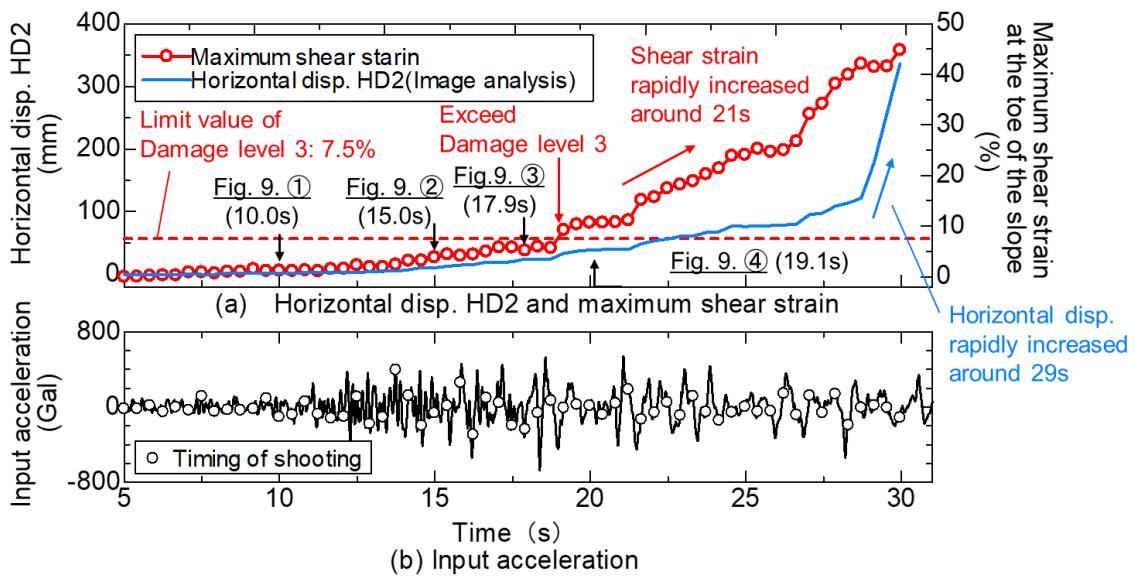


Figure 8. Time history of the maximum shear strain at the toe of the slope in Case 1 (1:1.0 slope gradient).

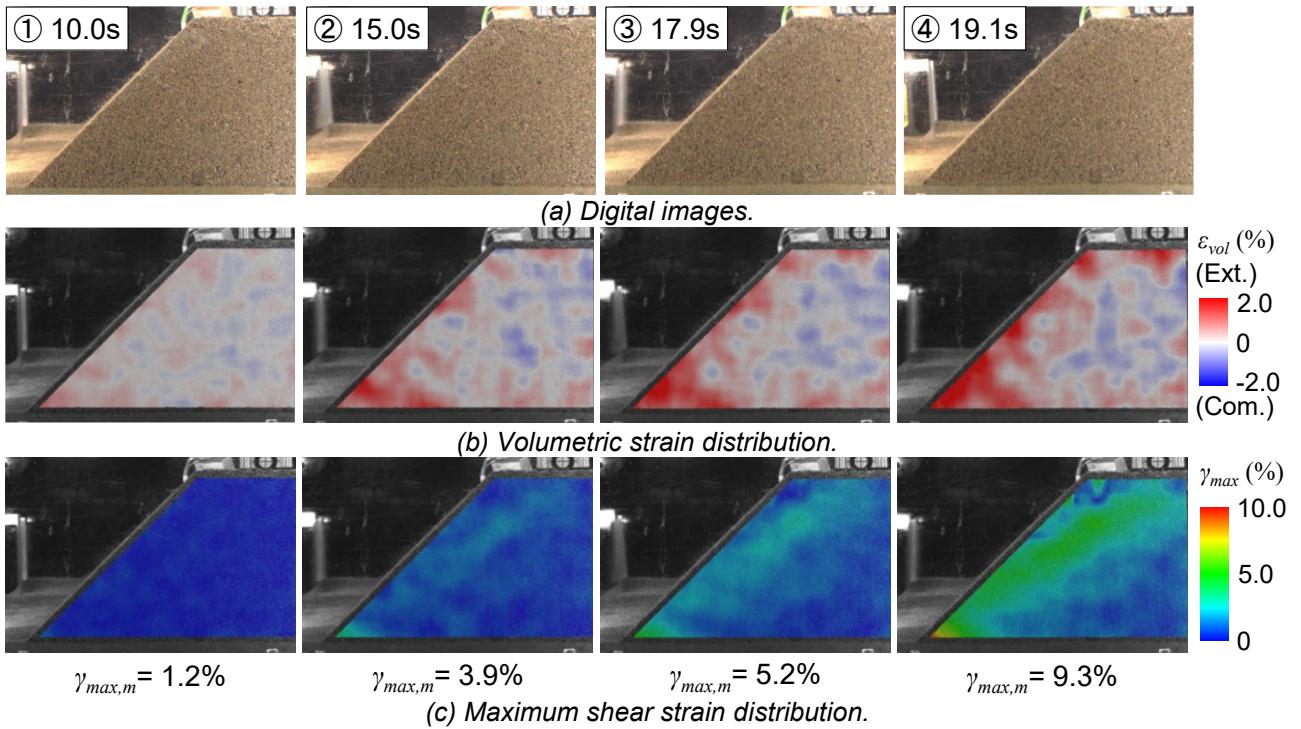


Figure 9. Digital images and result of image analysis in Case 1 (1:1.0 slope gradient).

toe of a slope locally leads to shear failure and progressive failure begins, resulting in overall sliding failure. In addition, Figure 9(b) shows that the volumetric strain tends to expand in the surface layer of the embankment and slightly compress in the central part. However, the magnitude of the compressive volumetric strain is only about 1%. Therefore, if compaction is sufficient and uniform, it is unlikely that the volume change will occur in the center of the embankment.

Case3 (1:1.5 slope gradient embankments)

Figure 10 shows the time histories of the input acceleration, settlement VD1, horizontal displacement HD2, and shear strain at the toe of the slope calculated from image analysis in Case3. In addition, Figure 11 shows the model embankment after 8th shakings (Spectrum I, II, I and five 600Gal sinusoidal waves). In the Spectrum I and II shakings, the shear strain at the toe of the slope didn't reach Damage level 3 (7.5%), indicating that the settlement and the horizontal displacement only occurred. Similarly, in the subsequent 600Gal sinusoidal waves, deformation such as the settlement and the horizontal displacement progressed but the model embankment did not fail as shown in Figure 11.

Figure 12 shows the distribution of the maximum shear strain after the first to the third shaking. A shear deformation occurred in the entire model embankment after each shaking. Although the shear strain was concentrated in a slightly wider region at the toe of the slope after third shaking, the maximum value of the γ_{max} is approximately 5% during shaking and 4% after shaking. It was confirmed that the shear strain is less than 7.5% (limit value of Damage level 3) even when subjected to 3 large seismic motions. Therefore, it could be said that although shear strain occurs at the toe of a slope even for an embankment with standard slopes or gentler, there is a sufficient margin of safety against sliding failure due to that the localization of strain is not remarkable. In addition, the volumetric strain is similar to that in Case1, confirming that a small compressive volumetric strain was occurred in the central part.

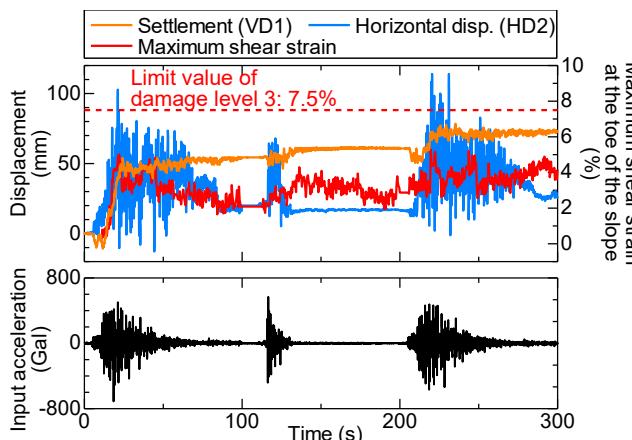


Figure 10. Time history waves in Case3 (1:1.5 slope gradient).

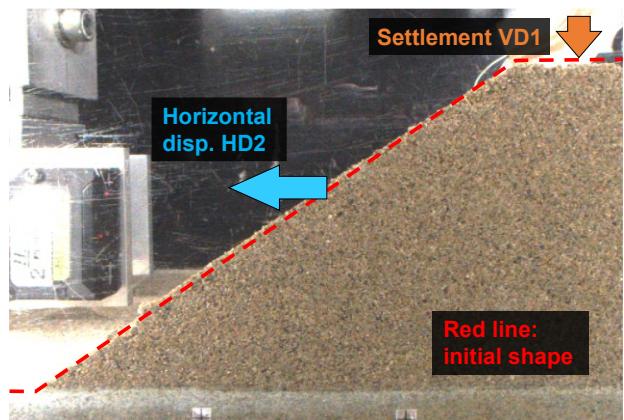
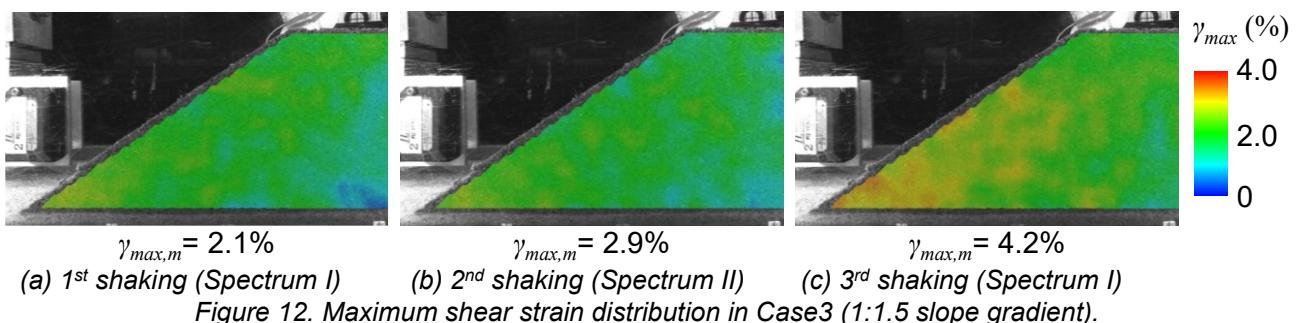


Figure 11. Model embankment after 8th shaking in Case3 (1:1.5 gradient slope gradient).



(a) 1st shaking (Spectrum I) (b) 2nd shaking (Spectrum II) (c) 3rd shaking (Spectrum I)

Figure 12. Maximum shear strain distribution in Case3 (1:1.5 slope gradient).

2.3. Damage Process

Figure 13 shows the relationship between a slope gradient and maximum shear strain at the toe of a slope, and a settlement at the top of an embankment after the first shaking in each case. From Figure 13 (a), the steeper a slope gradient, the greater the maximum shear strain at the toe of a slope. Specially, the maximum shear strain at the toe of a slope exceeds the limit value of Damage level 3 in Case1 with the slope gradient

of 1:1.0, which resulted in sliding failure. Additionally, in Case2 with the slope gradient 1:1.25, although sliding failure didn't occur during the first shaking, the maximum shear strain at the toe of the slope reached Damage level 3. It indicated a local shear failure occurred at the toe of the slope. In addition, the local shear failure progressed with the subsequent shaking. Consequently, sliding failure occurred at the sixth shaking in Case2. On the other hand, in Case3 with the standard slope gradient of 1:1.5, the shear strain at the toe of the slope was less than the limit value of Damage level 3 (7.5%). Hence, the model embankment didn't lead to sliding failure. As a result, it was confirmed that safety of an embankment against sliding failure could be evaluated by comparing the maximum shear strain at the toe of a slope and the damage level of an embankment material even when a slope gradient is different.

Figure 13 (b) shows that the settlements are less than 200mm in all cases, which is within Deformation level 2 (minor damage) described in the seismic design standard. However, in Case1, although the sliding failure occurred, the measurement position of settlement was inside than the sliding plane, an underestimated settlement was measured by the sensor. Measuring the displacement of the sliding soil block from images after the first shaking in Case1, the settlement is approximately 957 mm, which is much larger than 500mm that is limit value of Deformation level 4 (a degree of damage that requires a long time for restoration). By contrast, in Case2 and 3 that didn't occur sliding failure during the first shaking, the settlements were only about 50mm. In addition, no significant deformation such as sliding failure occurred, indicating that the deformation state in each case is consistent with the level of damage described in the seismic design standard. Therefore, proposed verification method can take into account the seismic damage process of an embankment, using shear strain at the toe of a slope as a verification index for safety against sliding failure, and when a safety is satisfied, using a settlement as a verification index for recoverability like before.

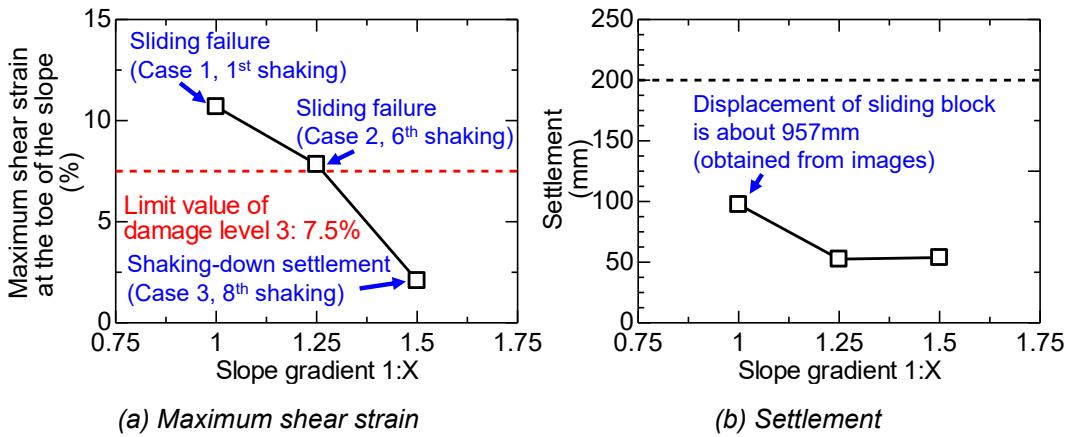


Figure 13. The relationship between slope gradient and deformations after 1st shaking each case.

3. Seismic response value calculations

3.1. Outline of numerical simulation

The above test results indicate that an embankment with steep slope may lead to sliding failure during earthquakes. Thus, safety verification against sliding failure is required in the seismic performance verification. Since the occurrence of sliding failure could be judged by whether or not shear strain at the toe of a slope reaches Damage level 3 of an embankment material, a seismic response value calculation method is necessary for a safety verification that can evaluate shear strain accumulated at the toe of a slope. Therefore, a method based on parameters obtained at seismic design was discussed with practical method in mind.

Here, as a practical response value calculation method, the effectiveness of FEM analysis method was verified. In FEM analysis, constitutive model was used that was combined with GHE-S model (Nogami et. al. (2012)), a nonlinear model of a ground that is standard in the seismic design of Japanese railways, and multiple shear spring model (Towhata and Ishihara (1985)). Figure 14 shows a conceptual diagram of multiple shear spring model. In this model, a number of shear springs applied GHE-S model are took into account a region of shear stress - axial differential stress relationship and shear strain - axial differential strain relationship. For example, by using two shear springs, shear behavior in the direction of $\theta = 45$ and 135° can be evaluated. Furthermore, by using four shear springs, $\theta = 22.5, 67.5, 112.5$, and 157.5° can be evaluated. In this study, shear behavior

at 5° intervals was evaluated by setting 18 shear springs. When carrying out a dynamic analysis using GHE-S model, GHE parameters are generally set by fitting shear stiffness - strain relationship obtained from dynamic shear tests. On the other hand, in this calculation of an embankment, here, it is necessary to properly evaluate a shear behavior of an embankment material up to around Damage level 3~4 (about 10% strain) in order to perform safety verification. Therefore, GHE parameters were set to fit the region around Damage level 3 of the used embankment material. The historical damping was set by fitting the historical damping-shear strain relationship up to the 1% shear strain level. However, it was confirmed that the historical damping does not significantly affect the analytical results of an embankment. An example of the analytical model is shown in Figure 15 and parameters used are shown in Table 4. Here, reference strain γ_r is calculated from the shear strength τ_f and initial shear stiffness G_0 as $\gamma_r = \tau_f / G_0$. The shear strength parameters were set as well as Table 3 for the central part of the embankment, while for the slope surface, the cohesion was reduced considering the drying of the embankment material. In addition, joint elements were placed between the surface layer of the embankment and the supporting ground because the toe of the slope was observed to slide toward the front of the slope during shaking.

In this calculation, first, an embankment was analyzed under its own weight as an elastic body with uniform shear stiffness. The shear stiffness was set based on a confining pressure near the center of the embankment (50kPa). Secondary, the shear stiffness G_0 was modified from Equation 1, that took into account a dependence of each element on confining pressure σ_m obtained from the own weight analysis.

$$G_0 = 10179 \cdot \sigma_m^{0.5} \quad (1)$$

Finally, dynamic analysis was carried out taking over the stress state obtained by nonlinear own weight analysis using the shear stiffness considered the dependence of confining pressure.

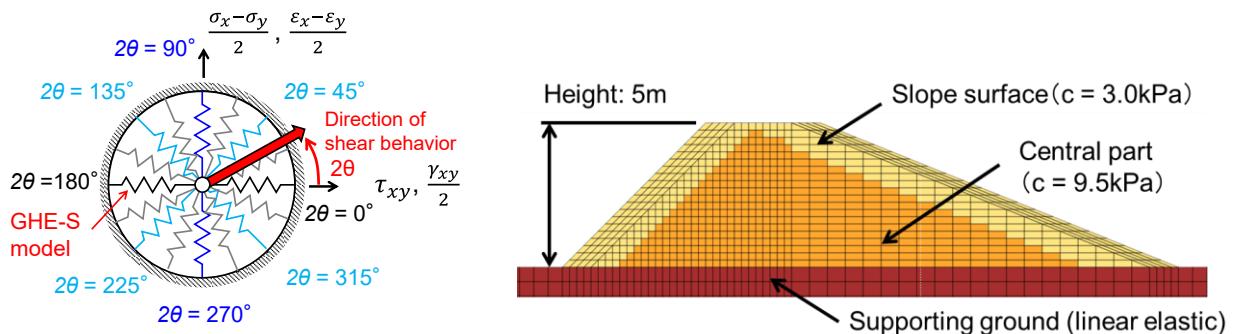


Figure 14. Conceptual diagram of multiple shear spring model.

Figure 15. An example of FEM analytical model in Case1 (1:1.0 slope gradient)

Table 4. Analytical parameters (physical properties)

Embankment	Supporting ground
Unit volume weight : γ 16.9 kN/m ³	18.0 kN/m ³
Poisson ratio : ν 0.499	0.499
Initial stress stiffness : G_0 10,179 kN/m ² *	165,306 kN/m ²
Cohesion : c 3.0 kPa (Surface) 9.5 kPa (Central part)	-
Internal friction angle : ϕ 32.5 deg.	-

*When the confining pressure is 1 kPa.

Table 5. GHE parameters

C1(0)	1.0
C2(0)	0.2
C1(∞)	0.11
C2(∞)	1.0
α	0.986
β	1.38

3.2. Numerical simulation results

This section describes the result of the reproduction analysis of the first shaking (Spectrum I) in Case1. Figure 16 shows the time histories of the settlement, the horizontal displacement, and maximum shear strain at the toe of the slope computed using FEM. It could be seen that each analysis results reproduce the increasing trend in the test. Since FEM model does not consider the deformation after shear failure, the behavior after sliding failure (around 29 seconds) is not consistent. However, the maximum shear strain at the toe of the

slope reaches Damage level 3 around 16 seconds. Thus, it can be judged from the analysis result that the embankment might lead to sliding failure. Comparing the timing when the toe of the slope reaches Damage level 3 between the test and the analysis, although the analysis reaches Damage level 3 a little earlier, the timings are generally in agreement. In addition, Figure 17 shows the distributions of the maximum shear strain at 10, 15, 16, and 20 seconds. As in the test, the damage process was adequately reproduced. Altogether, the shear strain was concentrated at the toe of the slope and the potential sliding plane occurred.

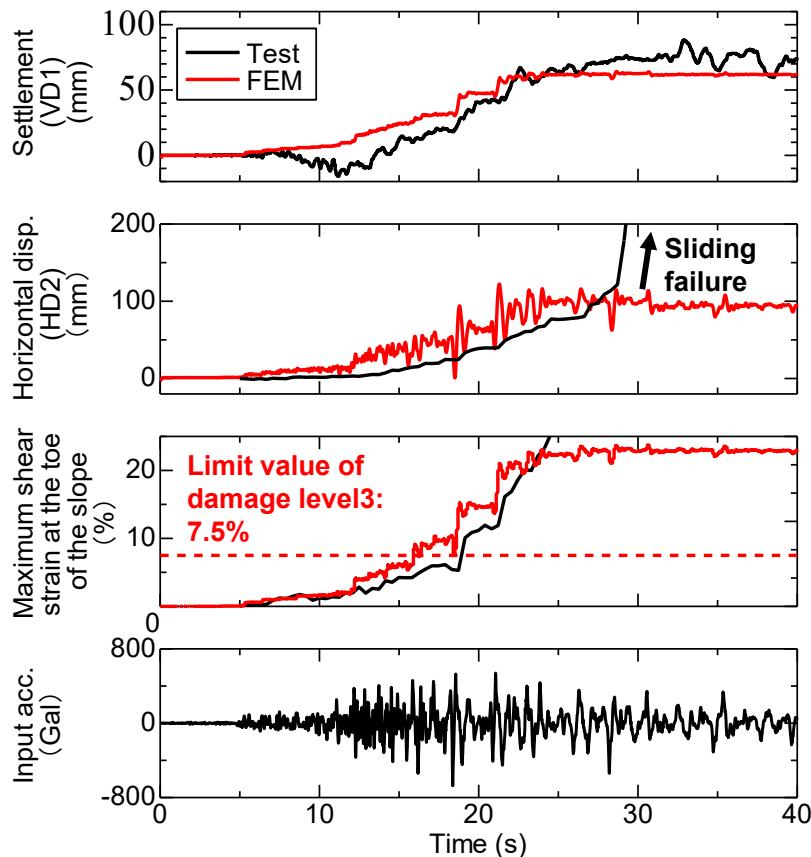


Figure 16. Time histories obtained from the FEM analysis and the test in Case1 (1:1.0 slope gradient).

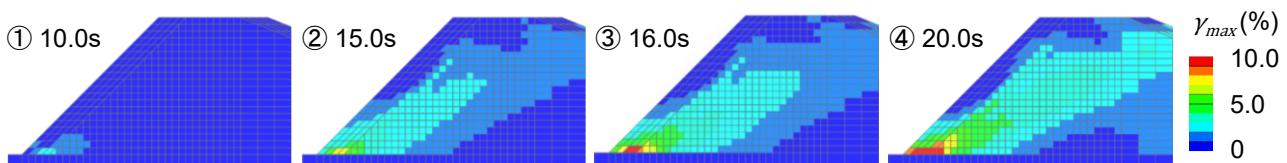


Figure 17. The calculated distribution of the maximum shear strain in Case1 (1:1.0 slope gradient).

4. Comparison of tests and calculations

In proposed performance verification method, shear strain at the toe of a slope is used as a safety verification index and a settlement is used as a reparability verification index. In this section, the validity of the seismic response value calculation method is discussed by comparing the tests and the analysis. Figure 18 shows the relationship between the slope gradient and the deformations after the first shakings obtained from the FEM analysis and centrifuge shaking table tests. Moreover, the settlement calculated by Newmark method using modified Fellenius method is also shown. In Newmark method calculations, the cohesion and internal friction angle are set in the same manner as in Table 4.

4.1. Safety

In proposed verification method, a safety against sliding failure is judged based on whether shear strain at the toe of a slope, where deformation is concentrated, exceeds a limit value of Damage level 3 (γ_{fail}) of an

embankment material. By referring to shear strain at the toe of the slope in the test, it can evaluate the safety of Case1 and 2, in which sliding failure occurred during the first shaking (Case1) and sixth shaking (Case2). Additionally, safety assessment was properly performed in the Case3 that didn't lead to sliding failure even after eighth shaking. On the other hand, the FEM analysis overestimates the maximum shear strain at the toe of the slope by 1.5 times than tests in Cases1 and 2. However, the computed shear strain exceeds the limit value of Damage level 3 when the sliding failure occurred in the tests (Case1 and 2) and doesn't exceed when the slope gradient is standard (Case3). Therefore, the trend of tests that deformation mode can be evaluated using shear strain and damage level was consistent. As a result, it was considered possible to calculate the shear strain at the toe of a slope, which is a safety verification index, using the FEM analysis.

4.2. Reparability

In proposed verification method, as usual, reparability is verified by comparing a settlement and the design limit value of residual displacement, which is determined by a degree of difficulty of restoration. For example, Deformation level 2 (minor damage) in the embankment of Japanese railway field is defined as a settlement of less than 200mm. In Case1 where sliding failure occurred during the first shaking, the FEM analysis underestimated the settlement because a deformation after shear failure was not taken into account in the FEM model. However, it can be seen that the safety verification is not satisfied in Case1. In contrast, the settlement can be evaluated with good accuracy in Case2 and 3, although its slightly underestimate. Although a volume change for dilatancy was not considered in this FEM analysis, the settlement can be calculated with high accuracy. For this reason, the volume change of the embankment is small in the test due to sufficient and uniform compaction. On the other hand, the calculated settlement by Newmark method increases rapidly as slope becomes steeper. Thus, there is a possibility of overestimating a settlement for an embankment with steep slope gradient. One of the reasons for this is that Newmark method assumes rigid-plastic deformation and does not take into account the damage process as observed in tests.

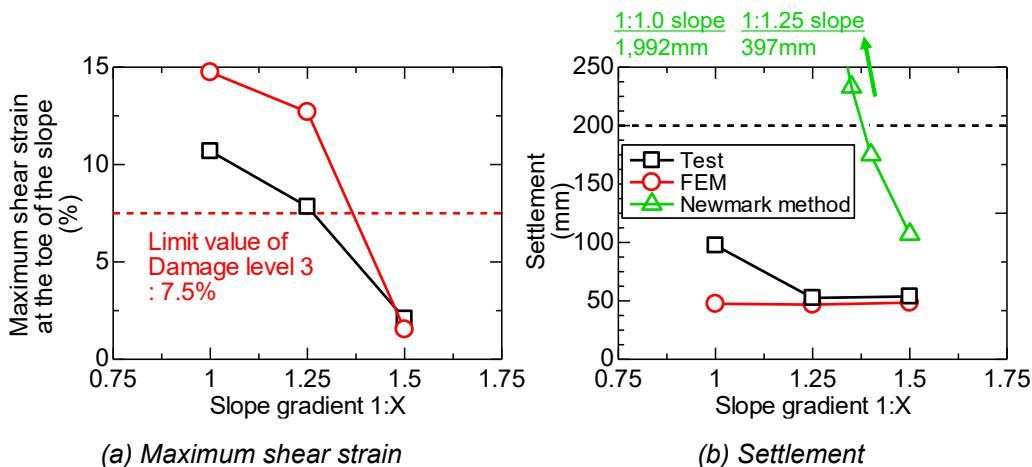


Figure 18. The relationship between slope gradient and deformations after 1st shaking each case on tests.

5. Conclusions

In this study, centrifuge shaking table tests were carried out on embankments with different slopes gradients. The reproduction analyses were also conducted using FEM analysis and Newmark method for developing a performance verification method that can take into account the seismic damage process of embankments. The findings are as follows:

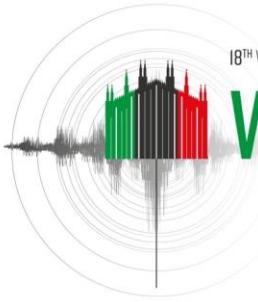
- (1) In the centrifuge shaking table tests, the camera fixed to the shake table due to capturing high-speed and high-resolution images of an embankment during shakings. Moreover, image analysis was carried out to observe a seismic damage process of an embankment in detail. As a result, the embankments with slope gradient steeper than 1:1.5, which is the standard slope in Japanese railway field, lead to sliding failure. In particular, the shear strain was concentrated at the toe of a slope, and a sliding plane occurred from that strain concentrated part. In contrast, the embankment with standard 1:1.5 slope did not lead to sliding failure, but only to deformation such as a settlement, a horizontal displacement. Therefore, it can be said

that embankments with slope gradient gentler than 1:1.5 are sufficiently safe against sliding failure if a supporting ground is stiff and adequately compacted an embankment.

- (2) Applying proposed verification method to test result, it was confirmed that can appropriately evaluate safety against sliding failure and recoverability. Furthermore, the verification index (safety: maximum shear strain at the toe of a slope, reparability: settlement) can be evaluated by the FEM analysis that combines multiple shear spring model and GHE-S model. As a result, it is possible to verify safety and reparability in the same way as for seismic design of bridges.

6. References

- Fujiwara, T., Nakamura. H., Taniguchi, Y. Takasaki, H. and Kaneda, J. (2015): A study about factors which caused railway embankment damages by circular slip analysis, Journal of Japanese Society of Civil Engineering A1, Vol. 71, No. 4, I_87-94. (In Japanese)
- Ibuki, R., Uemura, K., Doi, T., Izawa, J. and Sreng, S. (2022): High speed observation on damage process of embankments during earthquakes in a centrifugal acceleration field, 10th Physical Modelling in Geotechnics, 912-915.
- Izawa, J., Doi, T. and Kojima, K. (2022a): Centrifuge shaking table tests on damage level of embankments before sliding failure during earthquakes, 20th International Conference on Soil Mechanics and Geotechnical Engineering, 1117-1122.
- Izawa, J., Doi, T., Suzuki, A. and Kojima, K (2022b): Seismic design of embankments in consideration of damage process during earthquakes, Quarterly Report of RTRI, Vol. 63, Issue 1, 56-63.
- Nogami, Y., Murono., Y. and Morikawa, H. (2012): Nonlinear hysteresis model taking into account S-shaped hysteresis loop and its standard parameters, Proceedings of 15th World Conference on Earthquake Engineering.
- Newmark, N. M. (1965): Effects of earthquakes on dams and embankments, Geotechnique, Vol. 15, No. 2, 139-160.
- Railway Technical Research Institute (2012): The Design Standards for Railway Structures and Commentary (Seismic Design), Supervised by Ministry of Land, Infrastructure and Transportation, Maruzen. (In Japanese)
- Railway Technical Research Institute (2007): The Design Standards for Railway Structures and Commentary (Earth Structure), Supervised by Ministry of Land, Infrastructure and Transportation, Maruzen. (In Japanese)
- Sarma, S. K. (1975): Seismic Stability of Earth Dams and Embankments, Geotechnique, Vol. 25, No. 4: 743-761.
- Sreng, S., Okochi, Y., Kobayashi, K., Tanaka, H., Sugiyama, H., Kusaka, T., Miki, H. and Makino, M. (2015): Centrifuge model tests of embankment with a new liquefaction countermeasure by ground improvement considering constraint effect. 6th International Conference on Earthquake Geotechnical Engineering.
- Towhata, I., Ishihara, K (1985): Modelling soil behavior under principal stress axes rotation, 5th International Conference on Numerical Methods in Geomechanics, 523-530.



SEISMIC FRACTURE MODELING OF 3D GRAVITY DAM MONOLITHS USING THE SCALED BOUNDARY FINITE ELEMENT METHOD

X. Jiang¹, H. Zhong², D. Li³, J. Niu⁴ & B. Wu⁵

¹ Nanchang Institute of Technology, Nanchang, China, jiangxinxin@nit.edu.cn

² China Institute of Water Resources and Hydropower Research, Beijing, China

³ China Institute of Water Resources and Hydropower Research, Beijing, China

⁴ Nanchang Institute of Technology, Nanchang, China

⁵ Nanchang Institute of Technology, Nanchang, China

Abstract: This paper presents the seismic crack propagation analysis of a 3D non-overflow monolith of the Koyna gravity dam with initial cracks considering the effects of dam-reservoir interaction. A numerical model based on the Scaled Boundary Finite Element Method (SBFEM) is proposed to simulate the 3D fracture process of gravity dams. The SBFEM is a semi-analytical method with only the discretization on the boundary and analytical solution in the radial direction. The cracked polyhedrons are modelled by the SBFEM with the salient feature that the stress intensity factors are directly extracted from element stress modes, which are utilized to simulate cracks in the gravity dams. The dynamic equilibrium equations of motion for the dam-reservoir system is solved by the Newmark method to evaluate the dynamic response. The cracking process are then simulated numerically by introducing the 3D crack propagation criteria and local remeshing algorithm. Moreover, the opening and closing behaviour of each crack are monitored continuously during the earthquake. The cracking process and crack profile of the Koyna gravity dam under earthquake shocks are simulated using the developed polyhedral model to verify its validity. The effects of the mesh density on the seismic response are also examined and discussed.

1. Introduction

Cracks are existed in concrete dams due to the shrinkage of the concrete, variation of the internal and external temperature, and so on. The initiation and propagation of cracks under earthquake pose a serious threat to the safety of the concrete dams (Calayır et al., 2005). From the observed cracking process in concrete dams, it is often the case that the dangerous cracks are formed through the extension of surface cracks (Chopra et al., 1973). In 1967, the Koyna gravity dam in India was found to be serious cracked after the earthquake, with through-type cracks appeared in the non-overflow monoliths, which prompted the academic community to conduct in-depth research on the mechanism of earthquake-induced cracking and damage in gravity dams. Nonlinear fracture models primarily include the Discrete Crack Mode (Shi et al., 2014) and the Cohesive Crack Model (Yu et al., 2022; Branco et al., 2015), were proposed to model the seismic behaviour of concrete dams. And numerical techniques, typically represented by finite element method (Molnár et al., 2017), boundary element method (Batta et al., 1996), and extended finite element method (Zhang et al., 2013) were employed.

However, dynamic fracture analysis was mostly limited to two-dimensions (Yilmazturk et al., 2015; Li et al., 2022), while three-dimensional dynamic fracture analysis being relatively rare.

The Scaled Boundary Finite Element Method (SBFEM), as a semi-analytical numerical analysis method, combines the advantages of both finite element and boundary element methods (Wolf et al., 2000). It is characterized by the ability to reduce one-dimensional and radial analytical solutions (Yu et al., 2023). In recent years, the SBFEM has demonstrated salient features in fracture analysis with the description of singular stress fields at crack tips and a direct extraction of generalized stress intensity factors (SIFs) from the element stress modes (Song et al., 2017; Hu et al., 2023). The computational methods for extracting 2D and 3D generalized SIFs (Saputra et al., 2015; jiang et al., 2022) are proposed and validated. Moreover, a local mesh refinement technique based on polygonal SBFEM was utilized, which proved to be efficient and accurate for the description of crack propagation process. Shi et al., 2013 utilized SBFEM and polygon local mesh refinement, to perform the static fracture process in gravity dams. Li et al., 2019 proposed an SBFEM model for hydraulic fracturing in gravity dams, with a specific focus on the variation and impact of fissure water pressure during the crack opening-closure process.

This paper aims to extend the SBFEM to perform a 3D crack propagation analysis of gravity dam monoliths. The dynamic equilibrium equations for polyhedral SBFEM are derived in Section 2. A fully automated method for simulating the dynamic crack propagation in gravity dams is presented in Section 3. Numerical examples are presented in Section 4. The seismic fracture process of the Koyna gravity dam is simulated and compared with shaking table test to prove its accuracy. Conclusions and future work are summarized in Section 5.

2. Summary of the 3D SBFEM for dynamic fracture analysis

2.1. Basic concepts of the polyhedral SBFEM

The SBFEM is a numerical method in which only the domain boundary is discretized, while the interior of the domain is described using radial analytical solutions. The polyhedral SBFEM is that the domain is discrete using a polyhedral mesh, with the polyhedrons modelled by the SBFEM. The polyhedral scaled boundary element is shown in Figure 1(a). Polyhedral elements can adapt to complex boundary due to arbitrary number of polygons on the boundary, such as such as triangles, quadrangles, etc. The only requirement is to satisfy the scaling requirement, meaning that the entire domain is visible from the scaling centre denoted as 'SC'. The radial coordinate is denoted as ξ , where $\xi = 0$ corresponds to the scaling centre, $\xi = 1$ corresponds to the boundary, η and ζ are the circumferential coordinates defined on each surface. They are called the scaled boundary coordinates and constitute a right-hand coordinate system in three dimensions. As shown in Figure 1(b), the polyhedral scaled boundary finite elements are used to mesh a gravity dam with a pre-existing crack. The scaling centre is located at the crack tip to model the crack. The crack surfaces are formed by scaling from the boundary towards the scaling centre proportionally without any special treatment. The governing equations of the scaled boundary finite element are then established to evaluate the displacement field, strain field, and stress field within each element.

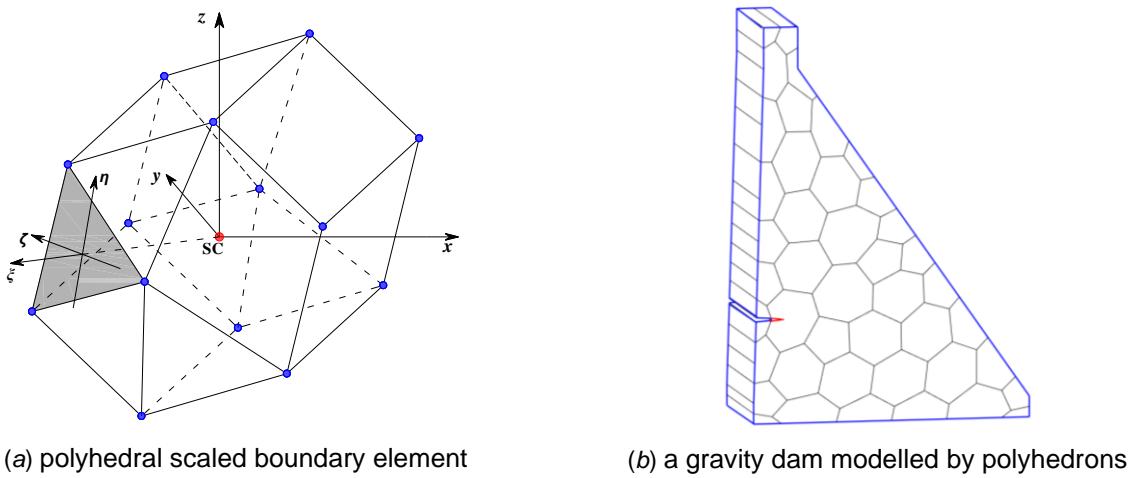


Figure 1. Polyhedral scaled boundary element model.

The governing equations for the polyhedral scaled boundary elements without considering body forces and side-face tractions are derived from the principle of virtual work (Saputra et al., 2015), which is expressed as

$$\xi \begin{Bmatrix} \xi^{0.5} \{u(\xi)\} \\ \xi^{-0.5} \{q(\xi)\} \end{Bmatrix}_{,\xi} = -[Z] \begin{Bmatrix} \xi^{0.5} \{u(\xi)\} \\ \xi^{-0.5} \{q(\xi)\} \end{Bmatrix} \quad (1)$$

where $[Z]$ are Hamiltonian coefficient matrices, $\{u(\xi)\}$ denote the displacement functions, and $\{q(\xi)\}$ are internal nodal forces.

The Eigenvalue decomposition or Schur decomposition method (Song et al., 2017) can be used to solve the equation (1). Eigenvalue decomposition is applied here to decompose the Hamiltonian coefficient matrices, the displacement functions and the internal nodal forces are expressed as

$$\{u(\xi)\} = \xi^{-0.5} [\Phi_b^{(u)}] \xi^{\langle \lambda_b \rangle} \{c\} \quad (2)$$

$$\{q(\xi)\} = \xi^{0.5} [\Phi_b^{(q)}] \xi^{\langle \lambda_b \rangle} \{c\} \quad (3)$$

where λ_b are the eigenvalues of $[Z]$, $[\Phi_b^{(u)}]$ and $[\Phi_b^{(q)}]$ are the corresponding eigenvectors, $\{c\}$ are the integral constant vectors.

The displacement at any point within the polyhedron can be represented as an interpolation along the circumferential boundary using the node displacement function, which are expressed as

$$\{u(\xi, \eta, \zeta)\} = [N_u] \{u(\xi)\} \quad (4)$$

with $[N_u]$ are the interpolation shape functions.

2.2. Derivation of the dynamic equation of SBFEM

The radial coordinate ξ equals 1 on the boundary. By substituting the boundary conditions of the element into equations (2) and (3), eliminating the integration constants, and rearranging, the element stiffness matrices $[K_e]$ are expressed as

$$[K_e] = [\Phi_b^{(q)}] [\Phi_b^{(u)}]^{-1} \quad (5)$$

Considering the boundary condition ξ equals to 1 on the boundary of the polyhedral element, by substituting it into equation (4), the integration constant vectors can be solved and expressed as

$$\{c\} = [\Phi_b^{(u)}]^{-1} \{d\} \quad (6)$$

with $\{d\}$ are the nodal displacements at the boundary.

By substituting equation (6) into equation (4), the shape functions $[N]$ of the element are expressed as

$$[N] = \xi^{-0.5} [N_u] [\Phi_b^{(u)}] \xi^{\langle \lambda_b \rangle} [\Phi_b^{(u)}]^{-1} \quad (7)$$

The mass matrices of the polyhedral element are assembled based on the mass matrices calculated for the pyramid formed by the boundary nodes of the element and the scaling centre, which are express as

$$[M_e] = \sum_e \int_V [N_p]^T \rho [N_p] dV \quad (8)$$

For any structural system discretized by polyhedrons, the global structural stiffness matrix and mass matrix are assembled in a manner similar to the finite element method through element assembly. Therefore, the dynamic equation is as follows

$$[M]\{\ddot{d}\} + [C]\{\dot{d}\} + [K]\{d\} = \{F\} \quad (9)$$

It is important to consider the effects of damping for practical dynamic analysis. The Rayleigh damping is expressed by a linear combination of the global stiffness matrix and the mass matrix as

$$[C] = \alpha_0 [M] + \alpha_1 [K] \quad (10)$$

with α_0 and α_1 are the coefficients related to the frequencies and damping of structures.

Equation (9) can be solved to evaluate the dynamic displacement field, velocity field, and acceleration field in time domain. Then it becomes convenient to calculate dynamic fracture parameters and then perform the dynamic fracture analysis.

3. Dynamic crack propagation simulation

3.1. Extraction of the generalized dynamic stress intensity factor

In the case of a crack with a propagation velocity of v in an infinite plane (Freund, 1998), the dynamic crack stress intensity factors can be expressed as

$$\begin{Bmatrix} K_I(t, c) \\ K_{II}(t, c) \\ K_{III}(t, c) \end{Bmatrix} = [k_I(c) \ k_{II}(c) \ k_{III}(c)] \begin{Bmatrix} K_I^{eq}(t) \\ K_{II}^{eq}(t) \\ K_{III}(t) \end{Bmatrix} \quad (11)$$

with the superscript 'eq' on the stress intensity factor represents the transient stress intensity factor calculated in the instantaneous stress field.

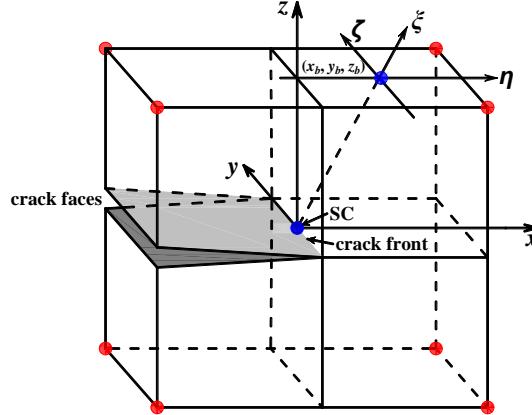


Figure 2. Representation of a polyhedral element containing a crack.

The generalized stress intensity factors are utilized to describe the dynamic stress singularity at the crack tip. As shown in Figure 2, any point within the polyhedral crack element simulated using SBFEM can be transformed into a local polar coordinate system. By introducing the crack characteristic length, the generalized SIFs can be evaluated at the local polar coordinate. A detailed discussion can be referred to Reference (Saputra et al., 2015; Jiang et al., 2022). For brevity, only the expression of the transient generalized stress intensity factors is presented, which is expressed as

$$\{K^{eq}(t)\} = \begin{Bmatrix} K_I^{eq}(t) \\ K_{II}^{eq}(t) \\ K_{III}(t) \end{Bmatrix} = \sqrt{2\pi L} \begin{Bmatrix} \Psi_{\sigma_{\theta\phi}L}^s \\ \Psi_{\tau_{r\phi}L}^s \\ \Psi_{\tau_{\theta\phi}L}^s \end{Bmatrix} \{c^s(t)\} \quad (12)$$

with the singular stress modes $\left[\Psi_{\sigma L}^s\right]$ defined as

$$\left[\Psi_{\sigma L}^s \right] = \left[\Psi_{\sigma}^s \right] \left(\frac{L}{r_b} \right)^{-[\left[S^s \right] + 1.5[I]} \quad (13)$$

where the superscript "s" represents the singular term, L denotes the chosen crack characteristic length, and r_b is the distance from the scaling centre to the point at the boundary.

It is important to note that the singular stress modes of polyhedral crack elements are only related to the element's shape. The values of the singular stress modes at the crack tip can be interpolated from adjacent element Gauss integration points. Additionally, the transient stress intensity factor can be calculated at any specified point, and the solution process is similar to the stress recovery process in the finite element method.

3.2. Automatic local remeshing algorithm

Due to the complexity of three-dimensional crack propagation and inapplicability of crack propagation criteria, a simplified model of 3D crack propagation for gravity dams is obtained by making two hypotheses. A through-crack is assumed on the crack front, which means the crack front is a straight line. And the direction of crack extension along the crack front is also assumed to be determined at the centre on the crack front. Thus, the crack front remains straight at each crack propagation.

Although the foregoing assumptions reduce the simulation of crack propagation to that of 2D plane cutting at the centre point on the crack front, this simplified 3D model demonstrates important improvements over a pure 2D model by simulating the geometrical conditions and loading condition accurately. The fracture parameters are calculated by the three-dimensional fracture analysis in the time domain. At each time step, the fracture parameters at the centre of the crack front are evaluated with the fracture toughness. When the fracture toughness is reached, the crack is considered to be in a critical state and about to propagate. The remeshing algorithm (Ooi, 2013) for polygon meshes was very efficient for crack propagation problems. In the cracking propagation process, only the local meshes near the crack tip and along the crack propagation path are minimally altered. Therefore, an automatic local remeshing algorithm for 3D gravity dams is realized.

4. Numerical examples

The Koyna concrete gravity dam experienced a damaging earthquake in 1967, resulting in penetrating cracks in several non-overflow monoliths (Chopra, 1973; Zhang, 2013). The cracks are most likely to start from the neck near the downstream face. Therefore, cracks are usually presupposed at the downstream neck to perform seismic cracking analysis. The tallest non-overflow monolith with a pre-existing horizontal crack of 1 m is shown in Figure 3. The monolith is 103 m high, 70.2 m wide at its base and 30 m along the transverse river. The concrete material parameters for the Koyna dam are: $E = 31 \text{ GPa}$, $\nu = 0.2$, $\rho = 2643 \text{ kg/m}^3$, and the dynamic fracture toughness of concrete is $K_{ld} = 1.8 \text{ MN}\cdot\text{m}^{-3/2}$.

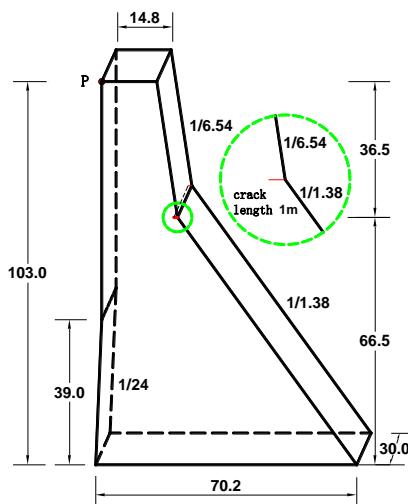


Figure 3. Typical concrete gravity dam monolith of the Koyna dam (units: m).

Figure 4 shows the time histories of the Koyna earthquake. The peak horizontal acceleration along the river is 0.49 g, and the peak vertical acceleration is 0.34 g. Peak acceleration in the cross-stream direction is 0.63 g but not considered here. The maximum reservoir water level is set as 92.0 m, which corresponds to the level when the earthquake occurred. In the dynamic analysis, damping equal to 5 percent is assumed, and an integration time step of 0.02 sec is employed. The Westergaard added mass is used to model the hydrodynamic effect of the reservoir water. The dam is considered to be fixed at the base while neglecting the effects of dam-foundation dynamic interaction. It should be noted that a crack will open and close cyclically in quick succession of the earthquake. The contact springs are applied to the crack surface to monitor the opening/closing behaviour of the cracks.

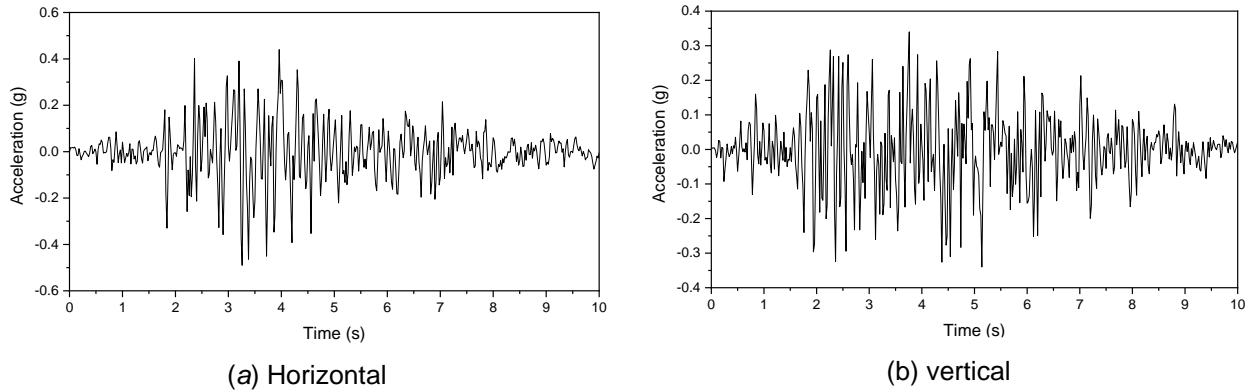


Figure 4. Time history of acceleration.

4.1. Numerical model

The gravity dam model is discrete into two types of polyhedral elements with different mesh densities, as shown in Figure 5. The numbers of polyhedral elements corresponding to the coarse mesh and fine mesh are 950 and 2375, and the numbers of nodes are 2640 and 6264, respectively. The pre-existing crack is simulated by polyhedral crack elements, with scaling centre of the polyhedral element positioned at the crack tip.

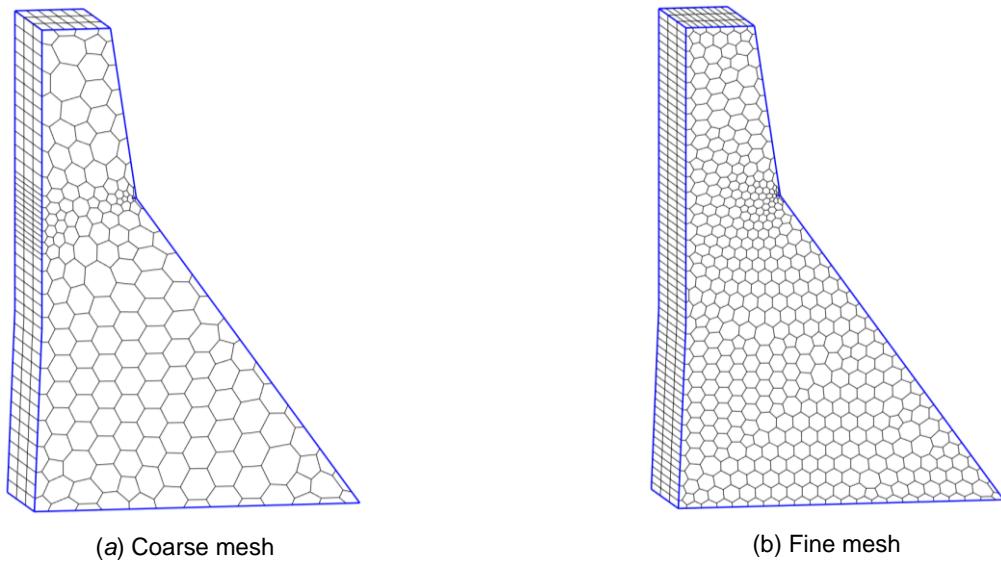


Figure 5. Polyhedral SBFEM model of the gravity dam monolith.

4.2. Seismic crack propagation analysis of 3D Koyna dam

Static analysis provides the initial state for the subsequent dynamic analysis. Applied loads include self-weight of the dam and hydrostatic. In the case of setting contact springs on the crack surfaces, the dam crest (point

P) horizontal displacement obtained from the coarse mesh and fine mesh are both 0.314 cm, and vertical displacement obtained from the coarse mesh and fine mesh are -0.237 cm and -0.236 cm., which shows good agreement with each other. It is indicated that the coarse mesh can lead to satisfactory result. Moreover, to verify the effectiveness of contact springs, the dam crest (point P) horizontal and vertical displacement obtained from the fine mesh without contact springs are 0.326 cm and -0.229 cm, respectively. It can be seen that whether the contact springs are applied has a great influence on the displacement of the dam crest. Figure 6 shows the deformation of polyhedral SBFEM model with or without contact springs. The cracks are embedded above and below when the contact spring is not applied, and the crack surface is in a state of compression after the spring is applied, indicating that it is necessary to consider the contact conditions of the crack surface.

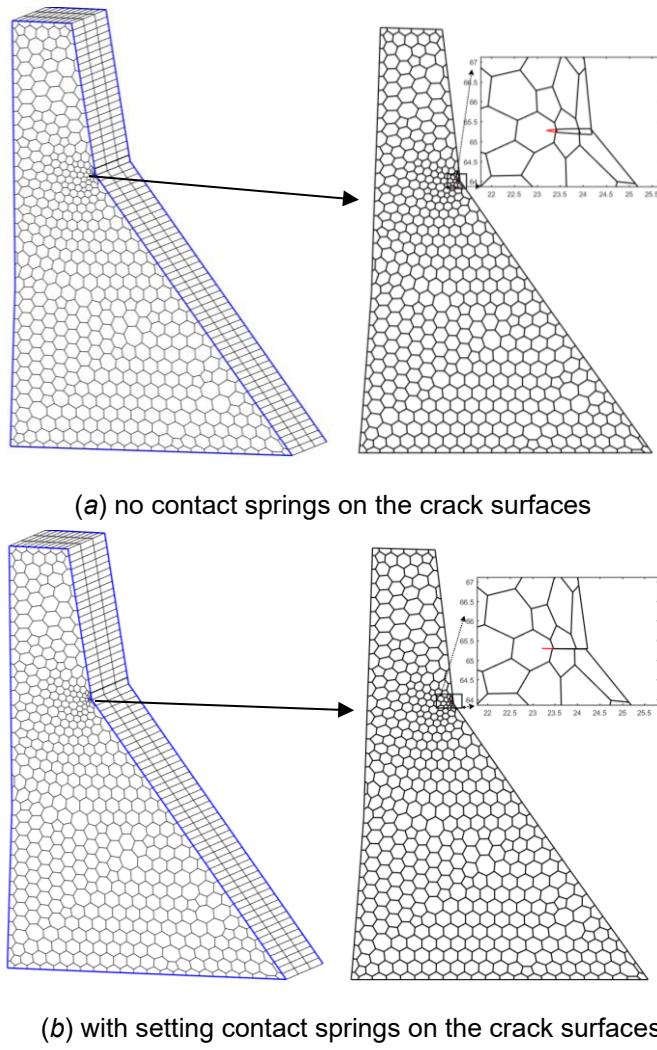


Figure 6. Deformation under static loading of the gravity dam.

The seismic response of the dam is investigated by comparison of the linear and nonlinear dynamic models. Figure 7 shows the seismic displacement response at observation point P, calculated using both coarse and fine mesh models of polyhedral SBFEM, and compares it with the results of linear elastic analysis. In this paper, the horizontal and vertical displacement in the downstream and upward directions are defined as the positive directions, respectively. The nonlinear dynamic responses before cracking initiation (2.06 s) are coincident with that of the linear elastic analysis. It means that the crack at the neck downstream side has not yet propagated. After 2.06 s, the crack begins to propagate. The peak horizontal displacement at the point P happens at 3.42 s, reaching 4.07 cm, and at the upstream happens at 3.76 s, reaching 9.69 mm. The peak vertical displacement at the point P happens at 3.42 s, reaching 1.00 cm, and at the downward happens at 3.76 s, reaching -1.65 mm. It is obvious that the nonlinear dynamic responses are much larger than that of the

linear elastic responses. The reason for this is mainly that the rigidity of the dam is gradually decreased due to crack propagation, thus generating greater dynamic response under the same seismic action. It is interesting that the nonlinear dynamic response of coarse mesh model and fine mesh model is very close, and the peak displacement occurs at the same time. This indicates that the polyhedral SBFEM with a coarse mesh achieves good computational accuracy.

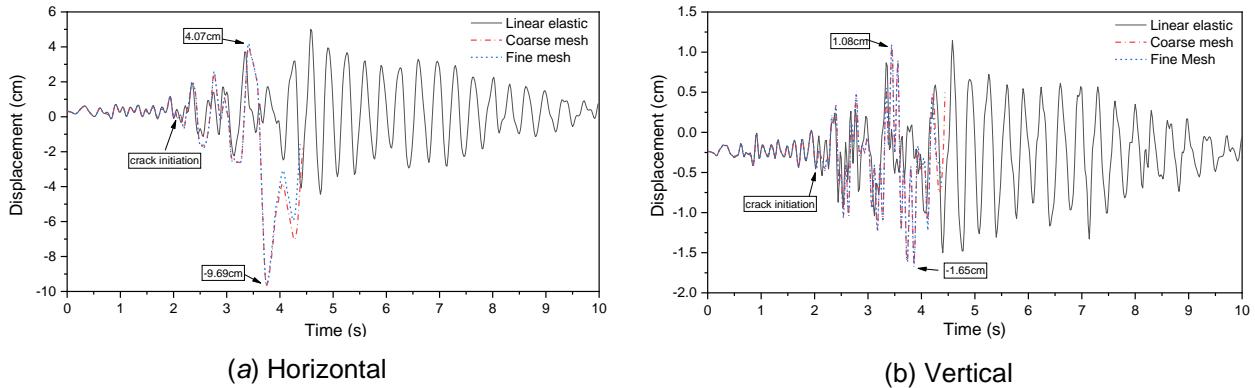


Figure 7. Seismic displacement at the dam crest of point P calculated by different models.

Figure 8 shows the predicted crack propagation profiles of Koyna dam during the Koyna earthquake using the two meshes of polyhedral SBFEM, comparing with the experimental observations. The results show that the computed results in this study are in agreement with the observation results of shaking table test (Hall et al., 1988), which verifies the correctness of the method in this study. Furthermore, the predicted crack propagation profiles obtained from the coarse and fine mesh are very close. When considering the dynamic response at observation point P, it can be concluded that mesh density in this study has a minimal impact on the 3D dynamic fracture model. Thus the coarse mesh exhibits satisfactory computational accuracy in dynamic fracture analysis.

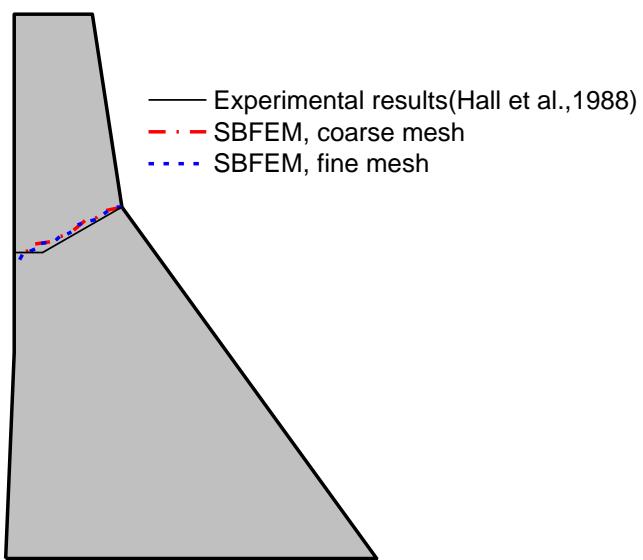


Figure 8. Comparison of predicted crack propagation profiles using different models.

The crack propagation process of Koyna dam during the Koyna earthquake predicted by the polyhedral SBFEM using the coarse mesh are shown in Figure 9. The initial crack firstly propagated at 2.06 s near the neck on the downstream face. The crack spreads in a direction perpendicular to the downstream surface. Figure 9(a) shows the crack trajectory at 2.60s, and crack was open at that station. As the earthquake continued, the crack expanded deeper in its original direction, which is shown in Figure 9(b) at 3.20s. At 3.60s,

the crack trajectory curved downward and extended, showing a trend towards the upstream surface. Moreover, the crack was found to be in a closed state. At 4.00 s, the downstream crack extends fully to the upstream face, with smooth curvature discrete crack penetrating the whole section of the dam.

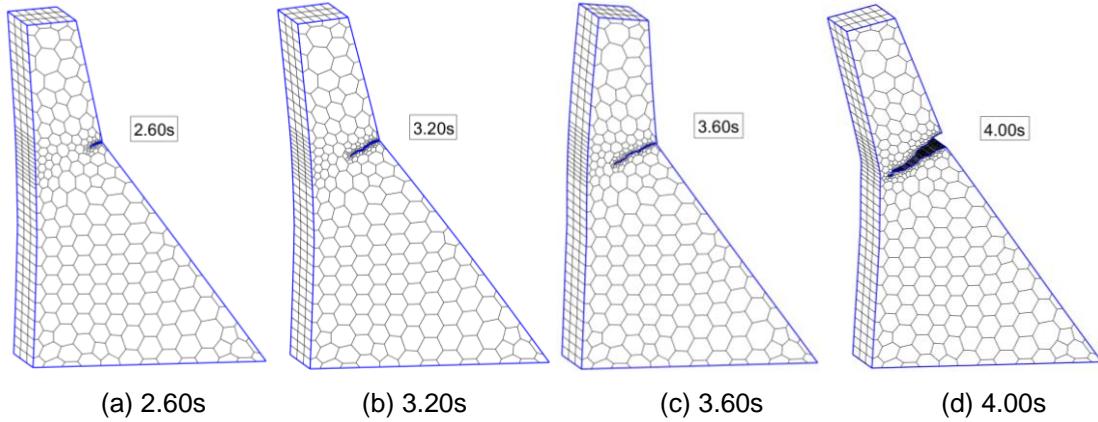


Figure 9. Crack propagation process of Koyna dam at four selected times (deformation scale: 200).

Figure 10 show the horizontal and vertical displacement cloud at times 2.60s, 3.20s, 3.60s and 4.00s during the crack propagation process. In terms of the horizontal displacement distribution, when the crack opens, the displacement of the dam crest tends to the upstream surface, and the value increases with the propagation of the crack, reaching a maximum value of about 45mm. At 3.60s, the crack closes and the dam crest point P shifts downstream, reaching a maximum value of about 17mm. According to the vertical displacement cloud, the absolute displacement of the observation point P increases with the expansion of the crack from 2.60s to 3.20s, reaching a maximum value of about 12mm. However, the vertical displacement of Koyna dam at 4.00 s decreases. This phenomenon may be influenced by vertical seismic components. By comparing the computed results with the Koyna dam prototype observation and model test, it may be concluded that the polyhedral SBFEM model can predict the crack propagation process very well in gravity dams.

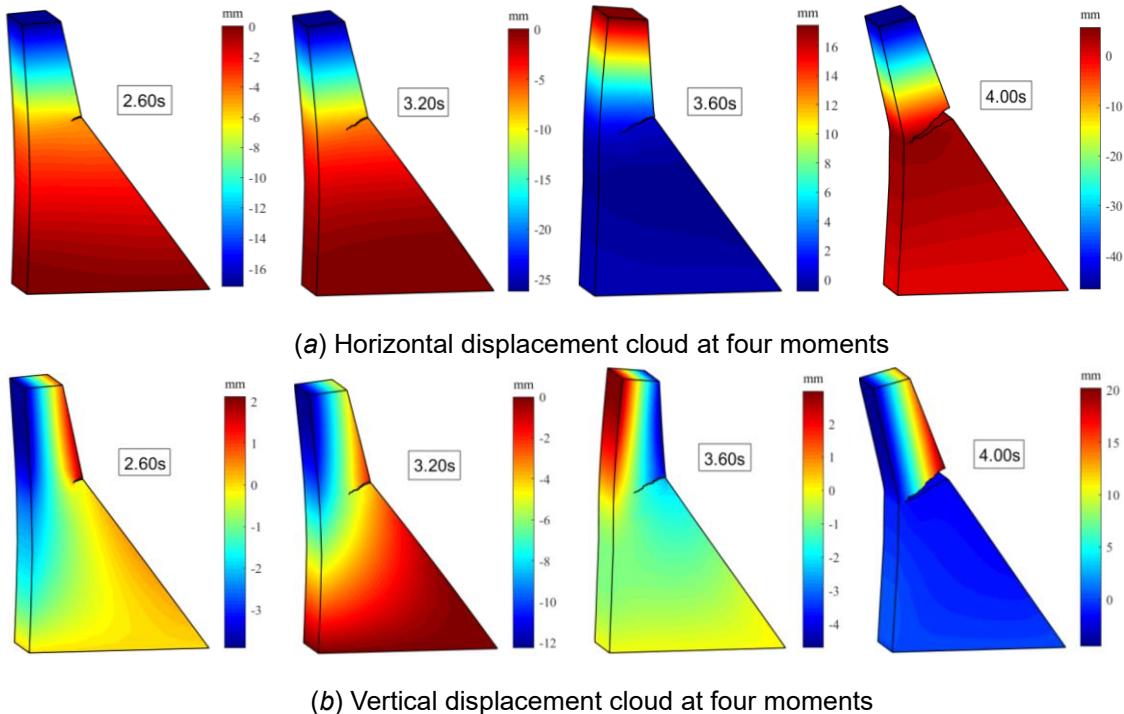


Figure 10. Displacement cloud maps at different time intervals for the coarse mesh model of Koyna gravity dam (deformation scale: 200).

5. Conclusion

A fully automated dynamic propagation analysis for 3D gravity dams is proposed by the combination of polyhedral SBFEM and local mesh refinement techniques. This model has successfully simulated the dynamic crack propagation process of the Koyna gravity dam. The method inherits the advantages of SBFEM in semi-analytically describing the singular stress field at crack tips. Furthermore, this method requires minimal additional nodes to describe the continuous-discontinuous displacement field during crack propagation, and it operates without the need for manual intervention, making it highly efficient for dynamic fracture analysis. From the view of calculation results, the coarse mesh of the polyhedral SBFEM can lead to satisfactory results.

In conclusion, the simplified 3D model demonstrates important improvements over a pure 2D model by simulating the geometrical conditions and loading condition accurately. It is a fully automatic numerical technique for dynamic fracture analysis in concrete dams. It can be extended to the dynamic simulation of interface cracks in concrete structures with further improvements.

6. References

- Batta, V., & Pekau, O.A. (1996). Application of boundary element analysis for multiple seismic cracking in concrete gravity dams. *Earthquake Engineering & Structural Dynamics*, 25, 15-30.
- Branco, R., Antunes, F.V., & Costa, J. (2015). A review on 3D-FE adaptive remeshing techniques for crack growth modelling. *Engineering Fracture Mechanics*, 141, 170-195.
- Calayir, Y., & Karaton, M. (2005). Seismic fracture analysis of concrete gravity dams including dam-reservoir interaction. *Computers & Structures*, 83, 1595-1606.
- Chopra, A.K., & Chakrabarti, P. (1973). The Koyna earthquake and the damage to Koyna Dam. *Bulletin of the Seismological Society of America*, 63(2): 381-397.
- Freund, L.B., & Hutchinson, J.W. (1998). Dynamic Fracture Mechanics. 2nd Ed., Berlin: Cambridge University Press.
- Hall, J.F. (1988). The dynamic and earthquake behaviour of concrete dams: review of experimental behaviour and observational evidence. *Soil Dynamics and Earthquake Engineering*, 7, 58-121.
- Hu, H. , & Chen, D. . (2023). uncertainty qualification in evaluating dynamic and static stress intensity factors using sbfem based on model order reduction. *Engineering Fracture Mechanics*, 109349.
- Jiang, X., Zhong, H., Li, D., Saputra, A. A., & Song, C. (2022). Three-dimensional dynamic fracture analysis using scaled boundary finite element method: A time-domain method. *Engineering Analysis with Boundary Elements*, 139, 32-45.
- Li, Y., Zhong, H., Pang, L., & Hu, Z. (2019). Influence of the water pressure distribution along crack faces on seismic fracture modelling of a dam-reservoir-foundation system. *Engineering Analysis with Boundary Elements*, 101(APR.):252-269.
- Li, Z., Wu, Z., Lu, X., Zhou, J., Chen, J., Liu, L., & Pei, L. (2022). Efficient seismic risk analysis of gravity dams via screening of intensity measures and simulated non-parametric fragility curves. *Soil Dynamics and Earthquake Engineering*, (Jan.):152-183.
- Molnr, G., & Gravouil, A. (2017). 2D and 3D Abaqus implementation of a robust staggered phase-field solution for modeling brittle fracture. *Finite Elements in Analysis and Design*, 130, 27-38.
- Ooi, E.T., Shi, M.G., Song, C., Tin-Loi, F., & Yang, Z. (2013). Dynamic crack propagation simulation with scaled boundary polygon elements and automatic remeshing technique. *Engineering Fracture Mechanics*, 106, 1-21.
- Wolf, J.P., & Song, C. (2000). The scaled boundary finite-element method – a primer: derivations. *Computers & Structures*, 78, 191-210.
- Saputra, A. A., Birk, C., & Song, C. (2015). Computation of three-dimensional fracture parameters at interface cracks and notches by the scaled boundary finite element method. *Engineering Fracture Mechanics*, 148, 213-242.
- Shi, M.G., Zhong, H., Ooi, E.T., Zhang, C., & Song, C. (2013). Modelling of crack propagation of gravity dams by scaled boundary polygons and cohesive crack model. *International Journal of Fracture*, 183, 29-48.

- Shi, Z., Nakano, M., Nakamura, Y., & Liu, C. (2014). Discrete crack analysis of concrete gravity dams based on the known inertia force field of linear response analysis. *Engineering Fracture Mechanics*, 115, 122-136.
- Song, C., Ooi, E.T., & Natarajan, S. (2017). A review of the scaled boundary finite element method for two-dimensional linear elastic fracture mechanics. *Engineering Fracture Mechanics*, 187, 45-73.
- Song, C., Tin-Loi, F., & Gao, W. (2010). A definition and evaluation procedure of generalized stress intensity factors at cracks and multi-material wedges. *IOP Conference Series: Materials Science and Engineering*, 10, 012042.
- Yilmazturk, S.M., Arici, Y., & Binici, B. (2015). Seismic assessment of a monolithic RCC gravity dam including three dimensional dam–foundation–reservoir interaction. *Engineering Structures*, 100, 137-148.
- Yu, C. (2022). A coupled smeared crack-plasticity model in incremental sequentially linear analysis for mixed failure modes. *Computers & Structures*, 269: 1-20.
- Yu, K., Yang, Z., Li, H., Tat Ooi, E., Li, S., & Liu, G. (2022). A mesoscale modelling approach coupling SBFEM, continuous damage phase-field model and discrete cohesive crack model for concrete fracture. *Engineering Fracture Mechanics*, 278: 1-26.
- Zhang, S., Wang, G., & Yu, X. (2013). Seismic cracking analysis of concrete gravity dams with initial cracks using the extended finite element method. *Engineering Structures*, 56, 528-543.

PERFORMANCE EVALUATION OF CONCRETE GRAVITY DAM IN THE EVENT OF SEISMIC AFTERSHOCKS

Shiyam Sundar K P¹, M K Shrimali², S D Bharti³, CVR Murty⁴, Nishant Roy⁵

¹Research Scholar, National Centre for Disaster Mitigation and Management, MNIT Jaipur, India,
shiyamsundarmnit@gmail.com

²Professor, National Centre for Disaster Mitigation and Management, MNIT Jaipur, India.

³Professor, National Centre for Disaster Mitigation and Management, MNIT Jaipur, India.

⁴ Professor, Indian Institute of Technology Madras, India.

⁵Assistant Professor, National Centre for Disaster Mitigation and Management, MNIT Jaipur, India

Abstract: The dams with unconventional cross sections are vulnerable to strong earthquakes, with most of the damages occurring at the neck region where there is an abrupt change in the slope of the downstream side. In the event of a sequence of mainshock and aftershocks, complete failure of the neck region is anticipated. The case of Koyna dam is taken as an illustrative example. A nonlinear time history analysis of a 2D cross-section of the tallest non-overflow monolith is performed for the 1979 Imperial Valley earthquake records of near and far field stations. The cross-section is analyzed for the mainshock and aftershock effects by joining the segments of the earthquake with an adequate time gap created by zero excitations. The time gap is decided such that the free vibration of the dam under the influence of one earthquake shock comes to rest with any possible residual displacement. The analysis considers the inelastic effect of the damage plasticity model available in ABAQUS. The results of the numerical study indicate that the neck region of the dam may be damaged entirely if the effect of aftershocks is considered in the analysis, even at a PGA level of 0.4g. However, no significant damage is anticipated elsewhere in the dam.

1 Introduction

Often, earthquakes are followed by aftershocks, resulting in severe damage or even the collapse of structures weakened by the initial seismic activity. Failure is not an option for large-scale structures like dams, as it could lead to catastrophic loss of life and property. Therefore, structures like dams must possess the ability to withstand multiple earthquakes to prevent such devastation. Dams are particularly prone to crack failures at the neck or sometimes near the base when subjected to significant seismic forces. The specific cracking pattern depends on the shape of the dam's cross-section. To mitigate these risks, extensive research has been conducted on the seismic vulnerability of concrete gravity dams. In 1972, Chopra (Chopra and Chakrabarti, 1972) analyzed the behavior of the Koyna dam under the influence of the earthquake. The study showed the stress distribution on the dam and proved that the tensile stress exceeded the strength capacity of the Koyna dam. Following the previous work, Chopra and Chakrabarti (Chakrabarti and Chopra, 1973) analyzed the dam's seismic behavior, including the interaction of hydrodynamic effects caused by the reservoir water. In 1982, Hall and Chopra (Hall and Chopra, 1982) conducted a seismic analysis of gravity dam in the frequency

domain, including dam-water interaction effects. Fenves (Fenves and Chopra, 1984) extended the study by considering the effect of sediments and silt deposits at the reservoir bottom. These materials partially absorbed hydrodynamic waves, leading to additional damping effects. In 1995, Tan and Chopra (Tan and Chopra, 1995) studied the earthquake behavior of Arch Dams, considering the effects of dam-water-foundation interaction. These research works have laid a foundation for understanding the seismic behavior of concrete gravity dams. Later, the research field was vastly extended to three-dimensional analysis, crack initiation and propagation, seismic behavior of dams considering material nonlinearity, etc.

Bhattacharjee and Leger (Bhattacharjee and Leger, 1993) established an approach for the nonlinear analysis of concrete gravity dams, which considered the effects of dam-reservoir-foundation interaction. Nonlinear seismic investigation of concrete gravity dam considering the hydrodynamic pressure exerted by the reservoir on the dam was investigated by Ghaemian and Ghobarah (Ghaemian and Ghobarah, 1998). They observed that accurate simulations of hydrodynamic effects were crucial for predicting the precise pattern of cracks in concrete gravity dams. In 2005, Bayraktar (Bayraktar et al., 2005) used the Lagrangian approach to examine the effect of rock properties on the stochastic dynamic response of dam-reservoir-foundation systems. Various other effects, like the sloshing of water on the surface and wave propagation through the foundation, were also considered in this study. For both near-fault and far-fault earthquakes, the Folsom gravity dam's seismic behavior was examined with the effect of reservoir length by Bayraktar (Bayraktar et al., 2010). Zhang (Zhang, Wang and Yu, 2013) introduced a computational method using the extended finite element method (XFEM), commonly employed for studying crack expansion, to predict how cracks spread in concrete gravity dams. This method was verified by comparing the results with simulating the 1967 Koyna earthquake on the Koyna dam. Guandi (Wang et al., 2017) studied the seismic behavior of a completed 3D dam, including the effects of contraction joints along with the effect of water interacting with the dam-foundation system. Alembagheri (Alembagheri, 2016) suggested a fresh approach for assessing earthquake damage in gravity dams. The static pushover analysis was employed to create a structured and logical method for estimating damage levels based on linear seismic analysis outcomes. The primary focus was on the potential damage caused by concrete undergoing tensile cracking. Hai-tao (Hai-tao et al., 2019) delved into how strain rate impacts the dynamic behavior of the dam during an earthquake by comparing results between high strain rate and quasi-static loading.

While a substantial amount of research is available on seismic analysis of concrete gravity dams, there is a notable scarcity of studies focusing on the impact of aftershocks on concrete gravity dam structures. Alliard (Alliard and Léger, 2008) introduced a method for conducting seismic response analyses of concrete gravity dams, considering the influence of aftershocks and decreased drainage efficiency caused by damage to the drainage system. This approach served as a foundation for establishing criteria based on displacement for evaluating the stability of existing dams that were being reevaluated for much higher ground motion intensities than they were originally designed for many years ago. Zhai (Zhai et al., 2022) developed a comprehensive model for the damage mechanics of both the dam body and its foundation. It took into account the deterioration of concrete properties caused by Alkali-Aggregate Reaction (AAR), as well as the effects of the main earthquake and any subsequent aftershocks. This enabled the calculation of the response of the interconnected system involving the dam, water, and foundation at various stages of its lifespan. The study established an overarching model for evaluating the seismic damage potential of the concrete dam affected by AAR, considering different operational periods. Zhang (Zhang, Wang and Sa, 2013) explored how aftershocks could impact the accumulated damage in concrete gravity dams. To do this, the researchers used 30 sets of recorded mainshock-aftershock seismic sequences. A two-dimensional model of a gravity dam was created and subjected to these recorded sequences. The findings revealed that the specific sequences of ground motions recorded had a substantial influence on both the accumulated damage and the design considerations for concrete gravity dams.

In the present paper, the seismic effect of mainshock and aftershocks on the concrete gravity dam is studied. Two-dimensional analysis is conducted on the tallest monolith of the Koyna dam. Material nonlinearity is included with the damage plasticity model in this study to understand the nonlinear behavior of the dam under subsequent earthquakes. The earthquake used for this analysis is synthesized with the similar earthquake of one mainshock and two short aftershocks. The maximum response of the dam, such as crest displacement, maximum and minimum principal stresses are observed for each shock. Further residual responses are noted to evaluate the effect of aftershocks on the dam.

2 Theory

Nonlinear time history analysis is a well-known method that is used by structural engineers to access the dynamic response of structures subjected to complex, time-varying loads, such as seismic events. Several time integration methods, such as the Newmark-beta method, are available, which help in solving the nonlinear problem. The concrete exhibits the behavior of material nonlinearity when it exceeds the elastic limit. To replicate this behavior, Concrete Damage plasticity models are used.

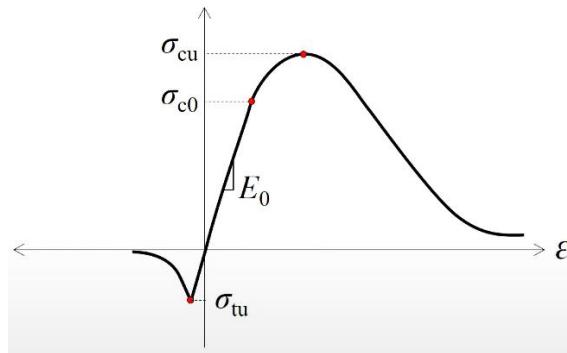


Fig 1. Stress-strain curve under compression and tension

The Concrete Damage Plasticity (CDP) model is a commonly employed material model to replicate how concrete behaves under different types of loads. This model integrates aspects from both plasticity theory and damage mechanics to accurately represent the nonlinear behavior of concrete. It considers factors like inelastic deformation and the gradual buildup of damage within the material. Fig. 1 shows the stress-strain curve of concrete under compression and tension obtained from the cylinder test. In the absence of stress-strain data, established formulas can be used to generate the stress-strain curve. One such example is the Eurocode 2 expression for concrete in compression.

$$\sigma = \sigma_{cu} \frac{k\eta - \eta^2}{1 + (k-2)\eta} \quad (1)$$

$$\eta = \varepsilon / \varepsilon_{c1} \quad (2)$$

$$k = 1.05 E_c \varepsilon_{c1} / \sigma_{cu} \quad (3)$$

Where σ_{cu} is compressive stress in the concrete at the ultimate compressive strain

ε_{c1} is the strain at the peak stress

E_c is the Young's modulus of concrete

Similarly, there are a number of expressions available in the literature, such as linear, bi-linear, and exponential curves to generate the softening behavior of concrete in tension (i.e., stress-cracking strain data). In ABAQUS, this data can be implemented through the concrete damage plasticity option in the form of inelastic stress-strain data under compression and cracking stress-strain under tension. The plasticity properties of concrete under compression and tension can be obtained from experiments. Table 1 shows the plastic flow parameters obtained from Lee and Fenves (Lee and Fenves, 1998), which are utilized for the concrete damage plasticity model.

Table 1. Plastic flow parameters

Dilation Angle	30~40
Eccentricity	0.1
f_{bo}/f_{co}	1.16
K	2/3
Viscosity parameter	0.0001

The response history analysis is done through the ABAQUS with the dynamics and explicit step. The software uses the central difference method to calculate the displacements in every time step. It approximates the acceleration at the next time step by taking a centered difference of velocities. The equations for central difference integration are shown below.

$$\text{Velocity, } \dot{u}_i = \frac{u_{i+1} - u_{i-1}}{2\Delta t} \quad (4)$$

$$\text{Acceleration, } \ddot{u}_i = \frac{\dot{u}_{i+\frac{1}{2}} - \dot{u}_{i-\frac{1}{2}}}{\Delta t} \quad (5)$$

$$\text{where, } \dot{u}_{i+\frac{1}{2}} = \frac{u_{i+1} - u_i}{\Delta t}; \dot{u}_{i-\frac{1}{2}} = \frac{u_i - u_{i-1}}{\Delta t}$$

substituting the above equations in (5) we get,

$$\ddot{u}_i = \frac{u_{i+1} - 2u_i + u_{i-1}}{(\Delta t)^2} \quad (6)$$

By substituting the above expressions in the equation of motion the response values can be obtained. Employing the central difference method in explicit dynamics simulations can yield precise results for a broad spectrum of dynamic situations. However, it is vital to carefully select a time step size that ensures both numerical stability and accuracy.

3 Numerical Study

For the numerical study, the cross-section of tallest non overflow monolith of the Koyna dam is taken. Two-dimensional nonlinear analysis is carried out using the commercial software ABAQUS. The material nonlinearity is taken into account by using the concrete damage plasticity model. Fig 2 shows the cross-section of the tallest monolith considered for this analysis.

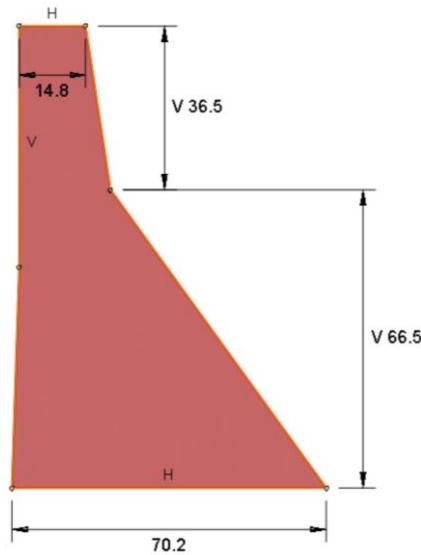


Fig. 2. Two-dimensional cross section of the tallest non overflow monolith of Koyna dam

The analysis utilises a two-dimensional Finite Element Method (FEM) using a 4-noded bilinear plane stress quadrilateral element with reduced integration and hourglass control (CPS4R) for the dam. The base of the dam is assumed to be fixed. The water in the reservoir is simulated using a 4-noded 2-D acoustic quadrilateral

element with reduced integration (AC2D4R). It is assumed that the fluid behaves as an incompressible and non-viscous medium, and a non-reflecting planar acoustic impedance boundary is applied at the far end of the reservoir water. At the free surface, a boundary condition of zero pressure is assumed to disregard surface wave effects in the reservoir.

Table 2. Material properties of concrete dam and reservoir water.

Properties	Value
Dam	
Density	2650 kg/m ³
Young's Modulus	31027 MPa
Poisson's ratio	0.2
Maximum permissible tensile strength	3.5MPa
Damping	5%
Water	
Density	1000 kg/m ³
Bulk Modulus	2.1 GPa

Table 2 shows the properties of concrete and water that were used for the analysis. For the nonlinear response history analysis, a seismic event sequence is synthesized, consisting of one mainshock followed by two aftershocks. Each shock is joined with the other with zero acceleration values over a time duration of 30 seconds. The time duration is selected such that the free vibration part of the response after each shock comes to rest. The earthquake data selected for this study is the 1979 Imperial Valley earthquake, recorded from two distinct stations—one in close proximity (near-field) and the other further away (far-field). The same earthquake is used for both the mainshock and aftershocks, but the ground motion is adjusted to yield peak ground acceleration (PGA) values of 0.4g and 0.6g. Consequently, four seismic scenarios are generated: two near-field earthquakes and two far-field earthquakes, each with PGA values of 0.4g and 0.6g. Fig. 3 displays the time history of the synthesized seismic event, comprising one mainshock followed by two aftershocks.

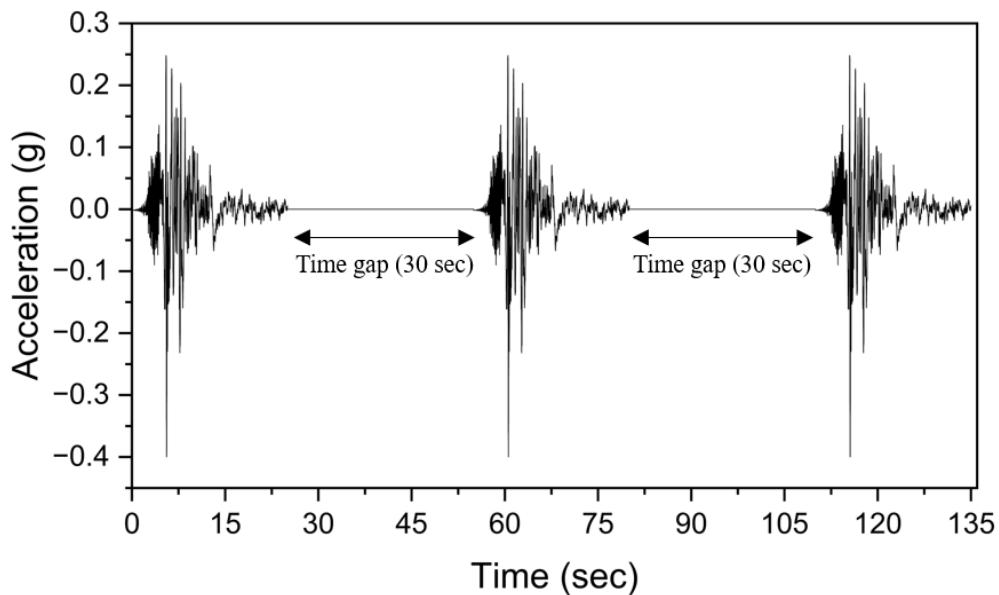


Fig. 3. Time History of the mainshock and two aftershock sequences considered in this study (Far-field scaled to 0.4g PGA)

4 Results and Discussions

Table 3 shows the first ten natural frequencies with and without water. It is seen from the table that the dam with reservoir water has less frequency as compared to the dry dam, as would be expected. Further, for higher modes, the frequency difference between dry Dam and Dam with reservoir increases. The first three mode shapes of the dry Dam and Dam with full reservoir are shown in Fig. 4. It is seen from the figure that the first three mode shapes of the dry Dam and the Dam with reservoir remain nearly the same. It shows that the water structure interaction during the free vibration of the dam does not significantly affect the first few mode shapes.

Table 3. Frequency values of ten modes for dam with and without water

Modes	Frequencies (Hz)	
	Dam with no water	Dam with a full reservoir
1	3.1	2.7
2	8.2	7.4
3	10.8	10.7
4	15.9	11.1
5	24.2	11.4
6	24.4	12.1
7	33.7	14.6
8	35.6	18.2
9	37.9	18.4
10	40.8	19.1

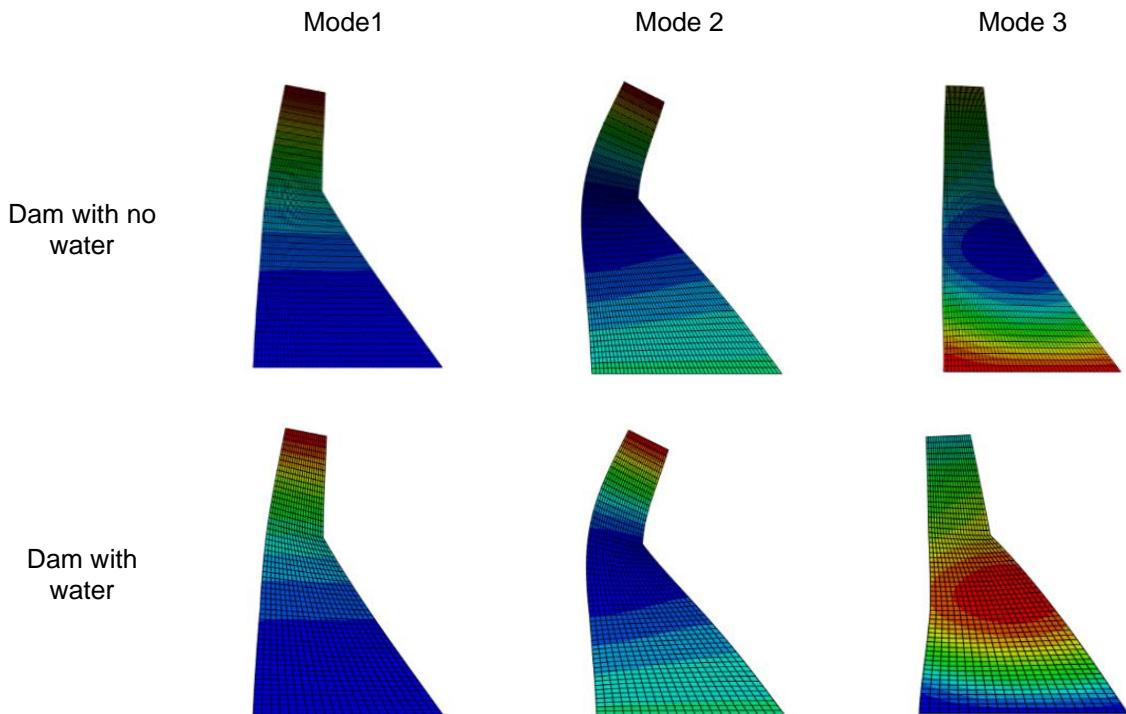


Fig.4. First three mode shapes of Koyna dam with and without reservoir water.

Fig. 5 shows the time history response of crest displacement of the main shock and the subsequent aftershocks for the far-field earthquake. It is seen from the figure that, at a PGA of 0.4g, the dam doesn't undergo much inelastic effect in the mainshock. However, for the subsequent aftershock, a significant inelastic effect in the dam is observed. At a PGA level of 0.6g, the dam experiences substantial inelastic deformation even during the primary seismic event. In the following aftershocks, this inelastic response is notably amplified. It may be noted that, for the second aftershock in the case of 0.6g PGA, the inelastic effect remains nearly the same as that of previous aftershocks.

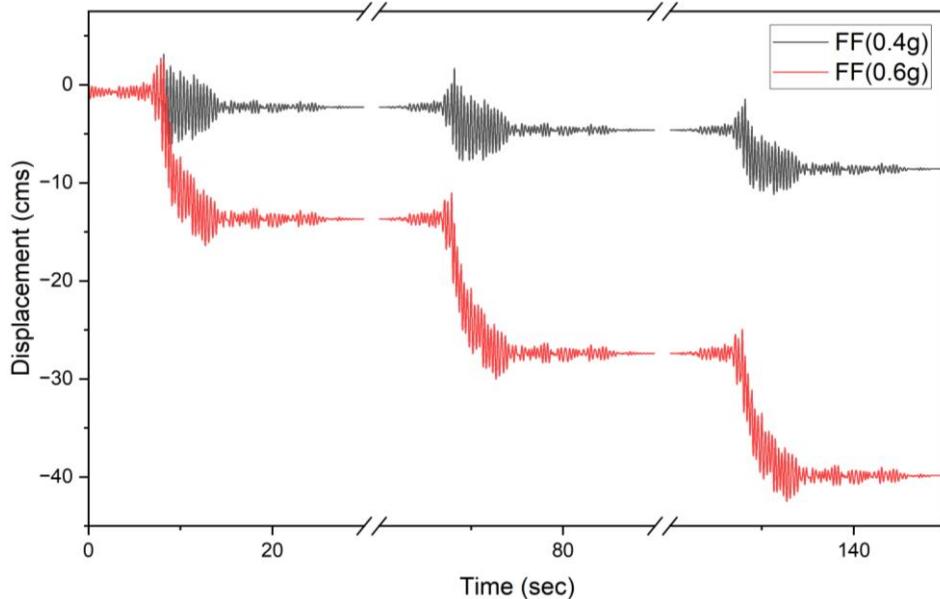


Fig.5. Response history of crest displacement for the Far-field earthquake

Fig. 6 shows the damages caused in the dam after the main shock and after all three shocks. The figure shows that for a PGA of 0.4g, very little damage is incurred at the neck portion of the dam. After the three shocks, the damage extends from the downstream of the neck portion and almost reaches the upstream side. The damage is mostly concentrated in the neck region and is not observed elsewhere in the dam. Because of the damage occurring across the width of the neck after the three shocks, the residual displacement, as shown in the figure, is exhibited more. For 0.6g PGA, the damage at the neck portion extends from the downstream to the upstream side in the mainshock itself. The extent of damage increases in aftershocks. For this level of PGA, the damage is again observed to be confined at the neck region.

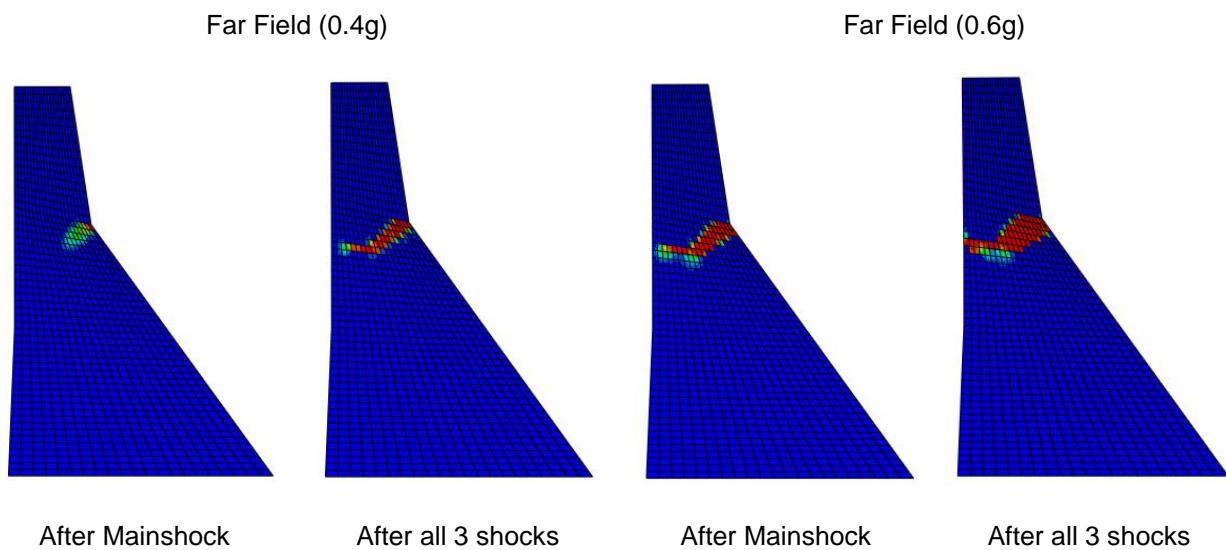


Fig. 6. Damage caused due to tensile failure under far-field earthquake.

Fig. 7 shows the time history of the crest displacement in the mainshock and aftershocks for the near-field earthquake. The trend of the time history of response remains nearly the same as that observed in the case of far-field earthquakes. At a PGA level of 0.6g, notable inelastic behavior occurs during the mainshocks and persists in the subsequent two aftershocks, while the degree of plastic deformation remains largely consistent.

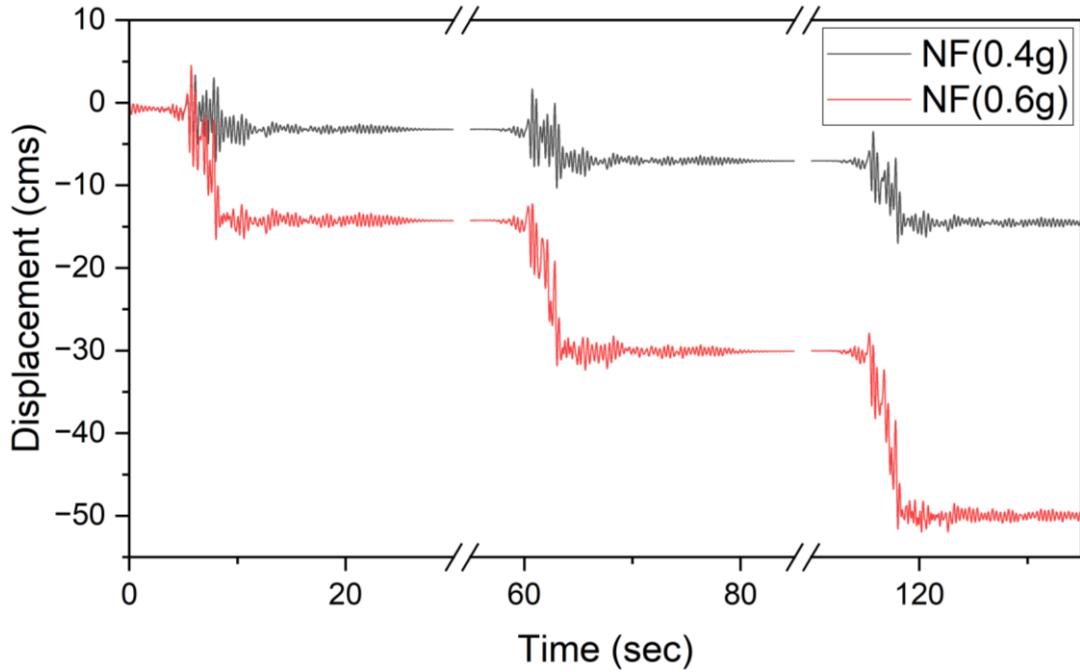


Fig.7. Response history of crest displacement for the Near field earthquake

Fig 8 shows the damage in the cross-section of the dam. The location and pattern of the damage are almost similar as compared to far-field earthquakes. However, it is observed that for PGA of 0.6g, the extent of damage after three shocks is considerably more as compared to that of far-field earthquake.

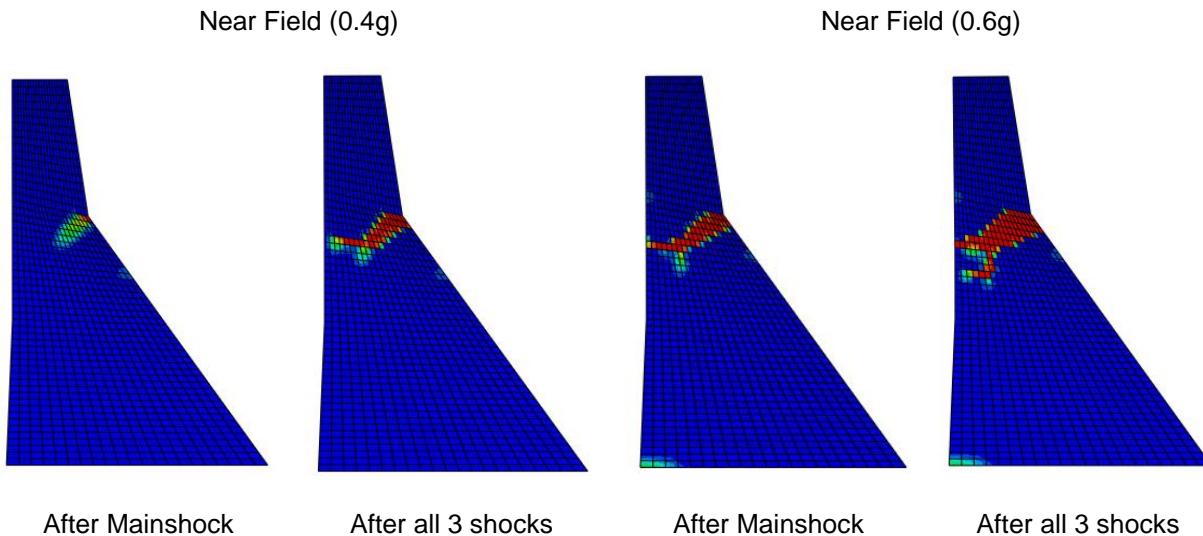


Fig. 8. Damage caused due to tensile failure under near-field earthquake.

Table 4 consolidates the values of the maximum response obtained during the mainshock and aftershocks. It is seen from the table that the maximum crest displacement remains nearly the same or varies within 10% for the mainshocks and aftershocks for 0.4g earthquake. Further, it is observed that a far-field earthquake provides less displacement as compared to a near-field earthquake. For 0.6g PGA, the far-field earthquake provides 15% less displacement as compared to the near-field earthquake. The tensile stress of the dam reaches the

maximum permissible tensile strength of the dam. As for the compressive stress, it is observed that the maximum principal stress remains nearly the same for that of the main shock and aftershocks. Further, it is seen that there is a 10 to 15% increase in the minimum principal stress when the level of PGA is increased from 0.4g to 0.6g, although there is a significant increase in the crest displacement. It is interesting to note that the crest displacement is less for the far field compared to the near field earthquake, while the maximum principal stress for both cases is almost the same.

Table 4. Peak response of the Koyna dam obtained after each shock

Shocks	EQ Type	PGA	Crest Displacement (cm)	Max Principal Stress (MPa)	Min Principal Stress (MPa)
Mainshock	Far-field	0.4g	5.98	3.5	15.65
		0.6g	16.39	3.5	17.41
	Near-field	0.4g	7.11	3.5	15.57
		0.6g	16.54	3.5	18.29
First Aftershock	Far-field	0.4g	5.45	3.5	15.69
		0.6g	16.31	3.5	15.46
	Near-field	0.4g	7.08	3.5	15.78
		0.6g	18.07	3.5	15.95
Second Aftershock	Far-field	0.4g	6.55	3.5	15.51
		0.6g	15.11	3.5	17.43
	Near-field	0.4g	9.96	3.5	14.85
		0.6g	21.9	3.5	17.13

Table 5 shows the residual displacement after the mainshock and each aftershock. It is observed from the table that the residual displacement is significantly increased for the higher level of PGA, i.e., 0.6g, as compared to 0.4g earthquake. Further, it is seen that the residual displacement considerably increases with each aftershock for both the PGA values. When the residual displacements are compared between the far-field and near-field earthquakes, it is observed that residual displacements are far less in the case of far-field earthquakes. This clearly demonstrates the severity of the near field earthquake on the response of the dam if aftershocks are considered in the analysis.

Table 5. Residual crest displacement obtained after each shock.

Earthquake Type	Near Field		Far Field	
	0.4g	0.6g	0.4g	0.6g
Mainshock	3.22	14.27	2.28	13.69
First Aftershock	7.04	30.07	4.61	27.4
Second Aftershock	14.58	50.1	8.56	39.75

5 Conclusions

The effect of aftershocks on the Koyna dam is investigated by considering a two-dimensional cross-section of the tallest nonover flow monolith. For this purpose, a mainshock and two aftershocks are considered in the analysis. A nonlinear time history analysis is performed for a simulated earthquake record in which a mainshock and two aftershocks are separated by a time length of about thirty seconds by inserting null values over the gap length of thirty seconds. In order to consider the damages induced in the dam due to the application of mainshock and aftershocks, a damage plasticity model is included in the analysis using ABAQUS. The dam is analyzed for two types of earthquakes, namely far-field and near-field earthquakes. It is scaled to two levels of PGA, namely 0.4g and 0.6g. The base of the dam is assumed to be fixed. The response quantities of interest include the maximum crest displacement, tensile and compressive stresses in both main and aftershocks, along with the residual responses at the end of each shock. The results of the numerical study indicate that.

- i. The first three mode shapes of the dry Dam and Dam with reservoir water remain almost the same, although the values of natural frequencies of the two cases differ.
- ii. For both far-field and near-field earthquakes, at a PGA level of 0.4g, not much inelastic effect is exhibited in the mainshock; however, in subsequent aftershocks, a significant inelastic effect is observed.
- iii. For the level of PGA 0.6g, a significant inelastic effect is exhibited in the mainshock, which subsequently increases in the aftershocks for both near-field and far-field earthquakes.
- iv. Damages in the Dam are concentrated only in the neck region; nowhere else, the damage is observed for the earthquakes considered in this study.
- v. For the PGA level of 0.4g, the damage occurs only at downstream of the neck portion during the mainshock, which extends towards the upstream side after the two subsequent aftershocks. For a higher level of PGA, i.e., 0.6g, the damage occurs at the neck portion across the downstream to the upstream side of the dam in the mainshock. The extent of the damage increases with the following two aftershocks.
- vi. Maximum response quantities remain nearly the same during each shock.
- vii. While a considerable increase in crest displacement is observed, when the PGA level is increased from 0.4g to 0.6g, the corresponding increase in the compressive stress is not significant. Further, the far-field earthquake provides fewer responses.
- viii. Residual displacement considerably increases after each shock and the level of PGA.
- ix. Near-field earthquake is observed to be highly severe as compared to far-field earthquake in terms of residual displacement.

6 References

- Alembagheri M (2016) Earthquake damage estimation of concrete gravity dams using linear analysis and empirical failure criteria. *Soil Dynamics and Earthquake Engineering* 90. Elsevier Ltd: 327–339.
- Alliard P-M and Léger P (2008) Earthquake Safety Evaluation of Gravity Dams Considering Aftershocks and Reduced Drainage Efficiency. *Journal of Engineering Mechanics* 134(1).
- Bayraktar A, Hançer E and Akköse M (2005) Influence of base-rock characteristics on the stochastic dynamic response of dam-reservoir-foundation systems. *Engineering Structures* 27(10): 1498–1508.
- Bayraktar A, Türker T, Akköse M, et al. (2010) The effect of reservoir length on seismic performance of gravity dams to near- and far-fault ground motions. *Natural Hazards* 52(2): 257–275.
- Bhattacharjee SS and Leger P (1993) *Seismic Cracking and Energy Dissipation in Concrete Gravity Dams*. EARTHQUAKE ENGINEERING AND STRUCTURAL DYNAMICS.

- Chakrabarti P and Chopra AK (1973) *Earthquake Analysis of Gravity Dams Including Hydrodynamic Interaction*. EARTHQUAKE ENGINEERING AND STRUCTURAL DYNAMICS.
- Chopra AK and Chakrabarti P (1972) *The Earthquake Experience at Koyna Dam and Stresses in Concrete Gravity Dams*.
- Fenves G and Chopra AK (1984) *Earthquake Analysis of Concrete Gravity Dams including Reservoir bottom absorption and Dam-Water-Foundation Rock Interaction*. EARTHQUAKE ENGINEERING AND STRUCTURAL DYNAMICS.
- Ghaemian M and Ghobarah A (1998) *Staggered Solution Schemes for Dam-Reservoir Interaction*. Journal of Fluids and Structures.
- Hai-tao W, Jiayu S, Feng W, et al. (2019) Experimental study on elastic-plastic seismic response analysis of concrete gravity dam with strain rate effect. *Soil Dynamics and Earthquake Engineering* 116. Elsevier Ltd: 563–569.
- Hall JF and Chopra AK (1982) *Two-dimensional Dynamic Analysis of Concrete Gravity and Embankment Dams Including Hydrodynamic Effects*.
- Lee J and Fenves GL (1998) Plastic-Damage Model for Cyclic Loading of Concrete Structures. *Journal of Engineering Mechanics* 124(8): 892–900.
- Tan H and Chopra AK (1995) *Earthquake Analysis of Arch Dams Including Dam-Water-Foundation Rock Interaction*. EARTHQUAKE ENGINEERING AND STRUCTURAL DYNAMICS.
- Wang G, Wang Y, Lu W, et al. (2017) Deterministic 3D seismic damage analysis of Guandi concrete gravity dam: A case study. *Engineering Structures* 148. Elsevier Ltd: 263–276.
- Zhai Y, Zhang L, Bi Z, et al. (2022) Seismic performance evaluation of AAR-affected concrete gravity dams under main aftershock sequence. *Soil Dynamics and Earthquake Engineering* 157. Elsevier Ltd.
- Zhang S, Wang G and Sa W (2013) Damage evaluation of concrete gravity dams under mainshock-aftershock seismic sequences. *Soil Dynamics and Earthquake Engineering* 50: 16–27.
- Zhang S, Wang G and Yu X (2013) Seismic cracking analysis of concrete gravity dams with initial cracks using the extended finite element method. *Engineering Structures* 56: 528–543.

USE OF THREE-DIMENSIONAL NUMERICAL ANALYSES IN SEISMIC DESIGN OF EARTH EMBANKMENTS

M.Kafash¹, Z. Karimi² & L. Yenne³

¹ AECOM, Denver, USA, masood.kafash@aecom.com

² AECOM, Denver, USA

³ AECOM, Denver, USA

Abstract: In last decades, the utilization of limit equilibrium, finite element, and/or finite difference methods for three-dimensional analysis has become a valuable tool for seismic design and analysis of earth and rockfill embankments, such as water storage and tailings dams. This advancement can be attributed to improvements in computational capabilities and the development of three-dimensional computer programs capable of effectively modeling various soil characteristics within a reasonable timeframe. However, the majority of existing criteria, including the required minimum factor of safety, are based on two-dimensional analysis. Merely comparing three-dimensional values with these criteria is insufficient and necessitates additional support for their application in design. This paper examines and contrasts the available database on two-dimensional and three-dimensional analysis while also establishes a foundation for the implementation of three-dimensional analysis in seismic design of earth embankments through a case study.

1. Introduction

Three-dimensional (3D) analysis using limit equilibrium methods (LEM), finite element, and/or finite difference methods has emerged as a robust tool in the seismic design and analysis of earth and rockfill embankments, including water storage and tailings dams, in the last decade. This is due to advances in computational capacities as well as advances in three-dimensional computer programs that are capable of modeling various characteristics of soils in a reasonable timeframe. However, most of the developed design criteria, including required minimum factor of safety (FOS), are based on two-dimensional analysis and simply comparing three-dimensional values with two-dimensional based criteria is not appropriate and requires additional support for use in practical design applications.

The establishment of 3D FOS stability criteria is not straightforward. Specific conditions and degrees of conservatism need to be considered to determine if a criterion is appropriate. Appropriate 3D FOS criteria must be established on a site-specific basis with consideration of the site geometric constraints, the uncertainties in the model, the degree of conservatism in the material property characterization and loading, and the consequences of failure. Currently, within the United States, a formal regulatory precedent that provides guidance for the development of 3D FOS design criteria is limited.

Researchers such as Stark and Ruffing (2017) have proposed a method to develop 3D FOS criteria based on recommended 2D FOS and by quantifying 3D effects and incorporating risk and potential consequences, as shown in Table 1. The proposed recommended minimum 3D FOS by Stark and Ruffing (2017) were set based on a relationship between the ratio of 3D/2D FS (R3D/2D) and width to height ratio (W/H) for three slope inclinations considered in the parametric study conducted by Akhtar and Stark (2017).

Table 1. Example of Recommended 3D FOS Values by Stark and Ruffing (2017)

Soil Strength Uncertainty	Imminent Threat to Human Life	Potential for Major Construction or Environmental Impact	Recommended Minimum 2D Factor of Safety	Minimum 3D Factor of Safety
small	low	low	1.3	1.4
small	high	high	1.5	1.7
small	low	high	1.3	1.5
small	high	low	1.5	1.7
large	low	low	1.5	1.7
large	high	high	2.0	2.3
large	low	high	1.5	1.7
large	high	low	2.0	2.3

In absence of well-defined criteria for use in design, this paper provides a framework and steps to identify the source of deviation between 2D and 3D factor of safety and describes how to incorporate the 3D effects in seismic design of embankments through a case history.

2. Two-dimensional vs three-dimensional factor of safety

The theory behind the 3D LEM has existed for decades and has been used by various researchers in calculating FOS as documented in literature by Hungr (1987), and Hungr et al. (1989). Review of the literature reveals that, as a general trend, 3D factors of safety tend to surpass their 2D FOS values. Several authors have made a comparison between 2D and 3D analysis methods in the context of analysis type and derivation (e.g., 3D LEM and Bishop's modified method), application (e.g., conical heaps, symmetrical), and slip surface geometry (e.g., central cylindrical with attached planar or curved side resistance components) (Kalatehjari and Ali 2013). In fact, Kalatehjari and Ali (2013) provide detailed summary of nearly 30 researchers in the context of a 2D and 3D limit equilibrium methos (LEM) FOS comparison. Of particular interest is the expected increase in FOS due to three-dimensionality. Table 2 presents a summary of literature reviewed and the attributes of each study as were provided by the available documentation. The ratio of the 3D to the 2D FOS is provided in Table 2 as the potential increase for each study. As presented in Table 2, the ratio of 2D to 3D, or the increase on FOS from 2D to 3D, varies based on multiple factors and is not unique.

Key factors affecting a 3D stability analysis include the type of failure mechanism, underlying topography, and side shearing resistance contributions. It is of no surprise that the influence of three-dimensionality would be specific to a particular case under evaluation. It is in this regard that care must be taken when evaluating a design with consideration of 3D FOS stability criteria. Therefore, it is important to identify and quantify this increase in factor of safety step by step, so it can be compared with the 2D FOS based criteria. When comparing 3D FOS to 2D FOS based criteria is important to understand the source for the increase in FOS and to identify whether the increase in the FOS is just an artifact of transitioning from 2D to 3D, i.e., incorporating the side resistance in estimation of FOS, or if there are other players such as change in material properties or condition.

In a study by Kafash et al. (2020), it was demonstrated that the 2D post-earthquake (PE) FOS for a critical section of a water storage dam located in a narrow valley, shown in Figure 1, was increased from 1.1 to 1.75, for the maximum section, by transitioning from 2D to 3D analysis. Figure 2 presents 2D LEM FOS for the maximum and right abutment sections. The main contributor to the PE FOS is the liquefiable layer located in the valley. Figure 3 presents the 3D PE FOS calculated, using the computer code FLAC3D — Fast Lagrangian Analysis of Continua (Itasca 2019), to validate the analysis. Kafash et al. 2020 performed a series of validation analysis to quantify the source for this increase in factor of safety. This 2020 analysis by the author will be used and expanded here to demonstrate the steps that engineers can follow on how to use 3D analysis in design.

Table 2. Summary of 2D and 3D FOS Comparison Literature Review

Author	Ratio 3D FOS/2D FOS	Application	Note
Lu et al. (2013)	1.15	3D Slope with Complicated Geometry	3D limit equilibrium ~ 3D strength reduction method
Aziz et al. (2018)	1.2-1.4	Single slope, symmetric berm, varied slope angles for comparison	Three dimensional slope stability analysis of open pit
Fredlund et al. (2017)	1.04-1.2	Uniform embankment, convex/concave geometry	The 2D-3D difference will not be constant for every case.
Pyke (2017)	1.6	Amorphous, Uniform embankment	3D geometry can occasionally reduce the calculated FOS, but more usually it increases the calculated FOS. The only way to know 3D impacts is to do the analysis.
Akhtar and Stark (2017)	Varies based on W/H	Uniform embankment	3D/2D LEM FOS ratios for all slope inclinations analyzed using finite element, finite difference, and limit equilibrium procedures are greater than unity
Report on Mount Polley Tailings Storage Facility Breach (2015)	1.3	Case History: Tailings embankment	3D/2D LEM with an aspect ratio (length to height) of 2.6 foundation layer strain softening
Geotechnical Assessment of the Alameda Dam (2015)	2	Case History: earthen embankment	3D/2D LEM with an aspect ratio (width to length) of 0.6 to 0.75 foundation layer strain softening
AECOM Case History 1	1.4	Water storage embankment	3D/2D LEM liquefiable material was located in a narrow channel within the foundation
AECOM Case History 2	1.2	Tailings dam embankment	3D/2D LEM liquefiable tailings, narrow valleys
AECOM Case History 3	1.3	Tailings dam embankment	3D/2D LEM and Strength reduction method, liquefiable tailings
AECOM Case History 4	1.7	Water storage facility	3D/2D Strength reduction method, liquefiable alluvium in narrow valley



Figure 1. Embankment Plan View and Location of Max and Abutment Sections

NO.	MATERIAL DESCRIPTION	UNIT WEIGHT (pcf)	DRAINED STRENGTH		POST-EARTHQUAKE STRENGTH	
			COHESION (psf)	FRICION ANGLE (degrees)	COHESION (psf)	FRICION ANGLE (degrees)
1	CORE (SILTY CLAY) Zone 1	133	0	26.5	0	22
2	EMBANKMENT SHELL (SILTY SAND AND GRAVEL) Zone 2&3	140	0	37	—	—
3	UPPER ORGANIC ALLUVIUM – BENEATH EMBANKMENT	125	—	—	0	6
4	UPPER ORGANIC ALLUVIUM – FREE FIELD	125	—	—	0	4
5	SURFACE SOILS	130	0	35	—	—
6	DEEP ALLUVIUM	143	0	38	—	—
7	BEDROCK (SANDSTONE)	140	10,000	45	—	—

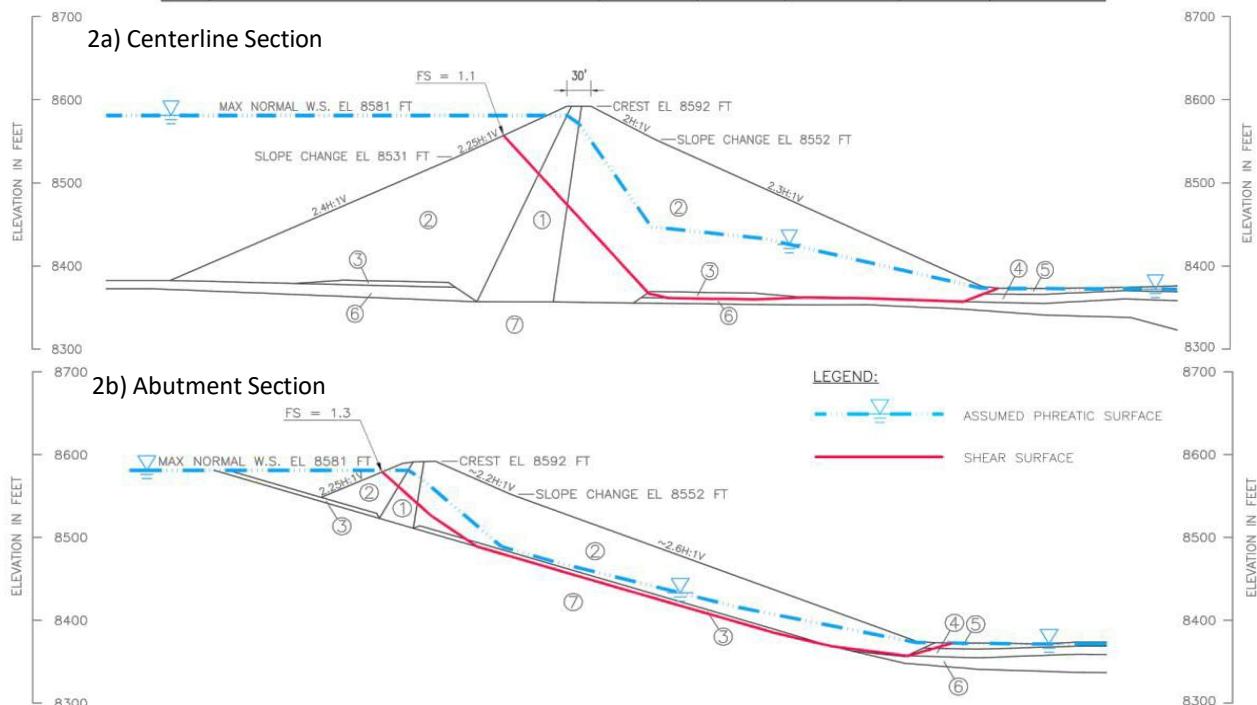


Figure 2. Model Geometry and Post-Earthquake Factor of Safety (Kafash et al. 2020)

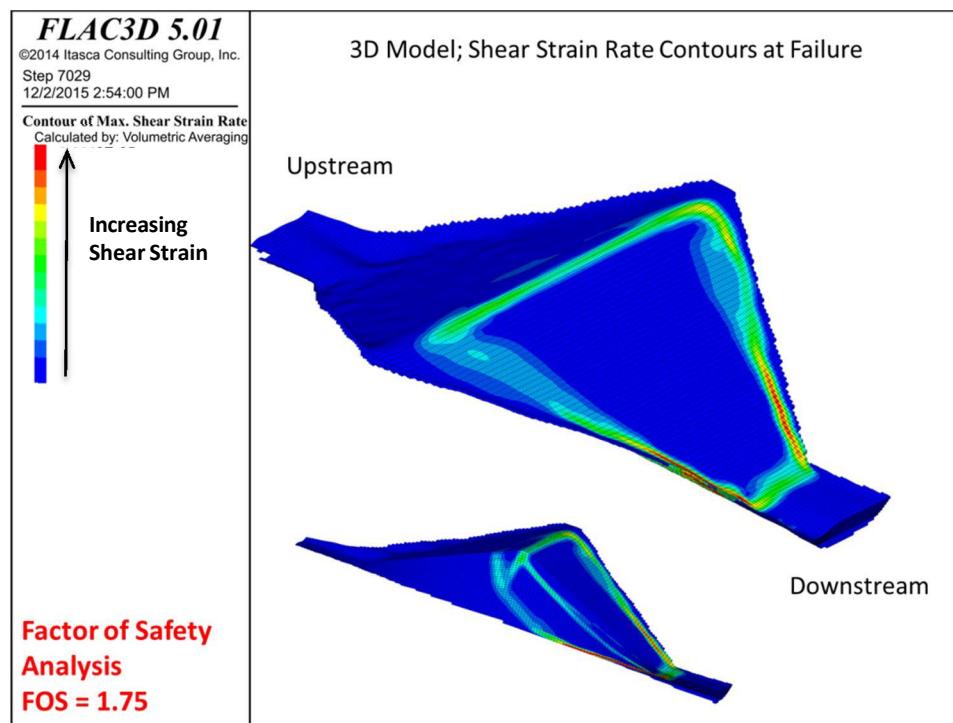


Figure 3. 3D FOS-Strength Reduction FOS

2.1 Steps to Identify the Contributor to 3D FOS

The first step in understanding 3D effects is to isolate the source(s) of FOS increase. The source of increase can be either from simply extending a 2D section to 3D by incorporating the side resistance, incorporating the change in geometry or material properties. Fredlund (2017) has proposed a general and practical methodology for moving from 2D to 3D which generally follows the steps below and are examined here through a case history for seismic design.

2.1.1 From side shear resistance of the failure surface

The increase in FOS from 2D to 3D due to the side shear resistance of the failure surface is the first step to quantify in analysis. This effect can be evaluated by extending a model in 3D. If a homogeneous slope is extended from 2D to 3D, the FOS increases as the side resistance of the failure surface is added to the estimation of 3D FOS.

The uncertainties on calculation of side resistance in LE have been investigated by several authors. For example, Akhtar and Stark (2017) has performed LE and FE/FD analysis to estimate the 3D FOS for translation sliding mass. Akhtar and Stark (2017) showed that using at rest (K_0) to estimate shear resistance along two vertical sides in LE method overestimates 3D/2D, and they proposed using an average of K_0 and K_a (Active earth pressure coefficient) for a better estimate of shear resistance acting along vertical sides of sliding mass.

While this factor is the first contributor to increase in an estimated FOS as move from 2D to 3D, it is essential to estimate its contribution to the final estimate of FOS. So, the first step involved extending the 2D cross section from 2D to 3D to the width of the embankment at crest and estimating the contribution from side resistance on FOS. Although not presented in the original paper by Kafash et al. (2020), Figure 4 illustrates the impact of including side resistance on the FOS calculation for the Kafash et al. 2020 case. As depicted, incorporating side resistance elevated the FOS from 1.05 to 1.3.

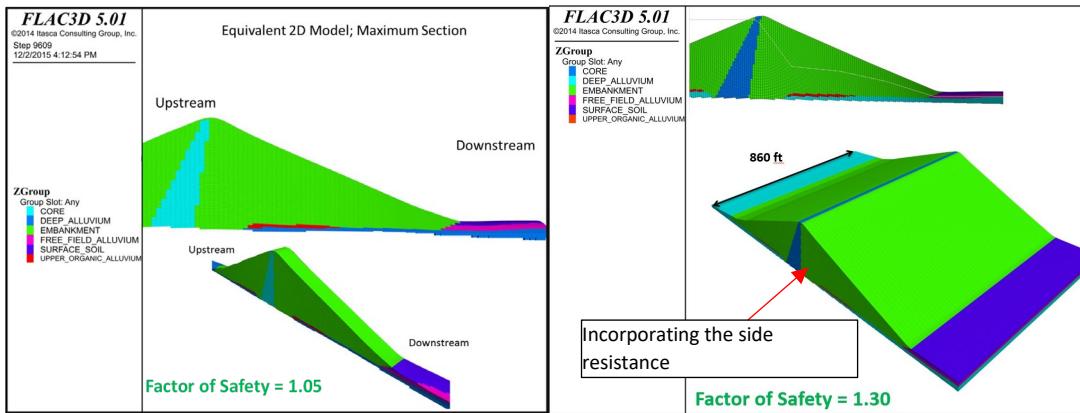


Figure 4. 2D vs 3D Analysis; Incorporating the Side Resistance in FOS

Other researchers, such as Akhtar and Stark (2017), have conducted similar analyses. Akhtar and Stark (2017) performed a parametric study on the effect of W/H ratios on 3D/2D FOS values. This study was later utilized by Stark and Ruffing (2017) to establish the criteria for 3D analysis, as outlined in Table 1 above and discussed earlier. Quantifying the influence of side resistance in the analysis can provide justification for employing appropriate 3D FOSs when compared to case histories based on 2D criteria.

2.1.2 From change in condition including geometry, subsurface condition, and/or material properties

The change in condition include change in geometry of the slope in 3D such as convex or concave geometry, change in subsurface condition, and change in phreatic condition and/or material properties such as change in the extent of liquefiable material. The change in condition can be counted as a raise that can be considered a “true” raise in FOS when comparing 3D FOS to 2D FOS criteria. The case study presented by Kafash et al. 2020, had 2D PE FOS of 1.05 for the maximum section that was passing through a localized liquefiable layer at the downstream toe of the embankment. The presence of a localized liquefiable layer purely suggested that 2D analysis are not appropriate for the embankment. As a next step to validate the analysis, Kafash et al. 2020 performed a weighted average of limit equilibrium FOSs for 2D sections across the embankment. The approximate 3D FOS from this method does not account for forces between slices in the direction of the dam axis or lateral earth pressure on the failure surfaces along sides of sliding mass and therefore, underestimates the 3D FOS but provides a level of cross-checking the 3D results. Four sections were considered, as shown on Figure 5, and their 2D limit equilibrium FOSs were averaged based on their representative length (cross-valley width). Results show an averaged 3D FOS of 1.5, as presented in the table below.

Section #	Model Base Elevation (ft)	Cross-valley width of section (ft)	2D Limit Equilibrium FS	Avg. FS
1	8365	70	1.05	
2	8365	65	1.4	
3	8455	110	1.6	
4	8505	75	1.8	
Σ	320		1.5	

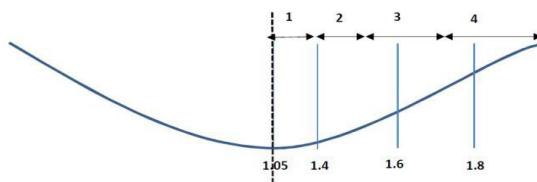


Figure 5. Weighted Average 3D FOS

This simple exercise breaks down the difference in PE FOS for the embankment from a 2D value of 1.05 for the maximum section to the 3D PE FOS of 1.75. As presented above, approximately 0.3 of the FOS raise is from side resistance effects (accepting the different shape of valley and extended 3D shape) and approximately 0.5 from the change in geometry and material characteristics, i.e., liquefiable layer. By performing this exercise, the designer now can judge what to incorporate and compare with the 3D FOS criteria for use in design. It is worthwhile to consider the inherent changes in stress condition and how material properties are assigned in 2D vs 3D as further discussed below in Section 2.1.3.

2.1.3 From change in the assignment of material properties

The other source of increase in the FOS could be due to how the properties are assigned in 3D vs 2D. Typically, the shear strength properties for post-earthquake analysis are assigned based on vertical stresses (S_u/p'). But the question is how the stresses are estimated in 3D limit equilibrium analysis across the failure mass and what mode of failure is appropriate (CIU vs DSS). This increase in FOS is not a true or valid raise and should be minimized in analysis by performing sensitivity analyses.

3. Use of three-dimensional numerical analyses in seismic design of earth embankments

As discussed above, establishment of 3D FOS stability criteria is not straightforward. Specific conditions and degrees of conservatism need to be considered to determine if a criterion is appropriate. Appropriate 3D FOS criteria must be established on a site-specific basis with consideration of the site geometric constraints, the uncertainties in the model, the degree of conservatism in the material property characterization and loading, and the consequences of failure.

As a 3D FOS design criteria guideline has not yet been established in the industry, the designer can follow the discussed steps to determine the appropriate 3D FOS on a case-by-case basis. In addition, in seismic design of embankments evaluating the 3D dynamic deformation behavior of the embankment provides a useful quantitative understanding of the performance of the section under various loading conditions. Kafash et al. (2020) and Kafash et al. (2021) provide examples of application of 3D seismic deformation analysis in design. The key design criteria for deformation analysis and performance-based design are to demonstrate tolerable deformation behavior for the loading condition applied. Seismically, meeting the tolerable deformation criteria is demonstrated under the loading from the maximum design earthquake by:

- The structural integrity of the slope is maintained with no release of tailings or water outside the embankment footprint;
- The slope does not undergo differential movement with strain levels above those that would indicate progressive failure or secondary potential failure modes, which could lead to cracking or piping, and release of water or tailings;
- A shear surface does not fully develop through the embankment structural section; and
- The embankment movement is stabilized after shaking based on the displacement time histories in the numerical deformation model.

The level of design ground motion should be tied to the site-specific seismic hazard. Three-dimensional effects contributing to dynamic deformation are similarly affected by site-specific factors and modeling uncertainties impacting the 3D FOS stability analysis.

Hence, the three-dimensional seismic design of embankments should include a 3D FOS examination and identification of contributors to 3D FOS, performing a 3D seismic dynamic deformation analysis, and performing sensitivity analysis incorporating uncertainties in design.

4. Summary and conclusion

The assumption of plane strain conditions in two-dimensional slope stability analysis can be limiting. If this assumption does not align with reality, a more advanced 3D analysis may be necessary. However, implementing 3D analyses introduces a higher level of complexity, demanding sufficient information to properly configure the model. Significant factors influencing a 3D stability analysis encompass the type and geometry of the failure mechanism, as well as underlying topographic and side shearing resistance.

Three-dimensional effects on stability analysis are site-specific and are very sensitive to geometric constraints, material properties, and loading conditions. There are no 3D FOS design criteria appropriate for all sites, nor unanimity of opinion in the selection of a general 3D FOS design criteria. Hence, designers need to build the case for appropriate 3D factor of safety in design by performing step by step analysis to quantify the source of increase in factor of safety. The review of information presented herein supports the adoption of performance-based design criteria by performing seismic deformation analysis in addition to a more conventional LEM FOS design criteria approach, especially in problems that have a significant 3D geometry.

5. References:

- Akhtar, K. and Stark, T. D. (2017). "Importance of side resistance in 3D stability analysis." Proc., Geo-Frontiers 2017 Specialty Conference, Orlando, Florida, 10-12 March 2017, ASCE, Geotechnical Special Technical Publication No.
- Fredlund, M.D., Fredlund, D.G., and Zhang, L. (2017). Moving from 2D to 3D in Unsaturated Slope Stability Analysis, PanAm Unsaturated Soils 2017, GSP 302, pp. 136-145.
- Geotechnical Assessment of the Alameda Dam (2015), Canadian Dam Association, Spring 2015, pp. 11-23
- Hungr, O. (1987). An Extension of Bishop's Simplified Method of Slope Stability Analysis to Three Dimensions, Geotechnique, 37(1), pp. 113-117.
- Hungr, O., Salgado, E.M., and Byrne, P.M. (1989). Evaluation of a Three-Dimensional Method of Slope Stability Analysis. Canadian Geotechnical Journal, Vol. 26, pp. 679-686
- Kalatehjari, R., and Ali, N. (2013). A Review of Three-Dimensional Slope Stability Analyses based on Limit Equilibrium Method, Electronic Journal of Geotechnical Engineering, 18: pp. 119-134, January 2013.
- Kafash, M.H, Sheykloo, P., Williams, J., Davidson, R., France, J. (2021). Application of Numerical Analysis in Design of Earth and Rockfill Embankments, USSD 2021, May 10th -May 21st, USSD 2021 Virtual Annual Conference.
- Kafash, M.H, Adams, T., Dawson, E., Williams, J. Raeburn, R. (2020). Seismic Evaluation of Electric Lake Dam Using Two-Dimensional and Three-Dimensional Methods, USSD 2018, April 30th -May 3rd, Miami, Florida.
- Lu, H.H., Xu, L.M., Fredlund, M.D. and Fredlund, D.G. (2013). 3D Shear Strength Reduction Finite Element Analysis, 18th Southeast Asian Geotechnical & Inaugural AGSSEA Conference, Singapore, May 2013.
- Fredlund M. D., Fredlund D.G., and Zhang L. (2017). Moving from 2D to a 3D Unsaturated Slope Stability Analysis.
- Pyke, R. (2017). How Great are 3D Effects in Slope Stability Analyses?, www.researchgate.net, publication information not available, 19 p.
- Seed, R. B., Mitchell, J. K. and Seed, H. B. (1990).
- Report on Mount Polley Tailings Storage Facility Breach, (2015). Independent Expert Engineering Investigation and Review Panel, January 2015, 147 p.

3D SEISMIC ANALYSIS OF ARCH DAM FOR RANDOM GROUND MOTION

D. Khandelwal¹, S. D. Bharti², M. K. Shrimali³, J. N. Arlekar⁴ & Dr. N. Roy⁵

¹ Department of Civil Engineering, Lecturer, Government Polytechnic College, Jaipur, India,
deepak.khandelwal10@gmail.com

² National Centre for Disaster Mitigation & Management, Professor, Malaviya National Institute Technology,
Jaipur, India,

³ National Centre for Disaster Mitigation & Management, Professor, Malaviya National Institute Technology,
Jaipur, India

⁴ National Centre for Disaster Mitigation & Management, Professor, Malaviya National Institute Technology,
Jaipur, India

⁵ National Centre for Disaster Mitigation & Management, Assistant Professor, Malaviya National Institute
Technology, Jaipur, India

Abstract: Most studies on the dam's seismic response considered earthquakes a deterministic process. There are very few studies for dams where the earthquake was considered a random process. The present study deals with the three-dimensional seismic analysis of the Morrow Point arch dam under the Kern County earthquake (1952), where the earthquake is considered a fully correlated ground motion. Assuming the ground motion to be an ergodic process, the power spectral density function (PSDF) of the Kern County earthquake represents the random ground excitation of the dam. C3D8R stress elements model the arch dam structure. The fluid-structure interaction is included by modeling the upstream water as AC3D8R acoustic elements. Direct spectral analysis is performed by obtaining the responses of the dam under harmonic base excitations considering fluid-structure interaction. The amplitude and frequency of the base excitation are varied to obtain the transfer function of the response quantities of interest; this part of the analysis is executed by ABAQUS. With the transfer functions of the responses known, the PSDF of response is determined by standard spectral analysis technique. For this purpose, a separate program is written using MATLAB code. The response quantities of interest are the mean peak top displacement at the top center of the arch dam and mean peak stresses at some critical locations. The mean peak values of response obtained from Kern County spectral analysis are compared with the peak responses obtained from the time history analysis.

1 Introduction

Seismic vulnerability evaluations were conducted for concrete dams commonly utilized in water and river management projects. These assessments covered Gravity and Arch dam designs and integrated water-structure interactions into the seismic response analysis. Gravity dam assessments used a simplified 2D slice analysis method, analyzing various dam sections for critical stress and displacements. However, this method wasn't suitable for dynamic analysis of arch dams, as it couldn't adequately capture their critical responses.

Hence, most analyses of arch dams now focus on a thorough 3D analysis, considering various interactions, to comprehensively evaluate their behavior. Höllinger and Wein presented solutions for the interacting vibrations of a linear elastic arch dam with a linear compressible, three-dimensional, irregularly shaped fluid body. The vibration response was derived for both time-harmonic excitation of the arch dam and nonstationary stochastic excitation processes relevant to earthquake analysis. In the time-harmonic solutions, a substructure synthesis method was utilized. The arch dam was treated using the finite element method, while the fluid domain employed a boundary integral equation method, also known as the boundary element method (Höllinger and Wein, 1983). Fok and Chopra studied how the Morrow Point arch dam responded to the Taft ground motion under different water levels and foundation rock conditions. Their findings indicated that the dam's earthquake response was amplified due to the interaction between the dam and water. At the same time, it was reduced by the reservoir boundary's capacity to absorb seismic effects (Fok et al., 1986). Duron and Hall conducted experiments and finite element studies to investigate how the Morrow Point arch dam responds to forced vibrations. Their work effectively isolated and analyzed the dam's response related to its fundamental vibration mode (Duron and Hall, 1988). Connor and Boot created a method for studying the reservoir system of an arch dam, with particular attention to considering the compressibility of water. Their analysis approach applied the Newmark implicit integration scheme (O'Connor & Boot, 1988). Yang et al. conducted a study analyzing a circular section spanning 90 degrees and extending infinitely on two sides. They formulated solutions for nonstationary random vibrations and hydrodynamic forces. Their main goal was to understand how a basic arch dam reservoir system responds to nonstationary random forces, effectively depicting earthquake ground movements. To simplify their analysis, they treated the dam as elastically deformable, primarily focusing on its first symmetric mode shape for simplicity. They described earthquake acceleration using a zero-start stationary process characterized by a Kanai-Tajimi spectral density function. The outcome of their study provided solutions for stochastic vibration and hydrodynamic force responses, which were expressed in generally nondimensional forms using nonstationary power spectral density functions and mean square functions (Yang et al., 1991). Tan and Chopra conducted a study focusing on the response of dam-foundation rock interaction to various ground motions. They examined critical factors like dam properties, rock properties, reservoir boundary materials, and boundary absorption. Their findings revealed that a flexible foundation lowered the dam's fundamental resonant frequency. They also observed that this interaction became more important as the ratio of the foundation rock's elasticity to the dam concrete's elasticity increased (Tan and Chopra, 1995). Sani and Lotfi assessed the interrelationships between the concrete arch dam, reservoir, and foundation rock concerning their seismic response (Sani and Lotfi, 2011). Akbari et al. studied the impact of nonuniform excitation due to spatially varying ground motions and explored the nonlinear responses of concrete arch dams. They analyzed a high arch dam, where the reservoir was treated as an incompressible material, and the foundation was assumed to be a massless medium. Contraction and peripheral joints were modeled, considering their ability to open and close. Monte Carlo simulation was employed to generate spatially nonuniform ground motion. The study investigated random seismic characteristics, including incoherence and wave passage effects, and compared their effects on structural response with uniform excitation at the design base level earthquake (Akbari et al., 2013). Ardebili and their research team conducted a study to investigate how hydrodynamic pressures under various reservoir operational conditions influenced the seismic performance of an arch dam. They chose the Dez Arch Dam in Iran as their case study. They utilized node-to-node contact elements to model all peripheral and contraction joints, allowing for simulations of tangential movement (Hariri-Ardebili et al., 2013). Løkke and Chopra conducted a comprehensive study on the nonlinear seismic analysis of a 3D arch dam model with reservoir water and foundation rock. They considered all the essential factors that affect how dams respond to earthquakes and their seismic performance. To achieve this, they created a direct finite element method to analyze the nonlinear dynamic behavior of these systems, using readily available finite element analysis software. Their analysis used viscous-damper type absorbing boundaries to simulate the semi-unbounded reservoir water and foundation areas. Additionally, they applied effective seismic forces at these boundaries based on deconvoluted ground motion data collected from a specific control point on the ground surface (Løkke and Chopra, 2019).

The available literature indicates a scarcity of studies regarding the seismic behavior of arch dams when earthquakes are treated as random occurrences. The challenge in conducting random vibration analysis for a dam with a reservoir lies in the complexity of constructing a frequency response function matrix due to the interaction between the dam and water. Unlike the dam alone, direct frequency domain spectral analysis is not feasible for the entire dam-reservoir system. The transfer function approach, commonly employed in

offshore structures, becomes essential to address this issue. Surprisingly, there is a lack of studies specifically evaluating the validity of spectral analysis using the transfer function approach for arch dam-reservoir systems. No previous research has explored a hybrid technique wherein the dam is modeled, and transfer functions of dam responses are obtained using standard methods. In this unique approach, a separate MATLAB program is developed to perform spectral analysis utilizing the extracted transfer functions. This current study focuses on conducting a 3D seismic analysis of the Morrow Point arch dam, assuming that earthquakes follow a random process. The earthquake is considered to be fully correlated ground motion. The analysis utilizing a transfer function approach is performed. The method is applied to a full reservoir dam. The approach is used to determine the response of the arch dam reservoir system. The earthquake's Power Spectral Density Function (PSDF) is assumed to follow the PSDF of the Kern County earthquake from 1952, treating it as representative of ergodic random excitation. The choice compares the response obtained from the spectral analysis using the transfer function approach with the time history analysis results. The critical response parameters of interest are the mean peak displacement values near the top of the crown cantilever section of the arch dam, and the mean peak stresses at specific critical locations.

2 Theory

Seismic analysis is conducted using spectral analysis, with earthquake excitation treated as a random process. The analysis utilizes both ABAQUS software and custom MATLAB code. MATLAB code is employed for the spectral analysis, while ABAQUS is used to create a model of the arch dam and reservoir water to extract its modal properties. The spectral analyses were carried out through the system's transfer function in MATLAB.

2.1 Modeling

In ABAQUS, the issue of Dam-water Interaction is approached by employing the coupled-acoustic-structural (CAS) finite element approach. Acoustics is the field of science that examines the generation, absorption, transmission, and reflection of sound waves in fluid environments. The acoustic wave equation can be expressed with pressure ' p ' as an independent variable as follows (Abaqus, F.E.A., 2014):

$$\frac{\partial^2 p}{\partial t^2} + v^2 \nabla^2 p = 0 \quad (2.1.1)$$

Where v is the speed of sound in the fluid media

$$v = \sqrt{\gamma / \rho_L} \quad (2.1.2)$$

Where γ is the Bulk modulus of the fluid, and ρ_L is the density of the fluid. The CAS (coupled-acoustic-structural) approach is a relatively straightforward and efficient numerical solution method that assumes no material flow and does not lead to mesh distortion in the material. In this approach, only pressure degrees of freedom are considered for the acoustic element at each node. This reduction in degrees of freedom results in shorter computational times for simulations. In the CAS approach, water is represented using acoustic elements based on linearized wave theory, while the dam is represented using Lagrangian elements. Impedance properties at the boundary connect the pressure within the acoustic element with the perpendicular motion at the interface between the acoustic and structural elements. The acoustic element propagates in the fluid's outward perpendicular direction, which can be described in the following way.

\dot{u}_{out} (outward velocity) is related to the pressure, as follows

$$\dot{u}_{out} = \frac{1}{k_1} \dot{p} + \frac{1}{c_1} p \quad (2.1.3)$$

Where p is acoustic pressure; \dot{p} is time rate change of the acoustic pressure; $\frac{1}{k_1}$ is the Coefficient of proportionality between pressure and displacement in the perpendicular direction of the surface; $\frac{1}{c_1}$ is the Coefficient of proportionality between pressure and velocity in the perpendicular direction of the surface. Surface-based tie constraint governs the interaction between the water on the upstream surface of the dam. With this interaction, both surfaces can remain in contact throughout the simulation. Under this constraint, every node on the fluid surface of the acoustic element experiences the same pressure and motion. An eight-node 3D acoustic continuum element with reduced integration (AC3D8R) is employed to model the water.

Eight-node 3D stress continuum elements with reduced integration (C3D8R) are used for the dam. The seismic analysis is carried out using the ABAQUS Explicit Module (Abaqus, F.E.A., 2014). The finite element analysis employs a dynamic explicit time integration method, which utilizes the central difference integration method incorporated within the ABAQUS software.

$$\dot{v}^{(i+1/2)} = \dot{v}^{(i-1/2)} + \frac{\Delta t^{(i+1)} + \Delta t^{(i)}}{2} \ddot{v}^{(i)} \quad (2.1.4)$$

$$v^{(i+1)} = v^{(i)} + \Delta t^{(i+1)} \dot{v}^{(i)} \quad (2.1.5)$$

Here, \dot{v} is the nodal velocity and \ddot{v} is the nodal acceleration. The initial acceleration of each increment is calculated as follows.

$$\ddot{v}^{(i)} = M_N^{-1} \cdot (F^{(i)} - I^{(i)}) \quad (2.1.6)$$

In this context, ' M ' denotes nodal mass, ' I ' signifies the internal forces acting on the water, and ' F ' represents the generalized force. To improve the simulation's accuracy, smaller time increments (Δt) are utilized, and this Δt remains consistent throughout the simulation. Ensuring precision is crucial and involves adhering to the Courant time limit, which specifies that Δt should be less than or equal to ' l/v '. Here, ' l ' corresponds to the smallest element length, and ' v ' represents the material's speed of sound wave propagation, known as the dilatational wave speed (Rawat et al. 2019). The wave reflection factor describes the interaction between water and the foundation, which accounts for the reflection of pressure waves in acoustic elements (such as water) in the vicinity of the structure. Consequently, it has an impact on the dynamic response of the structure. Hall and Chopra conducted a comprehensive study on this phenomenon in 1983 (Hall and Chopra, 1983). The properties of the foundation material determine the degree of reflection, and the extent of this reflection is quantified by the wave reflection factor, denoted as α . This α factor can be expressed as follows:

$$\alpha = \frac{1 - D}{1 + D} \quad (2.1.7)$$

$$D = \frac{\rho_w C_w}{\rho_f C_f} = \frac{\sqrt{\rho_w E_w}}{\sqrt{\rho_f E_f}} \quad (2.1.8)$$

In this equation, ρ_w represents the density of water, ρ_f is the density of the foundation or canyon material, C_w denotes the wave propagation speed in water and C_f signifies the wave propagation speed in the foundation or canyon material. E_w and E_f are modulus of elasticity of water and foundation, respectively. When α equals 1, the surface behaves as a complete reflector, and when α equals 0, the surface acts as a complete absorber.

2.2 Analysis Methodology

Spectral analysis is carried out for the dam with a full reservoir using the direct analysis method. In this analysis, a unit of sinusoidal excitation \ddot{x}_g is applied at the dam and reservoir water boundaries. The dam is represented using 3D elements, specifically C3D8R/C3D8 (3D stress elements). The sinusoidal excitation is defined by sampled amplitude values at intervals of Δt , spanning 10 cycles of oscillation to reach a steady-state response of the dam. The solution is computed using ABAQUS, and the steady-state response amplitude (A_j) is determined for various frequencies of excitation (Løkke and Chopra, 2019). The magnitude $|A_j|$ is referred to as the transfer function TR_j at the frequency ω_j for the response parameter. Once TR_j is established, it can be used to calculate the Power Spectral Density Function (PSDF) of the response quantity of interest, which is expressed as:

$$S(\omega_j) = |TR_j|^2 S_{\ddot{x}_g j}$$

Or

$$S(\omega) = |TR(\omega)|^2 S_{\ddot{x}_g}(\omega) \quad (2.2.1)$$

This formula represents the Power Spectral Density Function (PSDF) of the response quantity of interest $S(\omega)$, where $S_{\ddot{x}_g}(\omega)$ Signifies the PSDF of the excitation.

The n^{th} moment of the Power Spectral Density Function (PSDF) can be expressed as:

$$\lambda_n = \int_0^{\omega_c} \omega^n S(\omega) d\omega \quad (2.2.2)$$

The cut-off frequency of the Power Spectral Density Function (PSDF), denoted as ω_c , represents the frequency where the PSDF's tail portion is truncated. λ_0 corresponds to the mean square value of the ground acceleration. The central frequency Ω can be calculated as follows:

$$\Omega = \sqrt{\frac{\lambda_2}{\lambda_0}} \quad (2.2.3)$$

Ω serves as a metric for the frequency concentration within the Power Spectral Density Function (PSDF). Utilizing the provided parameters along with the earthquake's duration T_d , the mean peak ground acceleration / mean peak values of the response quantities of interest can be calculated (Datta, 2010).

$$\ddot{x}_{gmax} = \sqrt{2\lambda_0 \ln\left(\frac{2.8\Omega T_d}{2\pi}\right)} \quad (2.2.4)$$

2.2.1 Analysis of the Dam with a Full Reservoir

While modal spectral analysis can be applied to the empty dam, it cannot be used for analyzing a dam with a full reservoir. This limitation arises because the mode participation factor considers only the inertia forces and does not account for the added mass effect in the dam caused by ground excitation. In the case of a dam with reservoir water, an additional force acts on the dam due to hydrodynamic action in addition to the inertia force. This force can be divided into two components: the inertia force resulting from added mass and the hydrodynamic force generated by the movement of water particles. The mode participation factor cannot accommodate the second part of this force. Therefore, the analysis of the dam with reservoir water is conducted using a direct transfer function approach, similar to the approach used in offshore structures. The 3D acoustics stress elements (AC3D8R/AC3D8) are utilized for finite element modeling of the water. The complete dam-water model is subjected to harmonic ground motion at the sides and base of the dam reservoir system, aiming to calculate the transfer function for the response parameters of interest. The dam-water model is exposed to a unit amplitude ground acceleration with varying frequencies in this process. At each frequency, ten cycles of ground acceleration are applied as the boundary excitation. A time/response history analysis is carried out using ABAQUS software to determine the steady-state response, denoted as $|A|$. The resulting response amplitude is then used to calculate the transfer function. In the context of offshore structures, the steady-state amplitude $|A|$ is determined for harmonic waves of unit amplitude, accounting for nonlinearity resulting from hydrodynamic effects in the analysis. While spectral analysis is typically valid for linear systems, this approach is regularly employed for offshore structures to assess peak responses even in the presence of nonlinearity. In the case of a dam, the boundary excitations create water particle kinematics, leading to hydrodynamic pressure on the dam, which inherently involves nonlinearity. The transfer function TR, obtained for harmonic excitation using ABAQUS software, considers this water-structure interaction. Consequently, conducting spectral analysis for a dam with a full reservoir subjected to random ground motion is not strictly valid, similar to offshore structures, and necessitates validation.

3 Numerical study

A numerical analysis is conducted on the Morrow Point Arch dam, chosen for its availability of data required for 3D modeling from previous literature (Hall and Chopra, 1983). The Morrow Point arch dam is situated on the Gunnison River in Colorado, USA, with a total height of 465 feet. It is characterized as a double curvature thin arch dam. The dam's concrete properties include a Modulus of Elasticity (E_d) = 4×10^6 psi (2.75×10^{10} Pa), a density w_d = 155 pcf (2483 Kg/m³), a Poisson's ratio m = 0.2, and a damping ratio (ξ) of 5% for all vibration modes. The water has a density w = 62.4 pcf (1000 kg/m³) and a Bulk Modulus K = 3.19×10^5 psi (2.2×10^9 Pa). The value of α is set to 1, assuming fully reflective boundaries. In the ABAQUS software, suitable boundary conditions are applied to replicate fully reflective boundary conditions at the base and sides of the reservoir water. Plans are generated at each elevation level with 93-foot increments to generate 3D geometry of the Morrow Point arch dam. These plans are then lofted using AutoCAD software. AutoCAD

software is also utilized to model the 3D shape of the reservoir water. These 3D representations of the dam and reservoir water are imported into the ABAQUS environment. The reservoir water length is assumed to be nearly three times the height of the dam, with the cross-section of the reservoir matching the upstream surface profile of the dam. The upstream end of the reservoir is designed as a non-reflecting planar surface, as depicted in Figure 1. The boundaries of the dam are considered fixed. For the acoustics water medium, a natural boundary condition is assumed, which creates a fully reflective boundary due to the presence of a rigid wall around the fluid. No user input is required for this natural boundary condition in the acoustics medium. Surface-to-surface tie-type interactions are implemented between the dam's upstream surface and the water. At the top surface of the reservoir water, it is assumed that the acoustic pressure is zero. Finite element meshing is done, as depicted in Figure 2. A fine mesh is used to determine modal properties, while a coarse mesh is employed for the direct analysis method and time-history analysis of the dam with a full reservoir. Specific details of the finite element meshing are outlined in Table 1.

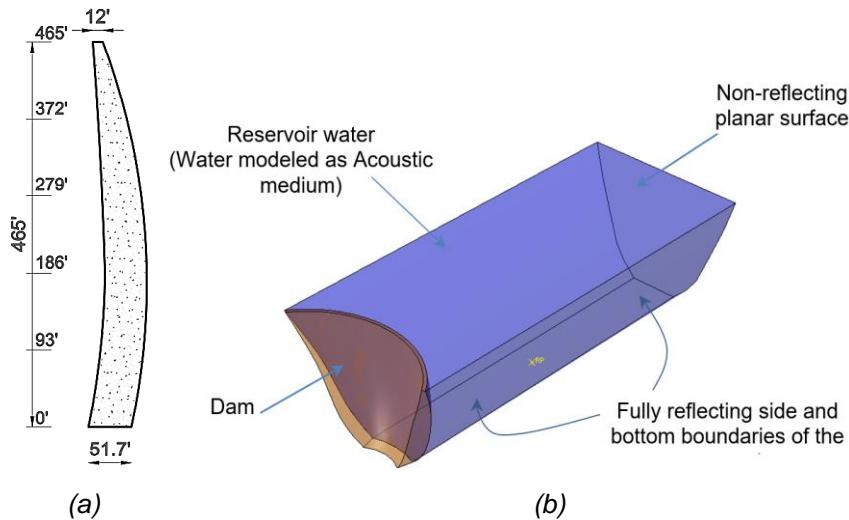


Figure 1. (a) Crown cantilever section of Morrow Point arch dam (b) 3D model of the arch dam – reservoir water.

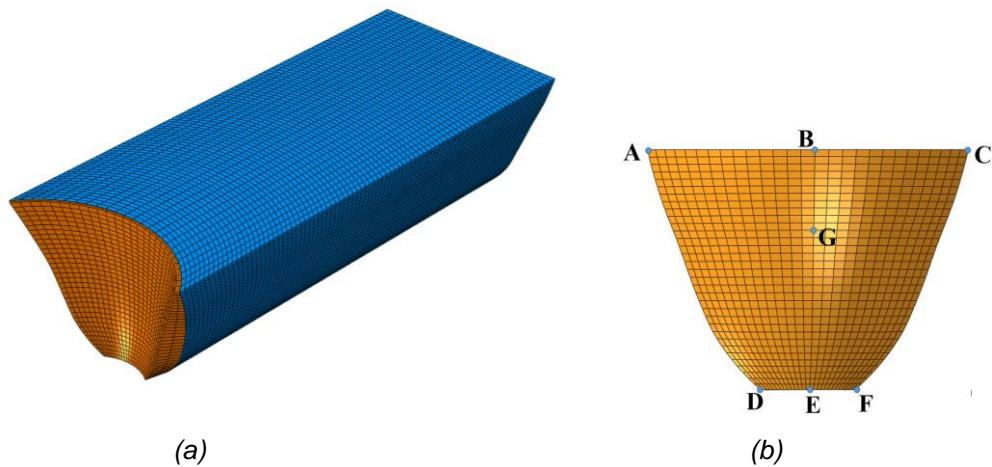
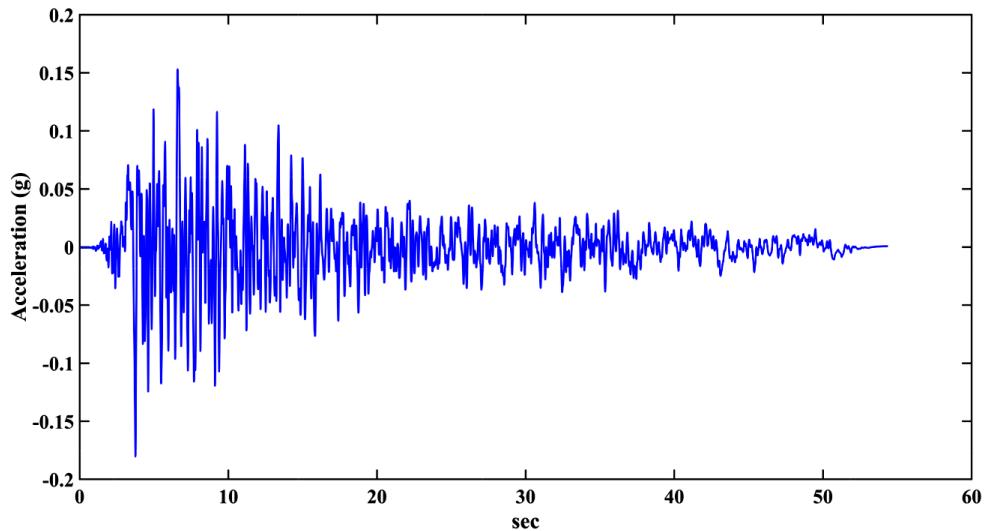
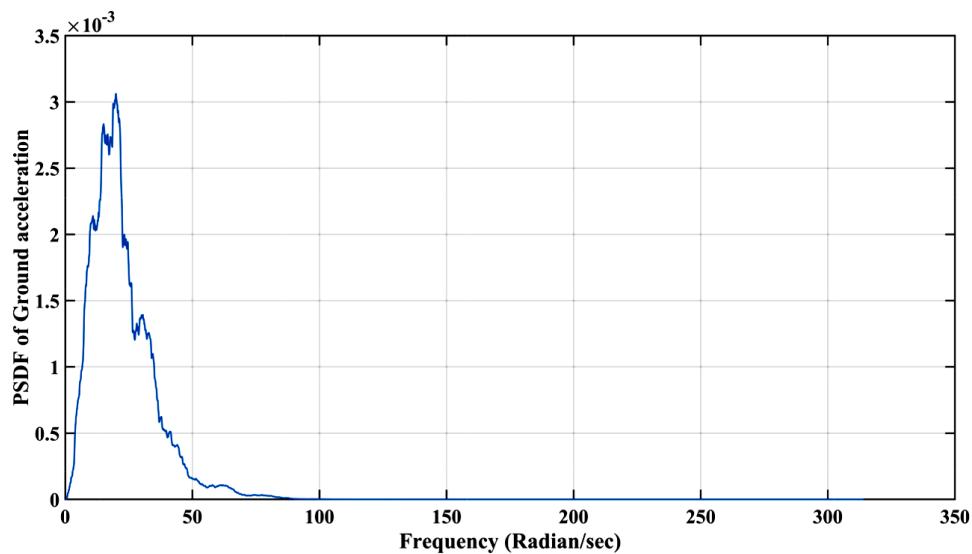


Figure 2. (a) Meshed 3D model of the Morrow Point arch dam - reservoir water (b) Selected critical points at the dam's upstream face

Table 1. Mesh properties of the dam-reservoir model

Part of the Model	Element type	Coarse Mesh	Fine Mesh
		Number of elements	Number of elements
Dam	C3D8R/C3D8	1782	13780
Reservoir water	AC3D8R/AC3D8	70400	583440

*Figure 3. Kern County (1952) acceleration time history**Figure 4. PSDF of the ground acceleration*

The acceleration time history of the Kern County earthquake from 1952 (depicted in Figure 3), specifically the Taft component 111 with a peak ground acceleration of 0.18g, is used as input at both the dam's base and sides. This same time history is also applied at a designated reference point (RP, as shown in Figure 1(b)). However, there is no application of time history in the vertical and cross-stream directions. A uniform earthquake loading is assumed at the dam and reservoir boundaries. The study includes conducting a time-

history analysis for the dam with a full reservoir. Figure 4 presents the Power Spectral Density Function (PSDF) of the ground acceleration for the Kern County Earthquake. The area beneath the curve is equivalent to the variance of the acceleration time history. A moving average filter method in MATLAB is employed to smooth the PSDF curve.

4 Discussion and results

Table 2 displays the first five mode shapes of the arch dam with a full reservoir. Conditions. Table 2 demonstrates that water–structure interaction reduces the dam's natural frequencies compared to the dam without water case. The decrease is more pronounced for higher frequencies.

Table 2. Modal shapes and Modal frequencies of the full reservoir dam

Mode No.	1	2	3	4	5
Modal Shape					
Modal Frequency (Hz)	2.84	2.97	3.24	3.71	4.48

Figure 5 displays the squared magnitude of the transfer function, denoted as $|TR|^2$, for the displacement at point B in the dam with a full reservoir. Figure 6 presents the corresponding Power Spectral Density Function (PSDF) for the displacement at point B. It's evident from Figure 6 that the PSDF of the displacement is narrow, with the peak occurring at the same frequency as the $|TR|^2$ plot. The nature of the PSDF and the $|TR|^2$ plot indicates that the fundamental mode of oscillation primarily governs the response. Figures 7 and 8 depict the PSDF of the arch and cantilever stresses at point B, respectively.

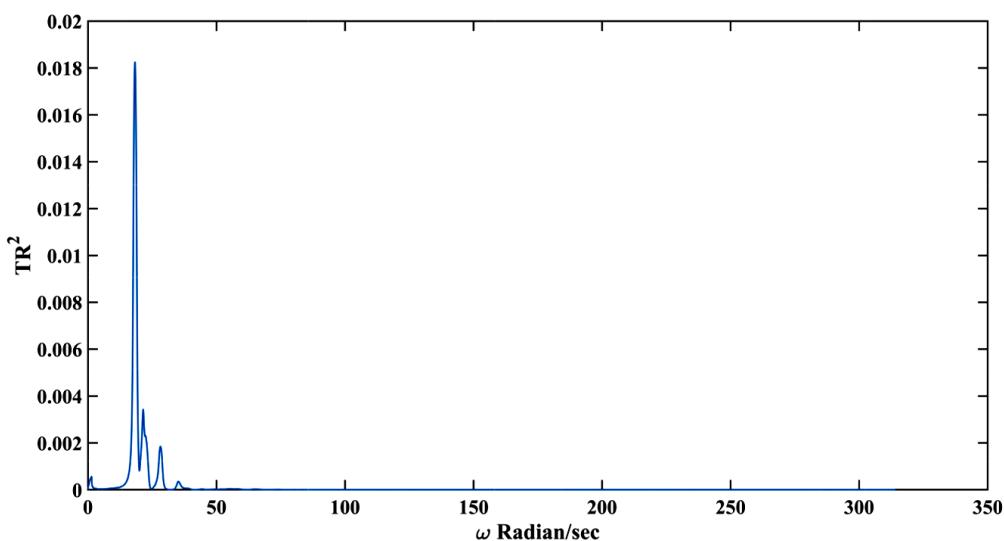


Figure 5. Square of the transfer function of displacement in upstream-downstream direction at point B of the full reservoir dam obtained by direct analysis

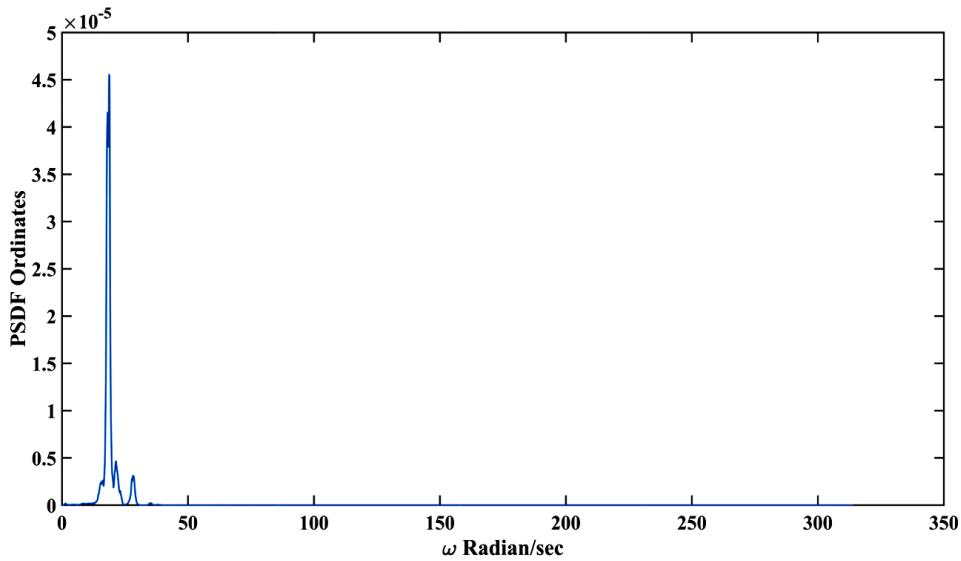


Figure 6. PSDF of the displacement at point B of the full reservoir dam in an upstream-downstream direction obtained by direct analysis (m)

Table 3 compares the absolute mean peak and RMS (root mean square) values of displacements obtained through spectral and time history analyses. The variation between these two responses falls within 10-15 percent. Consequently, the direct spectral analysis offers a reasonably accurate prediction of mean peak displacement. It's worth mentioning that the time history analysis yields slightly higher response values. Table 4 compares RMS and mean peak values of the arch and cantilever stresses at points A, B, C, D, E, F, and G, as determined by the spectral analysis (direct method) and the time history analysis. The disparities between these two stress values stay within a 15 percent range, with the time history stresses slightly higher.

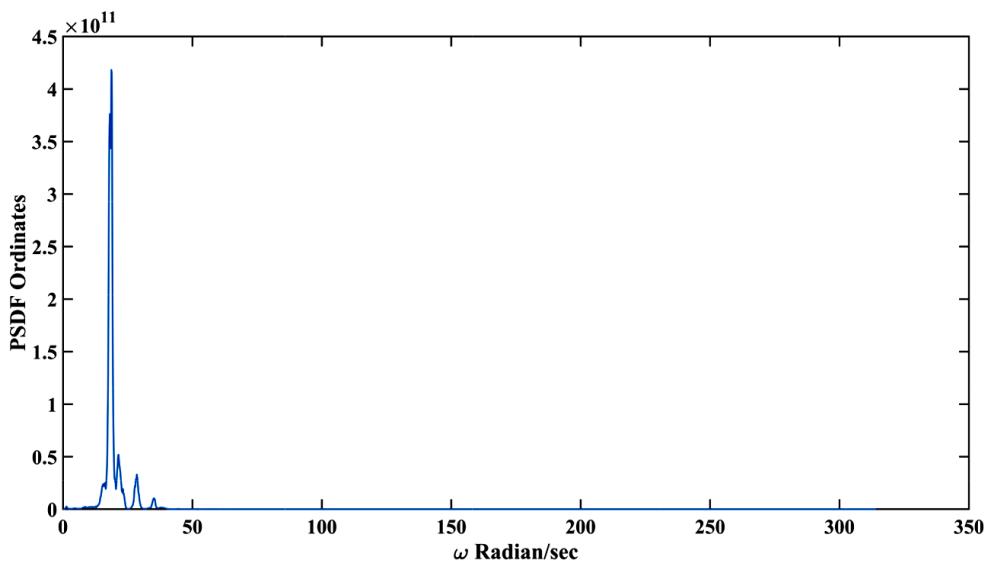


Figure 7. PSDF of the arch stress at point B of the full reservoir dam (N/m²)

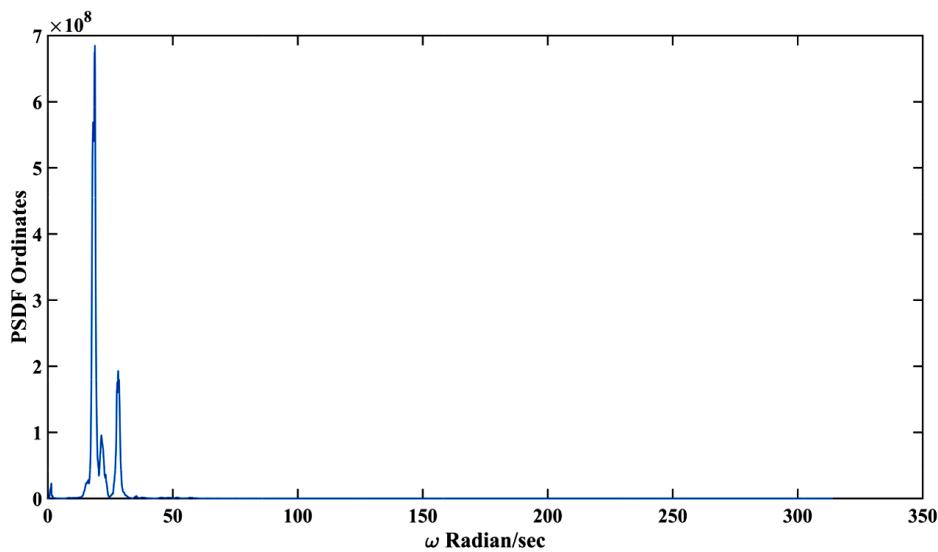


Figure 8. PSDF of the cantilever stress at point B of the full reservoir dam (N/m^2)

Table 3. Absolute mean peak and Root mean square (RMS) values of displacement (m) at point B

B(RMS values)	Spectral Analysis	Time History Analysis
	Direct method	
0.0098	0.0112	
B(absolute mean peak values)	0.0355	0.0408

Table 4(a). Absolute mean peak values of Cantilever and Arch stresses at points A, B, C, D, E, F, and G

Point	Arch Stress (Mpa)		Cantilever Stress (Mpa)	
	Spectral Analysis(Direct method)	Time History analysis	Spectral Analysis (Direct method)	Time History analysis
A	0.9026	1.0019	0.2104	0.2403
B	3.6632	4.2072	0.1557	0.1728
C	0.9026	1.0239	0.2104	0.2386
G	3.4244	3.7668	0.6004	0.6860
D	0.2418	0.2689	0.7489	0.8424
E	0.4076	0.4592	2.1936	2.4349
F	0.2418	0.2689	0.7489	0.9159

Table 4(b). RMS values of Cantilever and Arch stresses at points A, B, C, D, E, F, and G (All points located on the dam upstream face see Figure 2(b))

Point	Arch Stress (Mpa)		Cantilever Stress (Mpa)	
	Spectral Analysis (Direct method)	Time History analysis	Spectral Analysis (Direct method)	Time History analysis
A	0.2507	0.2660	0.0581	0.0614
B	1.0111	1.0665	0.0427	0.0440
C	0.2507	0.2660	0.0581	0.0614
G	0.9505	1.0054	0.1614	0.1625
D	0.0672	0.0715	0.2081	0.2211
E	0.1132	0.1202	0.6092	0.6470
F	0.0672	0.0715	0.2081	0.2211

Therefore, the direct spectral analysis accurately estimates dam responses when the dam and reservoir water are subjected to random ground excitation. Additionally, it's noted that arch stresses are substantially higher than cantilever stresses at the top, with the reverse trend occurring near the base.

5 Conclusion

The study involves conducting spectral analysis of the arch dam when subjected to random ground motion. Specifically, the Morrow Point arch dam is examined under the Power Spectral Density Function (PSDF) of the ground motion based on the PSDF of the Kern County earthquake. The ground motion is applied to the bottom and side boundaries of the dam-reservoir system. The applicability of the transfer function approach for spectral analysis of the dam with reservoir water under random ground motion is validated by the time history analysis. The Power Spectral Density Function (PSDF) reaches its highest value at the fundamental frequency of the dam. The frequency at which the excitation peak occurs is significantly distant from the first two natural frequencies of the dam. The Power Spectral Density Function (PSDF) of stresses for the dam with the reservoir is essentially characterized by a single peak, which aligns with the dam's fundamental frequency. The stresses in the arch section of the dam are considerably higher near the top compared to the cantilever stresses. However, near the bottom, the trend is the opposite.

6 References

- Abaqus, F.E.A., 2014. Dassault Systemes Simulia Corporation. *Providence, Rhode Island, USA*.
- Aftabi Sani, A. and Lotfi, V., 2011. An effective procedure for seismic analysis of arch dams, including dam-reservoir-foundation interaction effects. *Journal of Earthquake Engineering*, 15(7), pp.971-988.
- Akbari, M., Hariri-Ardebili, M.A. and Mirzabozorg, H., 2013. Nonlinear response of high arch dams to nonuniform seismic excitation considering joint effects. *Journal of Engineering*, 2013, pp.1-6.
- Chopra, A.K., 1988. Earthquake response analysis of concrete dams. In *Advanced dam engineering for design, construction, and rehabilitation* (pp. 416-465). Boston, MA: Springer US.
- Datta, T.K., 2010. *Seismic analysis of structures*. John Wiley & Sons.
- Duron, Z.H. and Hall, J.F., 1988. Experimental and finite element studies of the forced vibration response of Morrow Point Dam. *Earthquake engineering & structural dynamics*, 16(7), pp.1021-1039.
- Fok, K.L. and Chopra, A.K., 1986. Hydrodynamic and foundation flexibility effects in earthquake response of arch dams. *Journal of Structural Engineering*, 112(8), pp.1810-1828.
- Hall, J.F. and Chopra, A.K., 1983. Dynamic analysis of arch dams, including hydrodynamic effects. *Journal of Engineering Mechanics*, 109(1), pp.149-167.
- Hariri-Ardebili, M.A., Mirzabozorg, H. and Kianoush, M.R., 2013. Seismic analysis of high arch dams considering contraction-peripheral joints coupled effects. *Central European Journal of Engineering*, 3, pp.549-564.

- Höllinger, F., 1983. Time-harmonic and nonstationary stochastic vibrations of arch dam-reservoir systems. *Acta Mechanica*, 49, pp.153-167.
- Løkke, A. and Chopra, A.K., 2019. Direct finite element method for nonlinear earthquake analysis of concrete dams: Simplification, modeling, and practical application. *Earthquake Engineering & Structural Dynamics*, 48(7), pp.818-842.
- O'Connor, J.P.F. and Boot, J.C., 1988. A solution procedure for the earthquake analysis of arch dam-reservoir systems with compressible water. *Earthquake engineering & structural dynamics*, 16(5), pp.757-773.
- Rawat, A., Mittal, V., Chakraborty, T. and Matsagar, V., 2019. Earthquake-induced sloshing and hydrodynamic pressures in rigid liquid storage tanks analyzed by coupled acoustic-structural and Euler-Lagrange methods. *Thin-Walled Structures*, 134, pp.333-346.
- Tan, H. and Chopra, A.K., 1995. Dam-foundation rock interaction effects in frequency-response functions of arch dams. *Earthquake engineering & structural dynamics*, 24(11), pp.1475-1489.
- Yang, C.Y., Debessay, M. and Li, W.G., 1991. Random vibration of simple, flexible arch dam reservoir systems from earthquakes. *Probabilistic engineering mechanics*, 6(1), pp.18-32.

SEISMIC DAMAGE ANALYSIS OF HIGH CONCRETE ARCH DAM-FOUNDATION SYSTEMS: A COMPREHENSIVE STUDY

Liang Hui^{1,2}, Guo shengshan^{1,2}, Yan chunli^{1,2}, Tujin^{1,2}

¹ Earthquake Engineering Research Centre, China Institute of Water Resources and Hydropower Research, Beijing, China;

² State Key Laboratory of Simulation and Regulation of Water Cycle in River Basin, Beijing, 100048 China

Abstract: In this paper, seismic performance of a high arch dam is evaluated considering the material nonlinearity with a concrete damage model and the interaction between the steel reinforcement and the concrete mass with a distributed steel reinforcement model. Effects of the steel reinforcement on seismic damage of the dam under different water levels are of detailed discussion. Afterwards, a method i.e. seismic overload analysis is adopted to evaluate the ultimate seismic capacity of arch dams and the evaluation criteria i.e. the occurrence of upstream and downstream penetrating cracks of the dam is proposed. Thus, the ultimate seismic capacity of the dam is evaluated based on seismic overload factor and the effect of water levels and steel reinforcement on that is discussed.

1 Introduction

According to existing cases of high concrete dams subjected from strong earthquakes (Shen CK, et al. (1974); Chopra AK, et al. (1972)), tensile cracking may appear at dam body and the maximum stress criterion based on linear elastic material model cannot meet seismic safety evaluation of high concrete dams. Thus, except for various contact non-linearity, it is necessary and significant to consider material non-linearity of concrete in order to comprehensively reveal seismic performance of high concrete dams, which is an important trend in seismic analysis of high concrete dams in recent years.

In the early studies, material nonlinearity of concrete is considered based on classical plasticity theory, continuum damage mechanics and plasticity theory and fracture mechanics (J. Lubliner, et al. (1989); Lee J., et al. (1998); Ayari M. L., et al. (1990)). With gradual deepening of researches, material constitutive model characterized by the combination of plasticity theory and damage mechanics has been widely used and developed. Pan, et al. ((2007); (2009)) performs seismic damage cracking analysis of a high arch dam based on plastic-damage model. Effects of two different earthquake input mechanisms i.e. massless foundation model and viscous-spring boundary model on seismic response of an arch dam are of comparative analysis. A new conception to directly establish seismic damage model considering residual deformation based on experimental data is provided (Chen Houqun, et al. (2012); Chen H. Q., et al. (2014)). The proposed approach is verified by performing seismic damage analysis of Koyna gravity dam in India and Shapai RCC arch dam in China both subjected to strong earthquakes. It is demonstrated that the proposed model avoids to use commonly plastic damage model which is not suitable for concrete and greatly simplifies calculation process, resulting in more reasonable results. As shown in Reference (Guo Shengshan, et al. (2011)), based on fracture

energy and blunt crack zone model, cracking strain is proposed as a function of cracking displacement and element length at integral point, which is applied to plastic-damage model to ensure uniqueness of fracture energy and effectively eliminate effects of element size on plastic-damage analysis of concrete dams. Moreover, seismic damage and failure analysis of a gravity dam and foundation system is performed and effect of water levels on seismic damage response of a high arch dam is investigated using plastic-damage model (Guo Shengshan, et al. (2013); Guo S., Liang H., et al. (2020)). Li Deyu, et al (Li Deyu, et al. (2013); Alembagheri M., Ghaemian M. (2012)) perform a comparative analysis of seismic damage response of gravity dams using elastic damage model and damage model considering residual deformation. It is concluded that results with elastic damage model are unsafe. Seismic damage assessment of concrete gravity dams and arch dams are carried out using the plastic-damage model. Different damage indexes and damage states are proposed based on the results (Alembagheri M., Ghaemian M. (2013); Alembagheri, Mohammad. (2016)). Omidi O, Lotfi V ((2013); (2017)) propose a special finite element program coded in 3-D space based on a well-developed plastic-damage model and perform seismic damage analysis of concrete arch dams including contraction and peripheral joints.

In order to prevent further damage and cracking of dams subjected to strong earthquakes, it is necessary to take some engineering measures to improve seismic performance of concrete dams. Reinforcement in potential cracking regions has been adopted to reduce developments of dam cracking by engineers. Yuchuan Long, et al ((2008); (2009)) propose a modified embedded-steel model for evaluating effects of steel reinforcement on decreasing extension and opening of cracks and apply the proposed model on high concrete gravity and arch dams subjected to strong earthquakes. An embedded sliding model is used to simulate seismic response and failure of a concrete gravity dam with and without reinforcement, and effects of local reinforcement is evaluated (Zhang Shirong, et al. (2013)). Guo S, et al (2019) present a distributed steel reinforcement model which is easy to implement and can reflect interactions between steel reinforcement and concrete. Subsequently, effects of steel reinforcement on seismic damage of concrete gravity dams is studied. It is noted that few researches has been implemented to discuss effects of steel reinforcement on seismic performance of arch dams. Moreover, owing to great uncertainty of earthquakes, the actual peak ground acceleration (PGA) suffered by a dam may far exceed the corresponding design PGA. The ultimate seismic capacity of concrete dams is also a key issue. Currently, no unified evaluation standard and corresponding evaluation indexes has been recognized. Comprehensive analysis is required from various perspectives to study the ultimate seismic capacity of high arch dams.

Hence, seismic performance of a high arch dam is evaluated considering material nonlinearity and the interaction between the steel reinforcement and the concrete mass. Effects of the steel reinforcement on seismic damage of the dam under to different water levels are of detailed discussions. Afterwards, a method for evaluating the ultimate seismic capacity of arch dams is proposed by seismic overload analysis based on the proposed criteria i.e. the occurrence of upstream and downstream penetrating cracks of the dam. Seismic overload factor is adopted to represent the ultimate seismic capacity and discuss the effect of steel reinforcement on that.

The research ideas were determined by Liang hui and Jin Tu. Material preparation and data collection were obtained by Liang hui and Yan Chunli. The code was written by Shengshan Guo. Statistical analyses and computations were performed by Liang hui. All authors have read and approved the revised manuscript.

2 Calculation model

2.1 Damage model

For damage simulation of concrete material, in addition to elastic-plastic damage model, there are isotropic elastic damage and anisotropic elastic damage model, these elastic damage models do not consider the influence of residual deformation during the process of loading and unloading. Hence, a concrete damage model (Guo S., et al. (2019)) considering both residual deformation and stiffness reduction is used to simulate damage cracking of dam concrete. Figure 1 shows the damage model. The detailed description can be seen in reference (Guo S., et al. (2019)).

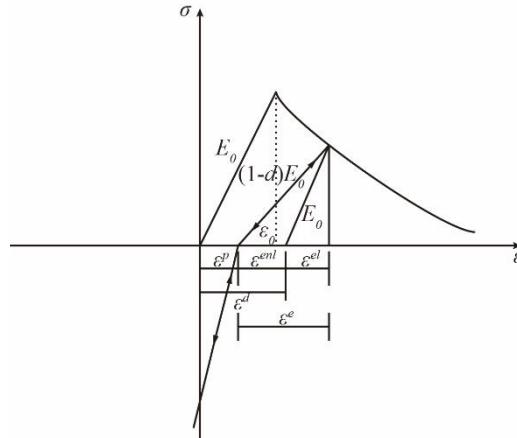


Figure 1 Damage model

2.2 Distributed steel reinforcement model

A distributed steel reinforcement model (Guo S., et al. (2019)) which is easy to implement and can reflect interaction between the steel reinforcement and the mass concrete is adopted to consider the effect of steel reinforcement on preventing damage cracking of the mass concrete. It is assumed that steel reinforcement is evenly distributed in the whole concrete element at a certain angle, and concrete and steel reinforcement are well bonded. Based on the assumption that strain of concrete and steel reinforcement is consistent, the stress-strain relationship of a compound element is obtained.

$$\sigma = D\varepsilon = \rho_c D_c \varepsilon + \rho_s D_s \varepsilon \quad (1)$$

where, ρ_s is steel reinforcement ratio of a compound element, $\rho_c = 1 - \rho_s$; $D = \rho_c D_c + \rho_s D_s$ is stiffness matrix of a compound element which is consist of stiffness matrix contributed by concrete element $\rho_c D_c$ and stiffness matrix contributed by steel reinforcement element $\rho_s D_s$; D_c is stiffness matrix of concrete element and D_s is stiffness matrix of steel reinforcement element.

Considering that steel reinforcement plays a role in the length direction, $\rho_s D_s$ can be written as follows.

$$\rho_s D_s = E_s \begin{bmatrix} \rho_{sx} & & & \\ & \rho_{sy} & & \\ & & \rho_{sz} & \\ & & & 0 \\ & & & & 0 \\ & & & & & 0 \end{bmatrix} \quad (2)$$

where, E_s is elastic modulus of steel reinforcement; ρ_{sx} , ρ_{sy} and ρ_{sz} are steel reinforcement ratio of a compound element in three directions.

The relationship between the steel reinforcement and concrete is established according to coordinate information. Steel reinforcement ratio of a compound element can be obtained based on finite element isoparametric transformation and Newton iteration method. The detailed description can be found in reference (Guo S., et al. (2019)).

3 Numerical modeling of high arch dams

3.1 Arch dam configuration

A double-curvature high arch dam is selected as a case study. Elevation of the dam crest is 880.5 m, and the maximum dam height is 167.5 m. Bottom thickness of crown cantilever is 44.81 m. Thickness-height ratio is 0.268 and chord-height ratio is about 1.50. A fine finite element model of dam-foundation system is established, shown in Figure 2(a) and (b). The dam body is divided into 12 parts along thickness direction with a mesh size of about 2.0 m. Total numbers of nodes and elements of the system are 652042 and 598133 respectively. Total degree of freedom of the system is about 196 million. Numbers of nodes and elements of the dam body is 177905 and 148207. The high arch dam is built as independent cantilever monoliths separated by 15 vertical

contraction joints shown in Figure 2(c). Figure 2(d) shows distribution of steel reinforcement. The steel reinforcement is divided by line element with a mesh size of about 0.1 m. The total numbers of nodes and elements are 2575645 and 2567395 respectively.

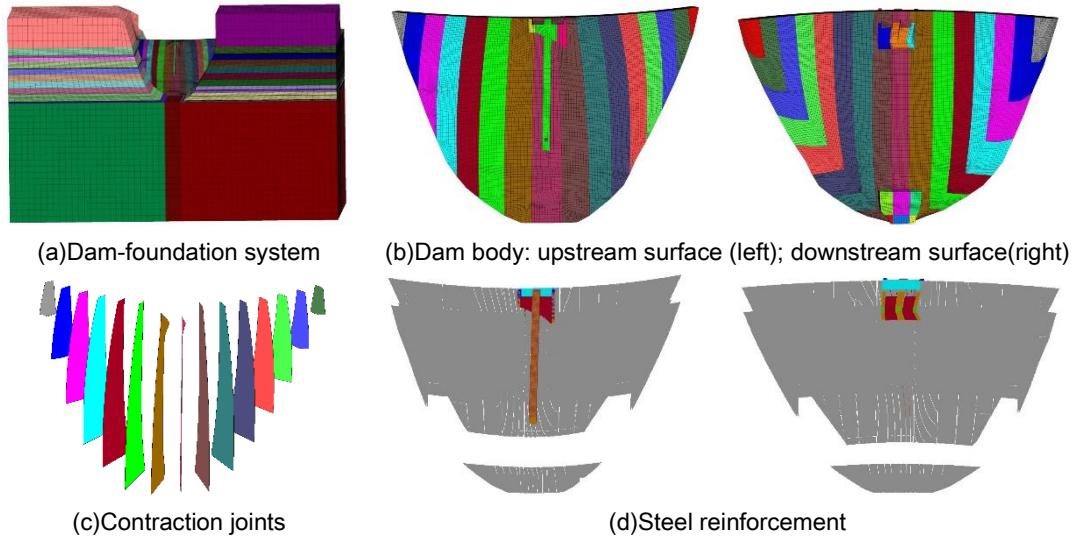


Figure 2 Finite element model of dam-foundation system

3.2 Material parameter

The unit weight of dam concrete is 24 KN/m³, the static elastic modulus is 22 GPa, the Poisson's ratio is 0.167, and the linear expansion coefficient is 8.0x10-6/°C. The static comprehensive deformation modulus of bedrock is shown in Table 1, and the Poisson's ratio is 0.25. Figure 3 shows the damage evolution of dam concrete used in this paper, which is characterized by cracking displacement-stress and cracking displacement-damage index. The fracture energy of concrete is 349 N / m.

Table 1 Material properties of foundation rocks (GPa)

Elevation (m)	713	720	740	760	780	800	820	840	860	880
Left bank	9.0	9.0	8.0	6.5	6.0	6.5	6.0	6.0	6.0	6.0
Right bank	9.0	9.0	9.0	7.5	8.0	8.0	6.0	6.0	6.0	6.0

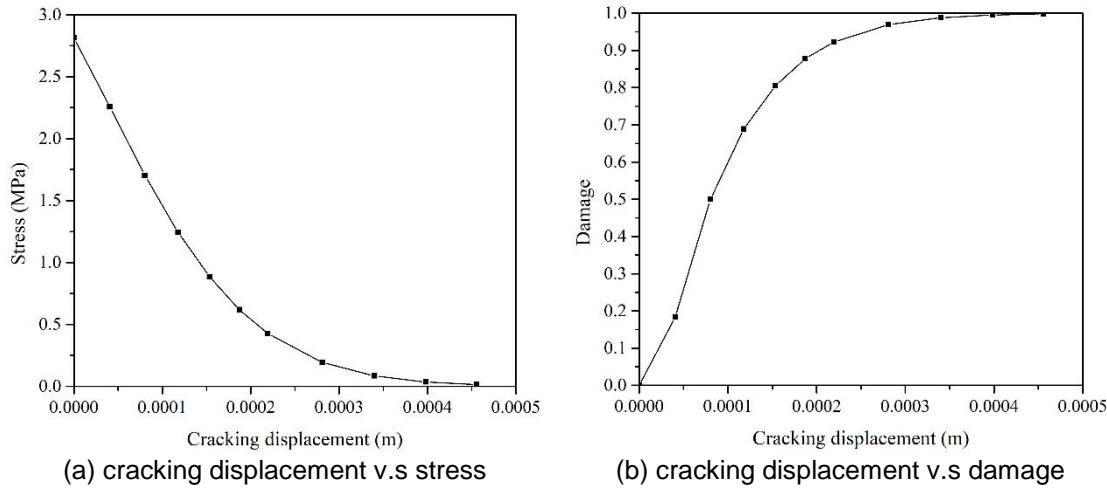


Figure 3 Damage evolution of dam concrete

3.3 Loading conditions

Independent cantilever dead load is considered for seismic damage analysis of the arch dam. The upstream

and downstream high water levels are 876 m and 738 m and corresponding low water levels are 814 m and 738 m. The sediment depth is 779.5 m. The buoyant unit weight of sediment is 9.0 KN/m³ and its frictional angle is assumed to be 12°. The sediment pressure is considered as hydrostatic pressure and applied on the upstream surface. The artificial earthquake motions are generated according to site-related design response spectrum and the peak ground motion of the design earthquake is 0.4225 g. The normalized input earthquake motions in three directions i.e. cross-river direction, stream-river direction and vertical direction are shown in Figure 4.

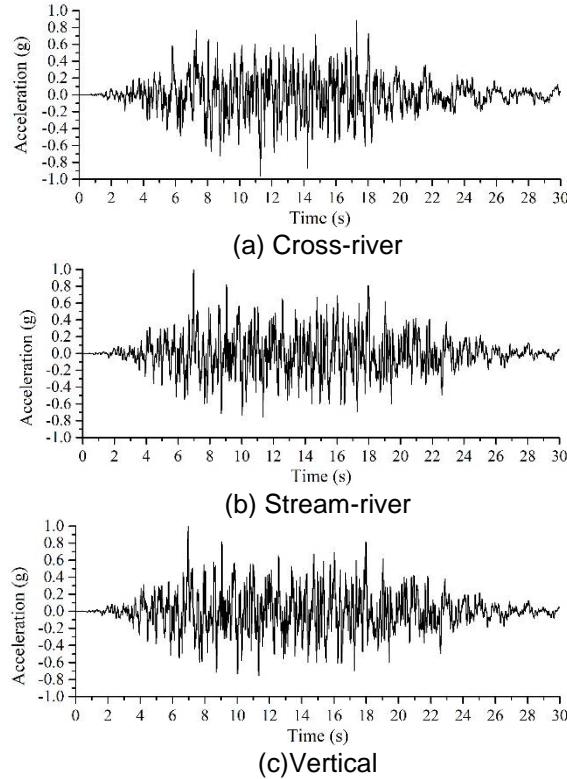


Figure 4 Input earthquake motions

4 Results and discussions

4.1 Results of seismic damage analysis

Seismic damage analysis is performed for four different cases which are shown in Table 2. All the cases are considered to obtain insight into the effects of steel reinforcement and water level on seismic damage of the dam.

Table 2 Case analysed

Case	Water level	Steel reinforcement
C1	high	without
C2	high	with
C3	low	without
C4	low	with

C1 and C2: High water level without and with steel reinforcement

Figure 5 describes damage contours of the arch dam for C1 and C2 under the maximum design earthquake. It can be seen that damage distributions of the dam are basically the same with and without steel reinforcement. Except for the damage located at the dam heel and toe, the dam is basically undamaged and slight damage occurs at the junction of the downstream pier and girder. According to damage contours of the crown cantilever, the macro crack depth at dam heel with damage variable (DV) greater than 0.8 is about 12.07 m without steel reinforcement. While, it decreases to 11.49 m when the steel reinforcement is considered.

Conditions	Upstream surface	Downstream surface	Crown cantilever
------------	------------------	--------------------	------------------

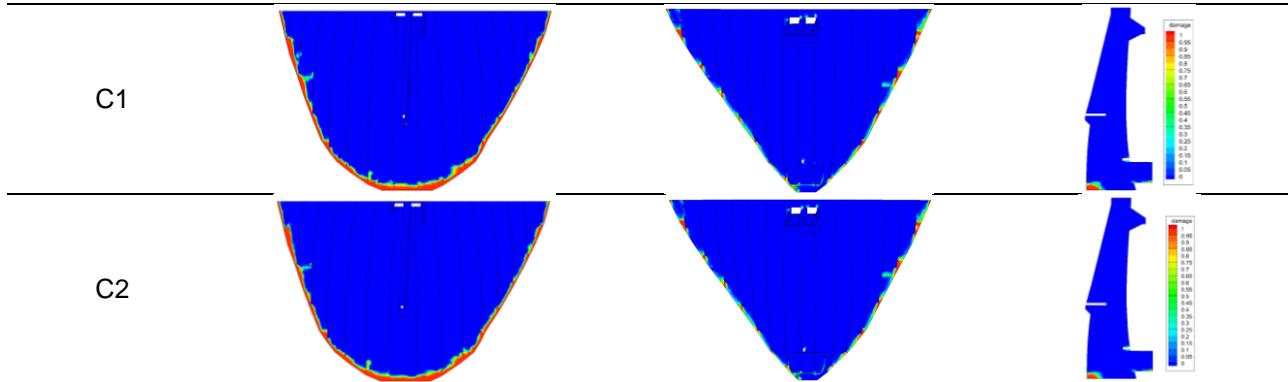


Figure 5 Damage contours of the arch dam for C1 and C2

C3 and C4: Low water level without and with steel reinforcement

Figure 6 describes damage contours of the arch dam for C3 and C4. It can be observed that damage at the junction of the pier and girder reduced significantly when the steel reinforcement is considered. According to damage contours of crown cantilever, damage occurs at downstream elevation of 790.6 m, and macro crack depth with DV greater than 0.8 is about 9.55 m without steel reinforcement. While it is about 8.16 m at elevation of 780.4 m with steel reinforcement.

Compared with C1 and C2, obvious damage of the dam occurs for C3 and C4, especially at downstream surface and the junction of downstream pier and girder. It can be explained that the occurrence of large opening of contraction joints significant increases of the dynamic cantilever stress of upper part of dam body under low water levels.

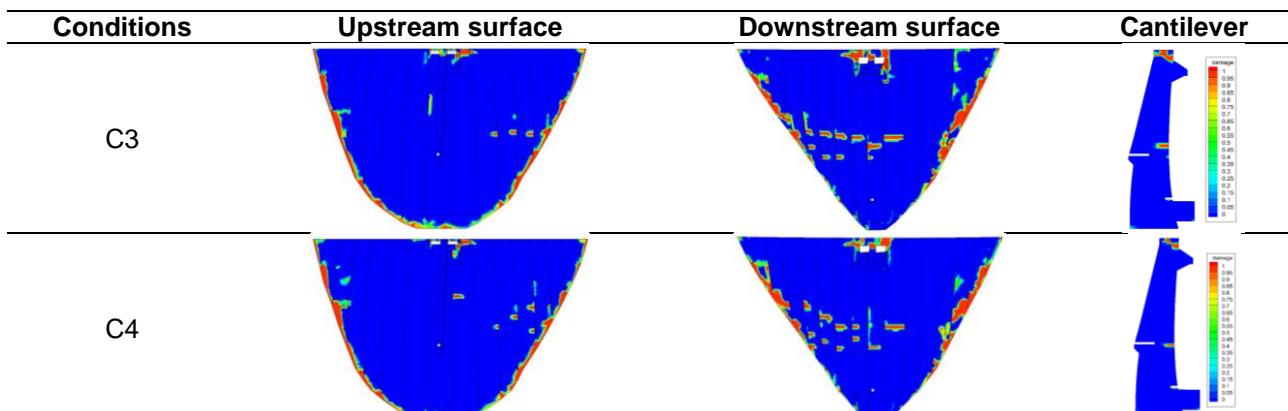


Figure 6 Damage contours of the arch dam for C3 and C4

4.2 Result of seismic overload analysis

The seismic overload analyses are performed to evaluate the ultimate seismic capacity of the arch dam-foundation system for all the cases. In the analyses, seismic load is scaled by multiplying seismic overload factor (OF) which is defined as the ratio of peak ground acceleration and that of maximum design earthquake herein.

C1 and C2: High water level without and with steel reinforcement

Damage contours of the arch dam at various overload factors for C1 and C2 are presented in Figure 7 and Figure 8 respectively. Obviously, damage of the dam mainly occurs at middle and upper part of upstream right abutment and at downstream middle part. Moreover, it develops and extends gradually with increasing OFs. Effect of the steel reinforcement on damage distributions and macro crack depths is apparent under different OFs. The macro crack depth with DV greater than 0.8 indeed decreases at the similar position when the steel reinforcement is considered. Moreover, penetrating cracks of 13# dam block occur at downstream elevation of 841.0 m with the OF of 1.60 for both C1 and C2. If the occurrence of upstream and downstream penetrating cracks of the dam is taken as the evaluation criteria, the corresponding OF of the dam reaching the ultimate

seismic capacity varies from 1.59 to 1.60, which can be taken as 1.59 i.e. the peak ground acceleration of 0.67 g.

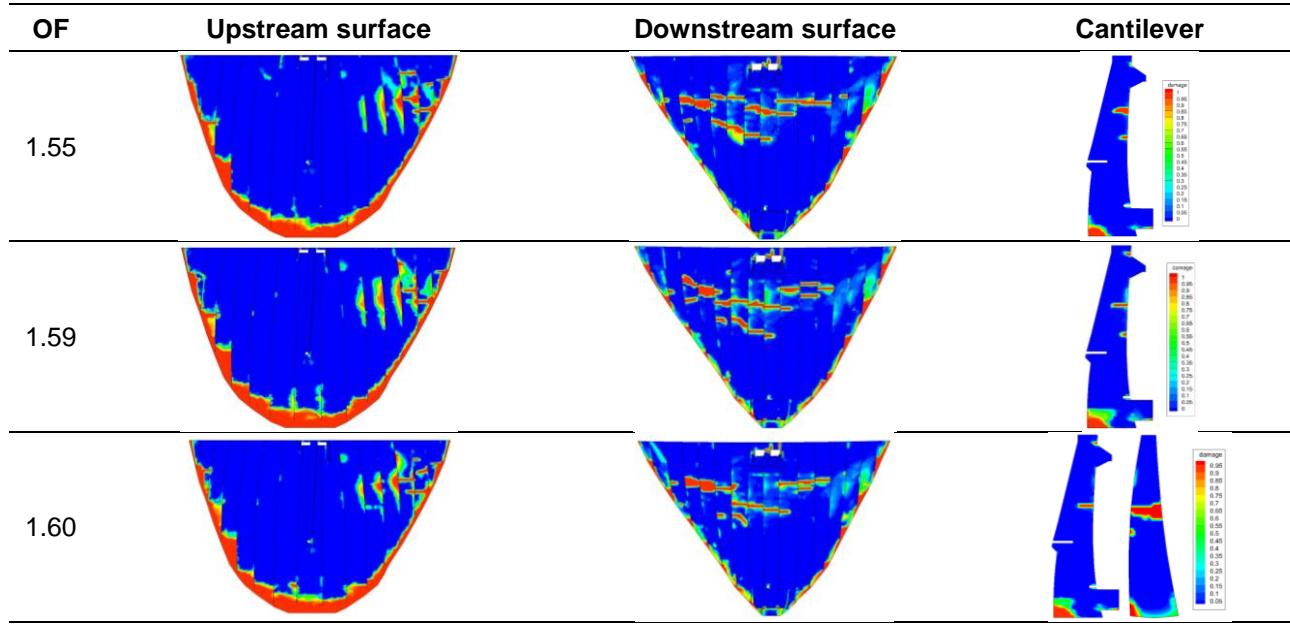


Figure 7 Damage contours of the arch dam at various overload factors for C1

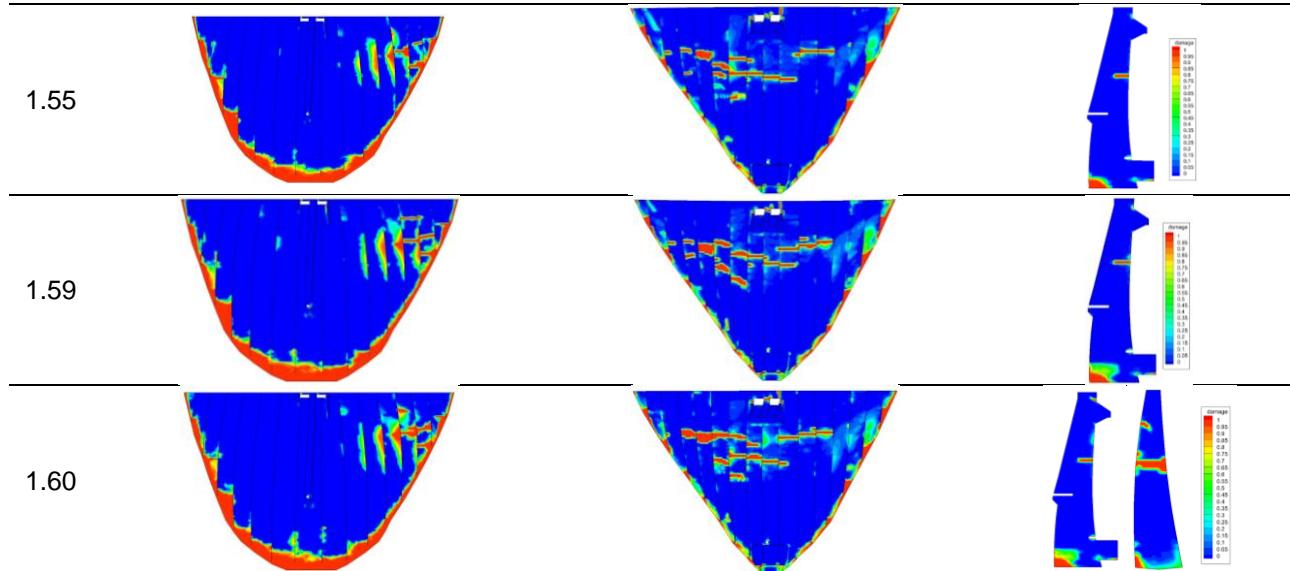


Figure 8 Damage contours of the arch dam at various overload factors for C2

C3 and C4: Low water level without and with steel reinforcement

Figure 9 and Figure 10 describe damage contours of the arch dam at various overload factors for C3 and C4 respectively. Similar to C1 and C2, damage region of the dam develops and extends gradually with increasing OFs. Moreover, damage distribution region at the junction of pier and girder and the pier root is smaller than that without steel reinforcement. According to Figure 9 and Figure 10, penetrating cracks of 7# dam block occur at downstream elevation of 811.44 m for C3 at OF of 1.30. While, they occur at downstream elevation of 820.57 m of the crown cantilever and 811.44 m of 7# dam block for C4. If the occurrence of upstream and downstream penetrating cracks of the dam is taken as the evaluation criteria, the corresponding OF of the dam considering steel reinforcement reaching the ultimate seismic capacity varies from 1.35 to 1.40, which can be taken as 1.35 i.e. the peak ground acceleration of 0.57 g. While it is 1.25 i.e. 0.53 g without considering steel reinforcement.

OF	Upstream surface	Downstream surface	Cantilever
----	------------------	--------------------	------------

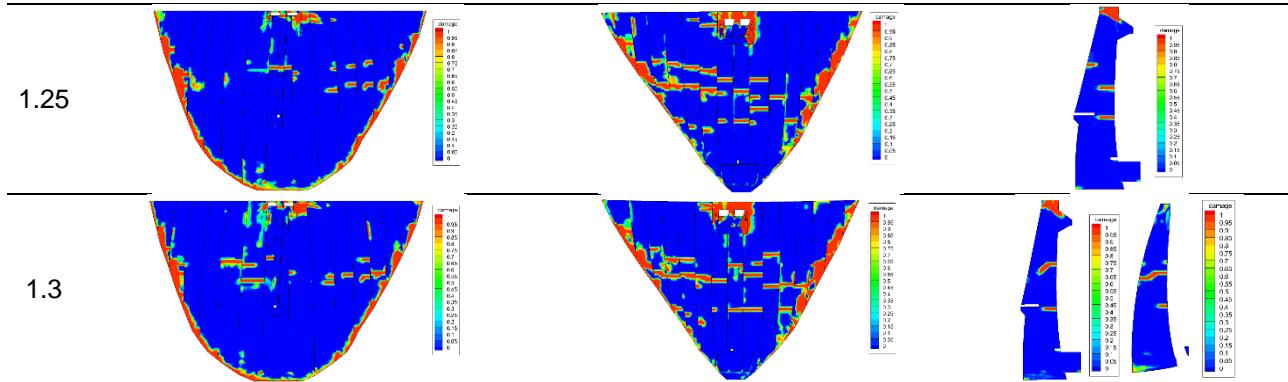


Figure 9 Damage contours of the arch dam at various overload factors for C3

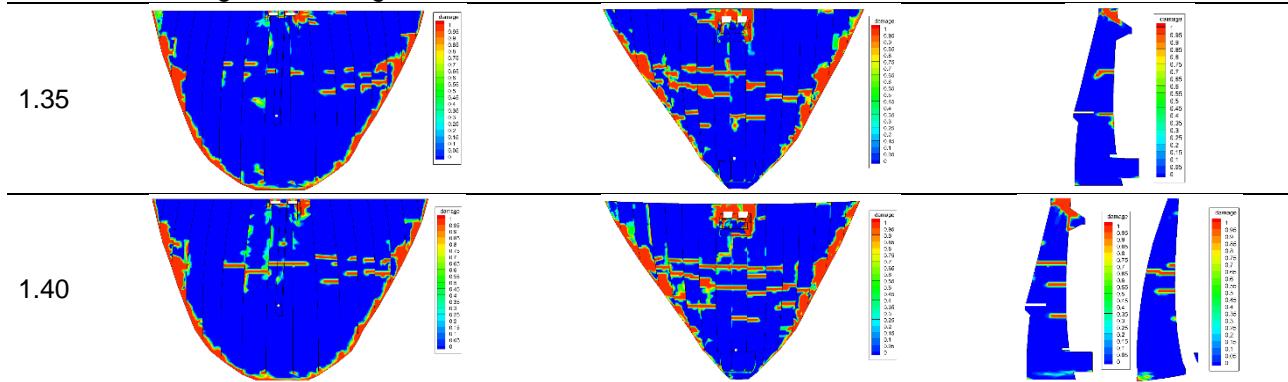


Figure 10 Damage contours of the arch dam at various overload factors for C4

5 Conclusions

Seismic performance of a high arch dam is evaluated considering material nonlinearity and the interaction between the steel reinforcement and the concrete mass with a comprehensive study. The effect of different water levels and steel reinforcement are of detailed discussion and seismic overload analysis is adopted to evaluate the ultimate seismic capacity of arch dams and the evaluation criteria i.e. the occurrence of upstream and downstream penetrating cracks of the dam is proposed. The main conclusions are as follows.

- (1) Compared with the results obtained under the high water level and design earthquake, obvious damage of the dam occurs under low water level and design earthquake, especially at downstream surface and the junction of downstream pier and girder. It is explained that the occurrence of large opening of contraction joints significant increases of the dynamic cantilever stress of upper part of dam body under low water levels.
- (2) Damage distributions of the dam are basically the same with and without steel reinforcement since the dam is basically undamaged and slight damage occurs at the junction of the downstream pier and girder under the high water level and design earthquake, while damage at the junction of the pier and girder reduced significantly under the low water level and design earthquake when the steel reinforcement is considered.
- (3) If the occurrence of upstream and downstream penetrating cracks of the dam is taken as the evaluation criteria, the corresponding OF of the dam reaching the ultimate seismic capacity varies from 1.59 to 1.60, which can be taken as 1.59 i.e. the peak ground acceleration of 0.67 g under the high water level.
- (4) If the occurrence of upstream and downstream penetrating cracks of the dam is taken as the evaluation criteria, the corresponding OF of the dam considering steel reinforcement reaching the ultimate seismic capacity varies from 1.35 to 1.40, which can be taken as 1.35 i.e. the peak ground acceleration of 0.57 g. While it is 1.25 i.e. 0.53 g without considering steel reinforcement under the low water level.

6 Reference

- Shen CK, Chen HQ, Zhang CH, Huang LS (1974). Earthquakes induced by reservoir impounding and their effect on the Hsingfengkiang dam. *Scientia Sinica*, 17(2):239–272.
- Chopra AK, Chakrabarti P (1972). The earthquake experience at Koyna dam and stresses in concrete gravity dams. *Earthquake Engineering and Structural Dynamics*, 1(2):151–164.
- J. Lubliner, J. Oliver, S. Oller and E. Onate (1989). A plastic-damage model for concrete, *Int. J. Solids. Struct.* 25(3): 299-326.

- Lee J., Fenves G. L. (1998). A plastic-damage concrete model for earthquake analysis of dams. *Earthquake Engineering & Structural Dynamics*, 27(9): 937-956.
- Ayari M. L., Saouma V. E. (1990). A fracture mechanics based seismic analysis of concrete gravity dams using discrete cracks. *Engineering Fracture Mechanics*, 35(1): 587-598.
- Pan Jianwen, Wang Jinting, Zhang Chuhan. (2007). Damage cracking analysis of arch dams under super strong earthquakes [J] *Journal of water conservancy*, (02): 143-149. (in Chinese)
- Pan J. W., Zhang C. H., Wang J. T., et al. (2009). Seismic Damage-Cracking Analysis of Arch Dams Using Different Earthquake Input Mechanisms [J]. *Science in China Series E: Technological Sciences*, 52(2): 518-529.
- Chen Houqun, Guo Shengshan. (2012). Seismic damage analysis of high concrete dam-foundation system [J]. *Journal of water conservancy*, 43 (S1): 2-7. (in Chinese)
- Chen H. Q., Li D. Y., Guo S. S. (2014). Damage–Rupture Process of Concrete Dams Under Strong Earthquakes [J]. *International Journal of Structural Stability & Dynamics*, 14(07): 1450021-1-1450021-21.
- Guo Shengshan, Chen Houqun, Li Deyu, et al. (2011). Study of element-size effect on dynamic plastic-damage analysis of concrete [J]. *Journal of hydropower*, 30 (6): 52-56. (in Chinese)
- Guo Shengshan, Chen Houqun, Li Deyu, et al. (2013). Seismic damage and failure analysis of gravity dam and foundation system [J]. *Journal of water conservancy*, 44 (11): 1352-1358. (in Chinese)
- Guo S., Liang H., Wu S., et al. (2020). Seismic damage investigation of arch dams under different water levels based on massively parallel computation[J]. *Soil Dynamics and Earthquake Engineering*, 129:105917-1-8.
- Li Deyu, Guo Shengshan, Chen Houqun, et al. (2013). Comparison of elastic damage model and damage model considering residue deformation for seismic damage analysis of gravity dams [J]. *Journal of hydropower*, 32 (5): 226-231. (in Chinese)
- Alembagheri M., Ghaemian M. (2013). Damage assessment of a concrete arch dam through nonlinear incremental dynamic analysis[J]. *Soil Dynamics & Earthquake Engineering*, 44:127-137.
- Alembagheri M., Ghaemian M. (2012). Seismic assessment of concrete gravity dams using capacity estimation and damage indexes [J]. *Earthquake Engineering & Structural Dynamics*, 42(1): 123-144.
- Alembagheri, Mohammad. (2016). Earthquake damage estimation of concrete gravity dams using linear analysis and empirical failure criteria[J]. *Soil Dynamics & Earthquake Engineering*, 90: 327-339.
- Omidi O., Lotfi V. (2013). Earthquake response of concrete arch dams: a plastic–damage approach [J]. *Earthquake Engineering & Structural Dynamics*, 42(14): 2129-2149.
- Omidi O., Lotfi V. (2017). Seismic plastic–damage analysis of mass concrete blocks in arch dams including contraction and peripheral joints[J]. *Soil Dynamics & Earthquake Engineering*, 95: 118-137.
- Yuchuan Long, Chuhan, et al. (2008). Numerical simulation of reinforcement strengthening for high-arch dams to resist strong earthquakes[J]. *Earthquake Engineering & Structural Dynamics*, 37:1739–1761.
- Long Y., Zhang C., Xu Y. (2009). Nonlinear seismic analyses of a high gravity dam with and without the presence of reinforcement[J]. *Engineering Structures*, 31(10): 2486-2494.
- Zhang Shirong, Wang gaohui, Pang Bohui, et al. (2013). Seismic cracking and reinforcement analysis of concrete gravity dam based on XFEM [J] *Vibration and shock*, (06): 137-142. (in Chinese)
- Guo S., Liang H., Deng Y., et al. (2019). The Effect of Steel Reinforcement on Seismic Damage to Concrete Gravity Dams Based on Distributed-Steel Model[J]. *Journal of Earthquake and Tsunami*, 14(2): 2050010-1-19.

INTENSIFYING DYNAMIC RESPONSE OF A CONCRETE DAM AFFECTED BY ALKALI-AGGREGATE REACTION

G. Mahdavi¹, and V.E. Saouma²

¹ University of Colorado, Boulder, USA, golsa.mahdavi@colorado.edu

² University of Colorado, Boulder, USA

Abstract: Seismic damage of aging infrastructures can pose a significant risk to the safety of people living downstream. Alkali-aggregate reaction (AAR) is a chemical reaction in concrete that occurs over time and causes concrete expansion and reduces the strength parameters, e.g., tensile strength, and module of elasticity. This study aims to investigate the impact of AAR on the performance of a concrete dam subject to seismic excitation. For this purpose, a detailed finite element model of the case study dam is prepared including the foundation.

Two pre-seismic models have been developed. In the first one, the coupled system is subjected to AAR expansion for the entire lifetime of the dam, while the second model is based on sound conditions (i.e., reference model). A high-fidelity AAR model is used to precisely predict the AAR expansion. Material properties are incorporated into the finite element model using the results of the core sampling tests. Both the sound and AAR-affected models are excited using intensifying artificial accelerations. To evaluate the response of the dam, the crest displacements are compared for the two models. The findings of this study contribute to understanding the seismic vulnerability of concrete dams affected by AAR and provide valuable insights for risk assessment and mitigation strategies.

1. Introduction

The seismic response of concrete dams, particularly in the context of alkali-aggregate reaction (AAR), stands as a critical concern in the context of structural engineering. AAR, a chemical reaction between alkaline substances in concrete and active components in aggregates, induces uneven expansion, cracking, and structural deterioration, significantly compromising the durability of concrete (Gillott, 1975). First identified in the United States in 1940, AAR poses a persistent challenge, as its continuous occurrence within concrete makes the repair and reinforcement of affected structures arduous and reconstruction a potential future necessity. The global impact of AAR has been particularly pronounced in hydraulic concrete structures, where elevated relative humidity and extended service life create ideal conditions for AAR development, magnifying the risk compared to ordinary concrete structures.

In recent years, heightened attention has been directed towards addressing the challenges posed by AAR in water conservancy projects. Alkali activity tests for aggregates have become a standard practice, allowing

proactive measures to prevent AAR-related damage. The recognition of AAR as a pervasive pathology in concrete structures has prompted the development of various models to assess its effects, with a primary focus on alkali-silica reaction (ASR), the predominant AAR type worldwide (Fournier and Bérubé, 2000). ASR involves a chemical reaction between unstable silica mineral forms in aggregates and alkali hydroxides in the concrete pore solution, resulting in the formation of alkali-silica gel that induces expansive pressures, microcracking, and degradation of material properties.

Despite advancements in understanding AAR, assessing its impact on aging infrastructure remains complex. Finite element (FE) models have emerged as a valuable tool for diagnosing current distress conditions and predicting potential future damage caused by AAR (Esposito, 2016). Notably, macro-models offer a proposer setting to capture the overall structural implications of ASR on large structures (Gorga et al., 2018). These models consider factors such as temperature, moisture, aggregate reactivity, alkali content, and exposure conditions, providing a detailed understanding of AAR's intricate interplay with structural elements.

As AAR-induced distress in aging dams can manifest heterogeneously, safety assessments become intricate endeavors. Non-destructive testing techniques offer avenues for identifying AAR-affected areas and evaluating the severity of the reaction. Complementing these techniques, numerical simulation methods facilitate the modelling of dam behaviour under diverse loads and environmental conditions, aiding in the prediction of AAR's impact on structural integrity. It is imperative to consider the age, design, and condition of dams when assessing safety, with a keen awareness that dams approaching the end of their design life may be more susceptible to AAR-induced damage, necessitating vigilant monitoring and maintenance.

In the context of seismic responses, the presented study endeavors to investigate the impact of AAR on the performance of a concrete dam subjected to seismic excitation. Utilizing a detailed finite element model, the study compares the response of a dam under AAR-affected conditions with a reference model under sound conditions. The findings contribute to a deeper understanding of the seismic vulnerability of concrete dams affected by AAR. This paper is a short paper from a Ph.D. thesis proposing a framework for aging and shaking analysis of concrete dams (Mahdavi, 2023).

There is limited research on the seismic response of AAR affected dams. The notable ones are: Gorga et al. (2018), Ben Ftima et al. (2023), Zhai et al. (2022), Pourbehi et al. (2019), Pan et al. (2014), and the detailed literature review can be found in Saouma and Hariri-Ardebili (2020).

2. AAR Constitutive Model

The theoretical underpinning of the AAR model used in this paper has been presented by the authors separately in Saouma and Perrotti (2006). The AAR expansion is a volumetric expansion described by the following equation:

$$\dot{\varepsilon}_V^{AAR}(t, \theta, RH) = \Gamma_t(f'_t | w_c, \sigma_l | COD_{max}) \times \Gamma_c(\bar{\sigma}, f'_c) \times g(RH) \times \dot{\xi}(t, \theta) \times \varepsilon^\infty|_{\theta=\theta_0} \quad (1)$$

where ε^∞ is the final volumetric expansion as determined from laboratory tests at temperature θ_0 . $0 \leq \Gamma_t \leq 1$ is a parameter which reduces the expansion in the presence of large tensile stresses (macro-cracks absorbing the gel), f'_t the tensile strength, and σ_l the major (tensile) principal stress. Similarly, $0 \leq \Gamma_c \leq 1$ is a parameter which accounts for the absorption of the gel due to compressive induced stresses, $\bar{\sigma}$ and f'_c are the hydrostatic stress, and the compressive strength of the concrete, respectively. $0 \leq g(RH) \leq 1$ is a function of the relative humidity (set to zero if the humidity is below 80%), and $\dot{\xi}(t, \theta)$ is the kinetics law given by:

$$\dot{\xi}(t, \theta) = \frac{1 - \exp(-\frac{t}{\tau_c(\theta)})}{1 + \exp(-\frac{(t - \tau_l(\theta))}{\tau_c(\theta)})} \quad (2)$$

where τ_l and τ_c are the latency and characteristic times, respectively. The former corresponds to the inflection point, and the latter is defined in terms of the intersection of the tangent at τ_l with the asymptotic unit value of $\dot{\xi}$. They are given by:

$$\tau_i(\theta) = \tau_i(\theta_0) \exp[U_i(\theta^{-1} - \theta_0^{-1})] \quad (3)$$

expressed in terms of the absolute temperature ($\theta^{\circ}K = 273 + T^{\circ}C$) and the corresponding activation energies. The i can be either l (latency) or c (characteristics). U_i presents the activation energies. Once the volumetric AAR strain is determined, it is decomposed into a tensorial strain in accordance with the three weight factors associated with the principal stresses. Finally, degradation of the material property, M , is accounted for as follows:

$$\frac{M(t, \theta)}{M_0} = 1 - (1 - \beta_M) \times \xi(t, \theta) \quad (4)$$

where M can be either tensile strength, f_t , or modulus of elasticity, E_c ; M_0 is the initial/original material property, and β_M is the residual fractional value (of f_t or E_c) when ε tends to ε^∞ . Figure 1 illustrates the AAR expansion curves at different temperatures, and the corresponding degradation curve (Saouma and Hariri-Ardebili, 2021).

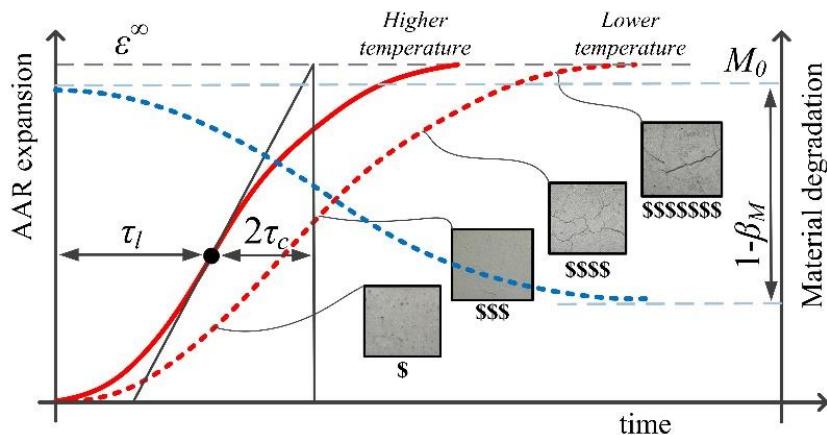


Figure 1 A sample AAR expansion curve at high temperature (solid red) including the inflection point. Reducing the temperature shifts the expansion curves to the right (dashed red). The corresponding material degradation curve is shown in dashed blue.

3. Dynamic Analysis Procedure

In order to assess the performance of the AAR- affected case study dam under seismic loading an Intensifying artificial acceleration was used which is described in section 5. Figure 2 Shows the overall procedure of dam analysis involving seismic loading. Based on this figure, the steps towards the dynamic analysis can be summarized as follows:

1. The first step involves performing a complete AAR analysis for an extended time; In this study it is assumed that the seismic excitation of the AAR-affected dam will occur after 50 years of AAR analysis.
2. An important step in the AAR analysis is to consider the material degradation such as concrete elastic modulus and tensile strength with time.
3. In the current study, for comparison purposes, an initial seismic analysis is performed considering the structure at its initial and sound condition. In other words, as shown in step 3 of figure 1, the seismic excitation is applied at the onset of AAR.
4. Next step is to perform an AAR analysis to be followed by another dynamic analysis. In this step the same seismic excitation is applied at the end of the 50 years of AAR analysis.
5. The final step is to compare the response of the structure for the 2 different analyses. At this stage, the Intensifying Artificial acceleration (IAA) allows us to determine and plot the maximum absolute value of our engineering demand parameter at different intensity measure levels, after applying a single IAA excitation and without having to perform multiple seismic analyses.

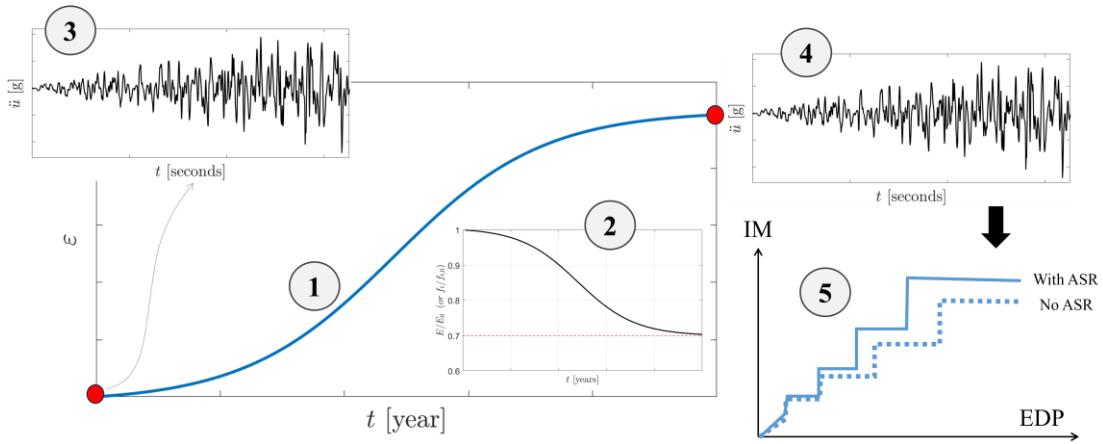


Figure 2 Step by Step Dynamic Analysis Procedure

4. Case Study

The case study is a concrete arch gravity dam which is modelled in Merlin (2021) finite element code. An AAR analysis using the described AAR model is performed for 50 years of aging dam followed by three IAA seismic excitations to assess the performance of the dam at different intensity levels. Then the response of the AAR affected dam was compared to that of the sound structure.

An important step prior to performing an AAR analysis is a parameter identification process to determine the AAR model parameters that best describe the real condition of the structure at each specific time. In the current study, an optimization technique is utilized to determine three most important parameters of the AAR model, ε^∞ , τ_c and τ_l such that the resulting crest displacements from the finite element analysis best matches the recorded displacements of the same location on the dam. The comparison of measured displacements at a specific point at crest with the computed ones is shown in figure 3.

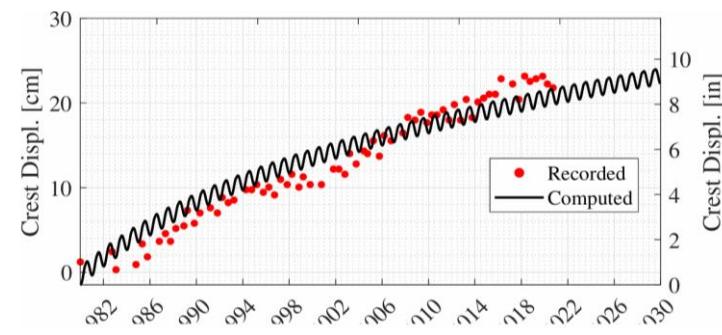


Figure 3 Matching displacements from Parameter Identification

Figure 4 shows the finite element mesh used for AAR and seismic analyses. This mesh includes vertical and peripheral joints surrounding the dam as well as the rock foundation to consider the effect of dynamic soil structure interaction (SSI). To include the effect of SSI, the Miura-Saouma (Saouma et al., 2011) model is used which involves considering the effect of free field motions on the dam-foundation system while having absorbing boundaries. As shown in the top left figure, varying material groups are considered through the dam body. The Elastic modulus is considered to be the highest at the lower portion of the dam, about 30 GPa at the base of the dam, and then it decreases with height to about 16 GPa at the crest.

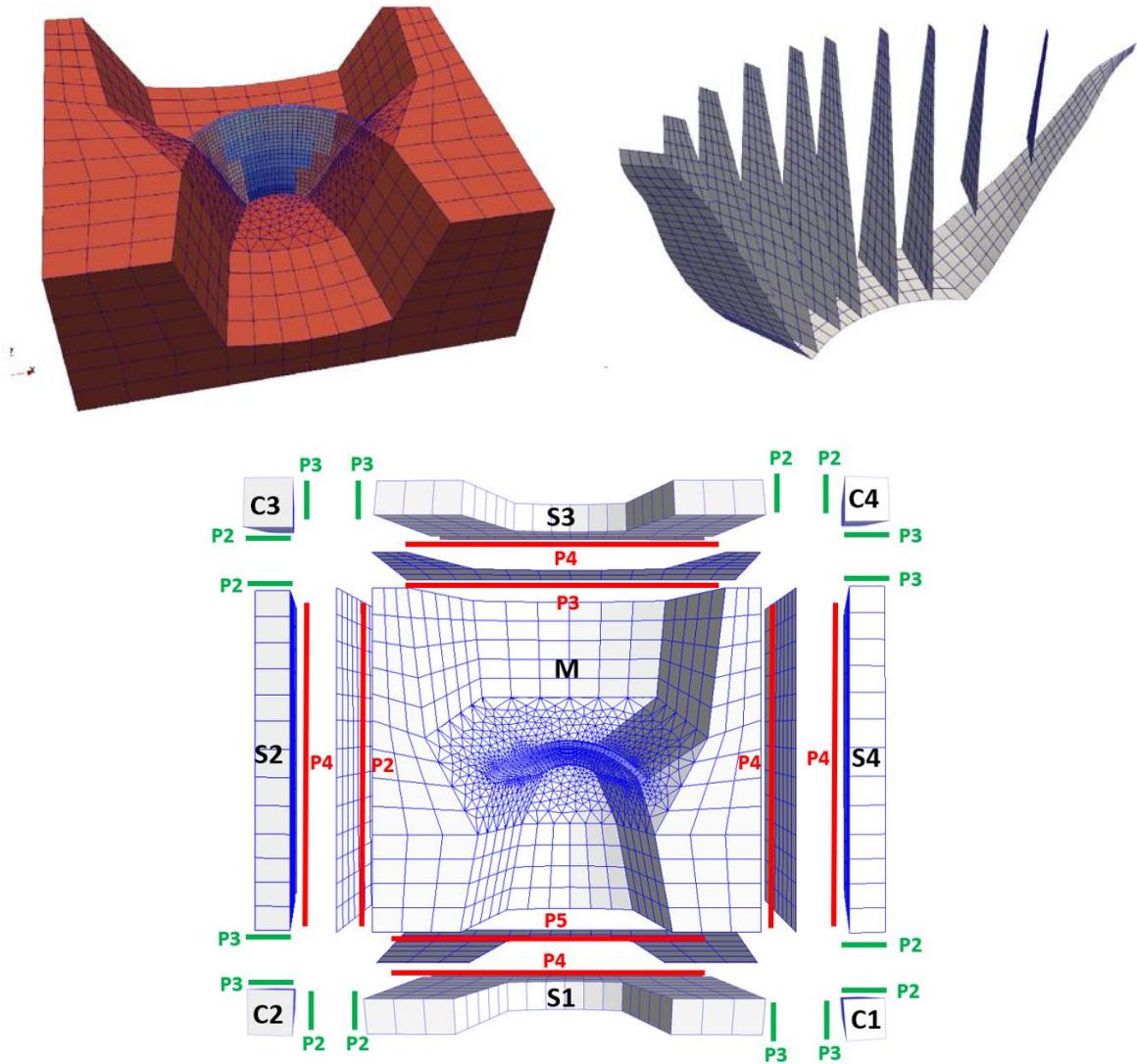


Figure 4 Top: Finite element model of case study dam, Bottom: Dynamic analysis mesh along with Free field meshes.

5. Intensifying Artificial Acceleration

To perform the dynamic analysis an Intensifying artificial acceleration (IAA) is selected. IAA is an artificially designed sequence of acceleration data, where one or more of its intensity measures (IMs), such as response spectra, follow a predefined time-dependent pattern (Estekanchi et al., 2020, Hariri and Sattar, 2023). In its most general form, an IAA can be represented as follows:

$$F_{IAA}(\ddot{u}_g) = \sum_{i=1}^n \left(\int_{\mu=1}^{\mu_{max}} \int_{T=0}^{T_{max}} \int_{t=0}^{t_{max}} \gamma_i [\Gamma_i(t, T, \mu) - \Gamma_i^*(t, T, \mu)]^{\beta_i} dt dT d\mu \right) \quad (5)$$

where \ddot{u}_g is the acceleration time series of the IAA, $\Gamma_i(t, T, \mu)$ is a desired intensity measure parameter to be used to optimize the IAA, and it can be a function of time, t , period, T , ductility ratio μ , or any other variable. Also $\Gamma_i^*(t, T, \mu)$ is the target function to be achieved through this process. γ_i is the weighting scale factor (i.e., optimization coefficient) that denotes the contribution of each term in the overall optimization process. β_i is the

power coefficient that typically takes values of one or two, depending on the objective function. Finally, n is the total number of IM parameters to be included in the optimization process.

The application of IAA in dynamic analysis of concrete dams has been already investigated in several publications such as Alegre et al., 2022, and has been used as part of ICOLD benchmark workshop in 2019 (Salamon et al., 2021, Hariri-Ardebili, 2024).

Figure 5 shows the intensifying acceleration applied to the structure in the stream direction to perform the dam seismic analysis. As shown in this figure the peak ground acceleration in this excitation increases from zero to around 0.76g within the duration of 20 seconds of analysis.

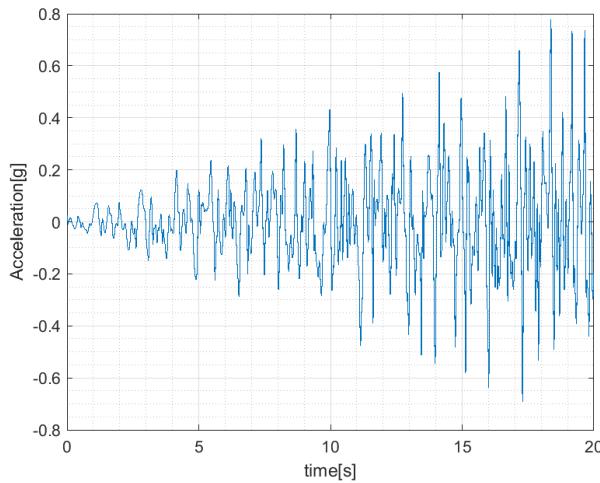


Figure 5 Intensifying Artificial Acceleration applied to the dam.

6. Results and Discussion

In this section the results of the seismic analyses for the two cases are compared in terms of displacements. The dam drift ratio is shown in figure 6 which is computed by dividing the difference of the top and bottom displacement at the crown cantilever by dam height. As seen, the drift ratio of the AAR affected dam starts at an offset of about 0.32% suggesting a critical initial state.

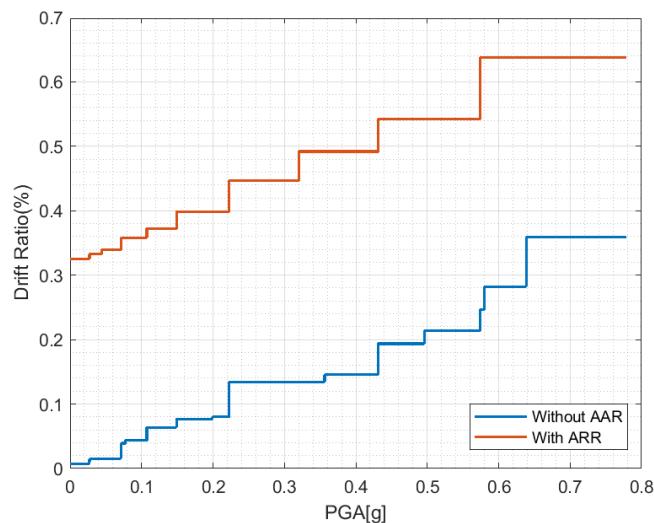


Figure 6 Dam Drift Ratio at different intensity levels

Figure 7 compares the crest displacements in the stream and vertical directions at a certain location on the crown cantilever. On the two left figures the displacements are shown with respect to time demonstrating an increasing trend as expected from the applied excitation. As seen the AAR affected system starts with an initial displacement of about 24 cm and thus continues to develop higher displacements over time compared to the sound system. In this figure the maximum absolute displacements occur in the positive direction which is towards the dam upstream. On the right side of figure 7, the maximum absolute displacements are plotted against the peak ground acceleration determined from the IAA. This figure shows the amount of crest displacements in the stream and vertical direction at each specific PGA.

As mentioned earlier, AAR causes the expansion of the concrete and thus results in additional initial displacements of the crest at the beginning of the dynamic analysis. In order to be able to judge the results based on only the dynamic analysis, and for the comparison purposes, the dynamic only displacements are plotted in figure 8 by removing the effect of AAR displacements from the total displacements that the dam is experiencing. It is worth mentioning that we are undertaking additional studies before we can opine on the "safety" of the dam.

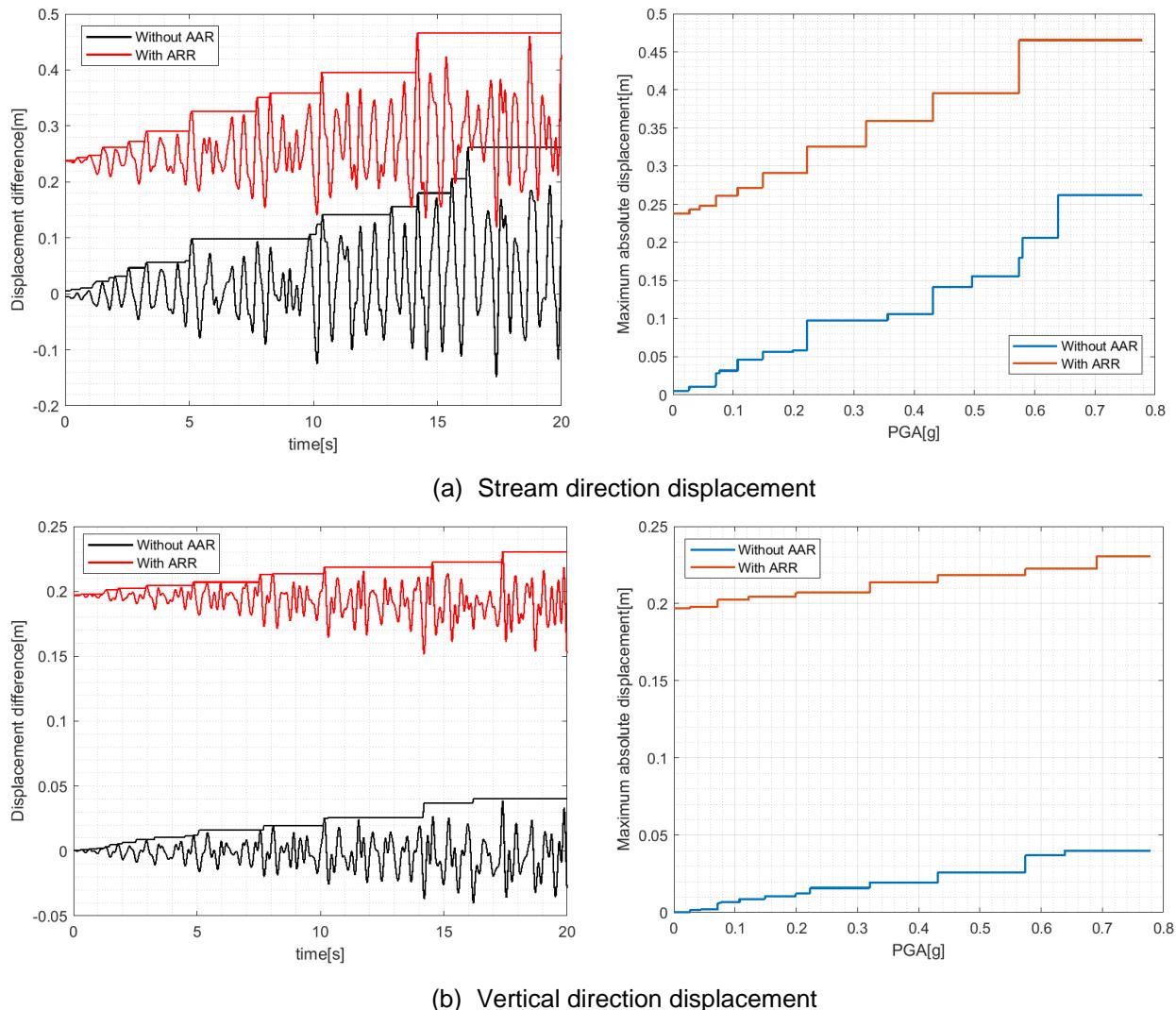


Figure 7 Comparison of Displacements for the two with and without AAR analyses

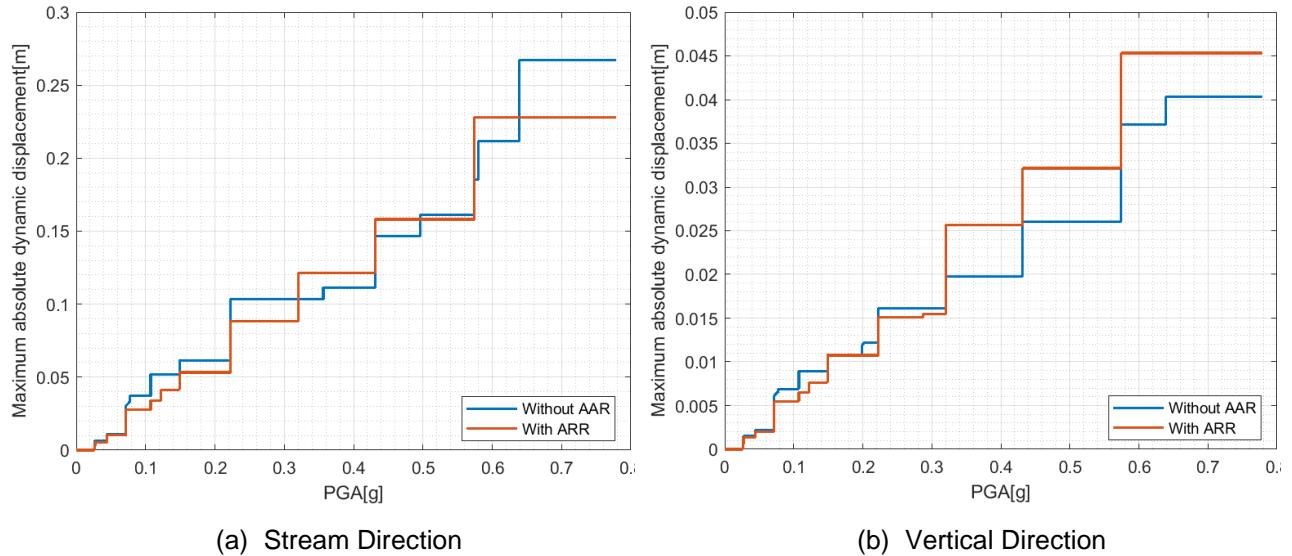


Figure 8 Maximum absolute horizontal and vertical displacements of dynamic response. note: The non-dynamic displacements are removed from both curves.

7. Conclusion

In this paper the effect of AAR on the seismic response of a concrete dam has been investigated. A macro level AAR model along with a parameter identification has been used to translate this chemical reaction into the finite element framework. The response of the AAR affected dam under intensifying artificial accelerations has been contrasted with its sound counterpart.

Looking at the maximum absolute displacement plots versus PGAs, it is shown that the AAR affected dam experiences an initial horizontal crest displacement due to the expansion prior to any seismic excitation. On the other hand, the sound dam is only likely to experience this level of displacements under a ground motion with a PGA of around 0.65g. In addition, under the PGA of 0.8g, the displacement of the sound dam reaches 60% of that of the AAR affected dam. These comparisons highlight the detrimental effect of AAR on the response of the dam.

8. Acknowledgements

The authors would like to acknowledge the financial support of the Bureau of Reclamation Assistance Agreement No. R18AC00055 for partially supporting this research.

The views and opinions expressed in this publication are solely those of the authors and do not necessarily reflect those of any other entity.

9. References

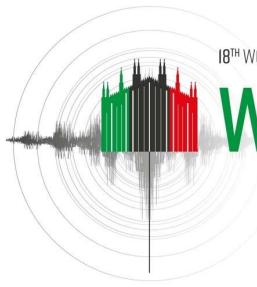
- Alegre, A., Oliveira, S., Mendes, P., Proen  a, J., Ramos, R., & Carvalho, E. (2022). Seismic Safety Assessment of Arch Dams Using an ETA-Based Method with Control of Tensile and Compressive Damage. *Water*, 14(23), 3835.

Ben Ftima, M., Bernard, P., Ch  ruel, A., & Argouges, M. (2023). Concrete Hydraulic Structures Affected by Alkali–Aggregate Reaction: Numerical and Experimental Investigations. *Journal of Performance of Constructed Facilities*, 37(6), 04023059.

Esposito, R. 2016. Vol. 1 of The deterioration impact of alkali-silica reaction on concrete. Parma, Italy: Ipskamp Drukkers

Estekanchi, H. E., Mashayekhi, M., Vafai, H., Ahmadi, G., Mirfarhadi, S. A., & Harati, M. (2020, October). A state-of-knowledge review on the Endurance Time Method. In *Structures* (Vol. 27, pp. 2288-2299). Elsevier.

- Fournier, B., & Bérubé, M. A. (2000). Alkali-aggregate reaction in concrete: a review of basic concepts and engineering implications. *Canadian Journal of Civil Engineering*, 27(2), 167-191.
- Gillott, J. E. (1975). Alkali-aggregate reactions in concrete. *Engineering Geology*, 9(4), 303-326.
- Gorga, R. V., Sanchez, L. F. M., & Martín-Pérez, B. (2018). FE approach to perform the condition assessment of a concrete overpass damaged by ASR after 50 years in service. *Engineering Structures*, 177, 133-146.
- Hariri-Ardebili, M. A. (2024). Quantifying modeling uncertainties in seismic analysis of dams: Insights from an international benchmark study. *Earthquake Engineering & Structural Dynamics*.
- Hariri-Ardebili, M. A., & Sattar, S. (2023). Uncertainty and bias in fragility estimates by intensifying artificial accelerations. *Probabilistic Engineering Mechanics*, 103545.
- Mahdavi, G. (2023). Probabilistic Nonlinear seismic analysis of AAR-Affected dams (Doctoral dissertation, University of Colorado Boulder).
- Merlin (2021). Finite element package for aging and shaking analysis of infrastructures. University of Colorado Boulder.
- Pan, J., Xu, Y., Jin, F., & Zhang, C. (2014). A unified approach for long-term behavior and seismic response of AAR-affected concrete dams. *Soil Dynamics and Earthquake Engineering*, 63, 193-202.
- Pourbehi, M. S., & van Zijl, G. P. (2019). Analysis of combined action of seismic loads and alkali-silica reaction in concrete dams considering the key chemical-physical-mechanical factors and fluid-structure interaction. *Engineering Structures*, 195, 263-273.
- Salamon, J. W., Wood, C., Hariri-Ardebili, M. A., Malm, R., & Faggiani, G. (2021). Seismic analysis of pine flat concrete dam: formulation and synthesis of results. In *Numerical Analysis of Dams: Proceedings of the 15th ICOLD International Benchmark Workshop 15* (pp. 3-97). Springer International Publishing.
- Saouma, V.E. and Hariri-Ardebili, M.A., (2021). Aging, Shaking, and Cracking of Infrastructures: From Mechanics to Concrete Dams and Nuclear Structures. Springer Nature.
- Saouma, V., Miura, F., Lebon, G., & Yagome, Y. (2011). A simplified 3D model for soil-structure interaction with radiation damping and free field input. *Bulletin of earthquake engineering*, 9, 1387-1402.
- Saouma, V. and Perotti, L., 2006. Constitutive model for alkali-aggregate reactions. *ACI materials journal*, 103(3), p.194.
- Zhai, Y., Zhang, L., Bi, Z., Zhang, H., & Cui, B. (2022). Seismic performance evaluation of AAR-affected concrete gravity dams under main aftershock sequence. *Soil Dynamics and Earthquake Engineering*, 157, 107258.



BEM-FEM SOLUTION OF ARCH DAM – FLUID INTERACTION USING ADAD-IZIIS SOFTWARE

V. Mircevska¹ & A. Nanevska²

¹ Institute of Earthquake Engineering and Engineering Seismology, University of "Ss. Cyril and Methodius", Todor Aleksandrov Str., 165, P.O. Box 101, 1000 Skopje, R.N. MACEDONIA e-mail: violeta@iziis.ukim.edu.mk (corresponding author)

² Institute of Earthquake Engineering and Engineering Seismology, University of "Ss. Cyril and Methodius", Todor Aleksandrov Str., 165, P.O. Box 101, 1000 Skopje, R.N. MACEDONIA e-mails: nanevska@iziis.ukim.edu.mk

Abstract: During an earthquake, the vibration energy is transferred by dam and the reservoir to the fluid. It is a function of the intensity and direction of the seismic excitation, dam and reservoir geometry, dam deformability, water level, compressibility and viscosity, energy absorption by deposits, and radiational damping. Various time domain direct-coupling algorithms and iterative-coupling algorithms integrate the advantages of both BEM and FEM techniques to simulate fluid-structure interaction effects. Both types of algorithms, however, show certain difficulties especially when solving more complex coupled BEM-FEM models. The direct-coupling techniques are affected by instability of the solution, whereas the iterative-coupling methods are based on time consuming iterations and often exhibit instability caused by equilibrium failure at the interface. To rapidly attain a stable solution, especially considering the complex influence of the combined vibration of the dam and the irregular terrain, an original method is developed applying a FEM-BEM fluid-structure interaction solution based on independent analysis of the two physically different domains. It is based on the determination of the matrix of hydrodynamic influence (HDI) that enables definition of the vector of hydrodynamic forces (HDF), (ADAD-IZIIS software).

Considered was a double-curved arch dam, 405 m long and 130 m high. In the simulations, the material behaviour is in the linear domain and the rock foundation was assumed as perfectly rigid. The dam-fluid-reservoir system was subjected to the well-known El Centro record of the 1940 Imperial Valley earthquake, measured at rock outcrop. Observational nodes at the centroids of the boundary elements providing insight into the hydrodynamic effects, whereas the dynamic response of the dam is displayed at the finite element interface nodes.

The presented analyses contribute to the improved understanding of the influence of the direction of the seismic excitation on arch dam-reservoir system considering the reservoir with regular and complex configuration. Compared to a reservoir with regular geometry, the vibration of the arch dam and the canyon walls with complex geometry generates different wave fields of compressive and dilatational waves. This results in modification of the distribution pattern of the hydrodynamic pressures and to considerably higher magnitudes.

1 Introduction

Various time domain direct-coupling algorithms, Yu et al. (2001), Czygan and von Estorff (2002) and iterative-coupling algorithms, Mansur (1983), Lin et al. (1996), Feng and Owen (1996), Kamiya et al. (1996), von Estorff and Hagen (2006), Soares et al. (2005) integrate the advantages of both BEM and FEM techniques to simulate fluid-structure interaction effects. Both types of algorithms, however, show certain difficulties especially when solving more complex coupled BEM-FEM models. The direct-coupling techniques are affected by instability of the solution, whereas the iterative-coupling methods usually involve time consuming iterations and often exhibit instability due to lack of equilibrium at the interface. To achieve stable and effective solution, especially when taking into account the complex influence of the combined vibration of the dam and the irregular terrain, a genuine method is developed. This is done with applying a FEM–BEM fluid–structure interaction solution based on independent analysis of the two physically different domains. Defined is the matrix of hydrodynamic influence (HDI) that enables definition of the vector of hydrodynamic forces (HDF), ADAD–IZIIS (2008). The interaction effect at the dam-fluid interface is enforced by adding the vector of hydrodynamic forces to the vector of inertial forces within the standard equation of dynamic motion of the FEM solid sub-domain, Equation 1. The incremental form of the general differential equation of motion of the system subjected to a dynamic action including effects of arch dam-fluid interaction is given as follows,

$$[M]\Delta\ddot{U}(t) + [C]\Delta\dot{U}(t) + [K]\Delta U(t) = -[M][R]\Delta a_g(t) + \Delta HDF(t) \quad (1)$$

2 Numerical model for analyses

The considered double-curved arch dam is 405 m long and 130 m high and is composed of 27 monolith blocks. The thickness of the crown cantilever is 26 m at the base and decreases gradually to 7.6 m at the crest. The material properties considered in the analyses were: Young's modulus $E=31.5$ GPa, mass density of concrete $\rho=2450$ kg/m³, Poisson's ratio $\nu=0.2$, mass density of water $\rho=1000$ kg/m³, and acoustic wave velocity in water $c=1440$ m/s. The water depth vs. dam height ratio is 0.77. In the simulations, the material behaviour is in the linear domain and the rock foundation was assumed as perfectly rigid. The dam-fluid-reservoir system was subjected to the well-known El Centro record of the 1940 Imperial Valley earthquake, measured at rock outcrop. Observational nodes at the centroids of the boundary elements (C1, D1, E, F and G) provide insight into the hydrodynamic effects exerted over the interface, whereas the dynamic response of the dam is displayed at the finite element nodes (A, B, C, and D), Fig. 1.

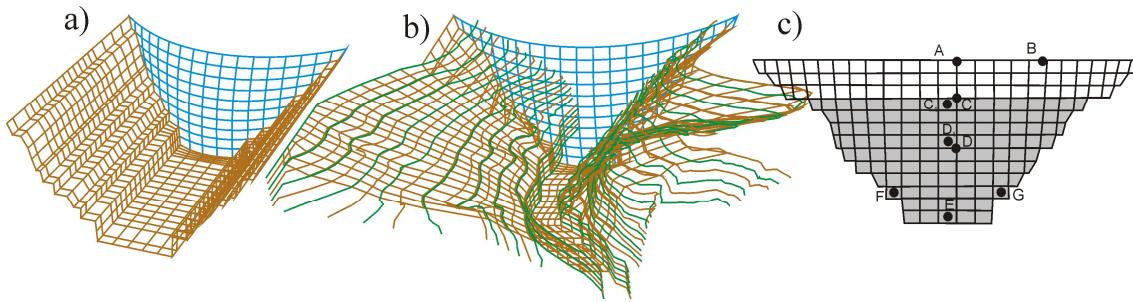


Figure 1. BEM discretization of the fluid-dam-foundation rock system for a) regular terrain, and b) complex terrain c) Location of the observational nodes.

2.1 Seismic excitation in the stream-wise direction

Time histories of relative displacement, velocity, and acceleration for node B (dam crest), where the highest dynamic response occurs, are given in Fig. 2. The response acceleration is undoubtedly the most relevant dam response parameter for quantifying the interaction effects. Namely, the dam and the fluid are dynamically interacting during the seismic action in a way that the dam acceleration exerted along the normal at the any point generates the energy of compressive or dilatational waves, which in return modify the dam acceleration response. In order to depict the influence of terrain irregularities on evaluation of the dynamic response along the crown cantilever, time histories of relative accelerations are presented for nodes A, C and D, Fig. 3.

As expected, it can be observed in Figs. 2 and 3 that, when comparing to results of the full and empty reservoirs, the dam response is strongly affected by the dam-fluid interaction. The ratio between the water

depth and dam height of 0.77 is sufficiently high to contribute to the development of considerable hydrodynamic forces. What is more important, these figures emphasize the influence of the considered direction of excitation and the terrain irregularities. A simple quantitative comparison made by means of the ratio between the observed maximal responses reveals that due to the effect of reservoir irregularities, the maximal relative displacement, velocity, and acceleration responses at the dam crest (node B) increase for 10%, 17% and 4%, respectively, Fig. 2. Likewise, the maximal relative acceleration responses increase for 4%, 4%, 14% and 49% with the increase of the depth of the water for nodes A, B, C and D, respectively, Fig. 3. Fig. 4 presents the developed hydrodynamic pressures at the centroids of the selected boundary elements (observational points C1, D1, E, F and G). The corresponding hydrostatic pressure HSP is also given. The influence of the reservoir irregularities is again quantified with the ratio between the maximal responses generated by reservoirs with complex and regular geometry respectively. Thus, the response is increased from 17% at the water mirror (centroid C1) to 170% close to the right canyon wall (centroid G). The relatively narrow canyon and twisted terrain topology particularly in the lower right corner part of the reservoir contribute to correspondingly stronger hydrodynamic shaking effects at the bottom of the dam. At dam height of 25 m close to the right canyon wall (centroid G), the angle between the dam and the terrain is acute and contributes to more than a two-fold increase of the magnitude of the maximal hydrodynamic pressure. At the same height on the opposite side of the dam, close to the left canyon wall (centroid F), the terrain is considerably smoother, which is translated in moderate amplification of the maximal hydrodynamic pressure of 19% in case of complex reservoir.

For the regular reservoir, simultaneously occurring pressures of the same order of magnitude are generated at centroids F and G (Figs. 4d and 4e). In the case of complex reservoir, however, the hydrodynamic pressures at these centroids differ considerably in magnitude and in phase (Figs. 4d and 4e). This is a result of the increased influence of the complex terrain, which is more emphasized at locations where canyon walls are configured in a way that the normal of the boundary elements points toward the dam and the generated compressive or dilatational waves act directly on the dam-fluid interface. The positive hydrodynamic pressure caused by the action of the dilatational waves, move away from the interface, and cancel the action of the hydrostatic pressure. In extreme case, the positive hydrodynamic pressure could become higher than the hydrostatic pressure, which may eventually cause erosion of the dam wall (cavitation effect). In the presented analyses, positive hydrodynamic pressure higher than the hydrostatic pressure was observed in Fig. 4a, where the generated wavefield by the irregular terrain gives cumulative effect of suction with small magnitude.

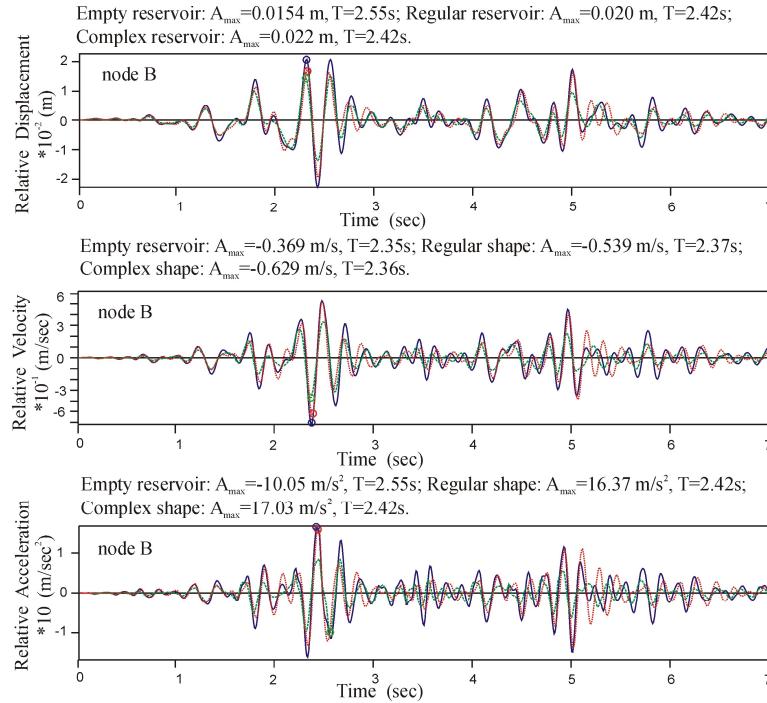


Figure 2. Dynamic response for seismic excitation in the stream-wise direction. Dashed line indicates response of empty reservoir, dotted line indicates response of reservoir with regular geometry, and solid line shows response of reservoir with complex geometry.

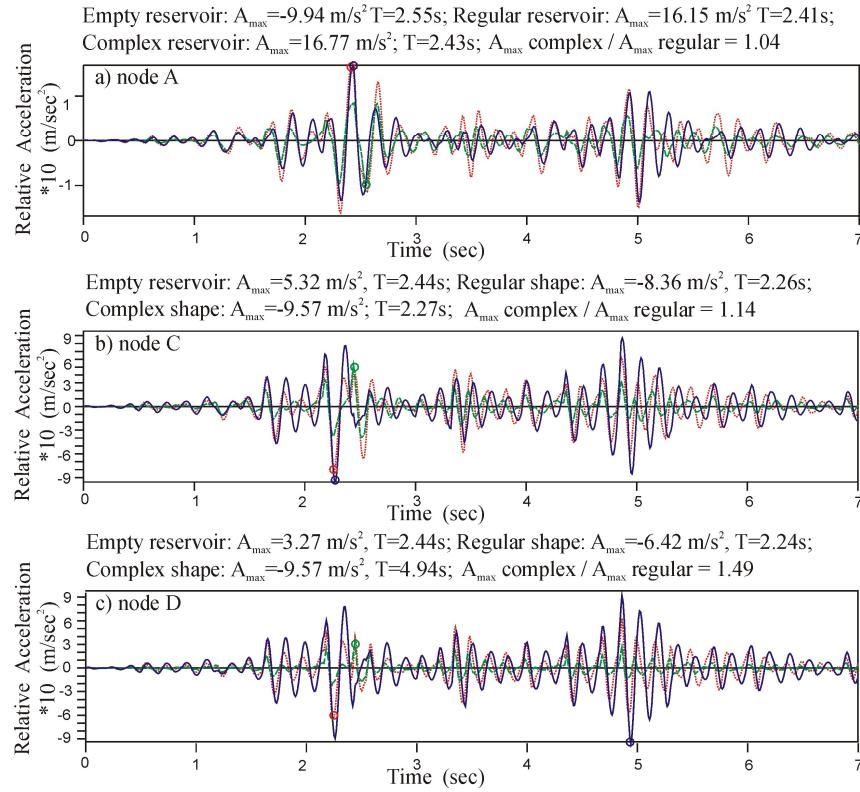
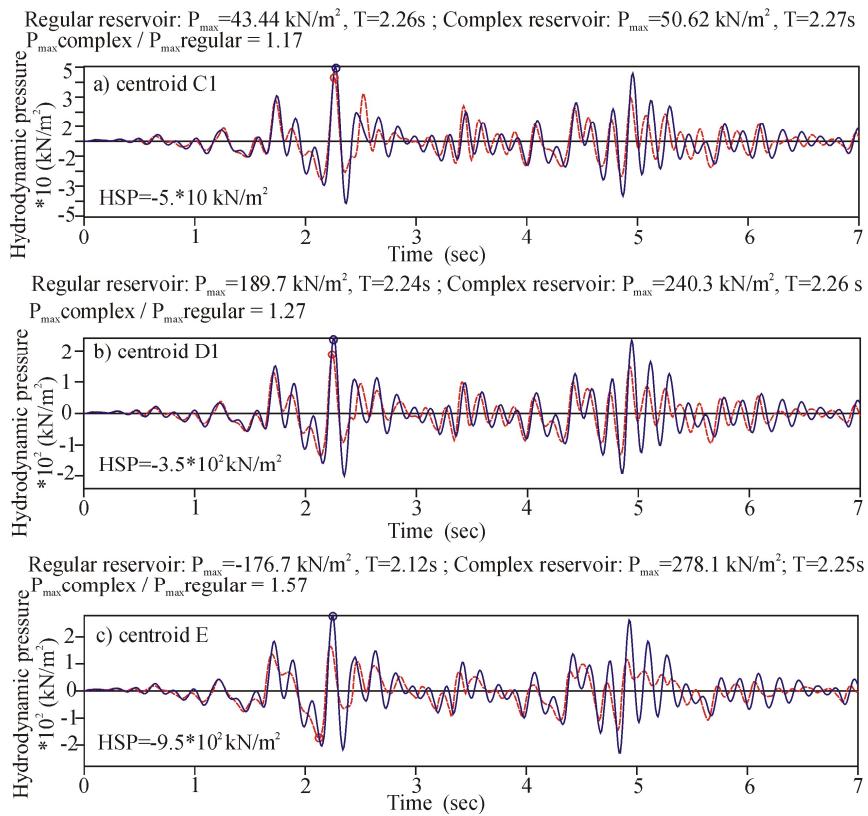


Figure 3. Relative acceleration response for seismic excitation in the stream-wise direction. Dashed line indicates response of empty reservoir, dotted line indicates response of full reservoir with regular geometry, and solid line shows response of full reservoir with complex geometry.



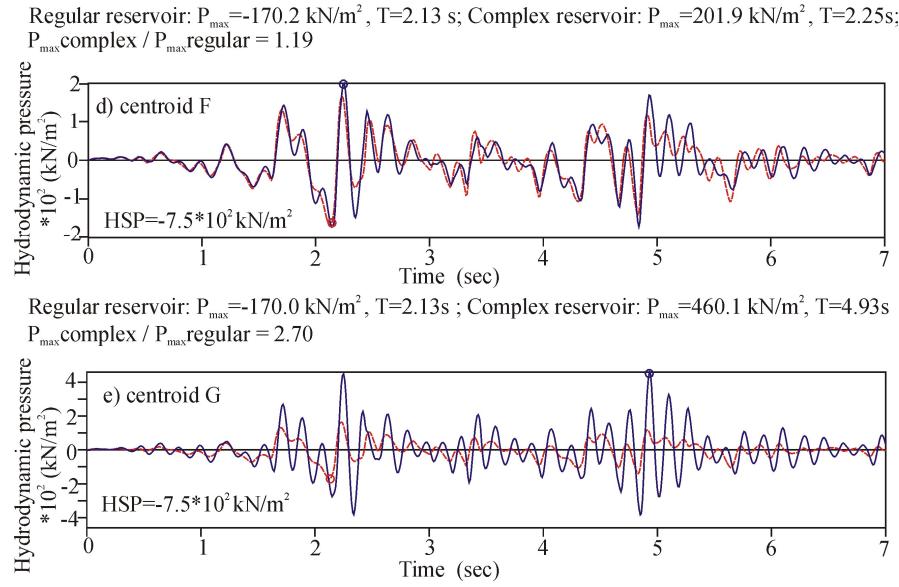


Figure 4. Hydrodynamic pressures under seismic excitation in the stream-wise direction. Dashed line indicates response of reservoir with regular geometry, and solid line indicates response of reservoir with complex geometry. The value of the hydrostatic pressure HSP is given at the respective centroid.

2.2 Seismic excitation in the cross-stream direction

Due to the cross-stream excitation, the dam exerts a buckling type of deformation with a deflection point somewhere along the central vertical axis of the dam. Therefore, in this zone are observed relatively low absolute accelerations, in particular, in the lower part of the dam. The geometric symmetry of the regular reservoir combined with the symmetric shape of the dam do not allow any significant hydrodynamic action to be exerted in the lower part of the dam, centroids D1 and E (Figs. 5b and 5c). In contrast, in the case of irregular reservoir, the analysis shows many-fold amplification of the hydrodynamic pressures in the lower part of the dam. Furthermore, the maximal hydrodynamic pressures at centroids F and G for regular terrain are of the same order of magnitude but in the opposite phase (Figs. 5d and 5e). At the right abutment, centroid G, the maximal hydrodynamic pressure of 63 kN/m² is generated at 2.44 sec, whereas at the left abutment, centroid F, the maximal hydrodynamic pressure is -59 kN/m² also at 2.44 sec. These slightly asymmetrical hydrodynamic pressures are consequence of the horizontal rotation of the dam central axis for 3 degrees with respect to the stream-wise direction decided during the dam design phase. In the case of complex terrain, however, the hydrodynamic pressure is significantly amplified by the vibration of a considerably irregular right wall close to the centroid G with a maximal value of 154 kN/m² observed at 2.21 sec, (Fig. 5e), but for the centroid F, the maximal hydrodynamic pressure is -52 kN/m² and computed at 4.98 sec. (Fig. 5d). The common characteristic of both scenarios is that the pressure waves generated by the left canyon wall are followed by dilatation waves generated by the right wall and vice versa.

2.3 Three-component seismic excitation

In the following example, the effects of the complex reservoir are considered under the same seismic action as in the previous cases but set at 45 degrees with respect to the dam axis. In the simulations, the horizontal component was decomposed into one stream-wise and another cross-stream component. The obtained dynamic responses of the dam (relative displacement, velocity and acceleration; not presented graphically) are considerably lower than that obtained for stream-wise excitation. For example, the maximal relative acceleration measured at node B in the stream-wise direction is 8.3 and 9.8 m/s² for the regular and complex reservoirs, respectively. At the same time, the seismic action in the stream-wise direction yields respective maximal relative accelerations of 16.4 and 17.0 m/s², Fig. 2. This was expected, as in this case the horizontal components of the seismic excitation are about 30% lower (PGA=0.21 g).

In Figs. 6 are shown the time histories of the cumulative (hydrodynamic + hydrostatic) pressures for node D1 and G. At these nodes, the hydrostatic pressure largely dominates the hydrodynamic pressure.

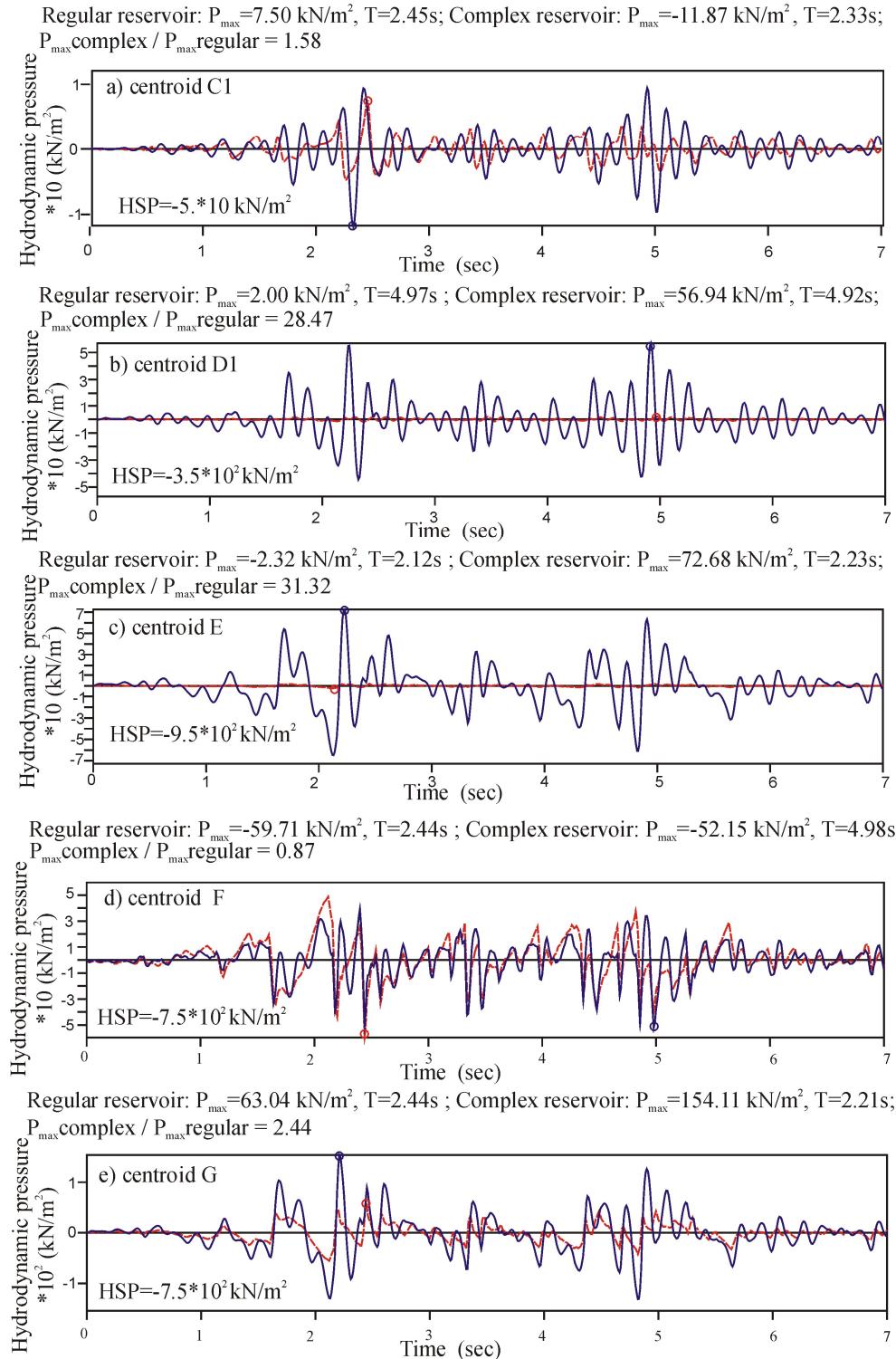


Figure 5. Hydrodynamic pressures under seismic excitation in the cross-stream direction. Dashed line indicates response of reservoir with regular geometry, and solid line indicates response of reservoir with complex geometry.

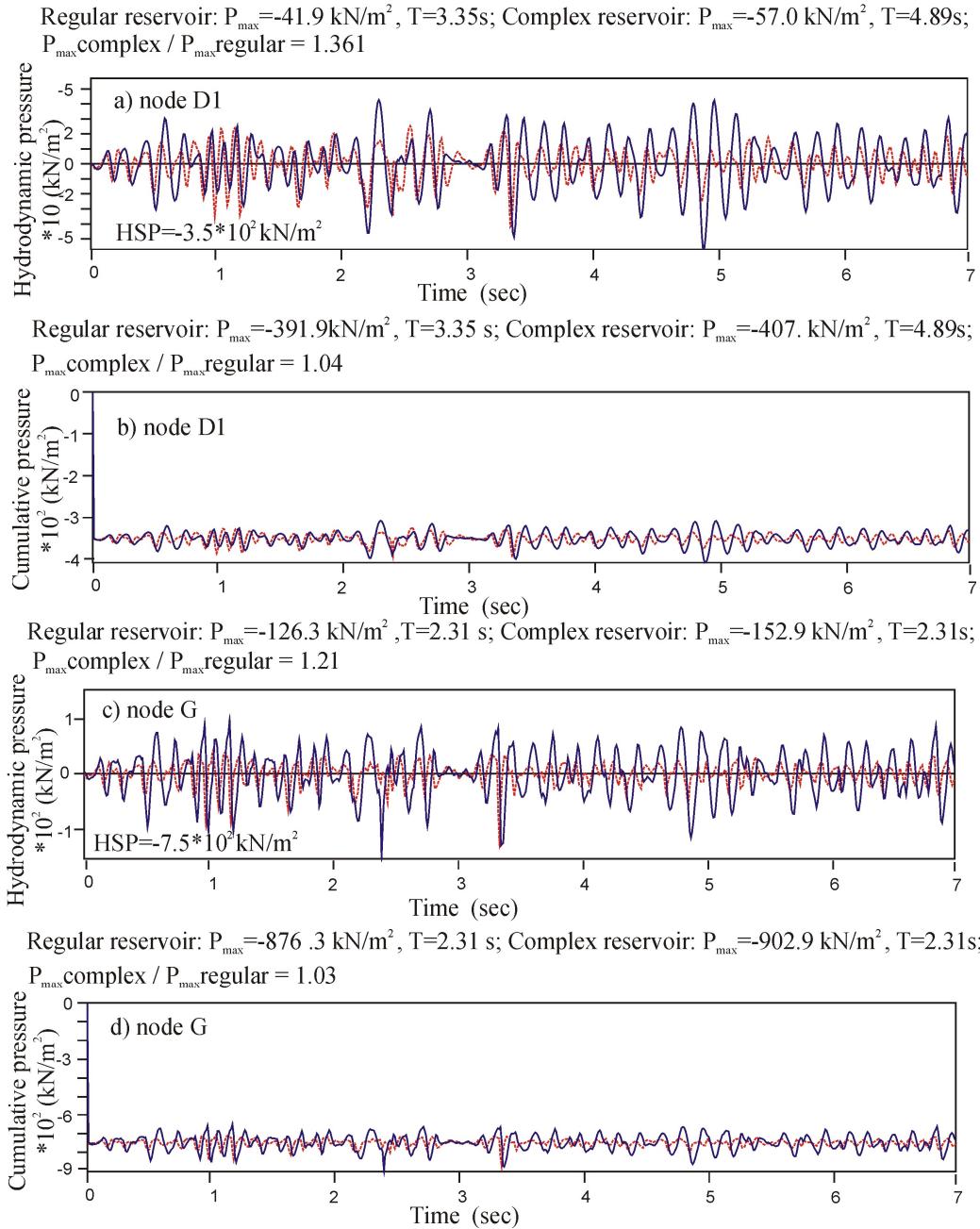


Figure 6. Hydrodynamic pressures under seismic excitation in the cross-stream direction. Dashed line indicates response of reservoir with regular geometry, and solid line indicates response of reservoir with complex geometry.

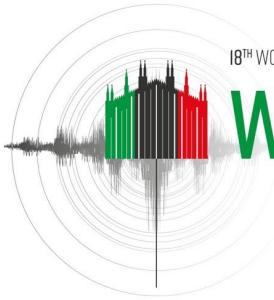
Thus, in the case of regular reservoirs, the ratio between the maximal hydrodynamic pressure and the hydrostatic pressure is 12% and 16.8% for nodes D1 and G respectively. In the case of complex reservoirs, these ratios increase to 16.3% and 20.4%. On the other side, whereas the ratios between the maximal hydrodynamic pressures developed in the complex and regular reservoirs are 36% and 21% for nodes D1 and G respectively, these ratios for the cumulative pressures decrease to only 4% and 3%. In the simulations, the hydrostatic pressure remains constant and contributes to the initial stress conditions in the dam before the seismic excitation actually takes place. During the seismic excitation, however, the hydrodynamic pressure varies considerably in intensity and distribution for both complex and regular reservoirs. It modifies the dynamic response of the dam respectively to the differences in the hydrodynamic loading. Note also that the above ratios depict the differences between the maxima only.

3 Conclusions

The presented analyses contribute to the improved understanding of the influence of the direction of the seismic excitation on the considered arch dam-reservoir system and its dynamic interaction with the water in the reservoir with regular and complex configuration. The analysis was conducted applying the BEM-FEM technique and the matrix of hydrodynamic interference. The considered direction of the seismic excitation was stream-wise, cross-stream and at 45 degrees with respect to the dam axis accompanied with a vertical component scaled at 75% of the horizontal ground motion. Highest hydrodynamic pressures are obtained for a three-component seismic excitation in the stream-wise direction. The vibration of the arch dam and canyon walls with complex geometry generates different wave fields of compressive and dilatational waves when compared to a reservoir with regular geometry. This results in considerably higher magnitudes and modified distribution pattern of the hydrodynamic pressures at the dam-fluid interface. For the stream-wise seismic excitation, the maxima of the response time histories of the hydrodynamic pressures calculated at selected observational points at the dam-fluid interface can be between 20% and 170% higher in the case of irregular reservoir. In the case of seismic force acting in the cross-stream direction, the hydrodynamic effects seem subdued for both reservoir configurations, however, the impact of the terrain irregularities is relatively higher and at selected nodes the maximal hydrodynamic pressure can be amplified for more than 10 times.

4 References

- ADAD-IZIIS (2008) ADAD-IZIIS software. *Analysis and Design of Arch Dams - User's Manual*, Institute of Earthquake Engineering – IZIIS, University of Ss. Cyril and Methodius, Skopje, Macedonia.
- Czygan O., Estorff von O. (2002). Fluid–structure interaction by coupling BEM and nonlinear FEM, *Engineering Analysis with Boundary Elements*, 26: 773–779.
- Estorff von O., Hagen C. (2006) Iterative coupling of FEM and BEM in 3D transient electrodynamics, *Engineering Analysis with Boundary Elements*, 30: 611–622.
- Feng Y. T., Owen D. R. J. (1996) Iterative solution of coupled FE/BE discretization for plate-foundation interaction problems, *Journal for Numerical Methods in Engineering*, 39(11): 1889–901.
- Kamiya N., Iwase H., and Kita E. (1996) Parallel computing for the combination method of BEM and FEM, *Engineering Analysis with Boundary Elements*, 18: 221–229.
- Lin C. C., Lawton E. C., Caliendo J. A., Anderson L. R. (1996) An iterative finite element-boundary element algorithm, *Computers & Structures*, 39(5): 899–909.
- Mansur W. J. (1983) *A time-stepping technique to solve wave propagation problems using the boundary element method*, Ph.D. Thesis, University of Southampton, England.
- Mircevska V., Bickovski V., Aleksov I., and Hristovski V. (2013) Influence of irregular canyon shape on location of truncation surface, *Engineering Analysis with Boundary Elements*, 37: 624–636.
- Soares Jr. D., Carrer J. A. M., and Mansur W. J. (2005) Non-linear elastodynamic analysis by the BEM: an approach based on the iterative coupling of the D-BEM and TD-BEM formulations, *Engineering Analysis with Boundary Elements*, 29: 761–774.
- Yu G., Mansur W. J., Carrer J. A. M., Lie S.T. (2001) A more stable scheme for BEM/FEM coupling applied to two-dimensional elastodynamics, *Computers & Structures*, 79: 811–823.



3D SEISMIC STABILITY ANALYSIS OF A CONCRETE SPILLWAY PIER AFFECTED BY AAR

A. Nour¹ & A. Cherfaoui²

¹ Hydro-Quebec, GISE/BORB, Montreal, QC, Canada, nour.ali@hydroquebec.com

² Hydro-Quebec, GISE/BORB, Montreal, QC, Canada

Abstract: A concrete Hydraulic structure located in north America is severely affected by Alkali-aggregate reaction (AAR). Indeed, AAR in concrete has been found to cause serious concerns for the operation and integrity of this structure. In this paper, a summary of the nonlinear analyses using elaborated finite element model (FEM) is presented. The nonlinear analyses consider the spatial distribution of temperature and relative humidity, slot-cutting (and grouting) modeling, nonlinear AAR kinetics, concrete creep, steel reinforcement and concrete damage. At first, the FEM was calibrated to measured structural and unit parameter data. Subsequently, the calibrated model was used to perform nonlinear AAR stress analyses to predict the future behaviour of this concrete structure. Considering the numerical model results and field observations, major crack patterns were identified. These crack patterns are in favor to form potential failure planes (sliding planes) of concrete blocks. The likelihood of occurrence of these identified sliding planes is discussed, and stability analysis was performed. AAR concrete expansion generates internal forces controlled by displacement. Once a concrete block starts moving through a sliding plane that has formed, these internal forces due to AAR are released. As a result, only loads controlled by external forces were considered in the stability analyses: gravity, water pressure, uplift pressure, ice load and earthquake including Westergaard load. In this context, this paper focuses on the presentation of the 3D seismic stability analysis results of the spillway pier. The nonlinear AAR stress analyses were performed using an inhouse AAR model. In fact, the effects of AAR are introduced in Abaqus Explicit solver by way of the VUEXPAN user subroutine jointly with the concrete damage plasticity (CDP) model of Abaqus. The Abaqus Explicit solver was chosen as it deals effectively with very large FE models simulating highly non-linear deformation due to AAR. The 3D seismic stability analysis of the identified concrete block is performed on a reduced FEM on Abaqus Explicit solver, by using the fully time history procedure based on accelerograms compatible with the Uniform Hazard Spectrum (UHS) of the site of study.

1. Introduction

Structural problems related to alkali–aggregate reaction (AAR) have been identified in concrete structures since the beginning of the 20th century (Stanton, 1940). Since it was known as a nefarious chemical reaction between alkalis in the cement and silica in the aggregates. For real structures, it may take several years (sometime up to 10 years) to show visible signs and it requires high relative humidity in concrete. Due to the complexity of the AAR and its multi-physical nature, the use of chemomechanical modelling is very helpful for making predictions in terms of displacements and concrete damage. Moreover, the macro modelling approaches are still always preferred to perform engineering work for real structures. In this frame, modelling of the nonlinear behavior of concrete is highly recommended for existing damaged and aged structures. Also, the use of elaborated numerical analyses based on the finite element method allow reproducing the present

behavior as well as making future predictions. In the phase of reproducing the present behavior, the calibration process is aimed to match the measured displacements and the observed damage (cracking).

In this context, a concrete Hydraulic structure located in north America is severely affected by Alkali-aggregate reaction (AAR). Indeed, AAR in concrete has been found to cause serious concerns for the operation and integrity of this structure. An overview of the nonlinear analyses using elaborated finite element model (FEM) is presented. The nonlinear analyses consider the spatial distribution of temperature and relative humidity, slot-cutting (and grouting) modeling, nonlinear AAR kinetics, concrete creep, steel reinforcement and concrete damage.

At first, the FEM was calibrated to measured structural and unit parameter data. Subsequently, the calibrated model was used to perform nonlinear AAR stress analyses to predict the future behaviour of this concrete structure. Considering the numerical model results and field observations, major crack patterns were identified. These crack patterns are in favor to form potential failure planes (sliding planes) of concrete blocks. The likelihood of occurrence of these identified sliding planes is discussed, and stability analysis was performed. AAR concrete expansion generates internal forces controlled by displacement. Once a concrete block starts moving through a sliding plane that has formed, these internal forces due to AAR are released. Therefore, the AAR thrust is ignored for the stability analyses (see also Ben Ftima et al. (2017)). As a result, only loads controlled by external forces were considered in the stability analyses: gravity, water pressure, uplift pressure, ice load and earthquake including Westergaard load. However, this paper focuses on the presentation of the 3D seismic stability analysis results of the spillway pier.

The nonlinear AAR stress analyses were performed using an inhouse AAR model. In fact, the effects of AAR are introduced in Abaqus Explicit solver (Hibbit et al., 2019) by way of the VUEXPAN user subroutine jointly with the concrete damage plasticity (CDP) model of Abaqus (Nour and Cherfaoui, 2022). The Abaqus Explicit solver was chosen as it deals effectively with very large FE models simulating highly non-linear deformation due to AAR. The 3D seismic stability analysis of the identified concrete block is performed using the pseudo-dynamic method and validated via a reduced FEM on Abaqus Explicit solver, by using the fully time history procedure based on accelerograms compatible with the Uniform Hazard Spectrum (UHS) of the site of study.

The authors strongly believe the adopted methodology in this paper, namely in managing and reducing the conservatism to a reasonable level, is particularly useful to engineers involved in the analyses of aged and damaged structures affected by AAR.

2. Chemomechanical macro model of AAR for concrete

As suggested by Pan et al. (2013), for the case of hardened concrete, the total strain increment $\Delta\varepsilon_{\text{Tot}}$ is assumed to be the superposition of the increments of the mechanical strain $\Delta\varepsilon_{\text{Mec}}$ (anisotropic), the thermal strain $\Delta\varepsilon_{\text{Th}}$ (isotropic), the creep strain $\Delta\varepsilon_{\text{Cr}}$ (anisotropic) and the AAR strain $\Delta\varepsilon_{\text{AAR}}$ (anisotropic) as follow:

$$\Delta\varepsilon_{\text{Tot}} = \Delta\varepsilon_{\text{Mec}} + \Delta\varepsilon_{\text{Th}} + \Delta\varepsilon_{\text{Cr}} + \Delta\varepsilon_{\text{AAR}} \quad (1)$$

In general, the factors directly affecting the AAR expansion of reinforced concrete structures are (i) the temperature and its variation in hardened concrete. (ii) kinetic of the reaction which depends on the percentage of alkali in the cement, the quantity of the cement used in the preparation of concrete mix and the reactivity level of the aggregate used in concrete mix. (iii) relative humidity and its variation in the hardened concrete. (iv) steel reinforcement in concrete (internal confinement). (v) compressive state of stress in concrete (confinement). (vi) effect of long-term creep of damaged concrete. Therefore, it is of interest to represent these effects in a macro scale model to perform engineering work. According to Leger et al. (1996) and Saouma (2014), the following uncoupled equation is adopted for the calculation of the AAR strain increment according to the principal stress σ_i axis i ($i = 1, 3$) as follow:

$$\Delta\varepsilon_{\text{AAR}}^{i, i=1,3} = \Gamma_t \cdot \Gamma_c \cdot g(H) \cdot W_i \cdot \Delta\xi(t, T) \cdot \varepsilon_V^{\max} \quad (2)$$

$\xi(t, T)$ is a scalar parameter, varying from zero to one, describing the progress of the chemical reaction or the kinetic of reaction function of temperature based on Larrive's (1998) model, and ε_v^{\max} is the maximum volumetric concrete free expansion. Here $g(H)$ is a reduction function that accounts for the effect of the relative humidity, also, Γ_t and Γ_c are the retardation factors of the AAR reaction due to tensile cracks and compressive stresses, respectively. W_i are the weighting factors for the anisotropic redistribution of volumetric AAR expansion depending on the level of the confinement caused by the compressive stresses. Further details are provided by Nour and Cherfaoui (2022) regarding the AAR model, the creep model, and the implementation in Abaqus Explicit solver, as well as validation examples at the material level.

The mechanical strain increment $\Delta\varepsilon_{Mec}$ is calculated using the Concrete Damage Plasticity (CDP) model of Abaqus considering that the mechanical properties will degrade further according to the chemical AAR progress. The Abaqus CDP model is a smeared cracking model, and it is appropriate for quasi-brittle materials subjected to cyclic loads. It uses concepts of isotropic damaged elasticity in combination with isotropic tensile and compressive plasticity to represent the inelastic behaviour of the material, where the two main failure mechanisms are the tensile cracking and the compressive crushing of the material. This model assumes that failure of the material can be effectively modelled using its uniaxial tension, uniaxial compression, and plasticity characteristics. The concrete tension softening is controlled by the fracture energy G_f and the seed size of the mesh h , which guarantee the mesh objectivity an important issue for a smeared cracking model.

Whereas the nonlinear structural analysis is realised using the explicit solver, the heat transfer and relative humidity transport analyses are performed on the implicit solver of Abaqus. According to Equation 1, AAR, creep, and thermal strain increments are calculated, for each increment, using the VUEXPAN.FOR user-subroutine. This subroutine allows imposing an anisotropic strain increment, which is the basis for the calculation of the induced stresses when the CDP model of Abaqus is used to represent the nonlinear behaviour of concrete. Moreover, the VUSDFLD.FOR subroutine is called for each increment to get information regarding the state of stress and to perform the mechanical properties degradation as function of the chemical reaction progress through internal Abaqus fields. Note that the exchange between the subroutines VUEXPAN and VUSDFLD is realised via the state variables (SDV).

3. Overview of nonlinear AAR analyses

3.1 Overview of the finite element model

The global finite element model (FEM) is presented by Figure 1, along with the adopted hexa-dominant mesh, where 1 m size seed is used for concrete. Here, the nonlinear analyses consider the spatial distribution of temperature and relative humidity, the slot-cutting (and grouting) modeling, nonlinear AAR kinetics progress function of temperature, concrete creep, steel reinforcement plastic behaviour, mechanical properties degradation due to AAR and concrete damage. The global FEM includes the steel reinforcement and the steel penstocks liners. The steel reinforcement was modelled as a surface element embedded in the concrete mass, whereas the steel penstock liners were modelled as shell elements.

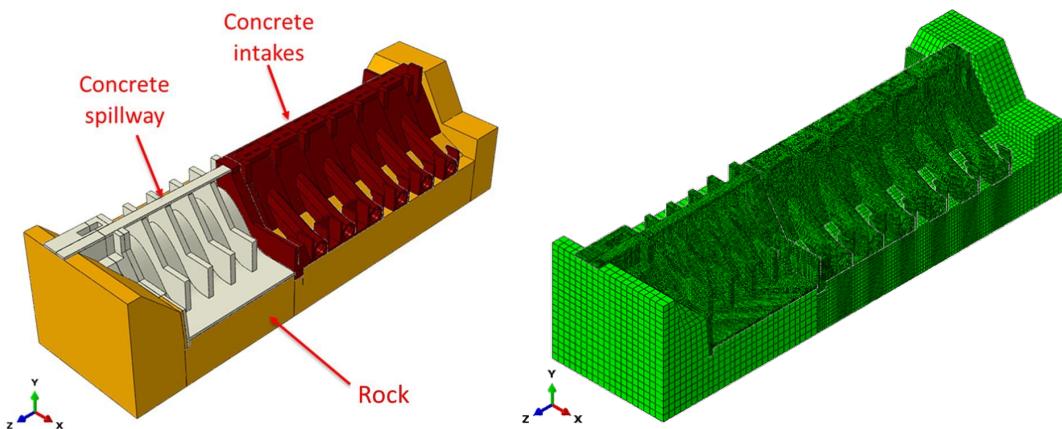


Figure 1. Global FEM.

The default material properties are summarised by Table 1. Sensitivity analyses were performed by varying the tensile strength (and the fracture energy) within plausible ranges to determine the impact on the emergence

of failure mechanisms. Moreover, the prerequisites multi-physical analyses for the nonlinear AAR mechanical analyses, namely the heat transfer analysis (spatial distribution of temperature) and the relative humidity transport analysis (spatial distribution of relative humidity) are also presented by Figure 2 and Figure 3, respectively. It is worthy to mention that the reference temperature is needed for AAR kinetics characterization as the chemical reaction obeys Arrhenius law. Hence, according to Paul and Tarbox (1991) and Leger et al. (1993), it is assumed to be the volume-weighted average temperature.

Table 1. Default material properties.

Concrete		
	Initial, $\xi = 0$	Final, $\xi = 1$
Elastic modulus (GPa)	25.0	15
Compressive strength (MPa)	25	25
Tensile strength (MPa)	2.5	1.5
Fracture Energy (N/m)	275	165
Rock		
Elastic modulus (GPa)	30.0	-
Poisson ratio	0.20	-
Density (kg/m^3)	2600	-

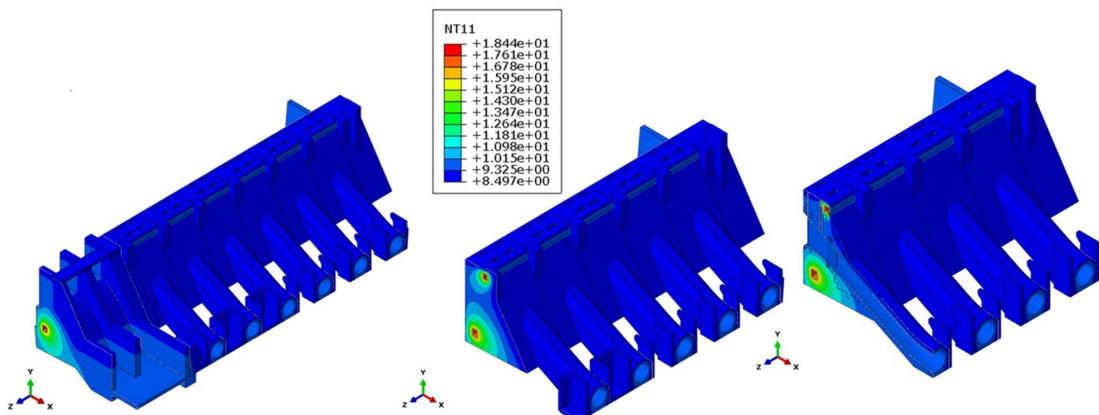


Figure 2. Heat transfer analysis results (NT11 stands for Temperature °C).

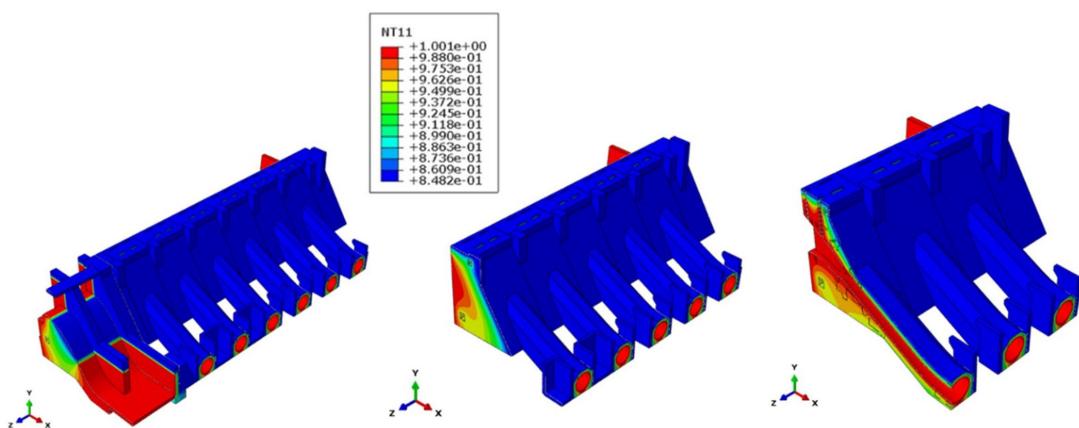


Figure 3. Relative humidity transport analysis results (NT11 stands for Relative Humidity H; $0 \leq H \leq 1$).

3.2 AAR parameters from calibration with measured displacements on concrete structure

Analysis of recorded displacements is a very important step for determining AAR parameters. The above-mentioned FEM was calibrated to a large amount of field measured structural and unit parameter data. The AAR parameters were obtained using the calibration procedure to achieve a satisfactory correlation of recorded displacements and predicted displacements by the numerical model. First, free expansion, latency time and characteristic time were determined by comparing vertical displacements. Next, lower and upper

confinement limits were determined by comparing horizontal displacements at the same time with the vertical displacements. It was an iterative process, until a satisfactory correlation with the selected displacement records was obtained. Table 2 shows the AAR parameters used for the nonlinear structural analyses. Subsequently, the calibrated model was used to perform nonlinear AAR stress analyses to predict the future behavior of the concrete structures.

Table 2. AAR parameters for nonlinear structural analyses

	Free expansion, ϵ_v^{\max}	Latency time, (years)	Characteristic time (years)	Reference temperature (°C)	Lower confinement limit (MPa)	Upper confinement limit (MPa)
Intake structure	0.079	5	105	10.4	-0.5	-6
Spillway	0.071	5	105	10.4	-0.5	-6

It is worthy to mention that providing the full comparison with the measured displacements is beyond the scope of this paper. However, a selection is presented by Figure 4 and Figure 5. Indeed, Figure 4 compares vertical displacement recorded by borehole extensometers in the intake and vertical displacement predicted by the model. The FEM results are in good agreement with the recorded displacements.

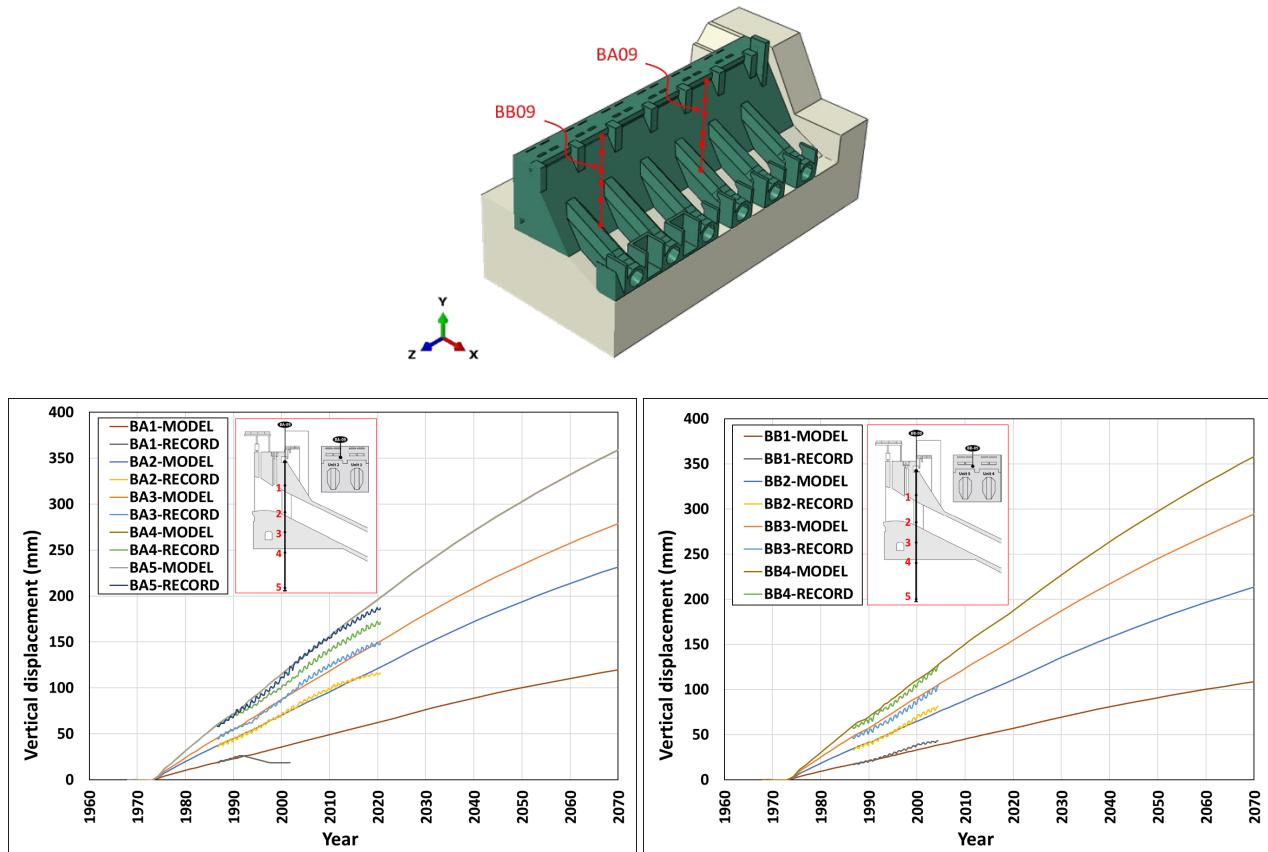


Figure 4. Modelled vs recorded displacement at BA-09 and BB-09 – intake (vertical).

Figure 5 compares modelled horizontal displacement and horizontal displacement recorded at invar extensometers BZ09-1 (unit expansion) and BZ09-2 (slot-cut closure). The correlation between recorded horizontal displacements and those predicted by the numerical model is quite satisfactory. The change in trend

of the predicted displacement observed in Figure 5 is due to the slot-cut injection (mitigation measure) implemented, in the numerical model, in 2020.

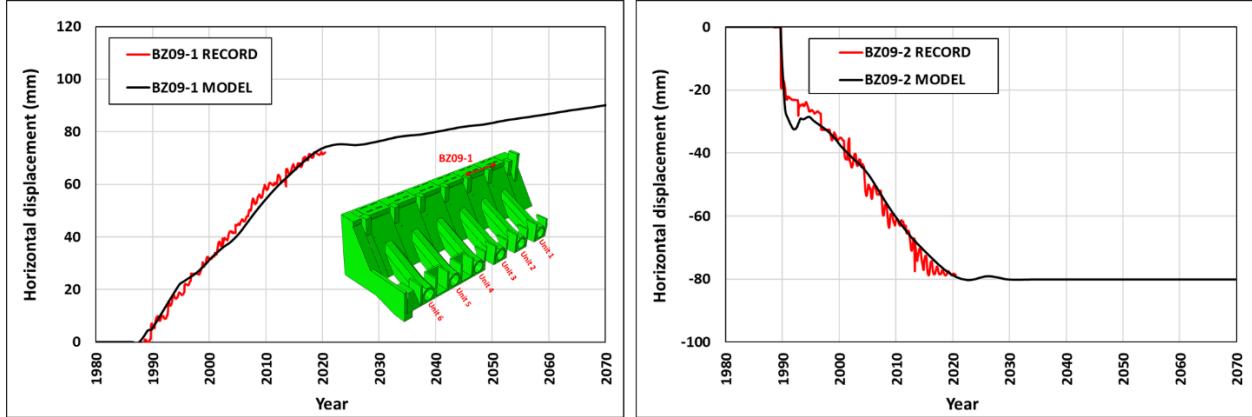


Figure 5. Modelled vs recorded displacement at BZ09-1 and BZ09-2 – intake (Horizontal, cross valley direction).

3.3 Potential sliding plane identification

The calibrated FEM was used to perform nonlinear AAR stress analyses to assess the structural behaviour of this concrete dam. Considering the numerical model results and field observations, major crack patterns were identified. These crack patterns could potentially form failure planes (sliding planes) of concrete blocks.

As mentioned before, sensitivity analyses were performed, by varying the tensile strength (and the fracture energy), to determine the potential structural failure mechanisms. Indeed, the zone highlighted in red in Figure 6-a is a hot spot of interest. In this zone, the spillway pier in contact with the intakes is not restrained according to the cross-valley direction (z-z direction). As illustrated by Figure 6-a, this pier is deforming under the effect of the thrust due to AAR from the intake upper blocks.

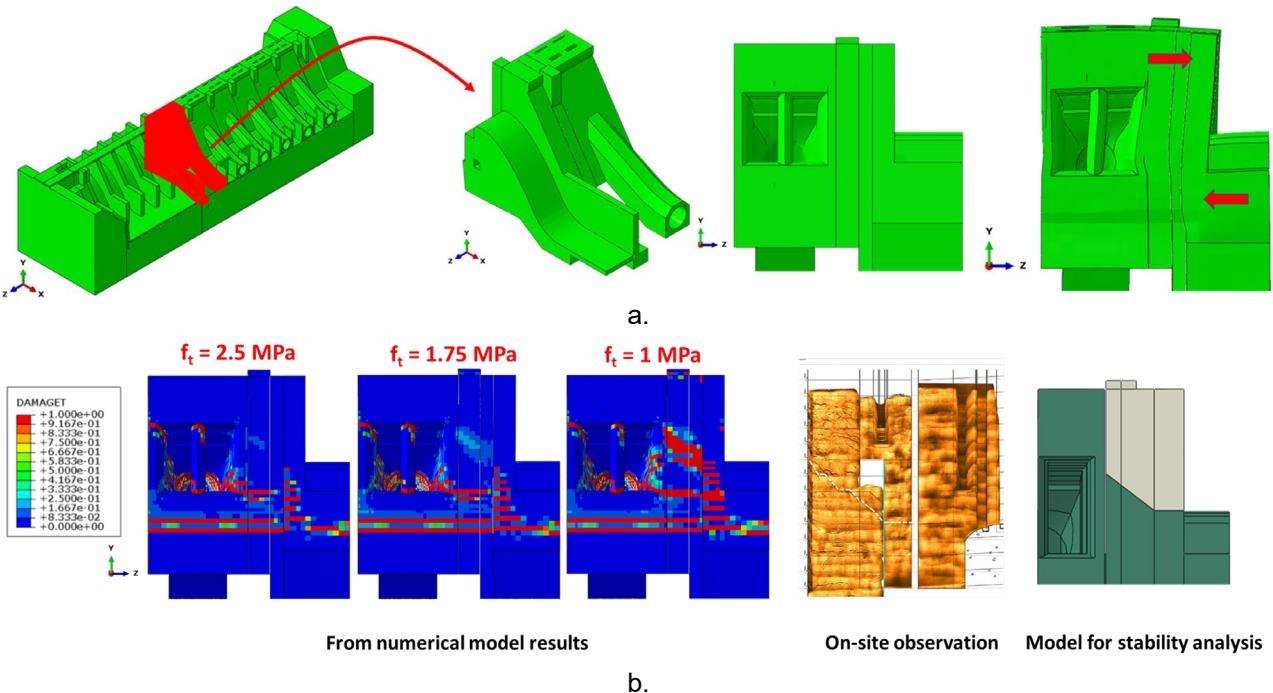


Figure 6. Potential sliding plane identification.

Because of the lift joints, the on-site observed cracks at the upstream face have a stepped shape (see Figure 6-b). However, there are no signs of presence of these cracks on the downstream face. Accordingly, the probability of occurrence of a sliding plane (from upstream to downstream), following the observed cracks pattern, is very low. On the other hand, when the initial tensile strength (f_t for $\xi = 0$) is reduced, the observed on-site cracks at the upstream face are captured by the numerical model. Note that the model does not show a completely cracked plane (from upstream to downstream) that could compromise the integrity or the stability of this zone, but nonetheless, the observed cracks (from on-site observations and the numerical model) are conservatively assumed to form a potential inclined sliding plane as shown by Figure 6-b. The stability of the conservatively assumed sliding concrete block is examined in the next section.

4. 3D seismic stability analysis

This section describes the stability analyses of the spillway pier concrete block according to the previously identified potentially sliding plane. The stability of this concrete block cannot be idealized as two-dimensional (2D) problem, it requires three-dimensional (3D) analysis. Note that the model does not show the identified plane as completely cracked, but it was conservatively assumed to be potential sliding plane. In this context, AAR concrete expansion generates internal forces controlled by displacement. Once a concrete block starts moving through a sliding plane that has formed, these internal forces due to AAR are released. As a result, only loads controlled by external forces were considered in the stability analyses: gravity, water pressure, uplift pressure, ice load and earthquake including Westergaard load.

As the loads combination involving the seismic action is the most critical, the presentation of other loads combination results is beyond the scope of this paper. However, one confirms that the anticipated safety factors of the water intake, under normal operating loads and flood conditions are meeting the CDA 2013 acceptance criteria.

4.1 3D Seismic stability analysis using the pseudo-dynamic method

It is worthy to mention that the first mode affecting the intake structure has a computed (FEM) and measured (from ambient vibration) frequency of ~ 7.5 Hz (period $T_1 = 0.13$ sec). This value indicates that the dam is relatively flexible, and an amplification is expected around that frequency. Also, this frequency is in accordance with the empirical formula $f_1 = 275/H = 6.88$ Hz (Ghrib et al., 1995), where $H = 40$ m (height of the dam). Note that this frequency accounts for reservoir and foundation interaction with the concrete dam. Therefore, the pseudo-static method is not acceptable (see FERC (2016)) for this flexible dam. By using the traditional check of sliding stability, the 3D seismic stability of the identified concrete block is conducted using the pseudo-dynamic method as recommended by ICOLD (2002). Here, the seismic action is defined by the Uniform Hazard Spectrum (UHS) obtained from a site-specific study of the dam (see Figure 7), considering 1/10000 return period ($p = 0.0001$), as recommended by the CDA (2013) for the assessment of strategic structures retaining water.

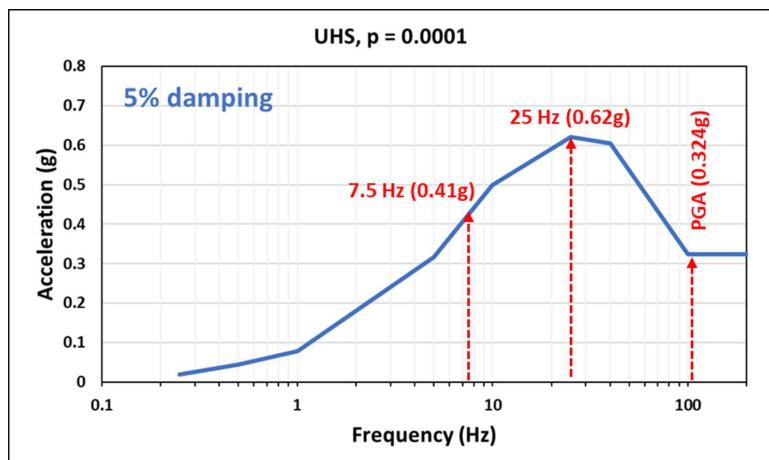


Figure 7. UHS obtained from a site-specific study (1/10000 return period).

For the site of the dam, the maximum acceleration is defined at the frequency of 25 Hz (Figure 7) based on Eastern North America (ENA) seismicity. As this dam is relatively flexible, the scenario for which the seismic action is determined according to the maximum spectral acceleration (at 25 Hz) is judged to be conservative. This conservative scenario was considered for the sensitivity analyses of the stability calculation.

It is well established in literature (EPRI, 1991; ICOLD, 2002; FEMA, 2005; USACE (2005 and 2007)) that the damping should be selected consistent with the expected level of deformation and the extent of nonlinear behaviour. Moreover, a damping value of 5% (without contribution of foundation and reservoir) is representative of concrete material behaviour in the elastic regime. The concrete damping value (without contribution of foundation and reservoir) can be increased to 10% when extensive cracking of the concrete structure is anticipated (valid for concrete structure already deteriorated by AAR), and when severe seismic action (return period = 1/10000 years) is considered. Nonetheless, one adopts a progressive approach where a sustained spectral acceleration (coefficient $\alpha = 0.67$, see Léger P and Javanmardi (2007)) at 5% global damping (including foundation and reservoir) was used, at first step. Thereafter, in perspective to reduce the conservatism, higher global damping values could be considered (7% global damping and higher but not more than 10% as recommended by USACE (2005 and 2007)) in the frame of a sensitivity analyses of the stability calculation. Factor conversion to determine spectral acceleration for other values of damping than 5% is obtained as indicated by Atkinson and Pierre (2004).

In this study, the existing steel reinforcement bars at the zone of interest were included to improve the safety factors for stability analysis. Indeed, tensile forces are known from the finite element analysis. In this case, Canadian concrete standard CSA-A23.3-19 recommends an interaction equation to compute allowable shear strength (see Figure 8). According to CSA-A23, if one assumes the steel will yield (or reach ultimate strength), the residual shear capacity is significantly reduced (only 20% or $0.2 V_f/V_r$ is allowed according to clause D 8.2 of CSA-A23.3). Here, V_f stands for shear demand and V_r for shear capacity. Due to AAR, as for shear friction, the vertical component of the tensile stress in the bar will induce an equal and opposite compressive normal stress (post-tension force) on the sliding plane, which will increase the shear strength. As explained by the flowchart in Figure 8, the axial force demand N_f in the interaction equation is determined from the FEM model. Allowed shear force is then calculated from the interaction diagram equation.

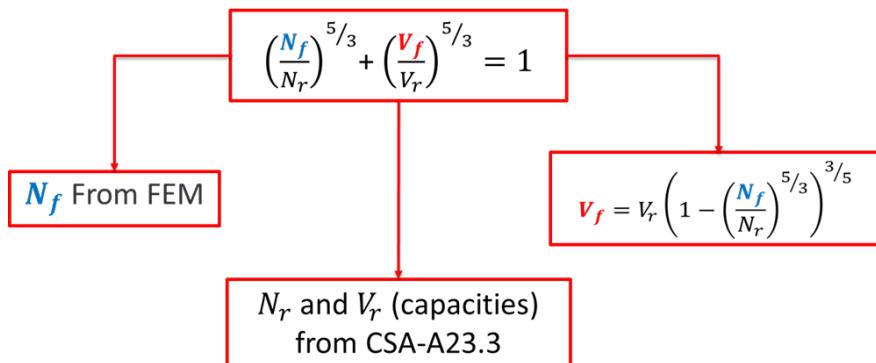


Figure 8. Flowchart for shear and tensile load interaction equation.

Note that the 30% rule of combination of the seismic action is adopted in a 3D context. Obtained results for stability analysis are summarised in Table 3 for 5%, 7% and 10% global damping values (including contribution of foundation and reservoir), and for both cases with and without existing steel reinforcement. Indeed, according to CDA (2013), for loads combination involving the seismic action, safety factor for sliding greater than unity is acceptable. As shown by Table 3, the CDA requirement for sliding is not met only for the conservative case when the contribution of existing steel reinforcement is ignored, with the seismic force obtained from the pseudo-dynamic method based on 25 Hz spectral acceleration (5% global damping). Despite this, the obtained factor of safety (FS) is close to 1 (0.9). For this case, because a 1/10 000-year earthquake is applied, the sliding safety factor could be below 1 for a short amount of time. Considering the high frequency content of the seismic excitation, a safety factor below 1 will typically induce a very small and acceptable residual displacement of the order of a few mm. However, accounting reasonably for the benefit effects of the existing reinforcement and the mobilised global damping allow enhancing the required safety factors as demonstrated by Table 3 (FS > 1). Therefore, the analysed concrete block is stable.

The traditional calculation of sliding stability involves computing a factor of safety against sliding based on a friction model of the interface zone and equivalent loads that represent the dynamic effects of an earthquake on the dam. However, the application of this procedure cannot represent the transient characteristics of the sliding response. Indeed, it is admitted that sliding will not occur when $FS > 1$, and no further analysis is required. However, design or evaluation of structures for zero relative displacement is unrealistic. It is recognized that an acceptably small amount of lateral displacement (even marginal) will likely occur during a major earthquake (USACE, 2005). Accordingly, $FS \approx 1$ could be interpreted as no sliding will occur or the resulting permanent relative displacement at the sliding plane is marginal and cannot compromise the stability of the concrete block. In this way, it is aimed in the next section to explore the transient response of the identified sliding plane, and to validate the obtained stability analysis results (Table 3) using the dynamic time history procedure.

Table 3. Safety factors for sliding from pseudo-dynamic method

Safety factors for sliding (friction angle $\phi = 45^\circ$ ($\tan \phi = 1$), Cohesion $c = 0$))		
Pseudo dynamic based on 25 Hz spectral acceleration		
	Without existing reinforcement	With existing reinforcement
5% global damping	0.9	1.22
7% global damping	1.02	1.35
10% global damping	1.13	1.48

4.2 3D Seismic stability analysis using dynamic time history analysis

In this section, validation of the obtained stability analyses results from the pseudo-dynamic method is realised using the dynamic time history procedure. To do so, a reduced FEM is prepared to perform the seismic analysis in time domain. It is worthy to mention that accounting for aleatory and epistemic uncertainties of the seismic action is beyond the scope of this paper. Therefore, only the TH1 time histories, compatible with the UHS for the site of study, which is selected for the dynamic time history analysis (see Figure 9).

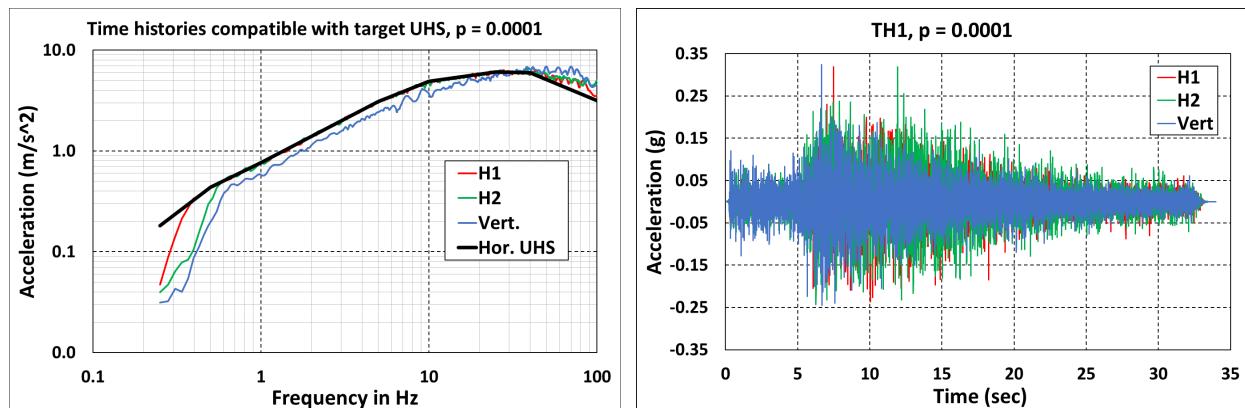


Figure 9. Time histories compatible with target UHS, $p = 0.0001$.

Here, the three components of the TH1 time histories are applied to the foundation FEM boundaries considering a massless representation of the rock foundation (density close to zero when using Abaqus Explicit solver). Therefore, the radiation damping is ignored. As mentioned by Koltuniuk et al. (2013), the seismic ground motions do not vary through the massless foundation mesh and are, consequently, independent of the size of the foundation FEM.

Also, the hydrodynamic effect of the water reservoir is considered as an added mass of water to the structure upstream face (Westergaard force). As water pressure will develop normal dynamic forces, then the added mass is assumed acting in a perpendicular direction (upstream-downstream), and the hydrodynamic force is considered according to Kuo (1982). Moreover, as Abaqus Explicit is used for the dynamic time history procedure, then only Rayleigh mass proportional damping (α) was used (Mills-Bria et al. (2008)), because the

inclusion of stiffness proportional damping (β) will lead to a very small stable time increment and will slow the computation time considerably. Indeed, α is a linear function of the fundamental frequency only, which means damping for higher modes will be underestimated leading to an overestimation of the global response (displacement, stresses, and internal forces). For this reason, the coefficient α is calculated using the mass proportional damping method proposed by Xiaoming et al. (2015). Note that a 5% critical damping is adopted for the determination of the α coefficient. The meshing for the FEM is illustrated by Figure 10, where the hexa-dominant meshing technique based on 0.5 m size seed is used for concrete. The analysis is performed assuming a contact with friction at the potentially sliding plane of the identified concrete block, by considering a friction angle $\phi = 45^\circ$ ($\tan \phi = 1$), and cohesion $c = 0$. Here, the zero-cohesion assumption is believed to be conservative, because the concrete does not lose all cohesive property under small deformation. Moreover, the existing steel reinforcement are ignored for the stability analyses. The static loads namely gravity, water pressure and uplift pressure are ramped from zero to over 5 sec and were applied at the first step, followed by the seismic action applied at the second step. As explicit analysis is dynamic by nature and solves every problem as a wave propagation problem, when statics forces are applied inertial forces must be monitored (checking kinetic energy/strain energy ratio) and reduced to ensure results are equivalent to a quasi-static case.

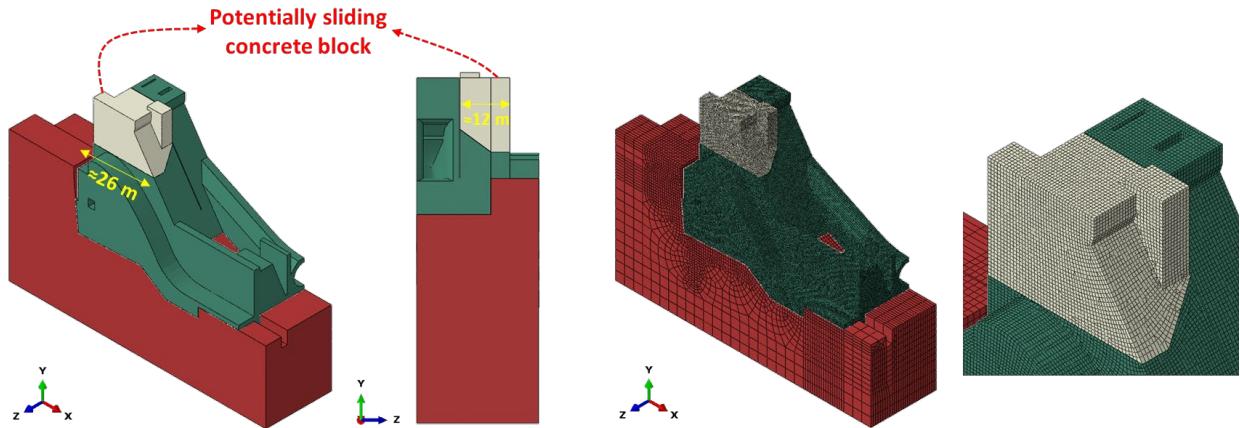


Figure 10. FEM for stability analysis and identification of the potentially sliding concrete block.

Obtained results are summarised by Figure 11, where the relative displacement at the identified potentially sliding plane is illustrated. Indeed, the maximum residual displacement according to the upstream-downstream direction is found to be 3.92 mm.

Generally, as mentioned by Fenves and Chavez (1996), the magnitude of the sliding displacement from dynamic analyses should be compared with a criterion for the maximum allowable displacement. However, CDA guidelines do not provide acceptance criteria for sliding displacements.

Here, the sliding displacement is obtained from conservative assumptions where several beneficial effects were ignored, namely the cohesion, the existing steel reinforcement, and the foundation radiation damping. For this reason, the 3.92 mm (as compared to the dimension 26 m, see Figure 10) sliding displacement according to upstream-downstream is judged to be marginal. This result is compatible with the previous traditional stability calculation. Consequently, the identified concrete block remains stable after the earthquake. Therefore, results obtained from the dynamic time history analysis validate the previously results obtained from the pseudo-dynamic analyses.

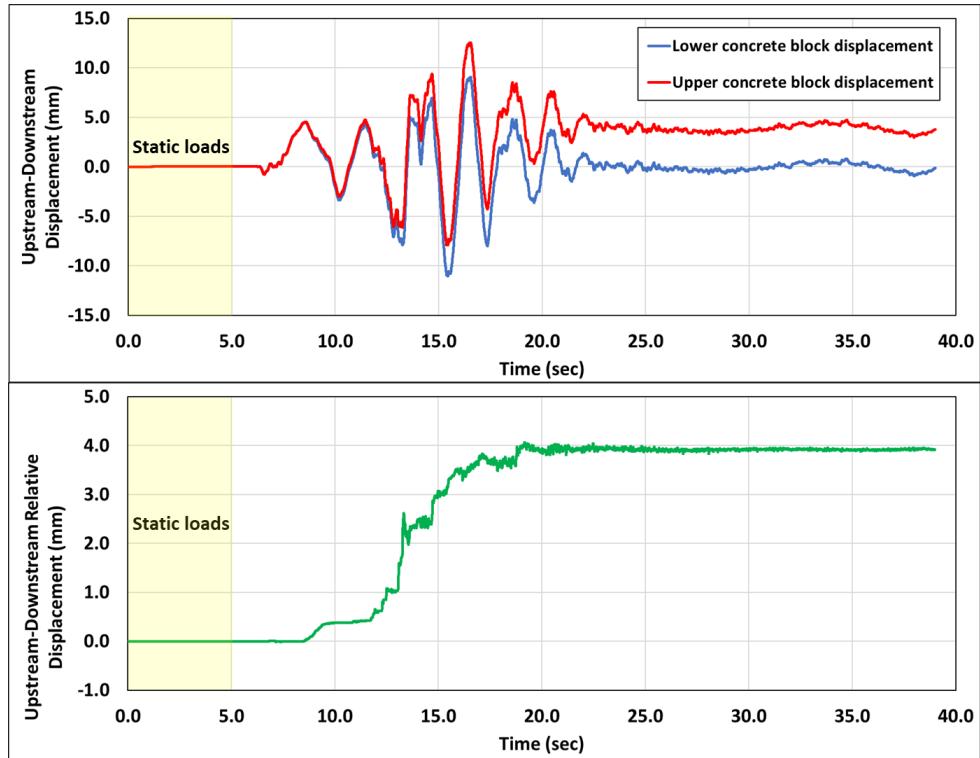


Figure 11. Relative displacement of the identified potentially sliding concrete block.

5. Conclusion

In the context of life extend of an existing concrete hydraulic structure affected by AAR, a detailed FEM was prepared to perform structural AAR analyses. The FEM was calibrated to measured structural and unit parameter data. Subsequently, this calibrated model was used to perform nonlinear stress analyses to predict the future behaviour of this concrete structure. Considering the numerical model results and field observations, major crack patterns were identified. These crack patterns may form potential failure planes (sliding planes) of concrete blocks. The likelihood of occurrence of these identified sliding planes was discussed, and stability analysis was performed.

The 3D seismic stability analysis of the identified concrete block is performed using the pseudo-dynamic method and validated using the fully time history procedure based on accelerograms compatible with the UHS of the site of study. The dynamic time history analysis is realised on a reduced FEM using the Abaqus Explicit solver.

One confirms that the identified potentially sliding concrete block is stable, and no catastrophic failure is likely to take place for the dam, during the extended service life of this facility. This is valid for the extreme action of floods and earthquakes as per CDA 2013 hazard classification and performance criteria.

Finally, the authors strongly believe that this case study is of value to the professional community and illustrates the benefit of using advanced numerical analyses for the assessment of existing dams. The adopted methodology in managing and reducing the conservatism to a reasonable level is particularly useful to engineers involved in the analyses of aged and damaged structures affected by AAR.

6. References

- Atkinson GM, J-R Pierre (2004). Ground-motion Response Spectra in Eastern North America for Different Critical Damping Values. *Seismological Research Letters*, pp. 541-545.
- Ben Ftima M, Léger P, Boussaha F. (2017). Nonlinear finite elements for the assessment of hydraulic concrete structures affected by alkali-aggregate reaction: a case study. In *Swelling Concrete in Dams and Hydraulic Structures*. pp 176-187. ISTE Ltd and John Wiley & Sons, Inc.

- CDA (2007, Revision 2013). Dam Safety Guidelines, Canadian Dam Safety Association.
- CSA A23.3:19. (2019). Standard and Redline, Design of concrete structures.
- EPRI (1991). A methodology for assessment of nuclear power plant seismic margin, EPRI NP-6041-SL, revision 1, project 2722–23, final report.
- FERC (2016). Chapter III Gravity Dams.
- FEMA (2005). Federal guidelines for dam safety.
- Fenves GL, Chaves JW. (1996). Evaluation of earthquake induced sliding in gravity dams. 11th WCEE, paper No 2069, Elsevier Science Ltd.
- Ghrib F, Léger P, Tinawi R (1995). Une approche progressive de vérification sismique des barrages en béton d'Hydro-Québec. Vol. I Rapport No. EPM/GCS 1994-19, Revision 0.1, April; Vol. II (analyses transitoires linéaires et non linéaires) Rapport No. EPM/GCS 1996-02 Revision 02, September 1996.
- Hibbitt HD, Karlson BI, Sorensen EP. (2019). Abaqus version 2019, Finite Element Program. Providence, RI, USA.
- Koltuniuk R, Percell P, Mills-Bria B. (2013). State-of-Practice for the Nonlinear Analysis of Concrete Dams 2013. U.S. Department of the Interior Bureau of Reclamation Technical Service Center Denver, Colorado.
- Kou. JSH. (1982). Fluid-structure interactions: Added mass computations for an incompressible fluid. August. NSF Report, University of California, No UCB/EERC-82/09.
- Larive C. (1998). Apports combinés de l'expérimentation et de la modélisation à la compréhension de l'alkali réaction et de ses effets mécaniques. Paris: Laboratoire central des ponts et chaussées.
- Léger P, Côte P and Tinawi R (1996) Finite element analysis of concrete swelling due to alkali–aggregate reactions in dams. Computers and Structures 60(4): 601–611.
- Léger P, Venturelli J, Bhattacharjee SS. (1993). Seasonal temperature and stress distributions in concrete gravity dams. Part 1: modelling. Can J Civ Eng. 20(6):999-1017.
- Léger P, Javamardi F (2007). Seismic stability of concrete gravity dams strengthened by rockfill. Ninth Canadian Conference on Earthquake Engineering Ottawa, Ontario, Canada 26-29 June.
- Mills-Bria B, Nuss L, Chopra A. (2008). Current methodology at the bureau of reclamation for the nonlinear analyses of arch dams using explicit finite element techniques. The 14th World Conference on Earthquake Engineering October 12-17, 2008, Beijing, China.
- Nour A, Cherfaoui A (2022). Finite-element modelling of alkali–aggregate reaction in a concrete hydraulic structure. Proceedings of the Institution of Civil Engineers – Construction Materials, Volume 175 Issue 3, June 2022, pp. 109-124. <https://doi.org/10.1680/jcoma.21.00057>.
- Pan J, Feng Y, Jin F, Zhang C. (2013). Numerical prediction of swelling in concrete arch dams affected by alkali-aggregate reaction. Eur J Environ Civ Eng. 17(4):231-247.
- Paul JW, Tarbox GS. (1991). Definition of critical thermal states in arch dams - a prerequisite for cracking analysis. Dam Fracture Proceedings from the International Conference, Boulder, Colorado, pp 643-657.
- Saouma VE. (2014). Numerical Modeling of AAR. London, UK: CRC Press. Taylor & Francis Group.
- Stanton TE (1940) Expansion of concrete through reaction between cement and aggregate. Proceedings of the American Society of Civil Engineers 66(10): 1781–1811.
- US Army Corps of Engineers (USACE). (2005). Stability analysis of concrete structures. EM1110-2-2100.
- US Army Corps of Engineers (USACE). (2007). EM-1110-2-6053, “Earthquake design and evaluation of concrete hydraulic structures.
- Xiaoming C, Jin D, Yungui L. (2015). Mass proportional damping in nonlinear time-history analysis. Proceedings of the 3rd International Conference on Material, Mechanical and Manufacturing Engineering. Published by Atlantis Press.

IMPACTS OF CONSTITUTIVE MODEL AND INPUT GROUND MOTION SELECTION ON THE SEISMIC RESPONSE OF AN EARTH DAM

A.G. Özcebe^{1*}, D. Gioffré², A. Famà¹, E. Zuccolo³, F. Bozzoni¹ & C.G. Lai^{1,2}

¹ EUCENTRE, Pavia, Italy (*corresponding author: ali.ozcebe@eucentre.it)

² DICAr, University of Pavia, Pavia, Italy

³ OGS, Udine, Italy (*formerly a researcher at EUCENTRE*)

Abstract: This work presents a case study for numerical assessment of the seismic response of an earth dam in Italy. Following the presentation of the problem setup, model response, and fundamental benchmarking analyses, the focus is made on quantifying the sensitivity of the results on different input ground motions and material constitutive models. The set of analyses carried out contains three different hypotheses: (1) non-liquefiable dam and soil layers (e.g. Mohr-Coulomb) subjected to the input ground motion suite selected and scaled according to the Italian code spectrum, (2) liquefiable dam and soil layers (e.g. Finn-Bryne model) subjected to the input motions compatible with the Uniform Hazard Spectrum (UHS), and (3) non-liquefiable dam and soil layers subjected to the input motion set compatible to the conditional spectrum (CS). The results of analyses suggest that incorporating the excess pore water generation capability in the constitutive model increased the residual displacement demand in the order of 50 to 60% (Hypothesis 2 versus Hypothesis 1), whereas the selection of the input ground motion suite according to the CS reduced the permanent displacement demand of about 50 % (Hypothesis 3 vs Hypothesis 1).

1. Introduction

Analysis and design of earth dams or embankments have always certainly been one of the challenging and interesting subjects of earthquake engineering. The early works were based on a pseudo-static approach with uniform rigid-body motion-induced type of uniform acceleration, in which slope instability was considered to be the only mechanism of failure. The use of this simple and old approach ceased after contradicting experimental data (Keightley, 1966), case history observations (Okamoto et al., 1969), and finally being extensively investigated by Seed (1973). Starting from the mid-1970s, the general concept of considering the earth dams as deformable bodies was already widely accepted and often represented by 1D or 2D shear beam models, with the idea of obtaining the seismic coefficient associated with the deformed shape of the geometry (e.g., Makdisi and Seed, 1979; Gazetas, 1981). On the other hand, in parallel with the developments in computing power numerical modelling of the dams also started to attract attention starting with linear-equivalent models (e.g., Idriss et al., 1973; Martinez and Bielak, 1980) and eventually evolving into plasticity-based models (e.g., Prevost et al., 1985). At the end of the 1980s, the general conception of the potential seismic failure reasons of the dams was significantly more advanced, which already included the liquefaction of the sandy materials within the dam and its consequences in terms of loss of free-board due to settlement and lateral deformations (Gazetas, 1987). Together with the giant leaps in soil constitutive modelling, the predictive capabilities of the numerical models are significantly improved (e.g., Woodward and Griffiths, 1996; Rouainia and Muir Wood, 2000; Elgamal et al., 2002; Aydingun and Adalier, 2003).

In the last 20 to 25 years, as a result of having a significantly increased number of available engineering programs/platforms within the reach of engineers, the research in the field of seismic response of earth dams has significantly risen. Starting from the first examples (e.g., Prevost et al., 1985; Griffiths and Prevost, 1988), there are dozens of works published either on modelling the seismic response of earth dams (e.g., Parish et al., 2009; Elia et al., 2011; Boulanger et al., 2015; Pelecanos et al., 2015;) or explaining the impacts of various components of numerical modelling on the global response, such as the complexity of the soil constitutive model (e.g., Elia and Rouainia, 2013; Boulanger, 2019), the interaction between the reservoir and dam (e.g., Pelecanos et al., 2020), spatial variability on the soil profile (e.g., Lizarraga and Lai, 2014; Boulanger and Montgomery, 2016). Unfortunately, a complete review could not be fairly summarized in this limited space.

Although the numerical assessment of the seismic response of earth dams is fairly common in the scientific literature, the use of uniform hazard-compatible input records is still the current Italian practice. Furthermore, it is the authors' experience that the avoidance of modelling the excess pore water pressure generation may still be the default preferred modelling strategy in the civil engineering community due to difficulties associated with the use of advanced soil constitutive models. This work aims to document the impact of alternative modelling strategies on the already existing ones by providing two sets of sensitivity analyses for an earth embankment without significantly increasing the complexity of the modelling. The aforementioned sensitivity analyses are carried out in FLAC8 (Itasca, 2019) and they are focused on the selection of the (i) input motion and (ii) constitutive models. For the former, the classical Uniform Hazard Spectrum (UHS) based approach will be compared with an alternative Conditional Spectrum (CS) one (Baker, 2011), in which the conditioned period of vibration is set based on amplification characteristics of the system (embankment + soil below). For the latter, two simple constitutive models are used, the first one is based on the Mohr-Coulomb plasticity model associated with hysteretic unloading-reloading relationships according to the available models in the literature (e.g., Darendeli, 2001; Rollins et al., 2020), the second one shares all the plasticity and hysteretic characteristics of the first one but also includes a loosely coupled volumetric-shear strain coupling through Finn-Bryne formulation (Bryne, 1991).

2. Problem Definition

The embankment of interest is located in Italy. It has a crest height of about 9 meters with 1.5 meters of top width and shell dimensions of about 15-20 m. The freeboard is roughly 2 meters. Both the shell and the core are characterized by $\phi'=33^\circ$ and $c'=0.1$ kPa and toes with $\phi'=40^\circ$ and $c'=1$ kPa. Below the embankment, there are silty ($\phi'=28^\circ$ and $c'=0.1$ kPa), gravelly ($\phi'=33^\circ$ and $c'=0.1$ kPa), and clayey ($\phi'=27$, $c'=5$ kPa) formations (Figure 1).

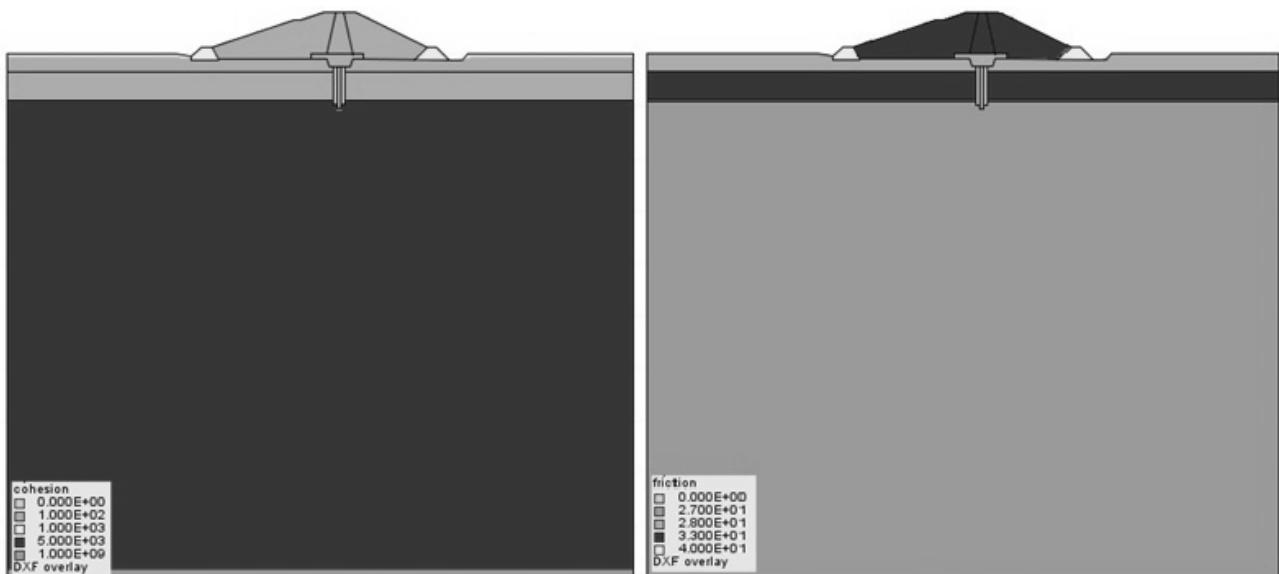


Figure 1. Mohr-Coulomb parameters used in the analyses (left: internal friction angle, right: cohesion)

The model box is defined with 100 m depth and 120 m width and the shear and skeleton bulk moduli profile are increased stepwise (Figure 2). Hydraulic conductivities range from 1.0e-7 m/s (core trench layer) to 1.0e-

4 m/s (toes) and they are defined in terms of mobility coefficients. On the other hand, porosity values 0.3 to 0.4 within the model. To damp out the small strain oscillations, a stiffness-proportional Rayleigh damping is defined as a 0.5% damping ratio at 4 Hz.

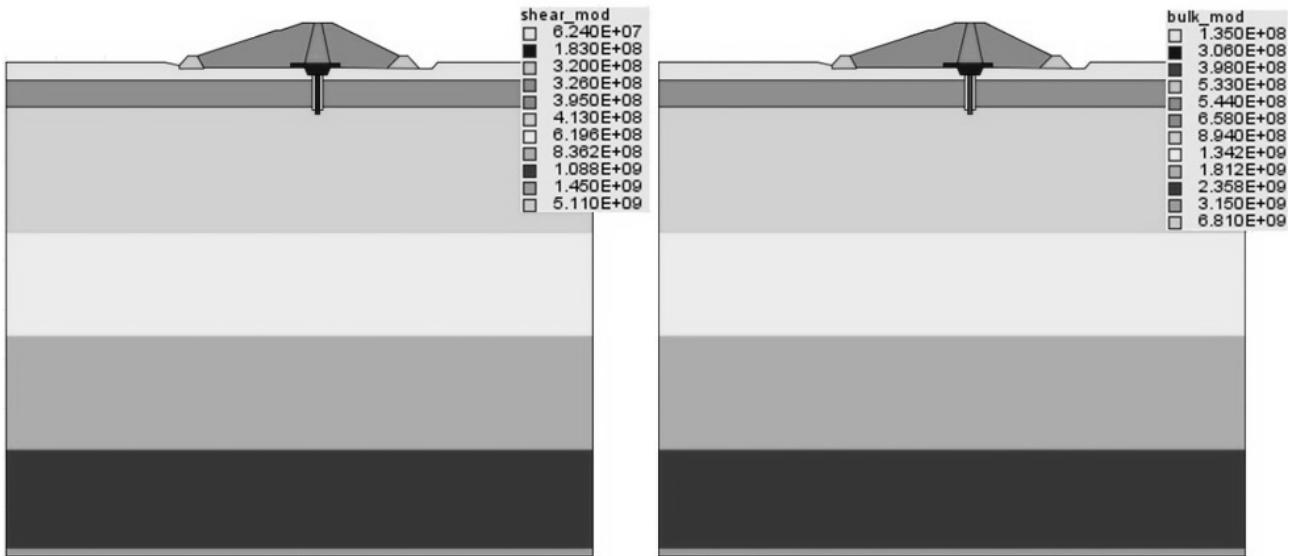
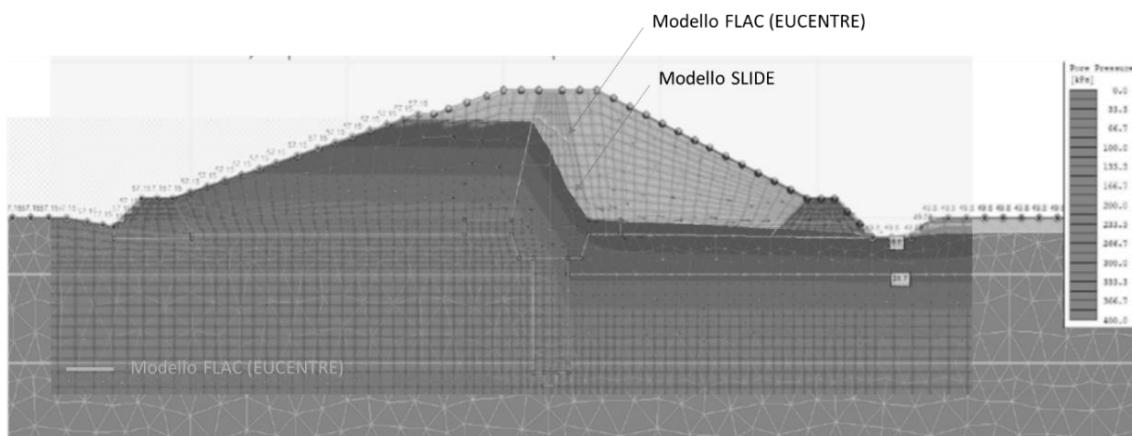


Figure 2. Elastic moduli used in the analyses (left: shear moduli, right: bulk moduli)

Before passing to the dynamic analyses, the following modelling steps are carried out in the sequence: (i) analysis without the presence of the dam, (ii) addition of the grout curtain and submerged part of the core, (iii) addition of the above-ground portion of the dam, (iv) filtration analyses with freeboard level, and (v) application of the hydrostatic pressure considering the water level at freeboard level. Between those steps, the model is cycled until the maximum unbalanced force is reached. It is important to note that all the static analyses are carried out by using static moduli (if there is an SPT test, that is used If not the dynamic moduli are reduced by 1/5-1/6, which roughly corresponds to 0.1% shear strain on the backbone curve).

Once the static phase is finished the phreatic surface and total settlement at crest level are blind-checked with another set of analyses carried out by the Client (SLIDE, Rocscience) and measured values (~9 cm), respectively. From the corresponding comparisons provided in Figure 3 (top) and Figure 3 (bottom), it could be inferred that the phreatic surface is generated per the previous solution and the model can capture the observed vertical deformations with acceptable accuracy.

Sigmoidal hysteretic reloading-unloading rules are calibrated based on the publications of Darendeli (2001), Park and Kishida (2019), Lanzo (2018), and Rollins et al. (2020), corresponding to different zones. A sample calibration is shown in Figure 4 for the gravelly layer. The strain ranges of calibration are obtained from the preliminary site response analyses by using the seven input ground motions under linear conditions.



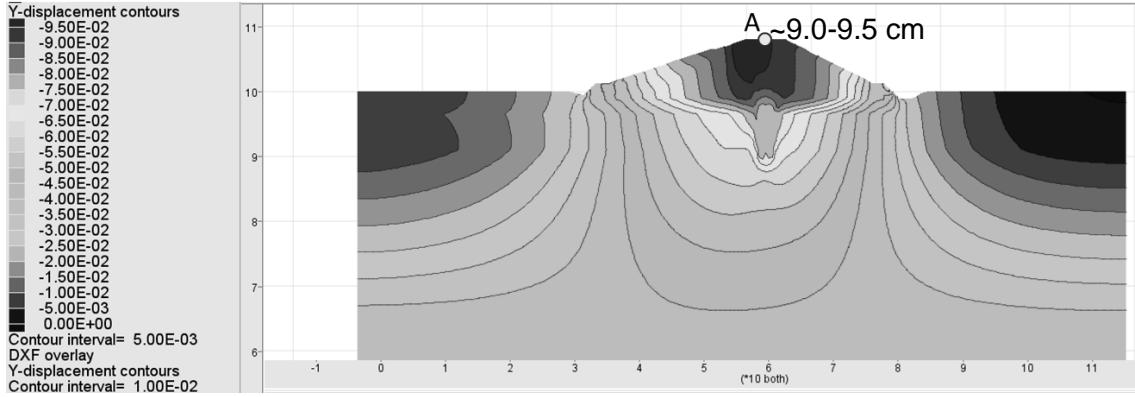


Figure 3. Benchmarking the static analyses (top: phreatic surface development, bottom: vertical displacement contours)

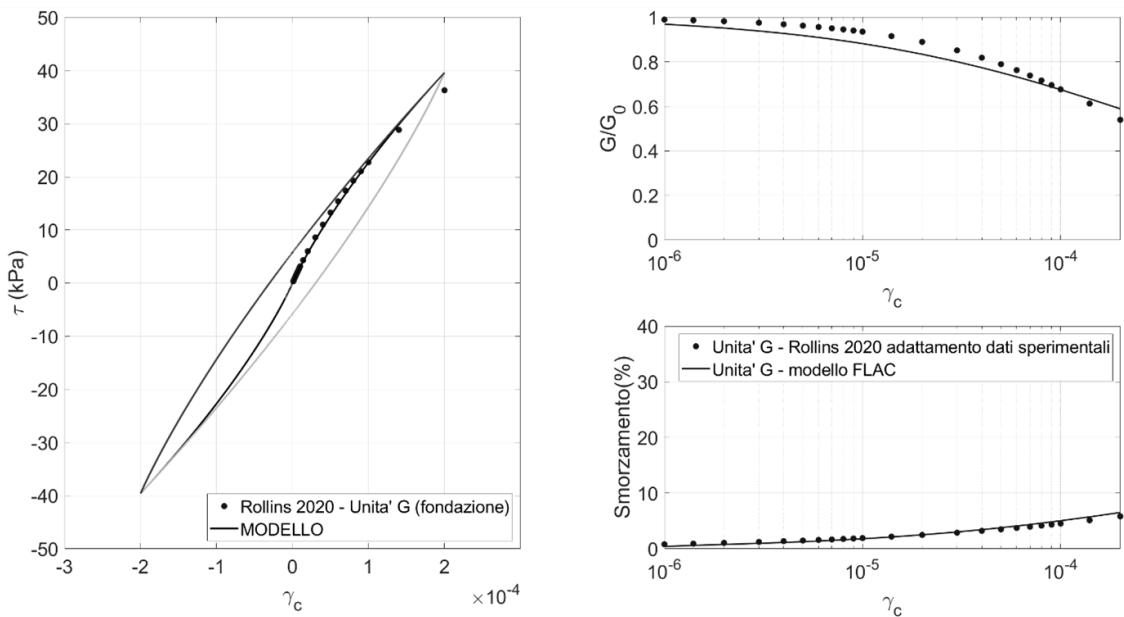


Figure 4. Calibration of the hysteretic model (left: stress-strain, right-top: shear modulus degradation-shear strain, right-bottom: damping ratio-shear strain)

Input motions are provided from the base as stress time histories with two components (i.e., compression/tension and shear stress) together with silent boundary conditions at the base (Lysmer and Kuhlemeyer, 1969) and lateral boundary conditions are assigned as free-field boundaries (Cundall et al., 1980). The finite difference mesh is structured to propagate up to 30 Hz. Further details regarding the dam and the analysis parameters could not be shared due to the classified information between EUCENTRE and the Client.

3. Model dynamic benchmarking

Before proceeding with the results of the analyses, a simple check of model reliability is made by considering the linear viscoelastic propagation (i.e., without the hysteretic and plasticity models). Instead of an earthquake strong ground motion, a two-component Ricker wavelet stress history is provided from the base. The response at the ground level near the free-field boundary is compared with a 1D analytical solution carried out by using STRATA (Kottke and Rathje, 2009). As shown in Figure 5, the comparisons between the numerical solution and the analytical one are found convincing to conclude that the finite difference mesh and the boundary conditions are structured well enough to accurately propagate the seismic waves.

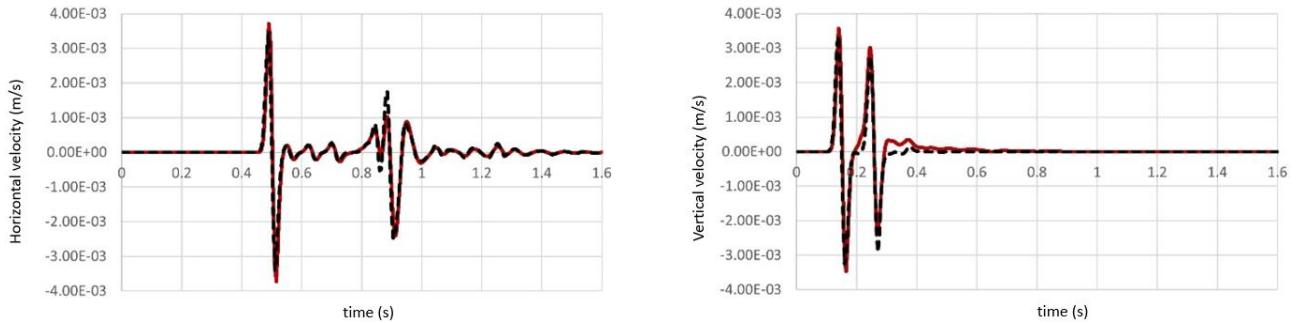


Figure 5. Checking the wave transmissibility of the finite difference model by comparing its results on the soil surface (near the free-field column) with a frequency-domain code STRATA (left: horizontal velocity time-history, right: vertical velocity time-history)

4. The effect of the input ground motion selection approach

Input ground motion selection constitutes a crucial part of the dynamic assessment of structural and geotechnical systems. Apart from the very peculiar cases, there exists a target elastic (usually 5%-damped) (acceleration or displacement) spectrum according to which the mean of the spectral values of the selected signals should be defined. In the current practice, the aforementioned target spectra are often based on uniform hazard spectra (UHS), which are defined at specific return periods. This classical approach is criticized for ending up with ground motion sets having non-realistically rich content over a broad frequency range (Baker, 2011). The alternative is constructing a Conditional Spectrum (CS) in which the spectral content of a period of vibration is conditioned to the hazard level of interest, meanwhile, all the other periods of vibrations do not share the same hazard level and have relatively lower demands.

The period of conditioning the spectrum is selected as a function of the vibratory characteristics of the dynamic system of interest. For the case of an embankment, the period of vibration of interest becomes a range since the amplification phenomenon is twofold: one coming from the site response below the embankment and the other from the embankment itself. To examine the amplification characteristics, an amplification function is derived by taking the magnitude of the ratios of the Fourier coefficients of the signals recorded in the crest of the embankment and rock outcrop conditions. Back calculated amplification functions are shown in Figure 6.

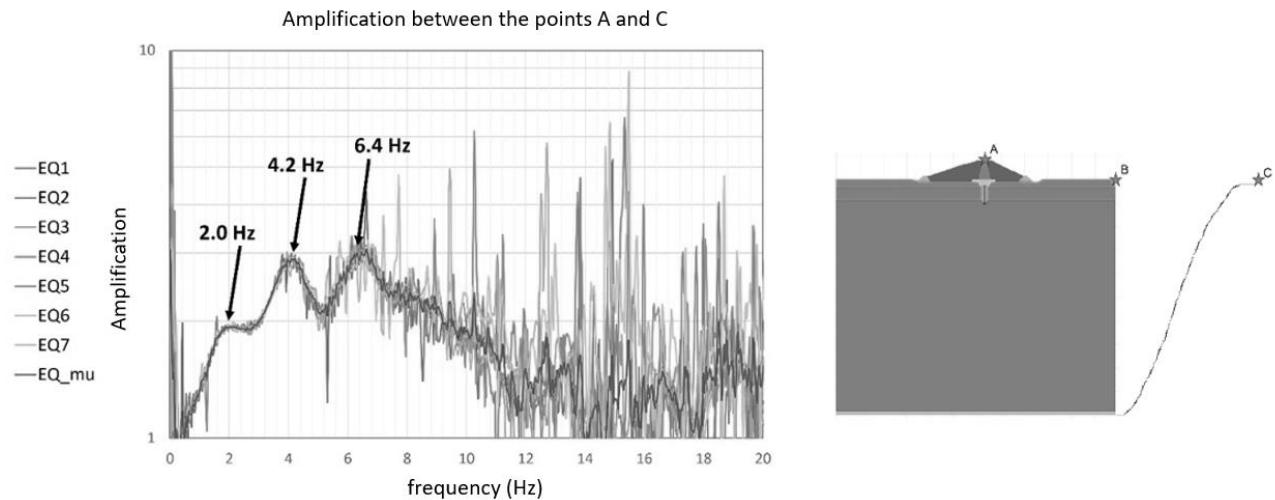


Figure 6. Finding out the natural frequencies of the combined system embankment plus soil. Left: Amplification function between A and C, right: Schematic illustration of the point locations: A, C, and B, where the results of the last one are not presented here.

From Figure 6, the first amplification peak is observed at 2.0 Hz, which is related to the soil profile itself. The second amplification peak at 4.2 Hz, instead, is the soil profile's second mode of vibration frequency further amplified by the presence of the embankment which becomes the first mode of vibration for the combined system. There is the third peak at 6.4 Hz, which is again an embankment-influenced soil profile response

result. Given the fact that there are two dominant peaks at 4.2 Hz and 6.4 Hz, it is decided to constrain the CS at T=0.2s. Acceleration response spectra corresponding to the sets of ground motions selected according to UHS and CS are shown in Figure 7 (left).

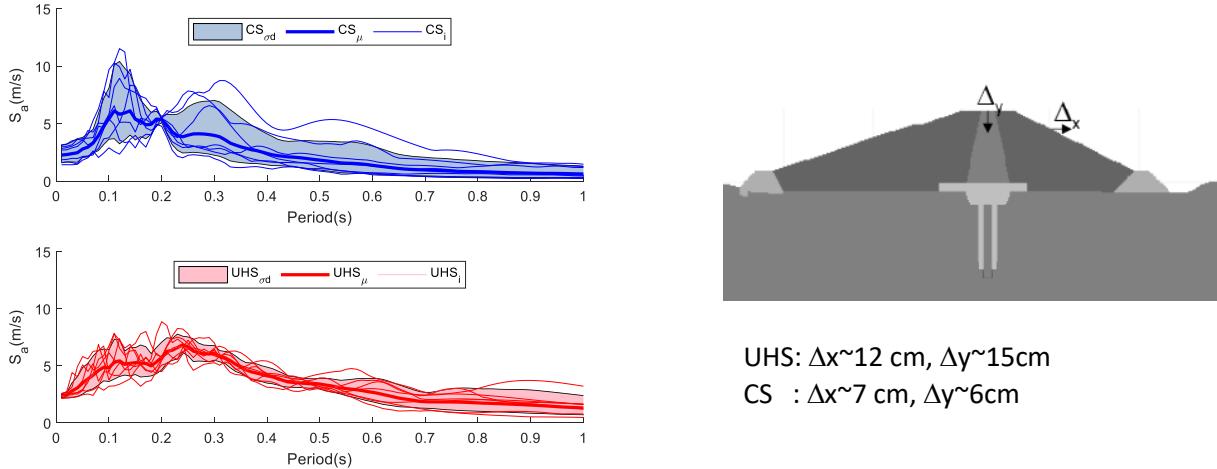


Figure 7. Left: Representation of the acceleration response spectra selected according to CS and UHS, right: residual displacement values obtained at two different locations of the embankment

When the two mean spectra (CS_{μ} and UHS_{μ}) shown in Figure 6 are compared, it can be observed that the spectral contents until the periods up to 0.25 s are somewhat similar, however, the CS (Conditional Spectrum) is progressively showing lower frequency content for the longer periods. On the other hand, the dispersion of CS is smaller or equal to that of UHS in the period range between 0.15-0.25 s, while it is less constrained for the rest of the periods.

As expected, analysis results show that less demanding motions selected according to the CS constrained at T=0.2s may substantially lower the residual displacement demands from 12 cm to 7 cm in terms of the horizontal displacement of the shell and from 15 cm to 6 cm in terms of the residual vertical displacement of the core (Figure 7, right). Finally, It should be noted that for an embankment system in which the initiation of the shear failure is closely linked to the amplification and the accumulated amount of plastic deformations will be more influenced by the longer period content due to period elongation as a result of soil plasticity. On the other hand, having exposure to an earthquake ground motion equally rich in such a broad frequency range remains still unlikely.

5. The effect of the constitutive model selection

The response of the embankment becomes rather more delicate if a potential increase is expected in the pore water pressures in the sandy zones within or below the embankment. Excess pore water pressure increase is a direct result of soil volumetric deformation tendency, which could be modelled through constitutive models connecting the shear deformation of the skeleton to the volumetric one. Shear-volumetric deformation coupling could be modelled through fully-coupled plasticity-based models (e.g., such as SANISAND, Dafalias et al. 2004; PDMDY, Yang et al. 2003; SD model, Cubrinovski and Ishihara 1998; PM4Sand, Boulanger and Ziotopoulou 2015, etc.) which guarantee accuracy provided that their numerous parameters are well-representative. In case of the absence of data, the simplified alternative becomes using a loosely coupled model (e.g. Bryne, 1991) in which the classical plasticity models (e.g., Mohr-Coulomb) could be enriched with an external empirical equation defining the volumetric deformation as a function of the shear deformation. With the compromise of accuracy loss in mimicking the actual dynamic response of the sandy layer, these methods require fewer parameters to be set.

Due to the limited information on the subsoil for conducting a more advanced analysis with fully-coupled models, in this work, the loosely coupled model proposed by Bryne (1991) is used (Itasca, 2019). In addition to the constitutive model discussed in Section 2, a set of additional equations are invoked, as defined in Equations (1) to (4). In those equations, $(\Delta\epsilon_{vd})_{1/2cycle}$ is the infinitesimal volumetric strain increment for an half cycle, C_1^c , C_1 , and C_2 are the model parameters, and γ is the shear strain.

$$\frac{(\Delta\epsilon_{vd})_{1/2\text{cycle}}}{\gamma} = C_1 \exp(-C_2(\epsilon_{vd}/\gamma)) \quad (1)$$

$$C_1^c = 7600(D_R)^{-2.5} \quad (2)$$

$$C_1 = 0.5C_1^c \quad (3)$$

$$C_2 = 0.4/C_1^c \quad (4)$$

In Figure 8, the shear bands formed with (right) and without (left) consideration of the effects of shear-volumetric coupling are compared for one of the ground motions within the UHS set. It could be noted that the shear strain demand is further amplified and extended due to the reduction of the effective stresses in the first layer beneath the embankment and sandy shell layers of the embankment. The strain band further penetrates the core of the dam, by ending up creating a mechanism.

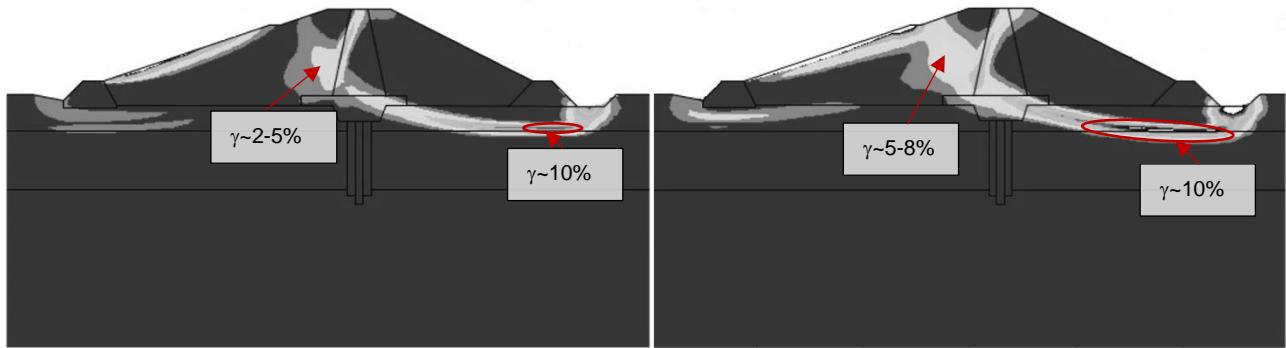


Figure 8. Residual shear strain (ssi) demands after a seismic motion. Left: Mohr-Coulomb model, Right: Mohr-Coulomb + Finn model

Although the increase in the shear strain demand may seem minor, the corresponding increase in the mean horizontal residual displacement demand of the shell is found to be increased by 60% (for some specific cases up to 100%) and the mean vertical residual displacement of the crest is found to be affected by 50%.

6. Concluding remarks

In this work, numerical modelling and its essential sanity checks are provided for an embankment dam in Italy. Once the model is shown to be performing acceptably well, two sets of sensitivity analyses are carried out to emphasize the influence of the selections of (i) input motion-scaling approach and (ii) constitutive model for sandy soil zones.

The former set of analyses shows that with the use of a CS-based ground motion selection, seismic demands are lowered by up to 50% of the demands obtained by using the UHS-based ground motion selection. The second set shows that taking into account the possibility of generation of the excess pore water pressure beneath the earth dam amplifies the deformation demand of about 60%. It should be taken into consideration that the seismicity of the site is moderate, hence for a site with higher seismic hazard demand, the additional displacement demand due to soil liquefaction is expected to be more prevalent.

7. References

- Aydingun O., Adalier K. (2003). Numerical analysis of seismically induced liquefaction in earth embankment foundations. Part I. Benchmark model. *Canadian Geotechnical Journal*, 40(4): 753-765.
- Baker, J. W. (2011). Conditional mean spectrum: Tool for ground-motion selection. *Journal of Structural Engineering*, 137(3): 322-331.
- Boulanger R.W., Montgomery J., Ziotopoulou K. (2015). Nonlinear deformation analyses of liquefaction effects on embankment dams. In *Perspectives on Earthquake Geotechnical Engineering: In Honour of Prof. Kenji Ishihara*. Cham: Springer International Publishing.

- Boulanger, R. W., Ziotopoulou, A.K. (2015). *PM4Sand (Version 3): A sand plasticity model for earthquake engineering applications*. Center for Geotechnical Modeling Report No. UCD/CGM-15/01, Department of Civil and Environmental Engineering, University of California, Davis, California.
- Boulanger R.W., Montgomery, J. (2016). Nonlinear deformation analyses of an embankment dam on a spatially variable liquefiable deposit. *Soil Dynamics and Earthquake Engineering*, (91): 222-233.
- Boulanger R.W. (2019). Nonlinear dynamic analyses of Austrian dam in the 1989 Loma Prieta earthquake. *Journal of Geotechnical and Geoenvironmental Engineering*, 145(11): 05019011.
- Bryne, P. (1991). A Cyclic Shear-volume Coupling and Pore-pressure Model for Sand. In *Proceedings: Second International Conference on Recent Advances in Geotechnical Earthquake Engineering and Soil Dynamics*, St. Louis, Missouri.
- Cubrinovski M., Ishihara, K. (1998). Modelling of sand behaviour based on state concept. *Soils and Foundations*, 38(3): 115-127.
- Cundall P.A., Hansteen H., Lacasse S., Selnes P. B. (1980). *NESSI, soil structure interaction program for dynamic and static problems*. Norwegian Geotechnical Institute, Report, 51508-9.
- Dafalias Y.F., Manzari M.T. (2004). Simple plasticity sand model accounting for fabric change effects. *Journal of Engineering mechanics*, 130(6): 622-634.
- Darendeli M. B. (2001). Development of a new family of normalized modulus reduction and material damping curves. *PhD Thesis*, The University of Texas at Austin.
- Elgamal A., Parra E., Yang Z., Adalier, K. (2002). Numerical analysis of embankment foundation liquefaction countermeasures. *Journal of Earthquake Engineering*, 6(04): 447-471.
- Elia G., Amorosi A., Chan A.H.C., Kavvadas M.J. (2011). Fully coupled dynamic analysis of an earth dam. *Géotechnique*, 61(7): 549-563.
- Elia G., Rouainia M. (2013). Seismic performance of earth embankment using simple and advanced numerical approaches. *Journal of Geotechnical and Geoenvironmental Engineering*, 139(7): 1115-1129.
- Gazetas G. (1981). A new dynamic model for earth dams evaluated through case histories. *Soils and Foundations*, 21(1): 67-78.
- Gazetas G. (1987). Seismic response of earth dams: some recent developments. *Soil Dynamics and Earthquake Engineering*, 6(1): 2-47.
- Griffiths D.V., Prevost J.H. (1988). Two-and three-dimensional dynamic finite element analyses of the Long Valley Dam. *Géotechnique*, 38(3): 367-388.
- Idriss I.M. (1973). *Quad-4: a computer program for evaluating the seismic response of soil structures by variable damping finite element procedures*. University of California.
- Itasca (2019). *FLAC—Fast Lagrangian Analysis of Continua, version 8.1. Computer program and user manuals*. Minneapolis: Itasca Consulting Group.
- Lizarraga H.S., Lai C.G. (2014). Effects of spatial variability of soil properties on the seismic response of an embankment dam. *Soil Dynamics and Earthquake Engineering*, 64: 113-128.
- Keightley W.O. (1966). Vibrational characteristics of an earth dam. *Bulletin of the Seismological Society of America*, 56(6): 1207-1226.
- Kottke A.R. and Rathje E.M. *Technical manual for Strata*. Berkeley, California: Pacific Earthquake Engineering Research Center, 2009.
- Lanzo G. (2018). Alcune considerazioni sulla rivalutazione della sicurezza sismica delle dighe di materiali sciolti. *CGT 2018* (In Italian).
- Lysmer J., Kuhlemeyer R.L. (1969). Finite dynamic model for infinite media. *Journal of the engineering mechanics division*, 95(4): 859-877.
- Makdisi F.I., Seed H.B. (1979). Simplified procedure for evaluating embankment response. *Journal of the Geotechnical Engineering Division*, 105(12): 1427-1434.
- Martinez B., Bielak J. (1980). On the three-dimensional seismic response of earth structures, *Proceedings of 7th WCEE*, Istanbul.

- Okamoto S., Hakuno M., Kato K., Kawakami F. (1969). On the dynamical behavior of an earth dam during earthquakes. In *Proc. 4th Worm Conf. Earthq. Engrg.*
- Parish, Y., Sadek, M., Shahrour, I. (2009). Numerical analysis of the seismic behaviour of earth dam. *Natural hazards and Earth system sciences*, 9(2): 451-458.
- Park D., Kishida T. (2019). Shear modulus reduction and damping ratio curves for earth core materials of dams. *Canadian Geotechnical Journal*, 56(1): 14-22.
- Pelecanos, L., Kontoe, S., Zdravković, L. (2015). A case study on the seismic performance of earth dams. *Géotechnique*, 65(11): 923-935.
- Pelecanos, L., Kontoe, S., Zdravković, L. (2020). The effects of dam–reservoir interaction on the nonlinear seismic response of earth dams. *Journal of Earthquake Engineering*, 24(6): 1034-1056.
- Prevost J.H., Abdel-Ghaffar A.M., Lacy S.J. (1985). Nonlinear dynamic analyses of an earth dam. *Journal of Geotechnical Engineering*, 111(7): 882-897.
- Rollins K.M., Singh M., Roy J. (2020). Simplified equations for shear-modulus degradation and damping of gravels. *Journal of Geotechnical and Geoenvironmental Engineering*, 146(9): 04020076.
- Rouainia, M. and Muir Wood, D., 2000. A kinematic hardening constitutive model for natural clays with loss of structure. *Géotechnique*, 50(2): 153-164.
- Seed H.B. (1973). *Stability of earth and rockfill dams during earthquakes*. Publication of Wiley (John) and Sons, Incorporated.
- Woodward P.K., Griffiths D.V. (1996). Influence of viscous damping in the dynamic analysis of an earth dam using simple constitutive models. *Computers and Geotechnics*, 19(3): 245-263.
- Yang Z., Elgamal A., Parra E. (2003). Computational model for cyclic mobility and associated shear deformation. *Journal of Geotechnical and Geoenvironmental Engineering*, 129(12): 1119-1127.

IMPACT OF UNCERTAINTY ASSOCIATED WITH GROUND MOTION SELECTION ON FRAGILITY ASSESSMENT OF DAMS

Bikram Kesharee Patra^{1*}, Rocio L. Segura² & Ashutosh Bagchi¹

¹ Dept. of Building, Civil & Environmental Engineering, Concordia University, Montreal, Canada

² Dept. of Civil, Environmental, and Sustainable Engineering, Santa Clara University, Santa Clara, CA, USA

*b_patra@live.concordia.ca

Abstract: This study explores the influence of uncertainties associated with ground motions on the fragility assessment of a concrete gravity dam. Aleatory uncertainty, inherent to natural processes, and epistemic uncertainty, arising from knowledge gaps, are crucial factors in ground motion selection. The Pine Flat Dam in California is used here as a case study and a 2D dam-foundation-reservoir model of the dam has been developed using ABAQUS software. Solid elements are used in the dam and foundation, while acoustic elements are used in the reservoir, and infinite elements are used at the foundation periphery. The dam experiences gravity, hydrostatic, and hydrodynamic loads alongside combined horizontal and vertical ground motions. Material nonlinearity is accounted for using the concrete damaged plasticity model. Ground motions are selected based on the target spectrum as proposed by ASCE 7-16 and the conditional mean spectrum method. The study uses ground motion records selected considering return periods, ranging from 475 to 10,000 years. System response parameters, including crest displacement and damage area ratio, are compared across return periods and ground motion selection methods. To this end, fragility curves are developed as a function of the damage area ratio and the normalized crest displacement. Results indicate that CMS-derived ground-motion models provide more conservative fragility estimates for low return periods than those from ASCE 7-16 for damage area ratio limit states. Similarly, CMS-derived fragility estimates as a function of the normalized crest displacement provide more conservative probabilities of exceedance for moderate to severe damage states when compared to those from ASCE 7-16.

1 Introduction

In the realm of structural engineering, dams serve as vital infrastructural lifelines, ensuring the supply of water, controlling floods, and generating power for communities globally. However, the resilience of these massive structures is consistently challenged, particularly in regions prone to high seismic activities. Recent studies have revealed that many dams worldwide have surpassed their fifth or even sixth decade of service, underscoring the urgent need for thorough evaluations and retrofitting procedures guided by contemporary standards. Notably, in the United States, a country boasting a significant number of large dams, the average age of these structures is now 65 years and steadily increasing. This trend raises significant concerns about the safety and structural integrity of these dams, especially under seismic pressures [1]. The potential consequences of dam failures, including loss of life, economic setbacks, and environmental devastation, emphasize the paramount importance of dam safety. As our understanding of seismic risks deepens, it becomes evident that many dams do not meet the updated safety standards. This convergence of aging infrastructure, emerging challenges, evolving methods for estimating seismic loads, and society's heightened safety expectations necessitates a comprehensive reassessment and enhancement of seismic analysis techniques for dams [2]. Further, in recent years, there has been a substantial increase in understanding of

seismic hazards, leading to a heightened emphasis on enhancing safety measures for dams. Considering this, deterministic methods have often been criticized for their excessive caution and, in certain cases, perceived lack of adequate safety. This criticism arises from their tendency to overlook the various uncertainties inherent in structural analysis. This oversight is compounded by the reliance on extreme load scenarios with exceptionally low probabilities of occurrence [3-5]. To address these limitations and establish a more rational approach to evaluating the safety of concrete gravity dams, there is a growing demand for methods that can effectively prioritize risks. Moreover, a shift toward a probabilistic framework has become essential. Such an approach allows for the comprehensive management of the diverse uncertainties that significantly impact dam performance and the decisions associated with it [4]. Within this probabilistic paradigm, fragility analysis has emerged as a promising solution. Specifically designed to assess the seismic vulnerability of structures, this method excels in estimating the likely extent of damage resulting from seismic events.

In this context, this paper undertakes a distinctive investigation, exploring the influence of ground motion selection techniques and record-to-record (RTR) variability on the fragility assessment of a concrete gravity dam. This work uniquely addresses both epistemic and aleatory uncertainties. Addressing the former, by employing two distinctive ground motion selection techniques, ASCE 7-16 and Conditional Mean Spectrum (CMS), each grounded in a unique theoretical framework. Meanwhile, for aleatory uncertainty, the study considers RTR variability within a return period and across different periods. With a careful selection of 110 ground motions (55 for each method) and five return periods for each method, the study delves into the intricacies of system response variations. Damage area ratio, and displacement-based damage indicators are the focal points for quantifying this variation. The study culminates in a comprehensive fragility assessment of a coupled 2D DFR system. This evaluation accounts for the nuances in ground motion within a return period and across five different periods, providing a nuanced understanding of their collective impact. Fragility curves, developed through displacement, and damage area ratio-based indices, offer a holistic perspective on the influence of ground motion selection techniques and RTR variations on the fragility assessment of the concrete gravity dam.

2 Literature review

The seismic fragility assessment of critical infrastructure, such as concrete gravity dams, is a paramount concern in ensuring their resilience and safety in earthquake-prone regions. In recent years, extensive research has been conducted to comprehensively explore these facets and their collective influence on seismic fragility assessment. This literature review delves into the body of work that addresses the impact of ground motion variation, material uncertainties, and the choice of damage indices on seismic fragility assessments for concrete gravity dams, shedding light on the evolving methodologies and insights that contribute to enhanced structural resilience.

Ellingwood et. al.,[4] studied the fragility analysis of concrete gravity dams. Basic fragility concepts are presented, and databases required to support the fragility assessment are identified. The method is illustrated using a concrete monolith from the Bluestone dam in West Virginia, designed in the late 1930s. Tekie and Ellingwood,[6] investigated fragility curves for a gravity dam, considering various limit states such as material failure at the toe and neck, sliding at the dam-foundation interface, and deflection of the crest near the dam heel. The seismic analysis involved twelve ground motions scaled to a range of 0.1g to 1.2 g. Their findings indicated the potential for sliding along the dam-foundation interface and tensile cracking at the dam's neck during an earthquake with a magnitude equivalent to the maximum credible earthquake (MCE) defined by the U.S. Army Corps of Engineers. Jayaram et. al.,[7] propose a computationally efficient and theoretically consistent algorithm to select ground motions that match the target response spectrum mean and variance. The proposed algorithm is used to select ground motions for the analysis of sample structures in order to assess the impact of considering ground-motion variance on the structural response estimates. Patra et al., [8] emphasize the significance of selecting a consistent numerical model, particularly in the context of evaluating system response variations. This consideration is crucial due to the influence of model variability and the solution procedure on the outcomes of any fragility assessment. The process of fragility assessment entails a multitude of simulations, making computational efficiency a key concern. In this context, the utilization of the time-dependent spectral finite element method (TDSFEM) presents a significant advantage over the conventional finite element method (FEM) due to its reduced computational time, while maintaining comparable accuracy. Sarkar et al.,[9] demonstrate this computational efficiency by contrasting the

computation times between TDSFEM and conventional FEM. Ghanaat et al., [10] utilized non-linear time-history analysis with Latin Hypercube Simulation (LHS) for developing the fragility curves for two failure modes: sliding at the dam base and sliding at the lift joint. Baker, [11] estimated fragility functions using multiple stripe analysis and Incremental dynamic analysis, highlighting the superior efficiency of multiple stripe analysis over the incremental approach. The article also introduces a method to calibrate structural fragility functions directly from nonlinear time-history responses, eliminating the need for extensive simulations.

The accurate estimation of fragility functions requires a proper selection of ground motion records at different intensity levels. Most of the available fragility assessments of concrete dams use the same records at all intensity levels and often selects them with an inadequate target spectrum. In order to improve the fragility assessment of such structures [12] it is proposed to use the records selected with the Conditional Spectrum (CS) method within a multiple stripes analysis. Hariri-Ardebili et al., [13] explored fragility curves for gravity dams subjected to solely horizontal and combined horizontal and vertical ground motions, determining that the addition of a vertical component elevates the likelihood of failure. Hariri-Ardebili et al., [14] addressed the probabilistic seismic demand model (PSDM) which is the relationship between the intensity measure (IM) (such as spectral acceleration) and the engineering demand parameter (EDP) (such as displacement and crack ratio i.e., the ratio of crack length to the total crack path). When the results of the cloud analysis are aggregated, one can plot the seismic fragility curve which is the probability of EDP exceedance in terms of the IM parameter. Chandramohan et al., [15] evaluated the effect of considering ground motion duration when selecting hazard - consistent ground motions for structural collapse risk assessment. Ground motion selection procedures that employ causal parameters like magnitude, distance, and V_{S30} as surrogates for ground motion duration are also evaluated. The inherent variability in the ground motion as well as the difficulty of conducting the analyses for a large number of ground motions renders the selection as the most important factor in the analysis results. In the context, consistency implies obtaining consistent results for the same problem, reliability implies a reduction in the variability in the results while practicality implies the completion of the process with lesser effort. The selection and scaling of the ground motions for use in the nonlinear seismic analysis of the concrete gravity dams was investigated with the aforementioned goals focused on the efficient prediction of the seismic demands on these structures [16]. These methods require the selection of a representative suite of ground motion records, resulting in the need for a ground motion selection method that includes all the relevant ground motion parameters in the fragility analysis of this type of structure. Segura et al., [17] present the development of up-to-date fragility curves for the sliding limit states of gravity dams in Eastern Canada using a record selection method based on the generalized conditional intensity measure approach. Gorai et al., [18] deal with the time history analysis of dam-reservoir-foundation coupled system using finite element technique under near field and far field ground motions. Six ground motions, recorded near to the ruptured fault are selected as near field ground motions. Sevieri et al., [19] discusses the main issues behind the application of the performance-based earthquake engineering to existing concrete dams, with particular emphasis on the fragility analysis. After a critical review of the most relevant studies on this topic, the analysis of an Italian concrete gravity dam was presented to show the effect of epistemic uncertainties on the calculation of seismic fragility curves. Tidke et al., [20] worked on fragility analysis of Koyna dam, using 2D DFR model with layered foundation, ground motions are picked according to the Conditional Mean Spectrum approach. An Incremental Dynamic Analysis (IDA) method was used in which each ground motion was scaled at different intensity levels and directly these ground motions were adopted for the time-history analysis. In fragility analysis, the seismic risk of a gravity dam can be evaluated better using PGA and ASI as compared to PGV.

The reviewed literature underscores the significance of seismic fragility assessment in enhancing the resilience of concrete gravity dams and similar critical infrastructure. It is evident that the multifaceted world of uncertainties, ranging from ground motion variations to material behaviour, introduces complex challenges that demand meticulous consideration.

3 Case study

As mentioned earlier, the Pine Flat dam in California has been used here as a case study. The fragility assessment of the dam involves two crucial steps i.e., ground motion selection and numerical simulation, which are discussed in the following sections and the Figure 1 shows the methodology as adopted seismic performance assessment.

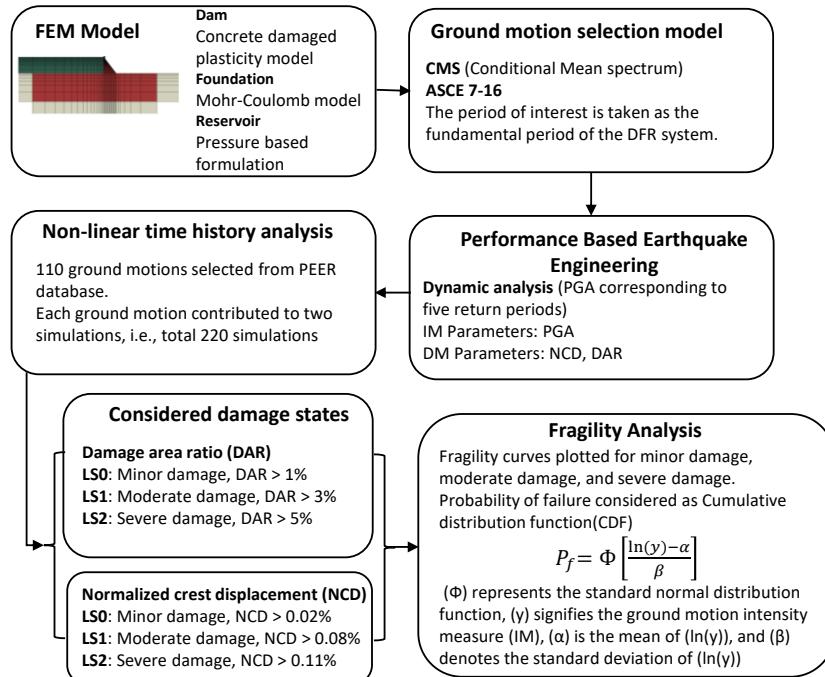


Figure 1. Outline of adopted methodology for fragility assessment of concrete gravity dam

3.1 Ground motion selection

In recent years, considerable research efforts have been devoted to enhancing the process of ground motion selection procedures for seismic analyses, considering the unique geological characteristics of each seismically active region. The importance of selecting input ground motions tailored to specific seismic site conditions must be emphasized, given the inherent diversity in geological settings across regions. The Conditional Mean Spectrum (CMS) method [21] has become widely utilized for selecting ground motions in dam fragility analyses. This technique aligns the mean spectrum of chosen ground motions with a predefined target spectrum at the structures fundamental period. Typically, this target spectrum is derived through Probabilistic Seismic Hazard Analysis (PSHA) specific to the dam site. Similarly, ASCE 7-16 provides guidelines for selecting ground motions applicable to seismic designs of various structures, including dams. This method adheres to a risk-consistent approach, ensuring that the chosen ground motions maintain a probability of exceeding the design limit state equal to the predetermined probability of exceedance.

Utilizing the U.S. Geological Survey (USGS) tool [22], a seismic hazard analysis was conducted for Pine Flat dam in California, USA. This analysis meticulously outlined potential earthquake scenarios across varied intensity levels, defined in terms of horizontal spectral acceleration at the structure's fundamental period. Spectral accelerations were chosen for return periods of 475,975, 2475, 5000, and 10,000 years. Ground motion selection was performed using the Pacific Earthquake Engineering Research Centre (PEER) ground motion database [23]. The Probabilistic Seismic Hazard Analysis (PSHA) for the dam's location, specifically for 0.50-second spectral period and considering a shear wave velocity of $V_{s30} = 760$ m/s (B/C boundary) [24], was carried out to generate the Uniform Hazard Spectrum (UHS).

For the UHS development, the conterminous U.S. 2014 (update) (v4.2.0) model [25] in the USGS tool was utilized. This model provided essential disaggregation information for 11 attenuation equations. The obtained disaggregation data were instrumental in developing the target spectrum and selecting ground motions using the CMS method. Specifically, the disaggregation information corresponding to the Campbell & Bozorgnia (2014) attenuation equation [26] in the PEER ground motion database closely aligned with the UHS at target period.

The target spectrum in the PEER ground motion database was generated using specific input parameters. These included a damping ratio of 5%, specifying the region as global/California, a magnitude of 6.42, and an R_{jb} (distance from the fault) of 46.13 km. Record selection criteria involved considering fault type as strike-slip.

The fundamental period of the Dam Foundation Reservoir (DFR) system, set at 0.551 seconds, was used as the conditioning period. For ASCE 7-16, magnitudes between 6 to 7.5, and Rjb values between 10 to 50 km were considered during spectrum generation. Each selection method comprised 55 ground motions, consisting of 11 unique motions per return period across five return periods.

Figure 2 (a) visually represents the mean target spectrum or CMS, alongside the CMS \pm conditional σ spectra and the spectra of the selected ground motions, where σ is the standard deviation. It's noteworthy that all these chosen ground motions fall within the CMS \pm conditional σ range, ensuring their suitability for the analysis. This stringent selection process guarantees that the chosen ground motions closely align with the specific seismic characteristics of the site.

ASCE 7-16 establishes a comprehensive framework for selecting ground motions. The latest edition offers detailed guidelines on how to specify these motions concerning acceptable hazard and risk levels. It mandates a minimum of 11 ground motion time histories for each target spectrum. ASCE 7-16 also allows the use of ground motions scaled to scenario spectra, providing an alternative to the risk-targeted uniform hazard spectrum. In this edition, ground motions were chosen based on spectral matching between $0.2T$ to $2.0T$, where T represents the fundamental period of the structure in its fundamental mode for the analysed response direction [27]. In the ASCE 7-16 process, the risk-targeted uniform hazard spectrum serves as the target spectrum. Figure 2 (b) visually represents the mean target spectrum, along with the $\pm \sigma$ spectra and the spectra of the chosen ground motions.

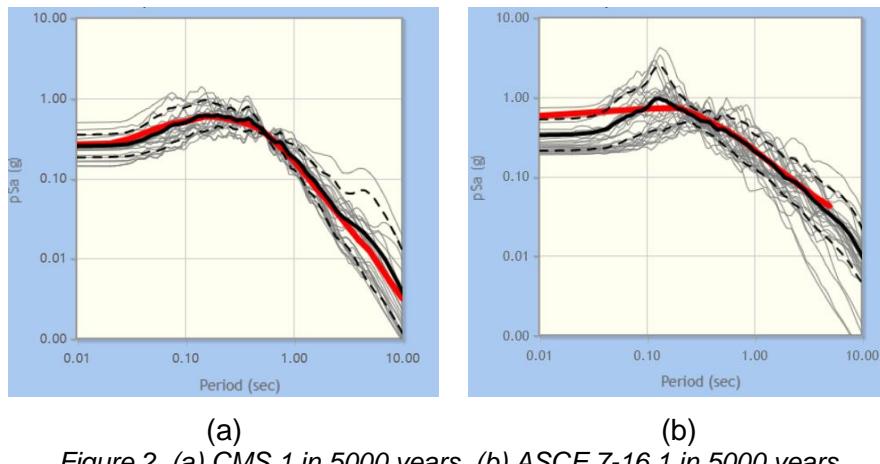


Figure 2. (a) CMS 1 in 5000 years, (b) ASCE 7-16 1 in 5000 years

3.2 Numerical model

The numerical simulation of the coupled DFR system, as well as the monolith of the Pine Flat dam, is shown in Figure 3 (a), (b). The simulation was conducted using the Abaqus 2022 standard version [28]. The model incorporates both fluid-structure interaction and soil-structure interaction. The reservoir is represented using acoustic elements (AC2D4), while the concrete dam and rock foundation utilize plain stress elements (CPS4R). Infinite elements (CINPE4) are employed for peripheral elements of the foundation. The material properties employed in the simulation are detailed in Table 1. Damping in the dam and foundation is implemented using Rayleigh damping. Tie contacts are established between the dam, foundation, and reservoir, and non-reflecting boundary conditions are defined at the periphery of the foundation. Additionally, a zero-pressure surface is defined at the top of the reservoir.

The model incorporates material nonlinearity through the concrete damage plasticity (CDP) model, with specific properties outlined in Table 2. The nonlinear dynamic analysis focuses on a singular loading scenario, encompassing self-weight, hydrostatic thrust, hydrodynamic effects, and seismic loads. Seismic loading is applied in combinations with both horizontal components either as H_1V or H_2V . Here, the ground motions have been applied at the base of the dam. Alternatively, they could be deconvoluted and applied to the base of the foundation [29]. These analyses maintained consistent parameters, including the dam's geometry, material properties, and contact characteristics, ensuring a uniform evaluation. The simulations yielded essential data, including the crest displacement history and tensile damage area ratio (DAR). This evaluation provided a

robust foundation for understanding the dam's response under varied seismic conditions, enabling comprehensive risk assessments, and strengthening the overall safety protocols of the Pine Flat Dam.

Table 1. Elastic material properties of dam, foundation, and reservoir for Pine Flat Dam [30]

Material properties	Concrete	Foundation	Reservoir
Density (ρ)	2482 kg/m ³	2640 kg/m ³	1000 kg/m ³
Modulus of elasticity (E)	22407 MPa	22407 MPa	-
Bulk modulus (K)	-	-	2070 MPa
Poisson's ratio	0.2	0.333	-
Rayleigh damping Alpha (α)	-	1.64	-
Rayleigh damping Beta (β)	0.004333	0.00668	-

Table 2. CDP properties for Pine Flat Dam

Ψ_c^*	σ_{co} (MPa)	σ_{cu} (MPa)	σ_{to} (MPa)	e	R
36.31°	12.08	22.41	2.24	0.1	1.16

* Ψ_c : dilatation angle; σ_{co} : compressive initial yield stress; σ_{cu} : compressive ultimate yield stress; σ_{to} : tensile failure stress; e: flow potential eccentricity and R: ratio of the initial equibiaxial to the uniaxial compressive yield stress.

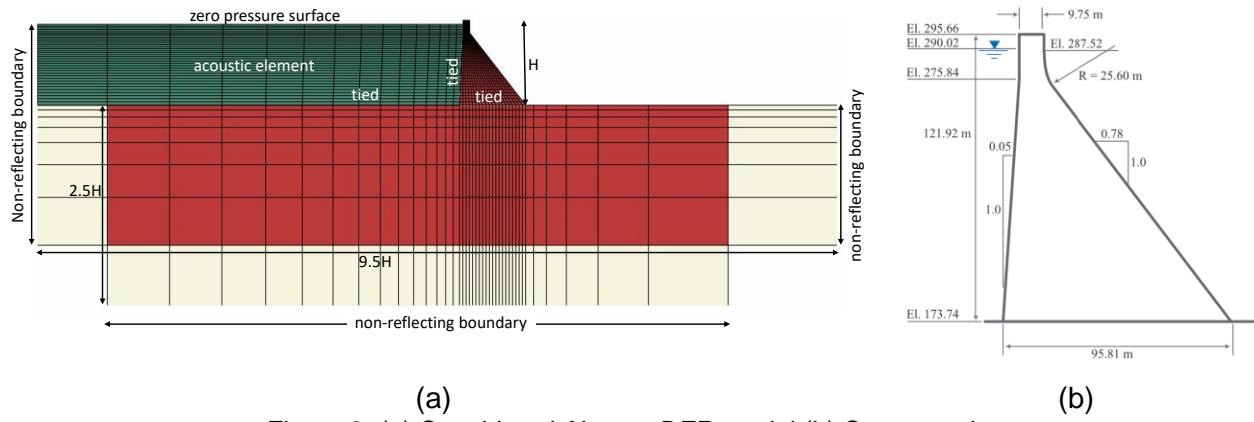


Figure 3. (a) Considered Abaqus DFR model (b) Cross section

4 Fragility analysis

4.1 Damage limit states

The key parameters under investigation, crest displacement, and damage area ratio, are vital indicators of the dam's structural integrity. DAR as shown in Equation 1, represents the percentage of the dam cross-section area that is damaged due to the exceedance of tensile stress during seismic events. The elements with DAR values between 0.6 to 1 are considered damaged. Excessive crest displacement not only signifies potential damage to the dam itself but also raises concerns about the integrity of ancillary structures. Crest displacement and tensile damage area ratio, when combined with ground motion return periods, facilitate the development of fragility curves. These curves serve as probabilistic representations of the likelihood of specific damage states occurring. In this study, limit states as a function of the DAR and crest displacement were defined. The crest displacement values were normalized with respect to the height of the dam. Normalized crest displacement (NCD) was calculated using Equation 2.

$$DAR = \frac{\text{dam cross section area that is damaged}}{\text{total cross section area of dam}} \quad (1)$$

$$NCD = \frac{\text{crest displacement}(m)}{\text{height of the dam}(m)} \quad (2)$$

The considered limit states are provided in Table 3.

Table 3. Damage limit States

Limit State	Range	
LS ₀ - Minor damage	DAR > 1%	NCD > 0.02%
LS ₁ - Moderate damage	DAR > 3%	NCD > 0.08%
LS ₂ - Severe damage	DAR > 5%	NCD > 0.11%

4.2 Fragility framework

Fragility analysis is a crucial technique in assessing the vulnerability of engineered systems to specific events, often used in seismic engineering and other fields where structural integrity is paramount [6]. The fragility function, $P_f(y)$, as shown in Equation 3 indicates the likelihood of structural failure given a specific ground motion intensity measure (IM) level. In this context, y represents the demand variable measured in the same units as the IM. D is the probability of exceeding a failure threshold. d_i refers to different damage states, such as minor, moderate, and severe (IM) represents the Intensity measure parameters.

$$P_f(y) = P[D > d_i | IM = y] \quad (3)$$

In the context of a gravity dam, the fundamental failure modes encompass sliding, overturning, tensile cracking, and compressive crushing. In this study, the structural limit states considered are tensile crack failure and normalized crest displacement, as proposed in the previous section. To construct fragility curves, the log-normal cumulative distribution function (CDF) is employed. The failure probability (P_f) can be calculated using Equation 4.

$$P_f = \Phi \left[\frac{\ln(y) - \alpha}{\beta} \right] \quad (4)$$

In this equation, Φ represents the standard normal distribution function, and α and β are the mean and the standard deviation of the lognormal CDF, respectively.

4.3 Fragility function

The fragility curves generated for the 5-intensity-level correspond to five return periods. In each of the 22 nonlinear dynamic analyses conducted for each return period, combined H₁V or H₂V ground motion records were utilized. This resulted in a total of 110 analyses per selection method. For each simulation, DAR and NCD were computed. Table 4 and Table 5 provides a summary of fraction of collapse, i.e., samples where NCD and DAR values exceeded the limit state, for CMS and ASCE 7-16 respectively. The limit states were considered based on DAR and NCD as detailed in section 4.1. The results from Table 4 and Table 5, representing the five fragility point estimates, were used to develop fragility curves for the three considered limit states.

Table 4. Fraction of collapse for CMS

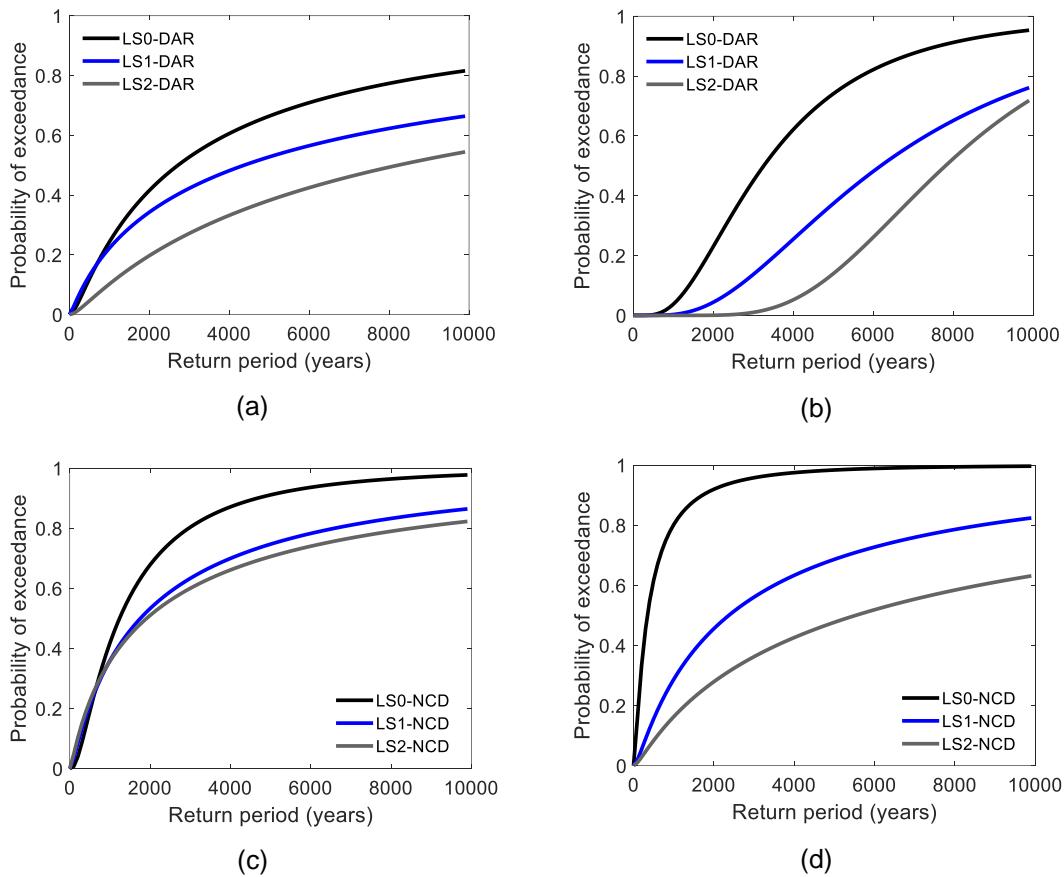
Return Period	1in10000	1in5000	1in2475	1in975	1in475
DAR Limit state					
LS0	18/22	16/22	8/22	7/22	2/22
LS1	15/22	11/22	8/22	7/22	1/22
LS2	12/22	9/22	4/22	3/22	1/22
NCD Limit state					
LS0	22/22	19/22	16/22	11/22	2/22
LS1	16/22	15/22	15/22	9/22	2/22
LS2	17/22	16/22	15/22	9/22	2/22

Table 5. Fraction of collapse for ASCE 7-16

Return Period	1in10000	1in5000	1in2475	1in975	1in475
DAR limit state					
LS0	20/22	17/22	7/22	1/22	1/22
LS1	17/22	8/22	2/22	1/22	0/22
LS2	16/22	3/22	1/22	1/22	0/22
NCD Limit state					
LS0	22/22	22/22	20/22	18/22	13/22
LS1	18/22	15/22	12/22	5/22	4/22
LS2	14/22	11/22	6/22	4/22	2/22

4.4 Fragility curves

The Figure 4 (a) and (b) shows the fragility curves based on DAR for CMS and ASCE 7-16. The fragility curves depict a progressive shift from minor to severe damage states as the return period increases, aligning with the expected behavior of the dam structure under seismic loading. Across all limit states, the fragility results show an increased probability of exceeding the damage states as the the return period increases. CMS appears to be more sensitive to lower intensity levels than ASCE 7-16, especially evident in LS1. CMS predicts slightly higher failure probabilities than ASCE 7-16 for similar return periods. This indicates that for the same ground motion, the structure is more likely to experience damage at lower return period values when using CMS.

*Figure 4. Fragility curves (a) CMS-DAR, (b) ASCE 7-16-DAR, (c) CMS-NCD (d) ASCE-NCD*

Similarly, the Figure 4 (c) and (d) shows the fragility curves based on NCD for CMS and ASCE 7-16. NCD fragility curves show similar trends for minor damages (LS0), aligning closely with DAR based fragility curves. For moderate damages (LS1), DAR and NCD fragility show differences, especially in CMS predictions. NCD tends to predict higher probabilities of moderate damages than DAR. Similarly, for severe damages (LS2), the difference between DAR and NCD is more pronounced. The fragility estimates based on NCD show higher probabilities for severe damages compared to those based on DAR. Here, NCD-based fragility appears to

provide more conservative estimates, especially for moderate and severe damages, compared to DAR. Considering that, the choice between DAR and NCD should be made based on the desired level of conservatism and the risk tolerance of the project. Further as observed in DAR based fragility, CMS tends to be more conservative across all limit states, especially for moderate and severe damages. Depending on the specific requirements of the project and the acceptable level of risk, the DAR or NCD based fragility, or a hybrid type can be selected for a comprehensive and accurate evaluation of a structure's vulnerability.

4.5 Impact of the record selection method: ASCE 7-16 vs. CMS

Figure 5 (a) and (b) shows the comparison of DAR and NCD fragility curves based on ASCE 7-16 and CMS. The choice of ground motion selection based on ASCE 7-16, or CMS depends upon the project-specific risk tolerance and the desired level of conservatism in the analysis. ASCE 7-16 provides reliable fragility estimates for minor and moderate damages, making it suitable for structures where conservative estimates are acceptable. CMS exhibits a more cautious approach, especially for severe damage states, making it valuable when a more conservative risk assessment is necessary. For minor and moderate damages: both methods offer reasonable predictions, but CMS leans towards a more conservative estimate, which could be advantageous in risk-averse scenarios. Similarly, for severe damages CMS provides a more conservative estimate, which might be essential for critical structures where understanding worst-case scenarios is crucial. The divergence between the methods underscores the importance of understanding and addressing uncertainties in seismic fragility assessments. Careful consideration of site-specific parameters and ground motion records is vital in producing accurate predictions, especially for critical infrastructures like dams. This analysis highlights the significance of comprehensively evaluating different limit states and considering multiple methodologies to obtain a holistic view of a structure's vulnerability under seismic stress. It emphasizes the need for a nuanced approach, considering both the practical implications and the level of conservatism required for a given engineering scenario.

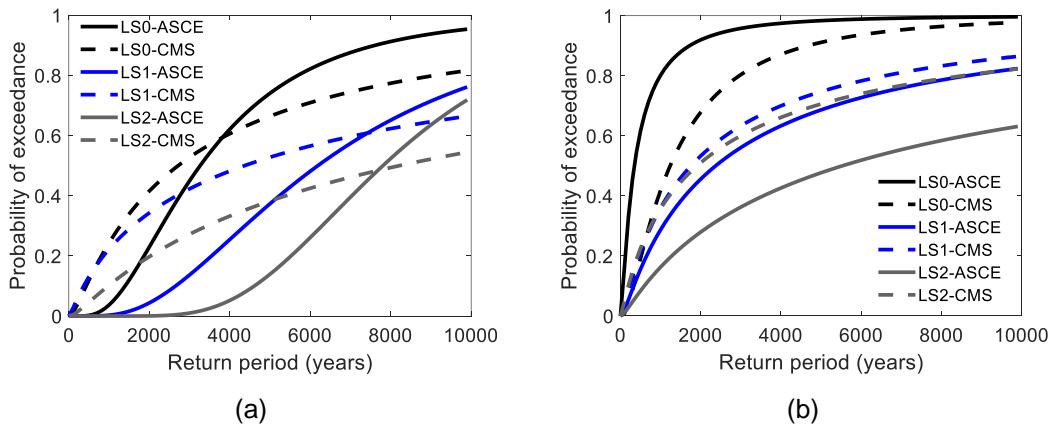


Figure 5. Fragility curves comparison between ASCE 7-16 and CMS: (a) DAR, (b) NCD

5 Conclusion

Seismic performance assessment is an important step in dam safety evaluation, especially in the regions of high seismic activities. This study has delved deep into the uncertainties in ground motion selection, scrutinizing their impact on the seismic response of dams. An extensive analysis, incorporating fragility analysis based on DAR, NCD, limit states has been conducted to understand their interrelationships in the context of dam vulnerabilities under seismic hazard. The key inferences drawn from the analysis are detailed below.

- (i) Practical and precise definition of limit the states is crucial; minor variations significantly influence fragility predictions, emphasizing the need for clear and consistent standards in structural assessments.
- (ii) ASCE 7-16 method of ground motion selection strikes a balance between accuracy and practicality, making it suitable for general applications where moderate conservatism is acceptable. On the other hand, CMS, being

more conservative, is vital in scenarios where a higher degree of safety is paramount, especially for critical infrastructure and risk-averse projects.

(iii) Both DAR and NCD based fragility assessment offer valuable perspectives on structural vulnerability. DAR captures a broader overview of damage states, while NCD provides detailed displacement-based insights. The choice between them depends on the assessment objective.

The findings underscore the importance of robust ground motion selection methodologies, and use of multiple damage indices for fragility assessment. The nuanced insights gained from the fragility plots pave the way for informed decision-making in dam engineering, urging for a paradigm shift towards probabilistic frameworks and fragility-based analyses.

6 Acknowledgement

Support of the Natural Sciences and Engineering Research Council of Canada (NSERC) is gratefully acknowledged.

7 References

- [1] ASCE, "2017 infrastructure report card," in *American Society of Civil Engineers*, 2017.
- [2] R. L. Segura, J. E. Padgett, and P. Paultre, "Metamodel-Based Seismic Fragility Analysis of Concrete Gravity Dams," *J. Struct. Eng.*, vol. 146, no. 7, Art. no. 7, Jul. 2020, doi: 10.1061/(ASCE)ST.1943-541X.0002629.
- [3] L. B. Lave, D. Resendiz-Carrillo, and F. C. McMichael, "Safety goals for high-hazard dams: Are dams too safe?," *Water Resources Research*, vol. 26, no. 7, pp. 1383–1391, 1990.
- [4] B. Ellingwood and P. B. Tekie, "Fragility Analysis of Concrete Gravity Dams," *J. Infrastruct. Syst.*, vol. 7, no. 2, Art. no. 2, Jun. 2001, doi: 10.1061/(ASCE)1076-0342(2001)7:2(41).
- [5] M. T. Schultz, B. P. Gouldby, and J. Simm, "Beyond the factor of safety developing fragility curves to characterize system reliability," 2010.
- [6] P. B. Tekie and B. R. Ellingwood, "Seismic fragility assessment of concrete gravity dams," *Earthquake Engng. Struct. Dyn.*, vol. 32, no. 14, Art. no. 14, Nov. 2003, doi: 10.1002/eqe.325.
- [7] N. Jayaram, T. Lin, and J. W. Baker, "A Computationally Efficient Ground-Motion Selection Algorithm for Matching a Target Response Spectrum Mean and Variance," *Earthquake Spectra*, vol. 27, no. 3, pp. 797–815, Aug. 2011, doi: 10.1193/1.3608002.
- [8] B. K. Patra, R. L. Segura, and A. Bagchi, "Modeling Variability in Seismic Analysis of Concrete Gravity Dams: A Parametric Analysis of Koyna and Pine Flat Dams," *Infrastructures*, vol. 9, no. 1, p. 10, 2024.
- [9] A. Sarkar, S. Ghodke, and A. Bagchi, "Performance of 2D-spectral finite element method in dynamic analysis of concrete gravity dams," *Structures*, vol. 59, p. 105770, Jan. 2024, doi: 10.1016/j.istruc.2023.105770.
- [10] Y. Ghanaat, R. C. Patev, and A. K. Chudgar, "Seismic Fragility Analysis of Concrete Gravity Dams," in *15th World Conference on Earthquake Engineering*, lisbon,Portugal, Sep. 2012, p. 10. [Online]. Available: https://www.iitk.ac.in/nicee/wcee/article/WCEE2012_4524.pdf
- [11] J. W. Baker, "Efficient Analytical Fragility Function Fitting Using Dynamic Structural Analysis," *Earthquake Spectra*, vol. 31, no. 1, pp. 579–599, Feb. 2015, doi: 10.1193/021113EQS025M.
- [12] C. Bernier, R. Monteiro, and P. Paultre, "Using the Conditional Spectrum Method for Improved Fragility Assessment of Concrete Gravity Dams in Eastern Canada," *Earthquake Spectra*, vol. 32, no. 3, pp. 1449–1468, Aug. 2016, doi: 10.1193/072015EQS116M.
- [13] M. A. Hariri-Ardebili and V. E. Saouma, "Collapse Fragility Curves for Concrete Dams: Comprehensive Study," *J. Struct. Eng.*, vol. 142, no. 10, Art. no. 10, Oct. 2016, doi: 10.1061/(ASCE)ST.1943-541X.0001541.
- [14] M. A. Hariri-Ardebili and V. E. Saouma, "Probabilistic seismic demand model and optimal intensity measure for concrete dams," *Structural Safety*, vol. 59, pp. 67–85, Mar. 2016, doi: 10.1016/j.strusafe.2015.12.001.

- [15] R. Chandramohan, J. W. Baker, and G. G. Deierlein, "Impact of hazard-consistent ground motion duration in structural collapse risk assessment," *Earthquake Engineering & Structural Dynamics*, vol. 45, no. 8, pp. 1357–1379, 2016, doi: 10.1002/eqe.2711.
- [16] B. F. Soysal, B. Özer Ay, and Y. Arici, "Evaluation of the Ground Motion Scaling Procedures for Concrete Gravity Dams," *Procedia Engineering*, vol. 199, pp. 844–849, Jan. 2017, doi: 10.1016/j.proeng.2017.09.014.
- [17] R. L. Segura, C. Bernier, R. Monteiro, and P. Paultre, "On the Seismic Fragility Assessment of Concrete Gravity Dams in Eastern Canada," *Earthquake Spectra*, vol. 35, no. 1, pp. 211–231, Feb. 2019, doi: 10.1193/012418EQS024M.
- [18] S. Gorai and D. Maity, "Seismic response of concrete gravity dams under near field and far field ground motions," *Engineering Structures*, vol. 196, p. 109292, Oct. 2019, doi: 10.1016/j.engstruct.2019.109292.
- [19] G. Sevieri, A. De Falco, and G. Marmo, "Shedding Light on the Effect of Uncertainties in the Seismic Fragility Analysis of Existing Concrete Dams," *Infrastructures*, vol. 5, no. 3, Art. no. 3, Feb. 2020, doi: 10.3390/infrastructures5030022.
- [20] A. R. Tidke and S. Adhikary, "Seismic fragility analysis of the Koyna gravity dam with layered rock foundation considering tensile crack failure," *Engineering Failure Analysis*, vol. 125, p. 105361, Jul. 2021, doi: 10.1016/j.engfailanal.2021.105361.
- [21] J. W. Baker, "Conditional Mean Spectrum: Tool for Ground-Motion Selection," *Journal of Structural Engineering*, vol. 137, no. 3, Art. no. 3, Mar. 2011, doi: 10.1061/(ASCE)ST.1943-541X.0000215.
- [22] USGS, "Unified Hazard Tool," Earthquake Hazards Program. Accessed: Oct. 29, 2023. [Online]. Available: <https://earthquake.usgs.gov/hazards/interactive/>
- [23] "PEER Ground Motion Database - PEER Center." Accessed: Oct. 29, 2023. [Online]. Available: <https://ngawest2.berkeley.edu/>
- [24] D. F. McPhillips, J. A. Herrick, S. Ahdi, A. K. Yong, and S. Haefner, "Updated compilation of VS30 data for the United States," *US Geol. Surv. Data Release*, 2020, doi: <https://doi.org/10.5066/P9H5QEAC>.
- [25] A. Shumway, M. D. Petersen, P. M. Powers, and S. Rezaeian, "Additional period and site class maps for the 2014 National Seismic Hazard Model for the conterminous United States," US Geological Survey, 2018.
- [26] K. W. Campbell and Y. Bozorgnia, "NGA-West2 Ground Motion Model for the Average Horizontal Components of PGA, PGV, and 5% Damped Linear Acceleration Response Spectra," *Earthquake Spectra*, vol. 30, no. 3, pp. 1087–1115, Aug. 2014, doi: 10.1193/062913EQS175M.
- [27] J. W. Baker and M. Lew, "Ground motion selection and acceptance criteria when multiple seismic sources contribute to MCE ground motions".
- [28] D. Systèmes, "Abaqus analysis user's guide, version 6.22." Dassault Systèmes, 2022. Accessed: Oct. 29, 2023. [Online]. Available: https://docs.software.vt.edu/abaqusv2022/English/?show=SIMULIA_Established_FrontmatterMap/DSDochome.htm
- [29] G. S. Sooch and A. Bagchi, "A new iterative procedure for deconvolution of seismic ground motion in dam-reservoir-foundation systems," *Journal of Applied Mathematics*, vol. 2014, pp. 1–10, 2014, doi: <https://doi.org/10.1155/2014/287605>.
- [30] M. N. Viladkar and A. M. S. Al-Assady, "Nonlinear analysis of pine flat dam including base sliding and separation," in *Proceeding of the 15th World Conference on Earthquake Engineering (15 WCEE), Lisbon*, Lisbon: 15th World Conference on Earthquake Engineering (15 WCEE), 2012, p. 9. [Online]. Available: https://www.iitk.ac.in/nicee/wcee/article/WCEE2012_3374.pdf

DECONVOLUTION OF REAL AND ARTIFICIAL ACCELERATIONS FOR DYNAMIC ANALYSIS OF DAMS

M. Poul¹ and M.A. Hariri-Ardebili²

¹ Pacific Gas & Electric (PG&E), San Francisco, CA, USA, masoud.poul@pge.com

² University of Maryland, College Park, MD, USA

Abstract: This paper examines the impact of the deconvolution process on the dynamic response of concrete gravity dams built on rock foundations, considering both actual ground motions and intensified artificial accelerations (IAAs) in soil-structure interaction (SSI) analysis. In SSI analysis, deconvolution is a common process used to compute effective earthquake loads at the depth of the rock profile. A detailed nonlinear finite element simulation of a concrete dam with a massive foundation is conducted to explore two scenarios: (1) where all selected motions are deconvolved to the depth, and equivalent nodal forces are used, and (2) where input motions are treated as outcrop motions, and the corresponding effective earthquake loads are directly applied to the depth. The rationale for the second input motion mechanism is that, since the shear wave velocity of the rock foundation is very high and damping is low, the deconvolution process may be ignored, as the effect of wave propagation in a finite foundation depth would not be significant. Results for both real ground motions and IAAs are presented. It has been found that ignoring the deconvolution process in real ground motions and IAAs (without any further post-processing) leads to an overestimation of the structural response, and the rock-damping ratio plays a critical role. However, it is noted that the results follow a very similar pattern, and ignoring the deconvolution process only impacts the amplitude of the results.

1. Introduction

Structural safety and risk analysis are of paramount importance for critical infrastructure, encompassing bridges, dams, nuclear facilities, and more (FEMA956 and FEMA 2015). A key component in this analysis is the consideration of ground motion records. Time history-time integration procedures are widely used to model structural responses, but their accuracy hinges on the quality of ground motion records, introducing inherent uncertainties.

To address this issue, probabilistic seismic analysis techniques, including incremental dynamic analysis, cloud analysis, and multiple-stripe analysis, are recommended for their ability to account for record-to-record variability. However, these methods necessitate a substantial number of simulations, which can be computationally expensive, making them impractical for certain types of infrastructure, such as dams.

This paper explores the impact of the deconvolution process on the dynamic response of concrete gravity dams built on rock foundations, considering both real ground motions and intensifying artificial accelerations (IAA) in soil-structure interaction (SSI) analysis. The study employs nonlinear finite element simulations for a concrete dam with a massed foundation, comparing scenarios with and without deconvolution for real ground motions and IAAs. Results reveal that neglecting deconvolution leads to overestimated structural responses,

influenced by ground motion variability and damping. The paper also proposes a practical framework for IAAs that avoids deconvolution, maintaining accuracy and expediting risk assessment for complex geostructures.

2. Intensifying Artificial Acceleration

In endurance time analysis (ETA), generating IAAs is a key challenge (Estekanchi et al. 2020). IAAs mimic the dynamic response of the structural system, ranging from elastic to nonlinear behavior and structural failure in a single transient analysis (Saouma and Hariri-Ardebili, 2021).

Creating IAAs is a nonlinear optimization process that initially focuses on acceleration response spectra but can extend to displacement response spectra, energy dissipation, nonlinear displacement, and effective cycle count. A review of the optimization of IAAs, their variabilities, and their correlation with various ground motion sets can be found in Hariri-Ardebili and Sattar (2023). Unconstrained nonlinear optimization is the core method for constructing IAAs by iteratively matching their dynamic characteristics to target values.

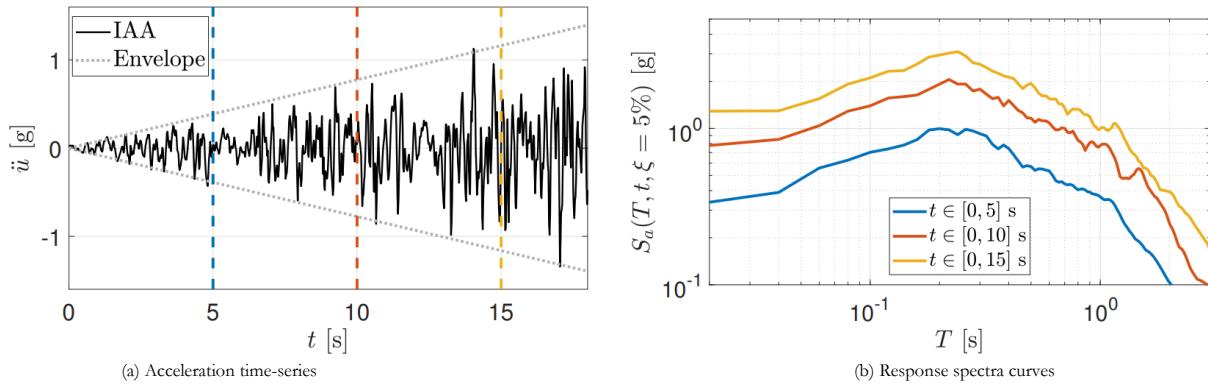


Figure 1: A sample intensifying artificial acceleration, and some of its intensity measures.

The IAA comprises a purposefully devised acceleration time series characterized by two distinct attributes. Firstly, the envelope of the acceleration time history escalates linearly with time (see Figure 1(a)). Secondly, the response spectra of the IAA, for any interval $t \in [0, t^*]$, demonstrate a linear increase over time, showcased in Figure 1(b). This figure illustrates a representative IAA along with its response spectra at three distinct time instances (0-5 s, 0-10 s, and 0-15 s). Notably, the response spectrum for the interval $t \in [0, 10]$ s is nearly twice that of the interval $t \in [0, 5]$ s, while the spectrum for the interval $t \in [0, 15]$ s is approximately three times larger than that of $t \in [0, 5]$ s. It is noteworthy that the response spectra can be extrapolated indefinitely for any chosen time interval $t \in [0, t^*]$, forming a comprehensive response spectrum surface instead of a mere curve.

3. Deconvolution of dynamic excitation for SSI Analysis

Concrete gravity dams are built on rock foundations. To manifest a pragmatic numerical model for the analysis of this coupled system, it's imperative to directly incorporate the domains of the dam, foundation, and reservoir, as visually depicted in Figure 2. Including the effect of SSI is advantageous, as neglecting it typically leads to higher structural responses.

The most direct and commonly used method for modeling a rock foundation in finite element methods is the utilization of a massless foundation system. The primary reasons for choosing this foundation system are as follows: (1) preventing the reflection of seismic waves at fixed boundaries, thereby eliminating the need for implementing absorbing boundary conditions; (2) avoiding the necessity for deconvolution analysis; and (3) directly applying free-field motion at the base of the rock foundation. While this approach is highly efficient, its application can lead to a significant overestimation of dam response in both linear and nonlinear finite element method analyses. It is important to note that this approach only considers the flexibility of the foundation, ignoring the full SSI effect.

To incorporate the full SSI effect, the mass of the foundation domain should be taken into account, proper boundary conditions need to be implemented to absorb outgoing waves, and the seismic motions should be precisely deconvolved to the foundation base.

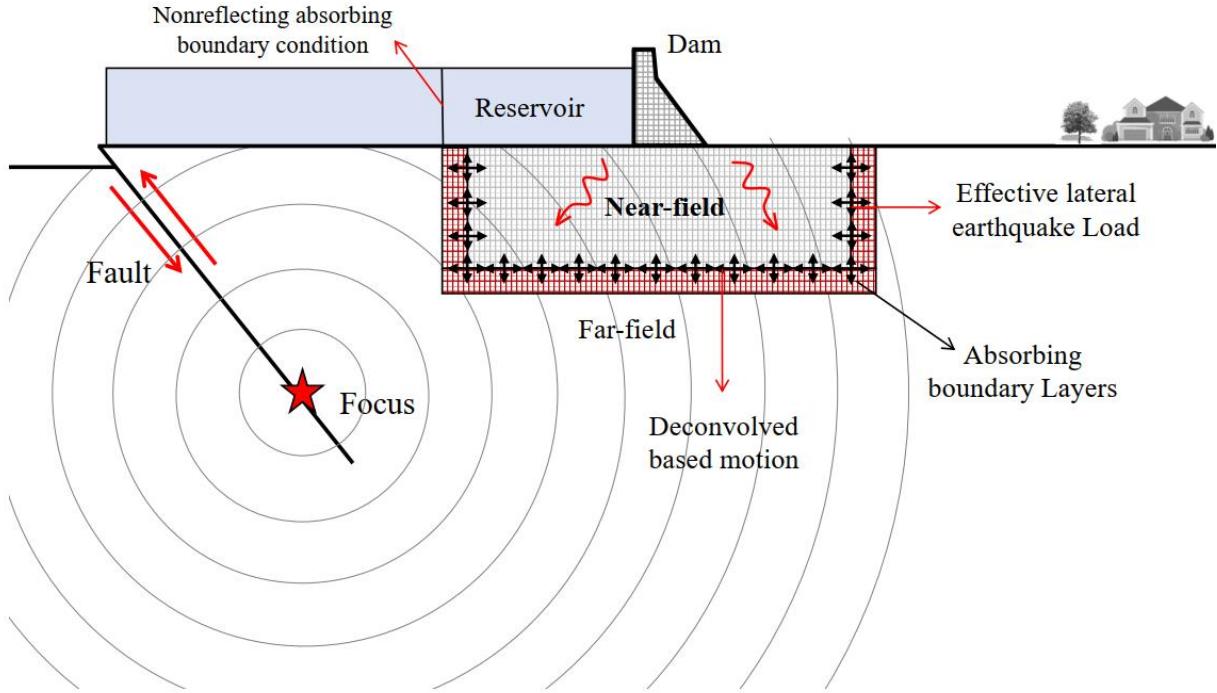


Figure 2: View of a geostructure including the fault rupture, earthquake wave propagation, and modeling of near-/far-field domains for the soil-structure interaction

The deconvolution technique, as introduced in Poul and Zerva (2018a, b), was employed in this study to determine the input excitation at the depth of the rock foundation, utilizing infinite-element absorbing boundary conditions. This method has proven to be reliable for foundation models equipped with viscous-type boundary conditions, including infinite elements, demonstrated through a few iterations as outlined in Poul and Zerva (2018c). The following explanation provides a brief overview of the procedure for both Perfectly Matched Layer (PML) and viscous-type boundary conditions.

(1)- Establish a FEM model of the rock profile and apply the PML ABCs at the surfaces encompassing the finite foundation domain to absorb the outgoing waves at the boundaries.

(2)- Apply the horizontal and vertical time histories of the nodal forces caused by the incident waves at the bottom of the rock profile, i.e., the shared nodes of the interior and PML domains. Then, a dynamic time-domain analysis is required. The time histories of the nodal forces are defined as:

$$\mathbf{F}_s^{\text{Input}}(t) = 2\rho bt C_s^{\text{eq}} \dot{u}_s^{\text{Input}}(t) \quad (1a)$$

$$\mathbf{F}_p^{\text{Input}}(t) = 2\rho bt C_p^{\text{eq}} \dot{u}_p^{\text{Input}}(t) \quad (1b)$$

where $\dot{u}_s^{\text{Input}}(t)$ and $\dot{u}_p^{\text{Input}}(t)$ are the velocity time history of the incident waves at depth for S- and P-waves, respectively. C_s^{eq} and C_p^{eq} are the equivalent shear and compressional wave velocities in the layer at which the time histories of the nodal forces are applied. In the first iteration, assume that: $\dot{u}_s^{\text{Input}}(t) = 0.5\dot{u}_s^{\text{Target}}(t)$ and $\dot{u}_p^{\text{Input}}(t) = 0.5\dot{u}_p^{\text{Target}}(t)$, where $\dot{u}_s^{\text{Target}}(t)$ and $\dot{u}_p^{\text{Target}}(t)$ are the velocity time histories of the target motions at the free surface.

The velocity time histories of the incident waves at depth can be expressed in terms of their amplitude and phase by means of the Fast Fourier Transform (FFT):

$$\dot{u}_s^{\text{Input}}(\omega) = 0.5\dot{u}_s^{\text{Target}}(\omega) = |\dot{u}_s^{\text{Input}}(\omega)| \exp[i\varphi_s^{\text{Input}}(\omega)] \quad (2a)$$

$$\dot{u}_p^{\text{Input}}(\omega) = 0.5\dot{u}_p^{\text{Target}}(\omega) = |\dot{u}_p^{\text{Input}}(\omega)| \exp[i\varphi_p^{\text{Input}}(\omega)] \quad (2b)$$

and the response ground motions at the free surface become:

$$\ddot{u}_s^{\text{Response}}(\omega) = |\ddot{u}_s^{\text{Response}}(\omega)| \exp[i\varphi_s^{\text{Response}}(\omega)] \quad (3a)$$

$$\ddot{u}_p^{\text{Response}}(\omega) = |\ddot{u}_p^{\text{Response}}(\omega)| \exp[i\varphi_p^{\text{Response}}(\omega)] \quad (3b)$$

(3)- Evaluate the effective phase shifts and the amplitude modification factors of the shear and compressional waves. The effective phase shifts are defined as the difference in phase between the surface ground acceleration and the phase of the input motion, namely

$$\bar{\varphi}_s^{\text{Shift}}(\omega) = \varphi_s^{\text{Response}}(\omega) - \varphi_s^{\text{Input}}(\omega) \quad (4a)$$

$$\bar{\varphi}_p^{\text{Shift}}(\omega) = \varphi_p^{\text{Response}}(\omega) - \varphi_p^{\text{Input}}(\omega) \quad (4b)$$

(4)- Generate the new input motions at the base of the system according to the following expressions:

$$\dot{u}_s^{\text{Input (new)}}(\omega) = \beta_s(\omega) \cdot |\dot{u}_s^{\text{Input}}(\omega)| \exp[i(\varphi_s^{\text{Target}}(\omega) - \bar{\varphi}_s^{\text{Shift}}(\omega))] \quad (5a)$$

$$\dot{u}_p^{\text{Input (new)}}(\omega) = \beta_p(\omega) \cdot |\dot{u}_p^{\text{Input}}(\omega)| \exp[i(\varphi_p^{\text{Target}}(\omega) - \bar{\varphi}_p^{\text{Shift}}(\omega))] \quad (5b)$$

The amplitude modification factors for the PML ABCs are defined as:

$$\beta_s(\omega) = |\dot{u}_s^{\text{Target}}(\omega)| / |\dot{u}_s^{\text{Response}}(\omega)| \quad (6a)$$

$$\beta_p(\omega) = |\dot{u}_p^{\text{Target}}(\omega)| / |\dot{u}_p^{\text{Response}}(\omega)| \quad (6b)$$

(5)- Perform an inverse FFT to obtain the new input motion from step (4) in the time domain.

(6)- Compute the new equivalent nodal force time histories from Eqs. 1a and 1b, apply them at the bottom of the rock profile, and evaluate the ground motions at the free surface. The results need to be compared with the target motions.

(7)- If required, perform iterations until acceptable results are obtained. Generally, the first or second iteration yield acceptable results. However, when absorbing boundaries, which impose minor nonlinearities in the system, are used, additional iterations can improve the precision.

Since the formulation of the PML and Infinite ABCs are different, the deconvolved base motions are not similar. Therefore, the target motions should be deconvolved separately for each of the foundation models.

In this study, the input motion for analyses with no deconvolution is defined as the time histories of nodal force resulting from half of the energy of the dynamic excitation at the free surface. The rationale is that the motion at the free surface results from the summation of incident and reflected waves. It should be noted that, in the FEM, half of the energy propagates downward; therefore, the nodal force is multiplied by a factor of two.

4. Case Study and Analysis Scenarios

This section discusses the impact of the deconvolution process on the nonlinear response of a concrete gravity dam (Koyna Dam) using both real ground motions and IAAs.

4.1. Analysis Scenarios

As previously discussed, the main objective of this paper is to assess the viability of applying Deconvolved IAAs (DIAAs) to problems involving SSI.

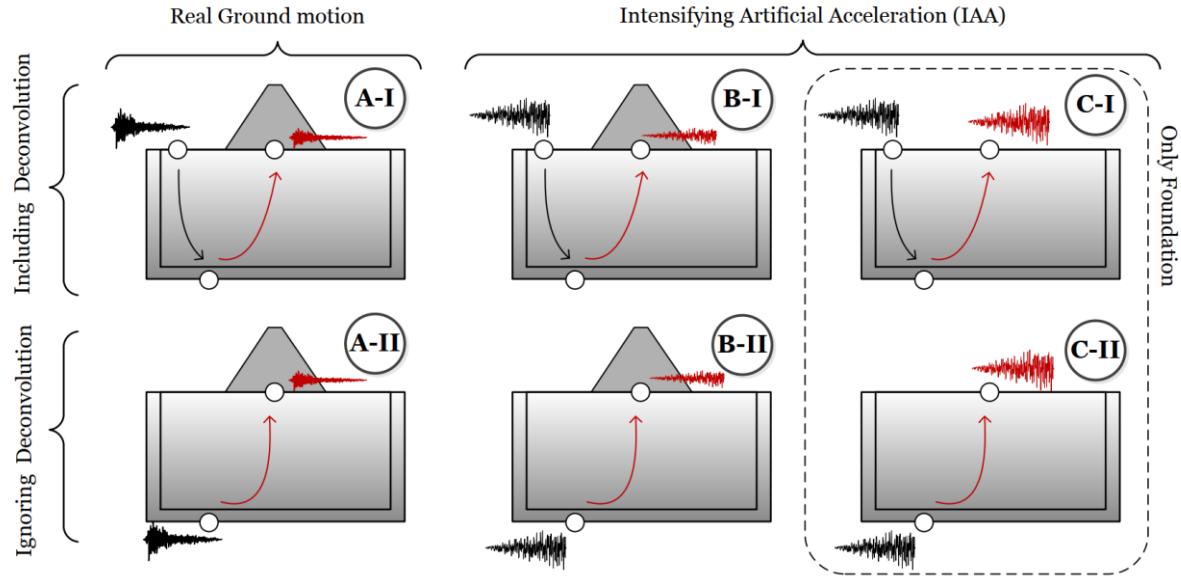


Figure 3: Comparison of different scenarios studied in this paper including the deconvolution process with real ground motions and IAAs

To accomplish this objective, six distinct scenarios are defined and depicted in Figure 3. Scenarios marked with the index “I” incorporate the deconvolution process. This implies that the initial motion is first subjected to deconvolution and subsequently applied at the bottom of the foundation. Conversely, scenarios marked with the index “II” bypass the deconvolution process, directly employing the dynamic excitations without deconvolution (whether it’s a real ground motion or an IAA) at the bottom of the massed foundation model. The scenarios labeled with the index “A” employ real ground motions, while those labeled “B” and “C” involve IAAs. In scenario “C,” the superstructure is excluded to facilitate a more precise exploration of upward seismic wave propagation.

The primary objective of scenario “C” is to precisely analyze the deconvolution process within the context of IAAs and evaluate the time-acceleration relationship. However, in scenarios “A” and “B,” the emphasis lies in illuminating the fundamental differences between a real ground motion and an IAA, especially concerning the deconvolution process.

4.2. Case Study

This paper employs the Koyna Dam as a case study, a well-established benchmark in research. The 2D finite element model of the dam-foundation-reservoir system, created in ABAQUS, assumes a homogeneous, isotropic, linear viscoelastic rock foundation (Poul and Zerva 2018a). Solid infinite elements at the foundation’s far end absorb outgoing waves. The foundation depth is modeled as twice the structure’s height. Four-node plane-stress elements (CPS4) were used for the modeling of the concrete dam and the plane-strain assumption for foundation rock (CPE4). The reservoir is represented as a linear compressible inviscid fluid employing four-node bilinear acoustic elements (AC2D4). Implicit time integration is used for all transient analyses, and surface-based fluid-structure interaction model interactions at the dam-reservoir and foundation-reservoir interfaces.

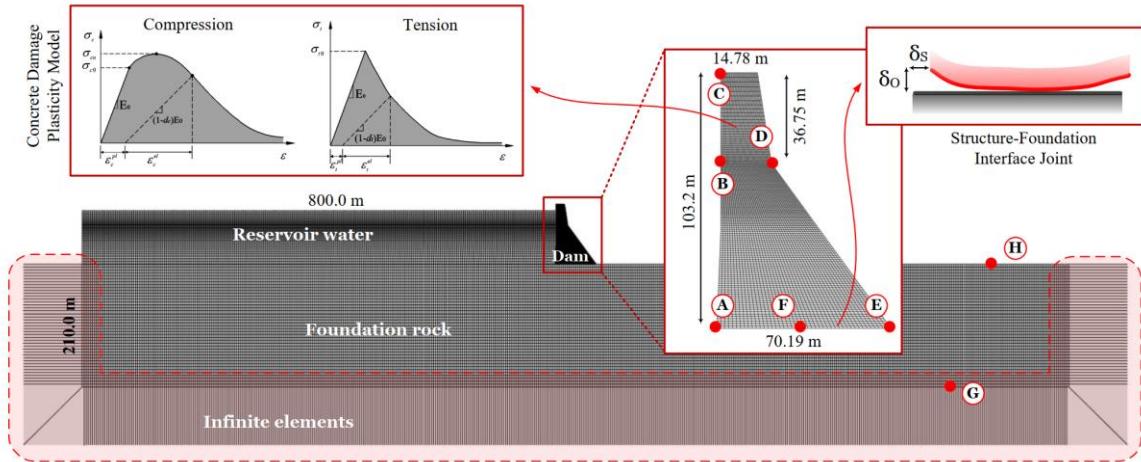


Figure 4: Finite element model of the coupled system including the index points, structure-foundation joint model, and nonlinear constitutive model of concrete under uniaxial loading.

This study introduces nonlinearities into the finite element model by incorporating both continuum and discrete damage models. The concrete damage plasticity model is employed to simulate material-level damage in the concrete, combining concepts of isotropic damaged elasticity with isotropic tensile and compressive plasticity. This approach considers both tensile cracking and compressive crushing by degrading the initial elastic stiffness of the concrete material, utilizing a scalar degradation damage variable denoted as "d," ranging from 0.0 (no damage) to 1.0 (full damage).

Moreover, the dam-foundation interface joint is modeled using surface-based contact pairs, assuming a rigid contact for normal interactions to facilitate contact pressure transfer and surface separation when the contact pressure reaches zero. Additionally, Coulomb's friction law, incorporating allowable slip, is applied to simulate tangential interaction.

5. Results

This section showcases the results of nonlinear transient analyses carried out on the coupled dam system using both IAA and a representative real ground motion record. It's crucial to emphasize that the primary focus of this paper is not to compare the results between IAA and real ground motions. Instead, the emphasis is solely on applying various IAA generations with and without the deconvolution process. It's worth noting that the sensitivity of the deconvolution process to damping ratios will be discussed in Section 5. For all simulations involving IAA and real ground motions, a constant damping ratio of 3.5% is utilized.

5.1. Real Ground Motion Record

In this section, the significance of the deconvolution process is explored for two records: Narrows-01 (Record 1) and Kobe Japan (Record 2). To assess scenario "A" in Figure 3, a total of four numerical simulations are carried out – two with the deconvolution effect and two without it. The detailed results, as depicted in Figure 5, are individually presented for the selected ground motion records, focusing on crest displacement, base joint sliding, and the concrete damage profile.

Analysis of the displacement time histories (Figures 5(a) and 5(d)) reveals an apparent phase shift in the results. Specifically, the finite element model with deconvolved motion exhibits a slight delay compared to the case without the deconvolution process. This delay stems from the wave travel between the foundation base and the surface. While this delay is not inherently significant, as it doesn't alter the structural analysis results, both crest displacement and base sliding demonstrate changes in response magnitude. Omitting the

deconvolution process leads to a higher structural response, with the differences dependent on the ground motion record, its inherent characteristics, and intensity.

For instance, in the case of Record 1, the difference in base sliding is merely 5%; however, for Record 2, this difference escalates to 20%. A similar trend holds true when examining the concrete damage profile. It is noted that the results follow a very similar pattern, and ignoring the deconvolution process in the rock foundation only impacts the amplitude of the results. Figures 5(b) and 5(e) also exhibit a similar pattern for the sliding of the dam with some discrepancies in amplitude.

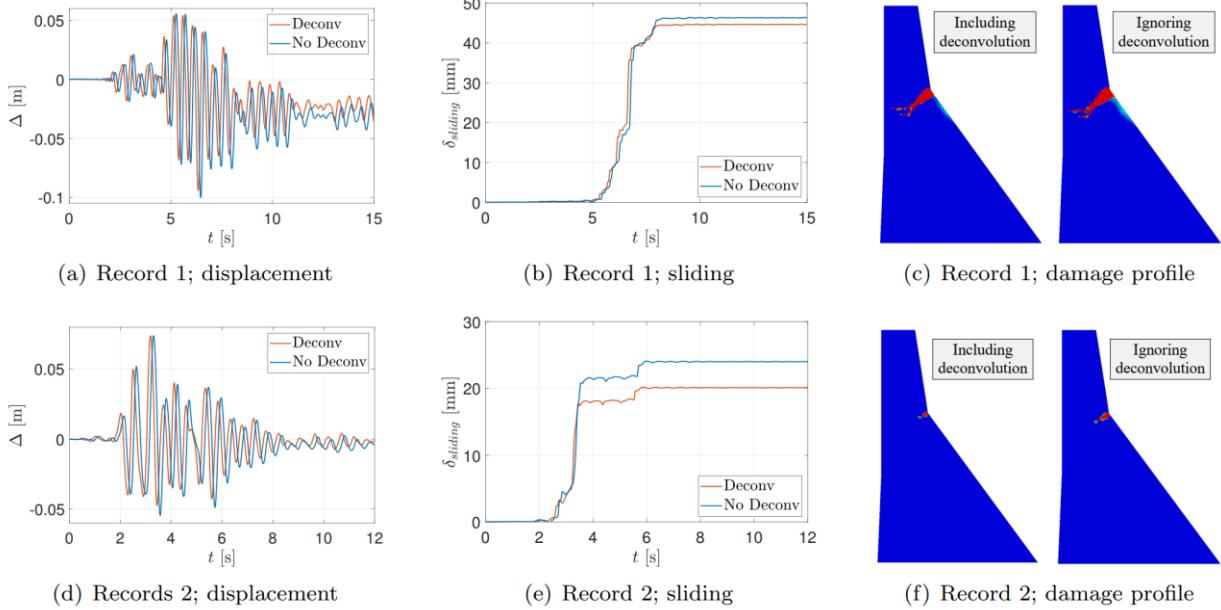


Figure 5: Comparison of structural responses from scenario “A” with two real ground motions.

5.2. IAA

Figure 6 compares the acceleration time series and response spectra of an IAA (selected from the 2nd generation of IAAs) with and without the deconvolution process. Additionally, Figure 6(b) depicts the acceleration time series and their envelopes for scenario “C” (foundation only). This illustrates how the IAA propagates within the foundation when the superstructure is absent.

Upon comparing the time series, it becomes evident that the wave with deconvolution shows a delay, indicated by a leftward phase shift. This observation aligns with what we previously reported for real ground motion as well.

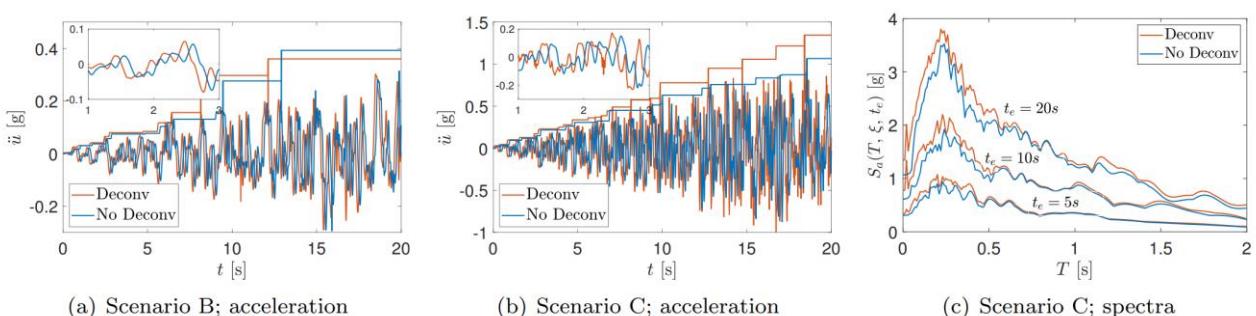


Figure 6: Anatomy of recorded acceleration with (Scenario “B”) and without (Scenario “C”) presence of the structure and including/ignoring the deconvolution process. The results are for G2S2 for sample.

Figure 7 assesses the sensitivity of the simulations to variations in the damping value, using G2S2 as an illustrative IAA. Consistent with the previous methodology, finite element models are generated both with and without the deconvolution process. In cases without the process, higher damping values lead to a reduced magnitude of the free-field acceleration (Figure 7a). This, consequently, results in decreased recorded structural responses, as seen in the displacement and joint sliding behaviors in Figures 7b and 7c, respectively.

For simulations involving the deconvolution process, our focus shifts to the nodal forces applied at the base of the foundation model (Figure 7d). The process aims to match the time histories of convolved surface ground motions to the target one. When a higher damping ratio is chosen for the rock foundation, a stronger input motion at depth becomes necessary. This explains why Figure 7d shows the derived input motion at depth for 5% damping being stronger than the one with 1% damping.

Figures 7e and 7f compare the crest displacement and joint sliding, respectively. We observe that when the deconvolution process is applied, similar dam responses are expected for different selected damping ratios of the rock foundation. It is noted that the results follow a very similar pattern, and ignoring the deconvolution process in the rock foundation only impacts the amplitude of the results.

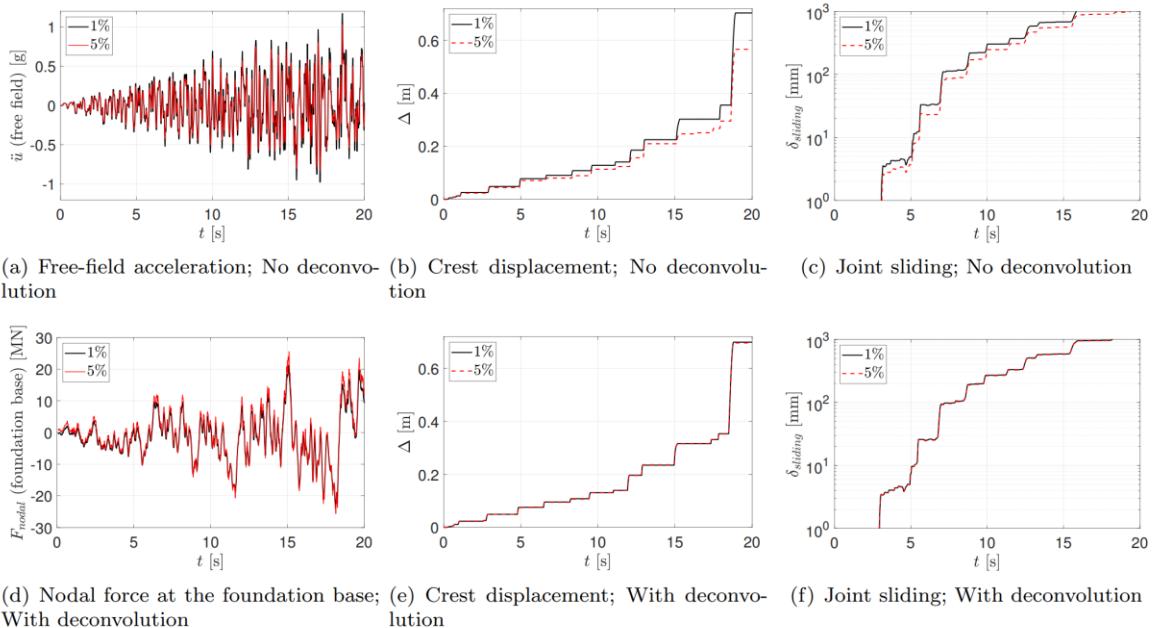


Figure 7: Sensitivity of IAA (G2S2) to damping ratio.

6. Conclusion

This paper explores the influence of the deconvolution process on the nonlinear response of a concrete dam when subjected to both real ground motions and intensifying artificial acceleration (IAA) motions. Through a comprehensive nonlinear finite element simulation of a concrete dam with a massed foundation, two scenarios are investigated: (1) where all selected motions are deconvolved to the depth with the use of equivalent nodal forces, and (2) where the input motions are considered as outcrop motions, and the corresponding effective earthquake loads are directly applied to the depth.

It has been found that ignoring the deconvolution process in real ground motions and IAAs (without any further post-processing) leads to an overestimation of the structural response, and the rock-damping ratio plays a critical role. However, it is noted that the results follow a very similar pattern, and ignoring the deconvolution process in the rock foundation only impacts the amplitude of the results.

7. References

- FEMA-956, Living With Dams: Know Your Risks, FEMA P-956, Technical Report, Federal Emergency Management Agency, Washington, DC, 2013.
- FEMA, Federal guidelines for dam safety risk management, Technical Report, Federal Emergency Management Agency, Washington, DC, 2015.
- Estekanchi, H. E., Mashayekhi M., Vafai H., Ahmadi G., Mirfarhadi S. A., Harati M., A state-of-knowledge review on the endurance time method, *Structures* 27 (2020) 2288–2299.
- Hariri-Ardebili, M. A., & Sattar, S. (2023). Uncertainty and bias in fragility estimates by intensifying artificial accelerations. *Probabilistic Engineering Mechanics*, 74, 103545.
- Saouma V. E., Hariri-Ardebili M. A., Aging, Shaking, and Cracking of Infrastructures: From Mechanics to Concrete Dams and Nuclear Structures, Springer, 2021.
- Poul M. K., Zerva A., Efficient time-domain deconvolution of seismic ground motions using the equivalent-linear method for soil-structure interaction analyses, *Soil Dynamics and Earthquake Engineering* 112 (2018a) 138–151.
- Poul M. K., Zerva A., Nonlinear dynamic response of concrete gravity dams considering the deconvolution process, *Soil Dynamics and Earthquake Engineering* 109 (2018b) 324–338.
- Poul M. K., Zerva A., Time-domain PML formulation for modeling viscoelastic waves with Rayleigh-type damping in an unbounded domain: Theory and application in Abaqus, *Finite Elements in Analysis and Design* 152 (2018c) 1–16.

DYNAMIC ANALYSES OF AN EARTH DAM WITH DIFFERENT INITIAL STRESS STATE

R. Previtali¹, R. Pellegrini², F. Carnevale² & P. Chemello³

¹ ISMES, Seriate, Italy, riccardo.previtali@ismes.it

² ISMES, Seriate, Italy

³ Enel Green Power, Rome, Italy

Abstract: This paper reports of the outcomes of the seismic assessment of a homogeneous earth dam located in Northern Italy carried out according to the Italian dam regulation. The assumed behaviour of the soil materials of the dam and its foundation follows a non-associated Mohr-Coulomb elasto-plastic law. A nonlinear hysteretic damping model is also included to reproduce cyclic elastic strain energy dissipation. The nonlinear seismic analyses, performed into FLAC2D, consider seven different natural horizontal and vertical accelerograms compatible with the reference spectra defined through a site-specific probabilistic seismic hazard analysis. The main parameters of the geotechnical model of the dam-foundation system are derived from specific experimental campaign. Since the dam is founded on clayey, normally consolidated, deformable soils, the progressive settlements of the embankment are calibrated through a back analysis of the measured dam settlements to get the current degree of consolidation, the spatial distribution of the interstitial overpressures and the residual time of the primary consolidation process. Focus is made on the effects of the initial distribution of stresses and pore pressures within the dam body and its foundation on its seismic response.

1. Foreword

The dam, about 90 years old, located in the Italian Alpine region, despite its modest highness (11.2m) guarantees 40 million cubic metres of water impounding because of its planimetric extension (its overall length is 1980m). This is the reason why it is a strategic existing dam according to the Italian Ministry of infrastructures and transport. The Italian Code for Dams (NTD14) and the Italian Building Code (NTC18) foresee in this case that seismic assessments be carried out by applying several natural earthquakes as time histories to the dam-foundation system, all ensuring spectral compatibility with the assigned hazard spectrum. To account for the expected strong shaking due to ultimate state earthquakes, the dam and its foundation have been modelled within a coupled non-linear approach by an elastic plastic constitutive model and by a nonlinear hysteretic damping model. A careful assessment of the initial condition of the dam and foundation system is therefore required.

Dams in service exhibit some long-term settlement. An almost linear relationship between settlement and the logarithm of time has been observed in many cases described in the literature of earth and rockfill dams (Hunter and Fell, 2003). Long term settlements are meant as a creep effect not involving changes of the in-situ stress.

Tedd et al. (1997) suggest that settlement index, as defined by Charles (Charles, 1986), exceeding 2% of the initial crest dam height may indicate in earth dams the presence of deformation mechanisms other than creep, recommending a more in-depth analysis. The values calculated for the dam under investigation are indeed higher than the 0.02 threshold, leading, therefore, to consider processes other than creep. In this case, the measured settlements are considered as an effect of the still progressing primary consolidation of the foundation soil, a thick layer of loamy clay; accordingly, some overpressures are still in place and modify the initial effective stresses and ultimate strength to shearing induced by the seismic action.

2. The Dam

2.1. Materials

The earth dam, of the homogenous type, with a simple originary trapezoidal section, has been built in 1927 with materials coming mostly from the eastern zone of the reservoir and, to a lesser extent, from the excavation site of a discharge canal in the interior of the lake. At the most depressed point of the foundation, the embankment reached a height of 10.50 m (original elevation 388.00 m a.s.l.).

At the western side, the embankment rests, for a short length, on a lithoid substratum of calcareous reddish marly sediments. This formation, distinctly stratified, dips towards east, with a low inclination, Figure 1, resulting in increased thickness of the upper loamy-clay layer. At dam's centre these clayey deposits reach the remarkable thickness of 180-200 m. On the eastern shore the embankment is founded on silty-clayey deposits, and it is very likely that the rocky base can be found, locally, at a depth not exceeding 35-45 m.

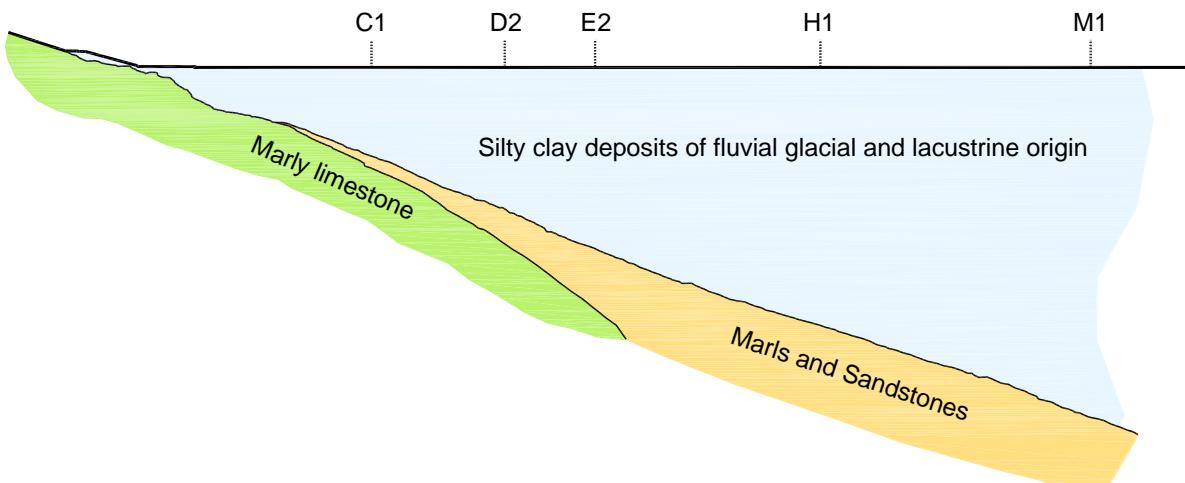


Figure 1. Geological section along dam longitudinal axis with evidence of relevant sections (C1, D2, E2, H1 e M1), after Milli (1986).

2.2. Construction and upgrades

The embankment was built in 1927, while normal operation of the dam began in 1930. Because of the consolidation of the soil foundation, the dam highlighted settlements of the downstream face and a longitudinal depression along the crest, both subject to periodic fills and reloading.

In years 1967-69 the dam has been raised from a crest elevation of 388.70 m a.s.l. to an elevation of 389.20 m a.s.l. to comply with the regulations on the admitted dam freeboard.

Between March 2006 and December 2009, the freeboard was reset (Figure 2), by increasing the elevation of the embankment up to 389.5 m a.s.l.. Work on the dam was carried out using loamy soil (named type A) of the same grain size of the existing dam body, compacted to 90% of the modified Proctor test density, and coarser soil (named type C) for the lower berm built on the downstream face. The fine soils have been taken from loan quarries located within the lake, near the eastern part of the dam, and the coarser soils in the bed of a tributary stream. Today dam's height is variable up to a maximum of 11.2m.

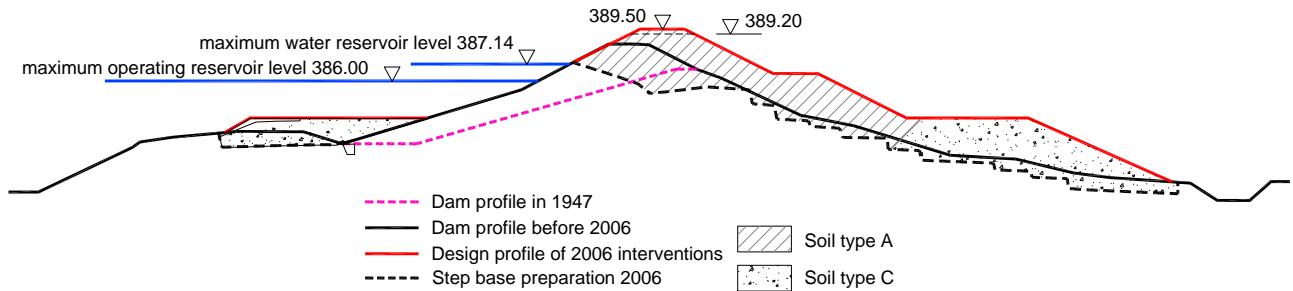


Figure 2. Dam section E2: today section of the dam with evidence of additions.

2.3. Dam behavior from monitoring data

Based on data gathered by the structural and hydraulic monitoring system, it has been possible to identify an overall regular behavior of the dam along its long service life. A peculiar aspect is dam settlement, with a rate of a few cm/year, still in progress since construction, which has been recognized as the response to loads of the low stiffness of the foundation clayey soils, which have been recognized as normally consolidated (Adami et al., 2010). Maximum values and higher rates are measured at the topographic survey points CLSD2, CSLC1, CSLE2, places nearby the dam crest on its upstream face (Figure 1, Figure 3).

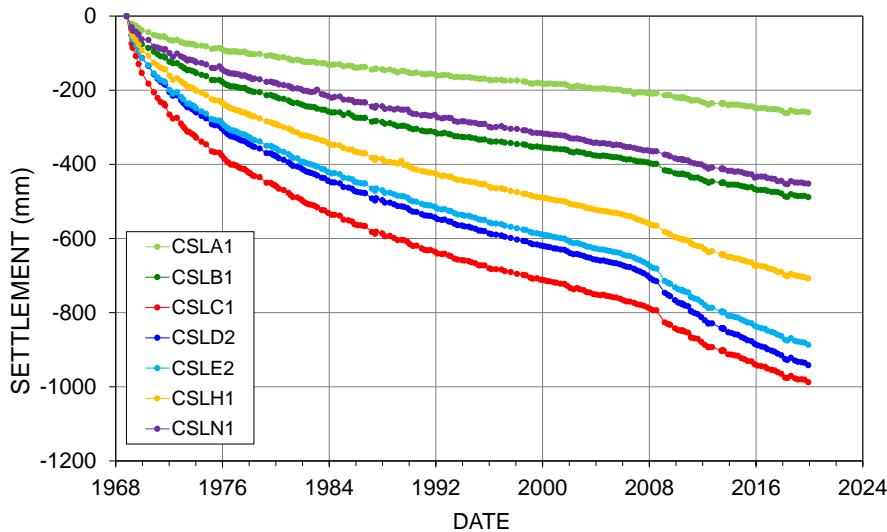


Figure 3. Settlement of the dam measured from 1968 to 2019 at significant topographical survey points.
CSLE2 refers to section E2.

2.4. Consolidation analysis

A PLAXIS2D® finite element model (FEM) of dam's Section E2 has been set up. The FEM model represents the entire soil foundation down to the stiff marly base lying about 104 m below the ground level.

The physical and mechanical properties of the dam and its foundation soils have been first determined by processing all the available experimental data and observations gained at different times from construction, typically in preparation of the restoration works, Table 1. Compliance related model parameters (C_r , C_s , e_0) and permeability (k_h , k_v) values of foundation soils have been calibrated seeking the most reasonable agreement with measured settlement values and evolution over time at the dam section E2, pertaining to the most settlement prone portion of the dam. By a process of back analysis, the better agreement has been obtained by varying values of some geotechnical properties as follows, in compliance with the geotechnical available evidence:

- by allowing for a slight overconsolidation of foundation soil down to 10m below the ground level assigning an overconsolidation ratio OCR decreasing from 4 to 1 in 10m.
- by increasing permeability of the deeper soils and assigning flow anisotropy (k_h/k_v) in the upper overconsolidated 10m of foundation soils.

- by increasing the compressibility in the normal consolidated range of deeper foundation soils (parameter C_c).

Table 1. Final geotechnical parameters of the dam and its foundation soils.

SOILS	γ_{wet} [kN/m ³]	$\gamma_{saturated}$ [kN/m ³]	c' [kPa]	ϕ' [°]	E' [MPa]	v' —	OCR	e_0	C_c	C_r	k_v [m/s]	k_h/k_v
Dam												
Type A	20.0	20.8	4	33	9	0.3	-	0.46	-	-	1e-7	1
Type C	23.0	23.3	-	40	50	0.3	-	0.19	-	-	1e-7	1
Overlay '67-'69	20.0	21.3	-	35	25	0.3	-	0.40	-	-	1e-7	1
Before '67	18.1	18.2	4	33	9	0.3	-	0.92	-	-	1e-7	1
Foundation												
From ground level 379m to el. 368 m	18.1	18.2	-	30	-	-	4÷1	0.92	0.3	0.035	1e-9	4
el. < 368 m	18.1	18.2	-	27	-	-	1	0.92	0.6	0.035	6e-10	1

where: γ : unit weight c' effective cohesion; ϕ' friction angle E': Young's modulus; v' Poisson's ratio

A hydro-mechanical coupled approach, in large deformations and providing for mesh update has been set. The mesh update allows to represent the effect of buoyancy on the portion of dam foundation settling below the water table, thereby reducing the effective load on foundation soils. A non-associated Mohr Coulomb constitutive model for the embankment soils and a Cam-Clay hardening plasticity model (Soft Soil Model of PLAXIS library) for the clayey foundation soils have been selected.

Settlements calculated at a Node of the model near to the dam crest (Node A) and at a Node nearer to the topographic survey point CSLE2 (Node B), which is placed nearby the crest on the upstream face of the dam, show a satisfying increase rate in time respect to measures. It is observed an almost constant gap of about 0.40 m between measures and model results in the early 30ties, when measures began. It is believed that early settlements measured at dam's operation start may be attributed to imbibition of the embankment material at the first filling of the reservoir, a known effect which cannot be predicted by this model. By increasing the calculated settlements by the 0.40m gap a satisfactory correspondence with measures is achieved starting from year 1940.

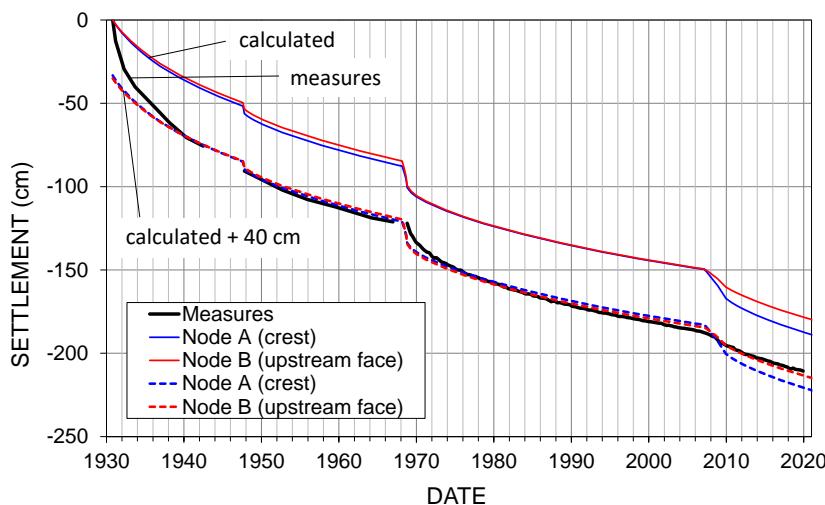


Figure 4 Calculated and measured crest settlement vs time. Dashed curves are obtained by adding to model calculated values (continuous line) a 0.40m settlement.

The current average degree of consolidation of the foundation soils, evaluated as the ratio between the developed and final settlement, is 74%; the final target value of 95% is achieved in about 160 years. According

to the model, the maximum final settlement predicted from construction at the foundation level is 3.42m including settlements developed before the start of the measures (year 1930).

The map of the residual overpressures predicted today, Figure 5, shows maximum values of approximately 59 kPa at a depth of 33 m from the ground level (elevation 346 m a.s.l.). The overpressures are zero in dam embankment. The bulb of residual overpressure is confined within the deeper clayey foundation soils.

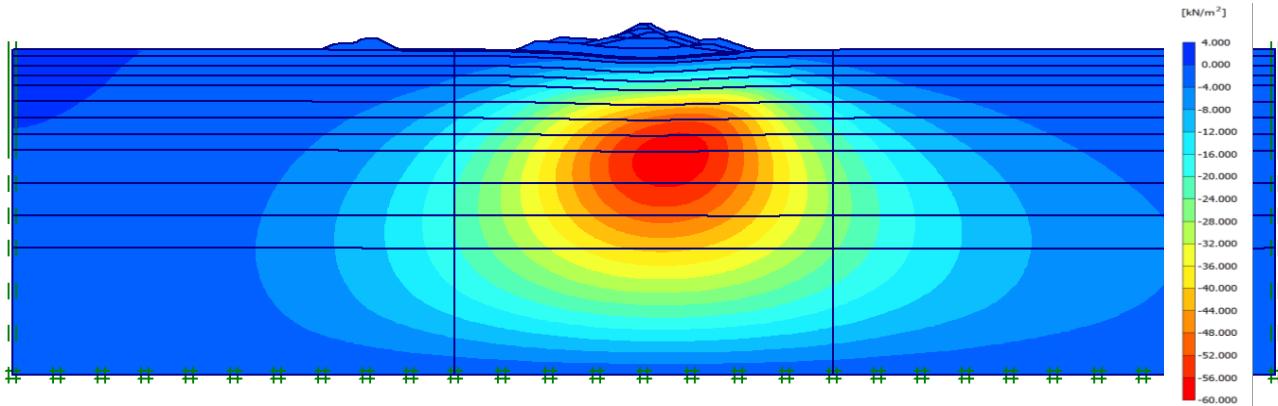


Figure 5. Contour map of predicted current residual water overpressures in Section E2 of the dam (PLAXIS). Maximum over pressure 58kPa. Pressure interval is 4kPa.

In 2001, Section E2 was equipped with a Casagrande piezometer in the foundation soil, placed at about 20 m below the dam foundation. In the period 2002-2006, prior to the last elevation of the dam, the height of the measured piezometric head was on average equal to 382.5 m a.s.l. very close to that predicted by this model. In 2010-2020 period, following the last elevation work, the average height of the measured piezometric surface (382.7 m a.s.l.) unexpectedly differs little from the value measured in the previous period, while the numerical model predicts a piezometric head rise 3m higher (385.6 m a.s.l.). Given the general consistency of the modelling approach with the experimental evidence provided by the dam and its foundation, it was concluded that the overpressure scenario calculated in the fine-grained soils of the dam foundation is a representative, and safe initial condition for the seismic analyses. The dynamic analyses have been however repeated under the scenario that overpressures in soil foundation have been completely dissipated before the seismic shaking to evaluate the sensitivity of results and effects on the seismic safety evaluation.

3. Seismic analyses

3.1. Earthquakes

Given the PSHA spectrum defined for a probability of occurrence of 5% which, according to NTD14 for strategic existing dams, corresponds to a return period $T_r=1950$ years, seven recorded earthquakes have been selected compliant to conditions such as the lithological quality of site (rock), the ruling momentum magnitude (M_w) - distance (D) couple defined by the site seismic hazard study, and the significant duration. The disaggregation analysis indicated the couple $M_w = 5.6 \div 6.3$ $D = 0 \div 20$ km for the assigned collapse ultimate limit state.

It was necessary to scale up the seven horizontal and vertical natural acceleration time histories to meet spectral compatibility to the target response spectrum. The range of vibrational periods identified to target the scaling was determined for both motion components as the estimated range between the fundamental period of the dam and its foundation, $T_0 = 0.22s \div 1.7s$.

Two of the seven acceleration time histories thus determined, which originate from the AQG and AQK recordings, appeared to herald significant seismic effects, due to their intensity and duration. Once applied to the E2 dam section, they are characterized also by a remarkable spectral amplification at periods corresponding to the fundamental period of the foundation soil, Figure 6.

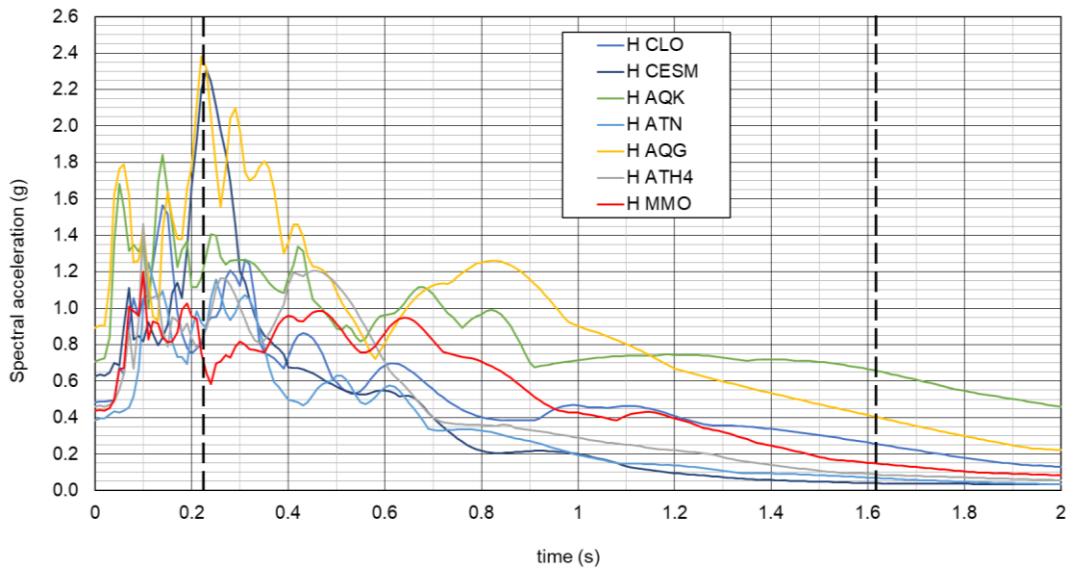


Figure 6. Horizontal response spectra of the seven earthquakes applied. The two dashed lines identify the fundamental period of the foundation ($T=1.61\text{s}$; $f=0.62\text{Hz}$) and that of the dam ($T=0.22\text{s}$; $f=4.5\text{Hz}$).

3.2. Seismic nonlinear coupled model

A plane strain finite difference model of the E2 section and the foundation down to the marly bedrock with the FLAC2D finite difference code.

The Masing nonlinear hysteretic damping model to reproduce cyclic elastic strain energy dissipation and the non-associated Mohr Coulomb constitutive model to describe plastic strain has been adopted. Small strain stiffness properties were determined by cross-hole geophysical tests performed on site, and from correlations with penetrometer CPT tests for the deeper soils, Table 2.

Dam and foundation cohesive soils have been assigned a decay law of dynamic shear stiffness properties (G_0) with the magnitude of induced shear deformation, based on the results of resonant column tests. Reference was made to curves published by Rollins et al., 1998 for granular materials (Type C, 'from ground level 379m to el. 368 m' in Table 2). The assigned evolution of shear stiffness and damping with shear deformation for the different materials has been described by the FLAC sigmoidal 4 parameter correlation function.

Table 2. Small strain properties assigned to the dynamic model.

SOILS	$\gamma_{\text{saturated}}$ [kN/m ³]	V_s [m/s]	G_0 [MPa]	[v] [-]
Dam				
Type A	20.8	126	29	0.46
Type C	23.3	240	137	0.46
Overlay '67- '69	21.3	200	29	0.46
Before '67	18.2	159	47	0.47
Foundation				
From ground level 379m to el. 368 m	18.2	170	54	0.48
274m < el. < 368 m	18.2	158 to 273 f(depth)	27	0.49
267m < el. < 274m	21.0	550	648	0.49
el. < 267m	21	800	1435	0.46

where V_s =Shear velocity G_0 =shear stiffness at small strains

To model the damping that occurs even for very small deformations, a 0.1% Rayleigh viscous damping has been applied, calibrated on the fundamental frequency of the dam, 4.5Hz.

Seven dynamic analyses have been carried out, applying at the compliant base of the model the vertical and horizontal time histories off each earthquake. The dam is subjected to the maximum operational reservoir level (386m a.s.l.) and the effective stress and pore pressure distribution resulting from the static consolidation model. The response to the seismic motion is the average value of results obtained by each earthquake applied.

3.3. Liquefaction potential

The model adopted assumes that the soils of the foundation and the dam body are stable towards liquefaction.

The grain size distribution of the site's soils, including fine-grained ones, requires carrying out checks of susceptibility to seismic liquefaction according to NTC18. The analysis was carried out by methods (Boulanger and Idriss, 2014; Robertson and Wride, 1998) based on correlations with the SPT and CPT penetrometer resistance values. It was possible to conclude that the granular soils of the dam body and its foundation are not prone to liquefaction. As fine-grained soils are regarded, based on the data available, they can be identified as 'clay-like' behaving soils according to Boulanger and Idriss (2006) and, therefore, not prone to liquefaction.

3.4. Results

The stress-strain response of the embankment is characterized by a deformation style consistent with that identified in the literature for earth dams (Swaisgood, 2003; Swaisgood, 2014), identifies as lateral spreading, but with a noticeably higher downstream displacement compared to that observed upstream. Deformation involves the dam body and the entire upper 10m silty foundation soil, Figure 8.

Horizontal displacements, Figure 7, involve dam's downstream portion and are of the same order of magnitude, and generally higher than the corresponding vertical ones: the maximum average value at the downstream face is 0.52 m while the maximum average crest settlement amounts to 0.37m. The observed trend is determined by shear strain bands; the most important originates on dam's upstream face and reaches its downstream toe and affects the upper silty foundation soils. For the most intense earthquakes a band develops in the dam body at the contact between the original 1930 dam and the new portion added in 2006-2009; it is again directed downstream and emerges below the upper berm. A local instability affects also the upstream face involving a thin portion of material where actually a concrete slab, not modelled, is in place protecting and confining most of the upstream face of the dam. Settlements are concentrated in the intermediate portion of the dam (Figure 9), while at the dam's toe some uplift is observed.

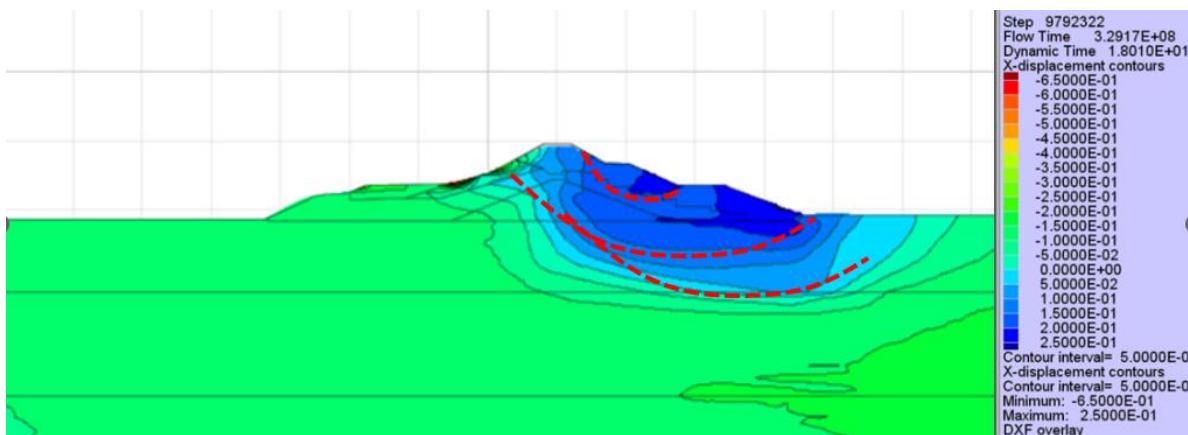


Figure 7. Contour of maximum horizontal displacements [m] and shear bands identifiers (in dashed red lines). CLO accelerogram, representative of the average effects.

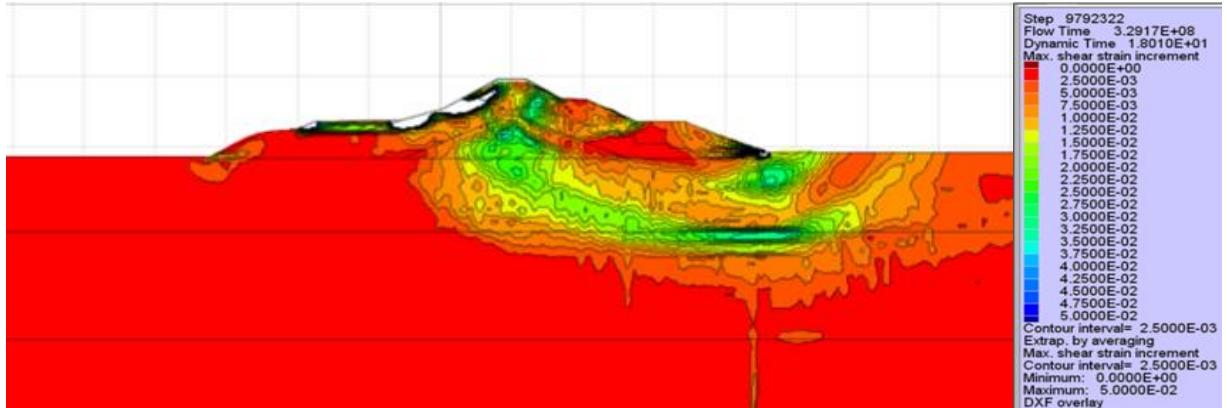


Figure 8 Contour of maximum shear strain increment [-]. CLO accelerogram, representative of the average effects.

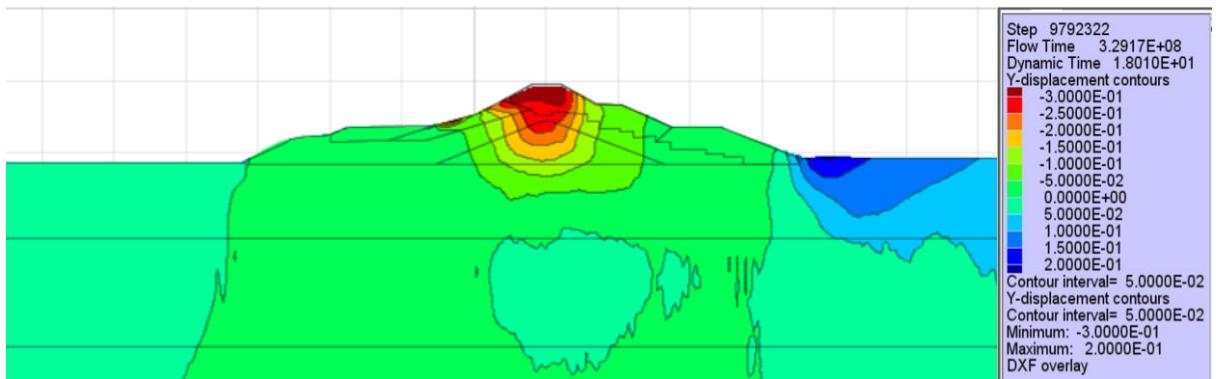


Figure 9. Contour of maximum vertical displacements [m]. CLO accelerogram, representative of the average effects.

The development of nonlinear shear strains and the effective damping of the thick foundation soils depress inertial effects in the dam body. The acceleration at crest (average $a_{max} = 5.49 \text{ m/s}^2$) is nearly de-amplified respect to that of outcrop (average $a_{max} = 5.59 \text{ m/s}^2$) and the amplification factor is lower than unity ($F_{AH} = 0.93$). The result is also consistent with findings by Lanzo (2018) on amplification ratios vs. base acceleration of as much as 30 existing embankment dams, Figure 10, Figure 11. The amplification ratio F_{AH} respect to the dam/foundation interface (average $a_{max} = 3.57 \text{ m/s}^2$) is 1.5 compliant to acknowledged ratios (Aliberti, et al., 2019), Figure 10.

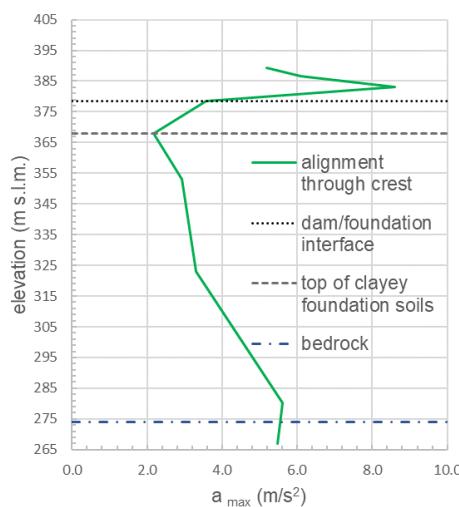


Figure 10. Envelope of maximum acceleration (average values) along the vertical alignment through dam's crest

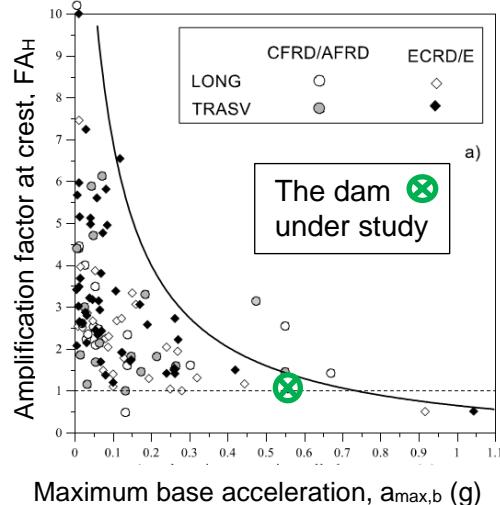


Figure 11. Amplification factor of acceleration at crest respect to base for dams. CFRD (Concrete Face Rockfill Dams); ECRD (Earthcore Rockfill Dam); E (Earthfill dam). After Lanzo (2018).

The shear stress vs. strain behavior sampled at single points of the model indicates that for this collapse ultimate state, hysteretic cyclic strains in the foundation coexist and are overcome by plastic irreversible strains in a large part of the upper foundation soil. Along the seismic induced shear bands, the plastic component prevails compared to the cyclic one. The shear stress-shear strain resulting in a point of the lower foundation soil (C3) and at the top foundation (C6) below the dam are given in

Figure 12 for two earthquakes: CESM, belonging to the group with minor seismic effects and AQG, one of the worse.

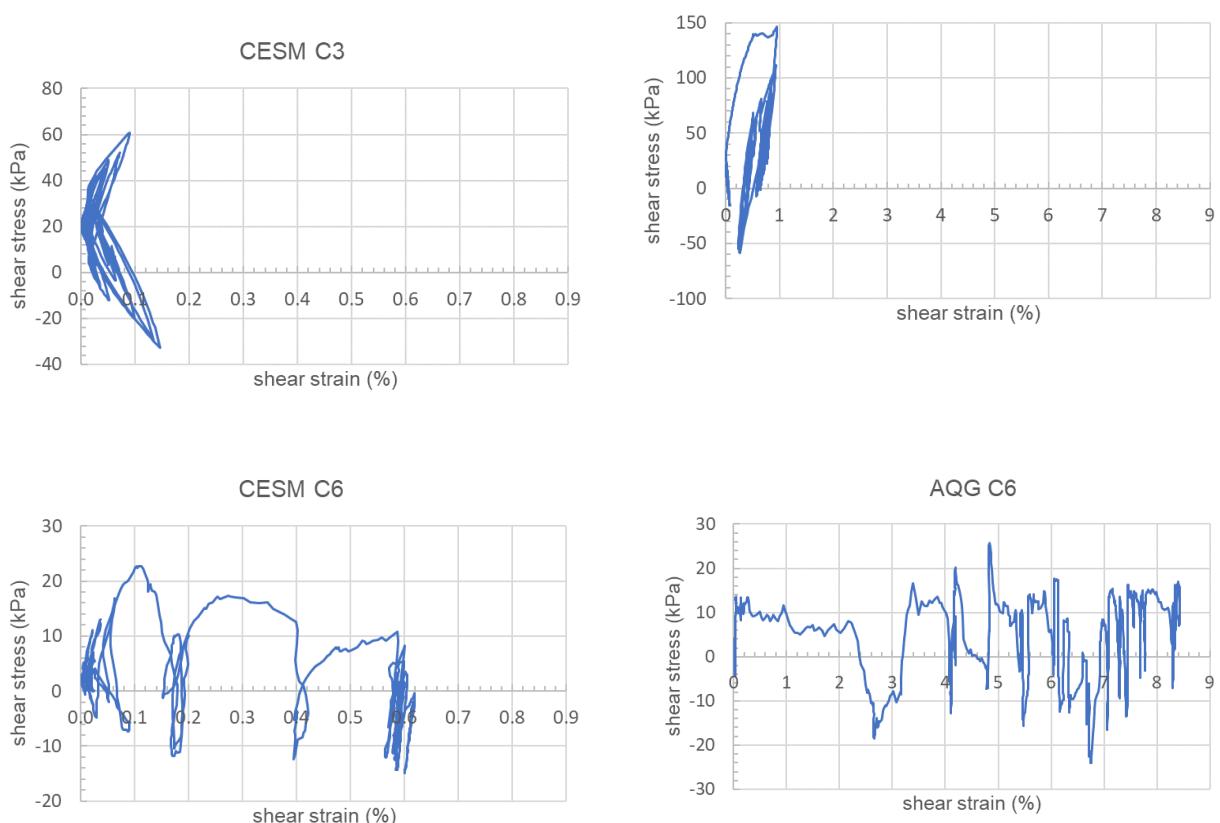


Figure 12. Earthquake AQG (left) and CESM (right) Shear stress vs shear strain during seismic shaking along crest's axis within the lower clay foundation (point C3) and at dam foundation interface (point C6).

The maximum shear strain values reached within the dam and its foundation lay in the range 0.1% to 15% for the seven earthquakes applied. These values are still compatible with the operational strength values assigned to the materials observed in laboratory tests; the final condition of the dam predicted by the model can therefore be still represented by the assigned strength. The settlements at dam crest are correlated with some well-known ground motion severity parameters associated to the input earthquakes, such as the Arias and the Housner intensities, Figure 13.

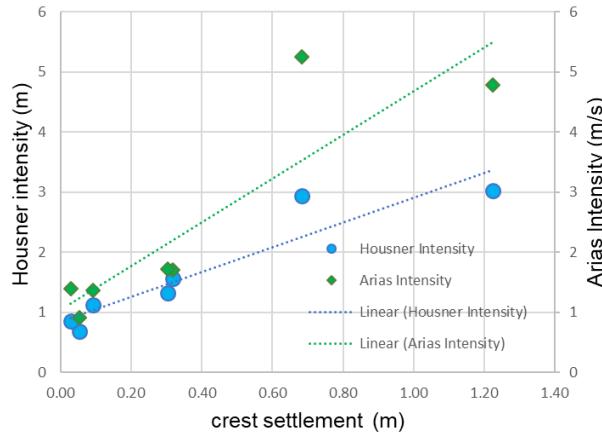


Figure 13. Crest settlement induced by the seven collapse limit state earthquakes as a function of Arias Intensity and Housner Intensity.

Crest settlement is an index of the potential damage suffered by the dam. The average settlement is in this case 0.37 m and is by 46% ascribed to the dam itself, while 42% to the upper foundation soils. It has been compared with thresholds defined by a collection of case studies (Swaisgood, 2003,2014; Pells and Fell, 2003; Sendir et al., 2007) where crest settlement could be associated with the damage occurred to earth dams, and thereby with conditions of post-seismic operativity. It could be concluded that the 0.37m is associated with severe damage which still does not induce the loss of the dam retention capacity of the reservoir water.

3.5. Analyses with no overpressures in dam foundation

The effects induced by the same earthquakes with an initial condition of full dissipation of overpressures within dam foundation leads to the same style of deformation, with effects of a lower magnitude. The dam and its foundation are subject to minor irreversible plastic deformations, Figure 14.

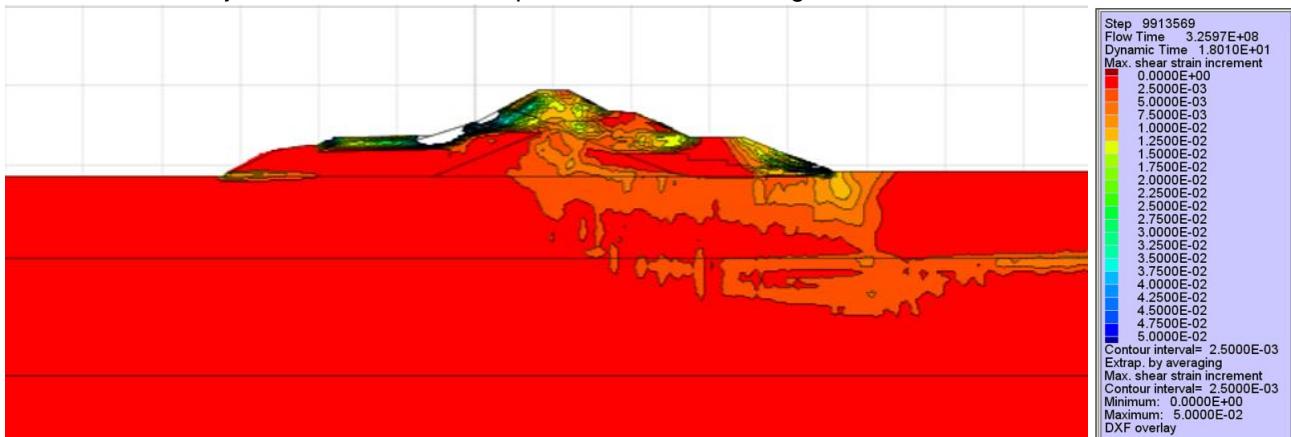


Figure 14. CLO accelerogram: maximum shear strain increment without initial overpressures.

In Figure 15 it may be appreciated how the initial condition with overpressures (left) for a CLO earthquake increases the portion of the model undergoing plasticity respect to the case without initial overpressures (right). In Figure 15 yellow dots indicate that plasticity has occurred and developed; pink areas have behaved according to the nonlinear elastic model applied.



Figure 15. Distribution of the state variable identifying occurrence of plasticity in the model during the time history of CLO accelerogram. Case with initial water overpressures (A) and with zero overpressures (B).

The average crest settlement stands in this case at 0.16m, while maximum horizontal displacement at 0.28m, almost half of the corresponding values obtained considering initial overpressures in dam foundation. The result is due to the lower confinement induced lower strength of the foundation soil when it is still affected by consolidation related overpressures. It could be concluded that the 0.16m is associated with important damage which does not induce the loss of the dam retention capacity of the reservoir water.

4. Conclusions

Nonlinear seismic numerical analyses have been carried out on a plane strain model of an old but still operating earth dam, which still shows crest settlement after about 90 years. The latter is due to the nature of the underlying foundation soils, a thick layer of normal consolidated loamy clay. A nonlinear coupled model in large deformations has used to identify the distribution and values of overpressures in the clay foundation, by which it was possible to conclude that consolidation is still in place, 74% being already developed. This analysis allowed to calibrate the stiffness of the foundation and its permeability.

Seismic analyses have been run applying at the seismic bedrock, placed 104m below ground level, seven ultimate state earthquakes, as horizontal and vertical time histories, with average $PGA=5.59m/s^2$. Results have been averaged as foreseen by NTC18 and NTD14. The dam and foundation constitutive model is hysteretic nonlinear, associated to a plasticity Mohr Coulomb plastic criterion.

Two different initial stress conditions of the foundation soils have been considered: the presence of interstitial water overpressures representative of the present day 74% consolidation of the deep foundation soils and their complete dissipation.

About two times higher vertical and horizontal residual displacements resulted when water overpressures are considered, due to the lower strength of foundation soils induced by lower effective stresses. The style of final displacement is maintained. The higher shear strains are of irreversible plastic nature; they are organized in broad shear bands that affect the dam and the soil foundation. The resulting strain values are consistent with the assigned strength of soils.

Damage is important, but in both cases the retention capability of the dam is maintained.

5. Acknowledgement

The support of Ing. Fabrizio Pelli and Marino Gotti is gratefully acknowledged.

6. References

- Adami S., Chemello P., Gigli P., Salvati S., Vanin V. (2010). Raising of an Earth Dam to Restore the Freeboard reduced by the Consolidation Settlements of the Foundation, *Proceedings of the ICOLD European Club 8th Symposium*, Topic C, Paper C-1:165-170, ATCOLD Ed., TU Graz Publ., Innsbruck, Austria, 22-23 September.

- Aliberti D., Biondi G., Cascone E., Rampello S. (2019). Performance indexes for seismic analyses of earth dams, *Earthquake Geotechnical Engineering for Protection and development of Environment and Constructions*, 1066-1073, Silvestri e Moraci Eds., Associazione Geotecnica Italiana Publ.
- Boulanger R.W., Idriss I.M. (2014). CPT and SPT based liquefaction triggering procedures, *Report No. UCD/CGM-14/01 Center for Geotechnical Modeling Department of Civil and Environmental Engineering, University of California, Davis, California*.
- Charles J.A. (1986). The significance of problems and remedial works at British earth dams, *Proceedings of the BNCOLD-IWES Conference on Reservoirs*, Edinburgh, Paper 9:123-141.
- Hunter G., Fell R. (2003). The deformation behaviour of embankment dams, *UNICIV Report No. R-416*, The University of New South Wales, Sydney.
- Idriss I.M., Boulanger R.W. (2004). Semi-empirical procedures for evaluating liquefaction potential during earthquakes, *Proceedings of the 11th International Conference on Soil Dynamics & Earthquake Engineering and 3rd International Conference on Earthquake Geotechnical Engineering*, pp. 32-56, Berkeley, California, USA, January 7-9.
- ITASCA. FLAC-fast lagrangian analysis of continua, Minneapolis, USA Itasca Consulting Group, Version 8.0, User's Guide.
- Lanzo G. (2018). Alcune considerazioni sulla rivalutazione della sicurezza sismica delle dighe di materiali sciolti, *Atti Conferenze di Geotecnica di Torino-XXV Ciclo*, Paper 11:1-43 Politecnico di Torino Publ. (in Italian), Torino, Italia. 8-9 Novembre.
- Milli E. (1966). Considerazioni geologiche e tecniche sui movimenti di assestamento e sulla stabilità dell'argine in terra di Santa Croce, *Technical report*, ENEL Compartimento di Venezia (in Italian).
- NTC18. (2018). Aggiornamento delle Norme Tecniche per le Costruzioni. Decreto del Ministero delle Infrastrutture e dei Trasporti, Gennaio 17, G.U. n.2018; 42 (in Italian).
- NTD14. (2014). Norme Tecniche per la progettazione e la costruzione degli sbarramenti di ritenuta (dighe e traverse), Giugno 26.G.U., vol.156 (in Italian).
- Pells S., Fell R. (2003). Damage and cracking of embankment dams by earthquakes and the implications for internal erosion and piping, *Proceedings of 21st Congress on Large Dams, ICOLD, Q83-R17*, ICOLD Paris Ed., Montreal, Canada.
- PLAXIS2D – Version 9.0 User manual (2008) R.B.J.Brinkgreve, Broere W., Waterman D. Eds.
- Robertson P.K., Wride C.E. (1998). Evaluating cyclic liquefaction potential using the cone penetration test. *Canadian Geotechnical Journal*, 35(3): 442-459.
- Rollins K.M., Evans M.D., Diehl N.B., Daily W.D. (1998). Shear modulus and damping relationships for gravels, *Journal of Geotechnical and Geoenvironmental Engineering*, 124(5): 396-405.
- Sendir S., Sato J.E., Towhata I. (2007). Shaking table tests on residual displacements of earth dams for their performance-based design, *Proceedings of International Workshop on Earthquake Hazard and Mitigation*, Guwahati, India, 7-8 December.
- Swaisgood J.R. (2003). Embankment dam deformations caused by earthquakes, *Proceedings of the Pacific Conference on Earthquake Engineering*, Paper No. 14: 1-8, Auckland, New Zealand.
- Swaisgood J.R. (2014). Behavior of embankment dams during earthquakes, *Journal of Dam Safety*, 12(2): 35-44.
- Tedd P., Charles J.A., Holton I.R., Robertshaw A.C. (1997). The effect of reservoir drawdown and long term consolidation on the deformation of old embankment dams, *Géotechnique*, 47(1): 33-48.

EFFECT OF NON-VERTICAL PROPAGATING SEISMIC WAVES ON THE BEHAVIOR OF GRAVITY AND ARCH DAMS

E. Robbe¹, N. Humbert², S. Cherubini³

¹ EDF, La Motte Servolex, France, emmanuel.robbe@edf.fr

² EDF, La Motte Servolex, France,

³ EDF R&D, Palaiseau, France,

Abstract: The more up-to-date finite-element analyses of concrete dams under earthquake loading generally consider the seismic input as compression and shear waves propagating vertically through the foundation until reaching the dam itself. Viscous-spring boundaries at the foundation boundaries can be used to correctly represent such assumptions. The vertical propagation is generally considered for lack of better knowledge. The aim of the paper is to present analyses with increasing complexity to demonstrate the effect of a slightly inclined propagation direction of the seismic wave on the behavior of concrete dams. First, finite-element analyses of a simplified 2D homogenous block of foundation will be performed to assess the capacity of the software used (open-source Code_aster) to correctly represent an inclined propagation wave. Next, a 2D section of Pine flat dam will be considered. Acceleration and displacement at the crest, shear safety factor and stresses at the dam-foundation interface will be compared with several inclinations of the seismic wave to evaluate the influence of the propagation direction on the results. Finally, 3D analyses of an arch dam is performed with various propagation direction. Results show that stability parameters are slightly affected by such assumption but remain in similar range when considering different accelerograms combination. From the authors point of view, such analyses are not necessary for the safety evaluation of concrete dams under earthquake considering that several time-history analyses are already performed with various combination of accelerograms.

1. Introduction

Seismic analyses of concrete dams gradually improve the representation of the seismic load from pseudo-static methods (seismic input is simplified as constant acceleration values in one or several direction) to advanced methods (seismic input represented as compression and shear waves propagating in the foundation toward the dam).

With increasing complexity of the methods to introduce seismic inputs into the analyses, new assumptions have to be chosen: with pseudo-static analyses the only required parameter was peak ground acceleration while time-history analyses with massless foundation required the choice of accelerograms. Up-to-date analyses involving mass of the foundation and thus propagation of compression and shear waves into the foundation require among other assumptions the direction of propagation of such waves. Generally, vertical direction is considered, with seismic waves travelling from the bottom to the top of the foundation. The aim of this paper is to evaluate the consequences of a slight angle in the direction of propagation in the analyses and

the consequences on the dam's behavior evaluation. Analyses are limited to concrete dams founded on homogenous rock foundation considering such cases provides an already sufficient level of complexity.

This topic has not been studied a lot in the past except by Garcia et al. (2016) who evaluate the relevance of incident angle of the seismic waves on the dynamic response of Morrow Point arch dam using boundary element model (BEM). High incident angles were considered (from 30 to 90 degrees) and the authors computed the variation of hydrodynamic load and relative displacements – accelerations compared to vertical propagating waves. They highlight than the assumption of vertical incidence of the incoming seismic waves, used very often, does not define the worst-case scenario. Previously, Milovanovitch (1996) presented in his thesis an impressive work based on an energy approach to evaluate the effect of incident angle of seismic waves for an arch dam, to optimize its position in the design process, also using BEM numerical analyses.

The novelties of this paper compared to the rare previous work on this topic are:

- The use of the more up-to-date methods for the numerical analyses of concrete dams under earthquake, briefly summarized in the following chapters,
- The effects of incident angle of seismic waves are evaluated by comparison on the concrete dam's behavior parameters: vertical stresses and shear safety factor for gravity dam, principals stresses for arch dams.

2. Taking into account non-vertical incident waves in finite-element analyses

From 2017 to 2019, Lokke and Chopra proposed the so-called 'direct finite-element method' for the linear or nonlinear earthquake analysis of 2D and 3D dam-water foundation rock systems. This method uses standard viscous-damper absorbing boundaries to model the semi-unbounded foundation rock and fluid domains and specifies the seismic input as effective earthquake forces at these boundaries. This method was integrated in the open-source finite-element software Code_Aster developed by EDF, validated with several benchmark workshop and back analyses of dams under earthquakes (Robbe 2017, 2017 et 2019).

In this method, the earthquake excitation is defined by 3 components (upstream, cross-stream and vertical) of free-field acceleration at a control point on the foundation rock surface. The free-field motion at the bottom and side boundaries of the foundation-rock domain can be determined from the surface control motion using a deconvolution-type analysis, assuming the incident wave field consist solely of plane SH, SV and P waves propagating vertically upward. As quoted by Lokke (2018), this is clearly a major simplification but seems a reasonable pragmatic choice considering the complexity of performing more realistic analyses such as briefly described in Figure 1 (A and B).

To consider compression and shear waves with non-vertical propagation, boundary conditions (and particularly at the vertical sides of the foundation) should be correctly defined for the problem to be correctly solved. The most difficult issue is to correctly evaluate the propagation and reflection of the compression and shear waves of the free-field column. For vertical propagation in a homogenous isotropic media without damping, the reflection is quite straightforward as both incident compression and shear waves going upward generate a similar reflected waves going downward. If the propagation is different from vertical, the reflection is slightly more complex as reminded in the following chapter.

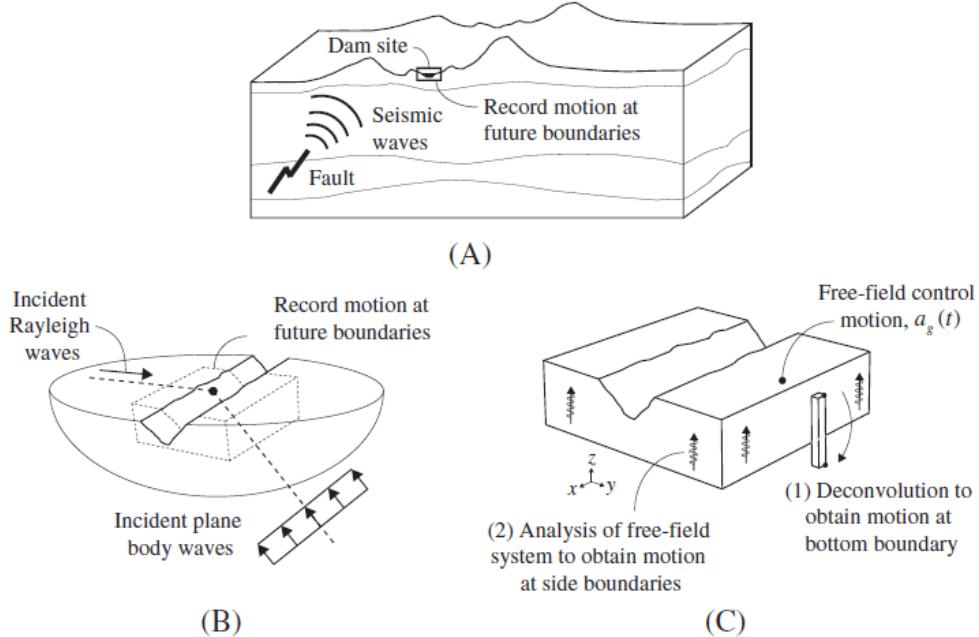


Figure 1 From Lokke (2018) : Schematic overview to obtain free field earthquake motion : from (A) large-scale fault rupture simulation, to (B) boundary element method with incident plane wave propagating at predefined angles, to (C) deconvolution analysis starting with a free field surface control motion.

2.1. Theory reminder for reflection of incident waves at the free surface

Sadd (2009) describes the reflection of compression and shear waves. As summarized in Figure 2, reflection of an incident compression wave with an incident angle θ_L generates 2 reflection waves:

- A compression wave with a similar angle θ_L
- A shear wave with an angle θ_T depending of θ_L and the speed of shear and compression waves (C_T and C_L) in the media.

Ratios of the amplitude between the incident wave and the reflections waves (r_{LT} and r_{LL}) are provided in the Figure 2. Reflection of an incident shear wave follows a similar pattern as summarized in Figure 3. The knowledge of all these theoretical parameters allows one to correctly compute the response of the free-field columns at the boundary of the foundation.

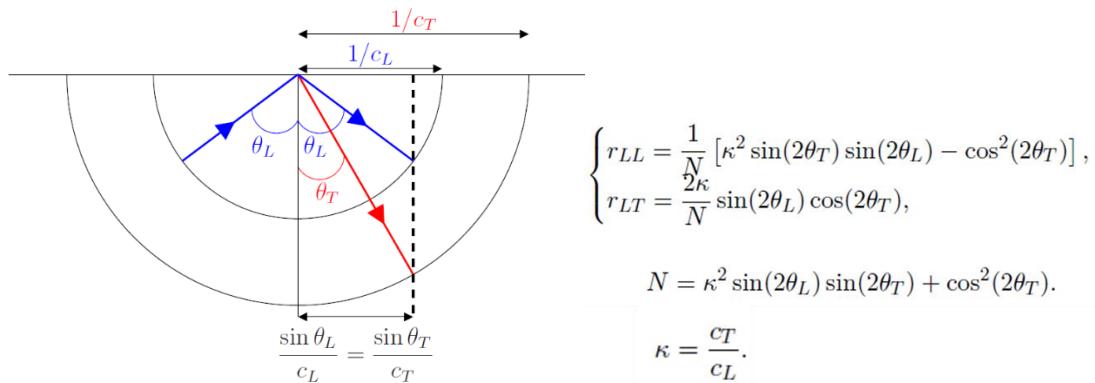


Figure 2 reflection of compression waves

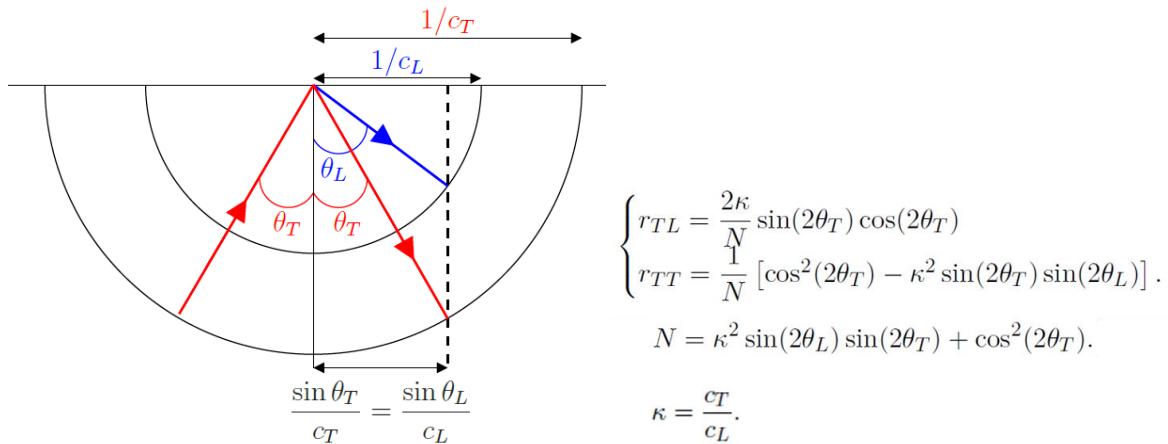


Figure 3 reflection of shear waves

2.2. Flat box test case of plane waves with tilted propagation

For the validation of such capabilities in the finite-element analyses with Code_Aster (or any FE software), a simplified 2D 'flat box' test case is proposed with the following assumptions:

- The box is 600 m wide and 500m high,
- Homogenous properties of the media: Young modulus = 22410 MPa, Poisson Coefficient = 0.2, density: 2483 kg/m³
- No damping,
- Absorbing finite-element on the vertical and bottom boundaries
- Compression incident simplified wave with 20° angles such as presented on the Figure 4.
- Linear time-history analyses are performed with Code_Aster.

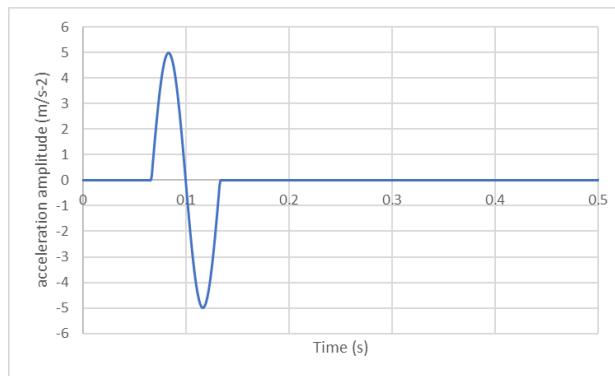


Figure 4 test wave

Figure 5 shows the evolution of the acceleration magnitude field at several time-steps of the analysis : 1) the incident wave propagates from the bottom-left corner with a 20° angle, 2) the reflection at the surface generates acceleration magnitude twice the introduced input at the bottom (sum of the incident and reflected waves), 3) reflected compression and then shear waves start to propagate toward the bottom-right corner, 4) later the 2 reflected waves can be clearly distinguished : first the compression wave with a similar 20° angle and then the shear wave with a different angle.

The clear pattern of the Figure 5 is proof that the boundary conditions are correctly set: there are no unwanted perturbation in the acceleration field. Qualification analyses with incident shear wave are also performed but not presented here.

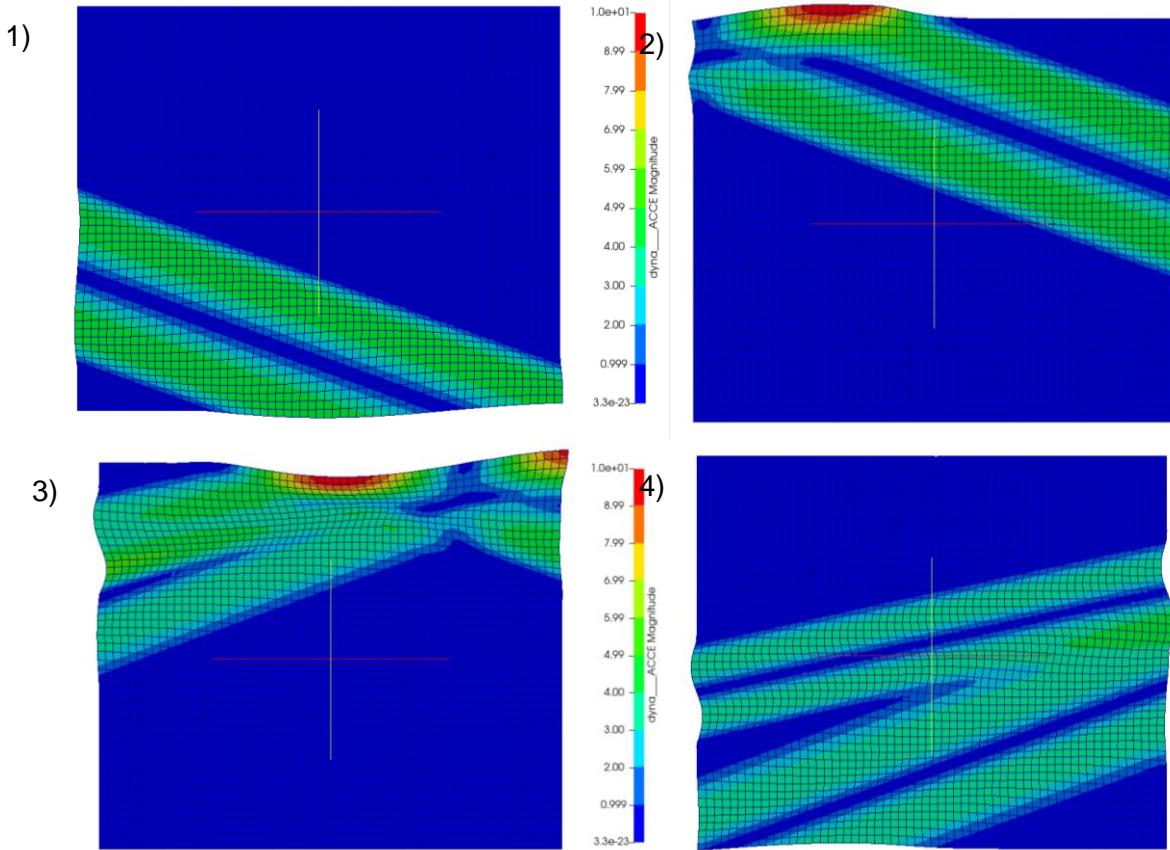


Figure 5 flat box test with compression waves with 20° incident angles at different time-steps

3. Effect on the seismic behavior of a 2D gravity dam

Now that the demonstration of the capability of the finite-element analysis software to take into account incident waves with angles, the aim of this chapter is to evaluate the effect on the behavior of a 2D gravity dam. In this purpose finite-element analyses on the Pine Flat test case are proposed. These analyses have been described in a previous paper (Robbe 2023) and only the main results are summarized here.

3.1. Pine Flat test case

In 2019, the international benchmark workshop organized by ICOLD in Milan proposed the seismic analysis of Pine Flat concrete dam as case study. Data from this case study are considered (ICOLD 2019):

- The simplified 2D geometry of the dam, foundation and reservoir, presented in Figure 6,
- Linear analyses are performed with the following material properties for concrete and foundation:
- Module of elasticity: 22,410 MPa,
- Density: 2,483 kg/m³,
- Poisson's ratio: 0.2,
- Rayleigh damping is considered, only for concrete with the following parameters: $\alpha=0.75$ (mass) and $\beta=0.005$ (stiffness)
- The winter reservoir level (EI 268.21) is considered, and the reservoir is modeled with acoustic fluid elements,
- Taft earthquake accelerations (Figure 7) with 0.17g horizontal peak ground acceleration.

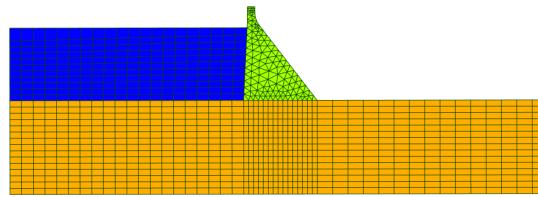


Figure 6 mesh of the dam, fluid and foundation

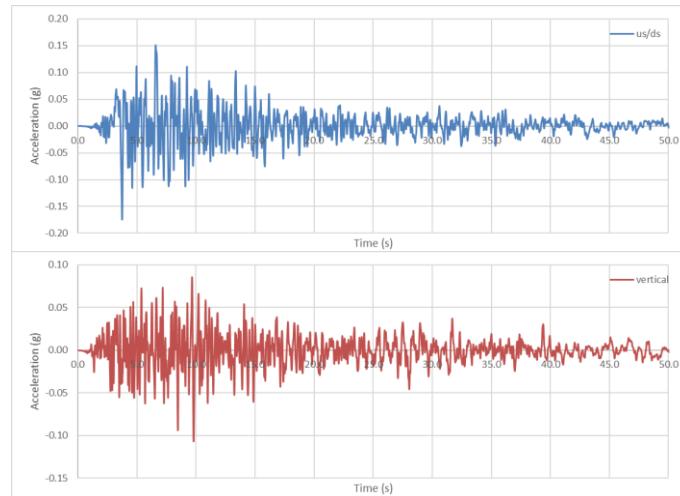


Figure 7 Taft acceleration records (us/ds at the top, vertical at the bottom)

3.2. Analyses with the dam: seismic behavior of the dam with vertical propagation

First the linear time-history analysis involving dam, foundation and reservoir is performed with a conventional vertical propagation direction with the Taft earthquake input components presented in Figure 7. The following results are computed at each time-step:

- Horizontal and vertical acceleration at the crest,
- Dynamic displacement at the crest,
- Shear factor of safety at the dam foundation interface with N and T the normal and tangential forces computed from static (stat) and dynamic (dyn) analyses:

$$SF(t) = \frac{N_{\text{stat}} + N_{\text{dyn}}(t)}{T_{\text{stat}} + T_{\text{dyn}}(t)}$$

- The linearized upstream and downstream stresses computed at the dam-foundation interface from the beam theory (with M the momentum at the center of the dam-foundation interface, L the length of the dam base and I the inertia):

$$\sigma_{\text{us or ds}} = \frac{N_{\text{stat}} + N_{\text{dyn}}(t)}{L} \mp \frac{(M_{\text{stat}} + M_{\text{dyn}}(t)) \frac{L}{2}}{I}$$

For the results involving static analyses, the following assumptions are considered:

- Uplift varies linearly from the reservoir level at the upstream toe to 30% of the load after 5 m (supposed position of the drainage), to 0 at the downstream toe.
- 45° friction angle is considered at the dam foundation interface with no cohesion.
- Water level is considered at elevation 268.21 (winter reservoir level).

Considering the results are strongly dependent on the accelerogram selection, several analyses are performed by successively changing the sign of the accelerograms. Results are summarized in Table 1. Obviously absolute dynamic acceleration and displacement remain identical. Minimum shear safety factor varies from 1.25 to 1.40 while max upstream tensile stress goes from 0.65 to 0.97 MPa.

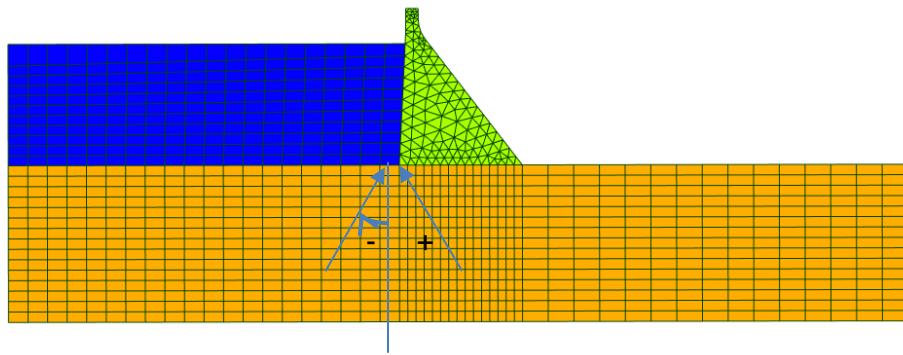
Table 1. results with change of sign of accelerograms

Set of accelerograms	Max horiz. acceleration (ms⁻²)	Max dyn horiz. displacement (mm)	Min shear safety factor	Max us tensile stress (MPa)	Max ds compression stress (MPa)
Us/ds ; vertical	11.1	43.4	1.39	0.70	3.28
-Us/ds ; vertical	11.1	43.4	1.40	0.65	3.26
Us/ds ; -vertical	11.1	43.4	1.25	0.97	3.5
-Us/ds ; -vertical	11.1	43.4	1.37	0.74	3.25

3.3. Analyses with the dam: effect of the incident angle on the seismic behavior of the dam

Using the capabilities of Code_Aster to take into account incident angle of the waves (as described in the first chapters of this paper), linear time-history analyses of Pine Flat dam are performed taking into account incident angle from -20 degrees to 20 degrees, with the sign convention defined in Figure 13 (negative angle when waves come from the upstream side). Results are compared with the reference case presented in the previous chapter in Table 2. Figure 14 shows the evolution of the upstream stress and shear factor of safety for different incident angle. The following comments can be made:

- When the waves are coming from the upstream side, stability parameters can be slightly more unfavorable: the tensile upstream stress slightly increases from 0.7 to 0.77 MPa while the safety factor remain quite similar. Change in the values remain lower than the change of values due to inversion of accelerograms.
- When the waves are coming from downstream, stability computed is increased: the maximum upstream tensile stress is lowered from 0.7 to 0.37 MPa for example.

*Figure 8 sign convention for incident angle**Table 2. results with change incident angle*

Incident angle (degrees)	Max horiz. acceleration (ms⁻²)	Max dyn horiz. displacement (m)	Min shear safety factor	Max us tensile stress (MPa)	Max ds compression stress (MPa)
-20	10.7	55.4	1.40	0.77	3.49
-10	10.8	49.9	1.39	0.76	3.43
0	11.1	43.4	1.39	0.70	3.28
10	9.7	37.2	1.49	0.56	3.12
20	9.0	34.4	1.58	0.37	2.92

4. Effect on the seismic behavior of a 3D arch dam

To evaluate the effect of non-vertical compression and shear waves on a 3D arch dam, the analysis of the arch proposed during the 12th ICOLD benchmark workshop (Zens 2013) is considered as test case. This is a fictitious 220m high symmetrical arch dam. The mesh is presented on Figure 9. Linear analyses are performed with the following material properties for concrete and foundation:

- Module of elasticity: 27000 MPa for concrete, 25000 MPa for rock, no change are considered for static or dynamic analyses
- Density of rock and concrete: 2,400 kg/m³,
- Poisson's ratio: 0.167 for concrete and 0.2 for rock,
- Rayleigh damping is considered, only for concrete with the following parameters: $\alpha=0.8767$ (mass) and $\beta=0.00074026$ (stiffness) providing 5% damping at 1.5 and 20 Hz but a lower 3% between 3 and 10 Hz.
- The full reservoir level is considered, and the reservoir is modeled with acoustic fluid elements,
- Earthquake are considered using 3 synthetics accelerations (Figure 10) with 0.22g peak ground acceleration. The vertical component is reduced by 2/3.

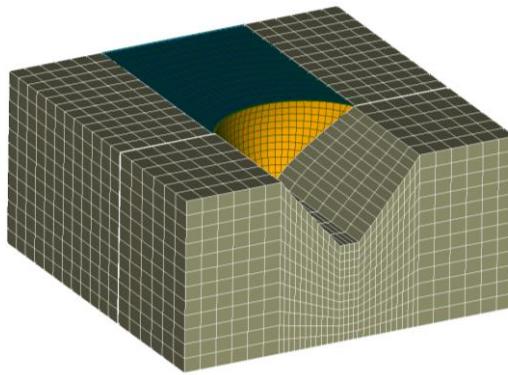


Figure 9 Mesh of the arch dam

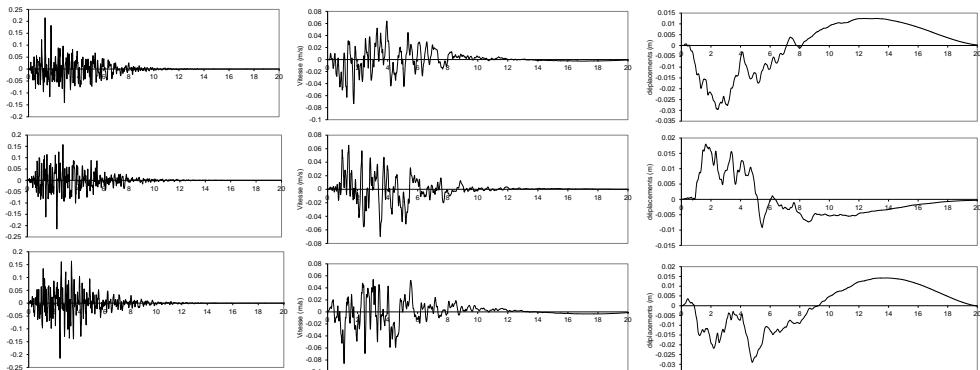


Figure 10 acceleration, velocity, and displacement for the arch dam analyses

1.2. Seismic behavior of the arch dam with vertical propagation

First, analyses with vertical propagation of the waves are performed, to provide reference results. First static analysis is performed considering self-weight on independent cantilever, and hydrostatic load with reservoir at the crest level.

For the dynamic analyses, 3 earthquakes (Eq1, Eq2, Eq3) are considered, combining accelerograms previously described (A1, A2, A3) :

- Eq1 : A1 in the X direction, A2 in the Y direction, 2/3 of A3 in the Z direction
- Eq2 : A2 in the X direction, A3 in the Y direction, 2/3 of A1 in the Z direction
- Eq3 : A3 in the X direction, A2 in the Y direction, 2/3 of A2 in the Z direction

As previously in §3, linear time-history analyses with acoustic fluid element and viscous-spring boundaries are performed. Rayleigh damping for concrete only is considered. Results of the static and dynamic analyses are summarized in Table 3. The following results are analyzed:

- Maximum acceleration (generally near the crest of the dam),
- Maximum displacement during the earthquake (static included), at the crest of the central cantilever,
- Maximum (tension) and minimum (compression) principals' stresses during the earthquake (static included) on the upstream and downstream face.

Under static load, the arch bend toward downstream, with a maximum displacement at the crest of 83 mm. Under the considered 0.22 pga earthquake, the displacement toward downstream can reach on average 129.6mm. This leads to compression stresses perpendicular to the dam-foundation interface near the abutment varying from 9.8 to 11.4 MPa under static and dynamic loads. Under earthquake, tensile stresses are also computed near the crest with an average maximum of 2.3 MPa.

Table 3. results with change of sign of accelerograms

load	Max acceleration (ms-2)	Max displacement (mm)	Max us tensile stress (MPa)	Min us compression stress (MPa)	Max ds tensile stress (MPa)	Max ds compression stress (MPa)
static		83	1.4	-7	0.5	-9.8
Static +Eq 1	18.5	129	2.8	-9.13	2.0	-11.6
Static +Eq 2	15.3	126	2.9	-9.37	2.6	-11.5
Static +Eq 3	17.3	134	2.6	-9.62	2.3	-11.2

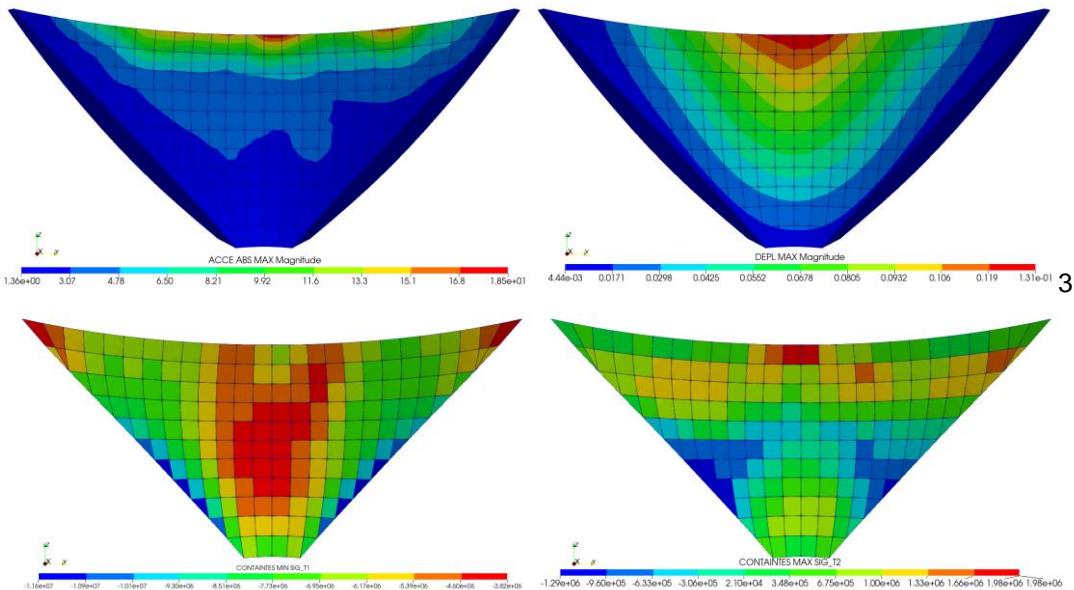


Figure 11 maximum acceleration, displacement (top) stresses on the downstream face (bottom) during the time-history analyses with static + EQ1 load.

1.1. Seismic behavior of the arch dam with non-vertical propagation

In the same spirit with what was done in the 2D case (§3), additional linear time-history analyses are performed considering Eq1 only, but taking into account incident angles of 20 degrees in the XZ and YZ plane (see Figure 12). 4 analyses are performed allowing to evaluate the influence of all incident angles on the main results, summarized in Table 4. Maximum principal's stresses on the downstream face are compared for each analysis in Figure 13.

Results show that different incident angle leads to rather small changes in the results, that remain in the range of difference that can be obtained when considering different earthquake. Generally, this won't bring any change regarding the judgement of the behavior of the structure.



Figure 12 definition of the incident angles

Table 4 results with static +EQ1 load considering several incident angle of the incoming seismic waves

Incident waves	Max acceleration (ms ⁻²)	Max displacement (mm)	Max ds tensile stress (MPa)	Max ds compression stress (MPa)
Vertical*	15.3-18.5*	126-134*	2.0-2.6*	-11.2 -11.6*
Inc 1	16.3	138	1.5	11.9
Inc 2	17	130	2.0	11.9
Inc 3	22	132	2.5	12.6
Inc 4	16.9	129	1.6	11.6

(*) range of results for the 3 earthquakes considered (from Table 3)

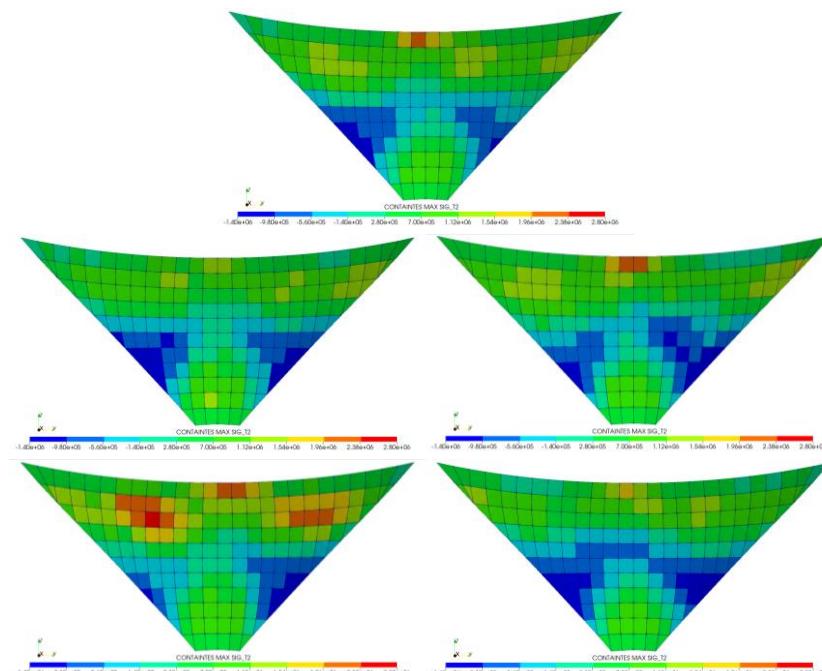


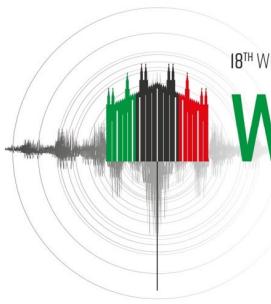
Figure 13 maximum principal stresses (static + dynamic) during the time-history analyses with vertical propagation (top) and 4 inclined incoming waves

5. Conclusion

Seismic analyses of concrete dams using direct finite-element analyses method proposed by Looke & Chopra, or similar methods, consider the seismic input as compression and shear waves vertically propagating from the bottom of the foundation toward the surface. This paper presents the development required to consider propagation with incident angle when homogenous media and no damping are considered for the foundation. The method is validated with a flat box test case and seismic analyses of a 2D gravity dam and a 3D arch dam under earthquake are performed to evaluate the influence of inclined direction of propagation of the waves. Results show that stability parameters are slightly affected by such assumption but remain in the range of variation computed when considering different accelerograms combination. From the authors point of view, such analyses are then not necessary for the safety evaluation of concrete dams under earthquake considering that several time-history analyses are anyway performed with various combination of accelerograms.

6. References

- Garcia F. (2016), Relevance of the incidence angle of the seismic waves on the dynamic response of arch dams, Soil dynamics and earthquake engineering,
- ICOLD - 15th International benchmark workshop on numerical analysis of dams (2019), Seismic analysis of Pine Flat concrete dam – theme A, Milan
- Liu YS, Chen DH (2013), Earthquake response analysis of a gravity dam considering the radiation damping of infinite foundation, APCOM & ISCM
- Milovanovitch V.D. (1992), Comportement dynamique des barrages en béton et prise en compte des effets de site sur les ondes sismiques incidents, Thesis, Ecole Nationale des Ponts et Chaussés (in French)
- Lokke A, Chopra A. K (2018), Direct finite element method for nonlinear earthquake analysis of 3-dimensional semi-unbounded dam-water-foundation rock systems, Earthquake engineering structure dynamic
- Robbe E. (2017), Seismic analyses of concrete dam, comparison between finite-element analyses and seismic records- World Conference on Earthquake Engineering, Santiago, Chile
- Robbe E. (2017) Seismic back analysis of Monticello arch dam – blind prediction workshop and additional analyses, USSD 2017 – Anaheim
- Robbe E. (2019), Seismic analyses of Pine Flat dam : simplified use of viscous spring boundaries and anisotropic damage in the principal directions with the ability of crack re-closure, 15th ICOLD benchmark workshop on numerical analyses, Milan
- Robbe E, Humbert N (2023), Seismic analyses of concrete dams : what if seismic waves do not propagate vertically, USSD 2023 Annual conference
- Sadd M. H. (2009) Wave motion and vibration in continuous Media, University of Rhode Island publication.
- Zens G, Goldgruber M, Proceedings of the 12th international benchmark workshop on numerical analyses of dams, Graz-Austria
- Zhang C, Pan J (2009), Influence of seismic input mechanisms and radiation damping on arch dam response, Soil Dynamic and Earthquake engineering, 29 (9), 1282-1293



CHALLENGES WITH DECISION MAKING FOR DAM SAFETY SEISMIC RISK IN A RISK INFORMED FRAMEWORK

M. Rocha¹, K.Z.Z. Lee² & P. Mott³

¹ Bureau of Reclamation, Denver, United States, mrocha@usbr.gov

² Bureau of Reclamation, Denver, United States

³ Bureau of Reclamation, Denver, United States

Abstract: The United States Bureau of Reclamation uses a Risk Informed Framework to make dam safety-related decisions and, when justified, modifies dams to reduce risk to the downstream public. Lately, the use of seismic risk models of dam failure is leading to extensive analyses to understand uncertainty and development of expensive dam modifications. The seismic risk analyses combined with large downstream populations are resulting in seismic hazards with return intervals greater than 20,000 years driving the risk. Reclamation is comparing our approach against other dam owners and industries and is finding that the seismic hazards developed for Reclamation dams exceed design standards used by other dam owners and other infrastructure.

The concerns have been narrowed down to the following two questions, focused on building confidence in Reclamation's approach and making the correct decisions by allocating limited funding to reduce greatest risks of dam failure.

1. At what threshold, either in frequency or cost, does the level of uncertainty in the seismic risk model, including seismic hazard and structural response, support the decision to modify a dam to improve its seismic resilience?
2. Is Reclamation's approach leading to decisions consistent with other dam owners and infrastructure?

This paper will identify the considerations around these questions and will summarize the effort Reclamation is undertaking to find answers.

The Bureau of Reclamation is an agency of the United States Government with a mission to manage, develop, and protect water and related resources in the Western United States. Reclamation is the largest wholesaler of water in the United States, bringing water to more than 31 million people and providing one out of five Western farmers with irrigation water for 10 million acres (4 million hectares). Reclamation owns 361 high hazard potential dams whose failure would lead to life loss.

1 Background

This paper identifies key questions surrounding seismic risks at Bureau of Reclamation (Reclamation) dams that compel a Risk Informed Decision Making Framework. Included is summary of Reclamation's Risk Informed Decision Making Framework, a description of uncertainty and analysis in Reclamation methodologies, and summaries of seismic standards for other dam owners, dam regulators, and infrastructure (primarily in the United States), including the International Commission on Large Dams (ICOLD), United States Army Corps of Engineers (USACE), United States Federal Energy Regulatory Commission (FERC), Australian National Committee on Large Dams (ANCOLD), American Society of Civil Engineers (ASCE), and American Association of State Highway and

Transportation Officials (AASHTO). The summary information is synthesized to identify two questions affecting Reclamation's research, decision making, and direction when evaluating seismic risks at Reclamation's dams.

Reclamation is a United States Federal bureau organized under the Department of the Interior. Reclamation was established in 1902 with the intent to invest in irrigation projects in the Western United States to encourage settlement and family farms. Irrigation was necessary in this area of the United States because of limited precipitation combined with snowmelt runoff that did not extend the full length of the growing season. Private and state sponsored storage and irrigation projects commonly failed due to lack of funding or engineering skill (Bureau of Reclamation, 2018). Over time, Reclamation's mission grew to include delivering water for municipal and industrial use and producing hydropower.

Reclamation is the largest wholesaler of water in the United States. We bring water to more than 31 million people and provide one out of five Western farmers with irrigation water for 10 million acres (4 million hectares) of farmland that produces 60% of the nation's vegetables and 25% of its fruits and nuts. Reclamation annually contributes more than \$72.9 billion to the economy and supports 618,000 jobs. Hydropower is generated through 78 hydropower plants, including Hoover Dam and Grand Coulee Dam. Reclamation is the second largest hydropower producer in the United States. Reclamation owns 364 high hazard potential dams whose failure would lead to life loss.

2 Risk Informed Decision Making

Reclamation implemented Risk Informed Decision Making in 1997, over 26 years ago. This practice has evolved with the current practices being described in the Public Protection Guidelines: a Risk Informed Framework to Support Dam Safety Decision Making published in December 2022. Risk analysis forms the quantitative component of the process and is described as follows:

"The basic objectives of a risk analysis are to: 1) develop a working set of potential failure modes (PFMs) addressing the key vulnerabilities of the facility, as understood by the risk analysis team based on their review of design, construction, and analysis information as well as other relevant information; 2) assign an occurrence probability estimate, termed the annualized failure probability (AFP), to each of the credible PFMs or develop a convincing set of arguments that explain why the PFM is not considered credible; and 3) assign a consequence (life loss) estimate to each of the credible PFMs and estimate the annualized life loss (ALL) for each PFM" (Bureau of Reclamation, 2022).

The quantified risk is plotted on a Risk Portrayal chart provided in Figure 1, a log-log scale with the y-axis representing the AFP and the x-axis the estimated life loss. The chart includes visual guidelines that are threshold values for determining whether action is justified to reduce or better understand risks. The thresholds are designed to provide a consistent level of protection. The threshold values themselves are relative lines on a drawing, and estimated risks must be interpreted through the dam safety case, which incorporates deterministic factors, probabilistic factors, and confidence in portrayal of the risks. ALARP is also shown on the chart and stands for As-Low-As-Reasonably-Practicable, as defined by Reclamation, the concept that risks should be evaluated for further risk reduction actions beyond those justified in the dam safety case when practicable and consistent with Reclamation's mission (Bureau of Reclamation, 2022).



Figure 1. Reclamation Risk Portrayal Chart (Bureau of Reclamation, 2022).

The visual guidelines can be divided into three segments. Segment 1 plotted at an AFP of $1\text{E-}4$ provides a consistent level of protection to residents downstream of the dam (regardless of how many people are located downstream). This value was set nearly two orders of magnitude less than the average probability that a selected individual will lose their life in a given year, called the average annual reference risk. Segment 2 is the diagonal component plotted along the contour $1\text{E-}3$ and reflects the idea that as the number of casualties increases, the standard should be higher. Segment 3 is plotted at an AFP of $1\text{E-}6$ and reflects a need to balance funding for dams with estimated AFP lower than 1 in 1,000,000 with a much higher consequence of failure. Three segments of visual guidelines are shown in Figure 2 (Bureau of Reclamation, 2022).

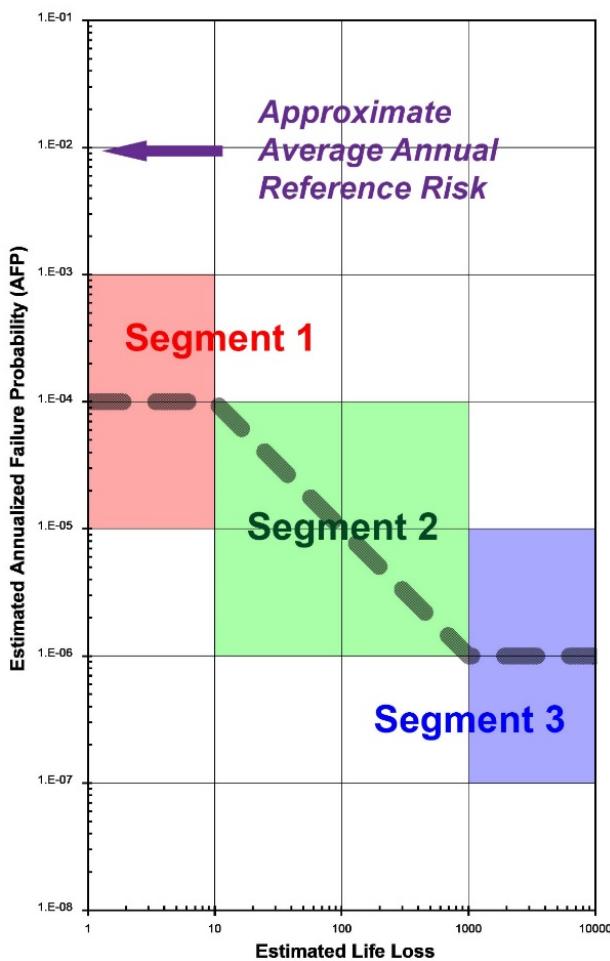


Figure 2. Visual Guidelines as three segments (Bureau of Reclamation, 2022).

Recent application of the guideline values is leading to an increasing number of efforts to understand seismic risks at Reclamation dams. Of the 255 identified evaluations, 74 are related to static PFM's such as internal erosion of the embankment, 62 are related to hydrology PFM's such as spillway failure or overtopping, and 119 are related to seismic PFM's.

Mathematically, the diagonal component of the visual guidelines, segment 2, creates a relationship between seismic loads and life loss estimates. For example, a dam with an estimated life loss of 100 must have an estimated conditional failure of probability less than 1 when evaluating a seismic event with a 1/100,000-year probability in order to plot below guidelines. The risk quantification process is more complex than presented here, but the general result is consistent in that as the estimated life loss increases, the dam must have the ability to withstand increasingly remote events. In other words, downstream changes in population could impact our perception of risk and may increase the justification for action. This is confirmed in the risk estimates for all 364 Reclamation dams. When the estimated life loss exceeds 1000, the threshold AFP is 1E-6.

Generally, Reclamation relies on our in-house seismic hazard group to develop site-specific probabilistic seismic loadings that rely on up-to-date ground motion attenuation models and a seismic source model that includes regional seismicity and fault studies. The maximum credible earthquake or deterministic methods are not currently used. Even with these labor and time intensive efforts, limited data points are leveraged to develop probabilities for infrequent events. The analyses focus on the mean loading condition with the 5th and 95th percentiles provided to convey a sense of the load uncertainty. The return periods for the earthquakes are not currently limited, and the entirety of the hazard is considered in the evaluation of the seismic risk to the dam.

Modifying an embankment dam to reduce the potential for a seismic failure typically requires removal of liquefiable material, construction of a stability berm, a drainage system, and installation of a downstream two-stage filter. The purpose of these modifications is to reduce the risk of liquefaction and deformation of the foundation and to filter any transverse cracks that may form in the embankment during the earthquake. The potential failure mechanisms are presented in Figure 3 and Figure 4. Figure 3 shows embankment deformation due to foundation liquefaction, where the foundation causes lowering of the crest leading to overtopping. Water flowing over the lowered crest initiates head cutting and eventually breaches the dam, releasing the entire reservoir. Figure 4 shows cracking in the embankment leading to internal erosion in the embankment. The internal erosion leads to cracks growing until the dam is breached. These modifications can range from \$100 million to over \$1 billion due to the extensive foundation material that must be removed and replaced, which can extend anywhere from 50 to 100 feet (15 to 30 m) in depth, and the high cost of the processed sand that is used for the two-stage filter.

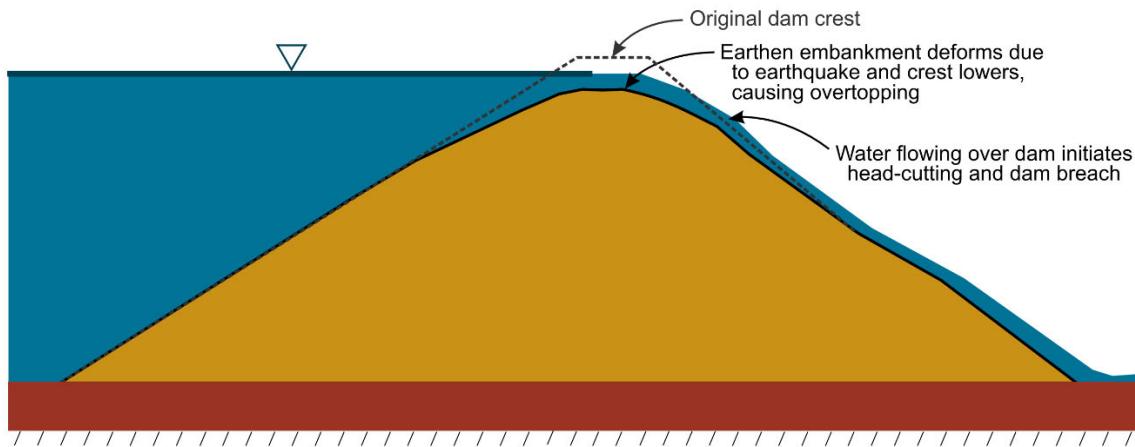


Figure 3. Embankment Deformation due to Foundation Liquefaction.

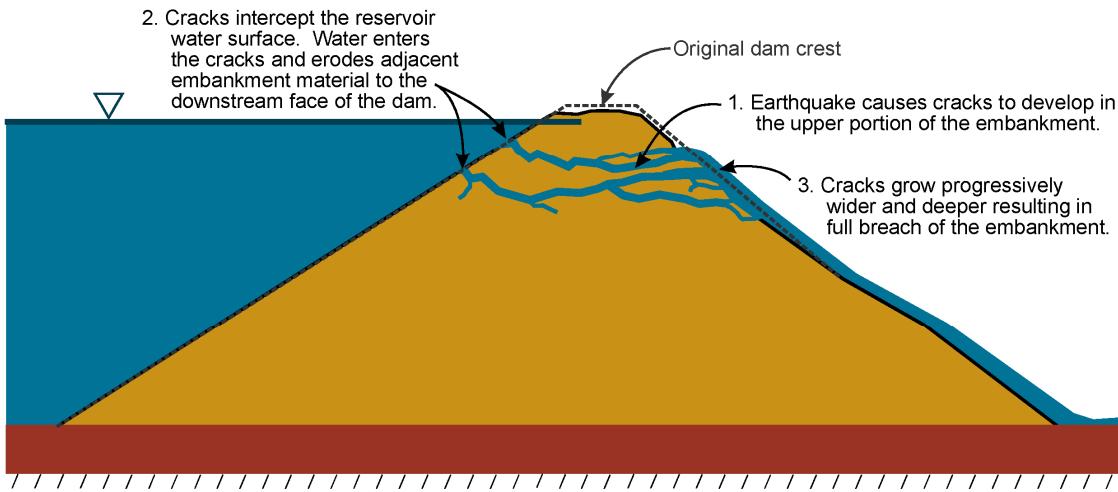


Figure 4. Transverse cracking in Embankment.

3 Analysis and Uncertainty

The level of analysis of dam response is scaled to the sensitivity of the risk. If a screening level risk analysis demonstrates that the dam is well built and not likely to be susceptible to increased earthquake induced ground shaking, the analysis will be streamlined to confirm assumptions and reduce uncertainty of the estimated risks. Other analyses for dams that are known to be susceptible to earthquake shaking, such as hydraulic fill dams, will

include the development of site-specific loadings and finite element and difference models of the structure. An example of finite element analysis of concrete dam damage is shown in Figure 5.

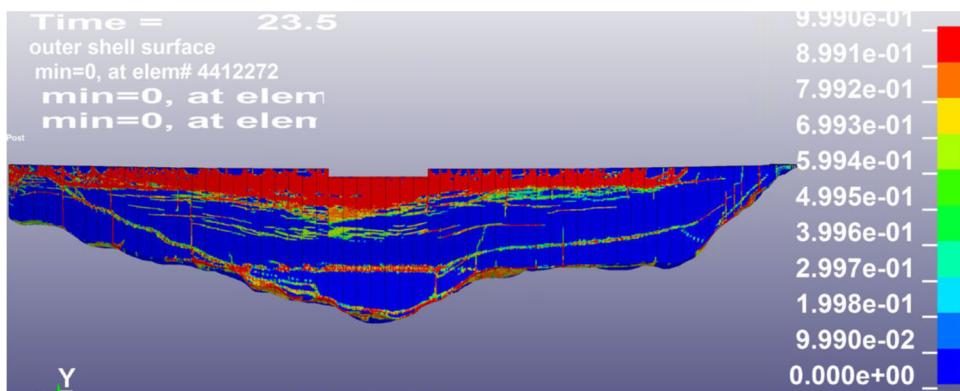


Figure 5. Damage plots from a finite element model of a concrete dam.

Analysis of the structural response can vary from 2-D to 3-D and pseudo-static to a non-linear analysis completed using finite element models for generally five or more sets of ground motions. The motions are deconvolved and applied to the base of the finite element model. Typically, the models are large and cover a significant area to ensure that the motions are propagated through the finite element model.

While the goal of the analysis is to reduce the level of uncertainty in the estimated risks, recognizing that the uncertainty can never be eliminated. Significant effort has been focused on reducing epistemic uncertainty in the finite element models, including industry workshops in the United States and comparison efforts with private consultants, academia, and other government agencies. For concrete dam analysis, Reclamation worked with the United States Society on Dams (USSD) and ICOLD to compare modeling efforts and techniques for an actual earthquake event. This effort led to improved best practices to reduce uncertainty in the model results. For embankment dam analysis, Reclamation has performed comparative efforts using known earthquake case histories such as Lower San Fernando Dam in California. This effort led to the development of a standard analysis guide that Reclamation has used to promote consistency. An industry-wide comparison is planned with USSD in 2025.

Even with efforts to reduce epistemic uncertainty, the actual events used for comparison with the analytical models involved lower intensity than the earthquakes evaluated in a risk analysis, for example, an actual PHA of 0.6g (Seed, et al., 1973) vs. 1.0g or even 1.2g analyzed in some models. As a result, the modeling to support the risk analysis is extending well beyond the bounds of validation for the finite element and finite difference models with real world events.

Another consideration when trying to understand the uncertainty in the analysis is from a series of documents prepared by the United States Committee on Large Dams, the precursor to USSD. Three documents of interest are the Observed Performance of Dams During Earthquakes, Volume I (1992), Volume II (2000), and Volume III (2014 by USSD). A summary of dam failures found that only a few dams have failed from an earthquake worldwide. Many of the dams that did fail were tailing dams or hydraulic fill dams with a known susceptibility to embankment liquefaction. The documents do include a caveat that this may be a result of the fact that few dams have experienced earthquakes of duration and intensity greater than their design criteria.

4 Summary of other Dam Owners and Industry

As Reclamation is considering the evaluation of seismic risks at our dams, it is also looking to other dam owners, regulators, and other industry to understand how methodology and results compare. Below are highlights from this comparison.

4.1 International Commission on Large Dams

The criteria of acceptable seismic dam performance suggested by ICOLD Bulletin 148 (2016) are that there should be no uncontrolled release of water from the reservoir from the shaking of a Safety Evaluation Earthquake (SEE). The SEE is the maximum level of ground motion for which the dam should be designed or analyzed. The deterministically evaluated maximum creditable earthquake (MCE) or the probabilistically evaluated earthquake with a long return period (e.g., 10,000 years) can be considered as an SEE. Deterministically evaluated earthquakes may be more appropriate in locations with relatively frequent earthquakes from known and well-identified sources.

Three levels of consequence rating are used to help determine the seismic input parameters. ICOLD consequence is loosely defined as the anticipated impact downstream of a dam failure; for example, socio-economic consequences can be expressed by the number of persons who would need to be evacuated in case of a dam failure. For extreme or high consequence dams, the SEE should be estimated at the 84th percentile level if developed by a deterministic approach or have a mean annual exceedance probability (AEP) greater than or equal to 1/10,000 if developed by a probabilistic approach. For moderate consequence dams, the SEE should be estimated at the 50th to 84th percentile level if developed by a deterministic approach or a mean AEP greater than or equal to 1/3,000 if developed by a probabilistic approach. For low consequence dams, the SEE ground motion parameters should be estimated at the 50th percentile level if developed by a deterministic approach or a mean AEP greater than or equal to 1/1,000 if developed by a probabilistic approach.

4.2 United States Army Corps of Engineers

The three design earthquakes presented in the USACE guidance (2016) are (1) MCE, (2) maximum design earthquake (MDE), and (3) operating basis earthquake (OBE). The MCE is evaluated using deterministic seismic hazard analysis (DSHA) methods informed by results from a probabilistic seismic hazard analysis (PSHA). An MCE is the largest earthquake that can be expected from a specific source. Multiple MCEs may be defined for a project site with multiple sources, and all MCEs need to be considered to identify the “maximum” ground motion parameters and loadings. There is no return period associated for an MCE. Results of DSHA ground motion studies should include both 50th percentile (median) MCE and 84th percentile MCE.

The MDE is the maximum level of ground motion for which a structure is designed or evaluated. The performance of a structure due to an MDE should not result in loss of life or a catastrophic failure (e.g., uncontrolled release of reservoir), although severe structural damage may be tolerated. For critical projects, the MDE is the same as the MCE. For all other features, the minimum MDE is an event with a 10 percent probability of exceedance in 100 years (or a return period of 950 years). The minimum MDE can be evaluated using PSHA with results from a site-specific DSHA. Note that MDE is the same as the SEE as specified in ICOLD (2016).

It is noteworthy that USACE’s focus on providing flood risk reduction generally results in reservoirs with lower storage levels, on average, resulting in increased freeboard that mitigates the risk of overtopping or cracking in the embankment.

4.3 United States Federal Energy Regulatory Commission

FERC (2018) establishes requirements of a seismic hazard evaluation at a particular dam site. The document requires that a deterministic evaluation should always be conducted to obtain the target spectrum for each seismic source significant to the site. In a DSHA, the median (50th percentile) of intensity measure distribution (e.g., natural logarithm of spectral acceleration or peak ground acceleration) from the empirical ground motion model (or attenuation relationship) is used when the seismic source has a relatively low degree of activity (i.e., faults with slip rates, SR \leq 0.3 mm/year), and the 84th percentile value is used when the seismic sources have high slip rates (i.e., faults with slip rates, SR \geq 0.9 mm/year). For a slip rate value between 0.3 and 0.9 mm/year, the fraction of standard error term ϵ as a function of slip rate can be estimated and then used to calculate the corresponding percentile. The maximum magnitude on each source, hence the MCE, is used for selecting the earthquake ground motions. For background seismic zone (i.e., a possible seismic source not associated with any known fault), the distance from the site to such a real seismic source typically varies from 5 to 15 km, and the maximum moment magnitude is typically $M = 6 \frac{1}{2} \pm \frac{1}{4}$.

When sufficient information for the seismic sources is available, a probabilistic seismic hazard analysis may be completed to supplement the deterministic evaluation. For comparison purposes, ground motion parameter values from the U.S. Geological Survey Unified Hazard Tool (USGS, 2023) for both return periods of 475 years (i.e., 10 percent in 50 years) and 2,475 years (i.e., 2 percent in 50 years) will be obtained and compared with those from the PSHA. Analysis and design should be based on site-specific results and not the USGS hazard values. However, if significant differences exist between the site-specific results and the USGS hazard values (e.g., in hazard curve and magnitude-distance de-aggregation data), possible causes for these differences should be explained and documented. In addition, if a PSHA is conducted, the uniform hazard spectrum (UHS) should be decomposed into two or more conditional mean spectra (CMS) to provide the more realistic expected spectral shapes.

4.4 Australian National Committee on Large Dams

ANCOLD (2012) defines the consequences of dam failure as the “outcome or result of a dam failure in terms of loss life and damage to property and/or services, as well as environmental damage.” The ground motion parameters are selected using the “Consequence Categories,” which is a seven-tier category system (i.e., Very Low, Low, Significant, High C, High B, High A, and Extreme) based on the potential effects of dam failure on the general community. The categories reflect the severity of potential damage and loss in conjunction with either the Population at Risk (PAR) or Potential Loss of Life (PLL).

The assessment of design seismic ground motions can be performed using the deterministic analysis or risk-based analysis according to the ANCOLD guidance (ANCOLD, 2019a). The deterministic analysis requires the selection of an OBE and SEE. Dam safety criteria of factor of safety and deformation are to be met so that there is a low likelihood of dam failure given the SEE loading. In the deterministic analysis, design ground motions at the dam site are defined in probabilistic terms and by ground motion resulting from the MCE on the active faults in the vicinity of the dam. The selection of design seismic ground motion for OBE and SEE using the deterministic analysis approach is summarized in Table 1. Conversely, the risk-based analysis approach requires assessment of the seismic ground motions at the dam site up to and beyond the SEE for use in risk analyses. For High and Extreme consequence category dams, ANCOLD guidance prefers the risk-based approach to the deterministic approach. “For Significant and Low consequence category dams, deterministic approaches will usually be adequate.”

Table 1. Brief Summary of Severity Levels for Various Impact Types (after ANCOLD, 2019b).

Dam Failure Consequence Category	Operation Phase	
	Operating Basis Earthquake	Safety Evaluation Earthquake
Extreme	Commonly 1 in 475 AEP up to 1 in 1,000 AEP	The greater of: Ground motion from the MCE on known active faults or Probabilistic ground motion Extreme: 1 in 10,000 AEP
High A, B, and C	Commonly 1 in 475 AEP up to 1 in 1,000 AEP	Probabilistic ground motion: High A: 1 in 10,000 AEP High B: 1 in 5,000 AEP High C: 1 in 2,000 AEP
Significant	Commonly 1 in 475 AEP	Probabilistic ground motion: 1 in 1,000 AEP
Low	Commonly 1 in 475 AEP	Probabilistic ground motion: 1 in 1,000 AEP

4.5 American Society of Civil Engineers – Building Code

The intents of building standards are to mitigate collapse of buildings and loss of life, and their use is generally not appropriate for dam applications. This section is included in the review for comparison purposes. Recent building

standards (e.g., ASCE, 2017) use the term Risk-Targeted Maximum Considered Earthquake (MCE_R), which represents a ground motion intensity (e.g., 0.2-second and 1.0-second spectral response acceleration) with a certain probability of exceedance in a given time period (i.e., a uniform risk of building collapse with 1 percent in 50 years probability or a return period of 4,975 or \approx 5,000 years). In a building design, the design ground motion intensity is usually based on an intensity of $\frac{1}{3}$ of the MCE_R . The two objectives of building standards are to (1) achieve a performance level of “life safety” (i.e., a building suffered from significant damage and may not be able to be occupied until after repairs are made) if the building site experiences ground motion intensity equal to the design ground motion intensity of $\frac{1}{3} MCE_R$, and (2) to achieve a performance level of “collapse prevention” (i.e., a building is on the verge of collapse) if the building site experiences a ground motion intensity equal to the MCE_R (Maxfield, 2016). The MCE_R ground motion intensity in building standards is different from the MCE of a scenario-based deterministic analysis, which is a maximum earthquake magnitude for a particular seismic source. As required by the building standards, the site-specific MCE_R spectral response acceleration at any period shall be taken as the less of the spectral response accelerations from the probabilistic ground motions and the deterministic ground motions.

4.6 American Association of State Highway and Transportation Officials

The seismic design of a bridge is different than that observed in dams, and this section is included for comparison purposes. The seismic design of a bridge is generally comprised of (1) determining the performance level required during the design earthquake, (2) performing demand analysis for loadings placed on the bridge, and (3) performing capacity design to withstand the demand for the required performance level (FHWA, 2014). In the capacity design, the ratio of demand to capacity needs to be less than 1.0. In the demand analysis, the seismic loads at the bridge site are determined using either the AASHTO design hazard maps or a site-specific seismic hazard assessment study. The design earthquake adopted by AASHTO for ordinary bridges has a probability of exceedance of 7 percent over an exposure period of 75 years (i.e., return period of about 1,000 years). However, in some circumstances, longer return periods (e.g., 1,500 or 2,500 years) have been used for important bridges and major critical water crossings (FHWA, 2014).

5 Conclusion and Next Steps

Reclamation has implemented a risk informed framework to prioritize modifications to our dams to reduce risk of failure that leads to life loss. This framework, in combination with the use of PSHA that include faults active in quaternary time, has led to increased evaluations of seismic risks at Reclamation dams and resulted in the need for a low conditional failure probability estimate under a relatively remote earthquake loading to meet the visual guidelines. Dam safety modifications for seismic hazards are expensive and becoming even more expensive due to specialized construction methods and materials necessary to ensure a robust modification with a reasonable level of success. In addition, there remains epistemic uncertainty given the limited ability to calibrate and validate the finite element and finite difference models to the modeled loads. Finally, the number of actual dam failures whose characteristics match Reclamation’s portfolio of dams is limited, leading to few real-world examples of the PFMs evaluated.

As Reclamation is responsible for the safety of 364 high hazard dams, which if they fail would lead to life loss, it is critical to ensure that funding and other resources are allocated to the dams that have the highest risk and greatest potential to fail. Investing significant effort in evaluating and modifying well-built dams where the only real vulnerability is the location of a fault that generates significant ground motions at a small probability leads to the first question we are trying to answer.

1. At what threshold, either in terms of loading frequency or modification cost, does the level of uncertainty in the seismic risk model, including seismic hazard and structural response, support the decision to modify a dam to improve its seismic resilience?

The comparison effort is demonstrating that if an earthquake with a 1/50,000 probability occurs in a specific location, the ground motions could significantly exceed those established for roads, bridges, and buildings. The life loss in the impacted area will be exceedingly high from failure of most of the infrastructure. In the event that

Reclamation is able to increase the resilience of a dam to withstand such an event, the dam may be the only structure standing. This level of resilience can be well beyond other dam owners in the United States, Australia, and the international standards published by ICOLD. Conversely, if an earthquake of this magnitude were to occur, and a dam upstream of the impacted population were to fail, recovery efforts would be impeded and likely made nearly impossible due to the flood waters and debris that result from the dam failure. The failure of the dam would compound the lives lost resulting from the earthquake.

As a result of the comparisons, a second question has arisen.

2. Is Reclamation's approach leading to decisions consistent with other dam owners and infrastructure?

Reclamation has invested significant resources into answering these questions, as demonstrated by the efforts to understand and reduce epistemic uncertainty in the finite element modelling for concrete dams and embankment dams. The next steps for this effort are provided below in no specific order.

- Continue efforts to reduce our epistemic uncertainty by:
 - Evaluating the use of conditional mean spectra and the uniform hazard curve
 - Performing a comparison effort with other organizations for embankment dam modeling
 - Evaluating the use of machine learning to streamline finite element modelling to increase evaluations of dam response
- Increase the extent of our comparisons to include nuclear infrastructure and other dam owners
- Evaluate our risk informed decision making framework and how PFM's are developed and evaluated to more systematically identify what should be considered as part of a dam safety study
- Complete an evaluation of the portfolio of dams, showing the impacts of seismic risk reduction activities against the portfolio-wide risks
- Follow a portfolio-wide approach using actuarial methods from the insurance industry
- Complete an external peer review of any changes to our approach

6 References

ANCOLD (2012). Guidelines on the Consequence Categories for Dams, Australian National Committee on Large Dams, Hobart, Tasmania, Australia.

ANCOLD (2019a). Guidelines for Design of Dams and Appurtenant Structures for Earthquake, Australian National Committee on Large Dams, Hobart, Tasmania, Australia.

ANCOLD (2019b). Guidelines on Tailings Dams Addendum - Planning Design, Construction, Operation and Closure, Australian National Committee on Large Dams, Hobart, Tasmania, Australia.

ASCE (2017). Minimum Design Loads and Associated Criteria for Buildings and Other Structures, ASCE 7-16, American Society of Civil Engineers, Reston, Virginia.

BUREAU OF RECLAMATION, 2018. The Bureau of Reclamation, A Very Brief History. Available online: <https://www.usbr.gov/history/borhist.html#:~:text=Congress%20passed%20the%20Reclamation%20Act,arid%20lands%20for%20human%20use> (accessed on 15 September 2023).

BUREAU OF RECLAMATION, 2022. Public Protection Guidelines: a Risk Informed Framework to Support Dam Safety Decision-Making, Denver, Colorado: Bureau of Reclamation.

FERC (2018). Chapter 13 - Evaluation of Earthquake Ground Motions, Engineering Guidelines for the Evaluation of Hydropower Projects, May 2018, Division of Dam Safety and Inspections, Office of Energy Projects, Federal Energy Regulatory Commission, Washington, D.C.

FHWA (2014). LRFD Seismic Analysis and Design of Bridges Reference Manual, NHI-15-004, National Highway Institute, Federal Highway Administration, U.S. Department of Transportation, Washington, D.C.

ICOLD (2016). Selecting Seismic Parameters for Large Dams Guidelines, Bulletin 148, International Commission on Large Dams, Paris, France.

- Maxfield, B. (2016). "Are You Communicating Seismic Concepts Correctly?", Structure Magazine, March 2016, pp. 32-34.
- Seed, H., Lee, K., Idriss, I. & Makdisi, F., 1973. Analysis of the Slides in the San Fernando Dams during the Earthquake of February 9, 1971. Earthquake Engineering Research Center, pp. Report No. EERC 73-2.
- USACE (2016). Earthquake Design and Evaluation for Civil Works Projects, Engineering and Design, ER 1110-2-1806, Department of the Army, U.S. Army Corps of Engineers, Washington, D.C.
- USGS (2023). Unified Hazard Tool, Earthquake Hazards Program, U.S. Geological Survey, U.S. Department of the Interior. Available online: <https://earthquake.usgs.gov/hazards/interactive/> (accessed on 8 September 2023).
- USCOLD (1992). Observed Performance of Dams During Earthquakes - Volume I, United States Committee on Large Dams, Denver, Colorado.
- USCOLD (2000). Observed Performance of Dams During Earthquakes - Volume II, United States Committee on Large Dams, Denver, Colorado.
- USSD (2014). Observed Performance of Dams During Earthquakes - Volume III, United States Society on Dams, Denver, Colorado.

NON-LINEAR SEISMIC ANALYSIS OF CONCRETE GRAVITY DAM USING TIME DOMAIN SPECTRAL FINITE ELEMENT METHOD

A. Sarkar¹ & A. Bagchi²

¹ Concordia University, Montreal, Canada, avirupsarkar9@gmail.com

² Concordia University, Montreal, Canada, ashutosh.bagchi@concordia.ca

Abstract: Concrete gravity dams are an important component of modern-day infrastructure industry due to their diverse utilities. The structural analysis and health monitoring of these structures is extremely important as failure of these structures could lead to huge scale devastations. Seismic events have caused damage to multiple dams and thus analysis of new and existing dams under seismic excitations is of utmost importance to evaluate the safety and stability of such structures under extreme events. The enormous size of these structures poses certain challenges with regards to the modelling and computational aspect as it requires huge computational time and space. Finite element method (FEM) is one of the most commonly used analysis tools in academics and industry to evaluate the performance of concrete gravity dams. FEM being integrated in most commercial packages also makes it a viable choice for modelling and analysis purposes. Dynamic analysis of large concrete gravity dams consumes huge computational time and space, thus leading to development of alternate modelling techniques in recent years. Time domain based spectral finite element method (TDSFEM) is one such modelling technique which reduces the computational effort compared to FEM while maintaining adequate level of accuracy. This article demonstrates the application of TDSFEM in the non-linear dynamic analysis of concrete gravity dams and illustrates its computational efficiency over the conventional FEM.

1 Introduction

In the field of civil engineering infrastructure, dams are a crucial component. In the last century, both industrialized and developing nations have built a large number of dams. These massive structures provide a variety of functionalities and practical utilities, such as producing hydropower and storing water. There have been cases where dam failure resulted in extensive destruction, loss of life, and damage to property. There are different reasons for the failure of dams: seismic events, material degradation, alkali-aggregate reaction, etc are some of the factors which have led to the failure of dams. The reasons for failure of dams also depend on the type of dam. In light of this, accurate dam analysis, design, and structural health monitoring are crucial in the context of contemporary civil engineering. Monitoring the structural health of big constructions, like dams, is not without its difficulties, though. The dams are massive constructions; thus, it takes a lot of computing power to simulate and analyse them numerically. Second, it's difficult to keep an eye on these constructions due to their massive size.

The Finite Element Method (FEM) stands out as a widely employed analytical tool across diverse engineering applications. Its seamless integration with modern digital computation facilities, due to the matrix methodology embraced in FEM formulations, has contributed to its extensive use. Over an extended period, FEM has proven to be versatile and applicable in nearly all engineering domains. In dynamic analysis, accurately capturing the higher vibration modes of a structure becomes crucial for a precise understanding of its behavior, especially in seismic excitation scenarios. Traditional FEM often necessitates fine mesh sizes to effectively capture these

high-frequency modes, with the mesh size ideally comparable to the wavelength of such modes. This requirement poses significant computational challenges, particularly for large and intricate structures like concrete gravity dams. The conventional FEM approach in dynamic analysis, in such cases, demands considerable computational resources, leading to challenges in time, space, and cost, potentially compromising solution accuracy.

Recent advances in the field of computational techniques in engineering have seen the development of several alternative methods with varied field of applications. While the versatility of the conventional FEM remains unparalleled, the alternative methods are more efficient in terms of the specific objective for which they are developed. A class of alternate methods are termed as spectral finite element methods. The basic objective of the development of these methods is to achieve computational efficiency over the conventional FEM in a wide range of structural engineering problems. These methods have their specific advantages and disadvantages. In this article, the authors discuss the applicability of the two most relevant spectral finite element methods in the context of dynamic analysis of concrete gravity dams. The novelty of the present work is in terms of the application of the suitable spectral finite element method for the dynamic analysis of concrete gravity dams and showcasing the computational efficiency over the conventional FEM. In this aspect, there has not been enough research in literature as per the knowledge of the authors. The authors however have showcased the computational efficiency of the spectral finite element method over the conventional FEM in some of their recent works, for example, Sarkar et al (2022), Sarkar & Bagchi (2023). The above-mentioned works are however limited to linear dynamic analysis. In the present work, the authors have extended their previous work on spectral finite element method in the dynamic analysis of concrete gravity dams using material non-linearity. The organization of the article is as mentioned next. Section 2 discusses in brief the literature review of application of FEM in dynamic analysis, the development of the spectral finite element methods, their respective advantages, and disadvantages, and finally the applicability of these methods in case of dynamic analysis of concrete gravity dams. In Section 3, the methodology of the Time domain spectral finite element method (TDSFEM) is discussed in detail. Section 4 presents the non-linear material modelling details adopted in this work. In Section 5, the seismic analysis of a concrete gravity dam using TDSFEM is showcased. Section 6 is focussed on the detailed discussions on the results obtained in the previous section. Conclusions and scope of future work are provided in Section 7 followed by a list of references.

2 Literature review

2.1 Finite Element method (FEM) and other alternative techniques

The traditional Finite Element Method (FEM) relies on shape functions that are static and independent of frequency. In recent years, there has been a pursuit of alternative analysis approaches to tackle dynamic problems with reduced computational time and cost. A pioneering idea in this direction involves the use of dynamic or frequency-dependent shape functions. The Dynamic Stiffness Method (DSM) is an early development that adopts frequency-dependent shape functions to accurately represent higher modes of a structure without requiring mesh refinement, resulting in increased precision. Another method following a similar approach and operating in the frequency domain is the Spectral Analysis Method (SAM). SAM utilizes the Fast Fourier Transform (FFT) to efficiently compute the frequency-dependent components of numerous high-frequency modes needed for a specific problem. The integration of key features from conventional FEM, DSM, and SAM has led to the creation of the Spectral Finite Element Method (SFEM). SFEM, often referred to as Frequency Domain-based Spectral Finite Element Method (FDSFEM) according to Doyle (1997) and Lee (2009), relies on FFT for its operations. Another alternative class of finite element method, focusing on computational efficiency over conventional FEM, is the Time Domain Based Spectral Finite Element Method (TDSFEM), introduced by Patera (1984). TDSFEM follows a distinct methodology from FDSFEM, operating in the time domain while incorporating spatial discretization. Although labeled as a 'spectral' method, TDSFEM integrates higher-order polynomials as interpolating functions, utilizing the Gauss-Lobatto-Legendre (GLL) integration technique for efficient computation. While TDSFEM doesn't directly provide frequency domain information, it offers computational advantages compared to traditional FEM.

2.2 Frequency domain based spectral finite element method (FDSFEM)

The Frequency Domain-based Spectral Finite Element Method (FDSFEM) operates with precise solutions to the governing differential equations, ensuring the utmost accuracy in modelling the dynamic properties of the system. This approach necessitates only a single element to model a section of a structure without any material or geometric continuity, thereby significantly reducing the size of matrices to be solved. By functioning in the

frequency domain, the method computes the response through the superposition of responses across various frequencies using FFT and Inverse FFT algorithms. The computational efficiency of FDSFEM was initially demonstrated by Doyle (1990) in the context of flexural wave propagation in Euler-Bernoulli beams. Subsequent work by his research team extended the application to Timoshenko beam theory by Gopalakrishnan et al. (1992). To illustrate the computational accuracy and efficiency of FDSFEM, a modal analysis comparison of Euler-Bernoulli beams using conventional FEM and FDSFEM was conducted by Lee & Lee (1996). Lee (2000) further developed Frequency Domain-based SFEM formulations for lattice structures. Based on the literature mentioned above, several notable advantages of FDSFEM can be highlighted. These include a reduction in the number of degrees of freedom and equations to be solved, leading to decreased computational time. Additionally, FDSFEM demonstrates high accuracy in addressing frequency domain problems, such as the calculation of eigenfrequencies. Nevertheless, there are specific limitations associated with employing FDSFEM for problems in structural engineering. The Frequency Domain-based Spectral Finite Element Method (FDSFEM) necessitates precise solutions for the governing equations of wave propagation, which are unavailable for structures with irregular geometry. Furthermore, the FDSFEM formulation incorporates throw-off elements at the boundary, consisting of one-noded semi-infinite elements that simulate the dissipation of energy from the structure. The requirement to model these throw-off elements at the element boundary limits the application of FDSFEM to structures with intricate geometries, a constraint that may not be suitable for many real-life practical structures. The impracticality arises from the necessity for the boundary element to be infinitely long in the FDSFEM formulation, making it challenging to apply to structures with complex geometry in real-world scenarios. The constraints in applying FDSFEM underscore the importance of ongoing research to explore alternatives within the realm of Spectral Finite Element Methods (SFEMs). Such research endeavours are crucial for overcoming these limitations and broadening the applicability of SFEMs in addressing diverse challenges in structural engineering.

2.3 Time domain based spectral finite element method (TDSFEM)

The spectral element method, initially introduced by Patera (1984) and later termed the Time Domain-Based Spectral Finite Element Method (TDSFEM), offers an alternative approach. It is noteworthy that in TDSFEM, the discretization occurs in the spatial domain. The distinction between TDSFEM and conventional FEM lies in the utilization of higher-order polynomials as interpolating functions, with integrating points connected to the element nodes rather than within the element domain. This characteristic leads to a diagonal mass matrix, resulting in reduced computation time compared to conventional FEM and thereby saving on computational costs. Witkowski et al. (2009) developed a Time Domain-Based Spectral Finite Element Method (TDSFEM) formulation specifically for Timoshenko beam elements, applying it to the task of damage detection in frames. Chróscielewski et al. (2009) conducted a similar study, focusing on steel truss structures. TDSFEM finds widespread application in 2D structures, as it circumvents the challenges encountered in Frequency Domain-Based Spectral Finite Element Method (FDSFEM). Zak (2009) introduced an innovative TDSFEM formulation tailored for isotropic plates. Rucka (2011) employed the TDSFEM formulation to model in-plane wave propagation in plates and conduct damage detection. Witkowski (2012) formulated 2D time domain-based spectral finite elements for wave propagation analysis using plane stress elements. Ostachowicz et al. (2012) provided a comprehensive guide for wave propagation analysis in structures using time domain-based spectral finite elements. Wang (2022) explored the vibration characteristics of simply supported beams, cantilever beams, and a four-edged rectangular plate using TDSFEM. The literature review indicates that FDSFEM exhibits higher computational efficiency compared to TDSFEM, as it requires only a single element to model dynamic properties without material or geometric discontinuity. However, the inclusion of a throw-off element in FDSFEM restricts its application to two-dimensional problems or structures with complex or irregular geometry. Furthermore, FDSFEM relies on solving governing differential equations for wave propagation, which is unavailable for irregular geometries. TDSFEM, with its different integration scheme compared to the Gauss Quadrature used in conventional FEM, gains significant computational efficiency. Palacz (2018) and Hafeez & Krawczuk (2023) have provided a detailed comparison of FDSFEM and TDSFEM. For the modelling of two-dimensional practical structures with complex geometry, TDSFEM emerges as a more suitable approach.

Notably, there is a lack of adequate research on modelling large civil engineering structures, such as concrete gravity dams with irregular geometries, using alternative techniques like TDSFEM. Concrete gravity dams, due to their immense size, demand considerable computational resources, space, and cost when employing conventional FEM, especially with a finer mesh to capture stress variations in critical dam locations. The

paper's objective is to apply efficient TDSFEM for dynamic time history analysis of concrete gravity dams and assess the computational efficiency achieved over conventional FEM in terms of saved computational time. The study considers the same order of polynomials for shape functions and degrees of freedom in both FEM and TDSFEM simulations to compare their performance effectively. As mentioned previously, the authors have performed dynamic analysis of concrete gravity dams using TDSFEM in some of their recent works. In this present article, the authors have extended their work on dynamic analysis using TDSFEM for the case of material nonlinearity. The objective of the present work is to showcase the application of TDSFEM in dynamic analysis of concrete gravity dams considering material non-linearity and the computational efficiency achieved over the conventional FEM.

3 Methodology of TDSFEM

The current section elaborates on the two-dimensional plane stress formulation within the framework of TDSFEM and delineates its distinctions from conventional FEM. The stiffness and mass matrices, along with the load vector, are expressed in the general form provided below.

$$\int_B C_{\alpha\beta\gamma\pi} w_{(\alpha,\beta)} u_{(\gamma,\pi)} dV \rightarrow K_{(e)} = h_0 \int_B B_{(e)}^T(\xi) E B_{(e)}(\xi) dx_1 dx_2 \quad (1)$$

$$\int_B \rho w_\alpha u_\alpha dV \rightarrow M_{(e)} = \rho h_0 \int_B L_{(e)}^T(\xi) L_{(e)}(\xi) dx_1 dx_2 \quad (2)$$

$$\int_B w_\alpha b_\alpha dV + \int_{\partial B_f} w_\alpha f_\alpha dS \rightarrow f_{(e)}^{ext} = h_0 \int_B L_{(e)}^T(\xi) b dx_1 dx_2 + \int_{\partial B_f} L_{(e)}^T(\xi) f dS \quad (3)$$

For transformation from the parent element to the mapped element, the Jacobian determinant needs to be used which takes the form:

$$j(\xi) = \frac{\partial x_1}{\partial \xi^1} \frac{\partial x_2}{\partial \xi^2} - \frac{\partial x_1}{\partial \xi^2} \frac{\partial x_2}{\partial \xi^1} \quad (4)$$

$$dV = h_0 j(\xi) \partial \xi^1 \partial \xi^2 = h_0 dx_1 dx_2 \quad (5)$$

For the total element load vector, the external load vector is added to the nodal load vector as below.

$$f_{(e)} = f_{(e)}^{ext} + f_{(e)}^{node} \quad (6)$$

$$f_{(e)}^{node} = \{P_1, P_2, \dots, P_N\}^T \quad (7)$$

$$P_a = \{P_{x1}, P_{x2}\}_a^T \quad (8)$$

Here, the vector P_a represents the nodal loads applied to the node 'a' of an element in the global co-ordinate system.

However, to obtain the element matrices, numerical integration needs to be performed.

$$K_{(e)} = \int_{-1}^1 B_{(e)}^T(\xi) E B_{(e)}(\xi) j(\xi) d\xi \approx \sum_{p=1}^{n_p} w_p B_{(e)}^T(\xi_p) E B_{(e)}(\xi_p) j(\xi_p) \quad (9)$$

$$M_{(e)} = \int_{-1}^1 N_{(e)}^T(\xi) \mu N_{(e)}(\xi) j(\xi) d\xi \approx \sum_{p=1}^{n_p} w_p N_{(e)}^T(\xi_p) \mu N_{(e)}(\xi_p) j(\xi_p) \quad (10)$$

$$f_{(e)} = \int_{-1}^1 N_{(e)}^T(\xi) f_{(e)}(\xi) j(\xi) d\xi \approx \sum_{p=1}^{n_p} w_p N_{(e)}^T(\xi_p) f_{(e)}(\xi_p) j(\xi_p) \quad (11)$$

In the above equations, n_p represents the number of integration points, ξ_p indicates the coordinates of the integration points, and w_p represents the associated weights of numerical integration. Notably, the departure of TDSFEM from conventional FEM lies in its utilization of the Gauss-Lobatto-Legendre (GLL) quadrature rule instead of the Gauss-Legendre quadrature rule employed in conventional FEM. The GLL quadrature rule, as described by Hilderbrandt (1956), expresses the coordinates of the integration points and their associated weights as given in the following equations.

$$(1 - \xi^2) \frac{dP^{M-1}(\xi)}{d\xi} = 0, M \leftarrow m_1, m_2 \quad (12)$$

$$w = \frac{2}{M(M-1)(P^{M-1}(\xi))^2}, M \leftarrow m_1, m_2 \quad (13)$$

Here, P^M denotes the Legendre polynomial of the M^{th} order given by the equation below

$$P^M(\xi) = \frac{1}{2^M M!} \frac{d^M}{d\xi^M} [(\xi^2 - 1)^M], \xi \leftarrow \xi^1, \xi^2 \quad (14)$$

The key characteristic of the GLL quadrature rule is its alignment of the coordinates of the integration points with the element nodes. This alignment occurs because of the interpolating polynomials used and the integration being conducted over the GLL nodes, resulting in the element mass matrix calculated by TDSFEM becoming a diagonal matrix. The global matrices are then formed from these element matrices through a standard aggregation procedure, akin to the process in conventional FEM.

4 Non-linear material modelling of concrete

Concrete like other quasi-brittle materials follows non-associative plasticity, which means the yield surface and the plastic flow potential are not the same. There have been quite a few plasticity models proposed for multi-dimensional plasticity behaviour of concrete. Damage in concrete is also modelled coupled with plasticity and them for multi-dimensional plasticity along with damage parameters are called as coupled damage plasticity models for concrete. The initial concrete damage plasticity models were provided by Lubiner et al (1989), Cervera et al (1995). However, those models work mostly in case of monotonic loadings as the defined damage variables are not separate for compression and tension. Lee and Fenves (1998) modified the damage plasticity variable proposed by Lubiner et al, (1989) by considering damage variables in tension and compression separately. This plastic damage model takes care of the different stiffness degradation behaviour in compression and tension and also the stiffness recovery effects during cyclic loading. Thus, this damage plasticity model is a comprehensive material model for concrete and has been adopted in this paper to model the behaviour of concrete under cyclic loading. For the return mapping algorithm, an elastic predictor-plastic corrector methodology is adopted along with the Newton-Raphson method for solving the set of non-linear equations as suggested by Simo and Taylor (1986). It needs to be pointed out here that in the recent years, several other concrete damage plasticity models have been developed for specific applications like Grassl (2009), Unger et al. (2011).

5 Seismic analysis of concrete gravity dam using TDSFEM

Given the substantial size of concrete gravity dams, adopting a computationally efficient analysis approach holds the potential to significantly reduce both computational time and costs. In this study, the Koyna dam

serves as a case study due as it was well-studied in the literature, especially in dynamic analysis studies (Chopra and Chakrabarti, 1973; Bagchi et al., 2019; Sooch and Bagchi, 2012, 2014; Sarkar et al., 2022; Sarkar and Bagchi, 2023). Additionally, the ABAQUS user's manual (2014) features Koyna dam as an example for seismic analysis of concrete gravity dams, making it a benchmark problem. The dam's geometry is illustrated in Figure 2a. Various meshing configurations were explored, with a representative mesh of 45 elements shown in Figure 2b. Similar meshing strategies were applied with 190 and 760 elements until reaching convergence. The Young's Modulus for the dam body is considered as 31,027 MPa, Poisson's ratio as 0.15 and density as 2,643 kg/m³. The non-linear material properties of the dam for biaxial loading are considered as per ABAQUS manual. Four-noded isoparametric quadrilateral elements have been considered for modeling the dam (shown in Figure 1). Dynamic time history analysis has been performed using the recorded horizontal and vertical ground motions at the location. The details of the ground motion records were obtained from ABAQUS manual. The magnitude of the earthquake was 6.7 (1967) on the Richter scale. The time histories of the ground motion are plotted in Figures 3 and 4. A computer program has been developed in the MATLAB environment (Matlab 2021) to integrate the material non-linear behavior in the TDSFEM formulation for the dam. In order to draw a comparison of the performance of FEM and TDSFEM, codes have been written for both FEM and TDSFEM and keeping the same degrees of freedom, non-linear time history analysis has been performed for both the cases.

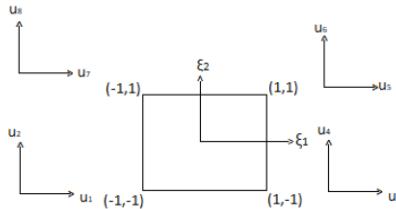


Figure 1. Typical 4 noded element with 2 degrees of freedom at each node.

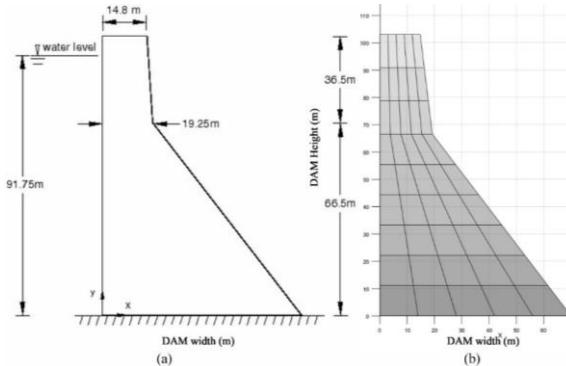


Figure 2. a) Dam geometry b) Typical meshing of dam geometry.

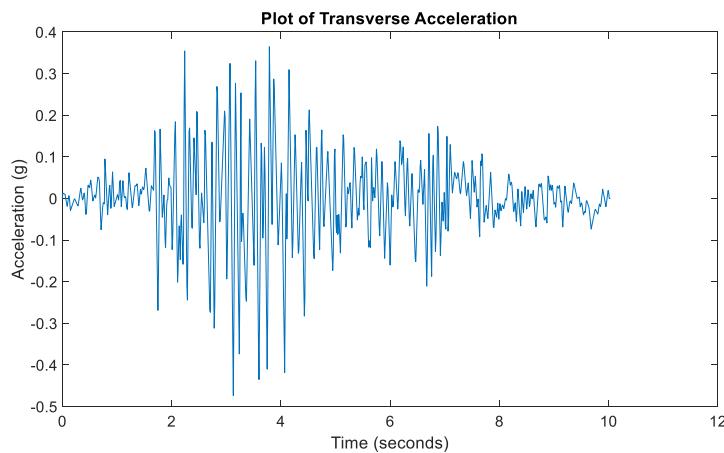


Figure 3. Horizontal ground acceleration.

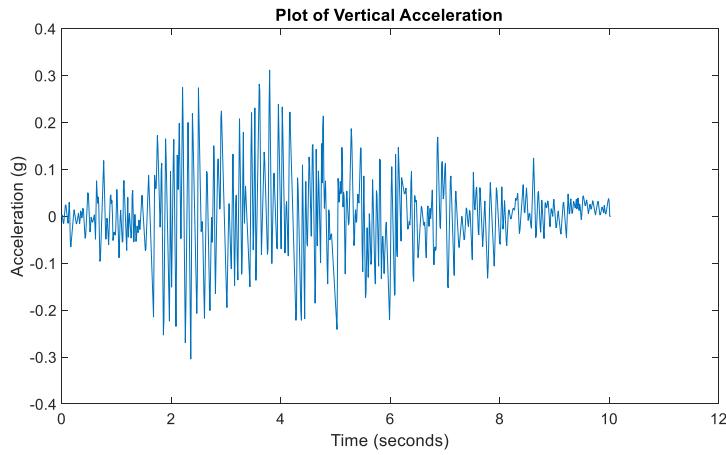


Figure 4. Vertical ground acceleration.

The time history of horizontal crest displacement has been shown in Figure 5 for both FEM and TDSFEM. The maximum displacement for FEM case was found to be about 50 mm and for FEM, it was 46 mm. Also, the time history plot shows the non-linear behavior sets in at 4 seconds, which is also reported in the ABAQUS manual. In Figures 6 and 7, the maximum principal stress plots over the dam body are shown for FEM and TDSFEM.

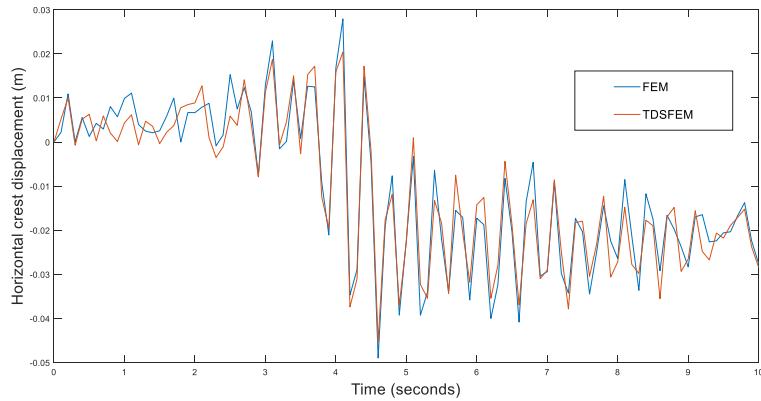


Figure 5. Horizontal crest displacement comparison for FEM and TDSFEM.

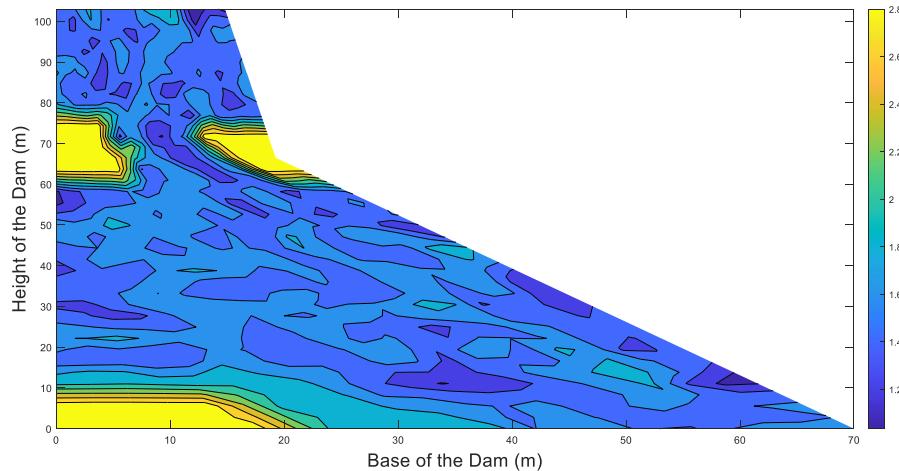


Figure 6. Plot of Maximum Principal Stress (FEM) in MPa units.

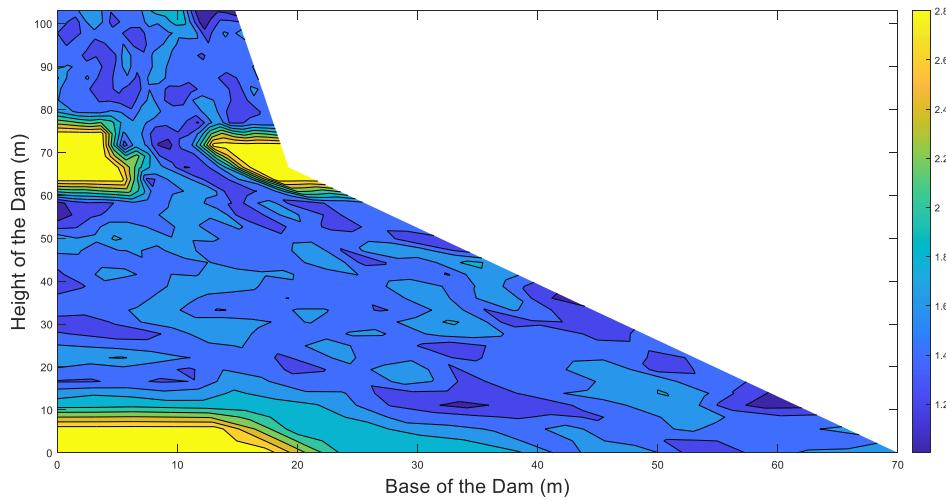


Figure 7. Plot of Maximum Principal Stress (TDSFEM) in MPa units.

6 Results and discussions

It can be observed from Figures 6 and 7 that the non-linearity in the dam body occurs at the locations of the dam heel and dam neck. The same has been reported in literature regarding the seismic analysis of the Koyna. The results of Figure 5, 6 and 7 for the displacement history and the stress plots also reveal the results obtained by FEM and TDSFEM match reasonably well. It needs to be pointed here that the computational time required by the TDSFEM model was 132 minutes, which is about 40 percent of the computational time required by the FEM model (320 mins). In case of dynamic analysis of large structures considering material non-linearity, this is a huge saving in time of computation. This saving in computation time is attributed to the nature of the mass and stiffness matrices obtained by the GLL quadrature scheme.

7 Conclusions and scope of future work

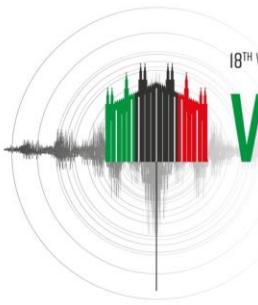
The results of the present study can be effectively used to conclude that the TDSFEM procedure is a viable alternative to the conventional FEM for dynamic analysis of concrete gravity dams and it produces results which are accurate and computational efficiency is achieved. In this study, the above has been demonstrated using a case study of the Koyna Dam. However, the developed methodology is applicable to any dam geometry and similar results can be obtained. The authors would like to point out that in this study, the dam has been considered as fixed base with empty reservoir condition as a preliminary study. As a scope of future work, this could be extended to the case where the reservoir and foundation are modelled and the whole dam-foundation-reservoir system is considered in the model. While modelling of the whole system, may be more complex, it would represent a more realistic scenario and provide more accurate prediction of the seismic response. As a larger computational model involving dam-foundation and reservoir (DFR) system and finer meshing would require much higher computation time due to the larger sizes of the system matrices to be solved, TDSFEM could provide a substantial benefit by reducing the computational time, particularly when a repetitive analysis is required for calculating the response of a DFR system for suite of multiple ground motions. While these aspects are out of scope of the present article, they would be taken up in future.

8 References

- Bagchi, S., Roy, T. B., & Bagchi, A. (2019, June). Multiple damage localization of gravity dam: Strain energy-based approach using random data. In *Proceedings, Annu. Conf.-Can. Soc. Civ. Eng.*
- Cervera, M., J. Oliver, and O. Manzoli, "A Rate-Dependent Isotropic Damage Model for the Seismic Analysis of Concrete Dams," *Earthquake Engineering and Structural Dynamics*, vol. 25, pp. 987–1010, 1996

- Chróscielewski, J., Rucka, M., Wilde, K., & Witkowski, W. (2009). Formulation of spectral truss element for guided waves damage detection in spatial steel trusses. *Archives of Civil Engineering*, 55(1), 43-63.
- Chopra, A. K., & Chakrabarti, P. (1973). The Koyna earthquake and the damage to Koyna dam. *Bulletin of the Seismological Society of America*, 63(2), 381-397.
- Doyle, J. F. and Farris, T. N. (1990), "A spectrally formulated finite element for flexural wave propagation in beams", *Int. J. of Analytical and Experimental Modal Analysis*, 99-107.
- Doyle, J.F. (1997) Wave Propagation in Structures: Spectral Analysis Using Fast Discrete Fourier Transforms, 2nd edn, Springer-Verlag, New York.
- D. Systèmes, "Abaqus analysis user's guide, version 6.14." Dassault Systèmes, 2014. [Online]. Available: <http://130.149.89.49:2080/v6.14/>
- Gopalakrishnan, S., Martin, M. and Doyle, J.F., 1992. A matrix methodology for spectral analysis of wave propagation in multiple connected Timoshenko beams. *Journal of Sound and Vibration*, 158(1), pp.11-24.
- Grassi, P. "On a damage-plasticity approach to model concrete failure". *Engineering and Computational Mechanics*. Volume 162, Issue 4, pp. 221-231, 2009.
- Hafeez, M. B., & Krawczuk, M. (2023). A Review: Applications of the Spectral Finite Element Method. *Archives of Computational Methods in Engineering*, 30(5), 3453-3465.
- Hildebrandt, F.B. Introduction to Numerical Analysis, McGraw-Hill Book Company Inc., 1956
- Lee, J., & Lee, U. (1996). Spectral element analysis of the structure under dynamic distributed loads. In *37th Structure, Structural Dynamics and Materials Conference* (p. 1494).
- Lee, U. (2009). *Spectral element method in structural dynamics*. John Wiley & Sons.
- Lee, U. (2000). Vibration analysis of one-dimensional structures using the spectral transfer matrix method. *Engineering structures*, 22(6), 681-690.
- Lee, J., and G. L. Fenves, "A Plastic-Damage Concrete Model for Earthquake Analysis of Dams," *Earthquake Engineering and Structural Dynamics*, vol. 27, pp. 937–956, 1998.
- Lubliner, J., Oliver, J., Oller, S. and Onate, E., 1989. A plastic-damage model for concrete. *International Journal of solids and structures*, 25(3), pp.299-326.
- Matlab, 2021 "Math. Graphics. Programming", Mathworks Inc., <https://www.mathworks.com/products/matlab.html>, last cited April 5, 2021
- Palacz, M. (2018). Spectral methods for modelling of wave propagation in structures in terms of damage detection—a review. *Applied Sciences*, 8(7), 1124.

- Patera, A. T. (1984). A spectral element method for fluid dynamics: laminar flow in a channel expansion. *Journal of computational Physics*, 54(3), 468-488.
- Rucka, M. (2011). Modelling of in-plane wave propagation in a plate using spectral element method and Kane–Mindlin theory with application to damage detection. *Archive of Applied Mechanics*, 81(12), 1877-1888.
- Sarkar, A., Bagchi, S. & Bagchi, A., 2022. Damage localization of concrete gravity dams based on modal strain energy using time domain spectral finite element method. In *SHMII-11: 11th International Conference on Structural Health Monitoring of Intelligent Infrastructure*.
- Sarkar, A. and Bagchi, A., 2023, August. Stress Analysis of Concrete Gravity Dams Using Time Domain Spectral Finite Element Method Under the Action of Seismic Ground Motion. In *International Conference on Experimental Vibration Analysis for Civil Engineering Structures* (pp. 623-631). Cham: Springer Nature Switzerland.
- Simo, J.C. and Taylor, R., 1986. A return mapping algorithm for plane stress elastoplasticity. *International Journal for numerical methods in engineering*, 22(3), pp.649-670.
- Sooch, G.S. and Bagchi, A., 2014, "A New Iterative Procedure for Deconvolution of Seismic Ground Motion in Dam-Reservoir-Foundation Systems", *Journal of Applied Mathematics*, Article ID 287605, 10 pages, DOI: <http://dx.doi.org/10.1155/2014/287605>.
- Sooch, G.S. and Bagchi, A., 2012, "Effect of seismic wave scattering on the response of dam-reservoir-foundation systems", In *Proc. Of 15th World Conference on Earthquake Eng.*, Lisbon, Portugal.
- Unger, Jörg F., Stefan Eckardt, and C. Koenke. "A mesoscale model for concrete to simulate mechanical failure." *Computers & Concrete* 8.4 (2011): 401-423.
- Wang, J., Li, H., & Xing, H. (2022). A lumped mass Chebyshev spectral element method and its application to structural dynamic problems. *Earthquake Engineering and Engineering Vibration*, 21(3), 843-859.
- Witkowski, W., Rucka, M., Wilde, K., & Chróscielewski, J. (2009). Wave propagation analysis in spatial frames using spectral Timoshenko beam elements in the context of damage detection. *Archives of Civil Engineering*, 55(3), 367-402.
- Witkowski, W., Rucka, M., Chróscielewski, J., & Wilde, K. (2012). On some properties of 2D spectral finite elements in problems of wave propagation. *Finite Elements in Analysis and Design*, 55, 31-41.
- Żak, A. (2009). A novel formulation of a spectral plate element for wave propagation in isotropic structures. *Finite Elements in Analysis and Design*, 45(10), 650-658.



APPLICATION OF GROUND MOTION-COMPATIBLE INTENSIFYING ARTIFICIAL ACCELERATION IN DAMS

G. Sevieri¹, M.A. Hariri-Ardebili², C. Resta³ & A. De Falco⁴

¹ Aon Reinsurance Solutions, Milan, Italy, giacomo.sevieri@aon.com

² University of Maryland, College Park, MD, USA

³ University of Pisa, Dept. of Energy, Systems, Territory and Construction, Pisa, Italy

⁴ University of Pisa, Dept. of Civil and Industrial Engineering, Pisa, Italy

Abstract: Assessing the progressive failure of concrete dams under seismic activity is crucial for evaluating the dam safety. However, traditional approaches, which involve probabilistic seismic hazard analysis, ground motion selection, and scaling techniques, are complex and time-consuming. An alternative method for seismic assessment of concrete dams is to use artificially generated intensifying acceleration functions. This paper investigates the application of a new generation of ground motion-compatible intensifying artificial acceleration (IAA) for linear and nonlinear analysis of concrete gravity dams. The generated IAA has a linearly intensifying nature and is compatible with the response spectrum of the target ground motion, enabling the model to be excited from the linear elastic range to the nonlinear range and eventually lead to failure. The results of IAA are tested and validated against the single-record Incremental Dynamic Analysis (IDA) method, which is a widely used approach for evaluating the seismic performance of structures. The accuracy of the IAA is evaluated for linear and nonlinear models, as well as for both massless and massed foundation models. In addition, a damage index is used to quantify the level of damage in the structures. The results of the study demonstrate promising compatibility between the IAA and IDA methods. Moreover, the IAA method substantially reduces the computational time required for the analysis compared to the IDA method. This makes the IAA method a highly efficient and practical tool for the seismic assessment of structures, especially for large-scale or complex systems that require numerous simulations.

1 Introduction

Seismic assessment of infrastructure plays a key role in quantifying risk due to natural hazards and enhancing the resilience of communities (Saouma and Hariri-Ardebili, 2021). Various methods have been developed to assess the seismic risk of structures; they can be broadly categorized as follows: a.) Seismic Coefficient Method (USACE, 2007); b) Equivalent Lateral Force Method; c) Response Spectrum Modal Analysis Method; d) Time History Modal Analysis Method; e) Time History-Time Integration (THTI) procedure.

The THTI method, the most accurate approach in the previous list, involves the direct integration of the equations of motion in the time domain. Given a ground motion record, this method allows for the comprehensive analysis of the seismic behaviour, at specific seismic intensity levels (SILs), of both linear and nonlinear systems. Uncertainties in the ground motion records, and in the input parameters, cannot be modelled explicitly. Therefore, the use of probabilistic methods becomes imperative. Some widely used

probabilistic methods include Incremental Dynamic Analysis (IDA) (Vamvatsikos and Cornell, 2002), Cloud Analysis (CLA) (Miano et al., 2018), and Multiple-Stripe Analysis (MSA) (Mackie and Stojadinović, 2005).

IDA overcomes the dependence on seismic input characteristics by considering multiple ground motion records at various SILs. The structural response, described in terms of one or more engineering demand parameters (EDPs), is then associated with the corresponding SIL through so-called IDA curves. This technique, however, requires compiling a suite of ground motion records and then selecting and scaling each of them. This entails numerous nonlinear simulations and is notably time-consuming, especially for complex structures like bridges and dams.

The Endurance Time Analysis (ETA) technique (Estekanchi et al., 2007) has been developed to reduce the computational burden of existing methods, while keeping the same level of accuracy. ETA is a time history-based dynamic pushover procedure that employs an intensifying artificial acceleration (IAA) input to analyse the structural behaviour. Unlike IDA, ETA utilizes a limited number of inputs (typically one to three, corresponding to directions of motion) to assess a structure's dynamic behaviour at various SILs. With ETA, the curve associating EDPs with SILs is thus fully defined after a single analysis. Further details about ETA can be found in (Estekanchi and Vafai, 2021) and (Estekanchi et al., 2020). ETA's initial application in Performance-Based Earthquake Engineering (PBEE) and its comparison with IDA have been discussed by (Hariri-Ardebili et al., 2014).

The successful application of the ETA method requires to generate IAAs consistently with the original ground motion record (Nozari and Estekanchi, 2011). Previous studies have used generic IAAs, optimized based on smoothed or codified response spectra. Uncertainty, bias, and validation of generic IAA series with respect to IDA with standardized ground motion sets have been discussed before (Hariri-Ardebili and Sattar, 2023a-b). However, for accurate validation, a structure's response must align with a specific ground motion record.

After discussing a conceptual methodology to compare the result of a ground-motion compatible IAA against a single-record IDA, this paper briefly introduces a simple approach to generate ground-motion compatible IAAs. A concrete gravity dam, interacting with the foundation soil, is finally analysed, considering both a massed and massless soil, to show the proposed approach.

2 Ground motion-compatible IAA

2.1 A conceptual framework for validating IAA against single-record IDA

The main idea behind the conceptual framework introduced in this section is to compare the IAA curve with the corresponding single-record IDA curve. The first step requires the generation of a ground motion-compatible IAA, applying it to the computational platform (e.g., a finite element model), and recording the system's continuous response (IAA curve). The ground motion record itself is then scaled to various SILs, and a series of nonlinear simulations are conducted, resulting in an Incremental Dynamic Analysis curve (Vamvatsikos and Cornell, 2002). The IAA and IDA curves are then compared, evaluating potential discrepancies under different modelling strategies. The paper considers both linear elastic and nonlinear models for the geo-structure, with and without wave propagation assumptions. Figure 1 schematically shows the comparison approach.

2.2 Generation of Ground Motion-Compatible IAA

The Endurance Time Analysis (ETA) is a dynamic pushover technique used to evaluate how structures perform under seismic motions, employing a pre-designed excitation function known as Intensifying Artificial Acceleration (IAA). This simulated acceleration function subjects the structure to a range of SILs, from low, where the structural response remains in the elastic range, to high, exploring nonlinear behaviour, and finally resulting in structural failure. This single dynamic analysis captures the full range of structural response variations. The structural performance is evaluated based on the duration the structure can endure under the imposed artificial excitation. Generally, a longer endurance time before failure indicates a more robust structure.

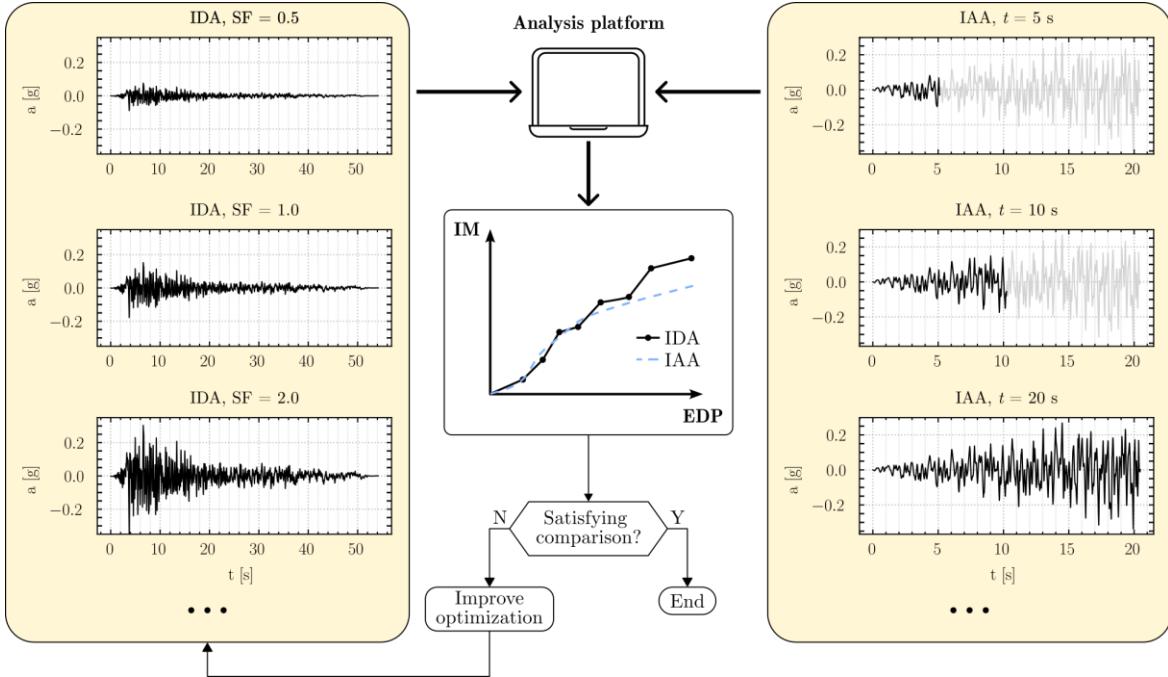


Figure 1. Conceptual scheme of the procedure for validation of IAA against single-record IDA.

The IAA is an artificially constructed acceleration time series, characterized by its response spectra that linearly increase with time. Ideally, both the acceleration time history and response spectrum profiles exhibit linear growth over time. Numerous studies have explored the generation and application of such intensifying acceleration time series. Pioneering work in this area was conducted by (Nozari and Estekanchi, 2011), who generated IAAs compatible with smoothed acceleration and displacement response spectra. Subsequent advancements include the introduction of the hysteretic energy concept and cumulative absolute velocity by (Mashayekhi et al., 2018).

Several approaches, based on different optimization processes and/or objective functions, have been proposed to generate IAAs, such as Wavelet Transform (Mashayekhi et al., 2019a), Evolutionary Algorithms (Mashayekhi et al., 2019b), Time-Domain Spectral Matching (Zhang et al., 2021). These methods make use of code or average spectra of ground motion records as target for the derivation of IAAs. In this paper, a procedure to generate IAAs consistently with specific ground motion records has been applied. The procedure has been detailed in Hariri-Ardebili et al. (2023). Specifically, this process considers acceleration spectra, nonlinear displacement, and absorbed hysteretic energy. Unconstrained nonlinear optimization must then be used to generate IAAs. The optimization aims at minimising the deviations between the dynamic features of IAAs and their intended target values, following the approach detailed in (Mashayekhi et al., 2018).

3 Case study: the Pine Flat Dam

3.1 The Finite Element model

In this paper, the Pine Flat Dam of Fresno County, California (US) has been analyzed. This case study has been chosen because of the large volume of research focusing on this structure, e.g., benchmark workshops organized by the United States Society of Dams (USSD) and the International Committee on Large Dams (ICOLD) in 2018 and 2019 (Salamon, 2018; Salamon et al., 2021). In addition to that, the Pine Flat dam has a notable history of research dating back to the 1970s and 1980s, with comprehensive studies conducted at the University of California at Berkeley (Chávez and Fenves, 1995; Chopra et al., 1980; Fenves and Chopra, 1986; Rea et al., 1972).

A dam is a perfect example to investigate the performance of the IAA approach in the presence of soil-structure interaction, a feature often overlooked in framed structures. It is also worth mentioning that the cost-effectiveness of applying IAA for seismic analysis is more pronounced in complex infrastructures like dams compared to simpler framed structures. Therefore, this paper prioritizes the analysis of a dam as a case study, although a similar methodology can be applied to other engineering structures.

A two-dimensional finite element model of the central non-overflow section has been analysed using ABAQUS 6.14 (ABAQUS, 2014). This model includes the dam, with a height of 121.9 m and a maximum width at the base of 95.80 m; a 700-meter-long foundation block with a depth of 122 m; and a 310-meter-long reservoir with a depth of 116 m. The foundation is represented as a linear elastic domain comprising 4,520 four-node plane stress elements, while the dam body employs either a linear elastic or concrete damage plasticity model (Lee and Fenves, 1998), depending on the analysis type. The reservoir is modelled with 4,012 four-node bilinear acoustic elements to account for compressible fluid effects. Figure 2 illustrates the finite element model, including the key points where responses will be extracted and discussed.

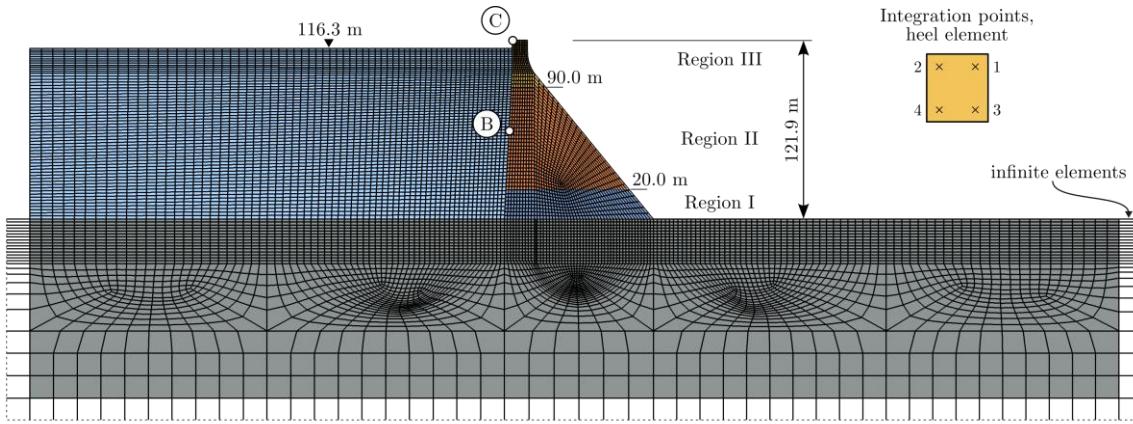


Figure 2. Finite element model of dam-reservoir-foundation system.

To explore the performance of AAIs in the analysis of structures with and without SSI, two foundation models have been considered: the massless model and the massed model. The massless model is widely used among practitioners, while the massed model is considered more reliable in the scientific community (De Falco et al., 2018; Løkke and Chopra, 2019). In seismic analysis using the massless model, the inertial component of soil-structure interaction is entirely neglected. Conversely, the seismic input of the massed foundation model, applied at the foundation base, must undergo deconvolution to achieve an acceleration at the free surface similar to that of the massless model (Wilson, 2002).

These modelling assumptions profoundly impact dynamic analysis outcomes. Selecting appropriate boundary conditions and pre-processing the seismic input to ensure comparability between the two assumptions is crucial. In our study, we employ ABAQUS built-in infinite elements to model the unboundedness of the soil domain (De Falco et al., 2018; Lysmer and Kuhlemeyer, 1969).

The Rayleigh damping has been assumed 2% for frequencies in the range of 1.5 to 2.8 Hz, with a damping matrix containing only the stiffness-proportional part: the stiffness coefficient β_K is greater than zero, while the mass coefficient α_M is set to zero. The application of Rayleigh damping to simulate dam-foundation systems and the advantages of using only the stiffness-proportional part of the damping matrix are discussed in (Løkke and Chopra, 2019). Table 1 presents the damping stiffness coefficients $\beta_{K,c}$ and $\beta_{K,r}$ alongside the elastic properties used in this study. Specifically, ρ_c and ρ_r represent unit weights, E_c and E_r are elastic moduli, and v_c and v_r are Poisson's ratios. The subscript c refers to concrete, while r denotes rock. Water is considered to have a unit weight of 1,000 kg/m³, with a compression wave velocity of $c_p = 1,439$ m/s.

Table 1. Elastic properties of concrete and rock foundation.

E_r [MPa]	ρ_r [kg/m ³]	v_r [-]	$\beta_{K,r}$ [s]	E_c [MPa]	ρ_c [kg/m ³]	v_c [-]	$\beta_{K,c}$ [s]
22410	2483	0.2	0.0044	22410	2483	0.2	0.0022

The nonlinear response of the dam is simulated using the concrete damage plasticity constitutive model (Lee and Fenves, 1998). This constitutive model has gained wide acceptance in structural and dam engineering applications due to its effectiveness in capturing the behaviour of non-reinforced concrete under cyclic loading. The model accounts for concrete damage, resulting from micro-crack development, by reducing the elastic modulus. This reduction is quantified by the scalar value $d_t \in [0,1]$, which is a function of plastic strain. The key material properties associated with this model, including concrete tensile and compressive strength (f_t and

f_c , respectively), fracture energy (G_f), and plastic flow parameters, are summarized in Table 2. The table includes the dilation angle Ψ , the eccentricity ϵ , defining the rate of flow potential approach to the asymptote, the initial equi-biaxial compressive yield stress to initial uniaxial compressive yield stress ratio $\sigma_{b0} / \sigma_{c0}$, and the ratio of the second stress invariant on the tensile meridian to that on the compressive meridian Λ .

Table 2. Concrete damage plasticity model parameters.

Ψ [-]	ϵ [-]	$\sigma_{b0} / \sigma_{c0}$ [-]	Λ [-]	f_t [MPa]	f_c [MPa]	G_f [N/m]
36.31	0.1	1.16	0.66	2	20	250

To assess and compare damage levels across various simulations at different locations, a straightforward damage index concept is employed. This index is calculated based on the intensity of damage, described by the aforementioned scalar parameter $d_t \in [0,1]$, with the ratio of damaged area to total area as a weight. It is expressed as $DI = \sum_{i=1}^{N_e} A_i \times d_{t,i} / A_t$, where A_i represents the elemental area, and A_t the total area under consideration.

Given that damage profiles and failure modes of brittle materials are significantly influenced by the applied seismic excitation, the structure is categorized into three distinct regions or zones. The damage index is then computed separately for each of these three regions, which are illustrated in Figure 2. These regions comprise the bottom 20 meters (Region I), the middle 70 meters (Region II), and the top 32 meters (Region III).

3.2 Ground motion characteristics

The primary focus of this study is on utilizing a ground motion-compatible IAA in the seismic analysis of structures. To demonstrate it, a proof-of-concept approach is taken, using the ground motion record recommended by ICOLD (Salamon et al., 2021). This specific ground motion record is sourced from the Taft Lincoln School Tunnel earthquake, which occurred on July 21, 1952, in Kern County, California.

Following the procedure outlined in Section 2, a horizontal IAA is obtained from the original ground motion record, as presented in Figure 3. This figure displays the acceleration time series alongside its envelope, referred to as the zero-period acceleration (ZPA), which corresponds to the Peak Ground Acceleration (PGA) in actual ground motion records. Throughout this paper, the term ZPA is used to describe the maximum absolute value of all acceleration time series, even though IAA is not an actual ground motion record.

The plot also showcases the acceleration response spectrum, denoted as $S_a(T, \xi, t_{trg})$, and the displacement response spectrum, known as $S_d(T, \xi, t_{trg})$, at the target time of 10 seconds for two different damping values. From a qualitative perspective, there is a strong alignment between the response spectra, demonstrating that the optimized IAA effectively estimates the majority of peak points. The application of a more robust error estimation metric, such as the mean absolute percentage error (MAPE), further substantiates the accuracy of the optimized IAA. Within the critical frequency range for structural analysis, the MAPE values consistently fall within the 10-20% range. This validates that the IAA is effectively optimized across the entire range of seismic intensities, and it is reasonable to anticipate a uniform structural response from them.

3.3 IAA vs. Single-Record IDA

The IAA is used to conduct multiple time history analyses on the finite element model of Pine Flat dam. As discussed already, the main goal is to validate the use of IAA against IDA to estimate the seismic performance and safety of the structure. To obtain results of broader applicability, a total of four analysis scenarios are considered, corresponding to different material behaviours and foundation modelling:

- a linear elastic system with massless foundation;
- a linear elastic system with massed foundation;
- a nonlinear, damaging system with massless foundation;
- a nonlinear, damaging system with massed foundation.

When the foundation is modelled as massless, no wave propagation is expected within its elements; the opposite is true in case of massed foundation. For nonlinear systems, the dam body is modelled using the aforementioned concrete damaged plasticity material, while the foundation is a linear elastic medium.

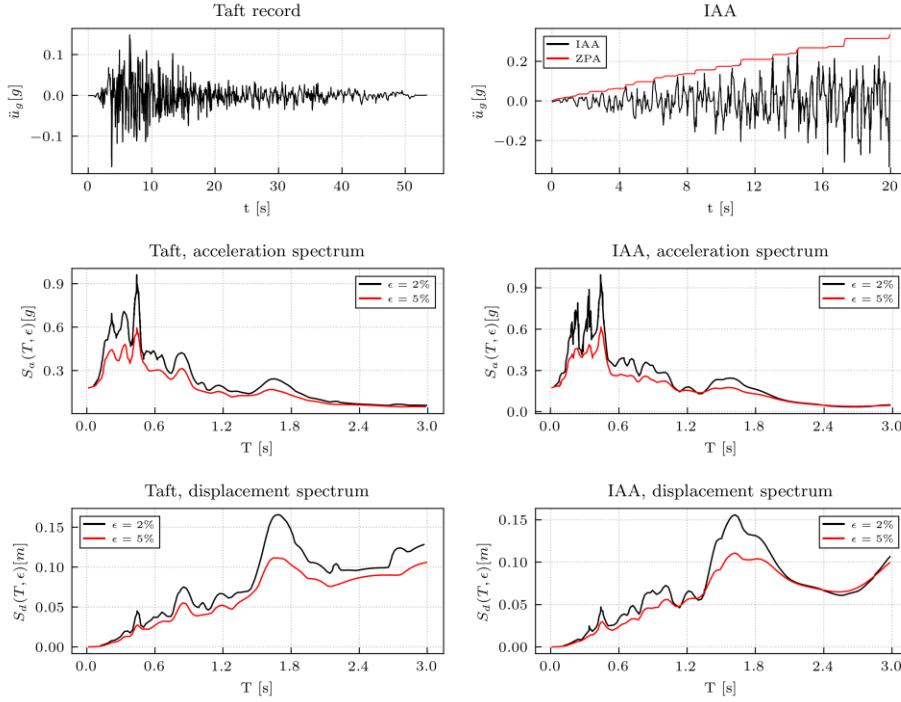


Figure 3. Characteristics of the target ground motion record (i.e., Taft record), the IAA, and their response spectra. Response spectra for IAA is plotted at the target time of 10 s.

The comparison between IDA and IAA is carried out in terms of capacity curves describing the relationship between engineering demand parameters (EDPs) of interest, such as displacements or damage, and a corresponding seismic intensity measure (IM). EDPs selected for this paper are the peak displacement in different locations (Figure 4), the first principal stress at the dam heel for LE models (Figure 5) and the damage index introduced in Section 3 for NL models (Figure 6).

Points defining the IDA curves are obtained from separate time history analyses, each employing the original ground motion amplified or reduced by a different scale factor. Scale factors can be spaced out evenly, or they can be obtained with a more optimized approach such as the hunt&fill method (Vamvatsikos and Cornell, 2002). For this paper, ten analyses are carried out for each scenario: the hunt&fill technique is employed for NL models, while for LE models, scale factors are evenly spaced. IDA capacity curves are developed from the results of analyses, connecting points in the EDP-IM plane with piecewise linear interpolation (although other options are available).

A different procedure is used to build capacity curves for IAA. Only one analysis is carried out for each scenario, and for each EDP the time history response $EDP(t)$ is recorded. It is worth mentioning that for nonlinear systems the response may be shorter than the input, either because of a numerical loss of convergence, or because a predetermined state corresponding to structural failure is reached. Next, a high envelope of the response is calculated, i.e., the maximum of its absolute value until any given time:

$$\Omega(t) = \max(|EDP(\tau)|) \text{ for } \tau \in [0, t]$$

the resulting stepwise increasing function is the desired capacity curve.

Finally, the comparison between IDA and IAA curves is made possible after a suitable conversion to ensure that both employ the same IM. IDA curves are naturally described as a function of a seismic intensity level, while IAA curves, due to the procedure detailed above, are naturally a function of time elapsed since the beginning of the analysis. A bijective relationship exists between IDA scale factors and analysis time, so conversion is possible in either direction. This paper presents results in the EDP-time plane. IDA scale factors are converted into equivalent time as

$$t_{SF} = 10s \times SF,$$

since 10 s is the target time employed for the IAA generation.

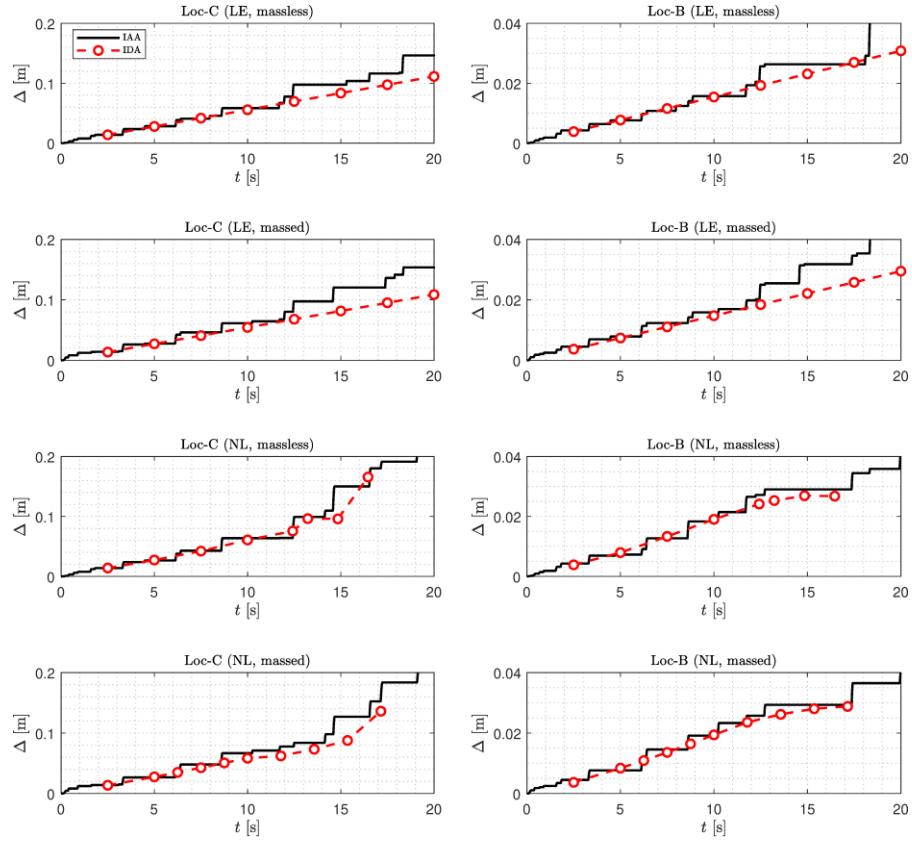


Figure 4. Comparison of peak displacement from IAA and IDA at two locations (C, crest; B, upstream mid-height), under the four considered modelling scenarios.

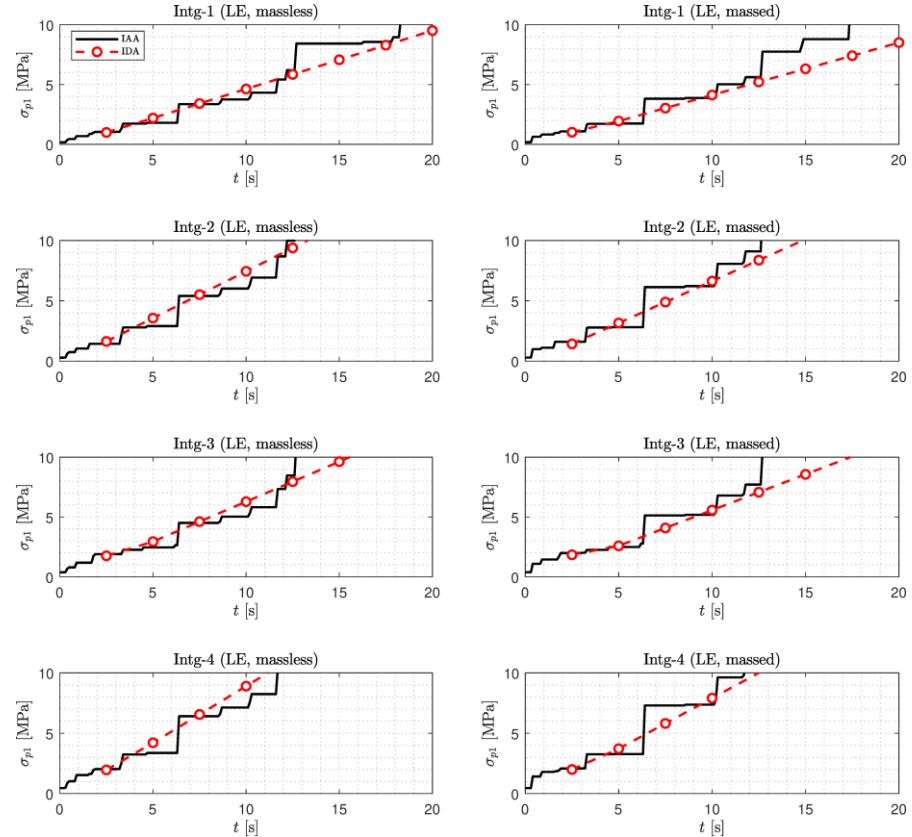


Figure 5. Comparison of IAA and IDA in terms of first principal stress in the four integration points of the finite element at the dam heel, for the two elastic finite element models.

Figure 4 shows the relationship between IM and peak displacement at two different locations on the dam: crest (Loc-C) and mid-height on the upstream face (Loc-B). A more precise localization of the two points is shown in Figure 2. For all four analysis scenarios, IAA curves provide a good prediction of the displacement response when compared with the results of IDAs. As might be expected, in most cases IDA and IAA curves coincide at target time ($t = 10$ s). Nonlinear behaviour is also well represented for both NL models. Both capacity curves for the dam crest are concave up, differently from what can be observed in the other location, pointing to a more severe damage in the upper portion of the dam.

Figure 5 and Figure 6 show, respectively, the value of the first principal stress σ_{p1} at the dam heel and the evolution of damage for increasing IM. Said EDPs are chosen to evaluate the accuracy of IAA in predicting the local response of the structure, as opposed to the global, systemic response represented by peak displacement. Damage is presented only for scenarios with NL models, while the first principal stress is shown only for LE models since cracking happens at the dam base in nonlinear ones, forcing a redistribution of stresses.

IAA curves for stress show good agreement with IDA values in all four integration points of the heel element of the dam (see Figure 2). At higher SILs, IAA overestimates σ_{p1} compared to IDA. It should be mentioned, however, that this happens when the stress levels are decidedly higher than the tensile resistance of concrete, suggesting that a nonlinear analysis may be more suitable in that range.

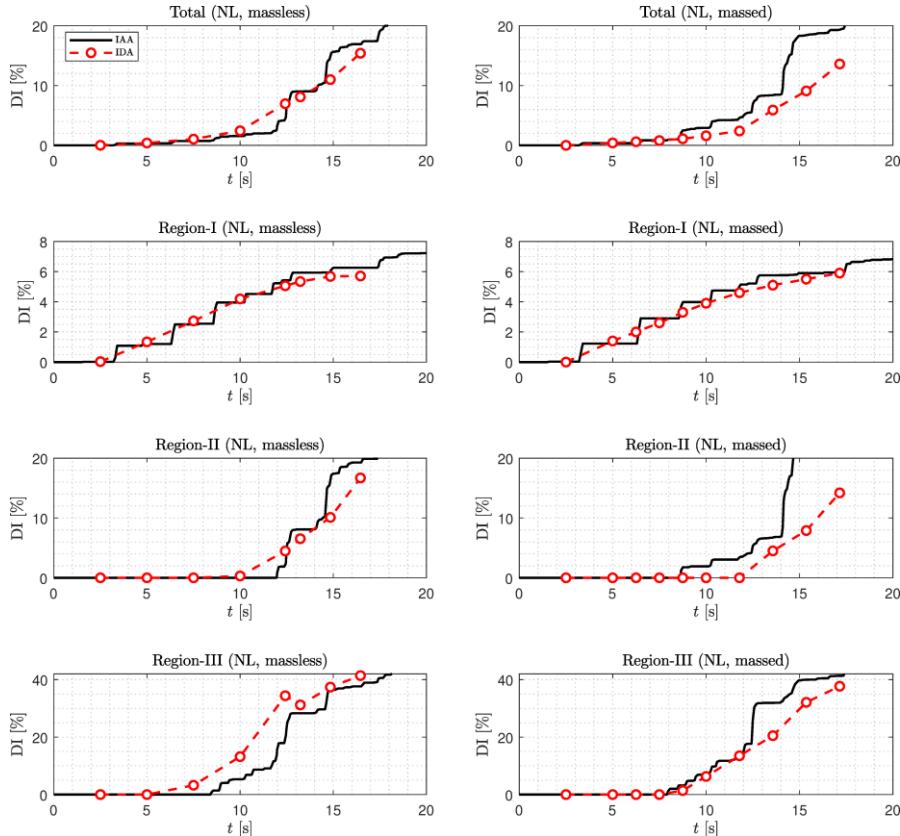


Figure 6. Comparison of damage index from IAA and IDA for the two nonlinear finite element models.

Comparison of damage index for NL modelling scenarios in Figure 6 is presented both for the whole dam and for the three regions in which it is subdivided, corresponding to the lower, middle and topmost portions (see Section 2). IAA-based curves show a remarkable precision in estimating DI in Region I, also capturing the concave-down shape of the IDA curve. A good agreement can also be found for Region II and Region III, especially in the case of massless foundation. The same is true for the whole model, with discrepancies between IAA and IDA curves in the range of 0 - 20%. This is a good result from an engineering perspective, and not an obvious one since the two analysis techniques involve very different cumulative inelastic durations.

Lastly, it should be noted that the total number of simulations required for IAA is four, while a total of 44 simulations were carried out for IDA. Total analysis time for IAA was substantially lower than that of IDA.

4 Conclusions

A proper seismic assessment of structures requires the evaluation of the system failure, accounting for the uncertainties in both the model parameters and the ground motion records. This can be achieved through probabilistic simulations, even though they are computationally intensive. Performing thousands of transient simulations may be feasible for simple framed structures but remains practically unattainable for complex infrastructure like bridges, nuclear power plants, tunnels, and dams.

This paper discusses the use of an alternative approach, the Intensifying Artificial Acceleration (i.e., IAA) to estimate the seismic response of structures. The IAA is an artificially constructed acceleration record, capable of estimating seismic responses ranging from linear elastic behaviour to the nonlinear regime and ultimately to collapse. The paper addresses two key questions regarding the application of IAA:

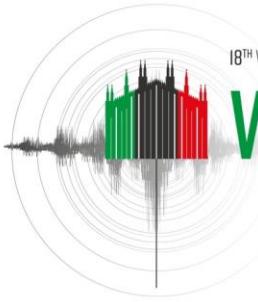
- IAA's validation concerning single-record Incremental Dynamic Analysis (IDA) is explored, encompassing various soil-structure modelling assumptions, including linear and nonlinear systems, as well as massed and massless foundation models.
- the IAA-based capacity function can estimate both global (e.g., displacement) and local (e.g., stress and cracks) engineering demand parameters. While the cumulative inelastic duration in real ground motion may differ from IAA, the damage response remains consistent. The development of cracks is sensitive to slight variations in input excitation, with the most significant discrepancies observed in the upper region adjacent to the neck, while damage indices in lower parts remain nearly identical.

The strong alignment between IAA and single-record IDA results highlights the computational advantages of the proposed framework. Despite the additional computational cost associated with generating ground motion-compatible IAA, it remains significantly more cost-effective than conducting multiple transient simulations in IDA. For a single deterministic model, IAA can substantially reduce finite element computational costs, considering both the number of required simulations and their duration.

5 References

- ABAQUS (2014). *ABAQUS Version 6.14 - Documentation manual*.
- Chávez J.W., Fenves G.L. (1995). Earthquake Response of Concrete Gravity Dams Including Base Sliding, *Journal of Structural Engineering*, 121: 865–875. [https://doi.org/10.1061/\(ASCE\)0733-9445\(1995\)121:5\(865\)](https://doi.org/10.1061/(ASCE)0733-9445(1995)121:5(865))
- Chopra A.K., Chakrabarti P., Gupta S. (1980). *Earthquake Response of Concrete Gravity Dams Including Hydrodynamic and Foundation Interaction Effects*, Berkeley, California University - Earthquake Engineering Research Center.
- De Falco A., Mori M., Sevieri G. (2018). Simplified Soil-Structure Interaction Models for Concrete Gravity Dams, *Proceedings of the 6th European Conference on Computational Mechanics (ECCM 6) and the 7th European Conference on Computational Fluid Dynamics (ECFD 7)*, Glasgow, UK, pp. 2269–80.
- Estekanchi H.E., Mashayekhi M., Vafai H., Ahmadi G., Mirfarhadi S.A., Harati M. (2020). A state-of-knowledge review on the endurance time method, *Structures*, 27: 2288–2299. <https://doi.org/10.1016/j.istruc.2020.07.062>
- Estekanchi H.E., Vafai H.A. (2021). *Seismic Analysis and Design using the Endurance Time Method*, CRC Press.
- Estekanchi H.E., Valamanesh V., Vafai A. (2007). Application of Endurance Time method in linear seismic analysis, *Engineering Structures*, 29: 2551–2562. <https://doi.org/10.1016/j.engstruct.2007.01.009>
- Fenves G.L., Chopra A.K. (1986). *Simplified Analysis for Earthquake Resistant Design of Concrete Gravity Dams*, Berkeley, California University - Earthquake Engineering Research Center.
- Hariri-Ardebili M.A., Sattar S., Estekanchi H.E. (2014). Performance-based seismic assessment of steel frames using endurance time analysis, *Engineering Structures*, 69: 216–234. <https://doi.org/10.1016/j.engstruct.2014.03.019>
- Hariri-Ardebili M.A., Sattar S. (2023). Uncertainty and bias in generic ground motion sets used for PBEE, *Structures*, 57: 105088.

- Hariri-Ardebili M.A., Sattar S. (2023). Uncertainty and bias in fragility estimates by intensifying artificial accelerations, *Probabilistic Engineering Mechanics*: 103545.
- Hariri-Ardebili M.A., Sevieri G., Resta C., De Falco A., Nikolou S., Sattar S. (2023). Conceptualizing and Validating IAA with IDA for Problems with Soil-Structure Interaction [*Unpublished manuscript*].
- Lee J., Fenves G.L. (1998). Plastic-Damage Model for Cyclic Loading of Concrete Structures, *Journal of engineering mechanics*, 124: 892–900. [https://doi.org/10.1061/\(ASCE\)0733-9399\(1998\)124:8\(892\)](https://doi.org/10.1061/(ASCE)0733-9399(1998)124:8(892))
- Løkke A., Chopra A.K. (2019). Direct finite element method for nonlinear earthquake analysis of concrete dams: Simplification, modeling, and practical application, *Earthquake Engineering & Structural Dynamics*, 48: 818–842. <https://doi.org/10.1002/eqe.3150>
- Lysmer J., Kuhlemeyer R.L. (1969). Finite Dynamic Model for Infinite Media, *Journal of the Engineering Mechanics Division*, 95: 859–877. <https://doi.org/10.1061/JMCEA3.0001144>
- Mackie K.R., Stojadinović B. (2005). Comparison of Incremental Dynamic, Cloud, and Stripe Methods for Computing Probabilistic Seismic Demand Models, *Proceedings of the Structures Congress 2005*, New York, United States. [https://doi.org/10.1061/40753\(171\)184](https://doi.org/10.1061/40753(171)184)
- Mashayekhi M., Estekanchi H.E., Vafai H. (2019a). Simulation of endurance time excitations via wavelet transform, *Iranian Journal of Science and Technology, Transactions of Civil Engineering*, 43: 429–443.
- Mashayekhi M., Estekanchi H.E., Vafai H., Ahmadi G. (2019b). An evolutionary optimization-based approach for simulation of endurance time load functions, *Engineering Optimization*, 51: 2069–2088.
- Mashayekhi M., Estekanchi H.E., Vafai H., Mirfarhadi S.A. (2018). Development of hysteretic energy compatible endurance time excitations and its application, *Engineering Structures*, 177: 753–769. <https://doi.org/10.1016/j.engstruct.2018.09.089>
- Miano A., Jalayer F., Ebrahimian H., Prota A. (2018). Cloud to IDA: Efficient fragility assessment with limited scaling, *Earthquake Engineering & Structural Dynamics*, 47: 1124–1147. <https://doi.org/10.1002/eqe.3009>
- Nozari A., Estekanchi H.E. (2011). Optimization of endurance time acceleration functions for seismic assessment of structures, *International Journal of Optimization in Civil Engineering*, 2: 257–277.
- Rea D., Liew C., Chopra A.K. (1972). *Dynamic Properties of Pine Flat Dam*, Berkeley, California University - Earthquake Engineering Research Center.
- Salamon J.W. (2018). *Evaluation of Numerical Models and Input Parameters in the Analysis of Concrete Dams (No. DSO-19-13)*, U.S. Bureau of Reclamation, Denver, Colorado.
- Salamon J.W., Wood C., Hariri-Ardebili M.A., Malm R., Faggiani G. (2021). Seismic Analysis of Pine Flat Concrete Dam: Formulation and Synthesis of Results, in: Bolzon, G., Sterpi, D., Mazzà, G., Frigerio, A. (Eds.), *Numerical Analysis of Dams, Lecture Notes in Civil Engineering*, Springer International Publishing: 3–97. https://doi.org/10.1007/978-3-030-51085-5_1
- Saouma V.E., Hariri-Ardebili M.A. (2021). *Aging, shaking and cracking of infrastructures: from mechanics to concrete dams and nuclear structures*, Springer Nature. ISBN: 3030574342
- USACE (2007). *Earthquake design and evaluation of concrete hydraulic structures*, Technical Report EM 1110-2-6053, Department of the Army, U.S. Army Corps of Engineers, Washington D.C., USA.
- Vamvatsikos D., Cornell C.A. (2002). Incremental dynamic analysis, *Earthquake Engineering & Structural Dynamics*, 31: 491–514. <https://doi.org/10.1002/eqe.141>
- Wilson E.L. (2002). *Three-dimensional static and dynamic analysis of structures: a physical approach with emphasis on earthquake engineering*, Computers and Structures Inc., Berkeley, California.
- Zhang R., Zhang L., Pan C., Chen Q., Wang Y. (2021). Generating high spectral consistent endurance time excitations by a modified time-domain spectral matching method, *Soil Dynamics and Earthquake Engineering*, 145: 106708. <https://doi.org/10.1016/j.soildyn.2021.106708>



COMPARISON OF DAMAGE PREDICTIONS FOR CONCRETE DAMS, FINITE ELEMENTS WITH SMEARED CRACK VS. DISCRETE ELEMENT MODELS

B.F. Soysal¹ & Y. Arici²

¹ Cankaya University, Ankara, Turkey

² Middle East Technical University, Ankara, Turkey, yarici@metu.edu.tr

Abstract: The seismic assessment of gravity dam monoliths has been treated within the framework of performance based earthquake engineering (PBEE) in the last decade. The necessary inclusion of the soil-structure-reservoir interaction in combination with predicting the damage on these structures for use in PBEE is a significant challenge. Within this context, smeared crack models with general purpose finite element codes became to be used generally as the assessment tool for these systems. Perhaps the most practical limitation in this approach is the difficulty with providing discrete cracks and the corresponding impediment to the rating of the damage on these systems leading to possibly subjective conclusions. On the other hand, discrete element techniques offer a proficient simulation alternative to the FE, enabling the interpretation of results from the main aspect of the damage on these system, i.e. cracking. A novel discrete element framework, incorporating dam-reservoir interaction, has been developed to this end as part of the doctoral studies of the first author. The model incorporates individual elements connected by multiple springs, successfully modelling initial continuum with the accurate prediction of discrete cracks at the latter stages of loading. The predicted damage and damage rating of a generic monolith is compared to the FE counterparts in this work. A comprehensive comparison with different ground motions at several levels focusing on crack widths is shown. The results showed the cracking on the system is very different in severe shaking compared to similar predictions in lower earthquake excitations. The FE simulations, commonly adopted for the investigation of these systems with smeared crack modelling, yielded less cracking as well as smaller propagation in severe shaking conditions.

1 Introduction

The investigation of the seismic response of gravity dam monoliths under the framework of performance based earthquake engineering (PBEE) has been undertaken recently in the last decade (Hariri-Ardebili et al., 2016). PBEE framework is based on moment frame structures with significant ductility, symmetry, and associated limit states, the extension of which to plain concrete monoliths is a significant research issue. The necessary inclusion of the soil-structure-reservoir interaction (Fenes and Chopra, 1985) in combination with predicting the damage on these structures further complicated the problem. In contrast to frame structures, the redundancy of these systems stems from extended crack paths, requiring modelling of propagation of cracking for response characterization (Ayari and Saouma, 1990, Espandar and Lotfi, 2003). The wide-spread use of general purpose finite element codes established the smeared crack model, with a range of different implementations, as the general canon in investigation of gravity dams (Arici and Soysal, 2022). The robust use of these tools for dam simulation enable recognizing variabilities in assessment, in modelling as well as variabilities in inputs (Hariri-Ardebili and Saouma, 2016, Sevieri et al., 2020). However, robustness of these

models have led to the inclusion of the well-known deficiencies of crack localization and mesh bias of these models to modelling uncertainties, while cracking is the main mode of damage (Hariri-Ardebili and Saouma, 2015, Soysal et al., 2016, Chen et al., 2021), and the acceptable damage to be rated for these systems.

Cracking, the main damage variable for gravity dams, is almost generally predicted with finite elements and smeared crack combination as the state of the art, in spite of the aforementioned issues (Arici and Soysal, 2022). Perhaps the most practical limitation is the difficulty with providing discrete cracks and the corresponding impediment to the rating of the damage on these systems leading to possibly subjective conclusions. These limitations of FEM, on the other hand, can be overcome by utilizing discrete element-based methods that simulate the discrete fracture phenomenon properly for gravity dams.

A novel discrete element framework, incorporating dam-reservoir interaction with mixed displacement/pressure based reservoir elements (Wang and Bathe, 1997), has been developed to this end as part of the doctoral studies of the first author. The seismic performance of a generic concrete monolith has been investigated using this tool, the modified applied element method, in this study. The model incorporates individual elements connected by multiple springs, successfully modeling initial continuum with the accurate prediction of discrete cracks at the latter stages of loading.

The primary intent of this study is to present a comparison of damage rating in a comprehensive fashion between the generally used FE tools and an appropriate discrete element tool. The comprehensive basis of comparison with FE with a different tool, focusing on a primary damage quantity, is an addition to the literature with scant comparison of different numerical approaches. The use of cracking directly as a novel damage measure, which can be measured or targeted, is also introduced. To this end, accurate crack propagation combined with improved stress prediction in the developed model, previously not combined in the dam setting, is an important advantage of the developed tool.

2 Mathematical model

A new framework, called the modified applied element method (MAEM), based on an existing discrete element technique, the applied element method (AEM, Meguro and Tagel-Din, 2000), is developed in this study. The modified applied element method is coupled with a fluid finite element, with mixed displacement/pressure (u/p) based formulation to investigate the behavior of dam-reservoir systems. A summary of the underlying theory is given below.

2.1 Modified applied element method

Similar to the AEM, MAEM also models the structure by rigid square elements with three degrees of freedom. In addition to the normal and shear spring pairs connecting the elements, the model is enriched by introducing diagonal springs between elements (Figure 1a). For the two-dimensional (2D) plane stress condition, the relationship between macro material constants such as elasticity modulus, E , and Poisson's ratio, ν , and the micro spring parameters k_n , k_s , and k_{nd} , which are the spring stiffness constants for normal, shear, and diagonal springs, respectively, are calculated based on the Cauchy-Born rule and hyperelastic theory (Zhao et al., 2011) using the concept of strain energy (Equations 1-3). This formulation also enables the representation of arbitrary Poisson's ratio in contrast to other discrete element methods that theoretically work for a single Poisson value or ignore the Poisson's effect (Soysal, 2021).

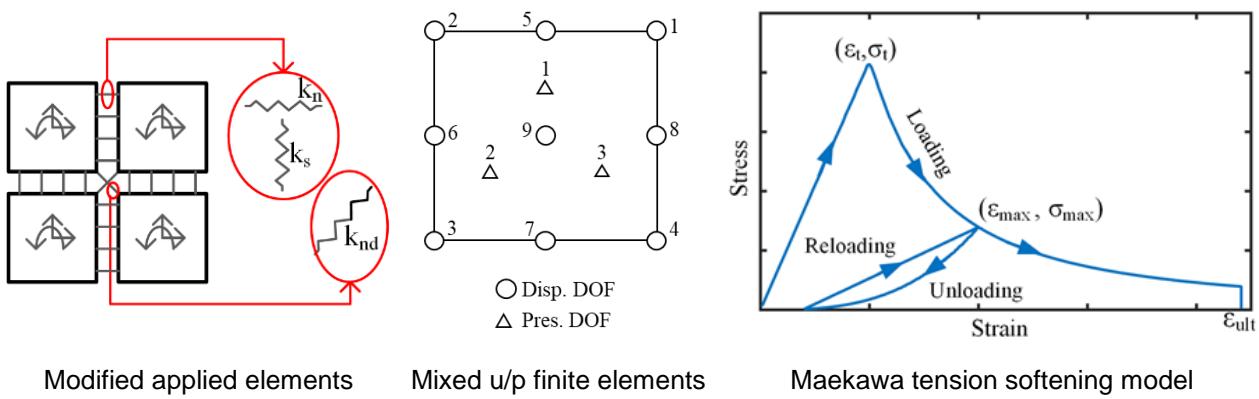


Figure 1. Modified applied element method and reservoir finite element

$$k_n = \frac{Et}{(1 + \nu)s} \quad (1)$$

$$k_s = \frac{Et(1 - 3\nu)}{(1 - \nu^2)s} \quad (2)$$

$$k_{nd} = \frac{Etv}{(1 - \nu^2)} \quad (3)$$

2.2 Theory and formulation for cracked media

The Maekawa model (Maekawa et al., 2003) was implemented for modeling the cracking of such brittle solids (i.e., concrete) using the modified applied elements by introducing tension softening to the normal springs on the model. A linear elastic response is assumed until the cracking point (ε_t, σ_t). Upon the exceedance of this limit, the loading curve has an exponential form, $\sigma_t(\varepsilon_t/\varepsilon)^c$, until the ultimate strain, ε_{ult} . The unloading portion is also nonlinear, and reloading is a straight line between the initiation of the reloading point and the past maximum strain ($\varepsilon_{max}, \sigma_{max}$) point (Figure 1c). Compressive behavior is assumed linear for all springs. The shear spring in any given spring pair cannot carry any force or contribute to the stiffness of the system post the peak stress in the normal spring (i.e., when tensile strain exceeds ε_t). The fracture energy for a horizontal crack, as computed in Equation 4, is mesh dependent. Mesh independence of the models is assured by the selection of the softening parameter, c , and the ultimate tensile strain limit, ε_{ult} , to obtain the required fracture energy in accordance with the modified applied element size (a).

$$b = 3 / \left(\frac{2G_f(1 + \nu)}{aE\varepsilon_t} - \varepsilon_t \right) \quad (4)$$

2.3 Dynamic solution - mass and damping matrices

The solution of the equation of motion is conducted using the half-step central difference method (Cook et al., 2000), where the velocity vector is lagged by half a time step (Equation 5). The global stiffness matrix is not assembled in each time step; instead, the internal force vector, \mathbf{F}_i^{int} , based on the element forces, is assembled to calculate the current displacement \mathbf{u}_{i+1} at the end of the time step Δt .

$$\frac{1}{\Delta t^2} \mathbf{M} \mathbf{u}_{i+1} = \mathbf{F}_i^{ext} - \mathbf{F}_i^{int} + \left(\frac{2}{\Delta t^2} \mathbf{M} - \frac{1}{\Delta t} \mathbf{C} \right) \mathbf{u}_i - \left(\frac{1}{\Delta t^2} \mathbf{M} - \frac{1}{\Delta t} \mathbf{C} \right) \mathbf{u}_{i-1} \quad (5)$$

For problems in the dynamic setting, the mass and damping matrices are also required to be set up. The mass matrix of the modified applied element is setup by assuming that the element mass and inertia are lumped at the centroid of the element for each degree of freedom. Rayleigh damping is implemented to obtain the global damping matrix, $\mathbf{C} = \alpha\mathbf{M} + \beta\mathbf{K}$. In order to improve the solution speed of the explicit time stepping, mass scaling technique suggested in Olovsson et al. (2005) is implemented. The modified global mass matrix $\bar{\mathbf{M}} = \mathbf{M} + \gamma\mathbf{K}$ is obtained using a positive stiffness multiplier γ , and global stiffness matrix \mathbf{K} .

2.4 Displacement/Pressure based mixed finite element formulation

A displacement/pressure based mixed finite element (Wang and Bathe, 1997) has been coupled with the modified applied elements for modeling the reservoir behavior. The element, as shown in Figure 1b, has nine displacement degrees of freedom (marked with circles) and three pressure degrees of freedom (shown with triangles). The formulation yields a set of coupled equations below to be solved in terms of the solution vectors of displacement and pressure, $\hat{\mathbf{u}}$ and $\hat{\mathbf{P}}$, respectively, with \mathbf{M} representing the mass term of the element and \mathbf{K}_{uu} , \mathbf{K}_{up} , \mathbf{K}_{pu} and \mathbf{K}_{pp} represent the stiffness terms (Equation 6). For a finite bulk modulus, the pressure unknowns can be statically condensed out to simplify the solution of the equation (Equation 7).

$$\begin{bmatrix} \mathbf{M} & \mathbf{0} \\ \mathbf{0} & \mathbf{0} \end{bmatrix} \begin{bmatrix} \hat{\mathbf{u}} \\ \hat{\mathbf{P}} \end{bmatrix} + \begin{bmatrix} \mathbf{K}_{uu} & \mathbf{K}_{up} \\ \mathbf{K}_{pu} & \mathbf{K}_{pp} \end{bmatrix} \begin{bmatrix} \hat{\mathbf{u}} \\ \hat{\mathbf{P}} \end{bmatrix} = \begin{bmatrix} \mathbf{R} \\ \mathbf{0} \end{bmatrix} \quad (6)$$

$$\mathbf{M}_{uu} \hat{\mathbf{u}} + \mathbf{S}_{uu} \hat{\mathbf{u}} = \mathbf{R} \quad (7)$$

where \mathbf{S}_{uu} is calculated as $\mathbf{S}_{uu} = -\mathbf{K}_{up} \mathbf{K}_{pp}^{-1} \mathbf{K}_{pu}$.

For an almost incompressible material (i.e., positive bulk, β , and shear modulus, G , with $\beta \gg G$), the displacement/pressure based mixed formulation fulfills the inf-sup condition eliminating the spurious zero-energy modes. A 2x2 Gauss-Quadrature scheme is utilized to obtain the stiffness terms in the above equations. At the far end of the reservoir, the Sommerfeld radiation boundary condition is employed. The damping coefficient, $q_s = 1/C_r$, is defined using the acoustic wave speed of water calculated as $C_r = \sqrt{\beta/\rho}$ with bulk modulus, β , and density, ρ of water (Bouaanani and Lu, 2009).

3 Validation studies

A number of validation problems were solved to demonstrate the capabilities of the developed framework.

3.1 Frequency response of a full-scale dam-reservoir system

The frequency response of a full-scale dam-reservoir system was investigated to validate the coupling of the discrete elements with the reservoir finite elements. To this end, the frequency response function of the idealized concrete gravity dam-reservoir system given in Fenves and Chopra (1987) and Lotfi et al. (1987) was regenerated (Figure 2a) using the computer code EAGD84 (Fenves and Chopra, 1984) with identical material and reservoir properties. In contrast to the frequency domain approach with constant damping through the whole frequency range, Rayleigh damping was utilized: the mass and stiffness proportional Rayleigh damping coefficients for the dam body were taken as 1 and 0.001, respectively, corresponding to 5% damping at 2 Hz and 14 Hz. For the reservoir, on the other hand, the mass and stiffness proportional Rayleigh damping coefficients were 0.2 and 0.0015, respectively, producing 5% damping at 0.5 Hz and 10 Hz. At the far end of the reservoir, viscous dampers were modeled to simulate the Sommerfeld radiation condition.

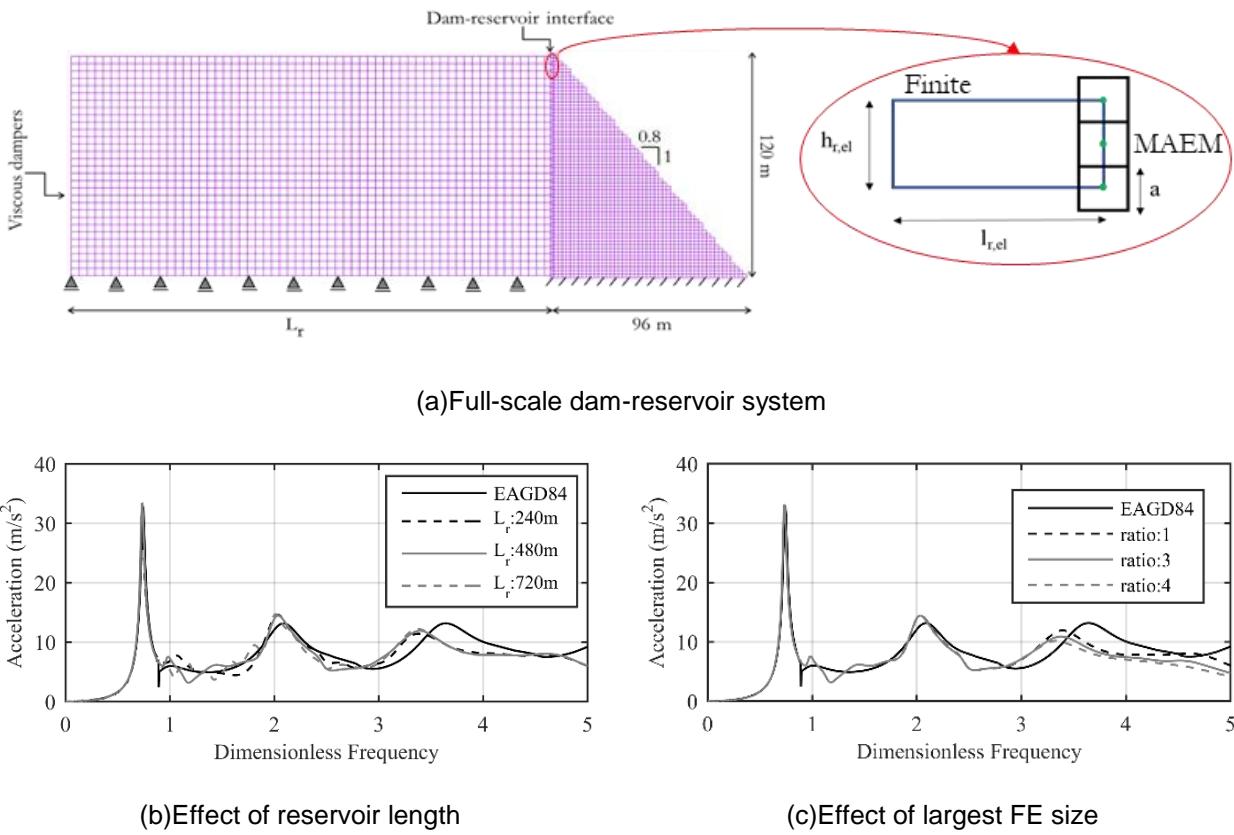


Figure 2. Coupled MAEM-Mixed Reservoir Element, Frequency Response Comparison

The model setup was first evaluated for the modeled reservoir size. The comparison of the solutions for models with 240 m, 480 m, 720 m reservoir lengths (L_r) and the EAGD84 benchmark is presented in Figure 2b. All models captured the general trend in the frequency response well, agreeing well with the EAGD84 benchmark results. The size of the reservoir seemed to affect the frequency response between the first and second frequencies to a small extent; however, even with modeling the reservoir two times the dam height, the

frequency response function appeared reasonable. The influence of the size and aspect ratio of the u/p based mixed finite element was investigated next. For a reservoir length of 480 m, the reservoir elements' aspect ratio was changed from 1 to 3 and 4, leading to finite element lengths, $l_{r,el}$, of 12 m and 16 m, respectively. The frequency response functions given in Figure 2c show that an increase in the aspect ratio of the elements affected the third mode only; even when the maximum element size was 16 m, the 9-node reservoir element appears to work well.

3.2 Nonlinear benchmarks

The capabilities for damage prediction of the model was tested for a range of benchmark cases with different types of loading. First, the uniaxial response of the model was compared to the well-known benchmark test of Gopalaratnam and Shah (1985). The tensile strength, modulus of elasticity, and the fracture energy of the specimen were reported as 3.41 MPa, 29.1 GPa, and 54 N/m, respectively, in this experiment. The satisfactory comparison of the load-displacement response to the experiment results using three different meshes with 0.01, 0.007 and 0.005m element sizes, is presented in Figure 3a. Next, the 1:40 scaled concrete gravity dam experiment by Carpinteri et al. (1992) is simulated. The specimen was loaded using a triangular load distribution in this test by displacement control until failure. Using the reported tensile strength, modulus of elasticity, and the fracture energy of 3.6 MPa, 35.7 GPa, and 184 N/m, respectively, the simulated load-CMOD response is compared to the experiment in Figure 3b. The results, obtained with element sizes of 0.05m, 0.03m, and 0.02m, show good agreement with the experiment.

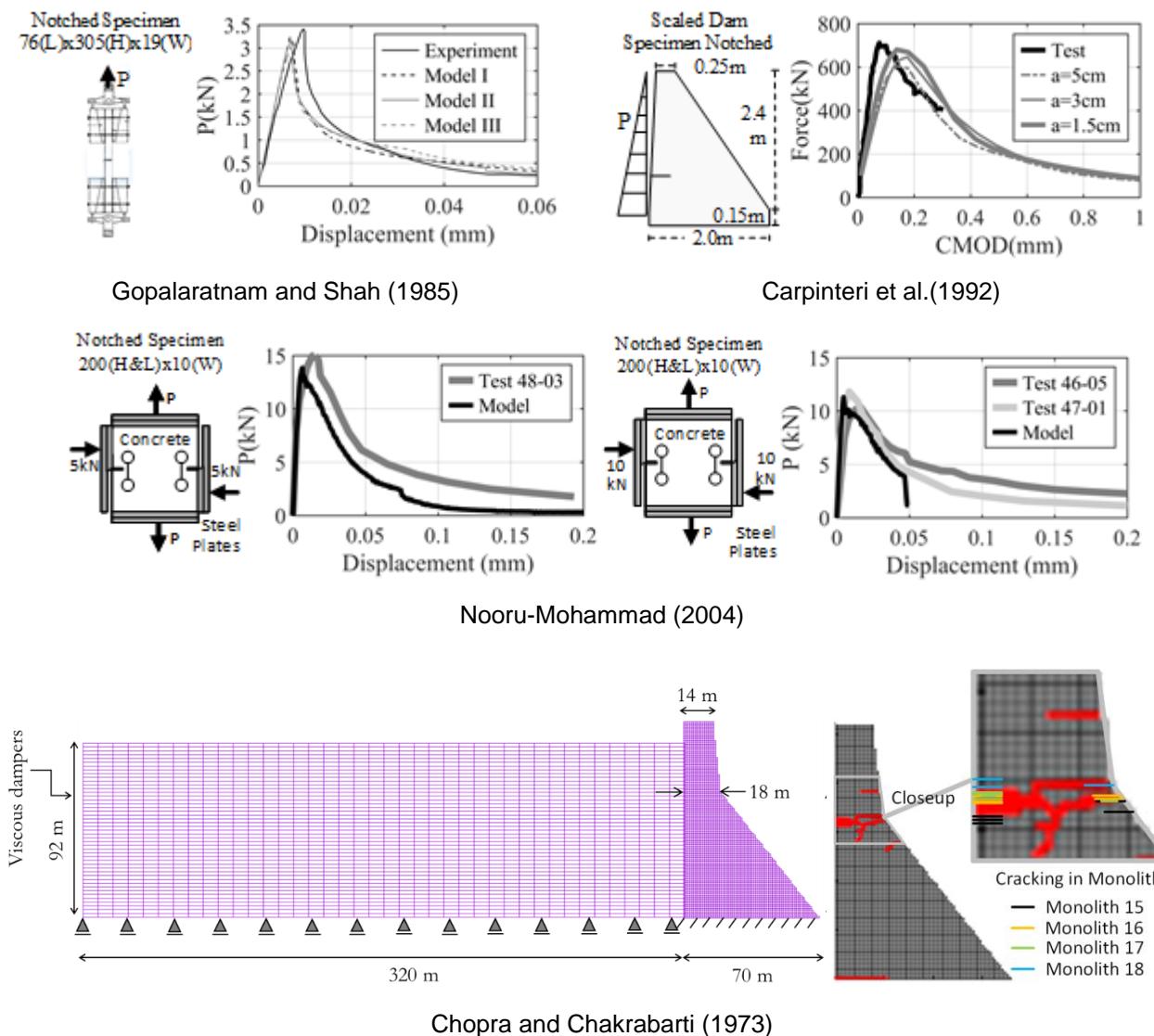


Figure 3. Model validation studies for crack response

Next, mixed mode failure is simulated. Double-edged notched specimens were applied tensile loading until failure under pre-existing lateral load in a series of tests performed by Nooru-Mohammad (1992). This complex failure state was simulated using an element size of 0.005m for different initial loading conditions. The predicted force-displacement response of the specimens under 5 and 10kN initial lateral loading were compared to test results in Figure 3c for tensile strength and fracture energy values of 2.55 MPa and 90 N/m, respectively. The results show satisfactory agreement with the testing.

The final validation case was for the nonlinear dynamic analysis of the Koyna Dam with explicit central difference method. The dam and reservoir were modeled with 1 m applied elements and 2 m x 8 m fluid finite elements, respectively. The Young's modulus and tensile strength of the dam were taken as 31027 MPa and 3 MPa, respectively, while for the reservoir, the Poisson's ratio, density, and acoustic wave speed of water were assumed as 0.4999, 1000 kg/m³, and 1440 m/s. Explicit time-stepping with $\Delta t = 2 \times 10^{-4}$ was used. The crack patterns on the dam, presented for maximum height monoliths 15-18, generally compare well with the obtained crack predictions. The cracking patterns given in Chopra and Chakrabarti (1973) appears to have moved upwards closer to the center monolith and the spillway cross-sections and generally show 3 cracks on the U/S per monolith near the EL2060ft level.

4 Simulation models and ground motions

The validations given above show the coupled discrete-reservoir finite elements framework is capable of simulating the reservoir-structure interaction as well as the nonlinear behavior of the concrete in the tensile range. The discrete element nature of the model allows cracking to be treated as a demand quantity in contrast to the general approach in the finite element method with the smeared crack approach. To this end, the response of a generic concrete gravity monolith under seismic loads was evaluated using the MAEM and FEM models described below.

4.1 Simulation models

A typical 100 m tall monolith was investigated with a vertical upstream face and a slope of 0.7H/1V at the downstream face, having a crest length of 6 m (Figure 4). The reservoir elevation was assumed as 98 m, with roller supports at the base, corresponding to a bottom absorption coefficient of 1.0. At the far end of the reservoir, Sommerfeld radiation boundary condition was applied. The Young's Modulus, Poisson's ratio, the mass density of concrete, tensile strength, and fracture energy were assumed as 28 GPa, 0.2, 2400 kg/m³, 2.4 MPa, and 200 N/m, respectively. The MAEM model was built with 1 m elements with a 400 m reservoir length. The softening parameter, c , and ultimate strain, ε_{ult} , of Maekawa tension softening material model were 13 and 0.01, respectively, leading to 200 N/m fracture energy for this mesh size. Shear springs were assumed as brittle: after the exceedance of cracking strain, ε_t in the normal spring of the spring pair, the shear spring lost its resistance, corresponding to no shear retention in the crack. The springs in compression were assumed to behave linearly. 10 connecting springs between each element were modeled with 32157 DOF. The nonlinear dynamic analyses were conducted utilizing the explicit nonlinear solution scheme with a time increment of 0.0002 sec. To ensure numeric stability, mass scaling was applied to the system with the stiffness multipliers as $\gamma = 1e - 6$ and $\gamma = 2e - 6$ for the dam-reservoir and viscous dampers, respectively. The reservoir was modeled with u/p based mixed finite elements as a nearly incompressible fluid with Poisson's ratio, acoustic wave speed, and water density as 0.4999, 1438.66 m/s, and 1000 kg/m³, respectively.

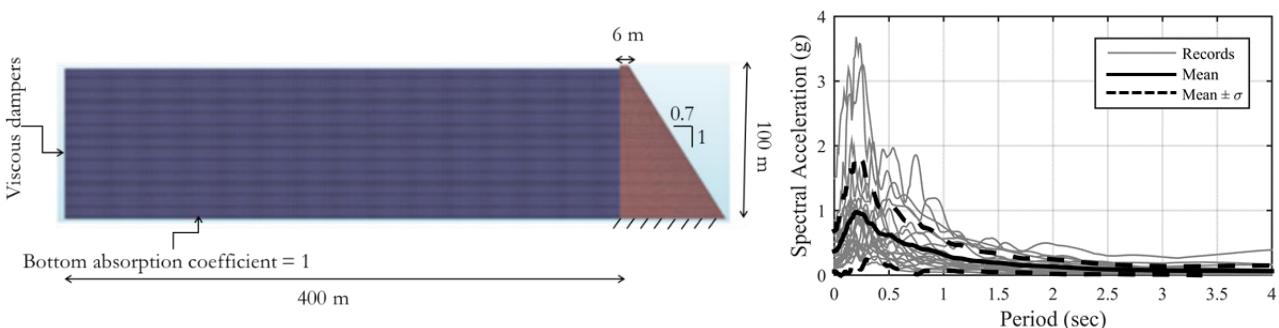


Figure 4. Dam-reservoir model and ground motions

The corresponding finite element models were identical to the models from a previous study by the authors (Soysal and Arici, 2016) conducted using the general-purpose finite element program DIANA (TNO Diana, 2014), with a robust implementation of the smeared crack model in time history solutions. Smeared crack formulation is widely used in the assessment of gravity dams (Hariri-Ardebili and Saouma, 2015). The classical smeared crack formulation with rotating crack and exponential strain softening was adopted for the modeling of cracking. The element size of the dam was approximately 0.7 m, while the fluid elements were modeled with 2.4 m length and 0.4 m height. The reservoir was modeled using compressible fluid elements with pressure degrees of freedom. In the nonlinear implicit transient analyses, a time increment of 0.005 sec was used.

4.2 Incremental dynamic analysis

The uncertainty in the seismic loading was included in the study using 21 different ground motions scaled and applied on the system using the incremental dynamic analysis approach (IDA). IDA is a commonly used procedure to determine a relationship between intensity measures of ground motions and engineering demand parameters of the structures: the ground motions are scaled with a positive scaling factor, increasing incrementally to a desired level (Vamsatsikos and Cornell, 2002). The IDA was performed by scaling the motions conventionally to the spectral acceleration at the first natural period of the dam-reservoir system. The ground motions selected from the Pacific Earthquake Engineering Research (PEER) database were from events recorded on Type A or B soils (USGS classification) with epicentral distances of 2 to 39 km and magnitudes ranging from 6 to 7.6. The spectra for the utilized motions are presented in Figure 4. The analyses were conducted at 17 levels, scaling the motions such that the spectral acceleration at the first natural period of the dam-reservoir system was varied from 0.2g to 1.0g, with 0.05g increments.

5 Incremental dynamic analysis results

A total of 714 nonlinear transient analyses were conducted for the FEM and MAEM models scaling each 21 ground motion at 17 different levels. A qualitative comparison of the crack patterns obtained from the FEM and MAEM is presented in Figure 5 for different shaking levels varying between 0.2-1.0g pga. For the sake of conciseness, results from only a few motions are provided. The results presented correspond to the overall envelope of cracking comprised of maximum crack strain values over the whole time history. An investigation of the crack response through the seismic loading shows that the cracks always initiate at the upstream toe of the dam. After the formation of this crack, cracks can occur on the upstream (more likely) and downstream faces depending on the ground motion time history. Cracks that occur on the downstream side propagate towards the core at approximately 45° inclination.

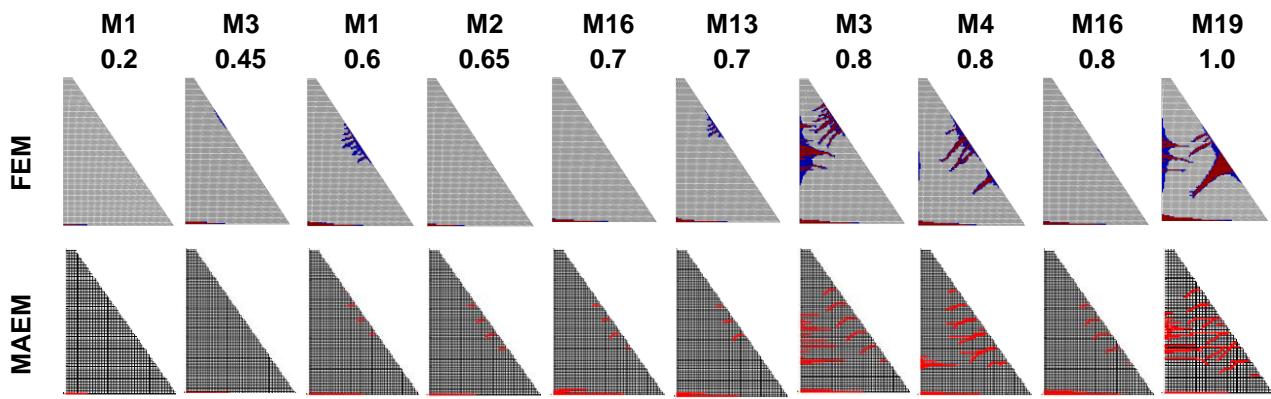


Figure 5. Cracking scheme comparison for FEM and MAEM models for selected results

The results of the analysis showed a similar pattern of damage in lower seismic excitations, with the pattern of cracking between the two approaches diverging as the seismic excitation was increased. For higher spectral accelerations ($>0.8\text{g}$), MAEM yielded more discrete cracking while the smearing of the cracking in finite elements increased considerably. The crack patterns for the M3 and M19 motions for 0.8 and 1.0g spectral acceleration levels clearly show a large distributed cracking in FEM over many elements on the upstream and downstream faces. There were more discrete cracks on the MAEM models for these higher excitations in

comparison to the formation of a large smeared crack mentioned above. The base crack is a consistent feature for both analyses; the results in this respect were comparable.

Such plain concrete structures are usually assessed on the basis of cracking (RILEM, 1991). The MAEM model offers the advantage of obtaining discrete cracks, and correspondingly their crack widths, on the continuum. Consequently, the use of cracking at the upstream face of the model as a damage indicator is investigated in the next section.

5.1 Cracking in the upstream face as a performance Indicator

A direct consequence of an earthquake event is the seepage through the dam. Cracking on the upstream face is, therefore, a primary concern in these systems. In this section, the quantifying of the seismic performance of the analyzed system in terms of the upstream cracking is investigated. The total cumulative cracking on the upstream face of the dam was chosen as the measure of cracking computed by summation of the maximum crack widths for each crack ($w_{max,i}$) that occurred in the upstream side of the dams, i.e., $w_{max,b} + w_{max,1} + \dots + w_{max,n}$, including the base crack. This measure formed an envelope quantity of the accumulated damage on the upstream of the dam.

Estimation of crack properties of an individual crack from the FEM models is much more challenging due to the smearing of the crack in the orthogonal direction to the crack propagation. Crack width estimates can be made based on the crack strains in the elements. Of the four Gauss points in each element, the crack width estimations for the FEM models were calculated based on the crack strains of the two Gauss points near the upstream face. The total crack width is likely to be much more representative in the FEM case: the total maximum crack width at the upstream face of the dam was computed by integrating the crack strains through the entire upstream face.

The corresponding variation of the crack widths with respect to the spectral acceleration of the motions is presented in Figure 6 for the FEM and MAEM models. The symbols M- represent the total damage accumulation, in terms of crack width, on the upstream face of the dam, for the event “-”. The overall mean \pm standard deviation bounds on the models are also shown, compiled from the considered 21 earthquake events. While the models' results were similar until 0.6g, both the maximum cracking and the standard deviation is widely different for stronger shaking. Smearing of the cracking, appears to be particularly important issue for assessment of these systems under very strong shaking. The smearing of cracks led to an underestimation of the total maximum crack width, by 50%, with respect to the MAEM model. While crack locations and propagation to minor extent appears to be similarly predicted, for the use of these models in extensive shaking, further work is required. Most damage estimates for these systems require such levels of assessment – corresponding assessment should be used with care.

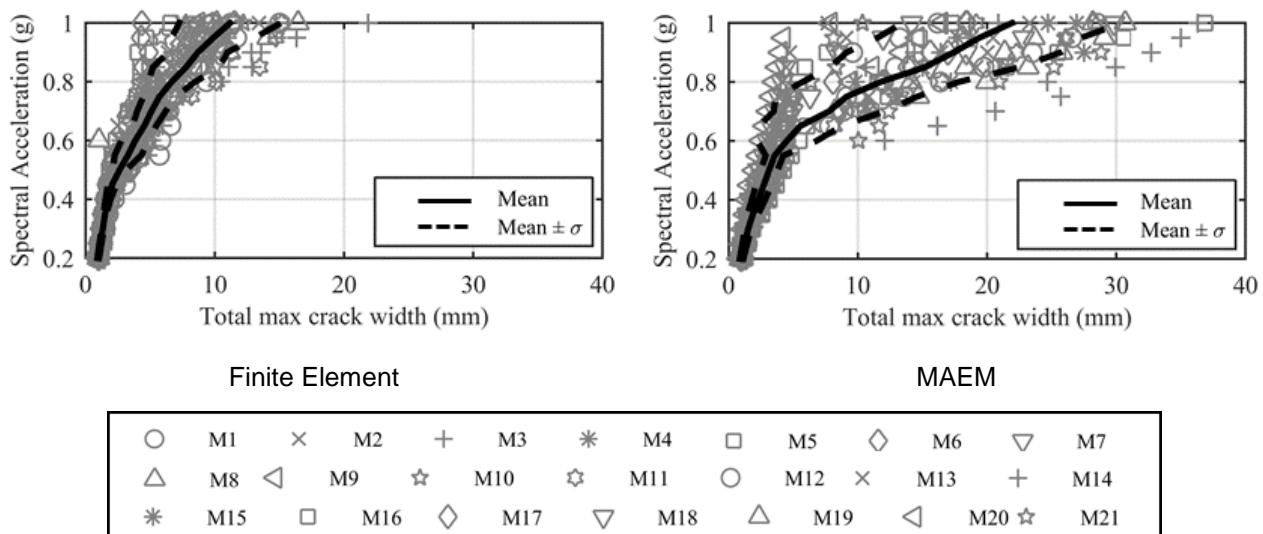


Figure 6. Total crack width on U/S Face

6 Conclusions

In this study, the damage predictions of the FEM-smeared crack model, generally used in assessment of dam monoliths, was compared with the results from a novel discrete element tool developed in the doctorate work of the first author. Building on the advantages of the discrete element model, crack widths on the upstream face of the dam monolith was introduced as a damage measure. A comprehensive comparison, including shaking level and focused on the primary damage measure in these systems was performed. The results from FEM and MAEM were compared with the goal of assessing the effects of smeared crack model on assessment of severe shaking of dams. The following conclusions were drawn from these analyses.

- The smearing of cracks occurring in the FEM model decreased considerably using the proposed MAEM model. Visual investigation of the incremental dynamic analysis results showed these cracks propagated more towards the core of the dam.
- The incremental dynamic analysis results showed the prevalence of base cracks until a specific limit of spectral acceleration, followed by the initiation and proliferation of cracking on the upstream face above the base. The MAEM and FEM models yielded similar results for the first phase, differentiating for the latter, higher levels of loading causing significant damage.
- The total crack width at the upstream side of the dam were computed. The width of the base crack was obtained similarly for the FEM and MAEM models. On the other hand, the total crack width at the upstream face was estimated 50% less by the FEM model compared to the MAEM counterpart for higher ground motion intensities.

Compared to continuum based finite element models, discrete element techniques such as MAEM are more proficient in simulating the discrete cracks. While the robustness of FE combined with smeared crack models is appreciated, the results in severe shaking and the well-known dispersing of cracks in the crack perpendicular direction can yield significant bias in damage predictions. Further work is planned on investigation of large displacements on these cracks as the discrete element model and explicit solution allow simulation of opening/closing or sliding along the cracks.

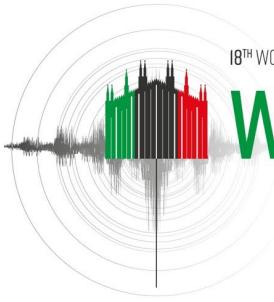
7 Acknowledgments

This study has been conducted with the funding provided by The Scientific and Technological Research Council of Turkey (TUBITAK) under the grant 116M524.

8 References

- Arici Y., Soysal B.F. Predicting seismic damage on concrete gravity dams: a review, *Structure Infrastructure Eng.* 2022.
- Ayari M.L., Saouma V.E. (1990) A fracture mechanics based seismic analysis of concrete gravity dams using discrete cracks, *Eng Fract Mech.* 1990;35(1-3):587-598.
- Bouaanan N., Lu F.Y. (2009). Assessment of potential-based fluid finite elements for seismic analysis of dam-reservoir systems, *Comput Struct.* 87(3-4):206-224.
- Carpinteri A., Valente S., Ferrara G., Imperato L. (1992). Experimental and numerical fracture modelling of a gravity dam. In: *Symposium Paper Special Publication*, 143:107-122.
- Chen D.H., Yang Z.H., Wang M., Xie J.H. (2019). Seismic performance and failure modes of the Jin'anqiao concrete gravity dam based on incremental dynamic analysis. *Eng Fail Anal.* 100:227-244.
- Chopra A.K., Chakrabarti P. (1973). The Koyna earthquake and the damage to Koyna Dam. Bulletin of the Seismological Society of America, 63(2): 381-397.
- Cook R.D., Malkus D.S., Plesha M.E., Witt R.J. (2001). *Concepts and Applications of Finite Element Analysis*, 4th Ed. Wiley.
- Espandar R., Lotfi V. (2003) Comparison of non-orthogonal smeared crack and plasticity models for dynamic analysis of concrete arch dams, *Comput Struct.* 81(14):1461-1474.
- Fenves G., Chopra A.K. (1984) EAGD-84 A computer program for earthquake analysis of concrete gravity dams, UCB/EERC-84/11, Berkeley, CA, USA.
- Fenves G., Chopra A.K. (1987) Simplified earthquake analysis of concrete gravity dams, *J Struct Eng.* 113(8).

- Fenves G., Chopra A.K. (1985) Effects of reservoir bottom absorption and dam-water-foundation rock interaction on frequency response functions for concrete gravity dams, *Eq Eng Struct Dyn*, 13(1):13-31.
- Gopalaratnam V.S, Shah S.P. (1985). Softening response of plain concrete in direct tension, *J Am Concr Inst*, 82(3):310-323.
- Hariri-Ardebili M.A, Saouma V. (2015) Quantitative failure metric for gravity dams, *Earthq Eng Struct Dyn*, 44(3):461-480.
- Hariri-Ardebili M.A., Saouma V.E. (2016). Probabilistic seismic demand model and optimal intensity measure for concrete dams, *Struct Safety*, 59:67-85.
- Hariri-Ardebili M.A, Seyed-Kolbadi S.M. (2015). Seismic cracking and instability of concrete dams: Smeared crack approach, *Eng Fail Anal*. 52:45-60.
- Hariri-Ardebili M.A., Seyed-Kolbadi S.M., Kianoush M.R. (2016). FEM-based parametric analysis of a typical gravity dam considering input excitation mechanism, *Soil Dyn Eq. Eng.* 84:22-43.
- Lotfi V., Roessel J.M., Tassoulas J.L. (1987) A technique for the analysis of the response of dams to earthquakes, *Eq Eng Struct Dyn*, 15(4):463-489.
- Maekawa K., Okamura H., Pimanmas A. (2003). *Non-Linear Mechanics of Reinforced Concrete*, 1st Ed. CRC Press.
- Meguro K., Tagel-Din H. (2000). Applied element method for structural analysis: Theory and application for linear materials, *Struct Eng./Earthq. Eng.,JSCE*, 17(1):21-35.
- Nooru-Mohamed M.B. (1992). *Mixed-mode fracture of concrete: an experimental approach*, Delft University of Technology, Delft, The Netherlands.
- Olovsson L., Simonsson K., Unosson M. (2005). Selective mass scaling for explicit finite element analyses, *Int J Numer Methods Eng*, 63:1436-1445.
- RILEM TC 104 (1991). Damage classification of concrete structures. The state of the art report of RILEM Technical Committee 04-DCC activity, *Materials and Structures*, 24(142):253–259.
- Sevieri G., De Falco A., Marmo G. (2020). Shedding light on the effect of uncertainties in the seismic fragility analysis of existing concrete dams, *Infrastructures*, 5(3).
- Soysal B.F., Binici B., Arici Y. (2016). Investigation of the relationship of seismic intensity measures and the accumulation of damage on concrete gravity dams using incremental dynamic analysis, *Eq Eng Struct Dyn*, 45(5):719-737.
- Soysal B.F. (2021). *Discrete element based analyses of structure-reservoir problem for gravity dams*, PhD dissertation, METU, Ankara, Turkey.
- TNO DIANA. (2014). Diana User's manual, R. 9.5; 2014.
- Vamvatsikos D., Cornell C.A. (2002). Incremental dynamic analysis, *Eq Eng Struct Dyn*, 31(3):491-514.
- Wang X., Bathe K.J. (1997). Displacement/pressure based mixed finite element formulations for acoustic fluid-structure interaction problems, *Int J Numer Methods Eng*, 40(11):2001-2017.
- Zhao G.F., Fang J., Zhao J. (2011). A 3D distinct lattice spring model for elasticity and dynamic failure, *Int J Numer Anal Methods Geomech*, 35(8):859-885.



CENTRIFUGE MODEL TESTS AND NUMERICAL SIMULATIONS OF IRRIGATION DAMS DURING EARTHQUAKE

K. Fukuda¹, S. S. Suzuki², H. Ishikawa³ & N. Takahashi²

¹ R & D Centre, Nippon Koei, Co., Ltd., Tokyo, Japan, fukuda-kt@n-koei.jp

² R & D centre, Nippon Koei, Co., Ltd., Tokyo, Japan

³ Sapporo Branch office, Nippon Koei, Co., Ltd., Hokkaido, Japan

Abstract: This study aimed to investigate the appropriate methods for evaluating the seismic behavior of irrigation dams during earthquake. Two cases of dynamic centrifuge model tests of irrigation dams using a material named as Edosaki sand (4.4 % of fine fraction content) were conducted in 50G of centrifugal force field. The model grounds of each case were prepared under the conditions of degree of compaction of 90 % and 95 % (optimum water content), respectively. The dam height was set to 15 m and the water level was 10.625 m. The input wave was obtained by adjusting the strong-motion earthquake record (NS component) observed at the Kobe Marine Meteorological Observatory of the Japan Meteorological Agency, considering the 1995 Hyogoken-Nanbu Earthquake at a maximum acceleration of approximately 6 m/s². An effective stress FE analysis program called LIQCA was used to simulate the results of the centrifuge model tests. A series of cyclic triaxial compression tests of Edosaki sand in saturated condition were conducted to determine the parameters for the LIQCA program. From the experimental and analytical results, the settlement, response acceleration, and deformation of the dams were compared to evaluate the deformation characteristics of the dams during the earthquake. It is found that analysis results approximately agree with the test results and the important fundamental data for evaluating the seismic assessment of irrigation dams were obtained from this study. More details of the comparisons between the results of the centrifuge model tests and the numerical analysis were discussed and presented in the paper.

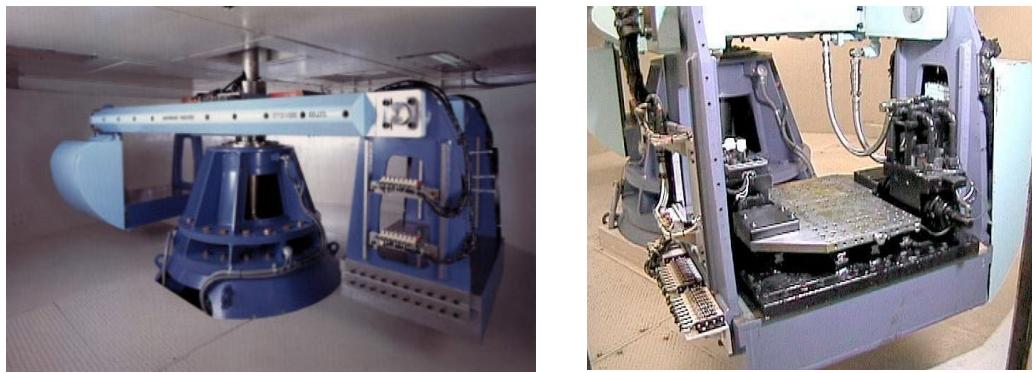
1. Introduction

The 2011 earthquake off the Pacific coast of Tohoku caused considerable damage to irrigation dams. There are approximately 0.15 million irrigation dams in Japan, and most of which were designed and constructed before aseismic design was established. In the future, the occurrence of massive earthquakes, such as the Nankai Trough Mega Earthquake, can be assumed. Therefore, a seismic assessment method for irrigation dams is required. In order to develop a seismic assessment method for irrigation dams, the authors have tried to investigate the seismic behavior of irrigation dams by conducting centrifuge model tests and their numerical analysis (Fukuda et al. 2017, Suzuki et al. 2019, Fukuda et al. 2022, Fukuda et al. 2023). This study presents the new results of dynamic centrifuge model tests and numerical analyses, in which degree of compaction of the dams were changed.

2. Centrifuge model tests

2.1. Test apparatus

The centrifuge model tests were conducted under a centrifugal acceleration of 50G. The centrifuge used in the test is a beam type with an effective radius of 2.6 m and is owned by Nippon Koei Co. Ltd. (Figure 1). Table 1 shows the specifications of the shaking table of Nippon Koei.



(a) Centrifuge

(b) Shaking table

Figure 1. Centrifuge of Nippon Koei.

Table 1. Specifications of the shaking table of Nippon Koei.

Item	Specification
Shaking control system	Electrohydraulic servo control
Max. centrifuge acceleration	100G
Max. shaking acceleration	25G
Max. payload	250 kg
Max. displacement	±3.0 mm
Frequency range	10-400 Hz
Max. velocity	40 cm/s

2.2. Model preparation and measurements

The material used in the test was "Edosaki sand", which was sampled from Ibaraki Prefecture, Japan. Figure 2 shows the grain size distribution curve of Edosaki sand. The Edosaki sand had a small fine fraction content of 4.4%. Table 2 shows the physical properties of Edosaki sand. Table 3 and Table 4 show the results of compaction test and consolidated drained triaxial compression test of Edosaki sand, respectively.

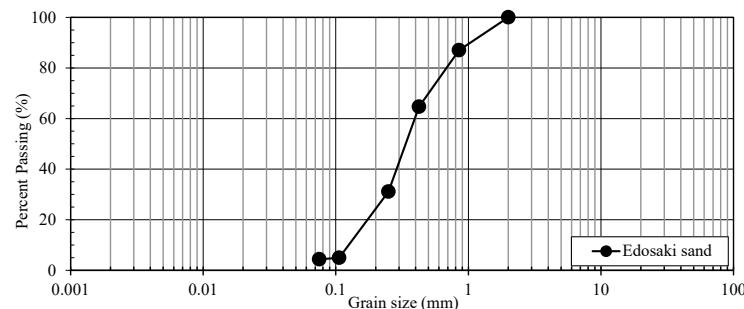


Figure 2. Grain size distribution curve of Edosaki sand.

Table 2. Physical properties of Edosaki sand.

Physical properties	Edosaki sand
Maximum grain size, D_{\max} (mm)	2.0
Mean grain size, D_{50} (mm)	0.335
Uniformity coefficient, U_c	2.56
Coefficient of curvature, U'_c	1.00
Fine fraction content (%)	4.4
Coarse sand fraction (%)	13.0
Medium sand fraction (%)	55.9
Fine sand fraction (%)	26.7
Density of soil particles, ρ_s (g/cm ³)	2.681

Table 3. Compaction test result of Edosaki sand.

Maximum dry density, $\rho_{d\max}$ (g/cm ³)	1.707
Optimum water content, w_{opt} (%)	15.0

Table 4. Consolidated drained triaxial compression test results of Edosaki sand.

Test cases	Case 1	Case 2
Degree of compaction, D_c (%)	90	95
Dry density, ρ_d (g/cm ³)	1.536	1.622
Water content (%)	15.0	15.0
Cohesion, c (kN/m ²)	0.1	4.5
Friction angle (deg.)	33.8	36.3

Table 5 shows the test cases and conditions. Figure 3 (a), (b) shows an outline of the centrifuge model tests. All test results were converted to the prototype scale (50G). The model grounds were prepared by compacting the material in a rigid soil container with 90 % ($\rho_d = 1.536$ g/cm³) and 95 % ($\rho_d = 1.622$ g/cm³) of the degrees of compaction, and a water content of 15 % (optimum water content). During the model preparation process, colored sand layers and targets were installed to observe the deformation of the dam during shaking.

A methylcellulose solution (metolose) fluid, which was adjusted to a kinematic viscosity of 50 mm/s², was used for the water storage of the dams. The input wave was obtained by adjusting the strong-motion earthquake record (NS component) observed at the Kobe Marine Meteorological Observatory of the Japan Meteorological Agency, considering the 1995 Hyogoken-Nanbu Earthquake at a maximum acceleration of approximately 6 m/s².

Figure 4 shows the observed seepage line after reaching 50G before shaking. The seepage line observed by the piezometer partially agreed well with the theoretical line of Casagrande's method (Casagrande 1937). However, in Case1, it was significantly higher than the theoretical line, resulting in the partial destabilization of the non-submerged side. This is because the degree of compaction of the dam was smaller than in Case 2. As a result, it is assumed that the permeability of the material became high in Case 1. Coefficients of permeability of Case1 and Case2 were 2.43×10^{-4} m/s and 9.38×10^{-5} m/s, respectively.

Table 5. Test cases and conditions.

Test cases	Height of dam (H) Degree of compaction (D_c) Water level (WL)	Input wave (Common condition)
Case 1	$H = 15 \text{ m}$ $\rho_d = 1.536 \text{ g/cm}^3, D_c = 90\%$ $WL = 10.625 \text{ m}$	A recorded wave of JMA Kobe Kaiyo station of the 1995 Hyogoken-Nanbu earthquake by adjusting the wave amplitude to a maximum acceleration of approximately 6 m/s^2
Case 2	$H = 15 \text{ m}$ $\rho_d = 1.622 \text{ g/cm}^3, D_c = 95\%$ $WL = 10.625 \text{ m}$	

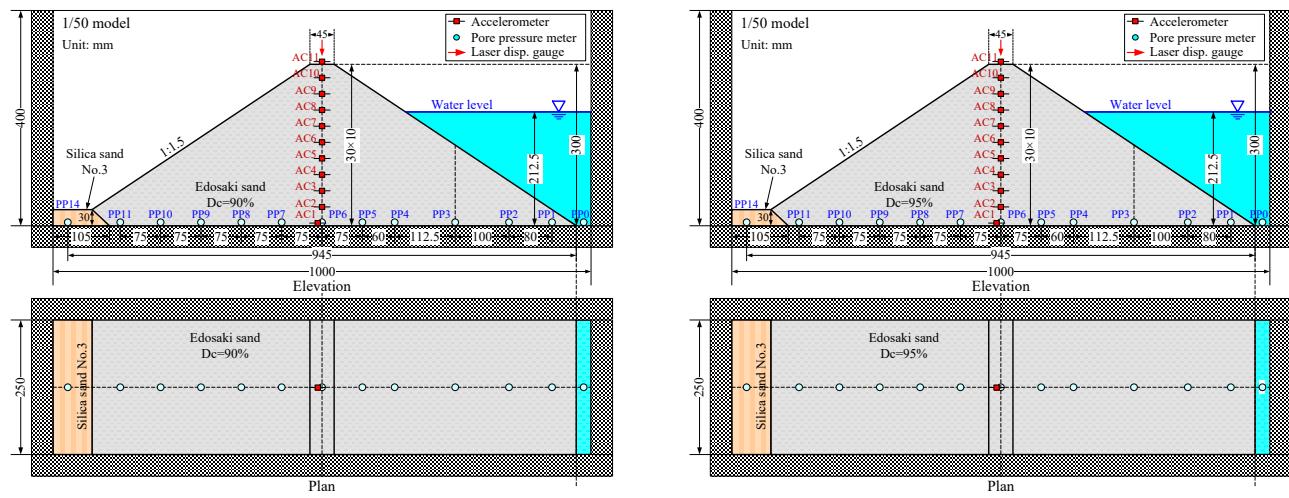
(a) Case 1 ($D_c = 90\%$, Water level = 10.625 m)(b) Case 2 ($D_c = 95\%$, Water level = 10.625 m)

Figure 3. Outlines of the centrifuge model tests.

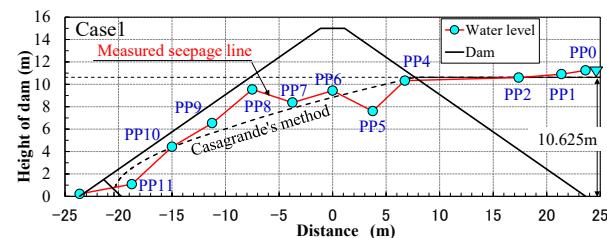
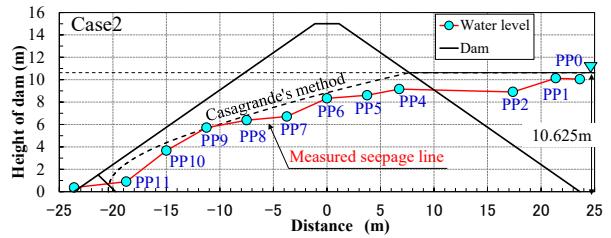
(a) Case 1 ($D_c = 90\%$, Water level = 10.625 m)(b) Case 2 ($D_c = 95\%$, Water level = 10.625 m)

Figure 4. Seepage line.

3. Test results

3.1. Response acceleration and settlement

Figure 5 shows the comparison of response acceleration between Case 1 and Case 2. From Figure 5, the maximum response acceleration of Case 2 is larger than that of Case 1. Figure 6 shows the comparisons of the maximum response acceleration (left side) and the amplification ratio of the maximum response

acceleration (right side), and the dam height obtained from the tests. From Figure 6, the response acceleration tends to attenuate in Case 1 and increase in Case 2 when the dam height is approximately 4 m or more. Furthermore, in Case 2, the amplification ratio of the maximum response acceleration was larger than 1 at the dam heights of approximately 13 m or more. The reason for the attenuation of the maximum response acceleration in Case 1 is considered to be due to the low stiffness in the degree of compaction of 90 %.

Figure 7 shows the comparisons of settlement and response acceleration at the top of the dam during the earthquake. It is shown that settlement of Case 1 was about 1 m larger than that of Case 2. Meanwhile, the response acceleration at the top of the dam of Case 1 was confirmed to be significantly attenuated compared to that of Case 2.

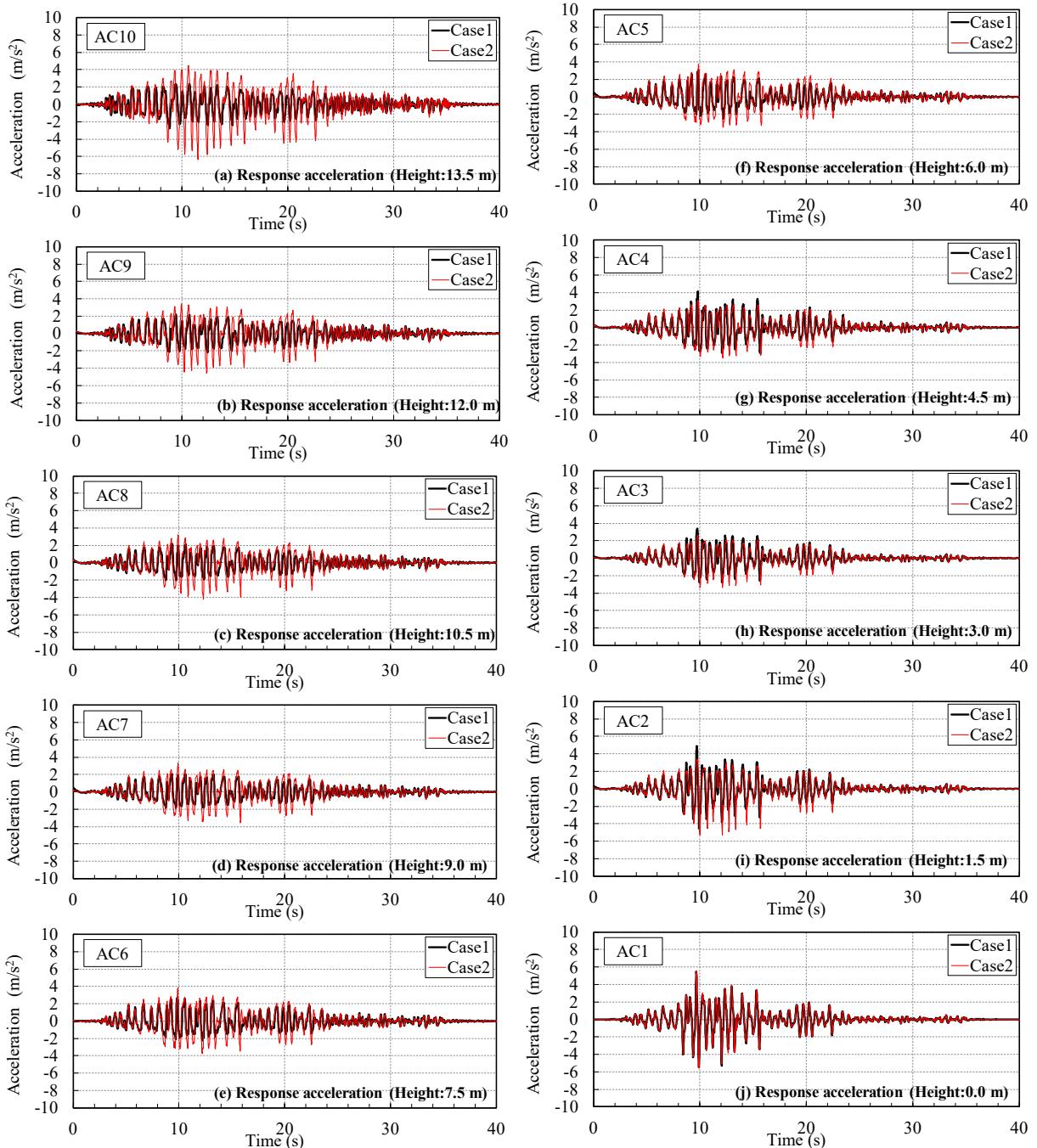


Figure 5. Comparison of response acceleration.

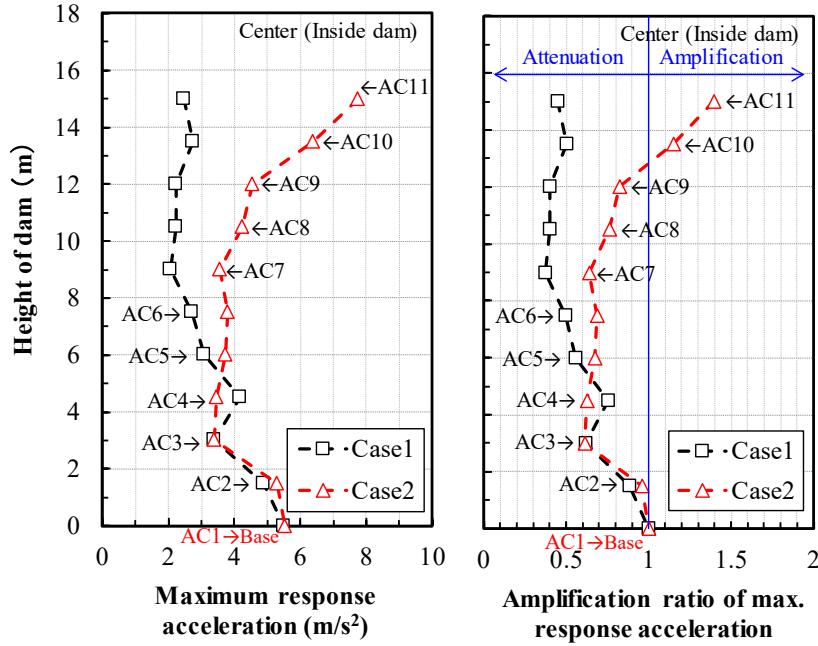


Figure 6. Comparison of maximum response acceleration (test).

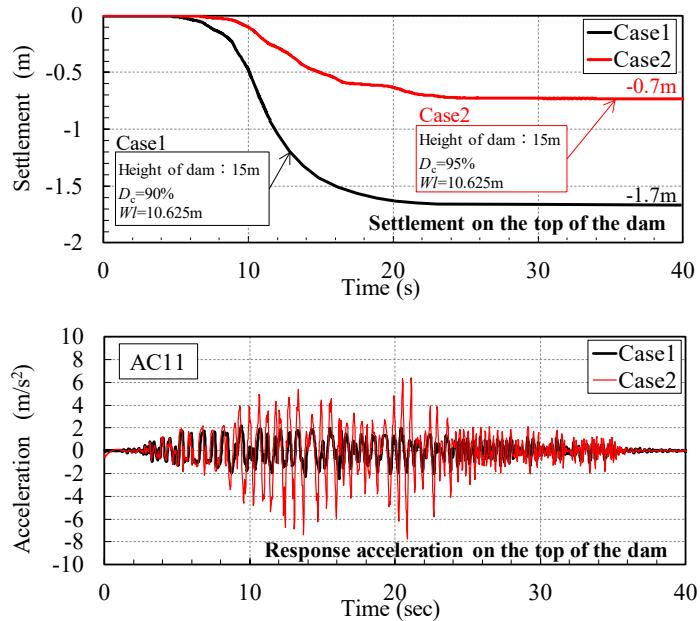


Figure 7. Settlement and response acceleration at the top of the dam.

3.2. Deformation mechanism

Figure 8 shows the deformation sketch of the target markers before and after the implementation of the shaking test. Figure 9 shows the states of the irrigation dam after the shaking tests. In Case 1, with $D_c = 90\%$, a large slip surface occurred from the top to the non-submerged side. This is the main reason why the settlement at the top of the dam in Case 1 increased to -1.7 m. On the other hand, in Case 2 ($D_c = 95\%$), no slip line occurred. Instead, small deformation occurred on the non-submerged side slope. And protrusion was observed near the toe slope of the submerged side. Protrusion near the toe slope of the submerged side was observed not only in Case 2, but also in Case 1. With regard to the non-submerged side, it is assumed that slip line occurs due to

the shaking and the top of the dam significantly subsides when the degree of compaction is low, and the seepage line is high.

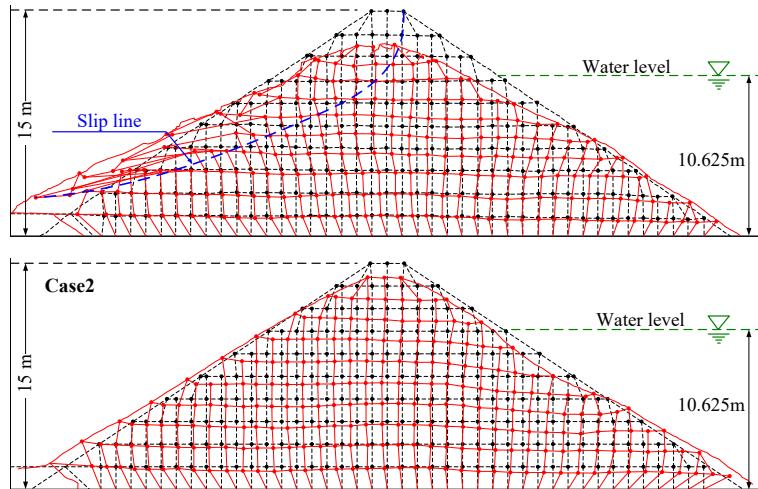


Figure 8. Deformation sketch of target markers before and after the implementation of the shaking test.

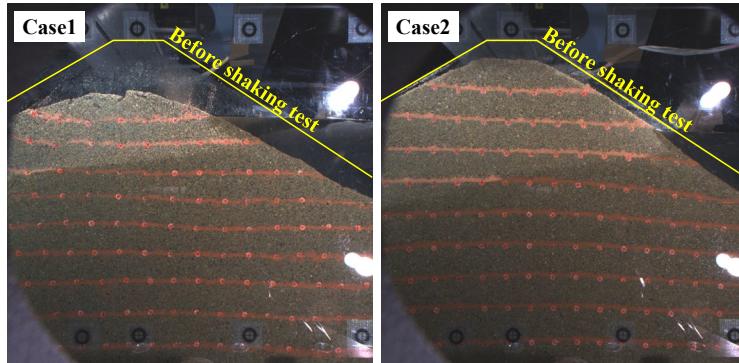


Figure 9. States after the shaking tests.

4. Numerical Simulation

The 3D version of LIQCA (Oka et al. 1991) was used to numerically simulate the test results. LIQCA3D is a fully coupled FEM for liquefaction analysis. Two cases of numerical simulation were conducted to simulate the centrifuge model tests.

4.1. Analysis model and boundary condition

Figure 10 shows the analysis models of Case 1 and Case 2. The centrifuge model tests can be considered as 2D problem; however, 3D analysis was conducted in this study to simulate the same scale as the model tests. The scale in the analysis model was converted to the prototype scale to simulate the centrifuge model tests. The dam height was 15 m, the upstream water level was 10.625 m, and the seepage line was applied as shown in Figure 10.

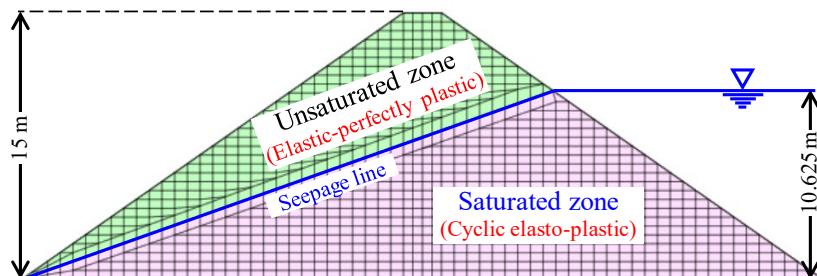


Figure 10. Model for Case1 and Case2.

4.2. Analysis parameters and input excitation motion

The soil parameters used in the analysis are summarized in Table 6 and Table 7. These parameters were determined from soil laboratory tests such as tests for physical properties, triaxial compression test (CU bar), and cyclic undrained triaxial test on soils. The input parameters for the cyclic elasto-plastic model were determined by simulation utility for laboratory test, as shown in Figure 11. The constitutive models used for each material are shown in Figure 10.

Figure 12 shows the input excitation motion for the numerical simulations, which is the response acceleration of the base obtained from the tests.

Table 6. Input parameters for cyclic elasto-plastic model.

(a) Case 1 ($D_c=90\%$)									
ρ	e_0	λ	κ	$G_0/\sigma'_m o$	k/γ_w	M^*_m	M^*_f	K_f	
1.963	0.746	0.018	0.0055	351.7	2.48×10^{-5}	0.870	1.105	2×10^6	
B^*_0	B^*_1	C_f	C_d	OCR^*	D^*_0	n	γ^{P*}_r	γ^{E*}_r	
2000	50	0.0	2000	1.0	13.0	3.0	0.0004	0.001	

(b) Case 2 ($D_c=95\%$)									
ρ	e_0	λ	κ	$G_0/\sigma'_m o$	k/γ_w	M^*_m	M^*_f	K_f	
2.018	0.652	0.018	0.0055	408.0	9.56×10^{-6}	0.821	1.108	2×10^6	
B^*_0	B^*_1	C_f	C_d	OCR^*	D^*_0	n	γ^{P*}_r	γ^{E*}_r	
6000	60	0.0	2000	1.0	3.0	10.0	0.0005	0.010	

Table 7. Input parameters for elastic-perfectly plastic model.

(a) Case 1 ($D_c=90\%$)					
Young's Modulus, E_0 (kN/m ²)	Poisson ratio, ν	Density, ρ (g/cm ³)	Internal friction angle, ϕ' (rad)	Cohesion, c (kN/m ²)	
93,394	0.333	1.763	0.585	1.25	

(b) Case 2 ($D_c=95\%$)					
Young's Modulus, E_0 (kN/m ²)	Poisson ratio, ν	Density, ρ (g/cm ³)	Internal friction angle, ϕ' (rad)	Cohesion, c (kN/m ²)	
121,742	0.333	1.866	0.586	18.7	

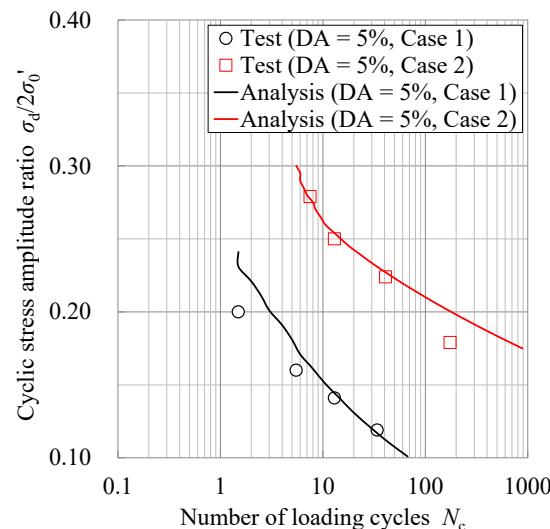


Figure 11. Simulation utility for cyclic triaxial test.

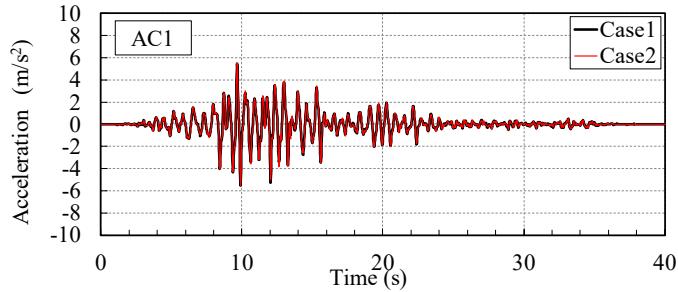


Figure 12. Input excitation motion for numerical simulations.

5. Comparisons of tests and analysis results

Figure 13 shows the comparisons of the maximum response acceleration and the dam height obtained from the analysis. In Case 1, the maximum response acceleration obtained from the analysis tended to be approximately similar to that obtained from the tests, but in Case 2, the maximum response acceleration obtained from the analysis was smaller than that obtained from the tests, and the difference of the maximum response acceleration became especially large at dam heights of approximately 9 m or more. This may be due to the fact that the soil parameter of shear stiffness of Case 2 used in LIQCA was lower than the actual shear stiffness.

Figure 14 (a), (b) show the comparisons of the settlement at the top of the dam obtained from the test and analysis results of Case 1 and Case 2. In Case 1, it shows that the settlement of the analysis result was 40 cm smaller than that of the test result. On the other hand, in Case 2, it shows that the settlement of the analysis result was 40 cm larger than that of the test result. Overall, the test results were approximately simulated by the numerical analysis using the LIQCA program.

Figures 15, 16 show the comparisons of the deformation of the dams between the test and analysis results of Case 1 and Case 2, respectively. For Case 1 (Figure 15 a, b), the test result shows that slip line occurred on the non-submerged side slope and small protrusion was observed on the submerged side slope, while the analysis result shows that a slip line didn't occur on the non-submerged side slope and large deformation was observed on the submerged side slope. For Case 2 (Figure 16 a, b), the test result shows that small deformation was observed on both side slopes, while the analysis result shows that small deformation was observed on the non-submerged side slope and large deformation was observed on the submerged side slope. The large deformation on the submerged side slope is due to the occurrence of liquefaction phenomenon caused by the increase of pore water pressure during shaking.

Overall, the deformation characteristics were similar between tests and analyses, but for future study, it is necessary to verify the validity of the constitutive model and the soil parameters in each zone.

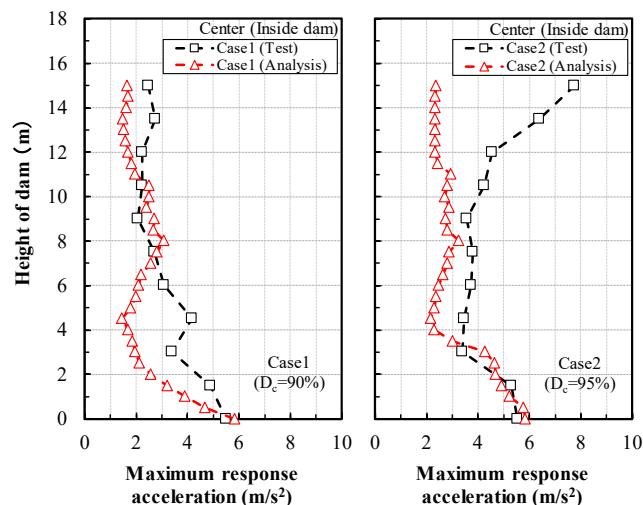


Figure 13. Comparison of maximum response acceleration (analysis).

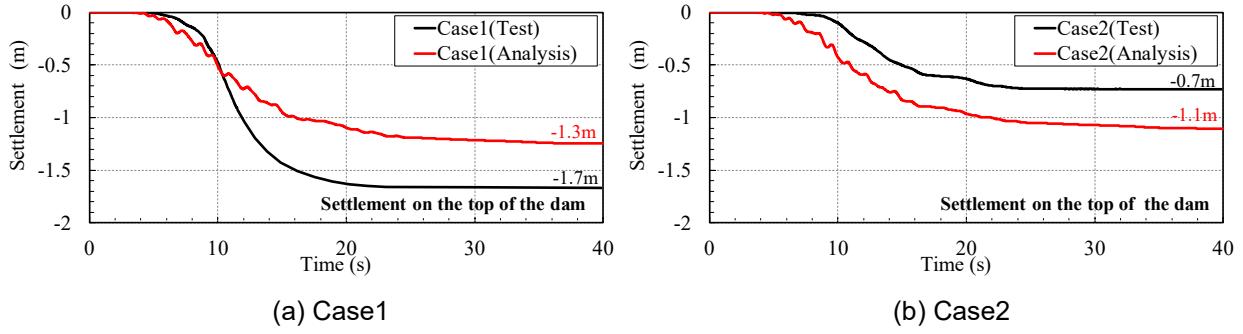


Figure 14. Comparison of settlement between tests and analysis.

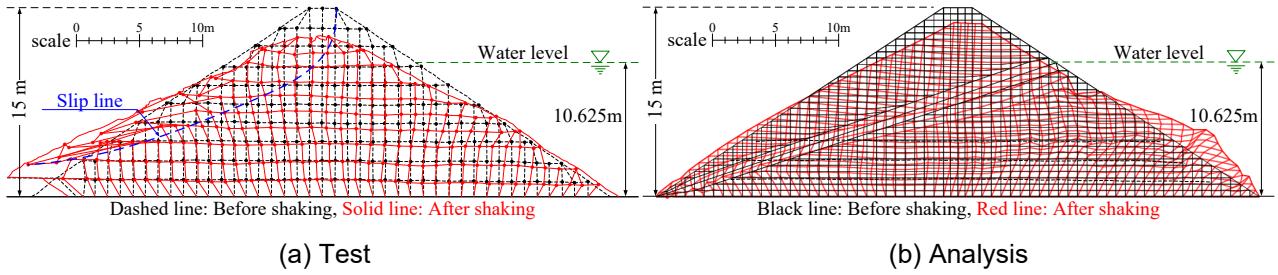


Figure 15. Comparison of deformation between tests and analysis (Case1).

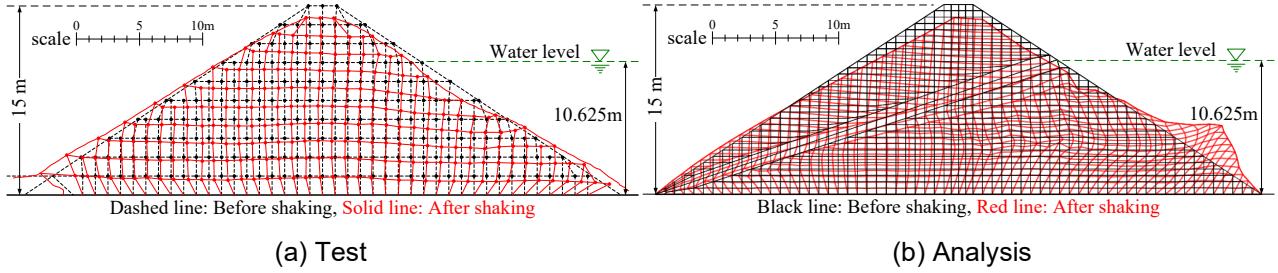


Figure 16. Comparison of deformation between tests and analysis (Case2).

6. Conclusions

Two cases ($D_c = 90\%$ and $D_c = 95\%$) of dynamic centrifuge model tests of irrigation dams and their numerical analysis were conducted. The results of this study are summarized as follows:

- (1) Important fundamental data of the dynamic behavior of the dams were obtained from the centrifuge model tests and their numerical analysis.
- (2) In the test case of $D_c = 90\%$ (Case 1), the seepage line was higher than that assumed during submergence. And the slip line occurred due to the shaking. The amount of settlement at the top of the dam increased significantly due to the slip.
- (3) In the test case of $D_c = 95\%$ (Case 2), the slip line did not occur, and a small deformation occurred on the non-submerged side slope during shaking, and a protrusion occurred near the toe of the slope on the submerged side slope. The amount of settlement at the top of the dam was significantly small.
- (4) The deformation characteristics in each test case were almost the same on the submerged side regardless of the degree of compaction.
- (5) An effective stress analysis program using cyclic elasto-plastic model called LIQCA3D was used to simulate the results of the centrifuge model tests. Overall, the test results were approximately simulated by the

numerical analysis using the LIQCA program. However, since the response acceleration obtained from the analysis tended to be small in both cases and the deformation on the submerged side slope was extremely large, it is necessary to verify the validity of the constitutive model and the soil parameters.

(6) For future study, tests and numerical analyses under different conditions should be conducted to investigate the dynamic behavior of the irrigation dam.

7. References

- Fukuda K., Sreng S., Sato S., Ishikawa K., Kobayashi K. (2017). Evaluation of seismic behavior of irrigation dam—Centrifuge model test and its analysis using LIQCA program, *Annual Conference of Japan Geotechnical Society*: 915-916 (in Japanese).
- Suzuki S.S., Koyama Y., Kobayashi K., Ishikawa H. (2019). Dynamic behavior of irrigation dams under water storage condition by centrifuge model tests and their numerical simulations, *7th International Conference on Earthquake Geotechnical Engineering*.
- Fukuda, K., Suzuki, S., S., Ishikawa, H. (2022). Experimental study on dynamic behaviors of irrigation dams by changing their heights and degree of compactions, *Physical Modelling in Geotechnics*, 916–919.
- Fukuda, K., Suzuki, S., S., Ishikawa, H., Sato, S. (2023). Study on seismic behaviors of irrigation dams by changing their height, *The 2nd International conference on Earth Resources and Geo-Environment Technology*.
- Casagrande A. (1937). Seepage through Dams, *Journal of New England Water Works Association*, 52(2): 131-172.
- Oka F., Yashima A., Shibata T., Kato M. (1991). A finite element analysis of liquefaction of seabed due to wave action, *Geo-Coast'91*: 621-626.

IMPACTS OF THE FEBRUARY 06, 2023, TURKEY EARTHQUAKE SEQUENCE ON RISK ASSESSMENT OF EMBANKMENT DAMS

H. Tosun¹, & M.A. Hariri-Ardebili²

² Mudanya University, Bursa, Turkey, hasan.tosun@mudanya.edu.tr

¹ University of Maryland, College Park, MD, USA

Abstract: On February 6, 2023, Kahramanmaraş, situated in the inner Mediterranean Region of Turkey, experienced two significant earthquakes. The initial event, registering a magnitude of 7.8, took place at a depth of 8.6 km, while the subsequent earthquake, measuring 7.5 in magnitude, occurred at a depth of 7 km. The epicenters of these earthquakes were approximately 90 km apart. The seismic sequence was characterized by additional magnitude 6+ earthquakes and over 10,000 smaller aftershocks. Tragically, the events resulted in the loss of more than 50,000 lives and caused extensive damage to critical infrastructure, including railways, highways, airways, and public structures. In addition, more than 40 embankment dams sustained varying degrees of damage. This paper explores the February 06 earthquake sequence, examining its mechanisms and consequences. Drawing insights from post-earthquake reconnaissance missions, the damage patterns observed in embankment dams are thoroughly explored. The study also offers evaluations of potential earthquake zones that may manifest following these seismic events, providing a comprehensive analysis of the dams' seismic hazards and overall risks. The aim is to contribute valuable insights for future seismic risk mitigation strategies and the enhancement of dam resilience in earthquake-prone regions.

1. Introduction

The seismic performance of dams, particularly embankment dams, has been a critical area of study in the field of civil engineering, driven by the imperative to enhance resilience in earthquake-prone regions (Swaisgood, 2003; Hirschfeld and Poulos, 1973). Dams, serving as vital components of water resource management, face the daunting challenge of withstanding the dynamic forces unleashed during seismic events. Embankment dams, characterized by their earthen structure, require precise evaluation of their response to seismic forces to ensure the safety of surrounding communities and the integrity of water storage (Marcuson et al., 2007). This study focuses on the seismic impacts experienced by embankment dams in the aftermath of the February 06, 2023, Turkey earthquake sequence, shedding light on the vulnerabilities and strengths revealed through these seismic events.

Embankments have become widely adopted globally due to their construction simplicity and the availability of cost-effective local materials. Despite their prevalence, the historical failure of dams has resulted in catastrophic consequences, leading to the loss of lives and substantial property damage. The stability of a dam is contingent upon ensuring that resultant forces or moments do not induce movement (Seed et al. 1969). Dam failures can manifest through various specific performance issues, such as cracking, internal erosion, piping, toppling, and failures in foundations, spillways, and slopes, particularly under dynamic loading conditions. Existing literature highlights that overtopping and internal erosion stand out as the most frequently

cited causes of earthen dam failures (Cristofano 1973; Wahl 1998). A notable historical example is the failure of the Augusta Dam, documented following the renowned earthquake in Charleston (South Carolina) in 1886 (Raja 2014). Comprehensive insights into recognized failures or damages in 58 earth dams attributed to earthquakes have been compiled by Ambraseys (1960).

Post-earthquake reconnaissance missions emerge as indispensable tools for gathering crucial data on the performance of structures, including embankment dams, in the wake of seismic disturbances (Yamaguchi, 2012; Seed et al., 1975; Sêco e Pinto, 2010; Mejia and Dawson, 2019). These missions provide firsthand insights into the physical effects of the earthquakes, enabling engineers and researchers to assess damage patterns, identify failure mechanisms, and collect essential information for subsequent analysis. The comprehensive understanding derived from post-earthquake reconnaissance missions plays a pivotal role in informing future design practices, retrofitting strategies, and emergency response plans, contributing significantly to the broader goal of mitigating seismic risks in dam infrastructure (Tosun et al., 2020; Darbre, 2004). Examples of such previous efforts can be found in Zhang et al. (2010) about May 12, 2008, Wenchuan earthquake impact on high embankment dams, Harder (1991) about Loma Prieta earthquake impact on earth dams, Park and Kishida (2019) about embankment dams performance in Japan, Yousif et al. (2019) about performance of a 128-m high rockfill dam under November 17, 2017 Iraq earthquake, Singh et al. (2005) about 2001 Bhuj earthquake impact on earth dams.

The importance of this endeavor transcends the immediate aftermath of seismic events. By scrutinizing the seismic performance of embankment dams and extrapolating lessons from the February 06, 2023 earthquake sequence, this study aims to enrich the discourse on dam safety and risk analysis (Hariri-Ardebili, 2018). The insights gained will be instrumental in refining seismic design criteria, establishing more robust safety protocols, and fortifying risk assessment methodologies. Ultimately, this research endeavors to bridge critical knowledge gaps, advancing our capacity to ensure the resilience of embankment dams in the face of seismic challenges and fostering a safer and more secure water infrastructure for communities in earthquake-prone regions. This conference paper is a condensed version derived from a more comprehensive journal article published by Hariri-Ardebili and Tosun (2024).

2. Seismic Performance Criteria

As per the guidelines outlined by ICOLD (2010), the criteria governing the seismic performance of dam structures are as follows:

- Dam Body under Operating Basis Earthquake (OBE): No structural damage, such as cracks, deformations, or leakage, affecting the dam's operation and reservoir is permissible. Minor, repairable damage is acceptable.
- Dam Body under Safety Evaluation Earthquake (SEE): Structural damage, including cracks, deformations, or leakage, is accepted as long as the dam's stability is maintained, and there is no uncontrolled release of large water quantities causing downstream flooding.

The performance criteria may be intricately linked to the definition of SEE. For instance, regions with high seismicity might have more stringent requirements, surpassing those specified by ICOLD (2010). In Germany, a sliding stability safety factor of slopes greater than 1.0 is mandated for an SEE with a return period of 2500 years, and in China, water stops in concrete dams must remain undamaged during an SEE with a return period of 5000 years (Wieland, 2012).

Safety-relevant components and equipment encompass bottom outlets, spillways, and associated gear (especially gates), control panels, power supply systems, software, etc. It is imperative that these components enable the regulation and lowering of the reservoir after an SEE. Considering the time needed for dam repairs post-earthquake, the ability to safely release a moderate flood with a return period of approximately 200 years is crucial. For embankment dams, specific safety criteria under SEE include preventing overtopping (i.e., maintaining reservoir level below the top of the impervious core), preserving internal erosion safeguards, and ensuring a sliding safety factor for slopes greater than 1 post-earthquake. In cases of earth-core rockfill dams located on fault lines, additional conservative designs are recommended for optimal safety.

3. Mechanism of February 06, 2023 Earthquake Sequence in Turkey

Turkey, strategically positioned at the convergence of the Anatolian plate and bordered by the Arabian, African, and Eurasian plates, finds itself in one of the most seismically active regions globally. Tectonic dynamics in this area are predominantly influenced by two major active faults—the East Anatolian Fault (EAF) and the North Anatolian Fault, with the former gaining prominence due to its NE-trending left-lateral strike-slip fault system, spanning about 450 km.

On the northern periphery, the Anatolian block undergoes westward movement at an approximate speed of 25 mm/yr relative to Eurasia. Between 1939 and 1999, a series of devastating Mw 7.0 or larger strike-slip earthquakes propagated westward along the North Anatolian fault system. Simultaneously, the southeastern edge of the Anatolian block experiences southwestward movement at approximately 15 mm/yr relative to the Arabian plate. While the East Anatolian fault did not witness Mw 7.0 or larger earthquakes in the century preceding 2023, it remained seismically active, as evident from the January 24, 2020, Mw 6.7 earthquake.

Throughout the 20th century, Turkey experienced 21 Mw 7 or larger earthquakes. Among these, eleven occurred on or near the North Anatolian fault, five within the extensional regime of western Turkey, three in the easternmost region of the country, and the two significant earthquakes in 2023, measuring Mw 7.8 and Mw 7.5, unfolded on the southernmost section of the East Anatolian fault.

At 04:17 a.m. local time on February 6, 2023, a seismic event of moment magnitude (Mw) 7.8 shook the EAF zone at Pazarcık ($N37.288^\circ$, $E37.043^\circ$), situated about 40 km northwest of Gaziantep and 33 km southeast of Kahramanmaraş. The earthquake occurred at a focal depth of 8.6 km. Approximately 10 minutes later, a significant aftershock measuring Mw 6.7 took place at Nurdağı ($N37.304^\circ$, $E36.92^\circ$). Subsequently, approximately 9 hours later, Elbistan ($N38.089^\circ$, $E37.239^\circ$) experienced an Mw 7.5 earthquake with a focal depth of 7.0 km. Another noteworthy seismic event, registering Mw 6.3, struck Hatay on February 20 ($N36.037^\circ$, $E36.021^\circ$) with a focal depth of 21.73 km.

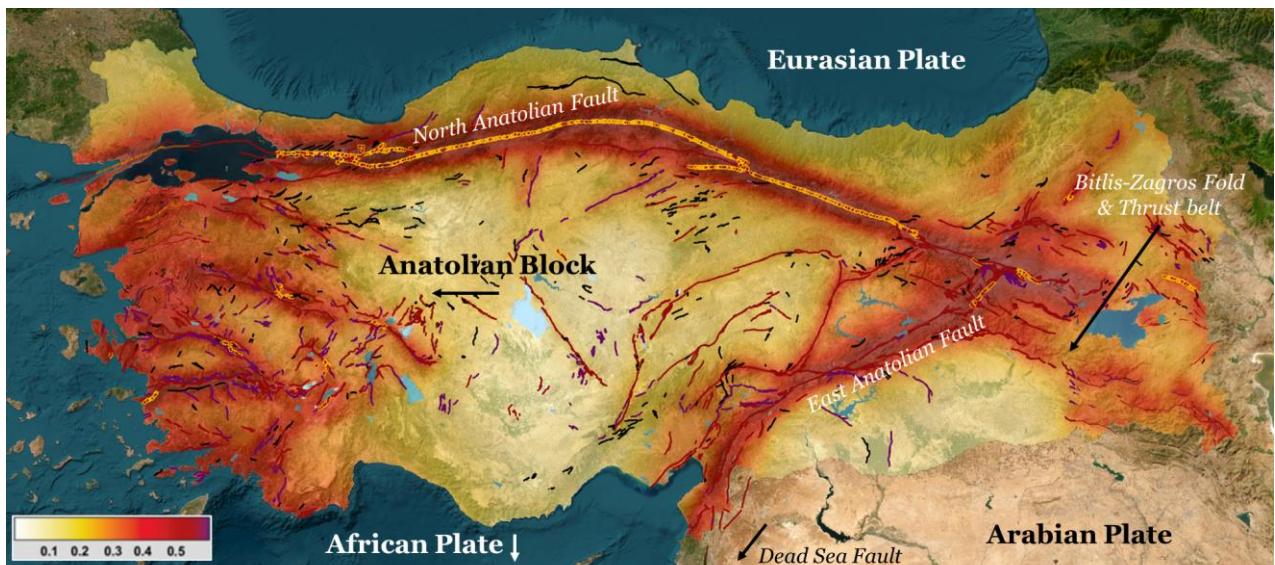


Figure 1. Location of the plate boundaries and active faults in Turkey. The background contour plot presents the PGA in [g] for the scenario with a 10% probability of exceedance in 50 years (475 years return period). Data collected and altered from <https://tadas.afad.gov.tr>.

The initial significant seismic event, registering a magnitude of 7.8 (Pazarcık earthquake) was initiated along the Narlı Segment situated at the northern end of the left-lateral strike-slip Dead Sea Fault Zone. Subsequently, the second major earthquake, with a magnitude of 7.5 (Elbistan earthquake), unfolded in proximity to the Çardak Fault, distinct from the East Anatolian Fault. The location of the Pazarcık earthquake, with a magnitude of 7.8, is approximately 9.1 km from the Narlı segment of the DSFZ and 6.6 km from the Sakçağöz segment of the same fault zone to the south. The epicenter lies 14.1 km west of the Amanos segment of the East Anatolian Fault Zone (EAFZ) and 18.6 km northwest and north of the Pazarcık segment of the EAFZ. This

seismic event resulted in the rupture of a segment spanning about 300 km (125 km of Amanos Segments, 90 km of Pazarcık fault, 60 km of Erkenek fault, and 25 km of Narlı fault) between Çelikhan, located in the Adiyaman district, and Hatay-Ovakent. The left-lateral fault exhibited a slip exceeding 6.0 m, with the largest vertical offset measured at 1.2 m. Some studies have suggested left-lateral slips reaching up to 8.5 m between the Amanos fault, covering 125 km of surface rupture, and the Pazarcık fault, encompassing 90 km of surface rupture with 3.5 m lateral slip (Tosun, 2023).

The earthquake, measuring 7.5 in magnitude and centered in Elbistan (Ekinözü), occupies a complex seismotectonic position. Its epicenter, located in close proximity (7.64 km) to the Çardak fault to the south, stands 26.0 km away from the Sürgü fault, which emerges as an eastward extension of the Çardak fault. Furthermore, it maintains an average distance of 49.6 km and 76.2 km, respectively, from the Beyyuda and Gurun faults, representing the continuation of the Savrun fault to the west. The Doğanşehir fault, recognized as one of the most active discontinuities in the region, is positioned 33.1 km from the earthquake base. Field observations confirm the epicenter's energy source, revealing a lateral separation exceeding 2.0 m in the relevant area. The road exhibits elevation changes, and rock units display splitting towards the northeast in higher elevations.

The seismic activity originating from the northern end of the Narlı segment of DSFZ triggered faults both to the south and north (up to Çelikhan), including the Antakya fault, resulting in a substantial energy release in the northern region. The additional energy accumulation, induced by the initial earthquake in the southern region, was partially mitigated by the subsequent Nurdağı (Mw 6.7) and İslahiye (Mw 6.5) earthquakes. At this stage, energy was further transferred to certain segments in the south, such as the İskenderun Fault Zone. The pronounced damage observed in Syria resulted from the ground movement triggered by the activation of other faults in this region. The second earthquake (Elbistan Mw 7.5 earthquake), occurring with accumulated energy on the Çardak fault, the weakest zone in the region, triggered the Sürgü fault. Effectively, the energy release just north of the Çardak fault set off a chain reaction, impacting all the faults in the region (Çardak, Sürgü, Doğanşehir, Malatya-Akçadağ, and Göksun), leading to significant damage in the area.

4. An Overview of Regional Dams

The repercussions of the February 2023 earthquake sequence have left a profound impact on the stability of numerous dams in Turkey, raising considerable concerns. Official reports indicate the presence of approximately 140 small and large dam structures in the region (Çetin and İlgaç, 2023). Fifteen dams, constructed between 1956 and 2015 within the borders of Adana province, include Seyhan (1956), Kesiksuyu (1970), Kozan (1972), Nergizlik (1996), Çatalan (1996), Yüregir Kılıçlı (2010), Yedigöze (2010), Sarıçam-Baklı (2015), PozantıYağlıtaş (2015), KozanPostkabasakal (2015), Kozan Bağtepe (2016), Kozan Zerdali (2016), Karaisalı Demirüt (2016), Aladağ Dölekli (2016), Kozan Meletmez (2020). The commissioning dates for these dams are detailed in the other publication.

Seven dams (Tahtaköprü-1976, Yarseli-1992, Yayladağı-2000, İskenderun-Pirinçcik-2015, Samandağ Çökek-2015, Kırıkhan Kutlusoguksu-2017, and Büyük Karaçay-2019) commissioned between 1992 and 2019 lie within the borders of Hatay province. Notably, Yarseli dam, one of these storage water structures, underwent elevation in 2006. Osmaniye houses four dams (Memetli-1973, Aslantaş-1985, Kalecik-1987, Düziçi Karacaören-2016) according to official records, with the Mehmetli dam being raised in 2013. Seven dams (Berdan-1984, Merkez Aslanköy-2006, Alaköprü-2015, Toroslar Gözne-2017, Silifke Kica-2019, Merkez Cemilli Çevlik-2019, and Merkez Değirmendere-2020) in the region are potentially at risk.

Official records also reveal eight dams (Kartalkaya-1970, Sır-1991, Menzelet-1992, Ayvalı-2007, Çağlayancerit Merk-2009, Çağlayancerit Zorkun-2012, and Adatepe-2013) within the borders of Kahramanmaraş province. Gaziantep province, part of the basin, has five dams (Hancagiz-1992, Kayacık-2006, Ardıl-2016, Nurdağı Kuzdık-2017, and İslahiye Bayraktepe-2017) operational between 1992 and 2017. Two dams (Çamgazi-1998 and Kahta Menzil-2011) in Adiyaman province and one dam (Seve-2005) in Kilis province complete the landscape.

Immediately following this earthquake sequence, the ICOLD Seismic Committee furnished the Turkish Society on Dam Safety with a list of dams within a 200 km radius of the earthquake, urging inspections. This list encompasses dams in the Asi, Ceyhan, and Fırat basins, serving purposes such as irrigation, drinking water, energy production, and flood protection, with heights ranging from 19 m to 201 m from the foundation. Dams

in Syria are also included in this list. The Turkish Society of Dam Safety identified dams at risk in the aftermath of four major earthquakes and conducted preliminary evaluations. The related report delineated areas susceptible to potential earthquake effects, emphasizing the dams within these regions (Tosun, 2023).

A detailed breakdown of the damages, categorized into levels of light, moderate, and severe, is provided by Tosun (2023), SBB (2023), and Çetin and İlgaç (2023).

- Severe damage: Malatya-Sultansuyu Dam; Osmaniye-Bahçe Ariklaş Pond; Kahramanmaraş-Kartalkaya Dam; Hatay-Yarseli Dam; Gaziantep-Nurdağı Hamidiye Pond
- Moderate damage: Hatay-Reyhanlı Dam; Malatya-Erkenek Pond; Malatya-Sürgü Dam; Hatay-Hassa Demrek Pond; Osmaniye-Kalecik Dam; Hatay-Samandağ Karamanlı Pond; Malatya-Çat Dam; Hatay-Kırıkkale Kurtlusoguksu Pond; Adıyaman-Çetintepe Dam; Kahramanmaraş-Kılavuzlu Dam
- Light damage: Hatay-Büyükkaraçay Dam; Osmaniye-Aslantaş Dam; Gaziantep-Islahiye Bayraktepe Dam; Kilis-Yukarı Afrin Dam

5. Embankment Dams under the Seismic Spotlight

In this paper, we delve into a technical assessment of select dams to understand their seismic response following the February 2023 earthquake sequence. Detailed scrutiny has been conducted on dams such as Akçadağ-Sultansuyu, Doğanşehir-Sürgü, Doğanşehir-Polat, Çelikhan-Çat, Pazarcık-Kartalkaya, Bahçe-Ariklaş, Bahçe-Kalecik, Antakya-Yarseli, and Reyhanlı-Reyhanlı (Figure 2). A specific focus is given to the Tahtaköprü Dam, notable for its resilience despite its proximity to a segment of the DSFZ in the region. Table 1 introduces the physical characteristics of the dams under consideration.

Table 1. Physical Characteristics of the dams considered for this study. Notes: height is measured from the foundation. I: Irrigation, DW: Domestic Water, EF: Earthfill dam, RF: Rockfill dam.

#	Dam	City	Basin	Height [m]	Function	Type	Body Volume [Mm³]	Construction period	Reservoir Capacity [hm³]	Irrigated Area [ha]
1	Ariklaş	Osmaniye	Ceyhan	33	I	EF	0.62	1994-1998	2.2	268
2	Kalecik	Osmaniye		80	I	RF	0.84	1978-1985	32.8	4 890
3	Kartalkaya	K.maraş		57	I+DW	EF	1.45	1965-1972	195.0	22 810
4	Çat	Adıyaman	Euphrates	78	I	RF	2.5	1985-1996	240.0	22 091
5	Polat	Malatya		56	I	EF	2.1	1985-1991	11.5	2 743
6	Sürgü	Malatya		55	I+DW	RF	1.22	1965-1969	70.9	10 090
7	Sultansuyu	Malatya		60	I	EF	3.2	1986-1992	53.3	17 614
8	Reyhanlı	Hatay		30	I	EF	20.73	2010-2020	480.0	58 460
9	Tahtaköprü	Hatay	Rebel	47	I	EF	2.0	1968-1975	200.0	11 900
10	Yarseli-Hatay	Hatay		45	I	EF	3.0	1985-1992	5.0	8 343

Several of these dams gained public attention post-earthquake, prompting us to offer concise insights into potential issues. Our discussions emphasize what we perceive as crucial aspects, drawing from our extensive inspections. Furthermore, a dedicated program has been devised for other dams known to have sustained damage (Tosun, 2023). These dams were visited, subjected to thorough inspections, and the findings are encapsulated in a separate publication. Figure 2 visually depicts the observed damage for each dam, represented by colored circles. Notably, two dams from this list exhibited no damage, while four sustained moderate damage and another four experienced severe damage. Large cracks, reaching up to 4.5 meters, have emerged in certain dam bodies, accompanied by slip surfaces on both upstream and downstream slopes. The inspection process revealed instances of lateral spreading and differential settlements. Furthermore, significant rock falls were observed, hindering road closure and impeding the timely delivery of essential first-aid services. The authors believe that further research into this matter is warranted.

For the seismic hazard analyses of dam sites across three water basins (Ceyhan, Euphrates, and Rebel), an exhaustive study was conducted, leveraging the macro seismo-tectonic model of Turkey. While the initial map

was provided by the National Disaster Organization and other Institutes for general use, a refined version tailored for dam projects was developed at the Earthquake Research Center in Osmangazi University. This program, utilized by the authors in numerous studies (Tosun and Seyrek, 2010; Seyrek and Tosun, 2011; Tosun, 2019), has proven effective.

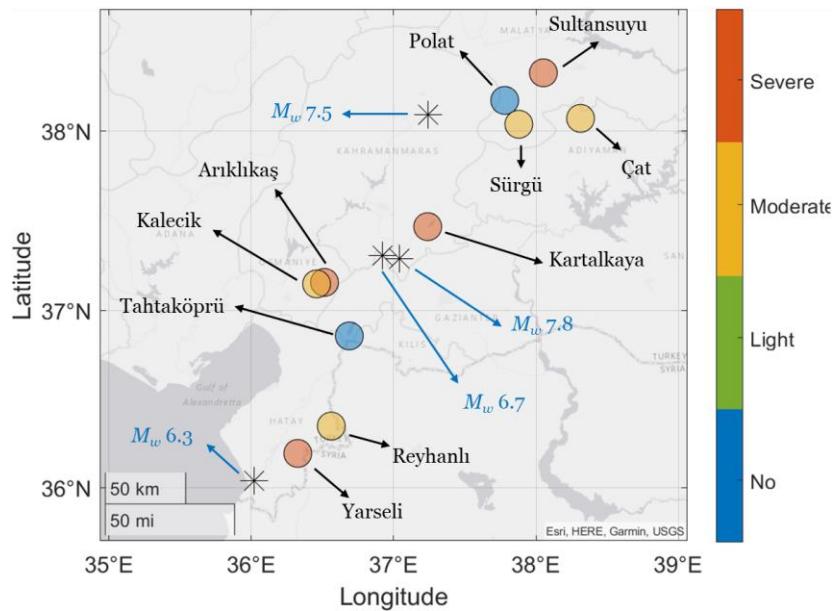


Figure 2. Location of the dams studied in this paper, as well as four main shocks and aftershocks from the February 2023, Turkey earthquake sequence. Note: The M_w values are based on initial assessment by USGS. AFAD reported differently.

Incorporating local geological features and seismic history, the seismic activity rates within the basins were quantified. Subsequently, the seismic stability of dams under consideration underwent a re-analysis, aligning with the new seismic zonation map and updated national regulations on seismic design. The comprehensive results of the seismic hazard analyses are presented in Table 2.

Table 2. Results of deterministic and probabilistic analyses. Notes: M_{max} : Maximum earthquake magnitude in M_w ; R_{min} : Minimum distance to fault segment; $PGA_{50\%}$: Mean PGA at the 50th percentile; $PGA_{84\%}$: Mean PGA at the 84th percentile; OBE: Operational Based Earthquake; MDE: Maximum Design Earthquake; SEE: Safety Evaluation Earthquake.

#	Dam	Deterministic Method				Probabilistic Method		
		M_{max}	R_{min} [km]	$PGA_{50\%}$ [g]	$PGA_{84\%}$ [g]	OBE [g]	MDE [g]	SEE [g]
1	Ariklikaş	7.0	7.6	0.311	0.505	0.304	0.407	0.562
2	Kalecik	7.7	5.7	0.363	0.591	0.379	0.525	0.591
3	Kartalkaya	7.6	7.5	0.354	0.569	0.228	0.331	0.497
4	Çat	7.4	2.8	0.471	0.762	0.322	0.434	0.607
5	Polat	7.6	3.4	0.470	0.761	0.408	0.548	0.754
6	Sürgü	7.4	1.2	0.463	0.761	0.369	0.520	0.766
7	Sultansuyu	7.6	8.5	0.351	0.563	0.162	0.239	0.370
8	Reyhanlı	7.3	3.2	0.453	0.733	0.310	0.423	0.597
9	Tahtaköprü	7.2	0.8	0.503	0.810	0.445	0.599	0.834
10	Yarseli	7.1	3.4	0.397	0.643	0.342	0.462	0.643

The seismic hazard analyses conducted through two distinct methods reveal a considerable variation in Peak Ground Acceleration (PGA) values across dam sites. Deterministic seismic hazard analysis indicates that the PGA values for the 50th percentile range from 0.311 g to 0.503 g, while those for the 84th percentile fall between 0.505 g and 0.810 g. Probabilistic seismic hazard analysis shows that PGA changes widely across all earthquake levels, depending mainly on the dam sites' positions and the nature of predictive relationships. In this study, six separate relationships were considered for determining horizontal PGA.

Notably, the Tahtaköprü dam, which showed no damage, exhibits PGA values (for both deterministic and probabilistic approach) that is highest among all dams considered in this study. Minimal capillary cracks were discerned as the sole visible impact. Situated proximately to the center and villages of Hatay province's Hassa district, most affected by recent earthquakes, the dam occupies a location between the Amanos Segment of the East Anatolian Fault Zone and the Yesemek Segment of the Dead Sea Fault Zone—regions instrumental in shaping seismic activity in the area. Figure 3 showcases images captured during the reconnaissance mission at Tahtaköprü dam. Furthermore, the presence of recently poured and laid material on the fill crest suggests a need for further investigation.



Figure 3. Views from the crest of Tahtaköprü dam (left) and fill materials in downstream slope (right).

Interestingly, the Tahtaköprü dam is equipped with three accelerometers—one in the crest and two installed in the left and right abutments. This configuration allows for the evaluation of the actual acceleration experienced by the dam during the earthquake sequence. Figure 4 presents the recorded acceleration time histories and their corresponding displacement time histories at the Tahtaköprü dam location during the first event (Mw 7.8). Notably, a PGA of approximately 0.25 g is observed in both the E-W and N-S directions at the crest, while the vertical acceleration reaches 0.2 g. A significant spike in the displacement time history of both horizontal components occurs around $t = 40$ s, reaching about 0.8 m. Figure 4(a) reveals that the recorded acceleration comprises two distinct strong motion phases, one around 10 s and the other around 40 s.

Unexpectedly, the recorded acceleration in the right abutment exhibits higher acceleration, potentially attributed to noise in recording. Removal of spikes in the acceleration time history reduces the PGA in the horizontal direction to about 0.20 g and 0.17 g in the vertical direction. The displacement time history of the vertical component at the right station displays a remarkably large displacement cycle and residual value. Importantly, none of the records shown in these plots underwent baseline correction. In the left abutment, a horizontal PGA of 0.16 g is observed with a vertical PGA of 0.11 g.

Polat and Sürgü dams' sites also experience relatively high PGA values due to their proximity to the energy source. It is crucial to highlight that all dams are impacted by a nearby energy source, with distances less than 10.0 km from fault line (Table 2). The results of total risk analyses are presented in Table 3. The hazard ratio identifies a risk class of IV with high risk for all dams, aligning with both ICOLD (1989) and DSI (2012) specifications. According to this study, Total Risk Factor (RF_{total}) values range between 173.6 and 244.5, signifying a high-risk potential for downstream life and structures.

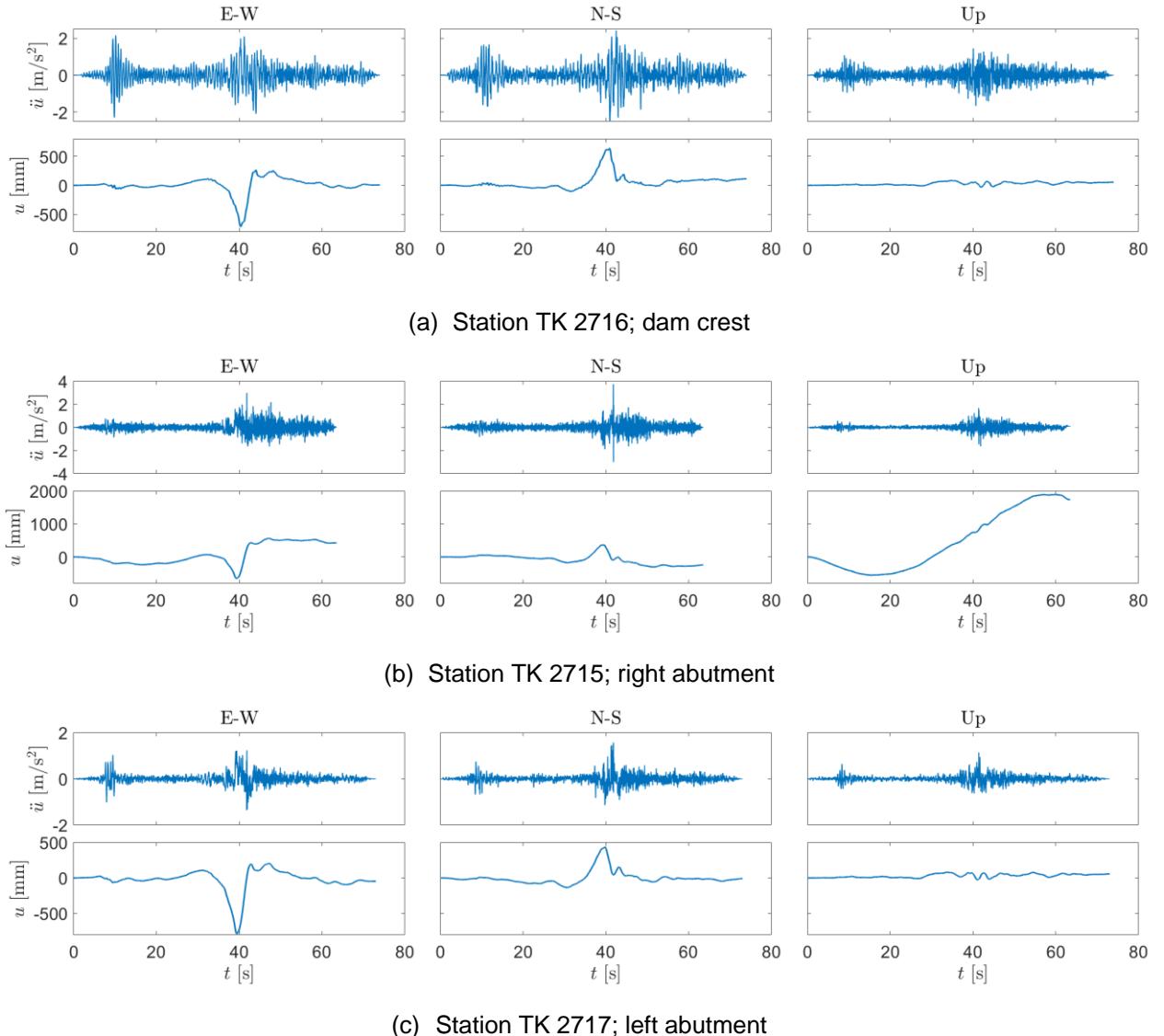


Figure 4. Recorded acceleration time histories and their corresponding displacement time histories at the location of Tahtaköprü dam measured during the first event (M_w 7.8)

Table 3. Results of total risk analyses for all dams considered in the study using two approaches.

#	Dam	Hazard Analysis		Total Risk (ICOLD, 1989)			Total Risk (Bureau, 2003)		
		Class	Hazard Ratio	Risk factor	Risk class	Risk ratio	Risk factor	Risk class	Risk ratio
1	Ariklikas	IV	Very high	28	IV	Very high	189.0	III	High
2	Kalecik	IV	Very high	34	IV	Very high	173.6	III	High
3	Kartalkaya	IV	Very high	34	IV	Very high	176.2	III	High
4	Cat	IV	Very high	36	IV	Very high	238.7	III	High
5	Polat	IV	Very high	34	IV	Very high	228.9	III	High
6	Surgu	IV	Very high	34	IV	Very high	244.5	III	High
7	Sultansuyu	IV	Very high	34	IV	Very high	225.5	III	High
8	Reyhanli	IV	Very high	32	IV	Very high	230.2	III	High
9	Tahtaköprü	IV	Very high	36	IV	Very high	236.7	III	High
10	Yarseli	IV	Very high	32	IV	Very high	165.5	III	High

6. Dams in Potential Earthquake Zones

In assessing the potential seismic hazards to dams in the region, three key factors emerge as areas of concern: (1) Ceyhan basin, (2) Euphrates upper basin- Perisuyu region, and (3) Elbistan-Çelikhan shear zone (transition zone between Ceyhan and Euphrates basins). Dams situated in this last potential area bore the brunt of the recent earthquake, as detailed in previous section, and will not be revisited in this section. However, the risk of damage to our associated dams, even in the event of a relatively modest earthquake in this area, remains significant (e.g., the damage incurred by the Sürgü dam in the 1985 Doğanşehir earthquake, M_w 5.8).

The Sürgü Fault system, configured as a shear zone, may not have fully ruptured, thus presenting a potential new seismic source in this region. The second major earthquake (Elbistan M_w 7.5) heavily loaded the southern region, west of the impact area of the first earthquake, with substantial energy. Recent seismic activities have also charged the Karataş, Yumurtalık, Misis, EcemİŞ, and Sarız fault zones in the region. In summary, the potential earthquake area includes the western part of Kahramanmaraş, Adana province, and the eastern section of Mersin province (Tosun, 2023).

In the northern region, the unruptured segment of the EAFZ between the Palu Segment (source of the Elazığ earthquake) and the Yedisu Segment is another potential seismic generator. The EAFZ extends from the junction point of the Sürgü Fault, Erkenek segment, Pütürge segment, continuing with the Palu segment to the Karlıova triple junction system. The Erkenek and Pütürge segments in this zone have not recently experienced earthquakes, signifying it as a potential earthquake-prone area.

The Pütürge Segment reaches Hazar Lake as a shear zone, transitioning to the Palu segment as another shear zone beyond this point. The 2020 Elazığ earthquake, with a magnitude of M_w 6.8, partially discharged energy in this region while also transferring energy to the Karlıova triple junction region in the northeast. Bounded by the Nazmiye Fault Zone, the Yedisu Segment of the North Anatolian Fault Zone, and the Sancak-Uzunpınar Fault zone parallel to the Palu segment, the north of the Palu Segment is defined as the third potential earthquake zone (Tosun, 2023).

The unruptured section of the EAFZ and the southern segments of the Dead Sea Fault Zone were unaffected by the first major earthquake in the region, ceasing at the southern ridge of the Antakyा fault (Samandağ region). Aftershock distribution indicates that this earthquake triggering and prolonging mechanism loads energy onto tectonic discontinuities in the south, creating a fourth potential earthquake zone. To summarize, two major earthquakes on February 06, 2023 (Pazarcık M_w 7.8 and Elbistan M_w 7.5) have introduced new potential earthquake areas. Therefore, focusing on four potential regions is deemed appropriate: (1) West and southwest of Kahramanmaraş province, Adana province, and the east of Mersin province, (2) The zone between Kahramanmaraş-Nurhak, Malatya-Doğanşehir, Adiyaman-Çelikhan, and Elaziğ-Sivrice, (3) The region between Elaziğ-Palu and Bingol-Yedisu, and (4) South of Hatay province.

7. Conclusions

In conclusion, the seismic events of February 06, 2023, in Turkey have left an indelible mark on the stability of numerous dams in the region, necessitating a comprehensive investigation into their response to the earthquake sequence. This paper discussed the seismic performance of embankment dams, focusing on the aftermath of the Pazarcık (M_w 7.8) and Elbistan (M_w 7.5) earthquakes. Through post-earthquake reconnaissance missions, we scrutinized the condition of several dams, including Akçadağ-Sultansuyu, Doğanşehir-Sürgü, Doğanşehir-Polat, Çelikhan-Çat, Pazarcık-Kartalkaya, Bahçe-Arıklıkaş, Bahçe-Kalecik, Antakyा-Yarseli, and Reyhanlı-Reyhanlı. Special attention was accorded to the Tahtaköprü dam, which, despite its proximity to a seismic fault, exhibited no damage, highlighting its robust seismic resilience.

The seismic hazard analyses, incorporating both deterministic and probabilistic approaches, revealed varying PGA values across dam sites. While the Tahtaköprü dam exhibited the highest PGA values, even those with no observed damage, other dams like Polat and Sürgü faced relatively high PGA values due to their proximity to the earthquake energy source. Total risk analyses categorized all dams as having a high risk, emphasizing the need for diligent safety evaluations and risk mitigation strategies. The study also identified potential earthquake zones in the region, shedding light on areas of concern for future seismic events.

In the exploration of individual dam responses, the Tahtaköprü dam's unique instrumentation provided invaluable data on actual accelerations during the seismic events. Despite recording moderate PGAs, this dam showed no damage, underscoring the significance of monitoring and instrumentation in understanding the true impact of earthquakes on dam structures. As we contemplate the findings of this study, it becomes evident that a holistic understanding of seismic performance, coupled with vigilant risk assessments, is imperative for enhancing dam safety in earthquake-prone regions.

8. References

- Ambraseys NN (1960) On the shear response of a two-dimensional truncated wedge subjected to an arbitrary disturbance. *Bull Seismol Soc Am* 50(1):45–56
- Cetin, K. and Ilgac, M (2023). Reconnaissance Report on February 6, 2023 Kahramanmaraş-Pazarcık (Mw=7.7) and Elbistan (Mw=7.6) Earthquakes, Technical Report, Turkiye Earthquake Reconnaissance and Research Alliance, Turkey.
- Cristofano EA (1973) Method of computing erosion rate for failure of earth fill dams; United States Department of the Interior, Engineering and Research Center: Denver, CO, USA, No. 727
- Dabre, G. R. (2004, August). Swiss guidelines for the earthquake safety of dams. In *Proceedings of the 13th WCEE*.
- Harder Jr, L. F. (1991). Performance of earth dams during the Loma Prieta earthquake.
- Hariri-Ardebili, M. A. (2018). Risk, Reliability, Resilience (R3) and beyond in dam engineering: A state-of-the-art review. *International journal of disaster risk reduction*, 31, 806-831.
- Hariri-Ardebili, M. A. and Tosun, H. (2024). Dams in the wake-up call of the 2023 Turkiye earthquake sequence: Insights from observed damages, risk assessment, and monitoring. *International Journal of Disaster Risk Reduction*, (in press).
- Hirschfeld, R. C., & Poulos, S. J. (1973). *Embankment-dam engineering*.
- ICOLD (2010). Selecting seismic parameters for large dams. Guidelines, Revision of Bulletin 72, Committee on Seismic Aspects of Dam Design, International Commission on Large Dams, Paris.
- Marcuson, W. F., Hynes, M. E., & Franklin, A. G. (2007, June). Seismic design and analysis of embankment dams: the state of practice. In *Proceedings of the 4th Civil Engineering Conference in the Asian Region, June 25-28, Taipei*.
- Mejia, L., & Dawson, E. (2019). Evaluation of Earthquake-Induced Cracking of Embankment Dams. In *Proceedings of the 2019 USSD Annual Conference, Chicago, USA*.
- Park, D., & Kishida, T. (2019). Seismic response of embankment dams based on recorded strong-motion data in Japan. *Earthquake Spectra*, 35(2), 955-976.
- Raja MA (2014) 2D Non-Linear Finite Element Analysis of Earthen Dam for Earthquake Loads, Dissertation MTech, Indian Institute of Technology, Roorkee, India
- SBB, (2023). Kahramanmaraş And Hatay Earthquakes Report, Technical Report, Presidency Of The Republic of Turkey, Presidency Strategy and Budget, Turkey, 2023.
- Sêco e Pinto, P. S. (2010). Understanding Seismic Embankment Dam Behavior Through Case Histories.
- Seed HB, Lee KL, Idriss IM (1969) Analysis of Sheffield dam failure. *J Soil Mech Found Div* 95:1453–1490
- Seed, H. B., Lee, K. L., Idriss, I. M., & Makdisi, F. I. (1975). The slides in the San Fernando dams during the earthquake of February 9, 1971. *Journal of the Geotechnical Engineering Division*, 101(7), 651-688.
- Seyrek E, H.Tosun, "Deterministic approach to the seismic hazard of dam sites in Kızılırmak basin, Turkey" *Natural hazards*, 59 (2), 787, 2011
- Singh, R., Roy, D., & Jain, S. K. (2005). Analysis of earth dams affected by the 2001 Bhuj Earthquake. *Engineering geology*, 80(3-4), 282-291.
- Swaisgood, J. R. (2003, February). Embankment dam deformations caused by earthquakes. In Pacific conference on earthquake engineering (Vol. 14).

- Tosun, H., Tosun, T. V., & Hariri-Ardebili, M. A. (2020). Total risk and seismic hazard analysis of large embankment dams: case study of Northwest Anatolia, Turkey. *Life Cycle Reliability and Safety Engineering*, 9, 329-338.
- Tosun H. Earthquake Safety Evaluation for Large Dams Located near the Energy Source and Case Studies. In Proceeding of 11th ICOLD European Club Symposium. Chania. Crete 2-4 October 2019
- Tosun, H. (2023) Second Report-Pazarcik (Mw 7.7) and Elbistan (Mw7.6) earthquakes dated February 06, 2023: Evaluation on damages inspected on dams in the region, Technical Report, Turkish Society on Dam Safety, Turkey.
- Tosun H, Seyrek E. Total risk analyses for large dams in Kizilirmak basin, Turkey. *Natural Hazards and Earth System Sciences*. 10 (5). 979, 2010.
- Wahl T (1998) Prediction of Embankment Dam Breach Parameters; Report DSO-98-004; Dam Safety Office: Washington, DC, USA, 67 p
- Wieland, M. (2012, September). Seismic design and performance criteria for large storage dams. In *World Conference Earthquake Engineering 15th, Lisboa*.
- Yamaguchi, Y., Kondo, M., & Kobori, T. (2012). Safety inspections and seismic behavior of embankment dams during the 2011 off the Pacific Coast of Tohoku earthquake. *Soils and Foundations*, 52(5), 945-955.
- Yousif, O. S., Zaidn, K., Alshkane, Y., Khani, A., & Hama, S. (2019, May). Performance of Darbandikhan Dam during a major earthquake on November 12, 2017. In *Proceedings of the EWG2019, 3rd Meeting of Dams and Earthquakes, An International Symposium, Lisbon, Portugal* (pp. 6-8).
- Zhang, J. M., Yang, Z. Y., Gao, X. Z., & Tong, Z. X. (2010). Lessons from damages to high embankment dams in the May 12, 2008 Wenchuan earthquake. In *Soil Dynamics and Earthquake Engineering* (pp. 1-31).

MONITORING AND SIMULATED RESPONSE OF DAMS TO THE FEBRUARY 2023 TURKEY EARTHQUAKE SEQUENCE

M.A. Hariri-Ardebili¹, & H. Tosun²

¹ University of Maryland, College Park, MD, USA, hariri@umd.edu

² Mudanya University, Bursa, Turkey

Abstract: This paper presents some monitoring results and preliminary analysis of the seismic behavior of typical dams in response to the February 2023 Turkey earthquake sequence, which commenced with a major earthquake measuring an Mw of 7.8. The seismic sequence encompassed a significant number of recorded earthquakes, including subsequent Mw 6.7, 7.5, and 6.3 events shortly after. The impact of these earthquakes resulted in the collapse of over 50 thousand structures, with an additional 180 thousand structures sustaining substantial damage. Notably, several dams were affected to varying degrees based on factors such as their proximity to fault rupture, the intensity of ground shaking at their sites, and the seismic capacity of each dam. Analysis of the recorded ground motions reveals the presence of accelerations exceeding 1.0 g within the vibration periods relevant to dam structures, specifically ranging from 0.3 s to 1.0 s. These high acceleration levels pose significant challenges to dam resilience. In the field of dam engineering, evaluating the seismic performance of existing dams typically involves subjecting them to a series of (scaled) ground motion time series recorded from past seismic events. Although such numerical simulations can provide insights into dam performance during earthquakes, it is crucial to acknowledge the inherent uncertainties associated with this approach. This paper aims to provide initial insights into the seismic behavior of dams when subjected to ground motion records from this event. Moreover, the recorded ground motions at the dam site (including the crest and abutment) are processed. The findings of this preliminary research are valuable for informing the seismic design of future dams or retrofitting existing dams to enhance their resilience.

1. Introduction

In the context of modern dam engineering, the integration of seismic instrumentation has become an indispensable facet for understanding and mitigating the seismic hazards confronting both existing and prospective dams (Bolt and Hudson, 1975). The incorporation of digital seismic accelerometers and recorders into dam safety monitoring systems has ushered in an era of real-time insights into the dynamic response of dams during seismic events. This paper offers an in-depth exploration of the seismic instrumentation landscape, tracing its evolution from the nascent stages of the 1930s to the contemporary era of sophisticated instruments.

The trajectory of advancements in seismic instrumentation has been defined by the proliferation of digital seismic accelerometers and recorders, with the accelerograph emerging as a paramount instrument. Originating in the 1970s, the accelerograph, equipped with servo-accelerometers, has become ubiquitous in monitoring strong ground movements. Noteworthy is the installation of the first strong motion instrument at

Hoover Dam by the United States Bureau of Reclamation (USBR) in 1936, marking a seminal moment that laid the foundation for subsequent global networks of strong motion seismometers (USBR, 1987).

In the present day, the Earth is surveilled by over 20,000 strong motion seismometers worldwide, delivering real-time data on seismic events (Adamo et al., 2021). These instruments play a pivotal role in recording various seismic factors, including frequency, amplitude content, magnitude, origin depth, and epicentral distance. The distinct characteristics of seismic events necessitate the use of records from the actual seismogenic region or, with caution, from regions exhibiting similar seismo-tectonic characteristics (Mihailov and Dojcinovski, 2001).

The indispensable role of seismic instrumentation in comprehending dam behavior in seismic areas is underscored by the categorization of strong motion seismographs based on their placement. Free field instruments are strategically positioned away from significant dam influences, input motion instruments are placed at the downstream toe and abutments, and response instruments are situated on the dam to assess its dynamic response.

Detailed discussion about the structural health monitoring and seismic instrumentation of dams can be found in several papers with notable ones as Hall (1998), Wieland (2010), Yang et al. (2017), Koufoudi et al. (2018), Seyed-Kolbadi et al. (2020), Oliveira and Alegre (2020), Sevieri and DeFalco (2020), Oliveira et al. (2022). Moreover, Hariri-Ardebili et al. (2023) provided a narrative review of different aspects of dam health monitoring using digital technologies.

This paper aims to provide preliminary insights into the monitoring data from dams in Turkey subjected to the February 2023 earthquake sequence. The seismic events, highlighted by a major earthquake measuring an Mw of 7.8, left an indelible impact on numerous structures, necessitating a thorough analysis of dams in the affected region. Specifically, this study explores the case of Feke II Dam, scrutinizing recorded motions in the dam crest and abutment rock. In addition to the empirical data, a low-fidelity finite element model is developed for dynamic response analysis, shedding light on the structural resilience (Hariri-Ardebili et al., 2018) of the dam amidst seismic events. This conference paper is partly inspired by a more comprehensive journal article published by Hariri-Ardebili and Tosun (2024).

2. February 2023 Earthquake Sequences in Turkey

Turkey, strategically positioned at the convergence of the Anatolian plate and bordered by the Arabian, African, and Eurasian plates, finds itself in one of the most seismically active regions globally. Tectonic dynamics in this area are predominantly influenced by two major active faults—the East Anatolian Fault (EAF) and the North Anatolian Fault, with the former gaining prominence due to its NE-trending left-lateral strike-slip fault system, spanning about 450 km.

On the northern periphery, the Anatolian block undergoes westward movement at an approximate speed of 25 mm/yr relative to Eurasia. Between 1939 and 1999, a series of devastating Mw 7.0 or larger strike-slip earthquakes propagated westward along the North Anatolian fault system. Simultaneously, the southeastern edge of the Anatolian block experiences southwestward movement at approximately 15 mm/yr relative to the Arabian plate. While the East Anatolian fault did not witness Mw 7.0 or larger earthquakes in the century preceding 2023, it remained seismically active, as evident from the January 24, 2020, Mw 6.7 earthquake.

Throughout the 20th century, Turkey experienced 21 Mw 7 or larger earthquakes. Among these, eleven occurred on or near the North Anatolian fault, five within the extensional regime of western Turkey, three in the easternmost region of the country, and the two significant earthquakes in 2023, measuring Mw 7.8 and Mw 7.5, unfolded on the southernmost section of the East Anatolian fault.

At 04:17 a.m. local time on February 6, 2023, a seismic event of moment magnitude (Mw) 7.8 shook the EAF zone at Pazarcık (N37.288°, E37.043°), situated about 40 km northwest of Gaziantep and 33 km southeast of Kahramanmaraş. The earthquake occurred at a focal depth of 8.6 km. Approximately 10 minutes later, a significant aftershock measuring Mw 6.7 took place at Nurdağı (N37.304°, E36.92°). Subsequently, approximately 9 hours later, Elbistan (N38.089°, E37.239°) experienced an Mw 7.5 earthquake with a focal depth of 7.0 km. Another noteworthy seismic event, registering Mw 6.3, struck Hatay on February 20 (N36.037°, E36.021°) with a focal depth of 21.73 km.

3. Dams Response to February 2023 Earthquake Sequences

1.1. Reported Damage

The aftermath of the February 2023 earthquake sequence reverberates significantly, marking a concerning impact on the stability of large dams in Turkey. An extensive toll has been exacted on more than forty large dams, resulting in varying degrees of damage. The Turkish State Hydraulic Works (DSİ) estimates the incurred cost for the restoration of these dams and reservoirs to be a staggering 150 million USD. A detailed breakdown of the damages, categorized into levels of light, moderate, and severe, is provided by Tosun (2023), SBB (2023), and Çetin and İlgaç (2023).

- Severe damage: Malatya-Sultansuyu Dam; Osmaniye-Bahçe Ariklaş Pond; Kahramanmaraş-Kartalkaya Dam; Hatay-Yarseli Dam; Gaziantep-Nurdağı Hamidiye Pond
- Moderate damage: Hatay-Reyhanlı Dam; Malatya-Erkenek Pond; Malatya-Sürgü Dam; Hatay-Hassa Demrek Pond; Osmaniye-Kalecik Dam; Hatay-Samandağ Karamanlı Pond; Malatya-Çat Dam; Hatay-Kırıkhan Kurtlusokuşu Pond; Adıyaman-Çetintepe Dam; Kahramanmaraş-Kılavuzlu Dam
- Light damage: Hatay-Büyükkaraçay Dam; Osmaniye-Aslantaş Dam; Gaziantep-Islahiye Bayraktepe Dam; Kilis-Yukarı Afrin Dam

The discussion regarding damaged dams falls outside the scope of the current paper and will be addressed separately. Detailed damage evaluation can be found in Hariri-Ardebili and Tosun (2024).

1.2. Monitoring and Instrumented Response

Beyond the damaged dams, numerous other dams in the region have encountered the February 2023 earthquake sequences to varying extents. Of particular interest are three dams equipped with sensors installed on both the dam and abutment, with recordings accessible through AFAD. These dams include Feke II Dam, Kavşak Bendi Dam, and Tahtaköprü Dam.

Tahtaköprü Dam, located in Hatay Province, is a 50-year-old earthfill dam, boasting a height of 55.5 meters and a crest length of 401 meters. Kavşak Bendi Dam, a concrete-faced rockfill dam, is approximately a decade old, standing at a height of 88 meters and a crest length of 186 meters. Feke II Dam (Figure 1), constructed with roller-compacted concrete in 2011, is the focus of detailed study in this paper. The dam stands at a height of 70 meters, with a crest length of 256 meters. The volume of RCC and the total dam volume are 194,000 and 227,000 m³, respectively. Concrete placement occurred in layers of 0.3 meters. The mix design comprises 60 kg/m³ of cement and 50-60 kg/m³ pozzolan (Low-lime fly ash - ASTM Class F).



Figure 1. A downstream view of Feke II Dam. Photo adopted from: <https://rccdams.co.uk/dams/feke-ii/>

4. Feke II Dam Seismic Monitoring System

This Roller-Compacted Concrete (RCC) dam is equipped with two AceBox sensors—one installed at the dam crest (TK0133) and the other on the abutment rock (TK0134). The AceBox is an advanced accelerograph designed for high performance. It features three Force Balance Accelerometers capable of recording seismic signals at a high resolution (up to 100 Hz frequency) and storing the data on the embedded USB memory.

Figure 2 depicts the dam's location in the canyon, showcasing the positions of the two recording stations in relation to the dam. Additionally, the figure provides an overview of the dam's location concerning the four main shocks and aftershocks from the February 2023 earthquake sequences. The plot displays all recorded earthquakes by the TK0133 station (located at the crest) from February to October 2023, amounting to approximately 280 events. The size of the circles corresponds to the Peak Ground Motion Acceleration (PGA) of each event recorded at station TK0133, with color variations representing the earthquake magnitude. Notably, the M_w 7.8 and M_w 7.5 shocks exhibit relatively moderate PGA at the dam site, while the impact of the M_w 6.3 event is practically negligible.

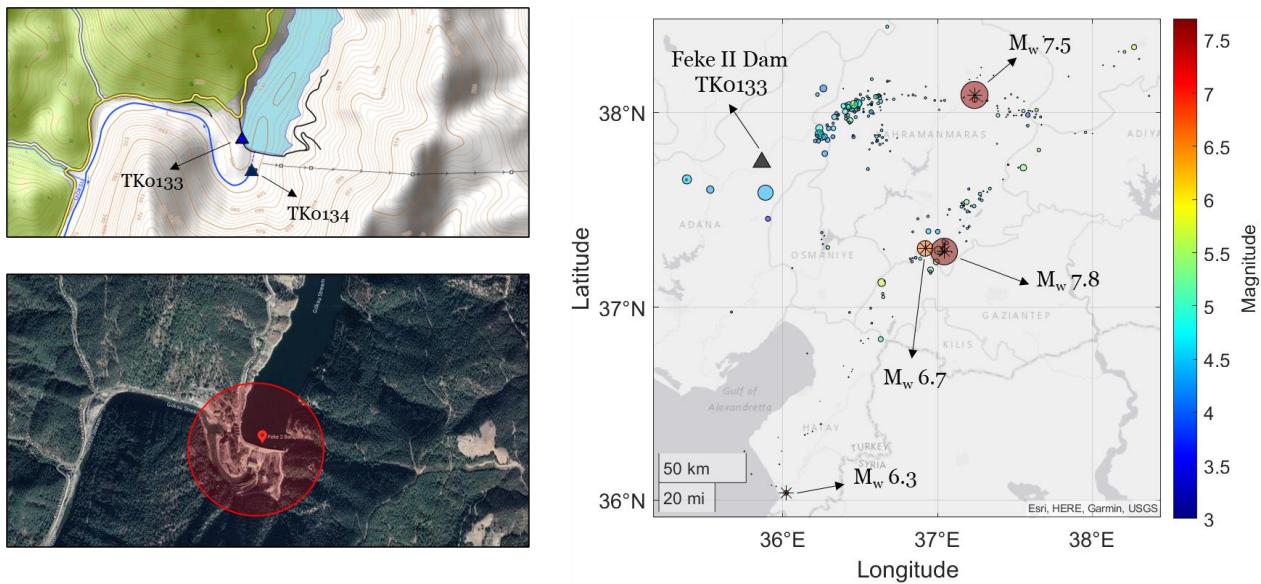


Figure 2. Location of the Feke II Dam and its two recording stations, as well as all the recorded motions including the February 2023. Note: The M_w values are based on initial assessment by USGS. AFAD reported differently.

5. Monitoring the Feke II Dam Recordings

Utilizing information sourced from the AFAD website, we retrieved four primary recordings from the February 2023 earthquake sequences for both TK0133 and TK0134 stations at the Feke II Dam site. Each recording encompasses three components in the N-S, E-W, and Up directions. Figures 3 and 4 present the acceleration time histories and their corresponding displacement time histories from four events in three directions. For this paper, we exclusively present the original recordings without any baseline correction. It is noteworthy that some displacement time history plots reveal the presence of cumulative residual displacement in the record, underscoring the necessity of filtering the records before deploying them in any numerical simulations.

Upon comparing the E-W and N-S components, a noticeable trend emerges: for TK0133 recordings at the dam crest, the E-W component typically induces a higher PGA compared to the N-S component. Conversely, for TK0134 station, the PGA from the N-S component is typically higher than that from the E-W component.

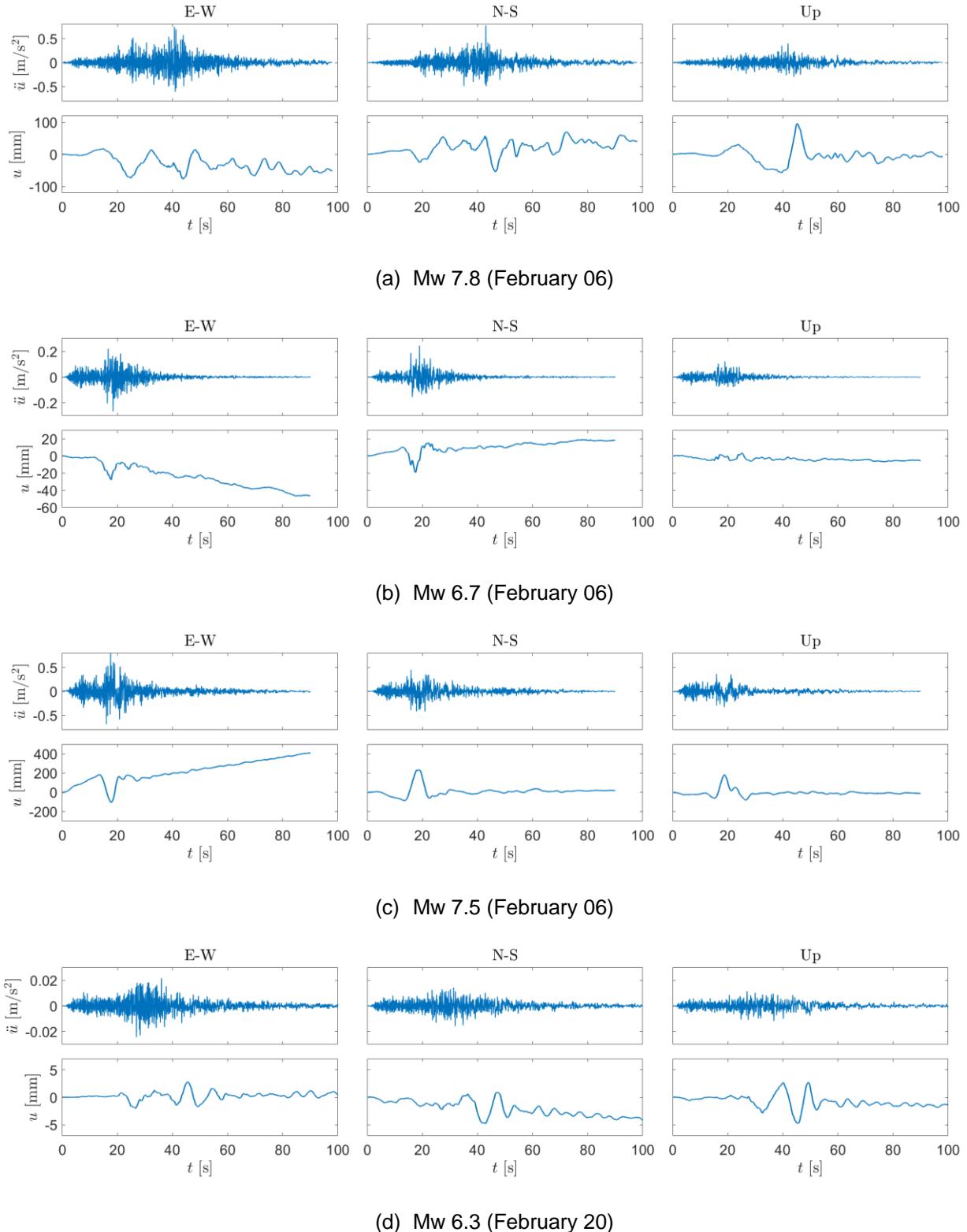


Figure 3. Recorded acceleration time histories and the corresponding displacement time histories at station TK0133, Feke II Dam crest.

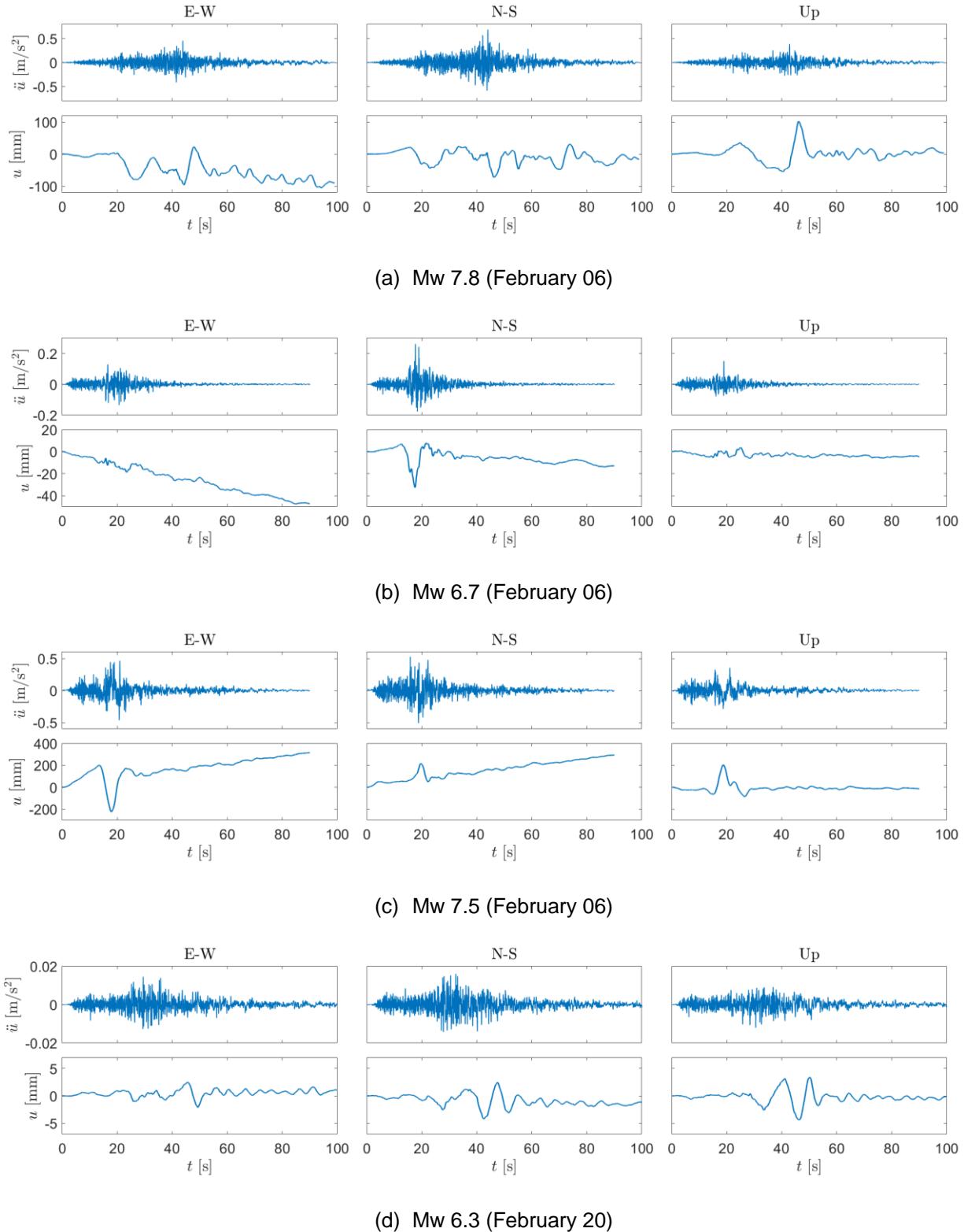


Figure 4. Recorded acceleration time histories and the corresponding displacement time histories at station TK0134, Feke II Dam abutment rock.

Figure 5 illustrates the acceleration and displacement response spectra derived from all four events across three components. A comparison is made between two stations: one at the dam crest and the other on the abutment rock. The figure also outlines the approximate location of the dam's fundamental period, determined to be 0.25 seconds through numerical modeling. A consistent observation with the PGA findings is evident here: for station TK0134, the N-S component of the spectrum surpasses the E-W component, while for TK0133, the E-W component predominates across the majority of frequencies. Furthermore, the estimated location of the dam's first period coincides with the peak interval of the acceleration response spectrum. According to this representation, the dam encountered a spectral acceleration of approximately 0.2-0.25 g during Mw 7.8 and 7.5 events. The displacement response spectra reveal instances where the vertical component matches or exceeds the two horizontal components for certain events.

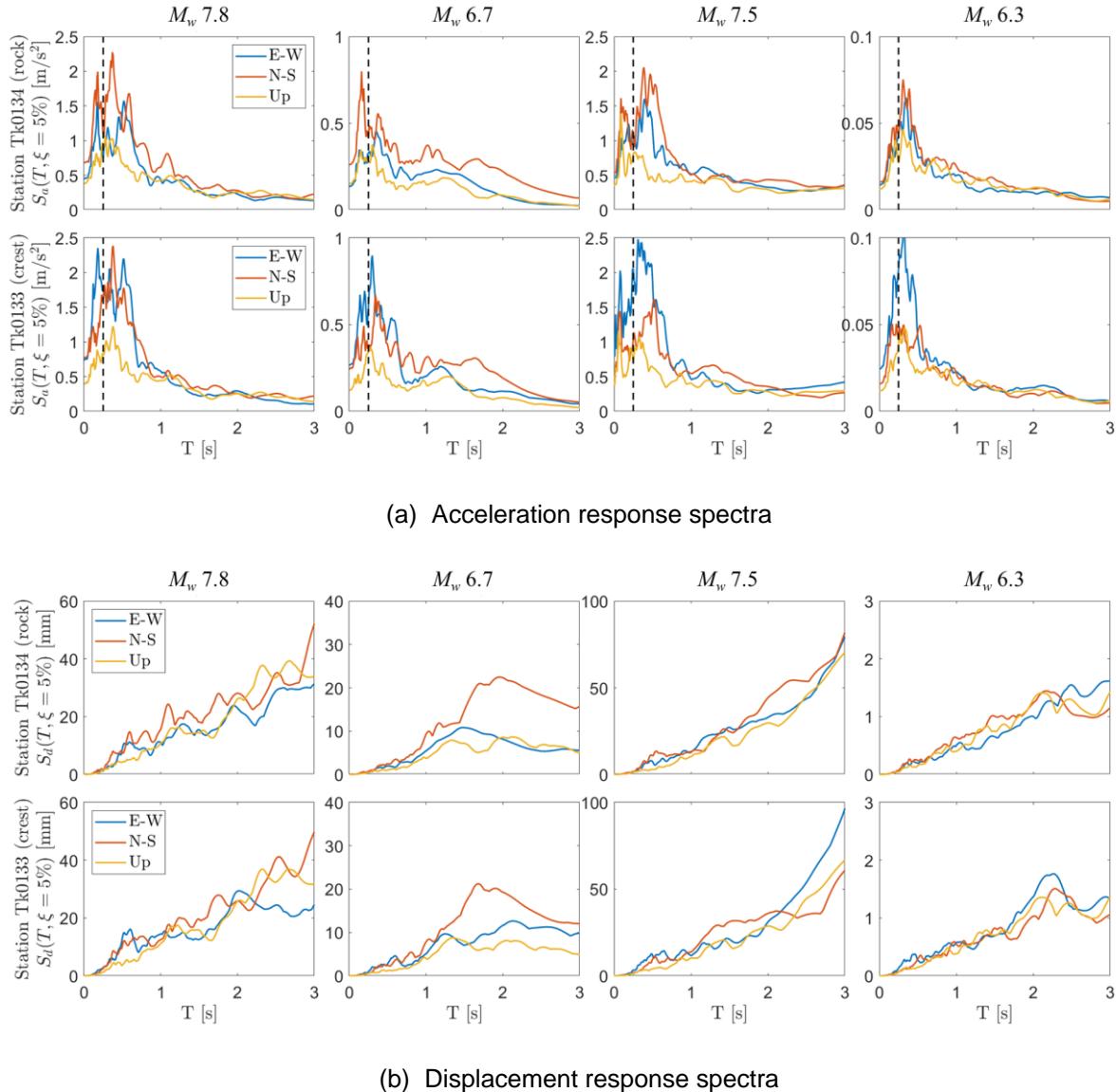


Figure 5. Comparing the response spectra from different events and stations.

Next, the amplitude spectrum of seismic records from two locations—dam crest (TK0133) and abutment rock (TK0134)—is examined. The time domain signals are transformed into the frequency domain using Fast Fourier Transform (FFT) techniques, allowing a comprehensive exploration of the frequency content. The resulting spectra highlight the amplitude variations across different frequencies, providing insights into the dynamic response of the dam under seismic events. The spectral analysis also involves the calculation of the amplitude ratio between the dam crest and abutment rock, showing the differential response at these key locations. Figure 6 represents the amplitude ratios across various frequency components and can interpreted

as a transfer function (TF). The location of spikes in this figure highlights frequencies where the amplitude response at the dam crest significantly differs from that at the abutment rock. These variations in amplitude ratio spikes could be associated with resonance or amplification effects at specific frequencies, showcasing the dam's unique vibrational characteristics. Identifying these spikes helps in understanding the dominant frequencies at which the dam responds most significantly to seismic input. For example, the E-W component of the Mw 7.8 event shows spikes at about 4 Hz and 20 Hz. The former matches the computed fundamental period of 0.25 s.

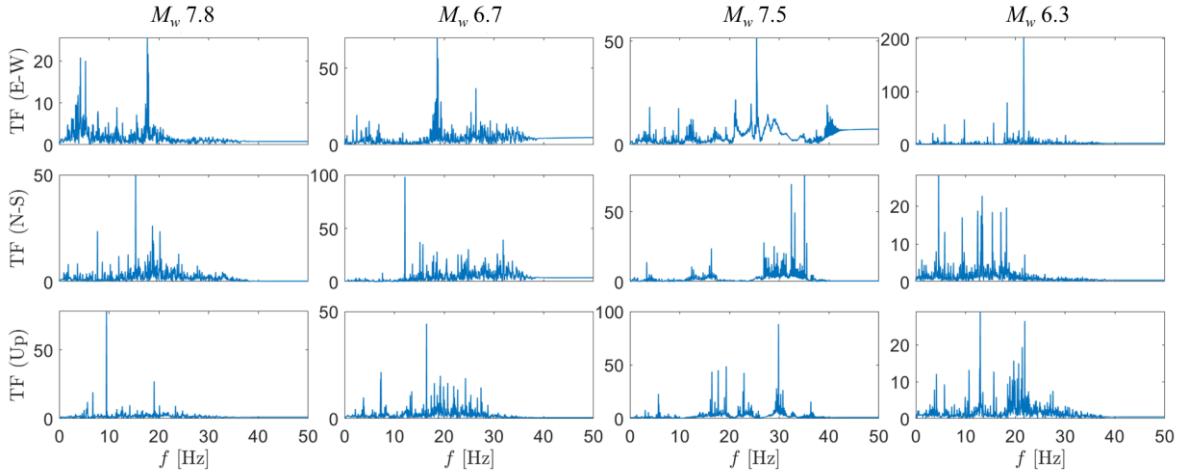


Figure 6. The transfer functions (TF) between the crest (TK0133) and abutment (TK0134) recorded acceleration time histories.

In addition to examining frequency response, the paper explores the comparison of six different Intensity Measure (IM) parameters between the dam crest and the rock abutment, as illustrated in Figure 7. Notably, the ratio of the vertical component remains consistently close to one across various cases. However, a distinctive observation emerges for the E-W component, where this ratio exceeds one, indicating that the dam amplifies the same ground motion at the crest. Conversely, for the N-S component, the ratio is slightly less than unity in the majority of cases, suggesting that the dam tends to dampen motion in this direction. These observations provide valuable insights into how the dam interacts with ground motion.

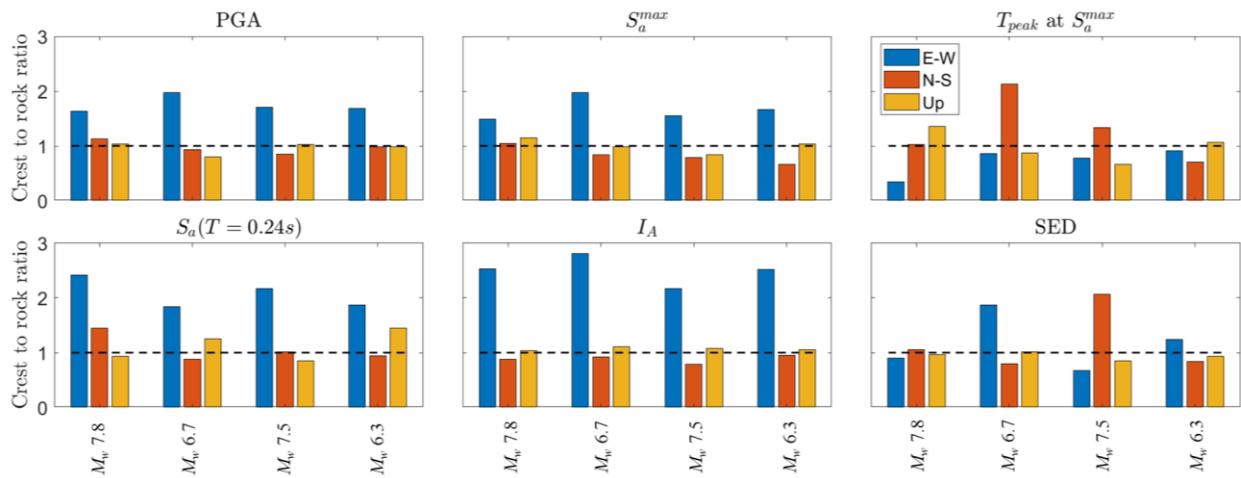


Figure 7. Comparing the ratio of different scalar intensity measure parameters from crest to abutment rock.

6. Preliminary Finite Element Simulations

This section offers initial glimpses into the dynamic response of the dam through finite element simulations. While the analyzed cross-section does not precisely mirror the actual dam due to unavailable dimensions, certain assumptions were made to approximate its geometry. Based on the literature, the dam features a height of 70 m, with upstream and downstream slopes of 1:0.07 and 1:0.8, respectively. Assumed dimensions include a crest width of 7 m, a neck height of 8 m, and a computed base width of 61 m derived from the geometric calculations. Additionally, a water freeboard of 3 meters is considered in the simulation. The RCC concrete properties were assumed to be: a modulus of elasticity of 20 GPa and, a mass density of 2400 kg/m³. An overall damping value of 3% is assumed for the dam and foundation.

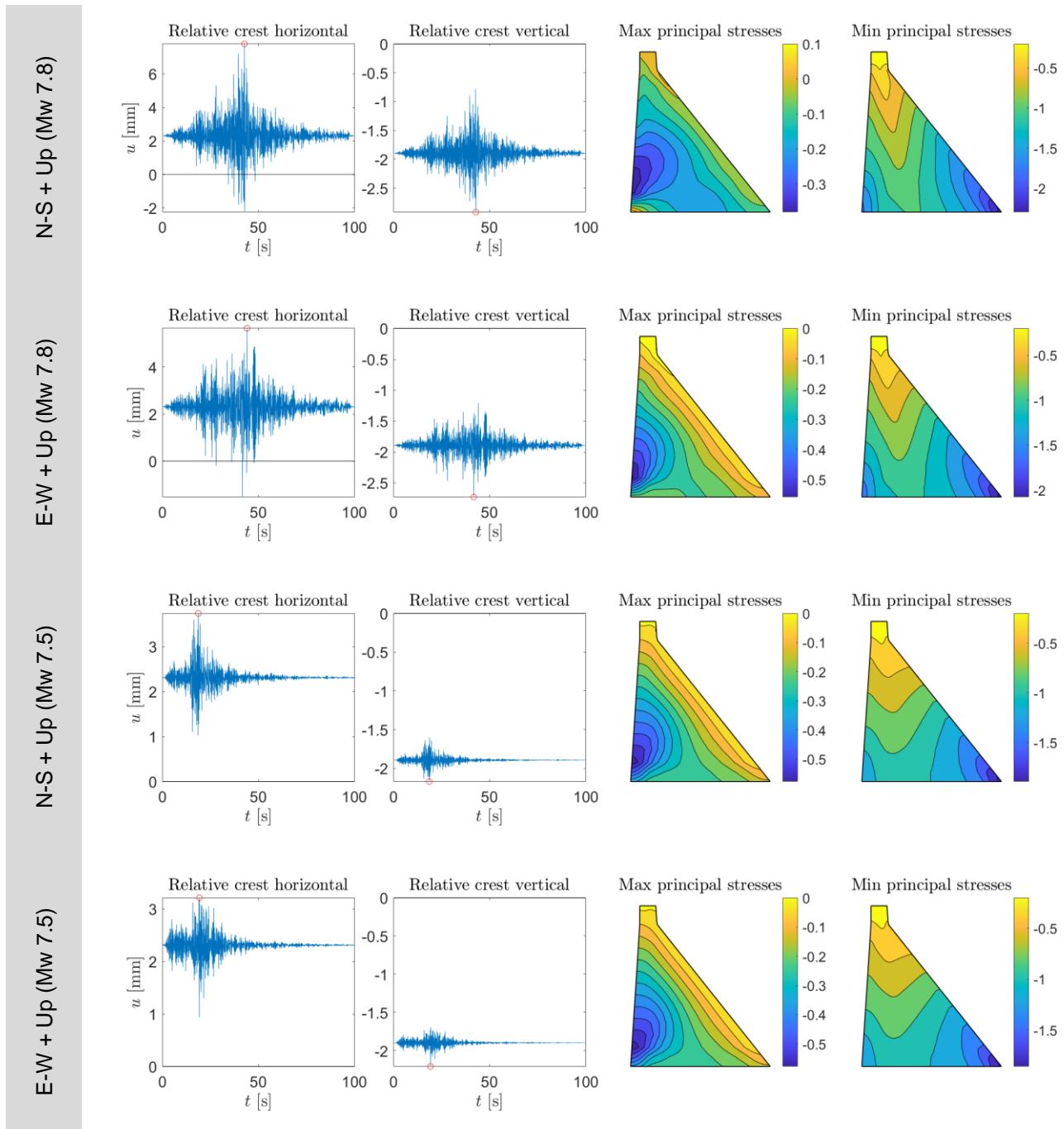


Figure 8. Seismic response of the assumed Feke II Dam subjected to two shocks of Mw 7.8 and Mw 7.5. Stress envelopes are in MPa, and the positive sign indicates tensile stress.

A series of low-fidelity finite element simulations were carried out on a coupled dam-foundation-reservoir system with linear elastic material properties, focusing on seismic events of magnitudes Mw 7.8 and Mw 7.5. Two-dimensional finite element models were utilized, considering two components of the earthquake: E-W and Up, or N-S and Up. Each simulation provided the crest's relative horizontal and vertical displacement time histories, along with the envelope of the maximum first principal stress and minimum third principal stress.

Figure 8 illustrates the outcomes of these preliminary simulations, revealing a horizontal displacement of 2 mm attributed to hydrostatic water pressure. A seismic drift of 0.01% is observed, well below the damage assessment threshold recommended by Hariri-Ardebili and Saouma (2015), set at 0.1%. Under the Mw 7.8 event, the dam experiences a tensile stress of 0.1 MPa, but practically no tension occurs for the Mw 7.5 event, mitigating the risk of cracking during the February 2023 earthquake sequences.

For a more in-depth assessment of the dam's response to potentially higher-intensity events, further numerical simulations were conducted using the N-S and Up component combination of the Mw 7.8 event. Ground motion records were scaled with linear scale factors (SF) of 2, 3, 5, and 8. Figure 9 presents the envelope of the maximum first principal stress in the dam body. Under the scenario of SF = 2, the dam experiences 0.89 MPa of tensile stress at the heel. As the scale factor increases, the tensile stress also rises but remains confined to the heel. With an SF of 3, the tensile stress escalates to 1.73 MPa. Assuming a dynamic tensile strength range of 1.6-2 MPa for intact RCC (Ferguson, 2023), the anticipation of cracking at the heel becomes imminent. It is essential to note that this paper employs only low-fidelity models with linear elastic simulation; more detailed nonlinear models may alter stress distribution and failure modes (Hariri-Ardebili and Seyed-Kolbadi, 2015).

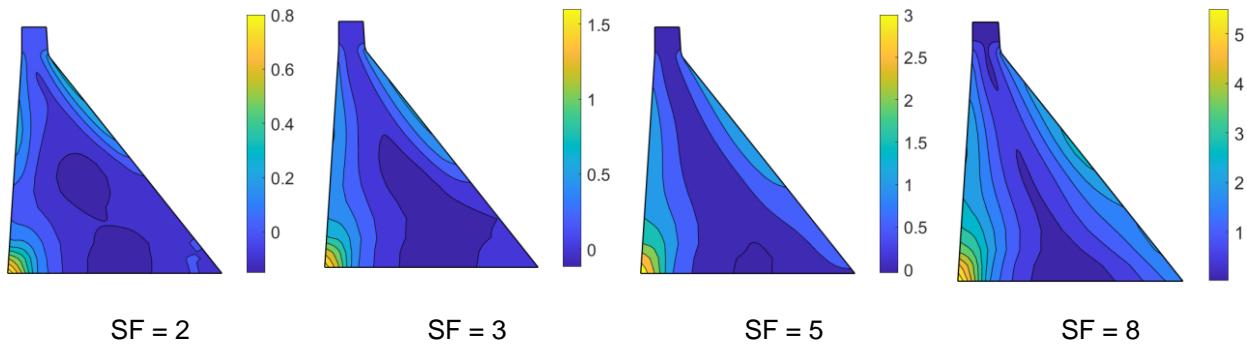


Figure 9. Tensile stress distribution in the dam body [in MPa] resulted from the Mw 7.8 event with N-S and Up components at different scale factors.

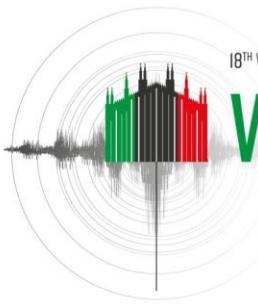
7. Conclusions

In summary, this paper contributes significant insights into the seismic resilience of dams in the context of the February 2023 Turkey earthquake sequence. The detailed monitoring of various dams, with a focused examination of the Feke II Dam, has furnished an understanding of their dynamic responses to seismic events. Leveraging low-fidelity finite element simulations, particularly focusing on seismic events of magnitudes Mw 7.8 and Mw 7.5, the study reveals commendable structural stability with minimal displacements and stress levels well within safety margins. The integration of seismic instrumentation facilitated the extraction of critical data, showcasing the Feke II Dam's robustness and its ability to withstand recorded seismic motions.

Looking forward, the paper extends its analysis to potential scenarios involving higher-intensity events. Numerical simulations, scaling ground motion records, and scrutinizing stress concentrations, provide crucial insights into the dam's response under varying seismic conditions. Despite the application of low-fidelity linear elastic models in this study, the acknowledgment of potential variations through more detailed nonlinear simulations underscores the paper's commitment to laying a robust foundation for seismic design considerations. This work not only contributes to the empirical understanding of dam behavior in seismically active regions but also serves as a reference for future endeavors in enhancing dam resilience and risk mitigation strategies.

8. References

- Adamo, N., Al-Ansari, N., Sissakian, V., Laue, J., & Knutsson, S. (2021). Dam Safety: Use of Seismic Monitoring Instrumentation in Dams. *Journal of Earth Sciences and Geotechnical Engineering*, 11(1), 203-247.
- Bolt, B. A., & Hudson, D. E. (1975). Seismic instrumentation of dams. *Journal of the Geotechnical Engineering Division*, 101(11), 1095-1104.
- Cetin, K. and Ilgac, M (2023). Reconnaissance Report on February 6, 2023 Kahramanmaraş-Pazarcık (Mw=7.7) and Elbistan (Mw=7.6) Earthquakes, Technical Report, Turkiye Earthquake Reconnaissance and Research Alliance, Turkey.
- Ferguson, K. A. (2022). Risk-informed design of RCC dams under extreme seismic loading. *Water*, 15(1), 116.
- Hariri-Ardebili, M. A. and Tosun, H. (2024). Dams in the wake-up call of the 2023 Turkiye earthquake sequence: Insights from observed damages, risk assessment, and monitoring. *International Journal of Disaster Risk Reduction*, (in press).
- Hariri-Ardebili, M. A., Mahdavi, G., Nuss, L. K., & Lall, U. (2023). The role of artificial intelligence and digital technologies in dam engineering: Narrative review and outlook. *Engineering Applications of Artificial Intelligence*, 126, 106813.
- Hariri-Ardebili, M. A. (2018). Risk, Reliability, Resilience (R3) and beyond in dam engineering: A state-of-the-art review. *International journal of disaster risk reduction*, 31, 806-831.
- Hariri-Ardebili, M. A., & Saouma, V. (2015). Quantitative failure metric for gravity dams. *Earthquake Engineering & Structural Dynamics*, 44(3), 461-480.
- Hariri-Ardebili, M. A., & Seyed-Kolbadi, S. M. (2015). Seismic cracking and instability of concrete dams: Smeared crack approach. *Engineering Failure Analysis*, 52, 45-60.
- Koufoudi, E., Chaljub, E., Douste - Bacqué, I., Roussel, S., Bard, P. Y., Larose, E., ... & Baillet, L. (2018). A High - Resolution Seismological Experiment to Evaluate and Monitor the Seismic Response of the Saint - Guérin Arch Dam, French Alps. *Seismological Research Letters*, 89(4), 1576-1582.
- Mihailov, V., & Dojcinovski, D. (2001). Strong Motion Instrumentations of Dams in Macedonia Some Experience and Results. In *Strong Motion Instrumentation for Civil Engineering Structures* (pp. 275-291). Dordrecht: Springer Netherlands.
- Oliveira, S., & Alegre, A. (2020). Seismic and structural health monitoring of Cabril dam. Software development for informed management. *Journal of Civil Structural Health Monitoring*, 10, 913-925.
- Oliveira, S., Alegre, A., Carvalho, E., Mendes, P., & Proença, J. (2022). Seismic and structural health monitoring systems for large dams: theoretical, computational and practical innovations. *Bulletin of Earthquake Engineering*, 20(9), 4483-4512.
- SBB, (2023). Kahramanmaraş And Hatay Earthquakes Report, Technical Report, Presidency Of The Republic of Turkey, Presidency Strategy and Budget, Turkey, 2023.
- Seyed-Kolbadi, S. M., Hariri-Ardebili, M. A., Mirtaheri, M., & Pourkamali-Anaraki, F. (2020). Instrumented health monitoring of an earth dam. *Infrastructures*, 5(3), 26.
- Sevieri, G., & De Falco, A. (2020). Dynamic structural health monitoring for concrete gravity dams based on the Bayesian inference. *Journal of Civil Structural Health Monitoring*, 10(2), 235-250.
- Tosun, H. (2023) Second Report-Pazarcık (Mw 7.7) and Elbistan (Mw7.6) earthquakes dated February 06, 2023: Evaluation on damages inspected on dams in the region, Technical Report, Turkish Society on Dam Safety, Turkey.
- United States Bureau of Reclamation. 1987. Concrete Dam Instrumentation Manual. USBR publication.
- Wieland, M. (2010). Features of seismic hazard in large dam projects and strong motion monitoring of large dams. *Frontiers of Architecture and Civil Engineering in China*, 4, 56-64.
- Yang, J., Jin, F., Wang, J. T., & Kou, L. H. (2017). System identification and modal analysis of an arch dam based on earthquake response records. *Soil dynamics and earthquake engineering*, 92, 109-121.



SEISMIC PERFORMANCE OF AN EARTH DAM WITH STRONG MOTION INPUT SIGNALS SELECTED WITH DIFFERENT CRITERIA

M. Tretola¹, G. Fiorentino², F. Sabetta², & S. Sica¹

¹ University of Sannio, Benevento, Italy, martretola@unisannio.it

² Roma Tre University, Rome, Italy, gabriele.fiorentino@uniroma3.it

Abstract: To assess the seismic performance of earth dams, nonlinear time-history analyses are required as prescribed by most advanced technical codes and standards. Usually, acceleration time-histories are adopted in the numerical simulations to characterize the seismic input signals. Once a proper geotechnical characterization of the dam and foundation soils has been achieved, for an earth dam the analysis results may be highly sensitive to the input signals adopted to represent the ground motion and the way these signals were obtained. The selection of proper natural accelerograms suffers from the limited availability of recordings consistent with the expected earthquake scenarios and the local features of the dam site. The paper describes a sensitivity analysis aimed at detecting how the performance of an existing earth dam may be affected by a different choice of the spectrum-compatible input accelerations. Two different selection criteria of the acceleration time-histories were considered. In one case, the acceleration input signals were selected from the Engineering Strong-Motion database (ESM) while, in another case, they were obtained from an up-to-date code used for the simulation of non-stationary stochastic ground motions.

1 Introduction

Dams are strategic and critical infrastructures that can be highly susceptible to earthquakes. Existing earth dams can often be more vulnerable than newly constructed ones due to their long operational times (fifty years or more) with soil aging, past earthquakes, floods and other detrimental factors that may have altered the original design of the dam.

Assessing the static and seismic safety of existing earth dams can pose additional challenges due to uncertainties regarding their recent and past loading history. Particularly for structures located in seismically active regions, predicting the seismic performance of the dam could be quite complicated and of utmost importance. In the event of a major earthquake, the stability of the dam can be compromised with all the catastrophic consequences involved, such as life loss, property damage and environmental devastation. In the case of earth dams in operation for many years, the continuous monitoring of the dam body and reservoir slopes together with a periodic evaluation of their response with an update of the level of knowledge on dam and foundation soils, seismic hazard and analysis methods, is essential to ascertain the resilience of these strategic infrastructures to earthquakes.

The time-domain nonlinear analysis, combined to suitable numerical techniques for the spatial discretization of the soil domain, is currently the most realistic approach to evaluate the seismic response of an earth dam through performance-based criteria. For such an aim, advanced constitutive laws are preferred to accurately reproduce soil behaviour from small to large strain levels together with suitable coupled formulations to model

solid - fluid phase interaction (Sica et al., 2008; Biondi et al., 2021; Cascone and Rampello, 2009). Everything stated could vanish if it were not accompanied by an adequate characterization of the seismic motion.

Spectrum-compatibility is usually invoked by the most advanced technical codes and standards. It implies that the difference between the average spectrum of the selected accelerograms and the reference code spectrum must not exceed a determined tolerance in a specific range of periods. The selected time series must also satisfy the requirement of seismic compatibility, i.e. they must be consistent with the regional seismotectonic and seismogenic context. In addition, other specific requirements may be needed, such as a limitation on the scaling factor of natural accelerograms. In Italy, for example, a scale factor in the range 0.5÷2 should be respected as specified by the current technical standards (MIT, 2014 and 2018) and guidelines (DGD, 2019). Unfortunately, especially for the higher return periods relevant to the ultimate limit states of a dam, the above conditions may be difficult to be fulfilled. Notwithstanding the higher number of accelerometric databases available worldwide to date, a sufficient number of natural accelerograms for all the required seismic scenarios may not always be found. It is worth noting that an erroneous input signal selection could strongly affect the outcomes of the performed numerical analyses and so the overall safety assessment (Bommer and Acevedo, 2004; Pagliaroli and Lanzo, 2008; Dello Russo et al., 2017; Sica and Dello Russo, 2021).

To overcome these limitations, a good solution could be the use of simulated time series, which can address the lack of sufficient natural accelerometric recordings. In the case of dynamic analyses related to geotechnical systems, in some countries (e.g. Italy) the use of simulated input motions is allowed providing that the seismogenetic characteristics of the source and the features of the propagation medium are adequately known (MIT, 2018).

This paper focuses on a sensitivity analysis aimed at understanding how a different choice of the input motion to analyze the seismic performance of a bituminous-faced rockfill dam, would impact the safety assessment of the structure with respect to typical damage indicators used in the field of earth dams, such as the freeboard loss. Specifically, the study explores two different approaches in selecting the acceleration signals to adopt as input for the seismic analysis of the reference dam. In the first approach, the natural records were retrieved from the Engineering Strong-Motion database (ESM). In the second, a novel code developed by Sabetta et al. (2021) and by Fiorentino (2022) for simulating non-stationary stochastic ground motions was employed. The adopted code had never been tested for seismic verification of geotechnical systems and its applications to earth dams represents a novelty of this study.

By comparing the results obtained from these two different sets of analysis, indications will be provided to engineers and dam owners in charge of dam safety assessment.

2 Seismotectonic of the dam site

The reference dam is located in southern Italy in an area characterized by a high seismicity. As illustrated in Figure 1, the dam site is very close to the surface projection of the normal faults indicated by ITIS077 (Colliano) and ITIS079 (Pescopagano) in the Database of Individual Seismogenic Sources (DISS, 2021).

In the lower part of Figure 1 are illustrated the main features of these faults which caused respectively the first and third shock of the 1980 Irpinia earthquake (moment magnitude $M_w=6.8$, macroseismic intensity $MCS=X$, 2735 victims, 9000 injured, according to Guidoboni et al., 2019).

Based on the Italian Macroseismic database (DBMI15, Locati et al., 2022), the strongest effects felt by the reference dam corresponds to the 1694 Irpinia-Basilicata event with an X degree MCS (Mercalli Cancani Sieberg scale) and an estimated magnitude of 6.7. The epicenter of that event is located 4.8 km far from the reference dam, as illustrated in Figure 1, where the epicenters of the historical and instrumental earthquakes reported in the catalogue CPTI15 (Rovida et al., 2020) are indicated with different symbols and colours. The 1694 earthquake can be therefore considered as the scenario earthquake for a Deterministic Seismic Hazard Assessment.

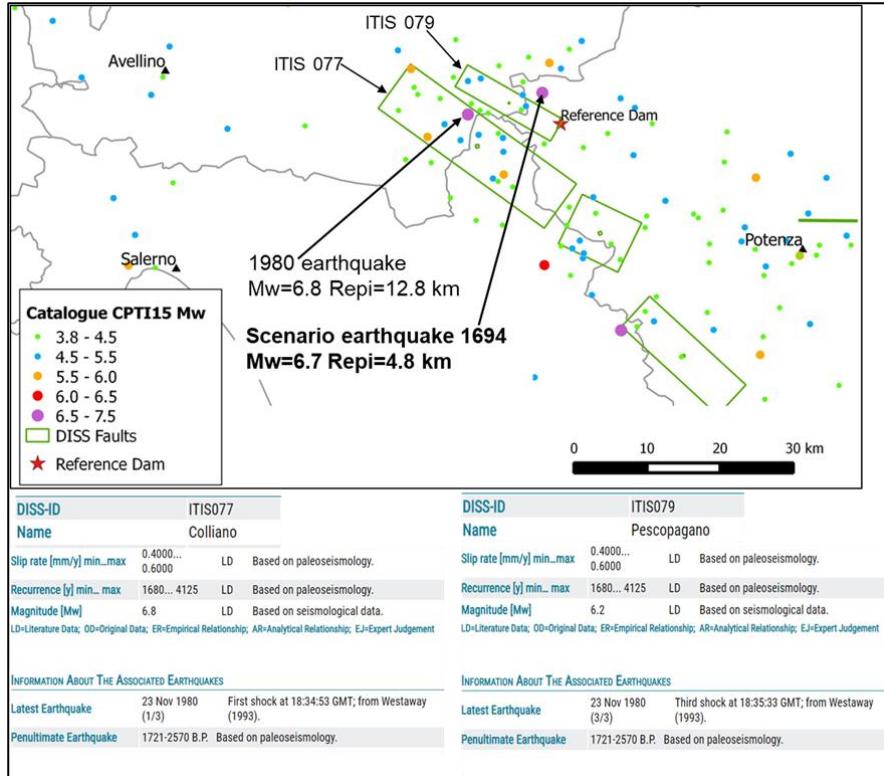


Figure 1. Faults and historical and instrumental earthquakes epicentres around the dam.

3 Input motion

The Italian building code (MIT, 2018) prescribes that the ultimate and operational limit states can be verified through dynamic analyses with the use of accelerograms, either recorded or simulated. The average spectral ordinates must not have a deviation of less than 10% or more than 30% with respect to the corresponding component of the elastic spectrum at any point in the range of the natural vibration periods for the reference structure and for the different limit states. In the last years, several databases containing many natural ground motion records, were created and updated (Bozorgnia et al., 2013; Luzzi et al., 2016).

Table 1. Main parameters of the strong motion records extracted from ESM with $Mw=6.5-7.0$, $R_{epi}=0-15$ Km, site class=A. The values of PGA, PGD and Arias Intensity refer to the maximum of two horizontal components. Duration is calculated as the time interval between 5-95% of Arias Intensity.

#	event time	Country	station	Mw	R_{epi} (km)	site class	PGA (cm/s ²)	PGD (cm)	Arias (cm/s)	Duration (s)
1	30/10/2016 06:40	Italy	T1213	6.6	12.6	A	850	12.4	609	6.5
2	21/06/2000 00:51	Iceland	502	6.5	6.5	A	821	24.2	273	4.9
3	21/06/2000 00:51	Iceland	107	6.5	6.5	A	613	35.1	154	3.0
4	17/06/2000 15:40	Iceland	502	6.5	8.4	A	519	11.9	137	4.3
5	30/10/2016 06:40	Italy	T1212	6.6	11.6	A	274	14.9	80	8.5
6	15/04/1979 06:19	Montenegro	ULA	6.9	13.1	A	210	8.8	73	12.2
7	21/06/2000 00:51	Iceland	112	6.5	11.2	A	126	9.7	22	5.3
8	21/06/2000 00:51	Iceland	101	6.5	10.6	A	175	8.3	18	5.3

As described above, the scenario earthquake for the reference dam has a magnitude of 6.7 and an epicentral distance (R_{epi}) of 4.8 km. To perform the local seismic response analysis at the dam site, the selected

accelerograms need to be recorded on a rock site ($V_{S30} \geq 800$ m/s or site class A). We choose to search compatible accelerograms in the Engineering Strong-Motion database, (ESM, Luzi et al., 2016) which currently includes 90478 three-component waveforms relative to events with magnitude ≥ 4.0 , mainly recorded in the European-Mediterranean regions and the Middle East. The search results, with the constraints of $Mw=6.5-7.0$, $R_{epi}=0-15$ Km, site class=A, provided only 8 three-component records (manually processed by Paolucci et al., 2001) whose main parameters are illustrated in Table 1. It is worth note the large variability of the parameters (e.g. PGA from 126 to 850 cm/s²) corresponding to recordings of similar magnitude, distance and site class.

These records must be scaled to achieve the spectrum compatibility with the dam design spectrum for the collapse prevention limit state, hereafter target spectrum (return period of 1950 years according to the Italian technical code NTC in MIT, 2018). This has been performed using the software Inspector (Acunzo et al., 2014) as shown in Figure 2, where are reported the elastic response spectra of the records, the target spectrum with the required tolerance interval and the resulting mean spectrum. The spectral compatibility has been implemented in the period interval of interest for the reference dam: 0.1-0.6 seconds. It must be noted that the high seismicity of the dam site and the long return period considered, give rise to spectral accelerations in excess of 1 g.

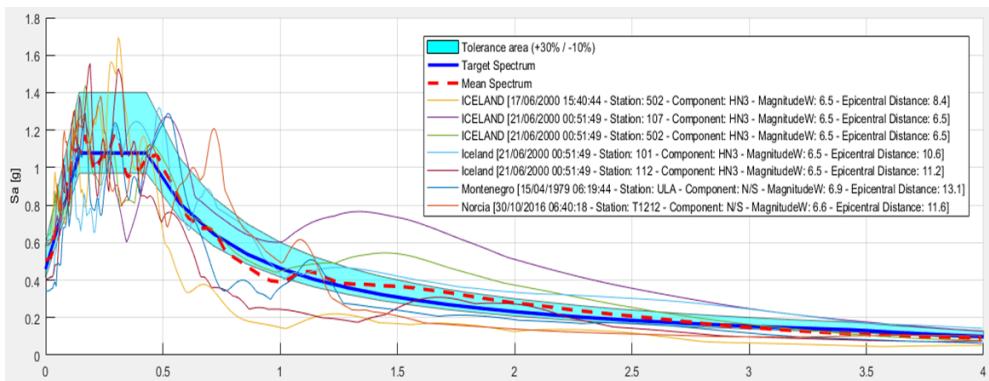


Figure 2. Software Inspector (Acunzo et al 2014): elastic response spectra of the selected records, target spectrum with tolerance interval, mean spectrum. Spectral matching in the interval 0.1-0.6 seconds.

The parameters of the N-S horizontal component of the scaled accelerograms are shown in Table 2 together with their scale factors and the parameter δ measuring the spectrum compatibility (Iervolino et al., 2010). The record of station T1213 (# 1 in Table 1) has been discarded for its lower spectrum-compatibility and to reach the desired number of seven accelerograms. The parameters in Table 2, even if corresponding to one horizontal component and not the maximum, are higher than in Table 1 because the scale factors are all, except one, greater than 1 and in some cases greater than 2 not respecting the prescribed requirements discussed in the introduction.

Table 2. Parameters of N/S horizontal component of the strong motion records scaled to the target spectrum in the interval 0.1-0.6 seconds, sorted by Arias intensity.

#	nation	station	PGA (g)	PGD (cm)	Arias (cm/s)	scale factor	δ
1	Italy	T1212	0.610	28.0	339.8	2.19	0.211
2	Montenegro	ULA	0.341	10.1	231.2	1.94	0.155
3	Iceland	101	0.408	28.2	208.2	3.40	0.197
4	Iceland	112	0.406	19.4	181.6	3.59	0.261
5	Iceland	107	0.586	37.1	172.2	1.06	0.212
6	Iceland	502	0.570	12.8	158.7	0.78	0.289
7	Iceland	502	0.633	18.3	156.1	1.08	0.156

Simulated accelerograms can be a suitable alternative to natural ground motions, which can be insufficient for some combinations of earthquake scenario and site conditions, especially for large magnitudes, short distances and rock site conditions, as shown before. Furthermore, they can avoid the use of large-scale factors to achieve spectrum-compatibility, which may not preserve the consistency of the scaled natural records with the original seismological parameters. For the time-history simulation we adopt the software SIGMA (Fiorentino, 2022) allowing to generate a chosen number of spectrum-compatible simulated ground motions giving magnitude, distance, and V_{S30} as input parameters. The time series are simulated with an up-to-date non-stationary stochastic model (Sabetta et al., 2021) calibrated using a ground motion predictive equation derived from the Italian strong motion database. In our case, 400 simulated accelerograms were generated with the constraints $Mw=6.5-7.0$, $R_{epi}=0-5$ km, $V_{S30}=800-900$ m/s. Figure 3 and Table 3 show the seven spectrum-compatible accelerograms selected by choosing the records with the smallest value of the parameter δ defined above. The variability of the parameters is lower than that of Table 2 because the scale factor is always nearly equal to 1 and the M-R- V_{S30} constraints are more rigorous. Figure 4 shows examples of two recorded and two simulated accelerograms.

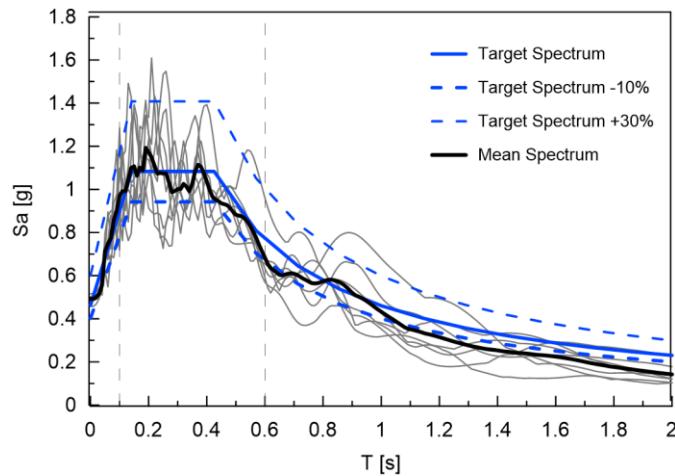


Figure 3. Software “SIGMA” (Fiorentino, 2022; Sabetta et al., 2021): elastic response spectra of seven simulated records, target spectrum, and mean spectrum. Spectral matching in the interval 0.1-0.6 seconds.

Table 3. Parameters of seven simulated accelerograms scaled to the target spectrum in the interval 0.1-0.6 seconds, sorted by Arias intensity.

#	Mw	R_{epi} (km)	V_{S30} (m/s)	PGA (cm/s ²)	PGD (cm)	Arias (cm/s)	Duration (s)	Scale factor	δ
60	7.0	1.1	806	485	10.1	223	9.6	1.08	0.171
210	7.0	5.0	840	490	7.5	221	8.6	0.95	0.173
26	6.9	0.0	867	506	7.3	217	8.5	1.01	0.199
178	7.0	4.9	833	480	10.4	203	9.4	0.99	0.202
19	6.8	0.0	803	493	7.4	200	7.3	1.04	0.202
87	6.9	2.2	835	474	7.3	192	11.0	1.03	0.206
24	6.9	0.0	867	449	7.8	151	10.1	1.11	0.211

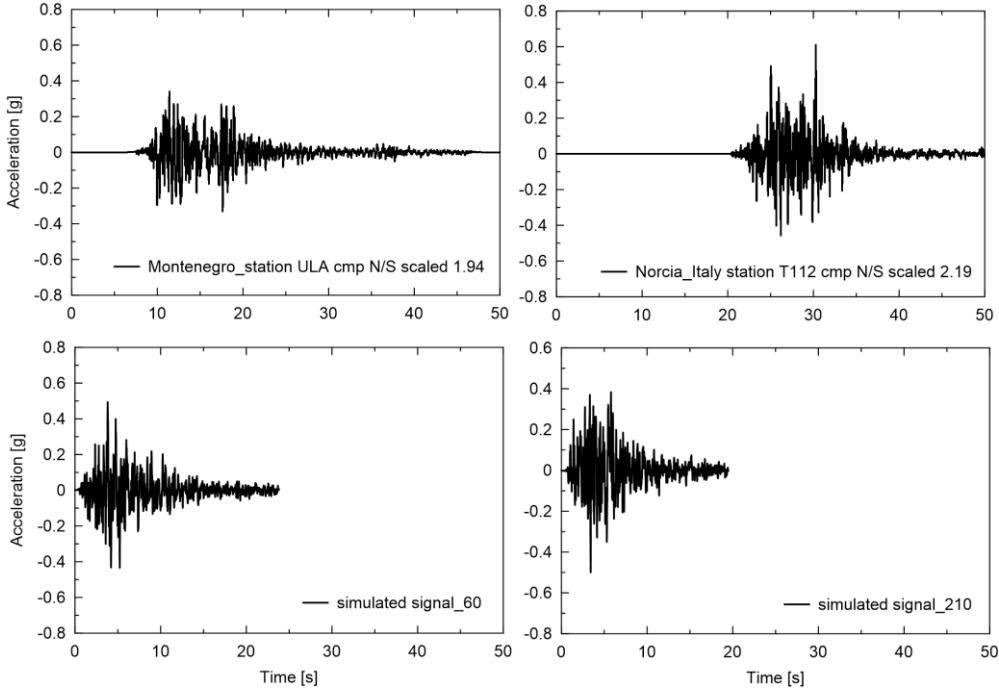


Figure 4. Examples of simulated and natural accelerograms.

4 Case study

4.1 Reference dam description

The case study concerns a reference earth dam located in Southern Italy. It has a volume of about 124000 m³ and retains 4.5·10⁶ m³ of water with a freeboard of about 3 m. The crest is 235 m long, 6.3 m wide, and about 16 m high above the foundation plane. The embankment was first constructed in the 1930s as a homogeneous dam. In the 1980s, it was largely removed and reconstructed in coarse-grained materials, changing the type to a bituminous-faced rockfill dam (BFRD). The new dam was completed in 1986 and the first reservoir filling began in 1991. Figure 5 shows a plan view and a picture of the dam.

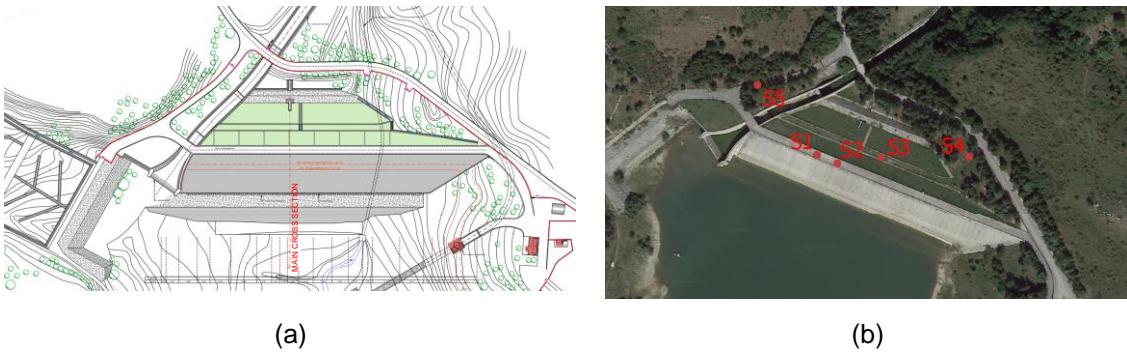
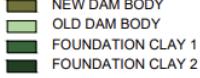


Figure 5. Plan view of the reference dam.

From the geological viewpoint, the subsoil of the reservoir area consists mostly of sandstones, while below the foundation plan of the dam embankment there are flyschoid formations. The most widespread formation is characterized by the so-called "Varicoloured Clays". It is made of variegated and flaky clayey marls, which incorporate limestone and calcarenite. Geotechnical investigations were carried out to characterize the dam body and the foundation soils. Specifically, three boreholes were drilled on the dam body (S1, S2 and S3) and another two on the abutments (S4 and S5) as shown in Figure 5-b. The boreholes show that the material of the new dam body consists of a weakly gravelly silty sand up to a depth of about 15 m. At higher depths, it is possible to find the material of the old dam body (around 7-meter thick), characterized by silty clayey sands that incorporate coarse-sized material. At a depth of approximately 22 meters from the crest of the dam, the formation of Varicoloured Clays is intercepted.

4.2 Numerical approach

Advanced dynamic analyses were conducted using the PLAXIS 2D (Brinkgreve, 2018) finite element (f.e.) software to ascertain how much the seismic performance of the sample dam could be affected by different selection criteria of the acceleration input signal. The main cross section of the reference dam including the foundation soil was modelled in 2D assuming plane strain conditions (Figure 6). In this first phase of the work, the dynamic analyses were carried out by applying the acceleration input in the horizontal direction only.


 NEW DAM BODY
 OLD DAM BODY
 FOUNDATION CLAY 1
 FOUNDATION CLAY 2

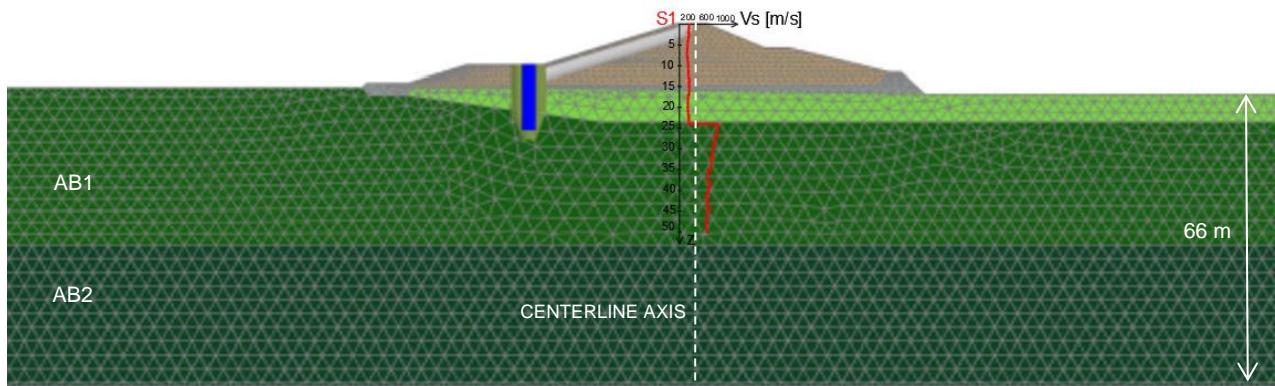


Figure 6. Analysis domain and finite element model adopted.

To accurately simulate the seismic wave propagation from the bedrock to the ground surface, a suitable portion of the soil deposit should be included underneath the dam embankment. In this specific case, the soil deposit includes the old layer of the dam as well as the flyschoid formation (Figure 6) divided into two clayey layers, an upper layer (AB1) and a lower one (AB2), based on the measured shear wave velocities. Considering the high value of the shear wave velocity ($V_s \approx 850$ m/s) measured in AB2 through in-situ tests (Cross-hole and Down-hole), this lower layer was considered as the reference bedrock for the dam site. The geometric model was discretized into a mesh of 10539 triangular elements whose maximum height were determined using the minimum wavelengths λ_{min} characterising the seismic propagation phenomenon, defined by the well-known Kuhlemeyer and Lysmer (1973) relation.

Table 2. HS-small parameters used in the numerical analysis.

Parameters	Unit	New dam body	Old dam body	AB 1	AB 2
γ_{sat}	[kN/m ³]	20.70	19.50	20.4	20.4
γ_{unsat}	[kN/m ³]	19.20	19.30	20.2	20.2
e	[-]	0.55	0.74	0.66	0.66
k_{sat}	[m/s]	1.123	0.156	0.124	0.124
c'	[kPa]	2	8	42	42
ϕ'	[°]	35	21	20	20
ψ	[°]	0	0	0	0
k_0	[-]	0.426	0.642	0.658	0.658
E_{50}^{ref}	[MPa]	13.33	28.75	62.50	75.00
E_{ed}^{ref}	[MPa]	10.67	23.00	50.00	60.00
E_{ur}^{ref}	[MPa]	40.00	86.25	187.50	225.00
m	[-]	0.50	0.50	0.50	0.50
G_0^{ref}	[MPa]	105.40	107.00	973.80	1.499E3
$\gamma_{0.7}$	[-]	0.08E-3	0.324E-3	0.4E-3	0.4E-3

To avoid wave reflection at the boundary of the analysis domain during the seismic stage, special absorbing elements (free-field boundaries) have been imposed along the lateral sides while a compliant base condition

was adopted at the bottom of the soil domain. As the nonlinear soil behaviour concerns, an elastoplastic constitutive law, defined *Hardening Soil with Small Strain Stiffness* (HS-small) implemented in Plaxis2D, was assigned to the different materials of the dam body and the foundation layers.

It is an advanced constitutive relation that is able to describe with sufficient accuracy the non-linear, hysteretic and plastic response of the soil from small to high strain levels. The model is able to predict soil stiffness decay with increasing strain amplitude by using two material parameters: G_0^{ref} representing the initial shear modulus of the soil, and $\gamma_{0.7}$, corresponding to the strain level at which the soil shear modulus is about 70% of the initial value. The experimental values of the shear modulus decay (G/G_0) obtained from cyclic triaxial tests performed on undisturbed samples of the foundation soils and the dam body were numerically reproduced through the HS-small constitutive law. The calibration of the advanced constitutive model for the dam materials was also carried out by comparing the computed dam settlements with the observed settlements during the construction stage. Table 4 summarizes the parameters of the soil constitutive relation used in the computation. The full reservoir condition was considered in the analyses. The presence of the reservoir water was modelled by applying a distribution of hydrostatic pressures to the upstream face of the dam, governed by the target reservoir height.

5 Results

5.1 Identification of the natural vibration frequencies of the dam

Through the application of a white noise signal at the base of the f.e. model, the horizontal and vertical fundamental frequencies of the dam body were identified, in both full and empty reservoir conditions. In particular, they were obtained through the transfer function between the acceleration signals computed in point A at the dam crest and point B at the base of the dam body, as shown in Figure 7.

It may be observed that the horizontal fundamental frequency of the dam in the full reservoir condition is equal to 4.5 Hz, slightly higher than that in the empty condition (about 4.32 Hz). This could be caused by the water reservoir pressure acting on the upstream bituminous face covering the upstream shell, with an increase in stress levels and therefore stiffness of the dam soils. As expected, the dam response in the vertical direction is more rigid with a fundamental frequency in the two conditions of full and empty reservoir, equal to about 7 Hz.

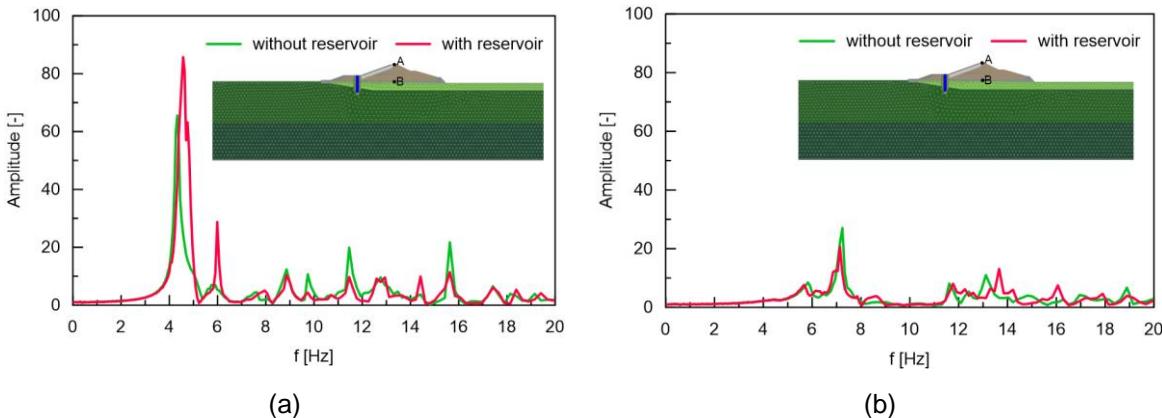


Figure 7. Identification of the horizontal (a) and vertical (b) fundamental frequency of the dam body in both full and empty reservoir conditions.

5.2 Displacements: recorded vs simulated input motion

With reference to the Collapse Limit State ($T_R = 1950$), the performance of the dam was evaluated in terms of vertical and horizontal displacements for both sets of accelerograms (recorded and simulated) applied at the base of the f.e. model in the x-direction only. Within the PLAXIS 2D software, each signal was scaled by a factor of 0.5 to take into account, in a simplified manner, the deconvolution between outcropping and inside rock. For all recorded and simulated input signals, Figure 8 shows the relative vertical and horizontal displacements (subtracting the displacements at the base of the model) calculated along the vertical axis passing through the centerline of the dam body.

Comparing the outcomes of the numerical analyses, it may be observed that the profiles of the permanent displacements computed with the set of natural signals (Figure 8, a-b) are more dispersed than those computed with the simulated input signals (Figure 8, c-d). This could be a consequence of the greater variability of the parameters of the natural accelerograms (Table 1) compared to the simulated ones, which were generated with a scaling factor close to 1. In particular, with reference to the recorded input signals, the permanent vertical displacement on the crest of the dam varies between a minimum of 19 cm (signal Iceland_502_48) and a maximum value of 35 cm (signal of Norcia). The average value of the seven recorded signals is 26 cm, similar to that obtained with the simulated ones (25.5 cm). The percentage difference between the two average values is approximately 3% (also in terms of horizontal displacement at the dam crest), therefore negligible. These results corroborate the use of the SIGMA code, especially when it is difficult to find a set of natural accelerograms consistent with the seismic scenario required to simulate spectrum-compatible signals.

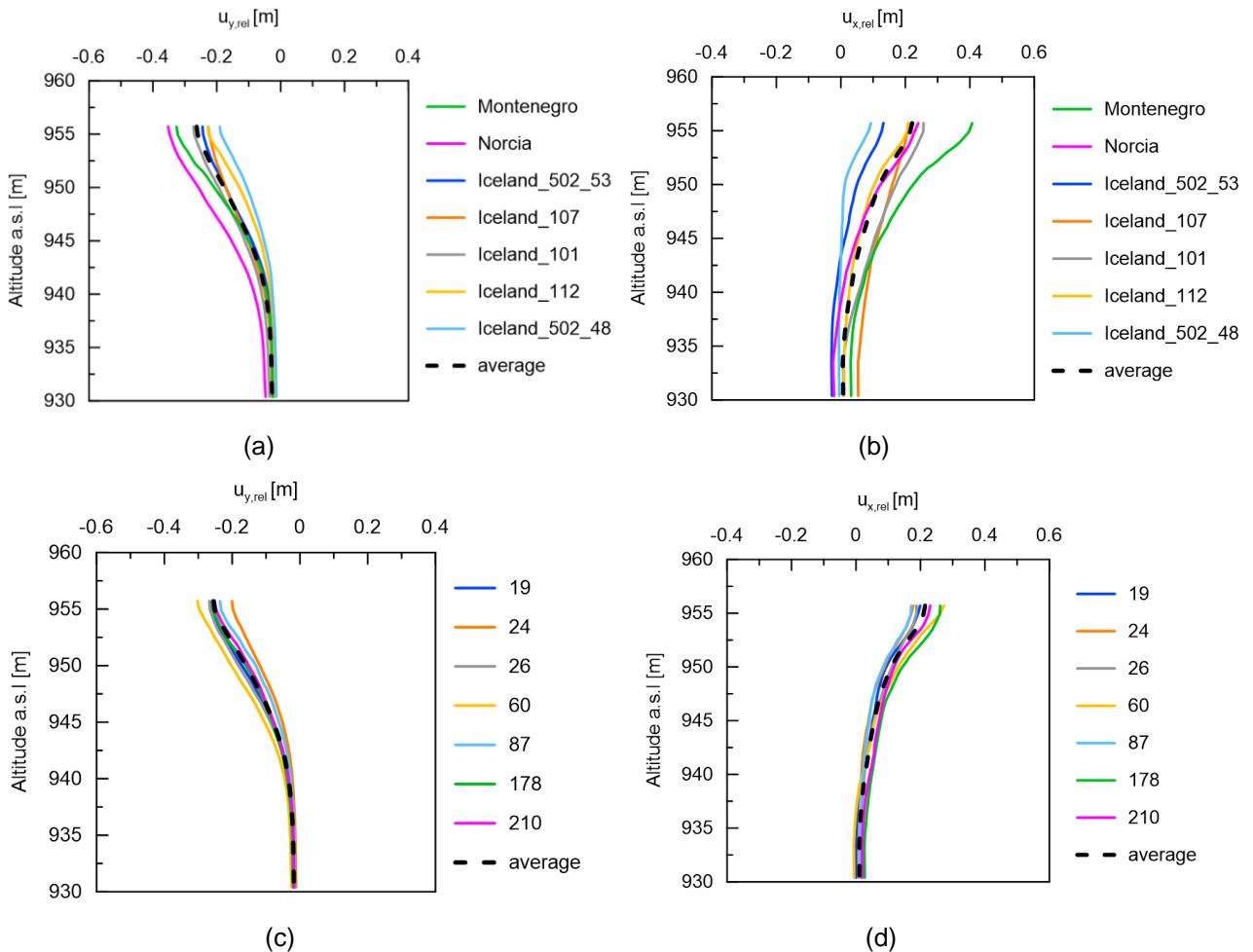


Figure 8. Seismic-induced vertical (a - c) and horizontal (b - d) displacements predicted with natural (a - b) and simulated (c - d) input signals.

With reference to dam performance against the freeboard loss damage, the average crest settlement excluding the foundation settlement (i.e. the settlement at the base of the dam), is about 20 cm for the recordings and 21 cm for the simulated signals, which in relation to the height of the embankment ($H=15$ m) gives a w/H ratio of about 1.4 % for both procedures of seismic input selection. When referring to the specific literature on dams (Pells and Fell, 2003; Swaisgood, 1995 - 1998), it can be stated that the expected damage of the reference dam for earthquakes representative of the Collapse Limit State scenario is significant (class 3 with $0.5\% < w/H < 1.5\%$). As regards the horizontal displacements, it can be seen that they are always positive and mostly involve the downstream side of the dam body with a typical first-mode deformation pattern (Sica & Pagano, 2009), for both sets of natural and simulated input signals. The horizontal displacement profiles obtained with the recorded signals are always more dispersed with respect to the mean value, unlike with the simulated ones. In particular, the maximum horizontal displacement was 40 cm, reached with the Montenegro signal,

whereas for the vertical displacements the maximum value was reached with the Norcia signal. This is maybe due to a more pronounced non-linear response of the dam body, with a greater accumulation of plastic deformations, when the Montenegro signal is implemented. Although this signal is originally less demanding in terms of PGA and AI compared to the Norcia signal, it amplifies more at the dam crest in the range of the dam fundamental vibration periods (T_h and T_v , as discussed in section 5.1), reaching a PGA of approximately 1.03 g (Figure 9).

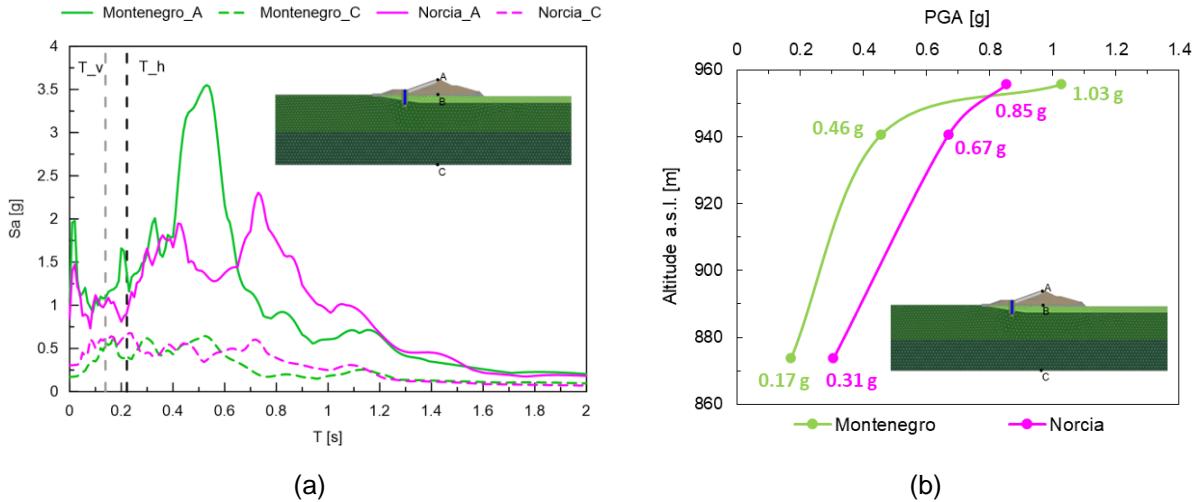


Figure 9. (a) Acceleration response spectra obtained at the bottom (point C) and at the crest (point A) of the f.e. model; (b) PGA profile along the centreline axis of the dam for the Montenegro and Norcia input signals.

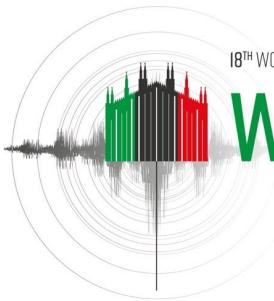
6 Conclusions

The paper focuses on a sensitivity evaluation carried out by performing dynamic analyses on an existing reference dam considering two different selection criteria of the acceleration time-histories. In the first case, the signals were retrieved from the European database (ESM), while in the second case, a novel code for simulating non-stationary stochastic ground motions was employed. The aim of the paper is to understand if the choice of different sets of input motions (recorded and simulated) significantly affects the safety assessment and damage indicators of earth dams, such as freeboard loss. Despite the increasing availability of accelerometric databases worldwide, finding natural recordings satisfying all the requirements of seismic compatibility, can be challenging, especially for high return periods relevant to the ultimate limit states of a dam. In this context, simulated signals can be particularly helpful by overcoming these limitations. It is worth noting that the simulated accelerograms can also avoid the use of large-scale factors to achieve spectrum-compatibility, which may not preserve the consistency of the scaled natural records with the original seismological parameters. The variability of the parameters in the simulated time series is less than that of natural records because they were extracted from a bunch of simulations selecting those showing the best spectral matching. The adopted simulation code had never been tested for seismic verification of geotechnical systems such as earth dams. Advanced dynamic analyses were carried out through the finite element software PLAXIS 2D to investigate the performance of the reference dam in terms of seismic induced displacement. It has been found that the average value of vertical and horizontal displacements at the dam crest resulted about the same and just slightly higher when considering the recorded accelerograms compared to the simulated ones. The assessment of the dam safety against freeboard reduction can be considered almost comparable with a w/H ratio of around 1.4% for both the seismic input selection criteria. By consulting the sector literature (Pells and Fell, 2003; Swaisgood, 1995 - 1998), it can be stated that the expected damage of the reference dam for earthquakes representative of the Collapse Limit State scenario is significant (class 3 with $0.5\% < w/H < 1.5\%$). The future perspective of the study includes additional dynamic analyses accounting for the vertical component of the input motions (neglected in this first study) and for the spectral compatibility with Uniform Hazard Spectra instead of standard spectra prescribed by the building code.

7 References

- Acunzo G., Pagliaroli A., Scasserra G. (2014). *In-spector*: un software di supporto alla selezione di accelerogrammi naturali spettro-compatibili per analisi geotecniche e strutturali, *Proceedings of 33rd conference of GNGTS*, Bologna, Italy ISBN 978-88-940442-2-5.
- Biondi, G., Cascone, E., Aliberti, D., & Rampello, S. (2021). Screening-level analyses for the evaluation of the seismic performance of a zoned earth dam. *Engineering Geology*, 280, 105954.
- Bommer, J. J., & Acevedo, A. B. (2004). The use of real earthquake accelerograms as input to dynamic analysis. *Journal of Earthquake Engineering*, 8(spec01), 43-91.
- Bozorgnia, Y., Abrahamson, N. A., Atik, L. A., Ancheta, T. D., Atkinson, G. M., Baker, J. W., & Darragh, R. (2014) NGA-West2 research project. *Earthquake Spectra*, 30(3):973-987.
- Brinkgreve, R. B. J. (2018). PLAXIS 2D Manuals. General Information, Tutorial Manual, Reference Manual, Material Models Manual, Scientific Manual. *Delft University of Technology & PLAXIS*. ISBN-13, 978-90.
- DGD (2019). Circolare della D.G. Dighe 3 luglio 2019, n. 16790 "Verifiche sismiche delle grandi dighe, degli scarichi e delle opere complementari e accessorie - Istruzioni per l'applicazione della normativa tecnica".
- Dello Russo, A., Sica, S., Del Gaudio, S., De Matteis, R., & Zollo, A. (2017). Near-source effects on the ground motion occurred at the Conza Dam site (Italy) during the 1980 Irpinia earthquake. *Bulletin of Earthquake Engineering*, 15, 4009-4037.
- DISS Working Group (2021). Database of Individual Seismogenic Sources (DISS), Version 3.3.0: A compilation of potential sources for earthquakes larger than M 5.5 in Italy and surrounding areas. *Istituto Nazionale di Geofisica e Vulcanologia (INGV)*. <https://doi.org/10.13127/diss3.3.0>
- Fiorentino G. (2022). SIGMA: a software tool to simulate non-stationary ground motions for engineering applications. *Proceedings of 3rd European Conference on Earthquake Engineering & Seismology*, Bucharest, Romania.
- Guidoboni E., Ferrari G., Tarabusi G., Sgattoni G., Comastri A., Mariotti D., Ciuccarelli C., Bianchi M.G., Valensise G. (2019). CFTI5Med, the new release of the catalogue of strong earthquakes in Italy and in the Mediterranean area. *Scientific Data* 6, Article number: 80 (2019). doi: <https://doi.org/10.1038/s41597-019-0091-9>
- Iervolino, I., Galasso, C., & Cosenza, E. (2010). REXEL: computer aided record selection for code-based seismic structural analysis. *Bulletin of Earthquake Engineering*, 8, 339-362.
- Kuhlemeyer, R. L., & Lysmer, J. (1973). Finite element method accuracy for wave propagation problems. *Journal of the Soil Mechanics and Foundations Division*, 99(5), 421-427.
- Locati M., Camassi R., Rovida A., Ercolani E., Bernardini F., Castelli V., Caracciolo C.H., Tertulliani A., Rossi A., Azzaro R., D'Amico S., Antonucci A. (2022). Database Macroseismico Italiano (DBMI15), versione 4.0. *Istituto Nazionale di Geofisica e Vulcanologia (INGV)*. <https://doi.org/10.13127/DBMI/DBMI15.4>
- Luzi, L., Puglia, R., Russo, E., D'Amico, M., Felicetta, C., Pacor, F., ... & Zare, M. (2016). The engineering strong - motion database: A platform to access Pan - European accelerometric data. *Seismological Research Letters*, 87(4), 987-997. <https://esm-db.eu/#/home>.
- MIT, Ministero delle Infrastrutture e dei Trasporti (2014). Norme tecniche per la progettazione e la costruzione degli sbarramenti di ritenuta (dighe e traverse). NTD2014. Decreto del Ministro 26 giugno 2014, Gazzetta Ufficiale n°156 del 08.07.2014 (in Italian).
- MIT, Ministero delle Infrastrutture e dei Trasporti (2018). Norme tecniche per le costruzioni e relative istruzioni. NTC2018. D.M. 17-01-2018 and C.M. 11-02-2019, *Italian Ministry of the Infrastructures and Transports*, Rome, Italy.
- Pagliaroli, A., & Lanzo, G. (2008). Selection of real accelerograms for the seismic response analysis of the historical town of Nicastro (Southern Italy) during the March 1638 Calabria earthquake. *Engineering Structures*, 30(8), 2211-2222.
- Paolucci, R., Pacor, F., Puglia, R., Ameri, G., Cauzzi, C., Massa, M. (2011). Record Processing in ITACA, the New Italian Strong-Motion Database. In: Akkar, S., Gülkán, P., van Eck, T. (eds) *Earthquake Data in Engineering Seismology. Geotechnical, Geological, and Earthquake Engineering*, vol 14. Springer, Dordrecht. https://doi.org/10.1007/978-94-007-0152-6_8

- Pells S., Fell R. (2003). Damage and cracking of embankment dams by earthquake and the implications for internal erosion and piping. *Proceedings 21st International Congress on Large Dams, Montreal. ICOLD, Paris Q83–R17, Paris.*
- Rampello, S., Cascone, E., & Grosso, N. (2009). Evaluation of the seismic response of a homogeneous earth dam. *Soil Dynamics and Earthquake Engineering*, 29(5), 782-798.
- Rovida A., Locati M., Camassi R., Lolli B., Gasperini P. (2020). The Italian earthquake catalogue CPTI15. *Bulletin of Earthquake Engineering*, 18(7), 2953-2984.<https://doi.org/10.1007/s10518-020-00818-y>
- Sabetta F., Pugliese A., Fiorentino G., Lanzano G., & Luzi L. (2021). Simulation of non-stationary stochastic ground motions based on recent Italian earthquakes. *Bulletin of Earthquake Engineering*, 1-29. <https://doi.org/10.1007/s10518-021-01077-1>
- Sica, S., Pagano, L., & Modaressi, A. (2008). Influence of past loading history on the seismic response of earth dams. *Computers and Geotechnics*, 35(1), 61-85.
- Sica, S., & Pagano, L. (2009). Performance-based analysis of earth dams: procedures and application to a sample case. *Soils and foundations*, 49(6), 921-939.
- Sica, S., & Russo, A. D. (2021). Seismic response of large earth dams in near-source areas. *Computers and Geotechnics*, 132, 103807.
- Swaisgood JR (1995) Estimating deformation of embankment dams caused by earthquakes. *Association of State Dam Safety Officials Western Regional Conference, Montana*
- Swaisgood JR (1998) Seimically-induced deformation of embankment dams. *6th US National Conference of Earthquake Engineering, Seattle, Washington*



EFFECT OF INTERNAL STRUCTURE OF LEVEES ON THE SEISMIC AND SEEPAGE BEHAVIOR

R. Uzuoka¹, S. Yamada² & K. Ueda³

¹ Kyoto University, Uji, Japan, uzuoka.ryosuke.6z@kyoto-u.ac.jp

² Kyoto University, Uji, Japan

³ Kyoto University, Uji, Japan

Abstract: The objective of this study is to clarify the effects of the internal structure of river levees on deformation and seepage performance during and after an earthquake. First the relationship between the internal structure of the river levee and the deformation caused by the earthquake was investigated based on the past damaged cases due to earthquake. By interpreting the open-cut survey results of past damaged river levees and classifying them according to the internal structure, we examined the relationship between deformation induced by earthquake and internal structure. Second, we investigated seismic deformation of embankments due to the difference in the internal structure during shaking and post-shaking seepage performance using dynamic centrifugal model tests. In the centrifugal model experiments, embankment models with two types of soil materials with different embankment histories were set up to examine the effect of internal structure on seismic and seepage behavior. After shaking the embankment model, a seepage experiment was carried out by giving a water level. In addition, we conducted cases without shaking, with weak shaking, and with strong shaking to investigate the effect of the intensity of the applied shaking. As the results, the seismic deformation of embankment in the shaking table test showed the similar tendency as observed in the past damaged cases. The difference in the internal structure caused different behavior in the seismic deformation during shaking and seepage performance after shaking.

1 Introduction

Earth structures such as river levees and roads have also suffered considerable damage from recent large earthquakes. In the earthquake response guidebook (MLIT, 2008) used for recovery from damage, the types of damage to river embankments are classified based on the damage that can be seen through surface observation only. There is also a classification method (MLIT, 2011) that focused on the damage mechanism. However, the soil distribution of levees varies widely, and the failure form caused by them also differ. It is necessary to consider the internal structure of levees and the failure form of damaged levee body.

Ikami et al. (2017) focused on the relationship between the deformed shape of river embankments by earthquakes and their infiltration performance and conducted centrifugal model experiments. A part of the levee foundation was adjusted to make it easier to liquefy, and a model embankment was built on top of it using a mixed sand of Toyoura sand and silica sand No. 7. After a shaking experiment in a 50G field, a seepage experiment was conducted. As a result, in cases where the amount of settlement was large due to shaking, there was a delay in the increase in seepage amount. This is because of an increase in the horizontal seepage distance due to lateral deformation by shaking. However, when the seepage flow continued for a long time, a

rapid increase in the amount of seepage was observed due to local seepage failure on the embankment slope. Oshige et al. (2020) conducted centrifugal model experiments to investigate earthquake-induced deformations and the resulting changes in the seepage performance of the embankment. A loose sandy ground adjusted to facilitate liquefaction was created at the foundation of the embankment, and a model embankment was built using sandy soil or clayey soil, and shaking and infiltration experiments were conducted in a 50G field. In both embankments with uniform embankment material, no density reduction was observed in the embankment bodies affected by seismic motion or river water infiltration. In addition, in the case of a sandy soil embankment, it was confirmed that the cracks caused by the shaking were blocked by the subsequent infiltration of river water, but significant increase in water leakage was not observed compared to the original embankment without shaking. On the other hand, in the case of a cohesive soil embankment, cracks caused by shaking tend to open larger overall than in the sandy soil embankment, and no crack closure due to seepage was observed. It was possible that the amount of water leaking from the levee after an earthquake may increase compared to a healthy levee without shaking.

In this study we examine the effects of the internal structure of river levees on deformation during shaking and post-shaking seepage performance. First the relationship between the internal structure of river levee and the deformation forms caused by the earthquake was investigated based on the past damaged cases due to earthquake. By interpreting the open-cut survey results of past damaged river levees and classifying them according to the internal structure, we summarized the relationship between deformation forms induced by earthquake and the internal structure. We examined four earthquake damaged cases such as the 1993 Kushiro-Oki Earthquake, the 1993 Hokkaido Nansei-Oki Earthquake, the 2011 off the Pacific coast of Tohoku Earthquake, and the 2016 Kumamoto Earthquake. Second, we investigated seismic deformation of embankments due to the difference in the internal structure during shaking and post-shaking seepage performance using dynamic centrifugal model tests. In the centrifugal model experiments, embankment models with two types of soil materials with different embankment histories were set up to examine the effect of internal structure on seismic and seepage behavior. After shaking the embankment model, a seepage experiment was carried out by giving a water level. In addition, we conducted cases without shaking, with weak shaking, and with strong shaking to investigate the effect of the intensity of the applied shaking.

2 Internal structure of river levee and failure types caused by earthquake

2.1 Typical damage cases and open-cut surveys

Of the survey locations that suffered major damage from the four earthquakes, open-cut surveys were conducted in six locations in eastern Hokkaido, three locations in southern Hokkaido, twenty-two locations in Tohoku region, and seven locations in Kumamoto Prefecture. We focused on the soil distribution in the embankment, the construction history of embankment, and the damage on the embankment.

At around 20:06 on January 15, 1993, a magnitude 7.8 earthquake occurred off the coast of Kushiro, causing human casualties and structural damage to eastern Hokkaido. Open-cut surveys were conducted at six locations, in the Kushiro River and Tokachi River systems (MLIT, 1994). Figure 1 shows the typical results of an open-cut survey in the Tokachi River levees. Numerous cracks were observed from the top shoulder of the land side of the levee to the river side of the levee, while a few cracks were observed on the land side of the levee. The damage occurred because the sandy gravel soil section of the foundation under the old levee body became a closed saturated zone and liquefied during earthquake. Here, the closed saturated zone is defined as the state in which saturated sandy soil mass exists on the settled foundation due to consolidation. There was a peat layer at the foundation, which had subsided significantly during and after construction of the embankment.

On March 11, 2011, at around 14:46, an earthquake with a magnitude 9.0 and tsunami occurred off the coast of Sanriku, causing human and building damage to be concentrated in Miyagi, Iwate, and Fukushima prefectures. Open-cut surveys were conducted at twenty-two locations in the Abukuma River system, Naruse River system, and Kitakami River system (MLIT, 2011). In the Edano area on the right bank of the Abukuma River shown in Figure 2, a new embankment made of sandy soil was built on the land side of the levee, covering the old embankment made of clayey soil on the river slide of the levee. The foundation ground was clayey soil, and part of the embankment had subsided and was below the groundwater level. Due to liquefaction in the closed saturated area, multiple longitudinal cracks occurred on the crown and back slopes.

Due to the subsidence of the crown and the lateral bulge of the land side of the levee, the embankment became almost horizontal after the earthquake.

In the Hashiura area of the lower reaches of the Kitakami River in Figure 3, the lower part of the levee body was mainly made of sandy soil and the upper part was made of clay material, and the gravelly soil was used to raise and widen the embankment on the land side. The foundation ground consisted of a thick layer of sand deposited on top of clayey soil. A groundwater level was usually formed at the ground level within the embankment. Due to liquefaction of a part of the foundation ground sand layer and the saturated sand layer at the bottom of the embankment body, vertical cracks appeared on the crest and river surface slope, causing the crest to sink and lateral bulge toward the river surface.

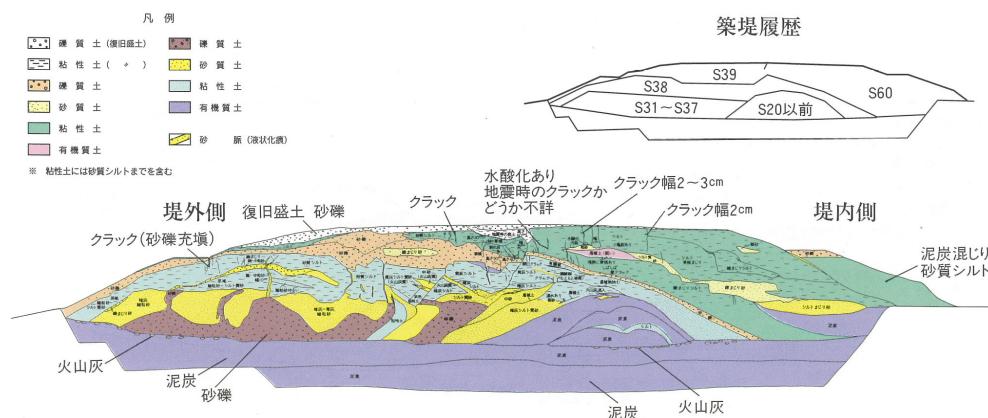


Figure 1. Open-cut survey of Tokachi River levee after the 1993 Kushiro-Oki Earthquake (MLIT, 1994). (yellow: sand, brown: gravel, green: clay, violet: peat)

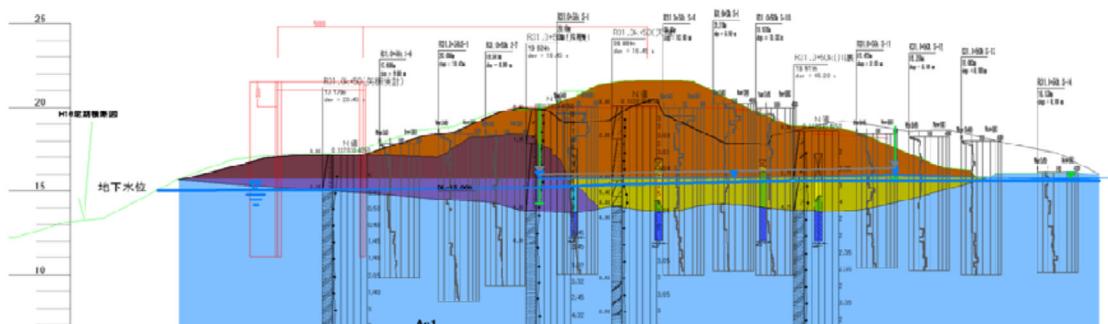


Figure 2. Open-cut survey of Abukuma River levee after the 2011 off the Pacific coast of Tohoku Earthquake (MLIT, 2011). (yellow: sand, brown: sand and gravel, blue: clay, violet: silt)

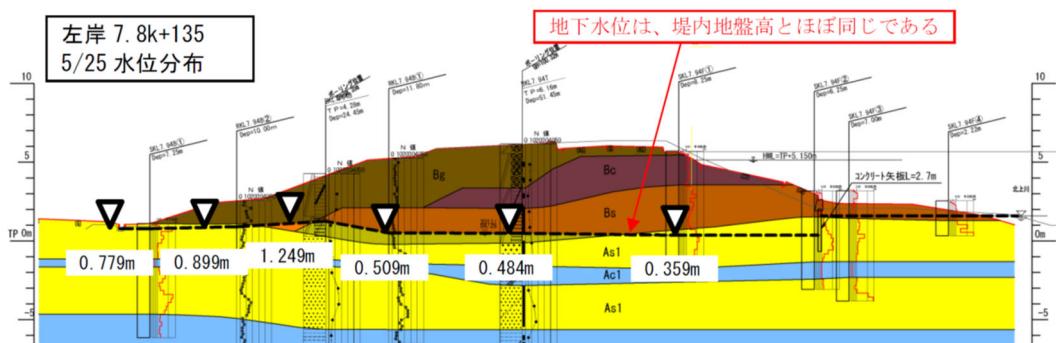


Figure 3. Open-cut survey of Kitakami River levee after the 2011 off the Pacific coast of Tohoku Earthquake (MLIT, 2011). (yellow: sand, brown: sand and gravel, blue: clay, violet: clay)

2.2 Classification of failure types in damage cases

Based on the results of open-cut surveys and damage forms of the four earthquakes, we simply classified liquefaction-induced failure forms into eight types based on soil distribution in the embankment and foundation ground. The results are summarized as follows shown in Figure 4.

A-1: Clayey soil embankment body on clayey soil foundation

This is a type in which a thin sandy soil layer is deposited between a clayey soil foundation and a clayey soil embankment body, and subsidence occurs when the sandy soil liquefies. Liquefaction in the closed saturated area causes settling, cracks, and bulges. The amount of subsidence tends to be particularly large at the crest of levee.

A-2: Clayey soil embankment body on sandy soil foundation

This type has a clayey soil embankment built on a sandy soil foundation. As the entire foundation ground settles, cracks tend to spread more than A-1.

B-1: Sandy soil embankment body on clayey soil foundation

This type often occurs when a sandy soil embankment is built on top of a clayey soil foundation, and the lower part of the embankment settles. The lower part of the embankment becomes a closed saturated zone, and liquefaction of the part causes cracks and bulges. On the other hand, as a characteristic of sandy soil embankments, crack damage is less than clayey soil embankments due to natural repairment of cracks.

B-2: Sandy soil embankment body on sandy soil foundation

This type applies to cases where a sandy soil embankment is built on sandy soil foundation, and cases where a natural levee is formed with sandy soil. During an earthquake, cracks and bulges occur due to liquefaction of the levee body and foundation ground.

C-1: Old sandy soil embankment covered with new clayey soil embankment on clayey soil foundation

A sandy soil embankment is built on a cohesive ground and then expanded with clayey soil, and when a part of the sandy soil embankment settles below the groundwater level, it becomes a closed saturated area, which can cause earthquake-induced liquefaction. As a result of liquefaction, it tends to settle toward the old sandy soil embankment. Cracks tend to occur more often on the new clayey soil embankment side. Regardless of whether the old embankment was on the land side or on the river side, similar damage occurred in cases with similar internal structures.

C-2: Old sandy soil embankment covered with new clayey soil embankment on sandy soil foundation

This is a type of sandy soil embankment built on sandy ground and then expanded with clayey soil, which tends to settle toward the old sandy soil embankment when the foundation ground and part of the old sandy soil embankment liquefy during an earthquake. Compared to C-1, the foundation ground subsides at the new clayey soil embankment side, so cracks and bulges tend to occur on the new clayey soil embankment side as well. As well as C-1, the influence of the positional relationship between the old levee body and the river on the failure form appears to be small.

D-1: Old clayey soil embankment covered with new sandy soil embankment on clayey soil foundation

A clayey soil embankment is built on a clayey foundation ground and then expanded with sandy soil, and when a part of the sandy soil embankment settles below the groundwater level, it becomes a closed saturated area, which can cause earthquake-induced liquefaction. As a result of liquefaction, cracks and bulges occur at the side of the new sandy soil embankment that covers the old embankment. There tends to be less damage on the old clayey soil embankment side. The same tendency was observed regardless of whether the old embankment was located on land or river side.

D-2: Old clayey soil embankment covered with new sandy soil embankment on sandy soil foundation

This type of embankment is constructed by building a clayey soil embankment on sandy ground and then expanding it with sandy soil. The foundation ground and part of the new sandy embankment body tend to liquefy during an earthquake, resulting in overall subsidence. Compared to D-1, the foundation ground at the old embankment side also settles, so cracks and bulges are more likely to occur on the old clayey embankment.

As well as D-1, the positional relationship between the old levee and the river seems to have insignificant effect on the failure form.

In summary the soil distribution of the embankment body has a considerable influence on the failure forms caused by earthquake-induced liquefaction. For types C and D where a new levee body is added to an old levee body, the positional relationship between the old levee body and the river does not have a significant effect, but the internal structure of the levee body, such as soil distribution and groundwater level, has a greater influence on the failure form. Types C and D with composite material embankments tend to deform asymmetrically and unilaterally, whereas types A and B with single material embankments tend to deform symmetrically. Cracks tended to be concentrated at the top of levee where the foundation ground was clayey soil as types A1 and B1, whereas cracks tended to occur over a wide range when the foundation ground was sandy soil as types A-2 and B-2. Based on the classifications, we set up a model for dynamic centrifuge model experiments.

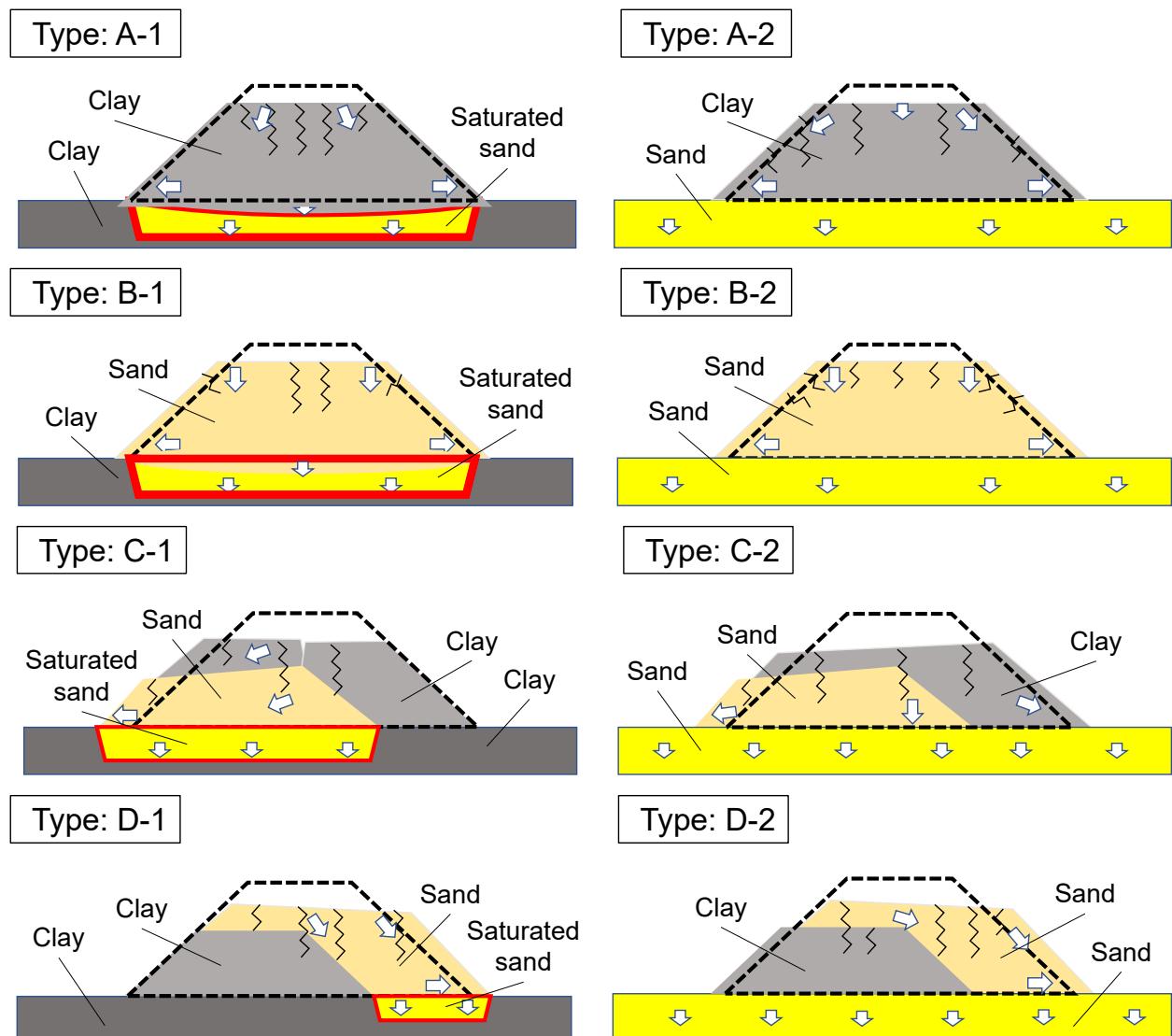


Figure 4. Classification of internal structure of river levee and failure types in past damage cases.

3 Dynamic centrifuge experiments

Although there are many studies that examine the deformation of embankments through shaking experiments, there are few studies that focus on the resulting changes in seepage performance. Also, among the eight types classified in the previous chapter, there are many experimental cases of types A and B, while there are few cases of C and D. Therefore, we discuss model embankments made of varied materials as cases C-1 and D-1 and conducted seepage experiments after shaking. Deformation during shaking and seepage performance after shaking were examined from responses of pore water pressure, acceleration, displacement, and water leakage.

3.1 Experimental conditions

We used a centrifuge facility (2.5 m radius) owned by the Disaster Prevention Research Institute, Kyoto University. This experiment was conducted in a 50G field, and the model scale was 1/50 of the prototype scale. Figure 5 shows an experimental model and Table 1 shows the experimental cases. The width of the bottom, the width of the top and the height of embankment were 17.5 m, 2.0 m, and 3.5 m in prototype scale, respectively. The foundation was made of an oil clay and the closed saturated area on the foundation was made of Toyoura sand. The clayey soil embankment body was made of a mixed soil of Toyoura sand and Kaolin, and the sandy soil embankment body was made of a mixed sand of Toyoura sand and silica sand No. 7. In cases 1-3, the old embankment body was made of sandy soil, and the new one was made of clayey soil. In cases 4-5, the old embankment body was made of clayey soil, and the new one was made of sandy soil. As shown in the figure, the test was conducted using twelve pore water pressure transducers (P^*), five accelerometers (A^*), two laser displacement gauges (D^*), and a high-speed camera. The oil clay foundation was shaped, and then sand was supplied to the closed saturated area with the target relative density of 50% using the air pluviation method. After that, the closed saturated area was saturated with Metolose fluid with fifty times viscosity as water, the old levee embankment with the target degree of compaction of 85% was compacted and shaped, and the new embankment body with the target degree of compaction of 85% was fabricated in the same way. Deaired water was used for seepage after shaking.

Three experimental cases were conducted on each model with different shaking intensities. Sinusoidal wave with tapers of the amplitude of 2 m/s^2 with twenty cycles was used for weak shaking, and sinusoidal wave with tapers of the amplitude of 3 m/s^2 with forty cycles was used for strong shaking. After the shaking, we conducted seepage experiments in which the water level was raised to 1.35 m and 2.70 m in prototype scale, and then

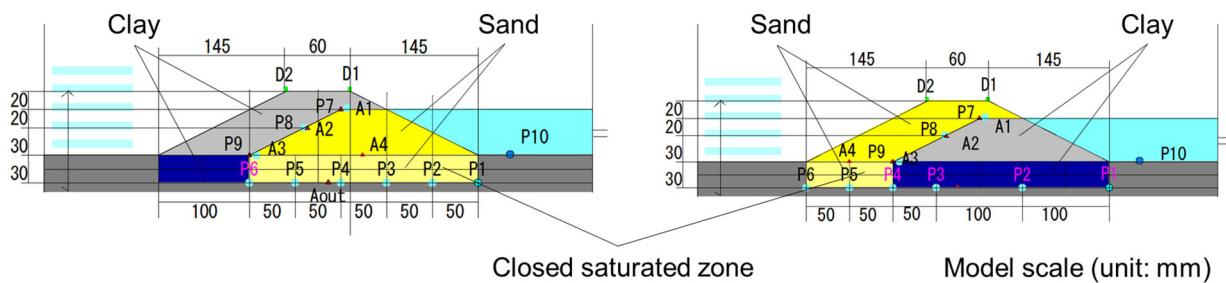


Figure 5. Centrifuge experimental models (left: Cases 1-3, right: Cases 4-6)
 P^* : pore water pressure transducers, A^* : accelerometers, D^* : laser displacement gauges

Table 1. Centrifuge experimental cases.

Case	Old embankment body	New embankment body	Shaking
Case 1	Sandy soil	Clayey soil	None
Case 2	Sandy soil	Clayey soil	Weak (2 m/s^2 with 20 cycles)
Case 3	Sandy soil	Clayey soil	Strong (3 m/s^2 with 40 cycles)
Case 4	Clayey soil	Sandy soil	None
Case 5	Clayey soil	Sandy soil	Weak (2 m/s^2 with 20 cycles)
Case 6	Clayey soil	Sandy soil	Strong (3 m/s^2 with 40 cycles)

the water level was maintained for 10 hours in prototype scale each water level, and finally the water level was raised to the embankment top with 3.5 m in prototype scale. The water level was controlled with intermediate water tank and electric bars to catch water existence. In addition, pore water pressure transducers were put in the upstream and downstream water tank to calculate infiltration and runoff amounts of water.

3.2 Experimental results

Figure 6 shows the excess pore water pressure ratio in closed saturated zone and vertical displacement during shaking in Case 3, where the old levee body was made of sandy soil and strong shaking was applied. At P1 in liquefiable closed saturated zone, the excess pore water pressure ratio exceeded one, and liquefaction occurred. The amount of subsidence was slightly larger on the old embankment side (D1) with sandy soil.

Figure 7 shows the results of Case 6, where the old levee body was made of clayey soil and was subjected to strong shaking. There was no place where the excess pore water pressure ratio exceeded one in closed saturated zone, and the amount of subsidence was larger on the new embankment side (D2) with sandy soil. If the old levee body was made of sandy soil as in Case 3, the old levee body settled and bulges, and cracks were concentrated at the top of the new clayey embankment body. When the old levee body was made of clay as in Case 6, the deformation of the old levee body was small as shown in Figure 7, and sliding failure occurred in the new sandy embankment body. The results of the dynamic centrifuge model experiment showed the similar tendency as the damage survey.

Figure 8 shows the time history of water level, infiltration amount and runoff amount regarding the seepage behavior after shaking in Cases 1 to 3, where the old levee body was made of sandy soil. The infiltration and runoff amounts were calculated with pore water pressure transducers in the upstream and downstream water tank, respectively. In Case 2, an increase in runoff amount was observed from an earlier stage than in Case 1, so it is possible that the shaking caused an increase in seepage flow. On the other hand, in Case 3, the time required for drainage to drain was longer than in Case 2. In a strong earthquake, the amount of subsidence

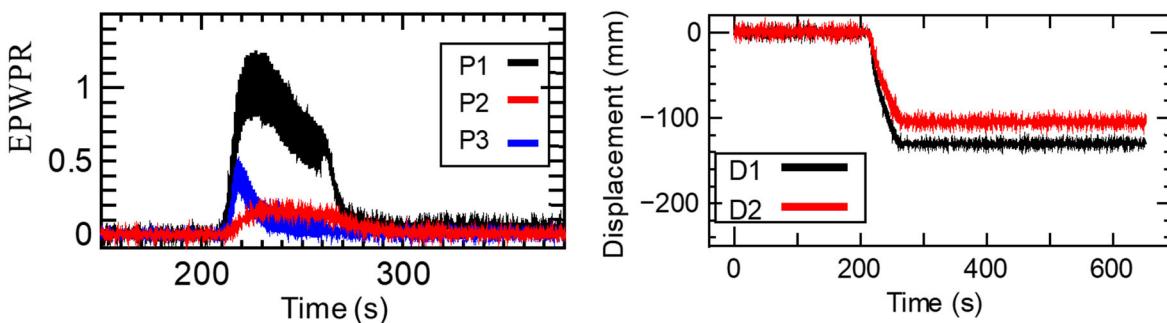


Figure 6. Excess pore water pressure ratio in saturated sandy soil and vertical displacement during shaking in Case 3

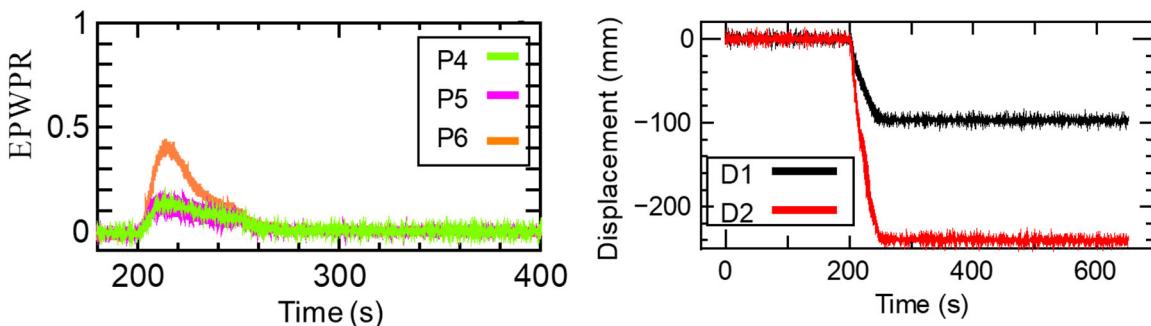


Figure 7. Excess pore water pressure ratio in saturated sandy soil and vertical displacement during shaking in Case 6

increased. It is possible that the amount of seepage decreased due to an increase in the density of the soil, which was seen in the experiment by Ikami et al (2017).

Figure 9 shows the top and sectional views of embankment models before and after seepage in Case 1 and 3. In Case 1, cracks occurred at the top of the new clayey soil embankment when the water level rose, and the middle of the slope suffered seepage failure when the water level was near the top. In Case 2, cracks induced by shaking became larger as the water level rose, and when the water level was 2.7 m, seepage failure occurred from the slope near both walls of the soil container. Traces of seepage flow were also visible in the center of the slope. In Case 3, there were many cracks due to the shaking compared to Case 2, and most of them were near the top. The cracks at the crown expanded as the water level rises. On the other hand, while the water level was maintained at 2.7 m, seepage failure occurred near the foot of the slope, and water was visible on the land side of the embankment. Oshige et al. (2020) found that cracks in clay soil widened due to seepage, leading to an increase in the amount of seepage. Similarly, in Case 3, the crack at the crown expanded as the water level rose, and there is a possibility that cracks caused by the shaking will increase the amount of seepage, however the clear increase in the runoff amount was not observed as shown in Figure 8.

Figure 10 shows the changes in pore water pressure at the bottom of clayey soil embankment on the river side during seepage after shaking in Cases 4 to 6, where the old levee body was made of clayey soil. In Case 4, where no shaking was applied, almost no change in the pore water pressure responses was observed. In Case 5, where weak shaking was applied, an increase was observed at P1 in response to water level changed. In the cases of homogenous cohesive soil embankment (Oshige et al. 2020), an increase in the amount of seepage was confirmed due to an increase in cracks, so it is possible that the increase at P1 is due to cracks

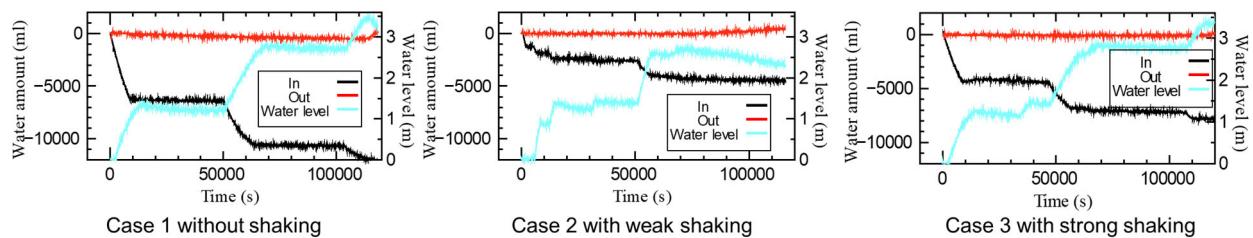


Figure 8. Water level, infiltration amount, and runoff amount during seepage in Cases 1-3

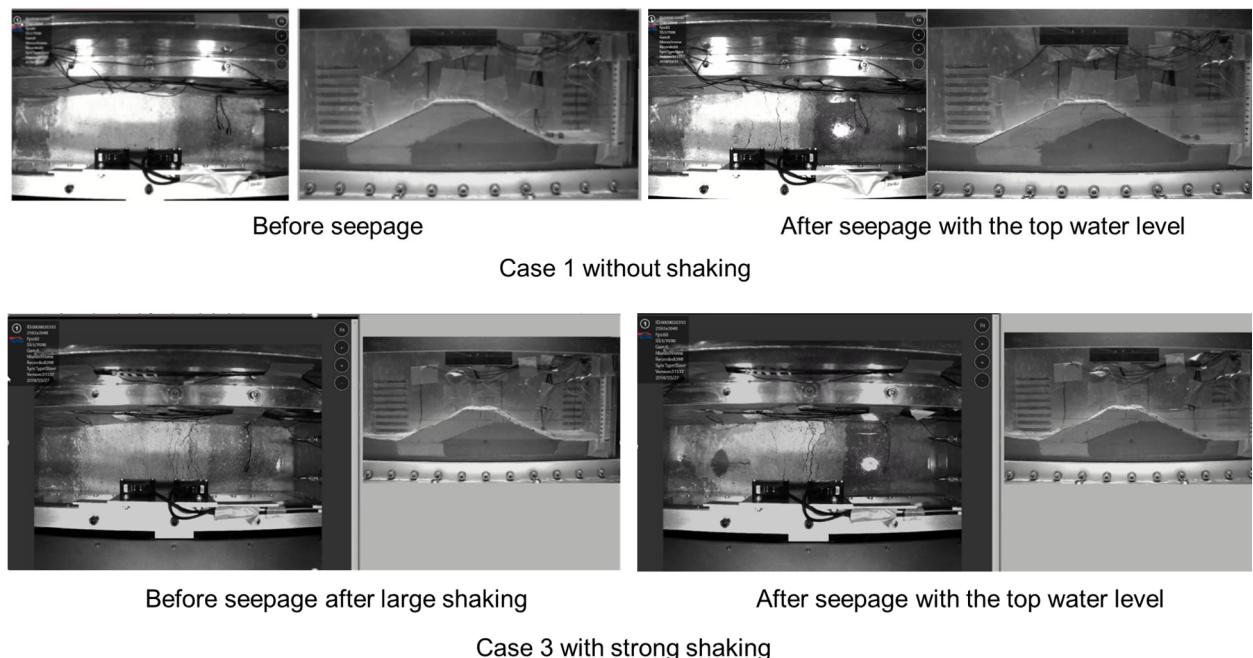


Figure 9. Top and sectional views of embankment model in Cases 1 and 3

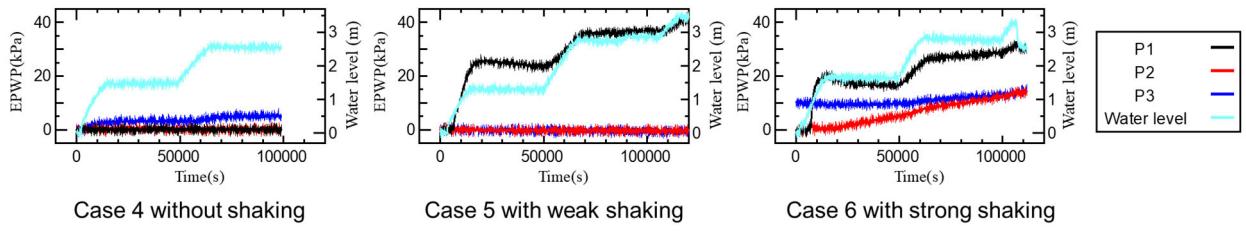


Figure 10. Pore water pressure at the bottom of clayey soil embankment during seepage in Cases 4-6

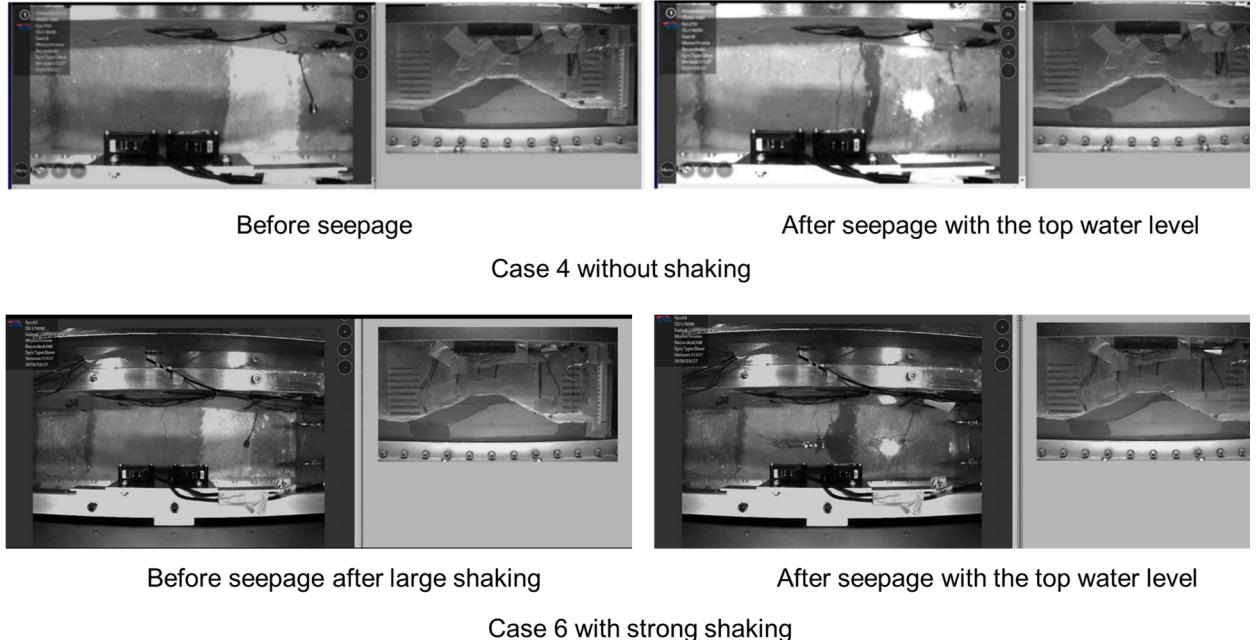


Figure 11. Top and sectional views of embankment model in Cases 4 and 6

caused by shaking. In Case 6, where strong shaking was applied, an increase in pore water pressure was observed not only at P1 but also at P2 and P3.

Figure 11 shows the top and sectional views of embankment models before and after seepage in Case 4 and 6. In Case 4, cracks occurred in the new sandy embankment as the water level rose, but seepage failure did not occur. In Case 5, when the water level rose, cracks appeared not only at the crown but also in the old clayey embankment body at a water level of 1.35 m. After that, when the water level reached near the top, there was no major deformation, and the water was drained from the foot of the slope. In Case 6, cracks at the top increased as the water level rose, and overflow occurred when the water level reached near the top.

If the old embankment body is made of sandy soil (Case 1-3), shaking will cause cracks in the new clayey embankment body and subsidence on the side of the old sandy embankment body. During seepage after shaking, cracks on the new clayey embankment body expand due to seepage, and the density of the old sandy embankment body increases due to subsidence. As the results an increase in the amount of seepage on the new clayey embankment body and a decrease in the amount of seepage on the old sandy embankment body. It is possible that seepage failure occurs near the foot of the new clayey embankment slope.

On the other hand, when the old embankment body is made of clayey soil (Case 4-6), shaking will cause cracks in the old clayey embankment body and sliding failure in the new sandy embankment body. During seepage after shaking, the seepage flow amount of the old embankment body increased, and the risk of overflow increases due to cracks and deformation in the new sandy embankment body.

4 Conclusions

This study examined the effects of the internal structure of river levees on deformation during shaking and post-shaking seepage performance. First the relationship between the internal structure of the river levee and the deformation caused by the earthquake was investigated based on the past damaged cases due to earthquake. By interpreting the open-cut survey results of past damaged river levees and classifying them according to the internal structure, we summarized the relationship between deformation forms induced by earthquake and internal structure. Second, we investigated seismic deformation of embankments due to the difference in the internal structure during shaking and post-shaking seepage performance using dynamic centrifugal model tests. In the centrifugal model experiments, embankment models with two types of soil materials with different embankment histories were set up to examine the effect of internal structure on seismic and seepage behavior. In the first case, the old embankment body was made of sandy soil, and the new one was made of clayey soil. In the second case, the old embankment body was made of clayey soil, and the new one was made of sandy soil. After shaking the embankment model, a seepage experiment was carried out by giving a water level. In addition, we conducted cases without shaking, with weak shaking, and with strong shaking to investigate the effect of the intensity of the applied shaking.

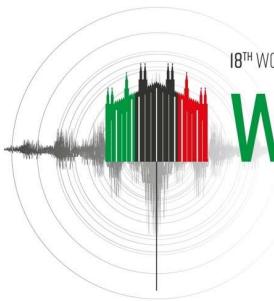
As the results, the seismic deformation of levee in the shaking table test showed the similar tendency as observed in the past damaged cases. The difference in the internal structure caused different behavior in the seismic deformation during shaking and seepage performance after shaking. When the old embankment body was made of sandy soil, the deformation of the old sandy embankment body was large due to the shaking induced softening, and cracks concentrated on the crest of the new clayey embankment body. During seepage after shaking, the seepage flow amount of the new clayey embankment body increased and that of the old sandy embankment body decreased. Seepage failure occurred near the foot of the new clayey embankment slope. When the old embankment body was made of clayey soil, the deformation of the old clayey embankment body due to shaking was small, and slip failure occurred on the slope surface of the new sandy embankment body. During seepage after shaking, the seepage flow amount of the old clayey embankment body increased, and the risk of overflow increased due to cracks and deformation in the new sandy embankment body.

5 Acknowledgements

This research was supported by JSPS KAKENHI Grant Number 21H04575. The authors would like to acknowledge the Technical Sub Committee on River Levee, Technical Committee on Geotechnical Engineering, Japan Society of Civil Engineers.

6 References

- Ikami Y., Uzuoka, R., Ueno, K. (2017). Centrifuge modeling for evaluation of seepage behavior of deformed levee after shaking, *Journal of Japan Society of Civil Engineers, Ser. C (Geosphere Engineering)*, 73(4). 442-449. (in Japanese).
- Ministry of Land, Infrastructure, Transport and Tourism, Hokkaido Regional Development Bureau (1994). Records of river disaster restoration after the 1993 Kushiro-oki Earthquake. (in Japanese).
- Ministry of Land, Infrastructure, Transport and Tourism, Tohoku Regional Development Bureau (2008). Guideline for restoration from earthquake-induced damage (in Japanese).
- Ministry of Land, Infrastructure, Transport and Tourism Hokkaido Regional Development Bureau (2011). Report on restoration technology of Kitakami River levee after the 2011 off the Pacific coast of Tohoku Earthquake (in Japanese).
- Oshige K., Kajitori, S., Tanimoto, S., Sasaki T. (2020). Centrifugal loading model test on levee mechanism after earthquakes, *Civil engineering journal*, 62(12). 24-27. (in Japanese).



SEISMIC ANALYSIS OF THE GARCIA DAM LOCATED IN THE BELICE VALLEY OF SICILY

Roberta Vincifora¹, Giuseppe Amato², Marco Filippo Ferrotto²,
Salvatore Pagnotta², Alphonso Cusmano³, Salvatore Volo²

¹ Harpaceas s.r.l., Milan, Italy

² Volo Engineering and Consulting s.r.l., Palermo, Italy

³ Freelance Engineer, Palermo, Italy

Abstract: In the present work the seismic analysis of the earth-dam located in the Belice Valley of Sicily is presented, as outlined in the "Circular D.G. Dams July 3 2019, N.16790 - Seismic verifications of large dams, discharges, complementary and ancillary works - Instructions for the application of the technical regulations according to the Ministerial Decree 26.06.2014 (NTD14) and the Ministerial Decree 17.01.2018 (NTC18)". The technical and the design description of the dam, the structural diagnostic, the soil, the seismic characterization and the analysis approach are discussed throughout the paper, highlighting the main results obtained according to the seismic demand of the site of interest.

The seismic analysis of the dam was performed by Flac2d, a geotechnical software general purpose by Itasca. The first step was the calibration of the soil stiffness parameters through a back analysis based on subsidence values monitored in 2006. The static analysis in the condition of full reservoir was performed for different values of the zone elastic moduli: the displacements computed by Flac2d were compared with the monitored ones in order to select the values of the elastic parameters best fitting the real situation. After the calibration of these parameters, the seismic analysis was performed assuming, for each Limit State considered, a set of seven spectrum-compatible real accelerograms selected from the European strong-motion database referred to the soil according to the Italian Code, obtaining the Peak Ground Accelerations (PGAs) by seismotectonic assessment. Moreover, the computation of the dynamic safety factor was performed to get additional information about the safety of the dam after the seismic excitation.

Given the possibility to perform the dynamic analysis by directly simulating the wave propagation through the continuum, Flac2d represented a very advanced tool to assess in detail the response to seismic excitation of the geotechnical work object of the present study, located in a relevant site from the seismic point of view such as the Belice Valley of Sicily. The presented study is of great interest in order to give quantitative measure of the response to seismic excitation of the Garcia Dam, a strategic structure built in the 70s.

1. Introduction

Several earth dams in Italy are located in areas prone to severe earthquakes, but they were designed and built before the introduction of the current seismic hazard classification of the Italian territory. In light of this, a seismic assessment of these structures is fundamental as their safety is crucial for the areas located on the downstream side (Makdisi and Seed, 1978; Seed, 1979). Researchers and practitioners have been focusing

on the seismic performance of existing earth dams in order to improve the reliability of their assessments on the basis of numerical analyses, parametric approaches and empirical methods (e.g. Vecchietti et al., 2019; Masini et al., 2020; Biondi et al., 2021; Bozzoni et al., 2023; Regina et al. 2023).

In this context, Italian government has promoted and funded the seismic assessment of existing dams over the last years, with the aim of verifying their seismic capacity and eventually retrofit them. In 2021 the Bonification Consortium 2 Palermo entrusted the company Volo Engineering and Consulting s.r.l., also known as Volo Ingegneria, with the task of preparing the "*Certificate of Structural Suitability for Reinforced Concrete Structures and Seismic Checks on the Mario Francese Dam - formerly known as the Garcia Dam*".

The campaign of "*In-situ and Laboratory Structural/Geotechnical Investigations*", preparatory for the collection of data required for this study, was carried out by the company Geolab s.r.l. of Palermo.

For the execution of this study, Volo Ingegneria has enlisted the following professional figures:

- Eng. Salvatore Volo, Ph.D. as Technical Director and Coordinator of investigation and study activities
- Eng. Alessandra Amato as Assistant to the Coordinator of investigation and study activities
- Dott. Geol. Gianvito Graziano as Geologist for the execution of geological studies
- Eng. Giuseppe Amato as Geotechnical Engineer for data processing and verifications
- Eng. Marco Filippo Ferotto, Ph.D. as Structural Engineer for data processing and verifications
- Eng. Salvatore Pagnotta, Ph.D. as Structural Engineer for data processing and verifications.

In the aforementioned sections, specialist collaboration was provided by Eng. Alphonso Cusmano, Geotechnical Engineer who possesses extensive and profound historical and technical knowledge of the dam and its associated structures.

The geotechnical analysis and calculation were performed using Flac2d, which is a geotechnical software general purpose of the American society Itasca, distributed in Italy by the company Harpaceas s.r.l. In this context, Eng. Samuele Perni and Eng. Roberta Vincifora, Technical Specialists for the Structural and Geotechnical Engineering Department of Harpaceas, provided technical support to model and analyse the dam with Flac2d.

The present paper illustrates the seismic assessment of the Garcia Dam as a significative case study because of the relevance of its location, that is the Belice Valley of Sicily. In order to select an effective methodology, among the above-mentioned papers particular attention was made to Vecchietti et al. (2019) and Biondi et al. (2021). The authors of these papers used the software Flac2d to analyse earth dams and evaluate their seismic performance. Among the criteria employed in those papers to evaluate the achievement of the dam limit states, the Swaisgood criterion was selected for this case study.

In this article reference is mainly done to the methods of geotechnical use and the carried-out computations. The adopted software allowed for the execution of this study in full compliance with the current technical regulations, in particular "*Decreto Ministeriale delle Infrastrutture e dei Trasporti 17/01/2018, Aggiornamento delle «Norme Tecniche per le Costruzioni» (NTC 2018)*" and "*Circolare D.G. Dighe 03/07/2019, n. 16790 – Verifiche sismiche delle grandi dighe, degli scarichi e delle opere complementari e accessorie – Istruzioni per l'applicazione della normativa tecnica di cui al D.M. 26/06/2014 (NTD14) e al D.M. 17/01/2018 (NTC18)*".

2. Description of the geographical context and the Garcia Dam

The valley, crossed by the Belice River, one of the main rivers in Sicily, spans the provinces of *Palermo*, *Trapani* and *Agrigento*.

The total area of the basin under the Garcia Dam section covers nearly 1,000 km² and is bordered by the mountains of *Piana degli Albanesi* to the North and the mountains of *Raitano*, *Camporeale*, *Cresta di Ruia*, *S. Ninfa*, *Partanna* and *Marinella* to the West. The eastern slope is delineated by *S. Caterina Gela*, *M. Leardo*, *Ficuzza*, *M. Barracù*, *Bisacquino*, *Santa Margherita Belice* and *Porto Palo* as shown in Figure 1.

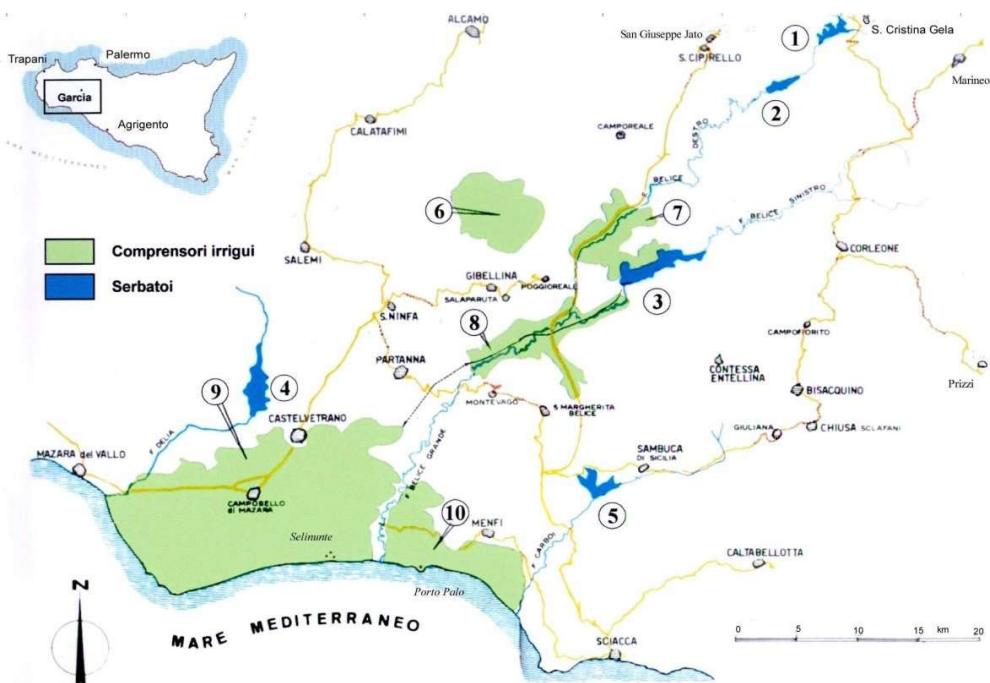


Figure 1. General chorography of the Use of Water from the Garcia Reservoir in the Belice Territory.
Reservoirs: 1 Piana degli Albanesi; 2 Piano del Campo; 3 Garcia; 4 Trinità; 5 Arancio; Irrigation areas: 6 Borghi (1300 ha); 7 Belice Destro (1400 ha); 8 Fondo Valle Belice (1300 ha); 9 Castelvetrano (14500 ha); 10 Menfi (2500 ha).

The river extends for over 100 km, from the mountains of *Piana degli Albanesi* to the Mediterranean Sea, which is reached between *Porto Palo* and *Marinella di Selinunte* in correspondence of the Natural Reserve *F. Belice e Dune Litoraneo*.

In the upper part of the basin, the river is composed by two distinct branches, “*Belice Destro*” and “*Belice Sinistro*”, which converge near the town of *Poggioreale*. Downstream of the confluence, the river is named “*Belice Grande*” and flows through the extensive alluvial plain most directly impacted by agricultural transformation.

The Belice River assumes a “Y” shape in correspondence of the *Carruba* district below *Poggioreale*, where the branches “*Belice Destro*” and “*Belice Sinistro*” converge.

“*Belice Destro*” originates at 1220 meters above sea level near *Piana degli Albanesi*, upstream of the reservoir with the same name, for which it is both tributary and outlet. “*Belice Sinistro*” has its source on *Rocca Busambra* (1613 meters above sea level).

The orography of the area surrounding the dam and the reservoir is gently hilly, typical of the prevalent clayey formations. The loose material dam is located in the immediate vicinity of the Garcia Lake, near *Rocca d'Entella*, which is a Natural Reserve named *Grotta d'Entella* of significant archaeological interest (Messana, 1998).

The flat areas of the valley floor are exploited for extensive agriculture. Here irrigation districts, served by the reservoir, have been established. Some are located in the middle part of the valley, around the same reservoir, but the largest ones are at lower altitudes, along the coastal strip, from *Mazara del Vallo* to *Castelvetrano* up to *Menfi*.

The main economic resource of the valley is indeed agri-food production, with the cultivation of grapevines and olive trees. High-value crops have been added following the new availability of irrigation, mainly in the districts of *Castelvetrano* and *Menfi*. The use of water from the Garcia Reservoir allows for continuity in the production of various agri-food products in the served areas.

The geotechnical work includes the loose material dam with central sealing core, the discharge and intake works and supplementary structures for access and security.

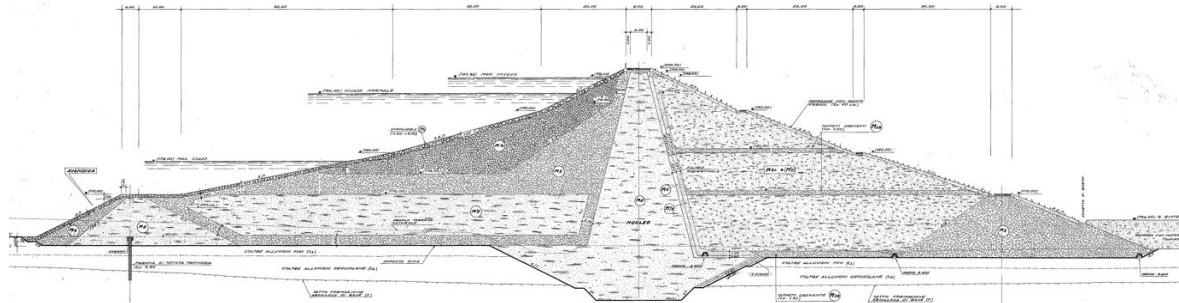


Figure 2. Scheme of the Garcia Dam.

The discharge works consist of a spillway, followed by a diversion channel and a dissipating basin, a bottom outlet and an auxiliary outlet, both of which are sectioned by floodgates and located in tunnels. Various diversion intakes are positioned at different elevations in the corresponding intake tower near the dam; the irrigation and drinking water diversion works are integrated into the discharge tunnel galleries.

The dam, with a reservoir capacity at the maximum regulation level of $80.00 \cdot 10^6 \text{ m}^3$, has currently undergone technical-administrative testing and is in the final phase of testing under Article 14 of D.P.R. 1363/59. At the time of drafting this article, the study is under examination and verification by the Ministry of Infrastructure and Transport - Directorate-General for Dams and Water Infrastructure - Technical Office for Dams.

3. Modeling of the Garcia Dam through FLAC2d

The Garcia earth-dam has been modelled through Flac2d in order to predict in a very precise way its response to seismic excitation according to the seismic demand of the site of interest.

Flac2d works in explicit dynamics on the basis of the finite difference method, allowing to simulate in a very precise way the seismic phenomenon according to the theory of wave propagation.

In particular, for each Limit State considered, it was performed a dynamic analysis under not-drained conditions after which the factor of safety was computed and evaluated.

The dam was modelled by distinguishing each portion of the geotechnical work characterized by different values of the stiffness and strength parameters. Figure 3 shows the relevant portions of the dam associated to the following soil typologies:

- Upstream shell: sandy silt, gravel with sand and fractured limestone
- Downstream shell: gravel with sand
- Core: sandy silt.
- Foundation: sandy silt.

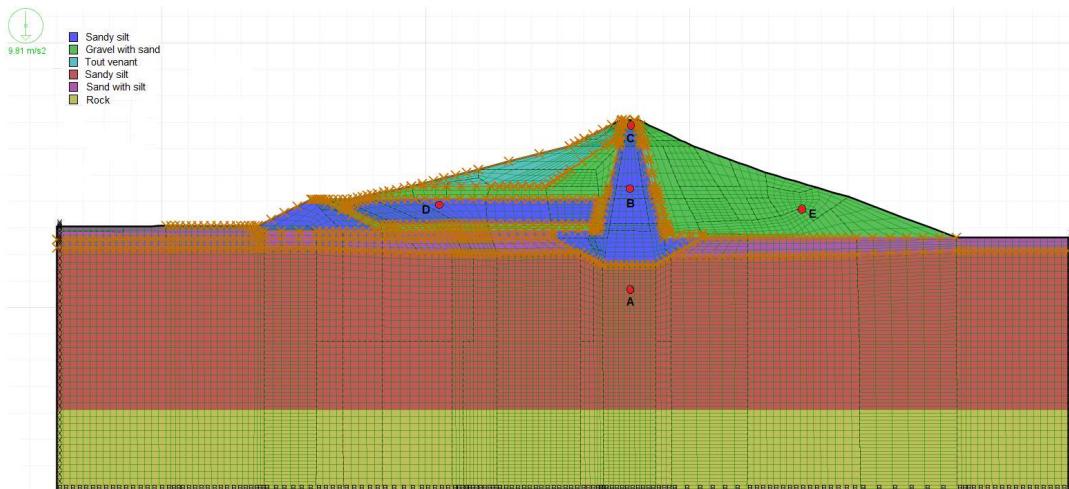


Figure 3. Flac2d modeling of the Garcia Dam and indication of five relevant points.

Among all the constitutive models available in Flac2d, the Mohr-Coulomb one was assumed for the entire model. As a matter of fact, this constitutive law requires a limited number of parameters to model the elastic behavior of the soil until failure is reached according to Mohr-Coulomb criterion.

The choice fell upon a constitutive model that required a limited number of parameters because the available data for the site characterization were incomplete, so a back analysis was needed and performed according to the following procedure:

- The resistance parameters, that is the friction angle and the cohesion, have been evaluated on the basis of the design values and the tests made during the construction stages.
- For the stiffness parameters there was lower availability of data, reason why a back analysis was performed to estimate the value of the Young modulus best fitting the subsidence values monitored in 2006 through a series of settlement gauges placed in six significant positions with a water height of 190 m a.s.l. (8 meters below the height of maximum regulation of the reservoir): first attempt values of the Young modulus were chosen on the basis of existing correlations for the soil typologies characterizing the site stratigraphy, then a series of analyses have been performed in Flac2d by progressively changing the value of the Young modulus until the monitored subsidence values were matched with a residual error of 13%.

For each attempt value of the Young modulus, a static analysis in long-term drained conditions was performed by means of an uncoupled computation, which involved a filtering hydraulic computation followed by a mechanical one. The water table was defined according to the pore-pressure values corresponding to a water height of 190 m a.s.l. The hydraulic boundary conditions were imposed by defining a waterproof edge in correspondence of the model base and filtering conditions for the lateral and top edges.

Previous reports indicate that the bedrock is located at a depth greater than 60 meters, hypothesis confirmed by the results of the MASW analysis conducted on the dam site. For this reason the bedrock has been modelled at a depth equal to 70 meters, its permeability coefficient was defined sufficiently small to consider the bedrock as waterproof and its stiffness was evaluated on the basis of the theory of elasticity by assuming a shear wave velocity $c_s = 800 \text{ m/s}$ for soil type A, a Poisson coefficient $\nu = 0.25$ and a density value $\rho = 2700 \text{ kg/m}^3$:

$$E = 2G(1 + \nu) = 2c_s^2\rho(1 + \nu) \quad (1)$$

The dynamic boundary conditions were inserted in the model as follows:

- quiet boundary conditions were assumed for the model base, which behaves as a viscous damper capable to absorb seismic waves
- free field boundary conditions were assumed for the lateral edges of the model, which let seismic waves pass through without reflecting them.

The dynamic analysis of the dam was carried out by means of the non-linear time history analysis method by using scaled spectrum-compatible real accelerograms.

The presence of quiet boundary conditions at the model base made it necessary to insert the seismic excitation in terms of shear stresses applied at the bedrock level, whose entity was evaluated according to the wave propagation theory by the following equation:

$$\tau(t) = -2\rho c_s v_s(t) \quad (2)$$

As Flac2d performs explicit dynamic analyses taking into account the non-linear behavior of the soil on the basis of the assumed constitutive model, the damping due to arising plastic deformations is automatically taken into account. However, there are some limitations, especially when less advanced constitutive models are assumed, such as in the case of the Mohr-Coulomb one. By defining a hysteretic damping it is possible to model the most advanced aspects of the damping phenomenon, such as the hysteretic cycles which can occur at low deformation levels due to previous plastic deformations. This is why, in the model of the Garcia Dam, it was introduced the hysteretic damping which takes into account the progressive reduction of the shear modulus on the basis of the reached deformation level.

For each scaled spectrum-compatible real accelerogram, a dynamic analysis has been performed by introducing the excitation in terms of tangential stresses at the model base according to Equation 2.

The dynamic analyses were performed by assuming undrained behavior in order to simulate the short-term condition characterizing the seismic event.

4. Geotechnical and structural checks

According to current National Code, geotechnical and structural checks have been carried out according to three different limit states: Damage Limit State (DLS) is the condition beyond which the dam experiences minor damages that can be easily repaired and do not reduce the retaining capacity or hinder the capability to carry out operations needed to ensure the dam safety; Life Safety Limit State (LSLS) is the condition beyond which the dam experiences major damages such as to trigger the uncontrolled release of retained water, which can endanger the safety of people and environment on the downstream side; Collapse Limit State (CLS) is the condition for which the collapse of the structure occurs, resulting in the uncontrolled emptying of the entire reservoir or part of it.

4.1. Preliminary static analysis and calibration of the dam model

As already mentioned, before the seismic analysis, a preliminary static study was conducted with the purpose of assessing the deformation and stress state during standard operational condition as well as the conditions of the hydrodynamic network. The numerical value obtained was in good agreement with the average experimental value recorded in 2006, and equal to 1.5 cm, confirming the reliability of the developed model and the geotechnical parameters used.

A further static analysis was carried out considering the reservoir full up to the height of maximum regulation (198 m a.s.l.). The analysis was carried out using a decoupled method aimed firstly at evaluating the filtration through the dam (hydraulic analysis) and then the stress state of the dam (mechanical analysis). Thus, the effective stress state and filtration through the dam under steady-state conditions were determined. The numerical results obtained were in good agreement with the expected stress state and pore pressure analytically calculated.

Once the stiffness parameters were calibrated, the factor of safety in static conditions was computed according to the strength reduction method. This is the method assumed by Flac2d to compute the FoS by progressively reducing the strength parameters until the first unstable condition is found.

4.2. Dynamic analysis under seismic excitation

With regard to seismic assessment, dynamic analyses are carried out by means of the non-linear time history analysis method, by using three different groups of seven scaled spectrum-compatible real accelerograms, considering one group for each limit state considered and by assuming soil type A.

The selection of the real accelerograms was performed by means of the software REXEL (Iervolino et al., 2009) on the basis of the target spectrum for several return periods associated with each limit state (101 years for DLS, 949 years for LSLS, 1950 years for CLS). According to the Italian National Code, these return periods are calculated considering a nominal life of the dam equal to 50 years and an importance class equal to IV (associated to a multiplying factor equal to 2), thus the reference period is equal to 100 years.

The earthquake, being an event lasting a few tens of seconds, is comparable to a cyclic load in undrained conditions, therefore capable of inducing interstitial overpressures within the dam body. These overpressures, as they accumulate, create an unbalanced situation that is rebalanced once drainage is allowed after the earthquake. The dissipation of this load leads to a change in effective stresses and therefore to the occurrence of deferred failure. This means that it is not sufficient to analyse what happens during the seismic event, but it is also necessary to analyse the phase immediately following the earthquake. In fact, if the subsidence is excessive, internal erosion (fracturing) or external erosion (overtopping) may occur. For these reasons, the phase of consolidation following the earthquake was evaluated considering the hydraulic overload generated within the dam body and its dissipation while monitoring subsidence. This analysis under drained conditions required the execution of a hydraulic computation coupled to a mechanical one in Flac2d, during which the software constantly updates the interstitial pressures and the variation of effective stresses that produce subsidence.

The acceptability of subsidence was evaluated using an empirical criterion available in literature and developed by Swaisgood (1998, 2003). The criterion allows four damage classes to be defined as a function of the relative displacement of the crest, calculated on the basis of the PGA and a ratio (Equation 3) depending on the

subsidence Δ , the dam height $DH=55\text{m}$ and the height $AT=45\text{m}$ of deformable soil layer on which it rests. This criterion makes it possible to identify the extent of damage to the dam.

$$\% Sttlmt = \Delta \cdot 100 / (DH + AT) \quad (3)$$

The global instability of a dam can occur either concurrently with the seismic event, as a direct effect of the inertia forces, or in the post-seismic phase, as a result of an unfavourable redistribution of the interstitial pressures accumulated during the earthquake. This eventuality was investigated through the calculation of the factor of safety on Flac2d. The FoS was calculated using the strength reduction method. This method involves the progressive reduction of the resistance parameters, that are the cohesion and the friction angle, until the first unstable condition is found in association to a collapse mechanism. Initially, the software calculates the global stability of the structure on the basis of the soil parameters, then a reduction factor is progressively applied until instability occurs. Therefore, the factor of safety is not the classic ratio between available and mobilized stress, but it is the reduction factor of the resistance associated to the first collapse mechanism.

4.3. Discussion of results and verifications

Generally speaking, non-linear time history analyses provided satisfactory results with respect to the overall behavior of the dam. The analysis of the acceleration response of the dam crest, performed in the frequency domain through the Fourier transform of the signal, returned a maximum peak in the vicinity of a frequency equal to 1.37 Hz, which is near to the frequency identified by environmental monitoring, i.e. 1.5 Hz, proving the reliability of the model.

At the DLS the displacements are such that the safety of the reservoir is still ensured and the normal functioning of the structure is guaranteed. The average subsidence recorded at the dam crest is equal to 0.111 m. Such value falls within the “minor damage” interval according to Swaisgood criterion, so these results do not give rise to any concern for the water tightness capacity or against overflow.

At the LSLS and CLS, the average subsidence recorded at the dam crest are much higher, equal to 0.615 m and 1.029 m, but not leading to the dam collapse. These values fall across the intervals “moderate damage” and “serious damage” according to Swaisgood criterion.

Regarding the instability checks of the dam, the factor of safety was computed in Flac2d according to the reduction strength method. For all the accelerograms considered, the factor of safety computed after the dynamic analysis under not-drained conditions was much greater than one, which made it possible to exclude instability problems associated to the seismic event.

The check of external erosion by overtopping consists of the calculation of the available distance between the water level and the dam crest. The height of the latter was evaluated considering the seismic and post-seismic settlements. The height of the dam crest was evaluated considering the overall subsidence, obtained as the sum of instantaneous subsidence caused by seismic action and deferred post-seismic subsidence caused by the dissipation of interstitial overpressures. The instantaneous subsidence is the sum of two components: the first one due to movement along a sliding surface and the second one due to plastic deformations, volumetric and distortional. The available distance is equal to the difference between the elevation of the dam crest and the elevation of the maximum water level increased of the semi-height of the greatest wind-generated wave. In absence of specific studies on the waves height generated by wind or earthquake, the Italian National Code suggests to use the maximum amplitude of the wave generated by the wind increased by the uplift against the dam upstream side, which can be assumed as a function of the dam fetch. For the Garcia Dam, the fetch to be considered is approximately 4 km and, in the worst condition with wind at 100 km/h, the wave amplitude to be considered is 0.53 m, while the uplift height to be taken into account is 0.12 m. The resulting available net is therefore equal to 1.625 m. This check was always satisfied as the average displacement of the dam crest was below this threshold.

As an example, an accelerogram belonging to the group used for the safety assessment in the case of CLS is shown in Figure 4, characterized by a PGA equal to 2.94 m/s^2 , which led to the most critical conditions. Figure 5 shows the time history of the horizontal displacements, obtained by using the above-mentioned accelerogram, in correspondence of the five relevant points of the dam, indicated in Figure 3. It can be seen that the maximum displacement is recorded at point E, which is located downstream, meaning that this is the portion of dam subject to the highest displacement rate.

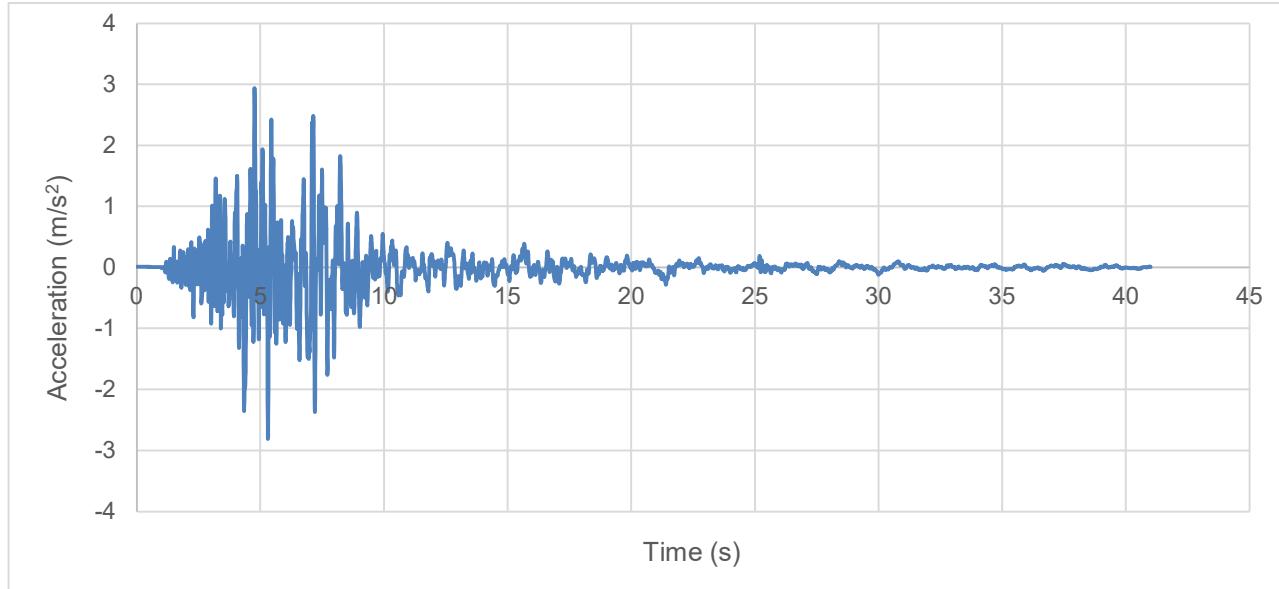


Figure 4. Collapse limit state accelerogram associated to a PGA=2.94 m/s².

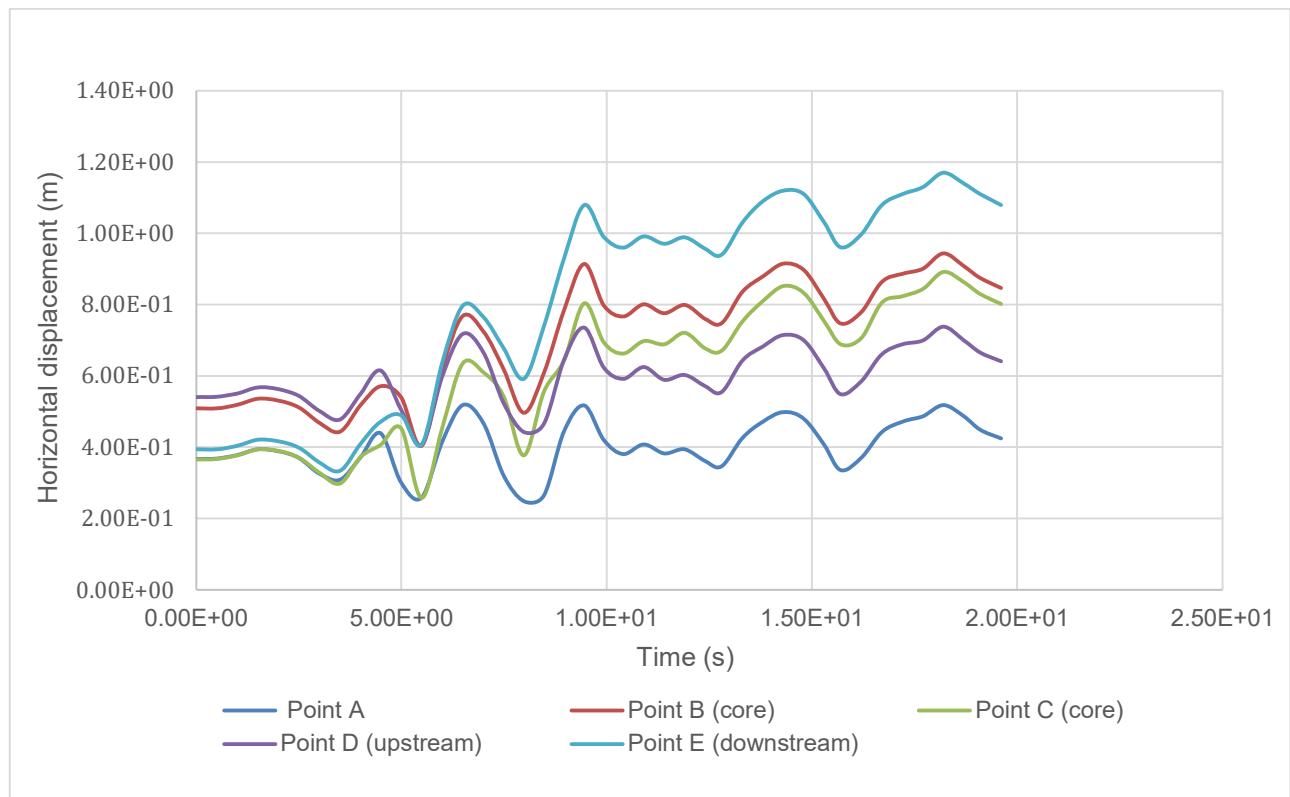


Figure 5. Time history of the horizontal displacements associated to five relevant positions.

In the end, after the occurrence of the seismic event, the FoS computation was performed according to the reduction strength method, leading to a value of the factor of safety equal to 1.92 associated to a collapse mechanism involving a big portion of the downstream shell, as shown in Figure 6. This is in accordance with the results regarding the maximum displacement recorded during the dynamic analysis, as discussed above and shown in Figure 5.

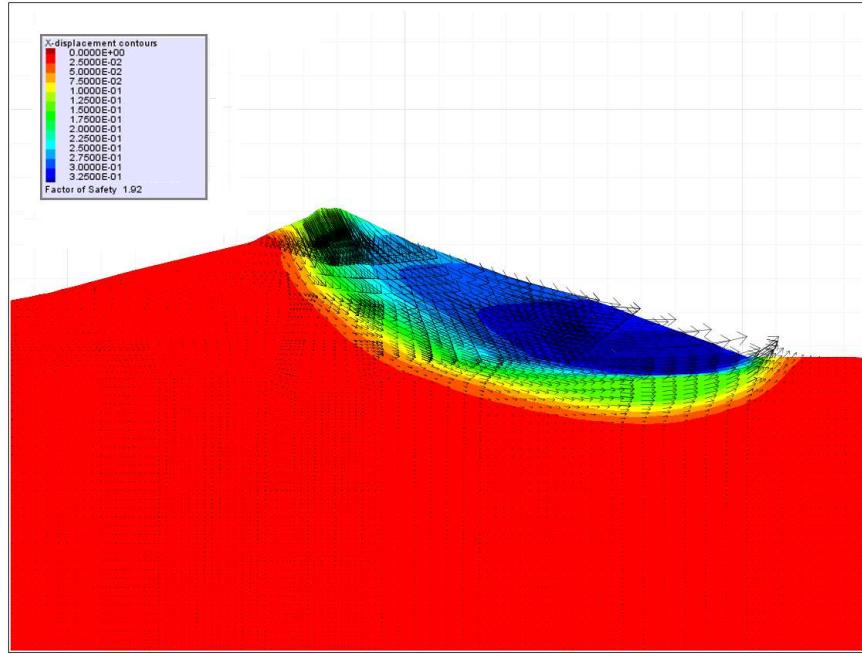


Figure 6. Factor of safety after the seismic event and associated mechanism.

5. Conclusions

This article provides the modeling and computation procedures used to perform the seismic analysis of the Garcia Dam through the geotechnical calculation software Flac2d. This software allowed for the execution of geotechnical checks through the creation of a geotechnical model taking into account the various zone materials (Core, Shells, Filters, etc.) that together constitute the dam.

Stiffness parameters were calibrated against the experimental values regarding average crest settlements. Model reliability was checked against the effective stress state and pore pressure for static analysis, against frequency identified by environmental monitoring for dynamic analysis.

The seismic assessment was carried out by means of the non-linear time history analysis method, by using three different groups of seven scaled spectrum-compatible real accelerograms, considering one group for each limit state (damage, life safety and collapse) and by assuming soil type A.



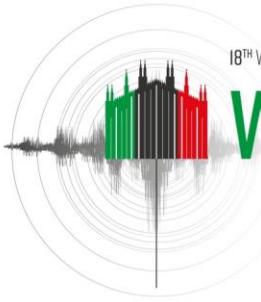
Figure 7. View of the Garcia Lake.

The results of the above-mentioned study have demonstrated that the dam does not exhibit seismic issues for all the dynamic analyses performed and the different limit states considered. The safety factors obtained for the dam are always greater than unity, reason why the dam structure can be considered seismically adequate in accordance with current regulations. At the time of drafting this article, the study is under examination and verification by the Ministry of Infrastructure and Transport - Directorate-General for Dams and Water Infrastructure - Technical Office for Dams.

Finally a thought and, in some cases a memory, is expressed towards the Designers Eng. Franco Bigalli, Eng. Alessandro De Boni, Eng. Giovanni Sallusto, Eng. Giancarlo Madoni (all members of the S.I.A. in Milan), the General Consultant in the Course of the Work Prof. Eng. Ruggiero Jappelli and the Works Director (as well as Site Laboratory Director and Collaborator of the General Consultant in the Course of the Work) Eng. Gianni Cusmano.

6. References

- Biondi G., Cascone E., Aliberti D., Rampello S. (2021). Screening-level analyses for the evaluation of the seismic performance of a zoned earth dam. *Engineering Geology*, 105954. DOI 10.1016/j.enggeo.2020.105954.
- Bozzoni F., Misiano G., Lai C.G. (2023). A multi-scale tool for assessing the seismic risk of small dams during emergency preparedness and response phase. *Natural Hazards*, 118:2069-2095. DOI 10.1007/s11069-023-06081-z.
- Iervolino I., Galasso C., Cosenza E. (2009). REXEL: computer aided record selection for code-based seismic structural analysis. *Bulletin of Earthquake Engineering*, 8:339-362. DOI 10.1007/s10518-009-9146-1.
- Makdisi F. I., Seed H. B. (1978). Simplified procedure for estimating dam and embankment earthquake-induced deformations. *Journal of the Geotechnical Engineering Division*, 104:849-867.
- Masini L., Rampello S., Donatelli R. (2020). Seismic performance of two classes of earth dams. *Earthquake Engineering and Structural Dynamics*, 50:692-711. DOI 10.1002/eqe.3352.
- Ministero delle Infrastrutture e dei Trasporti, NTC 2018 (2018). Aggiornamento delle Norme tecniche per le costruzioni.
- Ministero delle Infrastrutture e dei Trasporti, NTD 2014 (2014). *Norme Tecniche per la Progettazione e la Costruzione degli Sbarramenti di Ritenuta (dighe e traverse)*.
- Regina G., Zimmaro P., Ziotopoulos K., Cairo R. (2023). Evaluation of the optimal ground motion intensity measure in the prediction of the seismic vulnerability of earth dams. *Earthquake Spectra*, 39(4):2352-2378. DOI 10.1177/87552930231170894.
- Seed H. B. (1979). Considerations in the earthquake-resistant design of earth and rockfill dams. *Geotechnique*, 29(3):215-263.
- Swaisgood J.R. (1998). Seismically-induced deformation of embankment dams. *6th US National Conference on Earthquake Engineering*, Seattle, Washington.
- Swaisgood J., (2003). Embankment dam deformations caused by earthquakes. *Pacific conference on earthquake engineering*.
- Itasca Software Manual – FLAC (Fast Lagrangian Analysis of Continua) Version 8.1
- Vecchietti A., Cecconi M., Russo G., Pane V. (2019). Seismic Vulnerability of a Rockfill Dam through Different Displacement-based Approaches. *Journal of Earthquake Engineering*, 26(1):113-139. DOI 10.1080/13632469.2019.1662346.



COMPARISONS BETWEEN TWO REINFORCEMENT METHODS FOR A HIGH EMBANKMENT DAM ON THICK ALLUVIAL DEPOSIT

Z. Wang¹, R. Wang¹ & J.M. Zhang¹

¹ Tsinghua University, Beijing, China, zhao-wan19@mails.tsinghua.edu.cn

Abstract: Soil liquefaction can cause major damage to embankment dams constructed on alluvial deposit under strong earthquakes. Gravel columns and berms are often adopted as reinforcement methods to mitigate soil liquefaction in the alluvial deposit and reduce the settlement and deformation of the dam. This paper presents seismic analyses of a high embankment dam on thick liquefiable alluvial deposit with a less permeable silty interlayer, and make comparisons between the two different reinforcement methods. The simulations are conducted using a plasticity constitutive model for large post-liquefaction deformation of sand (CycLiq) with solid-fluid coupled analysis. The results show that while gravel columns primarily enhance drainage, their overall effect on dam deformation is limited. In contrast, berms are much more effective in reducing settlement and deformation by increasing the confining stress within the deposit.

1. Introduction

Southwest China is rich in hydropower resources and has become a major region for hydropower development (Li et al., 2018). Unfortunately, this region is also the extremely seismically active, having recorded numerous strong earthquakes including the 1950 Zayu-Medog Mw 8.6 earthquake and the 2008 Wenchuan Mw 8.0 earthquake (Zhao et al., 2023). The historical seismic activities have resulted in the riverbeds to widely consist of thick layered liquefiable alluvial deposits. For instance, the 124.5m-high Yele dam (Han et al., 2016) was constructed on 420m-thick alluvial deposit while the 240m-high Changhe dam (Liu et al., 2017) was constructed on 79.3m-thick alluvial deposit. Therefore, it is of great importance to investigate seismic reinforcement methods for such hydropower projects.

Traditional alluvial removal approach are unfeasible for very thick deposit. To accommodate for deep ground treatment, gravel columns are often adopted. Seed and Booker (1977) introduced the construction of gravel columns as a mitigation strategy to increase stability and prevent liquefaction of sand layer. Both centrifuge tests and numerical simulations have highlighted the mitigation mechanism of ground densification, enhanced drainage and shear reinforcement (Adalier et al., 2003; Badanagki et al., 2018; Tiznado et al., 2020, 2022; Zou et al., 2020). The 50m-high Kissir Dam in Algeria (Karech et al., 2017) lying on a 40m-thick alluvial filling of low mechanical characteristics was treated by gravel columns, which is effective in mitigating soil liquefaction. Toorourrong Reservoir (Avalle et al., 2012) in Australia also employed gravel columns with the area replacement ratio of 20%, increasing the stability coefficient of the dam slope from 1.0 to 1.2.

The construction of berms extending upstream and downstream from the dam surface are often adopted to improve slope stability by providing extra confining stress. The Thermalito Afterbay Dam (Haider et al., 1984) and Forty Mile Coulee East Dam (Chin et al., 1991) employed berms to prevent upstream sliding. A case study

of the Ghoocham earth dam in Iran demonstrated that berms improved the slope safety factor from 0.795 to 1.307 (Aminjavaheri & Karam, 2014).

In this study, numerical simulations are presented for a high embankment dam on thick alluvial deposit reinforced with gravel columns and berms. The efficacy of these two methods in enhancing the seismic performance of the dam is evaluated, in terms of dam deformation, acceleration, and ground excess pore pressure accumulation, which was seldom discussed in previous studies. The influences of gravel columns treatment depth and area and berm size are also discussed.

2. Numerical model and material properties

2.1. Model description

This study employs a two-dimensional plane strain model to simulate the behaviour of an embankment dam. Based on typical existing embankment dam projects on thick alluvial deposit, the model is designed as shown in Figure 1, the embankment dam consists of upstream and downstream rockfill with slope of 1:2.0 and a clay core with 10-meter width at the top and slope of 1:0.2. The alluvial deposit contains layers of clay, silt, sand, and gravel, extending to a depth of 535m. From bottom up, layer 1 is a 180m thick gravel layer, layer 2 is a 150m thick sandy gravel layer, layer 3 is a 140m thick sand layer, layer 4 is a 10m thick silt layer, layer 5 is a 50m thick sand layer, and layer 6 is a 5m thick sandy gravel layer. The sand layers could be subjected to excess pore pressure accumulation and liquefaction under earthquake. The clay and silt layer 4 has low permeability which could affect excess pore pressure dissipation. The lateral extension of the model is 6 times the embankment dam width to reduce boundary effects (Tiznado, 2022).

As reinforcement, gravel berms 70 meters in height and 300 meters in length are constructed at both upstream and downstream toes. For gravel columns, treatment is performed to a depth of 55 meters, with an area replacement ratio of 25% beneath the dam. Treatment depth is extend to 65 meters below berm toes to ensure penetration through layer 4, to allow for excess pore pressure dissipation. The treatment depth is adopted based on current construction capabilities.

Here, we present the results of four numerical simulation models to make comparisons between the effects of berms and gravel columns. Model 0 (BS) serves as a baseline, without berms and gravel columns, representing the untreated condition. Model 1 (GC) is treated with gravel columns only while Model 2 (BM) with berms only. Model 3 (BM-GC) incorporates both treatment methods, as depicted in Figure 1.

The properties of the embankment dam and alluvial deposit are given in Table 1.

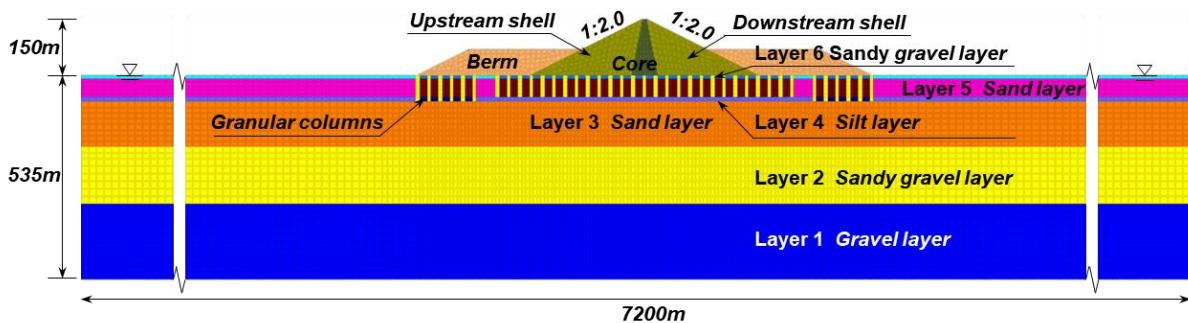


Figure 1. The geometry of the model

Table 1. The properties of the embankment dam and alluvial deposit

	Saturated density (kg/m ³)	Permeability coefficient (m/s)	Void ratio
Layer 6	2400	7.50E-05	0.4
Layer 5	2000	3.00E-05	0.55
Layer 4	1900	1.50E-07	0.7
Layer 3	2100	7.50E-06	0.5
Layer 2	2400	6.00E-06	0.2
Layer 1	2400	1.00E-06	0.2

Gravel column	2400	7.50E-04	0.4
Dry unit weight (kg/m³)			
Core	1709		0.7
Rockfill	1800		0.4
Berm	1800		0.2

2.2. Simulation process

The numerical simulation is performed using GEOSX, an open-source, multiphysics simulator (Fu et al., 2013; Settgast et al., 2016). The nonlinear, elastoplastic response and solid-fluid coupled analysis is modelled with a plasticity constitutive model for large post-liquefaction deformation of sand (Cycliq) (Wang et al., 2014), which has been integrated into GEOSX by Wang (2020) and Yu et al. (2023). The model has successfully been applied to the simulation of various liquefaction related problems(Liu et al., 2020; Zhu et al., 2021; Li et al., 2022; Qu et al., 2023), including gravel column improved ground(Wang et al., 2016; Zou et al., 2020). Model parameters of the embankment dam and alluvial deposit are presented in Table 2, which are adopted within typical ranges based on previous experience.

The simulation starts with the calculation of the initial stress field calculation. Subsequently, dynamic analysis is performed by inputting a horizontal 1995 Kobe earthquake motion at the base (Figure 2), of which the peak acceleration is 0.41g. The vertical motion corresponds to two-thirds of the vibration amplitude of the horizontal motion. The surface of the model is assumed fully drained, while the sides and base are undrained. The sides of the model are subjected free-field dynamic boundary conditions.

Table 2. Model parameters of the embankment dam and alluvial deposit

	G_0	κ	h	M	$d_{re,1}$	$d_{re,2}$	d_{ir}	α	$\gamma_{d,r}$	n^p	n^d	λ_c	e_0	ξ
Layer 6	360	0.003	2.8	2	0.55	38	0.95	30	0.05	0.5	18	0.018	0.85	0.7
Layer 5	300	0.007	1.3	1.4	1.4	30	1.4	30	0.05	2.2	6	0.0112	0.85	0.7
Layer 4	200	0.018	1.8	1.35	1.4	30	0.2	30	0.05	2.2	6	0.019	0.95	0.7
Layer 3	250	0.006	1.1	1.4	1.4	30	1.4	30	0.05	2.2	6	0.0112	0.75	0.7
Layer 2	330	0.005	3.8	1.8	0.55	30	0.95	30	0.05	0.5	18	0.018	0.9	0.7
Layer 1	360	0.005	3.8	2	0.55	30	0.95	30	0.05	0.5	18	0.018	0.9	0.7
Gravel column	360	0.003	2.8	2	0.55	38	0.95	30	0.05	0.5	18	0.018	0.9	0.7
Core	200	0.02	1.8	1.5	1.4	30	0.2	30	0.05	2.2	6	0.019	0.95	0.7
Rockfill	360	0.003	2.8	2	0.55	38	0.95	30	0.05	0.5	18	0.018	0.85	0.7
Berm	300	0.01	2.8	1.7	0.55	30	0.95	30	0.05	0.5	18	0.018	0.7	0.7

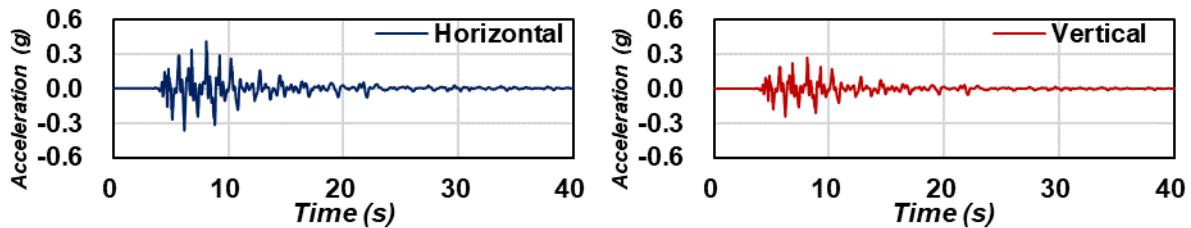


Figure 2. Input ground motions for the dynamic analysis

3. Results and discussions

3.1. Deformation response

The horizontal displacement time histories of the four models at the location of maximum deformation are shown in Figure 3. Both untreated and treated models exhibit near symmetry in both upstream and downstream results. Sliding circles exist in both shells and berms. The maximum deformation of the shells appear at 0.3 times of the dam height while that of berms appear near the top. The maximum horizontal displacement of Model BS is 0.55m (Figure 3 (a)). The gravel column has negligible effect in reducing dam

displacement, with Model GC displacement being only 0.02m smaller than Model BS. In contrast, the existence of berms significantly reduces dam displacement by 0.27m. The displacement of the berms is still quite large, but does not affect the safety of the dam itself. Combining gravel columns and berms in Model BM-GC does not show noticeable improvement compared with using berms alone.

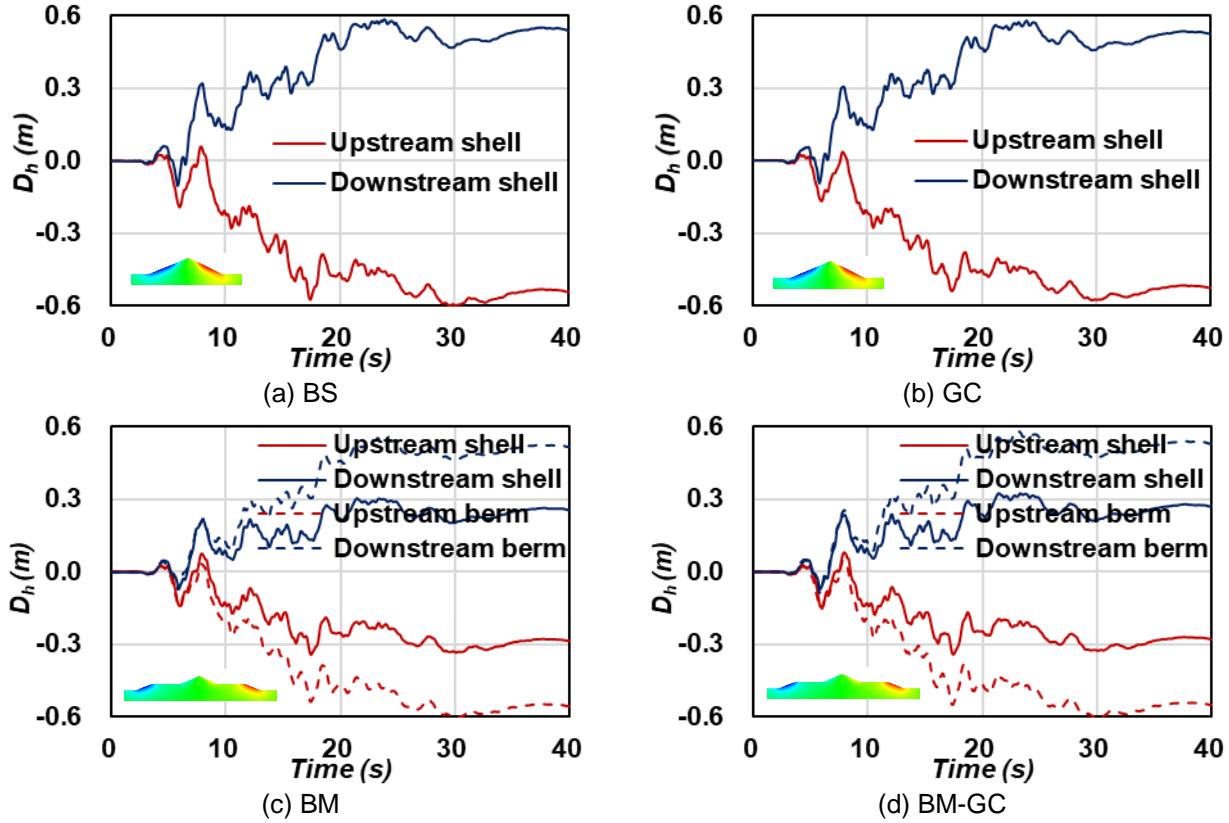


Figure 3. Horizontal displacement time histories of upstream shell (berm) and downstream shell (berm)

The differences between berms and gravel columns reinforcement effects can also be clearly demonstrated in the vertical displacement time histories in Figure 4 and Table 3. The reinforcement methods can reduce the seismic dam settlement to various degrees. The application of berms is clearly more effective in controlling settlement. The reason for this can be better explained by the settlement within each layer of material listed in Table 3. Settlement of the dam itself accounts for 57 percent of the total settlement, which is only slightly affected by the reinforcements. Through added confining stress, the berms reduce the settlement in the soil, especially in layer 5, which accounts for 9.5% of settlement without reinforcement. The effect of gravel columns is again quite small as the layer is already relatively dense with initial void ratio of 0.55 (Table 1), meaning that the densification effect of the columns is nonessential.

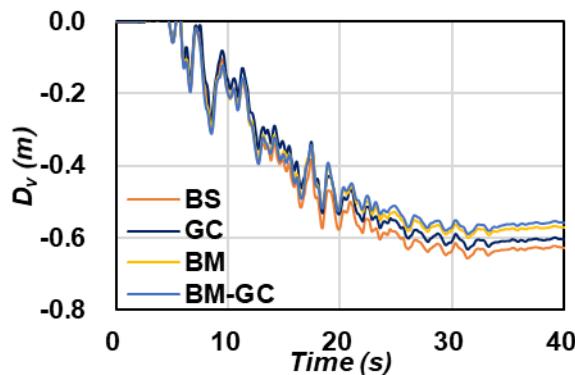


Figure 4. Vertical displacement times histories at the crest of the dam

Table 3. Vertical displacement times histories in different layers

	BS		GC		BM		BM-GC	
	Dv (m)	Proportion	Dv (m)	Proportion	Dv (m)	Proportion	Dv (m)	Proportion
Dam	0.359	56.7%	0.345	56.5%	0.337	58.6%	0.329	58.3%
Layer 6	0.004	0.6%	0.007	1.1%	0.004	0.7%	0.003	0.5%
Layer 5	0.060	9.5%	0.055	9.0%	0.040	7.0%	0.038	6.7%
Layer 4	0.016	2.5%	0.014	2.3%	0.011	1.9%	0.013	2.3%
Layer 3	0.108	17.1%	0.106	17.3%	0.105	18.3%	0.104	18.4%
Layer 2	0.053	8.4%	0.048	7.9%	0.044	7.7%	0.043	7.6%
Layer 1	0.033	5.2%	0.036	5.9%	0.034	5.9%	0.034	6.0%

3.2. Acceleration response

Figure 5 plots the acceleration time histories at the crest and base of the dam for the four models. The peak acceleration at the base of the dam is significantly reduced by about 60% at the base of the dam, due to the accumulation of excess pore pressure in the sandy deposit, to be discussed in the next section. There is a clear amplification of the acceleration within the dam. The amplification ratio of Model BS, GC, BM, and BM-GC are 3.00, 3.04, 2.53, and 2.43, showing that berms can significantly reduce the acceleration of the dam.

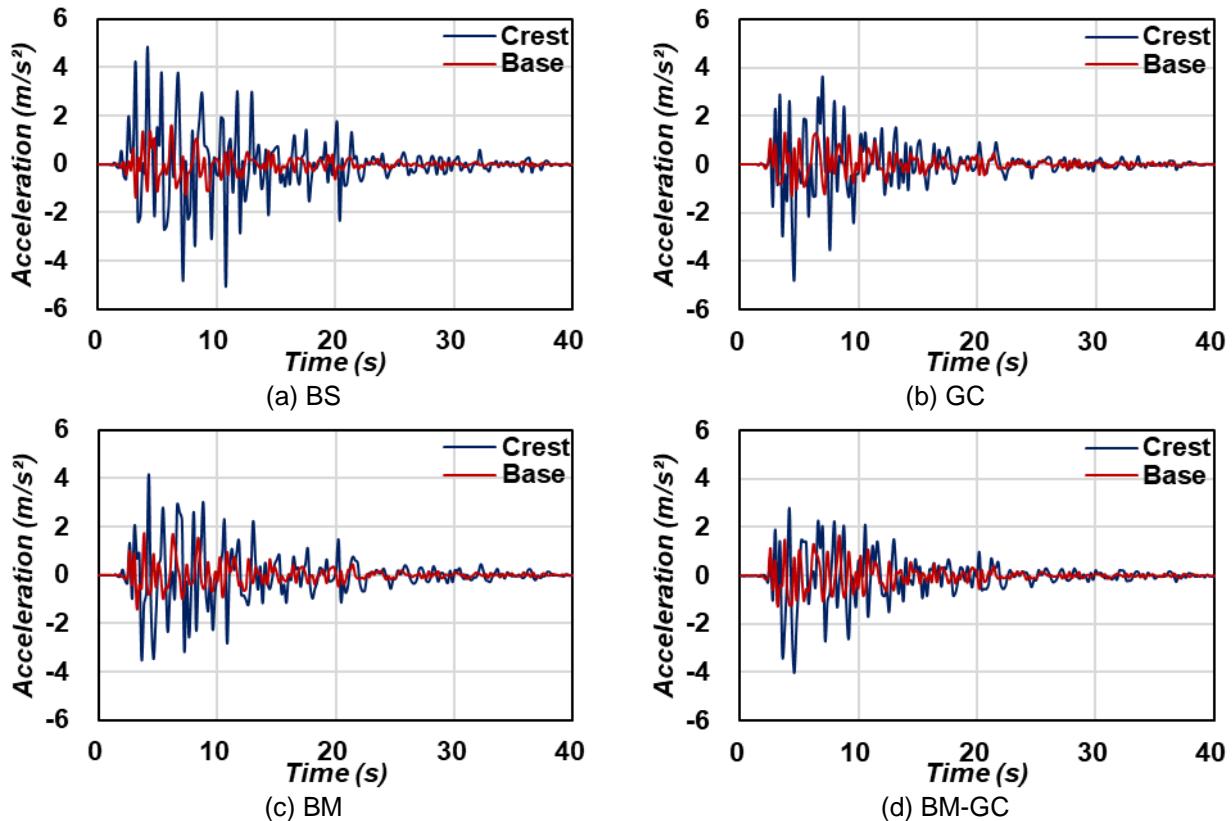


Figure 5. Acceleration response at the crest and base of the dam along the dam axis

3.3. Excess pore pressure ratios response

Figure 6 offers a comparative view of excess pore pressure ratios at the top of each layer for different models along the dam axis. The simulation results show that the excess pore pressure ratio at the top of layers 3 and 5 are the highest, reaching about 0.3 for the unreinforced model (Fig. 3 (a)), due to the low initial effective stress in layer 5 and the low permeability of layer 4. The drainage effect of gravel columns plays a role in suppressing the excess pore pressure ratio in layer 5 via increased permeability (Fig. 6 (b)). However, as the gravel columns do not penetrate the silt layer, the excess pore pressure ratio in layer 3 remains relatively

higher. Berms also help decrease excess pore pressure ratios due to its effect in increasing confining stress, especially in the relatively shallow layer 5.

The accumulation of excess pore pressure ratio in the deep Layers 1 and 2 and silt layer reach only approximately 0.1 and are not significantly affected by the reinforcement methods.

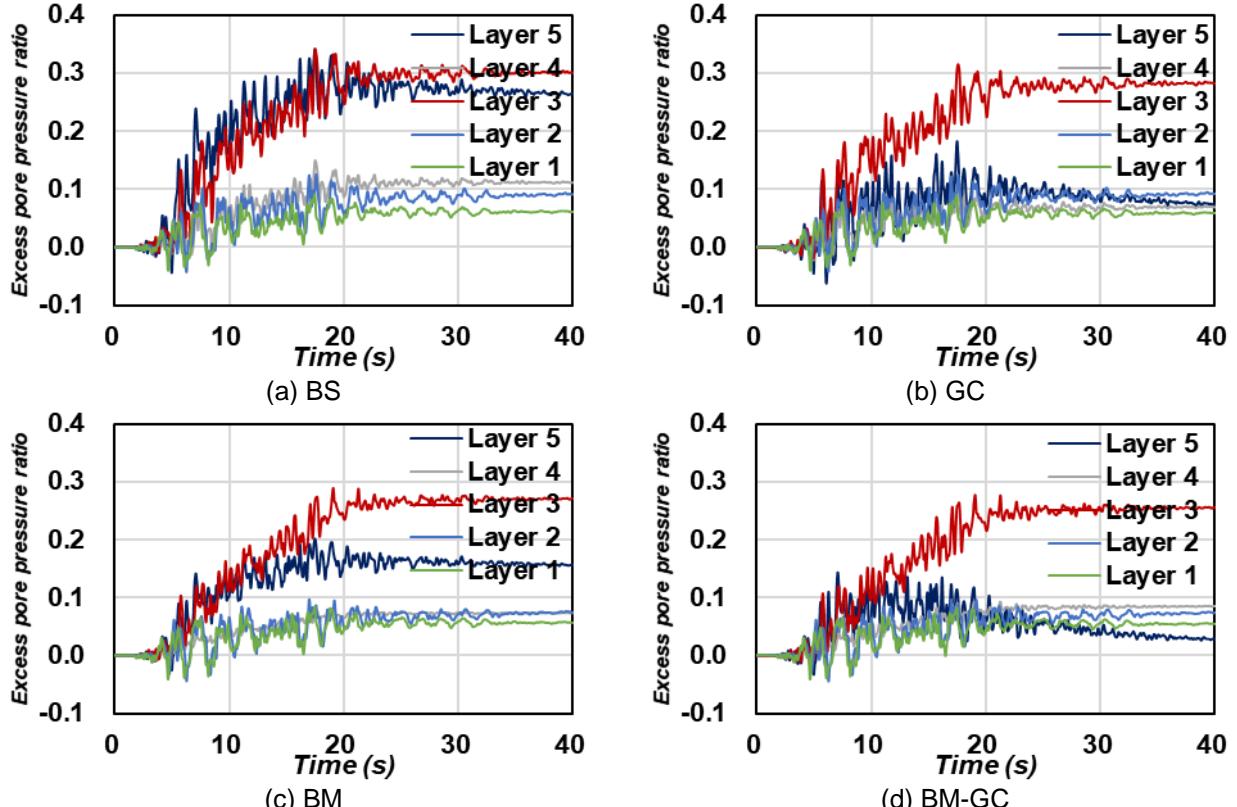


Figure 6. Excess pore pressure ratio time histories in different layers along the dam axis

3.4. Parametric study of berms and gravel columns

To further investigate the parametric sensitivity of berms and gravel columns, several numerical simulation models treated with different ways are analysed.

For models only treated by berms, both upstream and downstream berms are constructed with lengths ranging from 100m to 600m, while maintaining a consistent height of 70m. As depicted in Figure 7 and Table 4, an extension in berm length associates with a reduction in both dam settlement and horizontal displacement. The vertical settlement can be minimized from 0.62m to 0.53m, representing a 14.5% reduction compared to the initial measurement. Additionally, the horizontal displacement exhibits a 30% decrease with the extension of the berm.

Sensitivity analysis reveals that the most effective length is 400m to reach a minimum deformation. Further increases in the length of berms yield marginal additional improvements.

For models only treated by gravel columns, Figure 8 shows the local geometries of models treated with different treatment areas of columns. Figure 9(a) and Table 5 demonstrate the impact of varying treatment areas. Despite the treating area nearly tripling, the vertical settlement and horizontal displacement remain nearly the same, with no more than a 2% decrease. Figure 9(b) examines the effects of different depths (35m, 55m, and 65m) of gravel columns on dam and crest vertical displacements, while Table 6 examines the horizontal displacements, showing a limited decrease of no more than 1%. Thus, Varying treatment depths and areas of gravel columns make negligible difference in dam settlements, as well as horizontal displacements of both upstream and downstream.

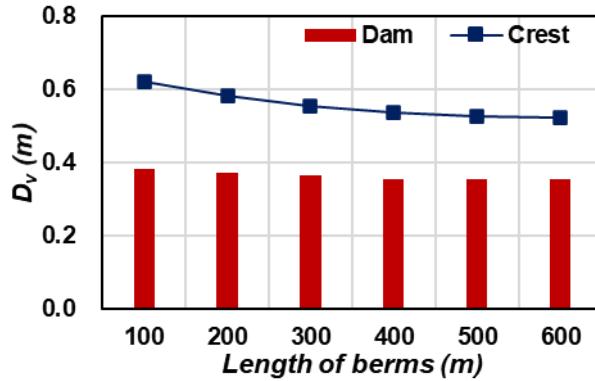


Figure 7. Vertical displacements of the dam treated by berms

Table 4. Horizontal displacements of the dam treated by berms

Length of berms (m)	100	200	300	400	500	600
Upstream Dh(m)	Berm	-0.541	-0.577	-0.570	-0.539	-0.540
	Dam	-0.383	-0.292	-0.274	-0.259	-0.247
Downstream Dh(m)	Berm	0.519	0.552	0.532	0.520	0.510
	Dam	0.336	0.254	0.229	0.222	0.219

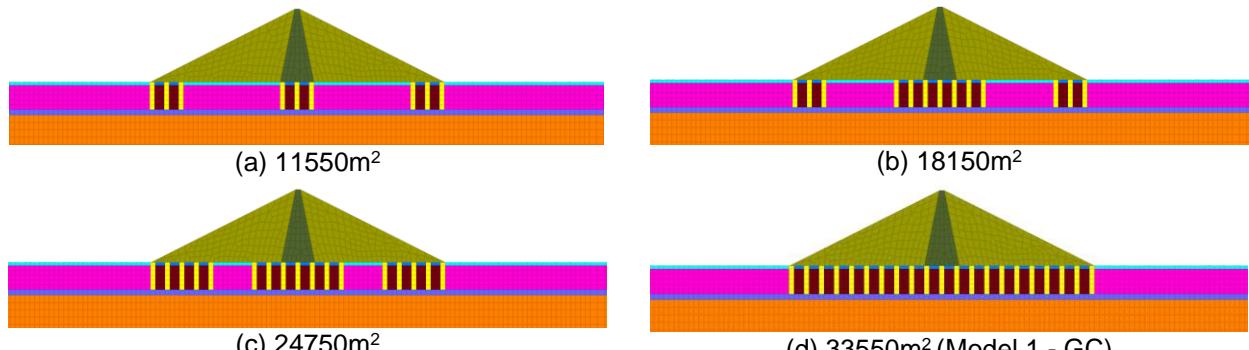


Figure 8 Local geometries of models treated with different treatment areas of columns

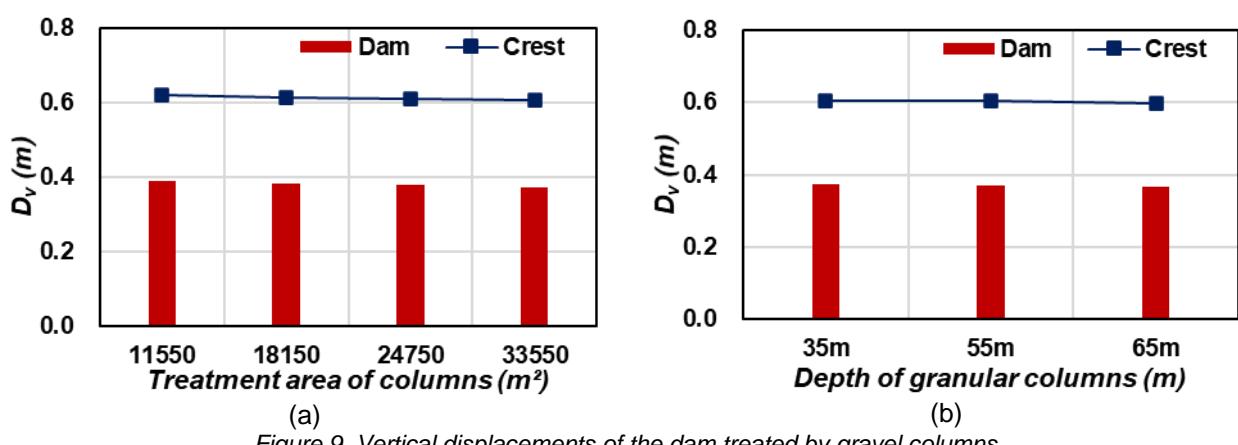


Figure 9. Vertical displacements of the dam treated by gravel columns

Table 5. Horizontal displacements of the dam treated by granular columns with different treatment area

Treatment area of columns (m^2)	11550	18150	24740	33550
Upstream Dh(m)	-0.536	-0.533	-0.532	-0.531
Downstream Dh(m)	0.530	0.530	0.523	0.519

Table 6. Horizontal displacements of the dam treated by granular columns with different depths

Depth of granular columns (m)	35	55	65
Upstream Dh(m)	-0.536	-0.531	-0.529
Downstream Dh(m)	0.522	0.519	0.516

4. Conclusions

Seismic analyses of an embankment dam on thick alluvial deposit treated by berms and gravel columns are conducted to compare efficacy of the methods. The findings are summarized below:

- (1) Berms demonstrate a substantial effect to reduce dam settlement and suppress the accumulation of excess pore pressure ratio within the sand layer.
- (2) The displacement the dam decreases with the extension of berms. The most effective berm length is found to be 400m. Further lengthening of berms is unlikely to produce significant additional improvements.
- (3) The gravel columns show limited effect in suppressing deformations and settlements, but provides noteworthy enhancement in drainage.
- (4) Changes in treatment depths and areas of gravel columns do not lead to substantial improvements in dam deformation.

Acknowledgements

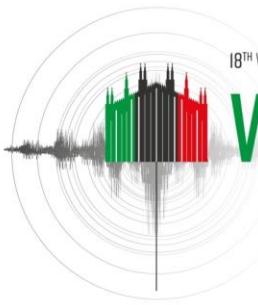
The authors would like to thank the National Natural Science Foundation of China (No. 52378349) for funding this study.

References

- Zhao B., Su L., Wang Y., Li W. and Wang L. (2023). Insights into some large-scale landslides in southeastern margin of Qinghai-Tibet Plateau. *Journal of Rock Mechanics and Geotechnical Engineering*, 15(8), 1960-1985.
- Liu T., Deng J., Zheng J., Zheng L., Zhang Z. and Zheng H. (2017). A new semi-deterministic block theory method with digital photogrammetry for stability analysis of a high rock slope in China. *Engineering Geology*, 216, 76-89.
- Li X.Z., Chen Z.J., Fan X. C. and Cheng Z.J. (2018). Hydropower development situation and prospects in China. *Renewable and Sustainable Energy Reviews*, 82, 232-239.
- Han B., Zdravkovic L., Kontoe S. and Taborda D.M.G. (2016). Numerical investigation of the response of the Yele rockfill dam during the 2008 Wenchuan earthquake. *Soil Dynamics and Earthquake Engineering*, 88, 124-142.
- Karech T., Benseghir A., Bouzid T. (2017). The behavior of dam foundation reinforced by stone columns: case study of Kissner Dam-Jijel. *International Journal of Civil and Environmental Engineering*, 11(8), 1187-1191.
- Avalle D., Kok B., Lennie T. (2012). Seismic retro-fit of an historic earth dam using grouted stone columns. *11th ANZ Conference on Geomechanics*, 692-697.
- Haider L.F., Hammond W.D., Ross P.S. (1984). Vibroflotation Compaction at Thermalito Afterbay. *Journal of Geotechnical Engineering*, 110(1), 57-70.
- Chin B.G., Davison D.M., Klohn E.J., Benson R.P., Cambell J.W. (1991). Construction performance of the Forty Mile Coulee East Dam on soft clay foundation. *Proc. 44th Can. Geotech. Conf.*, Calgary, Alberta, Canada, 91(1)-(9).
- Kirsch K. and Kirsch F. (2016). Ground Improvement by Deep Vibratory Methods.
- Jafarzadeh F. and Akbari Garakani A. (2013). Foundation treatment in rockfill dams with consolidation grouting.
- Shrestha R., Kotake N., Yang D. (2021). Application of Deep Mixing Method for Mitigation of Potential Seismic and Hurricane-Induced Hazards. 10.

- Agha A.M. (1975). Seepage control at tarbela dam through upstream blanket. Pakistan Engineering Congress, 15.
- Seed H.B., Booker J.R. (1977). Stabilization of potentially liquefiable sand deposits using gravel drains. *J. Geotech. Eng. Division, ASCE*, 107(7), 757–768.
- Adalier K., Elgamal A., Meneses J. and Baez J.I. (2003). Stone columns as liquefaction countermeasure in non-plastic silty soils. *Soil Dynamics and Earthquake Engineering*, 23(7), 571-584.
- Badanagki M., Dashti S. and Kirkwood P. (2018). Influence of Dense Granular Columns on the Performance of Level and Gently Sloping Liquefiable Sites. *Journal of Geotechnical and Geoenvironmental Engineering*, 144(9).
- Tiznado J.C., Dashti S., Ledezma C., Wham B.P. and Badanagki M. (2020). Performance of Embankments on Liquefiable Soils Improved with Dense Granular Columns: Observations from Case Histories and Centrifuge Experiments. *Journal of Geotechnical and Geoenvironmental Engineering*, 146(9).
- Tiznado J.C. (2022). Centrifuge and Numerical Modeling of an Embankment on Liquefiable Soils Treated with Dense Granular Columns. *Geo-Congress 2022*, 486-494.
- Zou Y.X., Zhang J.M. and Wang R. (2020). Seismic analysis of stone column improved liquefiable ground using a plasticity model for coarse-grained soil. *Computers and Geotechnics*, 125.
- Pham T.A. and Dias D. (2021). 3D numerical study of the performance of geosynthetic-reinforced and pile-supported embankments. *Soils and Foundations*, 61(5), 1319-1342.
- Das A.K. and Deb K. (2018). Experimental and 3D Numerical Study on Time-Dependent Behavior of Stone Column-Supported Embankments. *International Journal of Geomechanics*, 18(4).
- Ng K.S. and Tan S.A. (2014). Nonlinear Behaviour of an Embankment on Floating Stone Columns. *Geomechanics and Geoengineering*, 10(1), 30-44.
- United States Bureau of Reclamation (USBR). (1987). Design of Small Dams. United States Bureau of Reclamation, Washington D.C., 860.
- Aminjavaheri A., Karam M. (2014). Application of Shear Keys to Improve the Slope Stability of Earth Dams on Weak Alluvial Foundations. *Soil Behavior and Geomechanics*, 642–650.
- Kaniraj S.R., Abdullah H. (1993). Effect of berms and tension crack on the stability of embankments on soft soils. *Soils Foundations*, 33(4), 99–107.
- Araya B.B. (2000). Effects of berms on the factor of safety of an embankment. Doctoral dissertation, University of Louisville, Louisville, KY.
- Federal Emergency Management Agency (FEMA) (2015). Evaluation and monitoring of seepage and internal erosion. Federal Emergency Management Agency, 295.
- Fu, P., S. M. Johnson and C. R. Carrigan (2013). An explicitly coupled hydro-geomechanical model for simulating hydraulic fracturing in arbitrary discrete fracture networks. *International Journal for Numerical and Analytical Methods in Geomechanics* 37(14): 2278-2300.
- Settgast, R. R., P. Fu, S. D. C. Walsh, J. A. White, C. Annavarapu and F. J. Ryerson (2016). A fully coupled method for massively parallel simulation of hydraulically driven fractures in 3 - dimensions. *International Journal for Numerical and Analytical Methods in Geomechanics* 41(5): 627-653.
- Wang R., Zhang J.M. and Wang G. (2014). A unified plasticity model for large post-liquefaction shear deformation of sand. *Computers and Geotechnics* 59: 54-66.
- Wang R.X. (2020). Research on fluid-solid coupling analysis and visualization method for large-scale geotechnical engineering problems [D]. Tsinghua University. (in Chinese).
- Yu J.K., Wang R.X., Wang R., Zhang J.M., Sun J. L. and Wang Y.C. (2023). High performance dynamic elastoplastic solid-fluid coupled analysis of ultra large underground structural system in liquefiable site [J/OL].China Civil Engineering Journal. (in Chinese).
- Liu H.X., Zhang J.M., Zhang X. and Wang R. (2020). Seismic performance of block-type quay walls with liquefiable calcareous sand backfill. *Soil Dynamics and Earthquake Engineering* 132.
- Zhu T., Wang R. and Zhang J.M. (2021). Effect of nearby ground structures on the seismic response of underground structures in saturated sand. *Soil Dynamics and Earthquake Engineering* 146.

- Li Y.Y., Luo C., Zhang J.M., Liu F. and Wang R. (2022). Rayleigh Wave-Shear Wave Coupling Mechanism for Large Lateral Deformation in Level Liquefiable Ground. *Computers and Geotechnics* 143.
- Qu X.Q., Wang R., Zhang J.M. and He B. (2023). Influence of Soil Plug on the Seismic Response of Bucket Foundations in Liquefiable Seabed. *Journal of Marine Science and Engineering* 11(3).
- Wang R., Fu P.C. and Zhang J.M. (2016). Finite element model for piles in liquefiable ground. *Computers and Geotechnics* 72: 1-14.



PREDICTIVE MODEL FOR SEISMIC DISPLACEMENTS OF A GENERAL FLEXIBLE SLIDING BLOCK IN NEAR-FAULT REGION

Xiang Chenlin¹, Huang Dongliang², Zhang Yingbin¹ & Zhao Lianheng²

¹ Southeast Jiaotong University, Chengdu, China, xiangchenlin@my.swjtu.edu.cn

² Central South University, Changsha, China

Abstract: The use of Newmark displacement to evaluate the seismic performance of earth slopes has been widely accepted in geotechnical engineering. With the occurrence of near-fault seismic events in recent years, it has been found that vertical ground motions with large peak ground acceleration are generated in the near-fault areas. This phenomenon has not been fully addressed in traditional coupled analysis. To evaluate the seismic performance of earth slopes in near-fault areas, a general flexible sliding block model has been proposed, which can simultaneously consider the vertical and horizontal ground motions. Based on the proposed method, an empirical earthquake-induced permanent displacement prediction model was established. 318 pulse-like ground motions from 50 earthquake events with magnitudes 5-8 were selected. The proposed predictive model is a function of the maximum seismic coefficient-time history (k_{max}), maximum velocity coefficient of velocity-time history of the k -time history (k_{v-max}), yield acceleration (k_y), the spectral acceleration for a flexible sliding block with $1.5T_s$ ($S_a(1.5T_s)$), and period ratio (ratio of the natural period of the slope to the mean period of input motion, T_s/T_m). The dynamic response (k_{max} and k_{v-max}) was represented by two different functions. The proposed model has been proven to be feasible and more accurate in comparison with existing models. The results reveal that it can provide a more practical reference for probabilistic seismic demand analyses of flexible slope failure in the near-fault region.

1. Introduction

In recent years, a series of strong seismic events (1994 Northridge earthquake, 1999 Chi-Chi earthquake 2008 Wenchuan earthquake and 2018 Hualien earthquake et al.) has gradually made people realize that near-fault pulse-like ground motions cause significantly more damage to geotechnical structures than far-field ground motions. Some studies have shown that near-fault ground shaking may typically involve two features: (1) have the potential to produce intense vertical ground motions (Bozorgnia et al., 1995; Harrington and Liel, 2016; Li et al., 2007), and (2) have a correlation between landslide distribution and fault geometry (Chigira et al., 2010; Dai et al., 2011; Gorum et al., 2011; Xu et al., 2015). Therefore, the stability of slopes near faults needs to be further studied.

Permanent displacement estimation is an important approach for studying the stability of slope when considering earthquakes (Li et al., 2022, 2020; Macedo et al., 2020; Rathje and Antonakos, 2011). There are many methods used to evaluate the stability of seismic slopes, among which the Newmark sliding block method is widely used due to its simplicity and accuracy (Song et al., 2021). It is mainly divided into rigid sliding block, decoupled and coupled analysis. The rigid sliding block analysis was proposed by Newmark (1965) for evaluating brittle and shallow slope failures. In order to more accurately describe the permanent displacement

of seismic slopes, Rathje and Bray (1999) proposed flexible sliding block analysis with considering the deformation if the sliding block. With the increase in the number of near-fault ground motions, some studies concluded that vertical ground motion has effect on slope stability based on brittle and shallow landslides, however, few studies investigate the effect of vertical ground motions on the deep landslides. With advanced engineering constructions, analyzing the stability of the slope in a designated area became necessary in near-fault earthquakes prone areas. For convenience and accuracy, a predictive displacement model is proposed.

In this study, a general flexible sliding model was proposed to consider the vertical ground motion in near fault area. Based on proposed sliding model, a new predictive displacmenet model was developed, in which the adopted parameters could focus more on velocity pulse characteristic of pulse-like ground motion. In the proposed model, the predictive displacement is a function of PGA, PGV, T_m and T_s at small period ratios ($0 < T_s / T_m \leq 2.4$). At larger period ratios ($2.4 < T_s / T_m \leq 7.5$), it is a function of $S_a(1.5T_s)$, PGV, T_m and T_s .

The predictive model for the displacement of a flexible sliding system could be obtained using altered period ratios, which can be used in stability analysis of slope for probabilistic seismic hazard analysis.

2. Generalized Coupled displacement database

2.1 Near-fault Ground Motion

Many researchers have contributed to the identification and extraction of near-fault pulse ground motion (Chang et al., 2019, 2016; Shahi and Baker, 2014; Zhai et al., 2013). In this study, the Chang's algorithm (Chang et al., 2016) was used to identify the pulse-like ground motions. It mainly includes two criteria: (1) the peak ground velocity (PGV) greater than 30 cm/s, and (2) pulse indicator (E_p) of ground motion exceeding 0.34. 318 pulse-like ground motions were classified as pulse-like from ground motion database. Due to varying characteristics of pulse ground motion in different directions, all pulse motions were rotated to the direction of maximum pulse indicator. The distribution of peak ground acceleration (PGA) and PGV as shown in Figure 1.

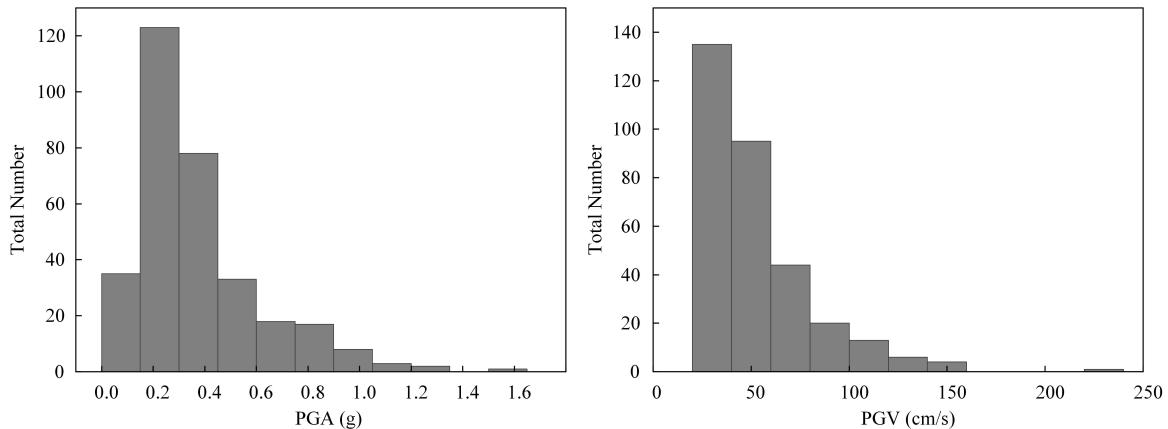


Figure 1. The distribution of 318 pulse-like ground motion records.

2.2 Generalized Flexible Sliding System

2.2.1 Critical acceleration

The Newmark sliding block method is widely used for evaluating the stability of earthquake-induced slopes. In traditional coupled analysis, the critical acceleration of sliding system is a constant. In fact, the critical acceleration of slopes should be a variable not a constant during the earthquake (Zhang et al., 2021). In this study, the critical acceleration becomes a time-varying variable by considering the vertical ground motion (Figure 2a). According to the equilibrium of forces, the critical acceleration can be obtained as follows:

$$k_y = \tan(\varphi - \alpha) + a_v \tan(\varphi - \alpha) + \frac{c}{\gamma H (\cos^2 \alpha + \sin \alpha \cos \alpha \tan \varphi)} \quad (1)$$

where φ represents the friction angle of the shear surface, α represents slope angle, c represents the cohesion, γ represents the weight of the sliding block, and H represents the height of the block.

2.2.2 Coupled sliding analysis

The displacement of the single degree of freedom system is expressed by the modal coordinates (Rathje and Bray, 1999), as follows:

$$u(y, t) = \sum_{i=1}^n \phi_i(y) Y_i(t) \quad (1)$$

where Φ_i represents the i -th mode shape of the sliding block, Y_i represents the modal coordinate corresponding to the i -th mode shape, and n represents the number of considered modes. The mode shape function has different analytical expressions. In this study, the mode shape function proposed by Idriss and Seed (1968) for calculating the response of sediment soils in earthquakes is adopted. The mode shape function is as follows:

$$\phi_i(y) = \cos\left[\frac{(2i-1)\pi y}{2H}\right] \quad (2)$$

When the sliding block is in a state of relative rest with the base, the dynamic differential equation of the sliding system can be obtained based on shear beam theory as follows:

$$\ddot{Y}_1 + 2\lambda\omega_1\dot{Y}_1 + \omega_1^2 Y_1 = -\frac{L_1}{M_1} a \quad (3)$$

where λ represents the material damping ratio; ω_1 represents the circular frequency of the sliding system; L_1 represents the distribution of input motion along the height of the sliding block, and M_1 represents the distribution of generalized mass along the height of the sliding block.

When the block begins to slide, there will be a relative displacement s between the block and the base (Figure 3). Unlike the rigid sliding block model, the driving force includes not only the input load but also the load associated with the sliding displacement. Therefore, the excitation on the right side of the motion differential equation becomes $\ddot{s}\cos\alpha + a$:

$$\ddot{Y}_1 + 2\lambda\omega_1\dot{Y}_1 + \omega_1^2 Y_1 = -\frac{L_1}{M_1}(\ddot{s}\cos\alpha + a) \quad (4)$$

where \ddot{s} refers to the relative acceleration between the sliding block and the base. The verification of the proposed method is shown in Figure 2b. It indicates the general flexible sliding block model proposed is correct.

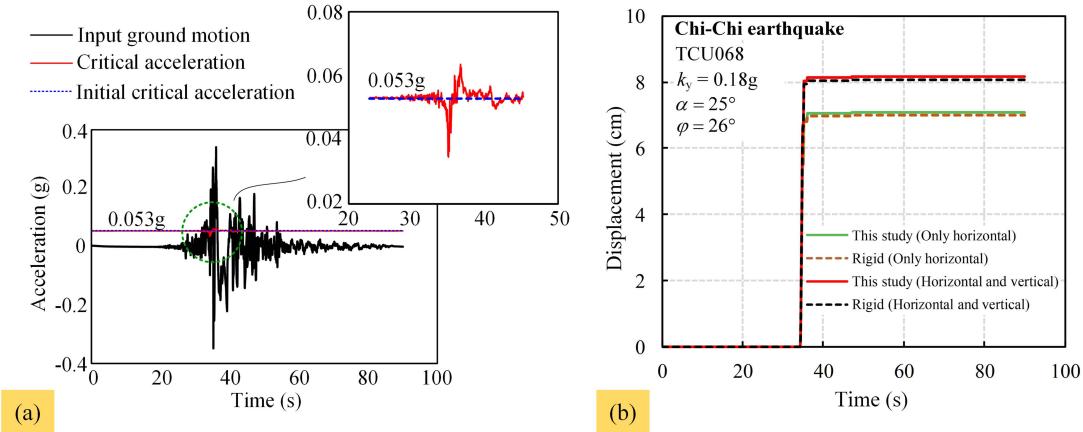


Figure 2. (a) The variation critical acceleration of sliding block model; (b) Comparison of the permanent displacement computed by the proposed general flexible and rigid sliding block model

Based on previous studies (Bray and Travasarou, 2007; Jafarian and Lashgari, 2016; Lashgari et al., 2021, 2018; Xiang et al., 2023), in this study, the permanent-displacement database of the general flexible sliding system was generated with different yield accelerations ($k_y = 0.02, 0.05, 0.1, 0.2, 0.3, \text{ and } 0.4 \text{ g}$) and fundamental periods of the slope ($T_s = 0, 0.5, 1, 1.5, 2, 2.5, 3, 3.5, 4, 4.5, 5, 5.5, \text{ and } 6 \text{ s}$). A total of 9508 effective displacements were used to establish the displacement model.

3. Prediction Model for Permanent Displacement

The selection of optimum ground motion intensity measures is the key step in constructing a predictive model for the seismic displacements of slopes. Based on previous study (Xiang et al., 2023), comparing the distributions of correlation coefficient between different parameters and permanent displacement, the parameter ($k_y^2/k_{\max} k_{v\max}$) exhibits the strongest correlation with permanent displacement. Therefore, this parameter is selected in this study to establish a functional expression for the relationship with permanent displacement. In order to better predict permanent displacement using the parameter ($k_y^2/k_{\max} k_{v\max}$) the period ratios were divided into 25 subclasses, and the relationship between the correlation coefficient and the period was plotted (Figure 3). The nonlinear fitting function and its standard deviation as follows:

$$\ln(D/k_y) = A \ln(k_y^2/k_{\max} k_{v\max})^2 + B \ln(k_y^2/k_{\max} k_{v\max}) + C + \sigma \quad (5)$$

$$\sigma_{\ln(D/k_y)} = -0.0051(T_s/T_m)^3 + 0.0487(T_s/T_m)^2 - 0.0799(T_s/T_m) + 0.8048 \quad (6)$$

where D is the permanent displacement of the flexible sliding block in centimeters; g is the gravitational acceleration; A , B , and C are the coefficients to be determined; and σ is standard deviation of the predictive model. Through an examination of the undetermined coefficients for each subclass, it was discovered that these coefficients exhibited a certain relationship with the period ratio and can be represented by the following equation:

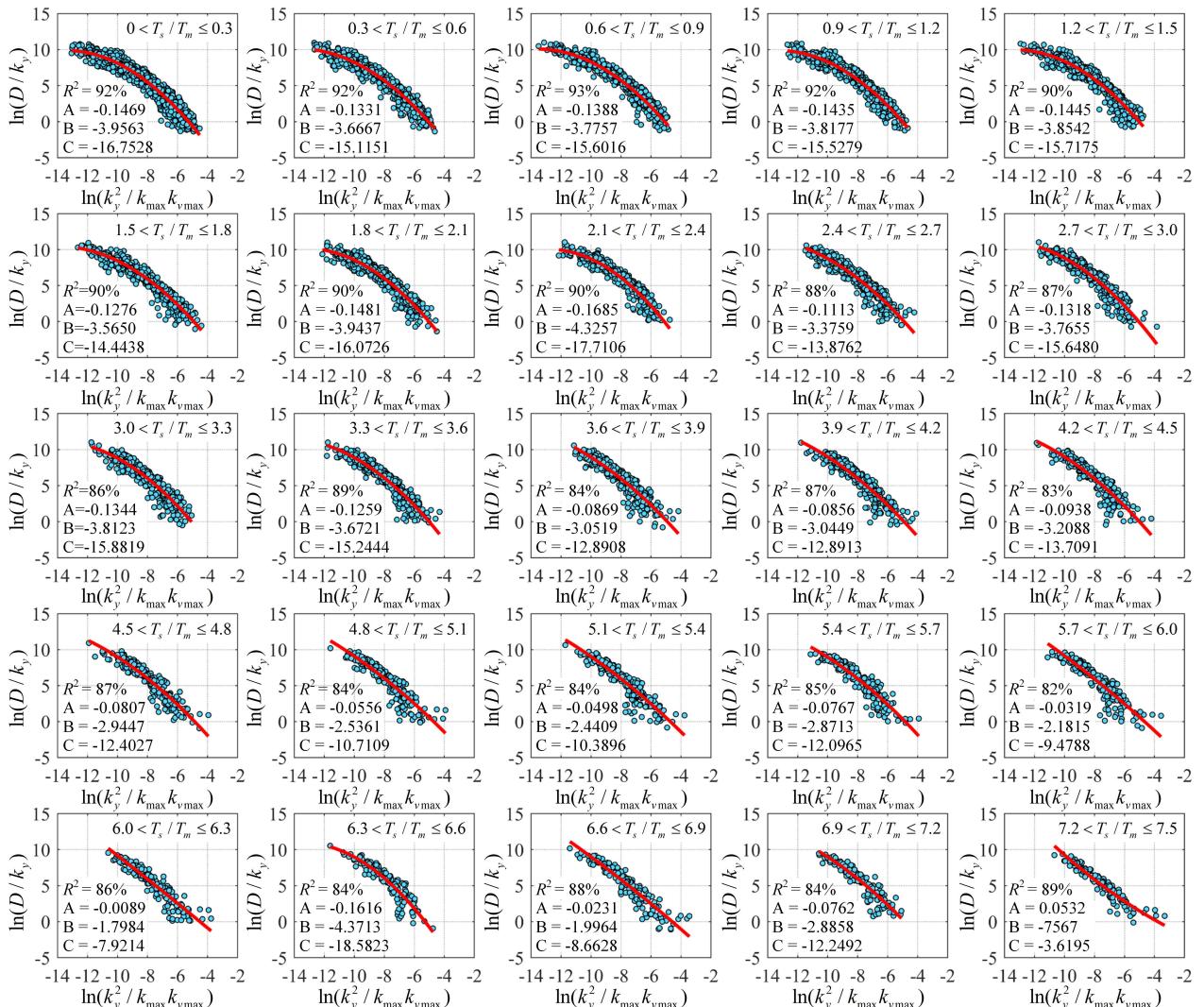


Figure 3. Variation of D/k_y versus $k_y/k_{\max} \times k_y/k_{v\max}$ under different period ratios.

$$\begin{aligned}
 A &= A_{01}(T_s/T_m)^2 + A_{02}(T_s/T_m) + A_{03} \\
 B &= B_{01}(T_s/T_m)^2 + B_{02}(T_s/T_m) + B_{03} \\
 C &= C_{01}(T_s/T_m)^2 + C_{02}(T_s/T_m) + C_{03}
 \end{aligned} \tag{7}$$

where A_{01} , A_{02} , A_{03} , B_{01} , B_{02} , B_{03} , C_{01} , C_{02} , and C_{03} are the undetermined coefficients in all ranges of period ratios. The values of these coefficients are listed in Table 1.

Table 1. Values of undetermined coefficients for estimating permanent displacement.

Constant coefficients								
A			B			C		
A_{01}	A_{02}	A_{03}	B_{01}	B_{02}	B_{03}	C_{01}	C_{02}	C_{03}
0.0020	0.0035	-0.1484	0.0373	0.0011	-3.8874	0.1441	-0.0100	-15.9919

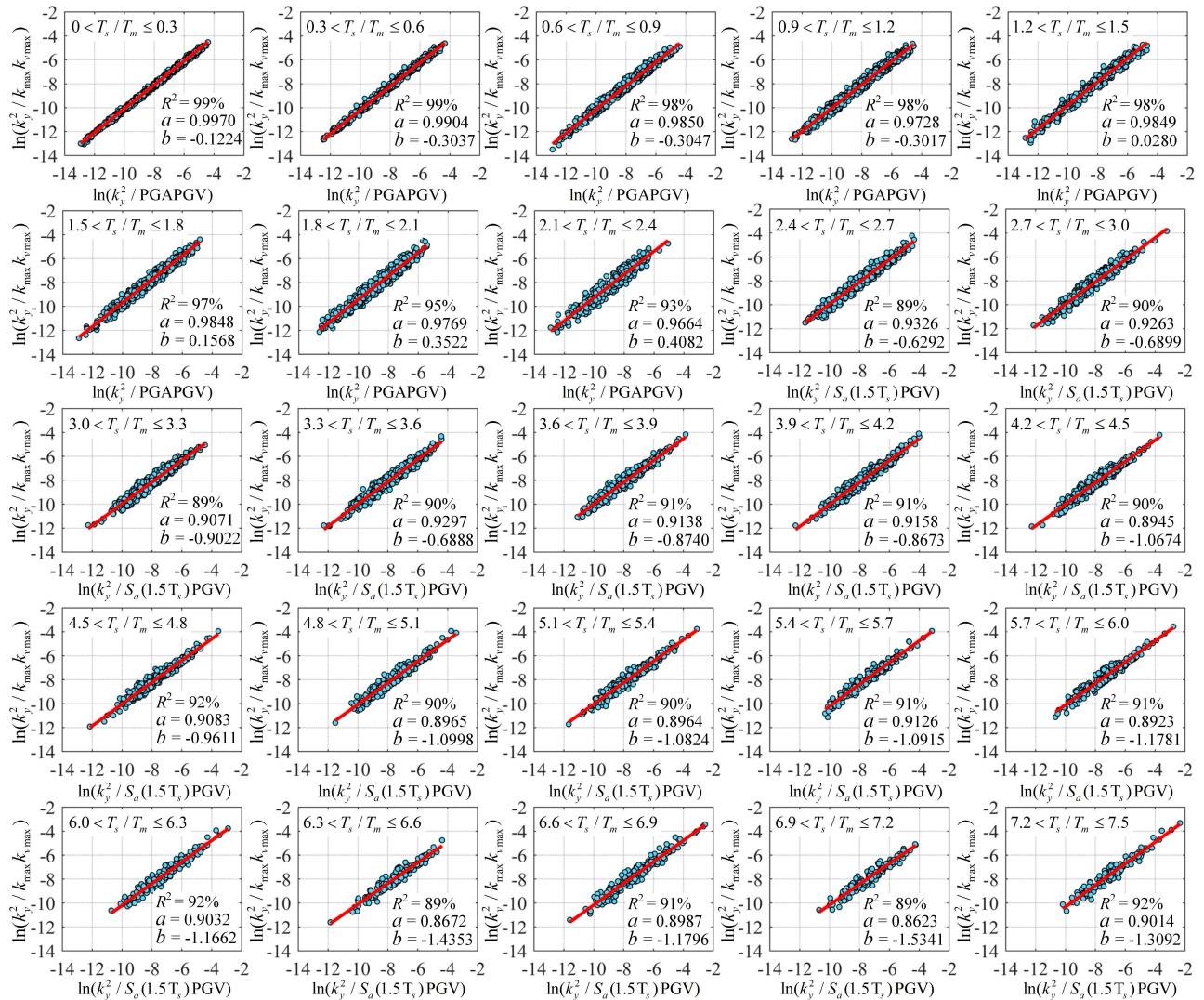


Figure 4. Variation of $k_y/k_{\max} \times k_y/v_{\max}$ versus $k_y/\text{PGA} \times k_y/\text{PGV}$ and $k_y^2/S_a(1.5T_s)\text{PGV}$ under different period ratios.

From the permanent displacement prediction model, it can be observed that, in addition to the critical acceleration, two dynamic response parameters are also required. Due to the dynamic response parameters cannot be obtained in a deterministic earthquake scenario, it is necessary to replace them with other easily predictable parameters. By analyzing the correlation coefficients between different intensity measures describing ground motion and dynamic response parameters, it was found that under small period ratio ($0 < T_s / T_m \leq 2.4$), where the sliding block exhibits rigid characteristics, the dynamic response parameter k_{\max} and $k_{v\max}$ can be directly replaced with PGA and PGV as shown in Eq.8. When the period ratio exceeds 2.4, the dynamic response parameters ($k_y^2/k_{\max}k_{v\max}$) exhibit a linear relationship with intensity parameters ($k_y^2/S_a(1.5T_s)PGV$), as shown in Figure 4. The functional expression for the linear relationship is as follows:

$$\ln(k_y^2/k_{\max}k_{v\max}) = a \cdot \ln(k_y^2/PGAPGV) + b + \sigma \quad 0 < T_s / T_m \leq 2.4 \quad (8)$$

$$\ln(k_y^2/k_{\max}k_{v\max}) = a \ln(k_y^2/S_a(1.5T_s)PGV) + b + \sigma \quad 2.4 < T_s / T_m \leq 7.5 \quad (9)$$

$$\sigma_{\ln(k_y^2/k_{\max}k_{v\max})} = 0.1272(T_s / T_m) + 0.0835 \quad 0 < T_s / T_m \leq 2.4 \quad (10)$$

$$\sigma_{\ln(k_y^2/k_{\max}k_{v\max})} = 0.0067(T_s / T_m)^2 - 0.0649(T_s / T_m) + 0.4586 \quad 2.4 < T_s / T_m \leq 7.5 \quad (11)$$

where $S_a(1.5T_s)$ is the spectral acceleration for a flexible sliding block with $1.5T_s$ in g; a and b are the coefficients to be determined; and σ is standard deviation. Through an examination of the undetermined coefficients for each subclass, it was discovered that these coefficients exhibited a certain relationship with the period ratio and can be represented by the following equation:

$$\begin{aligned} a &= a_{01}(T_s / T_m)^2 + a_{02}(T_s / T_m) + a_{03} \\ b &= b_{01}(T_s / T_m)^2 + b_{02}(T_s / T_m) + b_{03} \end{aligned} \quad (12)$$

where a_{01} , a_{02} , b_{01} , b_{02} , and b_{03} are the undetermined coefficients in all ranges of period ratios. The values of these coefficients are listed in Table 2.

Table 2. Values of undetermined coefficients for estimating parameters of dynamic response.

T_s / T_m	Constant coefficient					
	a_{01}	a_{02}	a_{02}	b_{01}	b_{02}	b_{03}
$0 < T_s / T_m \leq 2.4$	0.0020	-0.0330	1.0167	0.2554	-0.3440	-0.1327
$2.4 < T_s / T_m \leq 7.5$				0.0048	-0.2041	-0.1381

4. Discussion

To further verify the validity of the predictive model in considering vertical ground motions, the predicted permanent displacements and the displacements calculated using proposed sliding model are compared. The prediction model proposed by Song and Rodriguez-Marek (2015) was selected for comparison is to emphasize the significance of considering the vertical ground motions in predictive model. The permanent displacements estimated by the generalized flexible sliding system analysis were plotted against the displacements predicted by the predictive model as shown in Figure 5. The red dashed line represents the predicted permanent displacement, which is the same as the displacement calculated using the sliding system method. The distance of between the blue data points and the red dashed line is more smller, the more accurate the prediction. In this study, the Pearson Correlation Coefficient (PCC) is 93%. Moreover, the PCC values for Song and Rodriguez-Marek's model is 83%. It can be concluded that the vertical ground motions has effect on the permanent displacement. This means when assess the stability of slope in near fault area, the vertical ground motion need to be considered.

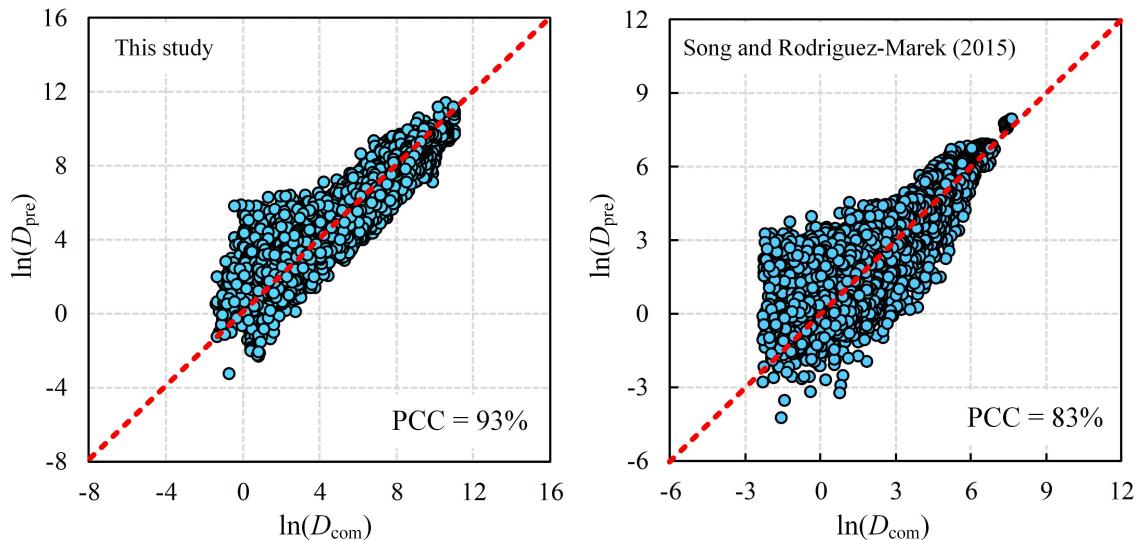


Figure 5. Comparison of the proposed predictive model with existing model.

5. Conclusion

This paper proposed a new predictive model for seismic slope based on a generalized flexible sliding system method in near-fault area. The results showed that the dynamic response parameters have a high correlation with displacement. At a small period ratio ($0 < T_s / T_m \leq 2.4$), the dynamic response parameters ($k_y^2/k_{max}k_{v-max}$) can be replaced by by PGA and PGV. When the period ratio exceed 2.4, the parameter ($k_y^2/Sa(1.5T_s)PGV$) has a high correlation with he dynamic response parameters ($k_y^2/k_{max}k_{v-max}$) compared with the parameter($k_y^2/PGAPGV$). The proposed model has been proven to be feasible and convenient to employ. It can provide a more practical reference for probabilistic seismic demand analyses of flexible slope failure in the near-fault region.

Acknowledgements

This study has received financial support from the National Natural Science Foundation of China (41977213, 51878668, 52278372); the National Ten Thousand Talent Program for Young Top-notch Talents; the regional project (R110121H01092), the Hunan Province Science Fund for Distinguished Young Scholars (No. 2021JJ10063), the China Scholarship Council (CSC, Nos. 202106370143, 202107000093) and China Road and Bridge Group project (P2220447). The financial supports are gratefully acknowledged.

References

- Bozorgnia, Y., Niazi, M., Campbell, K.W., 1995. Characteristics of Free-Field Vertical Ground Motion during the Northridge Earthquake. *Earthquake Spectra* 11, 515–525. <https://doi.org/10.1193/1.1585825>
- Bray, J.D., Travasarou, T., 2007. Simplified procedure for estimating earthquake-induced deviatoric slope displacements. *Journal of Geotechnical and Geoenvironmental Engineering* 133, 381–392. [https://doi.org/10.1061/\(ASCE\)1090-0241\(2007\)133:4\(381\)](https://doi.org/10.1061/(ASCE)1090-0241(2007)133:4(381))
- Chang, Z., De Luca, F., Goda, K., 2019. Automated classification of near-fault acceleration pulses using wavelet packets. *Computer-Aided Civil and Infrastructure Engineering* 34, 569–585. <https://doi.org/10.1111/mice.12437>
- Chang, Z., Sun, X., Zhai, C., Zhao, J.X., Xie, L., 2016. An improved energy-based approach for selecting pulse-like ground motions. *Earthquake Engineering and Structural Dynamics* 45, 2405–2411. <https://doi.org/10.1002/eqe.2758>
- Chigira, M., Wu, X., Inokuchi, T., Wang, G., 2010. Landslides induced by the 2008 Wenchuan earthquake, Sichuan, China. *Geomorphology* 118, 225–238. <https://doi.org/10.1016/j.geomorph.2010.01.003>
- Dai, F.C., Xu, C., Yao, X., Xu, L., Tu, X.B., Gong, Q.M., 2011. Spatial distribution of landslides triggered by the 2008 Ms 8.0 Wenchuan earthquake, China. *Journal of Asian Earth Sciences* 40, 883–895. <https://doi.org/10.1016/j.jseaes.2010.04.010>

- Gorum, T., Fan, X., van Westen, C.J., Huang, R.Q., Xu, Q., Tang, C., Wang, G., 2011. Distribution pattern of earthquake-induced landslides triggered by the 12 May 2008 Wenchuan earthquake. *Geomorphology* 133, 152–167. <https://doi.org/10.1016/j.geomorph.2010.12.030>
- Harrington, C.C., Liel, A.B., 2016. Collapse assessment of moment frame buildings, considering vertical ground shaking: Collapse of Moment Frame Buildings Considering Vert Ground Shaking. *Earthquake Engng Struct. Dyn.* 45, 2475–2493. <https://doi.org/10.1002/eqe.2776>
- Idriss, I.M., Seed, H.B., 1968. Seismic Response of Horizontal Soil Layers. *Journal of the Soil Mechanics and Foundations Division* 94, 1003–1031. <https://doi.org/10.1061/JSFEAQ.0001163>
- Jafarian, Y., Lashgari, A., 2016. Simplified procedure for coupled seismic sliding movement of slopes using displacement-based critical acceleration. *International Journal of Geomechanics* 16, 1–16. [https://doi.org/10.1061/\(ASCE\)GM.1943-5622.0000578](https://doi.org/10.1061/(ASCE)GM.1943-5622.0000578)
- Lashgari, A., Jafarian, Y., Haddad, A., 2021. Predictive model for seismic sliding displacement of slopes subjected to pulse-like motions. *Bulletin of Engineering Geology and the Environment* 6563–6582. <https://doi.org/10.1007/s10064-021-02314-2>
- Lashgari, A., Jafarian, Y., Haddad, A., 2018. Predictive model for seismic sliding displacement of slopes based on a coupled stick-slip-rotation approach. *Engineering Geology* 244, 25–40. <https://doi.org/10.1016/j.enggeo.2018.07.017>
- Li, C., Wang, G., He, J., Wang, Y., 2022. A novel approach to probabilistic seismic landslide hazard mapping using Monte Carlo simulations. *Engineering Geology* 301, 106616. <https://doi.org/10.1016/j.enggeo.2022.106616>
- Li, D.Q., Wang, M.X., Du, W., 2020. Influence of spatial variability of soil strength parameters on probabilistic seismic slope displacement hazard analysis. *Engineering Geology* 276, 105744. <https://doi.org/10.1016/j.enggeo.2020.105744>
- Li, X., Dou, H., Zhu, X., 2007. Engineering characteristics of near-fault vertical ground motions and their effect on the seismic response of bridges. *Earthq. Eng. Eng. Vib.* 6, 345–350. <https://doi.org/10.1007/s11803-007-0723-5>
- Macedo, J., Candia, G., Lacour, M., Liu, C., 2020. New developments for the performance-based assessment of seismically-induced slope displacements. *Engineering Geology* 277, 105786. <https://doi.org/10.1016/j.enggeo.2020.105786>
- Newmark, N.M., 1965. Effects of earthquakes on dams and embankments. *Geotechnique* 15, 139–160. <https://doi.org/10.1680/geot.1965.15.2.139>
- Rathje, E.M., Antonakos, G., 2011. A unified model for predicting earthquake-induced sliding displacements of rigid and flexible slopes. *Engineering Geology* 122, 51–60. <https://doi.org/10.1016/j.enggeo.2010.12.004>
- Rathje, E.M., Bray, J.D., 1999. An examination of simplified earthquake-induced displacement procedures for earth structures. *Canadian Geotechnical Journal* 36, 72–87. <https://doi.org/10.1139/t98-076>
- Shahi, S.K., Baker, J.W., 2014. An efficient algorithm to identify strong-velocity pulses in multicomponent ground motions. *Bulletin of the Seismological Society of America* 104, 2456–2466. <https://doi.org/10.1785/0120130191>
- Song, J., Rodriguez-Marek, A., 2015. Sliding displacement of flexible earth slopes subject to near-fault ground motions. *Journal of Geotechnical and Geoenvironmental Engineering* 141. [https://doi.org/10.1061/\(ASCE\)GT.1943-5606.0001233](https://doi.org/10.1061/(ASCE)GT.1943-5606.0001233)
- Song, J., Rodriguez-Marek, A., Feng, T., Ji, J., 2021. A generalized seismic sliding model of slopes with multiple slip surfaces. *Earthquake Engineering and Structural Dynamics* 50, 2595–2612. <https://doi.org/10.1002/eqe.3462>
- Xiang, C., Zhang, Y., Huang, D., Ueda, K., Fu, H., Liu, J., Zhao, L., 2023. Predictive model for seismic displacements of flexible sliding block subjected to near-fault pulse-like ground motions. *Engineering Geology* 320, 107134. <https://doi.org/10.1016/j.enggeo.2023.107134>
- Xu, C., Xu, X., Shyu, J.B.H., 2015. Database and spatial distribution of landslides triggered by the Lushan, China Mw 6.6 earthquake of 20 April 2013. *Geomorphology* 248, 77–92. <https://doi.org/10.1016/j.geomorph.2015.07.002>
- Zhai, C., Chang, Z., Li, S., Chen, Z.Q., Xie, L., 2013. Quantitative identification of near-fault pulse-like ground motions based on energy. *Bulletin of the Seismological Society of America* 103, 2591–2603. <https://doi.org/10.1785/0120120320>
- Zhang, Y., Xiang, C., Yu, P., Zhao, L., Zhao, J.X., Fu, H., 2021. Investigation of permanent displacements of near - fault seismic slopes by a general sliding block model. *Landslides* 19, 187–197. <https://doi.org/10.1007/s10346-021-01736-z>

DYNAMIC RESPONSE OF THE PUNTA NEGRA DAM UNDER THE 2021 SAN JUAN EARTHQUAKE

F. Zabala¹, N.G. Sánchez N.² & G.S. Zabala³

¹ Earthquake Engineering Research Institute, National University of San Juan, Argentina,
fzabala@unsj.edu.ar

² Earthquake Engineering Research Institute, National University of San Juan

³ Earthquake Engineering Research Institute, National University of San Juan

Abstract: The response of a 118 m CFRD dam to the 2021 San Juan earthquake in Argentina is analysed in this paper. The crest and mid-height acceleration records of the maximum height cross section are compared with the response of a two-dimensional Material Point Model (MPM) to the base accelerogram. The material behaviour was simulated using the Sanisand model (Dafalias & Manzari, 2004) calibrated with drained triaxial tests. The results show that despite the complex three-dimensional response of the dam, the two-dimensional model is able to reproduce the order of the response accelerations very well. The model response after the intense part of the earthquake has rather long period oscillations that are not present in the actual crest record, and this was interpreted as a lack of energy dissipation of the material constitutive model at small strains. The addition of a small amount of mass-proportional damping improved the model response results compared to the actual records. Additional model results such as vertical crest displacement, equivalent plastic shear strain contour lines, and pore pressure contour lines are also presented.

1. Introduction

The Punta Negra Dam (PN Dam) is a CFRD dam situated in the central south of the San Juan province in western Argentina, near the Andes. Constructed with well-graded gravels, it has a crest height of 118 meters above the foundation level and a length of more than 750 meters. The province of San Juan has a high seismic activity. Notable earthquakes include the Mw 7.0 earthquake of January 15, 1944, which caused 8,000 casualties in the city of San Juan. The PN Dam is located approximately 30 km upstream from the city of San Juan, while the Ullum Dam, a clay core earth dam, is located downstream between the PN Dam and the city (Figure 1). In the event of a collapse of the PN Dam, overpassing can cause the Ullum Dam to collapse too, leading to a catastrophic event. On January 18, 2021, an earthquake of magnitude 6.4 occurred, with an epicenter 39 km from the PN Dam and a depth of 8 km.

The dam is instrumented with five accelerometers, which recorded the event at the site and the response of the structure. Figures 2 indicates the location of the instruments in a satellite view of the dam. The maximum height cross section is shown in Figure 3. The dam's upstream zone reached rock level, allowing for the concrete face plinth to be anchored in the rock. A foundation zone of alluvial gravel remain untreated.

The recorded accelerograms at a rock zone near the base (accelerometer PP in Figure 2), mid-height (MP) and crest (CC) in the transverse direction are displayed in Figure 4, while the base response spectra are shown

in Figure 5. The seismic intensity at the site was moderate with peak accelerations of 0.14 g at the dam base and 0.47 g at the crest, in the transverse direction, resulting in an amplification factor of 3.35. The dam performed satisfactorily and showed no signs of damage.

The seismic safety of earth or rockfill dams and embankments is strongly dependent on the permanent displacements caused by earthquakes. In case of a severe earthquake, the permanent displacement pattern results from the combination of displacements caused by volumetric and shear strains distributed within the structure and those caused by the sliding of a soil mass along one or more failure surfaces. Numerical methods commonly used in practice do not take into account the phenomena of strain localisation at failure surfaces and the associated mesh dependence of the solution. Typically, non-linear finite element or finite difference codes provide an estimate of the distributed deformations and dynamic response without considering the plastic strain localisation problem. In addition, some of the numerical approaches used in practice do not consider the change in configuration caused by large displacements. To address these issues, we at the Earthquake Research Institute of the National University of San Juan have developed a Material Point Method (MPM) code named Geopart, Zabala et al (2005), for the static and dynamic simulation of geotechnical structures.



Figure 1. Location of Punta Negra dam, Ullum dam and the city of San Juan.



Figure 2. Location of accelerometers in Punta Negra dam

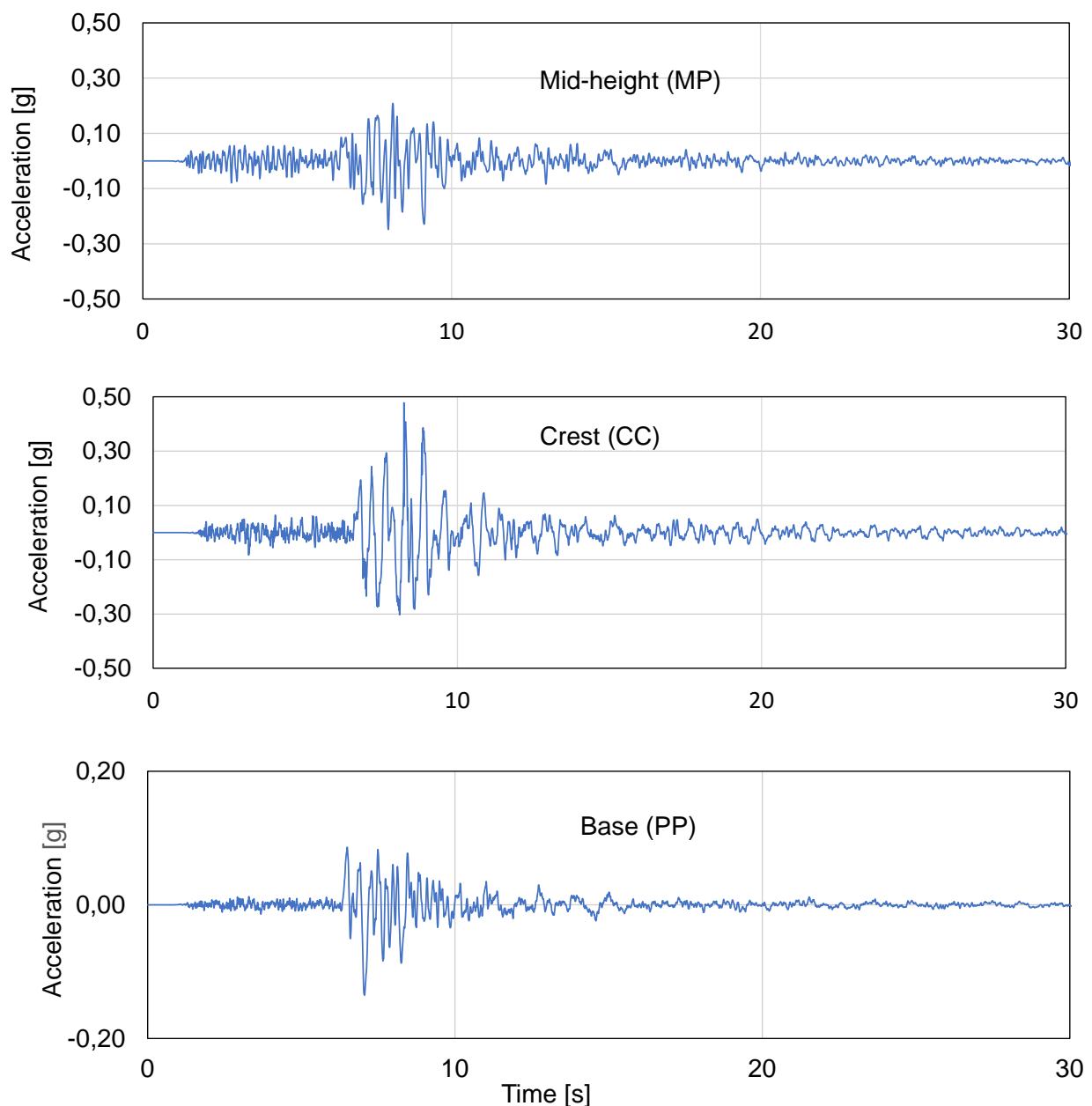
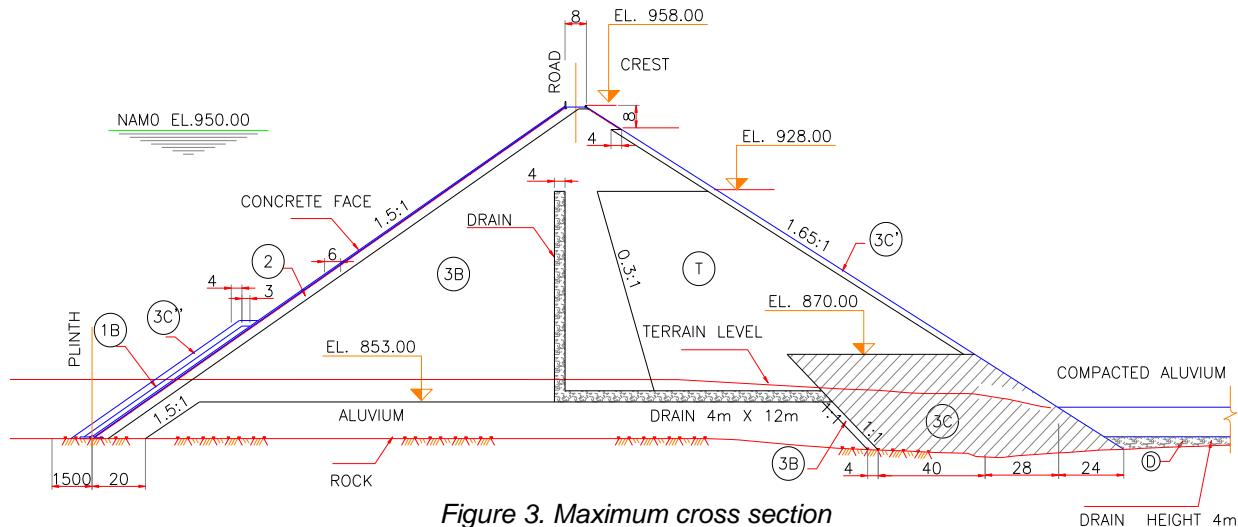


Figure 4. Acceleration records in transverse direction

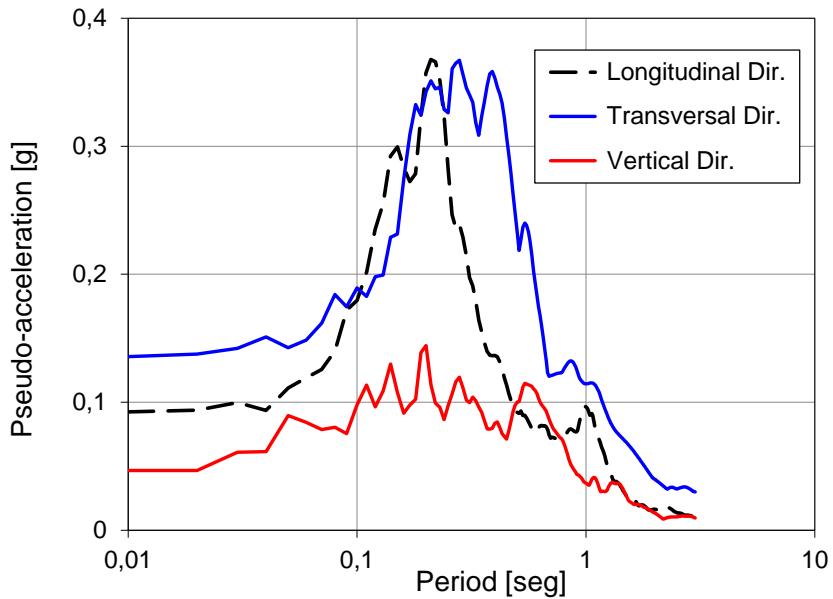


Figure 5. Base response spectra

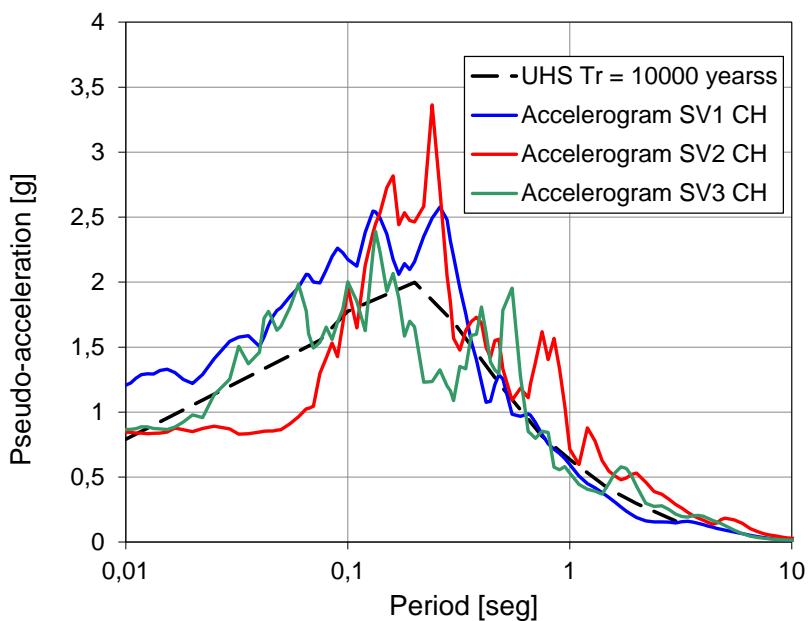


Figure 6. Uniform hazard spectra and spectra of selected movements

2. Material Point Method model

The structure was modelled using the Material Point Method with the aim of evaluating its response to extreme earthquakes, which could produce large displacements, similar to those postulated for the seismic safety assessment of the dam. Figure 6 shows the Uniform Hazard Spectra obtained for the site for a 10000 year return period and the spectra for the selected movements used for seismic safety assessment (Oldecop & Zabala, 2009). As it can be seen, the postulated peak ground acceleration is very high (0.79 g) compared to the maximum acceleration recorded near the base for the 01/18/23 earthquake.

MPM is a Lagrangian "particle mesh" numerical method (Sulsky et al 1994, 1995), in which "material points" or "particles", represent the continuum and store all the variables of the analysis,. The interaction between the particles is solved using a fixed grid or Eulerian mesh extended over the entire problem space. As the MPM does not rely on direct connections between particles, it is particularly useful for representing finite strains and large displacement problems.

The mechanical behaviour of the dam materials was simulated using the constitutive model of Dafalias & Manzari (2004) with parameters calibrated from drained triaxial tests which are detailed in Table 1. Only two different materials were considered for the analysis, a compacted well-graded gravel for the dam body, with a placing mean density of 2.4 t/m³, and an alluvial zone left in the foundation without treatment which was considered with the same parameters but with a density of 2.2 t/m³.

In order to consider the coupled hydro-mechanical behavior in the saturated zones near the dam's base, we employed a variant of the "u-p" displacement-pore pressure formulation (Zienkiewicz, 1981) that was adapted to the explicit version of MPM (Zabala & Alonso, 2010). For the saturated zone, a permeability of 10-3 m/s was considered.

Table 1. SANISAND constitutive model parameters.

Parameter		
Elasticity	G_0	50
	N	0,3
Yield surface	M	0,1
	M_c	1,722
	C	0,635
Critical state	e_0	0,25
	λ_c	0,014
	ξ	0,62
Bounding Surface	h_0	30
	c_h	0,7
	n_b	1,85
Dilatance Surface	A_0	2,1
	n_d	0,5
Fabric – Dilatance	z_{max}	4
	c_z	400

A two-dimensional plane strain model of the maximum cross-section of the dam is depicted in Figure 7 showing the two different materials considered and the saturated zone. The dam material above the downstream river level was considered unsaturated.

The mesh size varies with the height. Three superimposed hierarchical levels of mesh were considered, with the finer sizes being placed in the upper third of the dam to achieve a higher level of detail in the crest, where the higher strains and amplifications in the dynamic response of the dam are expected.

At the base of the model, the mesh has a cell size of 3 m horizontally and 2 m vertically. From one third of the height of the model, a 1.5 m x 1 m sub grid is superimposed. Finally, in the upper third, a third grid of 0.75 m x 0.5 m is added. The aspect ratio between the mesh dimensions permits to represent the upstream slope uniformly with one particle per cell at each mesh level. This option is useful for evaluating the interaction between the concrete face and the dam's body, which is not presented in this paper. Quadratic B-spline shape

functions (Steffen et al, 2008) were used for all three mesh levels. The model was initially consolidated by its own weight and under water pressure. At the time of the earthquake, the water level in the reservoir was 920.60 metres above sea level, thirty metres below the maximum normal water level.

The mesh nodes at the base were first fixed for static loads and in a second stage, for the calculation of the dynamic response, they were all connected to one node so that the displacement of all nodes of the base was equal. A Lysmer approach (Lysmer and Kuhlemeyer, 1969) with horizontal and vertical dampers connected to the node was used to consider the foundation as a semi-infinite elastic half space and to allow for the radiation of incoming waves to the foundation. The resulting damping force F_L for the single base node (Equation 1) is proportional to the shear velocity of the foundation (c_s) for the horizontal component, and to the pressure velocity of the foundation (c_p) for the vertical component.

$$\{F_L\} = -A \begin{Bmatrix} \eta_s v_{ix} \\ \eta_p v_{iy} \end{Bmatrix} \quad (1)$$

ρ = density, $\eta_s = \rho c_s$, $\eta_p = \rho c_p$

v_{ix} , v_{iy} = horizontal and vertical components of node velocity

A = base area

The recorded motion is introduced into the model by applying a force to the node proportional to the earthquake velocity as in Zhang et al. (2008).

$$\{F_E\} = -2 A \begin{Bmatrix} c_s v_{Ex} \\ c_p v_{Ey} \end{Bmatrix} \quad (2)$$

v_{Ex} and v_{Ey} are the components of the earthquake velocity history in the horizontal and vertical directions, which enter the model as shear and pressure waves, respectively.

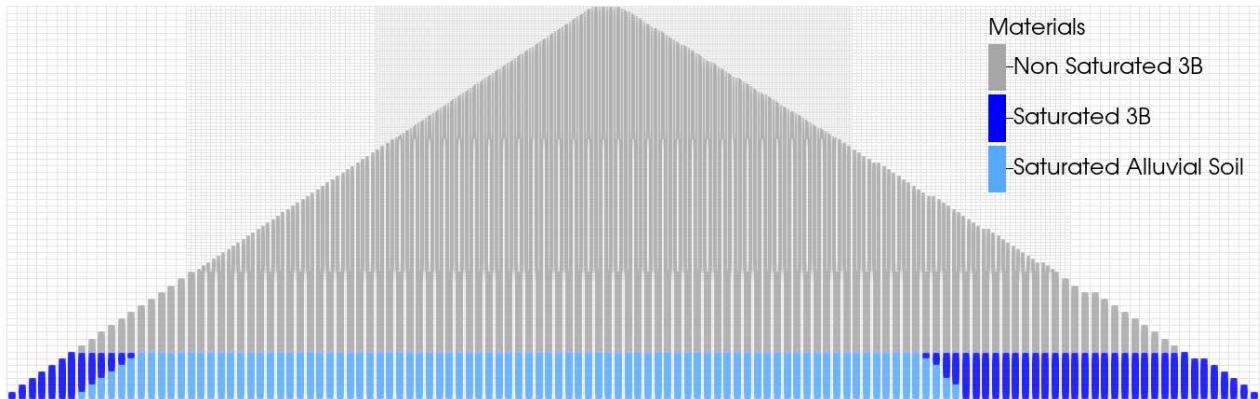


Figure 7. MPM model

3. Model response

The model response to the 2021 San Juan earthquake was first calculated without considering any additional damping. Under this condition the constitutive model provided the only mean for energy dissipation. The response accelerations at the crest of the dam are compared with the transverse acceleration records of the maximum cross section in Figure 8. Note that the acceleration record at the crest decreases rapidly after the most severe part of the earthquake while the calculated response continues to oscillate, indicating that the actual dissipation is higher. In a second analysis, Raleigh type damping proportional to mass was added. Two different damping ratios, 3% and 5% for a period of 1 second, were used to examine the influence of the damping on the response. Raleigh damping proportional to mass decreases inversely with frequency, so the effect on the model response is lesser for frequencies above 1Hz. Figure 9 shows the results of the second analysis, which appears to be more consistent with the recordings. In Figure 10, the crest record, the model response without damping and with a damping ratio of 3% are plotted between 10 and 20 seconds, showing

the better agreement of the response when damping is added. Figure 11 also compares the mid-height acceleration record with the model response for 3% and 5% damping.

Figure 12 shows the evolution of the vertical crest displacement of the model. The final calculated displacement is greater than the post-earthquake settlement, which was approximately 15 mm for the maximum cross section. Figures 13 show the line contours of the shear equivalent accumulated plastic strain (Equation 3), with quantities which are small in comparison with the usual maximum strength strains of the granular materials. In the zone near the crest, the equivalent shear plastic strain has maximum values corresponding to the maximum dynamic response and is distributed without strain localization. Figure 14 depicts the pore pressure distribution at the end of the analysis for a 3% damping ratio. The pore pressures are very small. The pore pressure ratio r_u is less than 0.10 in the zone of maximum confinement.

$$\varepsilon_{eq}^p = \sqrt{\frac{2}{3} e_{ij}^p e_{ij}^p} \quad (3)$$

ε_{eq}^p = equivalent plastic shear strain

e_{ij}^p = deviatoric plastic strain

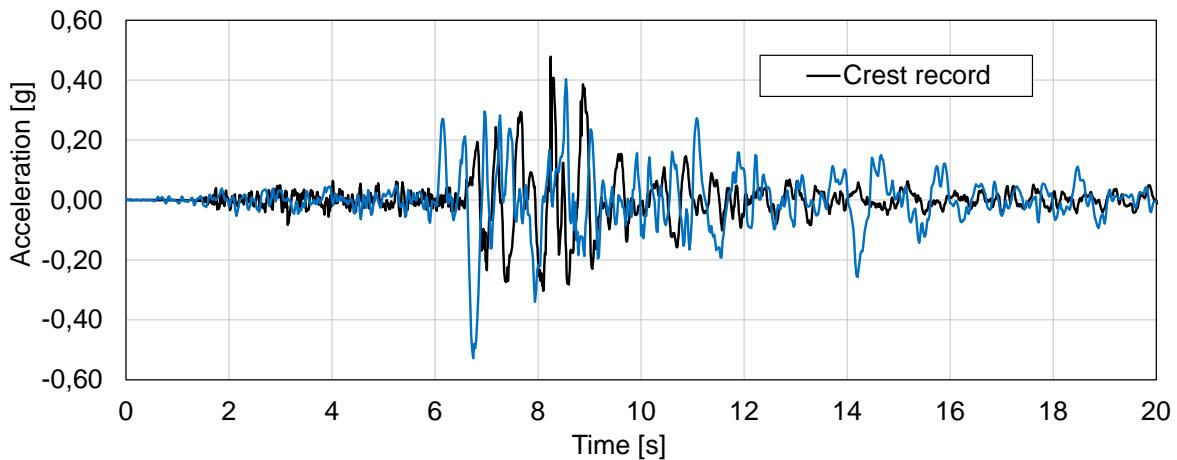


Figure 8. Comparison of crest transverse record with model response acceleration without additional damping

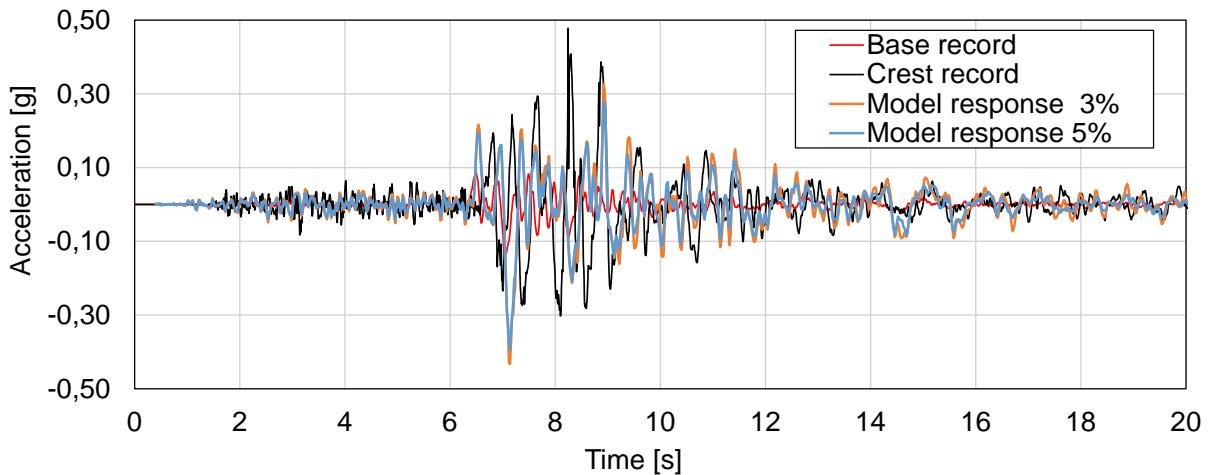


Figure 9. Comparison of crest and base transverse record with model response acceleration for damping ratio of 3% and 5%

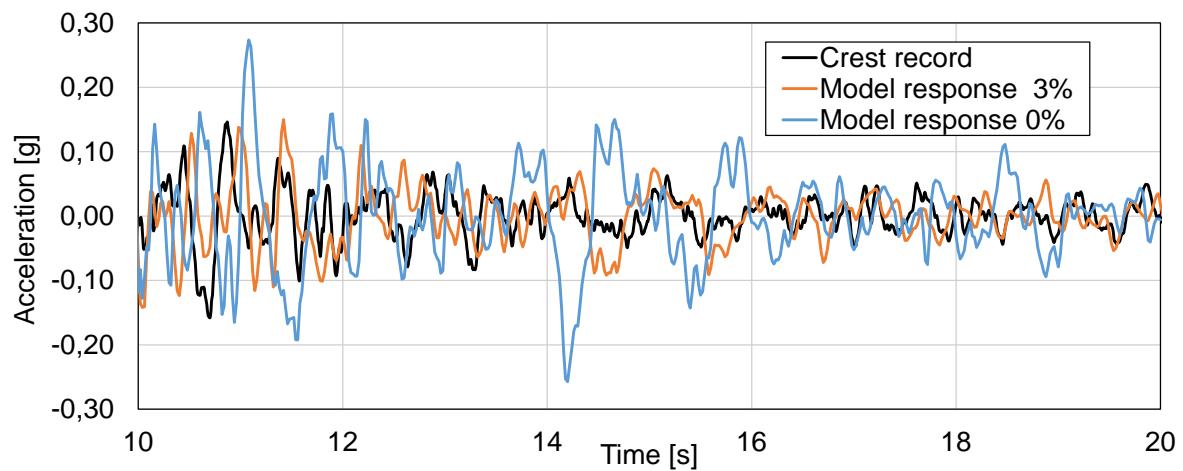


Figure 10. Comparison of crest transverse record with model response acceleration without added damping and with a damping ratio of 3%

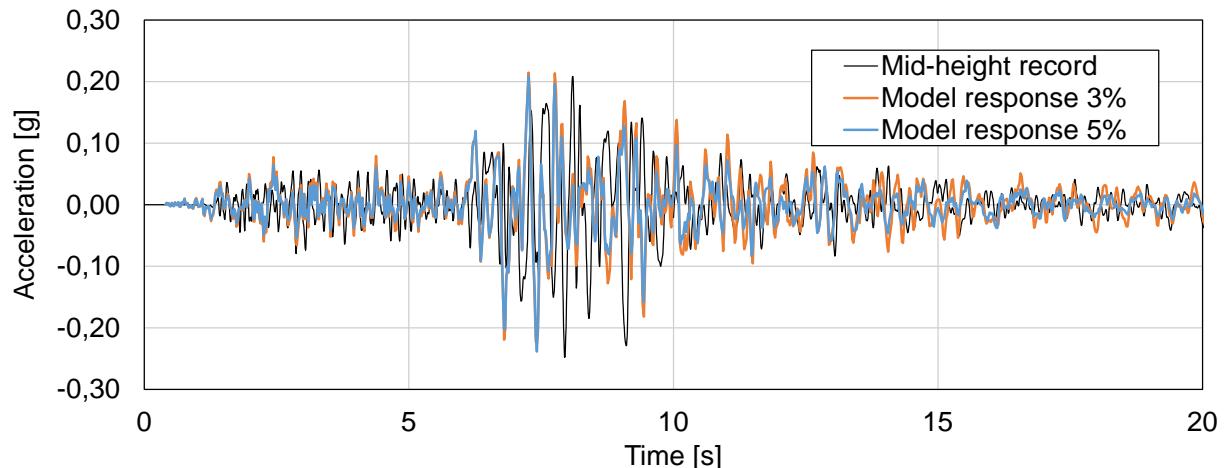


Figure 11. Comparison of mid-height transverse record with model response for damping ratio of 3% and 5%

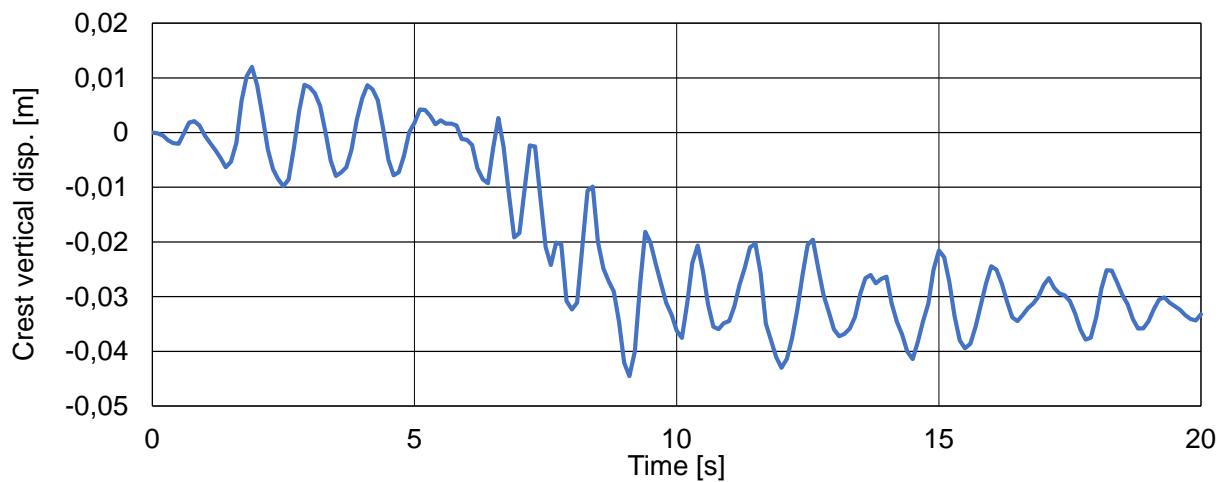


Figure 12. Crest vertical displacement

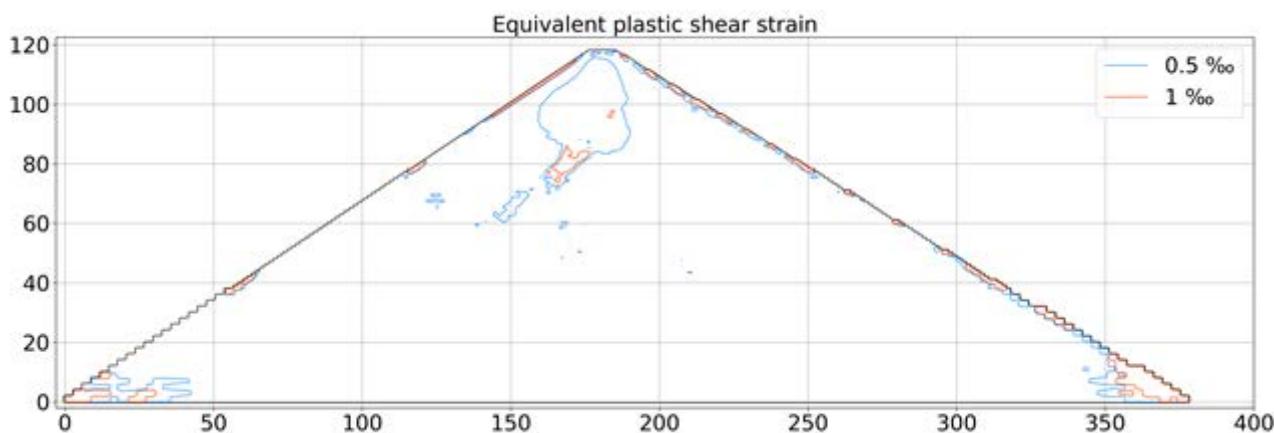


Figure 13. Contour lines of equivalent plastic shear strain at the end of the analysis

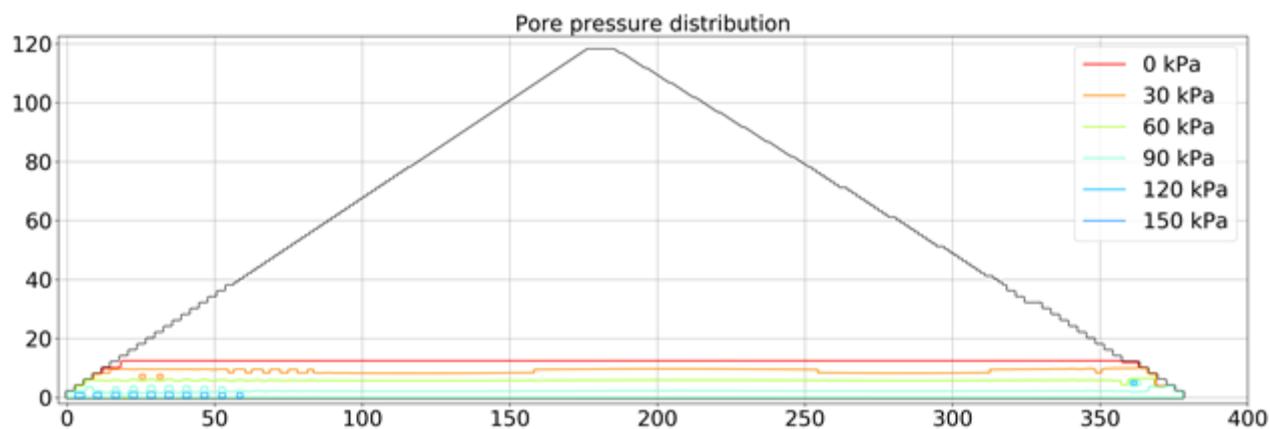


Figure 14. Contour lines of pore pressure at the end of the analysis

4. Conclusions

The availability of the Punta Negra dam acceleration records from the 2021 San Juan earthquake has allowed the feeding of a numerical MPM model of the dam, which can be used for further seismic safety assessments.

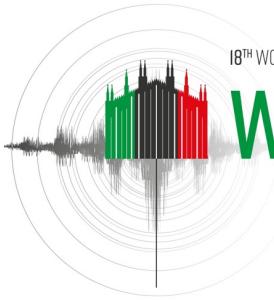
Despite the complex three-dimensional response of the dam, the two-dimensional model is able to reproduce the order of the response accelerations very well. The Sanisand constitutive model used for the dam materials, with parameters calibrated using a few drained triaxial tests, appears to represent the overall stiffness of the dam correctly, as the frequency content and amplification of the recorded accelerations are similar to the model response. However, it was noted that the model response after the intense part of the earthquake has rather long period oscillations, which are not present in the actual crest record, and this was interpreted as a lack of energy dissipation of the material constitutive model for small strains. The addition of a small amount of mass-proportional damping improved the model response results compared to the actual records.

The largest estimated plastic strains are relatively small compared to the strains that correspond to the materials' peak strengths. These strains occur in the zone near the crest. Additionally, the calculated ratio of pore pressure increase in the foundation is also small.

Acknowledgements: We would like to express our gratitude to the Dirección de Recursos Energéticos de la Provincia de San Juan for providing the acceleration records and to Energía Provincial Sociedad del Estado for the geometric and material data of the dam.

5. References

- Dafalias Y. F. & Manzari M. T. (2004). *Simple Plasticity Sand Model Accounting for Fabric Change Effects*. Journal of Engineering Mechanics, Vol. 130, No. 6, June 1, 2004. ASCE, ISSN 0733-9399/2004/6-622–634.
- Idia (2021) <https://idia.unsj.edu.ar/2021/02/22/registros-del-sismo-en-san-juan-del-18-de-enero-de-2021/>
- Lysmer J. and Kuhlemeyer R.L. (1969). *Finite difference model for infinite media*. Journal of Engineering Mechanics, 95: 859–877.
- Oldecop L & Zabala F. (2009) Evaluación de la amenaza sísmica para el proyecto hidroeléctrico Punta Negra. Instituto de Investigaciones Antisísmicas. Universidad Nacional de San Juan
- Steffen, M., Kirby, R. M., & Berzins, M. (2008). Analysis and reduction of quadrature errors in the material point method (MPM). *International journal for numerical methods in engineering*, 76(6), 922-948.
- Sulsky D, Schreyer HL, Zhou S-J (1995), “Application of a particle-in-cell method to solid mechanics”, Computer Physics Communications; 87: 236-252.
- Sulsky, D., Z. Chen, & H. L. Schreyer (1994). A Particle Method for History-Dependent Materials. Computer Methods in Applied Mechanics and Engineering. Vol. 118(1), pp 179-96
- Zabala F., Alonso E. E. (2011). *Progressive failure of Aznalcóllar dam using the material point method*. Géotechnique 61, No. 9, pp 795–808.
- Zabala,F, Rodari R. (2005) Geopart. Geotechnical MPM particle code
- Zhang, Y., Conte, J. P., Yang, Z., Elgamal, A., Bielak, J., & Acero, G. (2008). Two-dimensional nonlinear earthquake response analysis of a bridge-foundation-ground system. *Earthquake Spectra*, 24(2), 343-386.
- Zienkiewicz, O.C. (1981). *Basic Formulation of Static and Dynamic Behavior of Soil and Other Porous Media*. Applied Mathematics and Mechanics, Vol.3, No.4, Aug. 1982.



SEISMIC RESPONSE ANALYSIS OF WATER-SEDIMENT-FOUNDATION-ARCH DAM SYSTEM

J. Zhang¹, S. L. Chen^{1,2}

¹ College of Aerospace Engineering, Nanjing University of Aeronautics and Astronautics, Nanjing, China,
zhangjiao@nuaa.edu.cn

² College of Civil Aviation, Nanjing University of Aeronautics and Astronautics, Nanjing, China

Abstract: The seismic response analysis of high concrete dams, which generally constructed in river valleys with complex environments, should include the following factors: (i) the semi-unbounded extent of the impounded water and foundation domains; (ii) dam–foundation interaction considering mass, flexibility, and damping of rock; and (iii) dam–water interaction considering compressibility of water and the sediments that invariably deposit at the reservoir bottom. In this paper, the interaction of water-sediment-foundation-dam (WSFD) coupled system was interpreted as a scattering problem for an open system, which was decomposed into an auxiliary system (water-sediment-foundation system) and a bounded WSFD coupled system. The “free-field” motion of auxiliary system was treated as inputting for bounded WSFD coupled system and the seismic response was the disturbance of the free-field by dam. The main contents of this paper include: (1) realization of the free-field calculation of water-sediment-foundation system considering complex valley terrain based on the transfer matrix method and 2D FEM of coupled system of water-sediment-foundation; (2) realization of the 3D seismic analysis algorithm of the WSFD coupled system based on the unified framework of fluid-saturated porous media-solid. A valley model with consistent cross-section was used to validate this approach, by comparing its 3D FEM results with the 2D FEM results of one cross section perpendicular to the river direction. Finally, taking the concrete hyperbolic arch dam of Xiao-Wan Hydropower Station in China as an example, the FEM of WSFD coupled system is established considering the topography of foundation, the reservoir water at normal storage level, and the alluvium and sediment deposited at the reservoir bottom after years of operation. And the response modes of dam under the seismic load are discussed.

1. Introduction

The seismic response of concrete arch dams is influenced by a variety of factors, including but are not limited to: (1) dynamic water pressure of the reservoir and water compressibility; (2) wave absorption at the reservoir bottom; (3) dam–foundation interaction including mass, flexibility, and damping of the rock; (4) radiation damping associated with the semi-unbounded extent of the fluid and foundation domains (Westergaard, 1933; Nath, 1982; Fok et al., 1987; Domnguez et al., 1997; Chopra, 2012). As a result, the interaction of the reservoir-sediment-foundation-dam (WSFD) coupled system involves the dynamic coupling of fluids, saturated porous media, and solids.

In its early development, analytical methods such as wave function expansion were employed to solve the coupled problems (Liaw and Chopra, 1974; Fenves and Chopra, 1984; Wang et al., 2018). However, analytical methods are limited to regular boundary conditions for soil foundation, which to some extent restricted their

widespread application. Analysis procedures based on the substructure method (Chopra and Wang, 2009; Wang and Chopra, 2010) have long been available for analysis of linear frequency-domain 3D dam-water-foundation rock systems. Nevertheless, they show limitations in dealing with strong nonlinear problems, contact nonlinear problems, etc. In comparison, direct methods in the time domain have shown tremendous potential in the nonlinear aspect. Technicians only need to establish a reasonable finite element (FE) model and then compile finite element code (or directly invoke finite element software) to perform time-stepping simulations in the time domain. The advantages of direct methods are also evident in handling coupled problems (Zhao et al., 2003; Chen et al., 2023), employing domain partitioning parallel techniques (Farhat and Roux, 1991; Park, 2001), mature commercial software applications (Lokke and Chopra, 2017, 2018), and so on.

The seismic analysis of WSFD system can be viewed as a wave scattering problem in an open system. Time-domain simulations of such problems require determining the inputting mechanism of seismic, typically utilizing the free-field of an auxiliary system as the inputs. However, the complex terrain of an arch dam presents challenges for solving the free-field. A large-scale simulation of source-to-site would be the most general approach (Bao et al. 1998). However, they seem impractical for dam analysis for the lacking of details in the earthquake fault rupture process and the properties of the geological materials in the source-to-site path. Another approach would be to use boundary element methods (BEMs) to compute the free-field motions resulting from incident plane waves propagating from infinity to the dam site at predefined angles (Zhang and Chopra 1991). However, the directions and types (P, SV, SH, and surface) of waves are not known in advance, thus limiting the application of this approach to practical problems. Recently, a common approach starting with the Probabilistic Seismic Hazard Analysis (PSHA) for the site become a popular method. It establishes a design spectrum according to the results of PSHA, and then selects ground motions consistent with this spectrum. The free-field motion at the bottom boundary of the truncated foundation domain is determined by deconvolution of the ground motions specified at the surface. But this method rarely considers the effect of sediments or and alluviums.

In this study, we consider a variety of factors affecting the seismic response of dams, including the dynamic water pressure and compressibility of the reservoir, the radiation damping of the sediment and the foundation. The water, solid, and sediment are all treated as a saturated porous medium. The problem of the open WSFD system is decomposed into a free-field problem of an auxiliary system and a scattering problem of a bounded WSFD system. Firstly, we introduce a computational approach for solving the free-field problem in an irregular canyon terrain site. This approach, in comparison to previous approaches (Lokke and Chopra, 2018), considers the influence of sediment at the riverbed, providing a more realistic free-field, thereby reducing computational errors caused by boundary effects. Then, a unified computational framework for the coupled problem of generalized saturated porous media is employed for the analysis of the bounded WSFD system. In this computational framework, all various media are treated as generalized saturated porous media, and the unified solver is used for different media, which simplifies the complex coupling between various solvers. On the other hand, it rigorously considers the interactions between various media, such as fluid-structure interaction, soil-structure interaction, and saturated porous medium-structure interaction. This procedure is validated numerically by computing the response of a uniform canyon model with linear river under vertical pulse P-wave, comparing the responses of 2D system and 3D system. Finally, we analyse the response pattern of the Xiao-Wan Arch Dam under the real seismic load as a case study. The results indicate that the most unfavourable part of the arch dam when subjected to seismic loading occurs at the centre of the dam crest.

2. Basic theory

The seismic analysis of arch dams involves the coupled problem of the WSFD system. It can be treated as a wave scattering problem in an open system, as shown in Figure 1. In this case, the semi-unbounded WSFD system is decomposed into an auxiliary system and a bounded WSFD system. The auxiliary system includes the uniform channel with linear fluid and sediment Ω_R^+ , and the semi-unbounded, regular, linear foundation Ω_F^+ . The bounded WSFD system includes the dam and the irregular nonlinear parts of foundation Ω_F and fluid Ω_R . The free-field in the fluid boundary Γ_R and foundation boundary Γ_F of the bounded domain needs to be solved, which provides input for the bounded WSFD system. And the seismic response of the WFSD system can be regarded as the disturbance of the free-field by dam.

The auxiliary system involves interactions of water, foundation, and sediment. While the bounded WFSD system involves interactions of water, foundation, dam, and sediment. The presence of saturated porous media (sediment) contributes to the intricacy of the solution. In this study, we considered fluid, solid, and saturated porous media as a generalized saturated porous medium, which to some extent facilitates the treatment of interaction problems. Based on this concept, a free-field computational approach to the auxiliary system is presented and a direct FE procedure for solving the WSFD system is presented. The specific implementation is as described below.

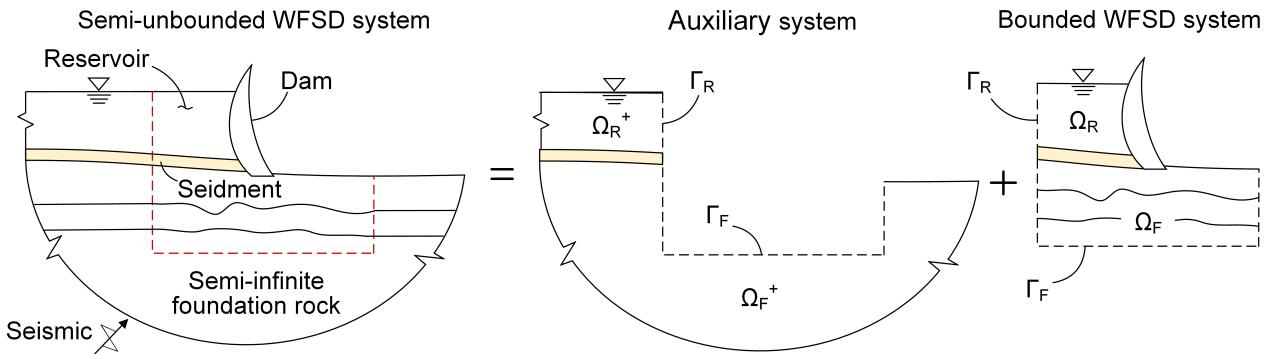


Figure 1. Decomposition of the coupled problem for the open WSFD system.

2.1. Free-field calculation methods for 3D irregular sites

As shown in Figure 2(a), the target free-field of the auxiliary system is decomposed into the bottom, four 2D irregular systems, and four 1D corner columns. Due to the irregularity of the 2D system, it presents some challenges to the solution. In this study, a common approach for calculating free-field is employed. The specific steps, as shown in Figure 2(b), can be summarized as follows:

1. Starting with Probabilistic Seismic Hazard Analysis (PSHA) for the site to establish a design spectrum, and then select ground motions consistent with this spectrum. The earthquake excitation is defined by three components of free-field motion specified on the ground surface: the stream component, the cross-stream component, and the vertical component. This motion is usually specified at the elevation of the dam abutments, but other choices are possible.
2. Computing free-fields of the bottom boundary and 1D corner columns by deconvolution of the free-field motion specified at the surface. Because probabilistic seismic hazard analysis typically does not consider topographic effects, the ground motions selected are intended for flat ground surface. The incident wave is assumed to consist solely of plane SH-, SV-, and P-waves propagating vertically upwards from the underlying semi-unbounded medium. Many procedures for deconvolution are available, such as Shake2000 (Ordonez, 2012), Deepsoil (Hashash et al., 2016), and transfer matrix method (Haskell, 1953; Thomson, 1950), among others.
3. Simulations for the free-fields of 2D auxiliary systems. The interactions between various media are considered through strict interfacial continuity conditions, which is described in detail in Section 2.2. The 1D free-fields obtained in Step 2 are used as the inputs for 2D systems. And the artificial boundary is adopted to eliminate outgoing (scattered) waves from the 2D systems.
4. Simulations for the 3D WSFD system. Likewise, the transmission boundary is employed for modelling the truncation effect of boundary. The 2D free-field motions are used as the inputs for the 3D system. The coupling method between various media is described in detail in the Section 2.2.

This approach to determining free-field has already been applied to the seismic response analysis of semi-unbounded dam-water-foundation systems (Løkke and Chopra, 2018). The difference lies in this paper's rational consideration of the impact of sediment at the riverbed, providing a more realistic free-field, thereby reducing computational errors caused by boundary effects. This approach seems to be a reasonable pragmatic choice compared to performing a large-scale simulation of seismic wave propagation from the earthquake source to the dam site (Moczo et al., 2007).

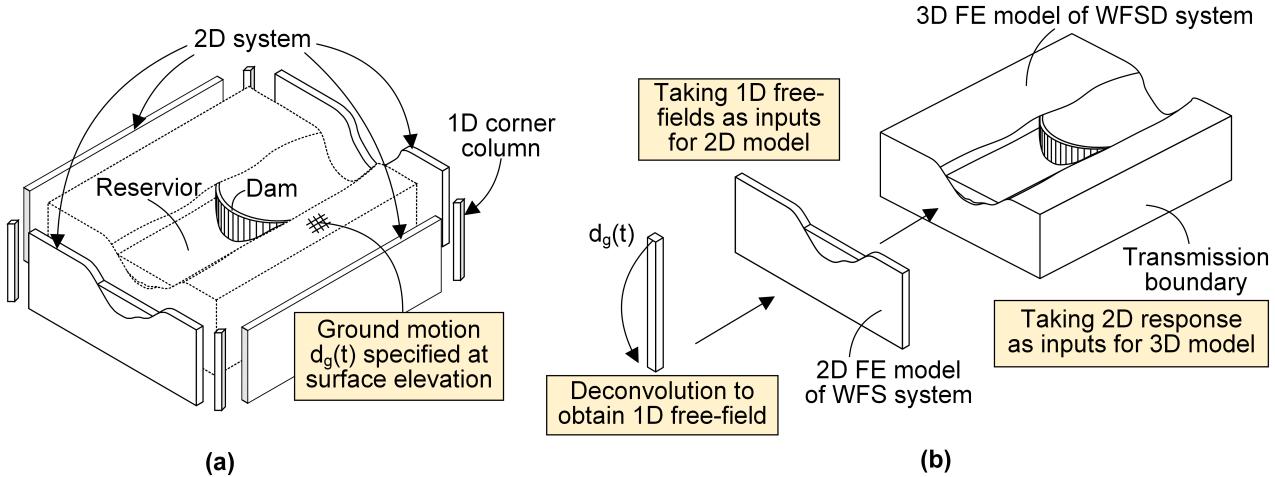


Figure 2. Approach for calculation of free-field: (a) decomposition of free-field system; (b) calculation steps of the free-field for irregular reservoir-sediment-foundation system.

2.2. Analysis Method for WSFD System

The seismic response analysis of the WFSD system involves the interaction problems between three media: fluid, saturated porous media, and solid. In this study, a unified calculational framework for generalized saturated porous media (Chen et al., 2023) is employed for dealing with this coupling problem. This method treats three various media as a generalized saturated porous medium, avoiding complex couplings between multiple solvers. The interactions between various media are considered rigorously by interfacial continuity conditions. An explicit solution strategy using central difference method and single difference method is adopted to realize the completely spatial discretization. Suppose that the computations have proceeded until $t = t^p$, the solutions of node i at time $p + 1$ can be expressed as

$$\mathbf{u}_i^{p+1} = 2\mathbf{u}_i^p - \mathbf{u}_i^{p-1} - (\Delta t)^2 (\mathbf{F}_{si}^p + \mathbf{T}_{si}^p - \mathbf{S}_{si}^p) / m_{si} \quad (1)$$

$$U_i^{p+1} = 2U_i^p - U_i^{p-1} - (\Delta t)^2 (F_{wi}^p + T_{wi}^p - S_{wi}^p) / m_{wi} \quad (2)$$

Where, \mathbf{u}_i and \mathbf{U}_i are displacement vectors for solid and fluid phase, respectively. m_{si} and m_{wi} are concentrated solid and fluid phase masses at node i . \mathbf{F}_i , \mathbf{T}_i and \mathbf{S}_i are vectors of constitutive force, viscous force and interface force applied at node i , respectively. The subscripts s and w represent the solid part and fluid part, respectively. The interface force presents when the node is at the intersection of media with different porosities. It is solved by the continuity conditions of a group of node pairings modeled at the interface (node i in the first medium and node k in the second medium). The interface force can be decomposed into normal and tangential components. Taking node i as an example, the normal part of the interface force can first be solved according to the following equations:

$$\mathbf{S}_{sNi}^p = (A_{22}\mathbf{B}_1 - A_{12}\mathbf{B}_2)/(A_{22}A_{11} - A_{12}A_{21}), \quad (3)$$

$$\mathbf{S}_{wNi}^p = (A_{21}\mathbf{B}_1 - A_{11}\mathbf{B}_2)/(A_{21}A_{12} - A_{11}A_{22}), \quad (4)$$

in which

$$A_{11} = (\Delta t)^2 \beta (m_{si} + m_{sk}), \quad (5)$$

$$A_{12} = (\Delta t)^2 m_{si}(\beta - \bar{\beta}), \quad (6)$$

$$B_1 = n_i [n_i^T (\hat{u}_k^{p+1} - \hat{u}_i^{p+1})] m_{si} m_{sk} \beta, \quad (7)$$

$$A_{21} = (\Delta t)^2 m_{wi} \beta (\beta - \bar{\beta}), \quad (8)$$

$$A_{22} = (\Delta t)^2 [m_{sk}\beta^2 + m_{wi}m_{sk}\bar{\beta}^2/m_{wk} + m_{wi}(\bar{\beta} - \beta)^2], \quad (9)$$

$$\mathbf{B}_2 = \mathbf{n}_i^T \{ \mathbf{n}_i^T [\bar{\beta}(\hat{\mathbf{U}}_k^{p+1} - \hat{\mathbf{u}}_k^{p+1}) - \beta(\hat{\mathbf{U}}_i^{p+1} - \hat{\mathbf{u}}_k^{p+1})] \} m_{wi} m_{sk} \beta, \quad (10)$$

in which, β and $\bar{\beta}$ are the porosities of the first and second media, respectively. \mathbf{n}_i is the unit exterior normal vector at node i . $\hat{\mathbf{u}}$ and $\hat{\mathbf{U}}$ are the “free displacements” of solid and fluid phase, solved by neglecting the interface forces. Similarly, the normal interface forces \bar{S}_{sNk}^p and \bar{S}_{wNk}^p at node k can be obtained. Since the part of fluid phase does not bear shear stress, the tangential interface force for the fluid phase is 0. The tangential interface force for the solid phase can be solved based on the continuity of solid phase displacements.

$$\mathbf{S}_{sTi}^p = \frac{(\hat{\mathbf{u}}_k^{p+1} + \Delta\mathbf{u}_{Nk}^{p+1} - \hat{\mathbf{u}}_i^{p+1} - \Delta\mathbf{u}_{Ni}^{p+1})m_{si}m_{sk}}{(\Delta t)^2(m_{si} + m_{sk})}. \quad (11)$$

Likewise, the tangential interface forces \bar{S}_{sTk}^p and \bar{S}_{wTk}^p at node k can be obtained. Finally, the displacement of the interface nodes at time $p+1$ is also solved according to equations (1) and (2).

2.3 transmission boundary

The boundary nodes are solved as the sum of scattered wave and free-field:

$$\mathbf{W}^{p+1} = \mathbf{W}_s^{p+1} + \mathbf{W}_f^{p+1} \quad (12)$$

in which, \mathbf{W} may represent the displacement vector of solid or fluid phase; \mathbf{W}_s and \mathbf{W}_f are the displacement vector of scattered wave and the free-field, respectively. The free-field displacement is calculated through the method described in Section 2.1. The solution of scattered wave can be solved using Multi-Transmitting Formula (MTF) proposed by Liao et al (Liao and Wong, 1984):

$$\mathbf{W}_s^{p+1} = \sum_{j=1}^N (-1)^{j+1} C_N^j \mathbf{W}_{sj}^{p+1-j}, \quad (13)$$

where the subscript j represents the transmitting nodes near the boundary nodes; N is the transmitting order; C_N^j is the binomial coefficient. Therefore, the displacements of boundary nodes can be expressed as:

$$\mathbf{W}^{p+1} = \sum_{j=1}^N (-1)^{j+1} C_N^j (\mathbf{W}_j^{p+1-j} - \mathbf{W}_{sj}^{p+1-j}) + \mathbf{W}_{fj}^{p+1-j}, \quad (14)$$

It should be noted that the transmitting nodes are not equivalent to the mesh nodes in FE model. They are virtual points at a distance of $j \cdot c_a \cdot dt$ from the boundary node determined by the wave velocity, wherein c_a is the artificial wave velocity. During the process of FE simulation, the displacements of the transmitting nodes can be determined by interpolating the displacements of the mesh nodes. This local artificial boundary condition is universal and has nothing to do with specific wave equations, which can be directly used for wave problems in saturated porous media (Chen and Liao, 2003).

2.4. Validation

The direct FE procedure for the WSFD system is validated numerically by computing the response of a uniform canyon model with linear river under vertical pulse P -wave, as shown in Figure 3(a). The foundation rock is assumed to be homogeneous, isotropic, and linearly elastic, with modulus of elasticity $E_s = 21.0 \text{ GPa}$, density $\rho_s = 2630 \text{ kg/m}^3$, and Poisson's ratio $\nu_s = 0.27$. The river is assumed to be linear fluid, with density $\rho_f = 2630 \text{ kg/m}^3$ and pressure wave velocity $V_p = 1500 \text{ m/s}$. The responses of the bottom and four side boundaries are firstly calculated by the approach described in Section 2.1, in which the responses of 2D irregular front-side and back-side are calculated by the 2D FE procedure. The response of the 3D canyon model is then calculated by the direct 3D FE procedure presented in Section 2.2, wherein the responses of boundaries are used as the inputs of 3D model. The interaction between the river and the bedrock is rigorously considered by equations (1) and (2). Because the canyon maintains a consistent cross-section in the river direction, theoretically, the 2D free-field at the front-side (or back-side) is consistent with the 3D response at one cross-section.

The comparison of 2D vertical waveform and 3D vertical waveform at the center of the river channel is shown in Figure 3(b). Wherein the displacement waveform in the river part is composed of the fluid-phase displacement of a generalized saturated porous medium with porosity of 1 (pure fluid). The displacement waveform in the rock part is composed of the solid-phase displacement of a generalized saturated porous medium with porosity of 0 (pure solid). The waveforms from 2D and 3D system coincide well in the bedrock

part and the river part. Slight differences exist in the river part but they are negligibly small. The comparison results confirm the effectiveness of the free-field calculation approach for the irregular site and the accuracy of the coupling analysis technique for the WSFD system.

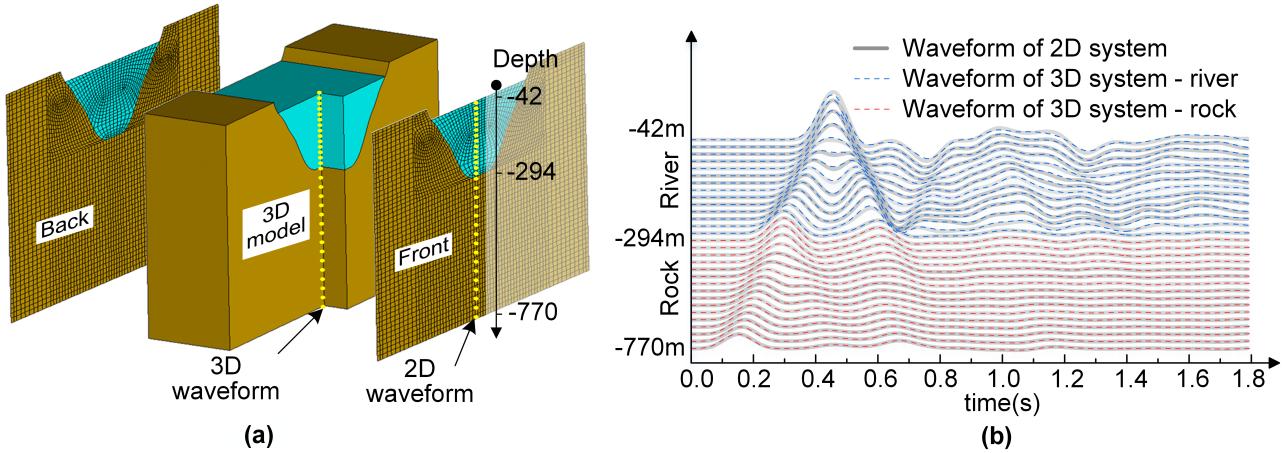


Figure 3. (a) 3D model of canyon with uniform channel of river; (b) comparison of waveforms at the centre of the river in 2D and 3D.

3. Seismic Response Analysis of Arch Dam

3.1. Mechanical Parameters and FE Model of Xiao-Wan Dam

The ability of the FE procedure for WSFD system to compute the dynamic response of concrete dams is evaluated numerically by analysing Xiao-Wan Dam, a 294-m-high, symmetric, double-curvature concrete arch dam located on the Lancang River in Yunnan of China. The elevations at the base and top of the dam are 953m and 1245m, respectively. Considering the radiation damping induced by flexible foundation and reservoir, the compressibility of water and the sediments that invariably deposit at the reservoir bottom, a water-sediment-foundation-dam coupled system FE model is established. The size of the truncated computational domain is 1200m×600m×770m. The reservoir water is modelled at normal storage level, with elevation of 1240m. And the sediment deposited at the reservoir bottom is modelled as porous saturated media with a thickness of 1/5 height of the reservoir. The overall model is shown in Figure 4(a), using a Cartesian coordinate system with the midpoint of the upstream dam crest as the origin. The X-axis represents the cross-stream direction of the river, the Y-axis represents the stream direction of the river, and the Z-axis represents the vertical direction. Eight nodes in the upstream surface of the dam are selected as monitors, as shown in Figure 4(b).

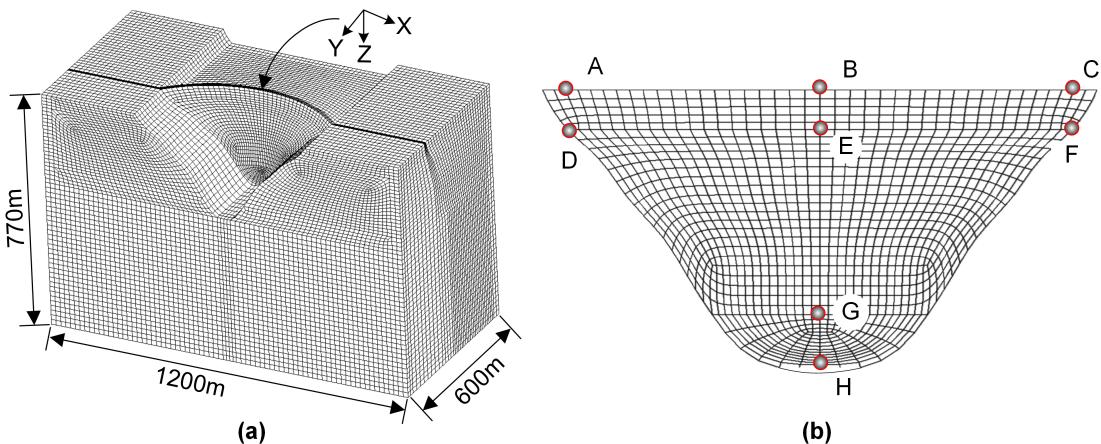


Figure 4. (a) FE model of WSFD system of Xiao-Wan Dam; (b) the monitoring points in at the upstream surface of the dam.

The foundation is assumed to a homogeneous isotropic elastic medium. For facilitating the interaction of various media, all media is modelled as generalized porous saturated media. In specific, the dam and foundation are treated as GSPM with a porosity of 0; the water is considered as GSPM with a porosity of 1. The material parameters (solid density ρ_s , fluid density ρ_w , Poisson's ratio ν , damping ratio ξ , elastic modules E , compressive velocity V_p , and shearing velocity V_s) for the concrete dam, reservoir water, sediment, and rock foundation are listed in Table 1. The interactions of various media are calculated by formulas described in Section 2.2

Table 1. Parameters of mechanical properties of materials.

Components	ρ_s (kg/m^3)	ρ_w (kg/m^3)	ν	ξ	E (GPa)	V_p (m/s)	V_s (m/s)
water	-	1000	0.49	0.005	-	1500	-
Dam	2400	-	0.20	0.033	28.6	3638	2228
Foundation	2630	-	0.27	0.020	21.0	3158	1773
Sediment	2083	1000	0.35	0.035	0.77	2582	754

The design response spectrum of the site is determined based on the results of the PSHA analysis. Then a strong ground motion record (the Iwate_Japan record) consistent with the design spectrum is selected from the PEER database, as shown in Figure 5(a). The seismic record with three components (stream direction, cross stream direction, and vertical direction) is specified on the ground surface near the shoulder of the dam. The peak acceleration of the horizontal component is scaled to 0.308g, and that of the vertical component is scaled to 0.205g. Considering a far-field seismic source, seismic waves are reasonably assumed to enter the WSFD system with a vertical incidence due to the continuous refraction of the bedrock profiles. The three components of the motion are used to calculate the free-field motion of the site employing the 1D deconvolution method and the 2D FE method for irregular canyon presented in Section 2.1. Finally, the seismic response of the dam under the inputs of free-field is solved by the 3D FE procedure of the WSFD system. In implementation, the overall model is divided into seven partitions and the MPI parallel algorithm is applied to enhance the computational efficiency and reduce the computational storage. The data exchanging between partitions is realized by directly transferring the displacements and forces at the interfaces of subdomains.

The acceleration histories of the dam are shown in Figure 5(b-d). The peak accelerations at monitors are marked at diagrams. The spatial variation of acceleration along the dam surface is evident. The crest of the dam displays a higher response compared to the other sites, and as the distance to the mountain decreases, the peak acceleration decreases proportionately. This trend is consistent across all three directions. In the cross-stream direction, the peak acceleration of 320 cm/s^2 at the base is amplified to 862 cm/s^2 at the dam crest. In the stream direction, the peak acceleration of 295 cm/s^2 at the base is amplified to 2972 cm/s^2 at the dam crest. In the vertical direction, the peak acceleration of 192 cm/s^2 at the base is amplified to 760 cm/s^2 at the dam crest. This implies that the dam suffers the most significant seismic loads in the stream direction, and the crest possesses the utmost hazardous section of the entire structure.

The displacement histories of three directions of the monitor B and the deformation of dam at various moments are shown in Figure 6. From the displacement response, it can be observed that the crest of the dam exhibits the maximum response in the stream direction, with a peak value close to 30 cm. Therefore, the deformations of dam are plotted at several specific moments of substantial displacement at the dam crest in the stream direction and magnified by 300 times for better visibility. It can be seen that the primary deformation modes of the dam occur as oscillation back and forth in the direction of the river, which is exactly the first-order mode of the dam body. In this study, the whole system is a linear system and the gravity is not considered, therefore the dam body is predominantly influenced by the seismic loads and the dynamic water pressure of reservoir. The dam deformation caused by hydrostatic pressure of reservoir water is not significant.

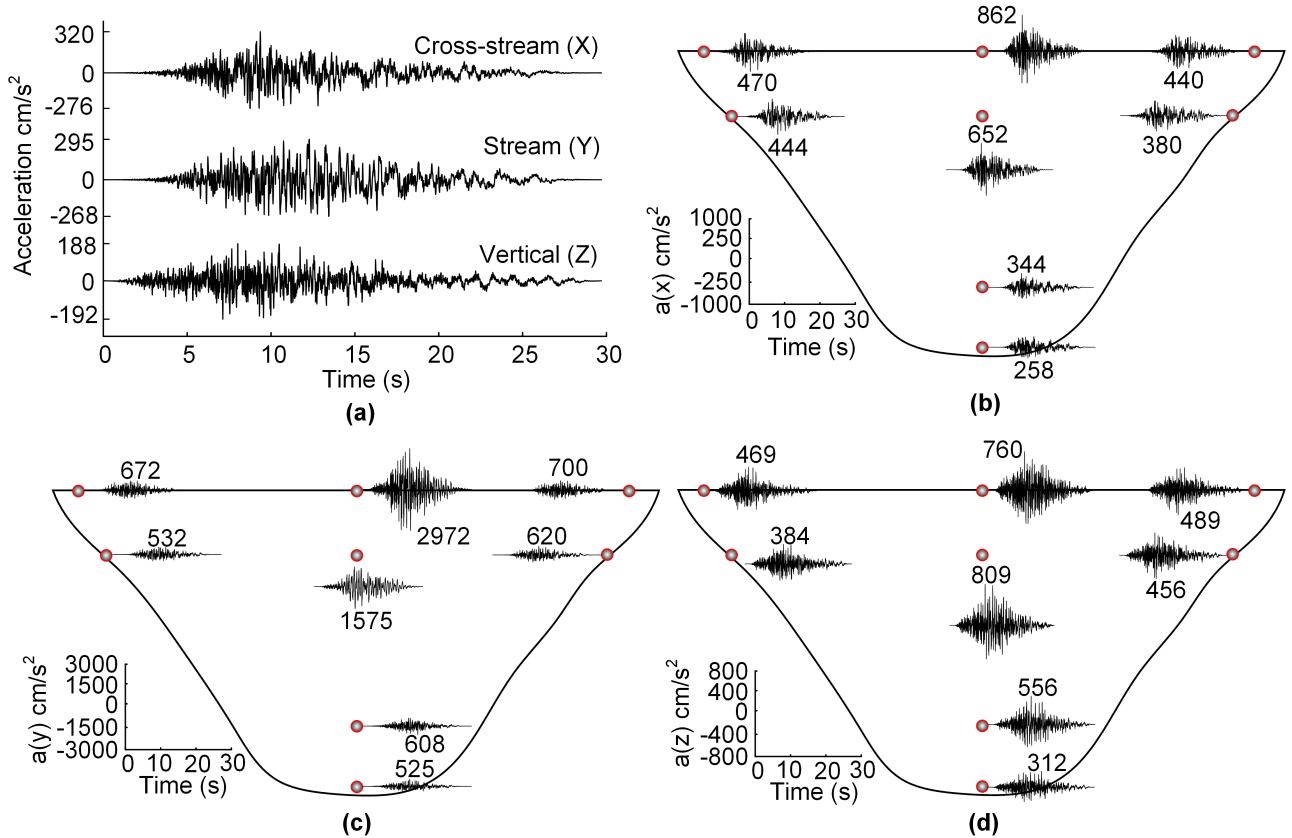


Figure 5. Inputs and acceleration responses of da : (a) is the acceleration history of Iwate_Japan record; (b), (c), and (d) are the acceleration histories of dam in the X, Y, and Z direction, respectively.

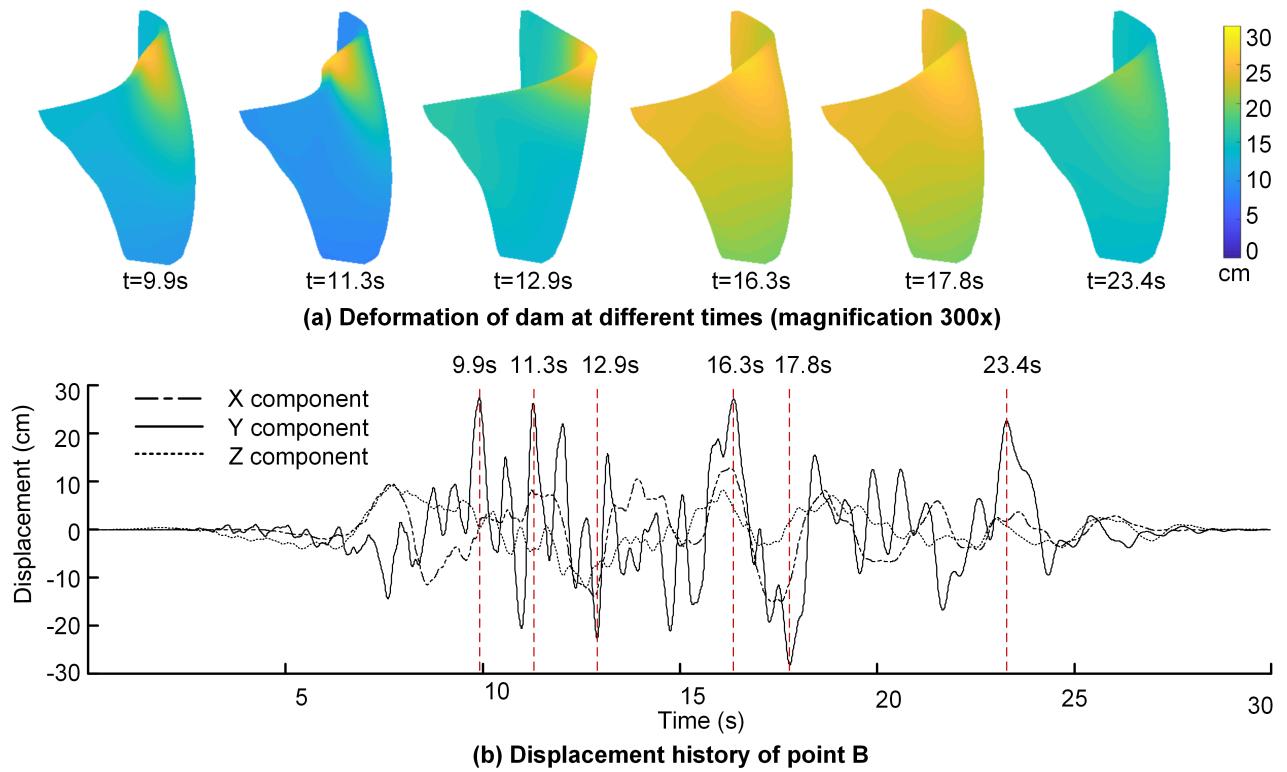


Figure 6. Displacement responses of dam: (a) the deformations of dam at different times; (b) the displacement history of three components at monitoring point.

The envelopes of the maximum (minimum) principal stresses are shown in Figure 7 (positive for tensile stress and negative for compressive stress). From the figure, it can be seen that the tensile and compressive stresses at the crest of the dam are higher compared to the bottom of the dam. The maximum tensile stress at the crest of the dam reached 9 MPa (Figure 7(a)), while the maximum compressive stress reached 7 MPa (Figure 7(b)). The occurrence of significant tensile stress is attributed to the fact that, in this study, the gravitational effects on the dam and the static hydrostatic pressure of the reservoir water were not considered. The stress envelope diagrams show that the dam crest experiences the highest and lowest levels of principal stress during seismic loading. This stress findings correspond to the results of the dam's displacement deformation. The dam crest is the most vulnerable component that requires careful consideration in the design process.

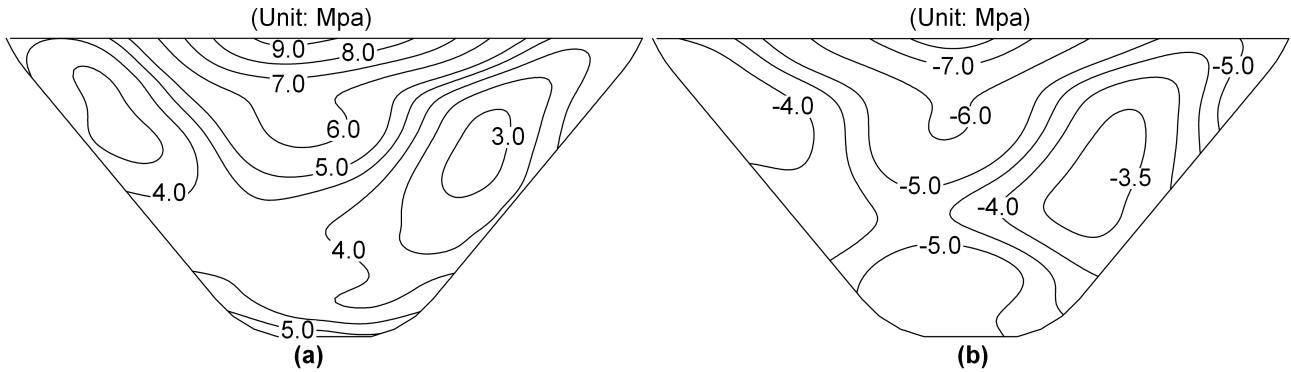


Figure 7. Stress responses of dam: (a) the envelope of the maximum principal stress; (b) the envelope of the minimum principal stress.

The seismic response indicates that the peak acceleration, deformation, and principal stress at the dam crest have maximum values across the dam during the seismic analysis. The peak acceleration in the stream direction of the dam crest is even amplified 10 times relative to that of the bedrock surface. The spatial variation of response along the dam surface can be approximately summarized as: the closer to the rock, the smaller the response. The response pattern aligns well with the modes of dam. This application of Xiao-Wan dam under seismic loads has well validated the effectiveness of the free-field calculation approach and the accuracy of the coupling method within the WSFD system, including the interaction of solid, fluid, and saturated porous media.

4. Conclusion

In this research, a practical approach is proposed for complex WSFD coupled systems. This approach splits the seismic response problem of the open WSFD system into a free-field problem of an auxiliary system and a coupled problem of a bounded WSFD system. In this case, the auxiliary system applies a combination of the 1D deconvolution method and the 2D finite element method for solving the free field of the irregular site involving the river, sediment, and bedrock. The free field of the auxiliary system is used directly as the inputs to the boundary of the bounded WSFD system in the form of displacements through the transmission boundary technique. The bounded WSFD system, on the other hand, effectively handles the interaction of reservoir water, sediment, dam, and foundation by means of setting up a group of node pairings modelled at the interface of various media with different porosities.

The advantages of this procedure for WSFD system presented in this paper include: (i) the free field calculational approach considers the influence of sediment at the riverbed, providing a more realistic free-field, thereby reducing computational errors caused by boundary effects; (ii) the unified solver (generalized saturated porous media solver) for all various media simplifies the complex coupling between various solvers; (iii) the treatment of the interfaces rigorously considers the interactions between various media, such as fluid-structure interaction, soil-structure interaction, and saturated porous medium-structure interaction.

This procedure is validated numerically by computing the response of a uniform canyon model with linear river under vertical pulse P -wave, comparing the responses of 2D system and 3D system. Finally, this approach is applied to analyse the seismic response of Xiao-Wan dams, located at Yunnan in China, under the Iwate_Japan seismic wave. The results reveal that the most unfavourable part of the arch dam when subjected

to seismic loading occurs at the centre of the dam crest. Its peak acceleration in the stream direction is even amplified 10 times relative to that at the bedrock surface. The seismic response of the dam to some extent validated the effectiveness of the free-field calculation method and the correctness of the coupling method of the WSFD system.

5. References

- Bao H., Bielak J., Ghattas O., Kallivokas L. F., O'Hallaron D. R., Shewchuk J. R., Xu J. (1998). Large-scale simulation of elastic wave propagation in heterogeneous media on parallel computers. *Computer Methods in Applied Mechanics and Engineering*, 152(1-2): 85-102.
- Chen S., Liao Z. (2003). Multi-transmitting formula for attenuating waves. *Acta Seismologica Sinica*, 16(3): 283-291.
- Chen S., Shen J., Zhang J., Cheng S., Sun J. (2023). Near-field seismoacoustic wave scattering due to an irregular interface: A unified framework. *Geophysical Journal International*, ggad358.
- Chopra A. K., Wang J. T. (2009). Earthquake response of arch dams to spatially varying ground motion. *Earthquake Engineering & Structural Dynamics*, 39(8): 887-906.
- Chopra A. K. (2012). Earthquake Analysis of Arch Dams: Factors to Be Considered. *Journal of Structural Engineering*, 138(2): 205-214.
- Domínguez J., Gallego R., Japón B. R. (1997). Effects of Porous Sediments on Seismic Response of Concrete Gravity Dams. *Journal of Engineering Mechanics*, 123(4): 302-311.
- Farhat C. (1991). A Lagrange multiplier based divide and conquer finite element algorithm. *Computing Systems in Engineering*, 2(2-3): 149-156.
- Fenves G., Chopra, A. K. (1984). Earthquake analysis of concrete gravity dams including reservoir bottom absorption and dam-water-foundation rock interaction. *Earthquake Engineering & Structural Dynamics*, 12(5): 663-680.
- Fok K., Chopra A. K. (1987). Water Compressibility in Earthquake Response of Arch Dams. *Journal of Structural Engineering*, 113(5): 958-975.
- Haskell N. A. (1953). The dispersion of surface waves on multilayered media. *Bulletin of the Seismological Society of America*, 43(1): 17-34.
- Hashash Y.M.A., Musgrove M.I., Harmon J.A., Groholski D.R., Phillips, C.A., Park D. (2016). DEEPSOIL 6.1, User Manual.
- Liao Z. P., Wong H. L. (1984). A transmitting boundary for the numerical simulation of elastic wave propagation. *International Journal of Soil Dynamics and Earthquake Engineering*, 3(4): 174-183.
- Liaw C. Y., Chopra A. K. (1974). Dynamics of towers surrounded by water. *Earthquake Engineering & Structural Dynamics*, 3(1): 33-49.
- Løkke A., Chopra A. K. (2017). Direct finite element method for nonlinear analysis of semi-unbounded dam-water-foundation rock systems: Nonlinear Earthquake Analysis of Dams. *Earthquake Engineering & Structural Dynamics*, 46(8): 1267-1285.
- Løkke A., Chopra A. K. (2018). Direct finite element method for nonlinear earthquake analysis of 3-dimensional semi-unbounded dam-water-foundation rock systems. *Earthquake Engineering & Structural Dynamics*, 47(5): 1309-1328.
- Moczo P., Robertsson J.O.A., Eisner L. (2007). The Finite-Difference Time-Domain Method for Modeling of Seismic Wave Propagation. *Advances in Geophysics*, 48: 421-516.
- Nath B. (1982). Natural frequencies of arch dam reservoir system-by a mapping finite element method. *Earthquake Engineering & Structural Dynamics*, 10(5): 719-734.
- Ordonez G.A. (2012). SHAKE2000 – A Computer Program for the 1-D Analysis of Geotechnical Earthquake Engineering Problems. *GeoMotions, LLC; Lacey, Washington, USA*.
- Park K. C., Felippa C. A., Ohayon, R. (2001). Partitioned formulation of internal fluid-structure interaction problems by localized Lagrange multipliers. *Computer Methods in Applied Mechanics and Engineering*, 190(24): 2989-3007.

- Shen J., Chen S., Zhang J., Cai P. (2023). Unified framework based parallel FEM code for simulating marine seismoacoustic scattering. *Frontiers in Earth Science*, 10: 1056485.
- Thomson W. T. (1950). Transmission of elastic waves through a stratified solid medium. *Journal of Applied Physics*, 21(2): 89-93.
- Wang J. T., Chopra A. K. (2010). Linear analysis of concrete arch dams including dam-water-foundation rock interaction considering spatially varying ground motions: linear analysis of concrete arch dams. *Earthquake Engineering & Structural Dynamics*, 39(7): 731-750.
- Wang P., Zhao M., Du X. (2018). Analytical solution and simplified formula for earthquake induced hydrodynamic pressure on elliptical hollow cylinders in water. *Ocean Engineering*, 148: 149-160.
- Westergaard H. M. (1933). Water Pressures on Dams during Earthquakes. *Transactions of the American Society of Civil Engineers*, 98(2): 418-433.
- Zhang L., Chopra A. K. (1991). Three-dimensional analysis of spatially varying ground motions around a uniform canyon in a homogeneous half-space. *Earthquake Engineering & Structural Dynamics*, 20(10): 911-926.
- Zhao C., Li W., Wang J. (2005). An explicit finite element method for dynamic analysis in fluid saturated porous medium-elastic single-phase medium-ideal fluid medium coupled systems and its application. *Journal of Sound and Vibration*, 282(3-5): 1155-1168.

Non-linear seismic response of an ultra-high arch dam. ETA-based safety assessment



BCI6 - SEISMIC ANALYSIS OF DAMS AND LEVEES

André Alegre^{1(*2,3)}, Sérgio Oliveira², Paulo Mendes³, Jorge Proença⁴, Rafael Ramos^{2,4}

¹ Kinematics Inc., Pasadena, CA, USA

² Concrete Dams Department - National Laboratory for Civil Engineering (LNEC), Lisbon, Portugal

³ Lisbon School of Engineering (ISEL-IPL), Lisbon, Portugal

⁴ CERIS – Instituto Superior Técnico, Lisbon, Portugal



LABORATÓRIO NACIONAL
DE ENGENHARIA CIVIL



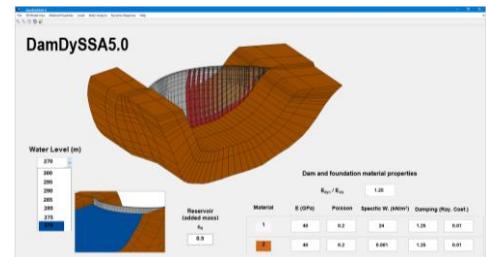
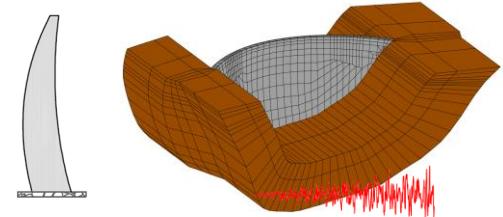
ISEL
INSTITUTO SUPERIOR DE
ENGENHARIA DE LISBOA



RESEARCH PROJECT
SSHM4DAMS
FUNDÉD BY  REPÚBLICA PORTUGUESA

1. INTRODUCTION

- Work focused on a very important and challenging topic in dam engineering: seismic analysis of large arch dams
- Main goal: conduct a complete study on the seismic behavior of a 300 m-high arch dam
 - Non-linear response analysis: test the developed finite element mesh
 - Performance assessment based on Endurance Time Analysis (ETA)
- Computational simulations carried out using a software developed by our research group



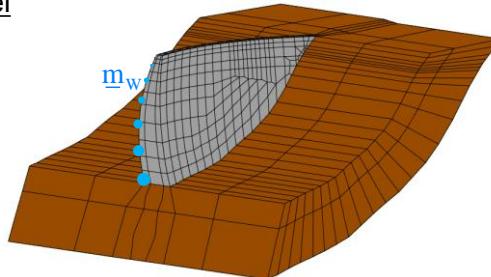
2. USED SOFTWARE: *DAMDySSA5.0*

- 3D finite element program for dynamic analysis of dam-reservoir-foundation systems
- Reservoir and dam-water interaction

Added water mass model

$$(\underline{m} + c_R \underline{m}_w) \ddot{\underline{u}} + \underline{c} \dot{\underline{u}} + \underline{k} \underline{u} = \underline{f}$$

↓
Added mass correction factor (Alegre, 2014)



Coupled model

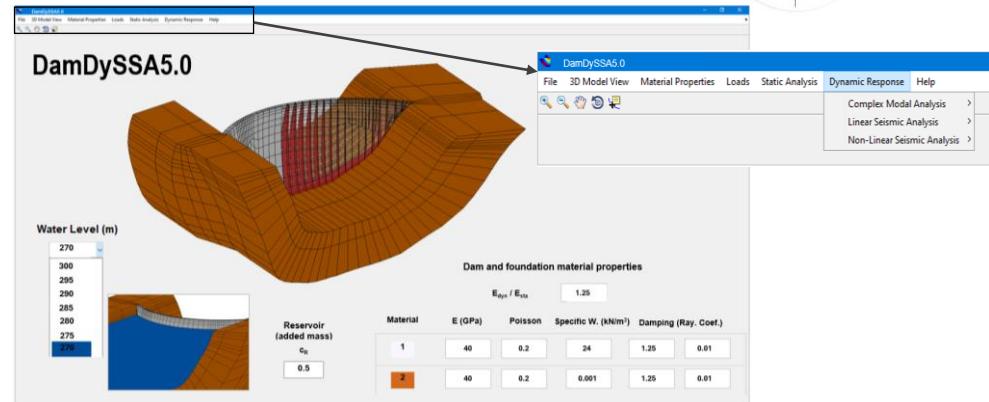
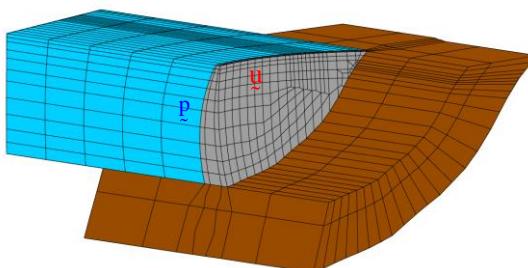
$$\begin{bmatrix} \underline{m} & 0 \\ \rho_w Q^T & S \end{bmatrix} \begin{bmatrix} \ddot{\underline{u}} \\ \ddot{\underline{p}} \end{bmatrix} + \begin{bmatrix} \underline{c} & 0 \\ 0 & R \end{bmatrix} \begin{bmatrix} \dot{\underline{u}} \\ \dot{\underline{p}} \end{bmatrix} + \begin{bmatrix} \underline{k} & -Q \\ 0 & H \end{bmatrix} \begin{bmatrix} \underline{u} \\ \underline{p} \end{bmatrix} = \begin{bmatrix} \underline{F}_s \\ \underline{F}_w \end{bmatrix}$$

(Zienkiewicz and Bettess, 1978)

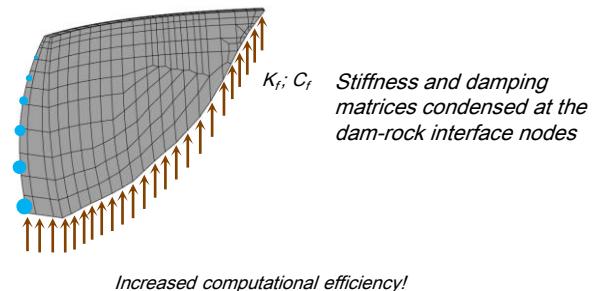
$$\underline{M} \ddot{\underline{q}} + \underline{C} \dot{\underline{q}} + \underline{K} \underline{q} = \underline{F}$$

$$\underline{q} = \underline{q}(t) = \begin{bmatrix} \underline{u} \\ \underline{p} \end{bmatrix}$$

(Alegre, 2021)



- Foundation: massless and elastic substructure

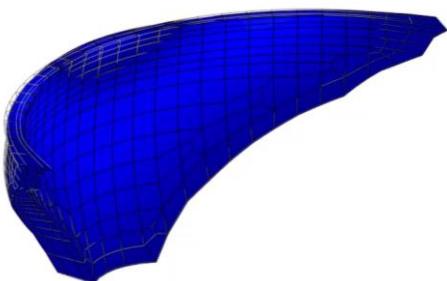


2. USED SOFTWARE: *DAMDYSSA5.0*

Seismic analysis

Time-stepping method

$$\underline{\mathbf{M}} \ddot{\mathbf{q}}_{t+\Delta t} + \underline{\mathbf{C}} \dot{\mathbf{q}}_{t+\Delta t} + \underline{\mathbf{K}} \mathbf{q}_{t+\Delta t} = \underline{\mathbf{F}}_{t+\Delta t}$$



Non-linear seismic analysis

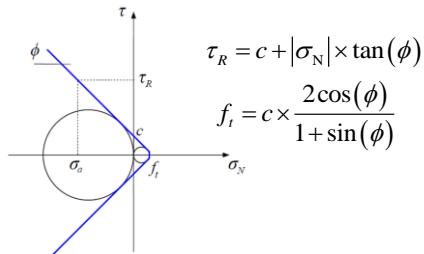
Time-stepping method + Stress-transfer method

$$\underline{\mathbf{M}} \ddot{\mathbf{q}}_{t+\Delta t} + \underline{\mathbf{C}} \dot{\mathbf{q}}_{t+\Delta t} + \underline{\mathbf{K}} \mathbf{q}_{t+\Delta t} = \underline{\mathbf{F}}_{t+\Delta t} + \Psi_{t+\Delta t}$$

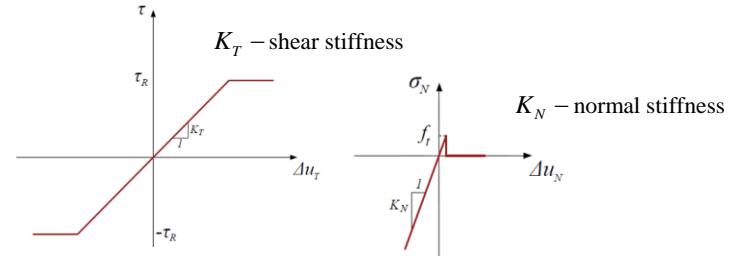
Stress redistribution simulated by applying nodal forces equivalent to the unbalanced stresses

- Non-linear joint model (opening/closing and shear sliding movements)

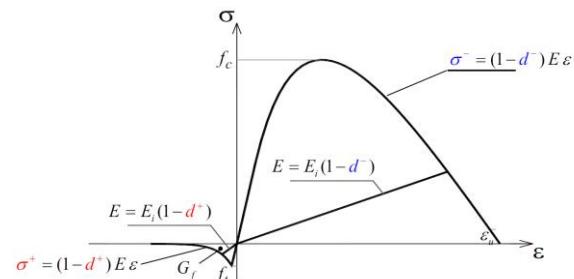
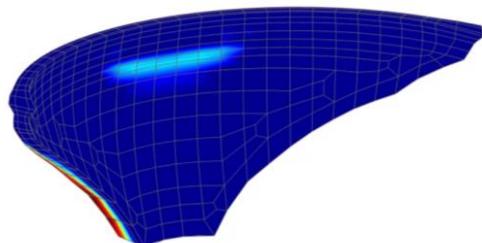
Mohr-Coulomb failure criterion



Stress-displacement relations



- Constitutive damage model with softening and two independent damage variables



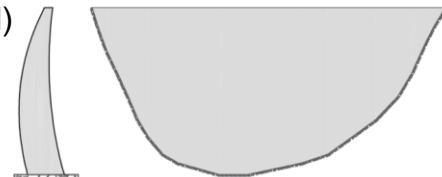
$$\sigma = (1-d^+) \tilde{\sigma}^+ + (1-d^-) \tilde{\sigma}^-$$

(Oliveira & Faria, 2006)

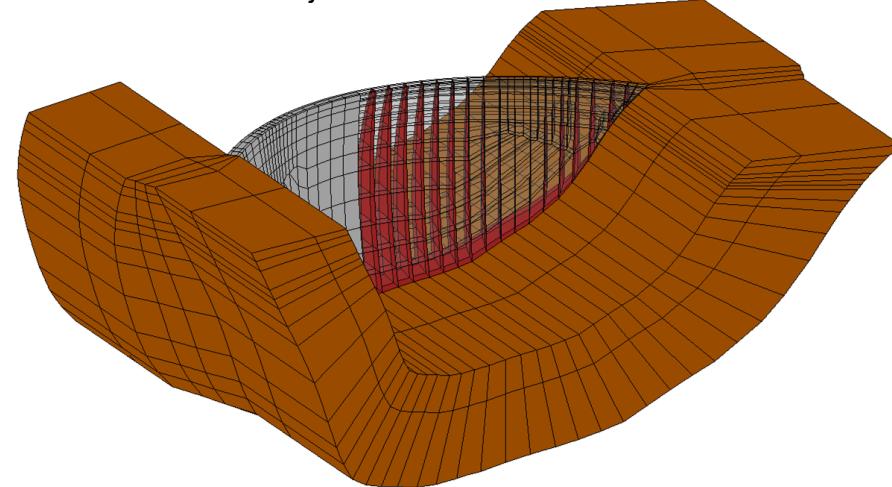
σ – real stress f_t – tensile strength
 $\tilde{\sigma}^\pm$ – effective stress f_c – compressive strength

3. CASE STUDY: 300 M-HIGH ARCH DAM

- Double curvature arch dam (non-symmetrical)
 - Height: 300 m
 - Crest length: 700 m



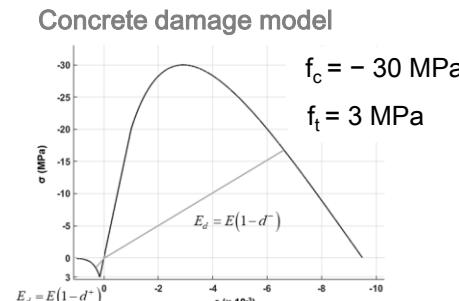
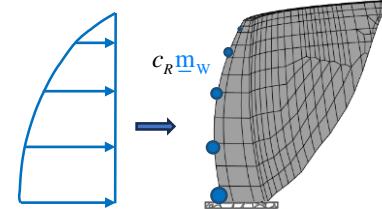
- Finite element mesh:
 - Dam structure: 1047 solid elements
 - Foundation: 602 elements
 - Vertical dam joints: 813 interface elements



Concrete (dam)
 $E = 25 \text{ GPa}$; $\nu = 0.2$
 $\gamma = 24 \text{ kN/m}^3$

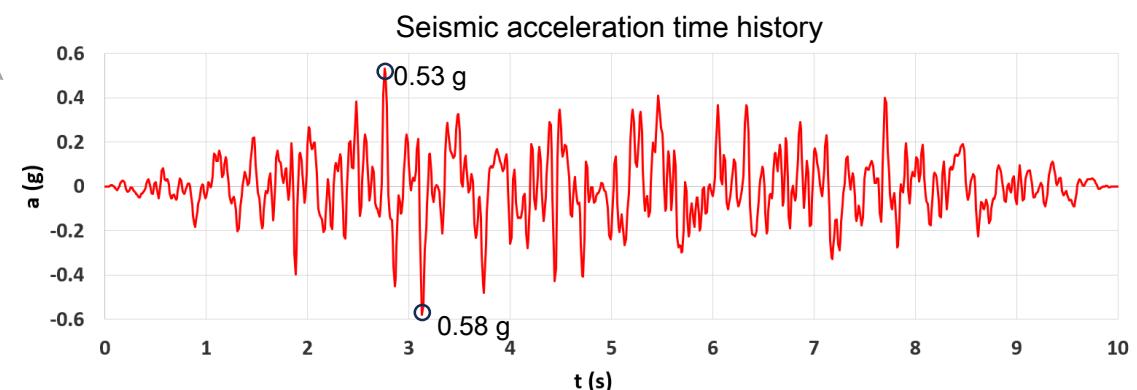
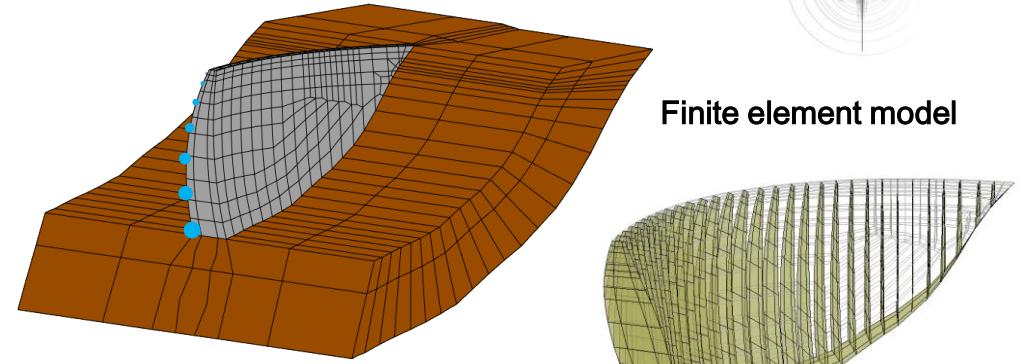
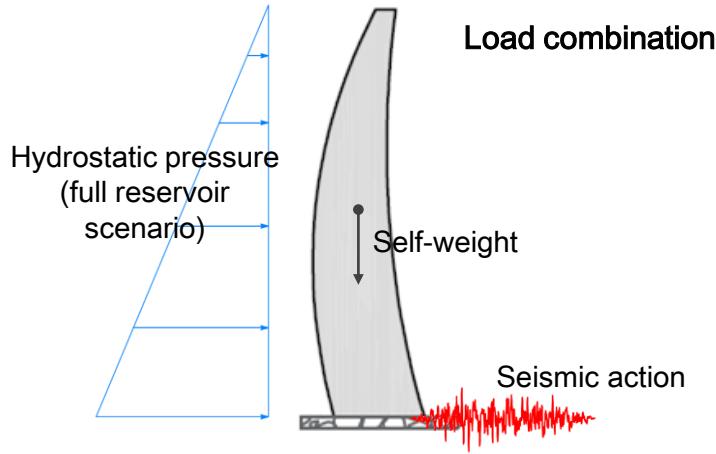
Rock (foundation)
 $E = 25 \text{ GPa}$; $\nu = 0.2$
 $\gamma = 0 \text{ kN/m}^3$ (massless model)

Reservoir
Added water mass model
 $c_R = 0.5$



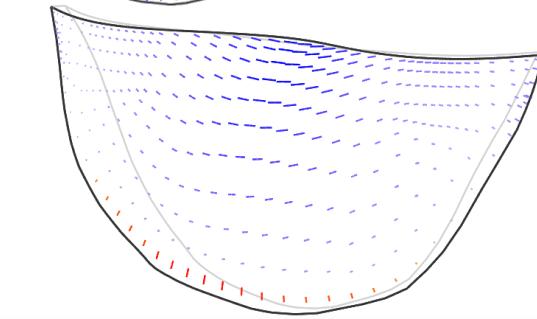
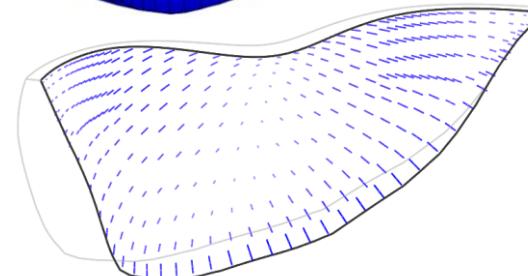
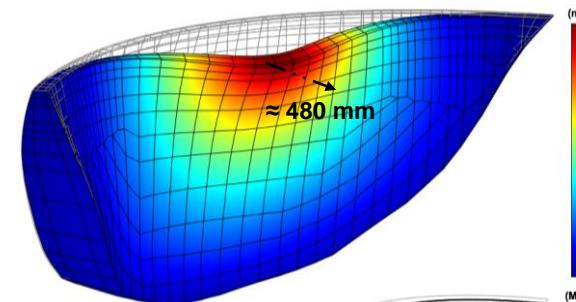
Vertical joints
 $K_N = 5 \times 10^7 \text{ kN/m}$
 $K_T = 0.5 K_N$
 $c = 0$; $\phi = 30^\circ$

4. NON-LINEAR SEISMIC RESPONSE ANALYSIS

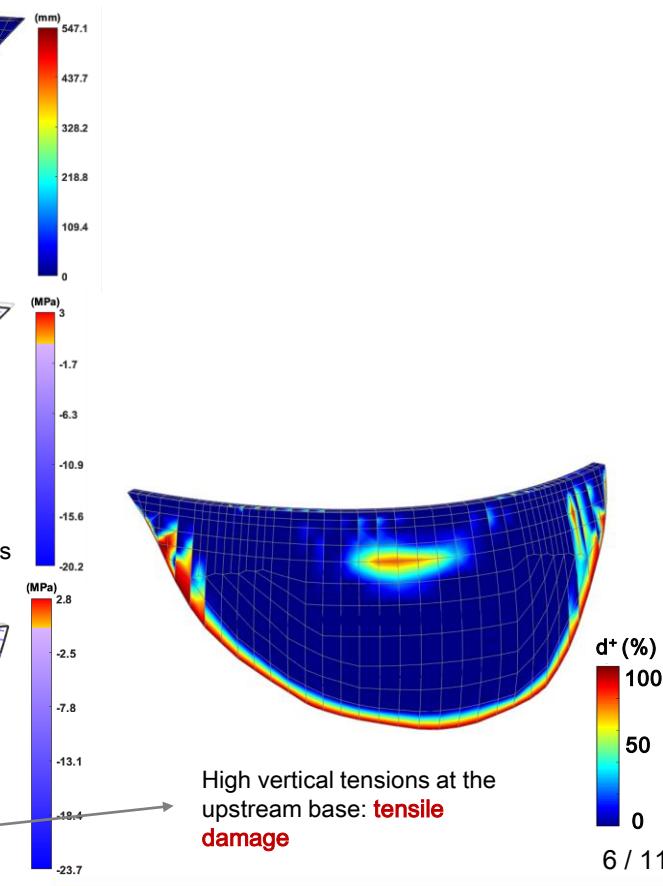
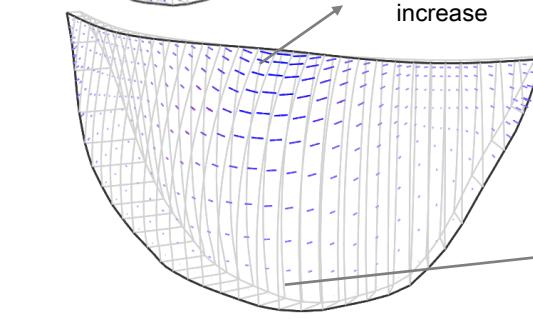
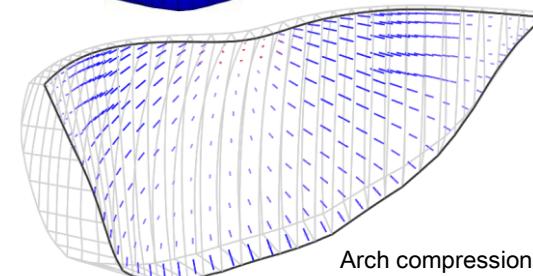
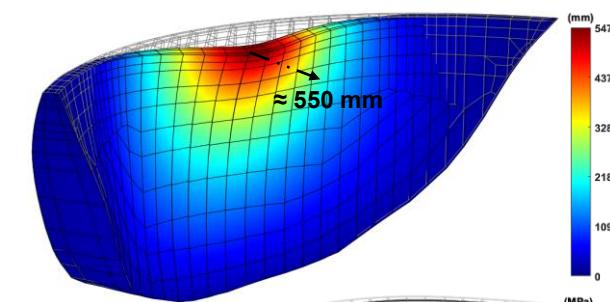


4. NON-LINEAR SEISMIC RESPONSE ANALYSIS

Linear response

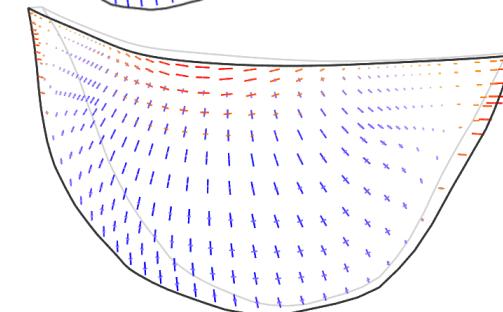
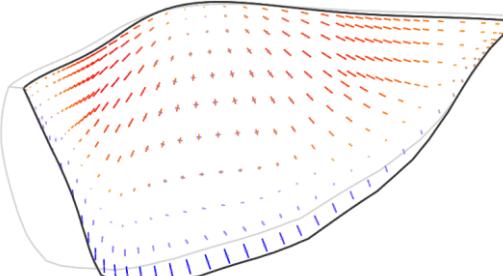
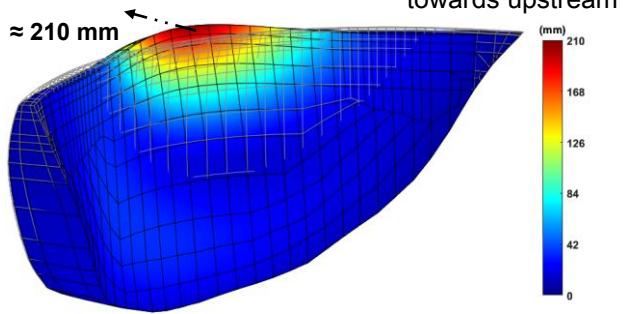


Non-linear response

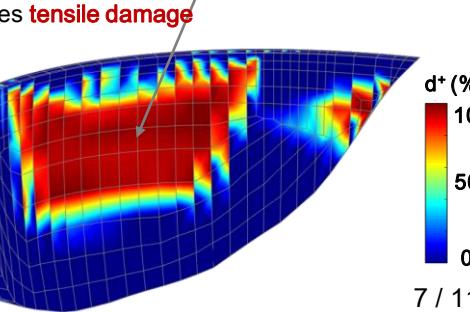
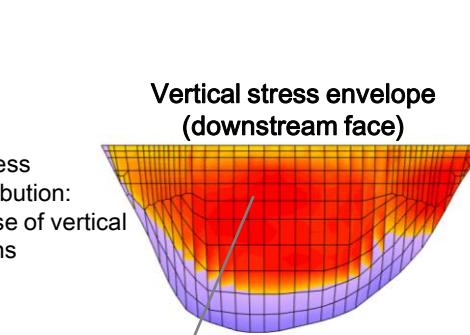
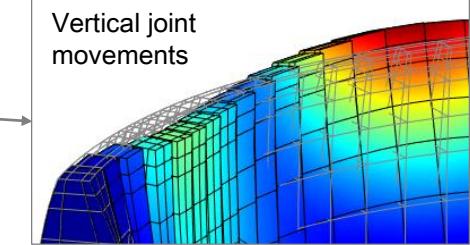
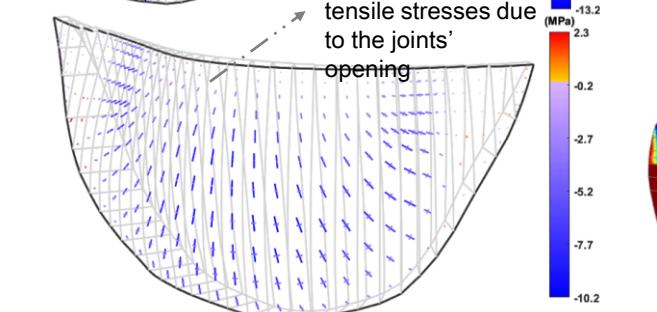
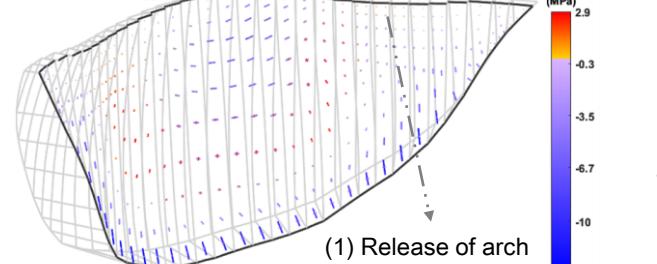
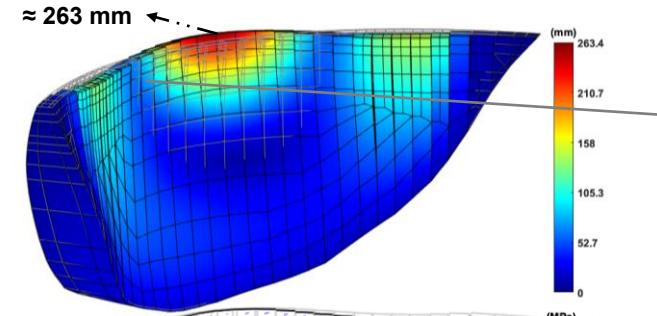


4. NON-LINEAR SEISMIC RESPONSE ANALYSIS

Linear response



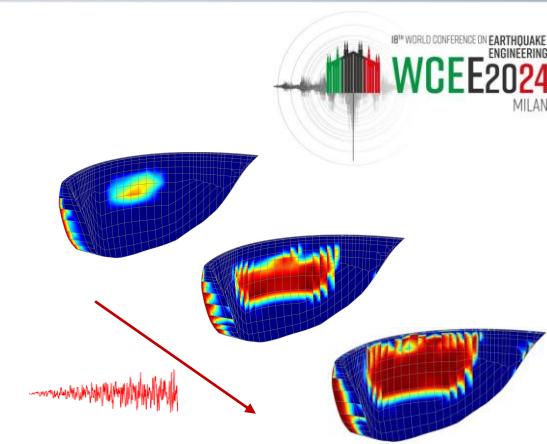
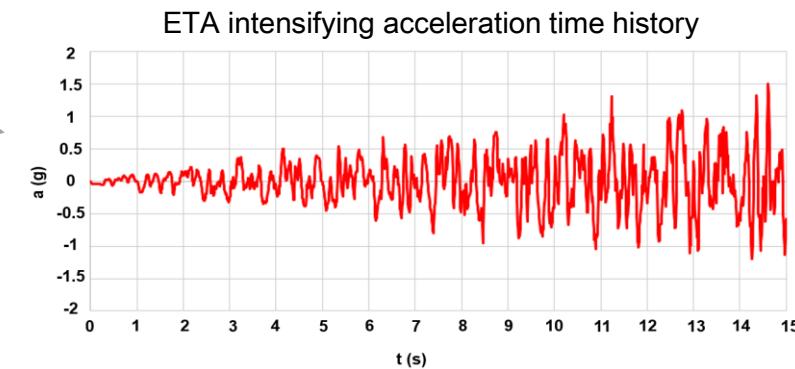
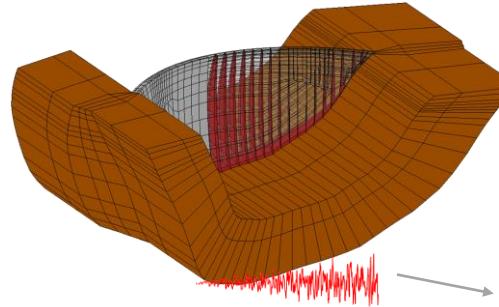
Non-linear response



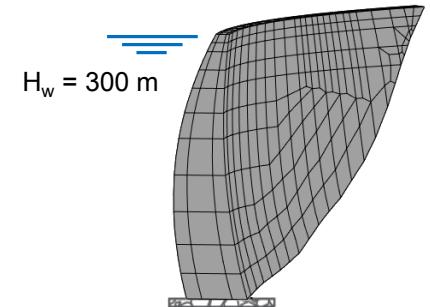
5. ETA-BASED SEISMIC PERFORMANCE ASSESSMENT

ETA-based methodology

- Seismic performance is evaluated by controlling the evolution of the tensile and compressive damage under dynamic excitation of increasing intensity
- Determine the maximum acceleration levels that the dam can withstand without presenting unacceptable damages



Full reservoir scenario

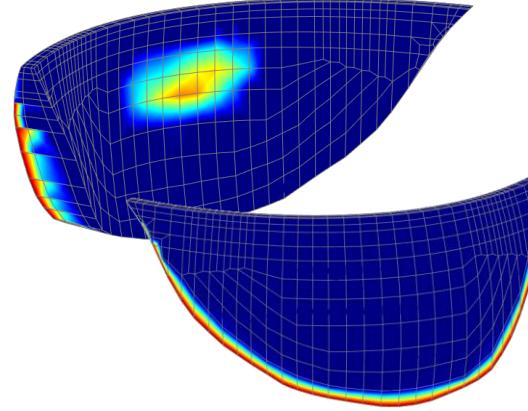


5. ETA-BASED SEISMIC PERFORMANCE ASSESSMENT

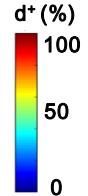
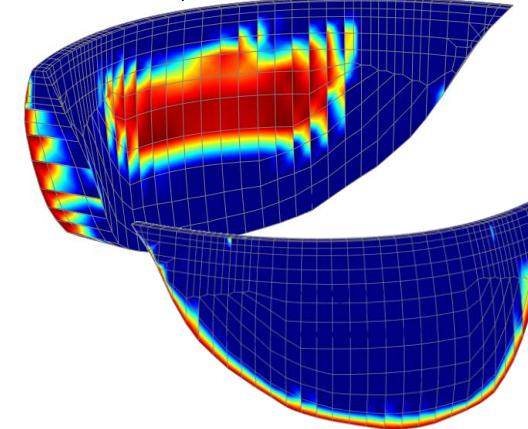
Tensile damage (d^+)



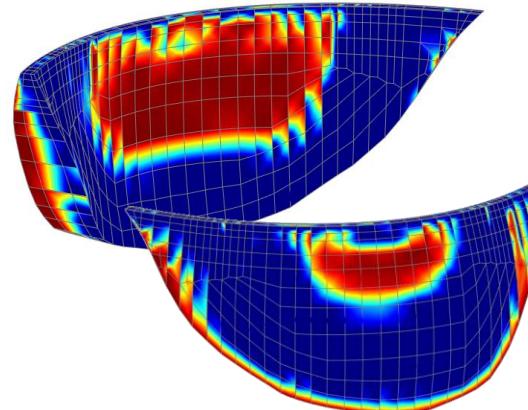
$t = 4 \text{ s}$ $a_p \approx 0.4g$



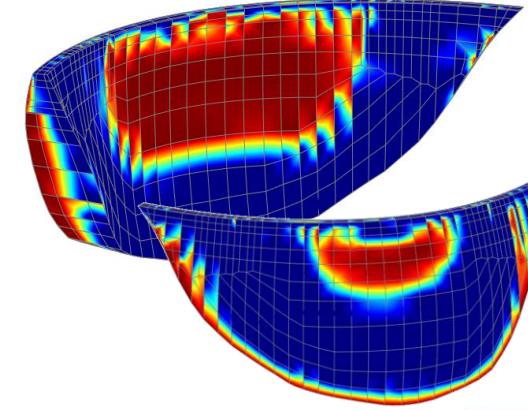
$t = 5 \text{ s}$ $a_p \approx 0.5g$



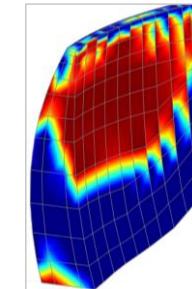
$t = 6 \text{ s}$ $a_p \approx 0.6g$



$t = 7 \text{ s}$ $a_p \approx 0.7g$



Tensile failure (cracking) from upstream to downstream:
unacceptable damage (service interruption)

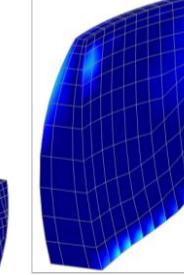
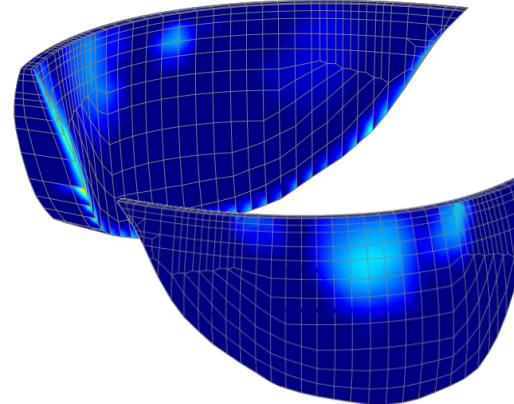


Seismic operational safety is verified for excitation levels up to 0.6g

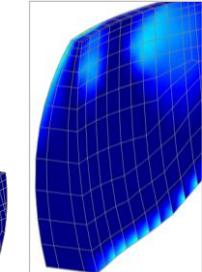
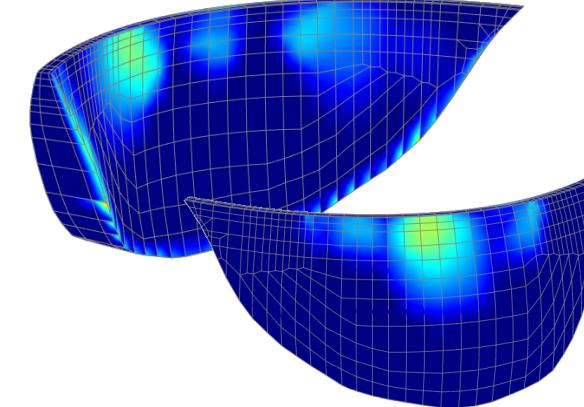
5. ETA-BASED SEISMIC PERFORMANCE ASSESSMENT

Compressive damage (d_c)

$$t = 9 \text{ s} \quad a_p \approx 0.9g$$



$$t = 11 \text{ s} \quad a_p \approx 1.1g$$



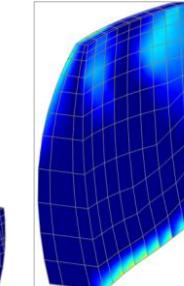
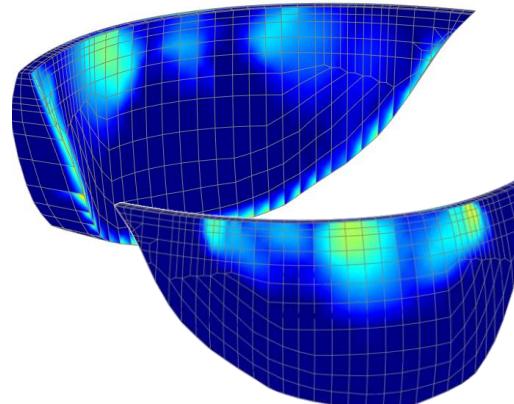
d_c (%)

100

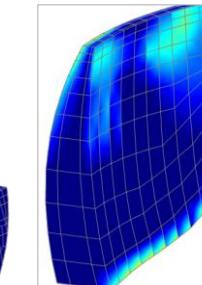
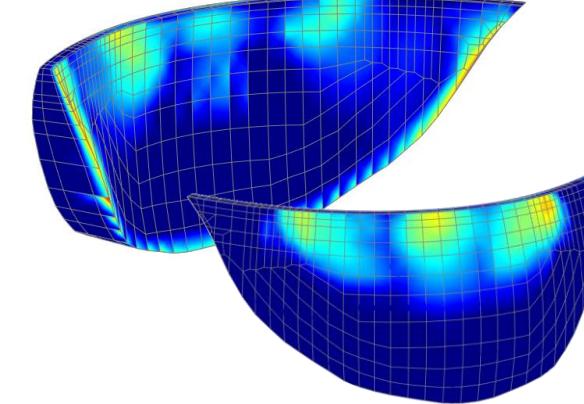
50

0

$$t = 13 \text{ s} \quad a_p \approx 1.3g$$



$$t = 15 \text{ s} \quad a_p \approx 1.5g$$



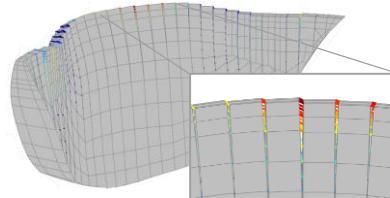
There is no compressive crushing in key areas (not a failure scenario)

Seismic structural safety is verified for excitation levels up to 1.5g

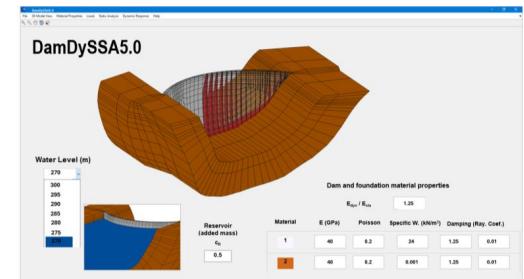
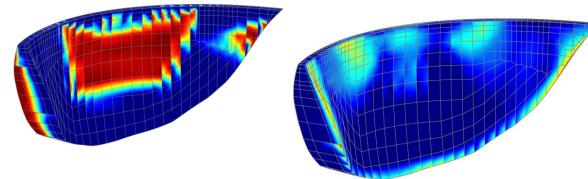
6. CONCLUDING REMARKS

- After years of research, our group developed *DamDySSA* and implemented a calculation module to conduct non-linear seismic analysis of arch dams

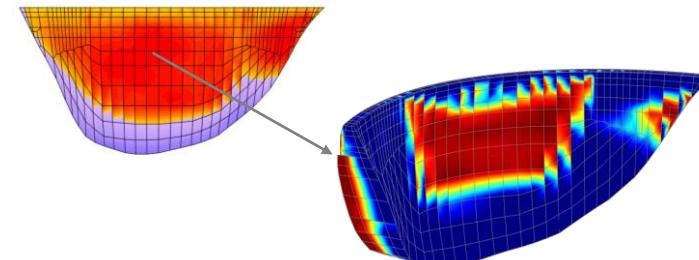
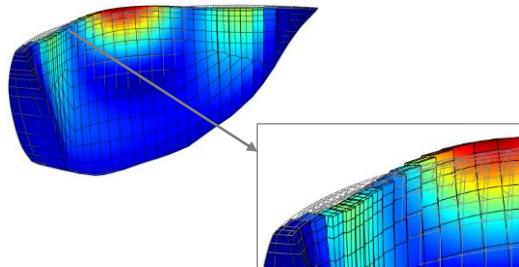
- Joint movements



- Tensile and compressive damage



- The results presented in this work for an ultra-high arch dam (as well as in many other studies) allowed to show the potential of *DamDySSA* to conduct efficient non-linear seismic analyses of arch dams, making it a reliable tool to support the seismic design and safety assessment studies



GRAZIE! THANK YOU!

Non-linear seismic response of an ultra-high arch dam.
ETA-based safety assessment

André Alegre^{1(*2,3)}, Sérgio Oliveira², Paulo Mendes³, Jorge Proença⁴, Rafael Ramos^{2,4}

¹ Kinematics Inc., Pasadena, CA, USA

² Concrete Dams Department - National Laboratory for Civil Engineering (LNEC), Lisbon, Portugal

³ Lisbon School of Engineering (ISEL-IPL), Lisbon, Portugal

⁴ CERIS – Instituto Superior Técnico, Lisbon, Portugal



RESEARCH PROJECT
FUNDÉD BY
 FCT para a Ciência
e a Tecnologia

REPÚBLICA
PORTUGUESA



BCI6, Tuesday Monitor 1, 14:30-14:40

Influence of nonlinearity of dynamic shear modulus on the seismic safety evaluation of arch dams

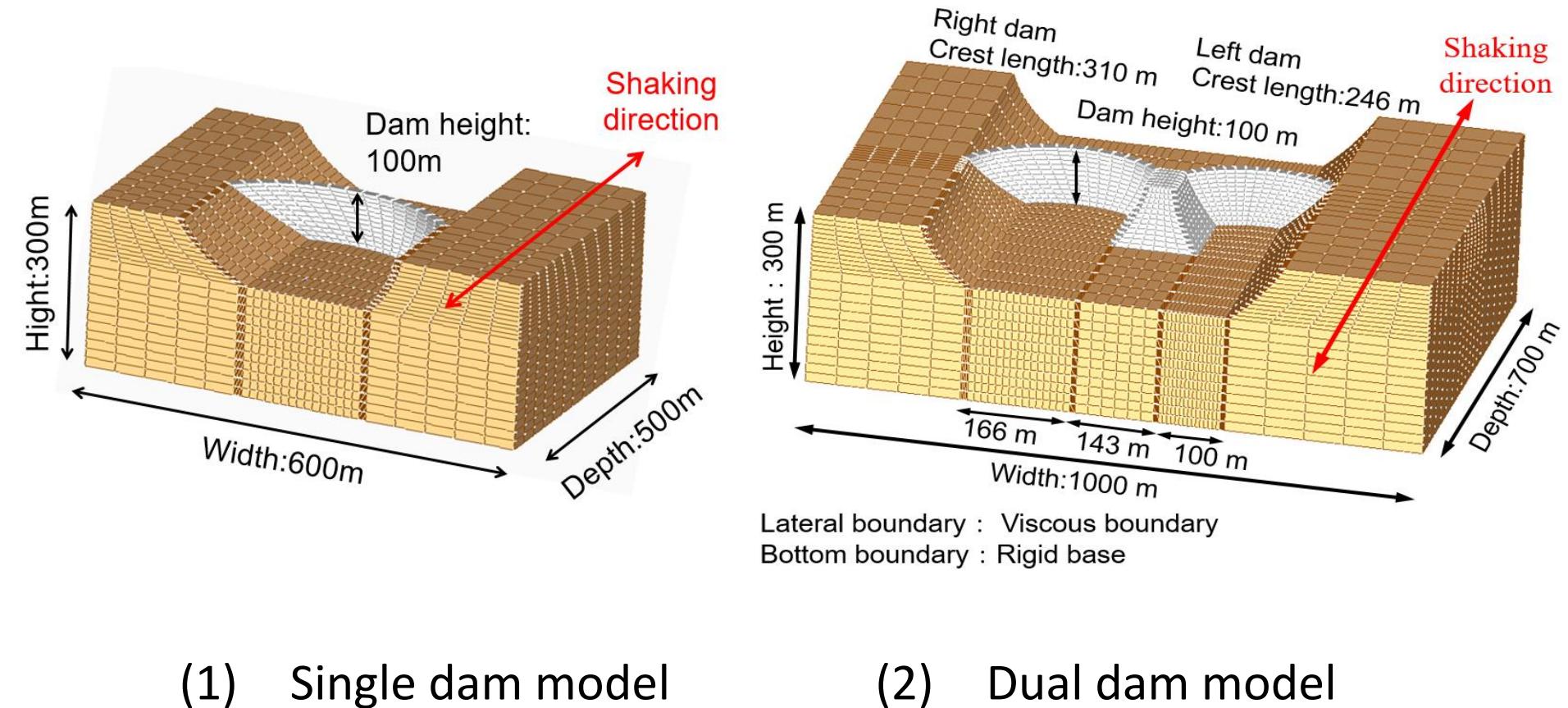
Y. ARIGA
Hirosaki University, Japan

Introduction

- When evaluating the safety of dams against strong earthquake motions, consideration of nonlinearity of dynamic deformation property of dam material becomes an important issue.
- So, we investigated the influence of decrease in dynamic shear modulus on the seismic tensile stresses in the dam body by 3-D dynamic FEM analysis.
- As for the strain dependence of dynamic shear modulus of dam body, we utilized the results of previous research for the reproduction analysis of actual earthquake behaviour of existing arch dam during the 2011 off the Pacific Coast of Tohoku Earthquake (Ariga. 2022).

3-D dynamic FEM analysis

- In order to examine the influence of nonlinearity of dynamic shear modulus on the seismic safety evaluation, 3-D dynamic analysis was executed by setting a simplified arch dam with a height of 100 m as the analysis object.
- As shown in Figure 1, two types of 3-D FEM model were set, or a single dam model and a dual dam model.
- The analysis program ISCEF (Integrated Software for Civil Engineering Fluid-structure interaction system), Century-techno (2023) was used.



(1) Single dam model

(2) Dual dam model

Figure 1. 3-D dynamic analysis model.

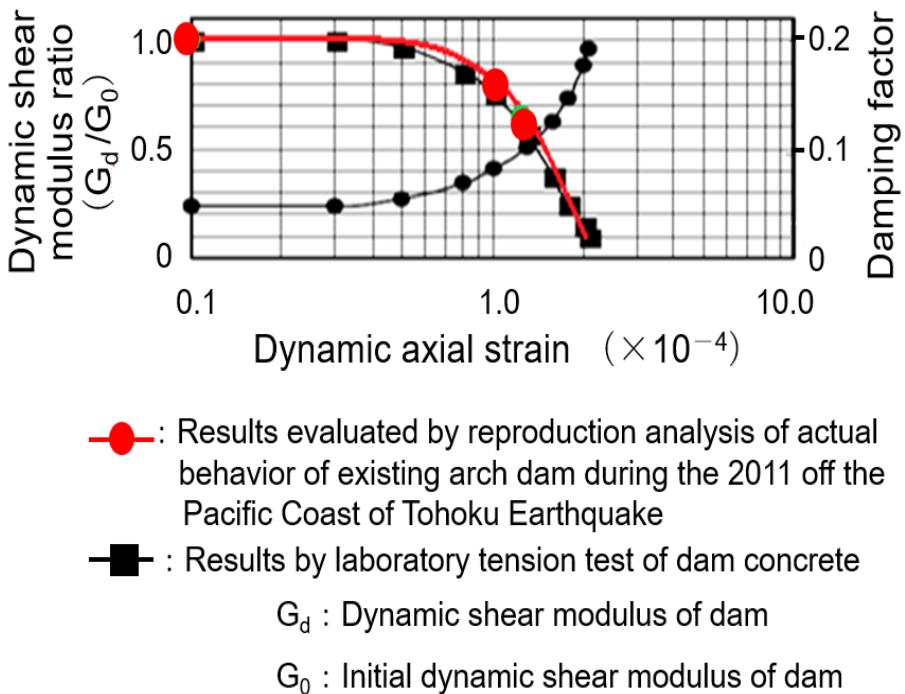


Figure 2. Nonlinear property of dynamic shear modulus and damping factor of dam

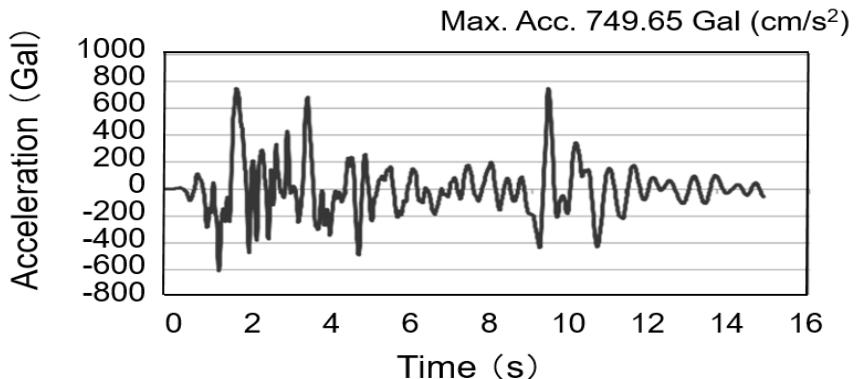


Figure 3. Input earthquake motion (JSCE, 2002).

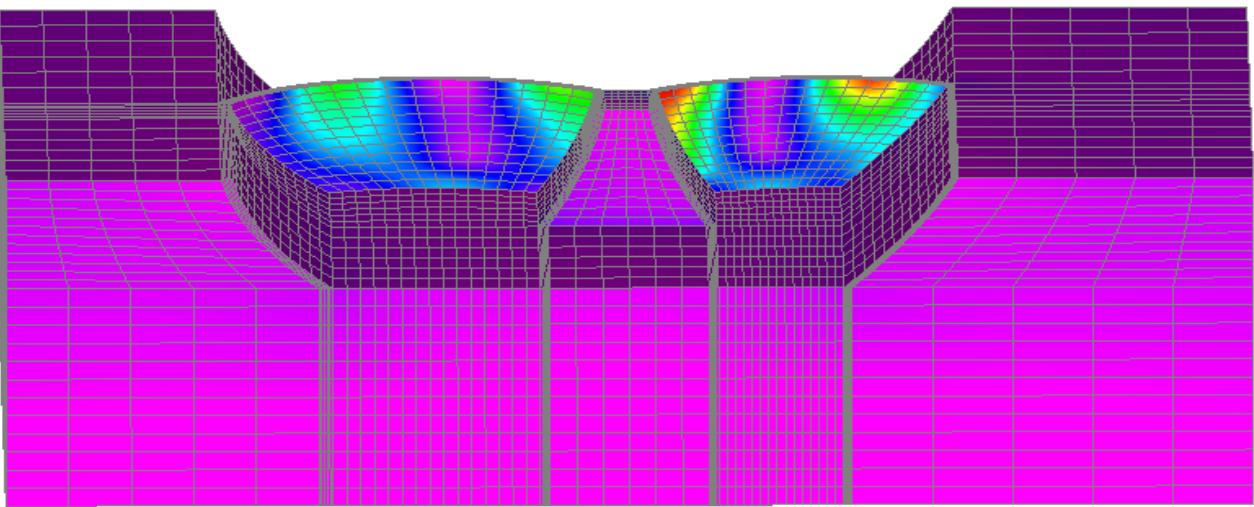
Table 1. Dynamic property values of dam and thrust block.

Case	G_d N/mm ²	Density	Poisson's ratio	Damping factor	G_d/G_0
Case-1	9250	2.40 t/m ³	0.20	0.05	1.0
Case-2	6000	2.40 t/m ³	0.20	0.05	0.65

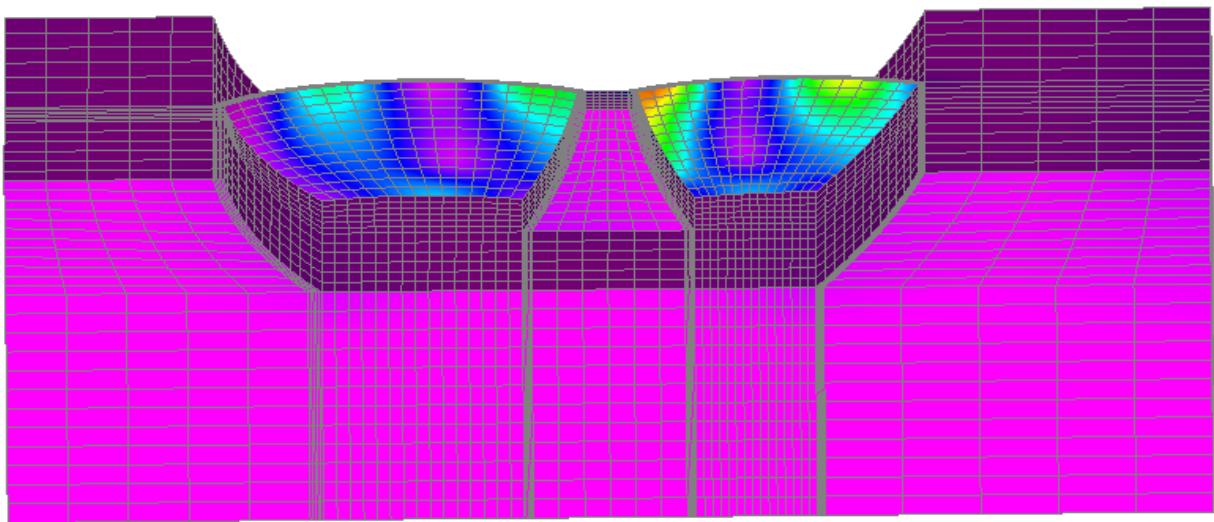
(Note) G_d : Dynamic shear modulus
 G_0 : Initial dynamic shear modulus
 G_d/G_0 : Reduction rate

Table 2. Dynamic property values of foundation rock.

Dynamic shear modulus (N/mm ²)	S-wave velocity (m/s)	Density t/m ³	Poisson's ratio	Damping factor
4500	1315	2.60	0.25	0.05



(1) $G=9250 \text{ N/mm}^2$ (Max. tensile stress : 32.59 N/mm^2)



(2) $G=6000 \text{ N/mm}^2$ (Max. tensile stress : 29.65 N/mm^2)

Figure 6. Distribution of seismic tensile stress in the case of dual dam.

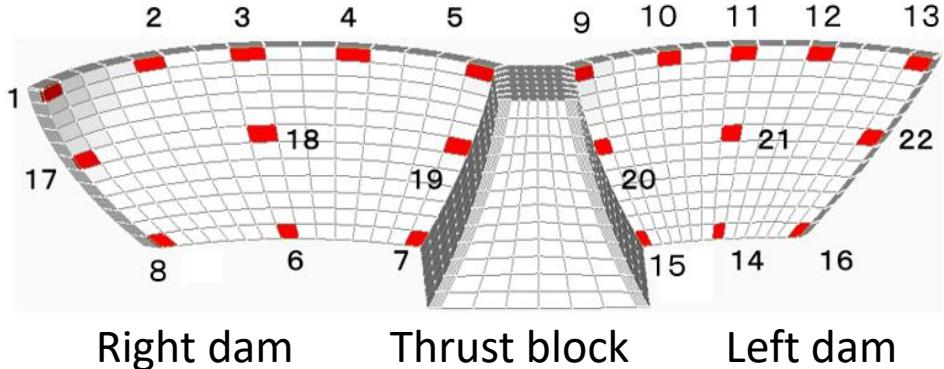


Figure 7. Representative output positions for dual dam.

Table 4. Seismic tensile stress at representative positions for dual dam.

(Unit : N/mm²)

Position				$G_d : 9250 \text{ N/mm}^2$	$G_d : 6000 \text{ N/mm}^2$
2	Right dam	Dam crest	Near right abutment	24.79	22.38
3	Right dam	Dam crest	Centre	20.13	14.65
5	Right dam	Dam crest	Thrust block connection	29.75	19.27
6	Right dam	Dam base	Centre	15.46	12.80
9	Left dam	Dam crest	Thrust block connection	32.60	29.66
10	Left dam	Dam crest	Near right abutment	18.78	< 23.97
12	Left dam	Dam crest	Near left abutment	32.07	26.62
14	Left dam	Dam base	Centre	14.61	11.42
17	Right dam	Middle level	Right abutment	10.53	< 11.42
22	Left dam	Middle level	Left abutment	21.16	19.98

Conclusions

1. Consideration on influence of dynamic shear modulus on stress evaluation

- ◆ The effect of reduced dynamic shear modulus on seismic tensile stresses in the dam body and foundation rock mass was investigated by three-dimensional dynamic analysis.
- ◆ The seismic tensile stresses in the dam body decreased in many locations as the dynamic shear modulus decreased.
- ◆ However, the seismic tensile stresses increased at some parts of the dam crest and the foundation rock as the dynamic shear modulus decreased.
- ◆ Since the seismic safety of an arch dam is highly dependent on the soundness of the foundation rock, careful safety verification is necessary when tensile stresses increase in the foundation rock and the abutments.

2. Consideration on seismic safety evaluation method for multiple arch dam

- ◆ A multiple arch dam is a dam consisting of two or more arch dams connected together.
- ◆ With regard to the seismic safety evaluation of dams with such composite structures, two methods can be considered, or individual evaluation and overall evaluation.
- ◆ The former is a method in which each dam is considered to be an independent structure and is evaluated individually.
- ◆ The latter is a method in which multiple dams are considered to be a single structure and the entire system is evaluated.
- ◆ The results of this study suggest that the seismic safety evaluation of multiple arch dams should be conducted not by individual evaluation but by overall evaluation.



Thank you for your attention



SEISMIC SLOPE STABILITY OF HYBRID TAILINGS DAMS: A PROBABILISTIC APPROACH

T S Aswathi¹, Saikat Kuili², Ravi S
Jakka³

^{1,2} Research Scholar, Indian Institute of
Technology Roorkee

³ Professor, Indian Institute of Technology
Roorkee

Contents

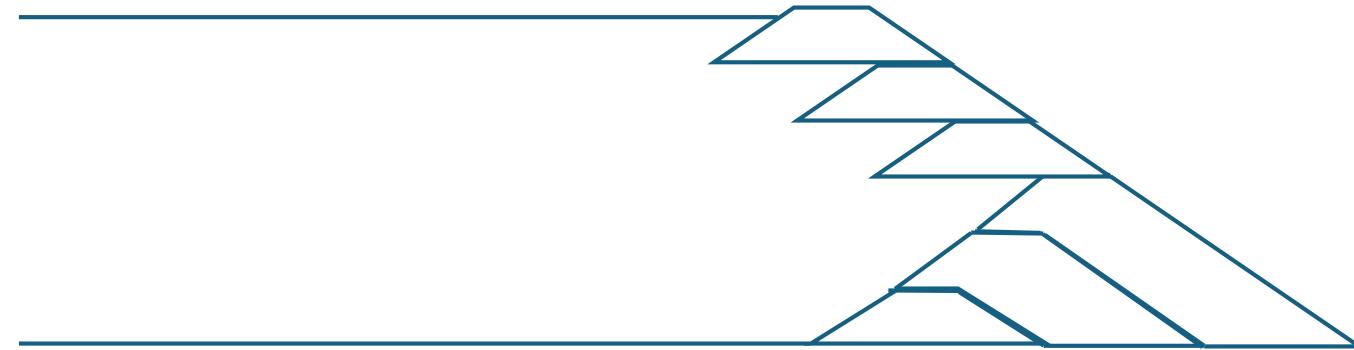


- What are tailings dams?
- Why probabilistic slope assessment of hybrid tailings dam?
- Problem statement
- Methodology
- Result and discussion
- Conclusion
- References



What are tailings dams?

- Tailings dams are earth structures used to store mining waste.
- Typically constructed using three conventional methods: upstream, downstream, and centerline - differ based on the movement of the dike crest with respect to the initial dike position during the construction process. (Vick, 1990).
- Upstream - most popular in the past for its cost effectiveness but now abandoned due to its poor performance.
- Hybrid tailings construction - uses two conventional constructional method to raise the tailings dam.
- Hybrid tailings construction can be useful in utilising the abandoned old tailings dam and reusing the disposal area. This also help in addressing the storage of disposal area hence enhancing the efficiency of tailings disposal.



Why probabilistic slope assessment of hybrid tailings dam?



- Contemporary soil strength assessments assume uniform properties, but the inclusion of slimes in dike impoundments introduces variability. Dikes are constructed in compacted layers, and ignoring soil property variations can compromise design integrity due to the mixture of different properties in slimes and tailings sand.
- Traditional deterministic stability analyses use a single Factor of Safety (FoS) and assume a slope is secure if the FoS exceeds 1. However, Duncan (2000) argues that this method fails to address soil property uncertainties adequately, as identical FoS values can correspond to different risk levels due to soil variability, as noted by Li and Lumb (1987).
- Probabilistic analysis, introducing the probability of failure (P_f) and reliability index (β), offers a comprehensive view of slope stability and risks. Traditional methods may miss risks, as minor disturbances can destabilize secure dams (Lade, 1992).
- Hamade et al. (2011) found that in the upstream construction method, the Factor of Safety (FoS) is lower, P_f is higher, and β is lower, indicating less stability. Further studies by Hegde and Das (2019), Sitharam and Hegde (2019), and Das and Hegde (2020) on tailings dam heightening revealed that soil property variability significantly impacts FoS values, underscoring the importance of probabilistic approaches for a realistic assessment of slope stability and risks. These studies considered both upstream and downstream raising methods for

Problem statement

The objective of this study is to analyse the probabilistic slope stability of hybrid tailings dams constructed using the upstream method. Key random variables include the variation in friction angle of slimes and tailings sand, as well as the position of the phreatic line. Both static and seismic loading conditions will be considered.

Additionally, this study aims to explore the feasibility of repurposing abandoned upstream tailings dams into hybrid structures.

Methodology

- Slope stability - LEM method (deterministic and probabilistic)
- Morgenstern-Price (M-P) method - static and pseudo static ($k_h = 0.1$ to 0.4)
- Deterministic analysis - considering mean value - critical slip surface
- Probabilistic analysis - deterministic critical slip surface - Monte Carlo Simulation (MCS) with 10,000 iteration.
- Mohr Coulomb material model
- Variation - friction angle of slimes and tailings sand - maximum permissible 25% CoV (Baecher and Christian, 2005; Hamade et al., 2011) as well as phreatic line variation.

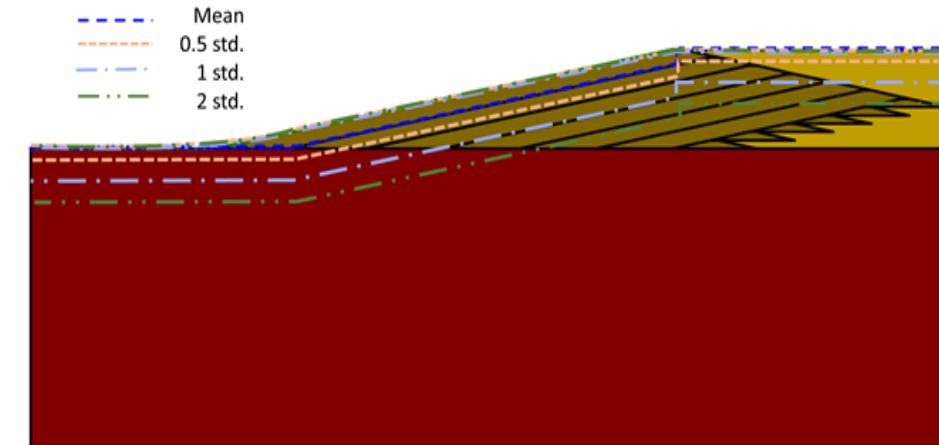


Figure 2. Typical illustration of phreatic line variation with 0.5 std., 1 std. and 2 std. along with mean phreatic line.

Table 1. Material properties along with their probability characteristics (Mabes et al., 1977 and McKee et al., 1978).

Material	Unit weight (kN/m ³)	Angle of friction (°)	Friction angle CoV (%)	Probability distribution
Slimes	14	31	5, 10, 15, 25	Normal
Tailings sand	17.5	35	5, 10, 15, 25	Normal
Foundation	20	40	-	-

Results and Discussions

Deterministic slope stability

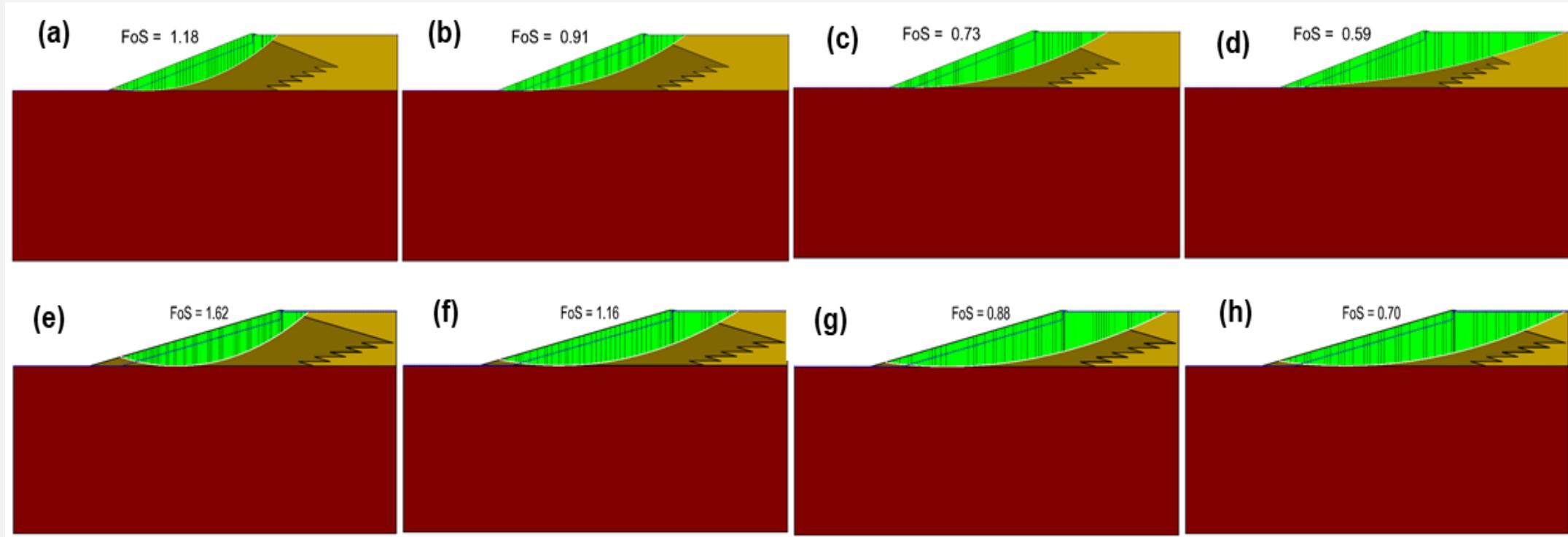
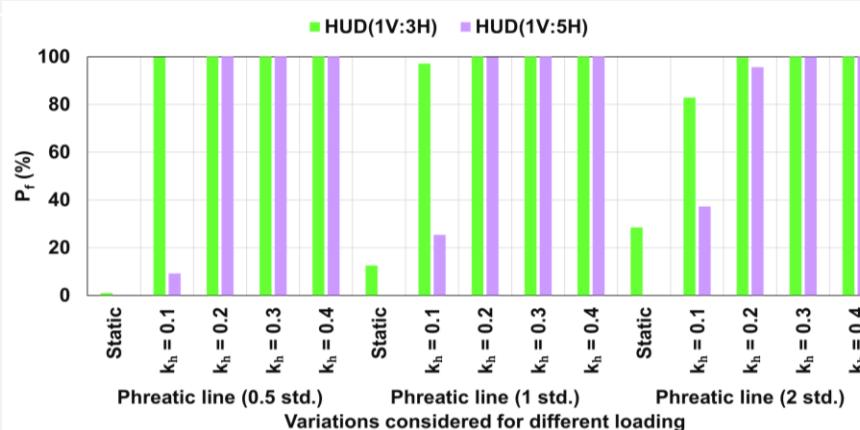
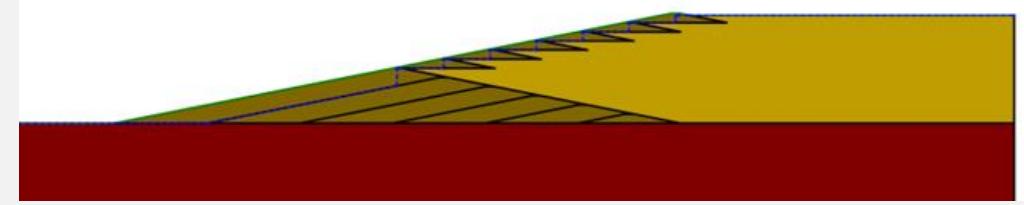


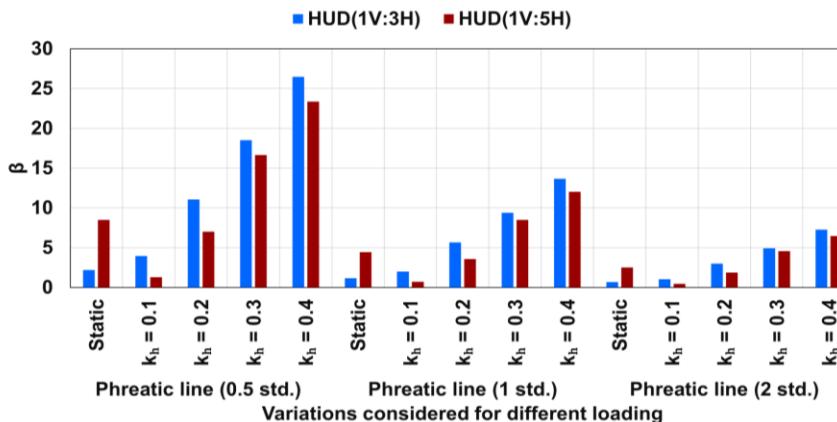
Figure 6. Critical slip surface pertaining to different pseudo-static loads of (a) $k_h = 0.1$, (b) $k_h = 0.2$, (c) $k_h = 0.3$ and (d) $k_h = 0.4$ for HDU(1V:3H) and correspondingly (e) $k_h = 0.1$, (f) $k_h = 0.2$, (g) $k_h = 0.3$ and (h) $k_h = 0.4$ for HDU(1V:5H).

Results and Discussions

Probabilistic slope stability



(a)



(b)

Figure 14. Probabilistic analysis outcomes of HUD with varying slopes and phreatic line variations, depicting (a) probability of failure and (b) reliability index.

Conclusions

- Evaluated stability of four hybrid tailings dam configurations under static and pseudo-static loadings.
- Stability assessed using the limit equilibrium approach and probabilistic analysis.
- HDU configuration consistently most stable, followed by HCU.
- Upstream method in the lower segment outperformed its use in the upper segment.
- Deterministic FoS decreased with increased seismic loading.
- Probabilistic analysis provided insights into failure risks under varying loading conditions. Friction angle variability had a greater impact on stability than phreatic line fluctuations.
- Higher seismic loading increased failure risk; variability affected failure probability trends.
- Comparison of P_f values:
 - Steeper slopes: HCU (23% static, 98.5% seismic) vs. HDU (9.71% static, 94% seismic).
 - Flatter slopes: HCU (2.5% static, 94% seismic) vs. HDU (1.4% static, 84% seismic).
 - HDU showed minimal failure risk under static and low seismic conditions.
- Probabilistic analyses are crucial for understanding slope stability and mitigating risks.⁹

References

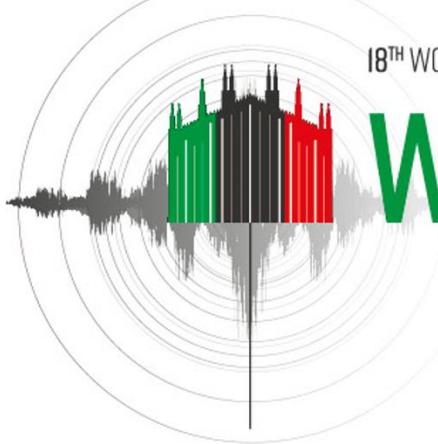
- ANCOLD (2019). *Guidelines on Tailings Dams Planning, Design, Construction, Operation and Closure - Addendum*.
- Baecher G. B., Christian J. T. (2005). *Reliability and Statistics in Geotechnical Engineering*, John Wiley & Sons.
- Chen Y., Wei Z. (2023). Stability of Tailings Dam Constructed by both Upstream and Centerline Methods, *Geotechnical and Geological Engineering*, 1-12.
- Das T., Hegde A. M. (2020). "A comparative deterministic and probabilistic stability analysis of rock-fill tailing dam", *Proceedings of the IACMAG Symposium 2019*, 607-617.
- Duncan M. (2000). Factors of safety and reliability in geotechnical engineering, *Journal of Geotechnical and Geoenvironmental Engineering*, 126(4): 307-316.
- El-Ramly H., Morgenstern N. R., Cruden D. M. (2002). Probabilistic slope stability analysis for practice, *Canadian Geotechnical Journal*, 39(3): 665-683.
- Elkateb T., Chalaturnyk R., Robertson P. K. (2003). An overview of soil heterogeneity: quantification and implications on geotechnical field problems, *Canadian Geotechnical Journal*, 40(1): 1-15.
- Ferdosi B., James M., Aubertin M. (2015). Investigation of the effect of waste rock inclusions configuration on the seismic performance of a tailings impoundment, *Geotechnical and Geological Engineering*, 33: 1519-1537
- Hamade T., Mitri H., Saad B., Pouliot S. (2011). "Stochastic analysis of tailing dams stability using numerical modelling", *Proceedings of the 14th Pan-American Conference on Soil Mechanics and Geotechnical Engineering 64th Canadian Geotechnical Conference*, Toronto, Canada, 1-8.
- Hegde A. M., Das T. (2019). Finite element-based probabilistic stability analysis of rock-fill tailing dam considering regional seismicity, *Innovative Infrastructure Solutions*, 4: 1-14.
- Jakka R. S., Ramana G. V., Datta M. (2011). Seismic slope stability of embankments constructed with pond ash, *Geotechnical and Geological Engineering*, 29: 821-835.
- Lade P. V. (1992). Static instability and liquefaction of loose fine sandy slopes, *Journal of Geotechnical Engineering*, 118(1): 51-71.
- Li K. S., Lumb P. (1987). Probabilistic design of slopes, *Canadian Geotechnical Journal*, 24(4): 520-535.
- Liu H., Yang C., Zhang C., Mao H. (2012). Study on static and dynamic strength characteristics of tailings silty sand and its engineering application, *Safety Science*, 50(4): 828-834.
- Lyu Z., Chai J., Xu Z., Qin Y., Cao J. (2019). A comprehensive review on reasons for tailings dam failures based on case history, *Advances in Civil Engineering*, 2019: 1-18.
- Mabes D. L., Hardcastle J. H., Williams R. E. (1977). "Physical properties of Pb-Zn mine-process wastes", *Proceedings of the Conference on Geotechnical Practice for Disposal of Solid Waste Materials*, ASCE, 103-117.
- McKee B. E., Robinson K. E., Urlich C. M. (1978). "Upstream design for extension of an abandoned tailings pond", *Proceedings of the 2nd International Tailings Symposium*, Denver, Colo, 2: 210-233.
- Özer A. T., Bromwell L. G. (2012). Stability assessment of an earth dam on silt/clay tailings foundation: A case study, *Engineering Geology*, 151: 89-99.
- Phoon K. K. (2002). "Potential application of reliability-based design to geotechnical engineering", *Proceedings of the 4th Colombia Geotechnical Seminar*, Medellin, 1-24.
- Psarropoulos P. N., Tsompanakis Y. (2008). Stability of tailings dams under static and seismic loading, *Canadian Geotechnical Journal*, 45(5): 663-675.
- Rico M., Benito G., Salgueiro A. R., Díez-Herrero A., Pereira H. G. (2008). Reported tailings dam failures: a review of the European incidents in the worldwide context, *Journal of Hazardous Material*, 152(2): 846-852.
- Sitharam T. G., Hegde A. M. (2017). Stability analysis of rock-fill tailing dam: an Indian case study, *International Journal of Geotechnical Engineering*, 11(4): 332-342.
- Sitharam T. G., Hegde A. M. (2019). A case study of probabilistic seismic slope stability analysis of rock fill tailing dam, *International Journal of Geotechnical Earthquake Engineering*, 10(1): 43-60.
- Vick S. G. (1990). *Planning, design, and analysis of tailings dams*, BiTech Publishers Ltd



Thank you!

Any questions?





18TH WORLD CONFERENCE ON EARTHQUAKE
ENGINEERING
WCEE2024
MILAN

MILAN, ITALY
30TH JUNE - 5TH JULY 2024

www.wcee2024.it

NEW EFFICIENT METHODS FOR THE SEISMIC ANALYSIS OF DAMS AND THEIR APPURTENANT STRUCTURES

Najib Bouaanani and Ramtin Kouhdasti



POLYTECHNIQUE
MONTRÉAL



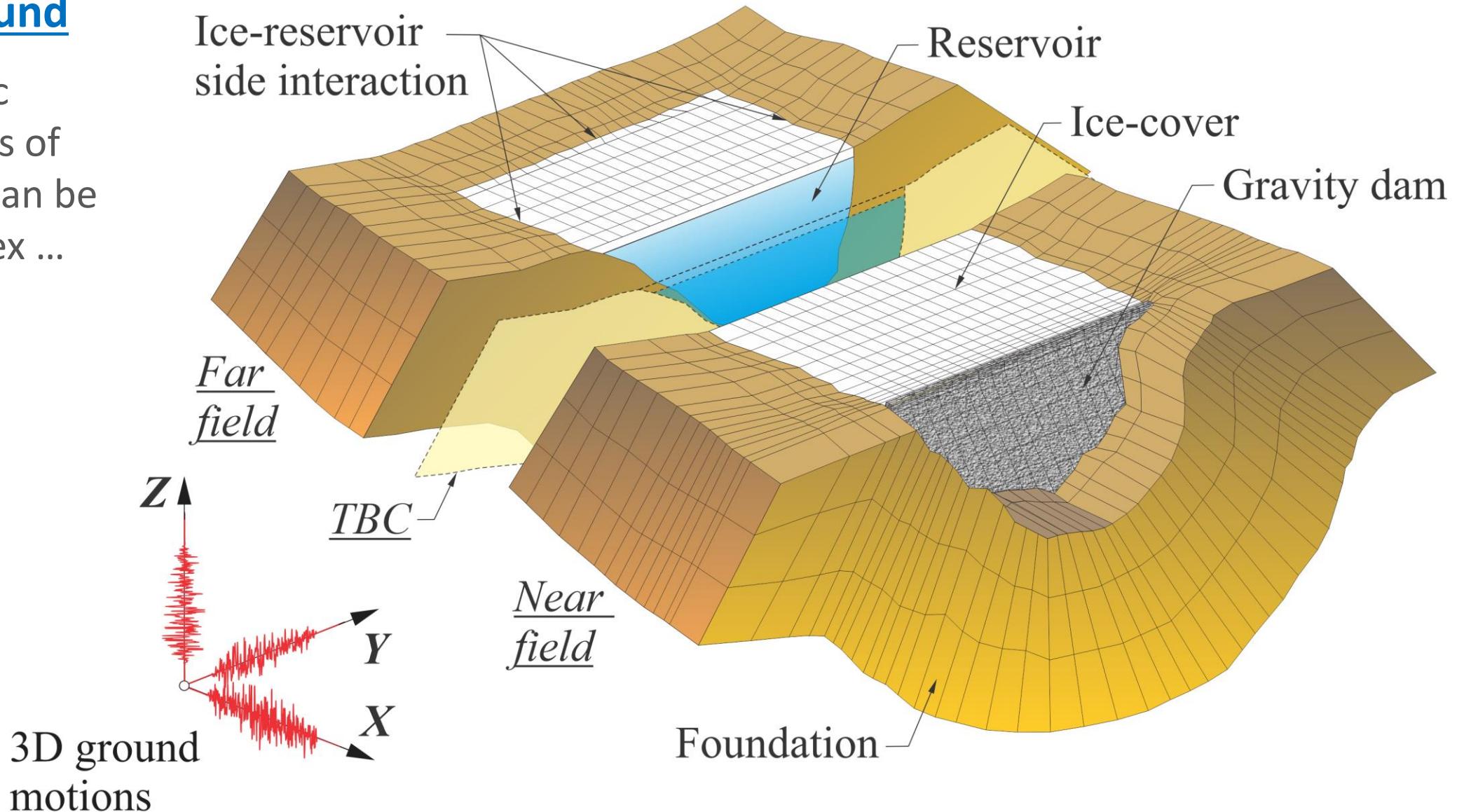
OUTLINE

- **Background**
- **Methodology**
- **Examples**
- **Conclusions**

INTRODUCTION

Background

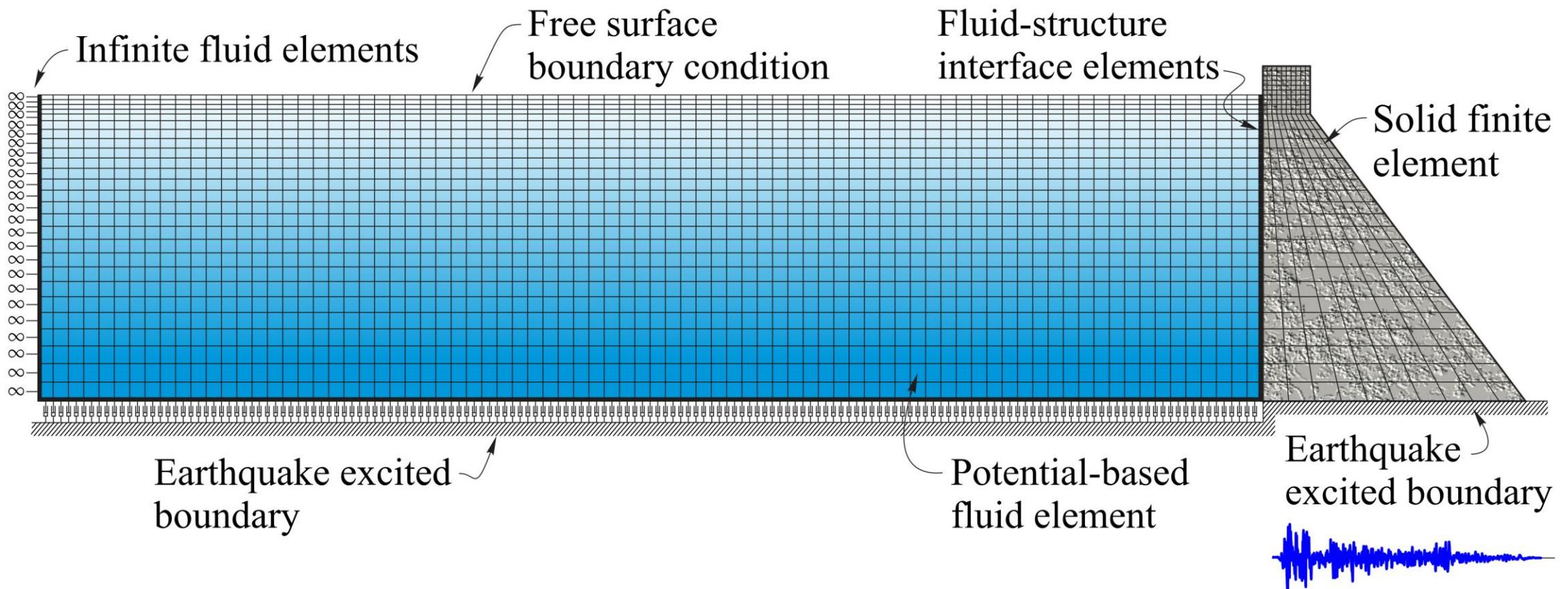
- Seismic analysis of dams can be complex ...



INTRODUCTION

Background

- Simplifications are necessary, e.g. from 3D to 2D analysis, etc.



INTRODUCTION

Background

- Despite their limitations, simplified methods remain valuable sources of information on the seismic behavior of dams and their appurtenant structures, particularly during the initial phases of design and/or safety evaluation

Main objective

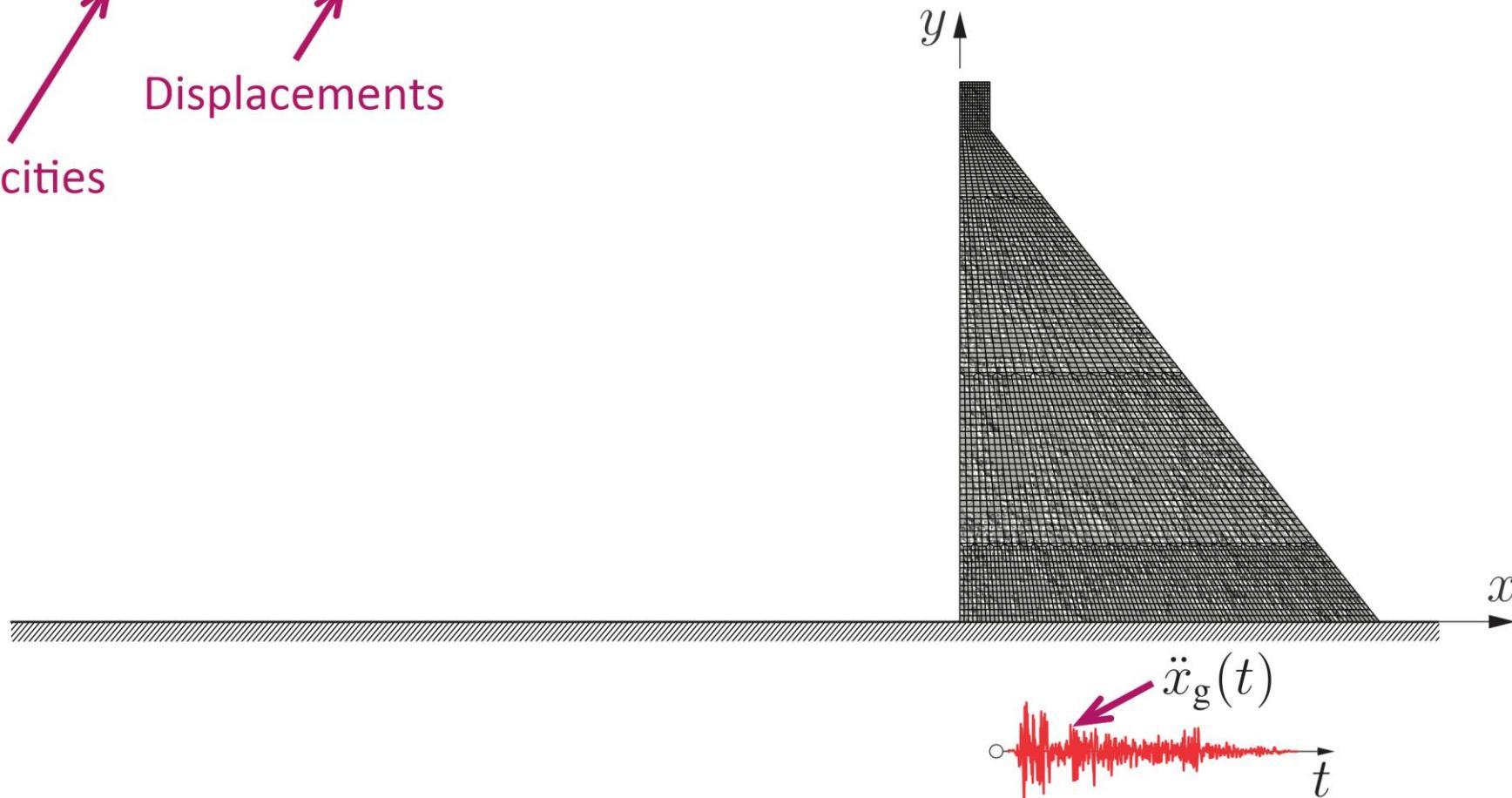
- Propose a simplified approach to conduct time-history modal superposition and response spectrum analyses of a dam-reservoir system
- The proposed method incorporates earthquake-induced hydrodynamic effects into modified versions of the input ground acceleration and its response spectrum
- The resulting seismic demands can be directly applied to the structure with empty reservoir (i.e. without water), thus eliminating the need for specialized software to account for fluid-structure dynamic interaction.

METHODOLOGY

Time-history modal superposition analysis (dry system)

$$M \ddot{U}(t) + C \dot{U}(t) + K U(t) = -M \mathbf{1}^{(x)} \ddot{x}_g(t)$$

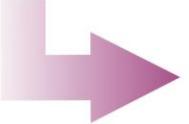
↑
Accelerations
↑
Velocities
↑
Displacements

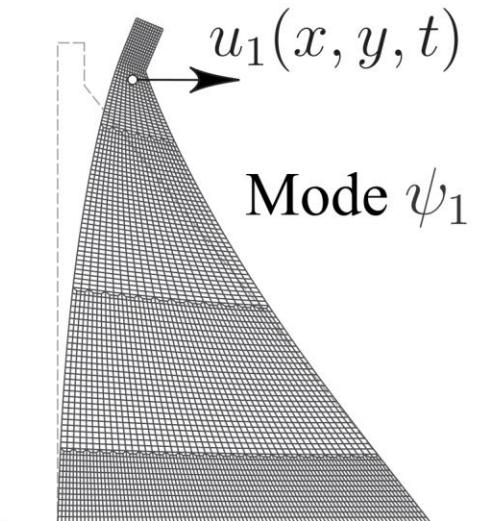


METHODOLOGY

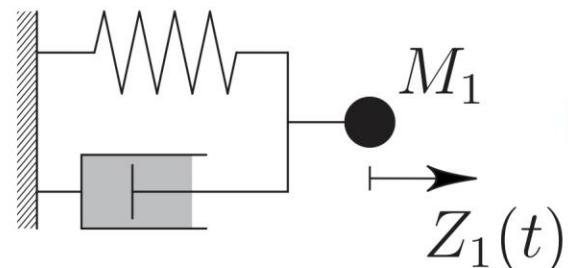
Fundamental mode analysis (dry system)

$$\mathbf{M} \ddot{\mathbf{U}}(t) + \mathbf{C} \dot{\mathbf{U}}(t) + \mathbf{K} \mathbf{U}(t) = -\mathbf{M} \mathbf{1}^{(x)} \ddot{x}_g(t)$$

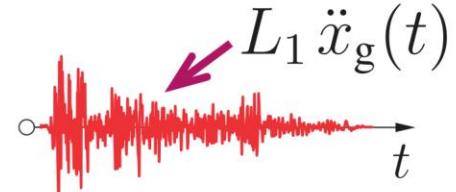

$$M_1 \left[\ddot{Z}_1(t) + 2 \xi_1 \omega_1 \dot{Z}_1(t) + \omega_1^2 Z_1(t) \right] = -L_1 \ddot{x}_g(t)$$



ESDOF




$$u_1(x, y, t) = \psi_1^{(x)}(x, y) Z_1(t)$$

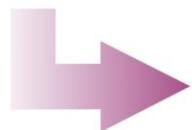



$$u(x, y, t) \approx u_1(x, y, t)$$

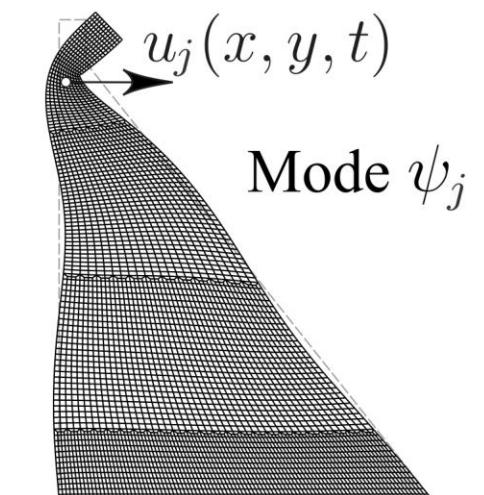
METHODOLOGY

Higher modes (dry system)

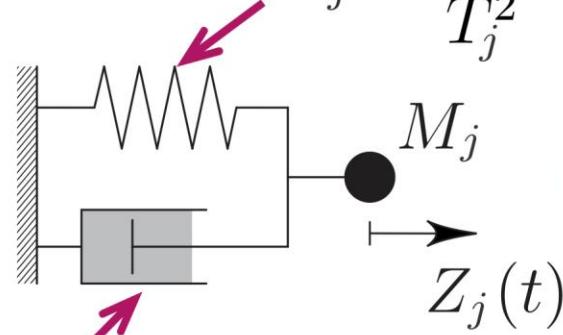
$$\mathbf{M} \ddot{\mathbf{U}}(t) + \mathbf{C} \dot{\mathbf{U}}(t) + \mathbf{K} \mathbf{U}(t) = -\mathbf{M} \mathbf{1}^{(x)} \ddot{x}_g(t)$$



$$M_j \left[\ddot{Z}_j(t) + 2\xi_j \omega_j \dot{Z}_j(t) + \omega_j^2 Z_j(t) \right] = -L_j \ddot{x}_g(t)$$



ESDOE



$$C_j = \frac{4\pi}{T_j} \xi_j M_j$$



$$Z_j(\omega) = \frac{L_j}{M_j(\omega^2 - 2i\xi_j\omega\omega_2 - \omega_j^2)}$$

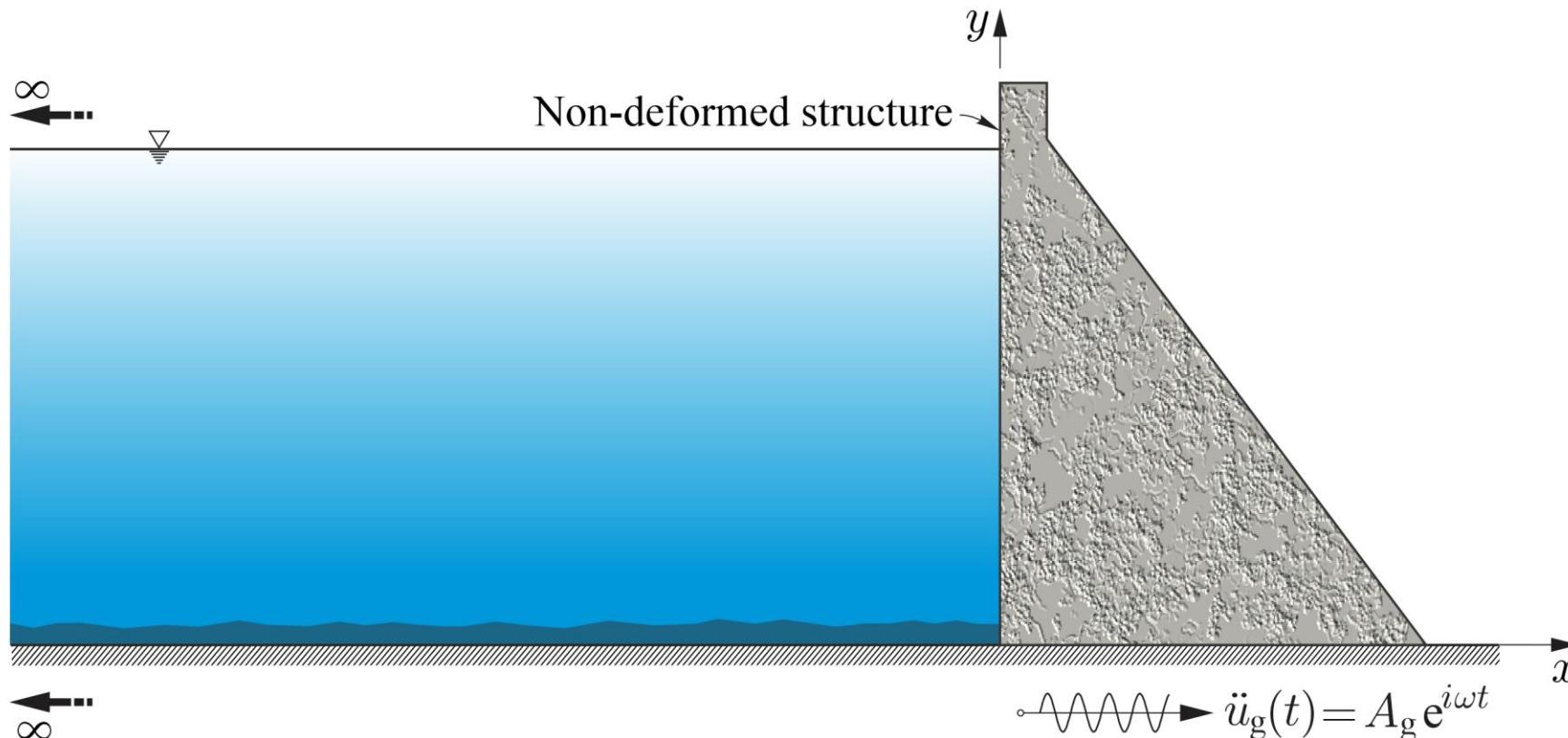
$$u_j(x, y, t) = \psi_j^{(x)}(x, y) Z_j(t)$$



$$u(x, y, t) \approx \sum_{j=1}^{N_s} u_j(x, y, t)$$

METHODOLOGY

Time-history modal superposition analysis (wet system)

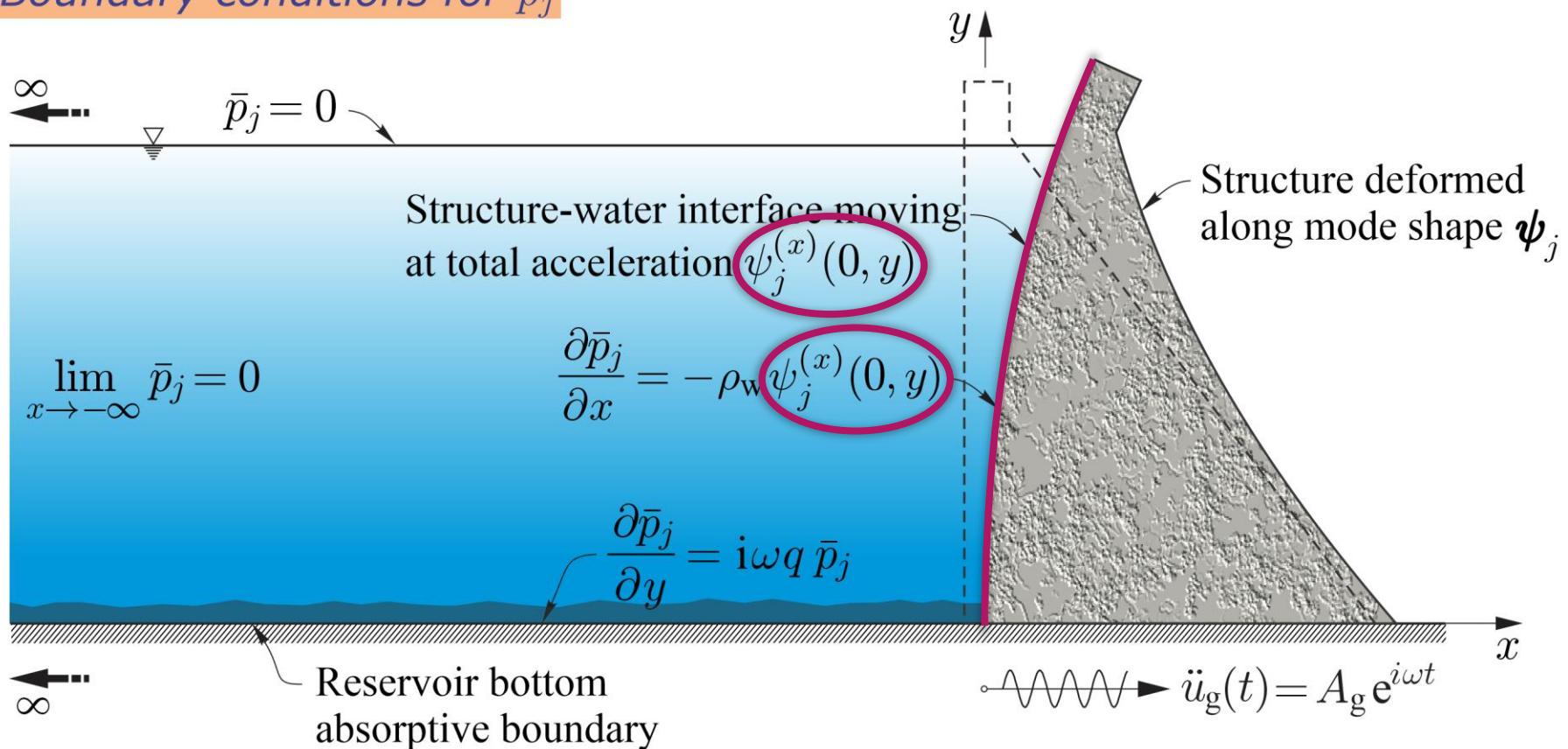


METHODOLOGY

Analytical approach (e.g. Chopra et al., Bouaanani et al., etc.)

$$\bar{p}(x, y, \omega) = \bar{p}_0(x, y, \omega) - \omega^2 \sum_{j=1}^{N_s} \bar{Z}_j(\omega) \bar{p}_j(x, y, \omega)$$

Boundary conditions for \bar{p}_j



METHODOLOGY

Time-history modal superposition analysis (wet system)

$$\mathbf{M} \ddot{\widehat{\mathbf{U}}}(t) + \mathbf{C} \dot{\widehat{\mathbf{U}}}(t) + \mathbf{K} \widehat{\mathbf{U}}(t) = -\mathbf{M} \mathbf{1}^{(x)} \ddot{x}_g(t) + \mathbf{F}_h(t)$$



$$\sum_{j=1}^{N_s} \left[\left(-\omega^2 + 2i\xi_n \omega \omega_n + \omega_n^2 \right) M_n \delta_{n,j} + \omega^2 \vartheta_{j,n}(\omega) \right] \widehat{Z}_j(\omega) = -L_n + \vartheta_{0,n}(\omega), \quad n = 1 \dots N_s$$

$$\psi_n^T \mathbf{M} \psi_n$$

$$\int_0^{H_w} p_j(y, \omega) \psi_m^{(x)}(y) dy$$

$$\psi_n^T \mathbf{M} \mathbf{1}^{(x)}$$

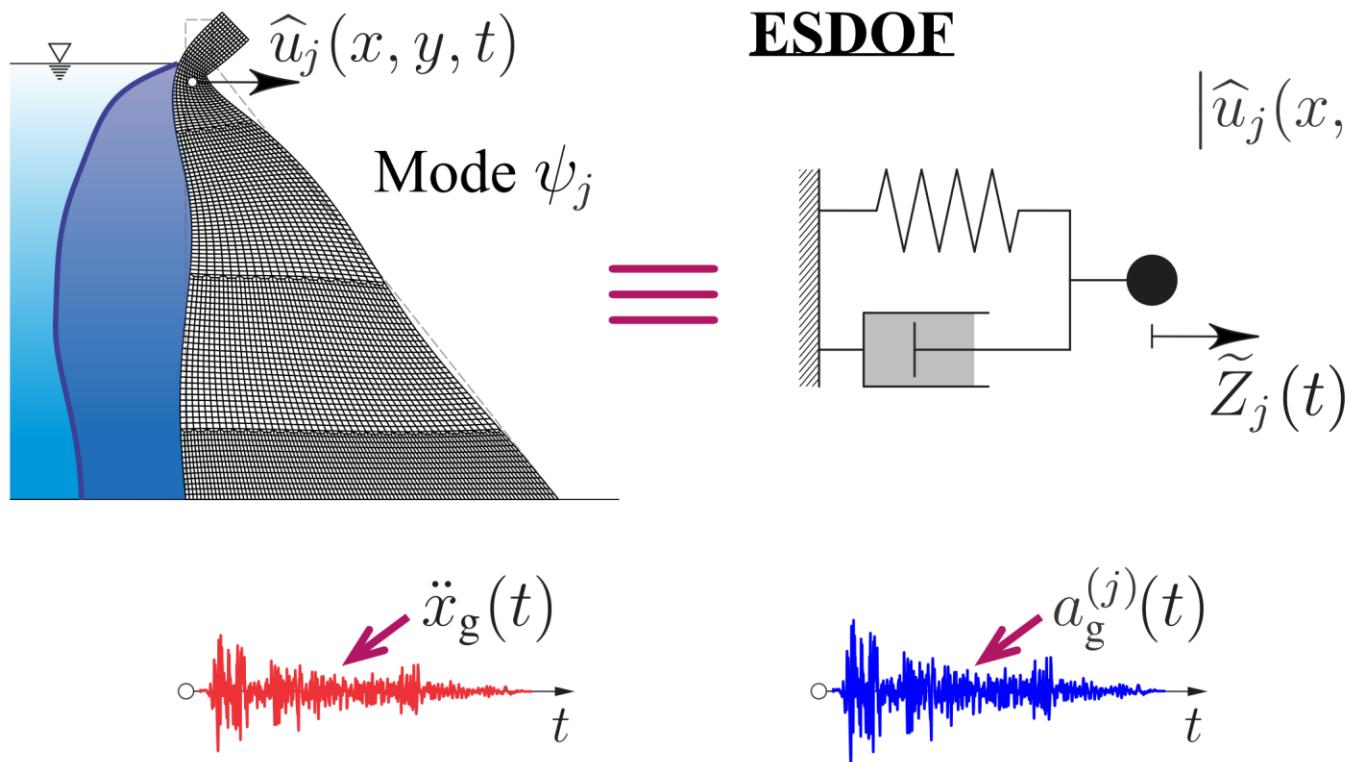
$$\int_0^{H_w} p_0(y, \omega) \psi_m^{(x)}(y) dy$$

- Simplified solutions are more difficult to obtain for the dam-reservoir system as the equations are coupled (i.e. fluid-structure interaction)

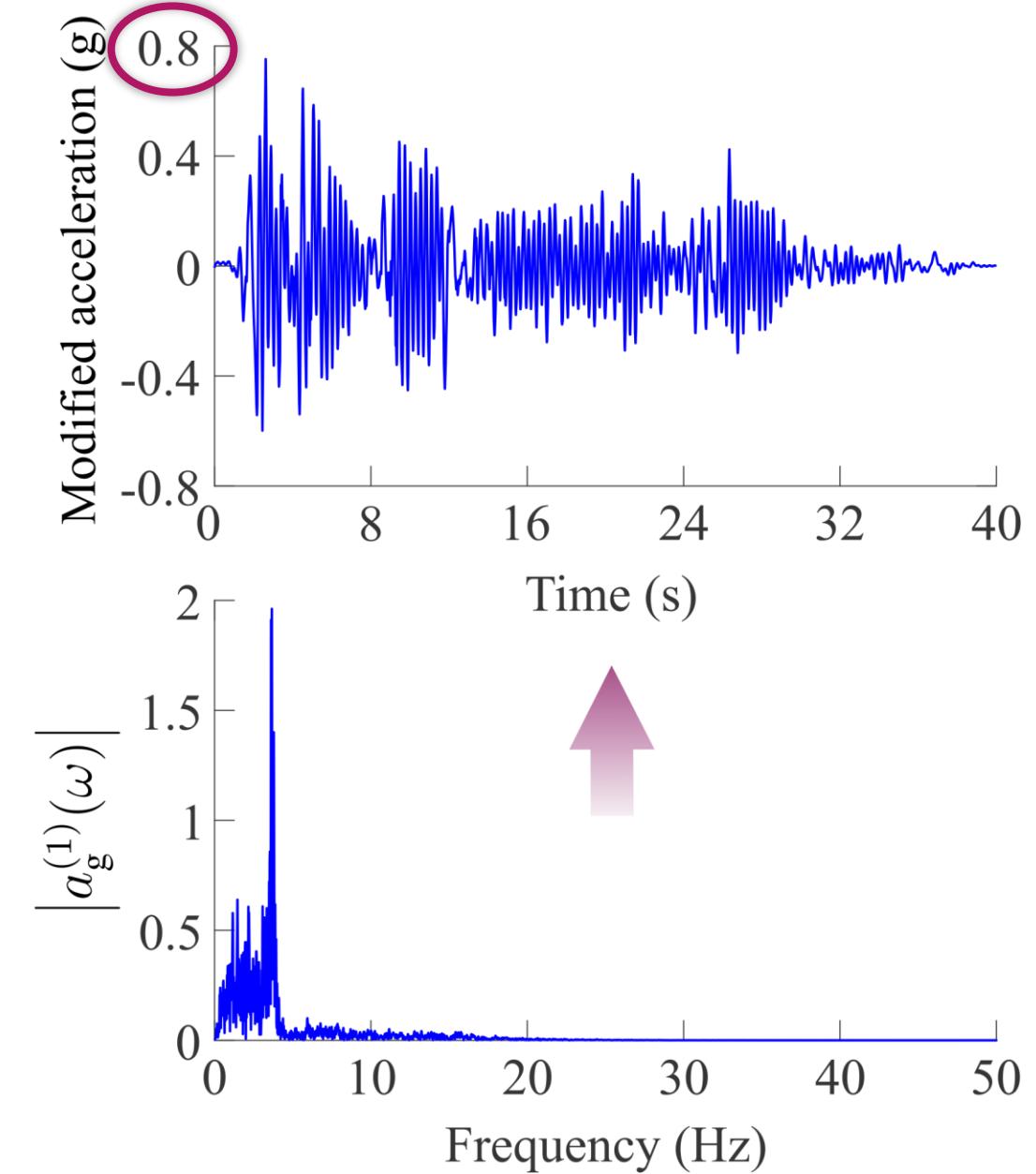
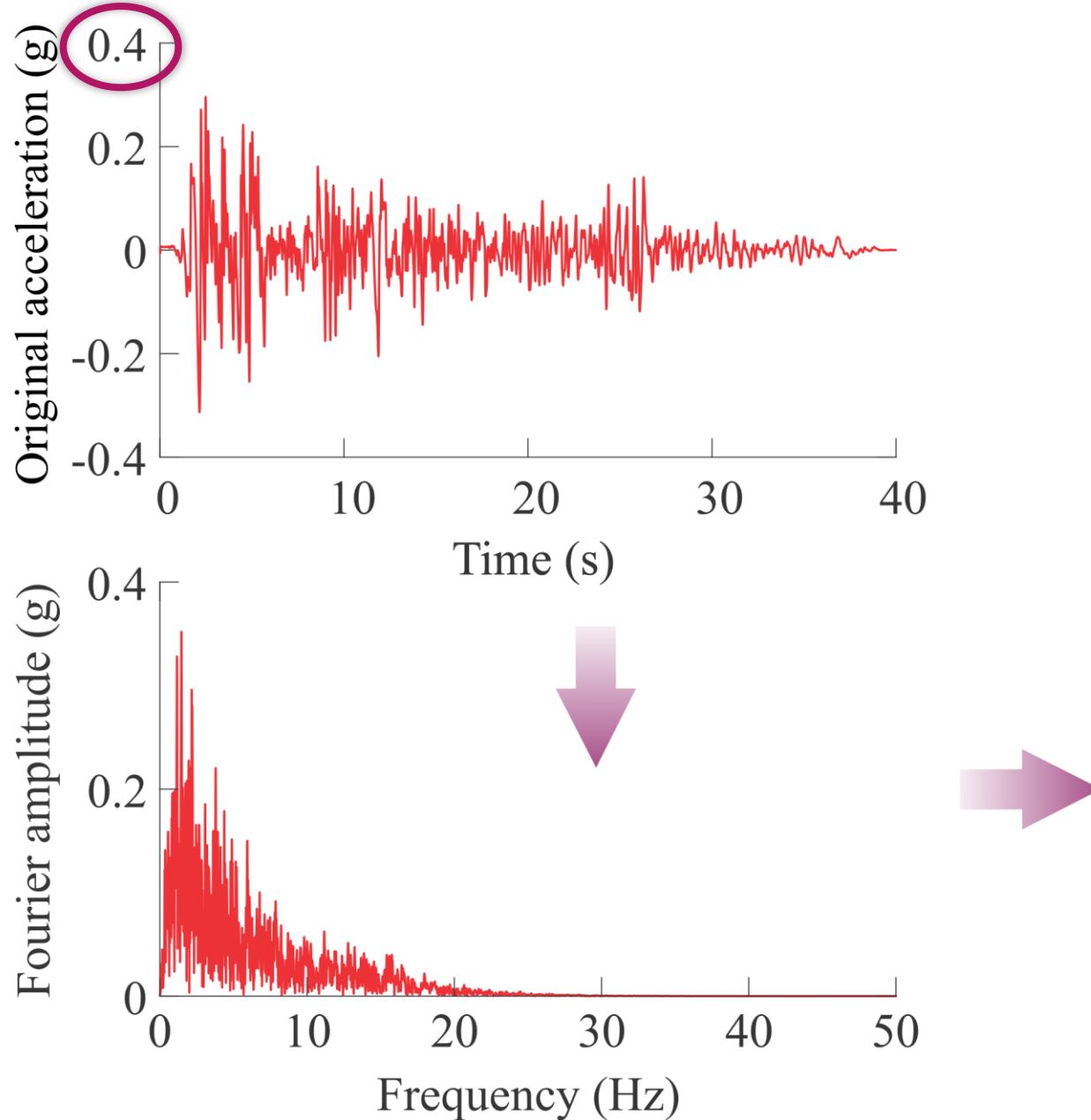
METHODOLOGY

Incorporating earthquake-induced hydrodynamic pressure into seismic input

$$a_g^{(j)}(\omega) = \ddot{x}_g(\omega) \frac{\hat{Z}_j(\omega)}{Z_j(\omega)} \rightarrow a_g^{(j)}(t) = \frac{1}{2\pi} \int_{-\infty}^{\infty} a_g^{(j)}(\omega) e^{i\omega t} d\omega$$

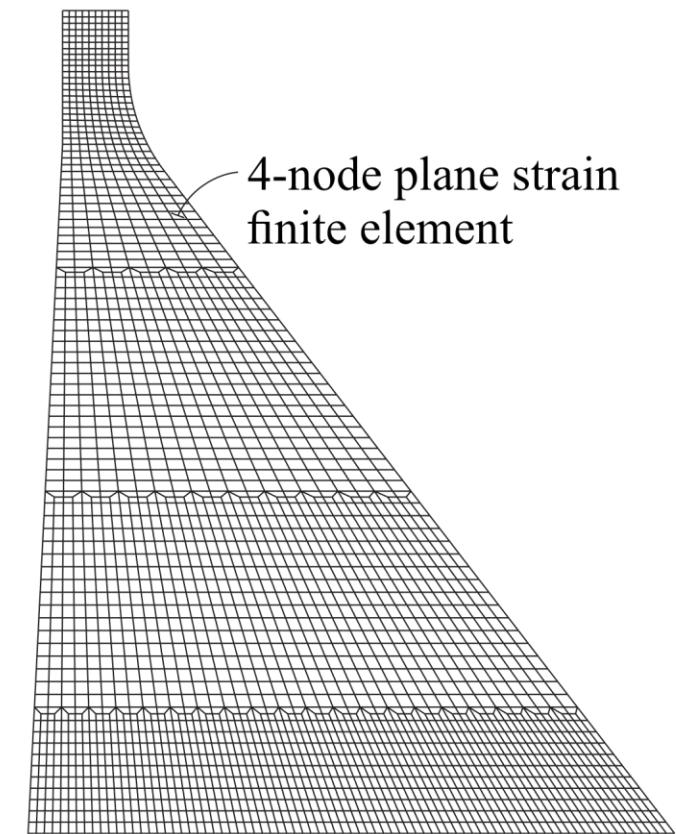
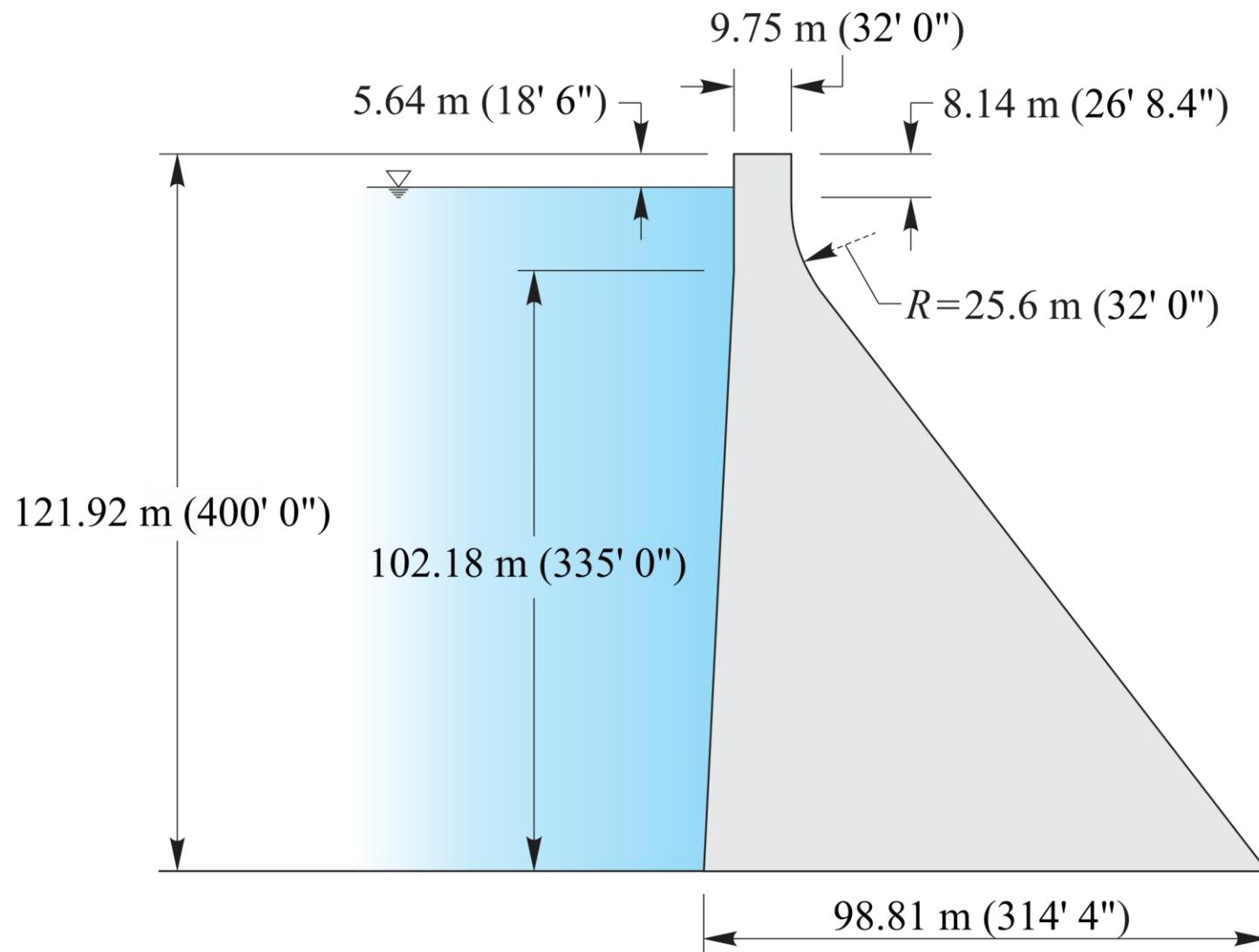


METHODOLOGY



EXAMPLES

Pine Flat dam



EXAMPLES

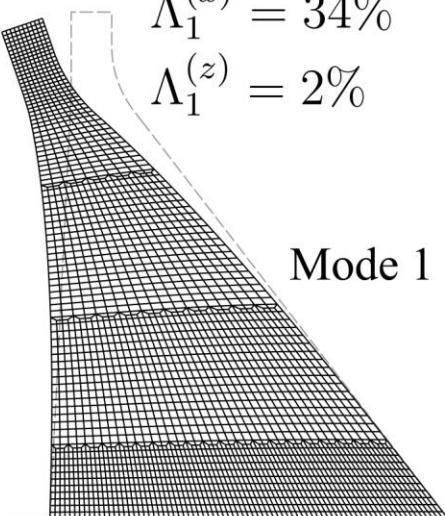
Pine Flat dam

$$T_1 = 0.309 \text{ s}$$

$$\Lambda_1^{(x)} = 34\%$$

$$\Lambda_1^{(z)} = 2\%$$

Mode 1

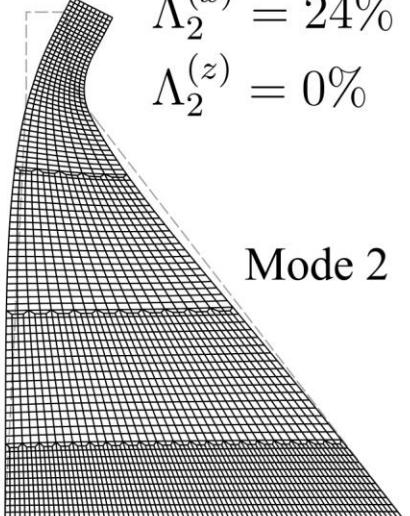


$$T_2 = 0.151 \text{ s}$$

$$\Lambda_2^{(x)} = 24\%$$

$$\Lambda_2^{(z)} = 0\%$$

Mode 2

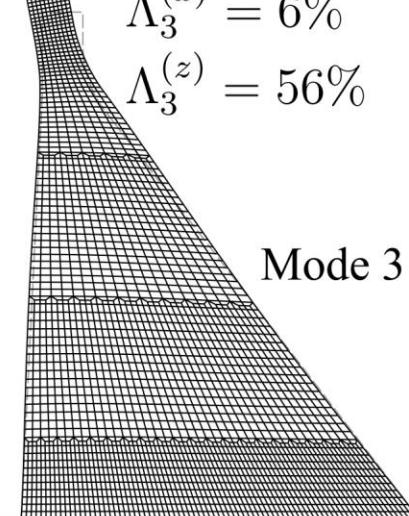


$$T_3 = 0.112 \text{ s}$$

$$\Lambda_3^{(x)} = 6\%$$

$$\Lambda_3^{(z)} = 56\%$$

Mode 3

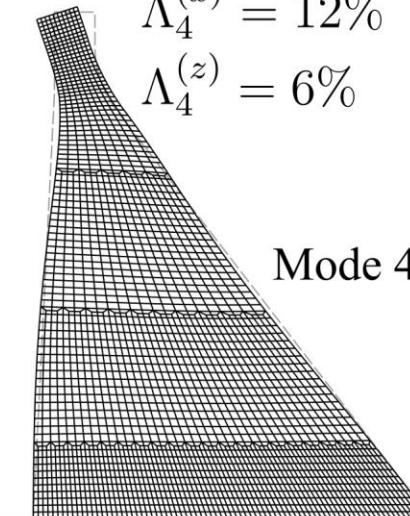


$$T_4 = 0.088 \text{ s}$$

$$\Lambda_4^{(x)} = 12\%$$

$$\Lambda_4^{(z)} = 6\%$$

Mode 4

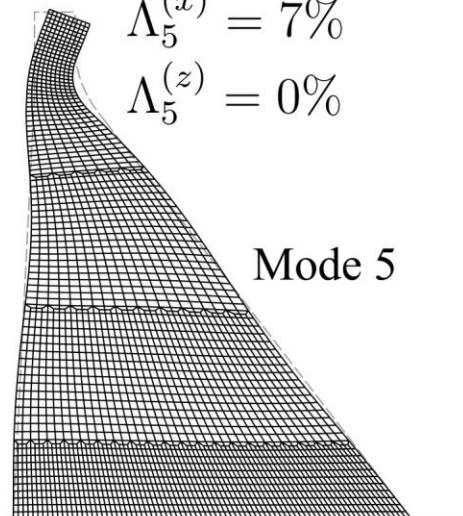


$$T_5 = 0.058 \text{ s}$$

$$\Lambda_5^{(x)} = 7\%$$

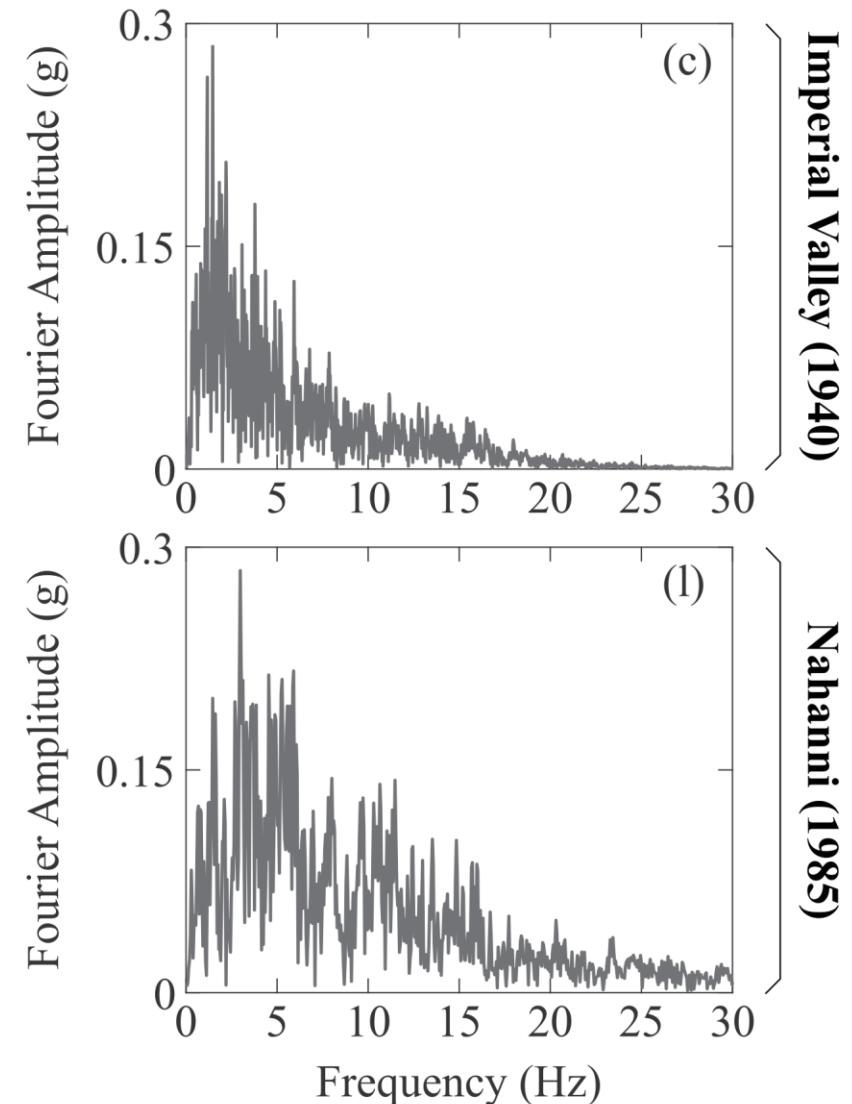
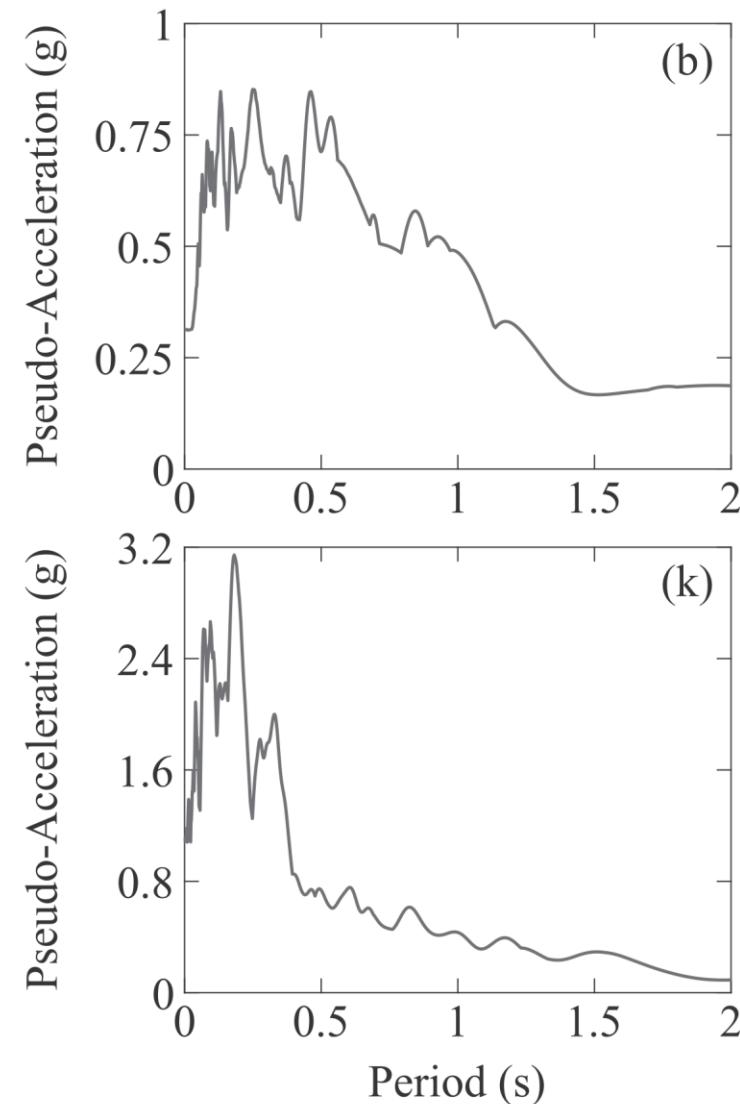
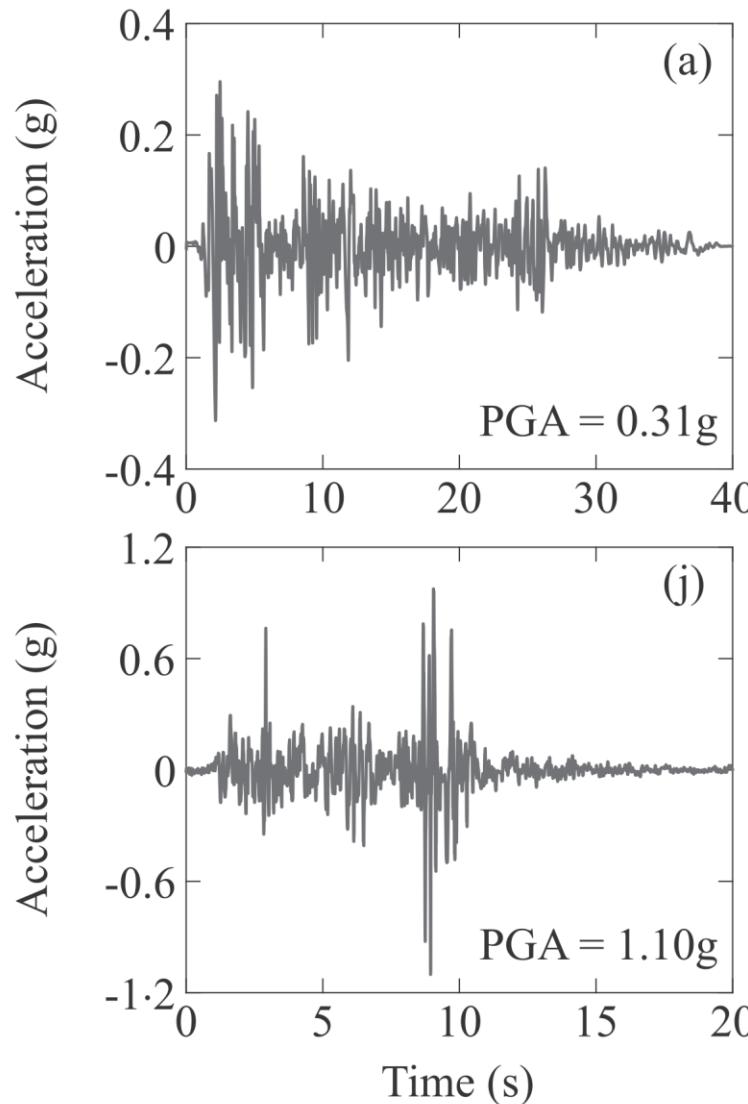
$$\Lambda_5^{(z)} = 0\%$$

Mode 5



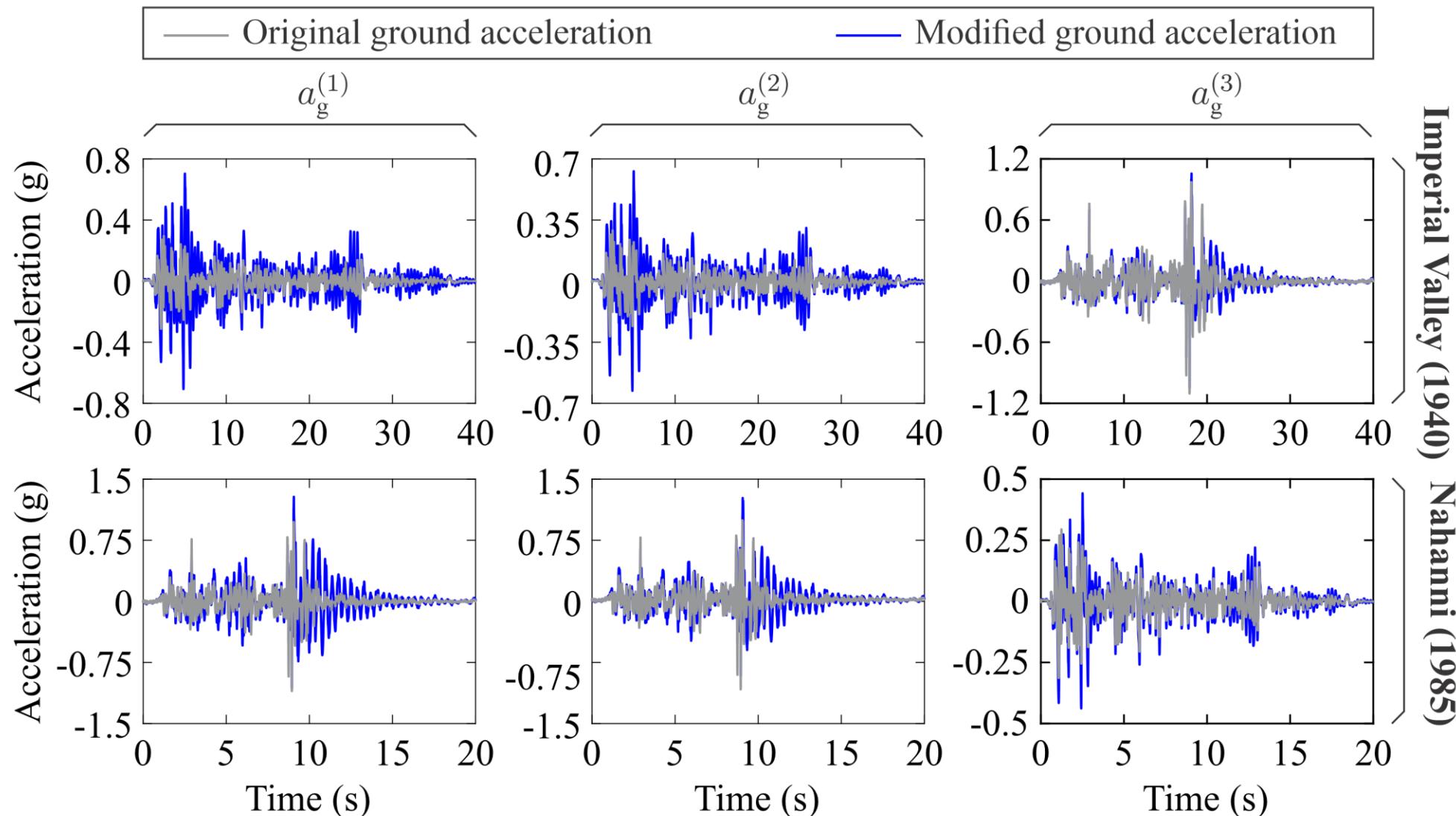
EXAMPLES

Earthquakes



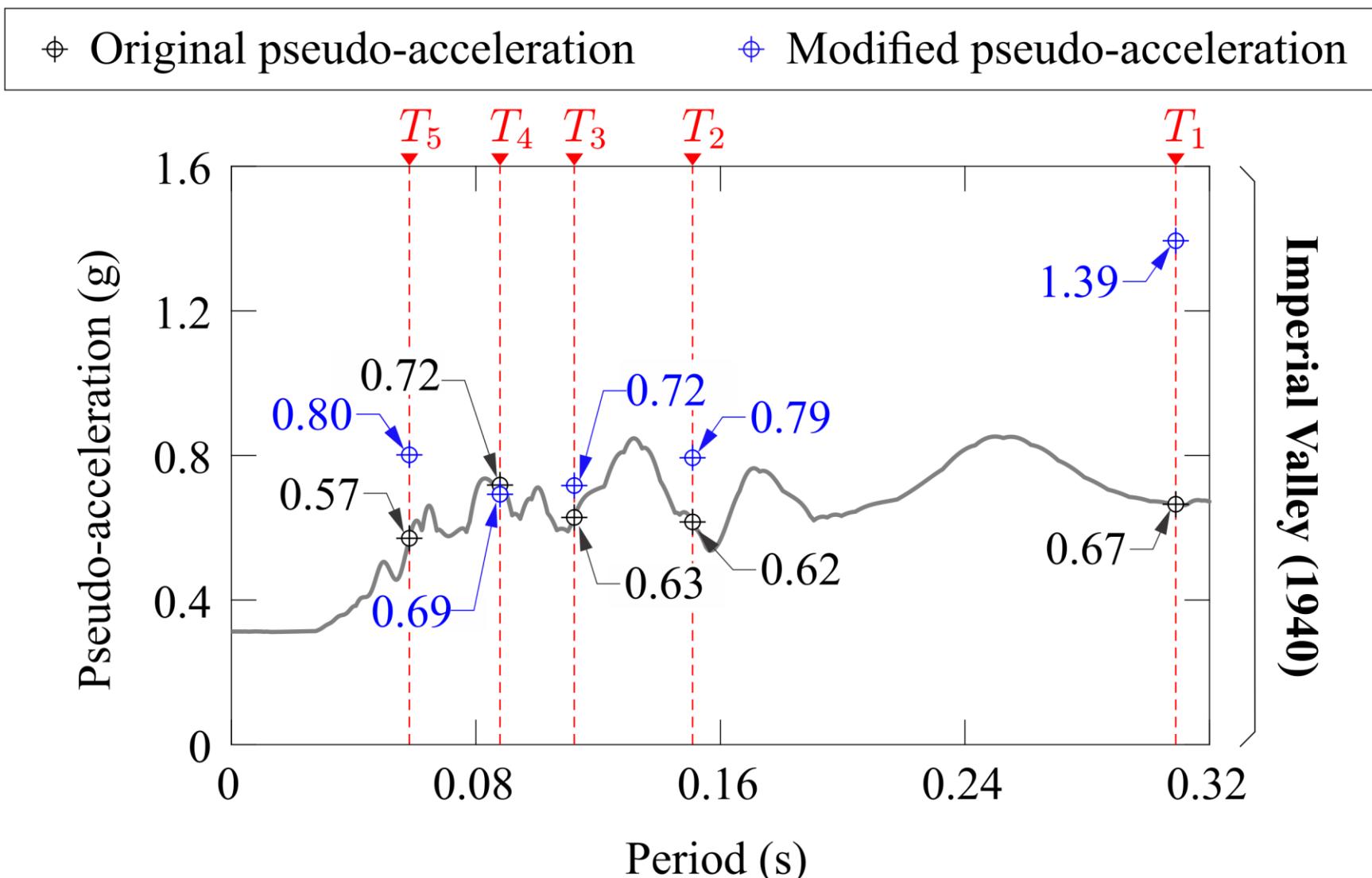
EXAMPLES

Modified accelerations



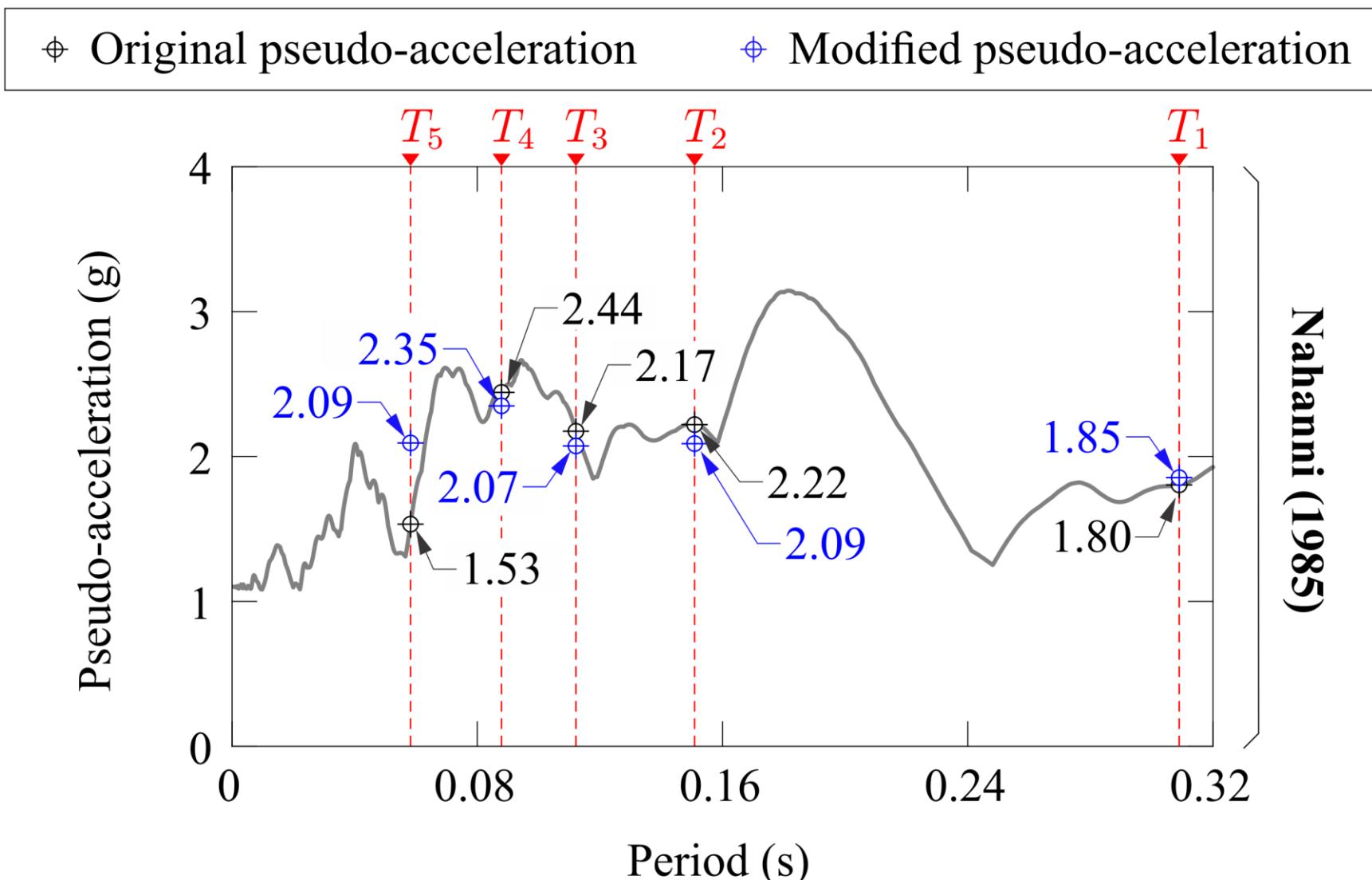
EXAMPLES

Modified spectral accelerations



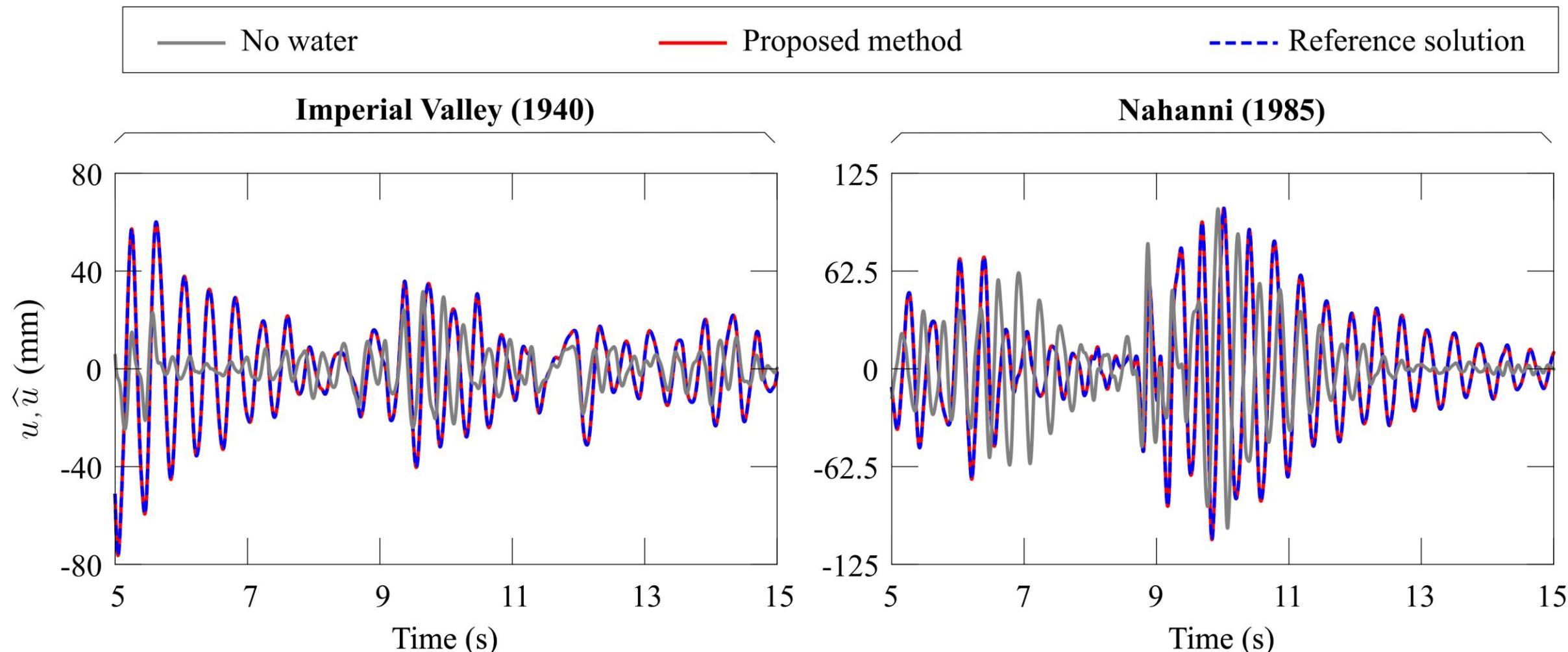
EXAMPLES

Modified spectral accelerations



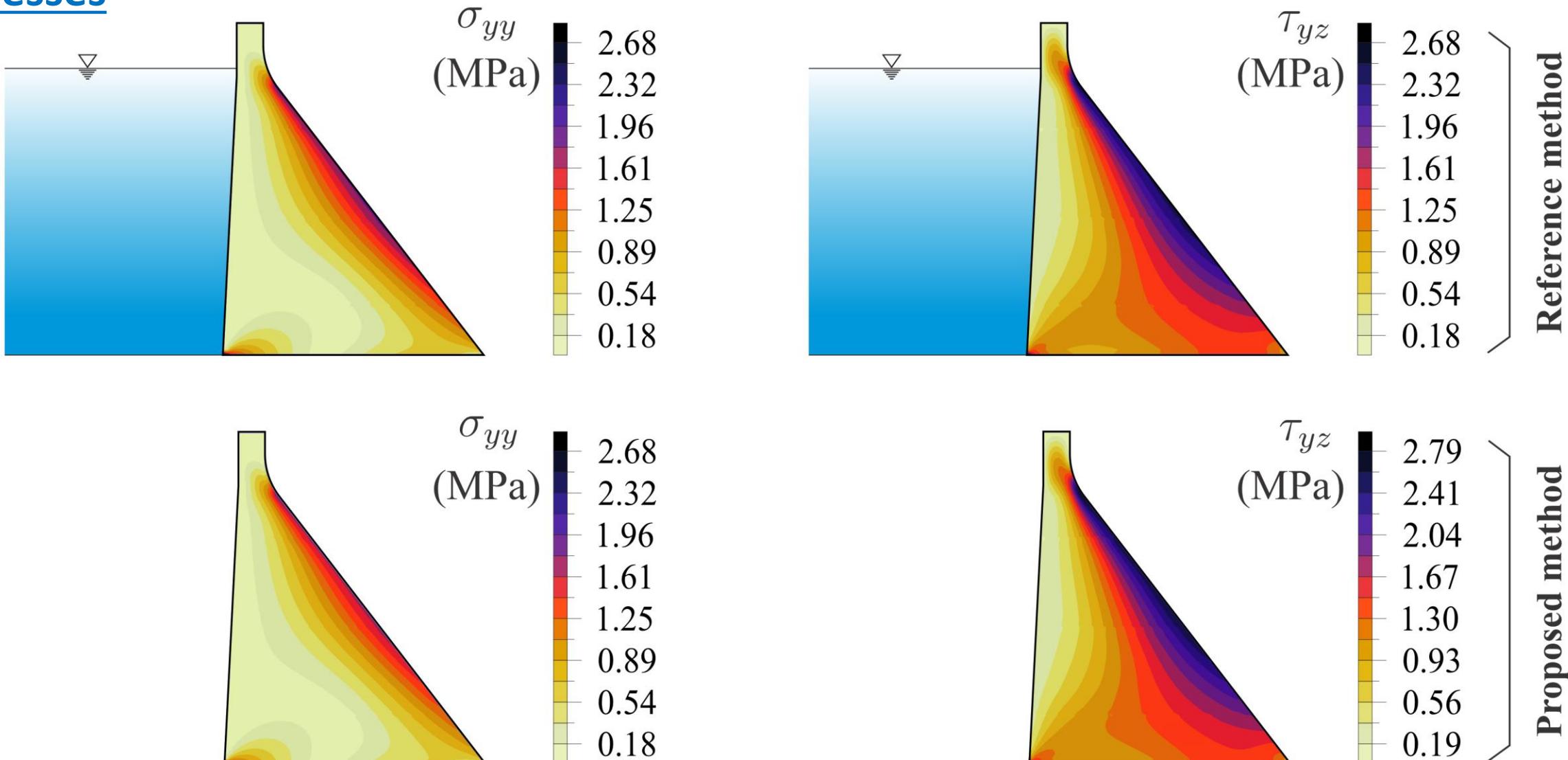
EXAMPLES

Displacements



EXAMPLES

Stresses

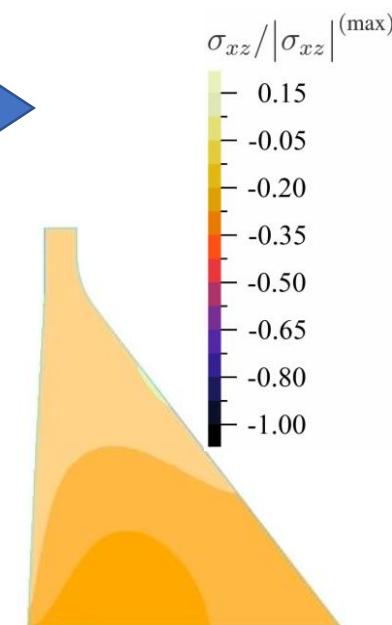
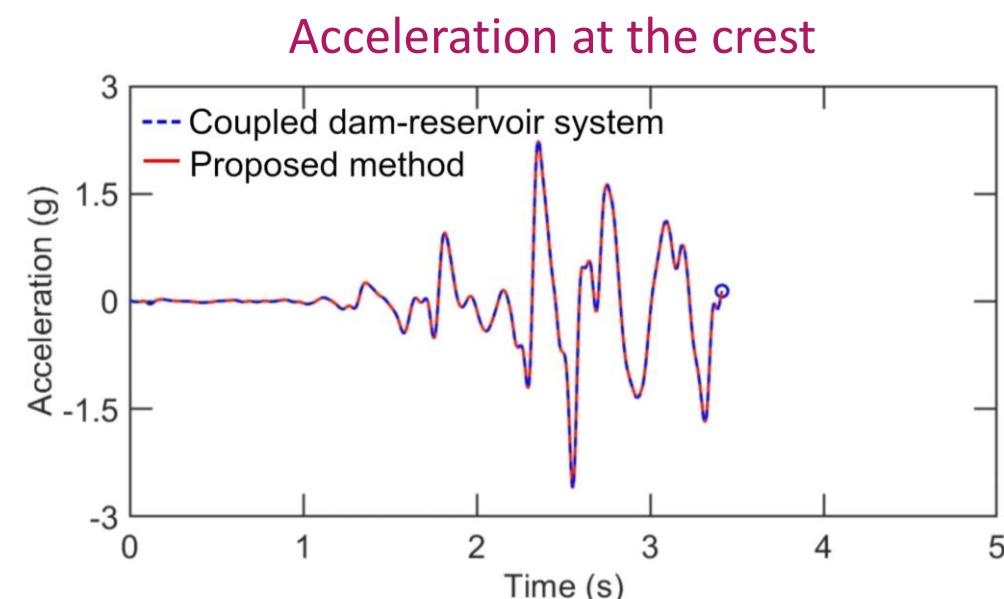
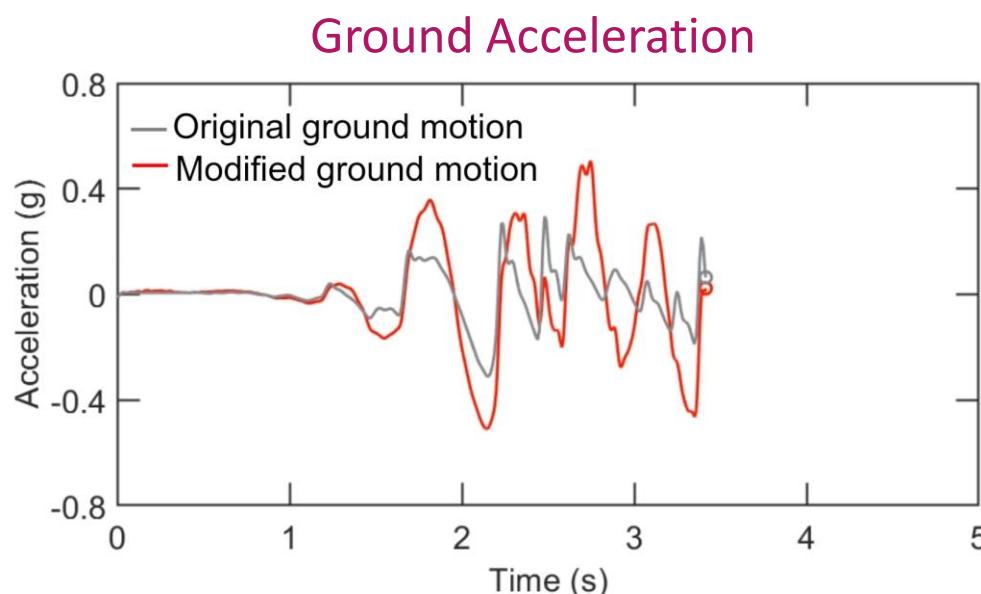


EXAMPLES

Hydrodynamic pressure

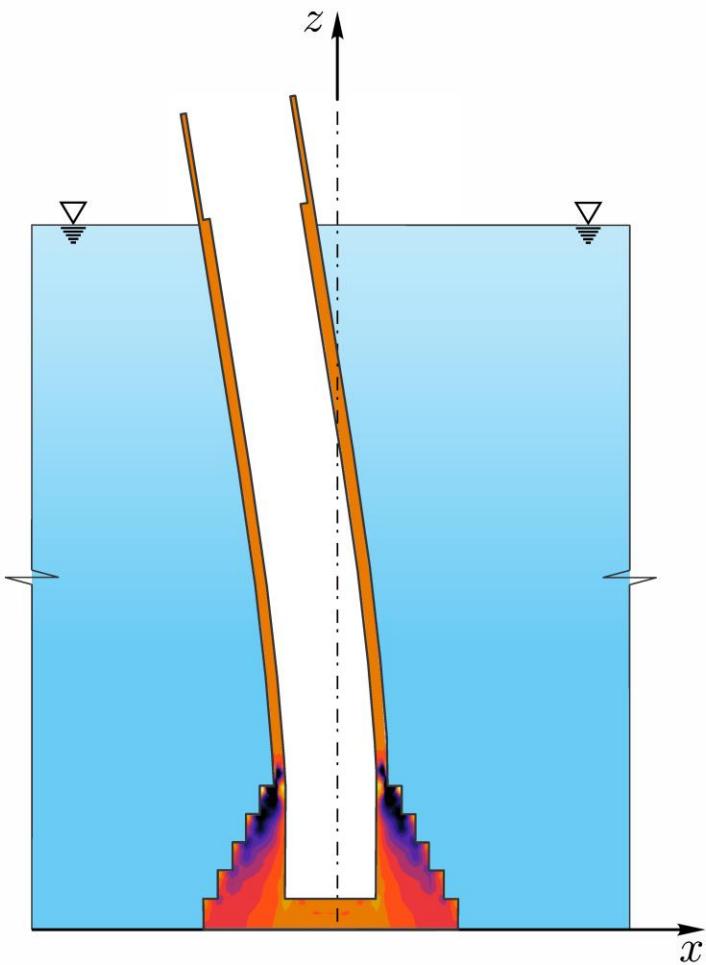


Stresses

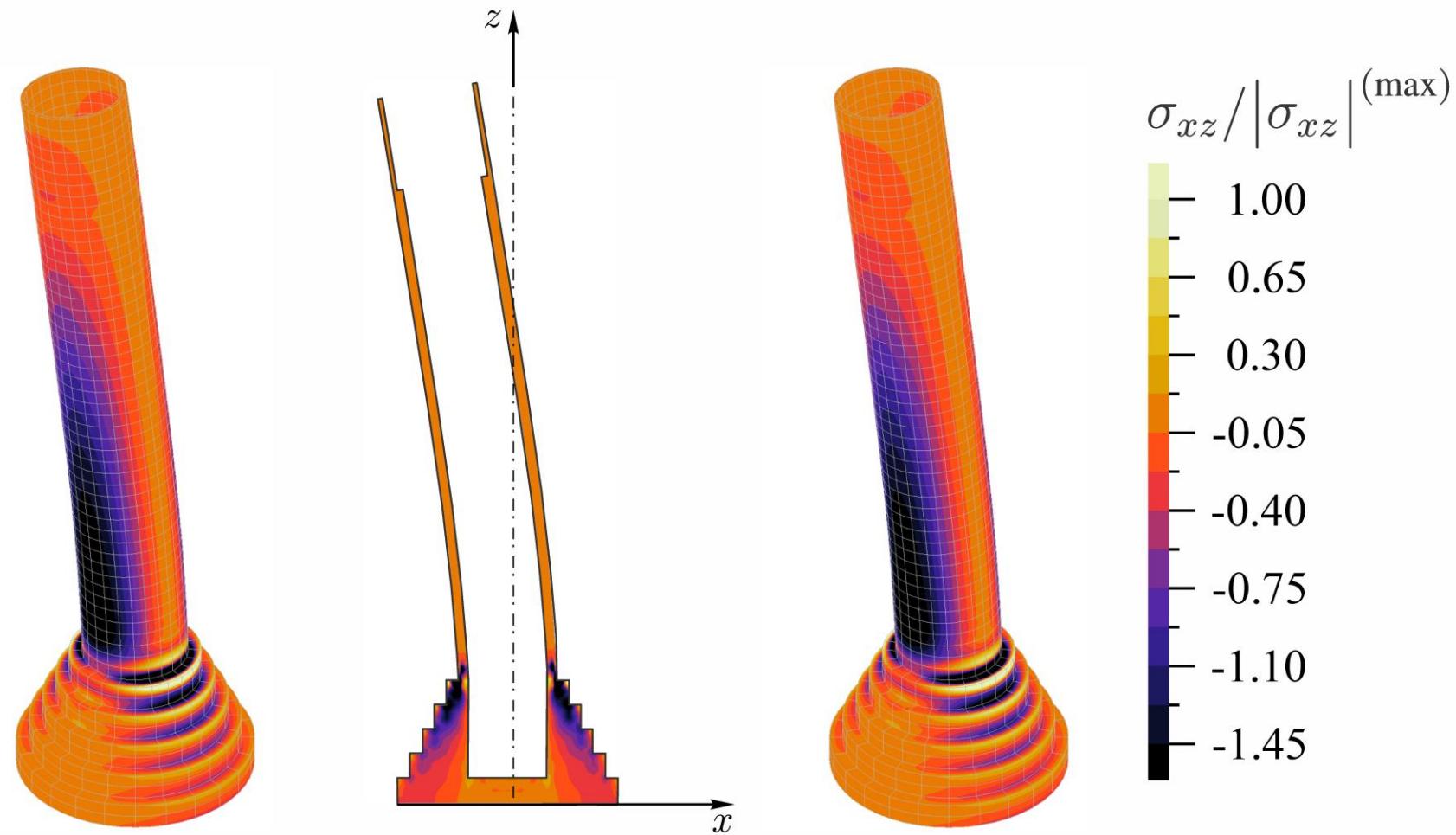


EXAMPLES

Reference method



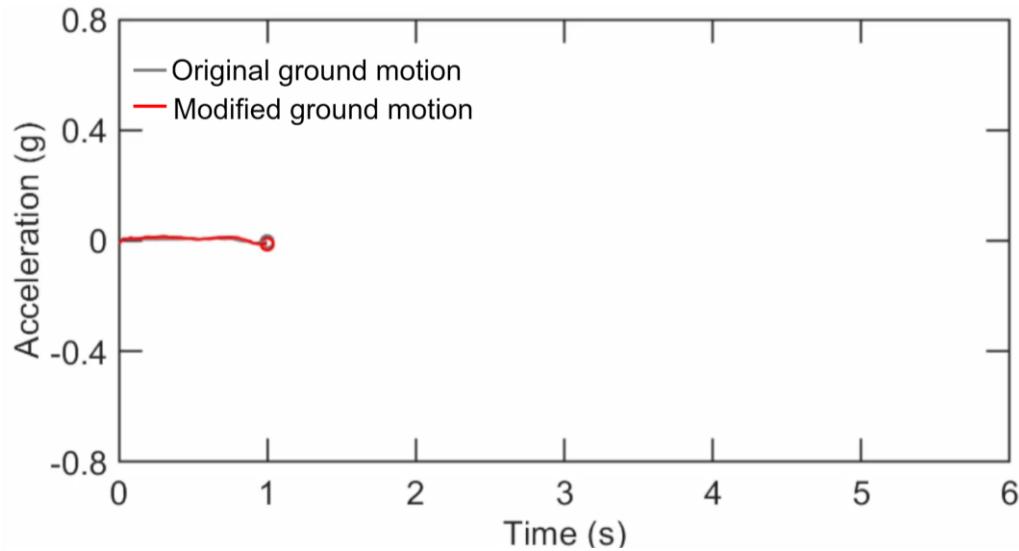
Proposed method



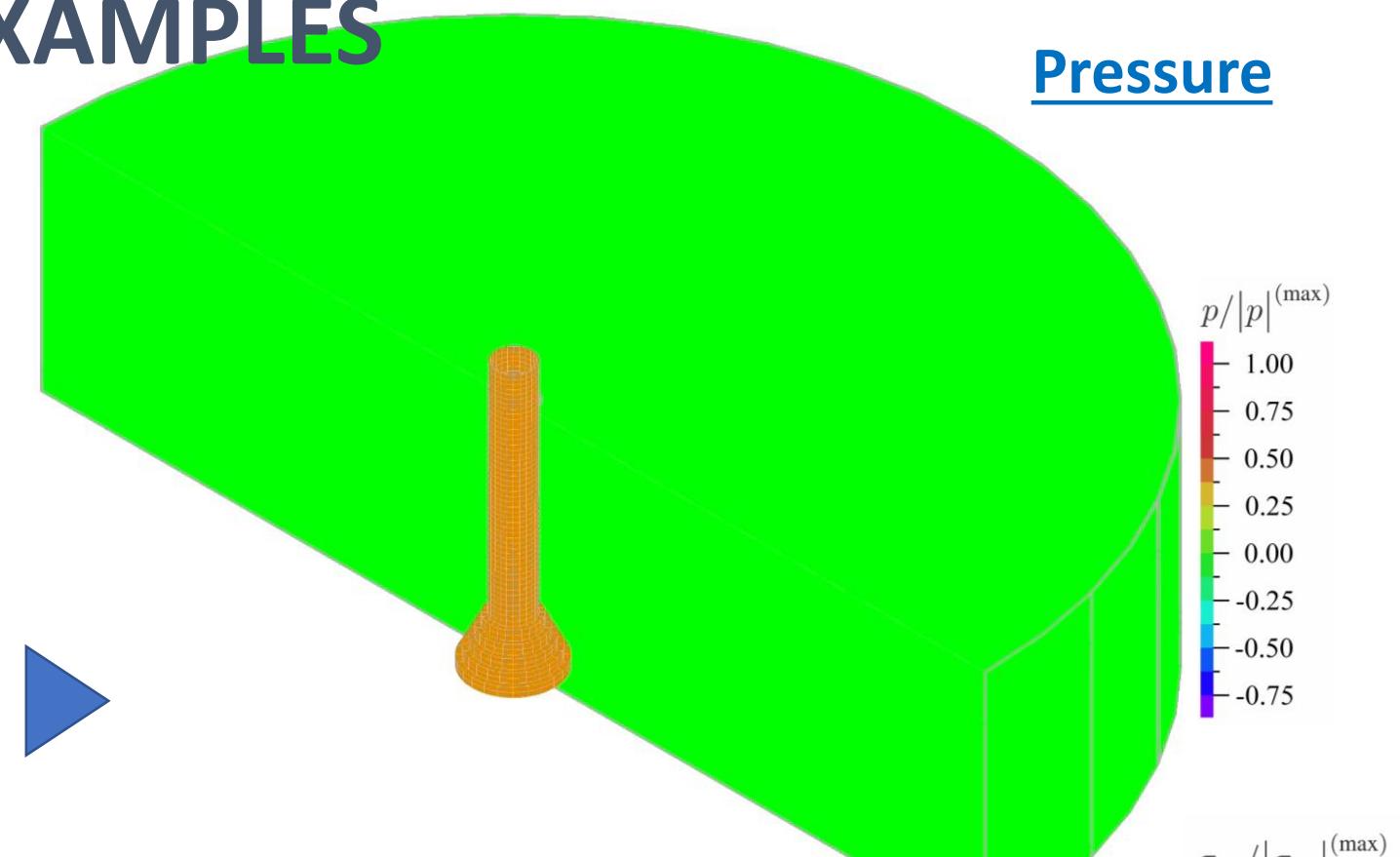
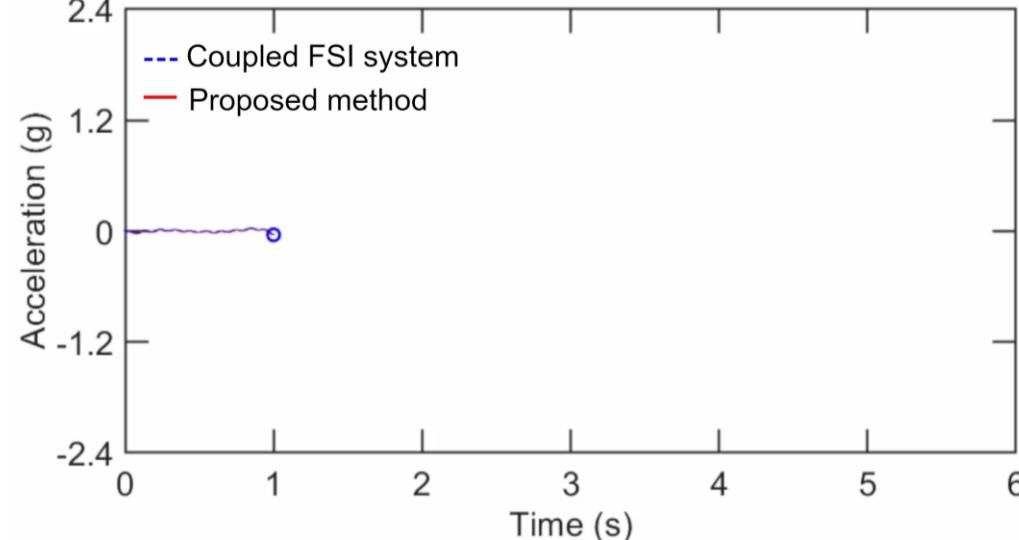
EXAMPLES

Pressure

Ground Acceleration



Acceleration at the Top



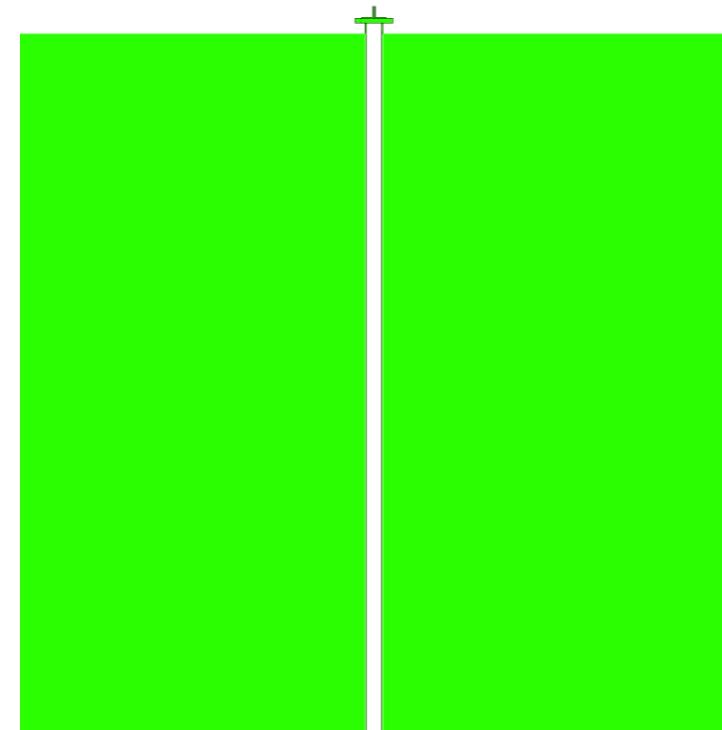
Stresses

EXAMPLES

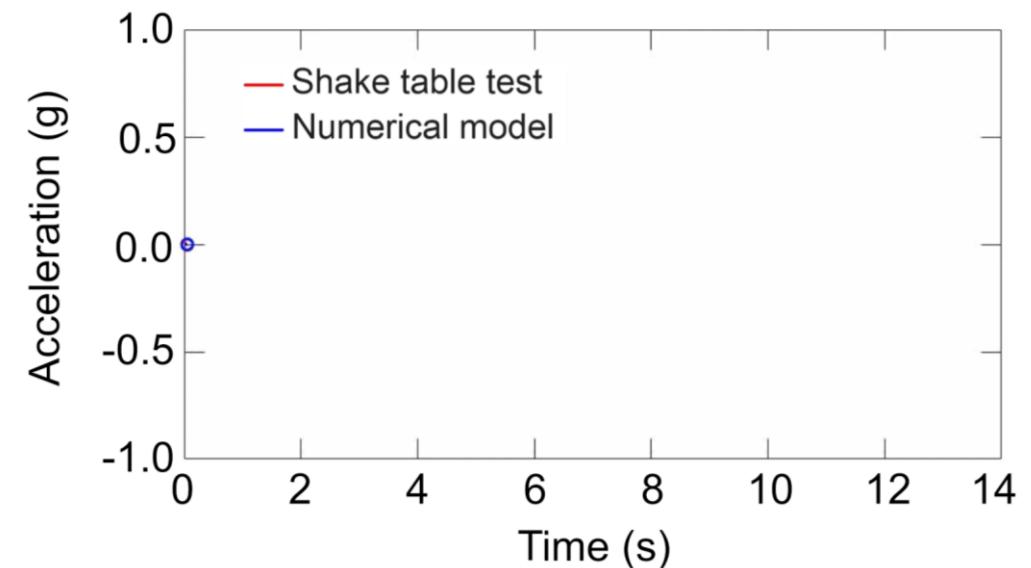
Experimental validation



Shake table test
(Polytechnique Montréal)



Coupled finite element model



CONCLUSIONS

- A new method was proposed to evaluate the seismic response of gravity dam-reservoir systems through dynamic modal superposition and response spectrum analyses.
- The main originality of the developed techniques is the inclusion of earthquake-induced reservoir effects into modified versions of the original ground motion acceleration and its response spectrum.
- The modified ground motion time-history and spectral accelerations can be applied directly to the dam with empty reservoir, thus eliminating the need for specialized software accounting for fluid-structure interaction dynamic effects.
- Extension of the method to include multidirectional earthquake loads and other types of water-structure systems is ongoing.



Welcome to
MONTRÉAL
October 1 to 6, 2028

CANADA counts
on your support!



THANK YOU!


19WCEE
Montréal Canada
2028

COLLABORATE, LEARN, INNOVATE AND IMPLEMENT
Building a safer and more resilient world **TOGETHER**

The seismic safety assessment of a multiple arch dam

M. Colombo, A. Frigerio

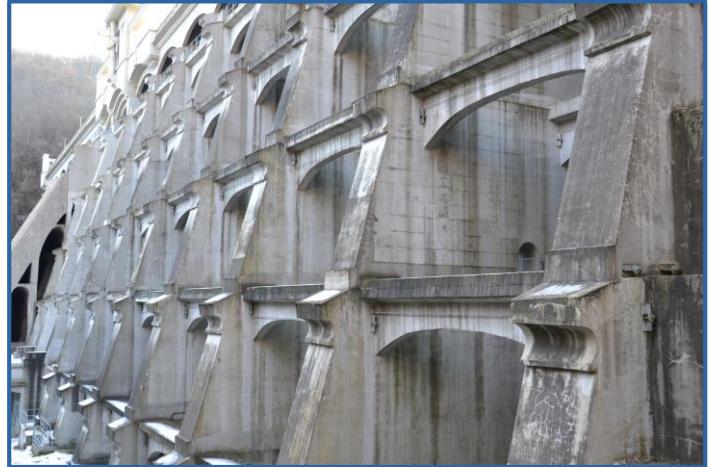
03/07/2024





Contents

- Introduction**
- Problems affecting buttress and slab/arch dams**
- Importance of numerical modeling**
- Case history of Molato dam**
- Conclusion**





Contents



Introduction



Problems affecting buttress and slab/arch dams



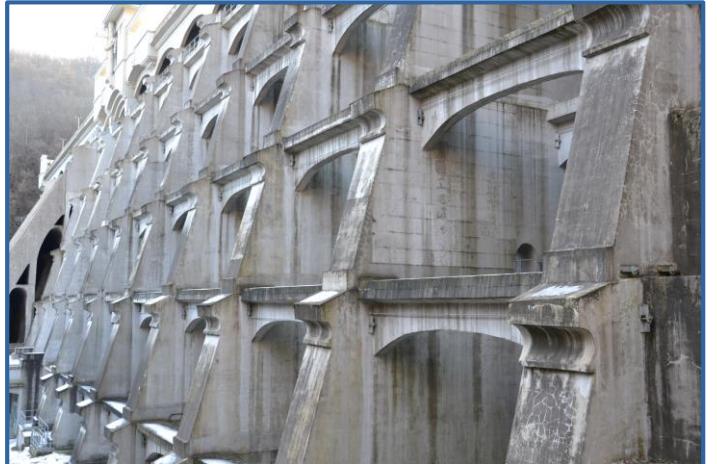
Importance of numerical modeling



Case history of Molato dam

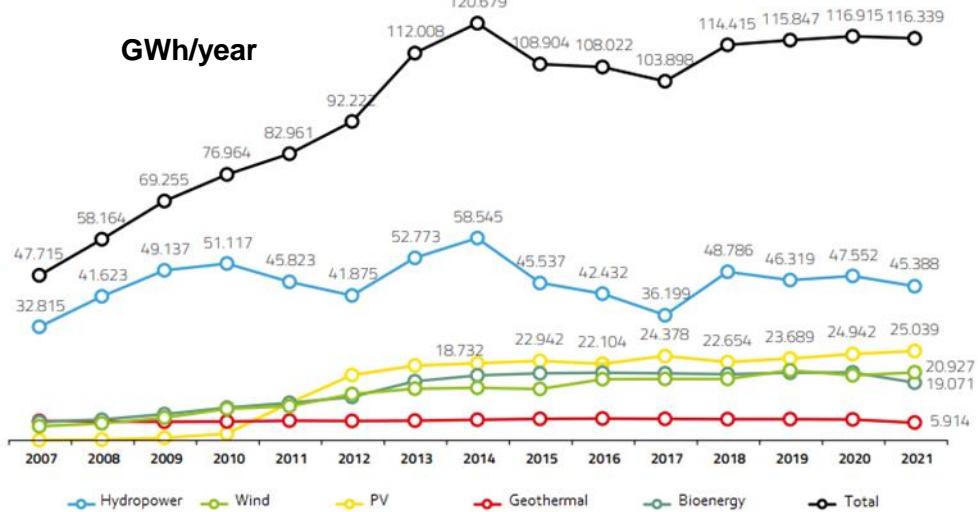


Conclusion





Introduction



- The need to exploit the water resources for the energy production accelerated the construction of large dams
- In Italy from a dozen of dams at the end of the nineteenth century to almost 400 large dams in the first half of the twentieth century
- Multiple use of water of dam reservoirs is a necessity and an opportunity

Use of dams

- hydropower generation
- storage of water for irrigation and water supply
- flood and sediments control
- navigation
- aqueduct support

In Italy hydropower is still the main renewable source and accounts for 15-17% of the national electricity production



Legend

The small green point means 1 dam; the number reported in all the other points stands for the number of dams in that area.

NORTH	=	46 %
CENTER	=	32 %
SOUTH	=	32 %
Total		531 dams



Introduction

Types of dams:

- gravity
- arch
- slab/arch
- earth fill, mixed



The first slab/arch dams were built in the first twenty-five years of the 1900 → The collapse of a mixed gravity and multiple arches dam (Gleno) in 1923 led to build more massive hydraulic structures



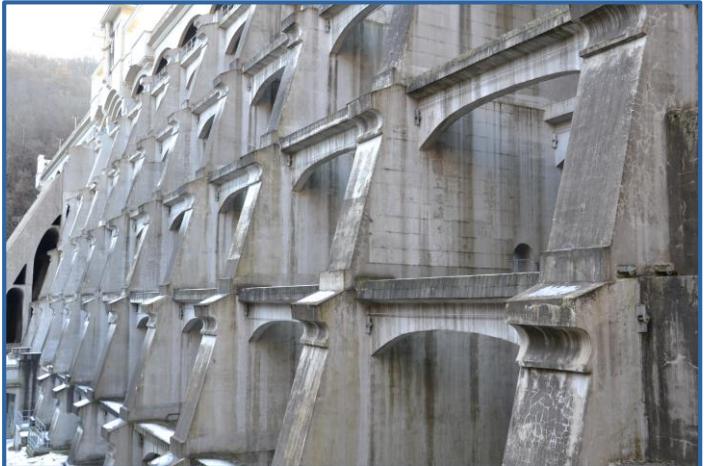
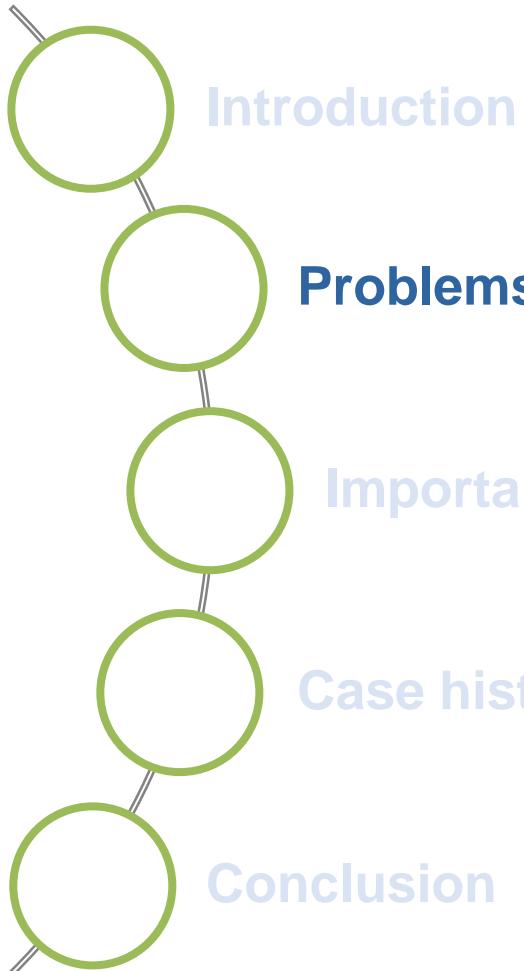
Downstream face view
after construction



Upstream face view
after collapse



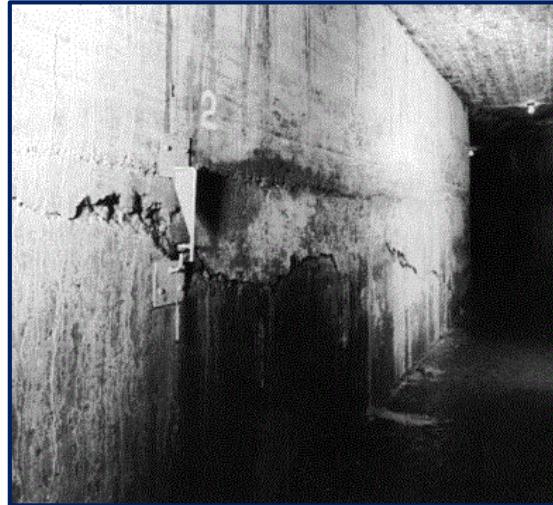
Contents

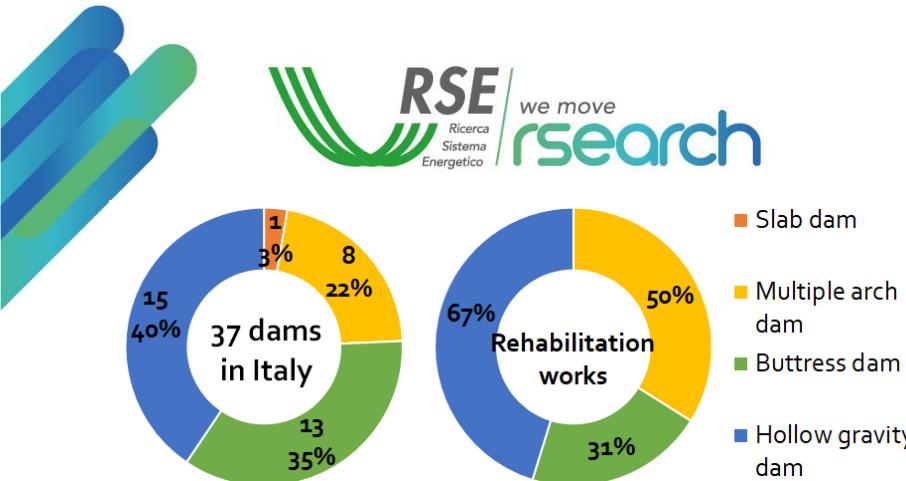




Problems affecting buttress and slab/arch dams

- The crack pattern due to thermal variations (heat of hydration, seasonal temperatures, solar radiation...) and geometric shapes (different height and thickness of the buttresses...)
- The aging of materials due to environmental conditions or chemical phenomena (alkali-silica reaction) and the corrosion of steel rebars
- The quality and the porosity of the material (concrete) contribute to aggravate its deterioration condition
- Possible loss of resistance to sliding (caused by the development of high uplift pressures), leakage through the upstream face and low resilience to seismic actions





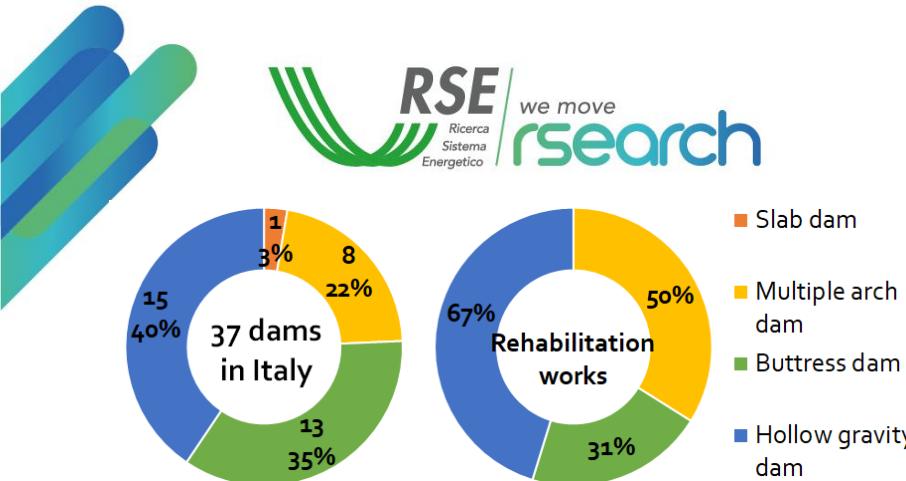
Problems affecting buttress and slab/arch dams

All of 37 slab/arch dams were built in the last century → some rehabilitation works have been required to respect the new regulations and guarantee their safe operation over time

The Italian Committee on Large Dams (ITCOLD) has set up the Working Group "Behaviour, problems, rehabilitation of hollow gravity, buttress and multiple arch/slab dams" → control and monitoring systems, criteria for safety assessment, rehabilitation works

Several case histories:

→ Ancipa dam (a hollow gravity infrastructure, located in Sicily and operated by ENEL Green Power): a steel insulating shield was built on the downstream face to reduce the seasonal thermal gradients and slow down the propagation of cracks in the buttresses



Problems affecting buttress and slab/arch dams

All of 37 slab/arch dams were built in the last century → some rehabilitation works have been required to respect the new regulations and guarantee their safe operation over time

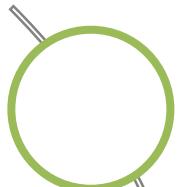
The Italian Committee on Large Dams (ITCOLD) has set up the Working Group "Behaviour, problems, rehabilitation of hollow gravity, buttress and multiple arch/slab dams" → control and monitoring systems, criteria for safety assessment, rehabilitation works

Several case histories:

- Ancipa dam (a hollow gravity infrastructure, located in Sicily and operated by ENEL Green Power): a steel insulating shield was built on the downstream face to reduce the seasonal thermal gradients and slow down the propagation of cracks in the buttresses
- San Giacomo di Fraele dam (a buttress infrastructure, located in Lombardy and operated by A2A): the partial closure of the buttresses with a sloped slab was created to reduce the effects of a reservoir located downstream the dam, thus prevent sliding



Contents



Introduction



Problems affecting buttress and slab/arch dams



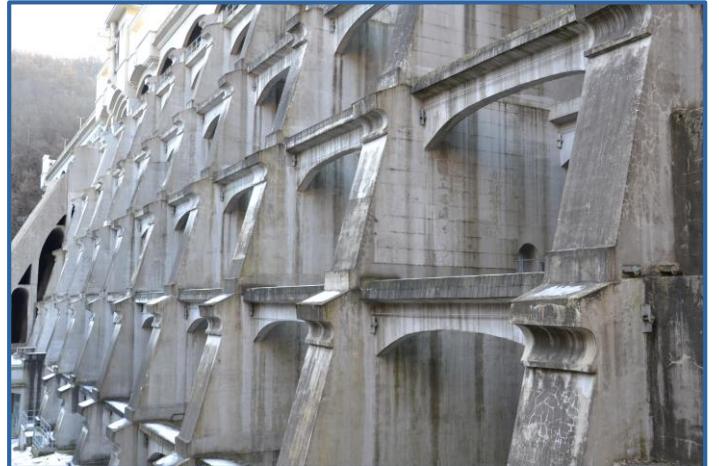
Importance of numerical modeling



Case history of Molato dam



Conclusion





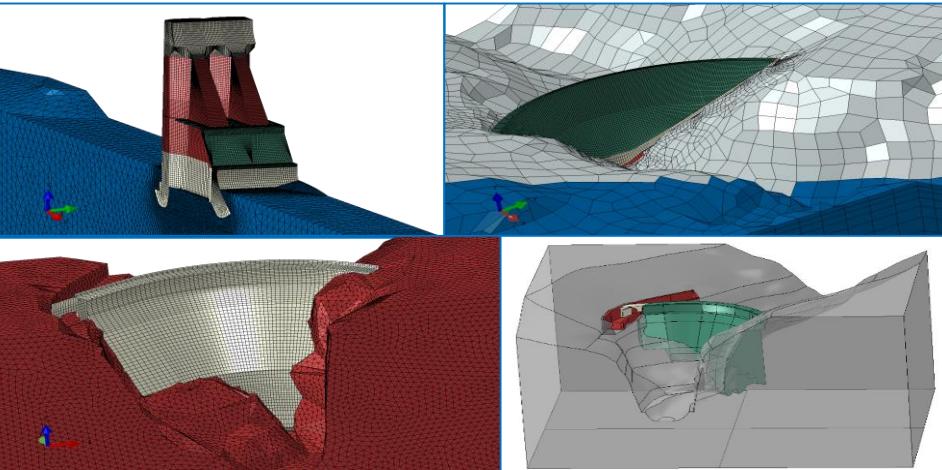
Importance of numerical modeling

To understand the influence of several impact phenomena (e.g., temperature, humidity, degradation of materials)

For diagnosis of possible damage in aged structures

To support in the choice of the most effective rehabilitation solution for keeping the structures in safety conditions over time

To assess the safety of dams

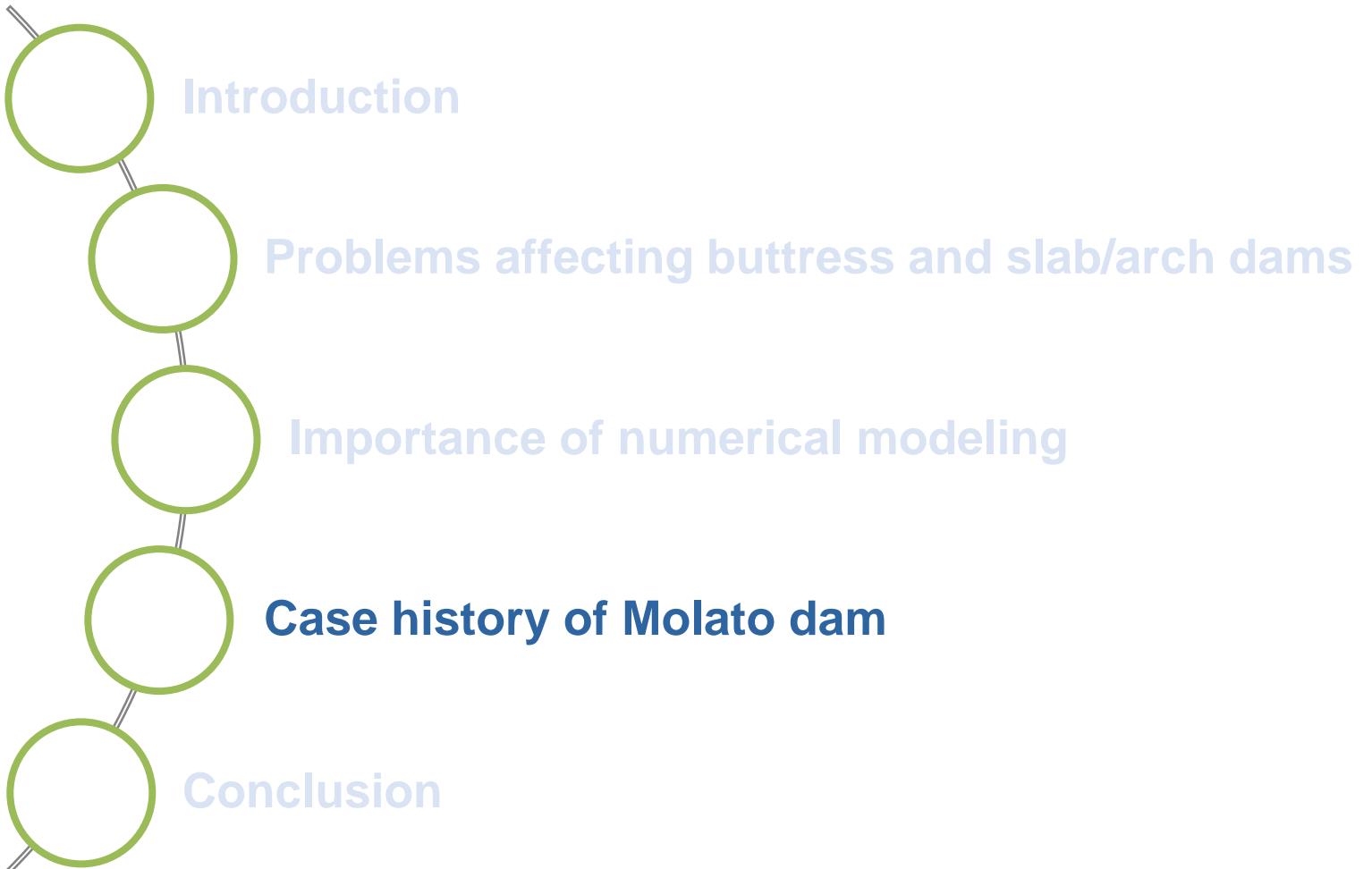


Different loading conditions and possible crack patterns are implemented

Advanced numerical modelling (e.g. finite element models) can help to remove the conservative assumptions



Contents





Case history of Molato dam

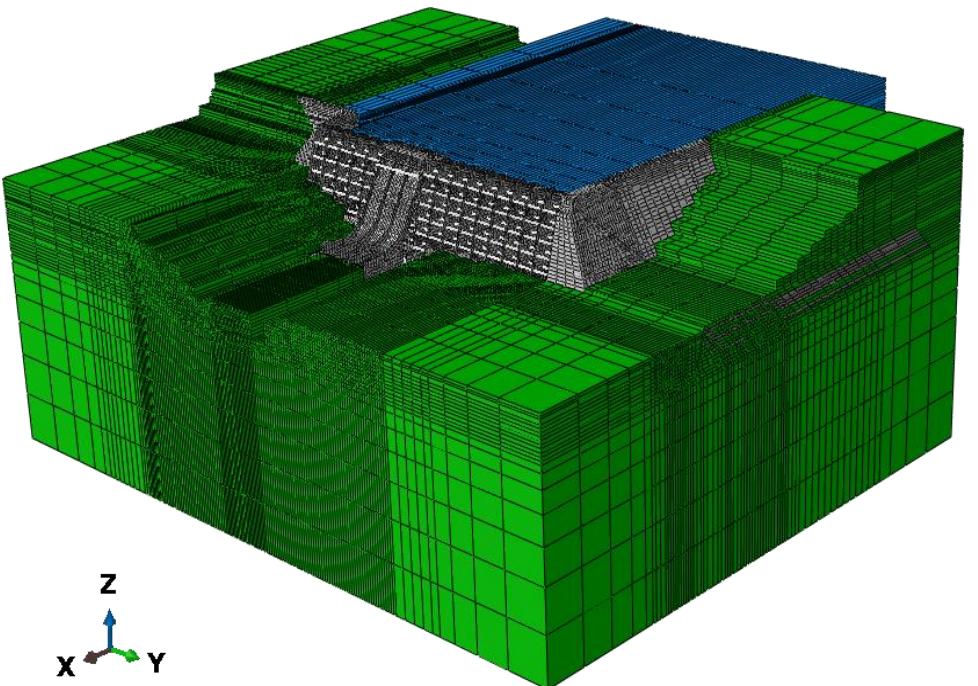
- Operated by the Consorzio di Bonifica di Piacenza and built in 1921-1928
- Provides water for irrigation with its total storage capacity of 13 Mm³
- Reinforced concrete multiple arch and buttress dam with two gravity lateral abutments
- 17 reinforced concrete arches, inclined 45° to the horizontal plane, resting upon intermediate buttresses, which are 10 m apart (connected by reinforced concrete T-shape beams in the transversal direction)
- At the base of the arches and the buttresses a concrete slab covers and protects the rock foundation





Case history of Molato dam

- The seismic response according to Italian standard by means of a numerical model capable of taking into account both the non-linear behaviour of the concrete and the dam-rock foundation interface
- The finite element model consists of solid elements for buttresses, concrete weightings among spans, gravity shoulders and rock foundation; beam elements for the T-shaped beams; shell elements for the multiple arches; acoustic elements for the reservoir





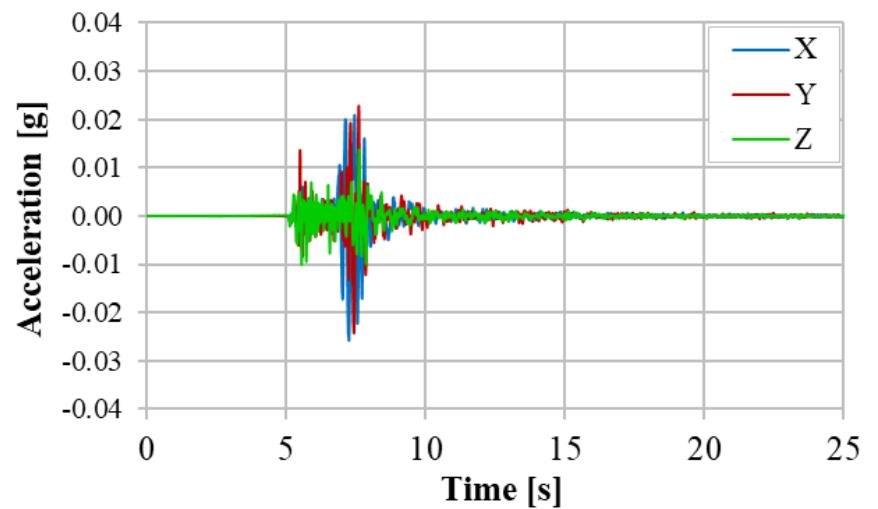
Case history of Molato dam

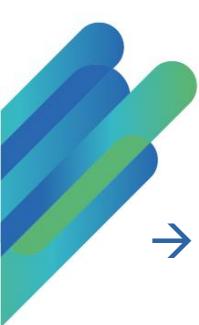
- The seismic response according to Italian standard by means of a numerical model capable of taking into account both the non-linear behaviour of the concrete and the dam-rock foundation interface
- The finite element model consists of solid elements for buttresses, concrete weightings among spans, gravity shoulders and rock foundation; beam elements for the T-shaped beams; shell elements for the multiple arches; acoustic elements for the reservoir
- A Mohr-Coulomb frictional model was assigned to the dam-rock foundation interface. A shell to solid coupling interaction was adopted to join shell elements to solid
- The nonlinear concrete behaviour was simulated using an elasto-plastic damage constitutive model (Lee & Fenves), while for the rock foundation a linear elastic behaviour was assumed
- The dynamic fluid-structure interaction was modelled according to the classic approach of the mechanical-acoustic coupling (Zienkiewicz). The acoustic approach allows to consider both the compressibility of water and the damping effects at the boundary of the fluid domain
- The traditional massless approach was adopted. This method is somewhat conservative because it does not take into account the energy dissipated in the rock foundation during the seismic motion



Case history of Molato dam

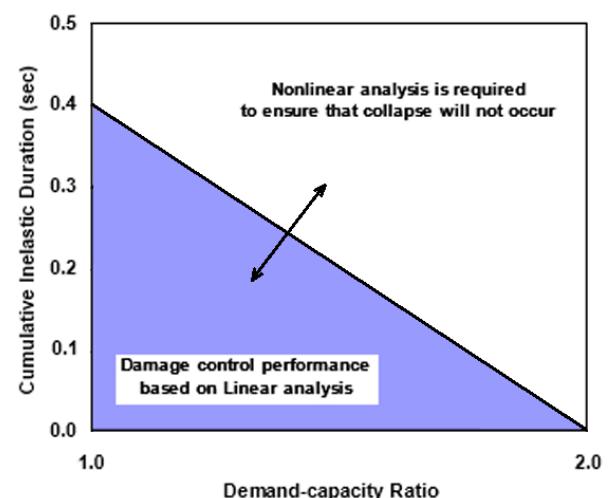
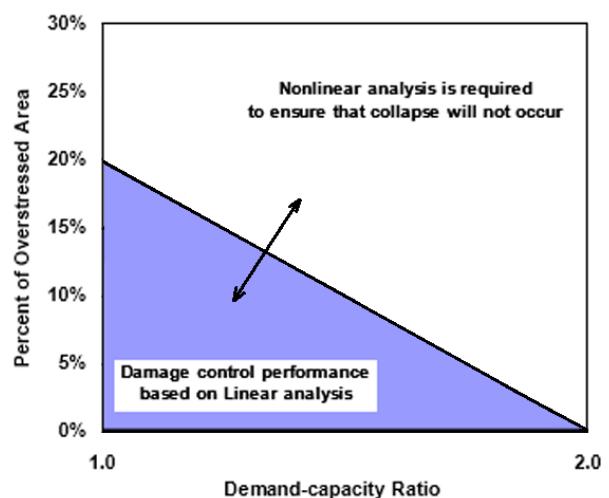
- Time history analyses applying gravity load, hydrostatic pressure and corresponding uplift, winter thermal load (the worst condition) and seismic forces (according to accelerogram)





Case history of Molato dam

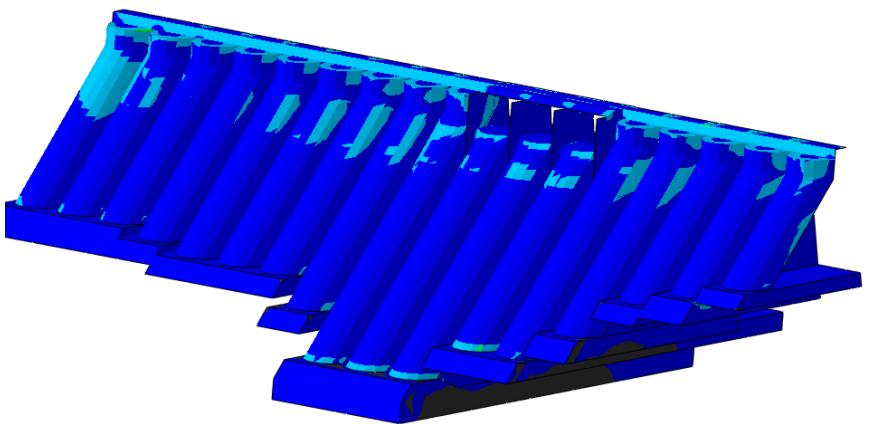
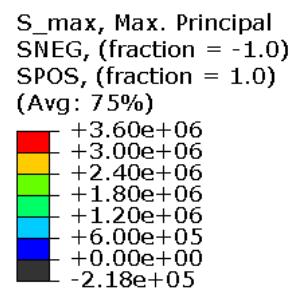
- Time history analyses applying gravity load, hydrostatic pressure and corresponding uplift, winter thermal load (the worst condition) and seismic forces (according to accelerogram)
- Stress verification according to US Army Corps of Engineers: the maximum principal stresses can be up to twice the tensile strength of concrete (equal to 1.8 MPa), but only up to a fifth of the total area of the upstream and downstream face and for a cumulative duration not exceeding 0.4 s





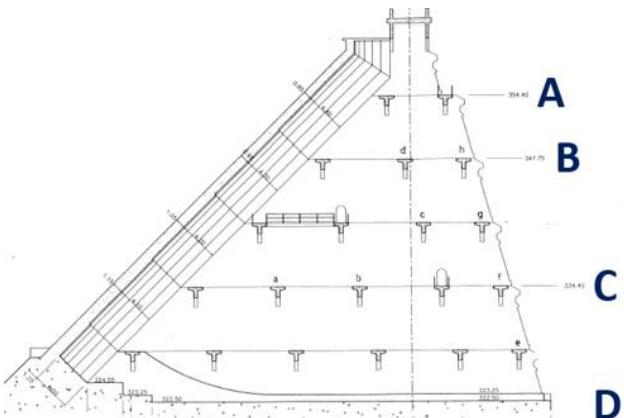
Case history of Molato dam

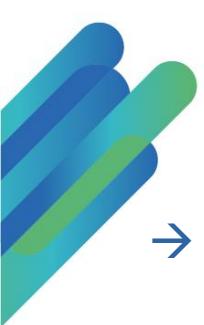
- Time history analyses applying gravity load, hydrostatic pressure and corresponding uplift, winter thermal load (the worst condition) and seismic forces (according to accelerogram)
- Stress verification according to US Army Corps of Engineers: the maximum principal stresses can be up to twice the tensile strength of concrete (equal to 1.8 MPa), but only up to a fifth of the total area of the upstream and downstream face and for a cumulative duration not exceeding 0.4 s
- Maximum principal stresses envelop does not overcome the tensile limit defined according to USACE (3.6 MPa) in all the multiple arches



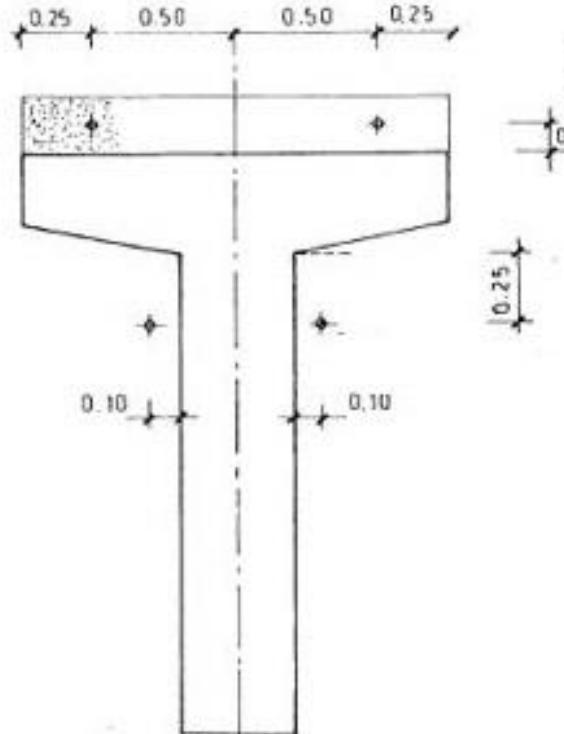
- Time history analyses applying gravity load, hydrostatic pressure and corresponding uplift, winter thermal load (the worst condition) and seismic forces (according to accelerogram)
 - Stress verification according to US Army Corps of Engineers: the maximum principal stresses can be up to twice the tensile strength of concrete (equal to 1.8 MPa), but only up to a fifth of the total area of the upstream and downstream face and for a cumulative duration not exceeding 0.4 s
 - Maximum principal stresses envelop does not overcome the tensile limit defined according to USACE (3.6 MPa) in all the multiple arches
 - For the buttresses and the shoulders (equivalent to gravity dams) sliding stability must be checked in horizontal sections: the verification is satisfied if for each section the ratio between the sum of horizontal forces (F_x) and the sum of vertical forces (F_y) is less than 1

Section	F_x [kN]	F_y [kN]	F_x / F_y [-]
A	47	4660	0.010
B	1540	9050	0.170
C	11300	35700	0.317
D	18000	46900	0.384

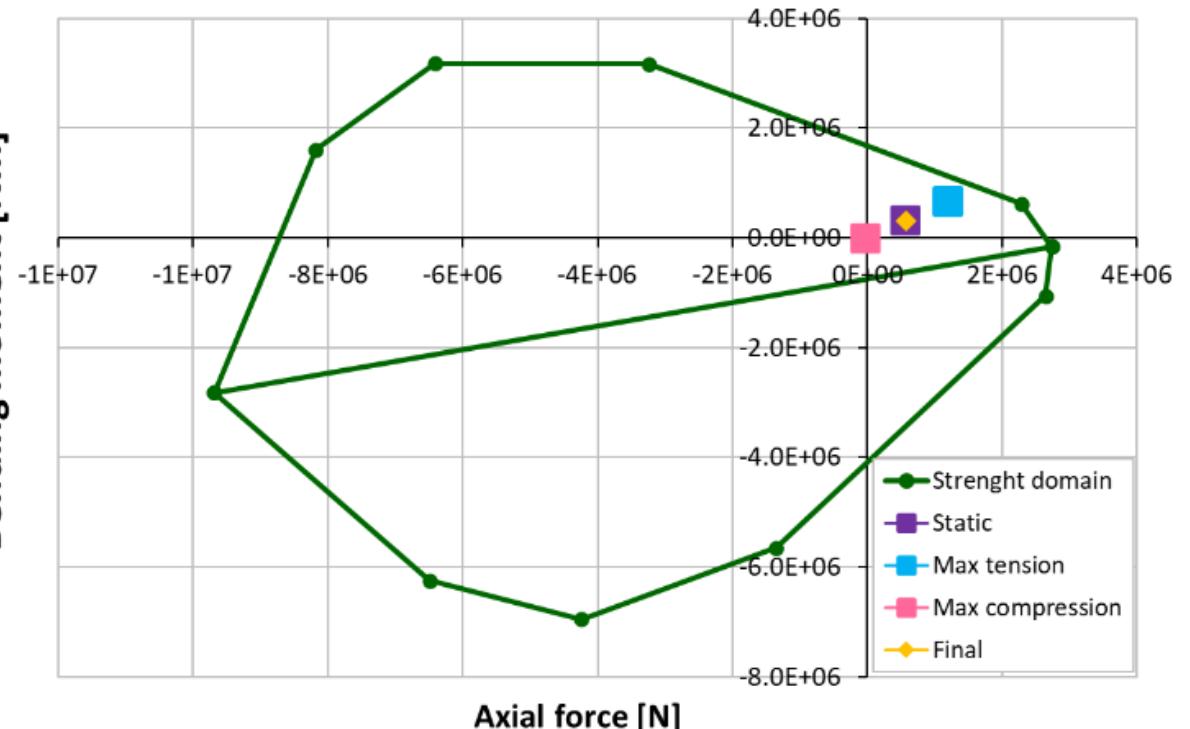




Case history of Molato dam

- Time history analyses applying gravity load, hydrostatic pressure and corresponding uplift, winter thermal load (the worst condition) and seismic forces (according to accelerogram)
 - Stress verification of the tensile stresses downstream
 - Maximum pressures in all the monitored sections
 - For the butt sections: the maximum of the sum of the bending moments and axial forces
 - For the reinforcement domain: a reinforcement domain at any time step of the analysis
- 
- The diagram shows a trapezoidal dam cross-section. The top width is 0.50, the side wall height is 0.25, the base height is 0.10, and the central thickness is 0.20.

s of
MP
on r
: ov
ent
h s
and
d if





Contents



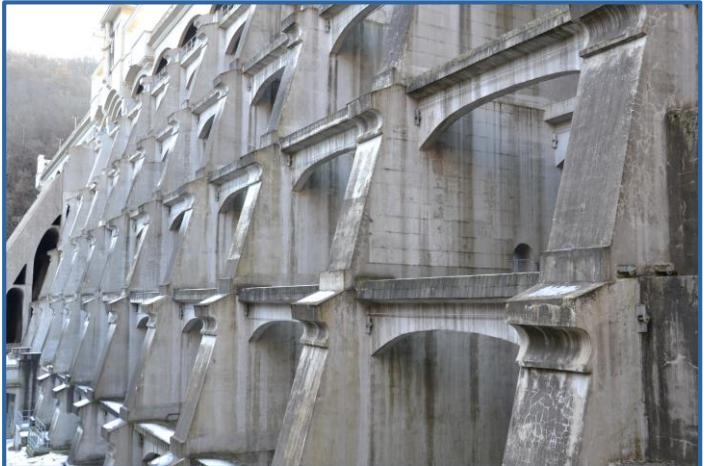
Introduction

Problems affecting buttress and slab/arch dams

Importance of numerical modeling

Case history of Molato dam

Conclusion



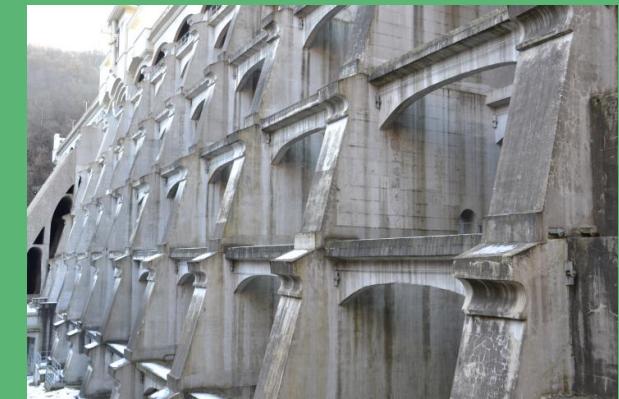


Conclusion

- The role of numerical modeling is fundamental for the evaluation of dam safety, for diagnostic investigation and for identifying the most effective rehabilitation works to guarantee long-term safety conditions
- The seismic analyses of Molato dam demonstrates how advanced numerical models and analysis allow evaluating the real response of all the structural elements of a strategic dam
- It is extremely evident that the properties of the materials, the constitutive laws, the geometric characteristics and the acting loads play a fundamental role in the evaluation of the seismic behavior of dams
- The work done by Colombo and Frigerio, except that related to the seismic assessment of Molato dam commissioned by Consorzio di Bonifica di Piacenza, has been financed by the Research Fund for the Italian Electrical System under the Three-Year Research Plan 2022-2024 (DM MITE n. 337, 15.09.2022), in compliance with the Decree of April 16th, 2018



THANK YOU
FOR YOUR KIND
ATTENTION





Université de
Sherbrooke



Low-to-high fidelity transformation function for the seismic fragility assessment of gravity dams

R.J.A Torres Filho ¹, R.L. Segura ², P. Paultre ¹

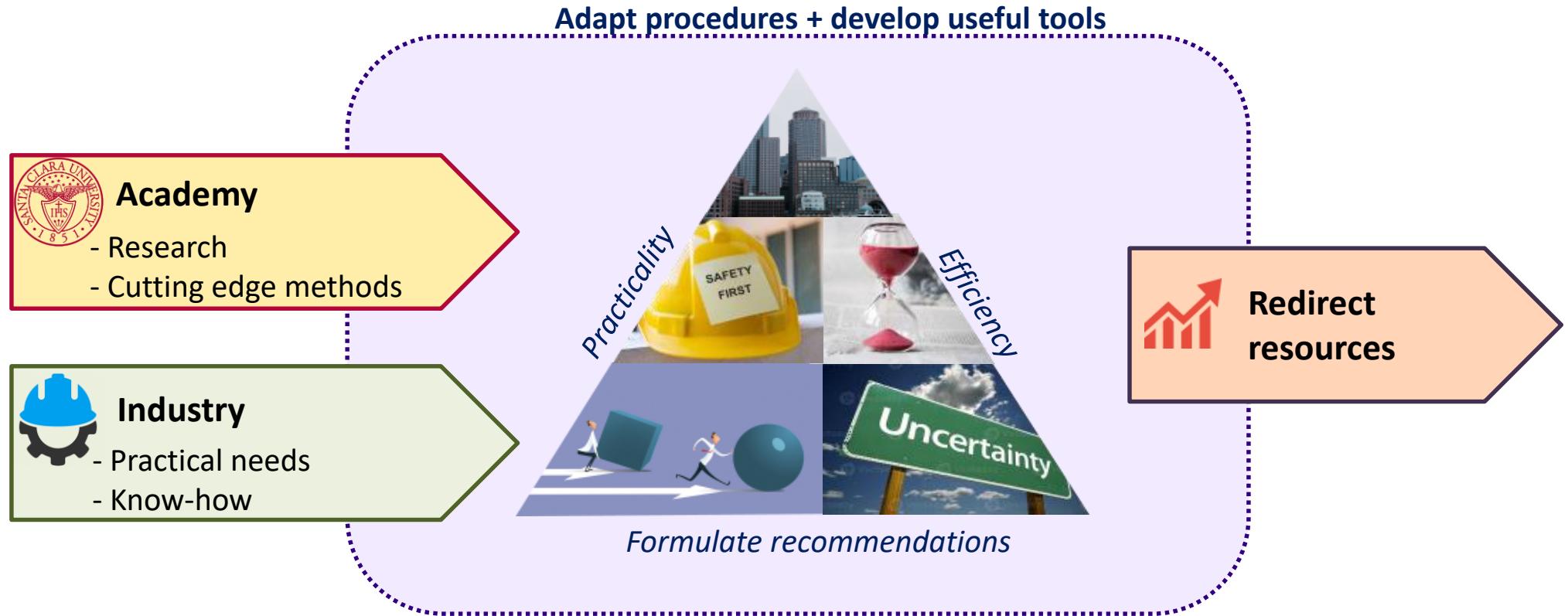
¹ Université de Sherbrooke, Sherbrooke, Canada

² Santa Clara University, Santa Clara, USA

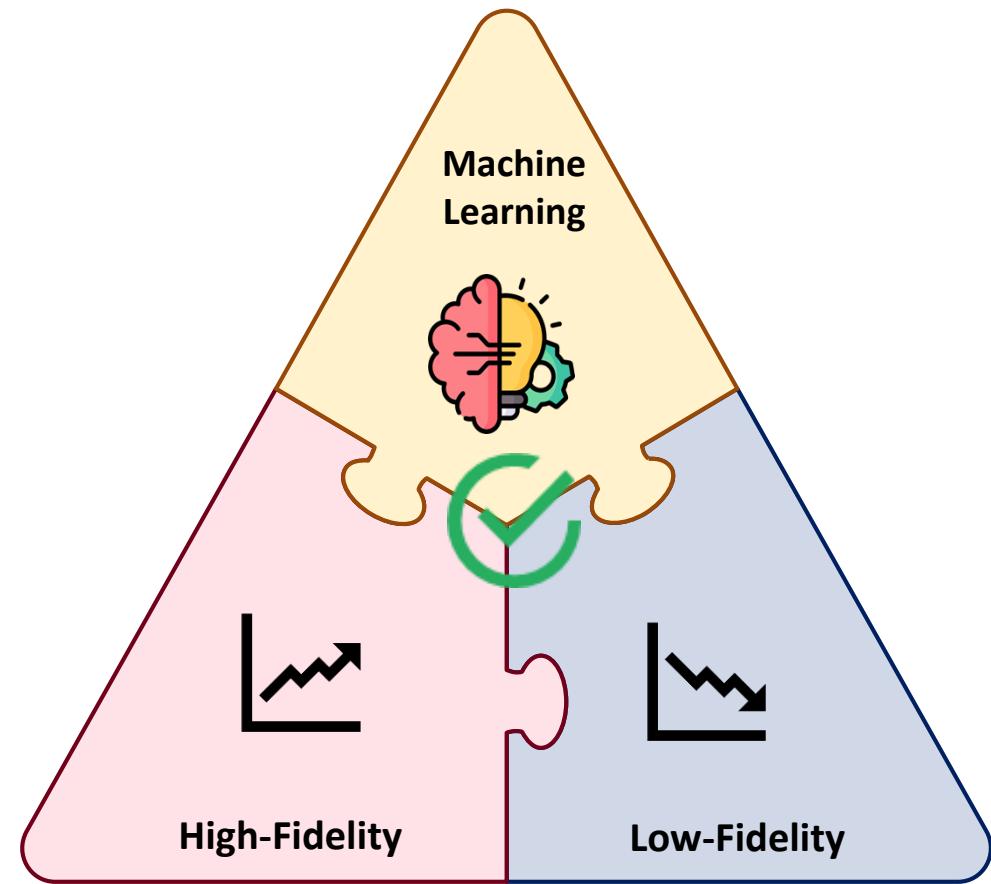
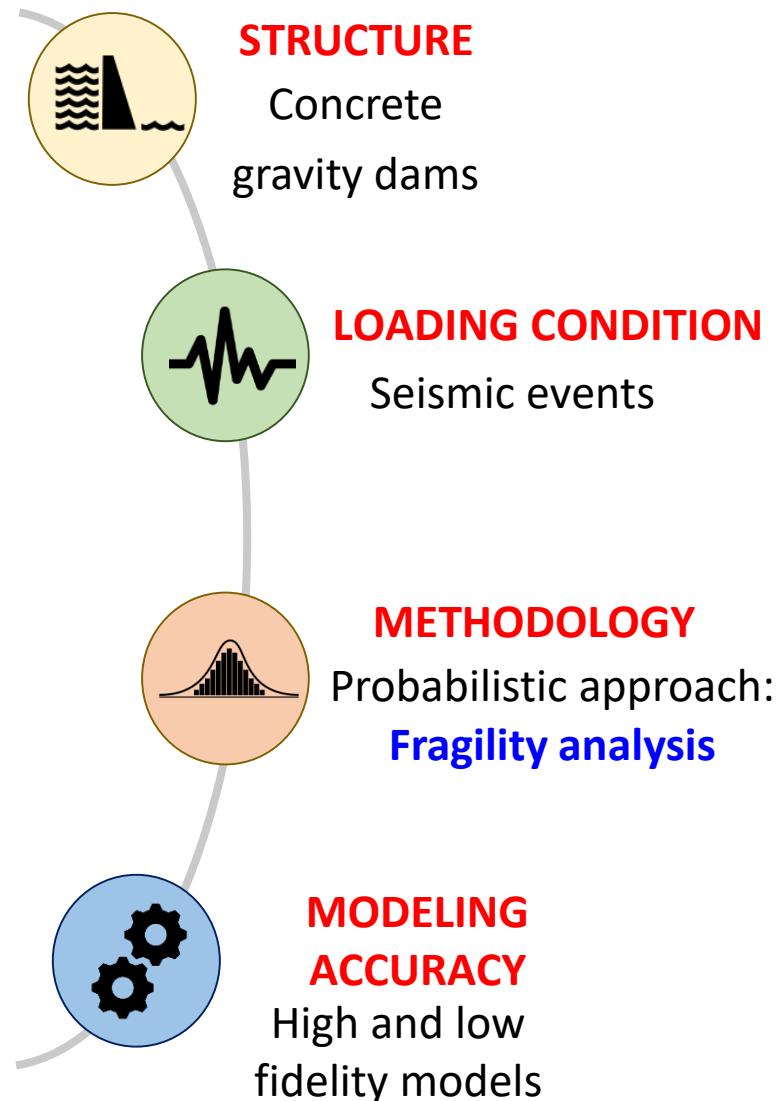


R.J.A Torres Filho, PhD.
Rodrigo.Jose.De.Almeida.Torres.Filho@usherbrooke.ca

Introduction: research project + Industry



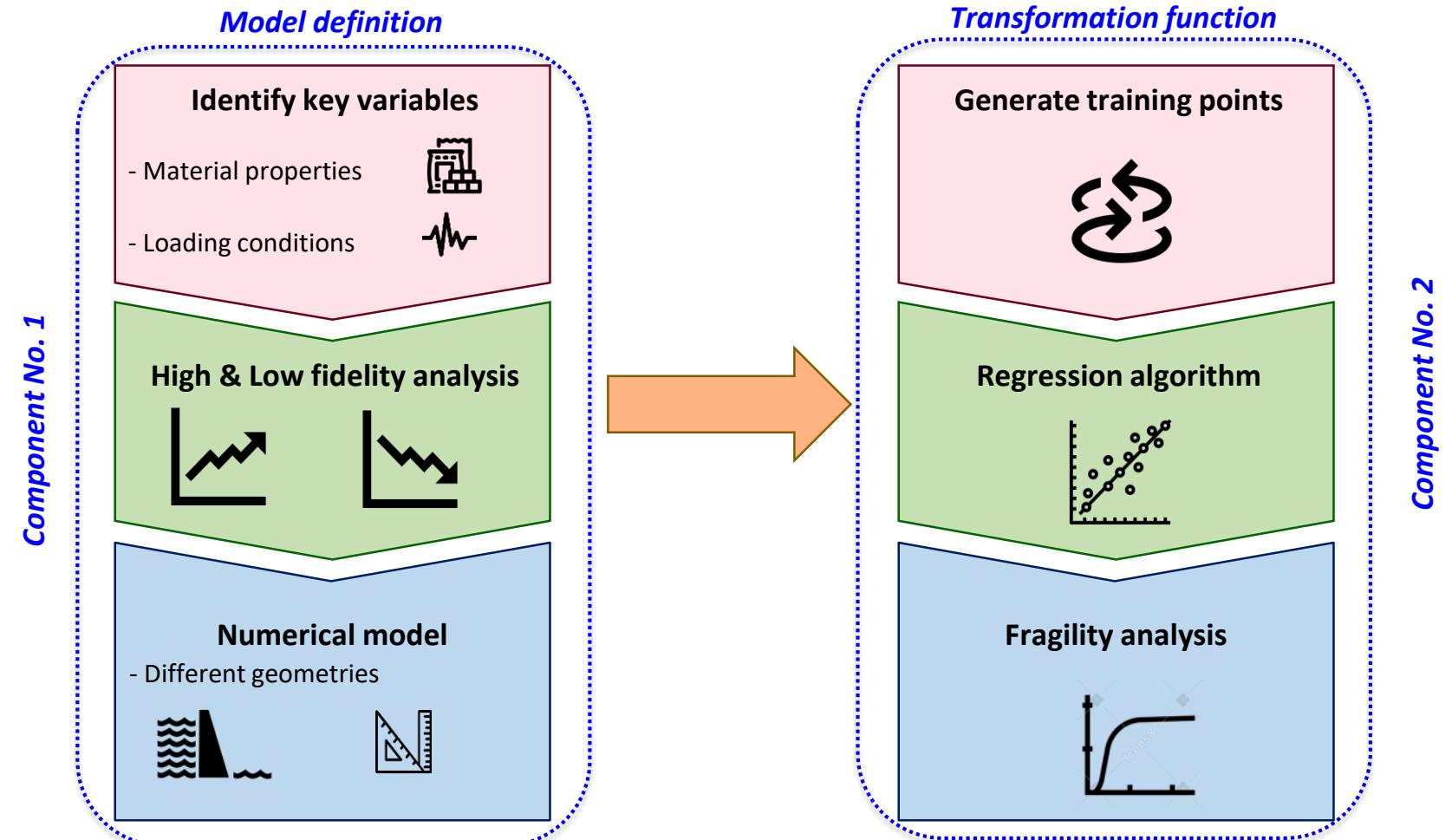
Introduction: context + problematic



HIGH +LOW Fidelity = Precise & low-cost

Introduction: Objective

Objective: develop a machine learning-based transformation function to **convert lower-fidelity observations into its high-fidelity equivalent** to perform seismic fragility assessment.



High and Low Fidelity Models

Model

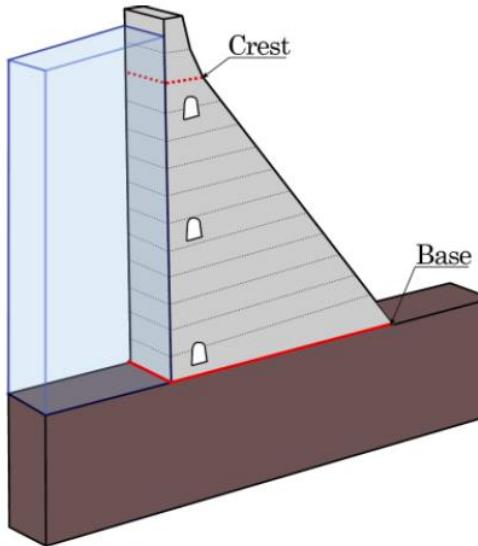
- Tallest monolith
- **Software:** CADAM3D (**Low-fidelity**) and LS-Dyna (**High-fidelity**)

Analysis

- Pseudostatic (**CADAM3D**)
- Non-linear time history (**LS-Dyna**)

Loads

- Self weight
- Hydrostatic load
- Hydrodynamic load
- Uplift
- Seismic loads



Parameters	Low Fidelity	High-fidelity
Seismic input	PGA	Ground motion time history
Water compressibility	Incompressible	Compressible
Foundation	Rigid	Flexible
Numerical representation	Cantilever	Finite elements
Output	Sliding factor of safety	Sliding displacement

Training dataset

→ **Input parameters:** 14

Sampling strategy: Latin Hypercube

- N=2500 samples

 2500 material parameters

 250 ground motions

 40 cross-section geometries

🎯 **Output of interest**



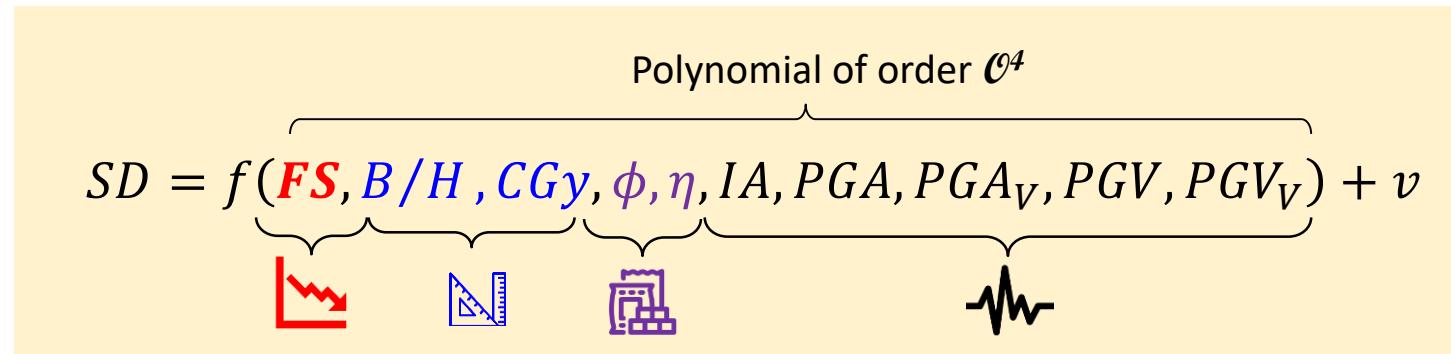
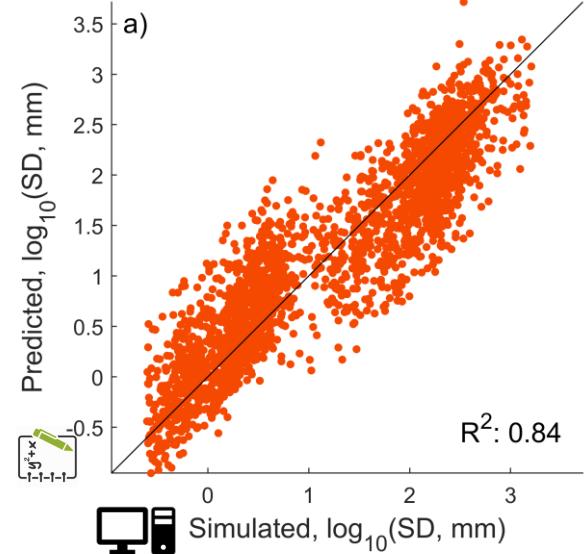
Variable	Uniform distribution parameters	
	Lower	Upper
 Tensile strength (MPa)	0.2	1.5
 Friction angle (°)	0.3	2.0
 Cohesion (MPa)	42	55
 Drain efficiency, η (%)	0	66
 PGA [Vertical] (g)	0.023[0.013]	1.115[0.429]
 PGV [Vertical] (cm/s)	0.820[0.302]	95.967[28.191]
 Arias intensity [Vertical] IA, (m/s)	0.004[0.001]	9.032[1.936]
 Spectral acceleration [Vertical] (g)	0.006[0.003]	4.598[1.200]
 Height (m)	30	210
 Base-to-height ratio, B/H	0.65	1.10

Transformation function

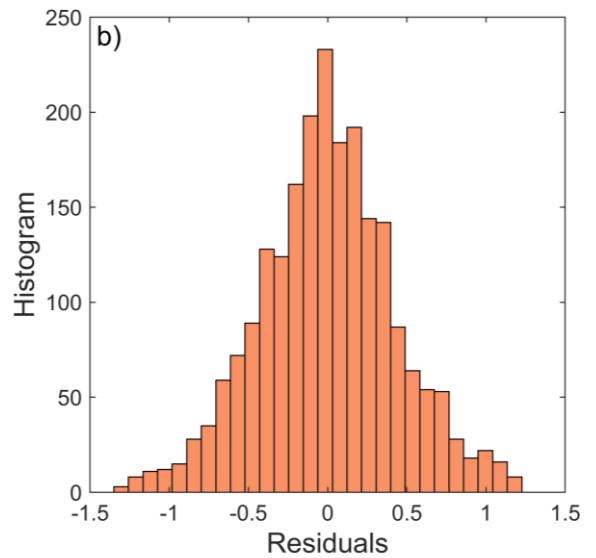
$$SD = g(X_i) + v \quad X_i = [x_1, x_2, \dots, x_n, SF]$$

Sliding displacement Algorithm Lack-of-fit error Covariate matrix





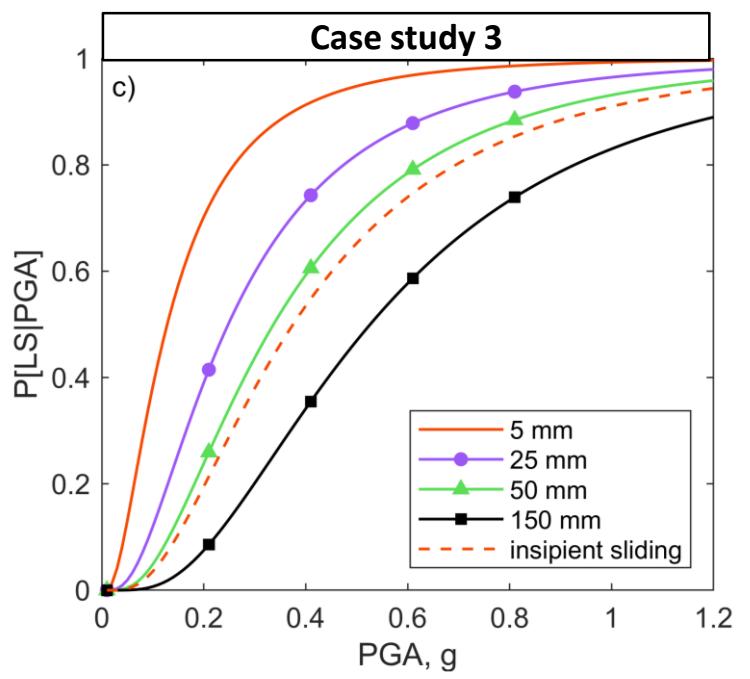
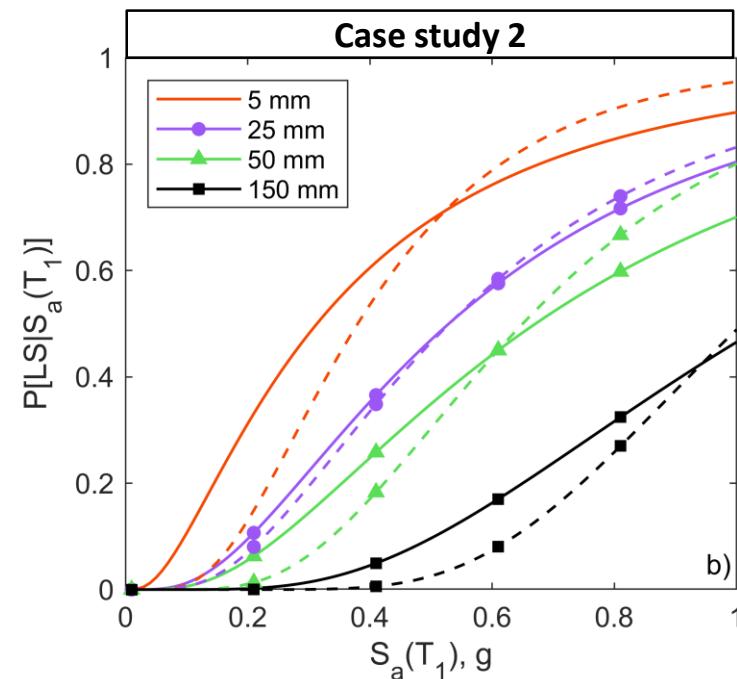
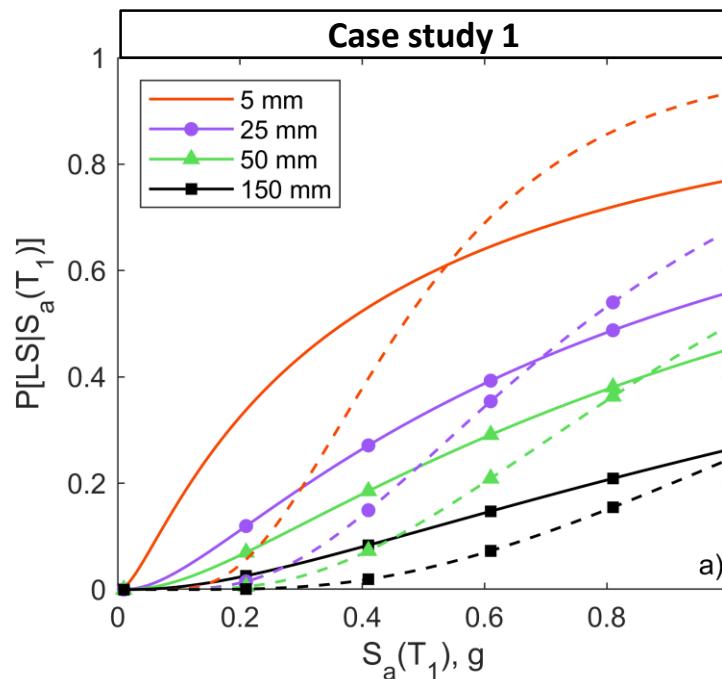
✓ SD \leftrightarrow SF with 10 parameters



Fragility analysis

- Comparison to 3 case studies
- 4 Sliding limit states
- Transformation function fragility curves (**continuous lines**)
- Reference fragility curves (**dashed lines**)

Parameters	Case study 1	Case study 2	Case study 3
Location	ENA	ENA	WNA
Height	78	78	80
Base-to-height ratio	0.79	0.79	0.75
Intensity measure	$S_a(T_1) = 0.1 \text{ to } 0.9 \text{ g}$	$S_a(T_1) = 0.1 \text{ to } 0.9 \text{ g}$	$\text{PGA} = 0.1 \text{ to } 1.2 \text{ g}$



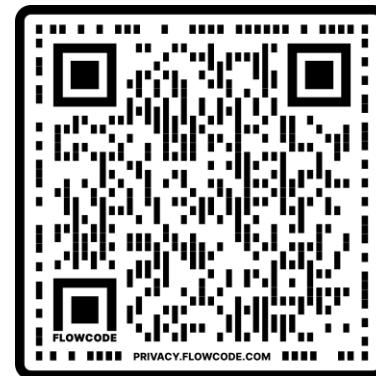
Conclusions

- ✓ The proposed transformation function provides a **cost-effective** and **accurate** method for generating **high fidelity observations**.
- ✓ The methodology is most effective for studies that align with the variables and hypotheses used during the transformation function's training.
- ✓ The transformation function-based fragility curves are a **valuable tool** for **preliminary assessments** with conservative and **safety-oriented** results.

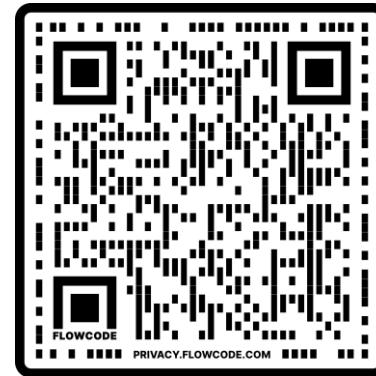
Questions?



Thank you for your attention



Torres Filho et
al. (2023)



Further information:

"Polynomial response surface-based transformation function for the performance improvement of low-fidelity models for concrete gravity dams".

Probabilistic Eng. Mech.



Rocio Lilen Segura

Analysis of the behaviour of a gravity dam in Central America subject to high seismic forces

A. De Paola¹, E. Baldovin² & S. Pavone³

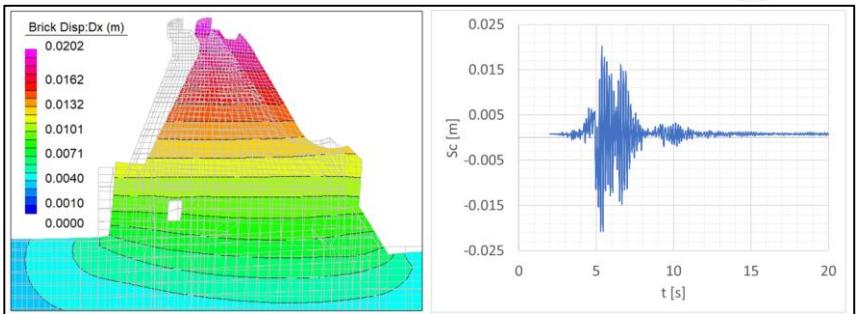
¹ Geotecna Progetti, Milan, Italy

² Geotecna Progetti, Milan, Italy

³ Geotecna Progetti, Milan, Italy

Introduction

Taking into account the verification criteria of the dams of the **U.S. Army Corps of Engineers (USACE)** recommendations, some aspects concerning the evaluation of the safety in seismic conditions of a gravity dam located in Central America in a context of high seismicity are presented.



3D dam view (Revit software) and a dam typical cross section

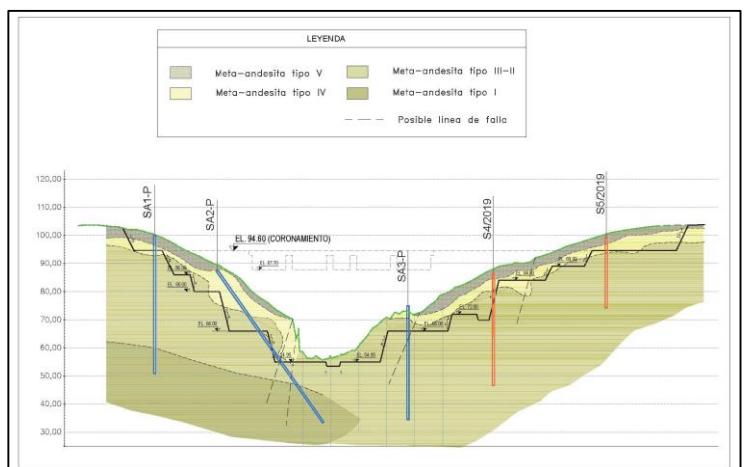
Concretes
 $f_c' = 21 \div 30 \text{ MPa}$



Principal characteristics of the analyzed dam

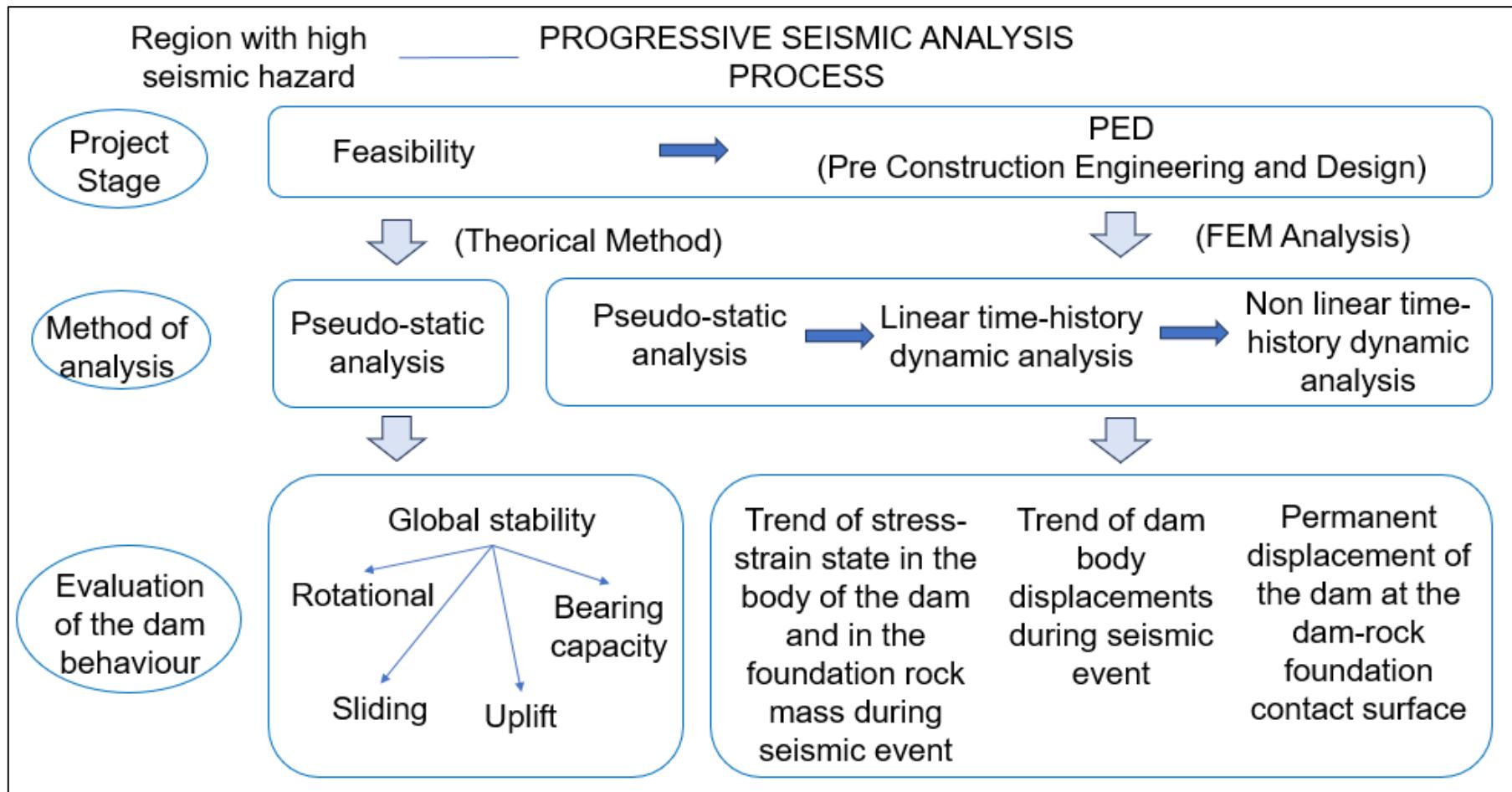
The analysed structure is a 39.65 m high conventional concrete gravity dam divided into 9 independent blocks of width ranging from 11.30 m to 25.20 m, for a total longitudinal extension equal to 153.50 m.

The dam foundation rock mass is composed by grey to light green-brown foliated metavolcanic rocks.



Problem statement

The analyses developed using various numerical methods and methodologies of increasing complexity, starting from a traditional calculation approach, based on the classic formulations of science of construction (called **Theoretical Method**), up to **FEM analyses** both in **the linear and nonlinear field**.



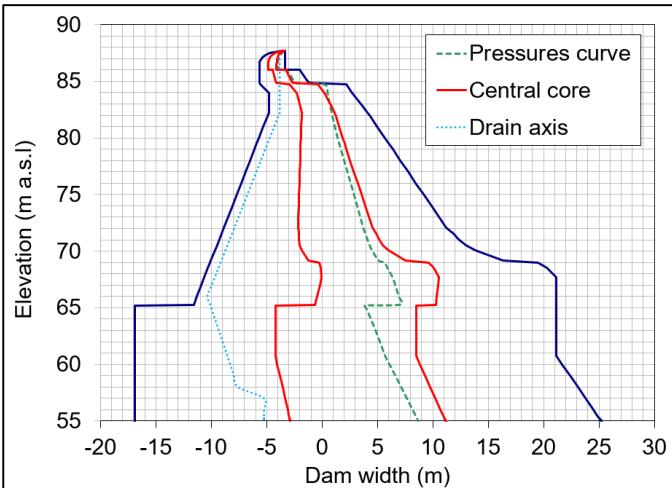
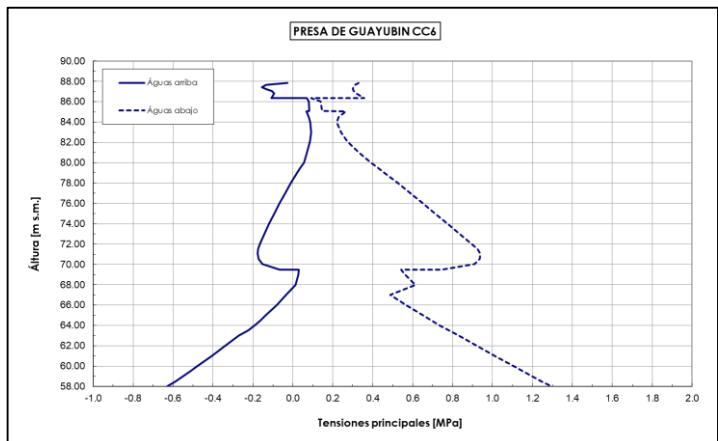
Evaluation of gravity dam seismic behaviour

The analyses were performed in **Safety Evaluation Earthquake (SEE)** and **Operating Basis Earthquake (OBE)** conditions.

Design Earthquake	Return period T (years)	PGA _h (g)	PGA _v (g)
OBE	144.3	0.179	0.099
SEE	5750	0.776	0.484

Analysis of the dam with the Theoretical Method

The dam has been analyzed through the calculation program “Gravity Dams Analyses” (G.D.A.) developed over the years by Geotecna Progetti and fully validated. In the dam seismic analyses the earth quake input has been considered according to a pseudo static approach.



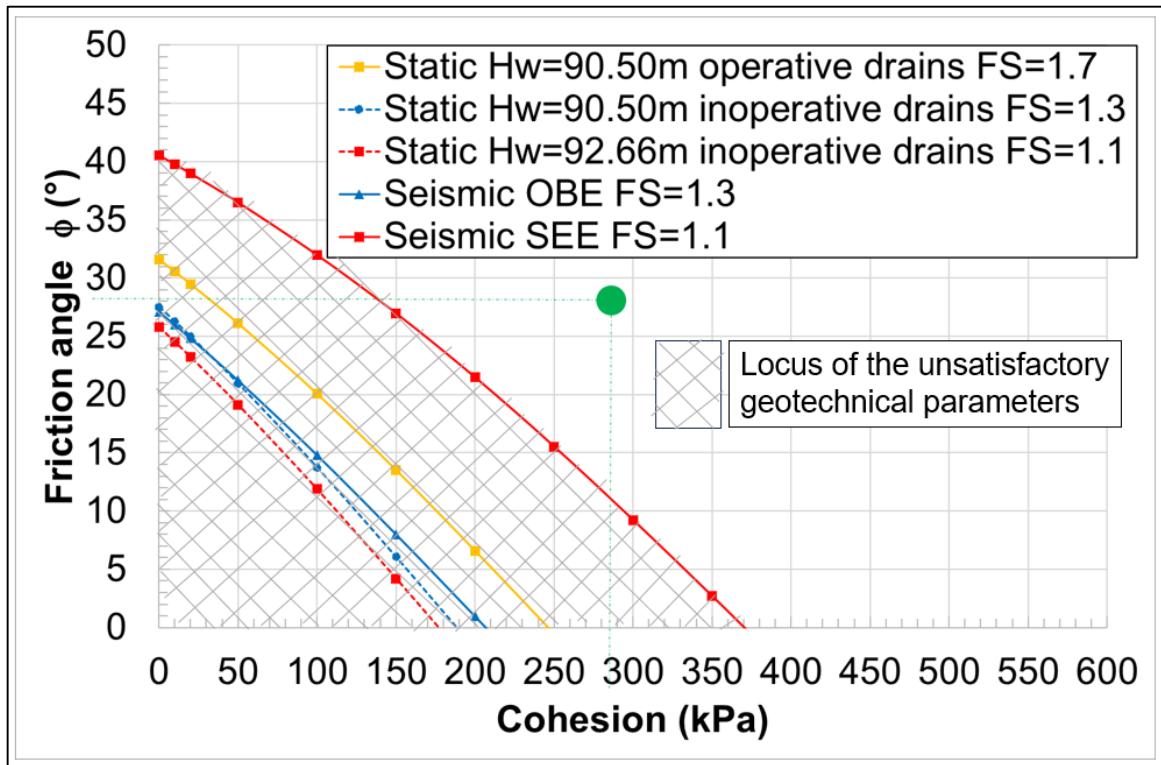
The stress values resulted lower than the materials strength limits.

It has to be considered that **sliding stability checks are of fundamental importance in the analysis of a gravity dam** and require correct evaluation of the shear resistance parameters of the concrete along the casting joints and the contact surface between dam and foundation rock mass.

Evaluation of gravity dam seismic behaviour

Analysis of the dam with the Theoretical Method

The **additional in situ geotechnical surveys** carried out returned shear strength characteristics of the rock mass **sufficient to verify the dam for sliding phenomena** (green point in figure).

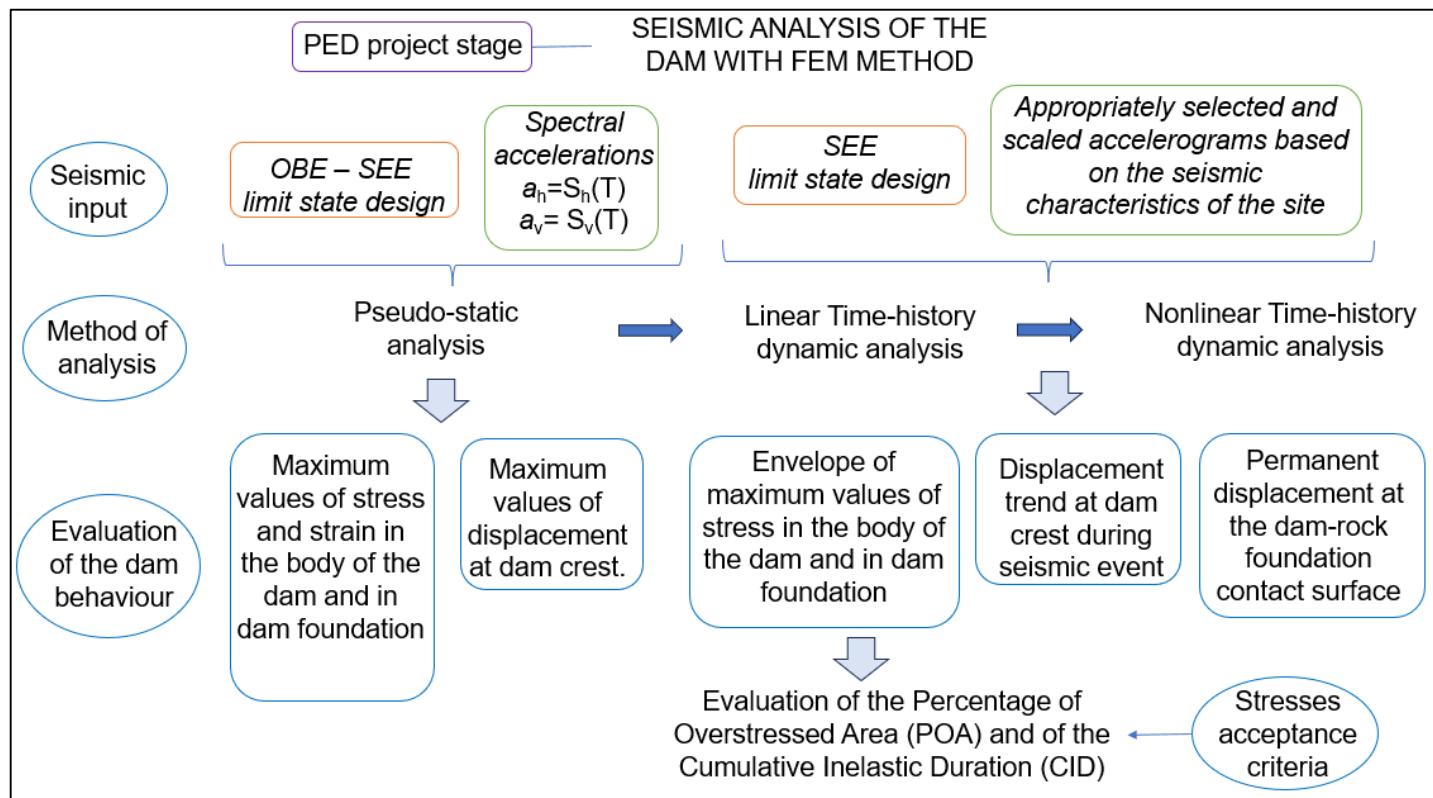
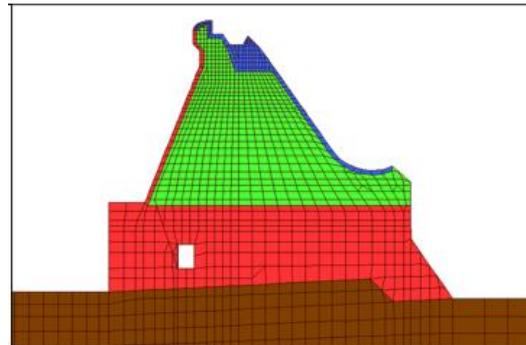


The geometries of the dam adopted in the **feasibility project stage were therefore confirmed and used as a starting point for the FEM analyses method**.

Evaluation of gravity dam seismic behaviour

Analysis of the dam with the FEM Method

The FEM numerical models of the dam analyzed typical cross sections have been realized with Straus7 calculation software using 3D brick type elements (8 nodes) 1 m in thickness.

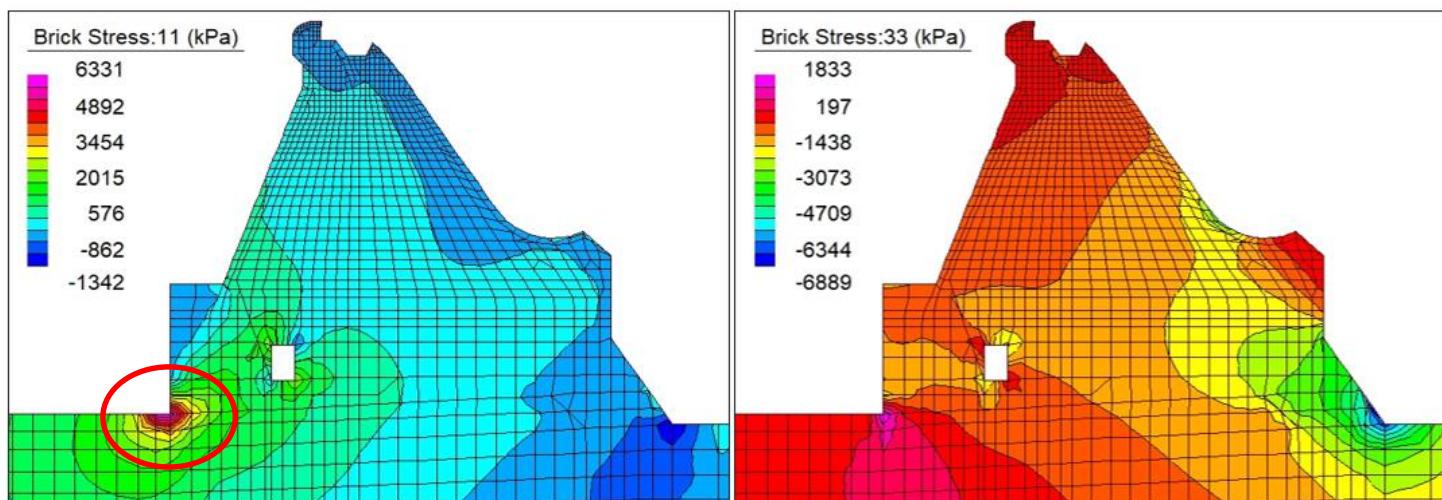
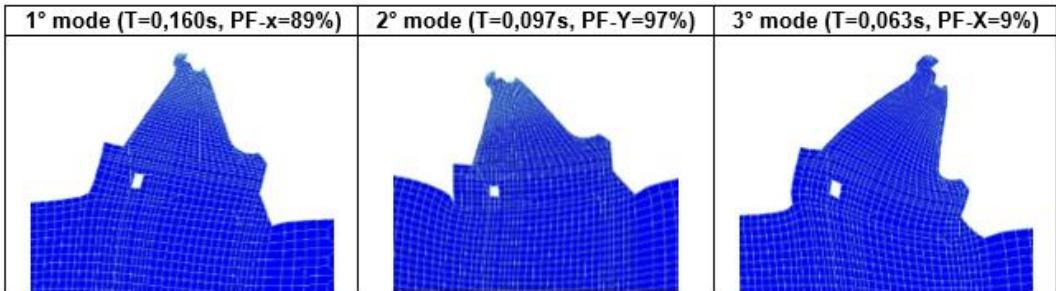


Evaluation of gravity dam seismic behaviour

Analysis of the dam with the FEM Method - Pseudo-static analysis

The FEM model was firstly **validated** comparing the analyses results obtained assuming the same pseudo static seismic action with those of the Theorical Method based on the PGA values evaluated for the site.

Analyses were performed considering the spectral accelerations values evaluated in correspondence of the fundamental periods that characterize the dam.

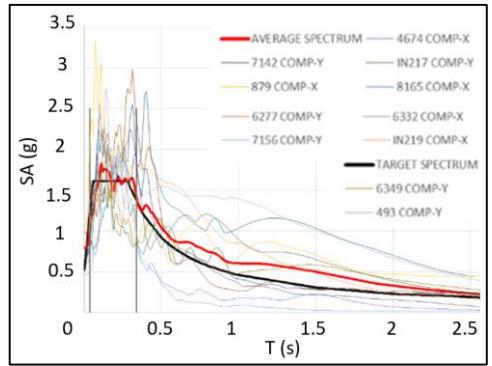


Trend of maximum and minimum stress values in the body of the dam and in the rock mass in SEE seismic condition

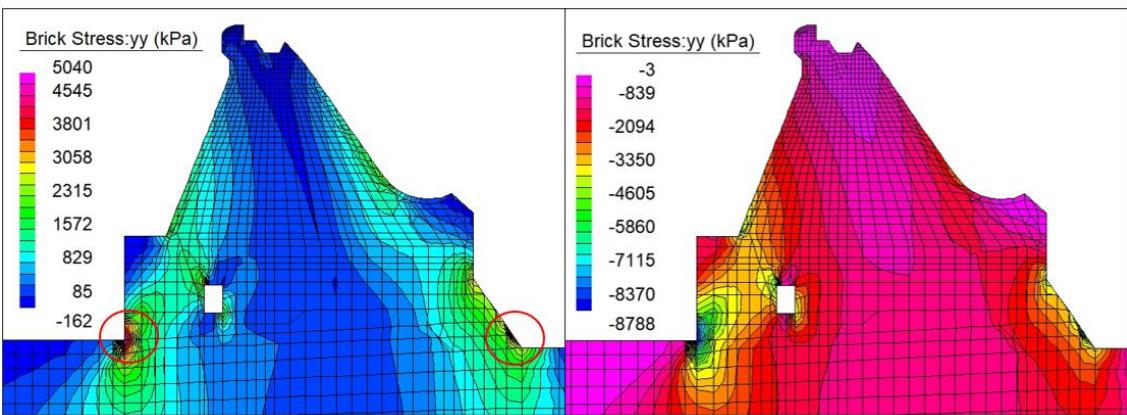
Evaluation of gravity dam seismic behaviour

Analysis of the dam with the FEM Method - Linear time history dynamic analysis

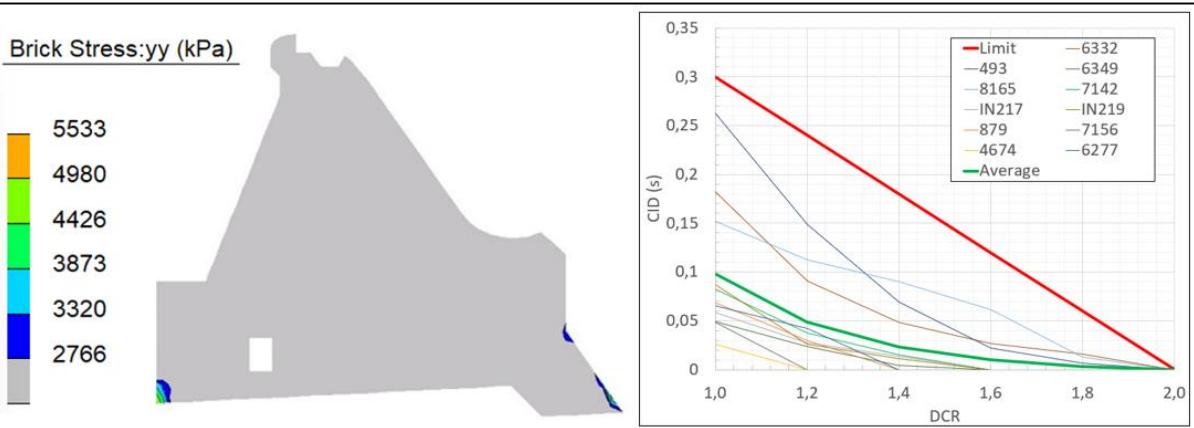
Time-history dynamic analyses have been performed using suitably selected accelerograms scaled to the site-specific response spectra values.



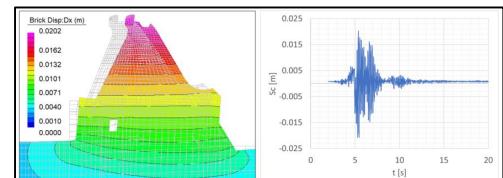
The maximum tensile stresses obtained are of the order of 4.5-5 MPa and exceed the static tensile strength of concrete



The acceptability of their values has been checked, according to USACE recommendations (EM 1110-2-6053).

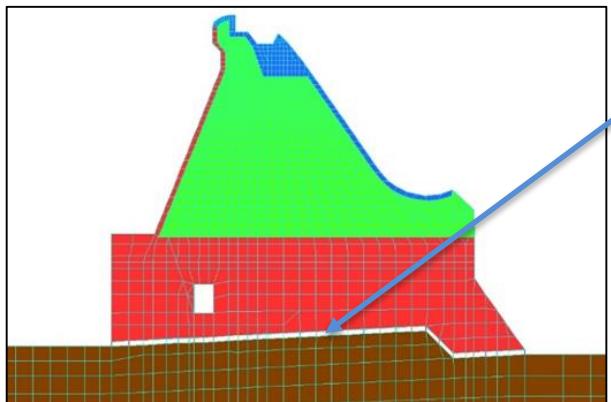


The maximum values of displacement "Sc" at the dam crest were of the order of 2 cm, such as the ratio between Sc and the dam height H resulted of the order of 0.061%.



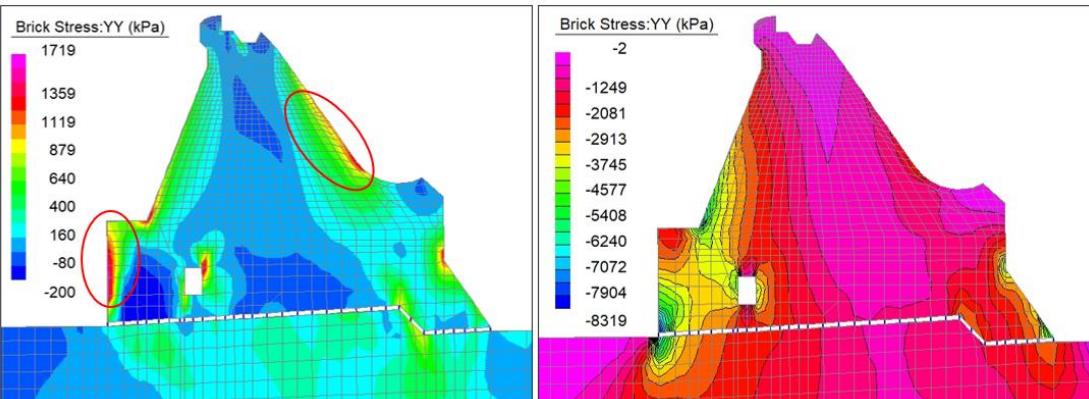
Evaluation of gravity dam seismic behaviour

Analysis of the dam with the FEM Method - Nonlinear time history dynamic analysis

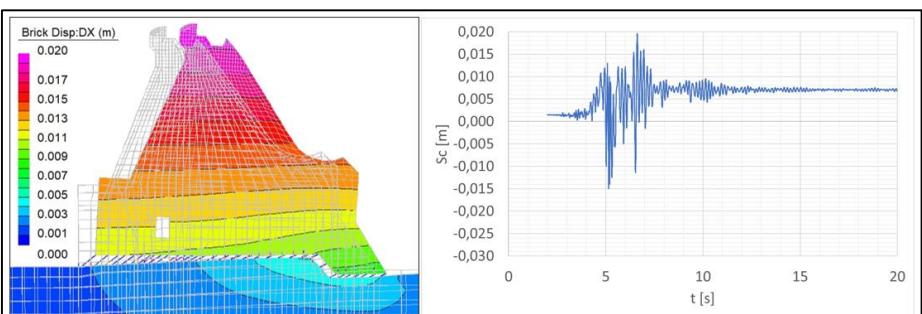


Specific beam type finite elements called "contact points" have been introduced in the FEM mesh between the nodes of the concrete dam brick type element and those of the foundation rock mass

The maximum stress value was equal to about 1.7 MPa, lower than the tensile strength of the several concrete types adopted for the dam.



The maximum value of the absolute displacement "Sc" at the dam crest was of the order of 2 cm, while the residual displacement at the dam base "Sb" was equal to about 7 mm ($Sb/H=0.035\%$).



Conclusions

- ❑ As confirmed by the present case study, in the design of a complex structure, such as a dam, it is **absolutely important to adopt a numerical approach of increasing complexity** during the several project stages.
- ❑ The analysis depends on the specific characteristics of the structure and on the related boundary conditions, which inevitably vary from a case to another and influence the design choices and the numerical verifications. In this context, **the preparatory activities for the definition of the boundary conditions of the structure are very important**. For this purpose, it is necessary to carry out a **geognostic and geotechnical survey** on site to obtain a reliable geomechanical characterization of the foundation rock mass and the execution of a **seismotectonic study** of the site to define adequate design seismic actions.
- ❑ A **basic numerical analysis** (methods based on the classical formulations of construction science), which allows to acquire a **good sensitivity of the general behaviour** of the dam, has to be followed by **more advanced modelling FEM** (e.g. pseudo static, dynamic, linear and non-linear analyses) which guarantees an extensive study of the stress-strain state and of the dam general behaviour.
- ❑ This approach appears fundamental to **develop solid numerical models and consequent reliable results representative of the real behaviour of the dam**.
- ❑ The seismic analysis process **cannot be completely standardized** and acritically applied to every gravity dam. It depends, in fact, on the specific characteristics of the analysed structure and on the related boundary conditions, which inevitably vary from a case to another, and influence the design choices and the numerical verifications.



Thank you!

Any questions?

Dam portfolio assessment for risk informed decision making

T. Elkhoraibi¹, A. Hashemi¹, A. Kottke², Y. Arici³

¹ Hashemi & Elkhoraibi Earthquake Engineering Inc., Berkeley, CA, USA

² Pacific Gas and Electric Company, San Francisco, CA, USA

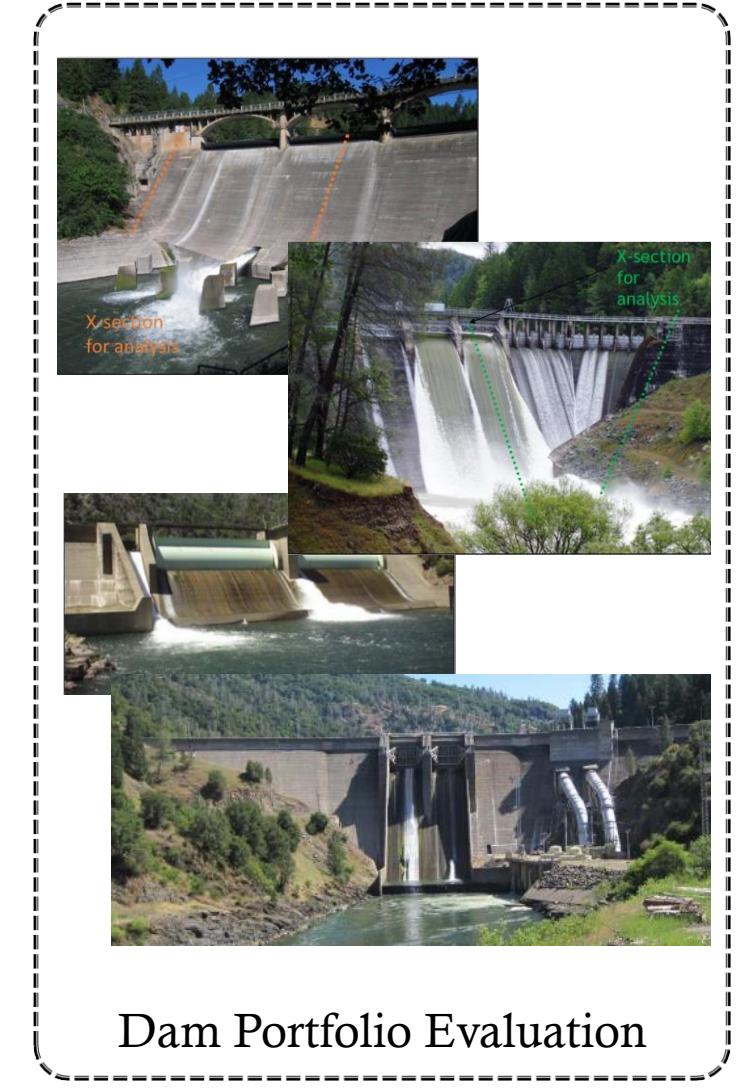
³ Middle East Technical University, Ankara, Turkey

INTRODUCTION

There is a large inventory of older gravity dams in North America. The performance of these systems under seismic hazard is a significant concern as the understanding of seismic hazard has changed significantly.

The management of a portfolio of dams requires collection/evaluation of site data, conditions, analysis and hazard assessment, and accompanying systematic comparison for decision making.

Even in the presence of well-procured site data, seismic assessment is a challenging task and requires consideration of natural (aleatory) variability and knowledge-based (epistemic) uncertainty.



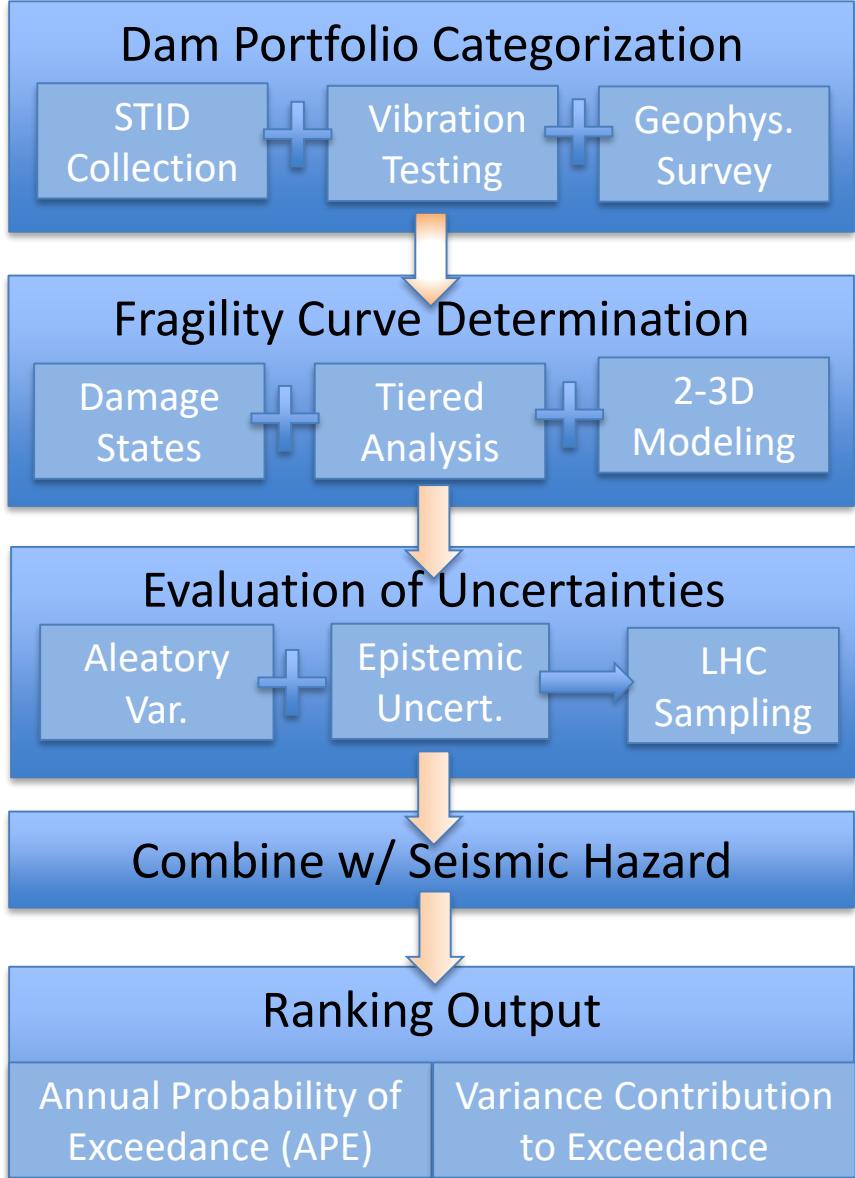
PROBLEM STATEMENT

For a dam portfolio comprised of a number of systems, with varied site conditions/materials and seismic hazard, a decision-making tool for prioritization is required to optimally allocate resources to systems with higher risk.

Accordingly, a methodology for comparative evaluation of risk for the dam stock is developed :

- Quantifying seismic risk in terms of fragility functions,
- Including two different damage states (incipient/severe),
- Explicit inclusion of uncertainties in the final assessment: the estimation of Annual Probability of Exceedance (APE) and ranking of the stock.

*Note that in addition to seismic risk of failure, the consequence of failure (not discussed here) plays an important role in ranking and prioritization of the dams.

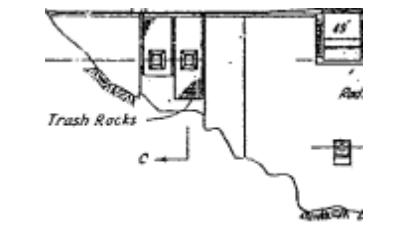


DAM PORTFOLIO CATEGORIZATION

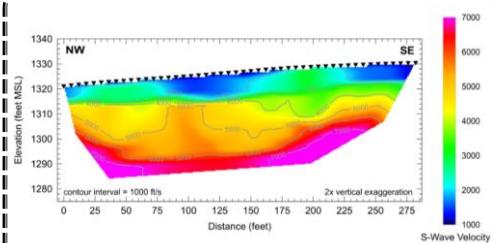
Detailed as built drawings and design data compiled, along with site reconnaissance and geophysical surveys



Site Visits



As-built Drawings



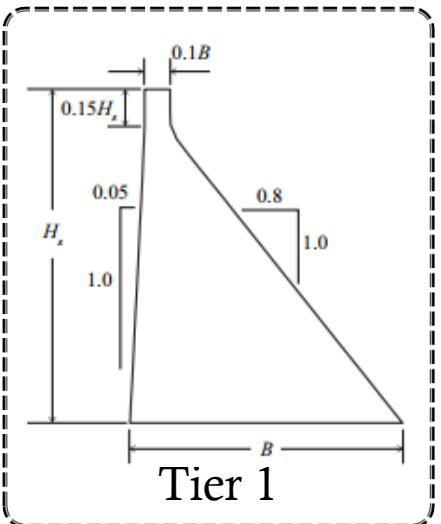
Geophysical Surveys

Multi-level screening approach making extensive use of simpler analysis techniques to consider uncertainty

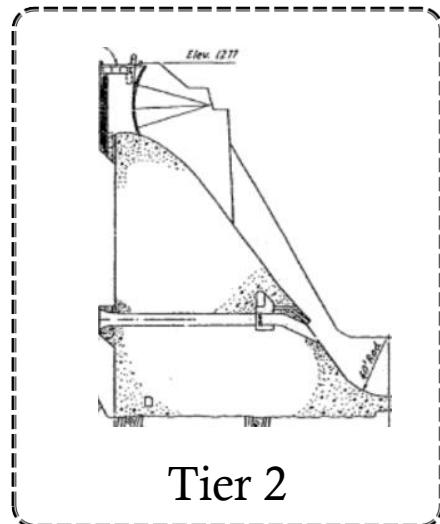
Tier 1: Standard sections, SRSA (Lokke and Chopra, 2013)

Tier 2: Non-standard section, EAGD84 (Fenves and Chopra, 1984)

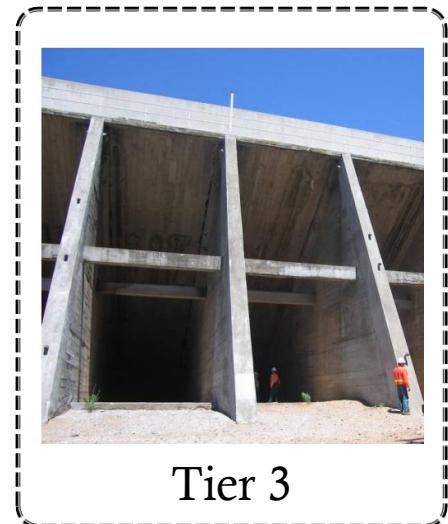
Tier 3: Significant 3D features – general purpose FEM



Tier 1



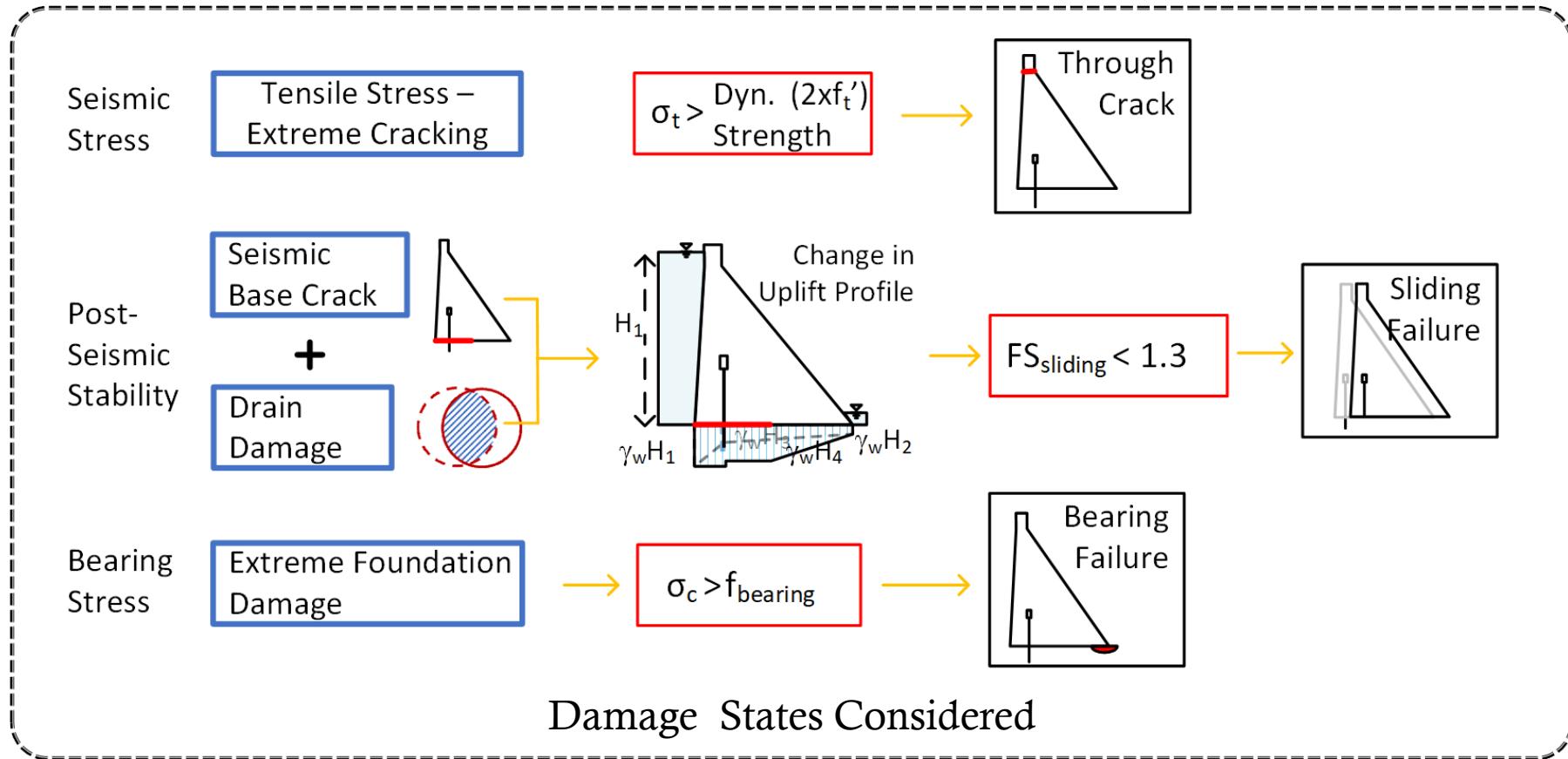
Tier 2



Tier 3

DAMAGE STATES

Damage limit states – tensile stress and bearing stress (during shaking), stability (post-shaking) – generally following FERC guidelines for assessment.



FRAGILITY CURVES

A clearly stated target performance objective is not available for concrete gravity dams, unlike buildings (such as an APE of 5e-5 for essential new buildings (ASCE 7-16))

Fragility curve is used to include the effects of uncertainties from various factors into the final estimate of APE.

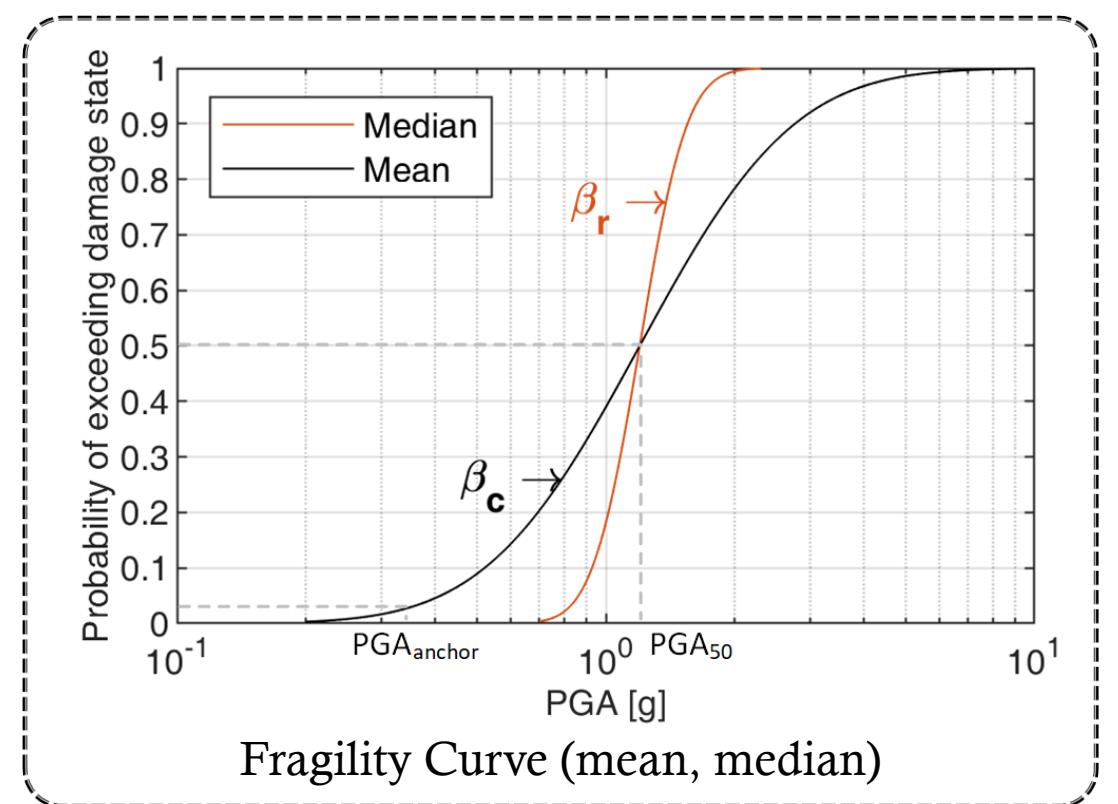
- Fragility curves defined using the anchor point using PGA as the primary intensity measure.
- Fragility curve includes the effects of composite uncertainty β_c .

$$a_{x\%} = a_{Ref} \times e^{\beta(\Phi^{-1}(x\%) - \Phi^{-1}(X_{Ref}))}$$

a_{Ref} IM for a reference point

X_{Ref} Corresponding prob. of exceedance

β^2 Variance



SOURCES OF UNCERTAINTY

The compiled data assessed to obtain the variabilities for all factors affecting the results of evaluation,

Data available from testing, surveys, measurements, for design documents.

$$\beta_c^2 = \beta_r^2 + \beta_{u,P}^2 + \beta_{u,M}^2$$

β_r^2 Aleatory, records

$\beta_{u,P}^2$ Epistemic+Ale., input

$\beta_{u,M}^2$ Epistemic, modeling

Variance Definition

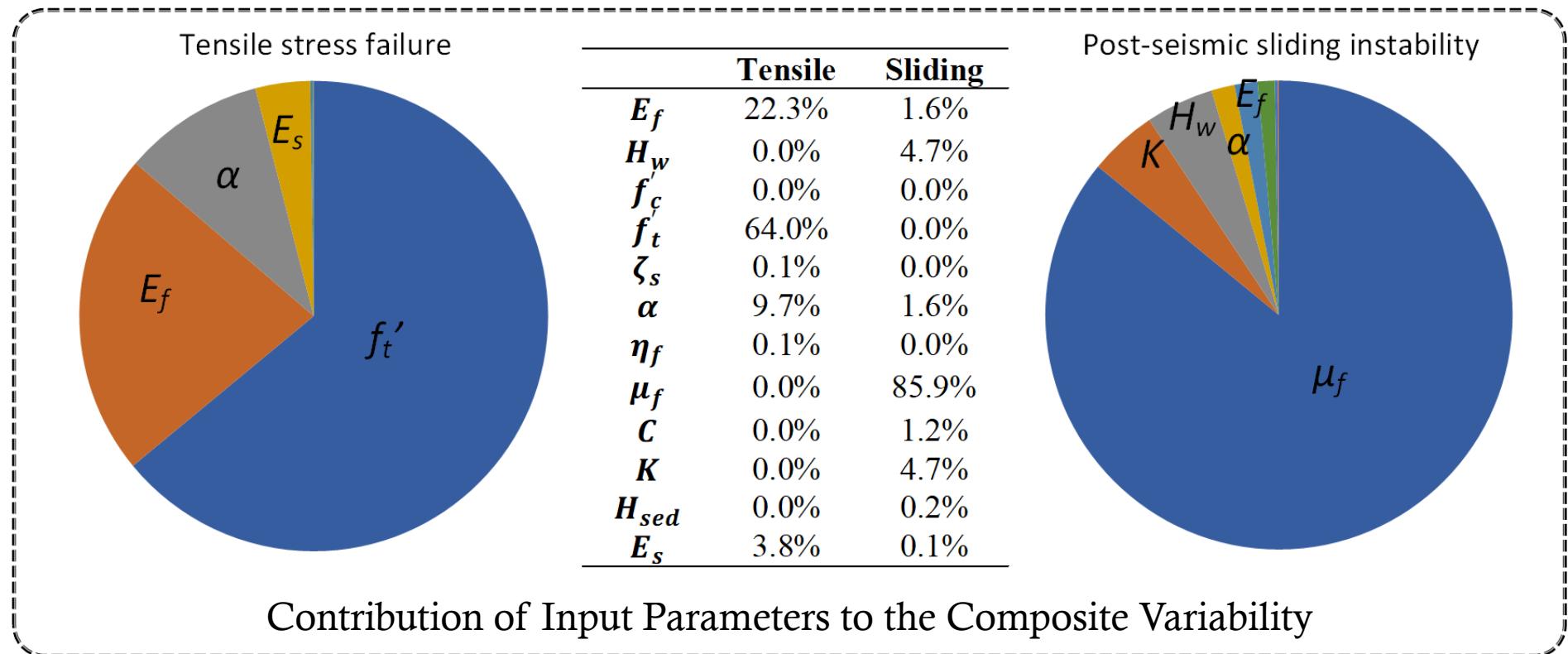
Sources of Uncertainty and Classification

Symbol	Source	Aleatory/Epistemic
β_r	Record-to-record variability	Aleatory
$\beta_{u,P}$	<ul style="list-style-type: none"> Concrete compressive and tensile strength Structural damping ratio Concrete elastic modulus Foundation elastic modulus Foundation hysteretic damping Wave reflection coefficient Friction angle/Cohesion Foundation bearing capacity Vertical drain effectiveness Height of reservoir water Height and density of sedimentation 	Epistemic
$\beta_{u,M}$	Modeling of analyzed system	Epistemic
β_c	Total (composite) aleatory and epistemic uncertainty with contributions from β_r , $\beta_{u,P}$ and $\beta_{u,M}$	Composite
$\beta_{u,H}$	Estimation of seismic hazard	Epistemic

FAILURE MODES AND VARIABILITY

Identifying the largest contributors to the variance allows better understanding of the most important parameters - guidance for allocating resources for reducing uncertainty.

The same set of analysis (120) repeated for each parameter with BE value assigned to other input to obtain individual parameter contribution to overall uncertainty.

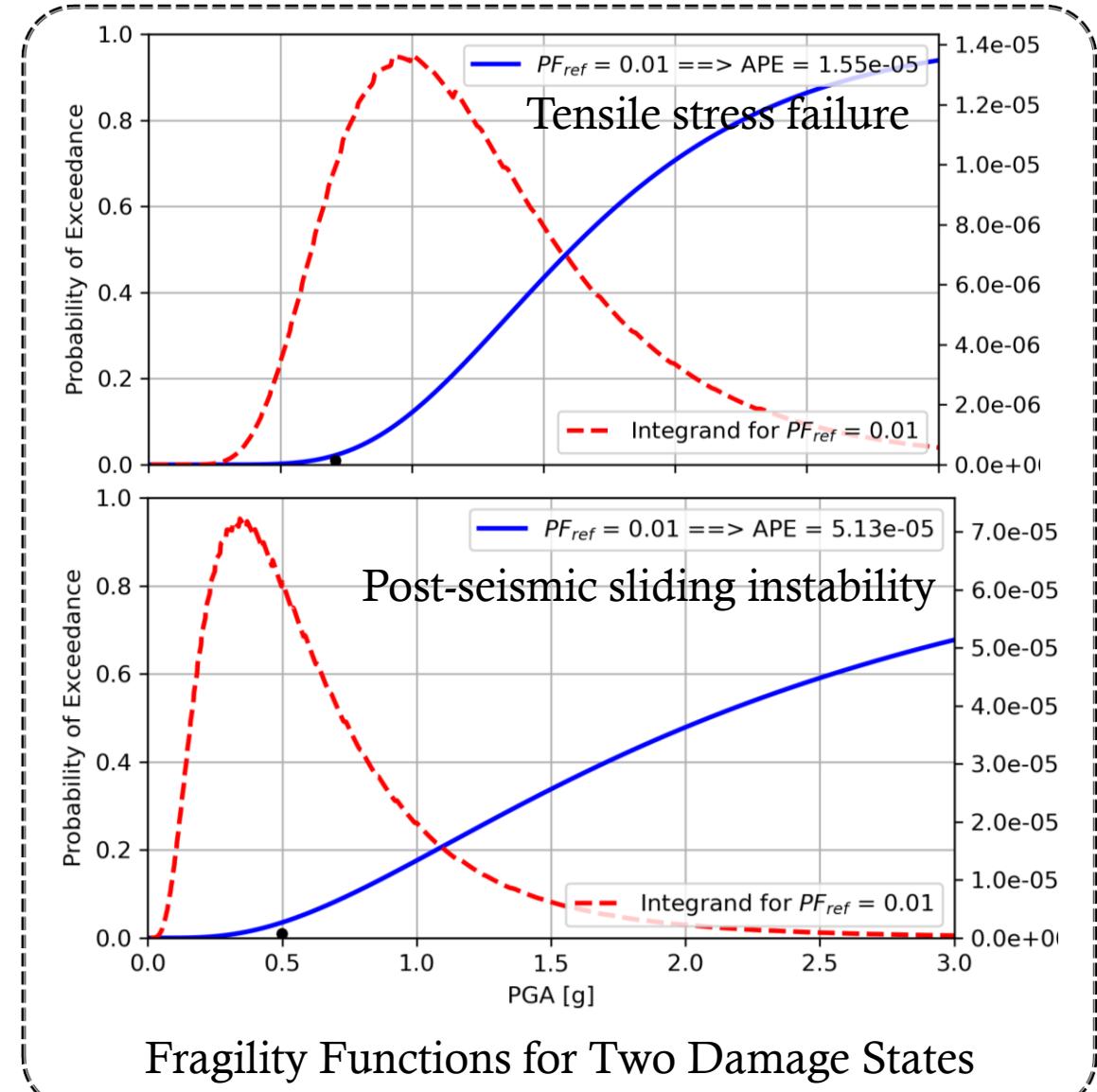


FRAGILITY FUNCTIONS AND AGGREGATE APE

Fragility functions for two damage states defined using the PGA at the anchor point with an associated probability of exceedance of 1%, PGA_{median} and the full composite standard deviation β_c .

Aggregate mean APE, for incipient and severe damage calculated as below – similar to values for essential facilities like hospitals and fire stations for this case.

Damage state	Incipient damage	Severe damage
Mean	3.58E-3	5.35E-5
Log-Mean	1.92E-3	0.46E-5
Log-SD	1.22	2.42
50 th Percentile	2.12E-3	0.51E-5



SUMMARY AND CONCLUSIONS

Tier 1 assessment of a proposed multi-level screening methodology is presented with a case example study. The development of fragility functions, including the estimation of associated uncertainty, is demonstrated, with the final goal of obtaining consistent, comparable risk estimates for systems within the portfolio.

- Fragility curves were determined for three different failure modes using anchor point IM and composite variability including aleatory and epistemic uncertainties.
- Input variability and its effect on assessment result was quantified using LHS with the goal of determining the parameters with overall largest contribution to uncertainty.
- In the case example, the effective friction angle at the dam-foundation interface was determined as the most dominant contributor to the risk.
- The overall seismic risk for Dam 1, in terms of APE, was determined to be 5.35E-5, which can now be considered for comparison to other dams in portfolio for prioritization.



Thank you!

Any questions?

Assessment of the seismic behaviour of concrete dams: from simplified to advanced methods

G. Faggiani, P. Maserati

02/07/2024





Contents

BACKGROUND



Progressive analysis methodology

CASE STUDIES



The seismic wave propagation model SAM-4D

FINAL REMARKS



Case Study: Pine Flat Dam



Main results



Final remarks



consists in **subsequent phases of increasing complexity**, starting from the **simplest method** appropriate to the problem, that provides **faster and more easily comprehensible results**, and progressing to the **most complex methods**, that are supposed to provide **more accurate and realistic results**



➤ Pseudo-static analysis

static analysis with additional static loads

- ✓ inertia forces of the structural mass
- ✓ hydrodynamic pressure on the upstream face of the dam

➤ Time-history analysis

dynamic analysis simulates the response of the dam to the entire ground motion

- ✓ dam-reservoir dynamic interaction: structural-acoustic coupling (Zienkiewicz, 1977)

with the massless approach

- ✓ dam-foundation dynamic interaction: neglects foundation inertial and radiation damping effects (Clough, 1980)

with the SAM-4D model

- ✓ dam-foundation dynamic interaction: simulates the propagation of seismic waves considering the dissipation effects through the boundaries of the artificially truncated massed foundation



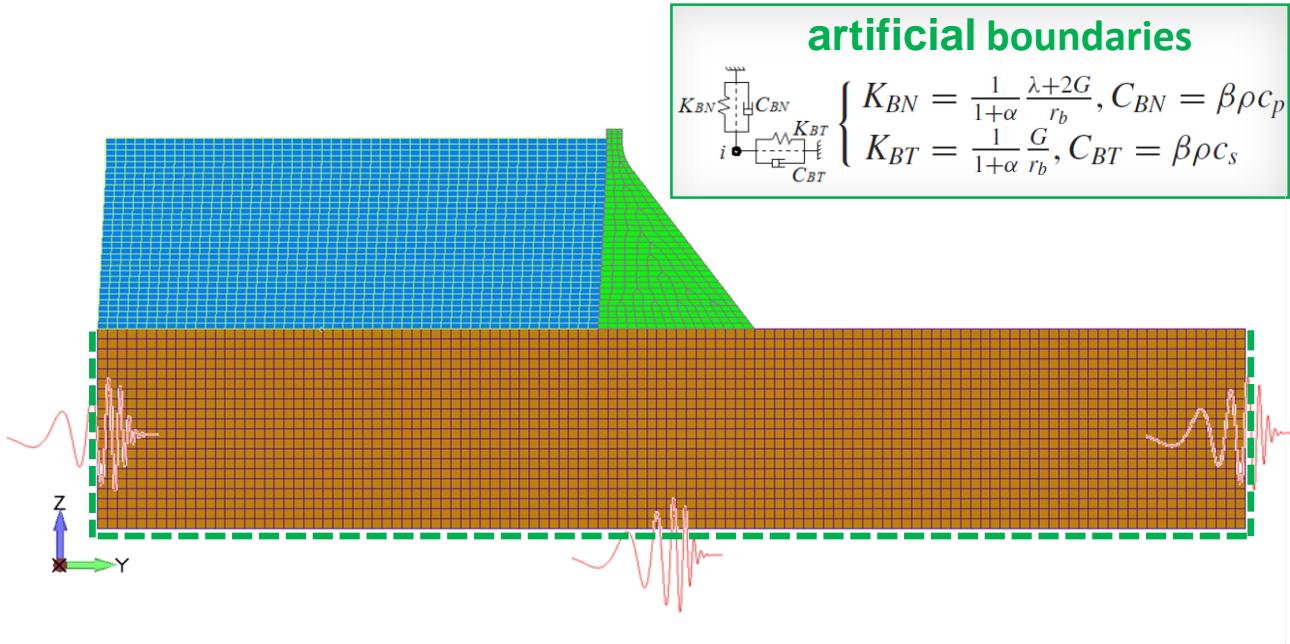


SAM-4D (Seismic Advanced Model for Dams)

The **dam-foundation seismic interaction method SAM-4D** (Chen et al. 2012, Liu et al. 2006, Liu et al. 2013, Zhang et al. 2009) allows to reproduce the behaviour of the real semi-unbounded foundation, representing the propagation in a domain delimited by **artificial non-reflecting (or absorbing) boundaries** and provided with mass.

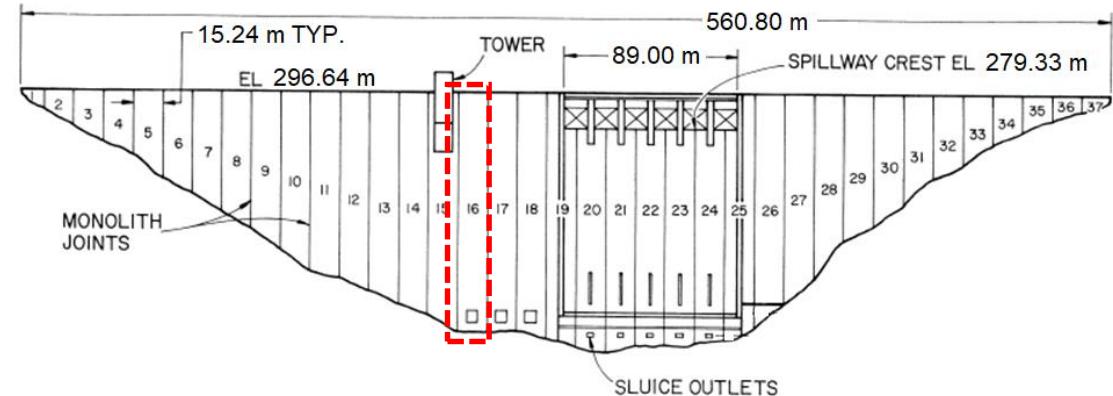
The incoming seismic waves are specified by means of **effective earthquake forces**, applied at the bottom and the side boundaries of the foundation and computed using the theoretical solution of the **vertically propagating elastic wave problem in a half-space**.

In case the **half-space is homogeneous** and **undamped**, the **incident motion at the bottom boundary** is equal to **one-half the free surface motion**: this simplification may be appropriate if the rock is assumed homogeneous and with no or little (up to 2%) material damping (Løkke and Chopra 2019).



Suitable modelling solutions (**infinite and orthotropic elements**) and pre-processing tools (to calculate and apply the **effective earthquake forces**) were developed and tested.

The model was implemented in the **commercial FEM code Abaqus** and in the **in-house FEM code CANT-SD**.



Case study: Pine Flat Dam



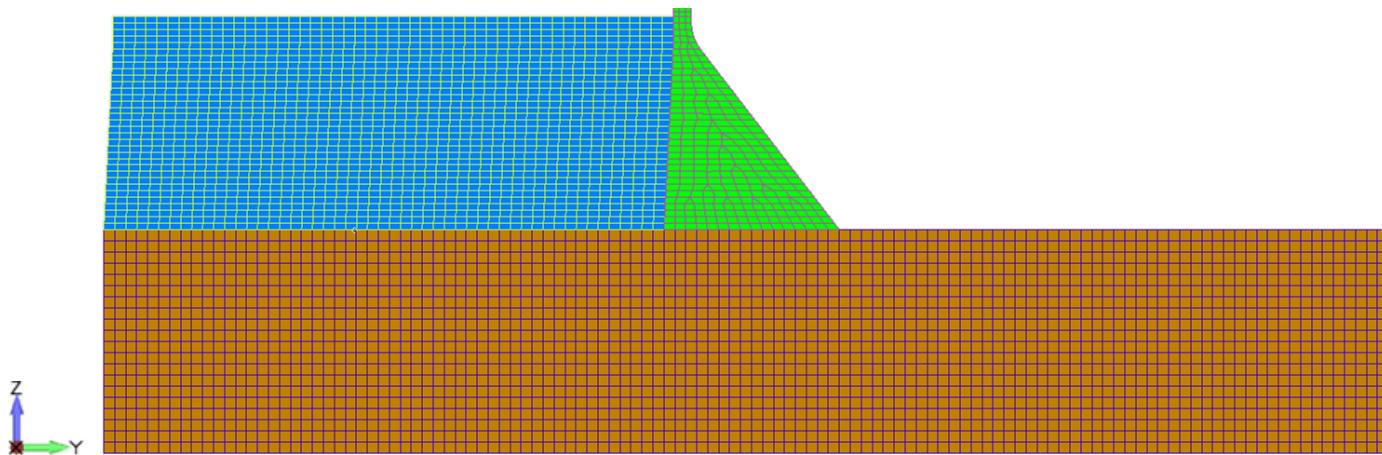
Analyses of increasing complexity

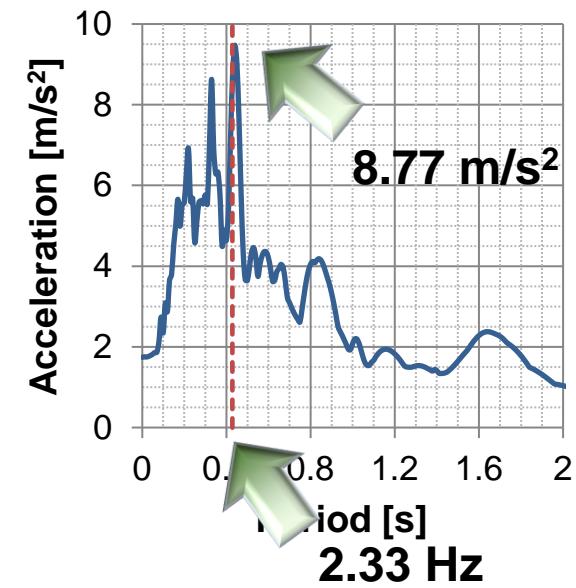
- ✓ linear elastic pseudo-static analysis
- ✓ linear elastic time-history analysis with **massless** approach
- ✓ linear elastic time-history analysis with **SAM-4D model**
- ✓ non-linear time-history analysis with **SAM-4D model**



Assumptions

- ✓ foundation: **linear elastic** model
- ✓ dam: **linear elastic** model
- ✓ dam: **Concrete Damaged Plasticity** (CDP) model (Lee-Fenves, 1998)



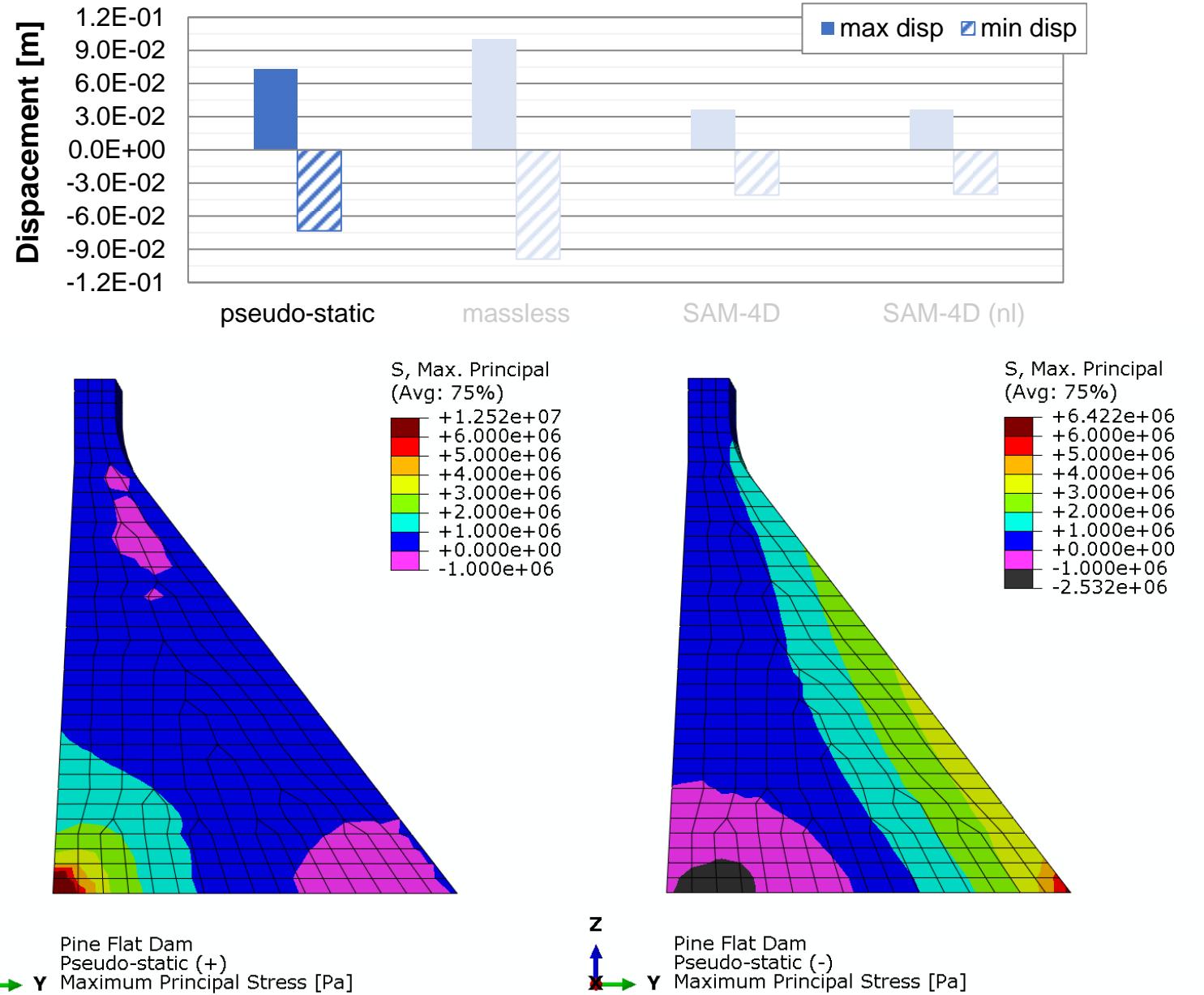


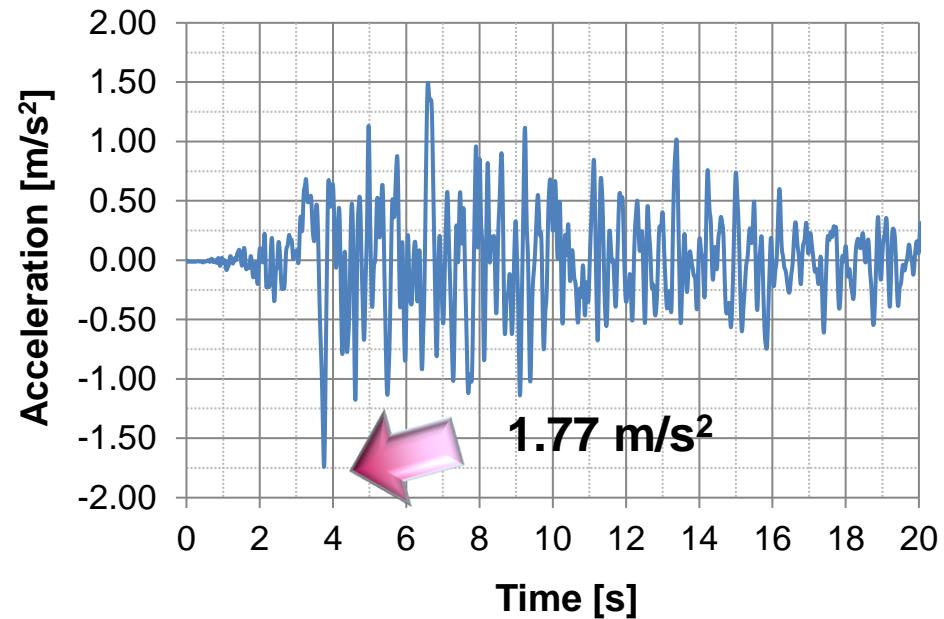
modal participation mass 68%

- Pseudo-static (+)**: seismic inertia load and hydrodynamic pressure towards **downstream**
- Pseudo-static (-)**: seismic inertia load and hydrodynamic pressure towards **upstream**



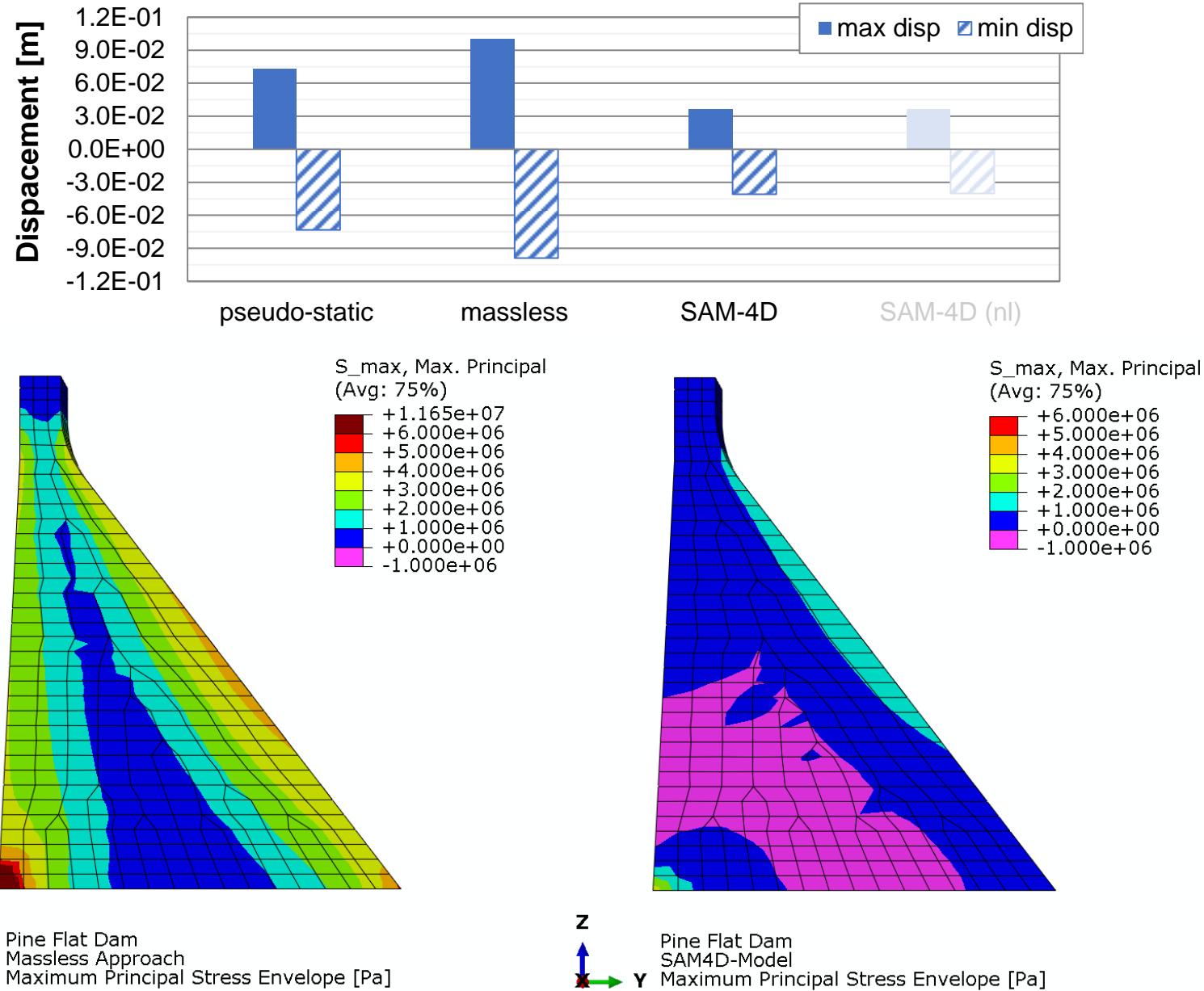
Results: pseudo-static analysis





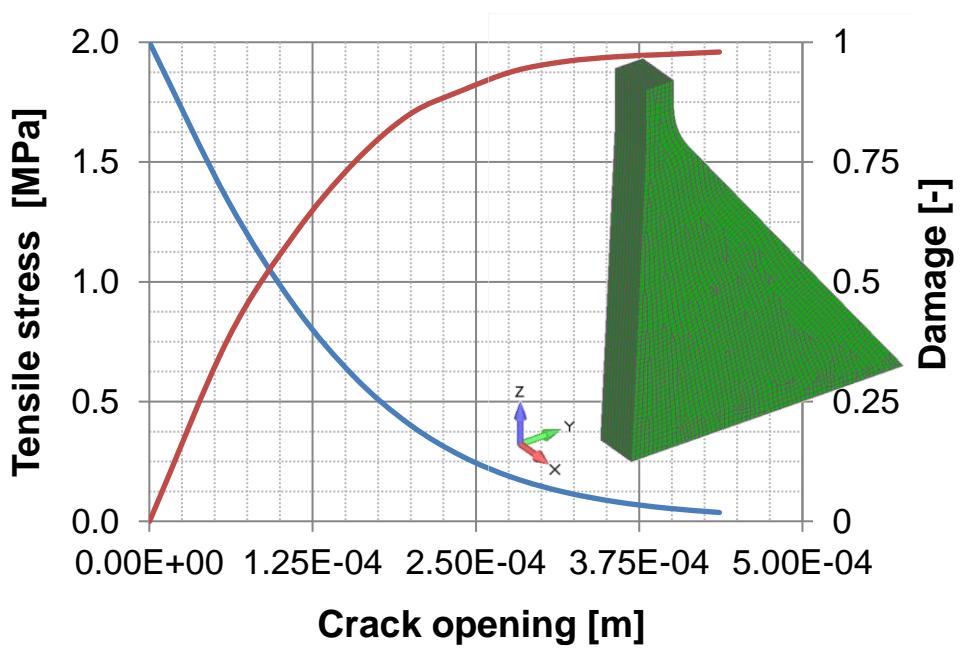
- Massless approach:** extensive tensile stress state (higher than the concrete tensile strength)
- SAM-4D model:** dramatically less severe tensile stress state (exceeding the concrete tensile strength only at dam heel)

Results: linear elastic time-history

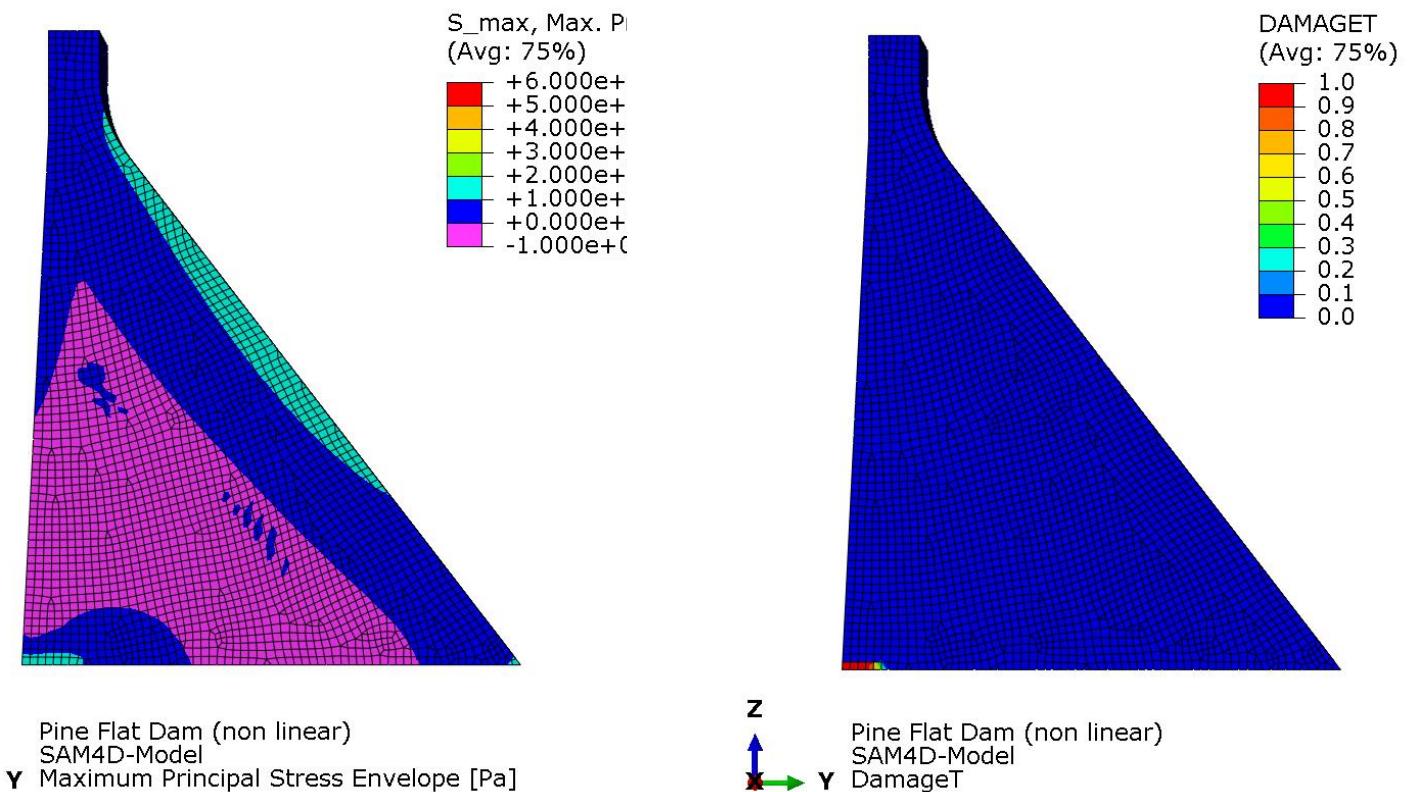
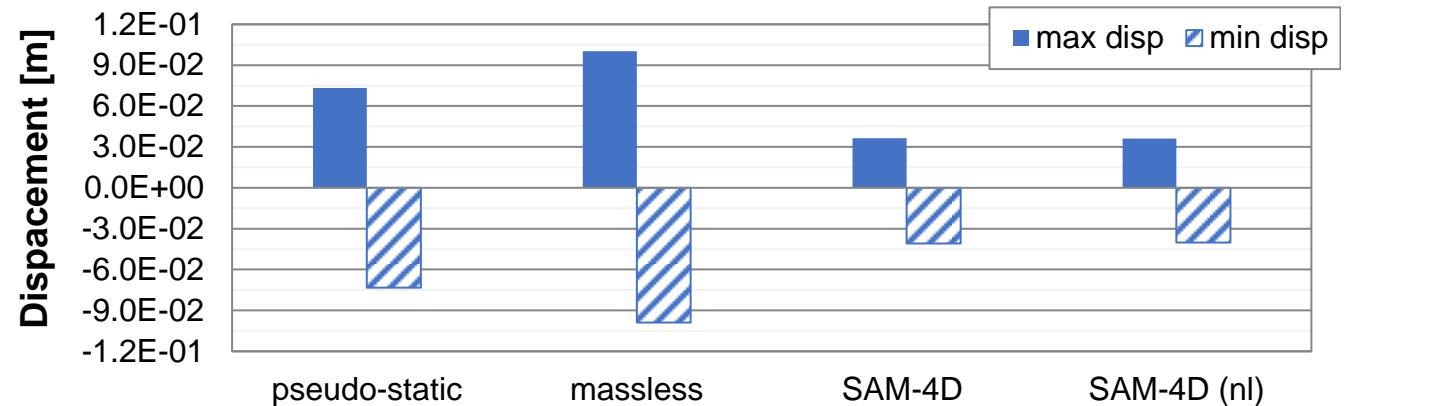




- **Tensile stress state:** comparable with that of the linear case (with a coarser mesh)
- **Damage variable:** only a small damaged area at dam heel



Results: non-linear time-history





Final remarks

- The case study of **Pine Flat Dam** used to apply the **progressive methodology** highlights that
 - ✓ In case of linear elastic analyses the **seismic response** obtained using the **SAM-4D model** is significantly **less severe** than that obtained with the traditional approaches
 - the stress state and the displacements resulting from the **SAM-4D** analysis are basically **consistent with a safe behaviour of the dam under the effect of Taft earthquake**
 - the stress state and the displacements resulting from the **massless** analysis are more **than two times greater** than those obtained with the SAM-4D model: the **tensile strength** of the concrete is in this case **overcome** on both the upstream and downstream faces of the dam
 - the stress state and the displacements resulting from the **pseudo-static** analysis are **comparable** to those resulting from the **massless** analysis and **slightly less demanding**
 - ✓ In case of non-linear analysis (time-history with the SAM-4D model) **no significant non-linear effect arises**: the structural behaviour is pretty unchanged with respect to the corresponding linear case
 - ✓ The **simplified pseudo-static analysis** can supply **useful hints** about the response of the dam, provided that the **inertia loads are correctly applied in both downstream and upstream directions** and that the **participating mass** of the first resonant mode of the system is **significant** enough



Giorgia Faggiani, Piero Masarati

This work has been financed by the Research Fund for the Italian Electrical System under the Three-Year Research Plan 2022-2024 (DM MITE n. 337, 15.09.2022), in compliance with the Decree of April 16th, 2018



Contacts

Always stay tuned with RSE because

#wemoversearch

Giorgia Faggiani



giorgia.faggiani@rse-web.it



www.rse-web.it



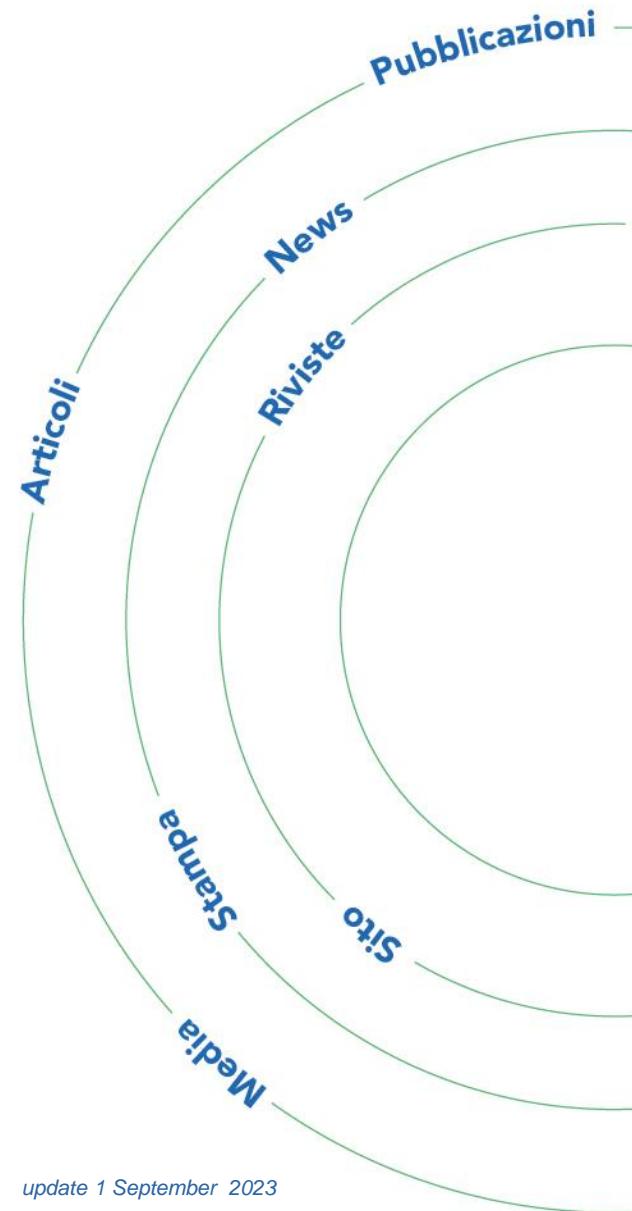
[@Ricerca sul Sistema Energetico - RSE SpA](#)



[@RSEnergetico](#)



[RSE SpA - Ricerca sul Sistema Energetico](#)



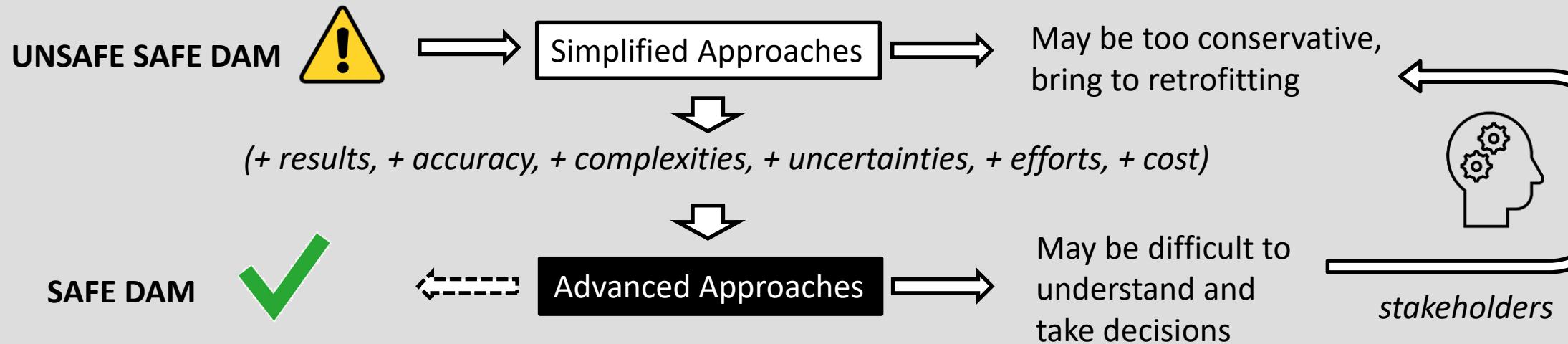


Non-Linear Seismic Response of Concrete Dams

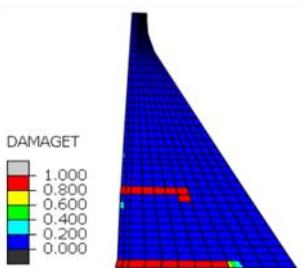
Luca Furgani ¹

¹ Mott MacDonald, Genoa

Introduction

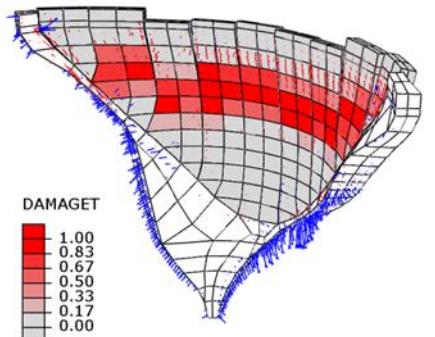


Gravity Dam Example



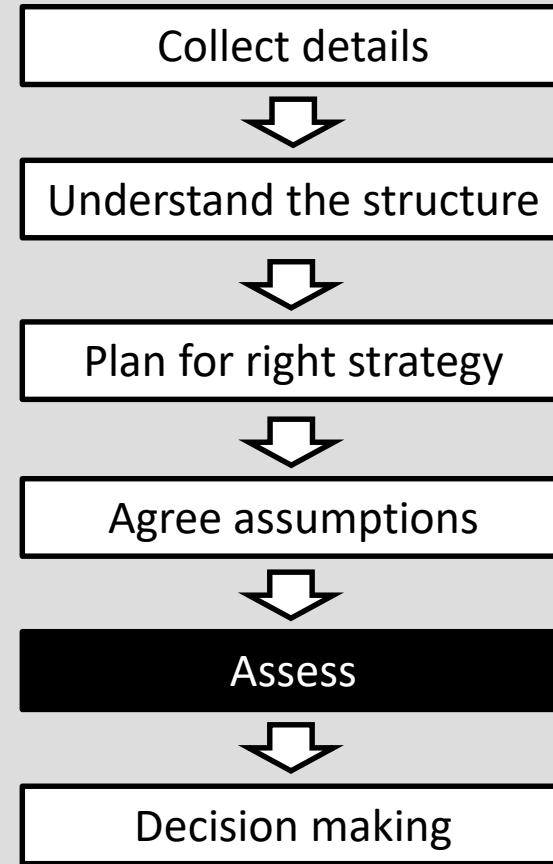
What do we expect to see from non-linear analyses of concrete dams?

Arch Dam Example



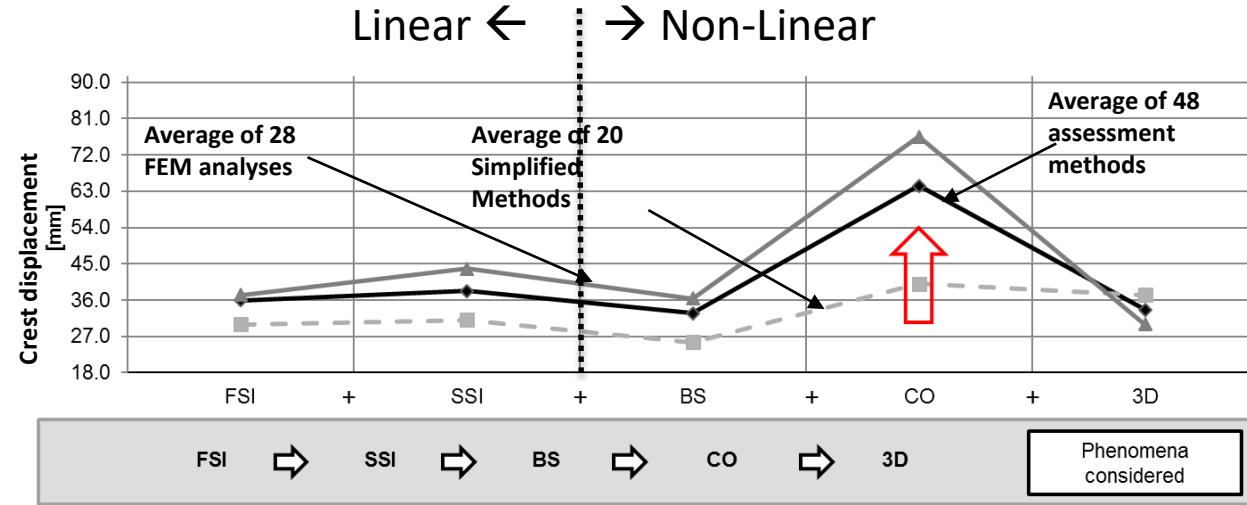
Introduction

Workflow example



Concrete dams can be analysed using several methods and it's crucial to know the pros and cons of them...

Variability of the relative displacements due to the introduction of different phenomena in 48 different analyses.



FSI: Fluid structure, SSI: Soil structure, BS: Sliding (Non Linear), CO: Crack opening (Non Linear), 3D: Three dimensional effects

... The assessment strategy is somehow more important than the specific method selected.



Why going for non-linear and how

For ultimate limit states we need to forecast something that has not been observed.

There are some **key aspects** to be covered for non-linear analyses:

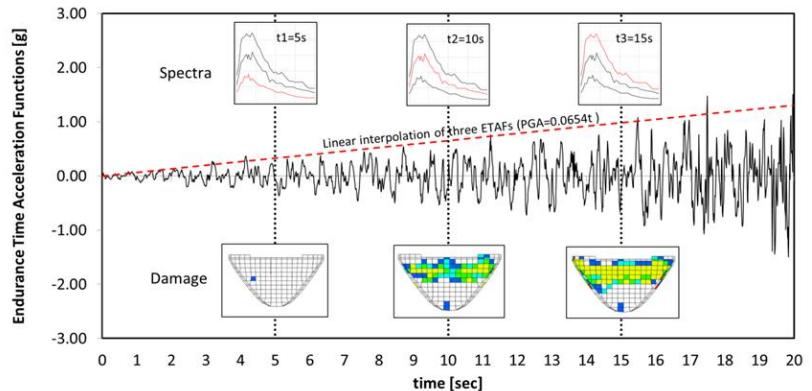
- Seismicity → accelerograms selection
- Existing conditions → existing cracks and stress state
- Geometric complexities → mesh simplification
- Material properties → testing and sensitivity analyses
- Assessment strategy → outcomes used for final checks

Non-linear results should merely confirm engineers expectations. The focus should be on the overall response and not the local failure.

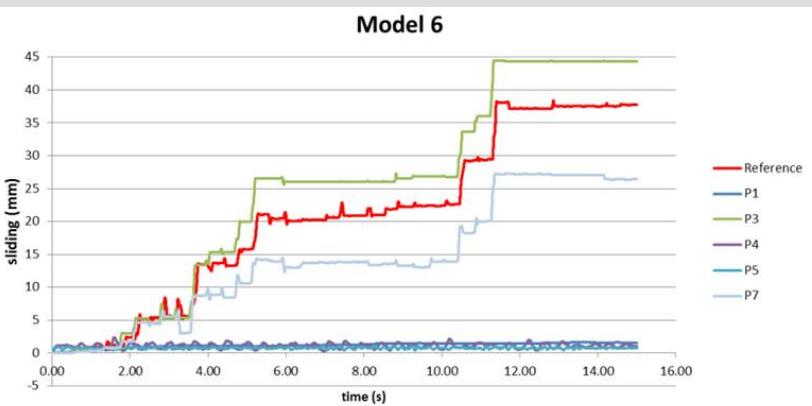
Even using an agreed method and same assumptions, different engineers may come to **conflicting conclusions** (see example from 14° ICOLD Benchmark).

Non-linear procedures, introduced in the paper, must be agreed before hand

The ETA method procedure example



14° ICOLD Benchmark results on sliding [mm]

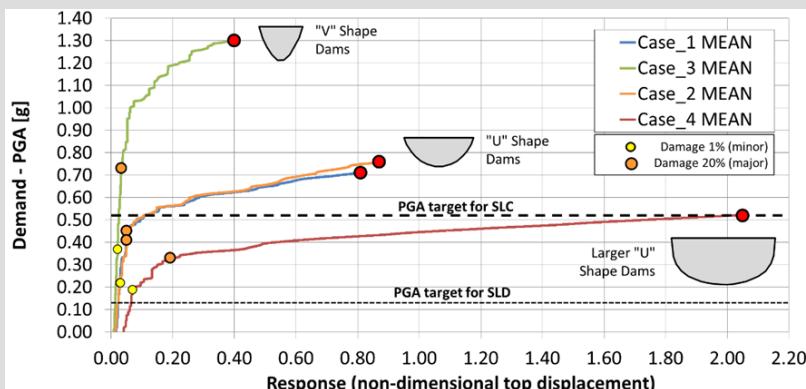


Case studies

Example of a complex shape dam



Capacity curves for typical dam shapes



Earthquakes are just one of the aspect affecting the structural safety of large infrastructures.

For existing dams, it is necessary to understand the **monitored behaviour** and study the static response first. Sometimes this is already affected by non linearities (existing cracks). After this we can consider the seismic response.

Non-linear response: Yes / No

Non-linear analyses: Yes / No

If the dam under assessment has a **non typical shape** and an unusual behavior, it may be more efficient to use simplified approach rather to increase the complexity using non linear analyses.

If the dam body is close to the typical ones it is suggested to use studies done by others as a reference for the assessment. In these cases **capacity curves** may be very effective to assess their seismic response. The capacity can be also considered independently from the real behavior such as a property of the dam.

It's essential to agree the expected outcome from the assessment study.

Further considerations on outcomes and stakeholders

For non-linear analyses we do not have agreed limits on acceptable cracks or plastic deformations.

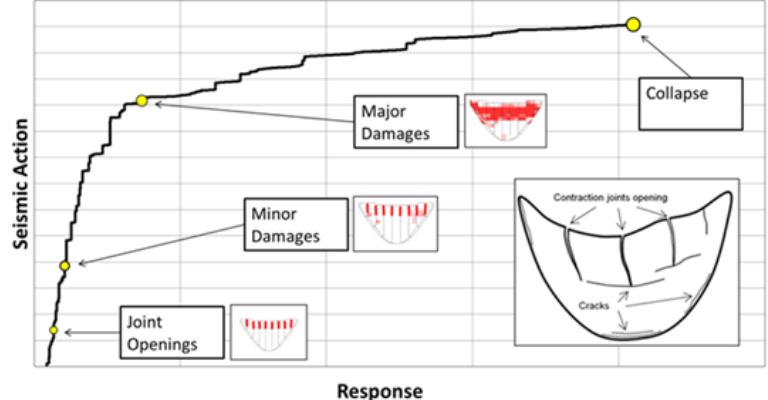
For this reason it is suggested to **focus on global response** rather than local damages to evaluate the response of the dam beyond the elastic behaviour.

Something like a capacity curve helps identifying **seismic action of global failures**. This is affected by many assumptions but it is providing what's needed for the seismic assessment.

If the results of the analyses demonstrate that there is a spare capacity of the dam compared to the expected ultimate limit state earthquake, the structure should be considered safe. The current issue is that a local damage may induce the decision makers to ask for **unnecessary mitigation actions**.

Independent checking should be introduced to be more comfortable on the analyses results.

Example of outcomes given by a capacity curve



Joint openings



Minor Damages



Major Damages



Collapse

Conclusions

- Results may be highly dependent on the approach used by engineers especially for non-linear analyses.
- As first step, we should move towards procedures that standardise the ground motion signals and focus on global failure mechanisms.
- Nonlinear analysis assessment procedures are still lacking in acceptance criteria. That's why stakeholders may request to go back to simplified approaches.
- With standard procedures and criteria it will be easier to establish dams' safety. This will help drive important decisions and fulfil the wider society's goals.

Takeaway



"Use the right method"

We have to select our tools according to the client request and our understanding of the most critical aspects.

"Step by step"

For high-risk structures where public safety is crucial is particularly important to follow a step-by-step approach to solve complex problems.



"Be open to new approach"

With endurance time analyses (ECG test) or similar methods we can test our structures (body) for increasing seismic actions.





Thank you!

Any questions?





NONLINEAR SEISMIC ANALYSIS OF GRAVITY DAMS INCLUDING LIFT AND BASE JOINTS

Dr. Shengshan Guo 305265331@qq.com

China Institute of Water Resources and Hydropower Research (IWHR)
Earthquake Engineering Research Center (EERC)

2024.7

1. Background

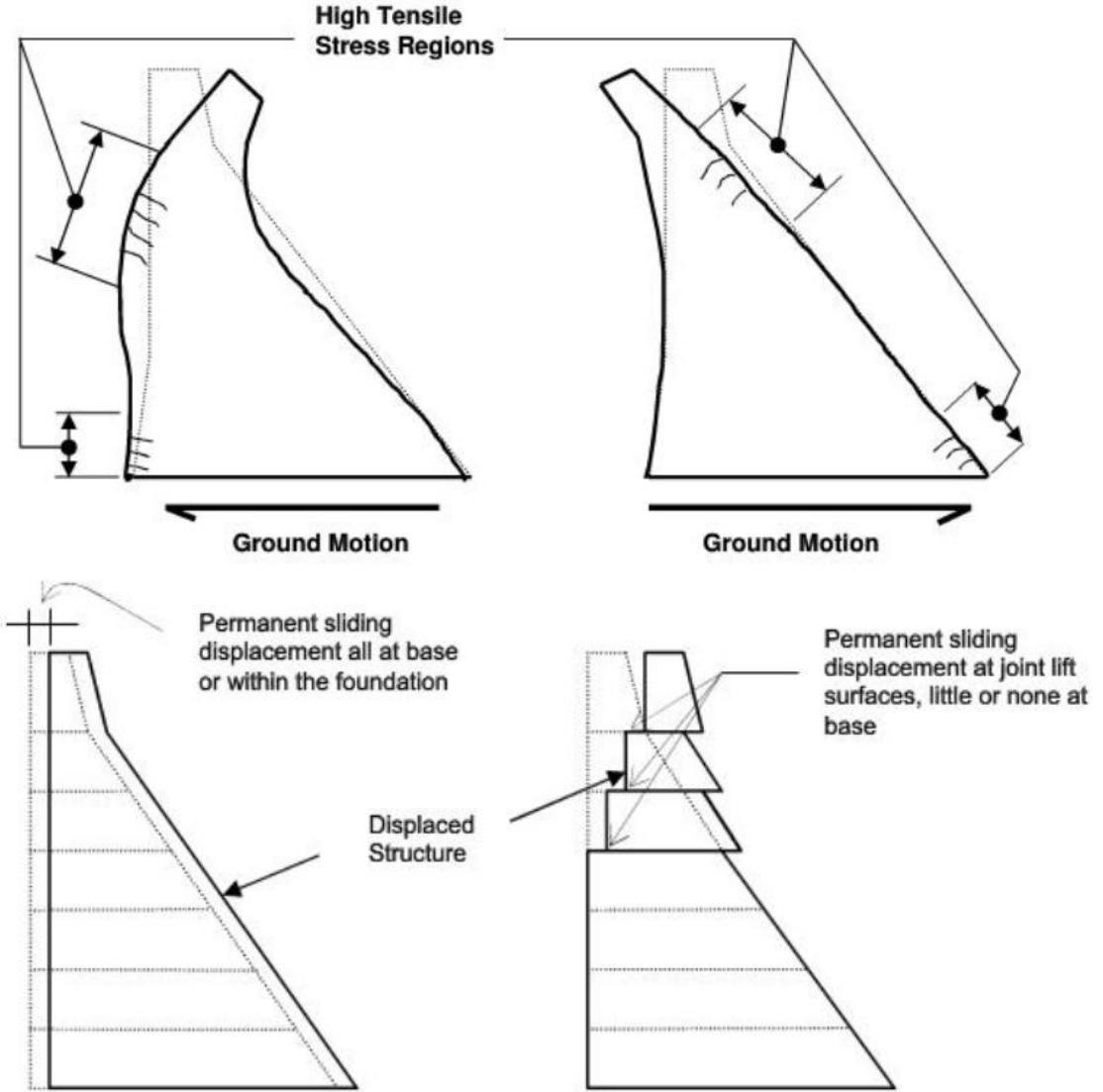
- In the international norms and guidelines on the seismic design of gravity dams, the fortification goals under MCE are mostly qualitatively defined as "**no uncontrolled discharge of reservoir water**".
- Due to the complexity of earthquake actions, although scholars are carrying out various failure modes to propose quantitative evaluation criteria, **there is no universally accepted criterion**.

- At this stage, the penetrating crack upstream and downstream of gravity dams is commonly selected as the evaluation index of ultimate seismic capacity.
- In fact this is only a conservative evaluation criterion, which does not mean that the dam loses its capacity.
- The penetrating crack has been observed on at the Hsinfengkiang dam in China subjected to an earthquake in 1962 and at the Koyna dam in India subjected to an earthquake in 1967. However, it still work well now after repairment.

1. Background

Seismic failure modes of gravity dams:

- **Tensile cracking at the changing position**
- **Tensile cracking at the dam heel and toe**
- **Sliding all at base or within the foundation**
- **Sliding at joint lift**

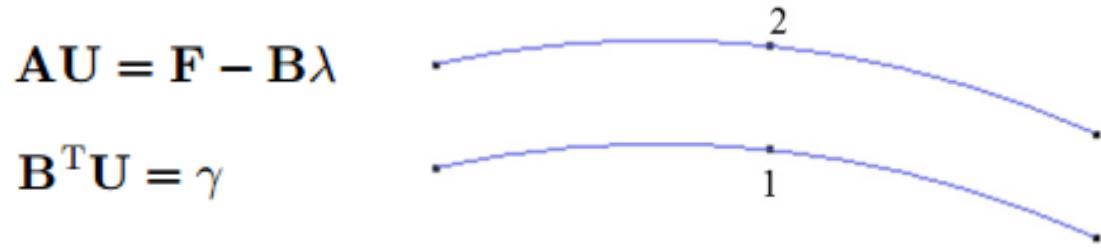


2. The Proposed Method

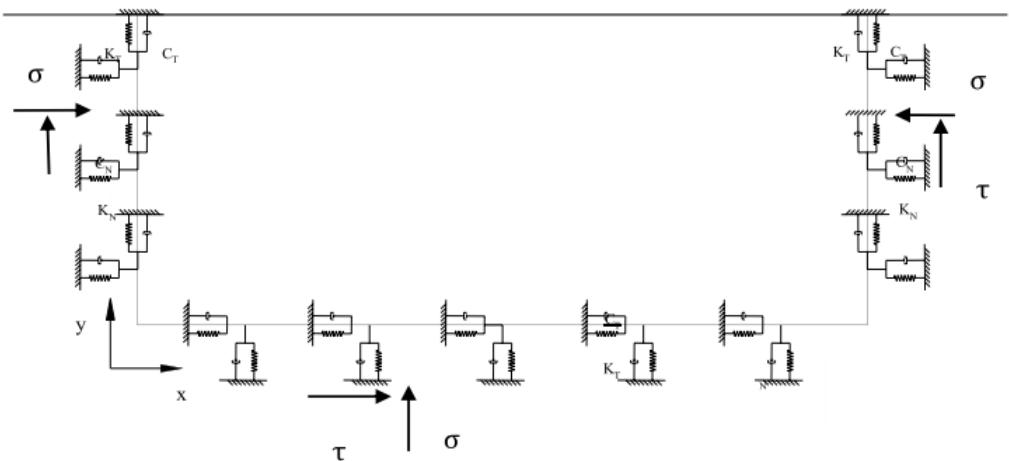
- A contact model considering the initial tension strength and shear strength of joints is presented, which can model **the whole process from crack initiation and crack propagation to overall sliding of blocks in the case of penetrated crack.**
- The nonlinear time history analysis can be performed for the lift joints and dam-foundation interface.
- The **post-earthquake static stability analysis** is recommended to evaluate its seismic safety once crack penetrates thoroughly.

2. The Proposed Method

- Contact model based on the Lagrange multiplier method:

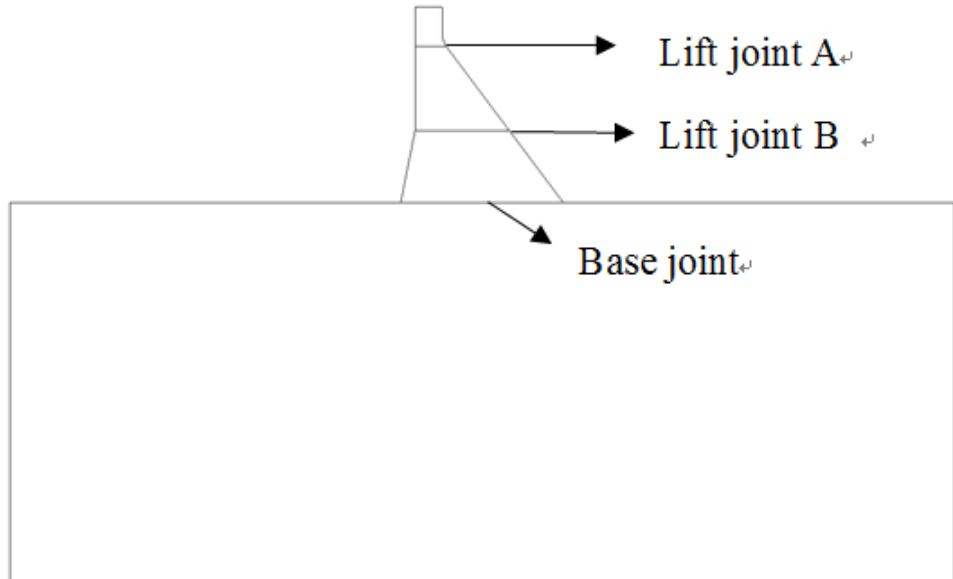


- A massed foundation model with viscoelastic boundary conditions is adopted to consider the effect of dam-foundation dynamic interaction and radiation damping of far-field foundation.



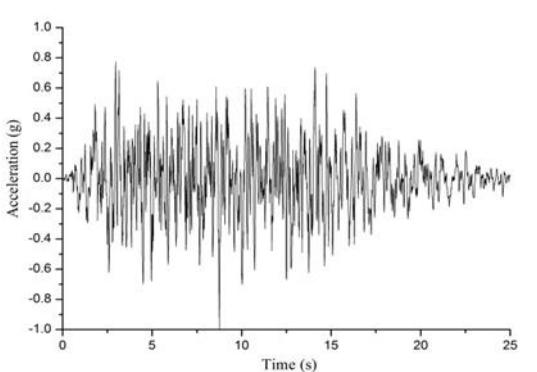
3. Application

- The typical gravity dam locates in China with the maximum dam height of 185 m. The horizontal PGAs of MDE and MCE are 338gal and 397gal respectively.
- Analyses are performed by a nonlinear finite element parallel computation program named PSDAP developed by authors.

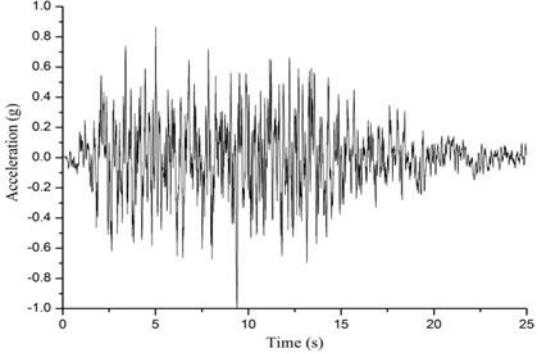


The location of joints

Strength parameters of joints			
Location	Lift joint A	Lift joint B	Base joint
Tensile strength (MPa)	1.61	1.61	2.00
Shear strength (MPa)	3.22	3.22	4.00
Friction coefficient	1.05	1.05	1.09
Cohesion strength (MPa)	1.50	1.50	1.09

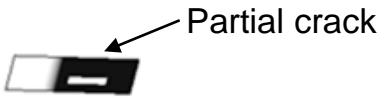


Time history of artificial wave acceleration in the stream and vertical direction



3. Application

MDE condition:



The distribution of the crack propagation
(black for damage, white for undamaged)

MCE condition:

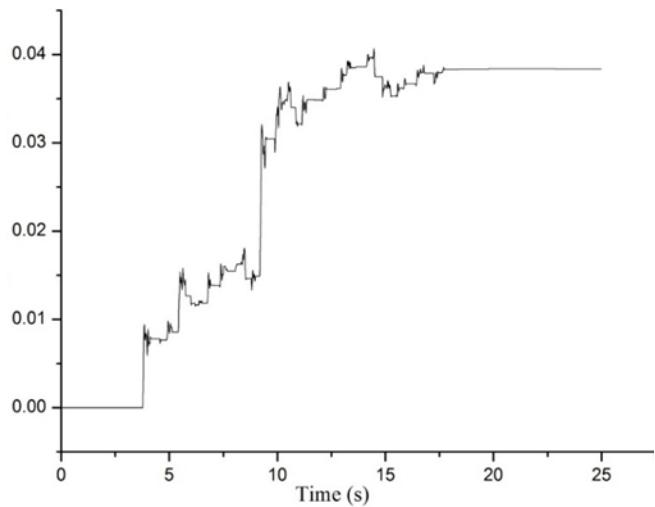
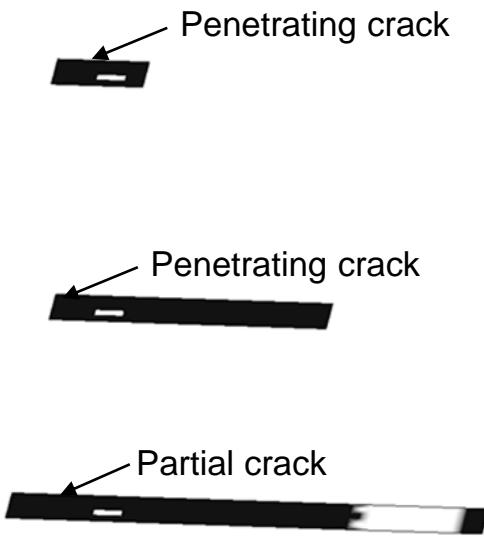


The distribution of the crack propagation
(black for damage, white for undamaged)

3. Application

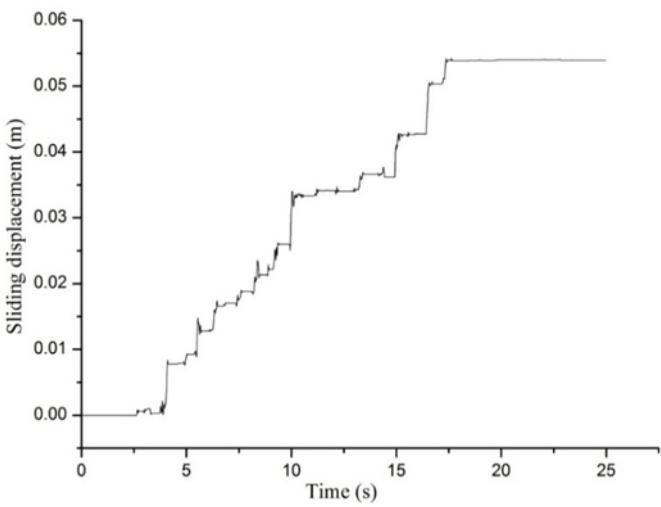
Overload factor of 1.5 condition:

- It can be obtained that the drainage hole may lose effectiveness owing to the excessive slippage.
- According to results obtained by the rigid limit equilibrium method, the safety factor of the static anti-sliding stability of the independent block above the lift joint B after the earthquake is only 0.47.



The distribution of the crack propagation
(black for damage, white for undamaged)

Sliding time history along
lift joint A

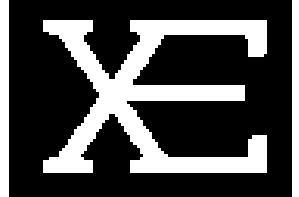


Sliding time history along
lift joint B

4. Concluding Remarks

- A method is proposed to model the crack propagation and the overall sliding of blocks caused by penetrated cracks in the framework of discrete model.
- Nonlinear time history analysis of a gravity dam with lift and base joints in China is performed. The propagation of cracks and the overall sliding of blocks along lift and base joints are investigated under different earthquake intensity levels to evaluate the seismic behavior of the dam.
- The analysis model and evaluation method provided in this paper can be used to evaluate the seismic safety of gravity dams.

Thanks for your attention !



Understanding the role of stress-dependent material damping in seismic analysis of concrete dams

M.A. Hariri-Ardebili ¹, M. Noorbakhsh ², S.M. Kolbadi ³, F. Pourkamali ⁴

¹ University of Maryland, College Park, USA

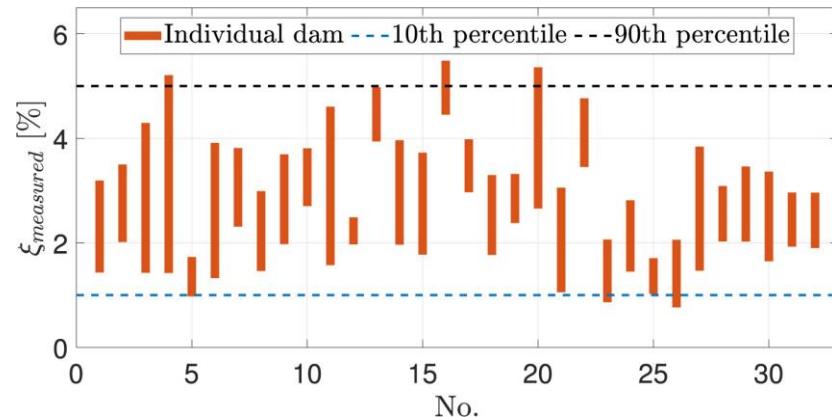
² University of Hawaii, Manoa, USA

³ X-Elastica LLC, Boulder, CO, USA

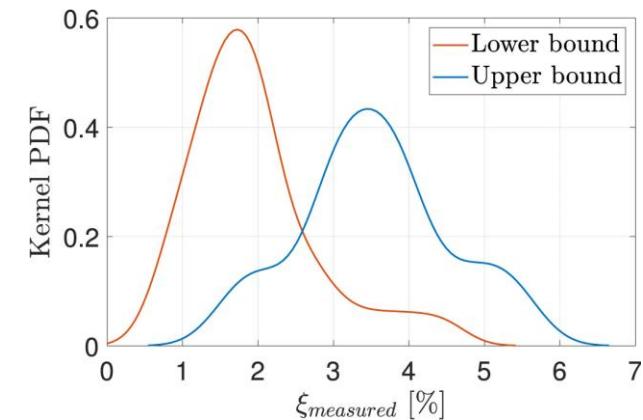
⁴ University of Colorado, Denver, CO, USA

Introduction

- There are many factors contributing to **seismic analysis** of concrete dams including fluid-dam-rock interaction, wave propagation, concrete damage model, etc.
- Among these parameters, the **damping mechanism** stands out as a critical factor that significantly influences the dynamic behavior of the dam.
- Damping in concrete dams is particularly challenging to model due to its **stress-dependent** nature.
- In seismic analysis, damping is often **assumed** rather than precisely **determined**, introducing **uncertainties** into the predictions of structural response.
- Some measured damping values
 - Forced vibration testing
 - 32 concrete dams



Chopra (2020)



Damping Sources and Mechanisms

- Three main classes of damping are (Kareem, 1996):
 - **Structural** damping measures the energy dissipation in a vibrating structure, bringing it to a quiescent state.
 - **Material** damping: This contribution arises from complex molecular interactions within the material and is generally applicable for low strain rates of loading and linear behavior of structures.
 - **Interfacial** (or frictional) damping: Developed through sliding contact between different connected components, interfacial damping contributes more than material damping and is highly nonlinear. Energy dissipation mechanisms through the structure are primarily displacement-dependent.
 - **Hysteretic** damping: It is typically modeled separately by capturing energy dissipation in a cycle independent of frequency.
 - **Aerodynamic** or **hydrodynamic** damping is experienced by structures vibrating in air or water, with both sources potentially contributing simultaneously to marine structures.

Generic Damping Models

- In a general form, damping can be defined as $f_d(x, \dot{x}) = \alpha \dot{x} |\dot{x}|^{\theta-1}$ with three main forms as:

$$f_d(x, \dot{x}) = \begin{cases} \mu \text{sign}(\dot{x}) & \theta = 0 \quad (\text{coulomb damping}) \\ c\dot{x} & \theta = 1 \quad (\text{viscous damping}) \\ q\dot{x}|\dot{x}| & \theta = 2 \quad (\text{quadratic damping}) \end{cases} \xrightarrow{\text{EVD}} \frac{2\mu}{\pi m \omega^2 A} \quad \frac{c}{\pi m \omega} \quad \frac{4qA}{3\pi m}$$

- Viscous damping
 - Rayleigh damping
 - Caughey damping
 - Wilson-Penzien damping
 - Modal damping

Select a desired amount of damping (ξ) and a frequency range, $[\bar{\omega}, R\bar{\omega}]$, covering important vibrational modes, ($R>1$)

Compute the bounds on the damping ratio using Δ parameter:

$$\Delta = \xi \frac{1+R-2\sqrt{R}}{1+R+2\sqrt{R}} \quad \begin{cases} \xi_{\min} = \xi - \Delta \\ \xi_{\max} = \xi + \Delta \end{cases}$$

If the upper and lower bounds are satisfactorily narrow, the constant mass-proportional, α_M , and stiffness proportional, β_K , coefficients are found from:

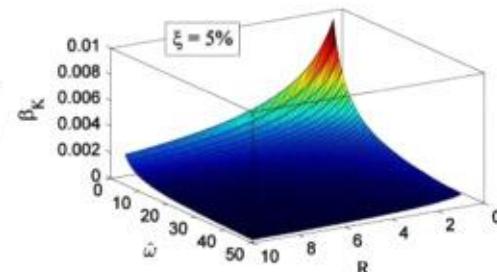
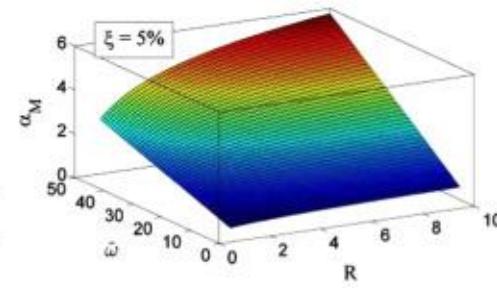
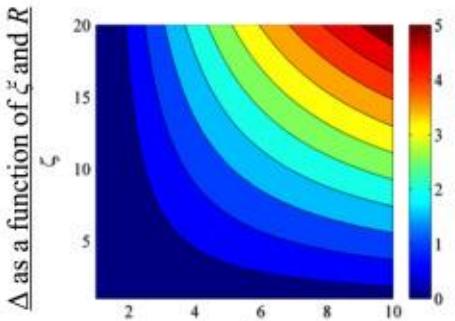
$$\alpha_M = 2\xi\omega \frac{2R}{1+R+2\sqrt{R}} \quad \beta_K = 2\xi \frac{1}{\omega} \frac{2}{1+R+2\sqrt{R}}$$

Compute the actual damping value, ξ_i , for i^{th} mode using the known ω_i :

$$\xi_i = \frac{1}{2\omega_i} \alpha_M + \frac{\omega_i}{2} \beta_K$$

Compute the Rayleigh damping for the system using the mass matrix and updated tangent stiffness matrix as:

$$[C(t)] = \alpha_M [M] + \beta_K [K(t)]$$



Stress-Dependent Material Damping

- For harmonic loading and steady-state resonance motion, the damping ratio, characterizing the energy dissipated by viscous damping in one cycle of harmonic vibration is:

$$\xi = \frac{1}{4\pi} \frac{E_D}{E_S} \quad \longrightarrow \quad E_D = \int_V f(\sigma_r) dV, \quad E_S = \frac{1}{2} \int_V \frac{\sigma_r^2}{E} dV, \quad f(\sigma_r) = J \sigma_r^n$$

- The following relation is used for unit dissipation energy, $f(\sigma_r)$ in this presentation. This is a complex experimental work proposed by Lazan (1968):

$$f(\sigma_r) = 6895 \left(\frac{\sigma_r}{\sigma_f} \right)^{2.3} + 41360 \left(\frac{\sigma_r}{\sigma_f} \right)^{8.0}$$

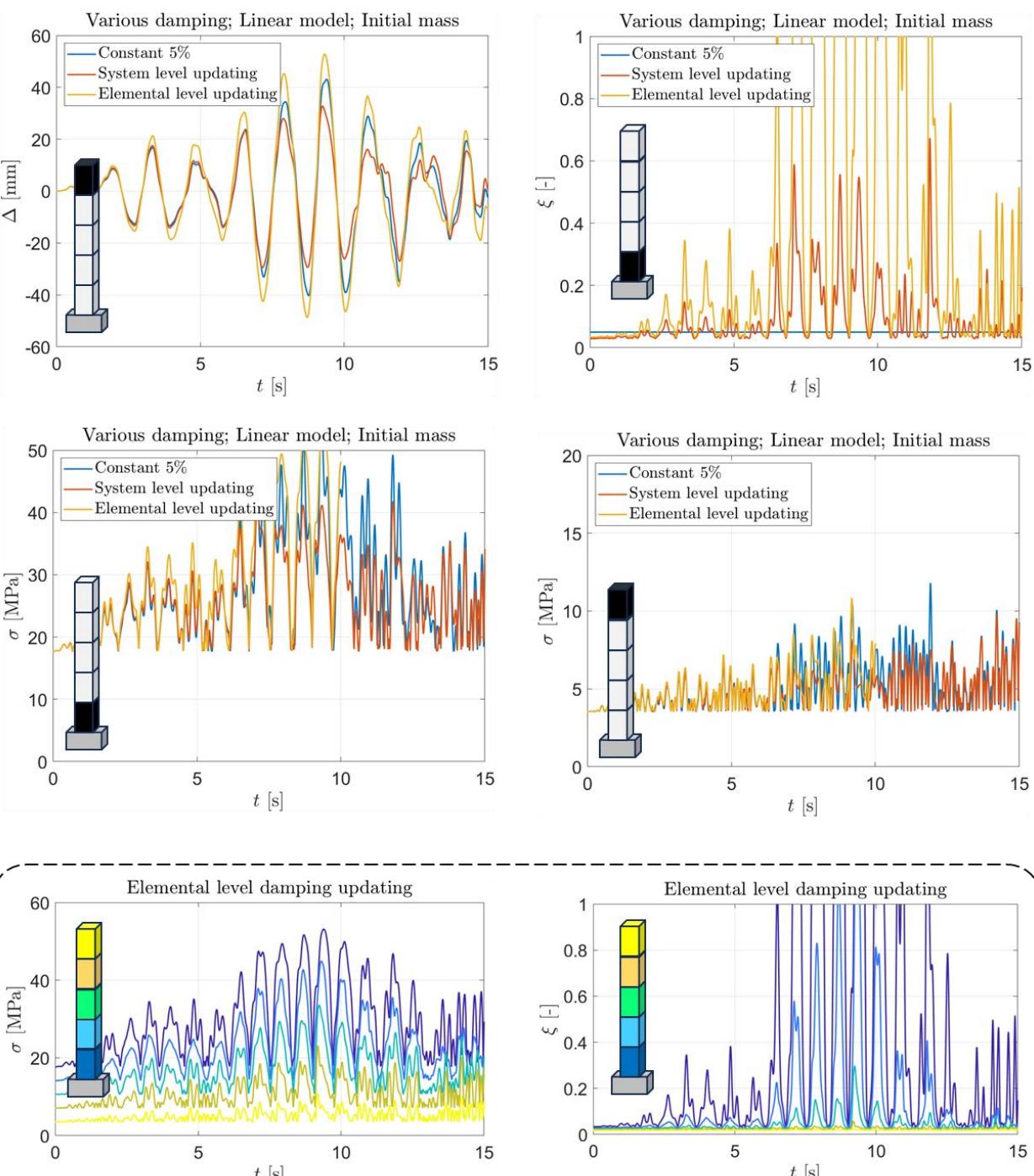
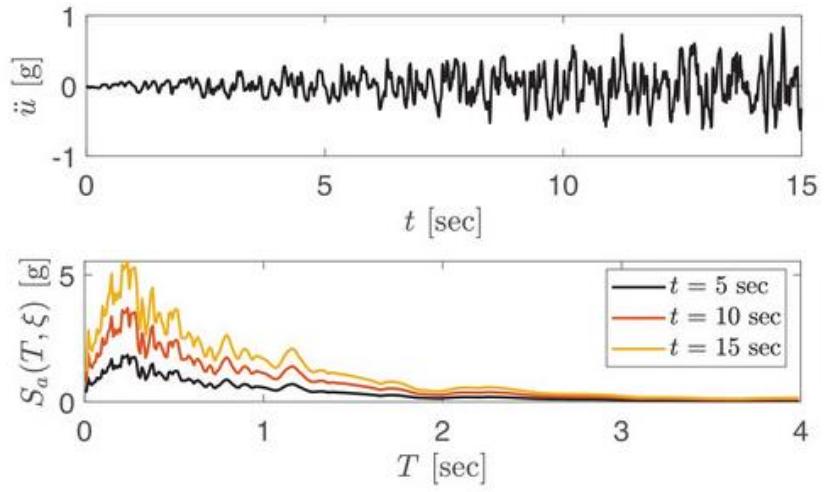
- The stress-dependent damping ratio at the elemental- and system-level are computed as:

$$\xi_{elem} = \frac{3E}{2\pi} \frac{2089.5 \left(\frac{\sigma_r^{elem}}{\sigma_f} \right)^{2.3} + 4595.5 \left(\frac{\sigma_r^{elem}}{\sigma_f} \right)^{8.0}}{\left(\sigma_r^{elem} \right)^{2.0}}$$

$$\xi_{sys} = \frac{3E}{2\pi} \frac{\sum_{i=1}^N \left(2089.5 \left(\frac{\sigma_r^{elem}}{\sigma_f} \right)^{2.3} + 4595.5 \left(\frac{\sigma_r^{elem}}{\sigma_f} \right)^{8.0} \right)}{\sum_{i=1}^N \left(\sigma_r^{elem} \right)^{2.0}}$$

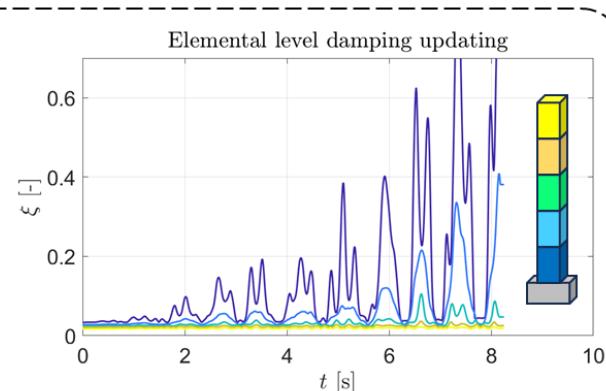
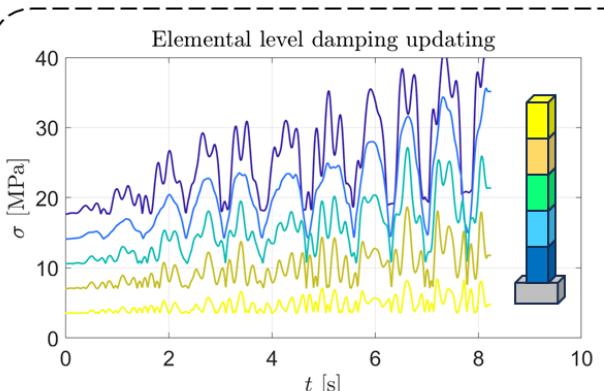
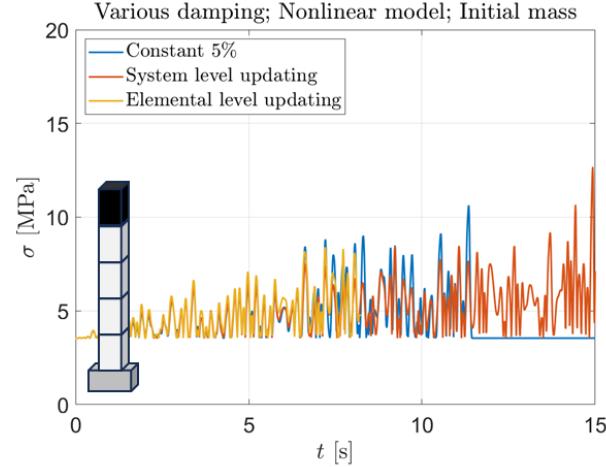
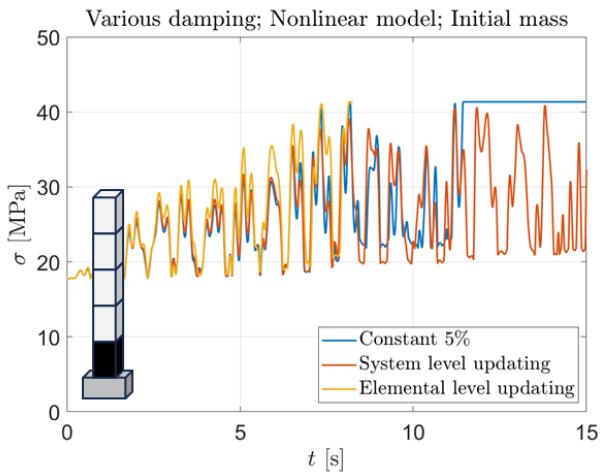
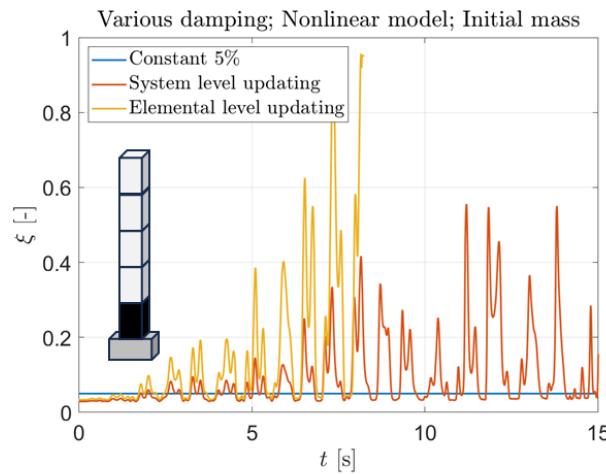
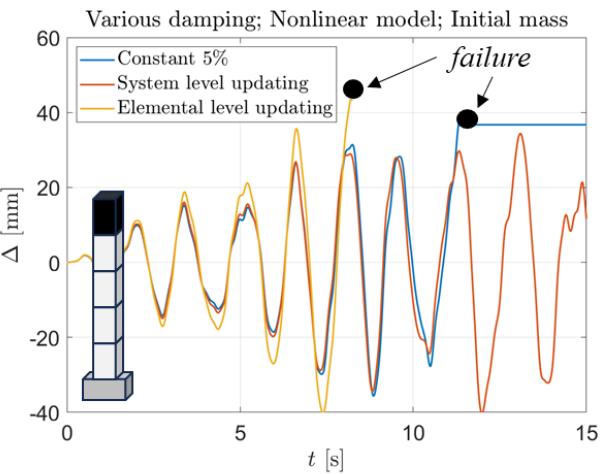
Cantilever Column: LE

- Simple column modeled using OpenSees with fiber elements.
- Only five elements along the height.
- Linear and nonlinear models are used with a pre-defined failure limit stress.
- Intensifying acceleration is applied.



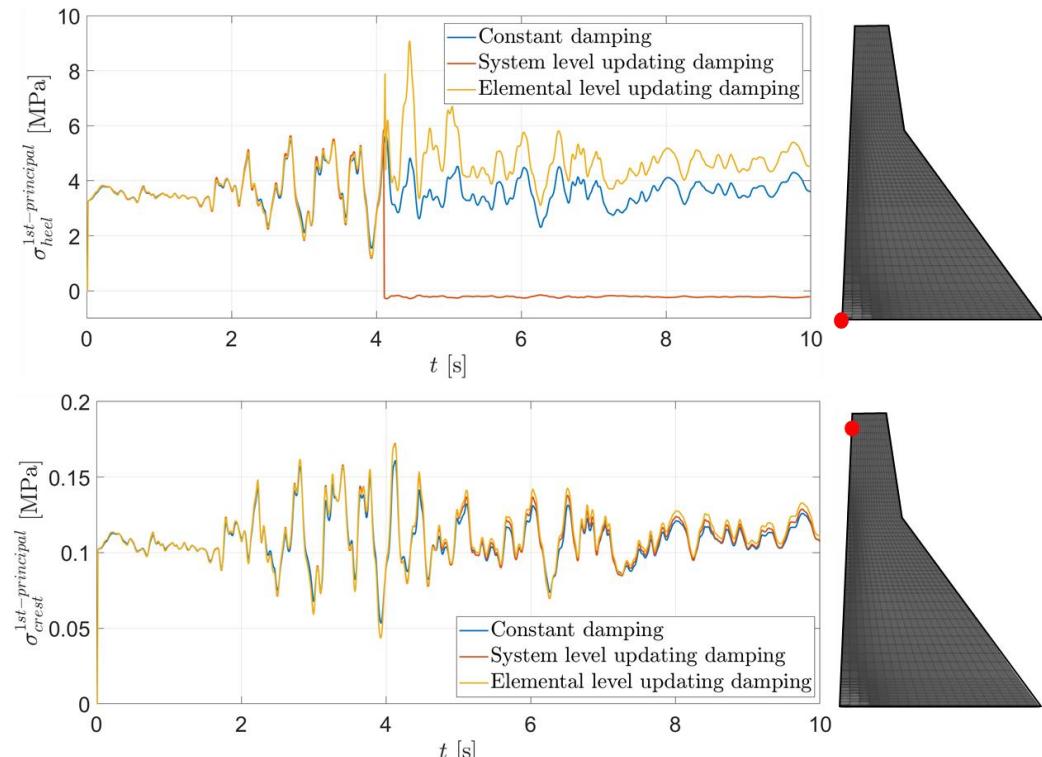
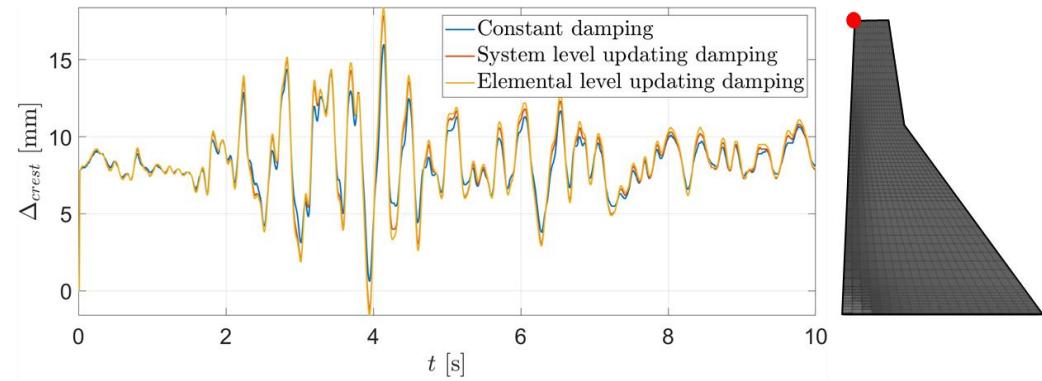
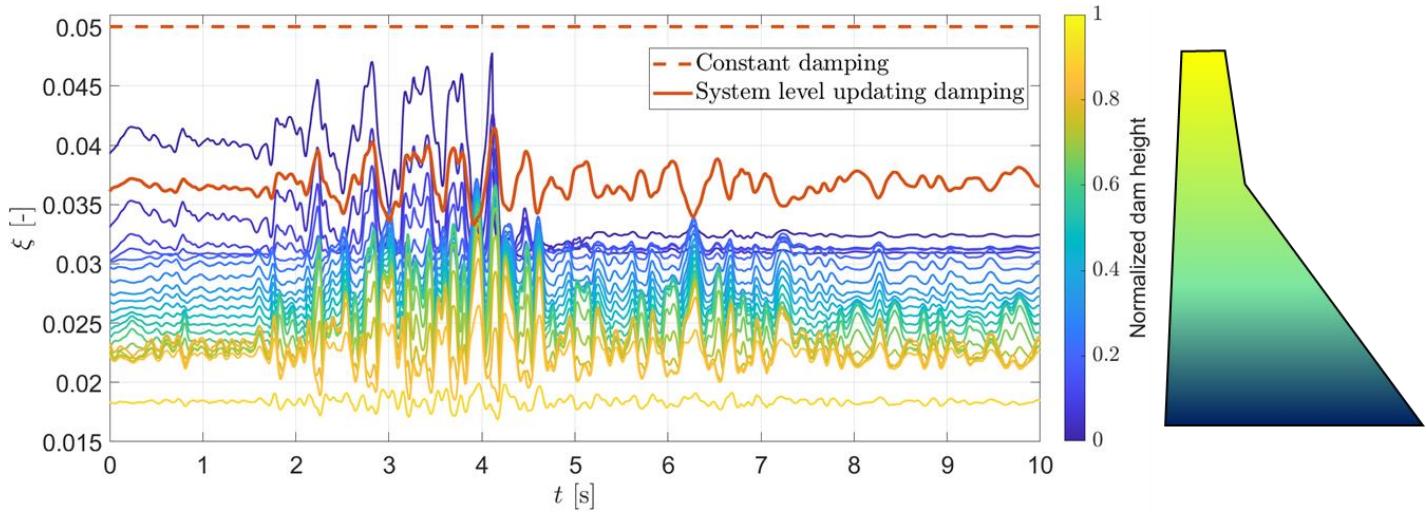
Cantilever Column: NL

- In the nonlinear models, an element automatically sustains damage, causing its stress values to plummet to zero.
- Given that this column comprises only one element at the base, its damage signifies the failure of the entire column.



Gravity Dam: NL

- Koyna Dam is modeled using a 3D sliced approach.
- 20 elements along the height.
- The smeared crack model is used for nonlinearity.
- It appears that a constant damping of about 3-4% is needed to align with all three modeling options.





Thank you!

Any questions?



BCI6 - SEISMIC ANALYSIS OF DAMS AND LEVEES



The role of modeling uncertainties in seismic analysis of concrete dams

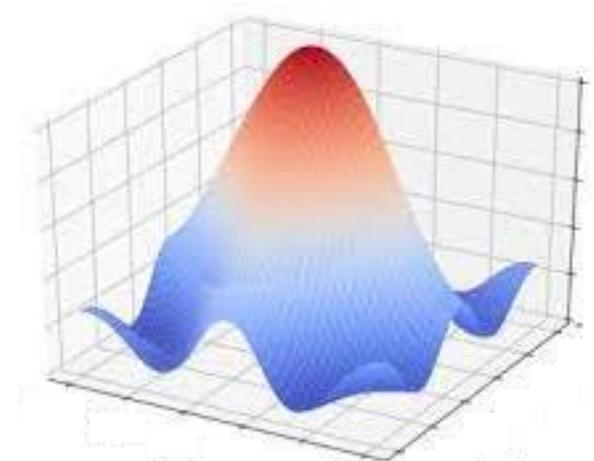
M.A. Hariri-Ardebili ¹, J.W. Salamon ²

¹ University of Maryland, College Park, USA

² U.S. Bureau of Reclamation, Denver, USA

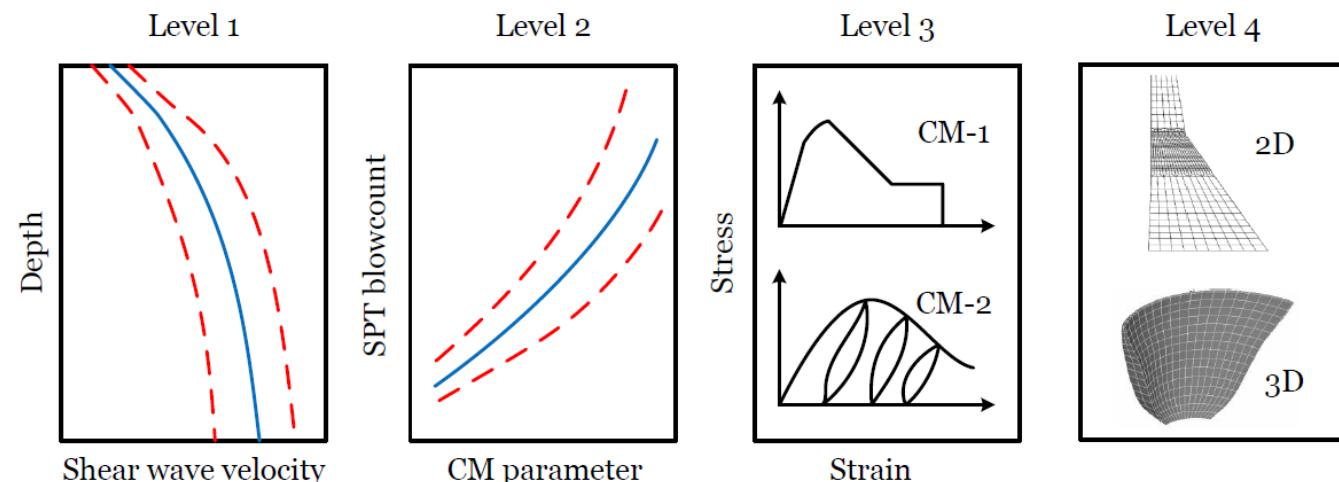
Problem Statement

- Any probabilistic simulation comes with some level of **uncertainty**.
- Uncertainties arise in simulation due to **randomness** or **lack of knowledge**.
- Uncertainty quantification (**UQ**) is defined as the process of quantifying uncertainties associated with model calculations of true, and physical quantities of interest.
- Overall uncertainty classification: Aleatory and Epistemic.
- Practical uncertainty classification in structural engineering problems (including dams and levees):
 - Loading uncertainty
 - Material uncertainty
 - **Modeling uncertainty**



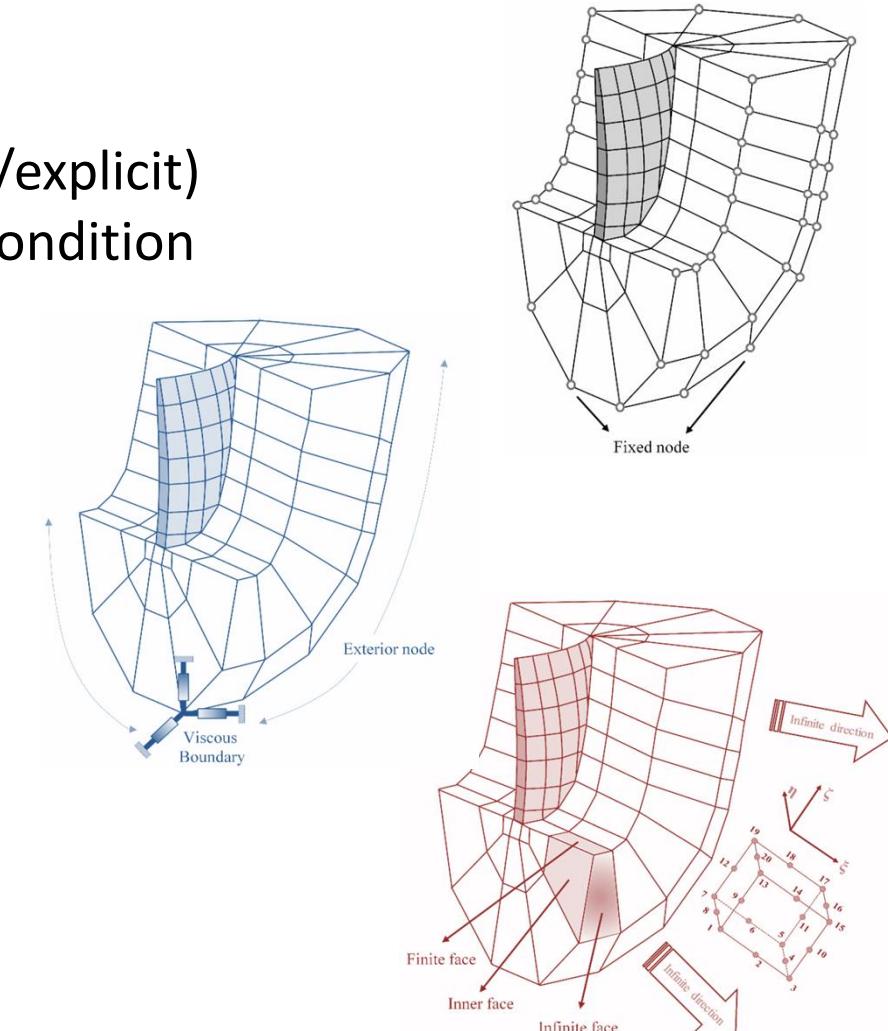
Modeling Uncertainty: Concept

- Modeling uncertainty encompasses the variability linked to the effectiveness of a model in accurately depicting the true structural response.
 - Level 1: uncertainties in the measurement of physical quantities
 - Level 2: uncertainty in the correlation between measurable physical quantities and constitutive model parameters.
 - Level 3: uncertainty in selecting a constitutive model
 - Level 4: uncertainty in the overall idealized model methodology



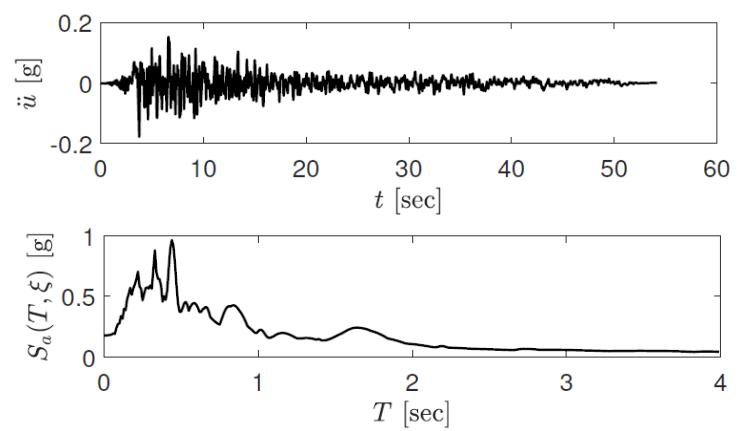
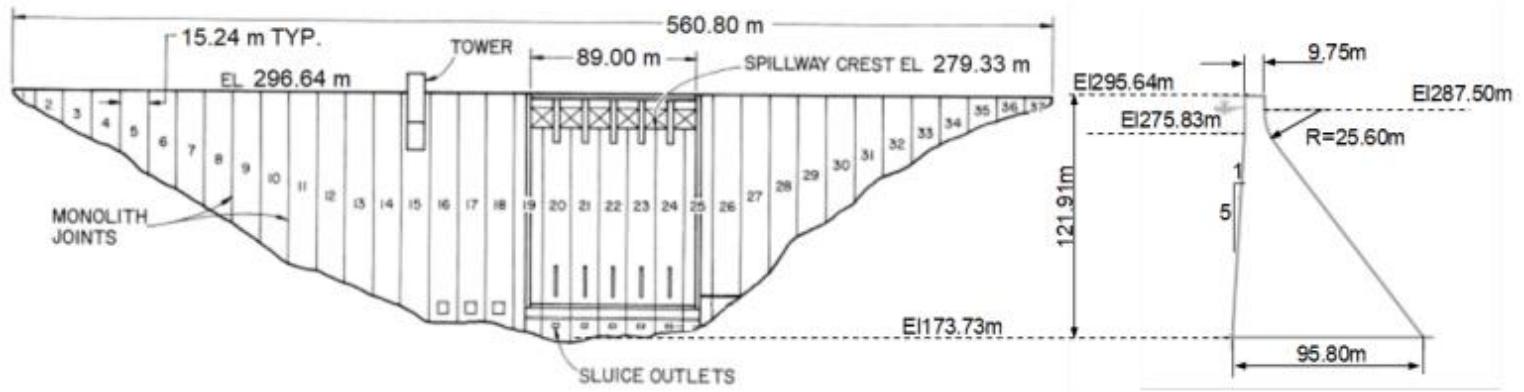
Modeling Uncertainty: Variables

- Modeling variabilities in concrete dams are:
 - 2D, sliced 3D, full 3D mesh
 - Mesh size, and element type
 - Time step, convergence criteria, solution algorithm (implicit/explicit)
 - Site topology and geology, foundation type, and boundary condition
 - SSI, wave propagation, heterogeneity, and deconvolution
 - FSI, uplift pressure, cavitation, surface sloshing, sediment
 - Concrete constitutive model, and damage mechanism
 - Conc/Conc and Conc/Rock interface joint
 - Geometric nonlinearity
 - Stage construction, gradual water impoundment, ...



ICOLD Benchmark Problem

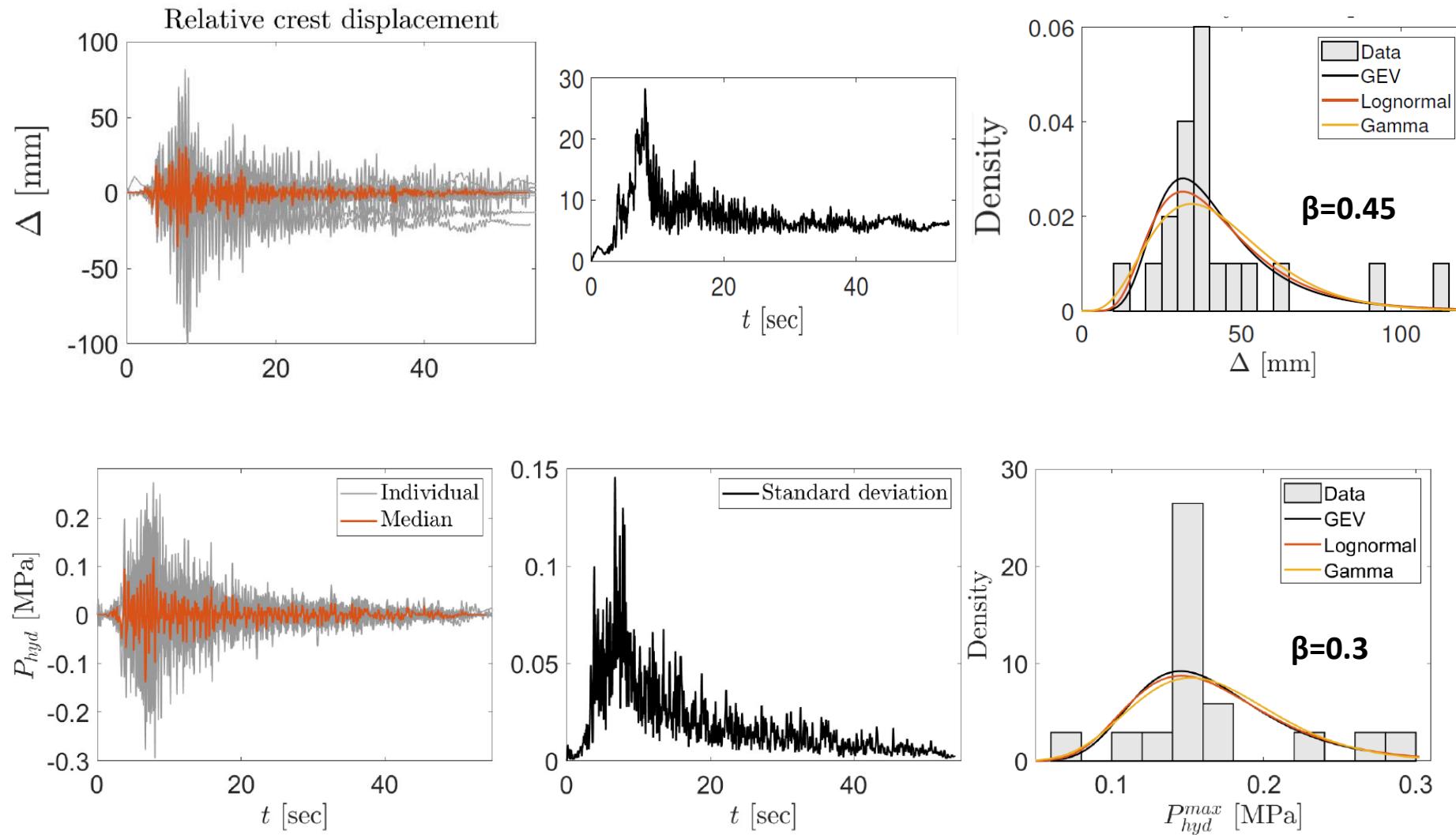
- This workshop design strategically isolates Level 3 and Level 4 modeling uncertainties by offering participants comprehensive data.
- The benchmark includes dam geometry, corresponding finite element mesh, essential material properties, and various reservoir water levels.
- Required loading scenarios encompass seismic loads, with both surface and foundation-based excitation provided, alongside damping value recommendations.



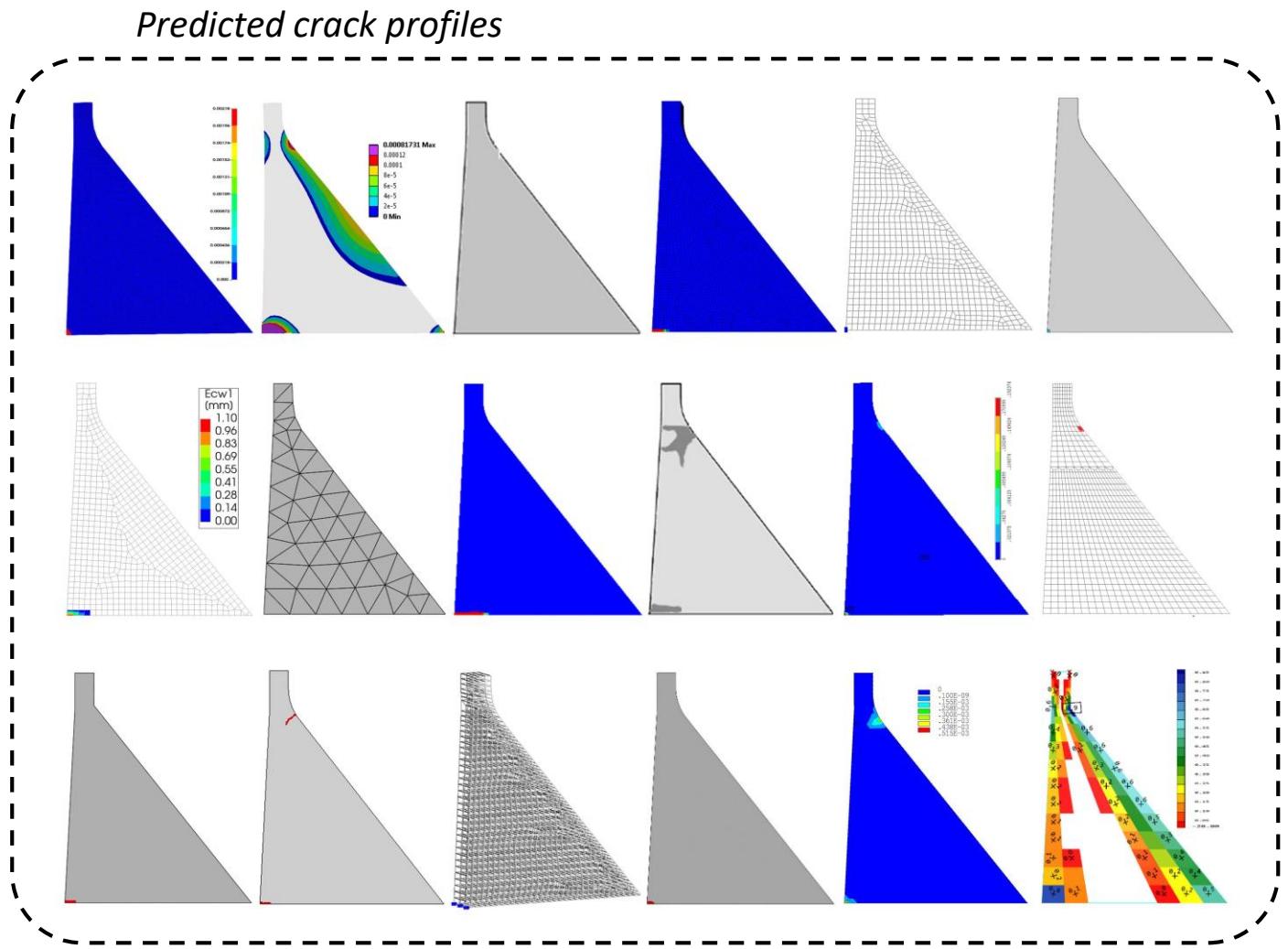
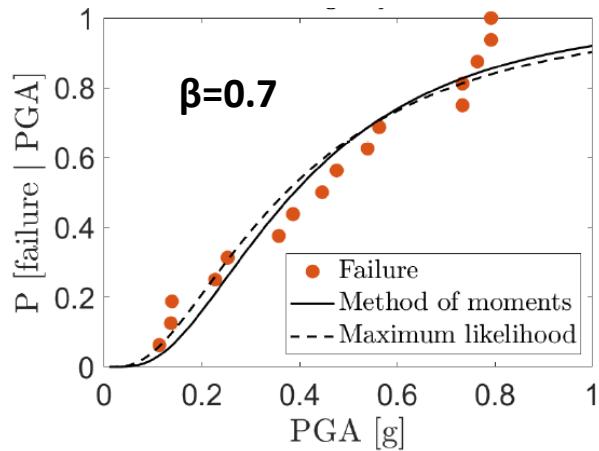
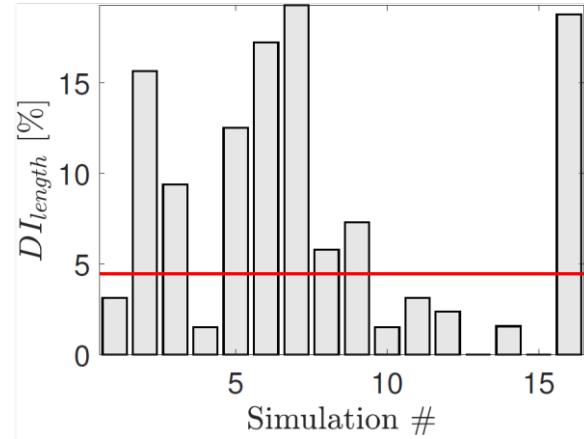
Processing the Results

ID	Mesh type	Mesh size [m]	Time step	Convergence criteria	Foundation type and boundary conditions	Fluid-structure interaction	Concrete constitutive (damage) model	Time integration	Software
11	2D plane strain	2		Norm of unbalance force	Domain reduction method with absorbing damping layers; No free-field BC	Finite volume mesh for fluid; compressible; acoustic-structural coupling		Implicit (solid); explicit (fluid coupling)	Real ESSI
12	2D plane strain	2.5 - 5.0	0.01	1%	Perfectly matched layers; Free-field BC only on the bottom of foundation	Incompressible fluid; acoustic-structure interaction	Total strain-based crack model with fixed-crack orientation including linear tensile curve	Explicit	Diana
13	2D plane strain	10	0.001	0.0001	Viscous-spring boundaries with massed foundation; With free-field BC	Compressible fluid; acoustic-structure interaction	Anisotropic damage model for pre-peak and orthotropic damage following Rankine criteria for post-peak; Isotropic damage under compression stresses using Drucker-Prager criteria	Implicit	Code-Aster
14	3D slice	2	0.01	Newton Raphson (Force)	Foundation bottom is kinematically constrained (Infinite radiation boundary); No free-field BC	Compressible fluid; acoustic-structure interaction	Drucker-Prager constitutive model with perfect plasticity	Explicit (Newmark)	Ansys
15	2D plane strain	1	0.01	Newmark	Simple supports; No free-field BC	Incompressible fluid; FSI with links-gap method	Concrete material in SAP with nonlinear properties	Explicit (Newmark and Linear)	Sap2000
16	3D slice	1.5	0.005	Nodal unbalanced forces	Viscous-spring artificial boundaries model with massed foundation; With free-field BC	Compressible fluid; acoustic-structure interaction	Concrete damage plasticity	Implicit (HHT)	Abaqus
17	2D plane strain	3	0.00005		Non-reflecting viscous boundary with free-field conditions at the lateral boundaries	Lagrangian displacement-based fluid with rotational penalty constraint; FSI	Discrete crack model with a bi-linear softening model in the normal and shear directions and Rokugo curve	Explicit (central difference)	DAMFA2D
18	2D plane strain	3	0.002	Hilber-Hughes-Taylor ($\alpha = -0.3$)	Non-reflecting boundary conditions using particular interface element characterized by a very low stiffness and damping coefficient; No free-field BC	Compressible fluid; acoustic-structure interaction	Crack width by multiplying elemental crack strain and the crack bandwidth (set to 0.5 m)	Implicit (HHT)	Diana
19	2D plane strain	15	0.001	First vibration frequency	Linear paraxial absorbing boundary elements; With free-field BC	Both acoustic fluid and Westergaard's added mass; FSI	Equivalent linearization technique (tensile-strain controlled)	Implicit (Newmark)	Code-Aster
20	2D plane strain	1.5	0.01	Packed scheme: moderate dissipation	Infinite element; With free-field BC	Compressible fluid; acoustic-structure interaction	Concrete damaged plasticity	Implicit (Direct)	Abaqus
21	3D slice	1.0 - 37.0	0.01	Relative convergence criterion : 10e-6	Fixed BC for massless model; No absorbing BC	Added mass and acoustic fluid	Nonlinear tensile behavior only	Implicit (Newton)	Code-Aster
23	2D plane strain	0.5 - 4.0	0.005	5% for force and moment, 0.01% for mass flow rate, 5% for displacement	Viscous-spring boundary condition; No free-field BC	Compressible fluid; acoustic-structure interaction	Coupled damage-plasticity model based on micro-plane formulation	Implicit	Ansys
24	3D slice	1.4	0.00000567		Viscous boundaries (Lysmer); Free-field elements for lateral boundaries only	Compressible fluid with mixed discretization scheme	Elastic perfectly plastic constitutive law for shear with Mohr-Coulomb failure criterion; elastic perfectly fragile constitutive law for tensile	Explicit	Flac3D
26	2D plane strain	1	0.01	Energy based	Infinite elements with free-field BC based on Lysmer	Compressible fluid; acoustic-structure interaction	Concrete damage plasticity	Implicit	Abaqus
27	3D slice	3	0.0001		Viscous boundary conditions proposed by Lysmer; With free-field BC	Lagrangian displacement-based fluid with only normal stiffness; FSI	Bi-linear softening model in tension and shear with Rokugo curve	Explicit (Central difference)	Parmac3D
28	2D plane strain	1.5	0.01		Lysmer boundary condition; With free-field BC	Compressible fluid; acoustic-structure interaction	Concrete damage plasticity	Implicit	Abaqus
29	2D plane strain	2.5	0.01		Viscous spring elements; No free-field BC	Compressible fluid; acoustic-structure interaction	Concrete plasticity with Menetrey-Willam criterion	Implicit	Ansys
30	2D plane strain	3.5			Infinite elements; free field rock-column and direct free field forces	Compressible fluid; acoustic-structure interaction	Concrete damage plasticity	Implicit	Abaqus
31	2D plane strain	1.5	0.001		Viscoelastic artificial boundary; No free-field BC	Compressible fluid; acoustic-structure interaction	Concrete damage plasticity	Implicit	Abaqus
32	3d slice	10	0.01	Tolerance for largest nodal value available in the system + energy norm	Non-reflecting BCs with damper elements	Compressible fluid-like structural elements; FSI	Concrete material according to EN norms	Wilson theta	SOFISTIK
33	Plane Strain	3	6e-4 to 0.01	to Force equilibrium	Infinite elements; No free-field BC	Compressible fluid; acoustic-structure interaction	Concrete damage plasticity	Implicit	Abaqus

Displacement and Pressure



Damage Index



Conclusions

- The presentation of varying levels of uncertainties in dynamic non-linear analyses of concrete dams serves as a primary avenue for assessing accuracy, thereby bolstering confidence and credibility in modeling and computational simulations.
- To enhance confidence in modeling and computational simulations for concrete dams, key recommendations are:
 - (1) Prioritize accurate hydrodynamic pressure representation on the dam's upstream face using compressible fluid elements in advanced analyses.
 - (2) Use appropriate non-reflecting boundary conditions, with a preference for free-field boundaries, to address foundation-dam dynamics.
 - (3) For intense seismic scenarios, introduce nonlinearity. Apply cohesive crack models at known crack/joint locations or use continuum damage models for the entire dam.
 - (4) Pay attention to mesh type/size, time step, convergence criteria, time integration schemes, and **damping models**, especially in nonlinear analyses.



Thank you!

Any questions?

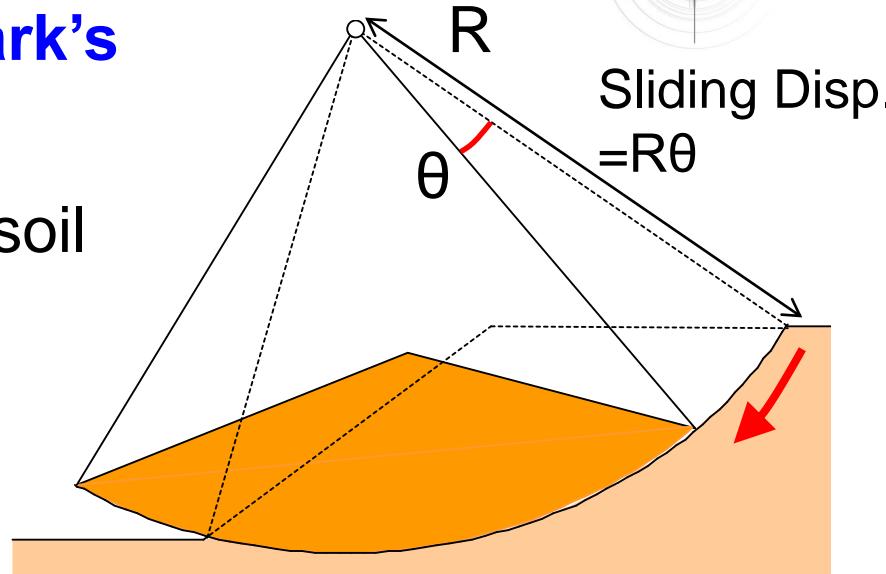


Centrifuge Shake Table Tests and Numerical Simulations on Seismic Damage Process of Embankments

R. Ibuki ¹, T. Doi ¹, J. Izawa ¹,
K. Uemura ², S. Sreng ²

- ¹ Railway Technical Research Institute, Tokyo, JAPAN
² Nippon Koei, Ibaraki, JAPAN

- In the seismic design of embankments, **the Newmark's sliding block method** has been often used.
- This method calculates sliding displacement of the soil block **after a sliding failure occurs**.
- However, some researchers have reported that this method **cannot simulate the actual damage** observed in the past large earthquakes.



- **Purpose:** To establish a design method, which can evaluate the damage process.
- **Means:**
 - ① Conducted a series of **centrifuge shake table tests**.
 - ② Clarified **the actual damage process** of embankments during earthquakes.
 - ③ Proposed an **evaluation method** to take account into the damage process.
 - ④ Considered a **calculation method** to simulate the damage process.

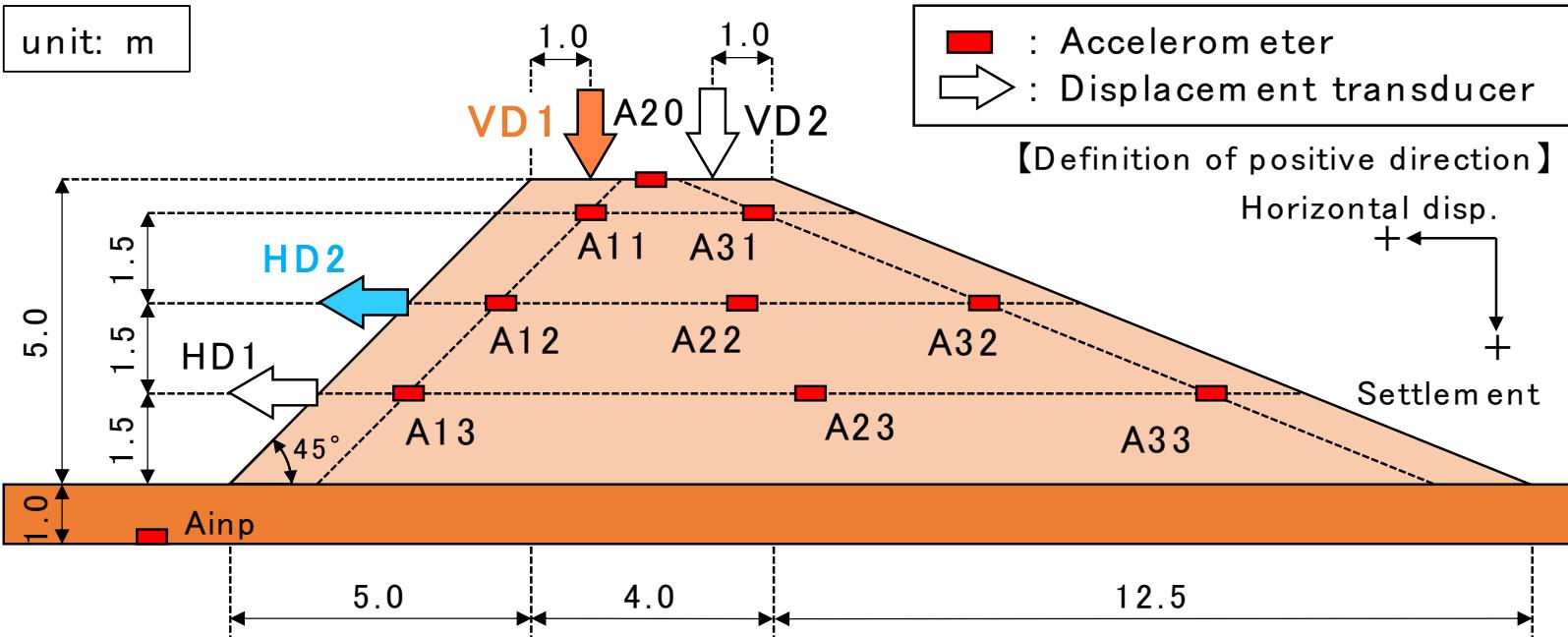
Introduction

1. Centrifuge Shake Table Tests
2. Seismic Damage Process of Embankments
3. Evaluation method up to Sliding Failure
4. Numerical Simulations

Conclusions

1. Centrifuge Shake Table Tests

Case 1 (left slope gradient 1:1.0, 50G)



Test conditions

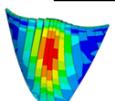
	Slope gradient of left side	Height (m)
Case 1	1:1.00	5.0
Case 2	1:1.25	5.0
Case 3	1:1.50	5.0

Today's topic is Case 1.

Physical & Mechanical properties of embankment material (the *Edosaki* sand)

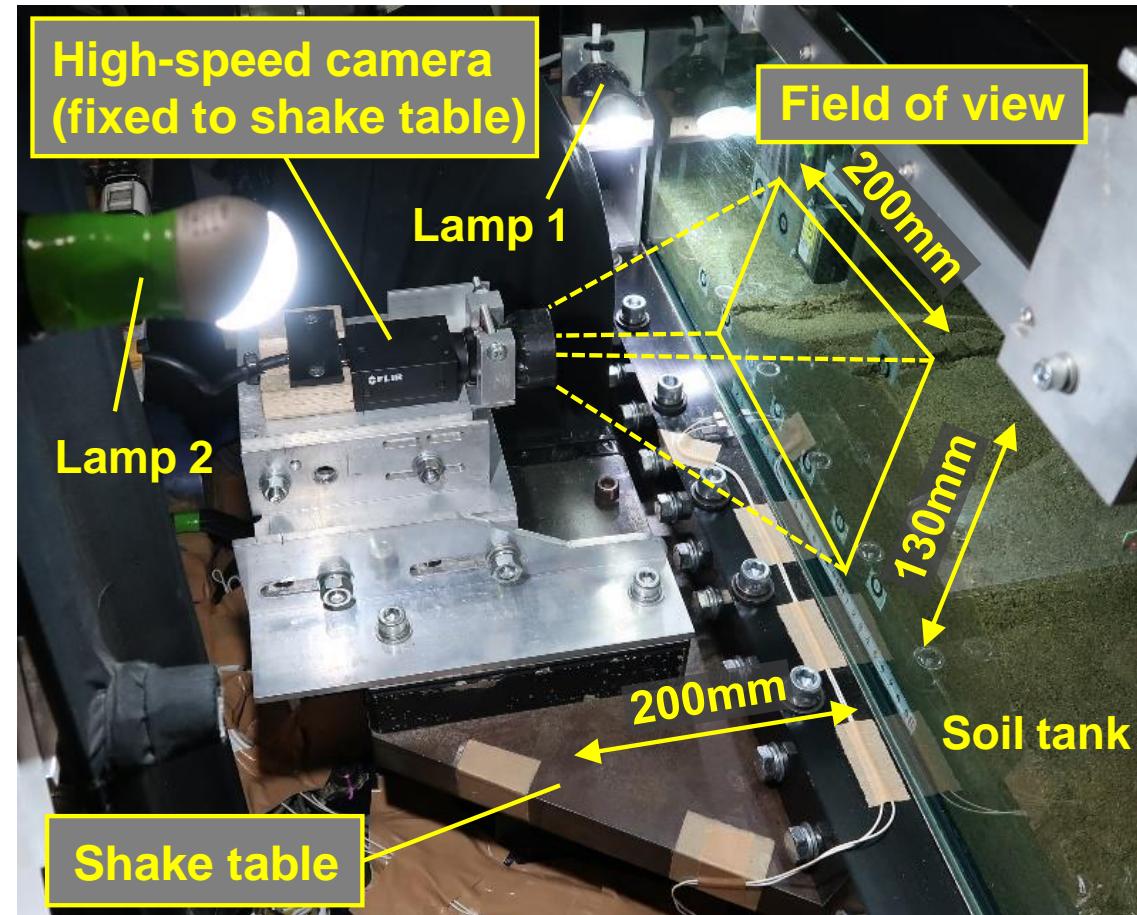
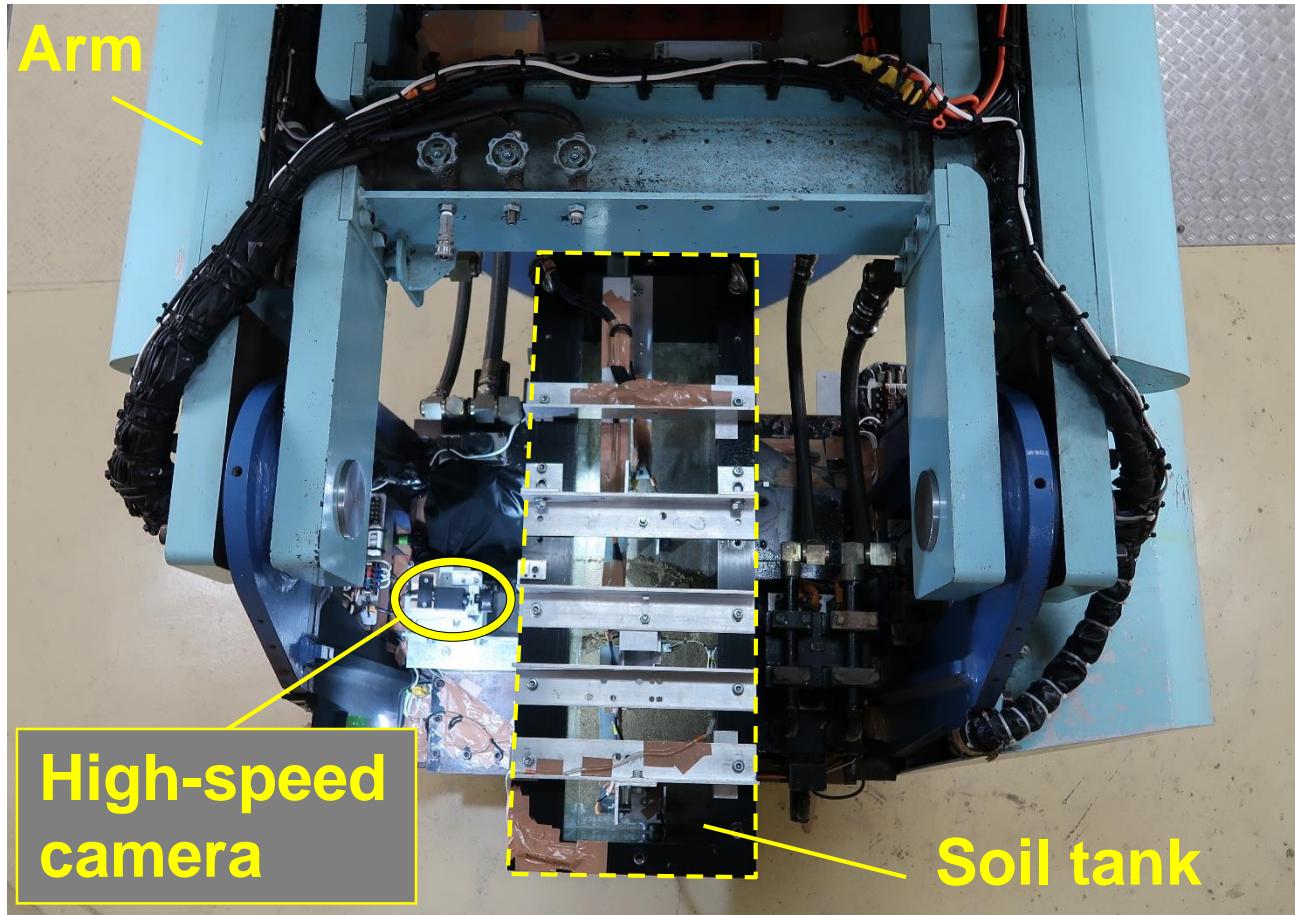
Degree of compaction	: D_c	95%
Dry density	: ρ_d	1.622 g/cm ³
Compression index	: C_c	0.055
Consolidation yield stress	: P_c	318.1 kPa
Cohesion	: c	8.65 kPa
Internal friction angle	: ϕ	36.4 deg.

Soil particle density	: G_s	2.68
Mean grain size	: D_{50}	0.34 mm
Effective grain size	: D_{10}	0.15 mm
Fine content	: F_c	4.8 %
Optimum water content	: w_{opt}	14.6 %
Maximum dry density	: ρ_{dmax}	1.707 g/cm ³

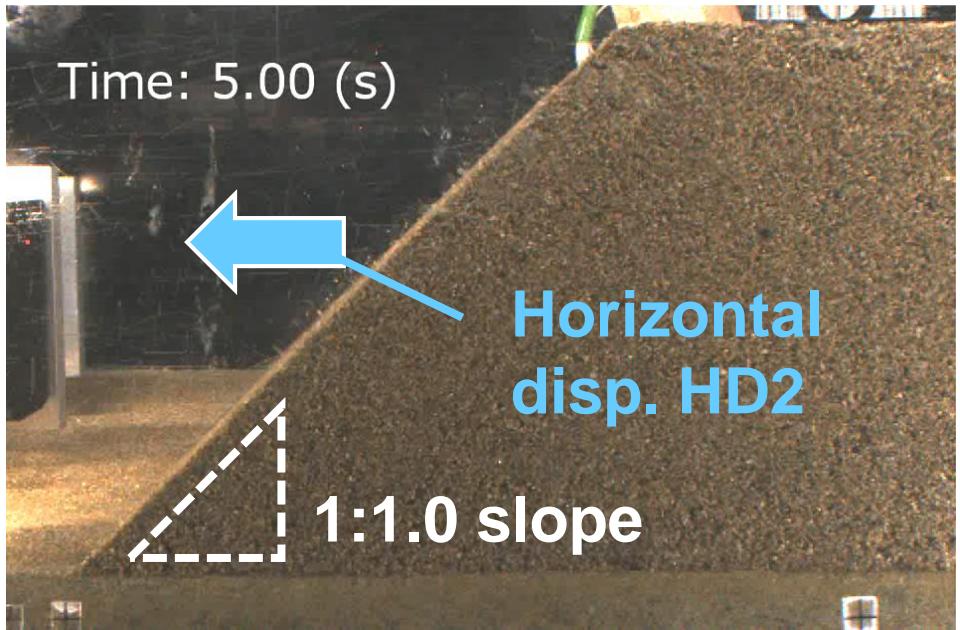


1. Centrifuge Shake Table Tests

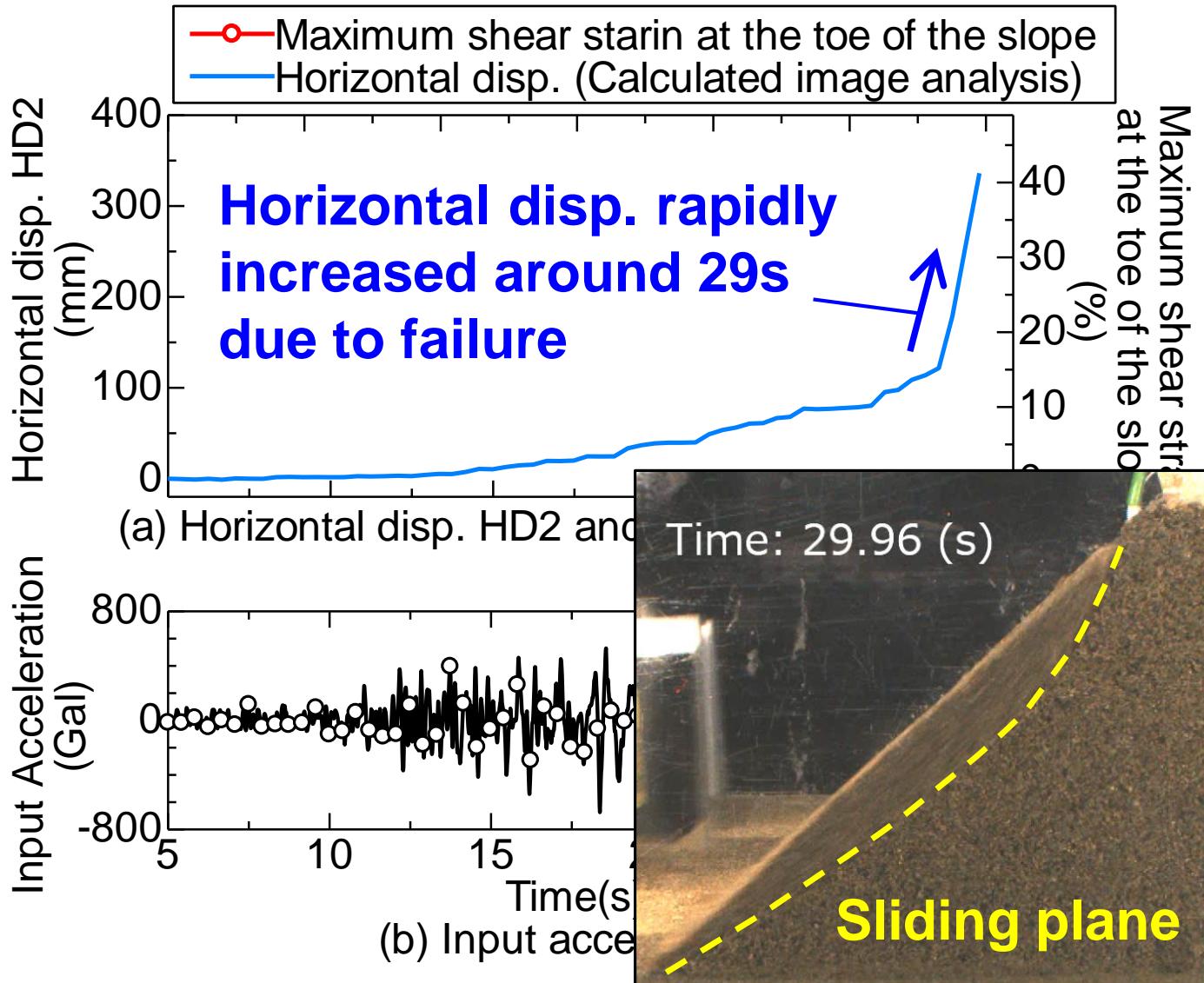
- Using a **high-speed and high-resolution camera** with global shutter.
- Fixed camera to the shake table **to exclude camera shake**.



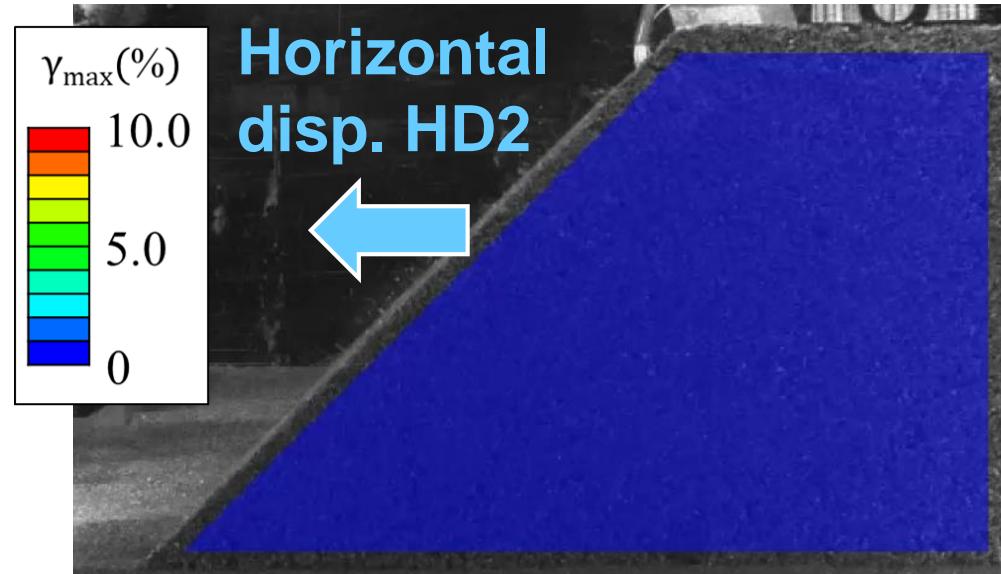
1. Centrifuge Shake Table Tests



- We could obtain **high-resolution images without camera shake** using the high-speed camera.
- **Sliding failure occurred** during 1st shaking.

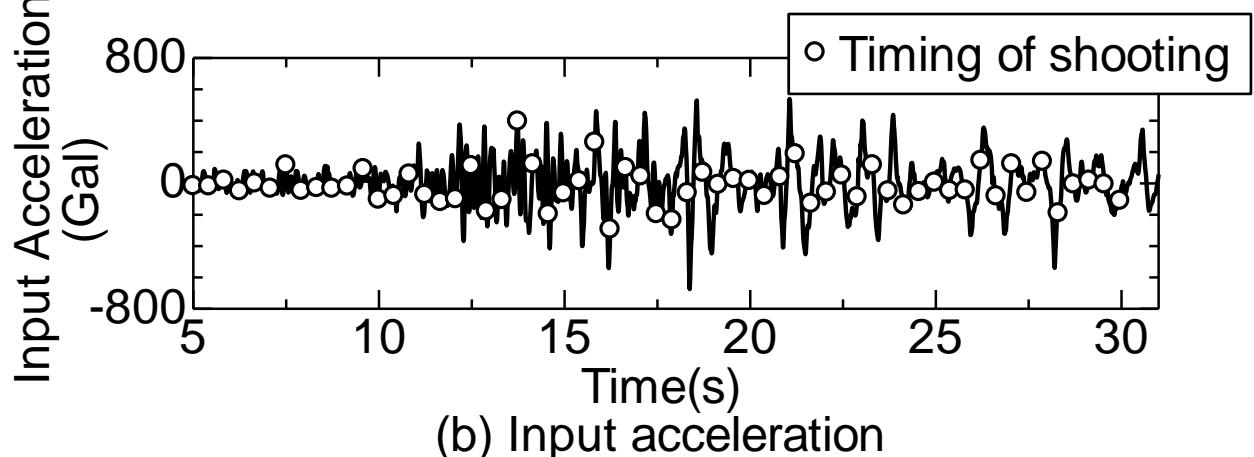
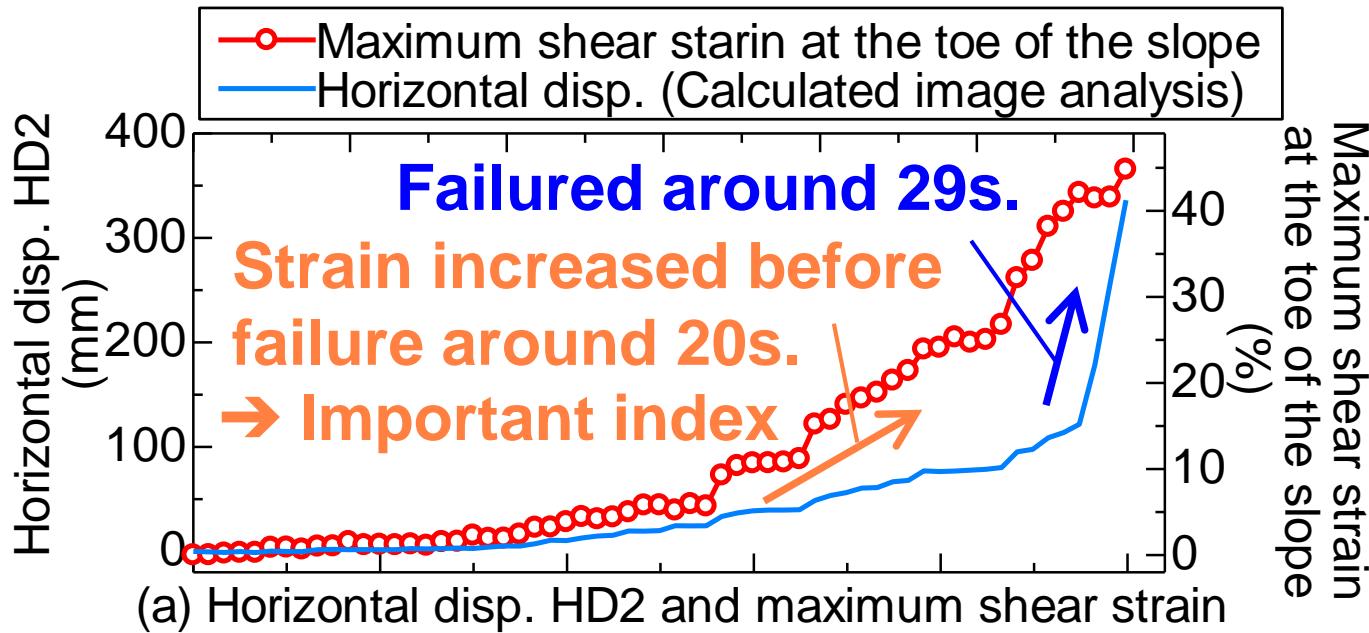


1. Centrifuge Shake Table Tests



Distributions of maximum shear strain

- Using the **image analysis**, strain distributions were obtained.
 - Shear strain tended to **concentrate at the toe of the slope** and sliding plane appeared.



2. Seismic Damage Process of Embankments

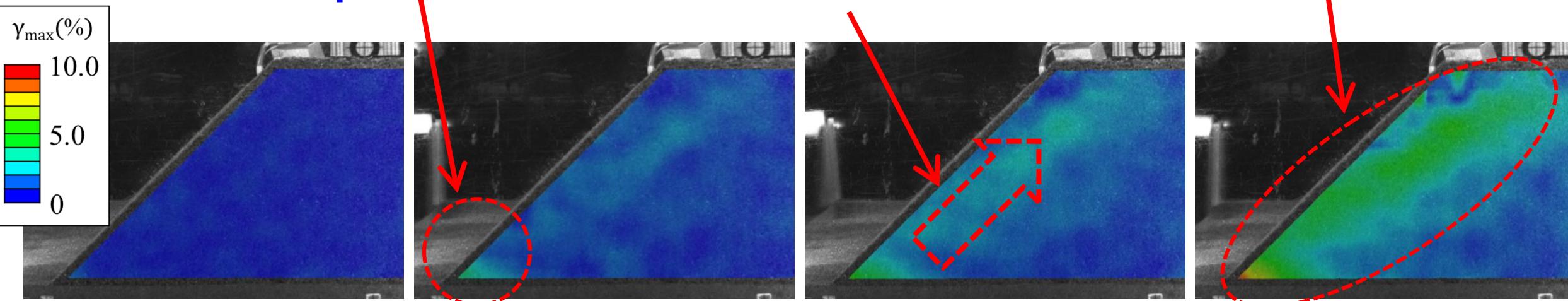
Damage process

We can explain the damage process up to the sliding failure using the shear strain near the toe of the slope.

i. The shear strain began to accumulate **near the toe of the slope**.

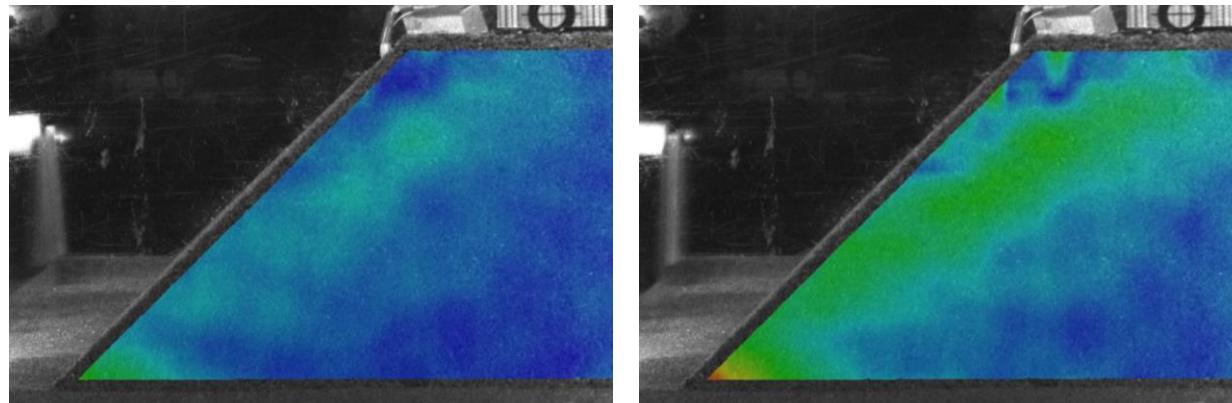
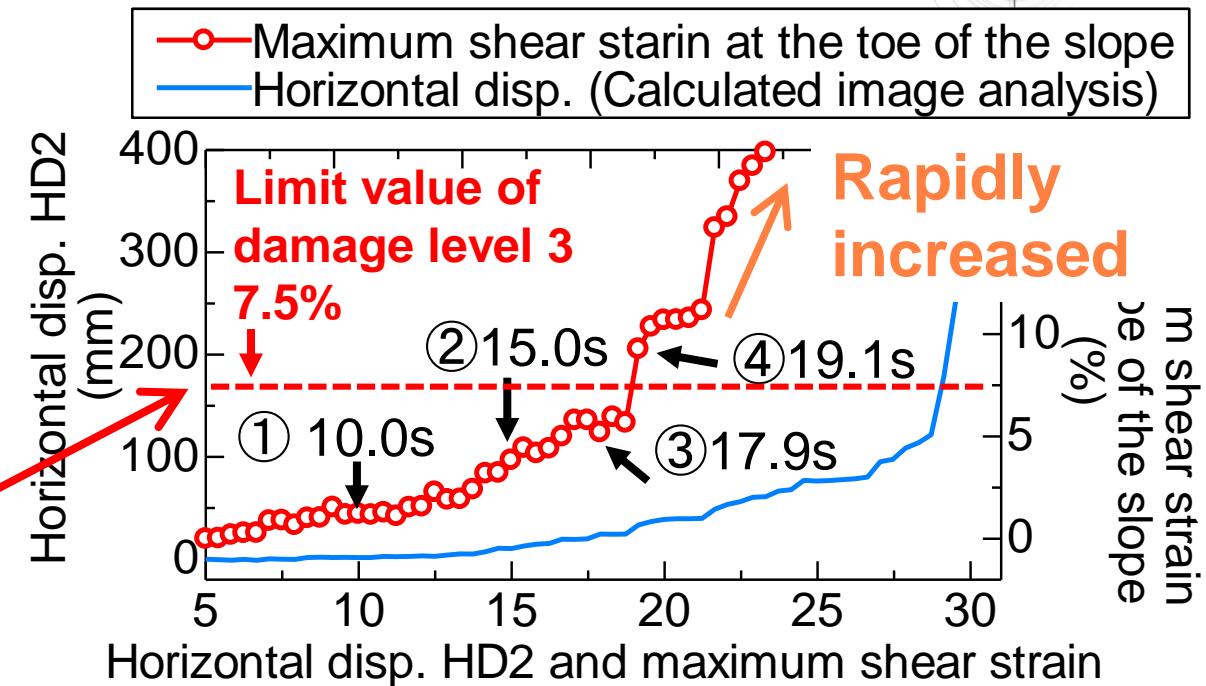
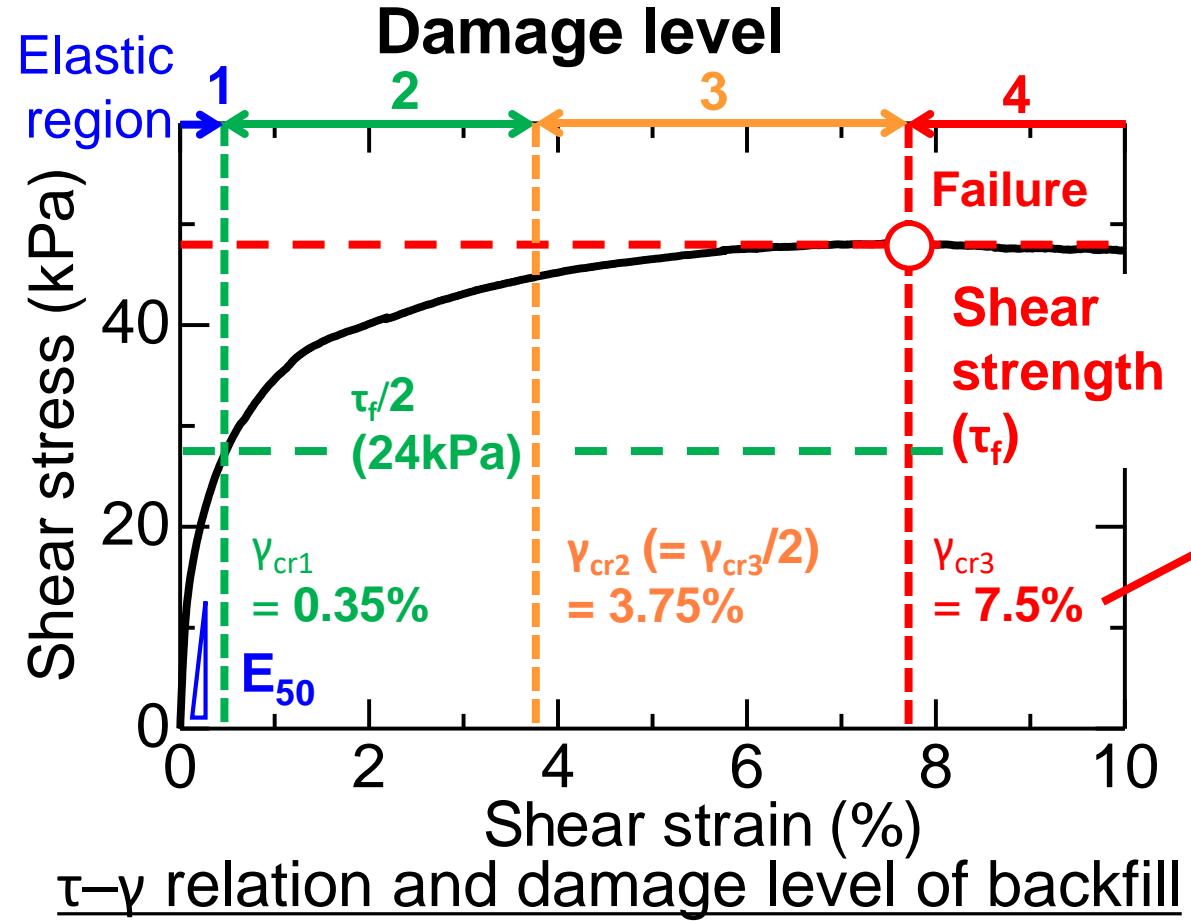
ii. The shear strain gradually progressed into the inside of the embankment.

iii. The sliding plane appeared.



Distributions of maximum shear strain(γ_{max})

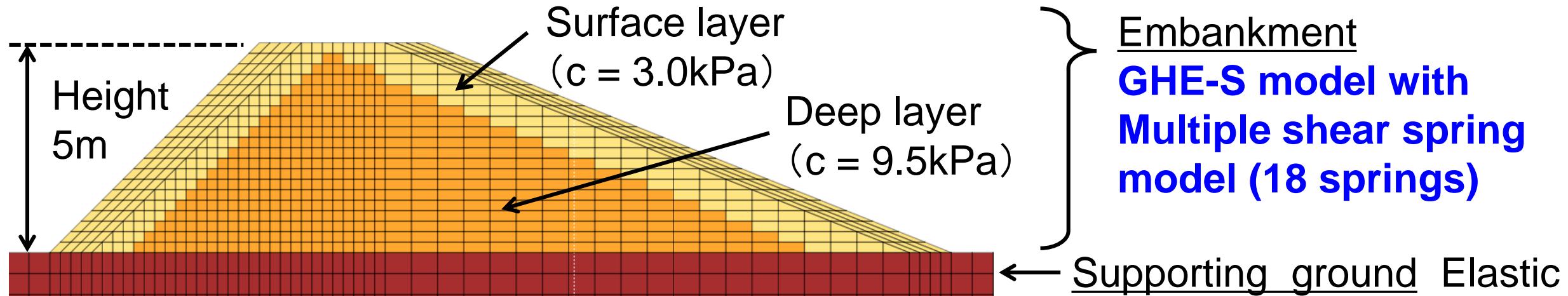
3. Evaluation Method up to Sliding Failure



② 15.0s $\gamma_{max,m}=3.9\%$

④ 19.1s $\gamma_{max,m}=9.3\%$

3. Numerical Simulations (1:1.0 slope)

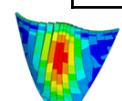


	Unit volume weight	Poisson ratio	Initial shear stress stiffness	Cohesion	Internal friction angle
Embankment	16.9 kN/m ³	0.499	10,179 kN/m ² ✕	3.0 kPa (Surface) 9.5 kPa (Deep)	32.5 deg.
Supporting ground	18.0 kN/m ³	0.499	165,306 kN/m ²	—	—

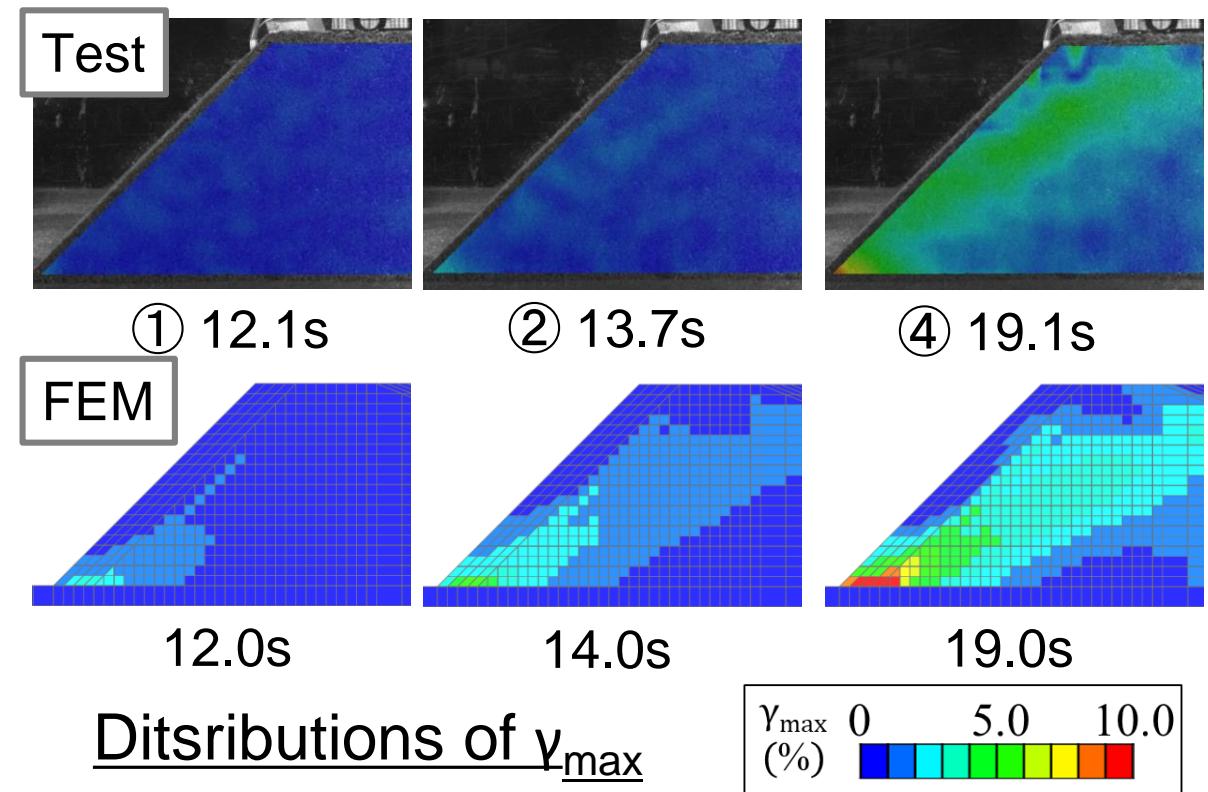
The GHE model parameter

✖ When the confining pressure is 1kPa.

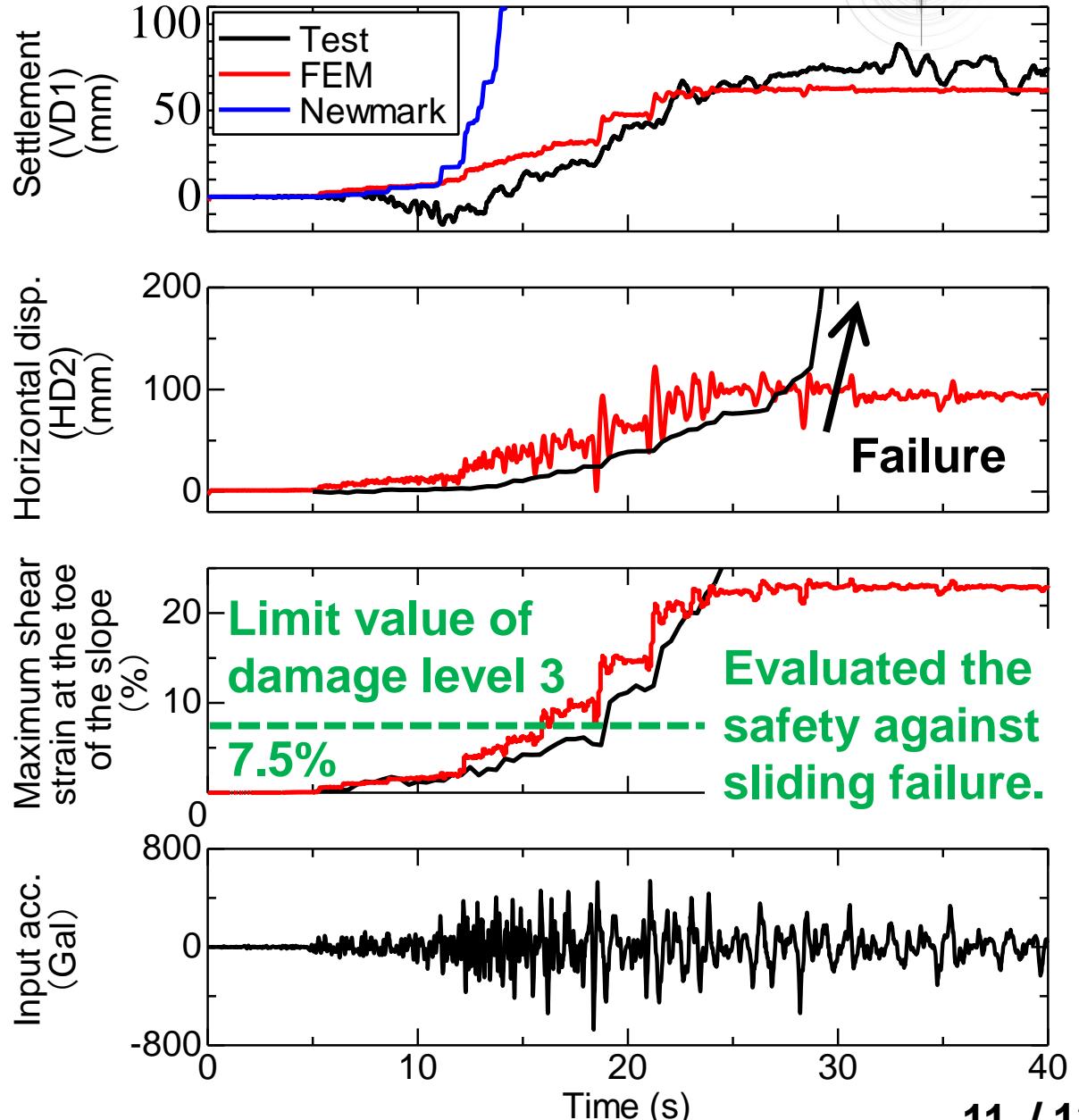
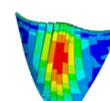
$C1(0)$	$C1(\infty)$	$C2(0)$	$C2(\infty)$	α	β
1.0	0.11	0.2	1.0	0.986	1.38



3. Numerical Simulations (1:1.0 slope)



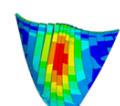
- Reproduced the damage process.
(Strain concentration and its progress.)
- Reproduced the deformation
before the sliding failure.



In this study, we conducted a series of centrifuge shake table tests and numerical simulations to consider the seismic damage process of embankments.

As a result, the following conclusions were obtained.

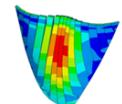
- **Damage process** before failure observed in the test was summarized as follows;
 - i. Shear strain began to **accumulate at the toe of the slope**.
 - ii. The shear strain at the toe of the slope gradually progressed into the inside of the embankment.
 - iii. The shear strain at the toe of the slope **exceeded the damage level 3** (specified from the deformation characteristics of the embankment material), **the sliding plane appeared**.
- The FE model using the GHE-S model with the multiple shear spring model could **reproduce the damage process** of the embankments observed in the test.
- Therefore, we could **evaluate the actual damage process** of embankments.

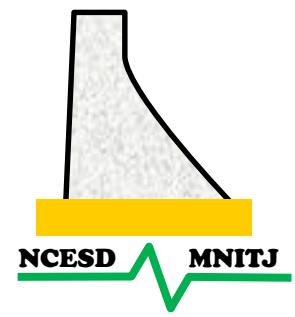




Thank you!

Any questions?





PERFORMANCE EVALUATION OF CONCRETE GRAVITY DAM IN THE EVENT OF SEISMIC AFTERSHOCKS

Shiyam Sundar K P¹, M K Shrimali¹, S D Bharti¹, CVR Murty²,
Nishant Roy¹

¹ Malaviya National Institute of Technology, Jaipur , India

² Indian Institute of Technology Madras, India

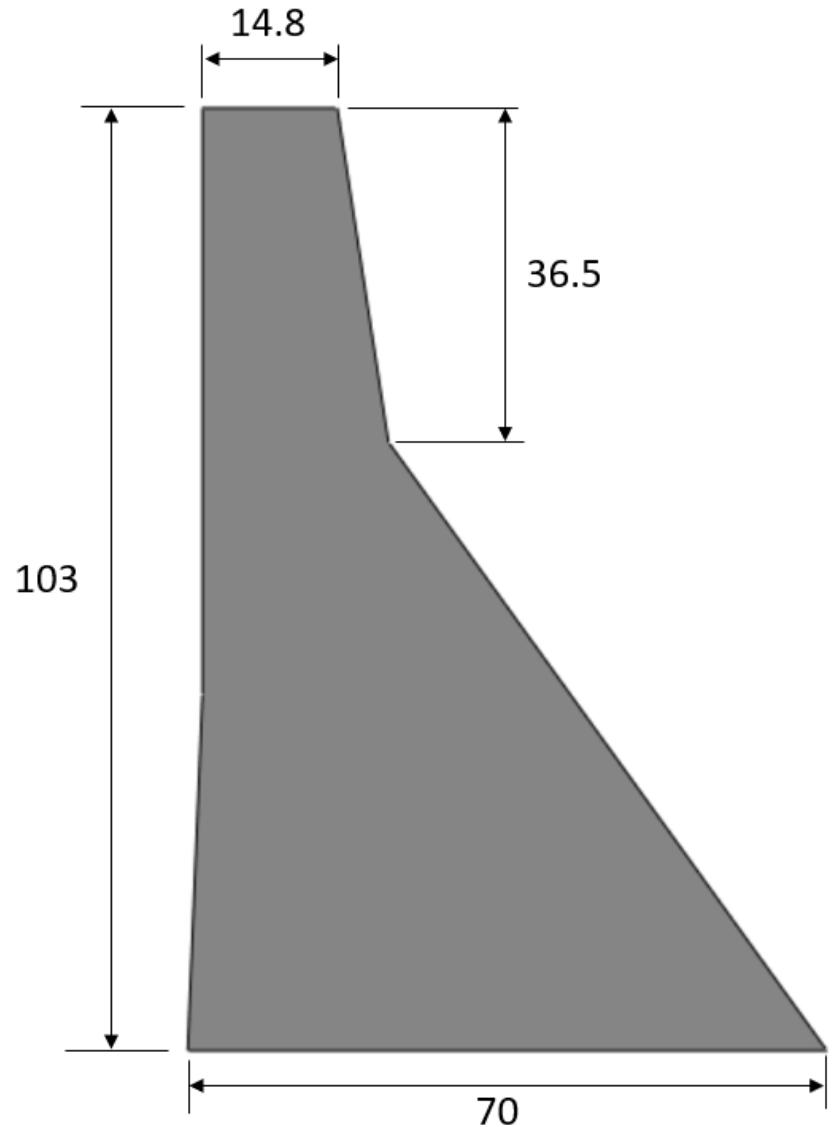
INTRODUCTION

- Dams with unconventional cross-sections are vulnerable to the sequence of mainshock and aftershocks.
- Literature on the effect of seismic aftershocks is scanty.
- A NTHA is essential to capture the damage response in a sequence of mainshock and aftershock.
- The complete evaluation of the seismic safety of dams requires 3D modelling, including foundation-structure interaction which is elaborate.
- A reasonably good idea about the seismic performance of the dam can be ascertained by 2D modelling of the tallest monolith of the dam with a rigid base.
- As a consequence, an attempt is made here to analyze the tallest monolith of a dam under the sequence of mainshock and aftershocks.

PROBLEM STATEMENT

- Tallest non-overflow monolith of the Koyna dam is analysed for the sequence of mainshock and aftershock.
- Concrete Damage Plasticity (CDP) model is utilized to capture the damages induced at the different portion of the dam.
- Frequencies and mode shapes of the dam with and without full reservoir are compared.
- Two types of earthquakes are considered such as Near-field and far-field earthquake and its PGA is scaled to 0.4g and 0.6g.
- The crack initiation and propagation is predicted for mainshock and aftershocks.

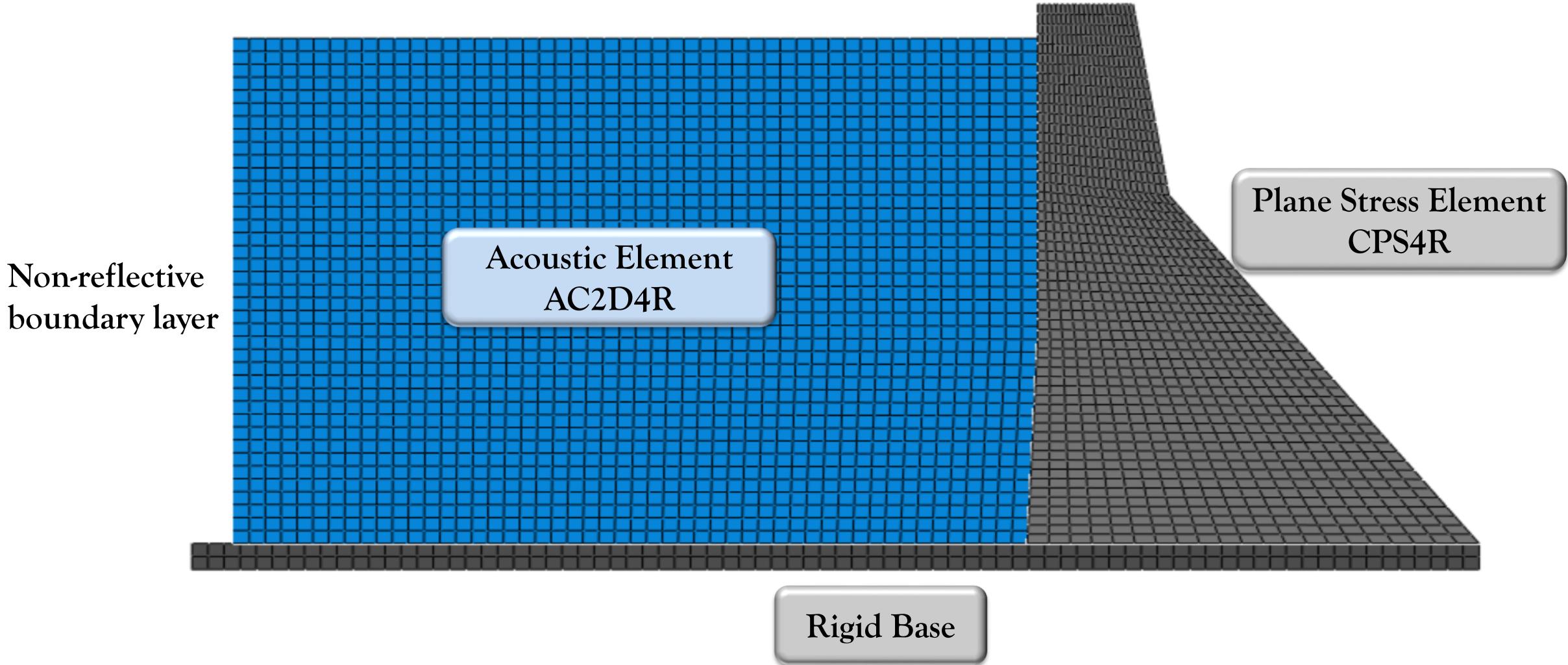
Koyna Dam Properties



Dam	
Density	2650 kg/m ³
Young's Modulus	31027 MPa
Poisson's ratio	0.2
Maximum permissible tensile strength	3.5 MPa
Damping	5%

Water	
Density	1000 kg/m ³
Bulk Modulus	2.1 GPa

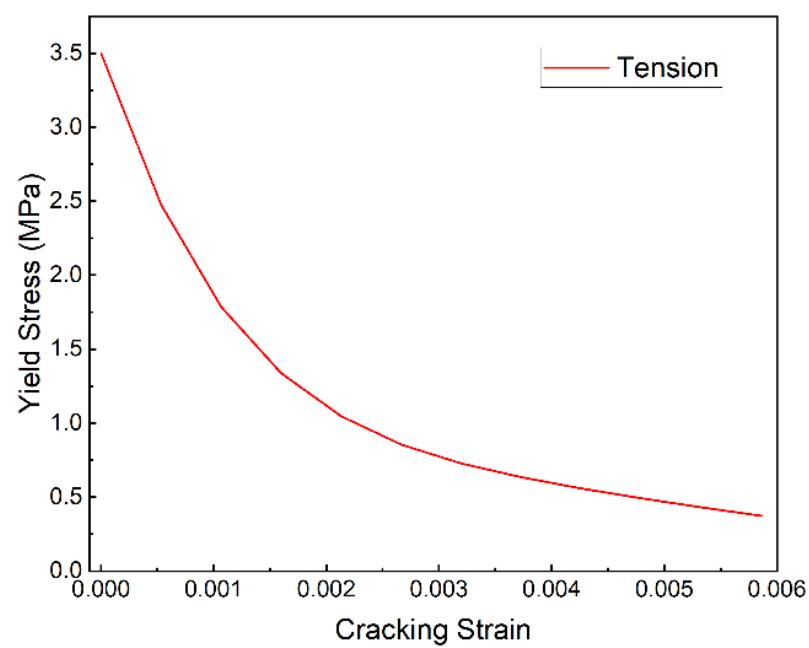
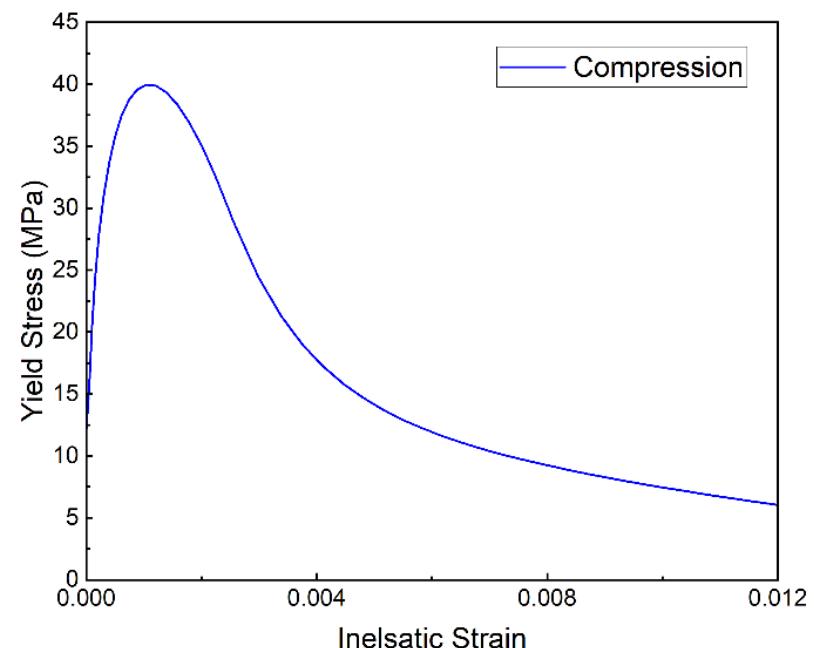
Finite Element Model



Concrete Damage Plasticity (CDP) Model

- For the CDP model, model code (1990) is used in this study.
- In the absence of stress-strain data, established formulas can be used to generate the stress-strain curve. One such example is Eurocode 2.

Plastic Flow Parameters	
Dilation Angle	30-40
Eccentricity	0.1
f_{b0}/f_{c0}	1.16
K	2/3
Viscosity parameter	0.0001

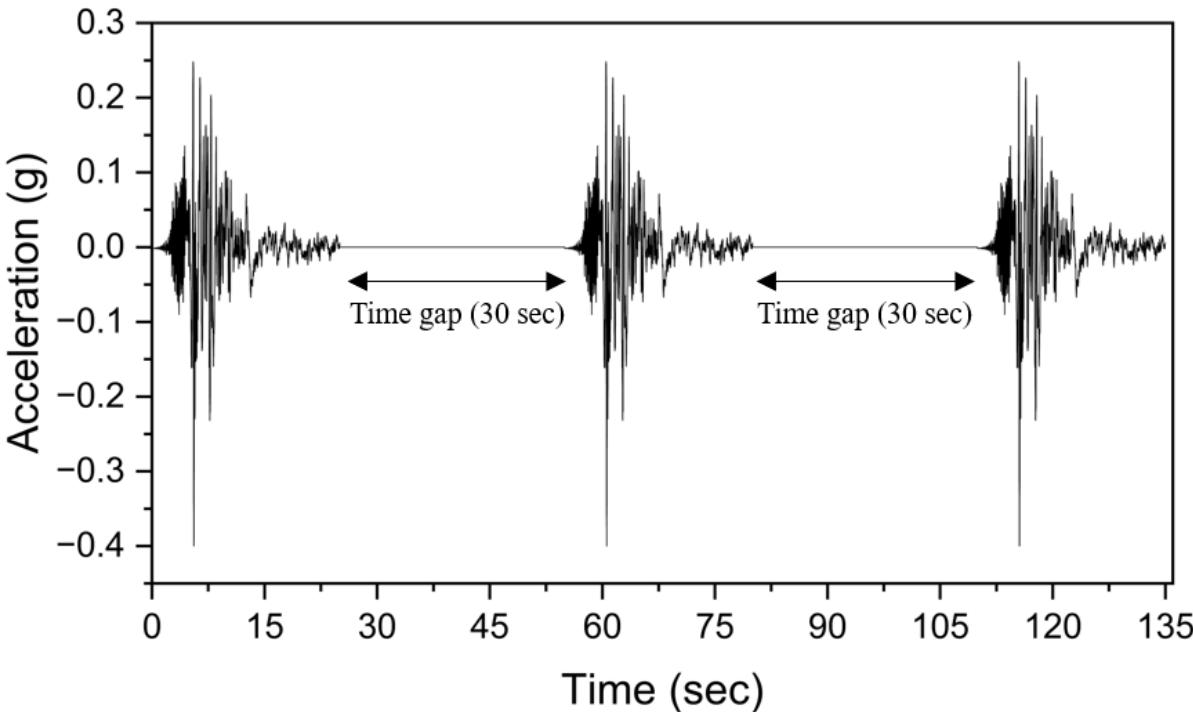


Nonlinear Time History Analysis

- The response history analysis is done through the ABAQUS with the dynamics and explicit step.
- The software uses the central difference method to calculate the displacements in every time step.
- It approximates the acceleration at the next time step by taking a centered difference of velocities.
- The time step of the explicit analysis are chosen in a way it is sufficiently smaller to ensure numerical stability.
- Rayleigh damping has been considered, with its coefficients evaluated considering the damping ratio of 5%.

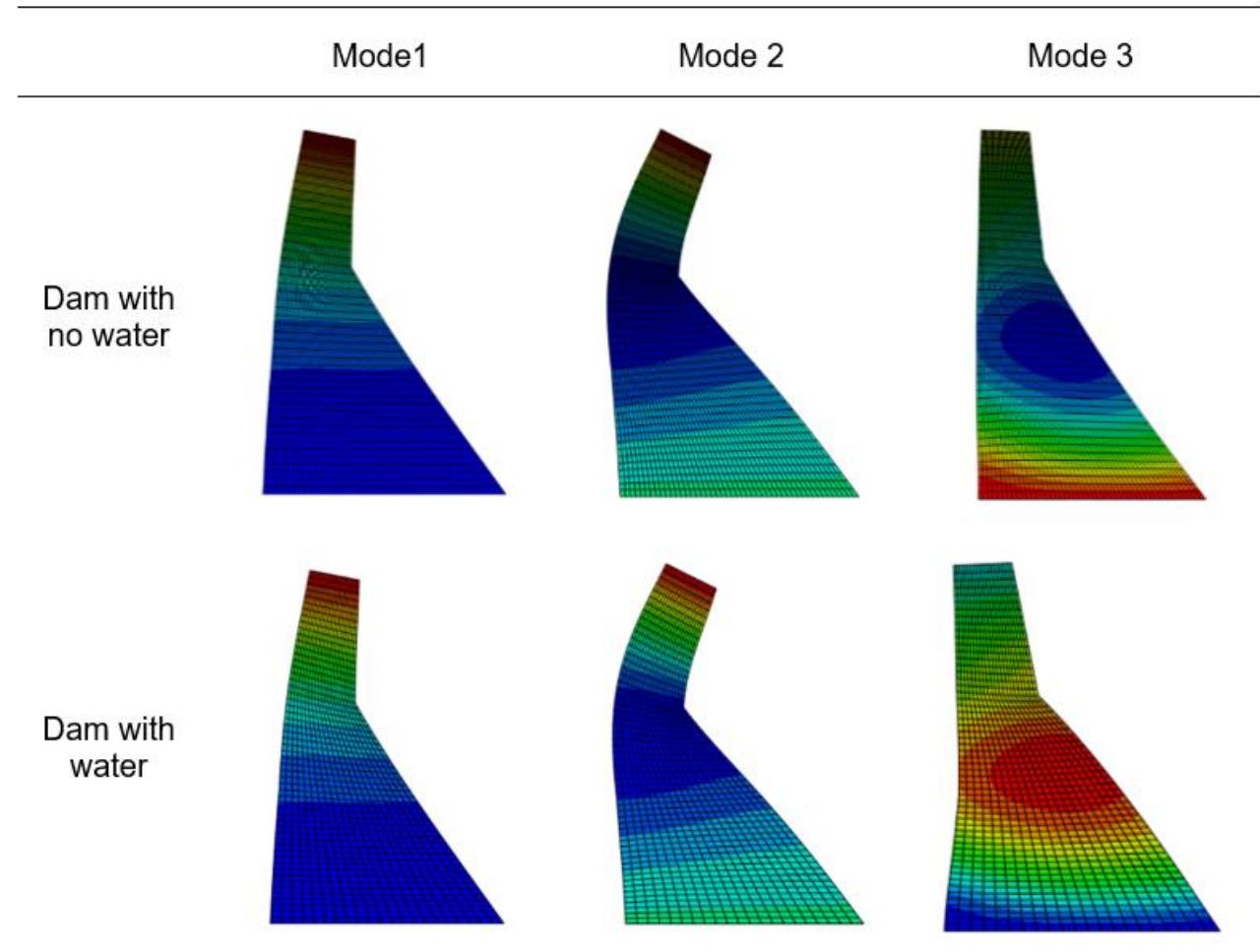
Ground Motion Data

- The earthquake data selected for this study is the 1979 Imperial Valley earthquake, recorded from two distinct stations—one in close proximity (near-field) and the other further away (far-field).
- The same earthquake is used for both the mainshock and aftershocks, but the ground motion is scaled to the peak ground acceleration (PGA) values of 0.4g and 0.6g.

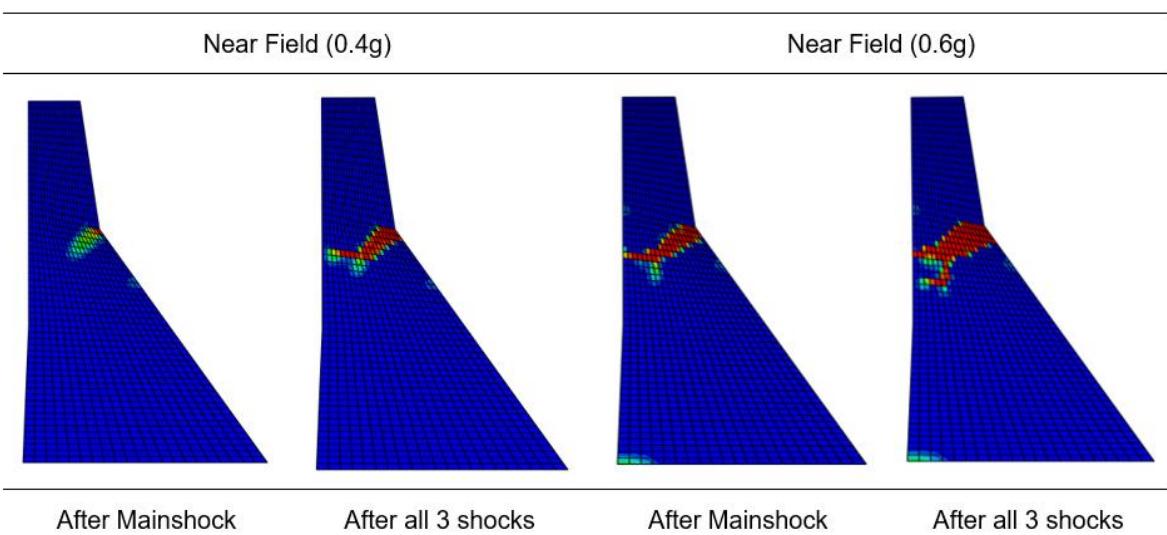
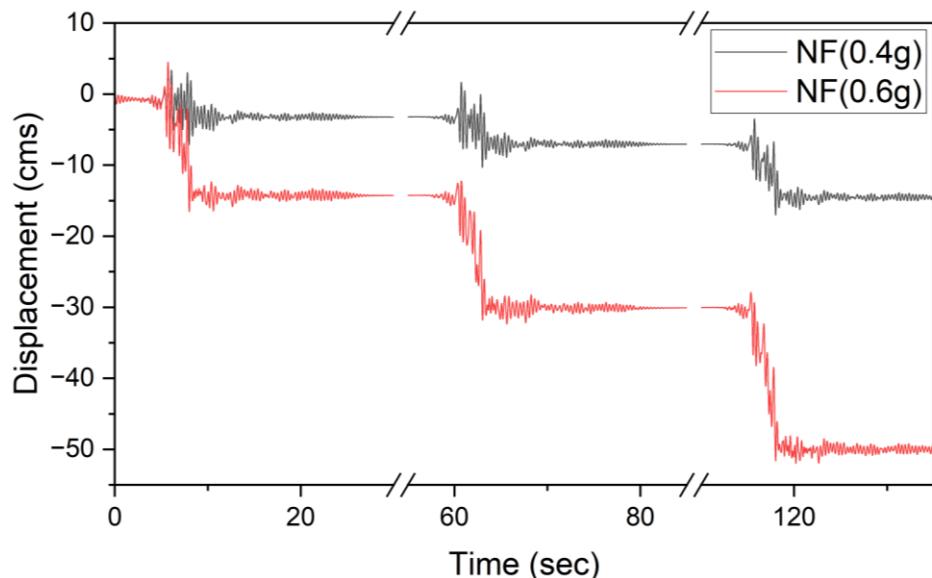
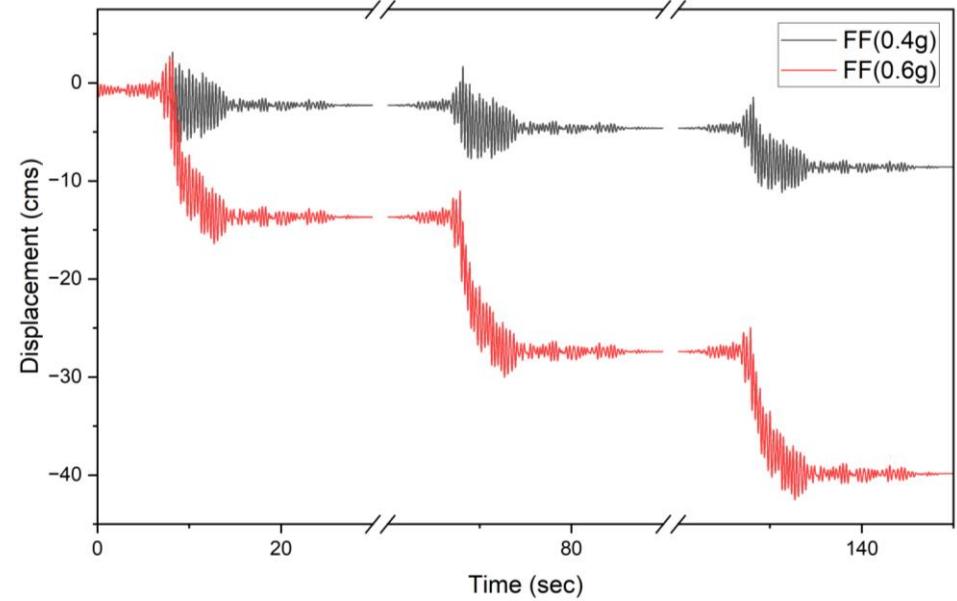
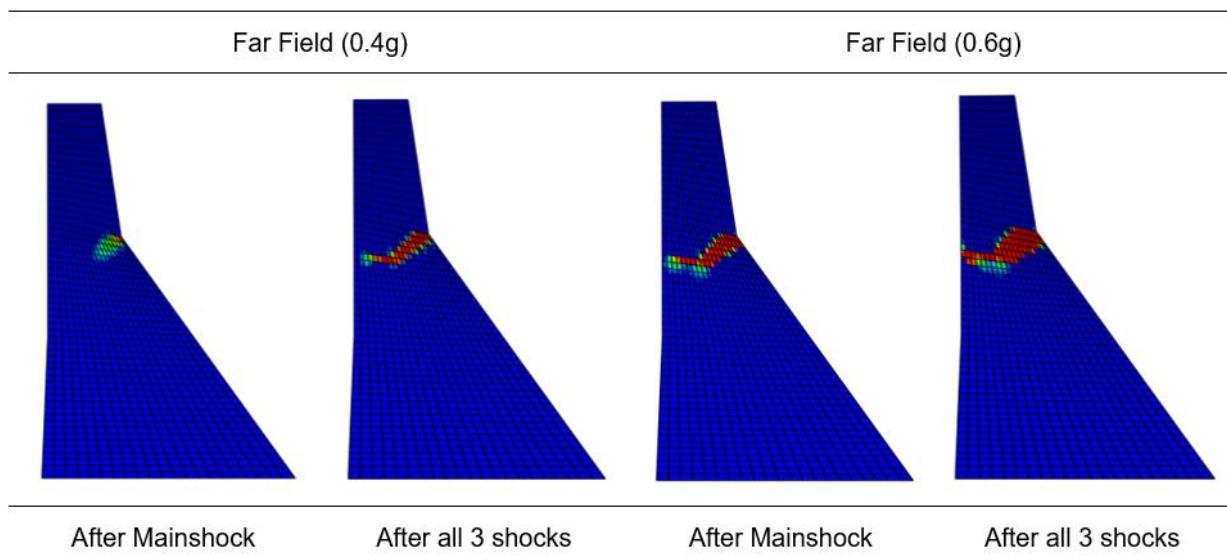


Frequency and Mode Shapes of Dam with and without Reservoir Water

Modes	Frequencies (Hz)	
	Dam with no water	Dam with a full reservoir
1	3.1	2.7
2	8.2	7.4
3	10.8	10.7
4	15.9	11.1
5	24.2	11.4



Damage Prediction and Crest Displacement

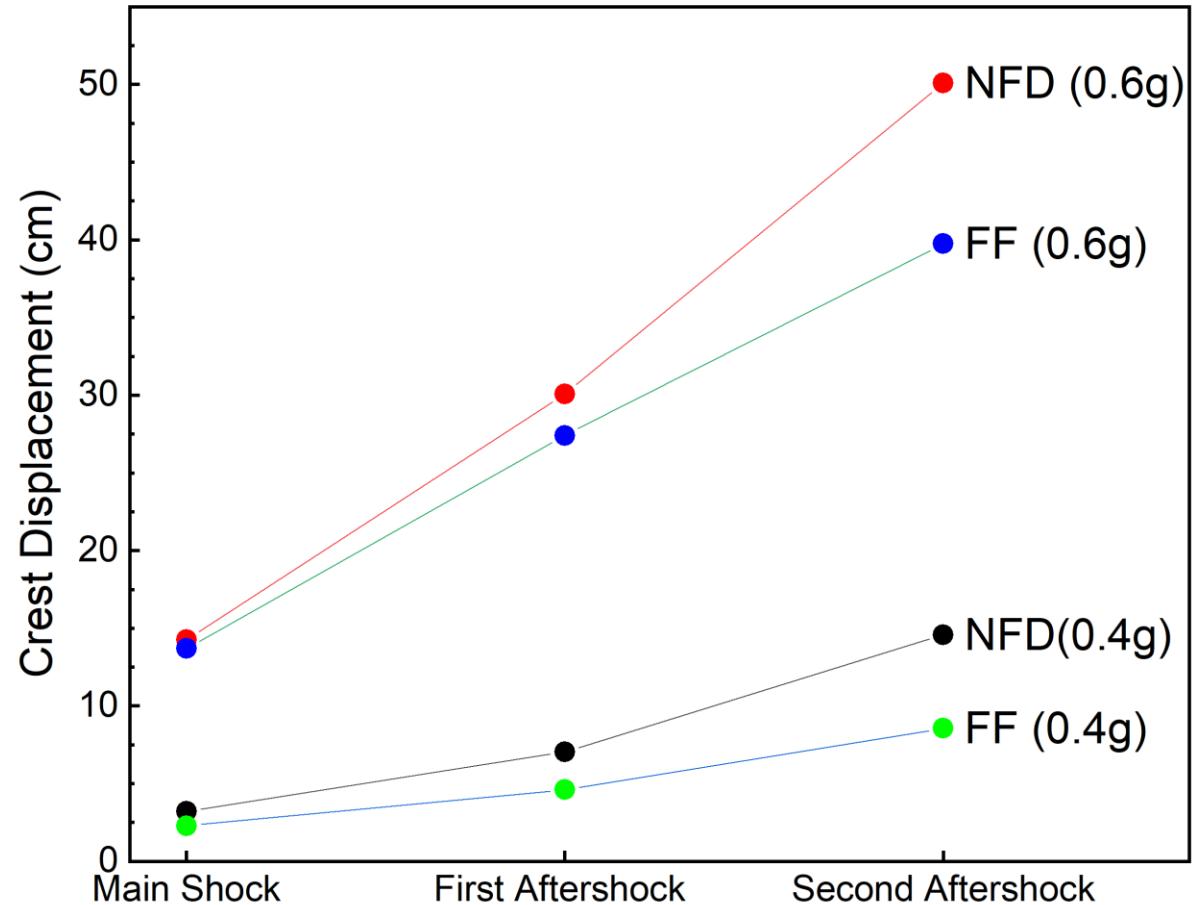


Peak Responses obtained after each shocks

Shocks	EQ Type	PGA	Crest Displacement (cm)	Max Principal Stress (MPa)	Min Principal Stress (MPa)
Mainshock	Far-field	0.4g	5.98	3.5	15.65
		0.6g	16.39	3.5	17.41
	Near-field	0.4g	7.11	3.5	15.57
		0.6g	16.54	3.5	18.29
First Aftershock	Far-field	0.4g	5.45	3.5	15.69
		0.6g	16.31	3.5	15.46
	Near-field	0.4g	7.08	3.5	15.78
		0.6g	18.07	3.5	15.95
Second Aftershock	Far-field	0.4g	6.55	3.5	15.51
		0.6g	15.11	3.5	17.43
	Near-field	0.4g	9.96	3.5	14.85
		0.6g	21.9	3.5	17.13

Residual Displacement after each shock

Earthquake Type	Residual Displacement (cm)			
	Near Field		Far Field	
	0.4g	0.6g	0.4g	0.6g
Mainshock	3.22	14.27	2.28	13.69
First Aftershock	7.04	30.07	4.61	27.4
Second Aftershock	14.58	50.1	8.56	39.75



Conclusions

- The first three mode shapes of the dry Dam and Dam with reservoir water remain almost the same, although the values of natural frequencies of the two cases differ.
- For both far-field and near-field earthquakes, at a PGA level of 0.4g, not much inelastic effect is exhibited in the mainshock; however, in subsequent aftershocks, a significant inelastic effect is observed.
- For the level of PGA 0.6g, a significant inelastic effect is exhibited in the mainshock, which subsequently increases in the aftershocks for both near-field and far-field earthquakes.
- In this study, Damages in the Dam are concentrated only in the neck region; nowhere else, the damage is observed for the earthquakes considered.
- For the PGA level of 0.4g, the damage occurs only at downstream of the neck portion during the mainshock, which extends towards the upstream side after the two subsequent aftershocks. For a higher level of PGA, i.e., 0.6g, the damage occurs at the neck portion across the downstream to the upstream side of the dam in the mainshock. The extent of the damage increases with the following two aftershocks.
- Residual displacement considerably increases after each shock and the level of PGA.



Thank you!

Any questions?



USE OF THREE-DIMENSIONAL NUMERICAL ANALYSES IN SEISMIC DESIGN OF EARTH EMBANKMENTS

Masood H. Kafash, Ph.D., P.E.

Lisa Yenne, P.E.

AECOM

Three-dimensional (3D) analysis

- *In last decades, the utilization of limit equilibrium, finite element, and/or finite difference methods for three-dimensional analysis has become a valuable tool for seismic design and analysis of earth and rockfill embankments*
- *However, many of industry and regulatory requirements are based on 2D analysis*

2014 Mount Polley Dam Failure

- Peak Undrained
 $S_u/p' = 0.25$
 (back calculated 0.22 to 0.27 to
 get FOS=1)

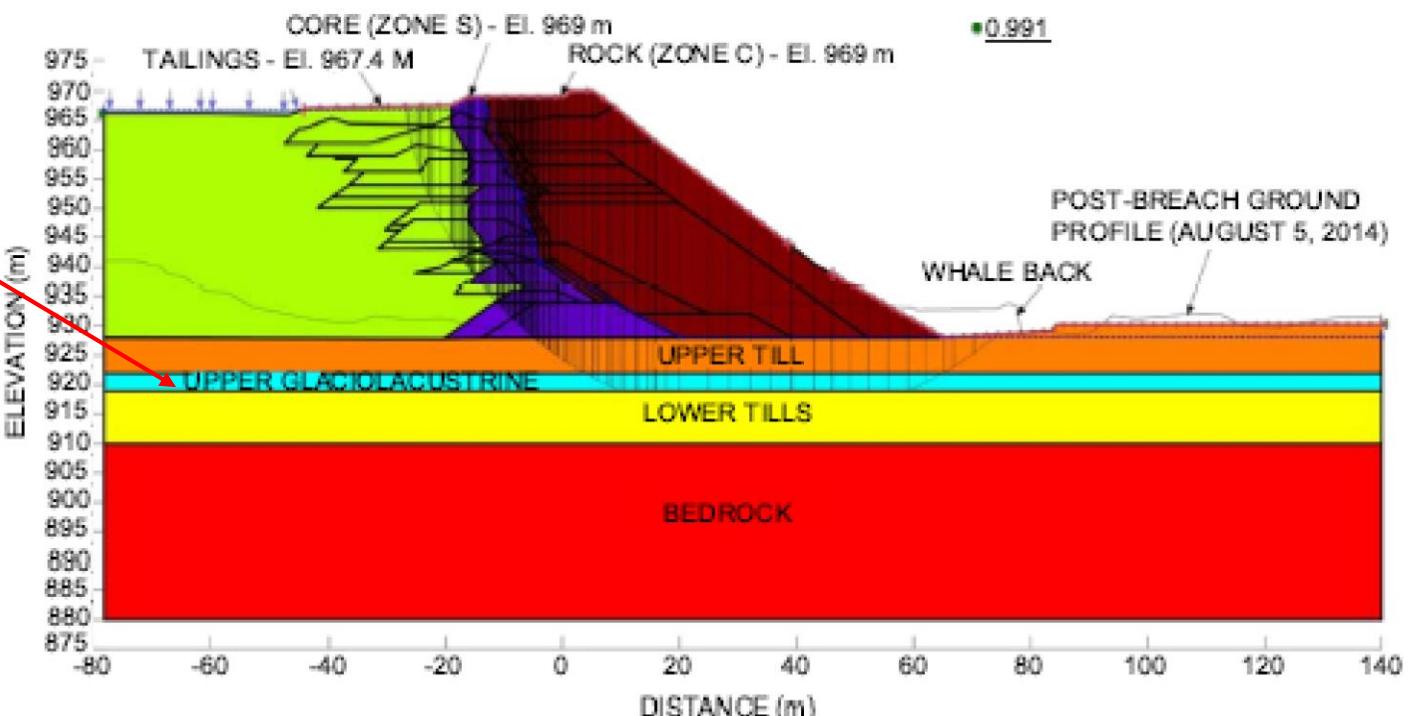
SECTION 3 - AUGUST 2014 AT FAILURE

Expert panel report (2015)

MATERIAL PROPERTIES:

CORE (ZONE S): MODEL: MOHR-COULOMB, UNIT WEIGHT: 20.5 kN/m³, 35°
 ROCK (ZONE C): MODEL: SHEAR/NORMAL FN., UNIT WEIGHT: 22 kN/m³
 TAILINGS: MODEL: MOHR-COULOMB, UNIT WEIGHT: 18 kN/m³, PHI: 30°
 UPPER TILL: MODEL: MOHR-COULOMB, UNIT WEIGHT: 21 kN/m³, PHI: 35°
 UPPER GLACIOLACUSTRINE: MODEL: S=F(OVERBURDEN), UNIT WEIGHT: 20 kN/m³, TAU/SIGMA RATIO: 0.27
 LOWER TILLS: MODEL: BEDROCK (IMPERMEABLE)
 BEDROCK: MODEL: BEDROCK (IMPERMEABLE)

ANALYSIS METHOD: MORGENTHORN-PRICE



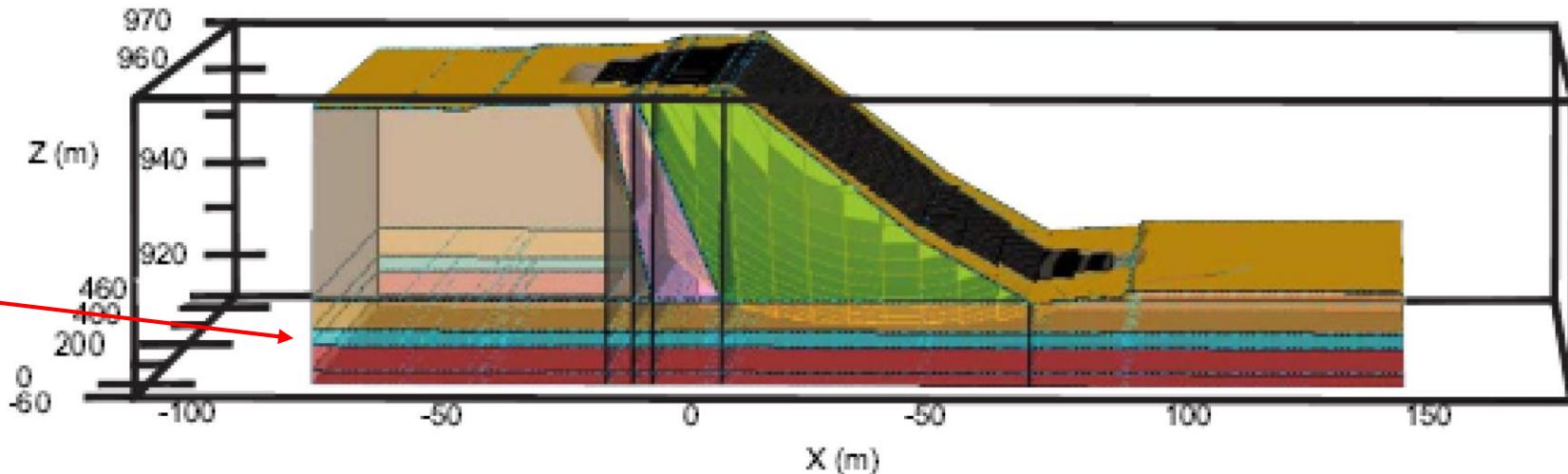
2014 Mount Polley Dam Failure

- 3D LE Analysis using Peak S_u/p' of 0.25
- 3D FOS=1.3

CALCULATION METHOD: M-P
SEARCH METHOD: ENTRY AND EXIT
FS: 1.288
CENTRE POINT: X: 37.591 Y: 200.000 Z: 981.233
ELLIPSOID ASPECT RATIO: 2.600, RX:70.168

Expert panel report (2015)

MODEL

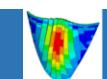


MATERIAL



MATERIAL PROPERTIES

MOHR COULOMB	UNIT WEIGHT = 18 (kN/m^3)	PHI=30°
MOHR COULOMB	UNIT WEIGHT = 21 (kN/m^3)	PHI=35°
VERTICAL STRESS RATIO	UNIT WEIGHT = 20 (kN/m^3)	RATIO=0.27
BEDROCK		
MOHR COULOMB	UNIT WEIGHT = 20.5 (kN/m^3)	PHI=35°
SHEAR NORMAL FUNCTION	UNIT WEIGHT = 22 (kN/m^3)	



Example of Recommended 3D FOS Values by Stark and Ruffing (2017)

Soil Strength Uncertainty	Imminent Threat to Human Life	Potential for Major Construction or Environmental Impact	Recommended Minimum 2D Factor of Safety	Minimum 3D Factor of Safety
small	low	low	1.3	1.4
small	high	high	1.5	1.7
small	low	high	1.3	1.5
small	high	low	1.5	1.7
large	low	low	1.5	1.7
large	high	high	2.0	2.3
large	low	high	1.5	1.7
large	high	low	2.0	2.3

How to incorporate the 3D effects in design

- Identify the contributors to the 3D FOS
- Evaluate the 3D seismic performance of the structure
- Perform sensitivity analysis and incorporate it in a risk informed design

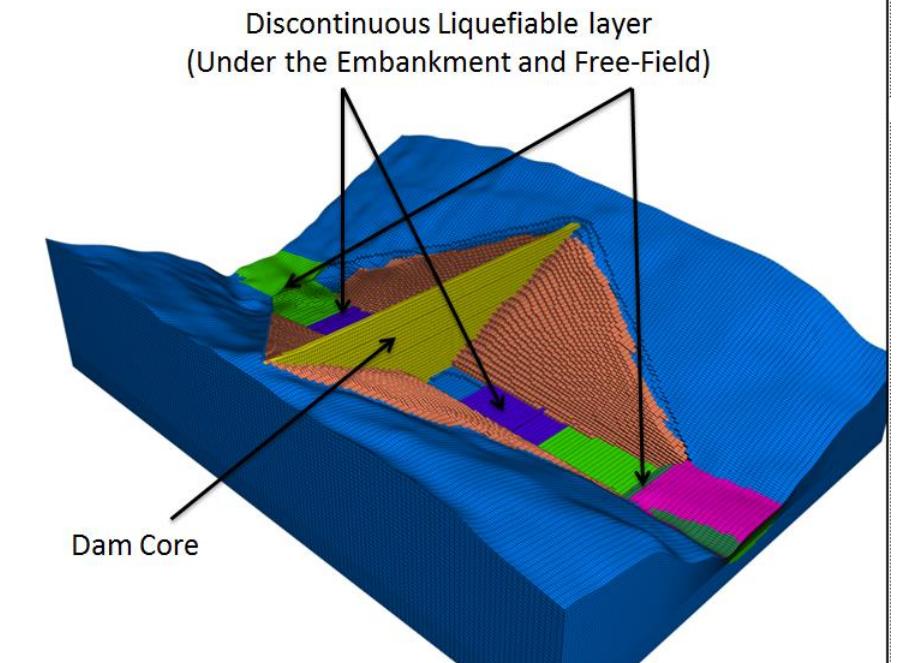
Map View with Boring Locations and 2D Cross Sections



Internal Geometry Foundation Conditions

- Embankment dam core founded directly on Bedrock.
- Upstream and Downstream shells founded on:
 - Left and Right Abutment Foundation (Colluvium)
 - Soft sandy CL; v. dense SM; and dense SC to CL
 - Valley Centerline Foundation (Alluvium)
 - Loose ML/SM
 - Dense to v. dense SM with gravel and GM with sand
- Free Field Foundation (Alluvium)
 - Soft / very loose mixtures of saturated ML/CL, SC, and SM
 - V. loose to v. dense SM and GM

Zone	Color by:	Group	Any
BEDROCK			
COLLUVIUM			
CORE			
DEEP_ALLUVIUM			
EMBANKMENT			
FREE_FIELD_ALLUVIUM			
SURFACE_SOIL			
UPPER_ORGANIC_ALLUVIUM			

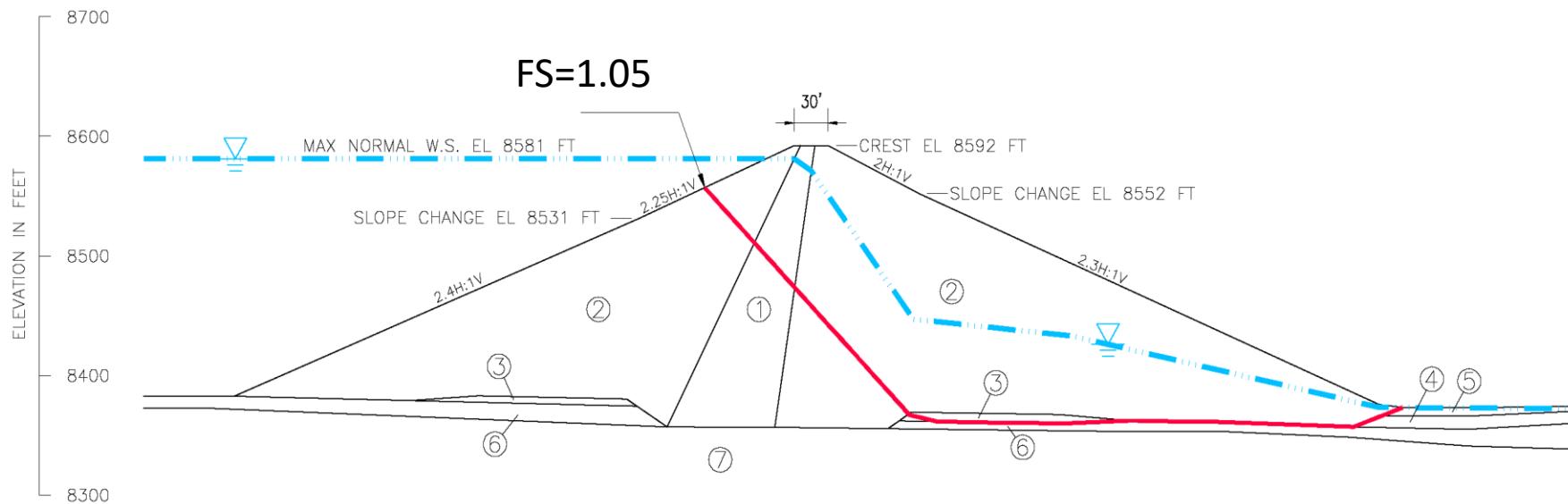


2D Post-Earthquake Limit Equilibrium Analyses

Valley Section



NO.	MATERIAL DESCRIPTION	UNIT WEIGHT (pcf)	DRAINED STRENGTH		POST-EARTHQUAKE STRENGTH	
			COHESION (psf)	FRICITION ANGLE (degrees)	COHESION (psf)	FRICITION ANGLE (degrees)
1	CORE (SILTY CLAY)	133	0	26.5	0	22 (3)
2	EMBANKMENT SHELL (SILTY SAND AND GRAVEL)	140	0	37	—	—
3	UPPER ORGANIC ALLUVIUM – BENEATH EMBANKMENT	125	—	—	0	6 (4)
4	UPPER ORGANIC ALLUVIUM – FREE FIELD	125	—	—	0	4 (4)
5	SURFACE SOILS	130	0	35	—	—
6	DEEP ALLUVIUM	143	0	38	—	—
7	BEDROCK (SANDSTONE)	140	10,000	45	—	—

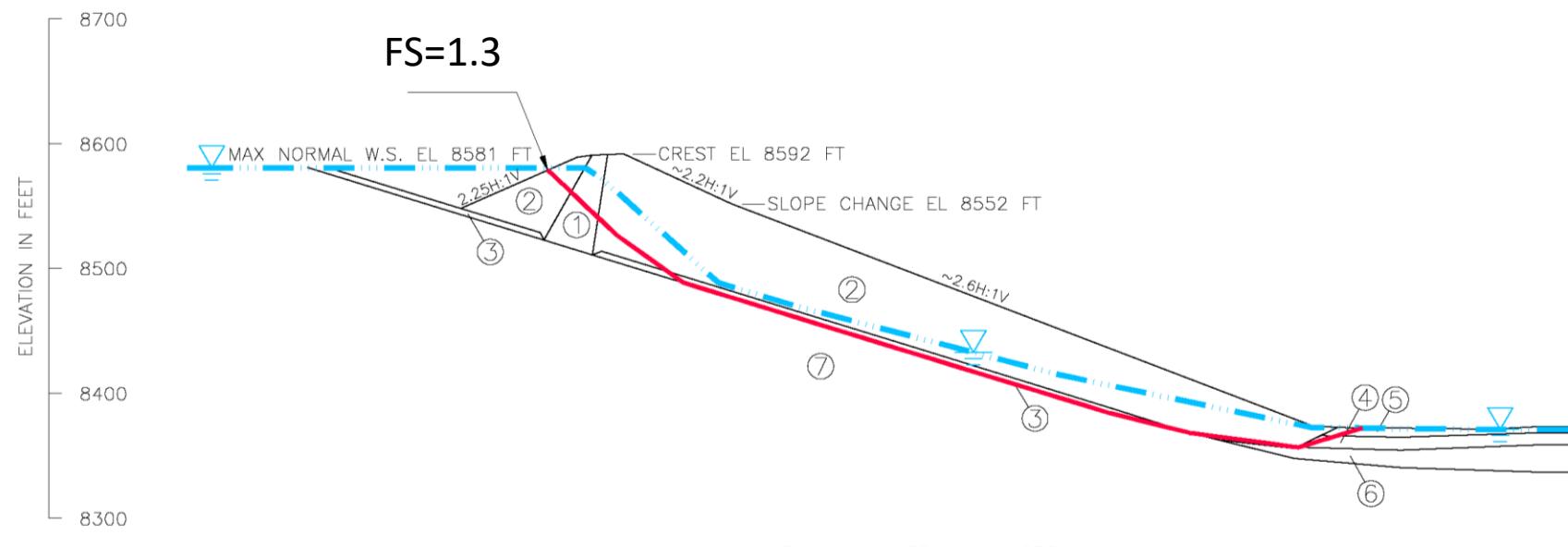


2D Post-Earthquake Limit Equilibrium Analyses

Abutment Section



NO.	MATERIAL DESCRIPTION	UNIT WEIGHT (pcf)	DRAINED STRENGTH		POST-EARTHQUAKE STRENGTH	
			COHESION (psf)	FRICITION ANGLE (degrees)	COHESION (psf)	FRICITION ANGLE (degrees)
1	CORE (SILTY CLAY)	133	0	26.5	0	22 (3)
2	EMBANKMENT SHELL (SILTY SAND AND GRAVEL)	140	0	37	—	—
3	ABUTMENT COLLUVIUM	125	0	35	0	26 (3)
4	UPPER ORGANIC ALLUVIUM – FREE FIELD	125	—	—	0	4 (4)
5	SURFACE SOILS	130	0	35	—	—
6	DEEP ALLUVIUM	143	0	38	—	—
7	BEDROCK (SANDSTONE)	140	10,000	45	—	—



FLAC3D 5.01

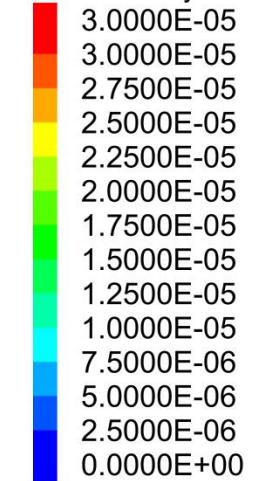
©2014 Itasca Consulting Group, Inc.

Step 7029

12/2/2015 2:54:00 PM

Contour of Max. Shear Strain Rate

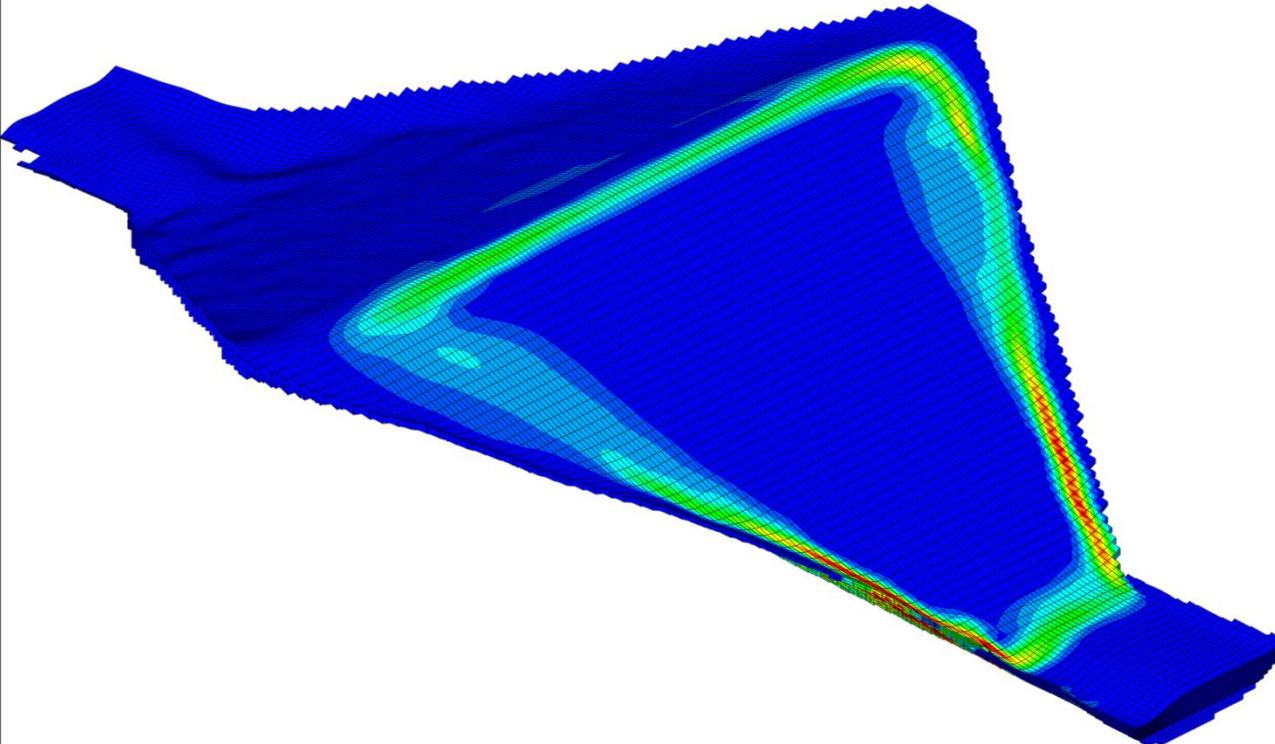
Calculated by: Volumetric Averaging



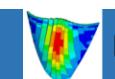
3-D Post-earthquake Slope Stability FOS Calculation using strength reduction technique



Critical failure mechanism illustrated by contours of
shear strain rate



FOS = 1.7

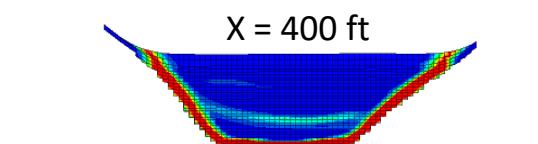
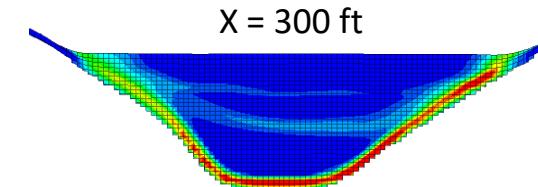
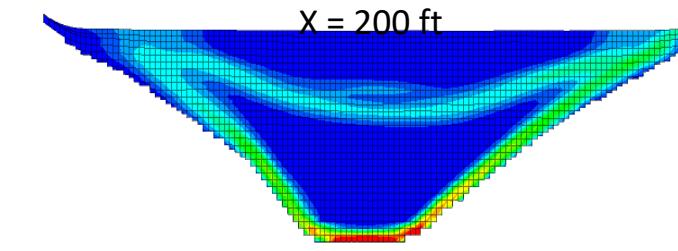
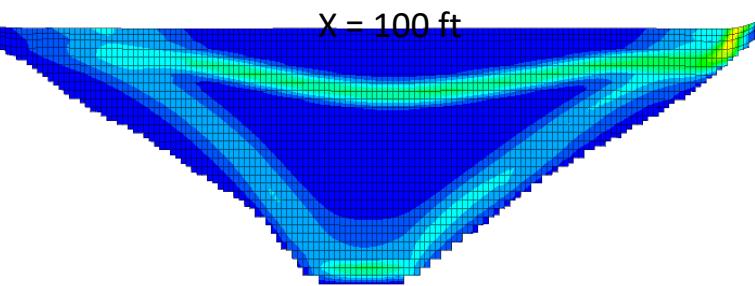
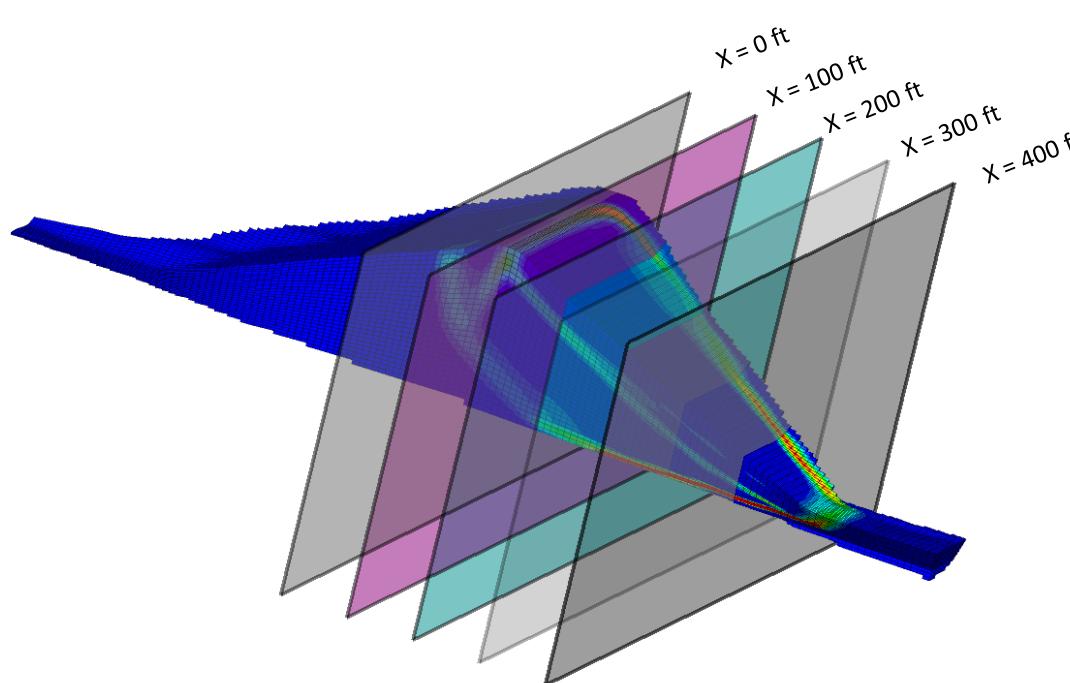
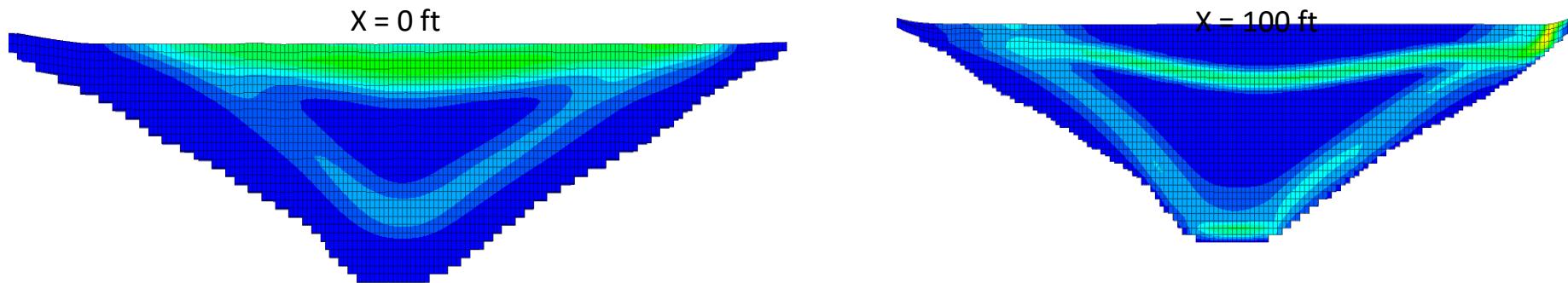


BCI6 - SEISMIC ANALYSIS OF DAMS AND LEVEES

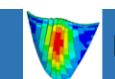
Shear Strain Rate Contours

3-D Post-earthquake Slope Stability FOS Calculation using strength reduction technique

Critical failure mechanism illustrated by contours of shear strain rate



FOS = 1.7



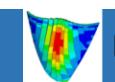
How to incorporate the 3D effects in design

- **Identify the contributors to the 3D FOS**
- Evaluate the 3D seismic performance of the structure
- Perform sensitivity analysis and incorporate it in a risk informed design

Steps to Identify the Contributor to 3D FOS

- From side shear resistance of the failure surface
- From change in condition including geometry, subsurface condition, and/or material properties
- From change in the assignment of material properties

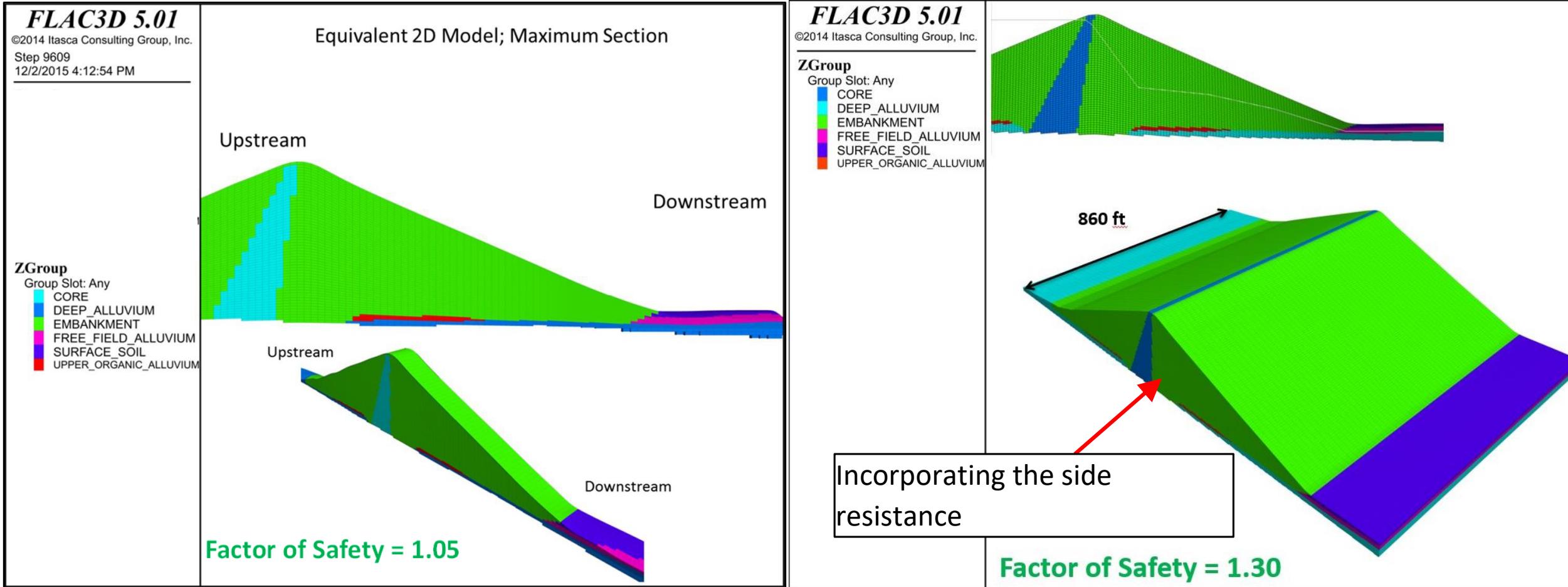
Fredlund et al. 2017



Steps to Identify the Contributor to 3D FOS

- **From side shear resistance of the failure surface**
- From change in condition including geometry, subsurface condition, and/or material properties
- From change in the assignment of material properties

From side shear resistance of the failure surface

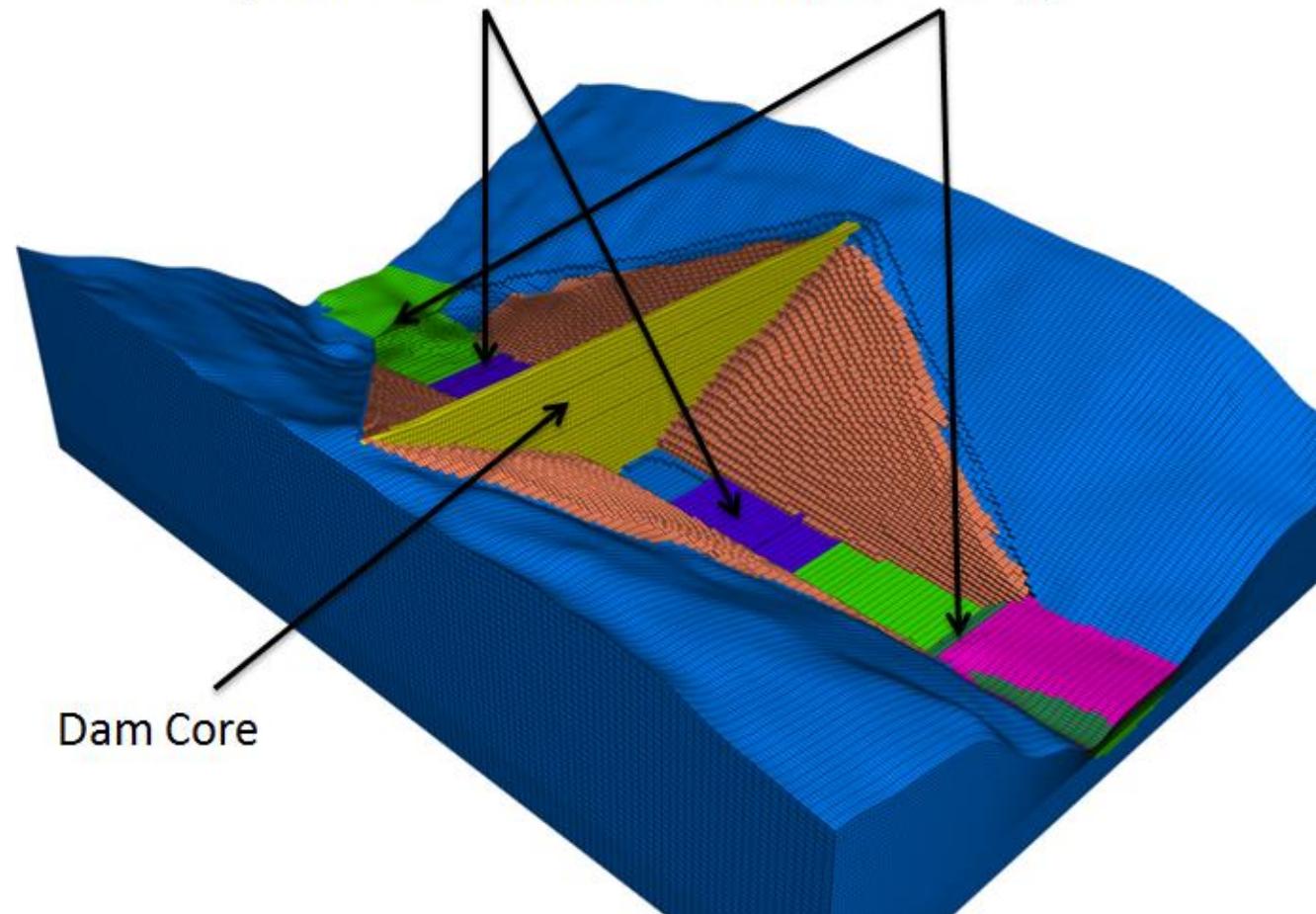


Steps to Identify the Contributor to 3D FOS

- From side shear resistance of the failure surface
- **From change in condition including geometry, subsurface condition, and/or material properties**
- From change in the assignment of material properties

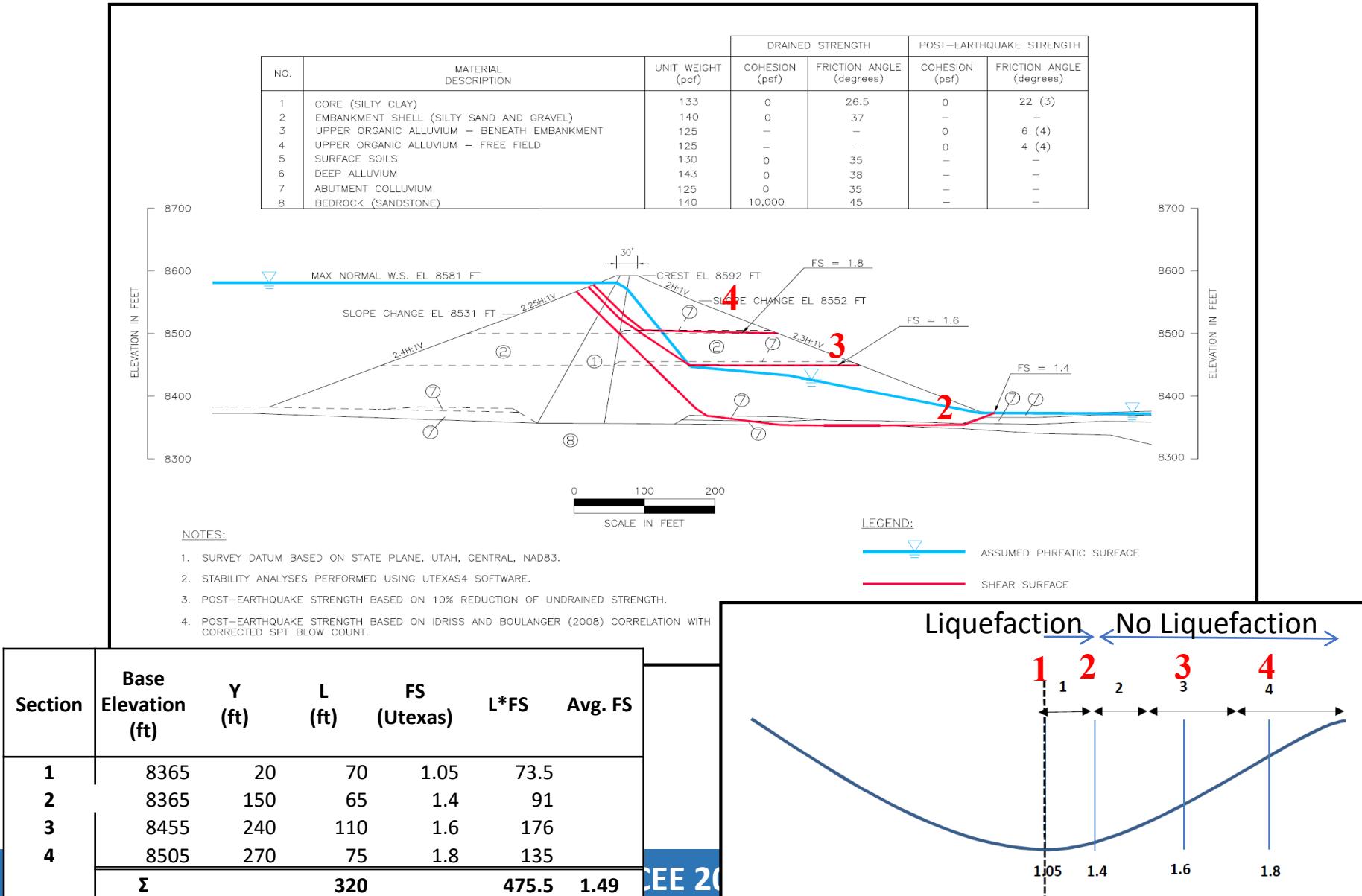
Change in Condition

Discontinuous Liquefiable layer
(Under the Embankment and Free-Field)



Zone	
Color by: Group	Any
BEDROCK	
COLLUVIUM	
CORE	
DEEP_ALLUVIUM	
EMBANKMENT	
FREE_FIELD_ALLUVIUM	
SURFACE_SOIL	
UPPER_ORGANIC_ALLUVIUM	

2D Weighted Average of Factor of Safety



Steps to Identify the Contributor to 3D FOS

- From side shear resistance of the failure surface
- From change in condition including geometry, subsurface condition, and/or material properties
- **From change in the assignment of material properties**

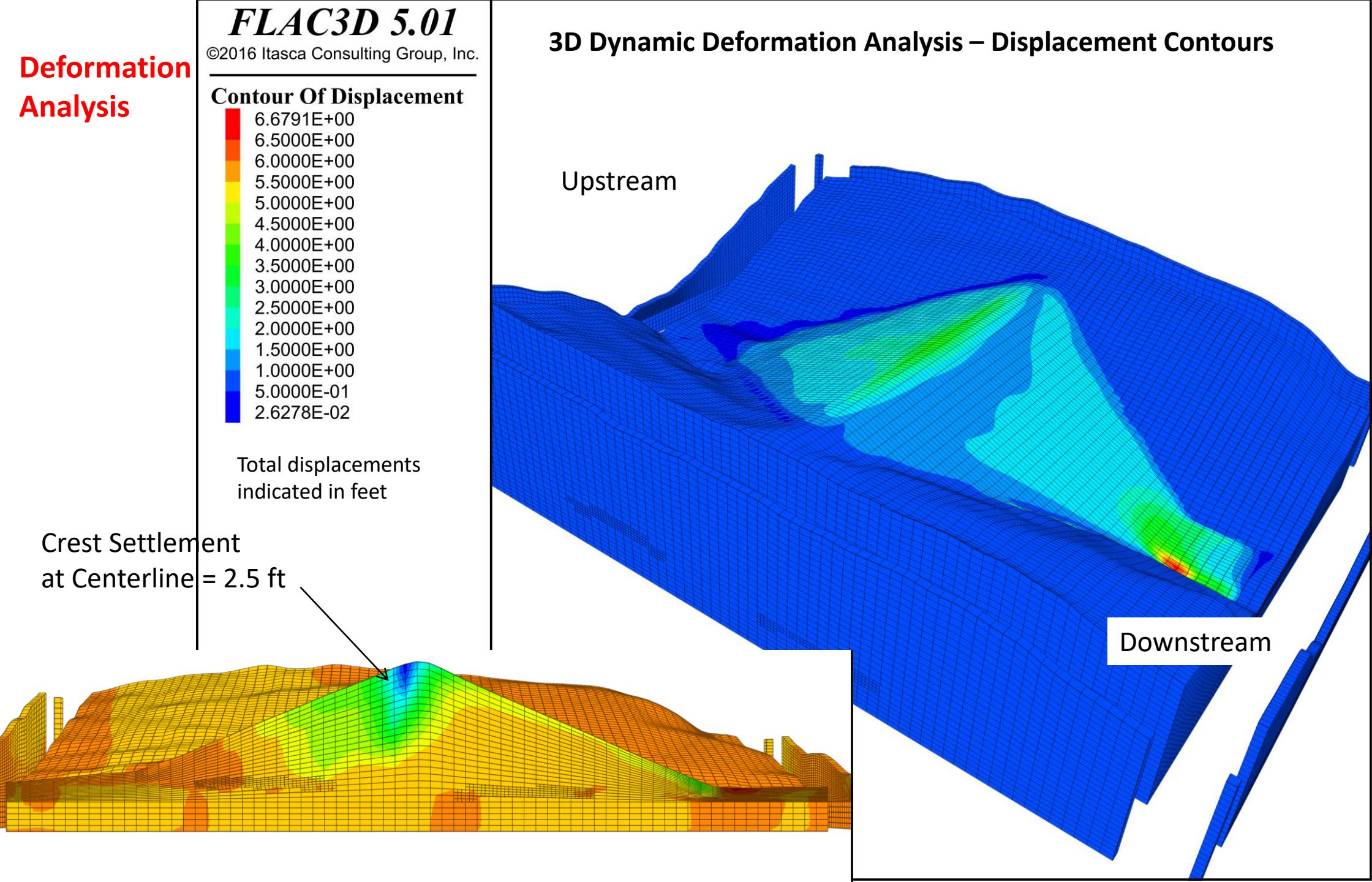
From change in the assignment of material properties

- The other source of increase in the FOS could be due to:
 - **how the properties are assigned in 3D vs 2D**

How to incorporate the 3D effects in design

- Identify the contributors to the 3D FOS
- **Evaluate the 3D seismic performance of the structure**
- Perform sensitivity analysis and incorporate it in a risk informed design

Deformation Analysis



How to incorporate the 3D effects in design

- Identify the contributors to the 3D FOS
- Evaluate the 3D seismic performance of the structure
- **Perform sensitivity analysis and incorporate it in a risk informed design**

Perform Sensitivity Analysis and Incorporate it in a Risk Informed Design

- Document uncertainties in design
- Perform sensitivity analysis:
 - Input parameters
 - Geometry
 - Seismic loadings
- Consider all the factors in your risk informed design

Time History		Polarity ²	Crest Displacements (feet) ³	
RSN ¹	Earthquake and Station Name ¹		X-direction ⁴	Z-direction ⁵
10,000-Year Return Interval Time Histories (PGA = 0.45g)				
178	1979 IMPERIAL VALLEY EC ARRAY #3 (230)	Positive	-0.48	0.60
		Negative	-0.51	-0.67
802	1989 LOMA PRIETA SARATOGA-ALOHA AVE (000)	Positive	-0.16	-0.31
		Negative	-0.60	-0.53
987	1994 NORTHRIDGE CENTINELA ST (245)	Positive	-0.54	-0.53
		Negative	-0.23	-0.41
MCE Event Time Histories (PGA = 0.82g)				
178	1979 IMPERIAL VALLEY EC ARRAY #3 (230)	Negative	-2.45	-2.49

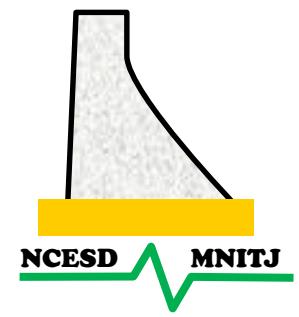
Summary and Conclusion

- Build the confidence on the calculated 3D FOS by performing step-by-step analysis
- Perform 3D seismic deformation analysis and consider both FOS and PBD in the design
- Use the 3D analysis results by considering all the uncertainties and risk factors in the design



Thank you!

Any questions?



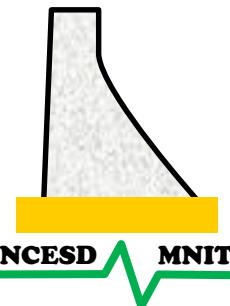
3D SEISMIC ANALYSIS OF ARCH DAM FOR RANDOM GROUND MOTION

D Khandelwal, S D Bharti, M K Shrimali, J N Arlekar, Nishant Roy

Malaviya National Institute of Technology Jaipur, India

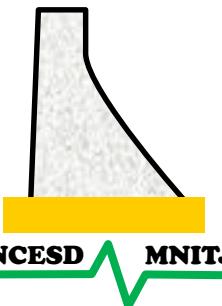
Introduction

- Majority of the studies on seismic response of dams considers earthquakes as deterministic process
- Studies dealing with dam-reservoir system with earthquake as random process are rare
- Challenging to conduct random vibration analysis in frequency domain
- Feasibility of spectral analysis using transfer function approach for arch dam-reservoir system needs evaluation
- Present study emphasizes on a hybrid technique: spectral analysis and transfer function

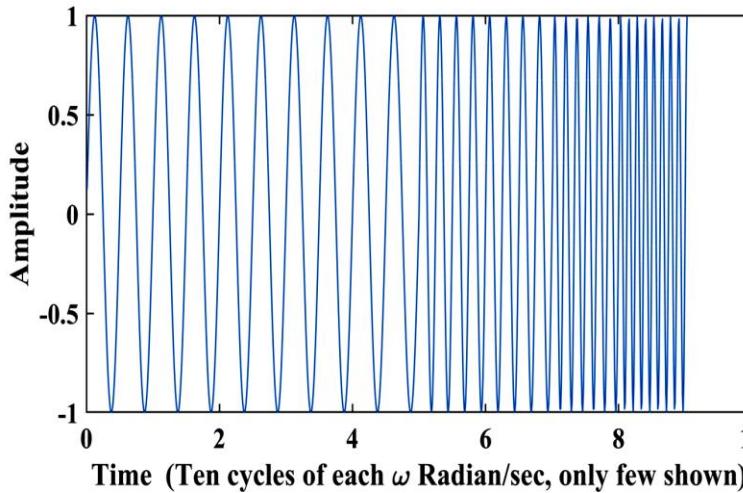


Problem Statement

- Frequency domain random vibration analysis of Morrow Point Arch Dam
- 3D model of arch dam with full reservoir
- Earthquake motion treated as random process, represented by PSDF, and applied at the base
- Response obtained by frequency domain spectral analysis compared with response history analysis
- 3 engineering demand parameters: maximum arch stress, maximum cantilever stress and peak top displacement



Random Vib Anal: (Spec Anal using Transfer Function)



Apply $a_g(t)$ at dam and reservoir boundaries

Find response history of analysis $A(t)$ (Steady State response) by dynamic time domain analysis (using ABAQUS)

$$TR(\omega) = \frac{A(\omega)}{a(\omega)}$$

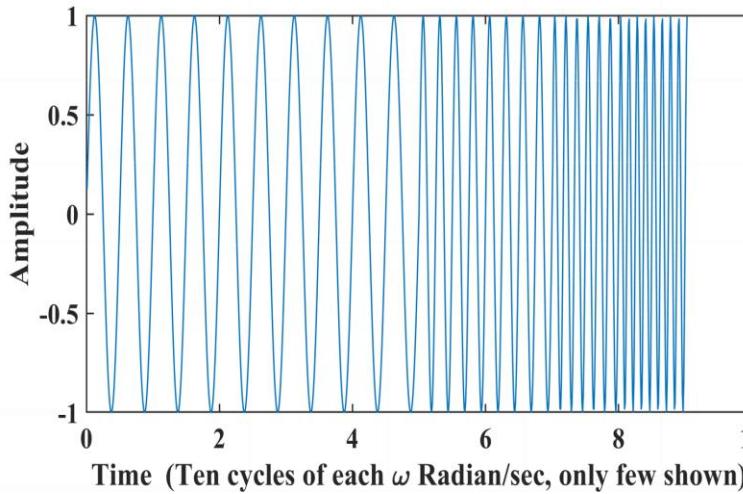
Developed a Unit Sinusoidal Signal $a_g(t)$ having frequencies (ω_j) from 2 Hz to 10 Hz (10 cycles for each frequency)

For the dry dam, a rigorous spectral analysis is possible using $S_r(\omega) = h(\omega)S_g(\omega)h(\omega)^*$

$h(\omega)$ is the frequency response function of the response obtained from modal analysis



Random Vib Anal: (Spec Anal using Transfer Function)



Apply $a_g(t)$ at dam and reservoir boundaries
Find response history of analysis $A(t)$ (Steady State response) by dynamic time domain analysis (using ABAQUS)

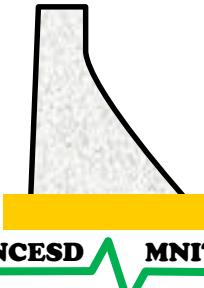
$$TR(\omega) = \frac{A(\omega)}{a(\omega)}$$

Developed a Unit Sinusoidal Signal $a_g(t)$ having frequencies (ω_j) from 2 Hz to 10 Hz (10 cycles for each frequency)

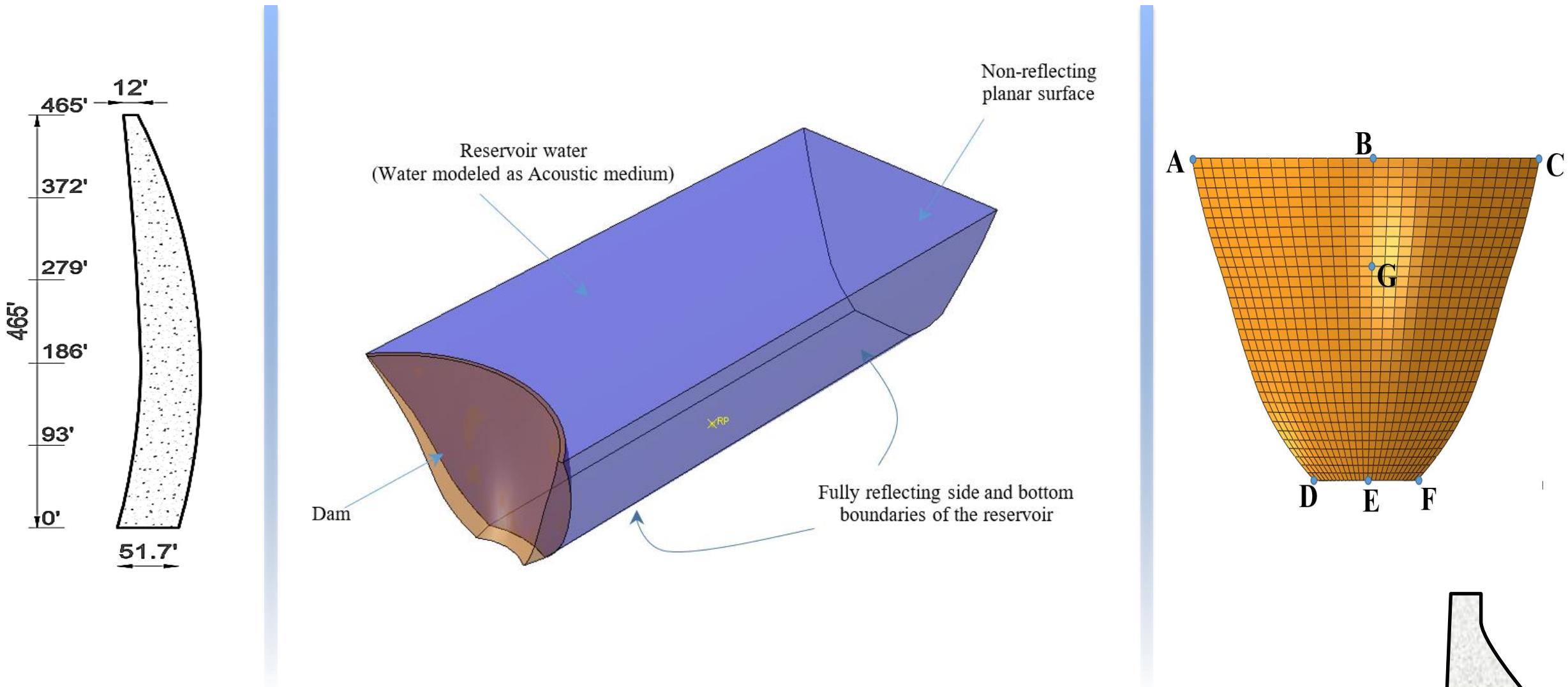
Plot curve between square of $|TR|$ and ω

PSDF of the interested response quantity $S(\omega)$
 $S(\omega) = |TR(\omega)|^2 S_{\ddot{x}_g}(\omega)$
 $S_{\ddot{x}_g}(\omega)$ is the PSDF of excitation

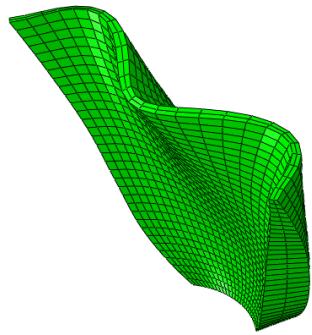
Find RMS and Mean Peak values of response quantities



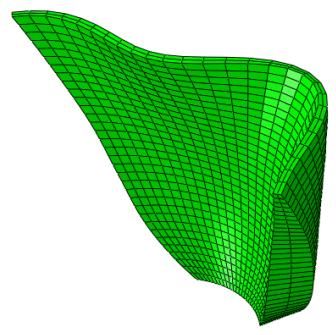
Model of Morrow Point Arch Dam



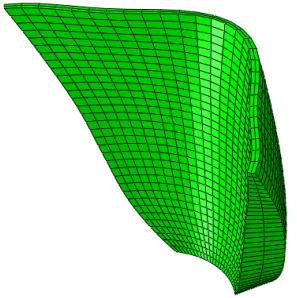
Mode Shapes and Modal Frequency



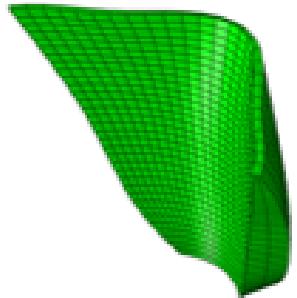
Mode 1



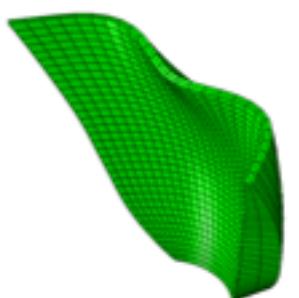
Mode 2



Mode 3



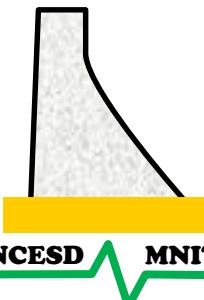
Mode 4



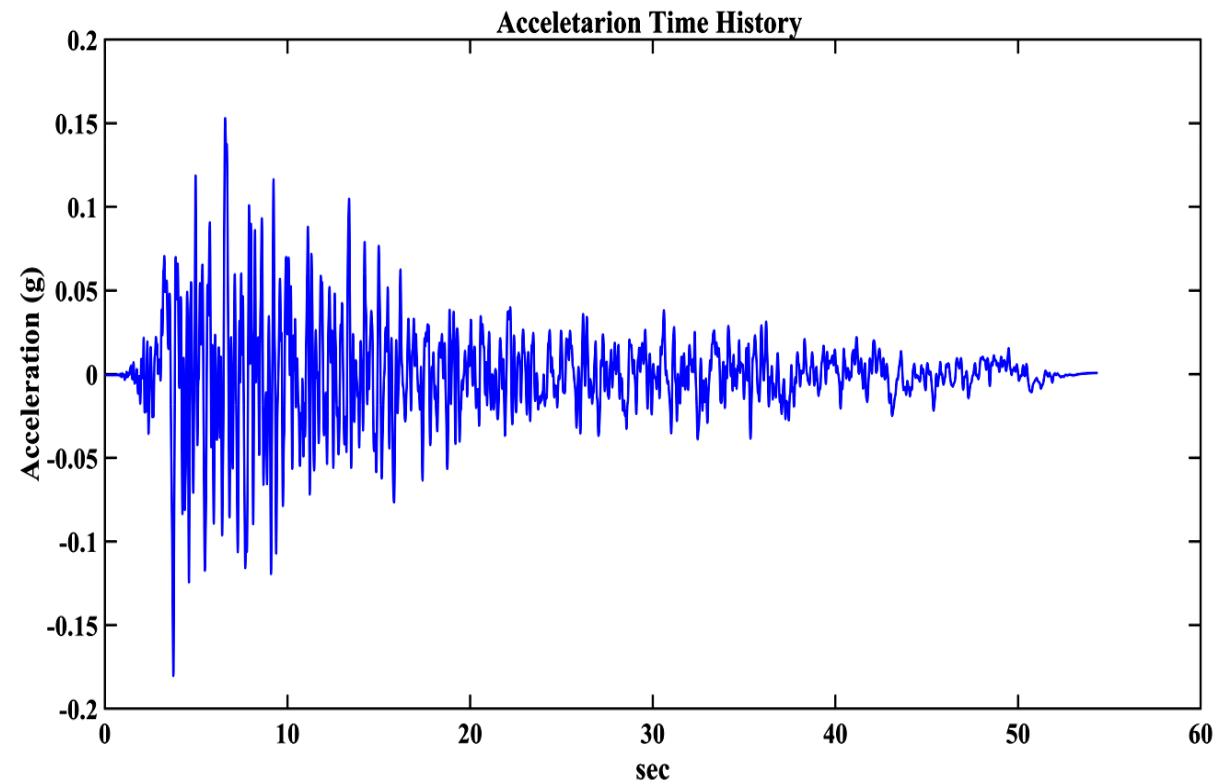
Mode 5

Modal Frequency (Hz)	
With Reservoir	Without Reservoir
2.84	3.62
2.97	4.14
3.24	5.81
3.71	6.69
4.48	7.13

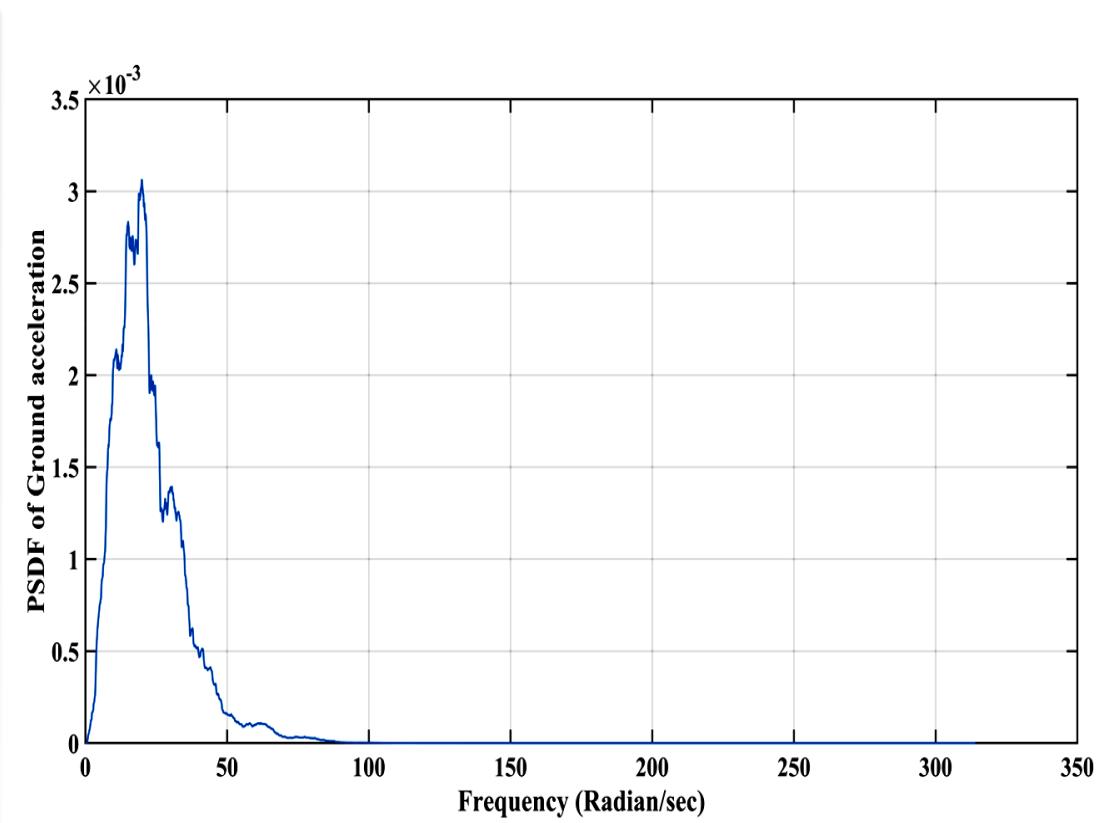
Water-structure effect reduces the natural frequency of the dam



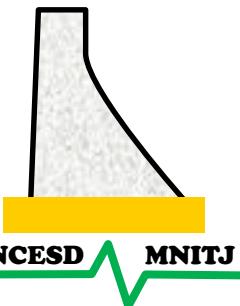
Earthquake Motion (treated as ergodic process)



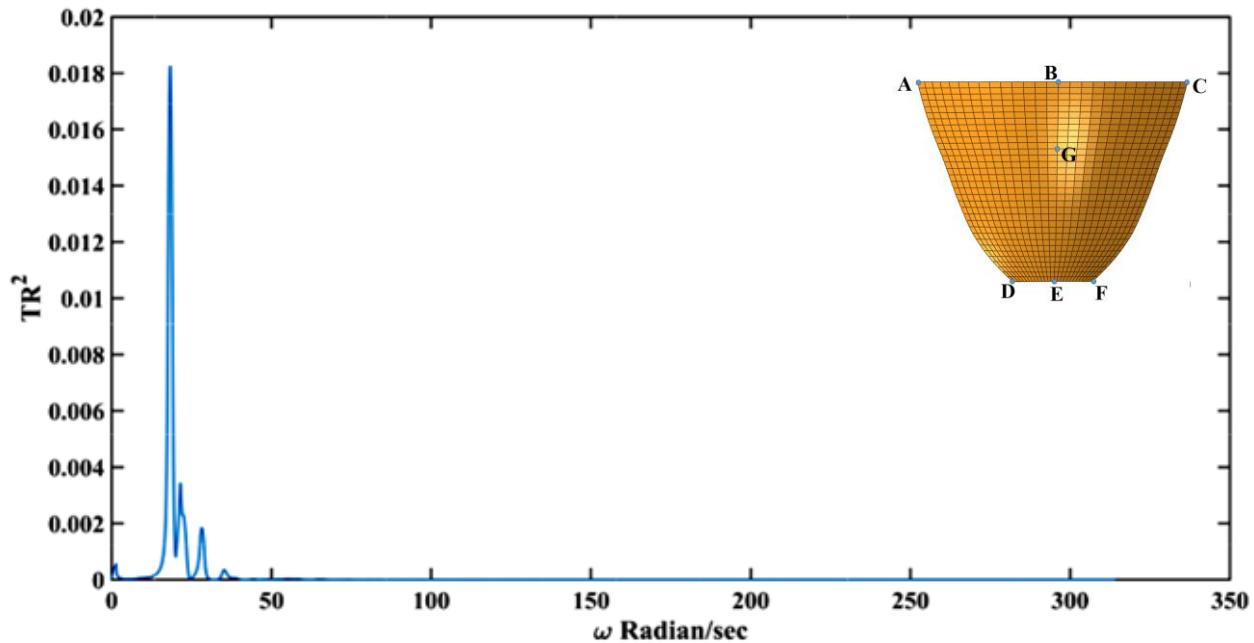
Earthquake applied in upstream–downstream direction



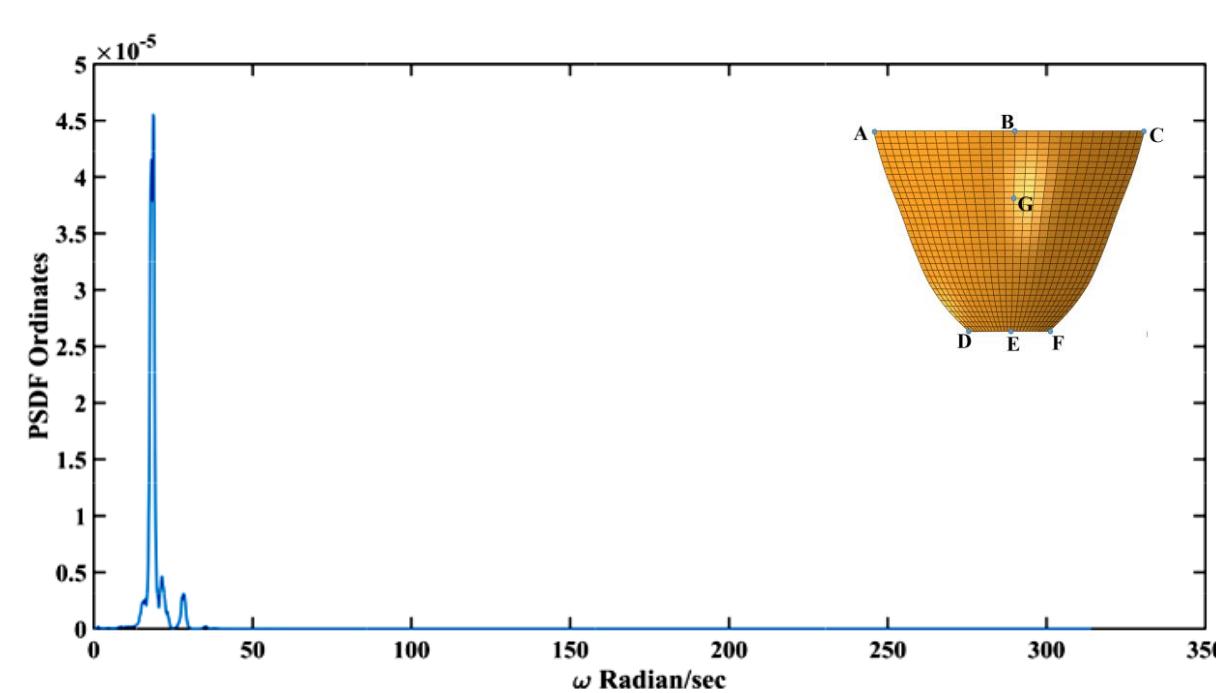
PSDF obtained after processing in MATLAB



Transfer Function and PSDF



Square of Transfer Function of Displacement at Point B



PSDF of displacement at point B

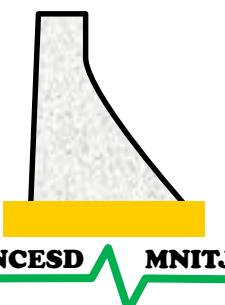
Spectral Analysis Direct Method: 0.0355 m
 Response History Method: 0.0408 m



Comparison of Response (absolute mean peak)

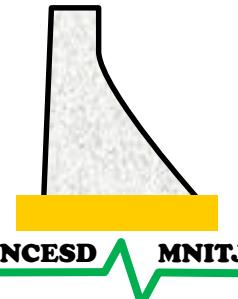
Point	Arch Stress (MPa)	
A	0.902	1.001
B	3.663	4.207
C	0.902	1.023
D	0.241	0.268
E	0.407	0.459
F	0.241	0.268
G	3.424	0.459

Point	Cantilever Stress (MPa)	
A	0.210	0.240
B	0.155	0.172
C	0.210	0.238
D	0.748	0.842
E	2.193	2.434
F	0.748	0.915
G	0.600	0.686



Conclusions

- 3D dam-reservoir system of Morrow Point Arch dam considered and the earthquake is treated as ergodic process
- Feasibility of spectral analysis using transfer function approach for arch dam-reservoir evaluated
- Engineering demand parameters considered are maximum arch stress, maximum cantilever stress and peak top displacement
- Response history analysis and frequency domain random vibration analysis are compared for the engineering demand parameters
- Results of spectral analysis using transfer function approach compare well with response history analysis





Thank you!

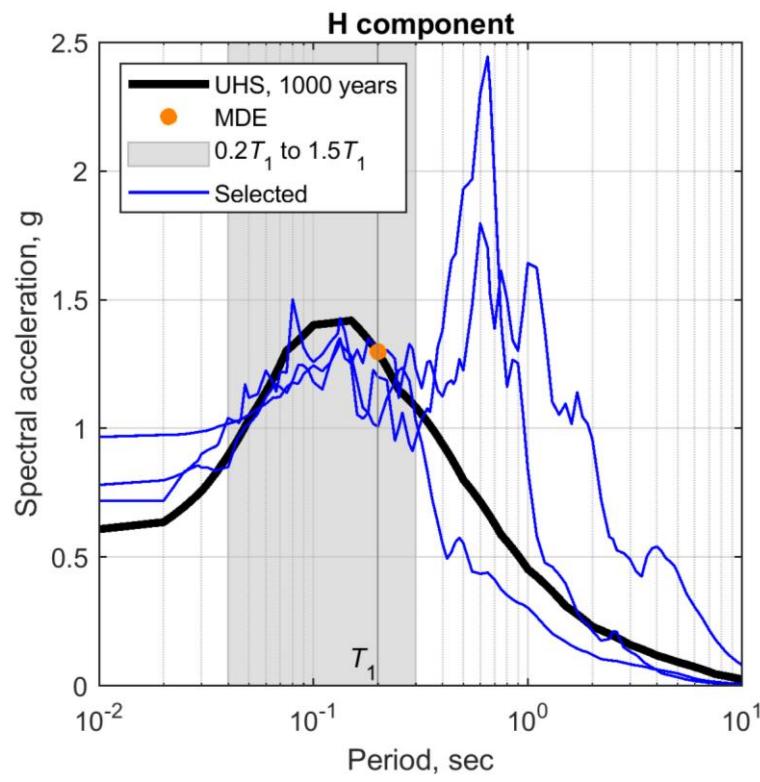
Challenges in developing vertical hazard for seismic analysis of concrete dams

N. S. Kwong ¹, S. Rezaeian ¹, A. J. Makdisi ¹, N. Luco ¹

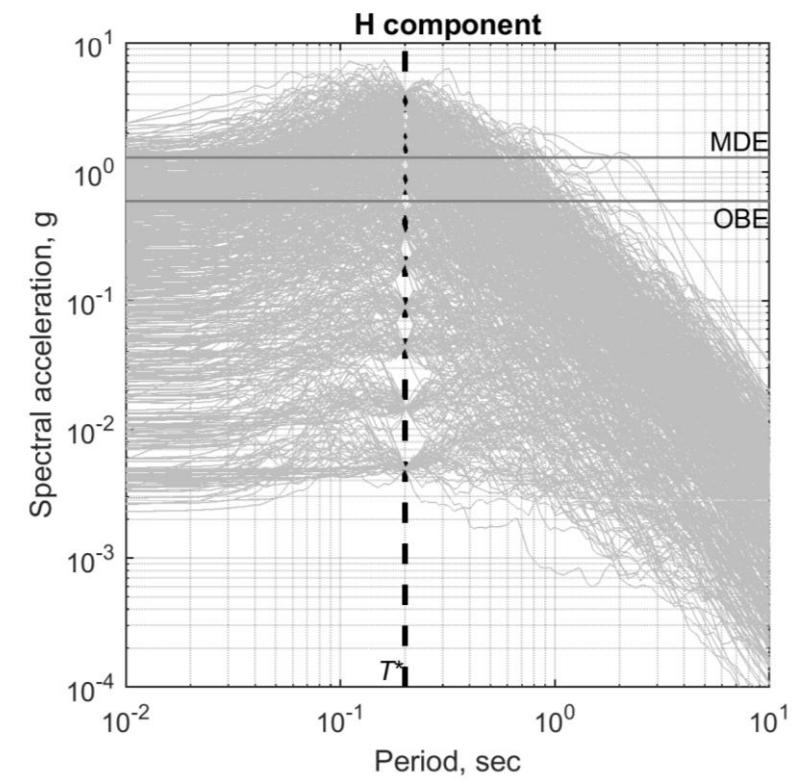
¹ U. S. Geological Survey, Golden CO, USA

Context

Building code evaluation



Seismic risk analyses



Problem statement

- How to develop vertical (V) hazard curves for any tectonic regime while including epistemic uncertainties?

3 approaches

Direct

- Conduct PSHA with GMMs for V component of GM

Indirect

- Combine GMM for H component of GM with a GMM for the V/H ratio

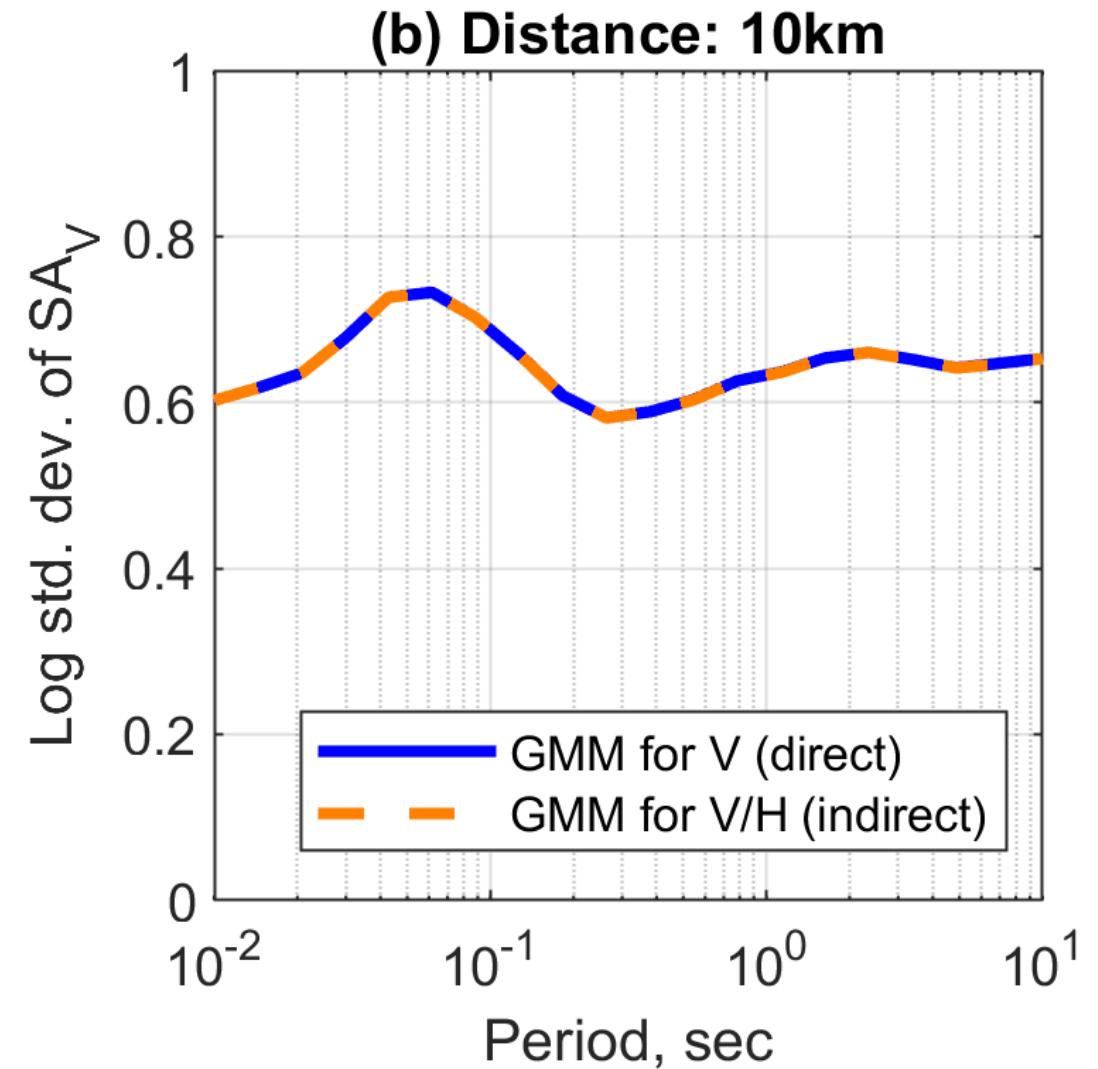
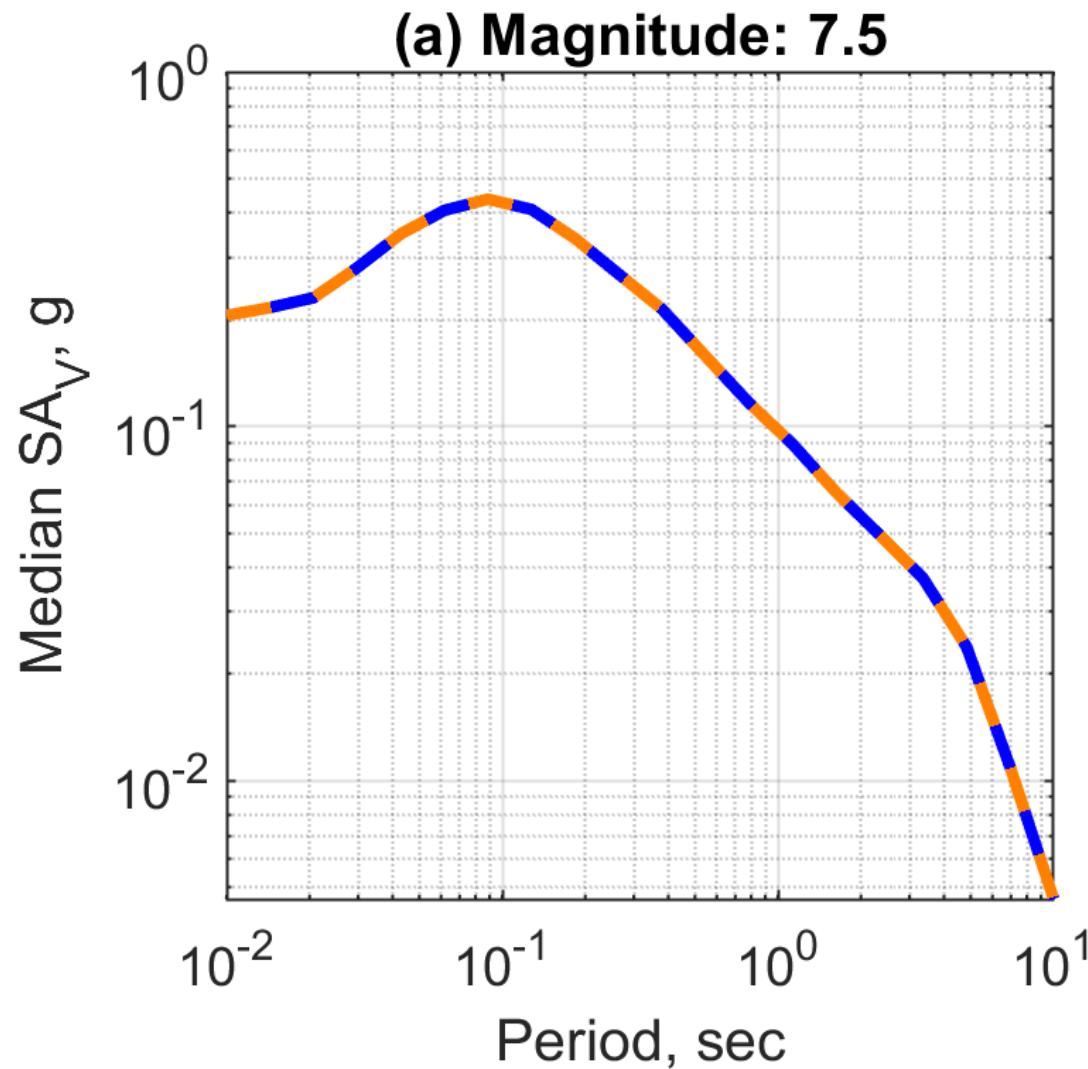
GMSM

- Derive V hazard curves from multiple suites of selected multicomponent GM time series that are consistent with H hazard

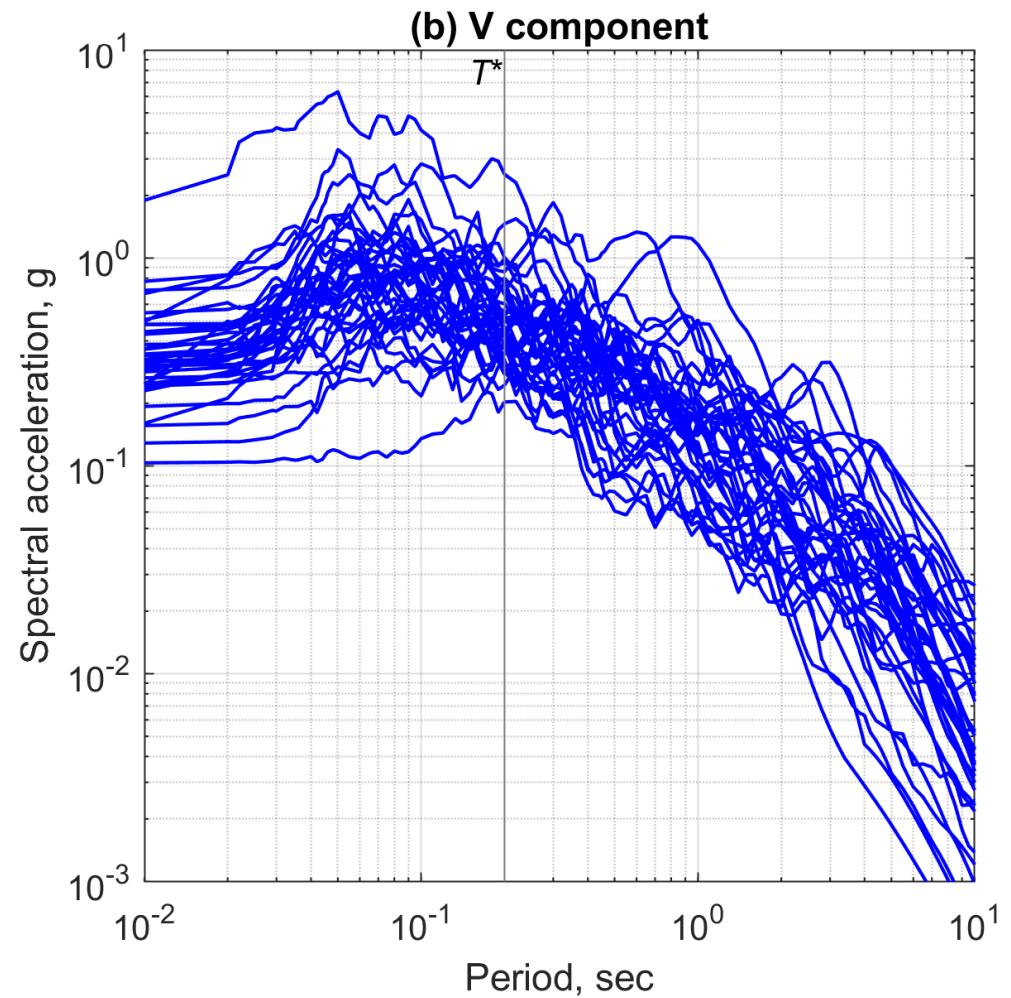
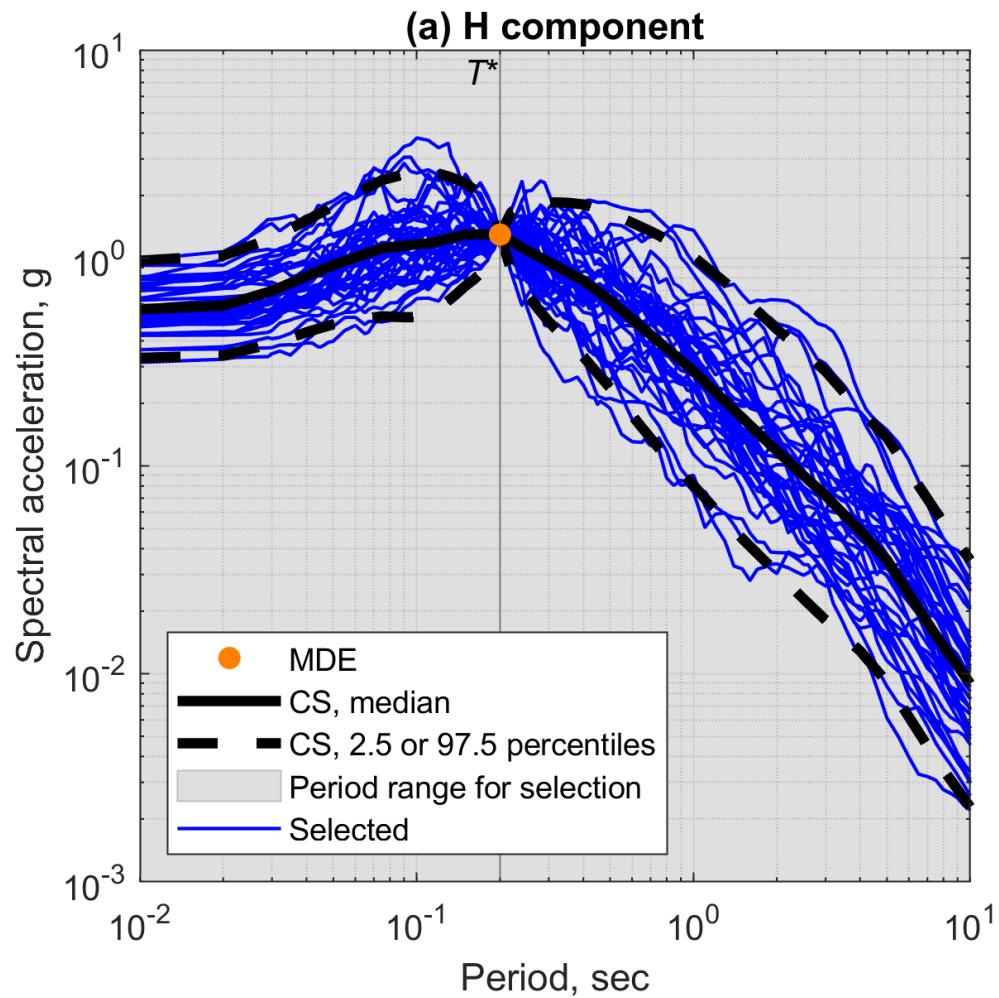
Case study

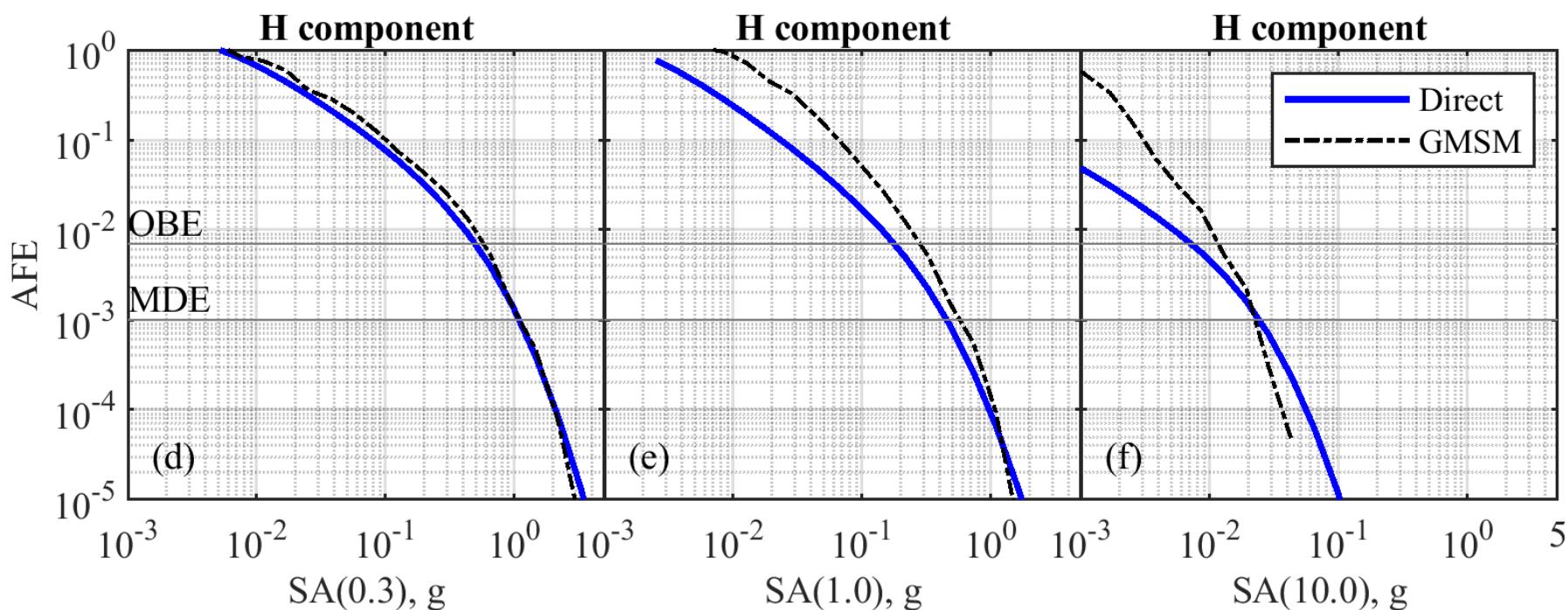
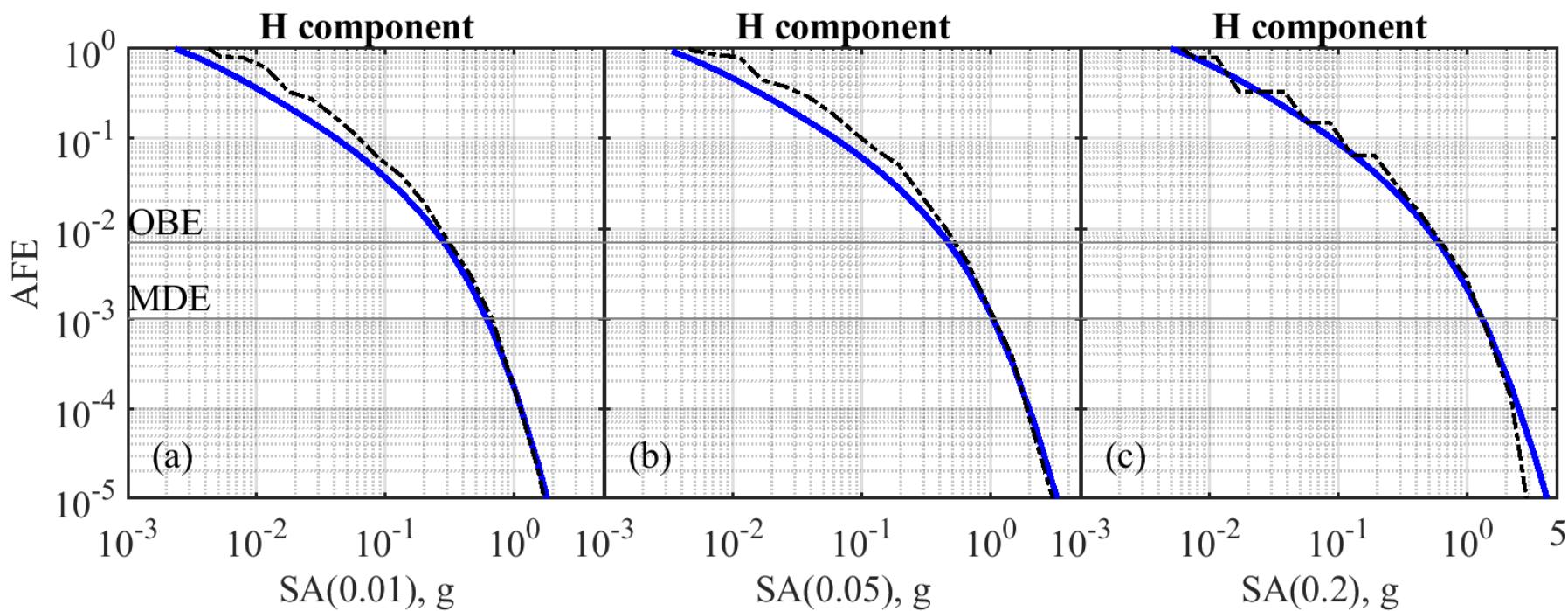
- San Francisco, California
- GMMs:
 - H component: Campbell & Bozorgnia 2014
 - V component: Bozorgnia & Campbell 2016
 - V/H ratio: Bozorgnia & Campbell 2016
- Fundamental period: 0.2 sec

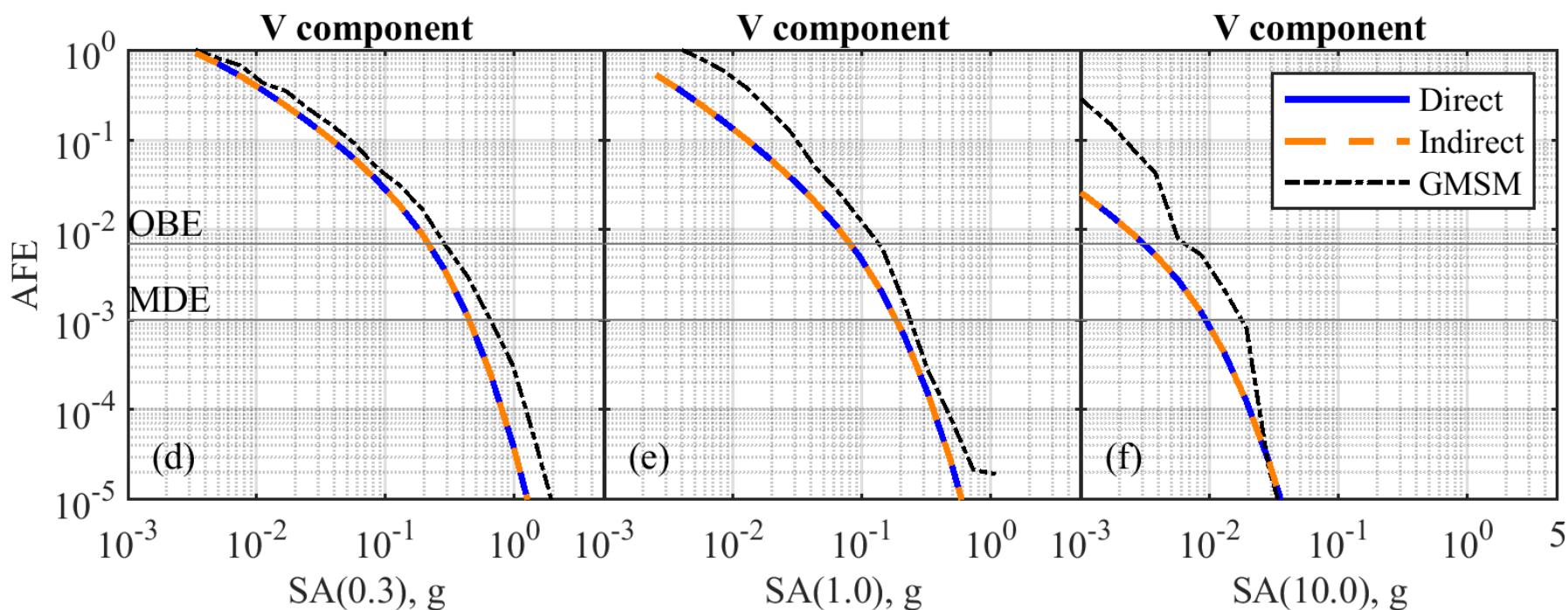
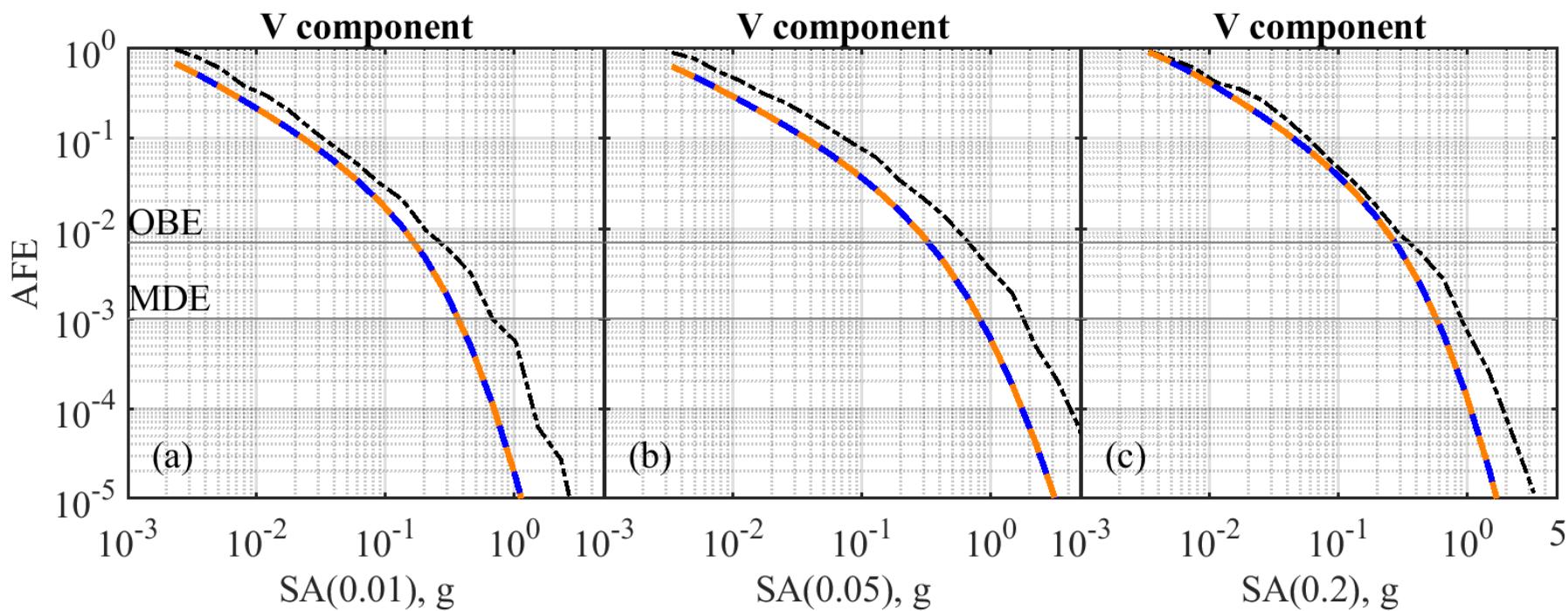
Direct and indirect approaches



GMSM approach







Pros and cons of approaches

Approach	Direct	Indirect	GMSM
Pros	1. Most rigorous	1. Can capture epistemic uncertainties via GMMs for H component of GM	1. Overcomes lack of GMMs 2. Can capture epistemic uncertainties without models for V/H or for correlations
Cons	1. Lack of GMMs for V component	1. V/H model may not be applicable to another tectonic regime 2. More complete quantification of epistemic uncertainties requires multiple models for V/H and correlations	1. Requires adequate number of candidate GMs 2. Involves much more work to derive hazard curves 3. Sensitive to inputs for GMSM

Conclusions

1. Vertical (V) hazard curves are important for evaluating input multicomponent ground motion time series for subsequent seismic risk analyses of concrete dams
2. Pros and cons of 3 different approaches for deriving V hazard curves were summarized
3. Indirect approach can also be supplemented with GMSM approach to capture epistemic uncertainties in hazard



Thank you!

Any questions?



Seismic damage analysis of high concrete arch dam-foundation systems: a comprehensive study

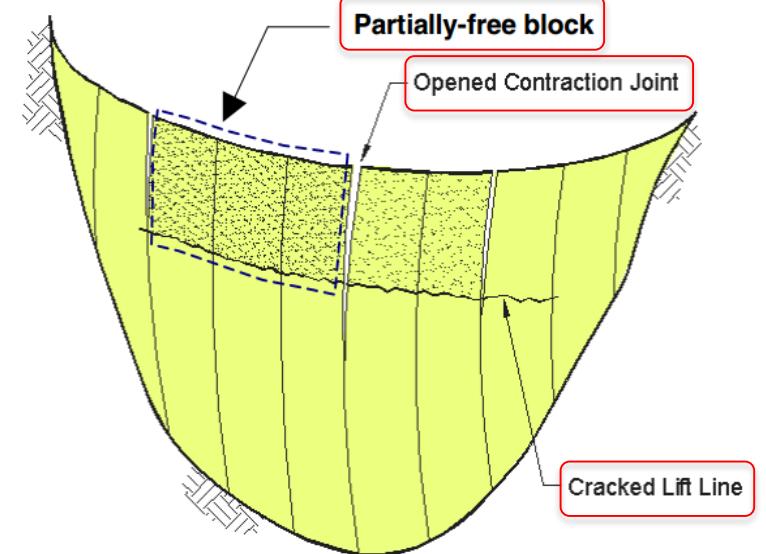
Hui Liang ^{1,2}, Shengshan Guo ^{1,2}, Chunli Yan ^{1,2}, Tujin ^{1,2}

¹ Earthquake Engineering Research Centre, China Institute of Water Resources and Hydropower Research, Beijing, China;

² State Key Laboratory of Simulation and Regulation of Water Cycle in River Basin, Beijing, 100048 China

1 Introduction

- ◆ **Contraction joint opening** may happen, causing the release of arch stress and the increase of cantilever tensile stress and **tensile cracking** may appear at the dam body under strong earthquakes.
- ◆ Once the crack penetrates through the dam thickness, the potential instability of the partially-free block caused by the penetrated cracks may lead to the failure of dams.



✓ **The maximum stress criterion based on linear elastic material model** cannot meet seismic safety evaluation of high concrete dams under strong earthquakes.

✓ **Reinforcement in potential cracking regions** is required to reduce developments of dam cracking.

Material nonlinearity

- classical plasticity theory
- continuum damage mechanics
- plasticity theory
- fracture mechanics
- the combination of plasticity theory and damage mechanics

Steel reinforcement

- embedded-steel model
- distributed steel reinforcement model

2 Problem statement

- **Limited researches** have been implemented to discuss effects of steel reinforcement on seismic performance of **arch dams**.
- **The ultimate seismic capacity** of concrete dams is also a key issue.
- **No unified evaluation standard and corresponding evaluation indexes** has been recognized.

- 
- ◆ **Contact nonlinearity:** contraction joints
 - ◆ **Material nonlinearity:** A new conception to directly establish seismic damage model considering residual deformation based on experimental data is adopted.
(Chen Houqun, Guoshengshan, et al.)
 - ◆ **Steel reinforcement:** Distributed steel reinforcement model

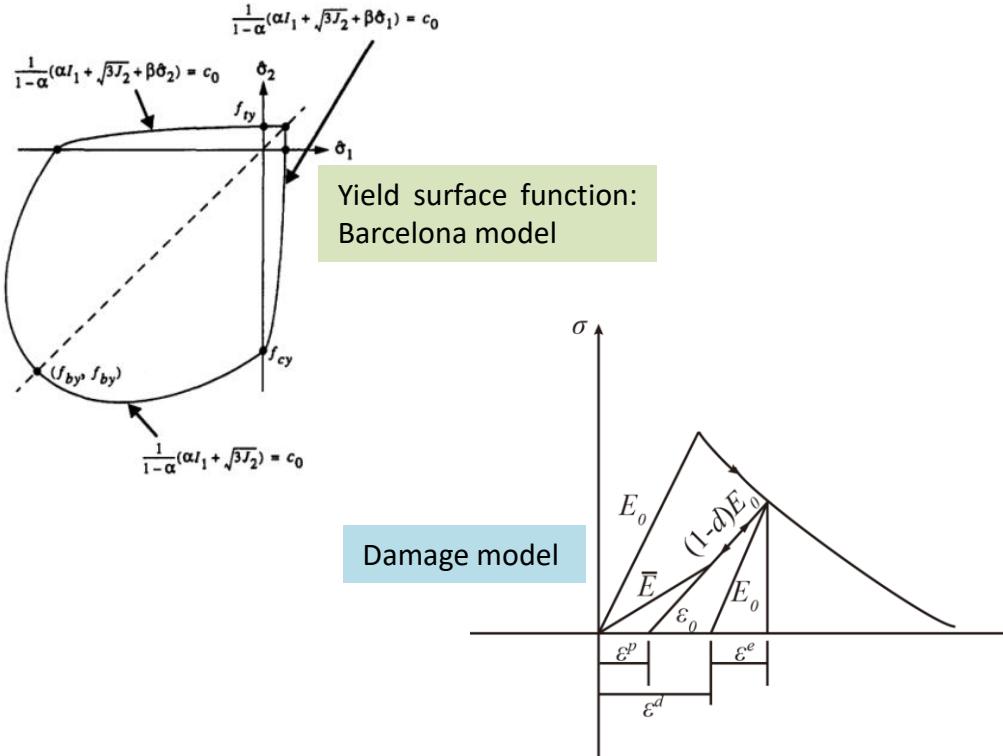


- **Effects of the steel reinforcement on seismic damage of the dam**
- Seismic overload analysis
- **The criteria** i.e. the occurrence of upstream and downstream penetrating cracks of the dam
- Seismic overload factor
- **Ultimate seismic capacity** of arch dams

3 Main paper

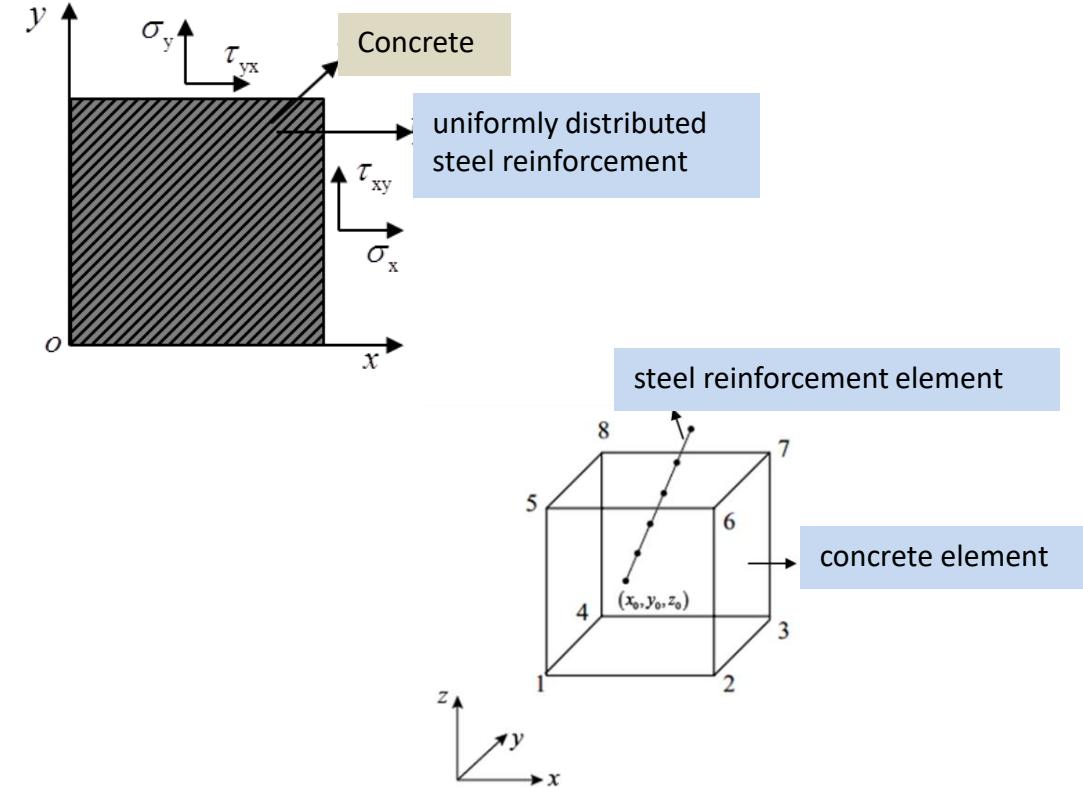
Seismic damage analysis of high concrete arch dam-foundation systems: a comprehensive study

➤ Damage model



- ✓ considering both residual deformation and stiffness reduction
- ✓ avoids to use commonly plastic damage model which is not suitable for concrete

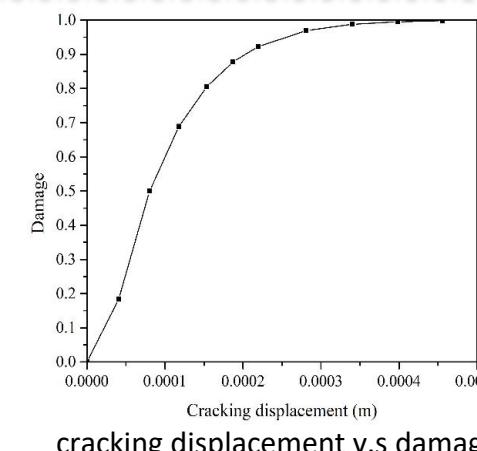
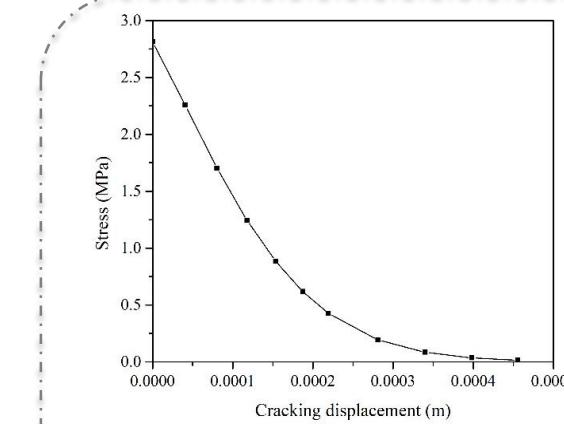
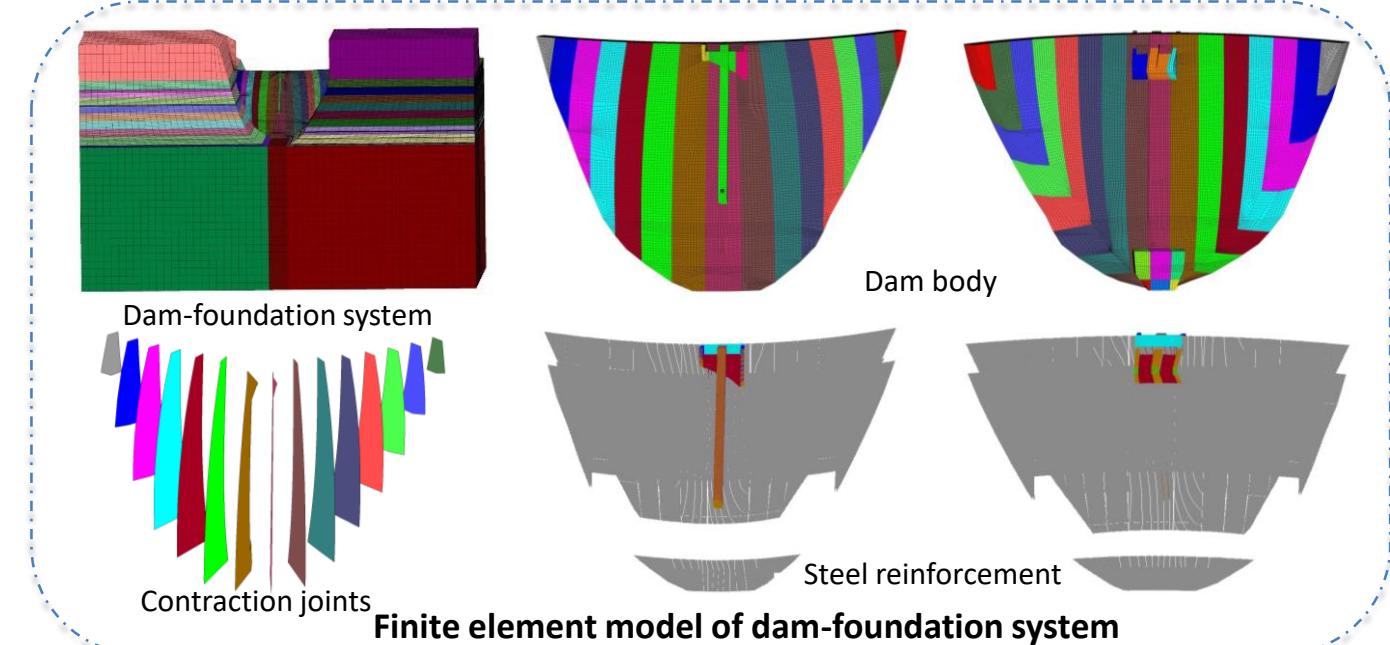
➤ Distributed steel reinforcement model



- Steel reinforcement is evenly distributed in the whole concrete element at a certain angle
- Concrete and steel reinforcement are well bonded.

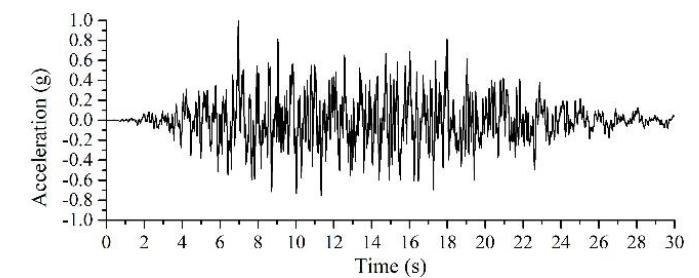
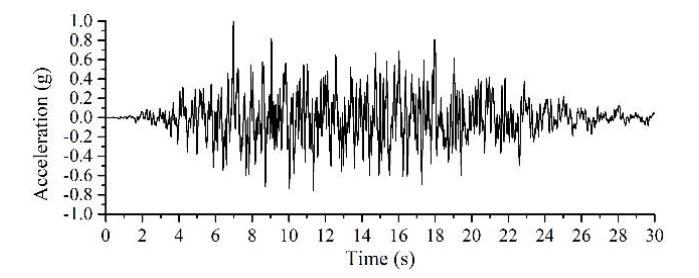
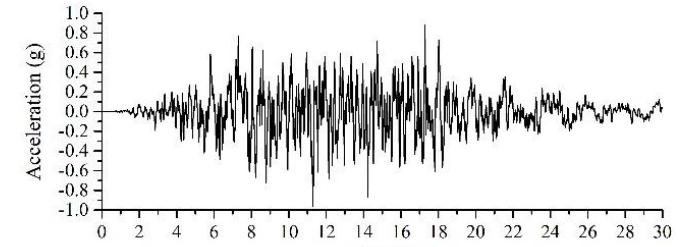
3 Main paper

Seismic damage analysis of high concrete arch dam-foundation systems: a comprehensive study



Damage evolution of dam concrete

- The upstream and downstream high water levels are 876 m and 738 m and corresponding low water levels are 814 m and 738 m. The sediment depth is 779.5 m.



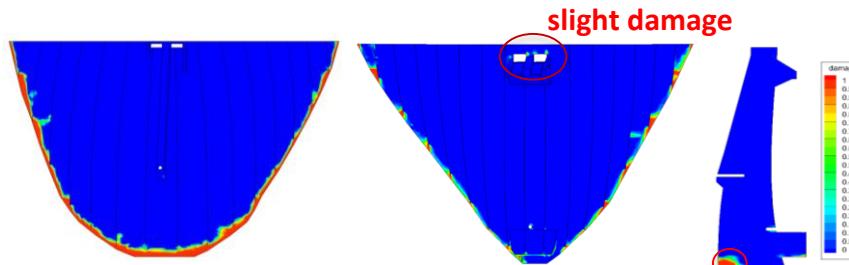
Input earthquake motions

the horizontal peak ground motion is 0.4225 g

3 Main paper

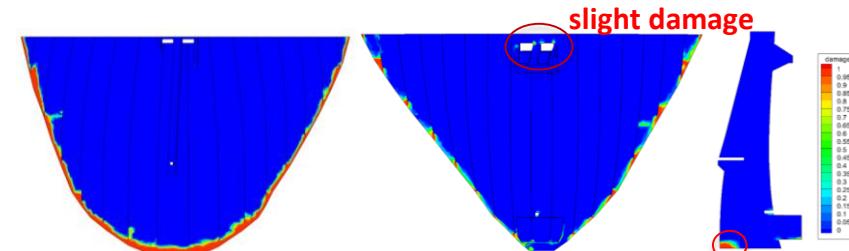
Seismic damage analysis of high concrete arch dam-foundation systems: a comprehensive study

Results of seismic damage analysis



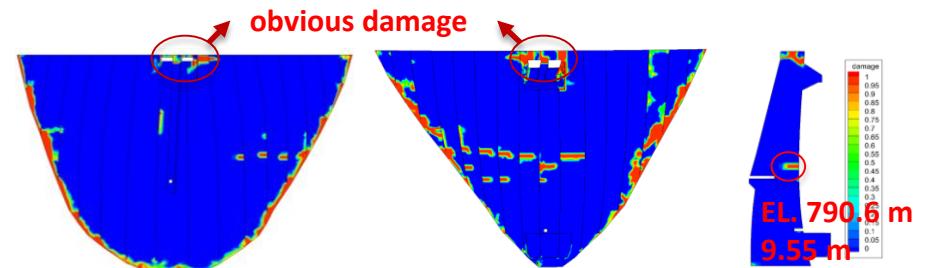
High water level without steel reinforcement

12.07 m



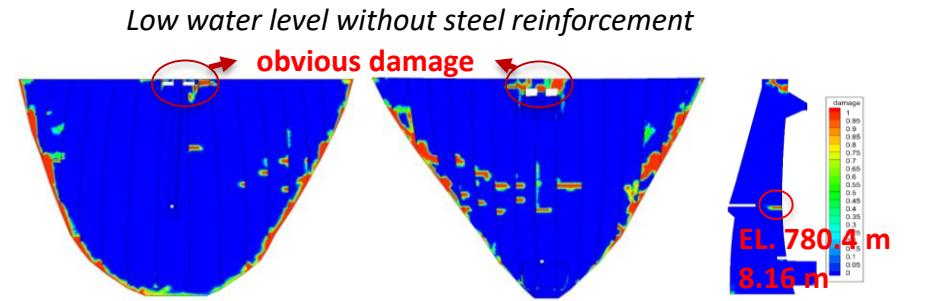
High water level with steel reinforcement

11.49 m



Low water level without steel reinforcement

EL. 790.6 m
9.55 m



Low water level with steel reinforcement

EL. 780.4 m
8.16 m

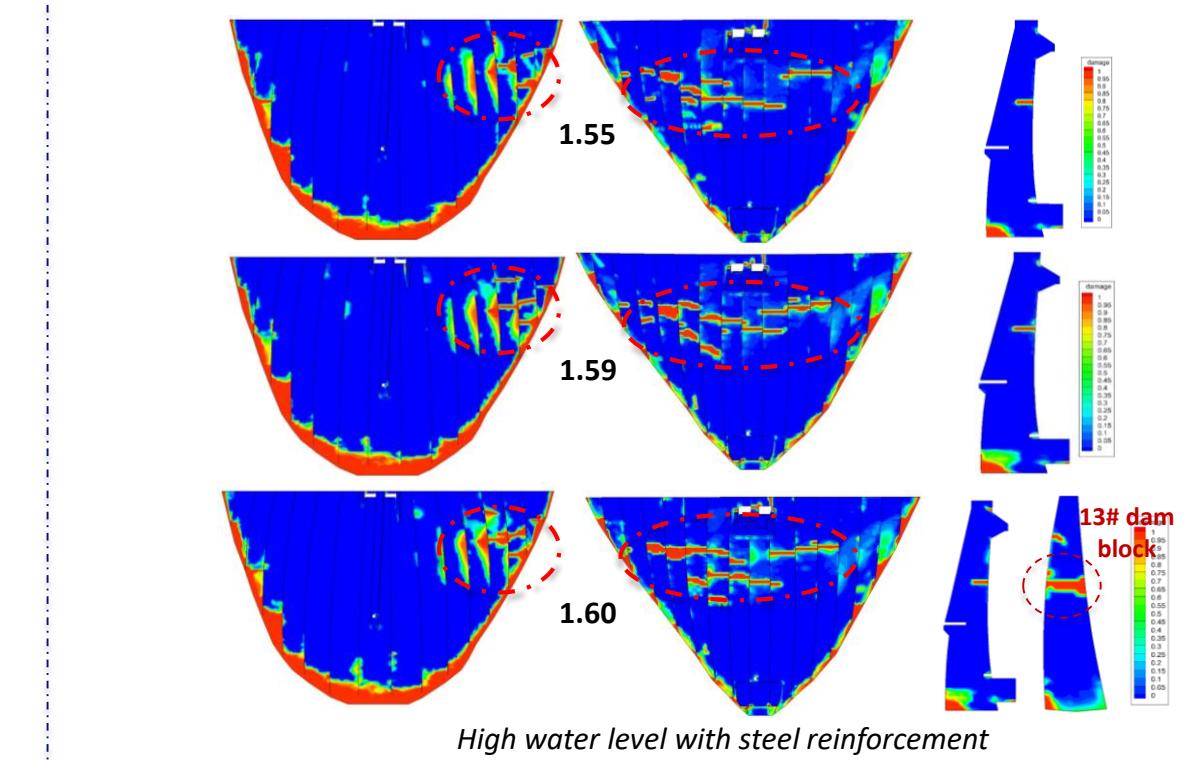
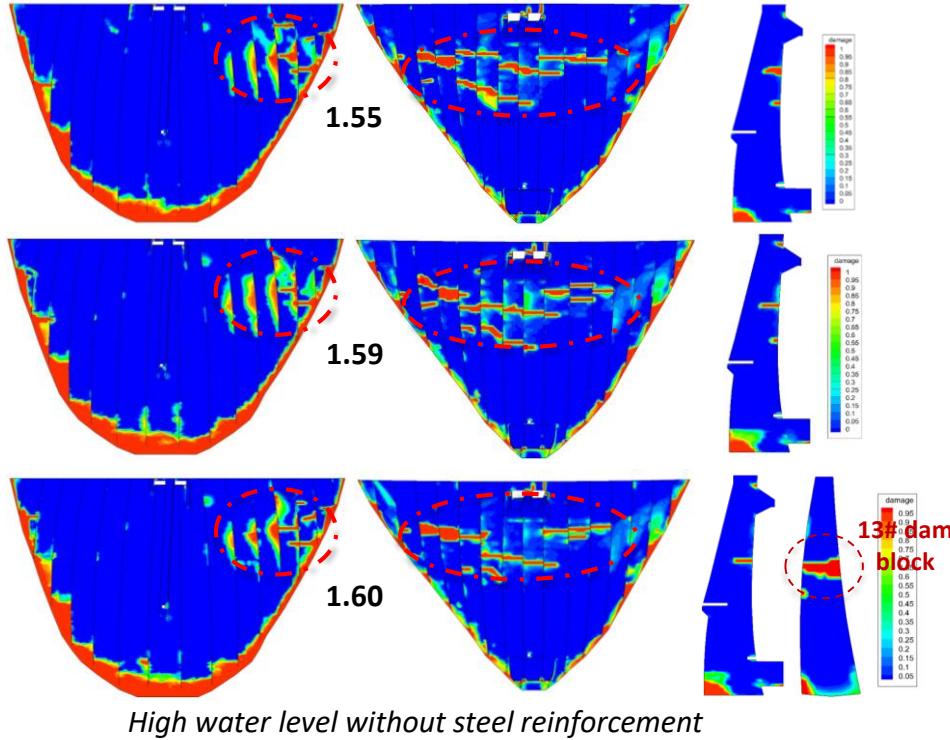
- The dam is basically **undamaged and slight damage** occurs at **the junction of the downstream pier and girder**.
- The macro crack depth at dam heel with damage variable (DV) greater than 0.8 is about **12.07 m** without steel reinforcement. While, it decreases to **11.49 m** when the steel reinforcement is considered.

- Damage at **the junction of the pier and girder** reduced significantly when the steel reinforcement is considered.
- According to damage contours of crown cantilever, damage occurs at downstream elevation of 790.6 m, and macro crack depth with DV greater than 0.8 is **about 9.55 m** without steel reinforcement. While it is **about 8.16 m** at elevation of 780.4 m with steel reinforcement.

3 Main paper

Seismic damage analysis of high concrete arch dam-foundation systems: a comprehensive study

Results of seismic overload analysis



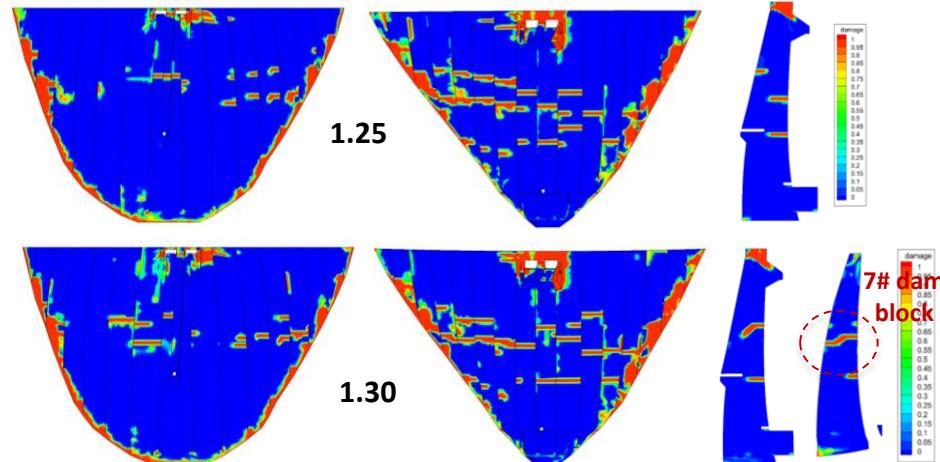
- ✓ Damage of the dam mainly occurs at **middle and upper part of upstream right abutment** and **at downstream middle part**.
- ✓ **The occurrence of upstream and downstream penetrating cracks** of the dam is proposed as the evaluation criteria.

- ✓ The corresponding seismic overload factor of the dam reaching the **ultimate seismic capacity** varies from 1.59 to 1.60, which can be taken as **1.59** for both models.

3 Main paper

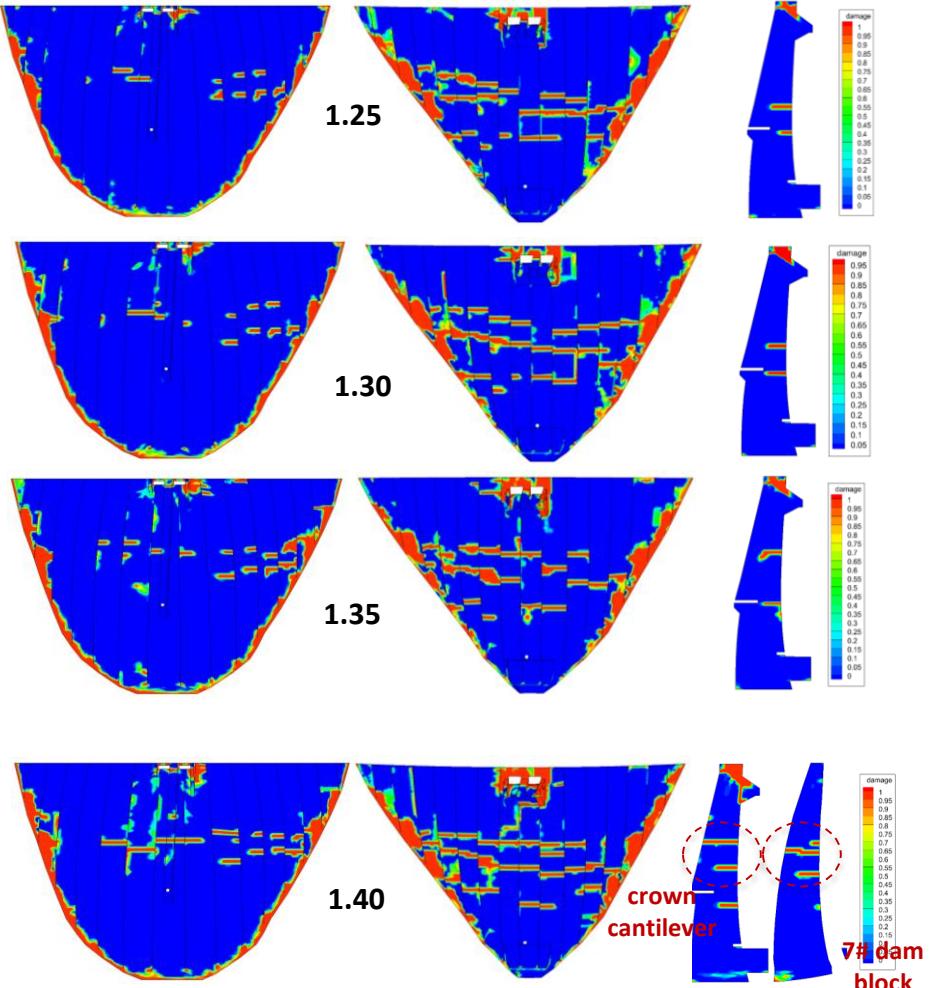
Seismic damage analysis of high concrete arch dam-foundation systems: a comprehensive study

Results of seismic overload analysis



Low water level without steel reinforcement

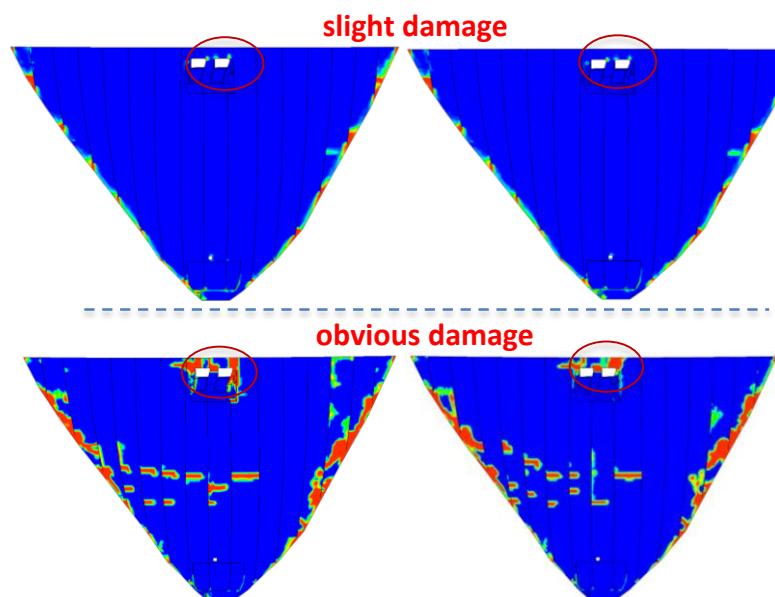
- ✓ for C3, penetrating cracks of 7# dam block occur at OF of 1.30. While, for C4, they occur at downstream elevation of 820.57 m of the crown cantilever and 811.44 m of 7# dam block at OF of 1.40.
- ✓ Compared with C1 and C2, the extent and distribution of damage for C3 and C4 is obviously different as well as the ultimate seismic capacity, which can be explained that the occurrence of large opening of contraction joints significant increases of the dynamic cantilever stress of upper part of dam body under low water levels.



Low water level with steel reinforcement

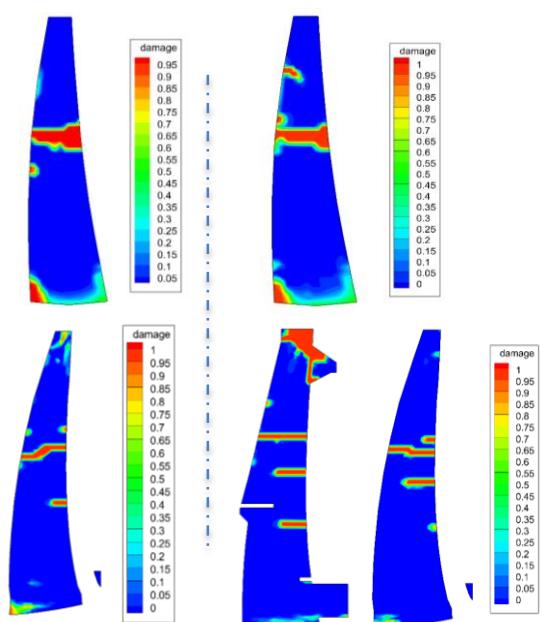
4 Conclusions

(1) Damage distributions of the dam are basically the same with and without steel reinforcement since the dam is basically undamaged and slight damage occurs at the junction of the downstream pier and girder under the high water level and design earthquake, while damage at the junction of the pier and girder reduced significantly under the low water level and design earthquake when the steel reinforcement is considered.



(3) If the occurrence of upstream and downstream penetrating cracks of the dam is taken as the evaluation criteria, the ultimate seismic capacity can be taken as 1.59 under the high water level. While, under the low water level, the ultimate seismic capacity can be taken as 1.35 and 1.25 with and without considering steel reinforcement, respectively.

(2) Compared with the results obtained under the high water level and design earthquake, obvious damage of the dam occurs under low water level and design earthquake, especially at downstream surface and the junction of downstream pier and girder. It is explained that the occurrence of large opening of contraction joints significant increases of the dynamic cantilever stress of upper part of dam body under low water levels





Thank you!

Any questions?





University of Colorado **Boulder**



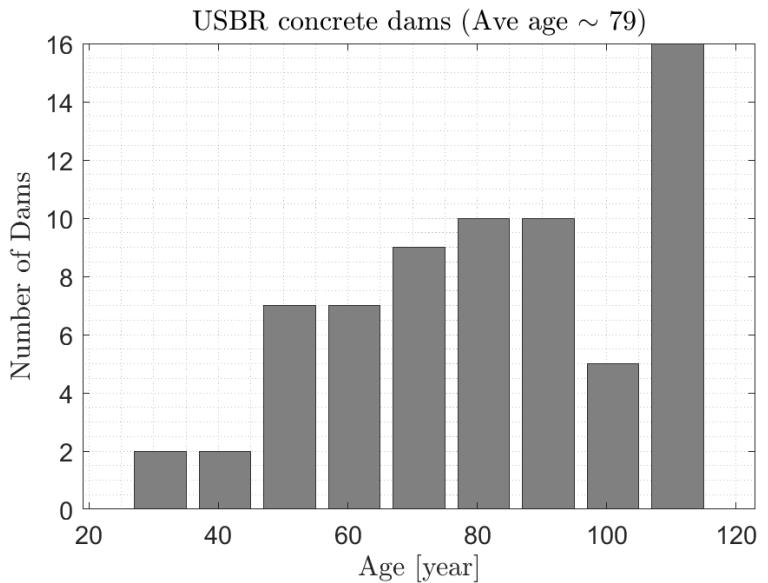
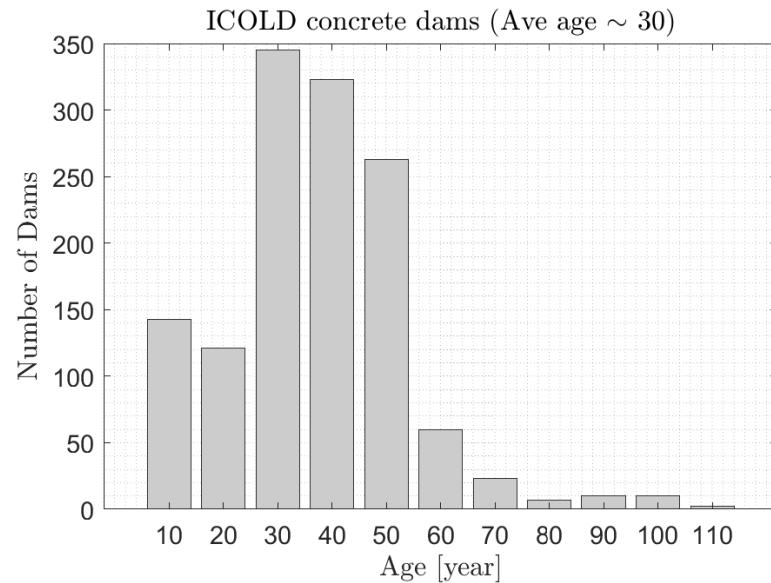
Intensifying dynamic response of a concrete dam affected by alkali-aggregate reaction

G. Mahdavi ¹, V.E. Saouma ¹

¹ University of Colorado, Boulder, USA

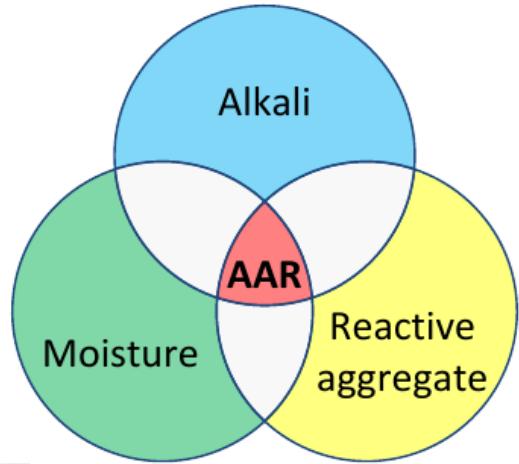
Introduction

- Dams are aging and many were designed at a time with limited technical data.
- Average age of the 91,000 dams in the US is ~60 years as of 2024.
- ASCE's Report Card for America's Infrastructure gave a D (A-F) grade for dams.
- Aging appears in different forms, i.e., creep, freeze & thaw, chloride attack, fatigue, alkali-aggregate reaction - AAR (first identified 1940), ...



What is AAR?

- Alkali aggregate reaction (AAR) is a reaction between the alkali hydroxides and certain types of aggregate.
- Produces gel that will induce expansion (akin to fracking)
- AAR causes concrete expansion, reduction of strength and elasticity, and reduction of fatigue life.
- AAR has different natures:
 - Alkali-silica reaction (ASR)
 - Alkali-carbonate reaction (ACR)



Dam



Bridge



NPP



RC

Road Map

Instrumentation

FE model

Nonlinear material

AAR model

Hazard analysis

Simulation algorithm

Sensitivity analysis

Model calibration

Uncertainty sources

Probabilistic simulation

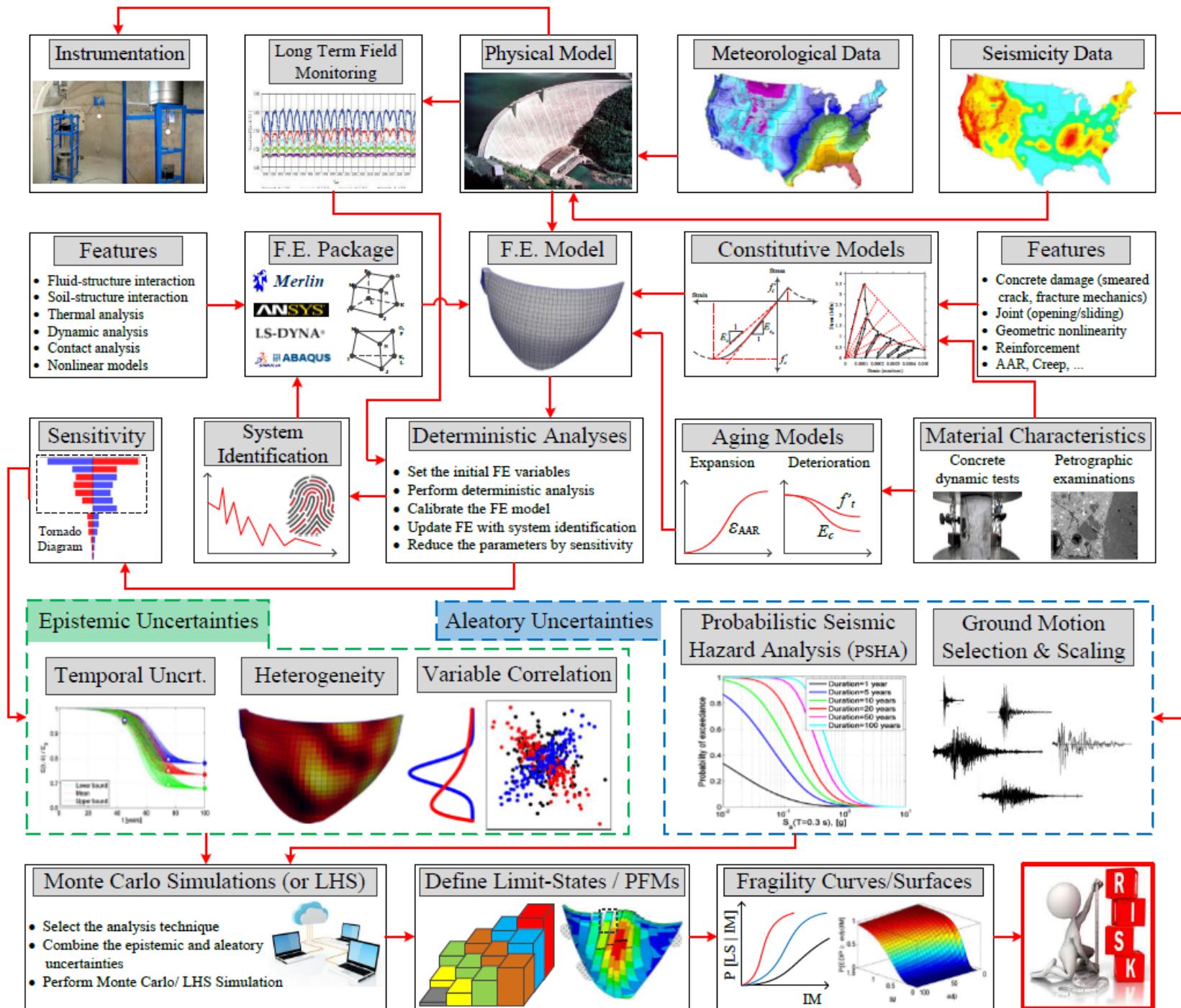
Damage index

Capacity models

Fragility functions

Risk assessment

Decision making



Formulation of AAR

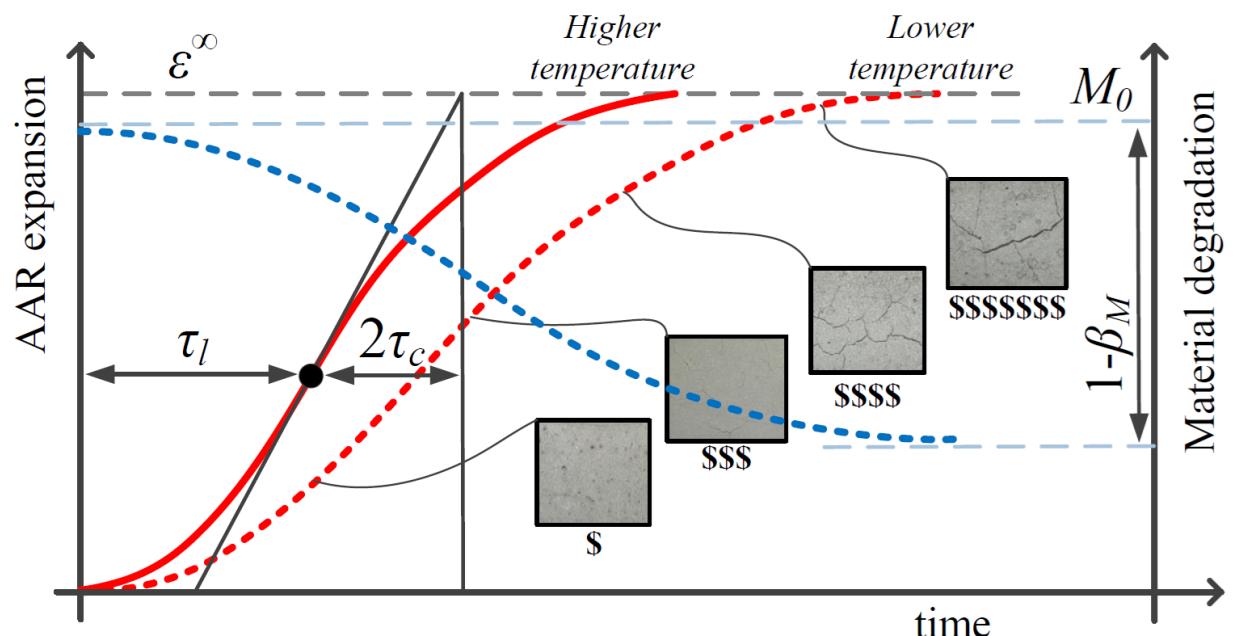
- Spatial and temporal distribution of temperature and relative humidity.
- Internal degradation of f'_t and E_c .

$$\dot{\varepsilon}_V^{AAR}(t, \theta, RH) = \Gamma_t(f'_t | w_c, \sigma_l | COD_{max}) \Gamma_c(\bar{\sigma}, f'_c) g(RH) \dot{\xi}(t, \theta) \varepsilon^\infty|_{\theta=\theta_0}$$

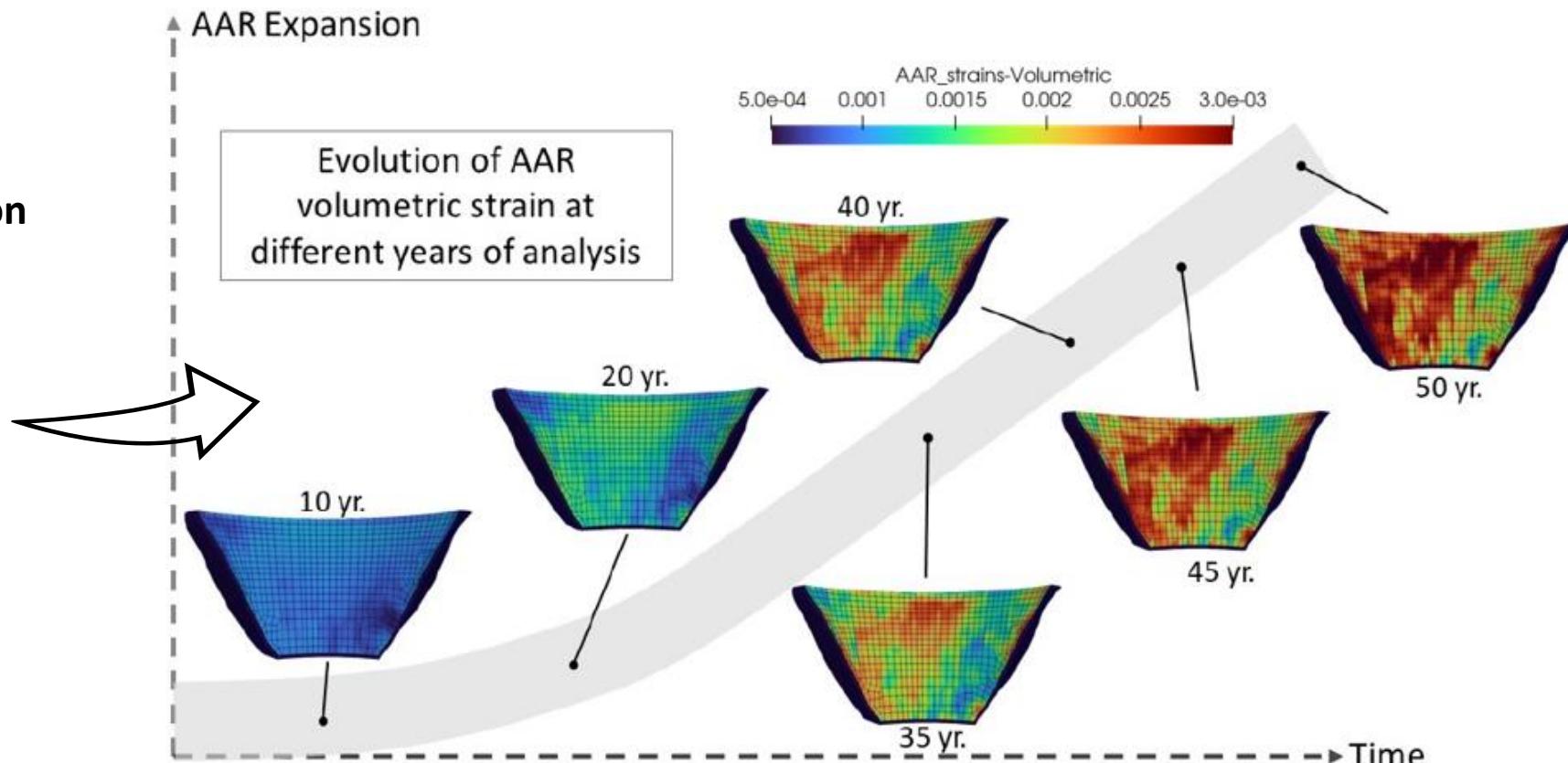
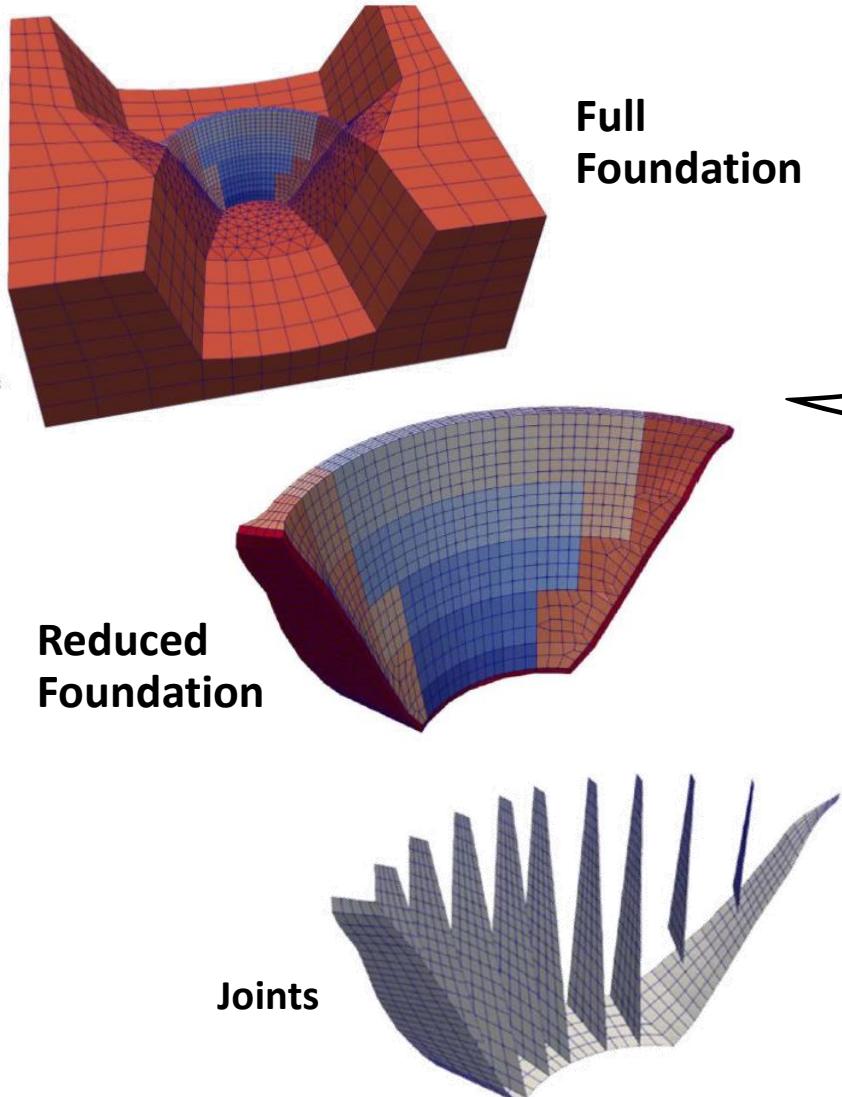
$$\xi(t, T) = \frac{1 - \exp(-\frac{t}{\tau_c(T)})}{1 + \exp(-\frac{(t-\tau_l(T))}{\tau_c(T)})}$$

$$\tau_l(T) = \tau_l(T_0) \exp \left[U_l \left(\frac{1}{T} - \frac{1}{T_0} \right) \right]$$

$$\tau_c(T) = \tau_c(T_0) \exp \left[U_c \left(\frac{1}{T} - \frac{1}{T_0} \right) \right]$$



Stress Analysis

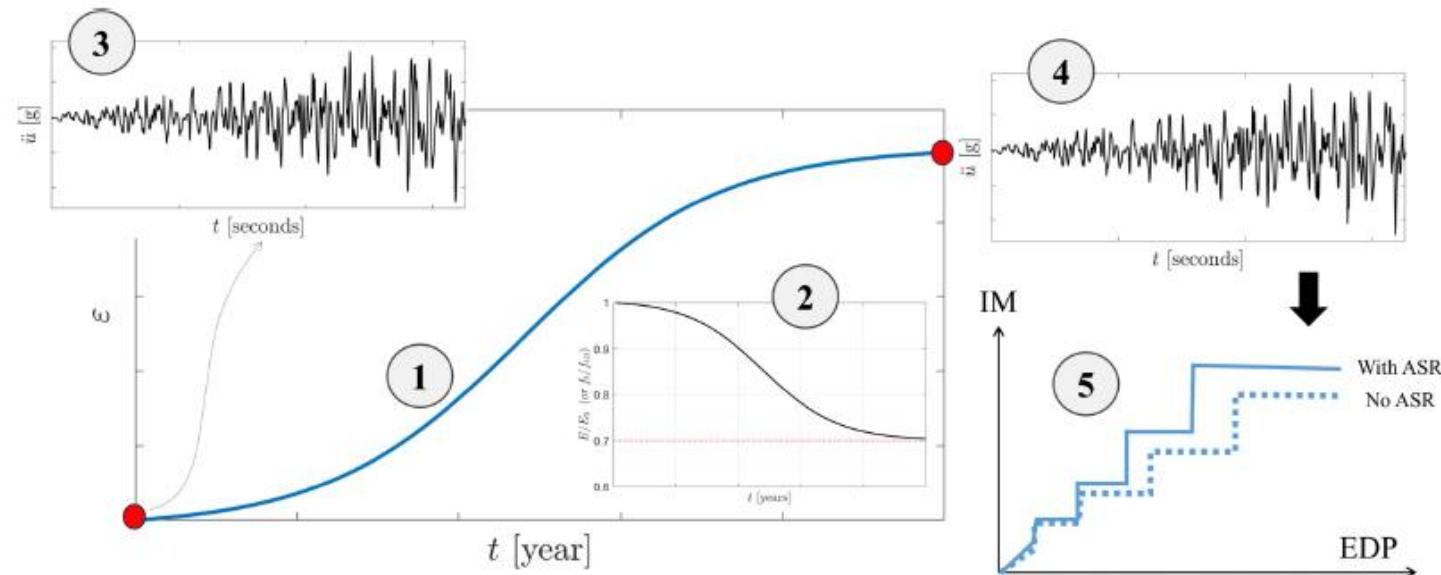
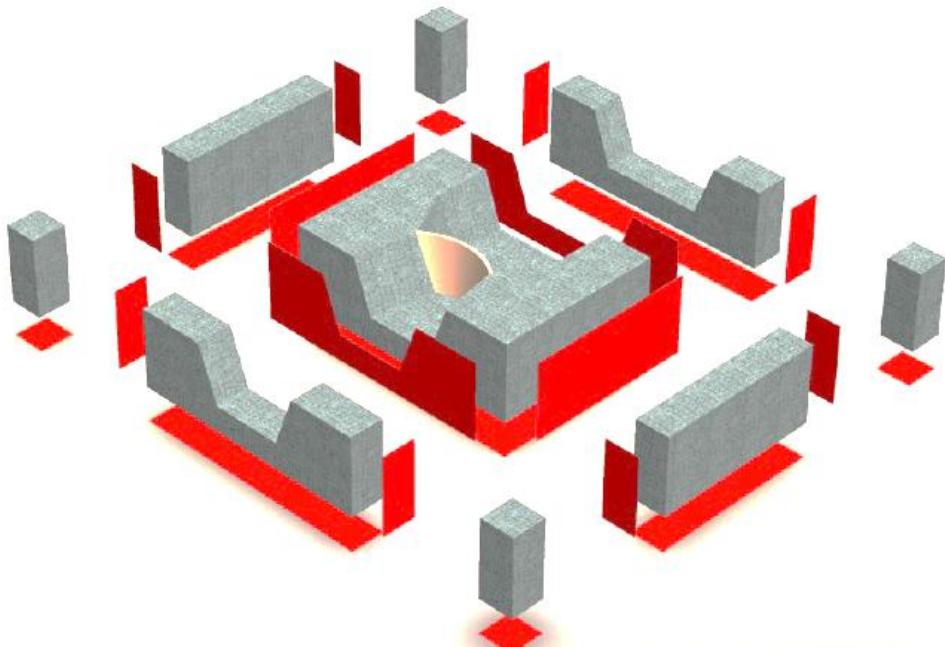


Results can be interpreted in terms of:

- **AAR volumetric strains**
- Stresses
- Joint opening and sliding
- Drift ratios
- Damage index
- Crest displacements

Seismic Analysis

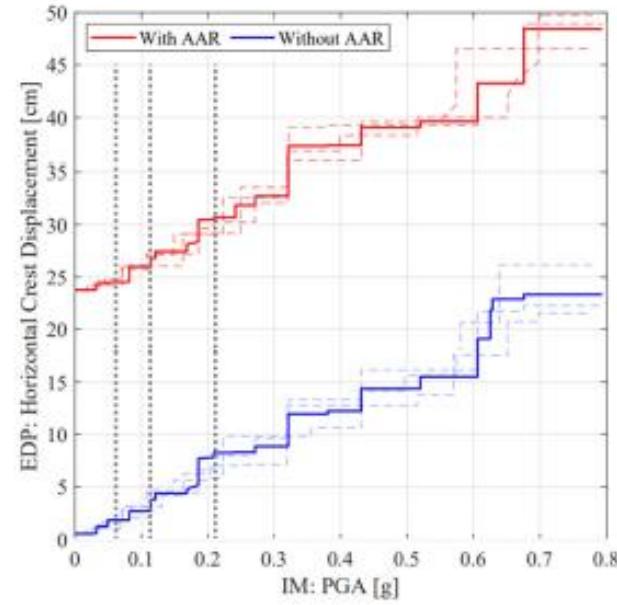
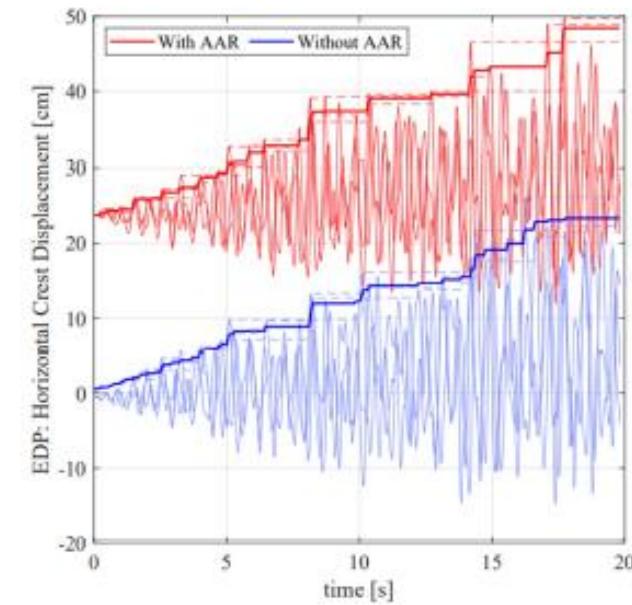
- The IAA is applied once at the onset of AAR and another time after 50 years of AAR analysis
- The major failure modes of arch dam:
 - Overstressing
 - Joint opening and sliding
 - Excessive deformation of dam
 - Leakage



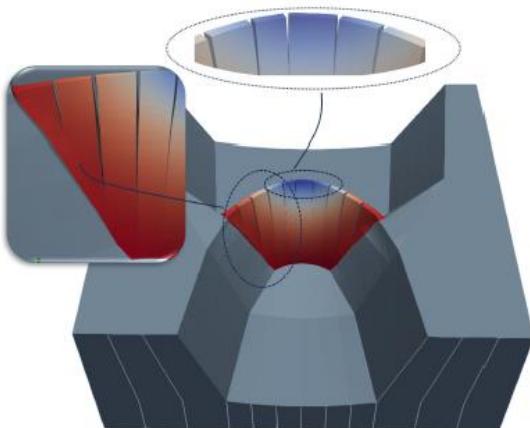
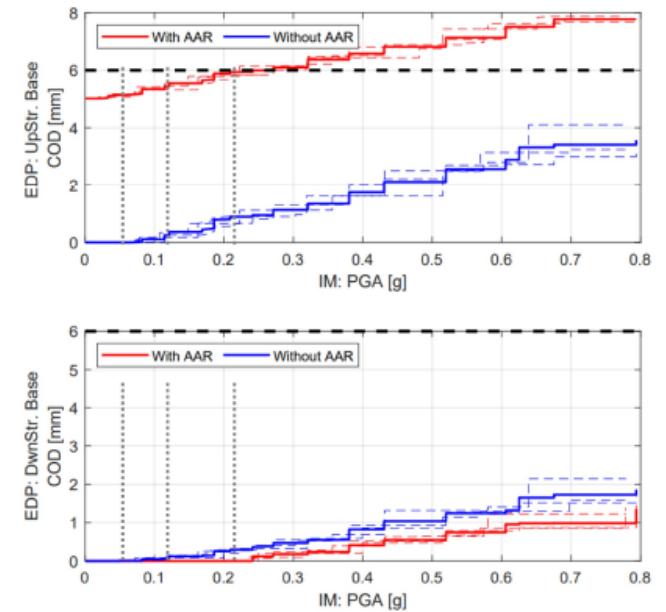
- EDP can be selected to be:
 - Crest Displacements
 - Joint opening and sliding
 - Stresses
 - Percentage of cracked concrete

Results

Horizontal crest displacements for the AAR affected and sound dam



Joint Opening displacements at the dam toe and heel





Thank you!

Any questions?

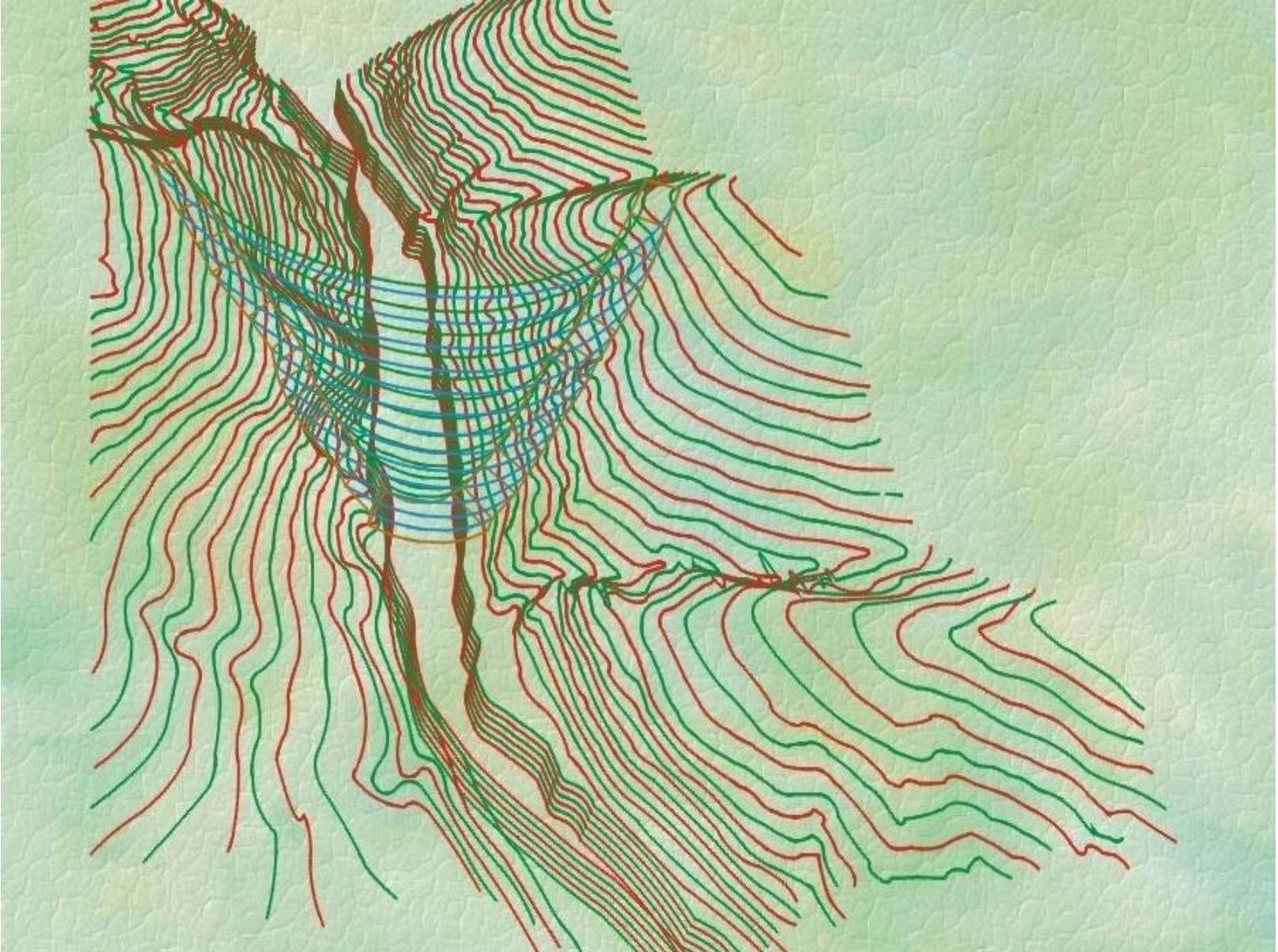


BEM-FEM SOLUTION OF ARCH DAM – FLUID INTERACTION USING ADAD-IZIIS SOFTWARE

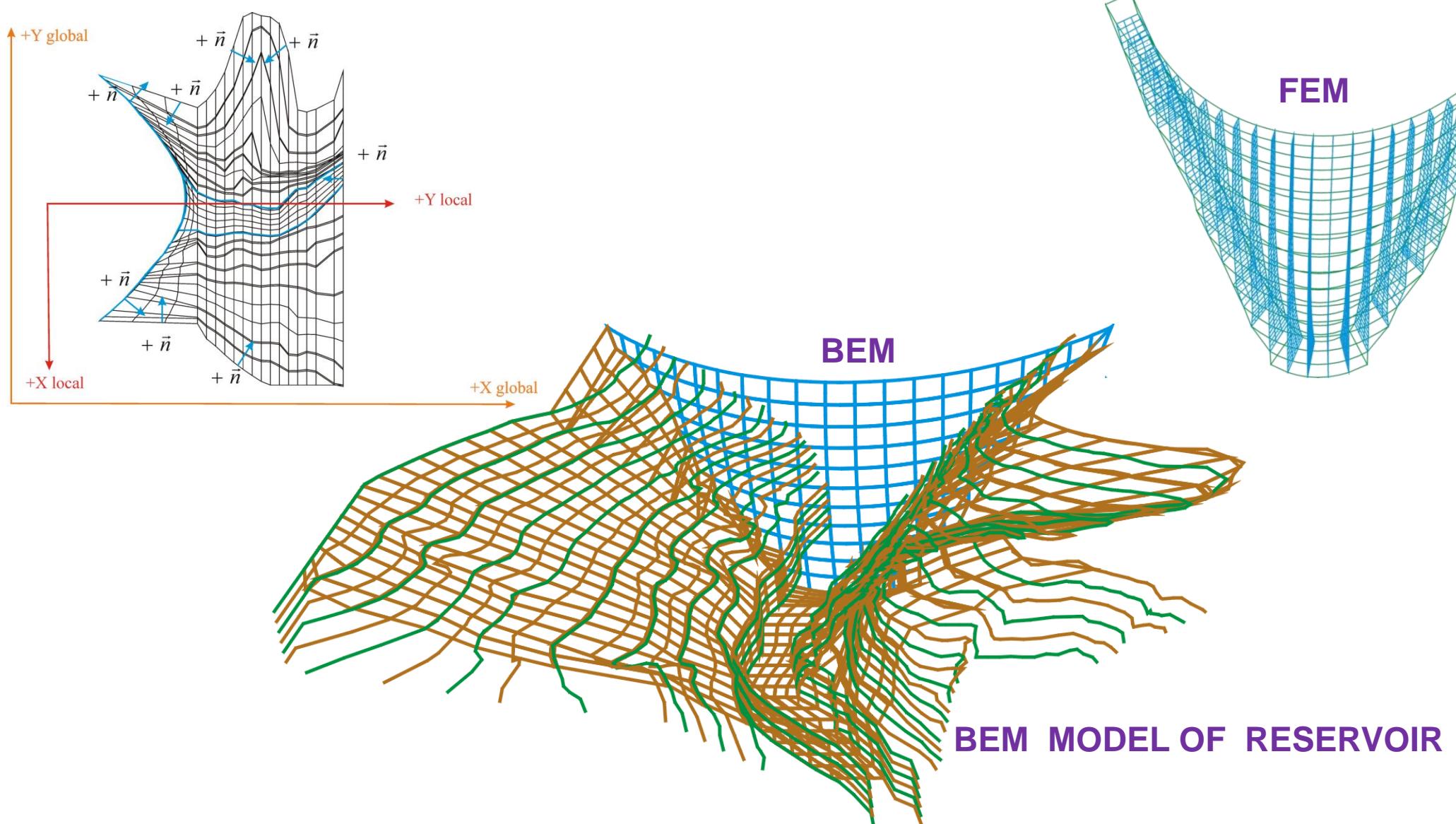
Violeta Mircvevska ¹, Ana Nanevska ¹

¹ Institute of Earthquake Engineering and Engineering
Seismology “Ss. Cyril and Methodius” – Skopje R.N. Macedonia

ADAD-IZIIS software – HDI matrix method



Uncoupled BEM-FEM technique



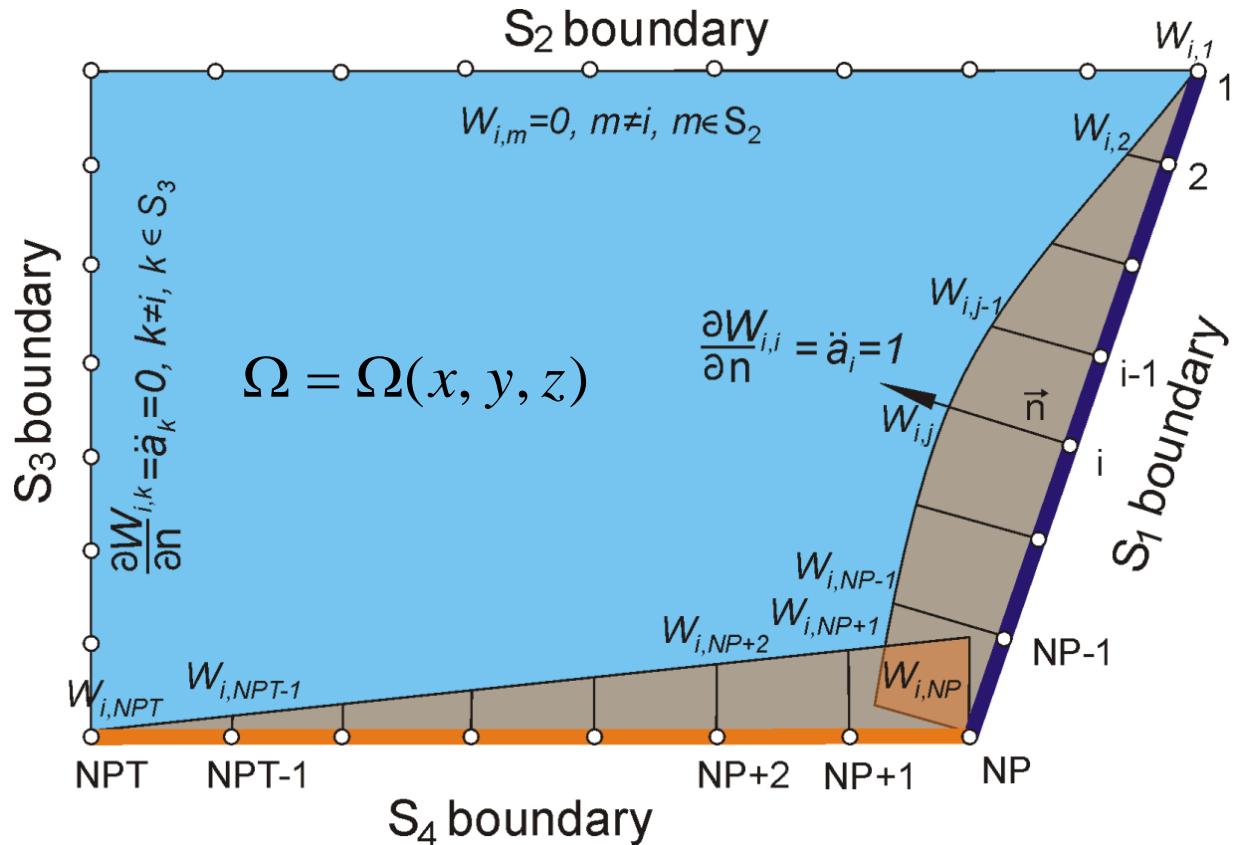
BEM MODEL OF RESERVOIR

HDI matrix method is derived on the principle of virtual work in the reservoir

$$\frac{\partial^2 W}{\partial x^2} + \frac{\partial^2 W}{\partial y^2} + \frac{\partial^2 W}{\partial z^2} = 0$$

$$W = W(x, y, z, t) \in \Gamma_1 \quad \frac{\partial W(x, y, z)}{\partial n} = \frac{\partial \bar{W}(x, y, z, t)}{\partial n} \in \Gamma_2$$

$$\frac{1}{2}W_i + \sum_1^{NBE} \int_{\Gamma_1} \left(\frac{\partial \{W\}^T}{\partial n} \{p\} - \{\bar{W}\}^T \frac{\partial \{p\}}{\partial n} \right) d\Gamma_1 + \sum_1^{NBE} \int_{\Gamma_2} \left(\frac{\partial \{\bar{W}\}^T}{\partial n} \{p\} - \{W\}^T \frac{\partial \{p\}}{\partial n} \right) d\Gamma_2 = 0$$



$$\{H\}_i^T = \{W_{i,1}, W_{i,2}, \dots, W_{i,i}, \dots, W_{i,NP}, \dots, W_{i,NPT}\}, \text{ for } i = 1, NPT$$

$$[HDI] = [W_{i,j}], \text{ for } i = 1, NPT \text{ and } j = 1, NPT$$

$$\{\Delta P_j\}_t^T = \{\Delta \ddot{U}_i^{tot}\}^T [W_{i,j}]$$

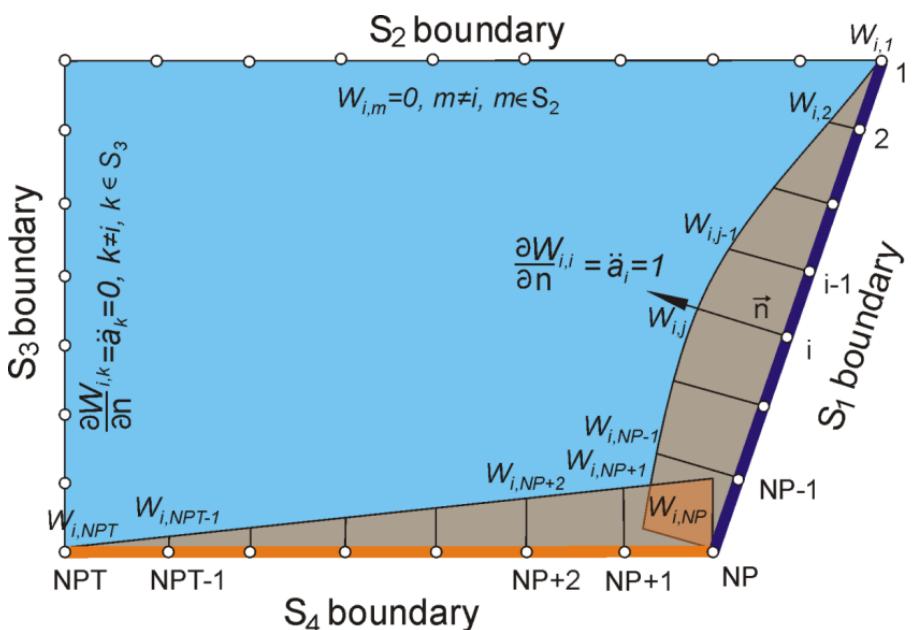
$$\{\Delta HDF(t)\} = \{N\} \int_A \{N\}^T \{\Delta P_j\}_t dA$$

$$[M]\{\Delta \ddot{U}(t)\} + [C]\{\Delta \dot{U}(t)\} + [K]\{\Delta U(t)\} = -[M][R]\{\Delta a_g(t)\} + \{\Delta HDF(t)\}$$

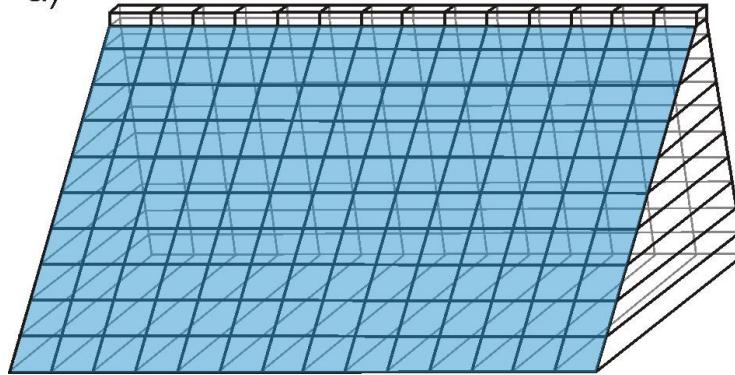
$$ENORM = \sqrt{\sum_{k=1}^{NP \times NS} (\{HDF(t)\}_k^i - \{HDF(t)\}_k^{i+1})^2 / (NP \times NS)} \leq 0.01$$

Conclusion :

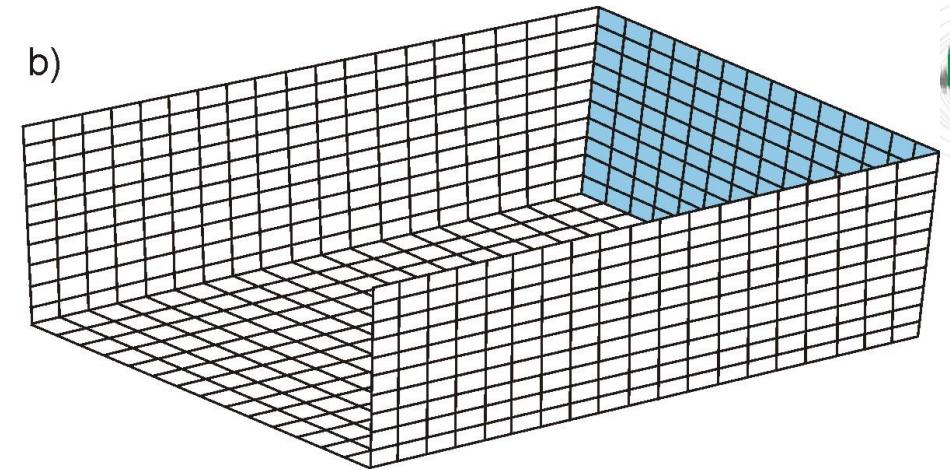
HDI matrix is characteristic of the analyzed fluid domain.



a)



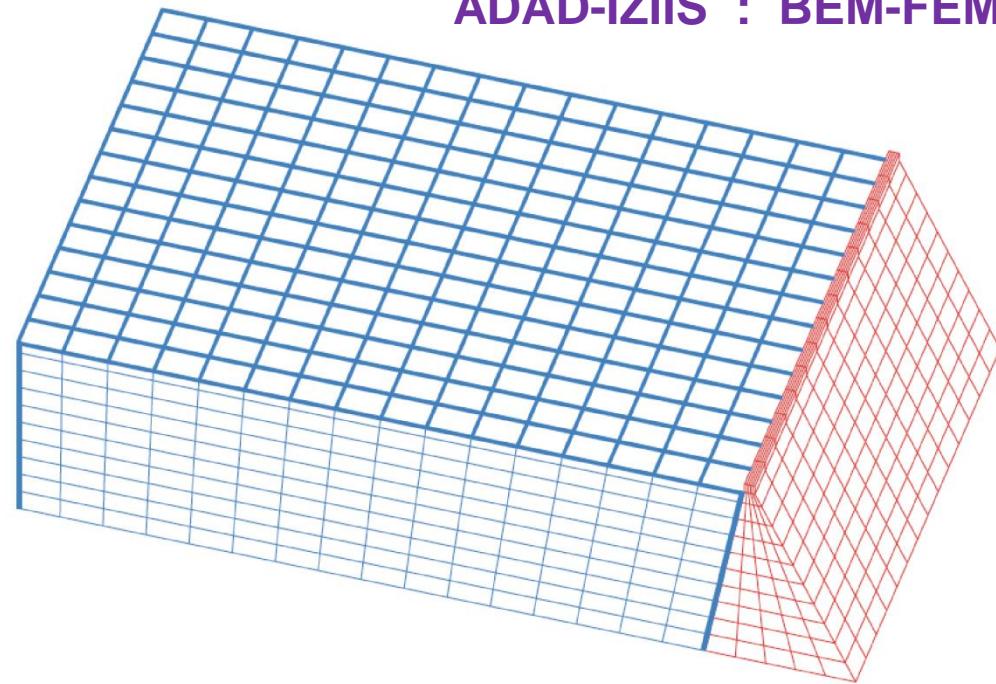
b)



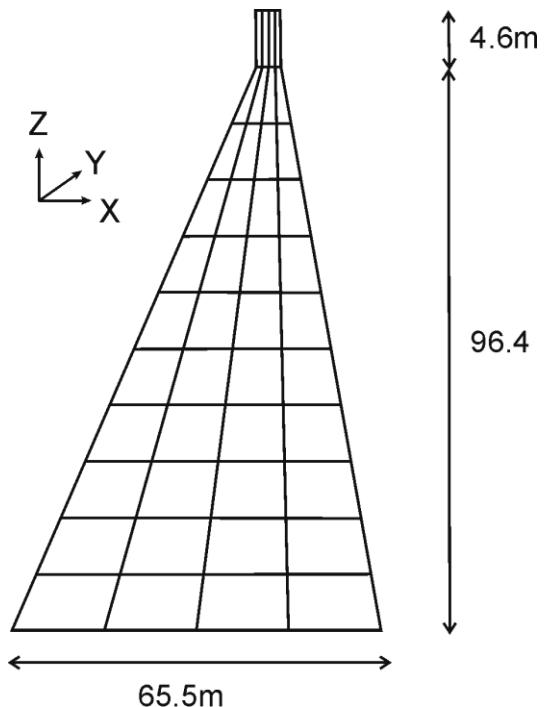
a) FE substructural mesh of dam domain

b) BE mesh of the fluid domain

ADAD-IIZIIS : BEM-FEM model

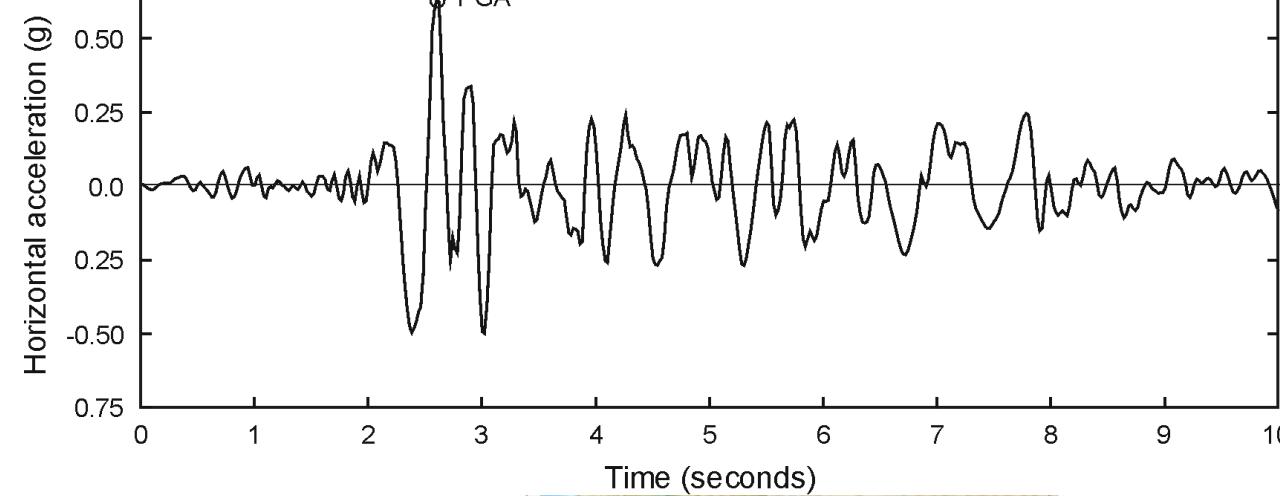


ADINA software FEM-FEM model

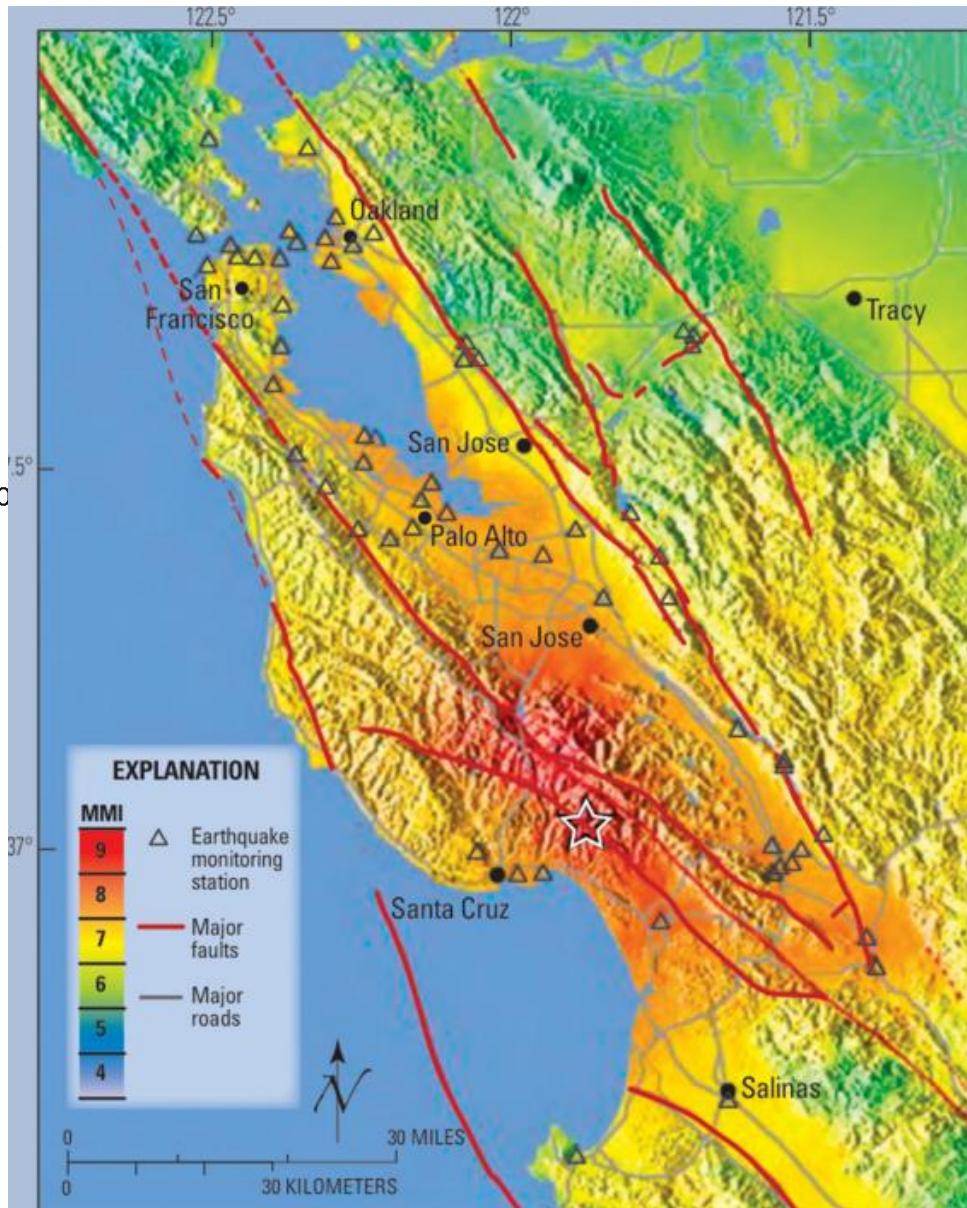


Dam cross section

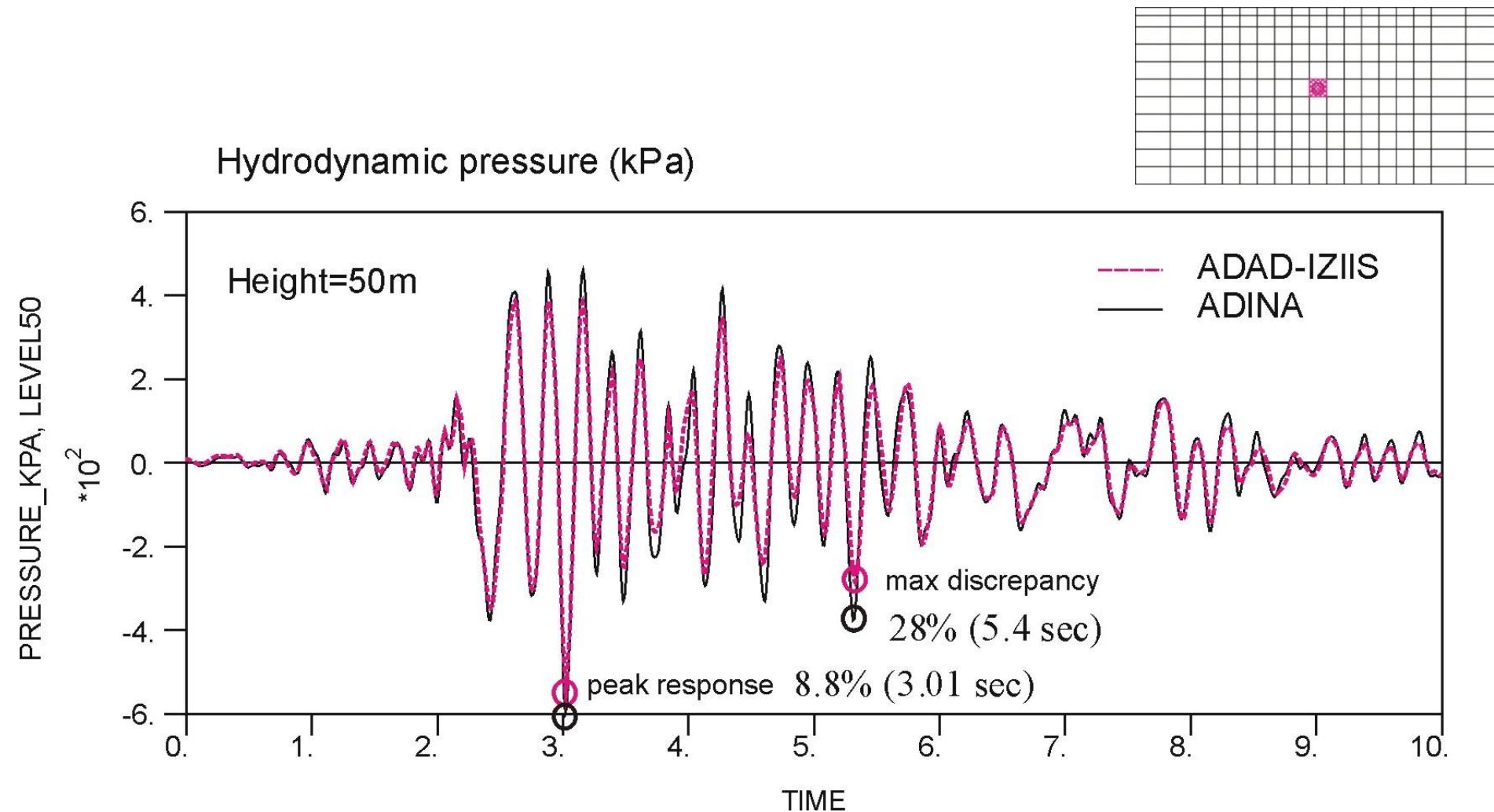
1989 Loma Prieta Earthquake



Date	October 17, 1989
Origin time	5:04:15 p.m. PDT [1]
Duration	8–15 seconds [2]
Magnitude	6.9 M_{w} [2]
Depth	12 mi (19 km) [1]



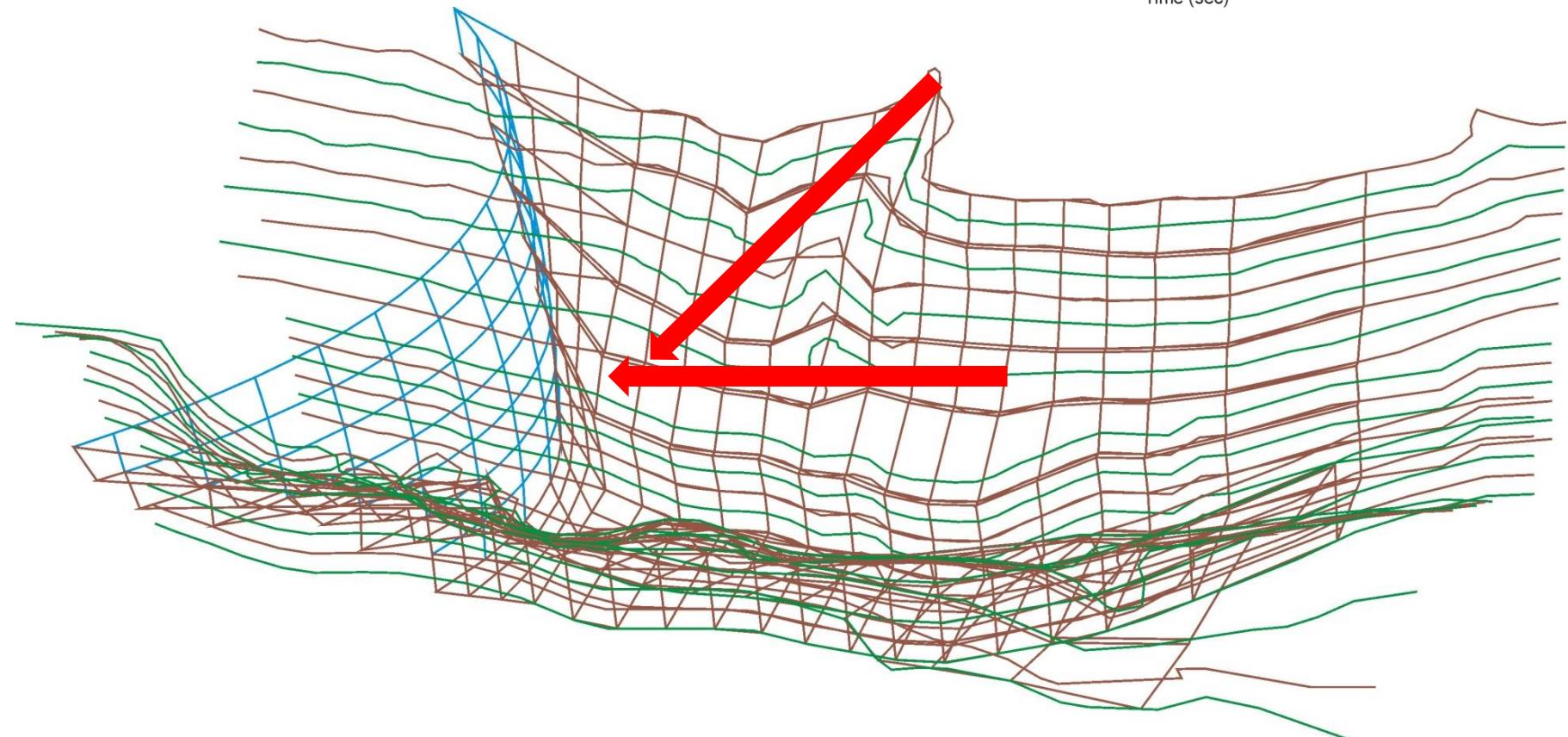
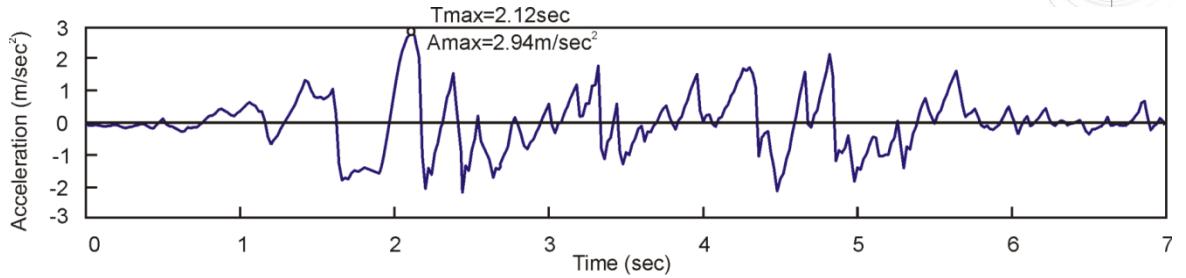
RESULTS: Comparison of HD pressures



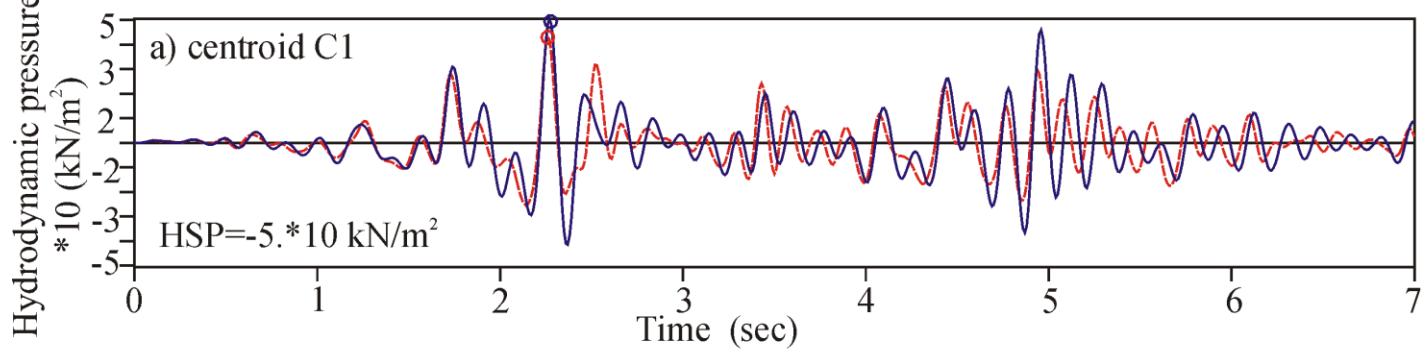
Conclusion: HDI matrix method yields accurate calculation and stable iteration process

ADAD-IZIIS software

PGA=0.3 g

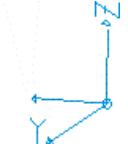
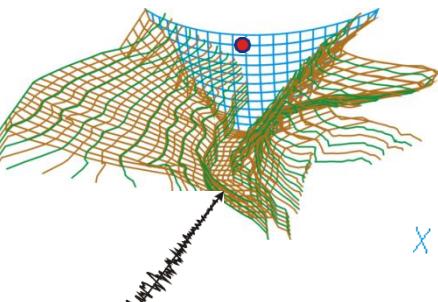


Regular reservoir: $P_{\max} = 43.44 \text{ kN/m}^2$, $T=2.26\text{s}$; Complex reservoir: $P_{\max} = 50.62 \text{ kN/m}^2$, $T=2.27\text{s}$
 $P_{\max \text{ complex}} / P_{\max \text{ regular}} = 1.17$

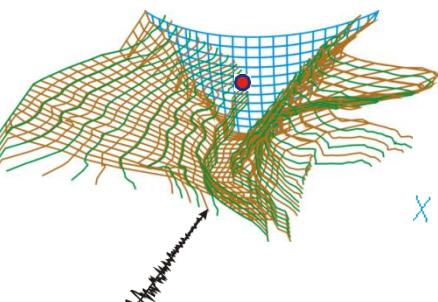
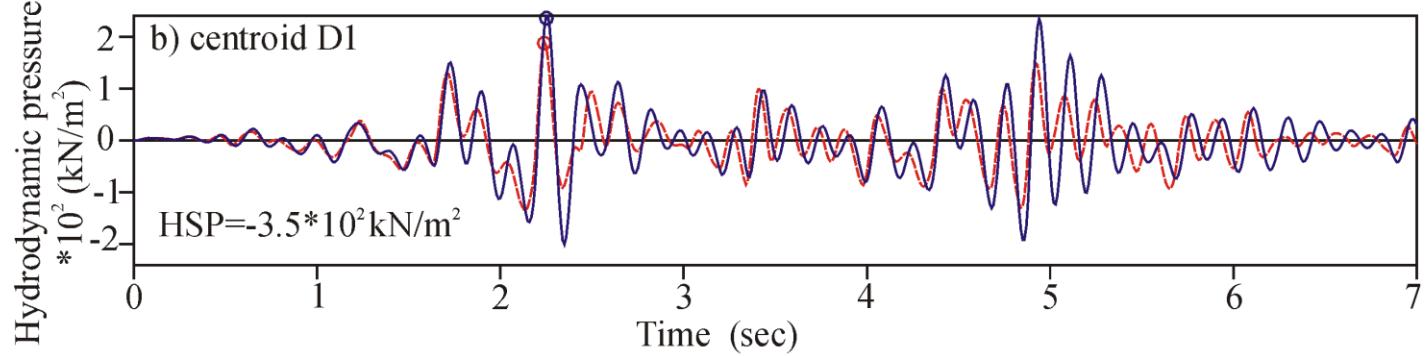


Regular Terrain

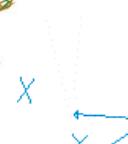
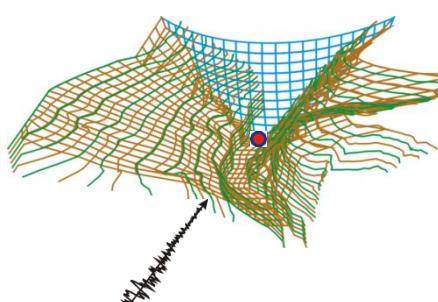
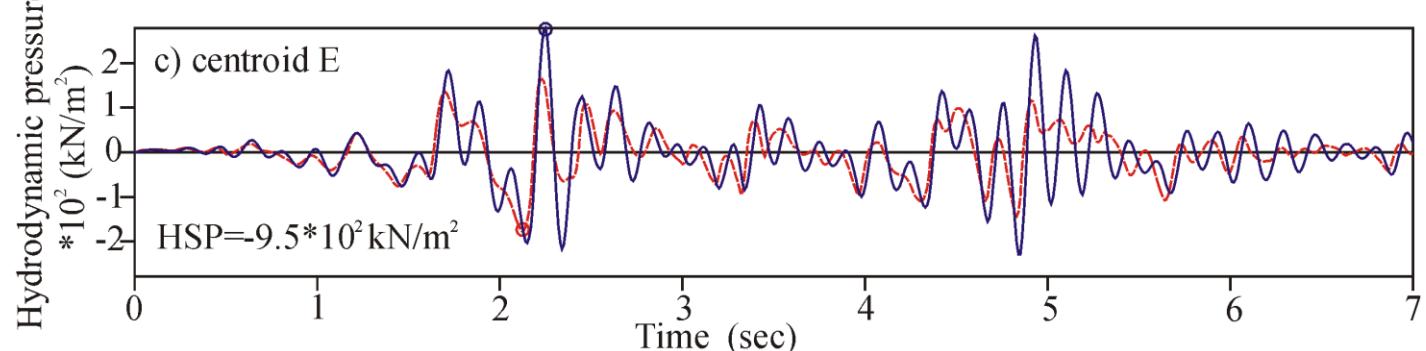
Irregular Terrain



Regular reservoir: $P_{\max} = 189.7 \text{ kN/m}^2$, $T=2.24\text{s}$; Complex reservoir: $P_{\max} = 240.3 \text{ kN/m}^2$, $T=2.26\text{s}$
 $P_{\max \text{ complex}} / P_{\max \text{ regular}} = 1.27$

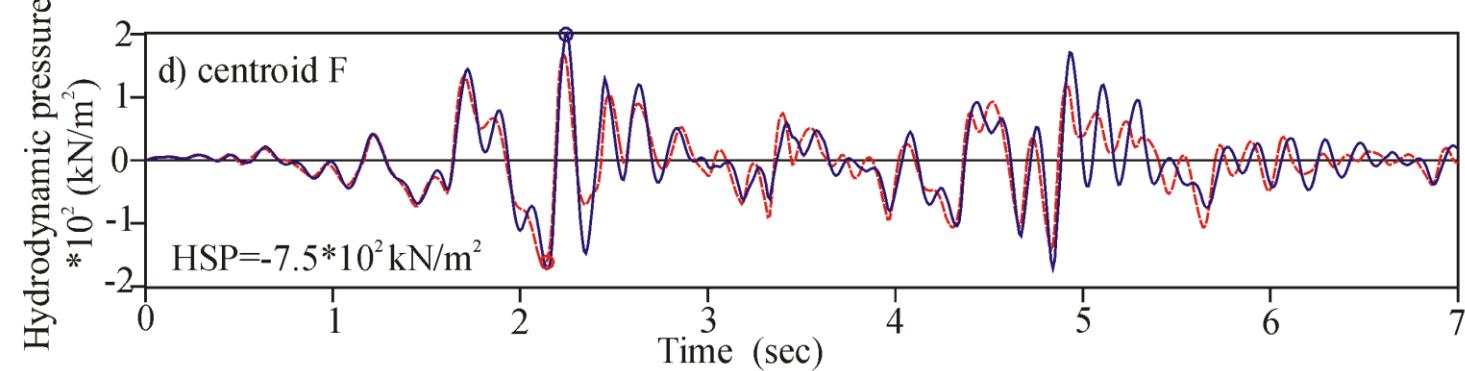


Regular reservoir: $P_{\max} = -176.7 \text{ kN/m}^2$, $T=2.12\text{s}$; Complex reservoir: $P_{\max} = 278.1 \text{ kN/m}^2$; $T=2.25\text{s}$
 $P_{\max \text{ complex}} / P_{\max \text{ regular}} = 1.57$



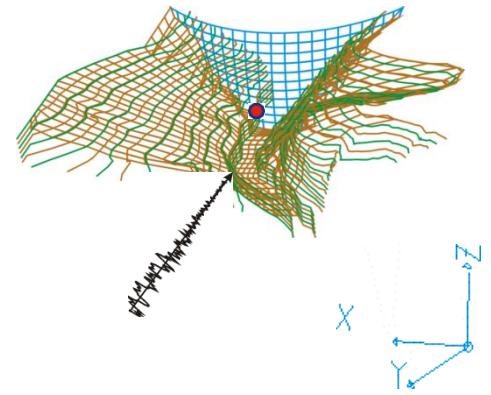
Comparison of HD pressures complex / regular reservoir

Regular reservoir: $P_{\max} = -170.2 \text{ kN/m}^2$, $T=2.13 \text{ s}$; Complex reservoir: $P_{\max} = 201.9 \text{ kN/m}^2$, $T=2.25 \text{ s}$;
 $P_{\max \text{ complex}} / P_{\max \text{ regular}} = 1.19$

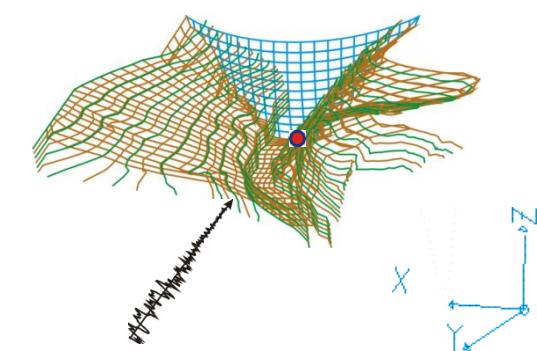
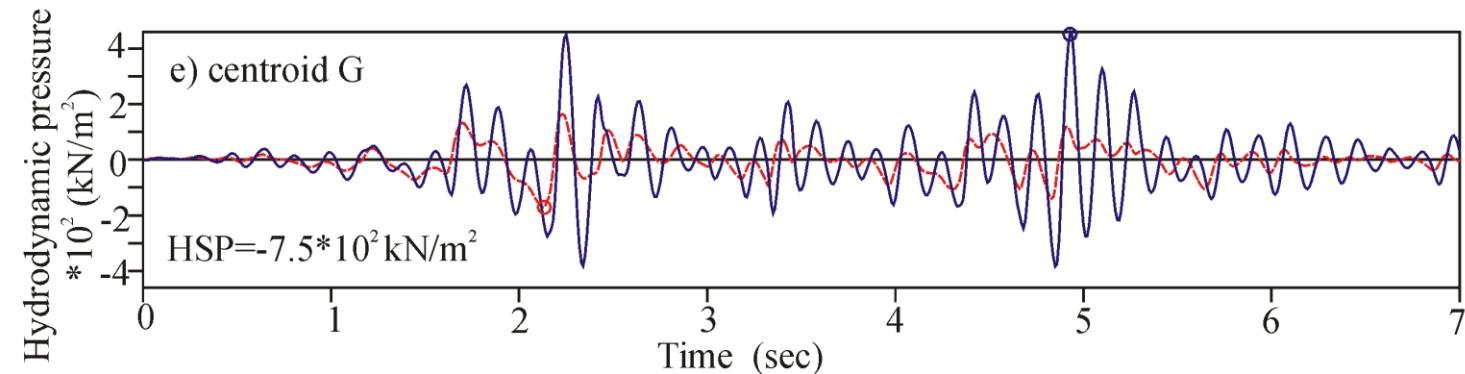


Regular Terrain

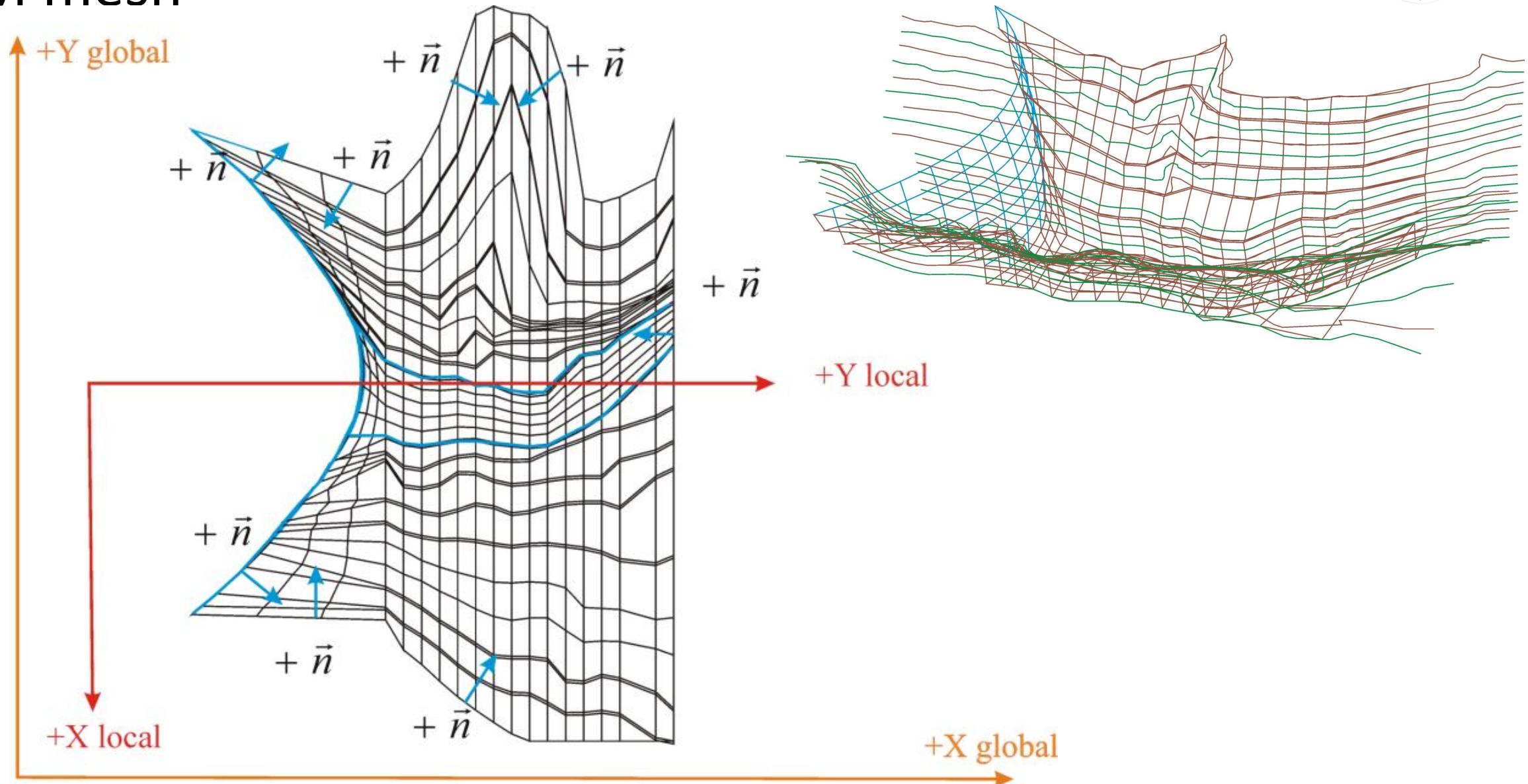
Irregular Terrain



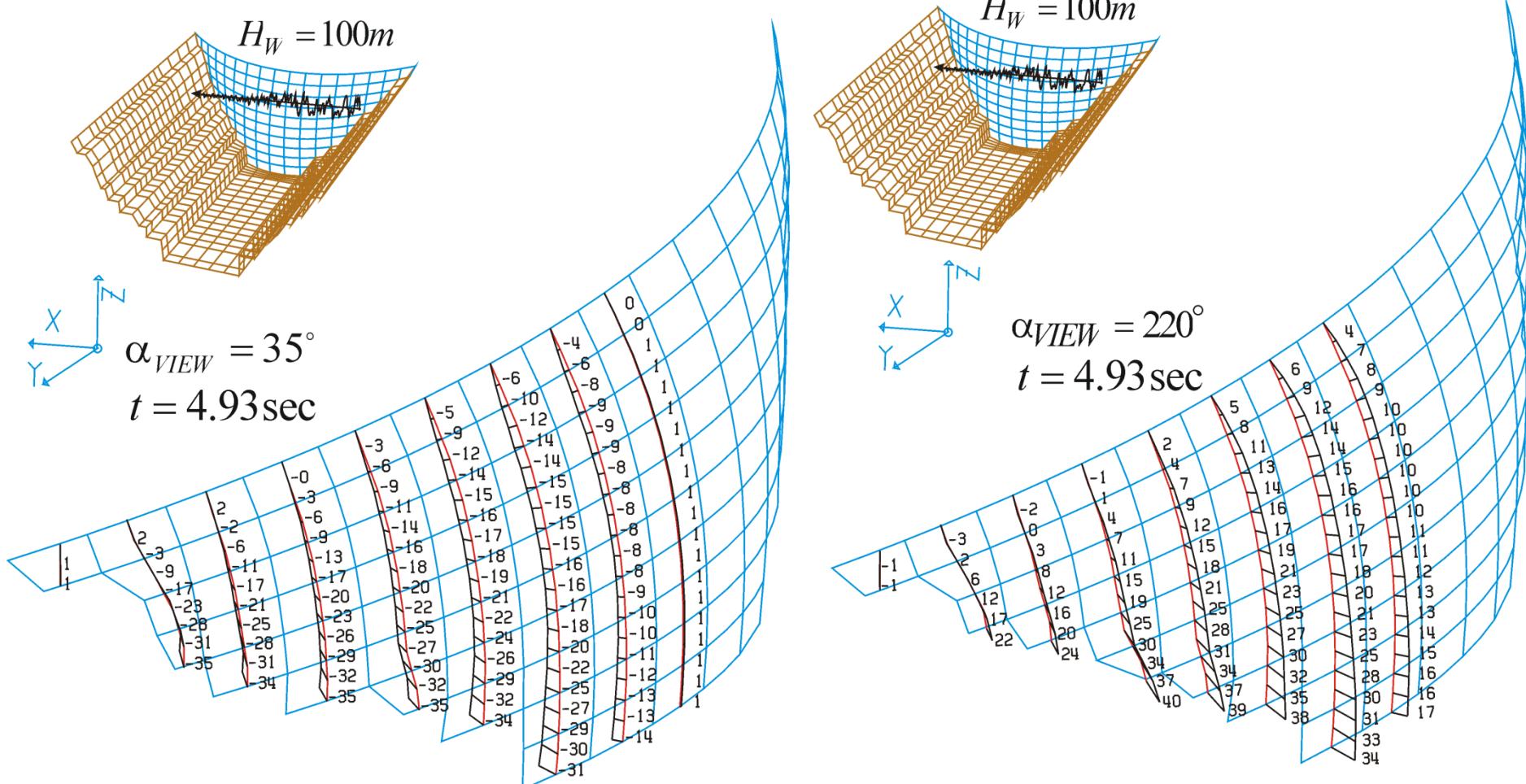
Regular reservoir: $P_{\max} = -170.0 \text{ kN/m}^2$, $T=2.13 \text{ s}$; Complex reservoir: $P_{\max} = 460.1 \text{ kN/m}^2$, $T=4.93 \text{ s}$
 $P_{\max \text{ complex}} / P_{\max \text{ regular}} = 2.70$



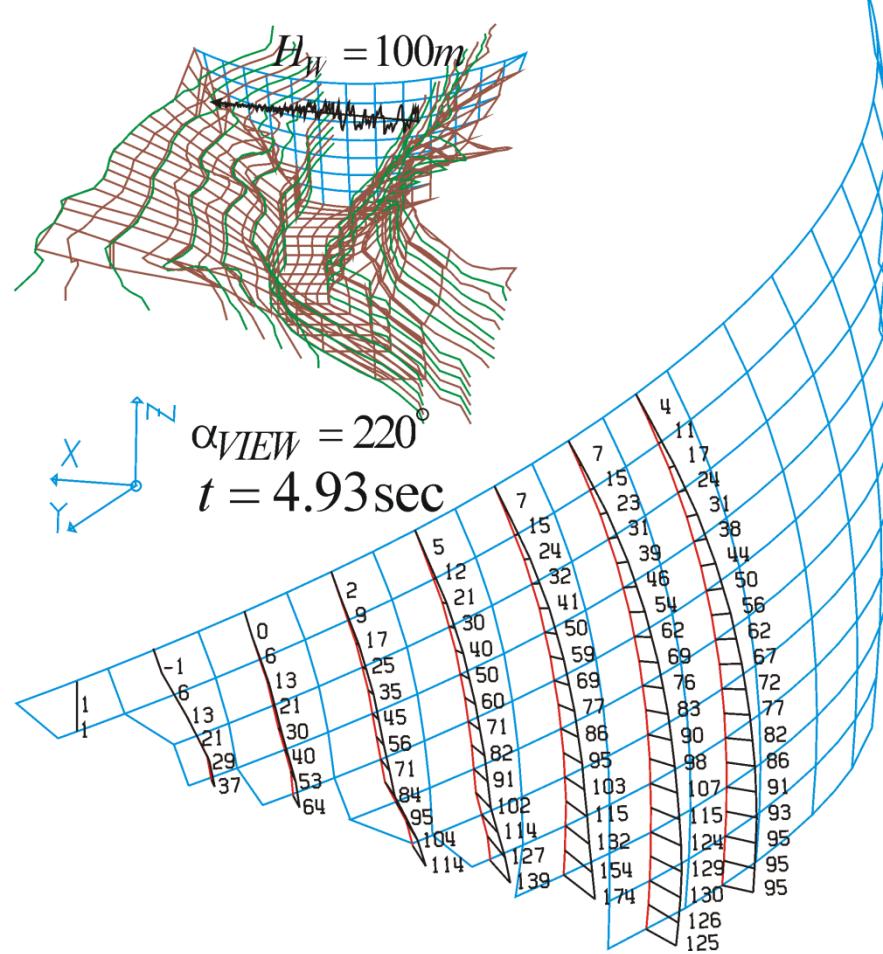
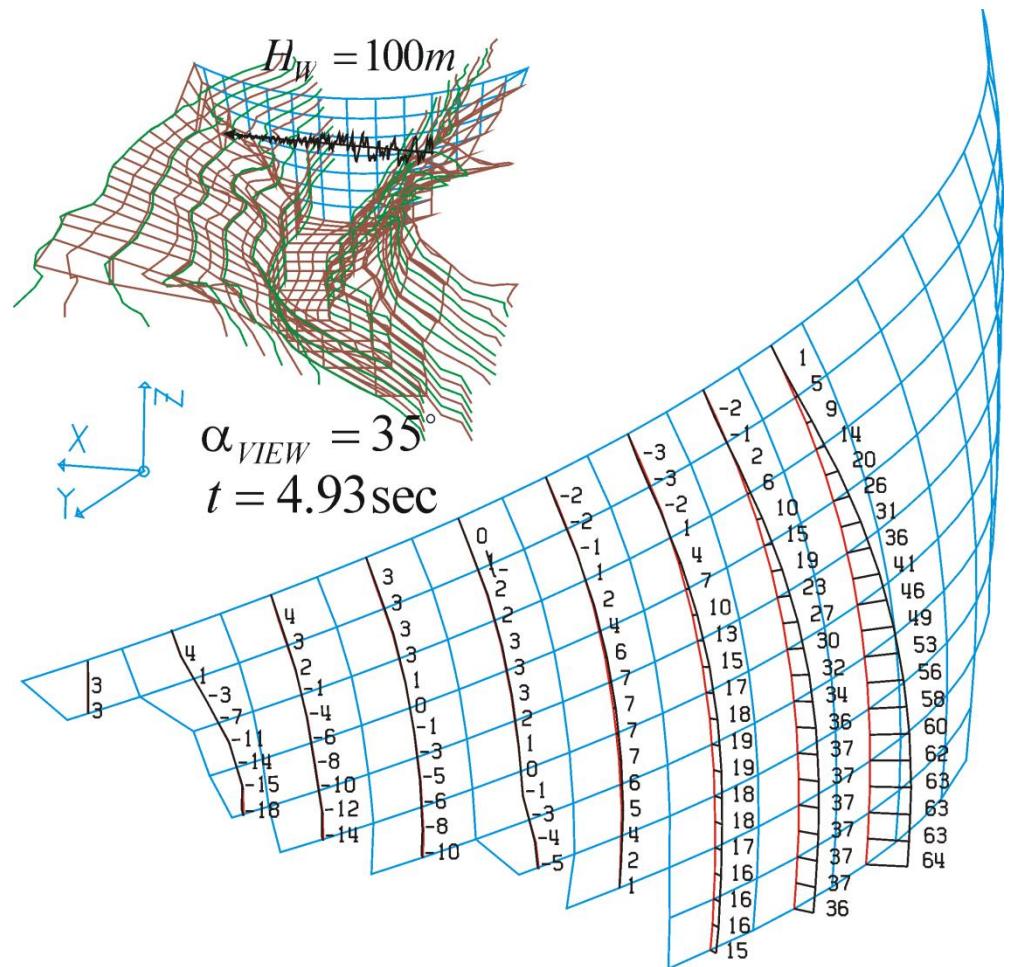
BEM mesh



HD pressures in [kPa] at dam-fluid interface of regular reservoir



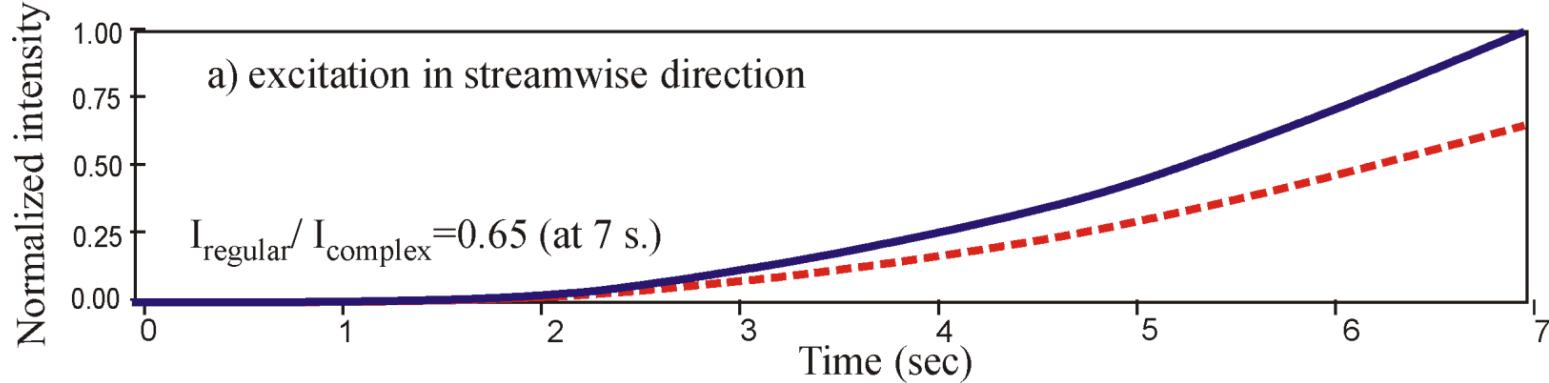
HD pressures in [kPa] at dam-fluid interface of irregular reservoir



Conclusion :

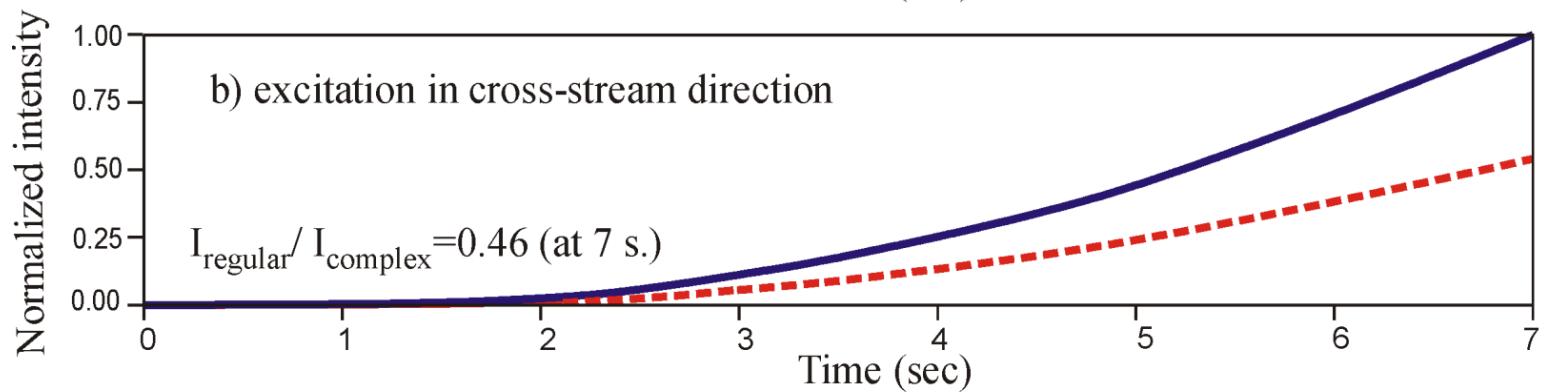
The method enables effective consideration of compound wave field.

$$I(tj) = \sum_{i=1}^{NP} \int_0^{t=tj} |f_i(t)| dt \quad tj = j * dt \quad j = 1,..nstep$$



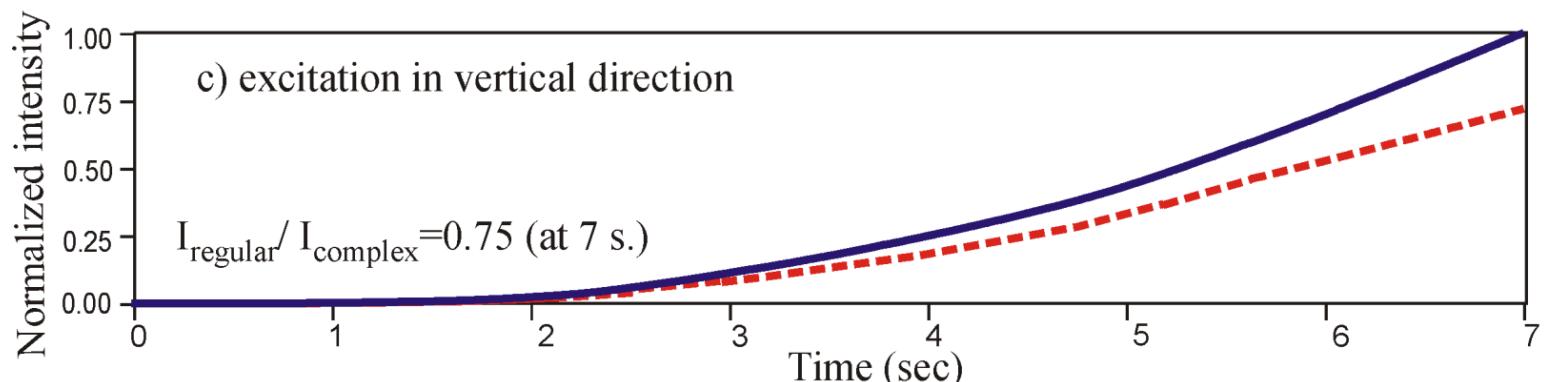
$$I_{\text{complex}} = 1.53 * I_{\text{regular}}$$

53%



$$I_{\text{complex}} = 2.1 * I_{\text{regular}}$$

100%



$$I_{\text{complex}} = 1.33 * I_{\text{regular}}$$

33%



Conclusion:

**Commercial software should consider topology
of the reservoir when calculating hydrodynamic
effects**



Thank you!

Any questions?



3D Seismic stability analysis of a concrete spillway pier affected by AAR

Ali Nour ¹, Abdelhalim Cherfaoui ¹

¹ Hydro-Quebec, GISE/BORB, Montreal, Qc., Canada

Outline

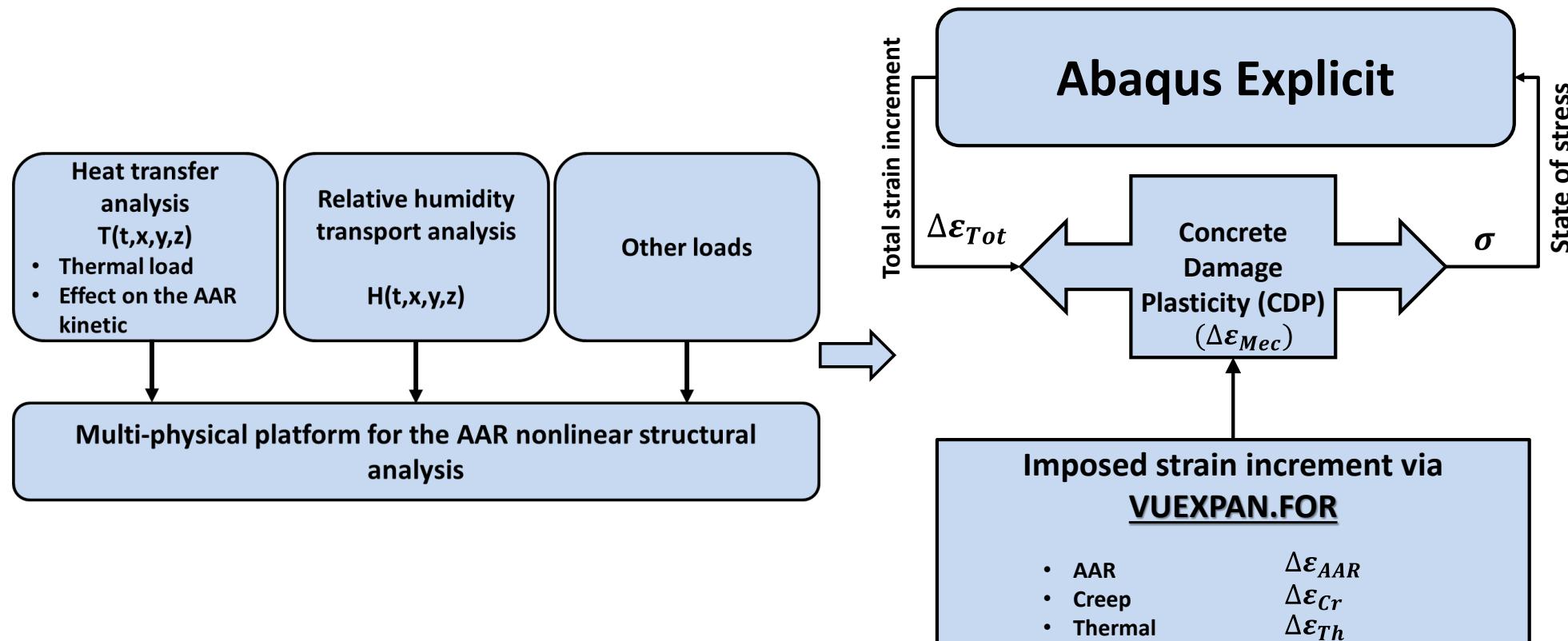
- Introduction
- Chemomechanical macro model of AAR for concrete
- Overview of nonlinear AAR analyses
 - *Overview of the finite element model*
 - *AAR parameters from calibration with measured displacements*
 - *Potential sliding plane identification*
- 3D seismic stability analysis
 - *Seismic stability analysis using the pseudo-dynamic method*
 - *3D Seismic stability analysis using dynamic time history analysis*
- Conclusion

Introduction

- A concrete Hydraulic structure located in north America is severely affected by Alkali-aggregate reaction (AAR).
- In this study, a summary of the nonlinear analyses using elaborated finite element model (FEM), based on an inhouse AAR model, is presented.
- At first, the FEM is calibrated to measured structural data. Then, the calibrated model is used to perform nonlinear AAR stress analyses to predict the future behaviour of this concrete structure.
- Considering the numerical model results and field observations, major crack patterns are identified. These crack patterns are in favor to form potential failure planes (sliding planes) of concrete blocks, and stability analysis is performed.
- In this study, the 3D seismic stability analysis results are presented for the spillway pier.
- The 3D seismic stability analysis of the identified concrete block is performed using the pseudo-dynamic method and validated using a reduced FEM in time domain using the Abaqus Explicit solver.

Chemomechanical macro model of AAR for concrete

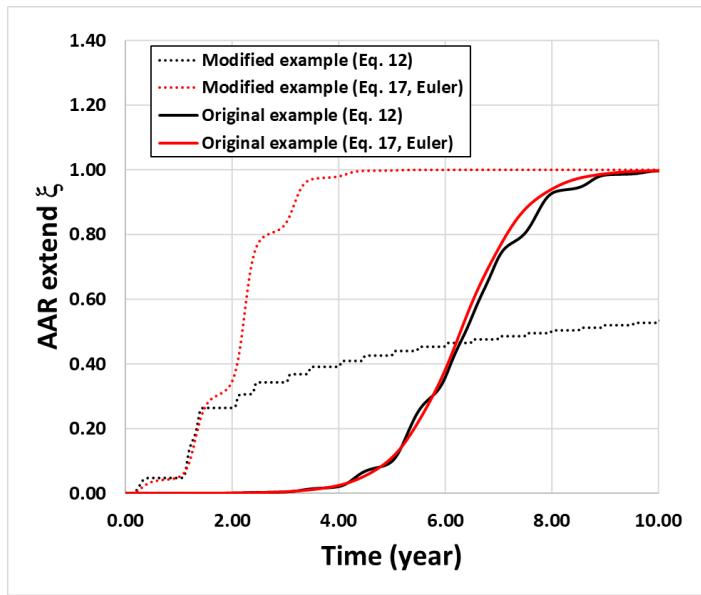
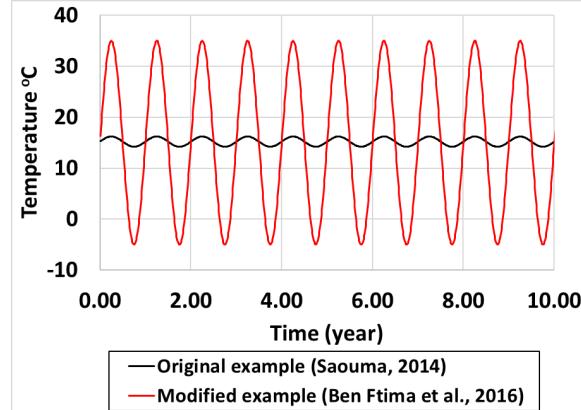
- The effects of AAR are introduced in Abaqus Explicit solver by way of the VUEXPAN user subroutine (inhouse macro scale AAR model) jointly with the concrete damage plasticity (CDP) model of Abaqus.



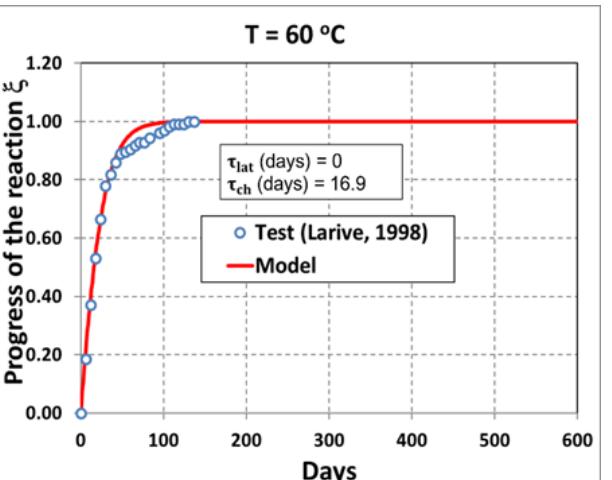
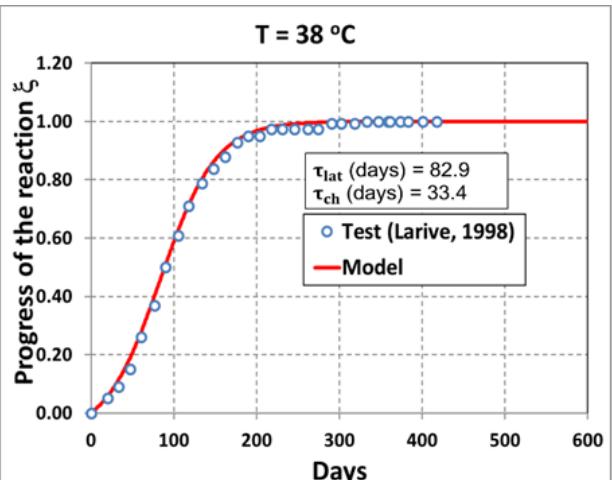
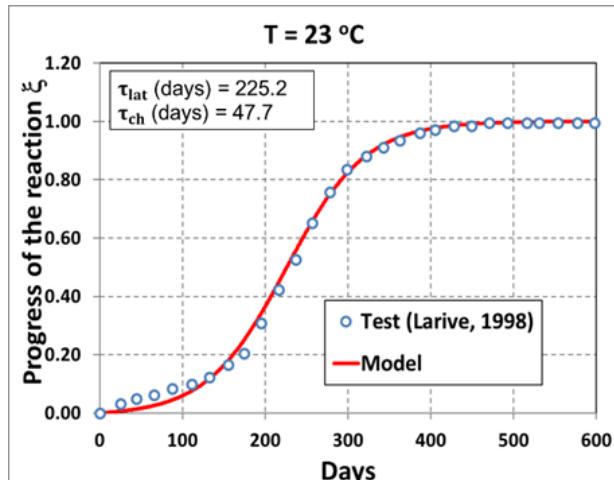
Chemomechanical macro model of AAR for concrete

Verification at the material level

Verification of AAR kinetic incremental scheme

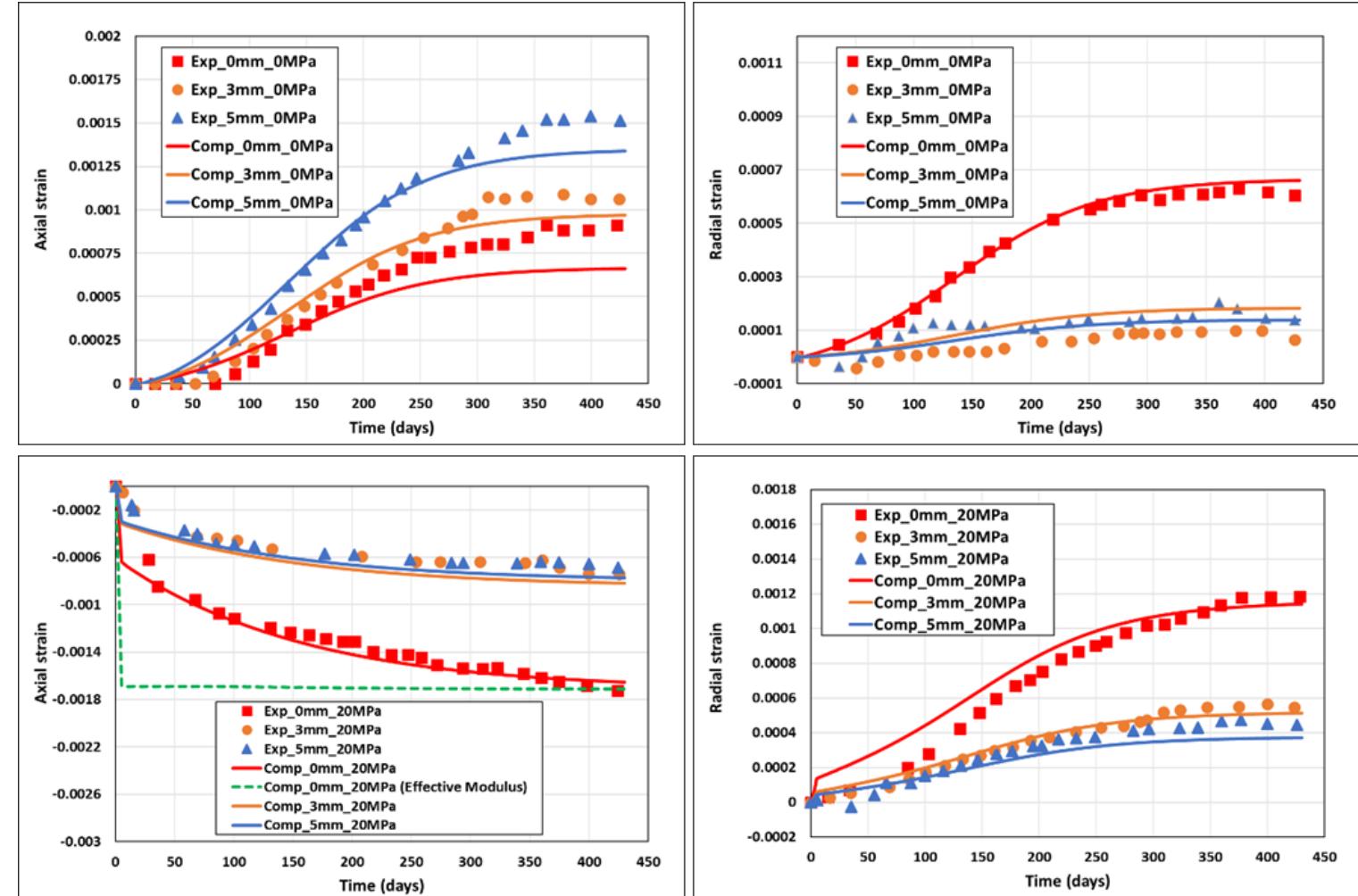
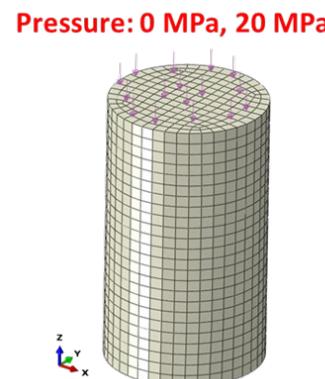
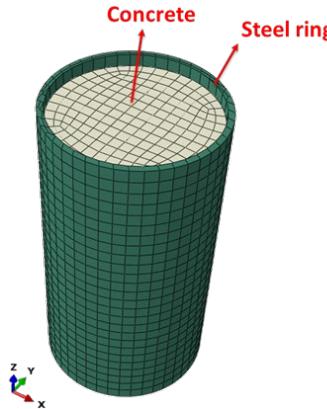


Verification of AAR kinetic progress using Larive's (1998) experimental data



Chemomechanical macro model of AAR for concrete

Validation of AAR expansion transfer from high to low confined direction (test results of Multon and Toutlemonde (2006))



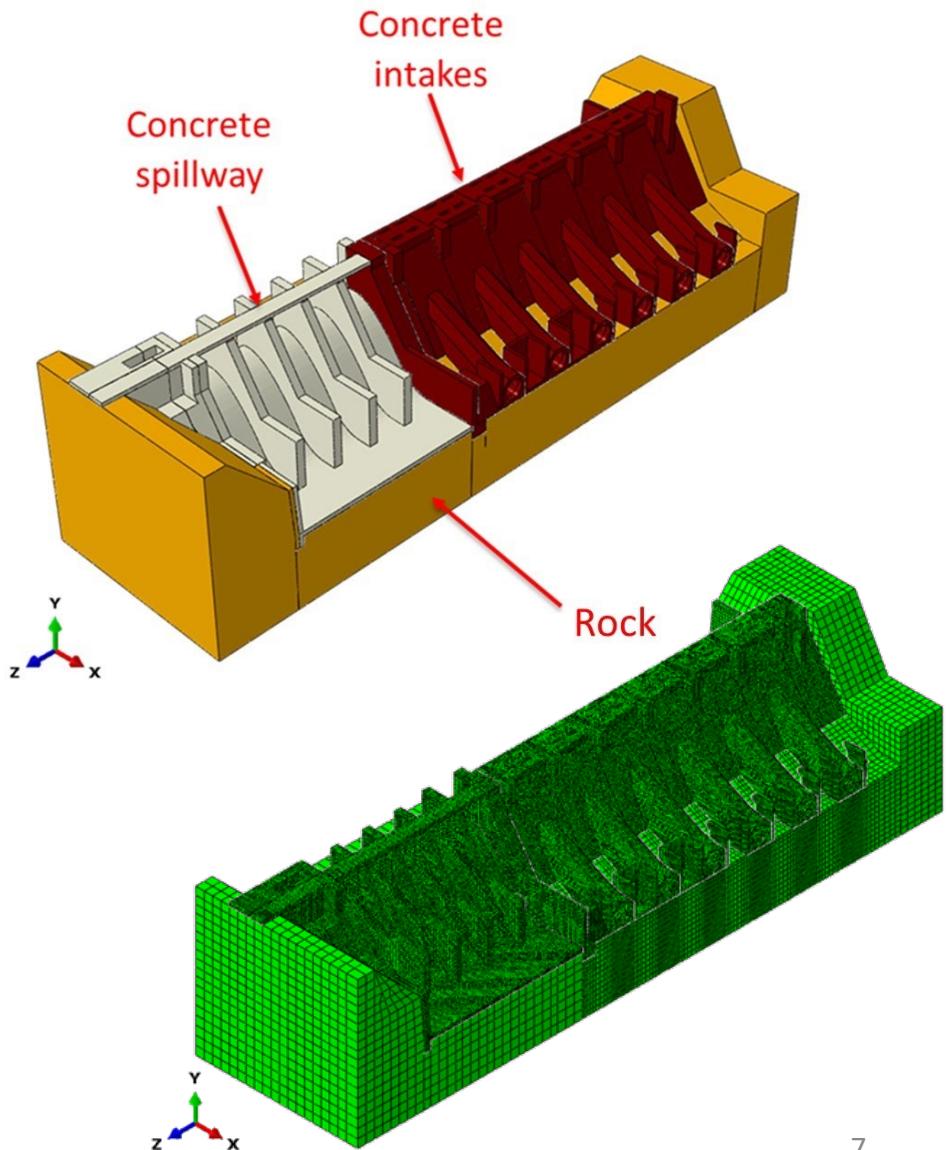
Overview of nonlinear AAR analyses

Overview of the finite element model

The nonlinear AAR analysis considers:

- The spatial distribution of temperature and relative humidity
- The slot-cutting modeling
- Concrete creep
- Existing steel reinforcement
- Mechanical properties degradation due to AAR
- Concrete damage

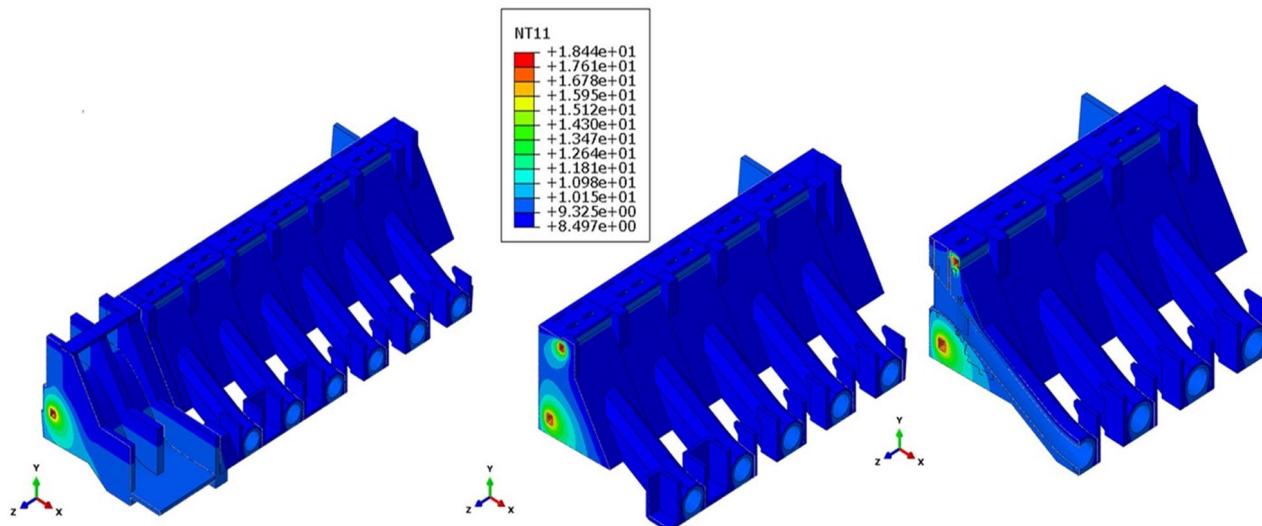
Concrete		
	Initial, $\xi = 0$	Final, $\xi = 1$
Elastic modulus (GPa)	25.0	15
Compressive strength (MPa)	25	25
Tensile strength (MPa)	2.5	1.5
Fracture Energy (N/m)	275	165
Rock		
	30.0	-
Elastic modulus (GPa)	30.0	-
Poisson ratio	0.20	-
Density (kg/m^3)	2600	-



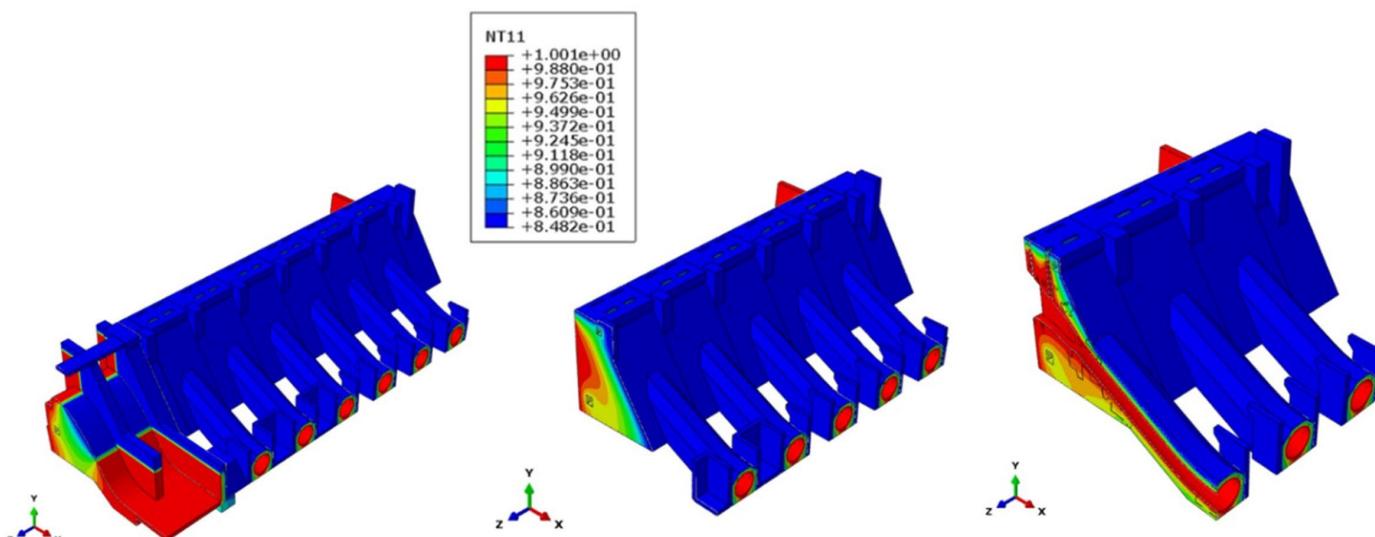
Overview of nonlinear AAR analyses

Overview of the finite element model

Spatial distribution of temperature



Spatial distribution of relative humidity

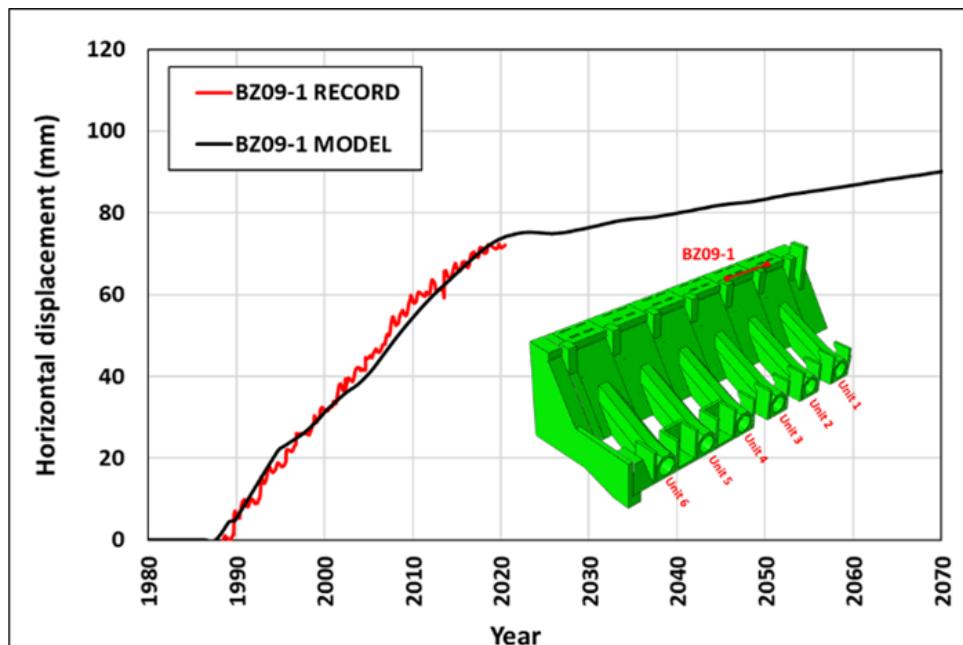
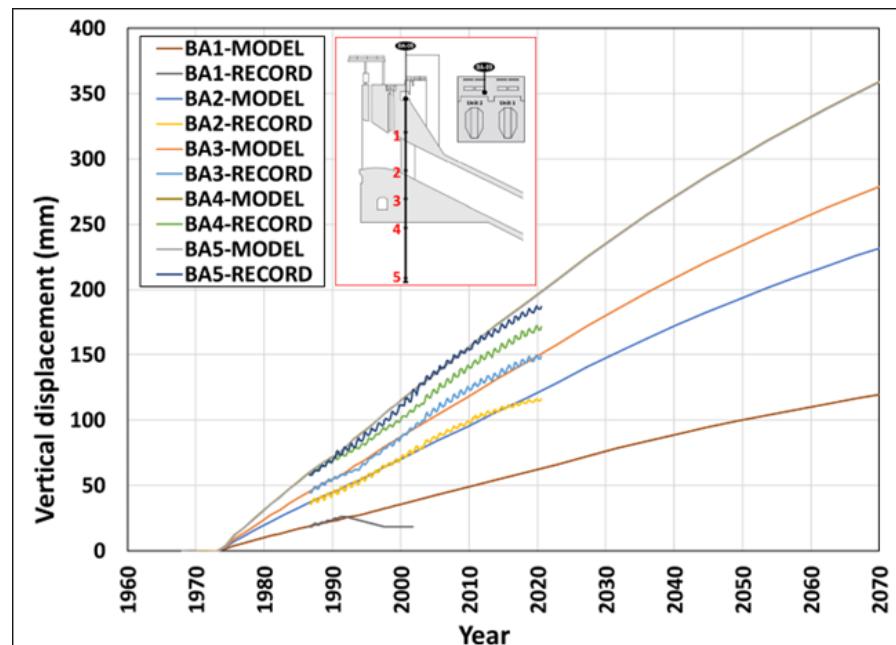


Overview of nonlinear AAR analyses

AAR parameters from calibration with measured displacements

	Free expansion, ϵ_v^{\max}	Latency time, (years)	Characteristic time (years)	Reference temperature (°C)	Lower confinement limit (MPa)	Upper confinement limit (MPa)
Intake structure	0.079	5	105	10.4	-0.5	-6
Spillway	0.071	5	105	10.4	-0.5	-6

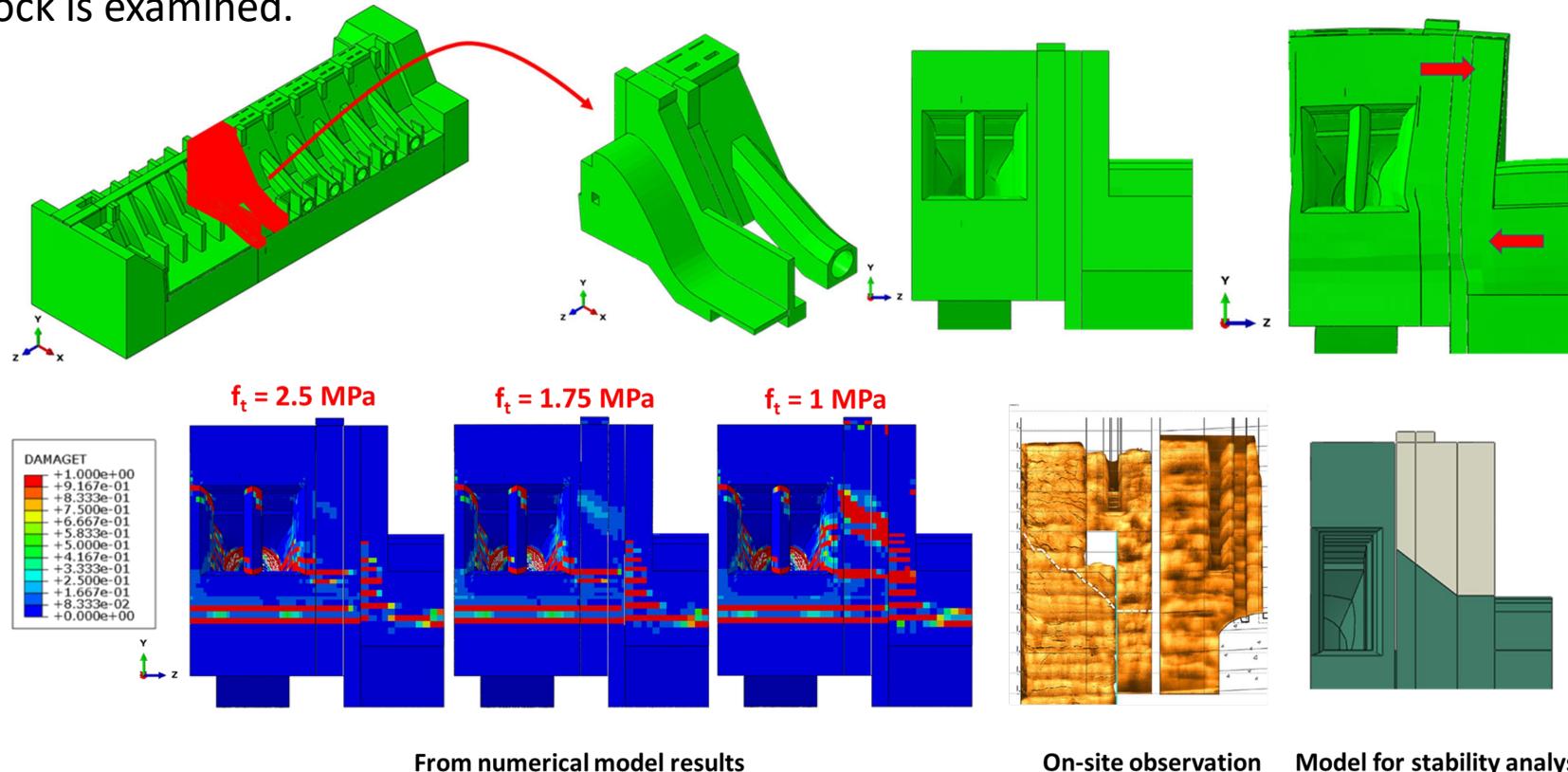
AAR parameters were obtained using the calibration procedure to achieve a satisfactory correlation of recorded displacements and predicted displacements by the numerical model



Overview of nonlinear AAR analyses

Potential sliding plane identification

- Sensitivity analyses were performed, by varying the tensile strength to determine the potential structural failure mechanisms.
- Considering numerical model results and field observations, major crack patterns were identified. These crack patterns could form failure planes (sliding planes) of concrete blocks. Therefore, the stability of the identified sliding concrete block is examined.

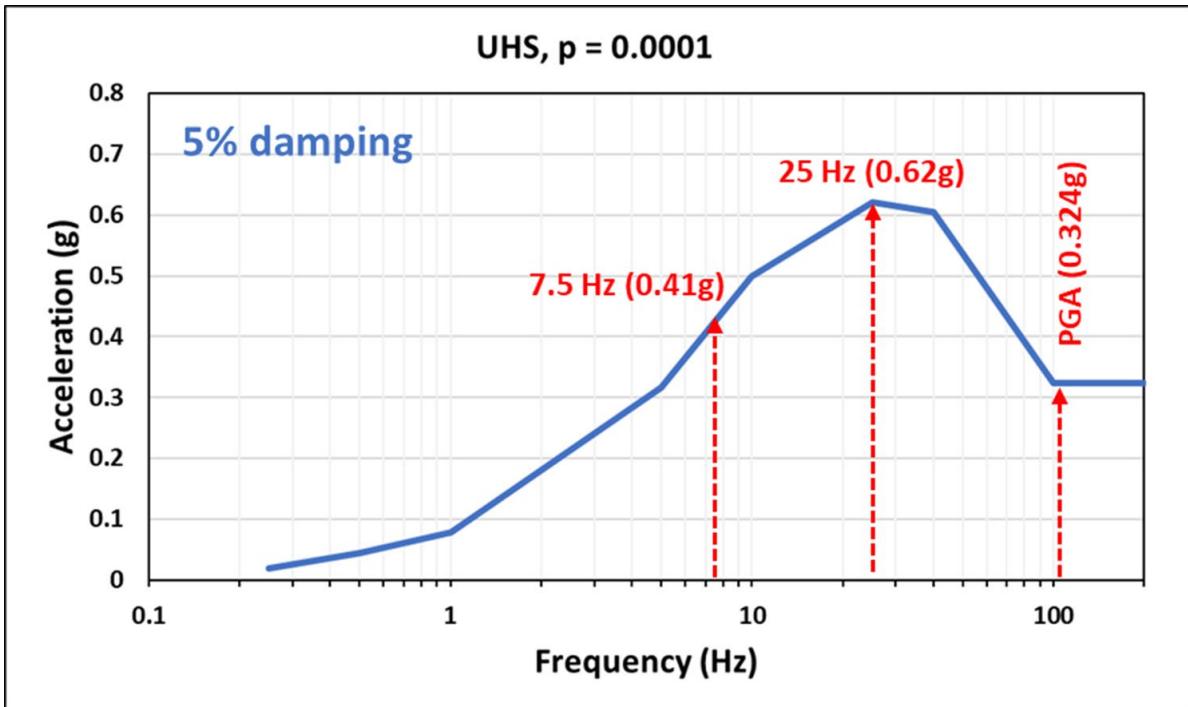


3D seismic stability analysis

- The stability of the identified concrete block cannot be idealized as two-dimensional (2D) problem, it requires three-dimensional (3D) analysis.
- AAR concrete expansion generates internal forces controlled by displacement.
- Once a concrete block starts moving through a sliding plane that has formed, these internal forces due to AAR are released.
- As a result, only loads controlled by external forces were considered in the stability analyses: gravity, water pressure, uplift pressure, ice load and earthquake including Westergaard load.

3D seismic stability analysis

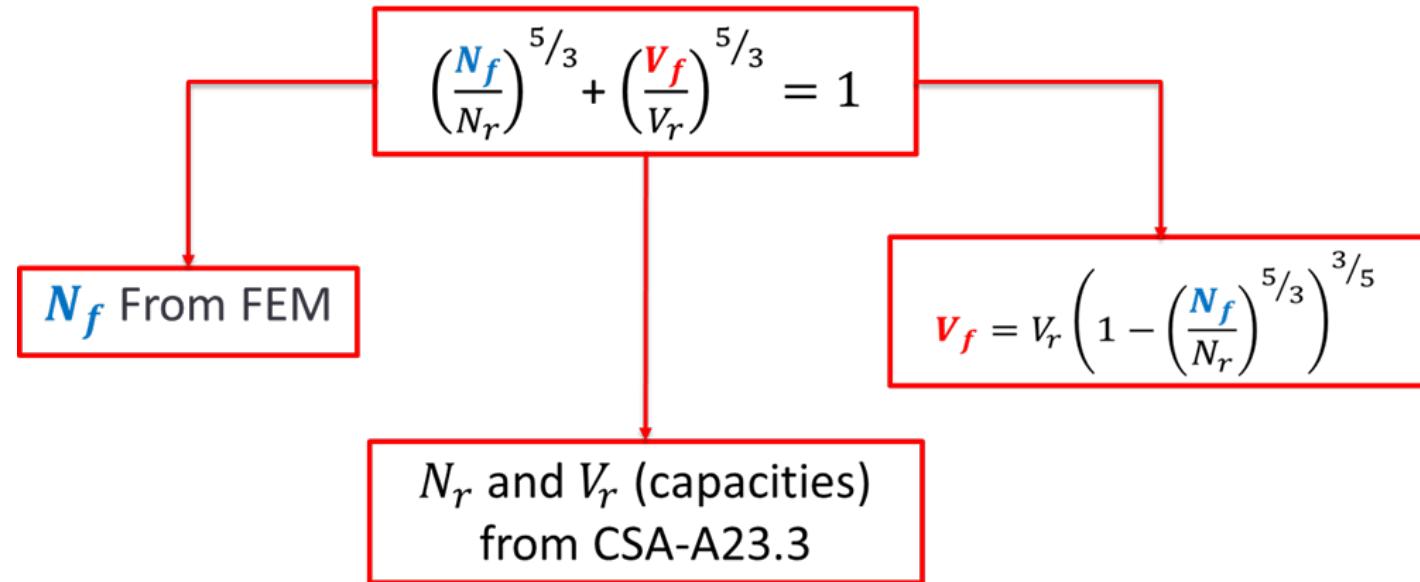
3D Seismic stability analysis using the pseudo-dynamic method



- The UHS is obtained from a site-specific study considering 1/10000 return period (CDA (2013)).
- The first mode has a computed (FEM) and measured (from ambient vibration) frequency of ~7.5 Hz.
- The dam is relatively flexible. Therefore, the pseudo-static method is not acceptable.
- The damping should be selected consistent with the expected level of deformation and the extent of nonlinear behaviour.
- In perspective to reduce the conservatism, higher global damping values could be considered (7% global damping and higher but not more than 10% as recommended by (EPRI, 1991; ICOLD, 2002; FEMA, 2005; USACE (2005 and 2007)) in the frame of a sensitivity analyses of the stability calculation.

3D seismic stability analysis

3D Seismic stability analysis using the pseudo-dynamic method



- In this study, the existing steel reinforcement bars were included to improve the safety factors for stability analysis.
- Due to AAR, as for shear friction, the vertical component of the tensile stress in the bar will induce an equal and opposite compressive normal stress (post-tension force) on the sliding plane, which will increase the shear strength.

3D seismic stability analysis

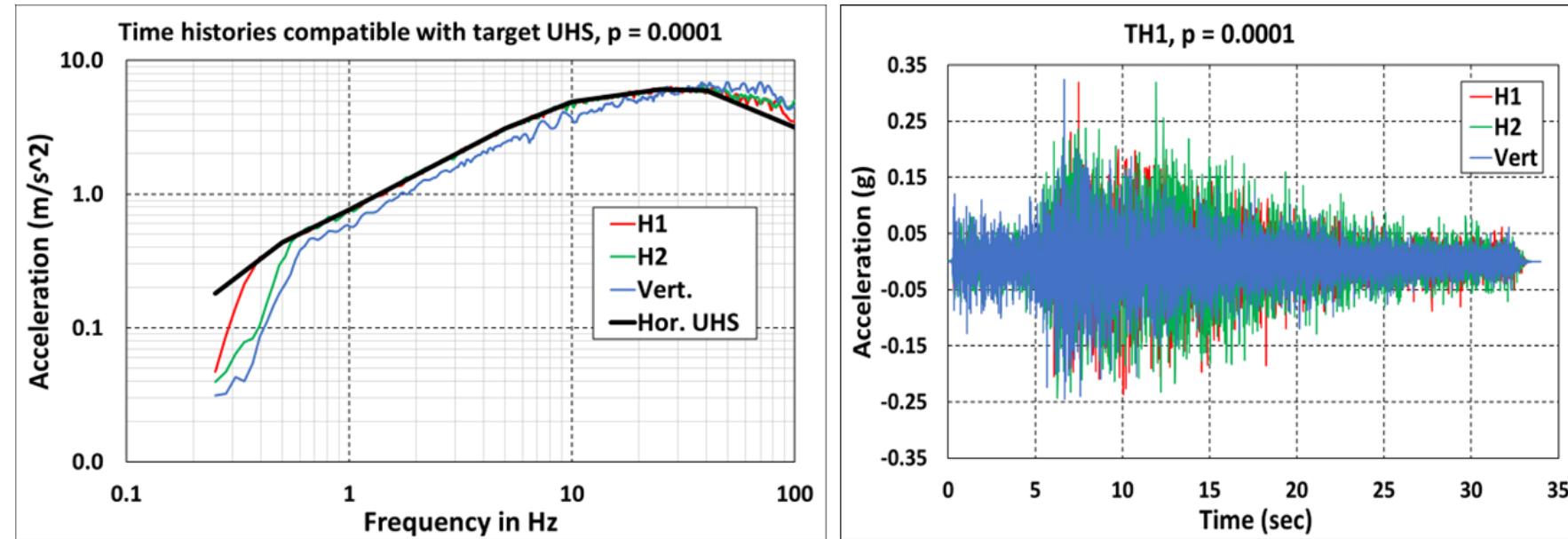
3D Seismic stability analysis using the pseudo-dynamic method

Safety factors for sliding (friction angle $\phi = 45^\circ$ ($\tan \phi = 1$), Cohesion $c = 0$)		
Pseudo dynamic based on 25 Hz spectral acceleration		
	Without existing reinforcement	With existing reinforcement
5% global damping	0.9	1.22
7% global damping	1.02	1.35
10% global damping	1.13	1.48

- The CDA requirement for sliding is not met only for the conservative case when the contribution of existing steel reinforcement is ignored (5% global damping). Despite this, the obtained factor of safety (FS) is close to 1 (0.9).
- Because a 1/10 000-year earthquake is applied, and considering the high frequency content of the seismic excitation, a safety factor below 1 will typically induce a very small and acceptable residual displacement of the order of a few mm.
- However, accounting reasonably for the benefit effects of the existing reinforcement and the mobilised global damping allow enhancing the required safety factors (FS > 1). Therefore, the analysed concrete block is stable.

3D seismic stability analysis

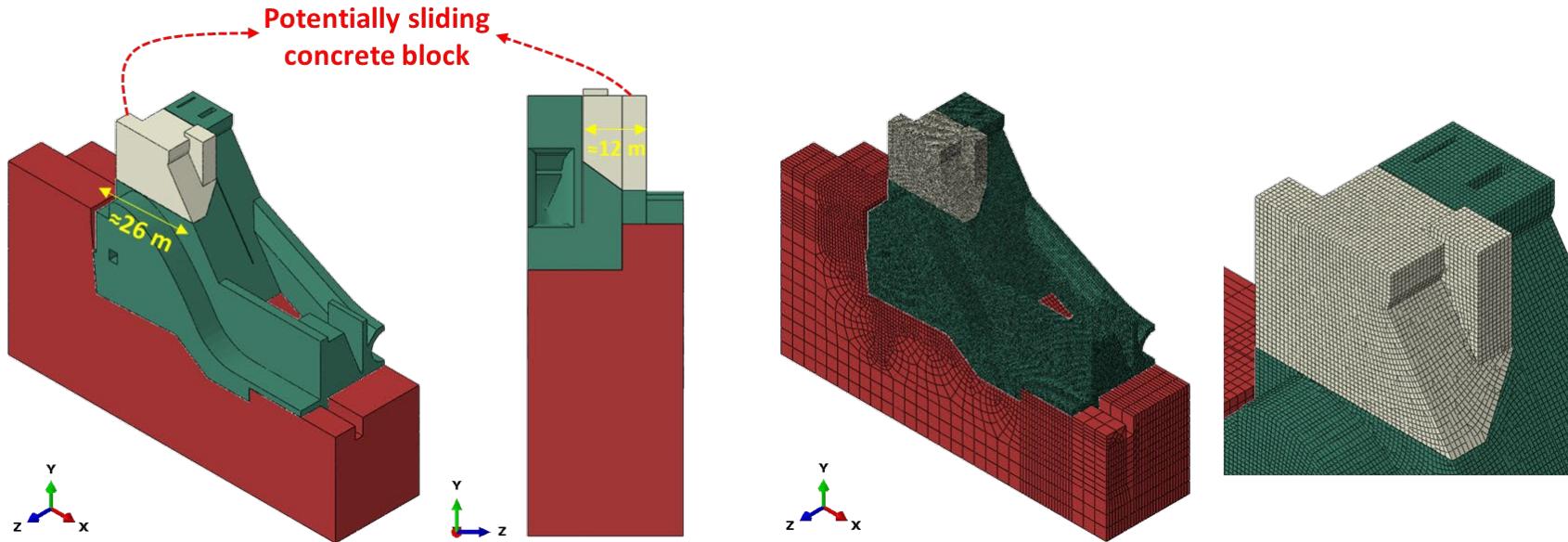
3D Seismic stability analysis using dynamic time history analysis



- The scope is to explore the transient response of the identified sliding plane, and to validate the obtained stability analysis results using the dynamic time history procedure.
- To do so, a reduced FEM is prepared to perform the seismic analysis in time domain.
- The three components of the TH1 time histories are applied to the foundation FEM boundaries considering a massless representation of the rock. Therefore, the radiation damping is ignored.

3D seismic stability analysis

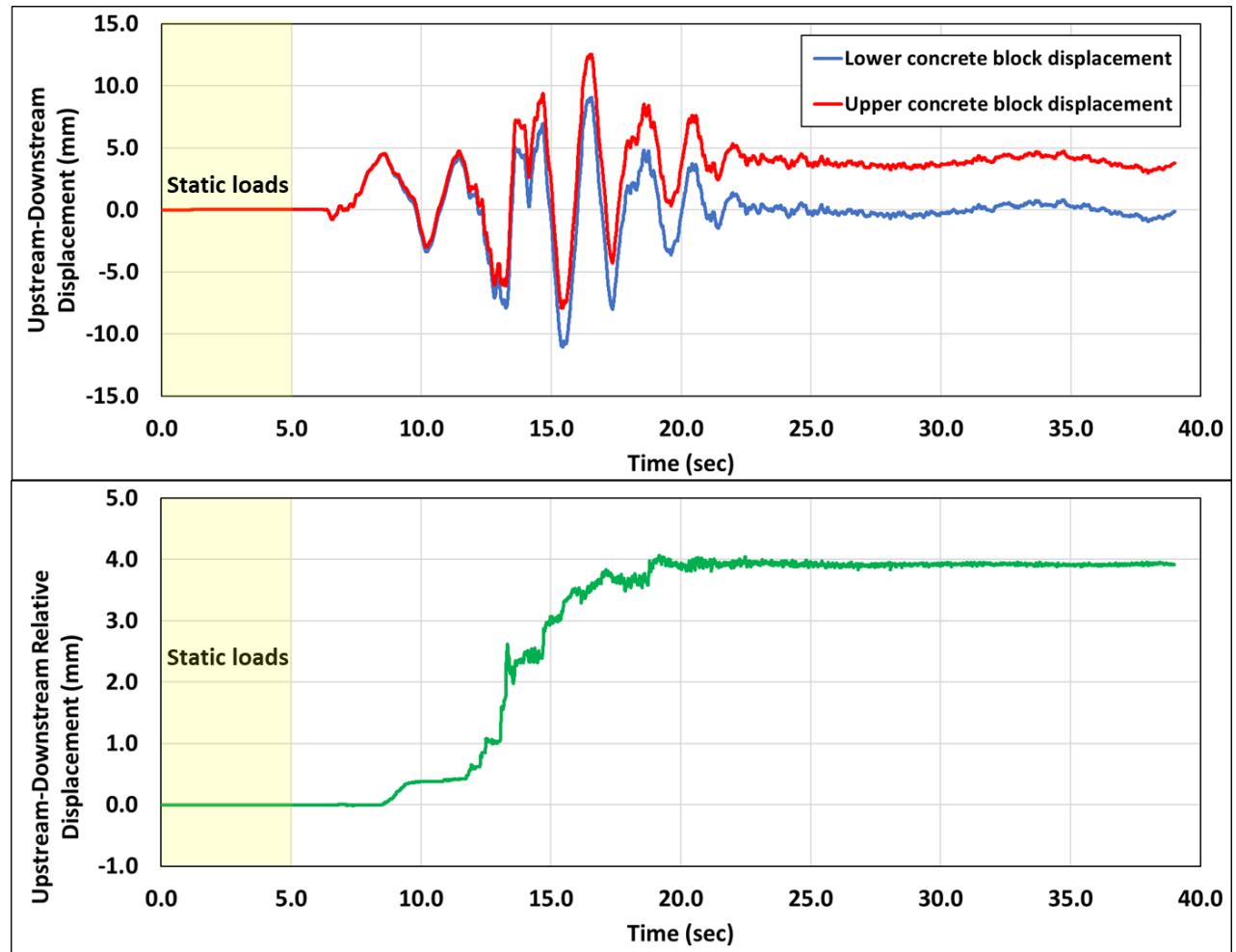
3D Seismic stability analysis using dynamic time history analysis



- The hydrodynamic effect of the water reservoir is considered as an added mass of water to the structure upstream face (Westergaard force).
- The analysis is performed assuming a contact with friction at the potentially sliding plane of the identified concrete block, by considering a friction angle $\phi = 45^\circ$ ($\tan \phi = 1$), and cohesion $c = 0$.
- CDA (2013) guidelines do not provide acceptance criteria for sliding displacements.

3D seismic stability analysis

3D Seismic stability analysis using dynamic time history analysis



- The maximum residual displacement according to the upstream-downstream direction is found to be 3.92 mm.
- The sliding displacement is obtained from conservative assumptions where several beneficial effects were ignored, namely the cohesion, the existing steel reinforcement, and the foundation radiation damping.
- For this reason, the 3.92 mm (as compared to the dimension 26 m) sliding displacement according to upstream-downstream is judged to be marginal.
- Consequently, the identified concrete block remains stable after the earthquake. Therefore, results obtained from the dynamic time history analysis validate the previously results obtained from the pseudo-dynamic analyses.

Conclusion

- In the context of life extend of an existing concrete hydraulic structure affected by AAR, a detailed FEM was prepared to perform nonlinear stress analyses to predict the future behaviour of this concrete structure and to identify major crack patterns.
- The 3D seismic stability analysis of the identified concrete block is performed using the pseudo-dynamic method and validated using the fully time history procedure.
- One confirms that the identified potentially sliding concrete block is stable, and no catastrophic failure is likely to take place for the dam, during the extended service life of this facility.
- We believe that this case study is of value to the professional community and illustrates the benefit of using advanced numerical analyses for the assessment of existing dams. The adopted methodology is useful to engineers involved in the analyses of aged and damaged structures affected by AAR.



Thank you!

Any questions?



EUCENTRE
FOR YOUR SAFETY.



Impacts of constitutive model and input ground motion selection on the seismic response of an earth dam

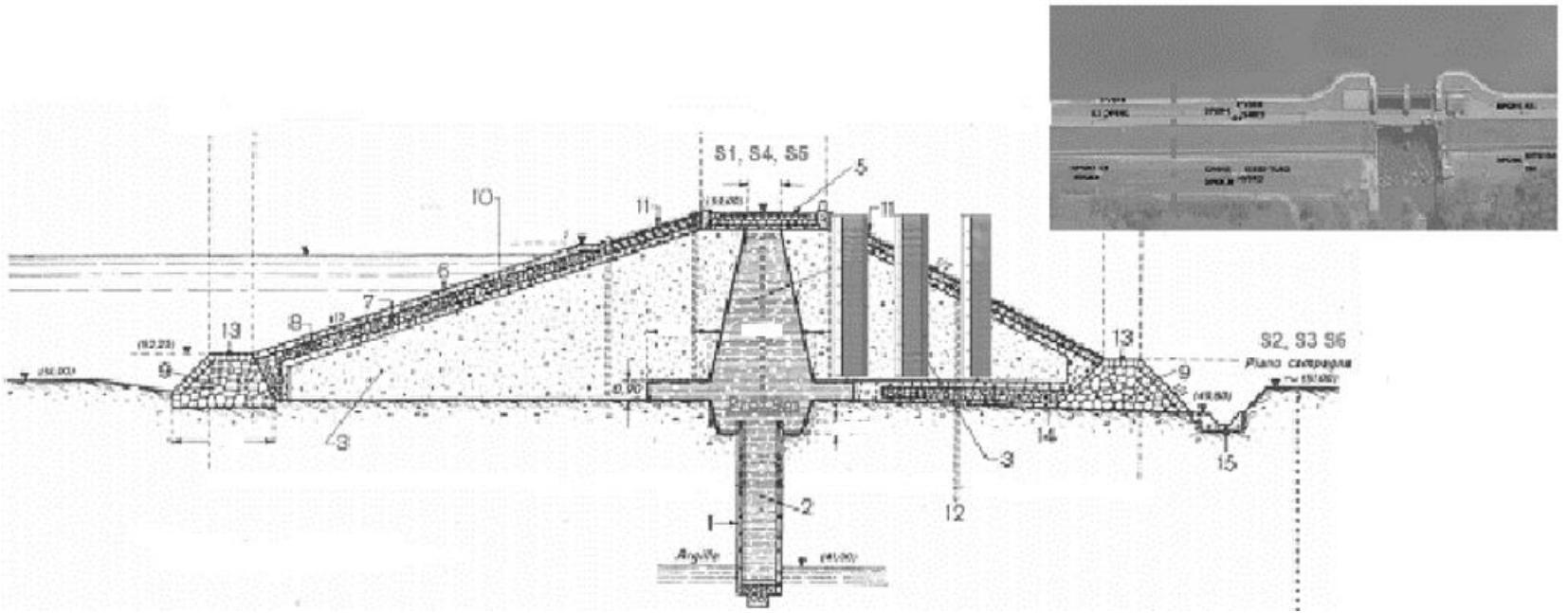
Özcebe AG¹, Gioffrè D², Famà A¹,
Zuccolo E³, Bozzoni F¹, Lai CG^{1,2}

¹ EUCENTRE, Pavia, Italy

² DICAr, University of Pavia, Italy

³ OGS, Udine, Italy

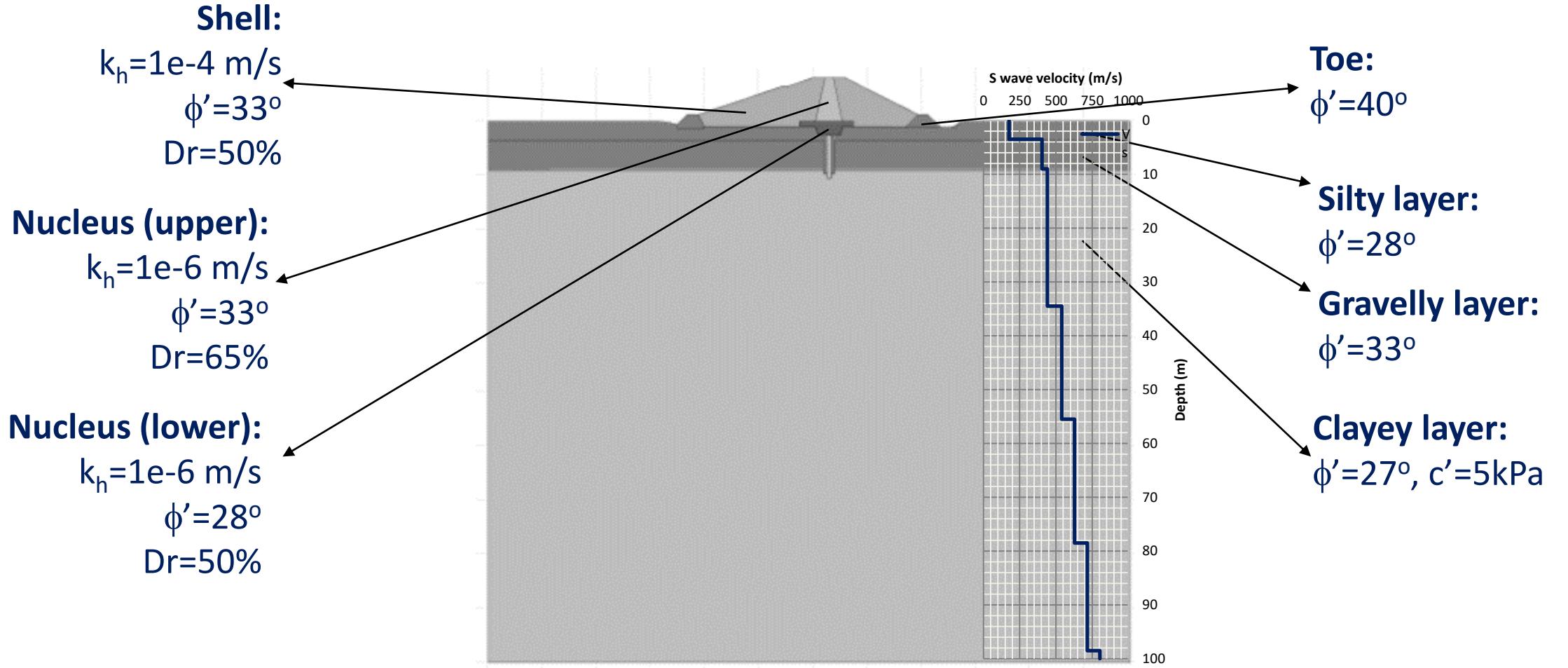
Background



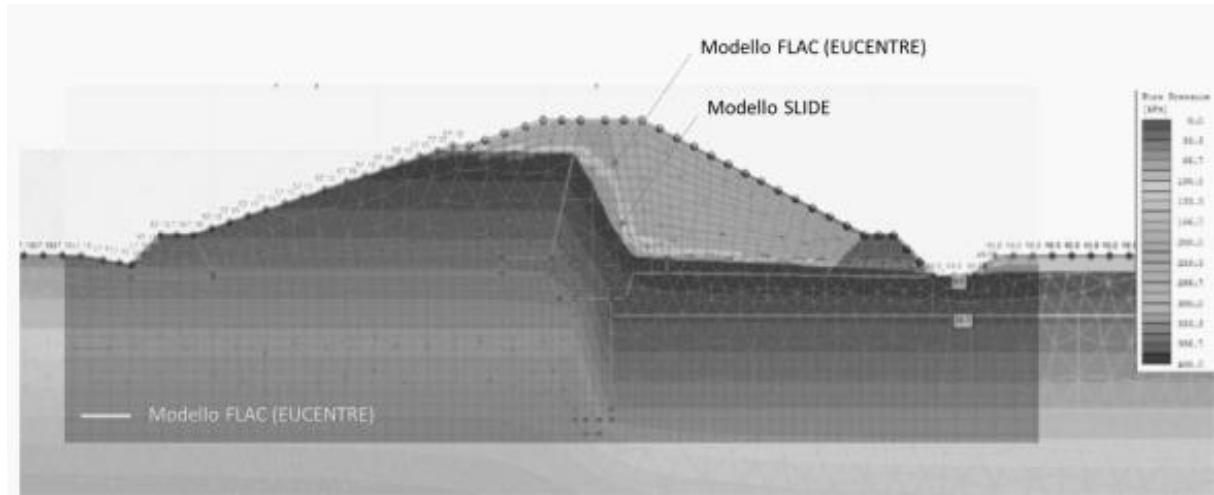
The earth dam is located in the Central Italy, with approximately ~10 meters of crest height and ~50 meters of plan dimension.

Nucleus made of a well compacted granular material with fine content of about 10%.

Setup and properties



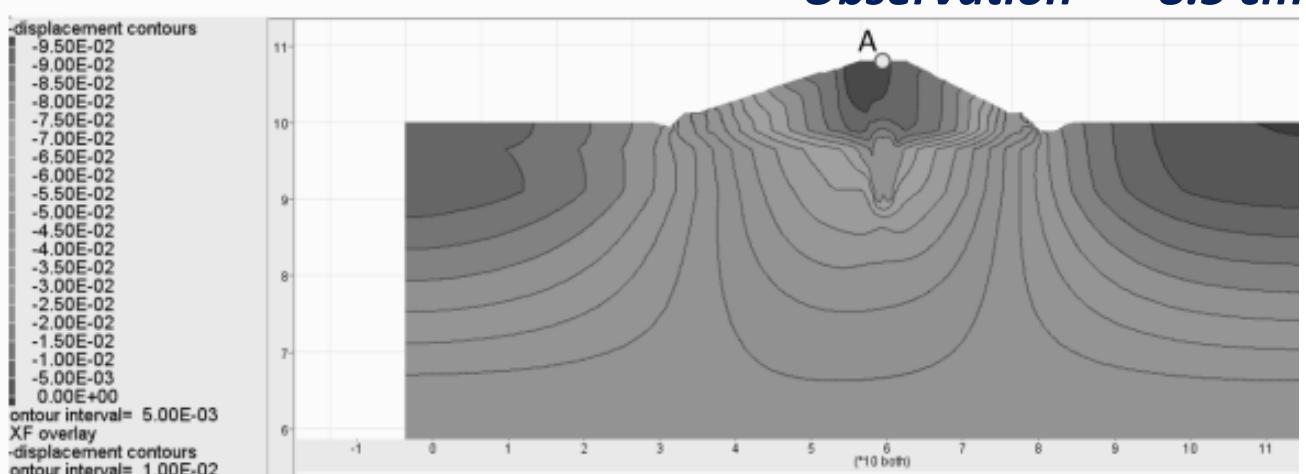
Static Analyses



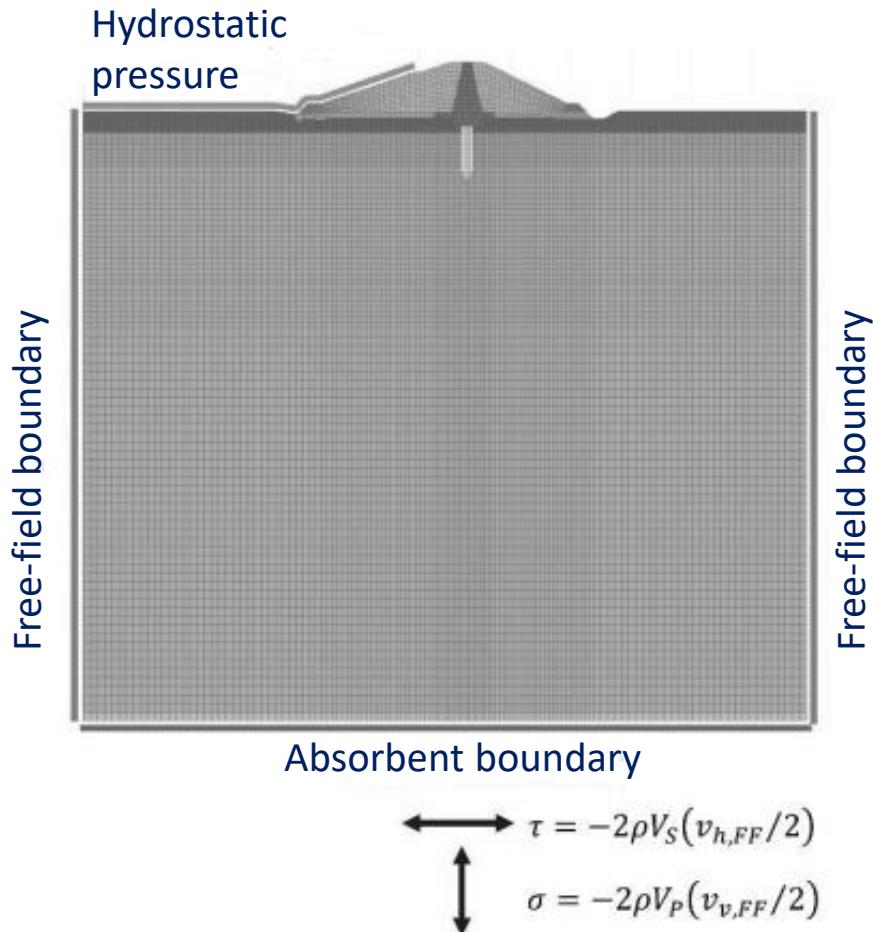
By providing the measured oedometric moduli for the fine grained layers and operative moduli ($\sim 1/6$) for the coarse grained materials, vertical settlement of the crest is compared with the observed value.

Water table location (phreatic surface) formed after Step 3 is compared (blindly) with an independent solution provided by the client, the comparison comes out to be quite convincing.

FLAC analyses = 9.4 cm
Observation = 8.5 cm



Dynamic Analyses - Setup

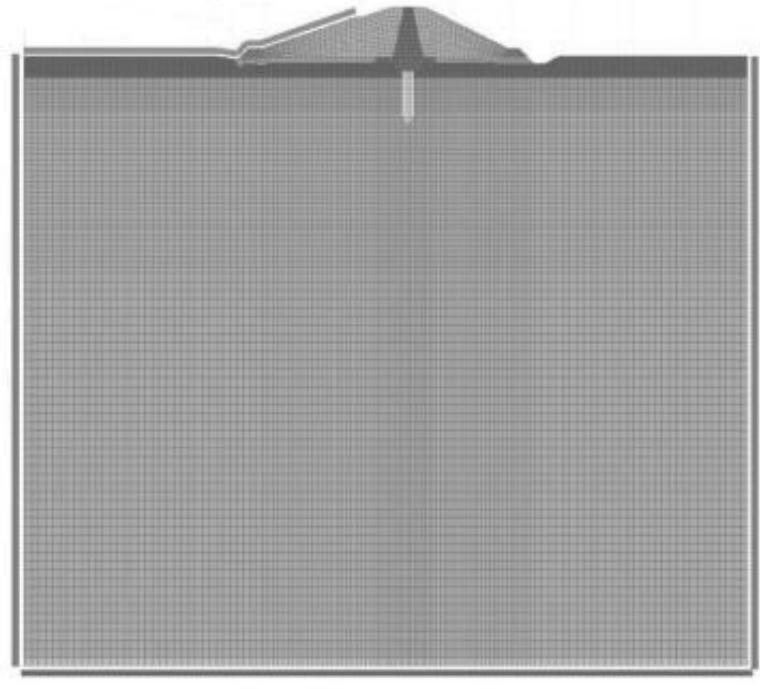


Dynamic boundary conditions are set up to minimize the unwanted reflections inside the numerical domain.

Numerical grid is capable to propagate frequency of the seismic waves up to 30 Hz.

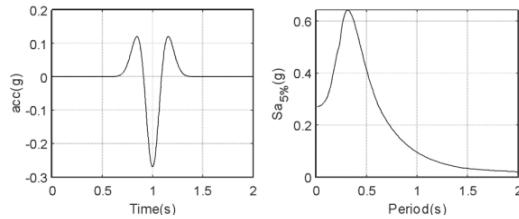
Two-component seismic motion (1H+1V) is provided in terms of shear and normal stress, which is applied at the level of absorbent boundary level.

Linear Dynamic Analyses

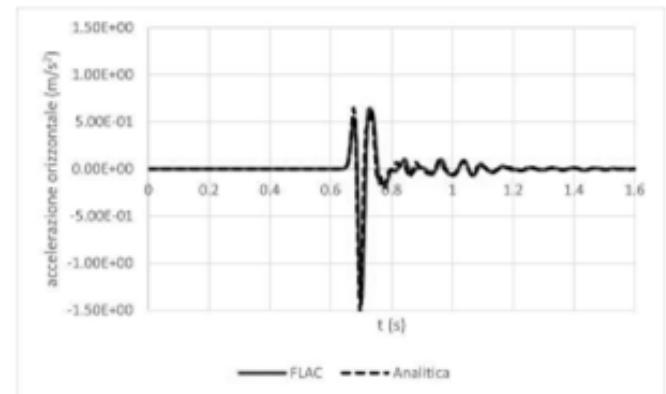
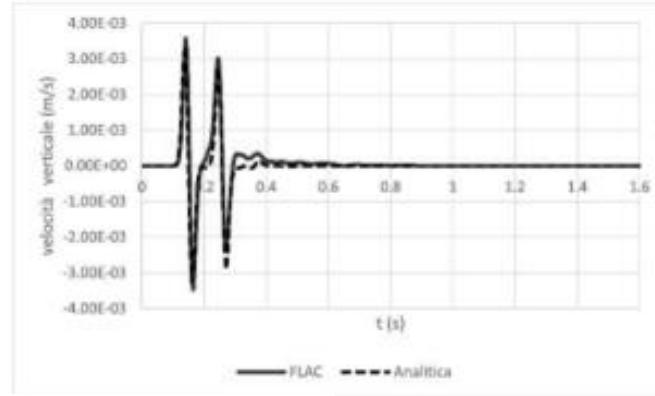
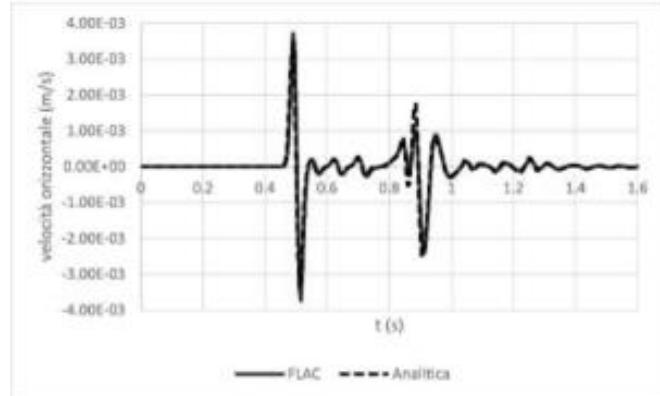


$$\tau = -2\rho V_S (v_{h,FF}/2)$$

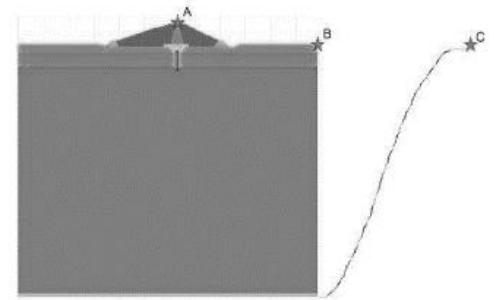
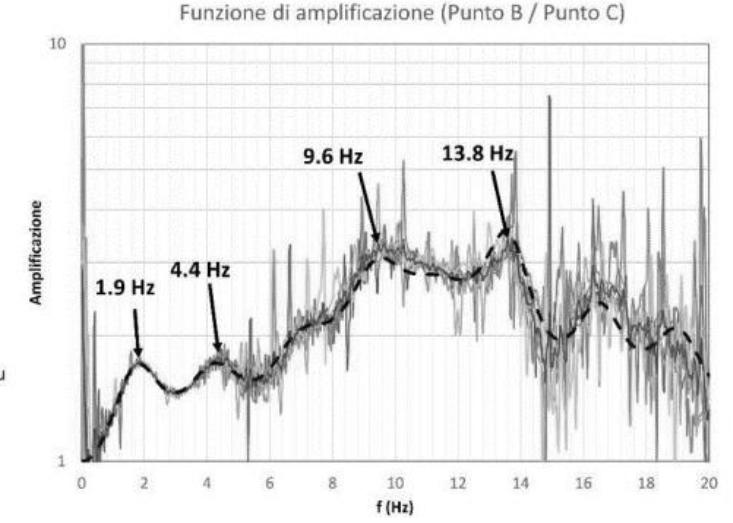
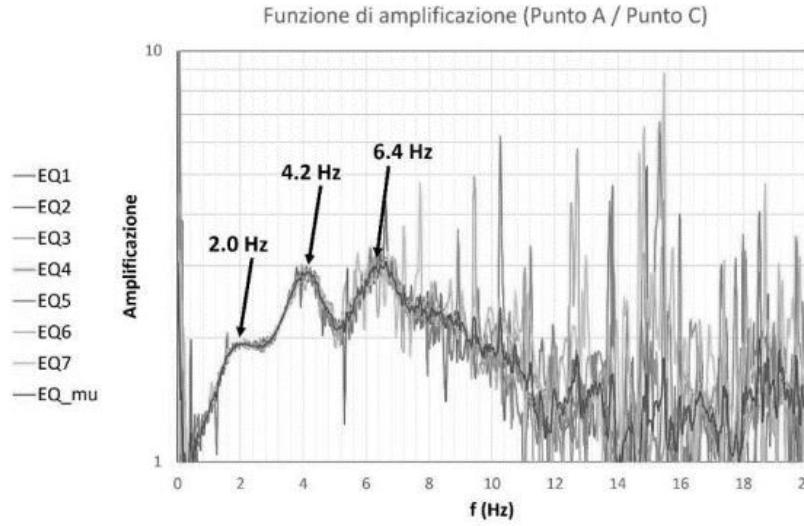
$$\sigma = -2\rho V_P (v_{v,FF}/2)$$



By applying a simultaneous 1H + 1V Ricker wavelet as the input motion, output at the surface nearby the FF-boundary is checked with an independent 1D code STRATA which provides the analytical solution.



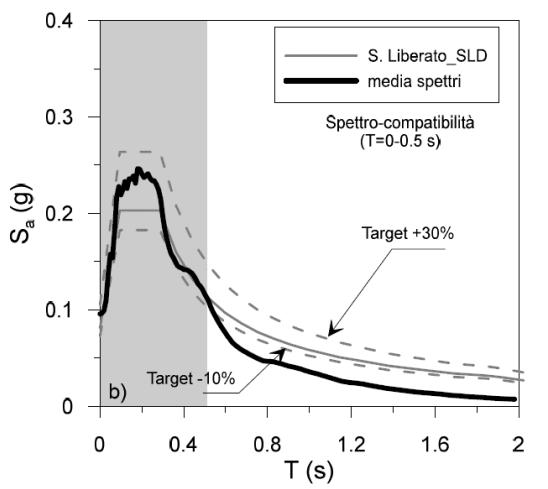
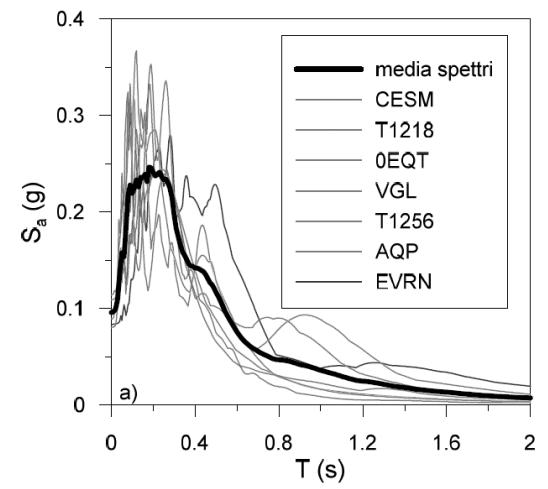
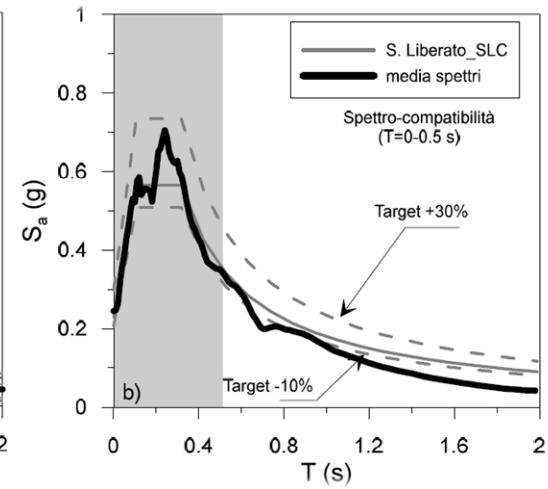
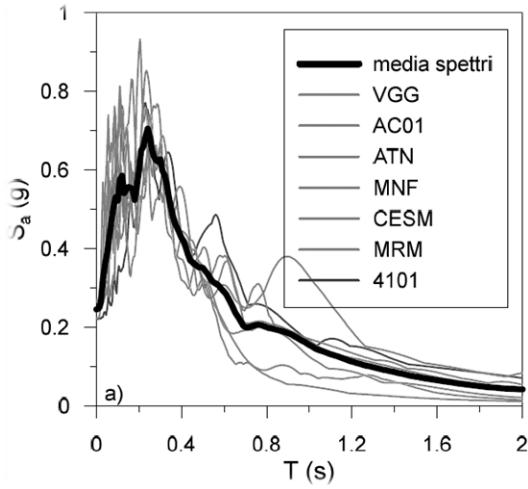
Linear Dynamic Analyses



Amplification characteristics of the embankment and the underlying soil layers are studied in linear viscoelastic domain (with small Rayleigh damping). It is noted that:

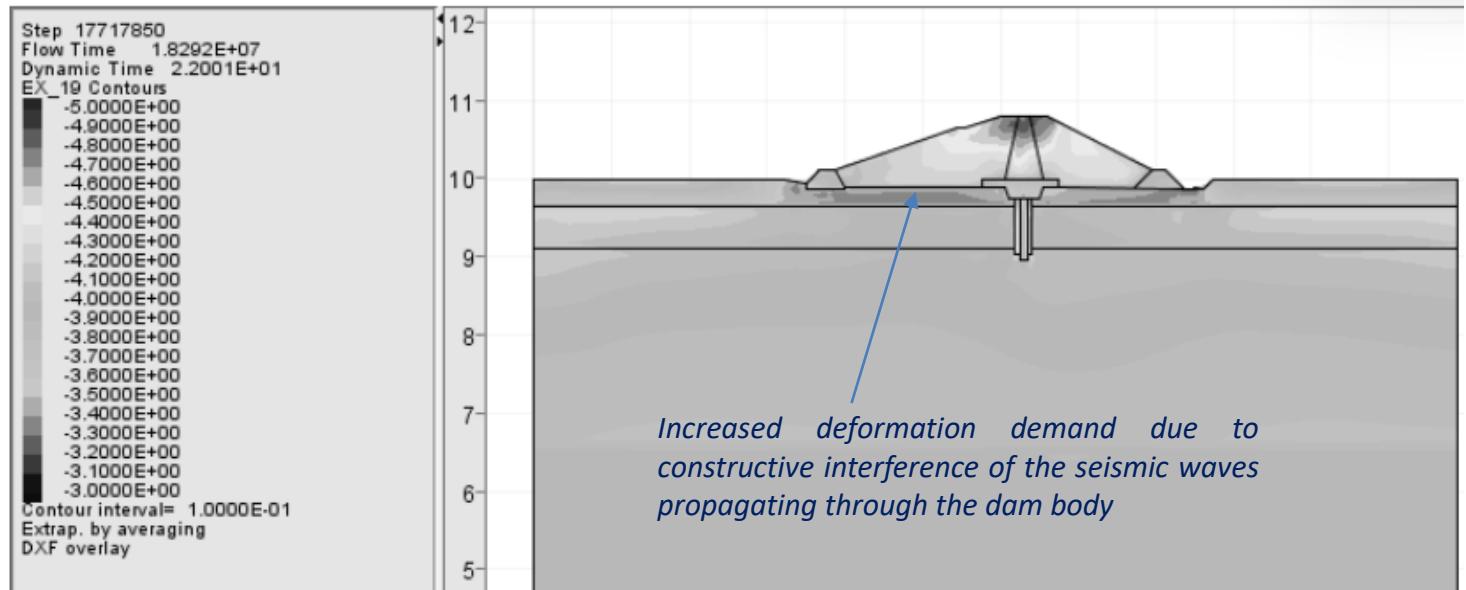
- The soil layers have the first natural frequency of about 2Hz which is slightly amplified by the dam
- The second natural frequency of the soil layers of about 4.4Hz is significantly amplified by the dam
- Third peak around 6.4 Hz appears as the second mode of the dam+soil layer system

Selection of the Ground Motions



While selecting the input motions, a UHS-based spectral compatibility ($f > 2\text{Hz}$) is enforced covering all the fundamental frequencies.

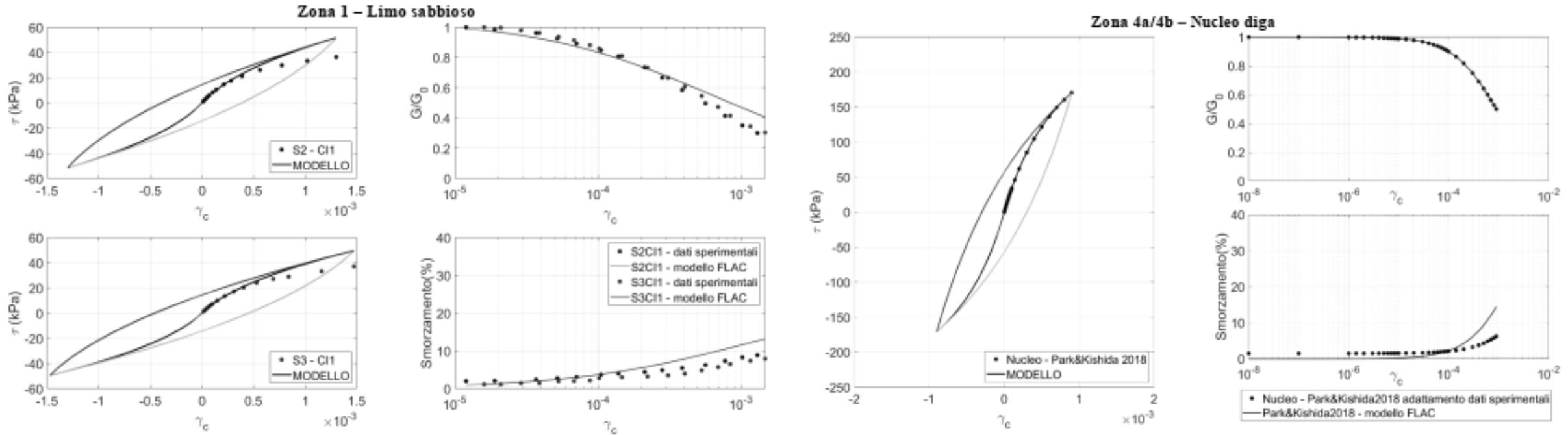
Linear Dynamic Analysis



A representative distribution of $\log(\gamma_{\max}/2)$ during a linear viscoelastic analyses

Using the same linear viscoelastic models, maximum linear deformation demands are calculated (for each ground motion pair).

Nonlinear dynamic analysis



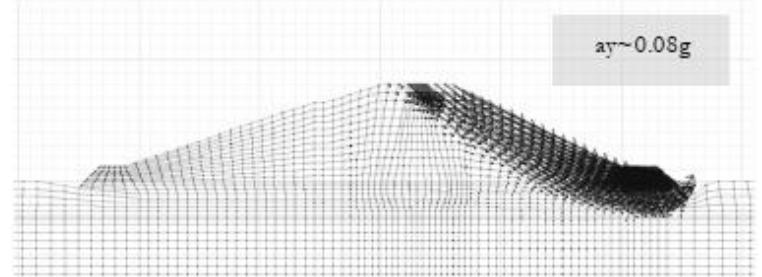
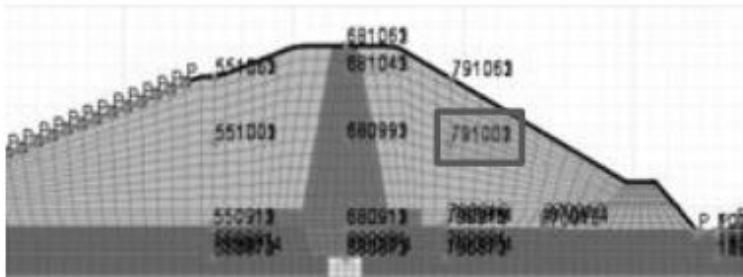
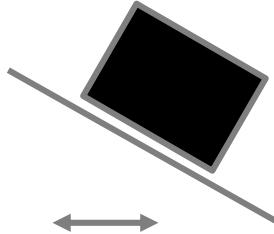
By using the resonant column data (when available) and material curve models present in the literature, G/G_{max} and DR curves are set up.

Nonlinear dynamic analysis

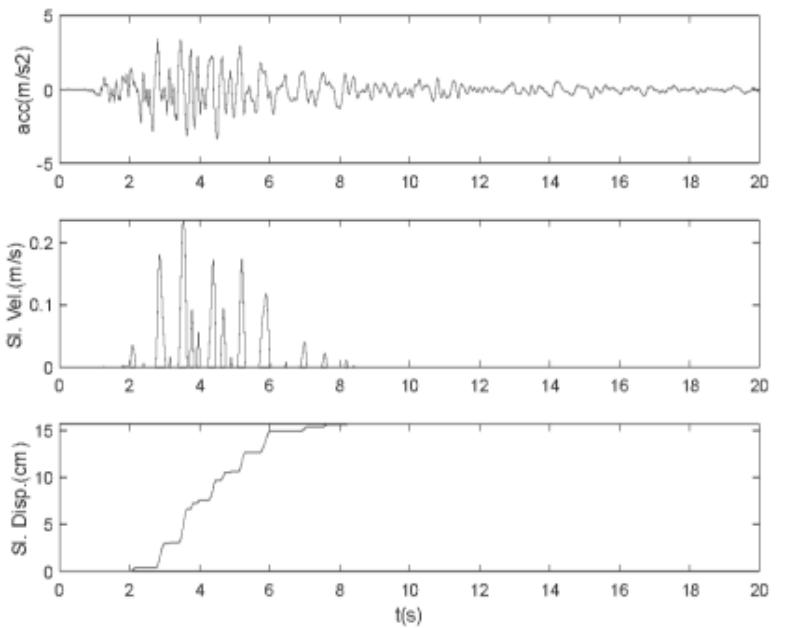
What is happening in a typical analysis?

1. Formation of two-three shear failure surfaces
2. Prevalently horizontal displacement of soil blocks in the shell
3. Vertical displacement of the crest due to dynamic instability
4. Reduced horizontal accelerations due to strong nonlinearity

Newmark Sliding Block Analysis

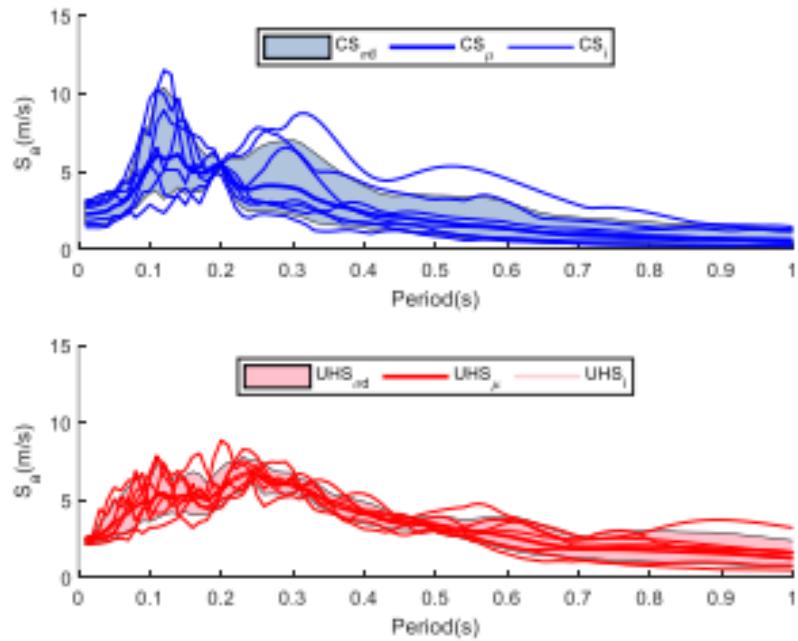


When one considers the acceleration time-history analysis and carries out Newmark-sliding block analyses, the slope displacement is estimated to be 15 cm, which verifies the dynamic analyses results.



Uniform Hazard versus Conditional Mean Spectrum

What would happen if we used a different input motion suite which is less demanding?



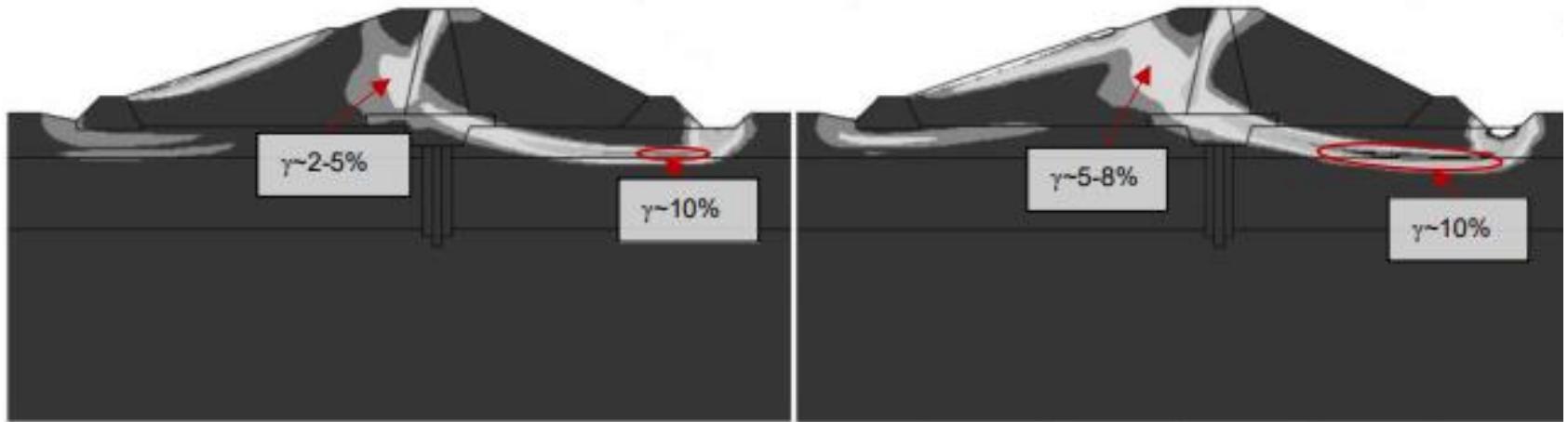
The concept of conditional mean spectrum compatibility is enforced for the period of 0.2s (between 4.2 and 6.4 Hz) instead of rather broadband UHS-compatibility.

The results show that the displacement demands are reduced by 40% for horizontal displacement and by 60% for vertical displacement demands.

Are we imposing a criterion that is too strict?

Effect of Soil Liquefaction

What would happen if we considered ground instability, soil liquefaction?



We are investigating the consequences of the soil liquefaction through the use of a loosely-coupled model (the dataset was not permitting the use of a more sophisticated model)

It is observed that the shear sliding surfaces are even more pronounced due to local softening of the shell zones.

Consequently, the increase of the horizontal and vertical displacement demands are in the order of 50% and 60%.

The use of soil liquefaction models must become a must in the analysis of liquefiable embankments.



Thank you!

Any questions?



Impact of uncertainty associated with ground motion selection on fragility assessment of dams

Bikram Kesharee Patra¹, Rocio L. Segura², Ashutosh Bagchi¹

¹ Dept. of Building, Civil & Environmental Engineering, Concordia University, Montreal, Canada

² Dept. of Civil, Environmental, and Sustainable Engineering, Santa Clara University, Santa Clara, CA, USA

Contents

- Introduction
- Problem statement
- Methodology
- Numerical model
- Results
- Conclusions

Introduction

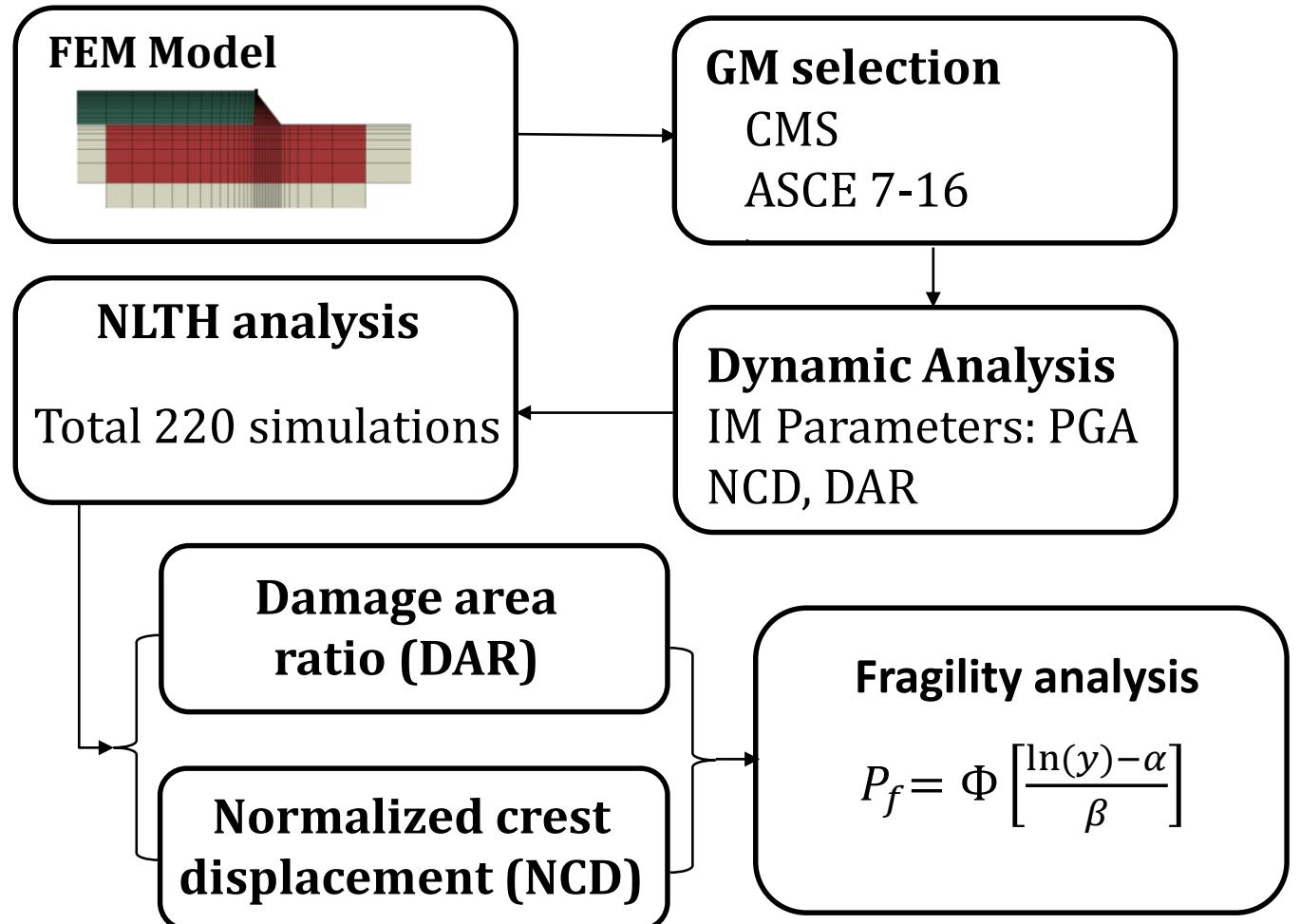
- Dams are critical national infrastructural assets that serve multifaceted roles for communities globally.
- Many dams worldwide are over 50 years old, requiring thorough evaluations and retrofitting based on current standards.
- Advances in the understanding of seismic hazards have led to a greater emphasis on enhancing safety measures for dams.
- Utilization of a probabilistic framework is essential for effectively managing uncertainties impacting performance evaluation and decision-making.
- The fragility assessment considering the impact of aleatory and epistemic uncertainty associated with GM selection and RTR variability is required.

Problem statement

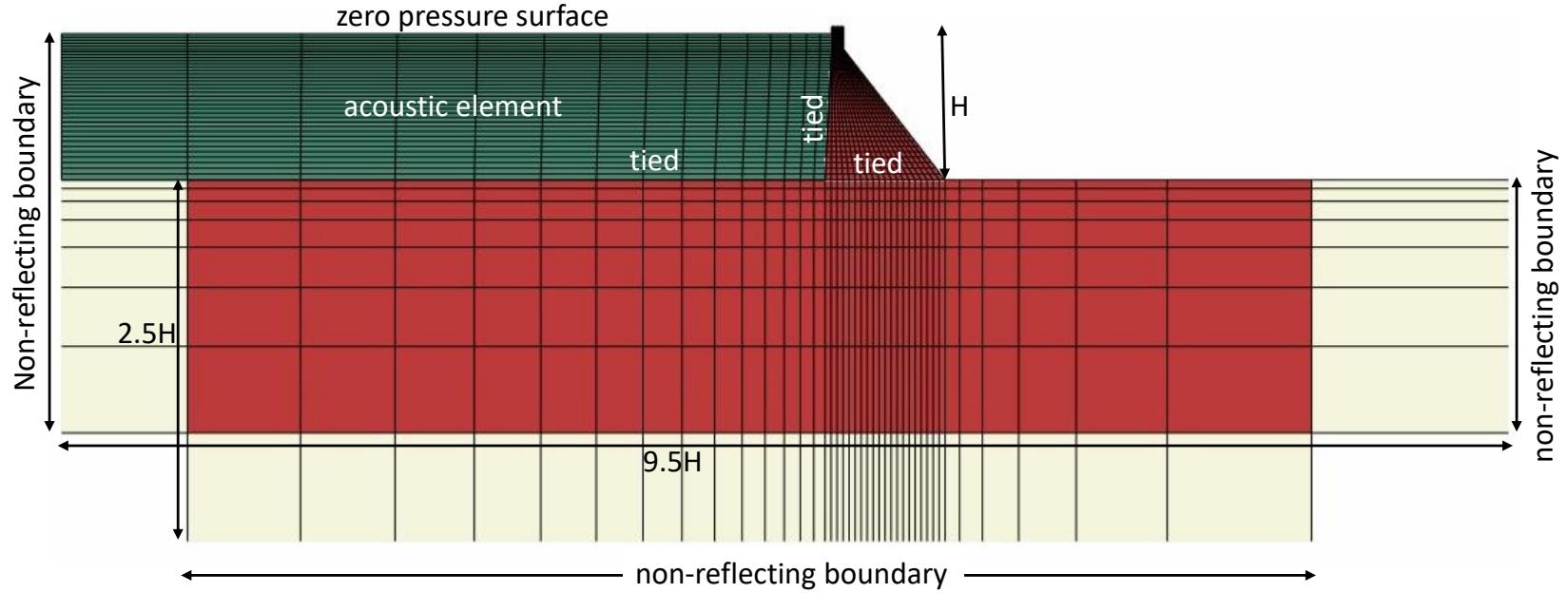
Evaluating the impact of ground motion selection method and RTR variability on seismic fragility assessment of a concrete gravity dam.

- A 2D DFR model, with the dam, and foundation modeled with structural elements and reservoir acoustic elements. the foundation periphery infinite elements.
- A total of 110 GM's selected for the dam location, ASCE 7-16, and CMS methods for 5 return periods (475 to 10000 years).
- A total of 220 NLTH analyses were carried out i.e., 110 NLTH per selection method, non-linearity implemented through CDP.
- Fragility curves are developed as a function of the damage area ratio and the normalized crest displacement.

Methodology



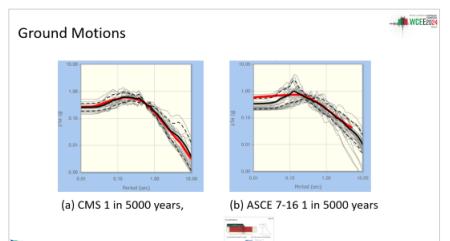
FEA | DFR Model



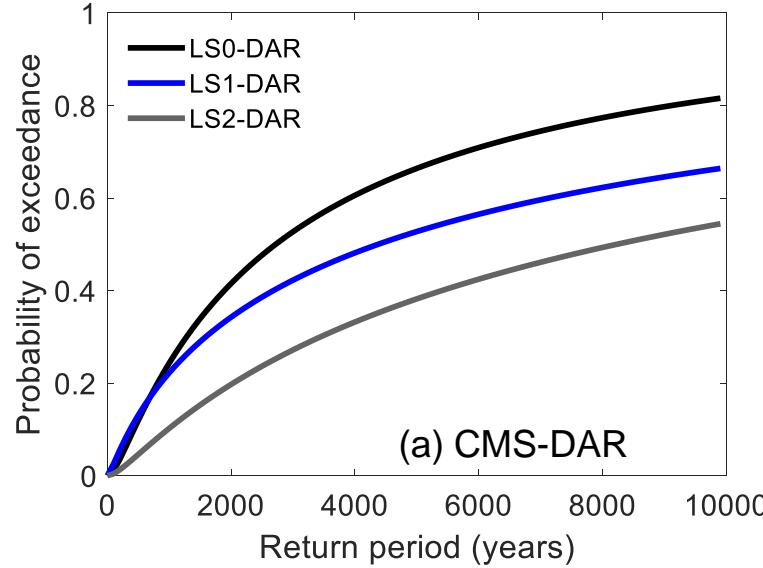
(a) Considered Abaqus DFR model

(b) Cross-section of Pine Flat Dam

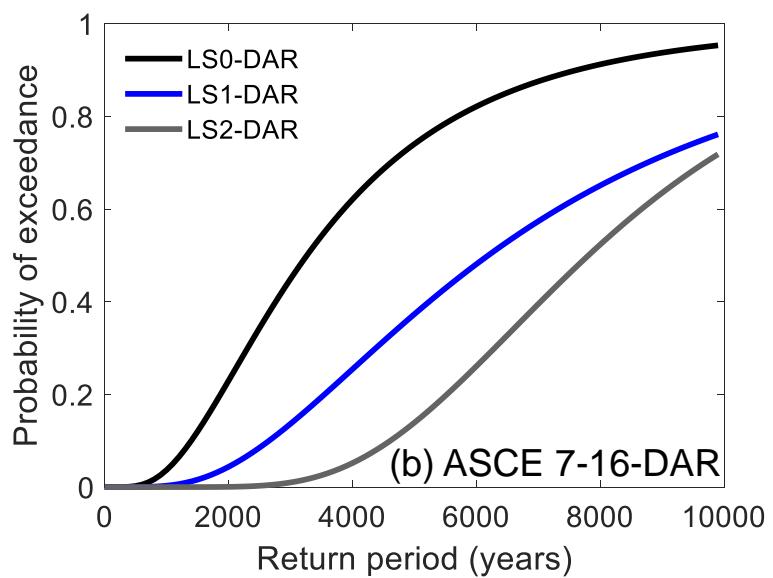
Material Properties			
Elastic material properties of dam, foundation, and reservoir for Pine Flat dam			
Material properties	Concrete	Foundation	Reservoir
Density (ρ , kg/m ³)	2482	2640	1000
Modulus of elasticity (E), MPa	22407	22407	-
Bulk modulus (K), MPa	-	-	2070
Shear modulus (G), MPa	0.2	0.33	-
Rayleigh damping Alpha (a)	-	1.64	-
Rayleigh damping Beta (b)	0.004333	0.00668	-
CDP properties for Pine Flat dam			
η_{C^*}	η_{C^*} (MPa)	η_{C^*} (MPa)	η_{C^*} (MPa)
36.33	12.08	22.41	2.24
e	e	e	e
0.1	0.1	0.1	0.1
R	R	R	R
1.16	1.16	1.16	1.16



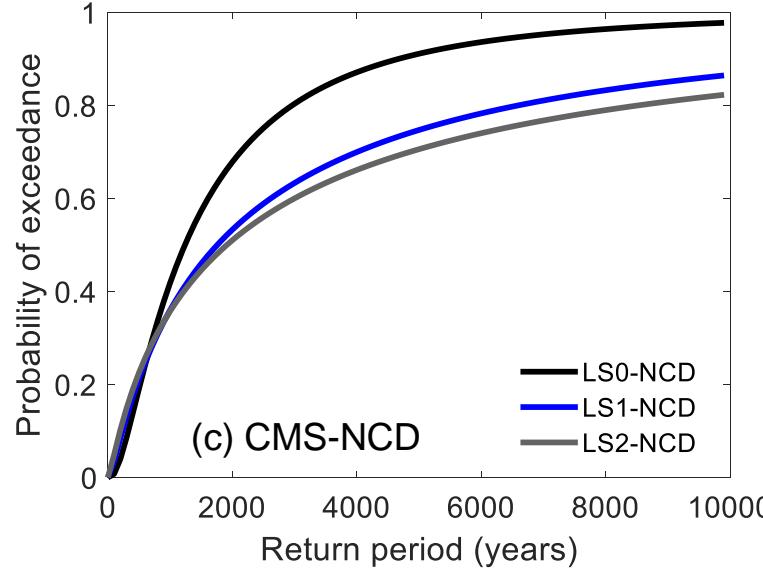
Results | Fragility curves



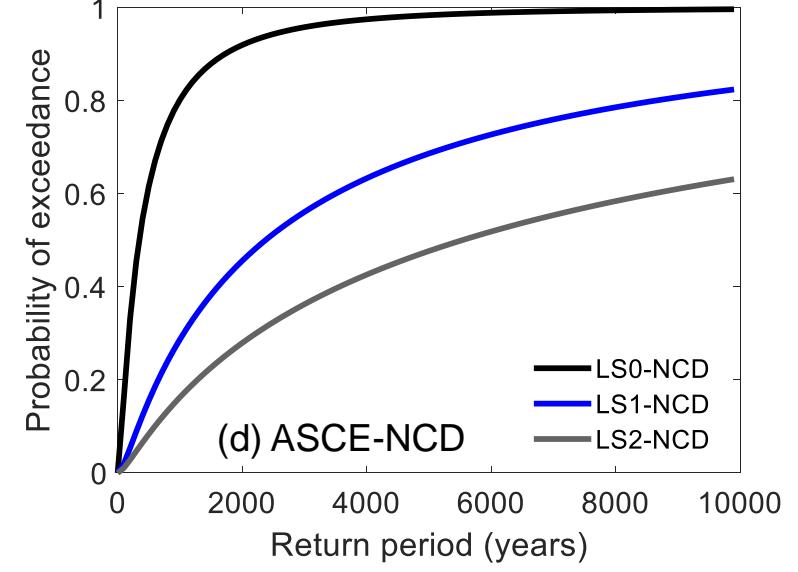
(a) CMS-DAR



(b) ASCE 7-16-DAR



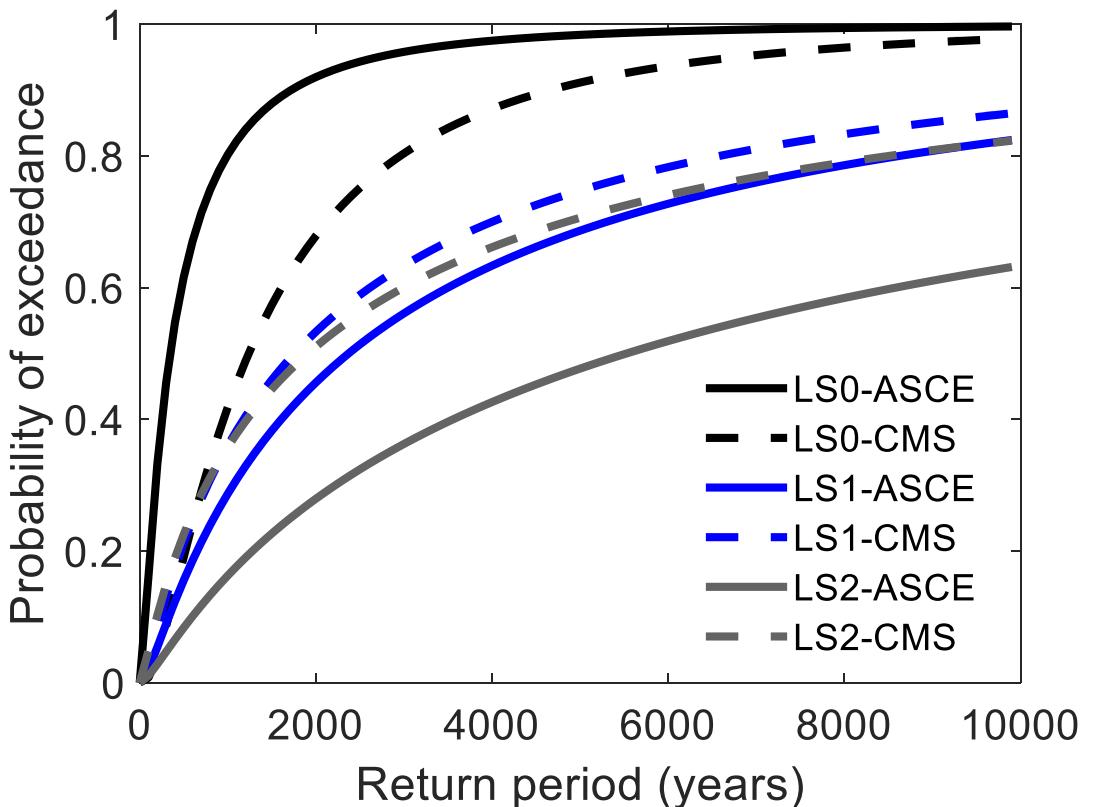
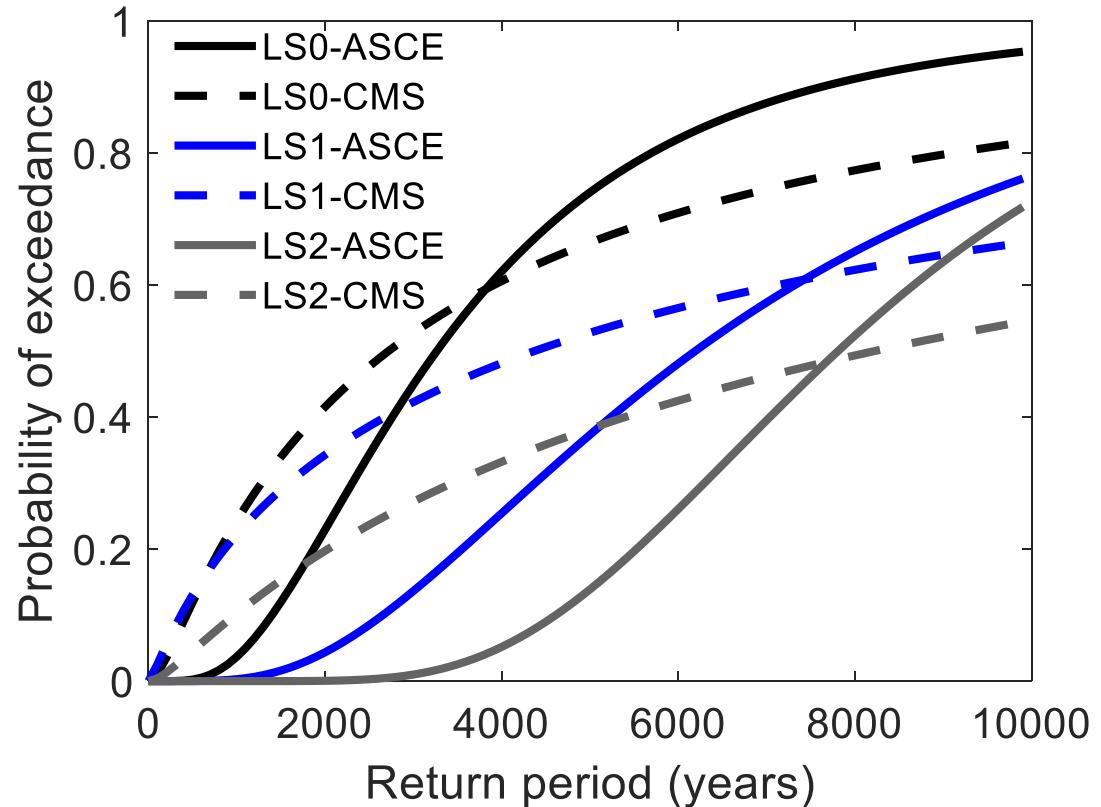
(c) CMS-NCD



(d) ASCE-NCD

- (a) CMS-DAR: Damage Area Ratio with CMS-based ground motion selection.
- (b) ASCE 7-16-DAR: Damage Area Ratio with ASCE7-16-based ground motion selection.
- (c) CMS-NCD: Normalized Crest Displacement with CMS-based ground motion selection.
- (d) ASCE 7-16-NCD: Normalized Crest Displacement with ASCE 7-16-based ground motion selection.

Results | Fragility curves



Fragility curves comparison between ASCE 7-16 and CMS: (a) Damage Area Ratio (DAR), (b) Normalized Crest Displacement (NCD)

Conclusion

- Seismic performance assessment is crucial for dam safety in high seismic activity regions.
- Clear and consistent standards for limit states significantly influence fragility predictions.
- ASCE 7-16 offers a balanced method for ground motion selection, suitable for general applications, while CMS is crucial for critical infrastructure requiring higher safety.
- DAR provides a broad overview of damage states, and NCD offers detailed displacement-based insights; the choice depends on the assessment objective.
- Robust ground motion selection methodologies and multiple damage indices are essential for fragility assessment, advocating for probabilistic frameworks in dam engineering.



Thank you!

Any questions?

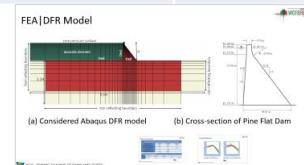
Material Properties

Elastic material properties of dam, foundation, and reservoir for Pine Flat dam

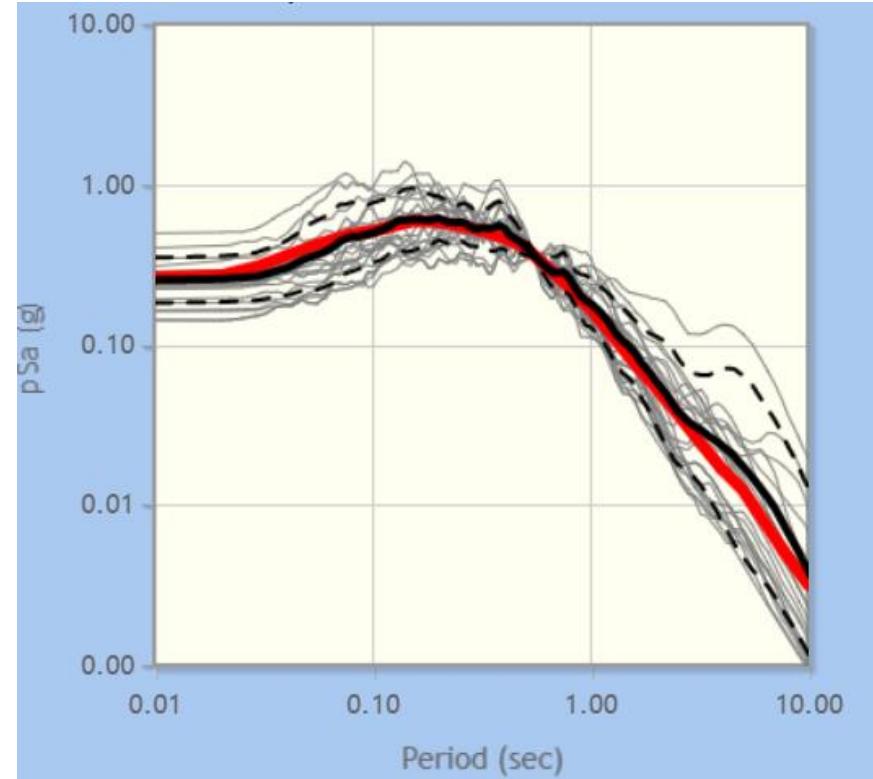
Material properties	Concrete	Foundation	Reservoir
Density (ρ), kg/m ³	2482	2640	1000
Modulus of elasticity (E), MPa	22407	22407	-
Bulk modulus (K), MPa	-	-	2070
Poisson's ratio	0.2	0.333	-
Rayleigh damping Alpha (α)	-	1.64	
Rayleigh damping Beta (β)	0.004333	0.00668	

CDP properties for Pine Flat dam

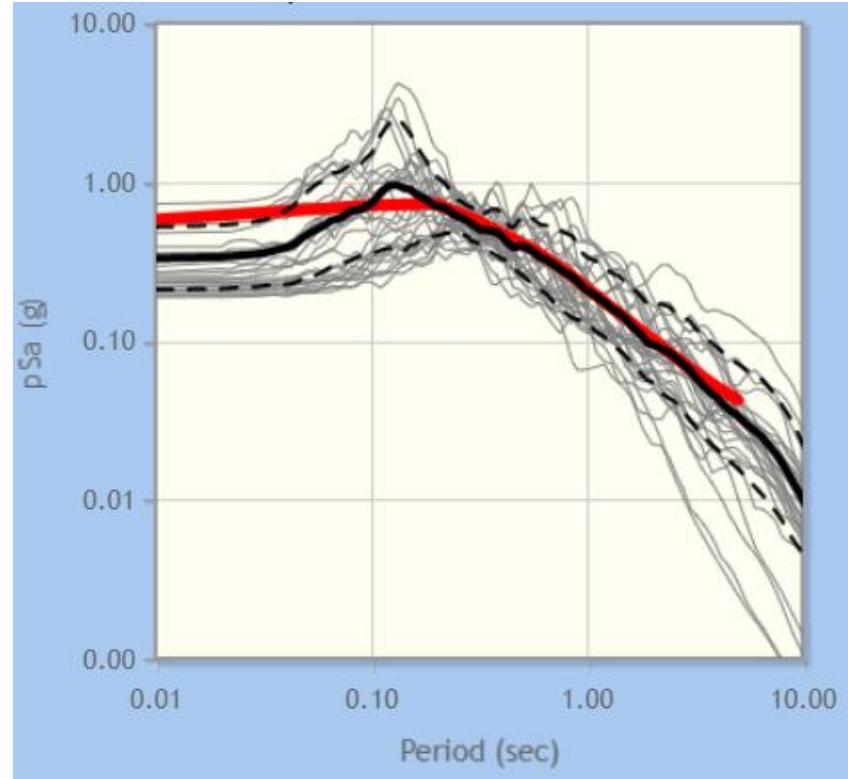
ψ_c^*	σ_{co} (MPa)	σ_{cu} (MPa)	σ_{to} (MPa)	e	R
36.31°	12.08	22.41	2.24	0.1	1.16



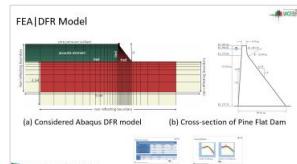
Ground Motions

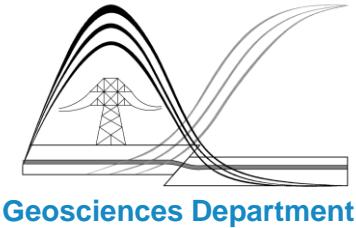


(a) CMS 1 in 5000 years,



(b) ASCE 7-16 1 in 5000 years





Deconvolution of real and artificial accelerations for dynamic analysis of dams

M. Poul ¹, M.A. Hariri-Ardebili ²

¹ Geosciences Department, Pacific Gas & Electric (PG&E), California, USA

² University of Maryland, College Park, MD, USA

Various factors influence the seismic response of dams:

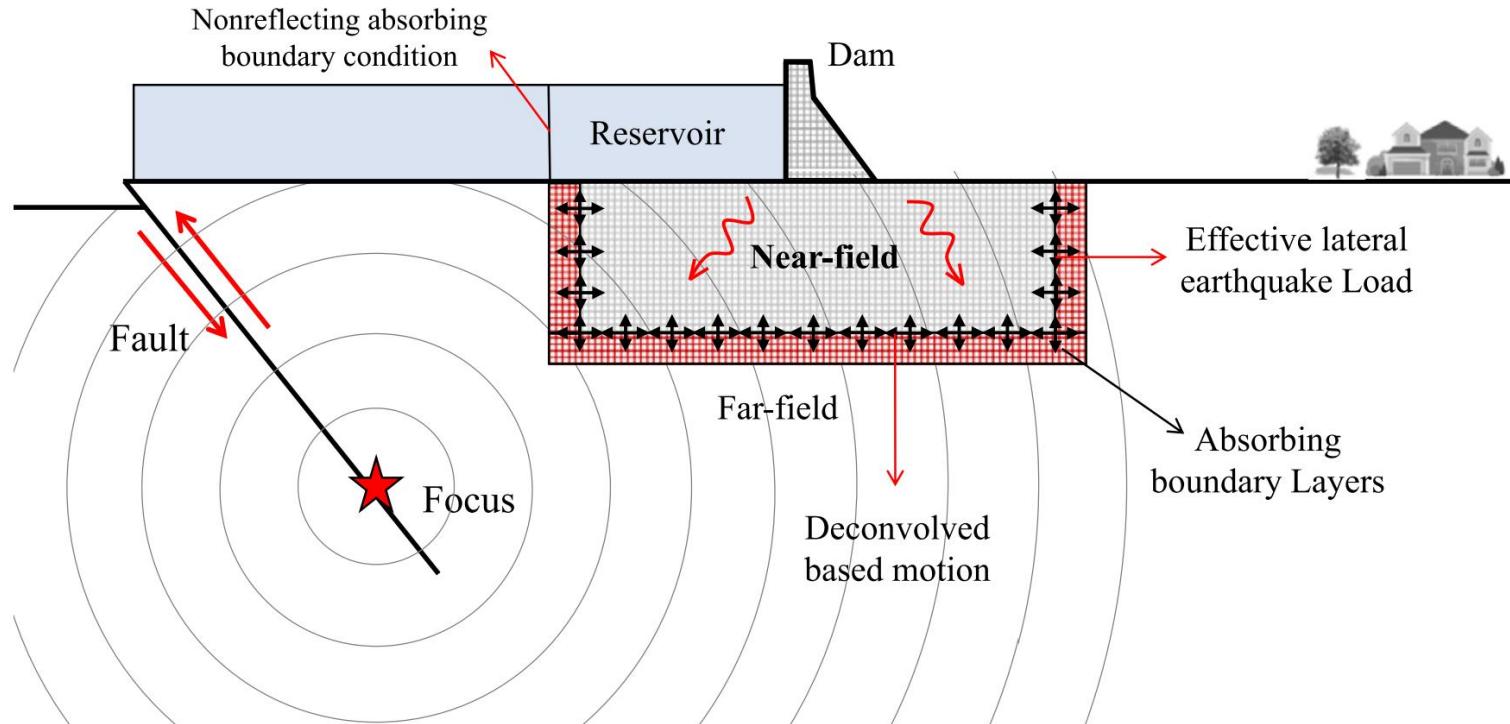
- Fluid-Structure Interaction (FSI)
- Soil-Structure Interaction (SSI)
- Concrete models
- Wave propagation
- ...

Importance of verification, validation, and uncertainty quantification:

- Provides confidence in the accuracy of the results
- Ensures reliability in performing and reporting analyses

This work focuses on deconvolution of seismic waves and wave propagation:

- Critical for understanding how seismic waves affect dam structures
- Impact of foundation modeling on dam response
- Addresses both real ground motions and artificial acceleration functions

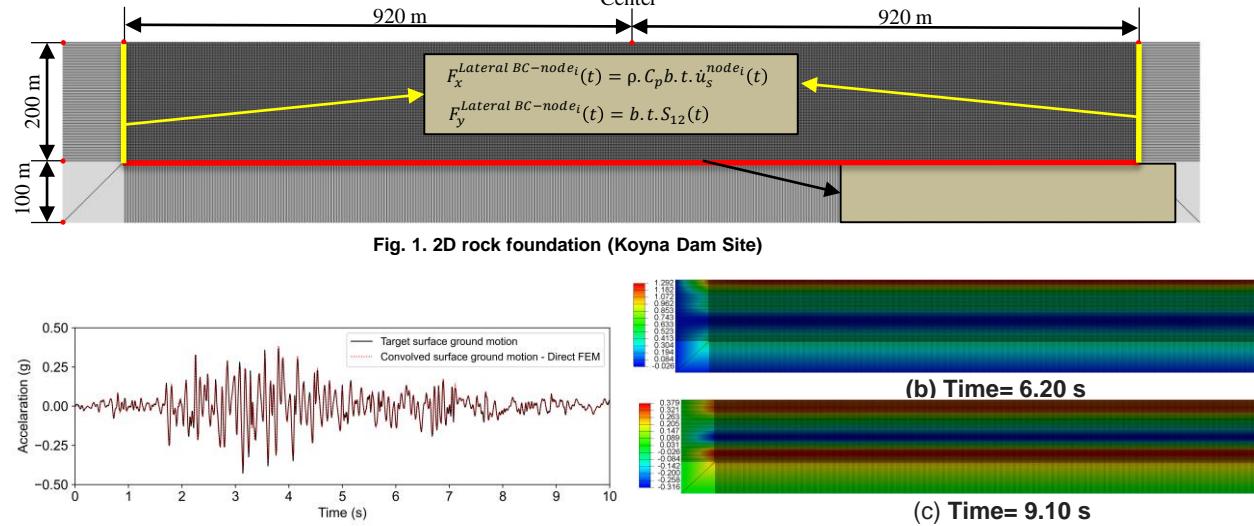


Outline:

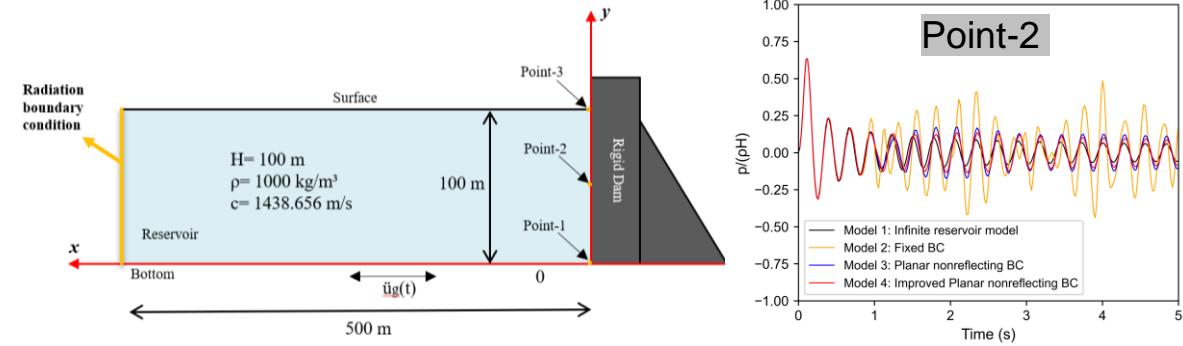
- Verification of Dam Modeling Technique in ABAQUS
- Impact of ABCs on Dynamic Response of Concrete Dams (PML vs. Viscous ABCs)
- Impact of Ignoring Mass of Foundation Domain
- When Can the Deconvolution Process Be Ignored?

Validation of Dam Modeling Technique in ABAQUS

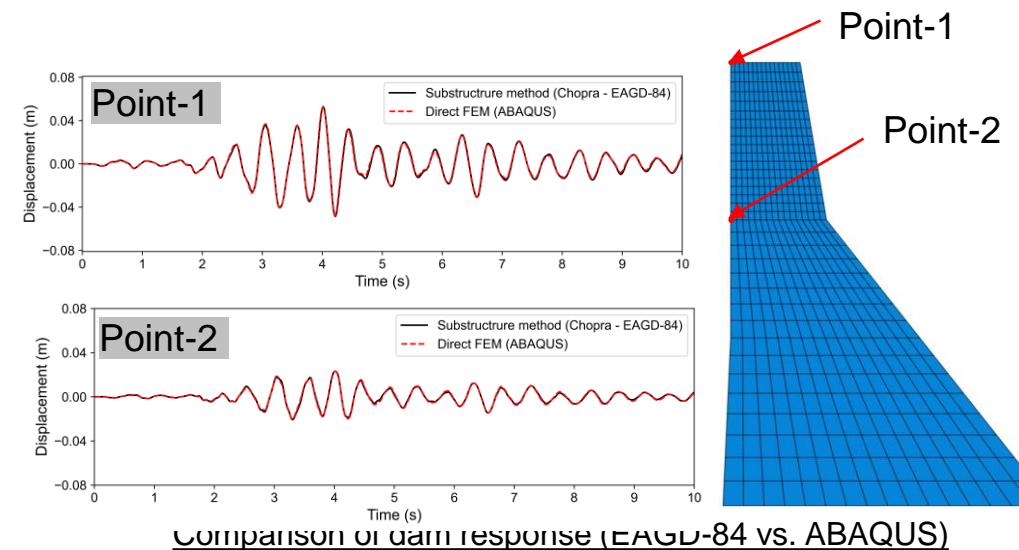
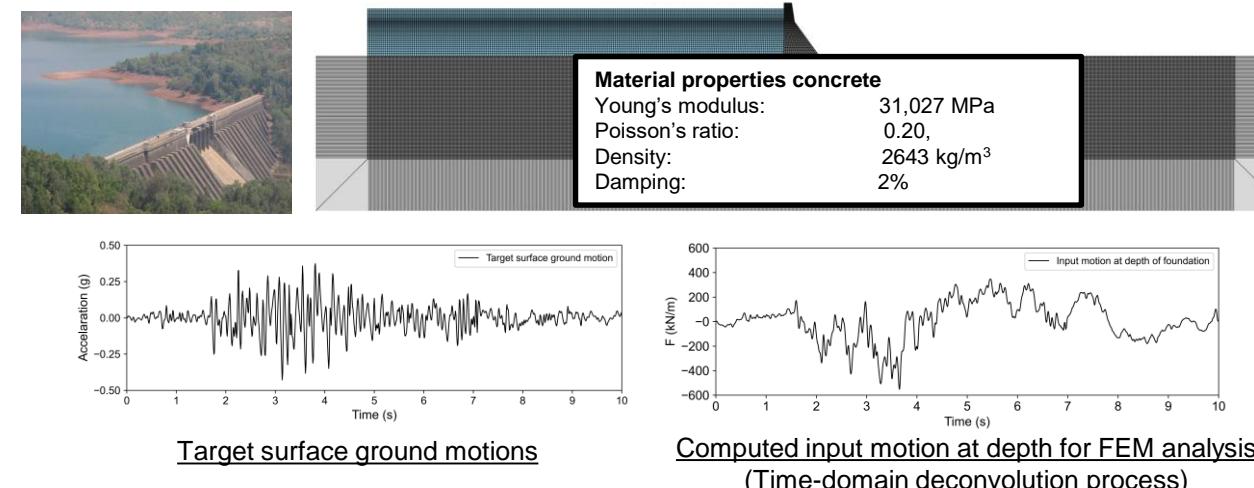
(a) Verification of input motion mechanism



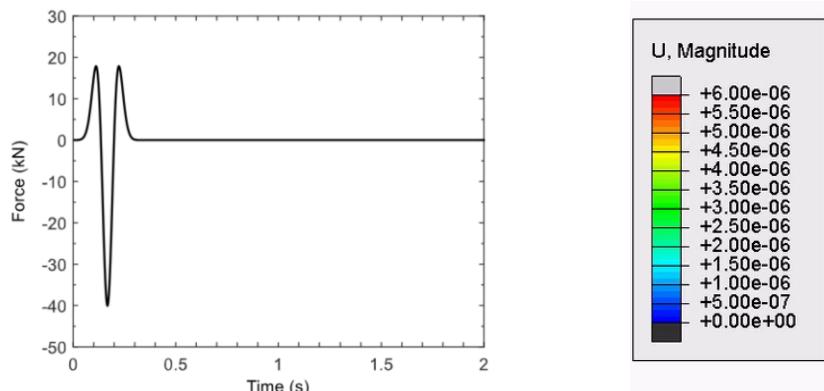
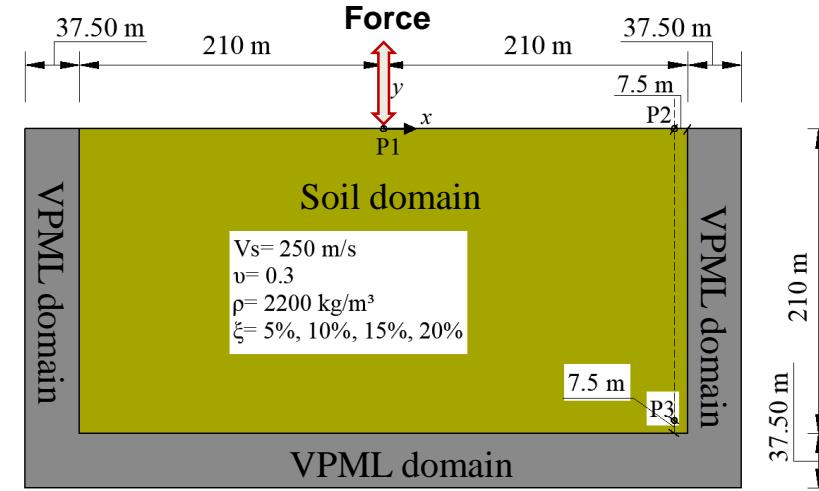
(b) Verification of hydrodynamic pressure on the dam-reservoir interface and BCs



(c) Verification of dam-foundation-reservoir system in ABAQUS vs. EAGD-84



Impact of ABCs on Dynamic Response of Concrete Dams (PML vs. Viscous ABCs)

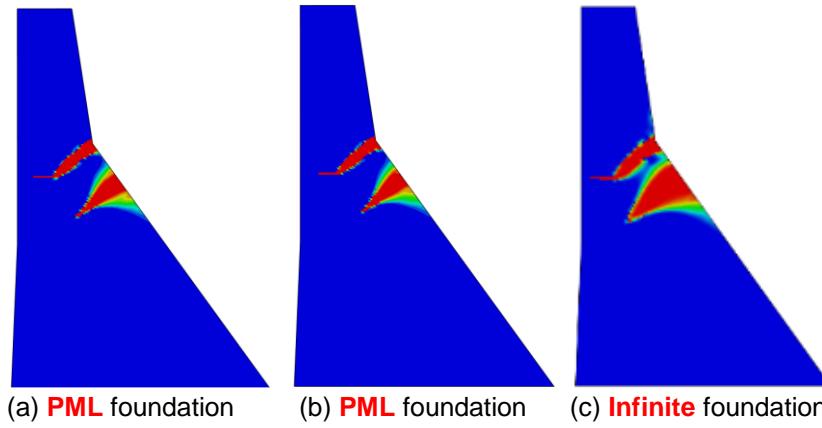


Applied Force at Point A

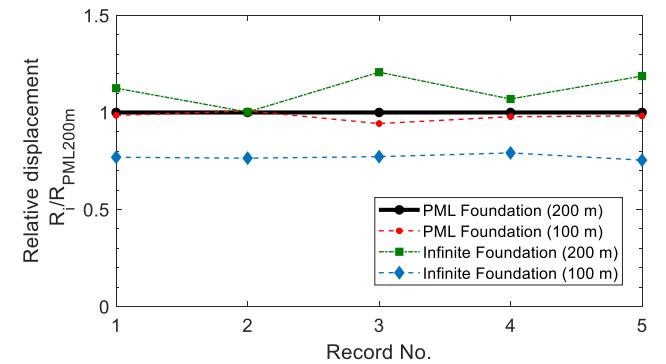
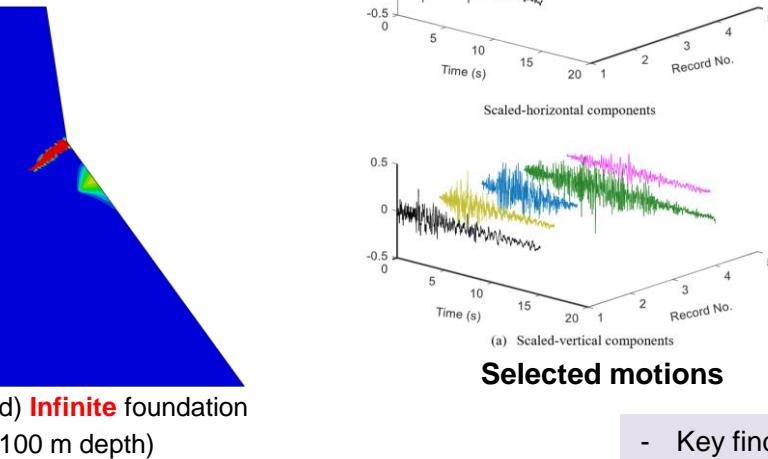


Impact of ABCs on DAM response:

- a) Rock foundation with **viscous/Infinite element** (100m and 200m)
- b) Rock foundation with **PML element** (100m and 200m)



Tensile failure profile for Koyna Earthquake



Maximum horizontal crest displacement

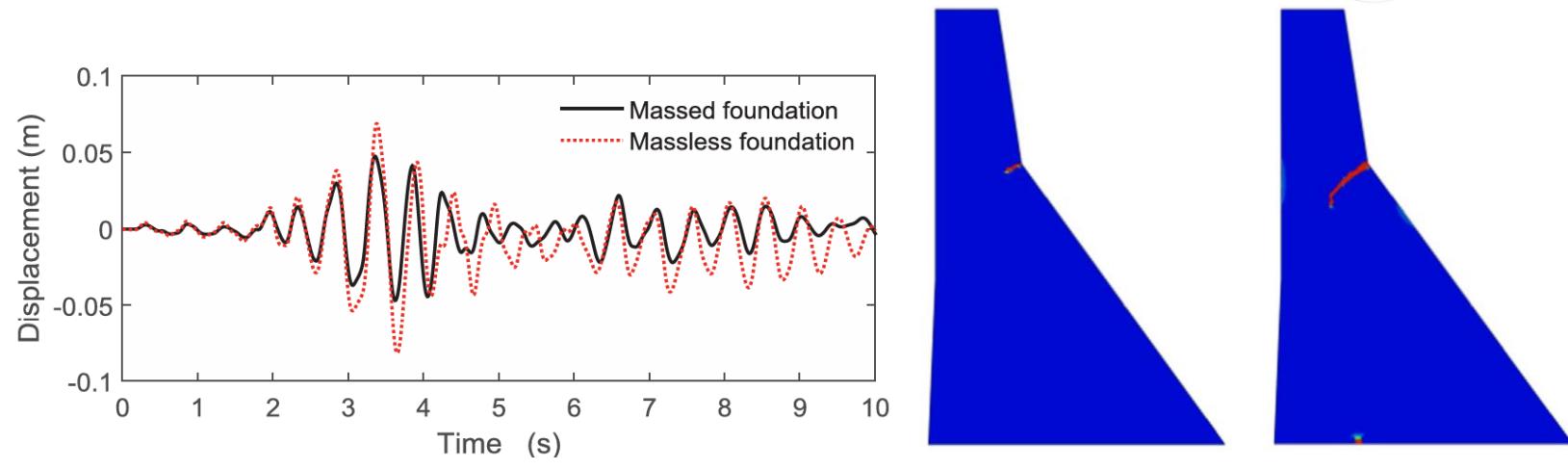
Selected motions

- Key finding:
- Shallow infinite foundation model **underestimates** dam response
- Deep infinite foundation model **provides satisfactory results**
- **Dam response is not impacted by depth of foundation with PML ABC**

Impact of Ignoring Mass of Foundation Domain

Key Points

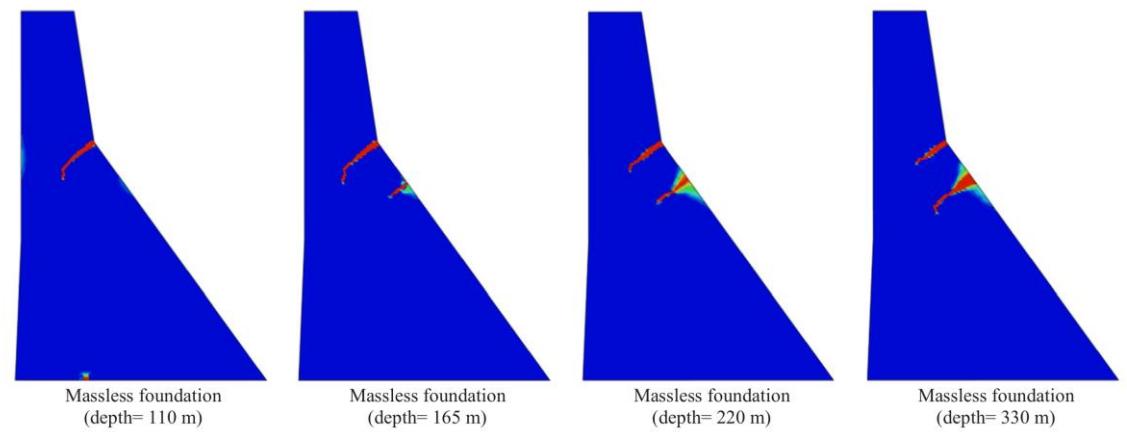
- Neglecting the dynamic effect of the foundation can lead to significant consequences.
- The degree of overestimation varies greatly with different seismic excitations.
- Average overestimation for a massless system (10 records):
 - Crest displacement: 57%
 - Crest acceleration: 45%
 - Contact opening: 152%
 - Sliding: 90%



Effect of massless foundation depth on the dam response

- Investigated the effect of massless foundation depths (110m, 165m, 220m, 330m) on dam response.

Increasing foundation depth significantly increases dam response.



Effect of massless foundation depths on the tensile failure mode of the dam

When Can the Deconvolution Process Be Ignored?

In certain cases, deconvolution can be ignored if the following conditions are met:

Low Damping.

- Low damping means minimal energy dissipation during wave propagation.
- Maintaining the original waveform over a short distance due to material damping.

High Shear Wave Velocity:

- A high shear wave velocity allows the wave to travel through the rock with minimal distortion.

Material Nonlinearity and Cracks:

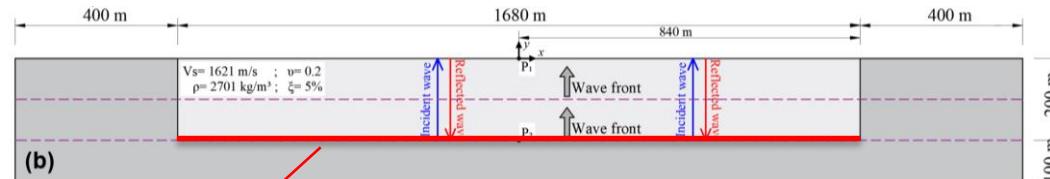
- The rock exhibits minimal material nonlinearity and has few cracks, ensuring that the wave propagation remains mostly linear and the waveform is less distorted.

Combined Factors:

- High shear wave velocity and low damping lead to minimal waveform changes over a short distance (200 meters).

Case 1. Applying deconvolved motion at the base

Target motion = convolved motions



$$F_s^{\text{Input}}(t) = 2\rho b t C_s^{\text{eq}} \dot{u}_s^{\text{Input}}(t)$$

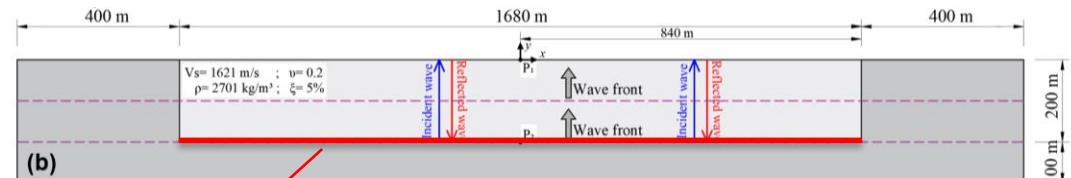
$$F_p^{\text{Input}}(t) = 2\rho b t C_p^{\text{eq}} \dot{u}_p^{\text{Input}}(t)$$

Determined through a deconvolution process

Velocities of incident waves

Case 2. Applying target motion directly at the base

Target motion \neq convolved motions



$$F_s^{\text{Input}}(t) = 2\rho b t C_s^{\text{eq}} \dot{u}_s^{\text{Input}}(t)$$

$$F_p^{\text{Input}}(t) = 2\rho b t C_p^{\text{eq}} \dot{u}_p^{\text{Input}}(t)$$

$$\dot{u}_s^{\text{Input}}(t) = 0.5 \dot{u}_s^{\text{Target}}(t)$$
$$\dot{u}_p^{\text{Input}}(t) = 0.5 \dot{u}_p^{\text{Target}}(t)$$

Velocities of incident waves

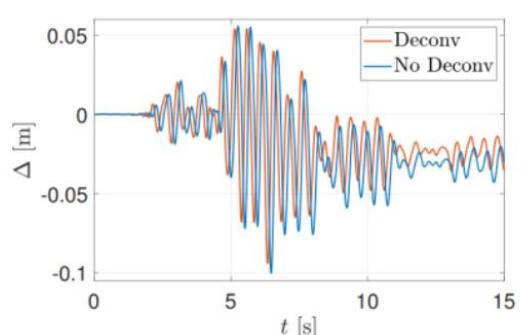


When Can the Deconvolution Process Be Ignored?

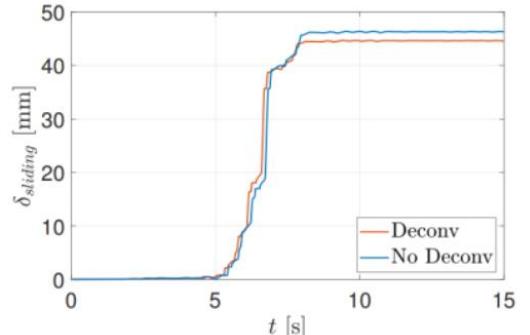
Real Ground Motions:

Responses are overestimated compared when deconvolution is ignored. But:

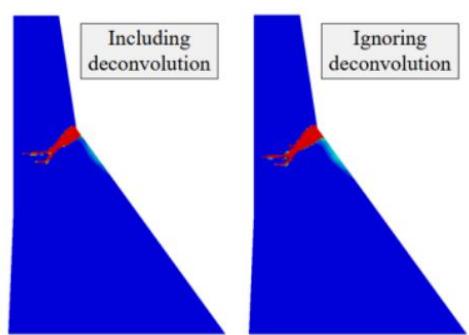
- Both models exhibit very similar patterns in the time histories of displacement and sliding.
- Ignoring the deconvolution process impacts only the amplitude of the results.
- The overall pattern of the responses remains very similar between the two models.



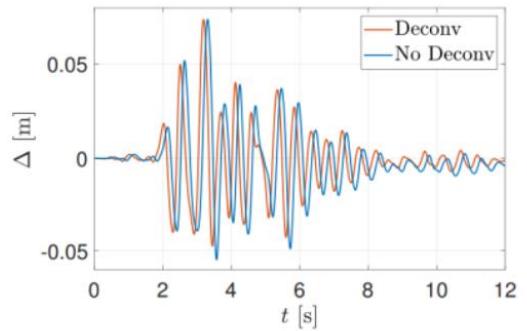
(a) Record 1; displacement



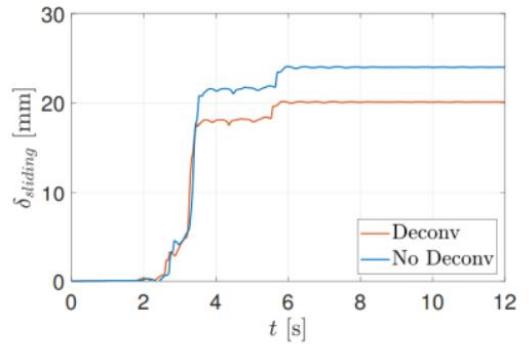
(b) Record 1; sliding



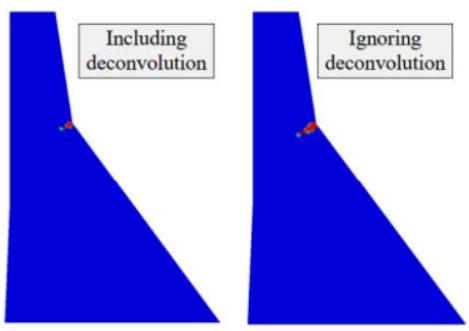
(c) Record 1; damage profile



(d) Records 2; displacement



(e) Record 2; sliding



(f) Record 2; damage profile

Comparison of structural responses from scenario "A" with two real ground motions

Intensifying Artificial Accelerations (IAAs)

IAA Method Overview

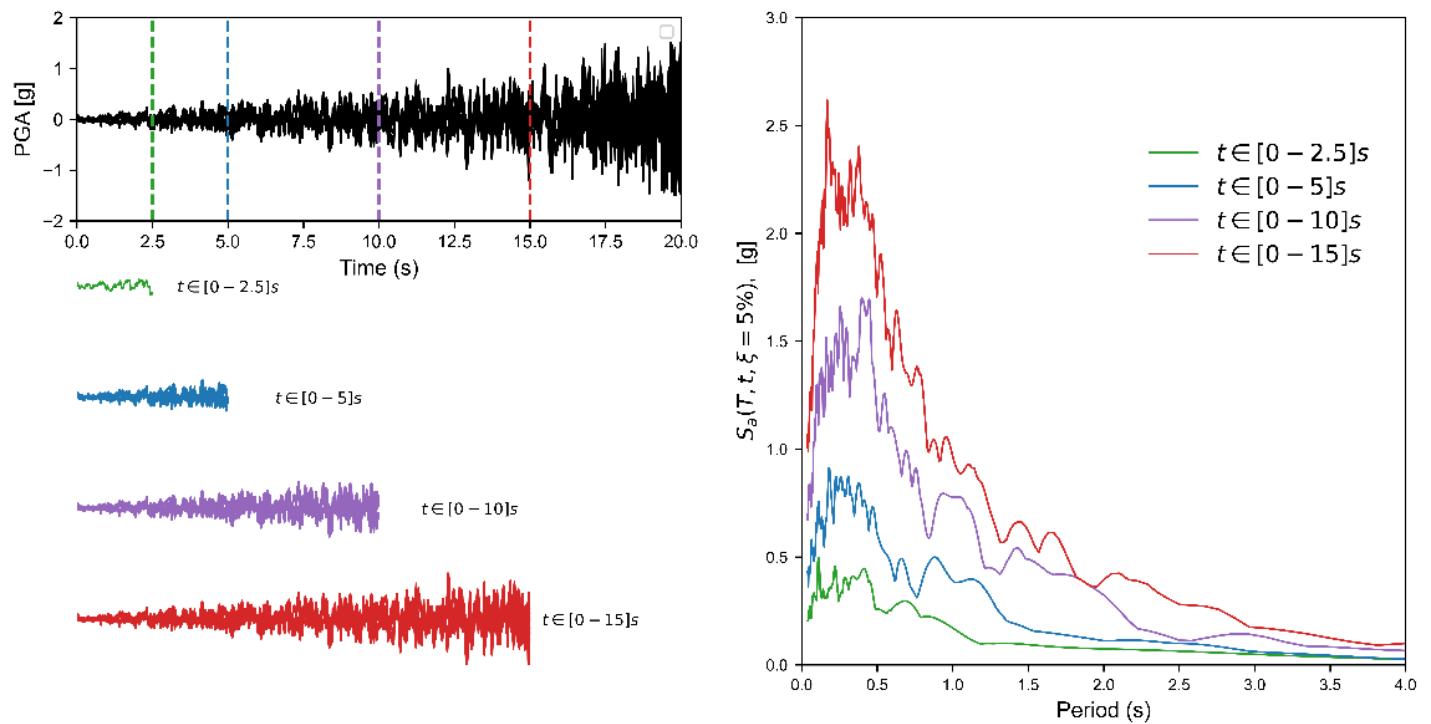
Dynamic time history analysis approach
Uses intensifying artificial accelerations (IAAs)
instead of real earthquake ground motions
Evaluates structure response at different intensity
levels with a single IAA

Characteristics of IAAs

Time reflects the intensity measure of earthquake
ground motions
Intensity increases as time increases

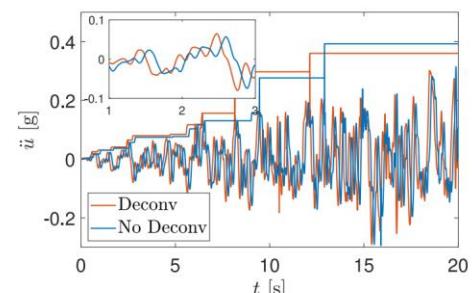
Evaluation Advantages

Direct relationship between engineering demand
and intensity measures

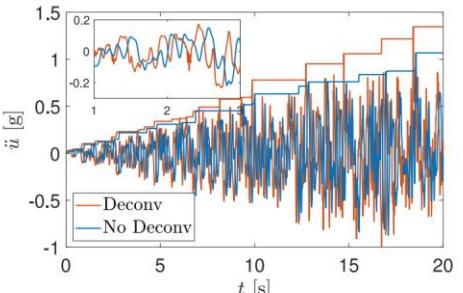


Sample of IAA record and response spectra at different time

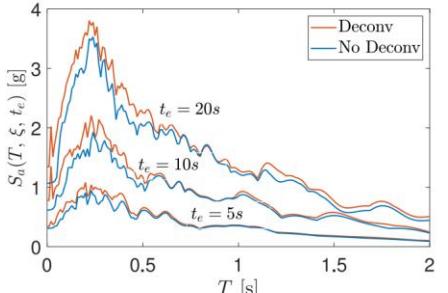
When Can the Deconvolution Process Be Ignored?



(a) Scenario B; acceleration



(b) Scenario C; acceleration



(c) Scenario C; spectra

Comparison of structural responses from scenario "A" with two real ground motions.

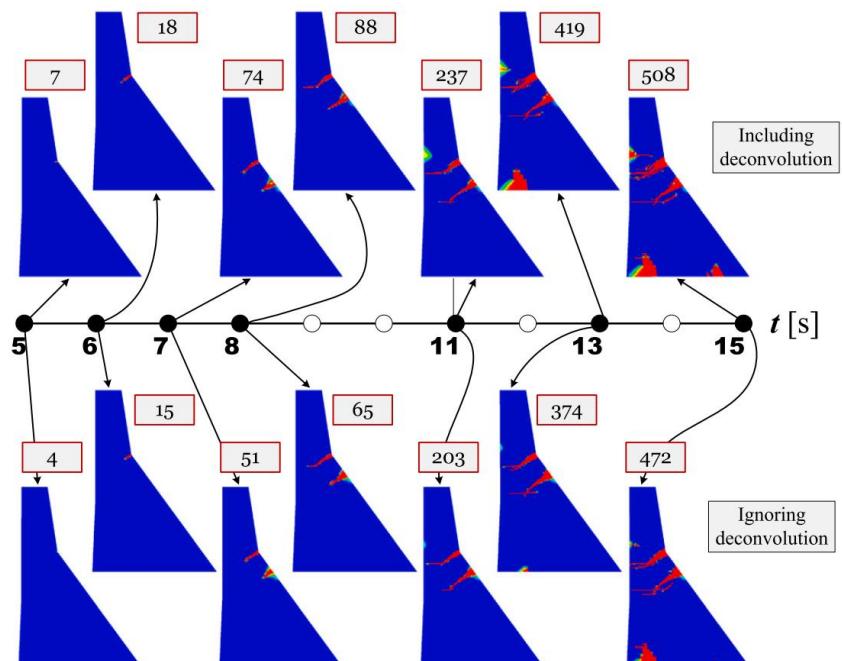


Illustration of the sample crack profile for the G2S2 IAA at various intensities, depicted at different time points.

Hariri-Ardebili, M. A., Poul, M. K., Nikolaou, S., & Zerva, A. (2024). Deconvolved Intensifying Artificial Accelerations (DIAA): Theory and application in geostructures. *Computers and Geotechnics*, 170, 106291.



Thank you!

Any questions?

DYNAMIC ANALYSES OF AN EARTH DAM WITH DIFFERENT INITIAL STRESS STATE

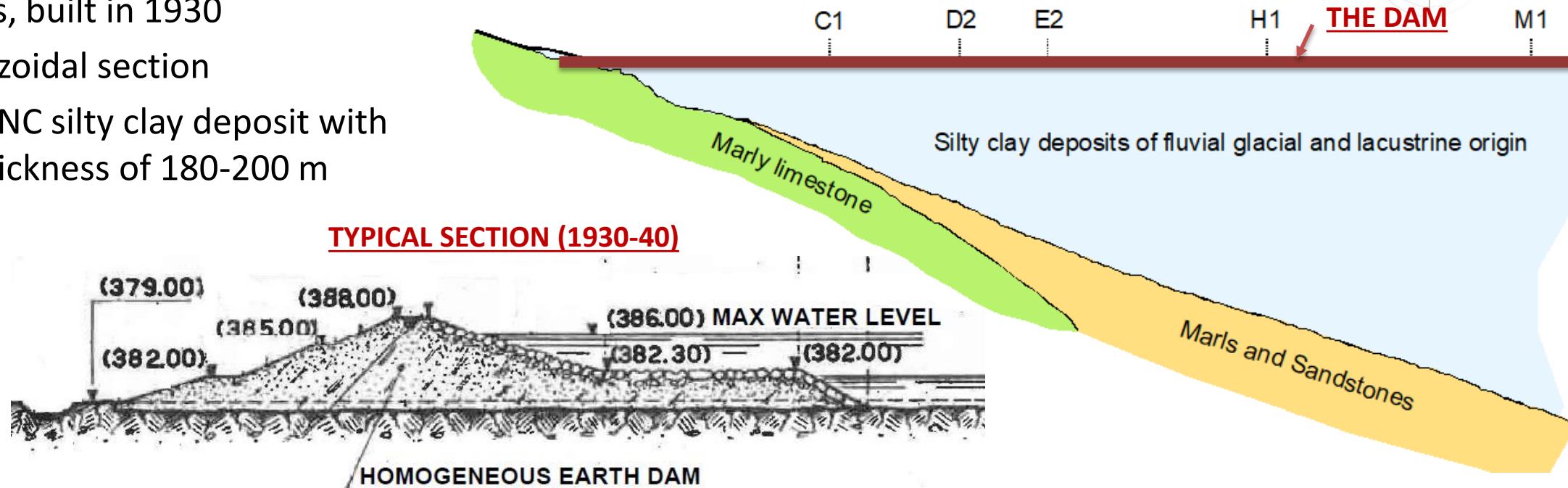
R. Previtali, R. Pellegrini, F. Carnevale ¹, P. Chemello ²

¹ ISMES, Seriate, Italy

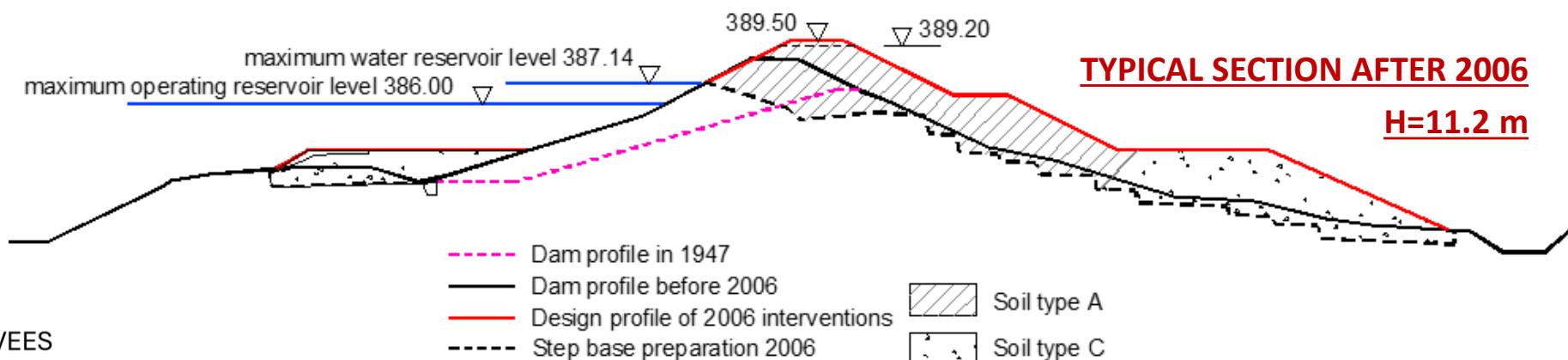
² Enel Green Power, Rome, Italy

DESCRIPTION OF THE DAM

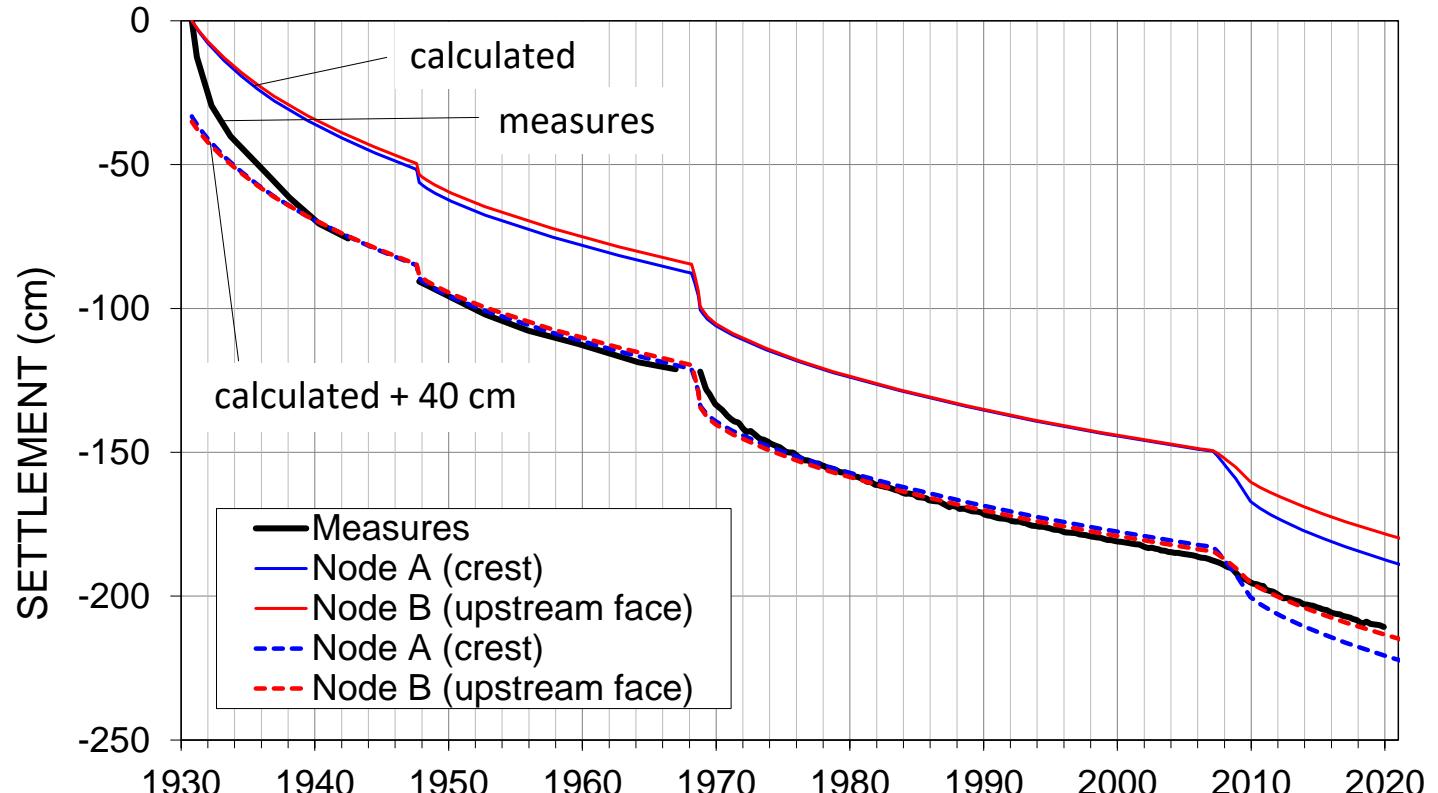
- Homogenous, built in 1930
- Simple trapezoidal section
- Foundation: NC silty clay deposit with maximum thickness of 180-200 m



- Continuous consolidation settlements → periodic work (first in 1948 and last in 2006) to comply with the regulations freeboard.



INITIAL STRESS STATE



- Overall regular behaviour
- Settlements: few cm/years (0.8 m/50 years), still in progress (N.C. clay)
- Numerical FE consolidation analysis with mesh update (M.C. dam - Cam Clay foundation)

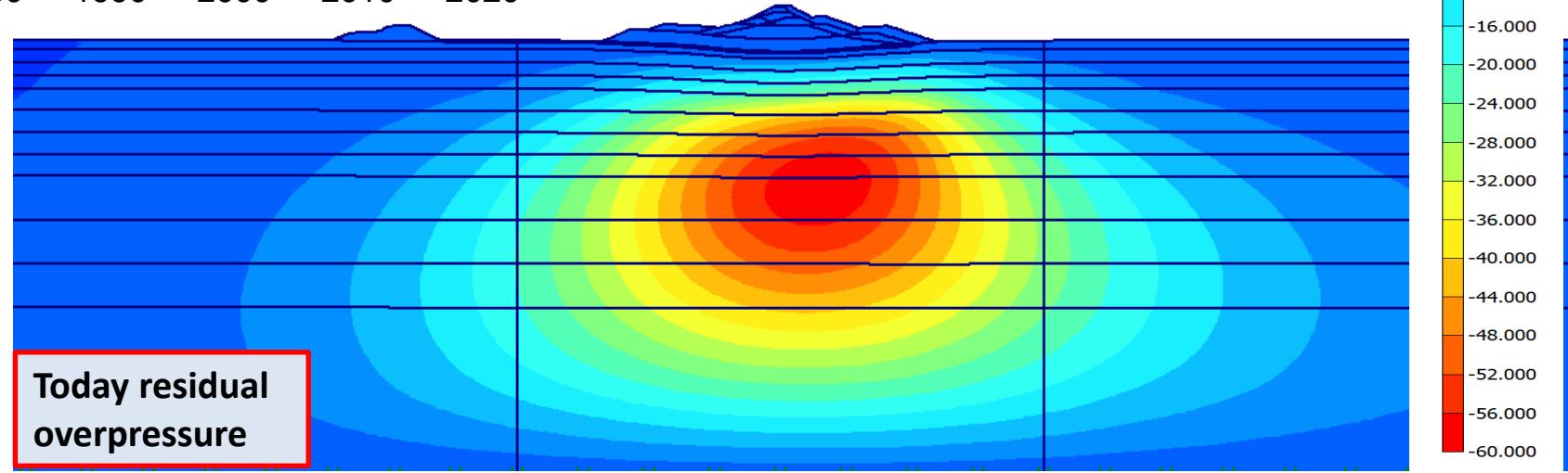


Both deformability and permeability have been calibrated starting from data available

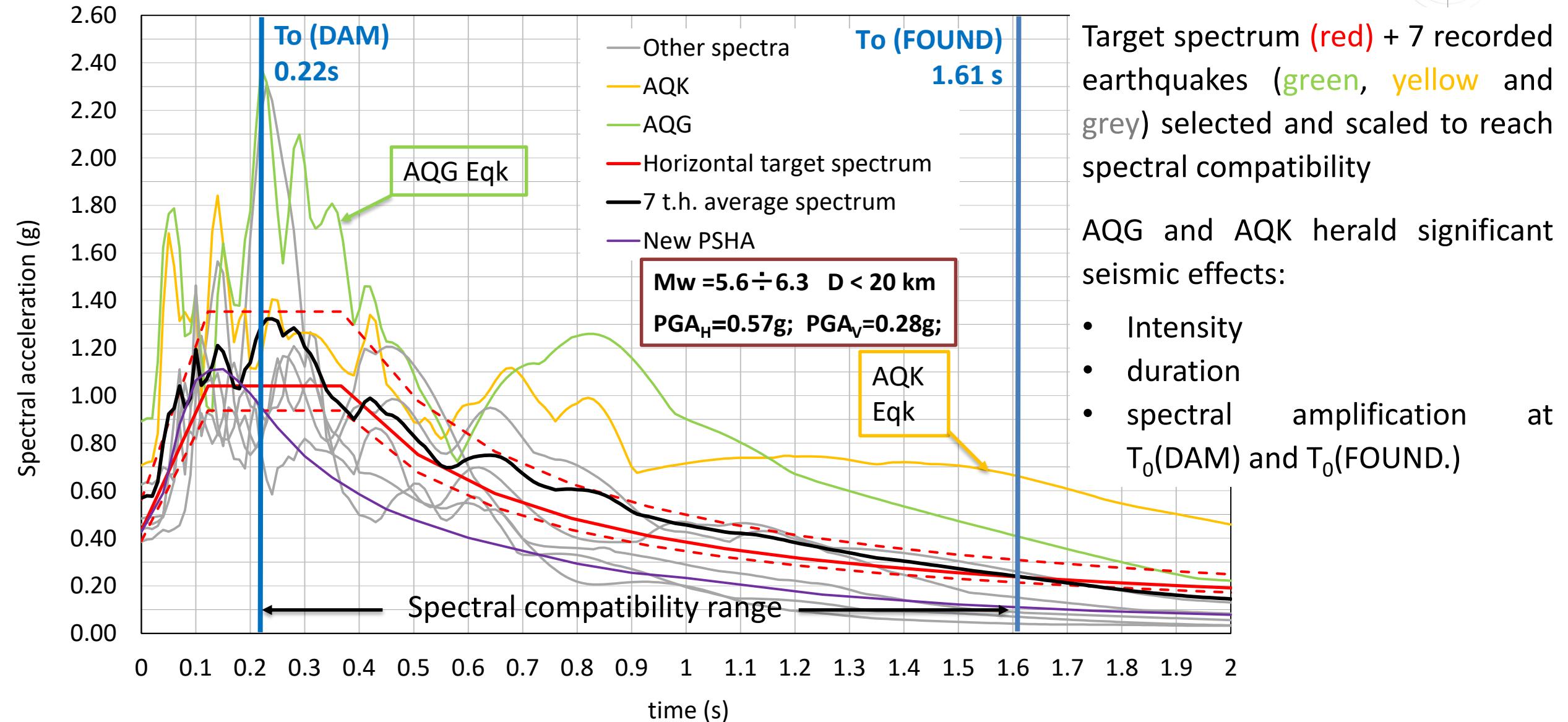


Good correspondence with measures (deformation and piezometric)

- Max residual overpressure: 59 kPa
- No overpressure in dam
- Current cons. degree: 74%
- Dissipation: 160 years

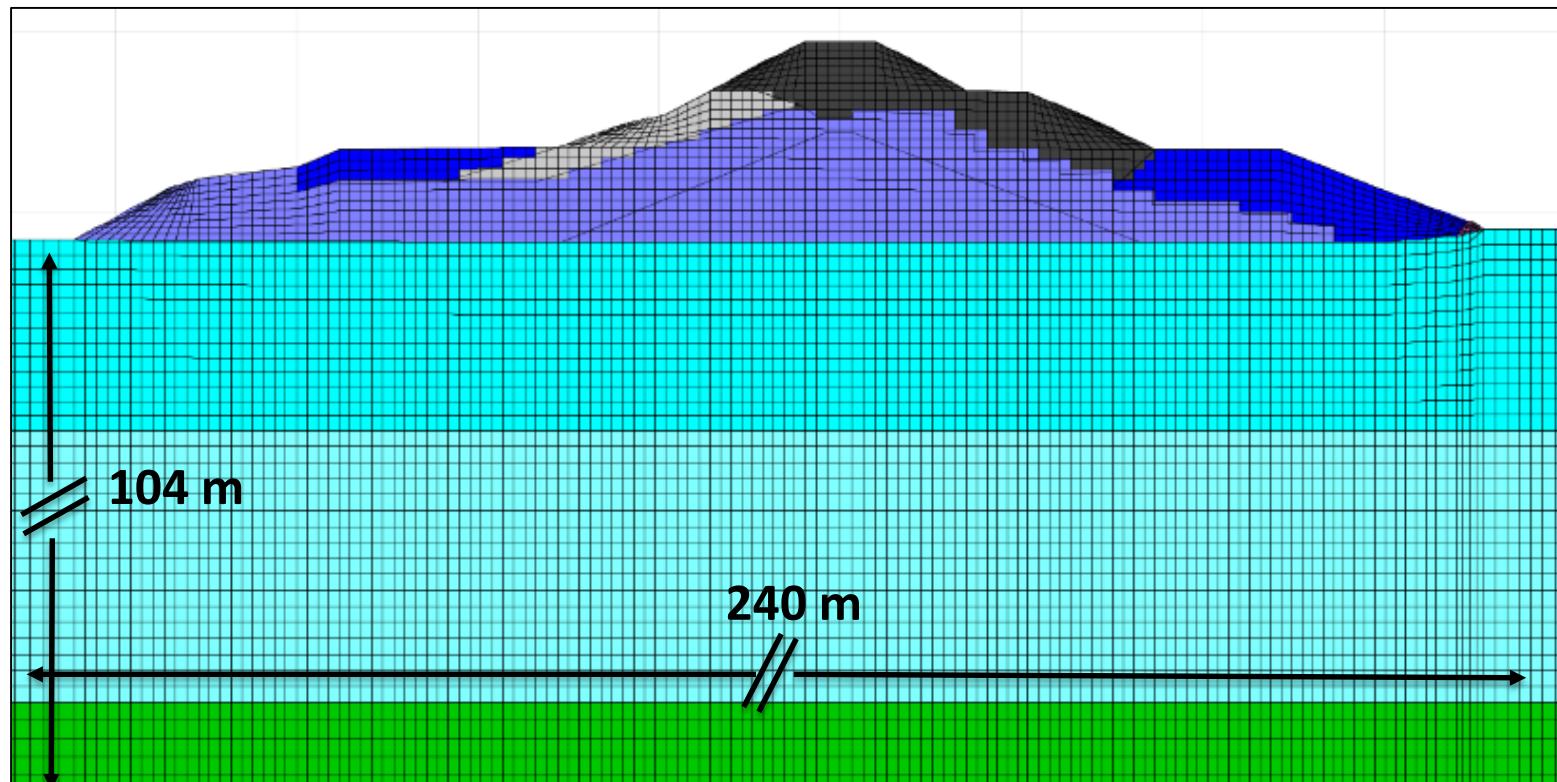
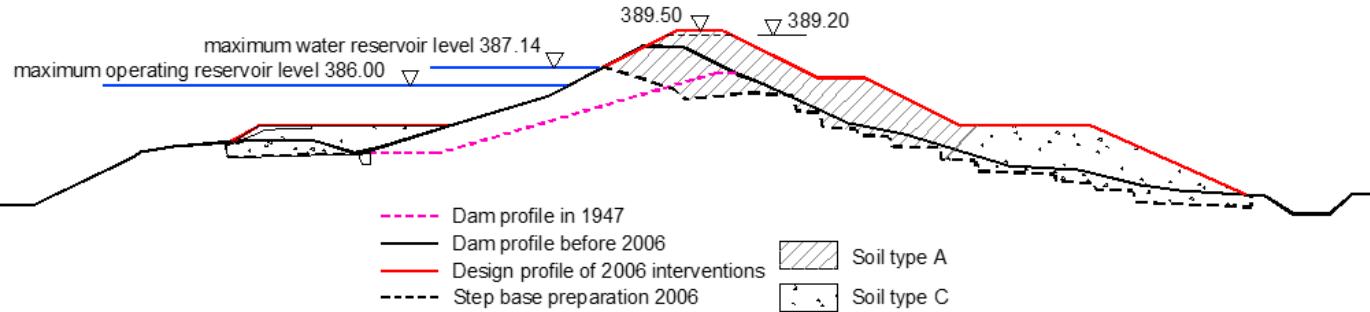


Collapse Limit State EARTHQUAKES (Tr=1950 years)



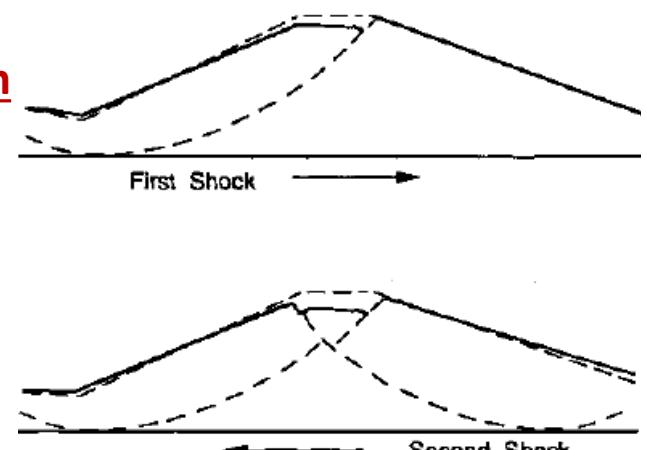
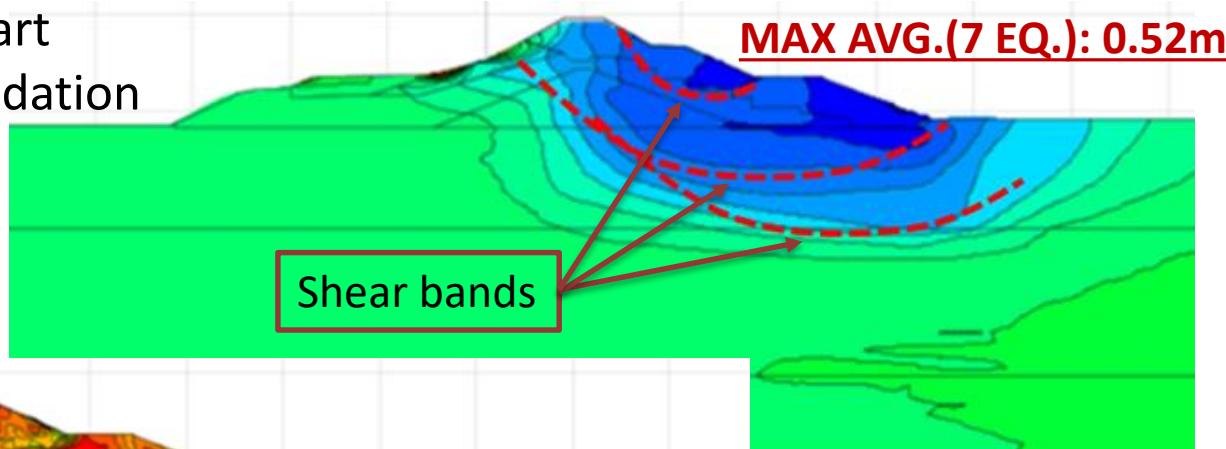
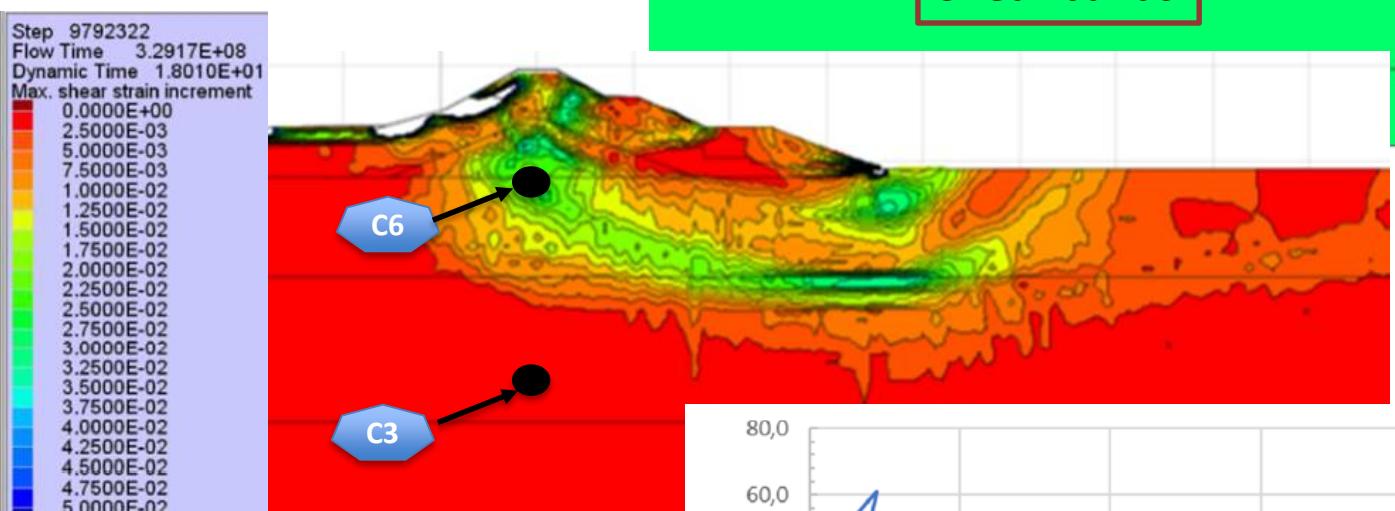
DYNAMIC ANALYSIS

- Plane strain finite difference model of the highest section (FLAC 2D)
- Boundary condition: Free Field boundary (lateral) + Quiet boundary (bottom)
- Hysteretic Damping Model: *Sig 4* Model (Masing criterion)
- Material constitutive model: Mohr Coulomb
- Small strain stiffness: obtained by cross-hole geophysical tests calibrated with HVSR + G reduction curves from laboratory test.



DEFORMATIONS AND STRAIN BEHAVIOUR

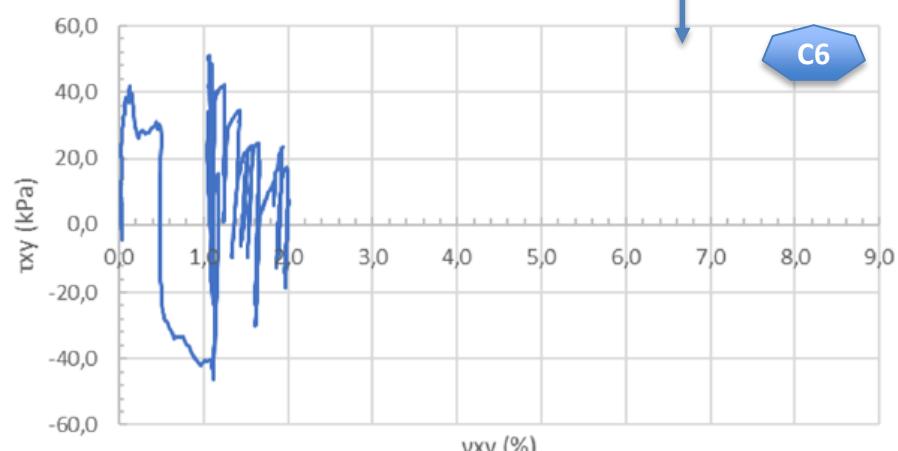
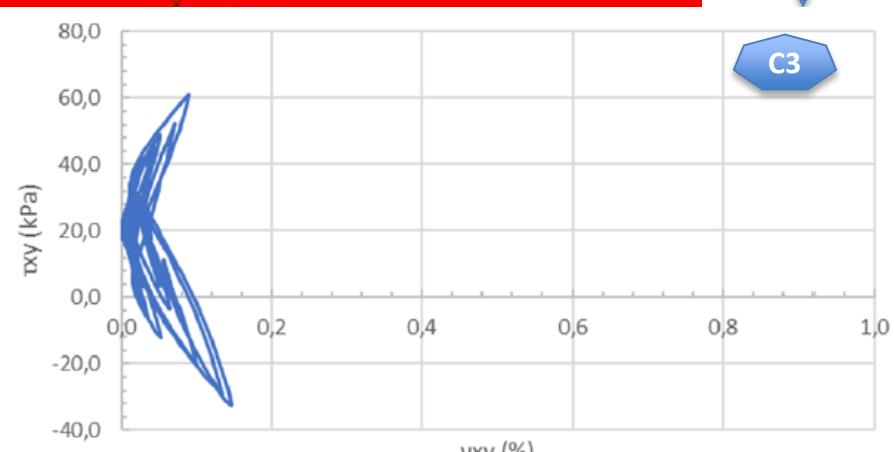
- Stress vs. strain response consistent with literature (lateral spreading)
- Higher for downstream part
- Involved upper 10 m foundation
- Shear strain bands



(After Ambraseys, 1958, taken from Yan, 1991)

Foundation: elastic behavior with hysteretic cyclic strains at deeper level.

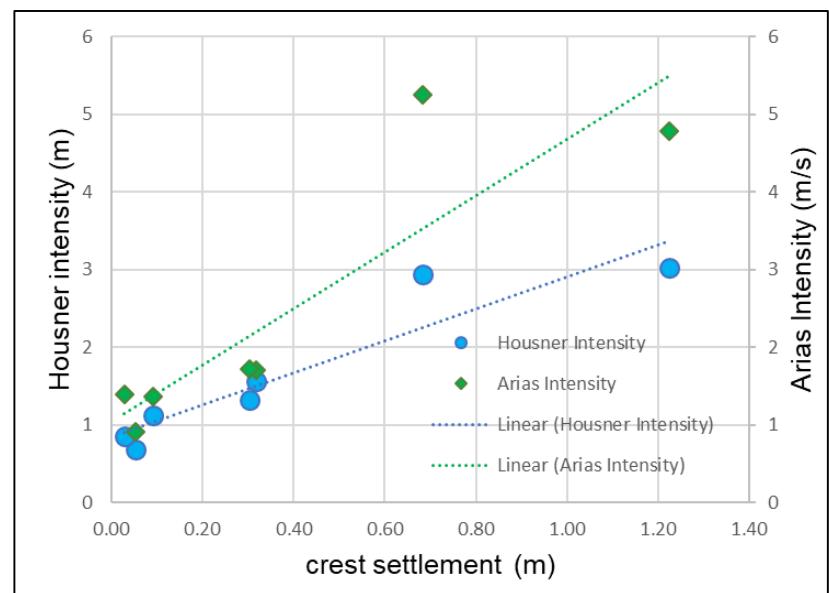
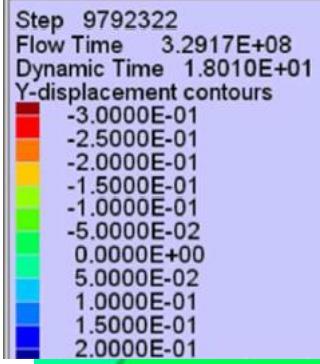
In the upper part irreversible strains develop



VERTICAL DISPLACEMENT

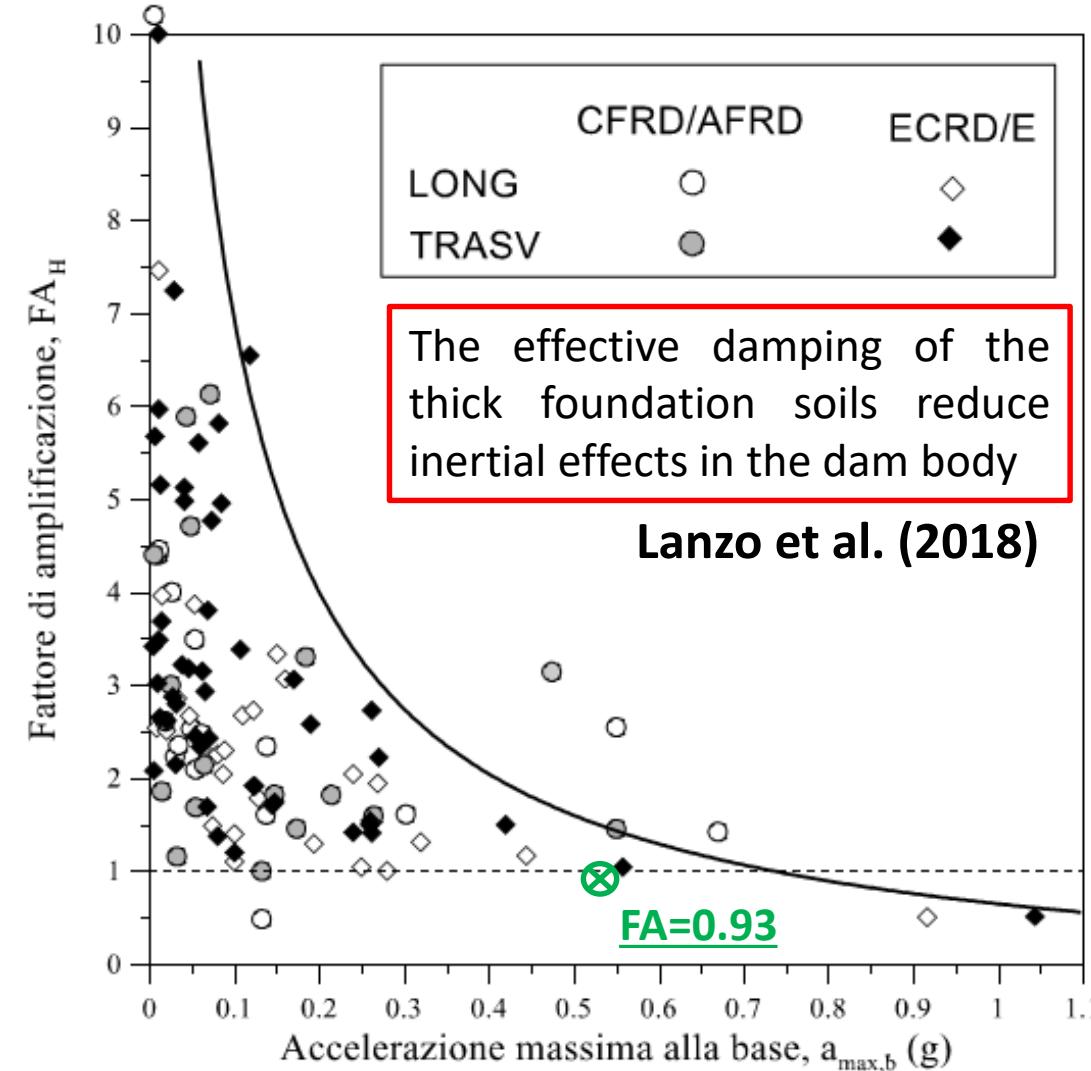
Vertical displacement are of the same order of magnitude of the horizontal ones

CLO EQ.

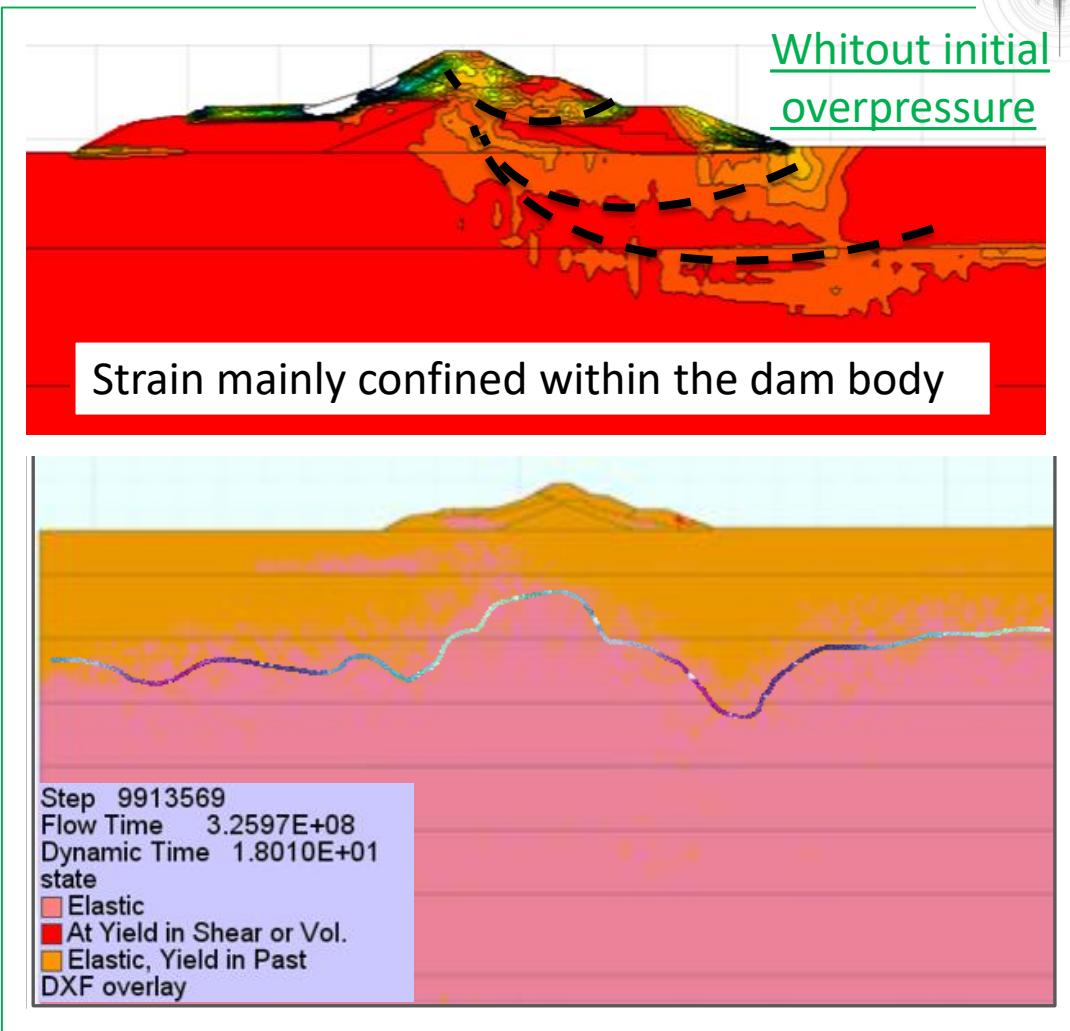
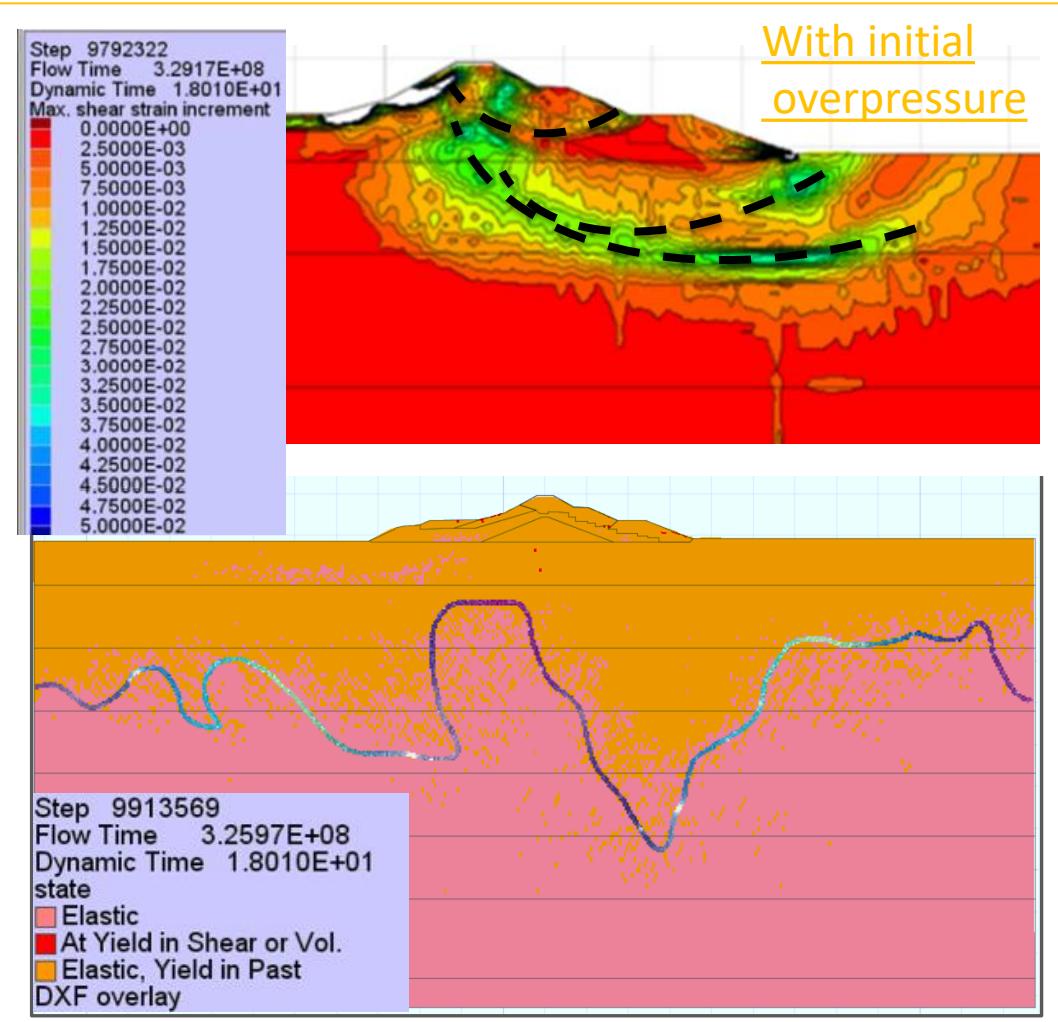


V.D. well correlated with seismic ground motion intensity parameter

MAX AVG. (7 EQ): 0.37m



COMPARISON WITH NO OVERPRESSURE CASE



- Effects with initial condition of full dissipation → same style of deformation with effects of a lower magnitude.
- The dam and its foundation are subject to minor irreversible plastic deformations.
- The initial condition with overpressures increases the portion of the foundation undergoing plasticity

COMPARISON WITH NO OVERPRESSURE CASE

Final average crest settlement:

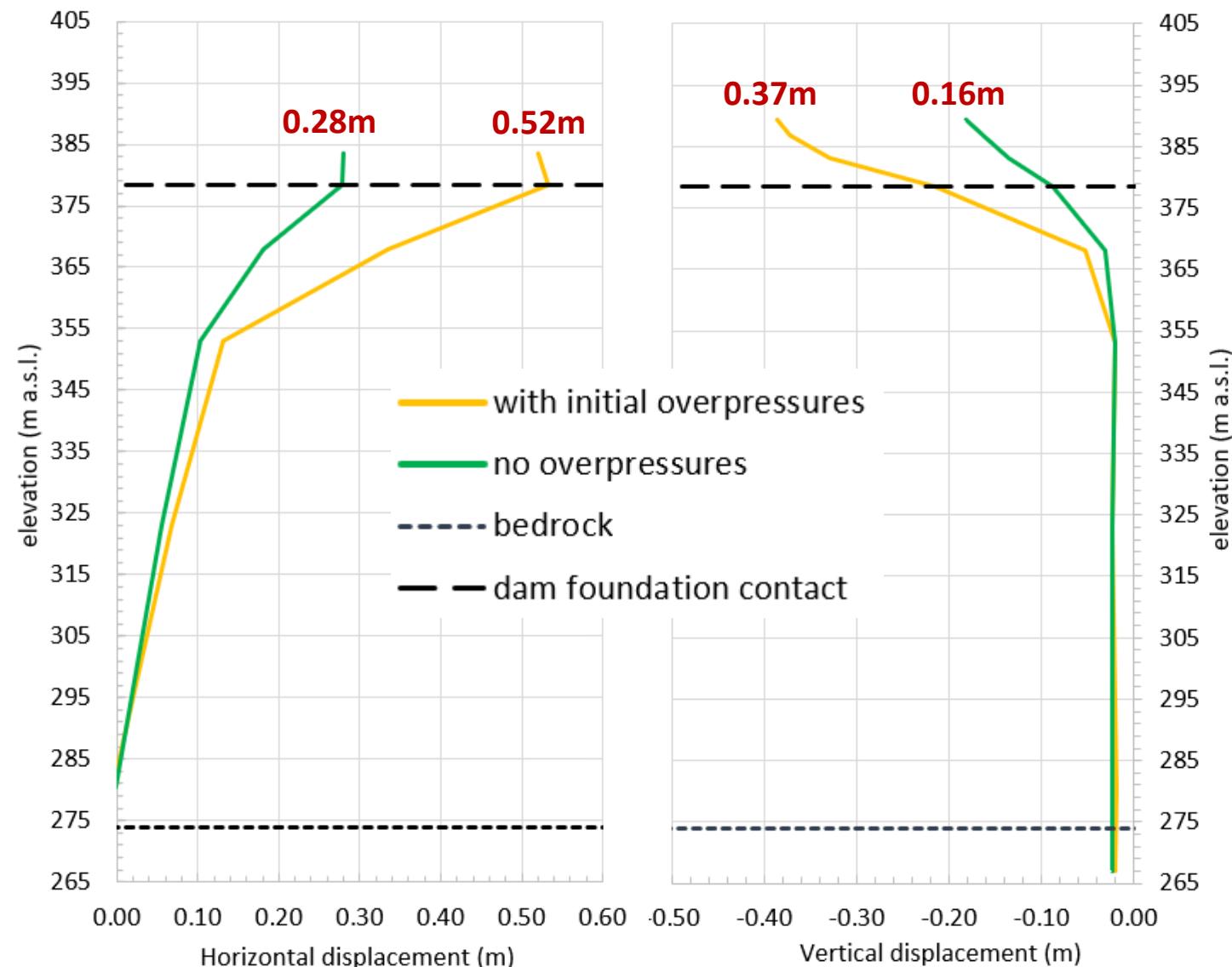
0.16m vs. 0.37m

Final average horizontal displ.:

0.28m vs. 0.52m

The average crest settlement is half of the corresponding values obtained considering initial overpressures.

The result is due to the lower confinement, induced lower strength of the foundation soil when it is still affected by overpressures related to consolidation.



CONCLUSIONS

- Two different initial stress conditions of the foundation soils have been considered: the calculated interstitial water overpressures resulted representative of a present day 74% consolidation of the deep clayey foundation soils to actual loads.
- By applying Collapse Limit State earthquakes, about two times higher final vertical and horizontal displacements resulted when water overpressures are considered, due to the lower strength of foundation soils induced by lower effective stresses.
- The style of final displacement is maintained. The higher shear strains are of irreversible plastic nature; they are organized in broad shear bands that affect the dam and spread in the soil foundation when initial overpressure are taken into account.



Thank you!

Any questions?



Effect of non-vertical propagating seismic waves on the behavior of gravity and arch dams

Humbert N.¹, Robbe E.¹, Cherubini S.²

¹ EDF (hydraulique center)

² EDF R&D

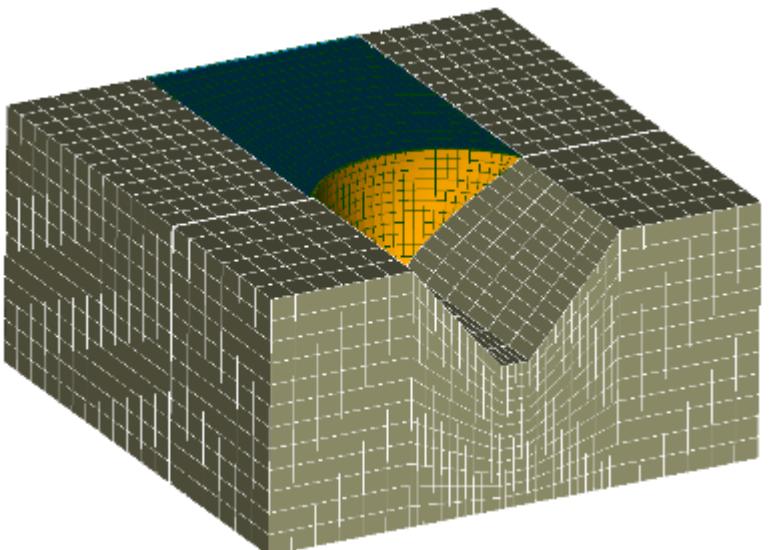
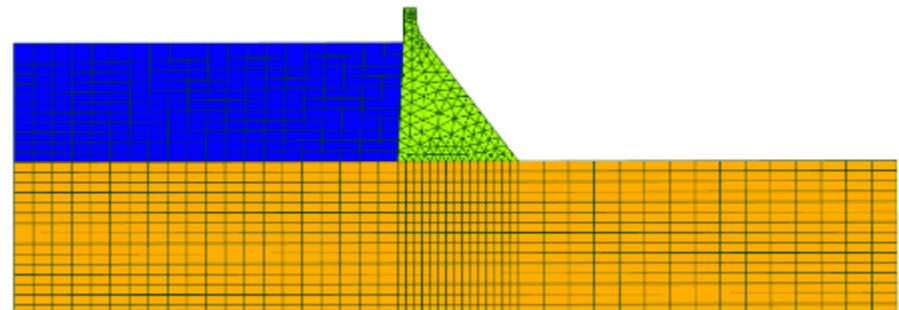
Introduction

The aim of the paper is to present analyses to demonstrate the effect of

- a **slightly inclined** propagation direction of the seismic wave
- on the behavior of **concrete dams**.

2 parts: 1- Validation of FE models

2- Evaluation of the effect on a 2D gravity dam et a 3D arch dam

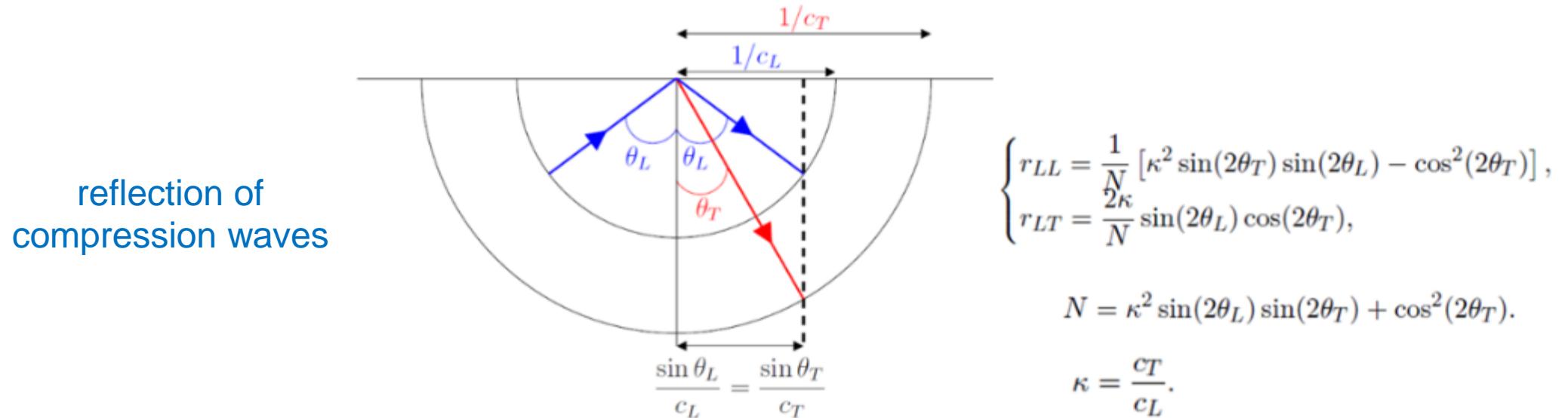


Taking into account non-vertical incident waves in finite-element analyses

Use and validation of Lokke and Chopra ‘direct finite-element method’

- Linear/nonlinear analysis
- 2D and 3D dam-water foundation rock systems

Theory reminder for reflection of incident waves at the free surface - Sadd (2009)

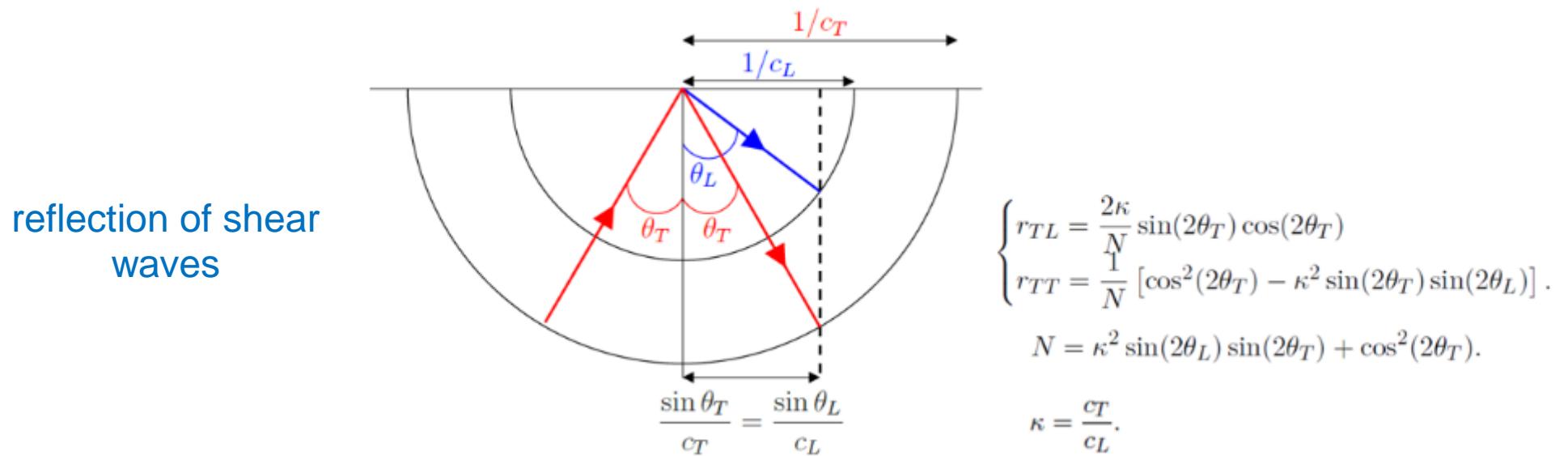


Taking into account non-vertical incident waves in finite-element analyses

Use and validation of Lokke and Chopra ‘direct finite-element method’

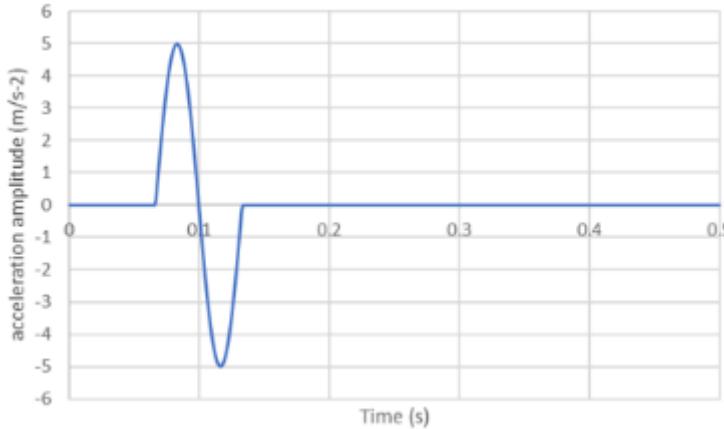
- Linear/nonlinear analysis
- 2D and 3D dam-water foundation rock systems

Theory reminder for reflection of incident waves at the free surface - Sadd (2009)

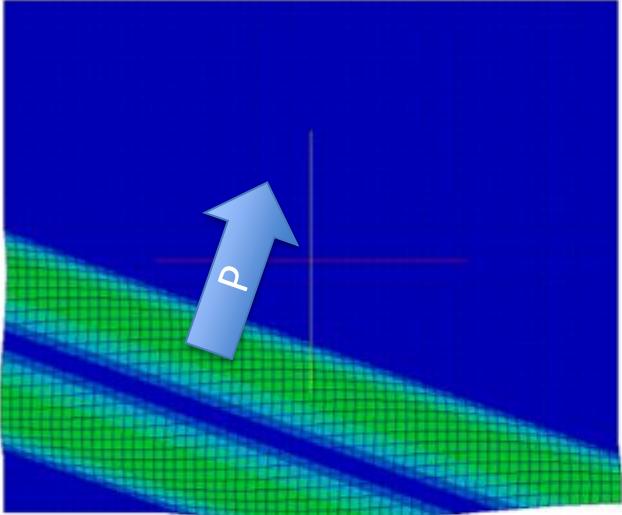


Taking into account non-vertical incident waves in finite-element analyses

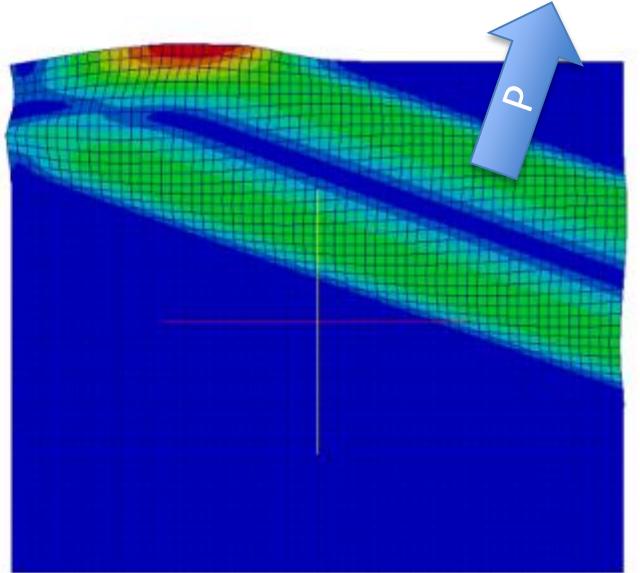
Validation on a simple “box”



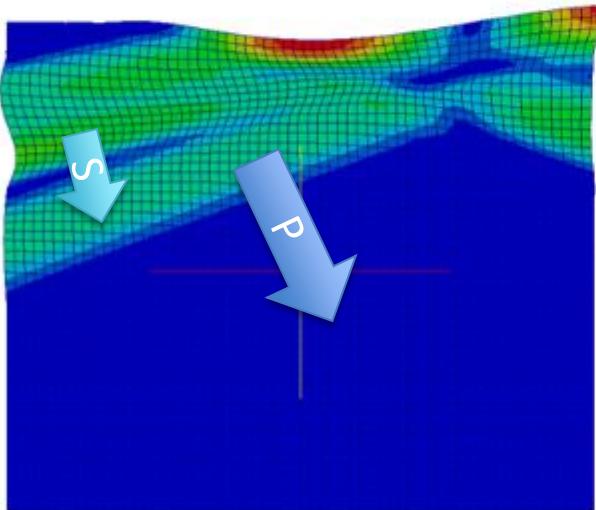
1)



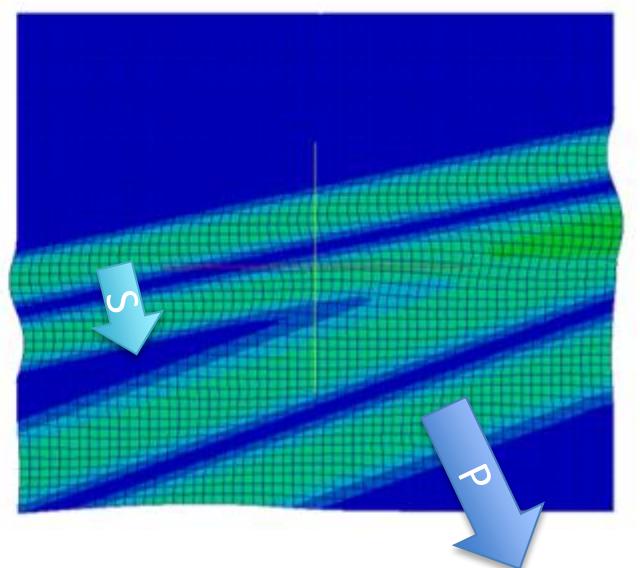
2)



3)

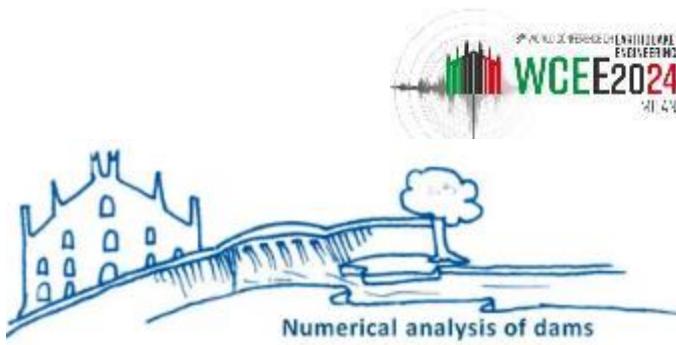


4)

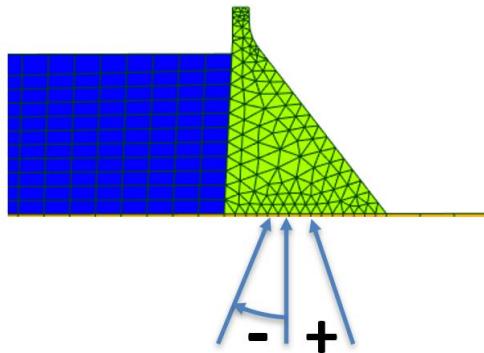
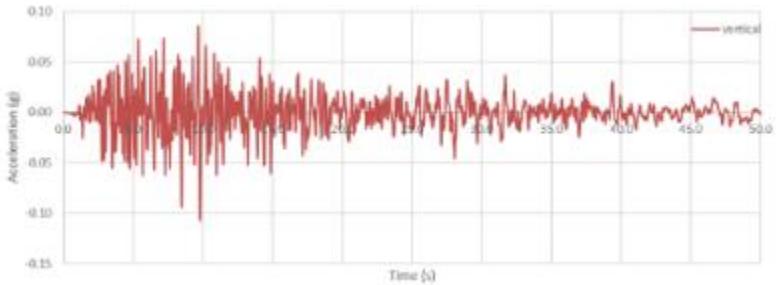
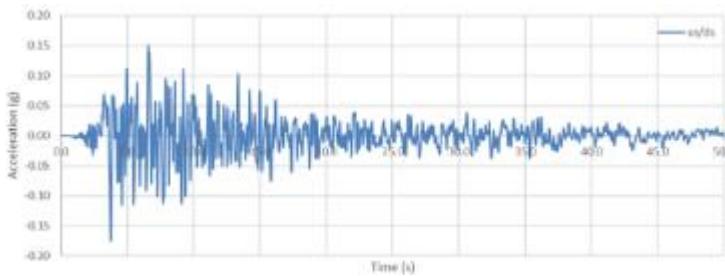


Case of gravity dam

Based on Pine Flat test case : workshop organized by ICOLD in Milano



- The simplified 2D geometry
- Linear analyses : Module of elasticity: 22,410 Mpa / Density: 2,483 kg/m³ / Poisson's ratio: 0.2 / Rayleigh damping only for concrete $\alpha=0.75$ (mass) and $\beta=0.005$ (stiffness)
- Wave propagation in reservoir (acoustic fluid elements)
- Taft earthquake accelerations (0.17g)



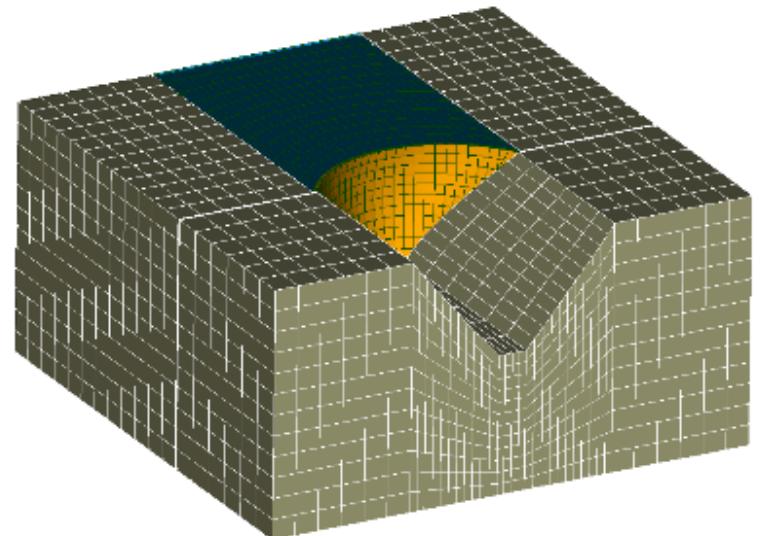
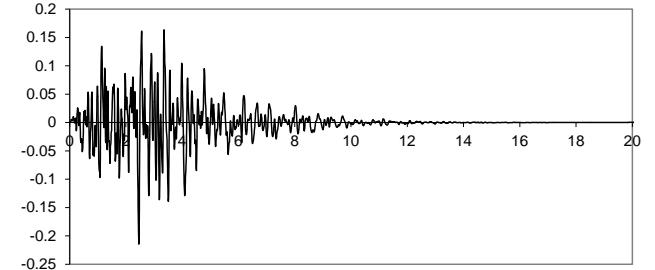
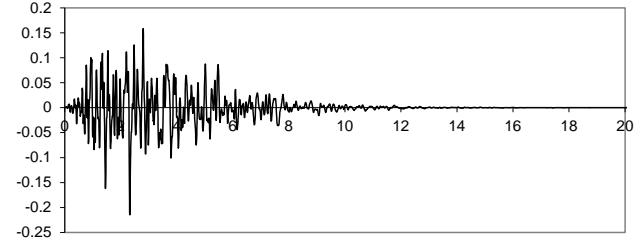
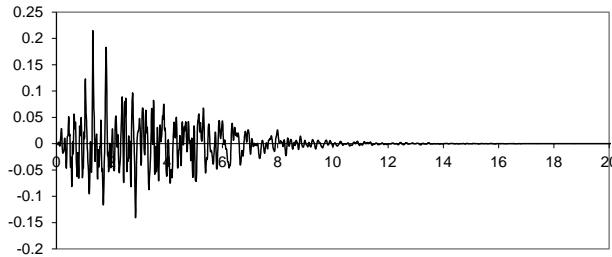
Evaluation of : Min shear safety factor / Max us tensile stress / Max ds compression stress

Set of accelerograms	Max horiz. acceleration (ms ⁻²)	Max dyn horiz. displacement (mm)	Min shear safety factor	Max us tensile stress (MPa)	Max ds compression stress (MPa)
Us/ds ; vertical	11.1	43.4	1.39	0.70	3.28
-Us/ds ; vertical	11.1	43.4	1.40	0.65	3.26
Us/ds ; -vertical	11.1	43.4	1.25	0.97	3.5
-Us/ds ; -vertical	11.1	43.4	1.37	0.74	3.25

Case of arch dam

Based on case proposed during the 12th ICOLD benchmark workshop (Zens 2013)

- 3D geometry
- Linear analyses : 27 000 MPa for concrete, 25 000 MPa for rock / Density of rock and concrete: 2,400 kg/m³
- Wave propagation in reservoir (acoustic fluid elements)
- 3 synthetics accelerations with 0.22g peak ground acceleration. The vertical component is reduced by 2/3.

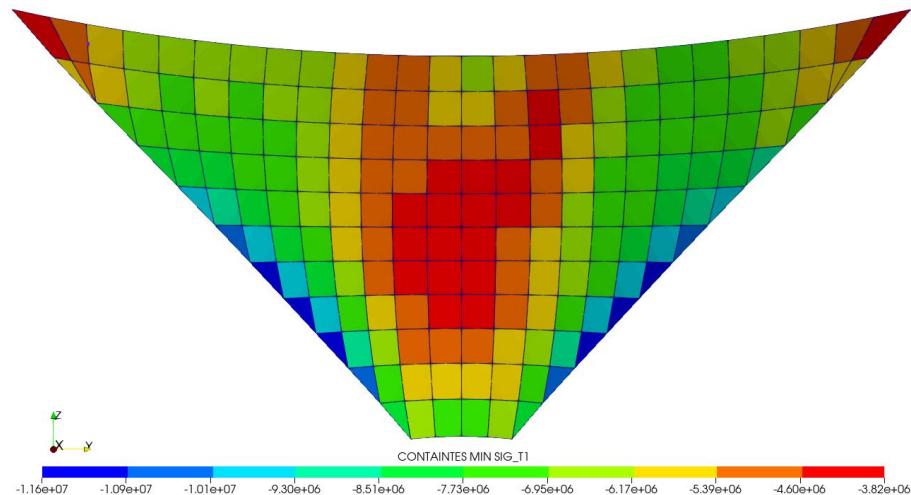


Case of arch dam

The following results are analyzed:

- Maximum acceleration (generally near the crest of the dam),
- Maximum displacement during the earthquake (static included), at the crest of the central cantilever,
- Maximum (tension) and minimum (compression) principals' stresses during the earthquake (static included) on the upstream and downstream face.

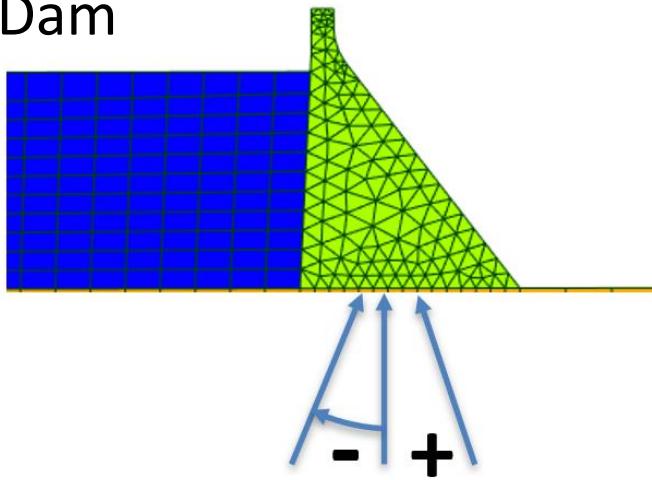
Results for vertical propagation:



load	Max acceleration (ms-2)	Max displacement (mm)	Max us tensile stress (MPa)	Min us compression stress (MPa)	Max ds tensile stress (MPa)	Max ds compression stress (MPa)
static		83	1.4	-7	0.5	-9.8
Static +Eq 1	18.5	129	2.8	-9.13	2.0	-11.6
Static +Eq 2	15.3	126	2.9	-9.37	2.6	-11.5
Static +Eq 3	17.3	134	2.6	-9.62	2.3	-11.2

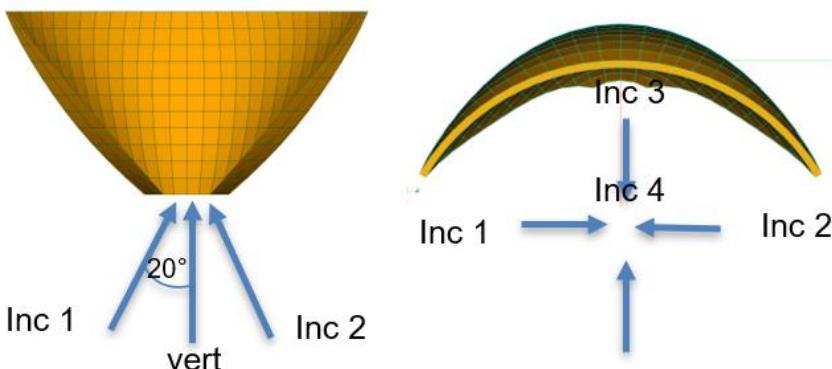
Results with inclined waves

Gravity Dam



Incident angle (degrees)	Max horiz. acceleration (ms ⁻²)	Max dyn horiz. displacement (m)	Min shear safety factor	Max us tensile stress (MPa)	Max ds compression stress (MPa)
-20	10.7	55.4	1.40	0.77	3.49
-10	10.8	49.9	1.39	0.76	3.43
0	11.1	43.4	1.39	0.70	3.28
10	9.7	37.2	1.49	0.56	3.12
20	9.0	34.4	1.58	0.37	2.92

Arch dam



Incident waves	Max acceleration (ms ⁻²)	Max displacement (mm)	Max ds tensile stress (MPa)	Max ds compression stress (MPa)
Vertical*	15.3-18.5*	126-134*	2.0-2.6*	-11.2 -11.6*
Inc 1	16.3	138	1.5	11.9
Inc 2	17	130	2.0	11.9
Inc 3	22	132	2.5	12.6
Inc 4	16.9	129	1.6	11.6

(*) range of results for the 3 earthquakes considered (from Table 3)

Conclusion

- This paper presents the development required to consider propagation with incident angle when homogenous media and no damping are considered for the foundation.
- The method is validated with a flat box test case and seismic analyses of a 2D gravity dam and a 3D arch dam under earthquake are performed to evaluate the influence of inclined direction of propagation of the waves.
- Results show that stability parameters are slightly affected by such assumption but remain in the range of variation computed when considering different accelerograms combination.
- From the authors point of view, such analyses are then not necessary for the safety evaluation of concrete dams under earthquake considering that several time-history analyses are anyway performed with various combination of accelerograms.



Thank you!

Any questions?





— BUREAU OF —
RECLAMATION



Decision making for Seismic Risks

World Conference on Earthquake Engineering
30th June to 5th July, 2024

- United States Bureau
- Irrigation, Municipal and Industrial Water
 - 31 million people
 - 4 million hectares of farmland

www.usbr.gov

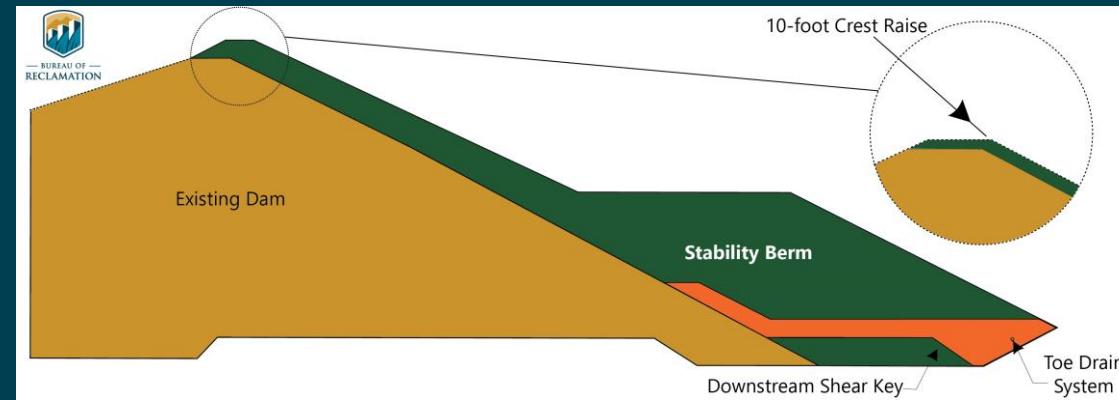


- 364 high hazard dams
- 78 powerplants
- 172 km³ storage
- 290 bridges
- 1,300 buildings
- 10,000 miles of canals
- 90 million visits per year

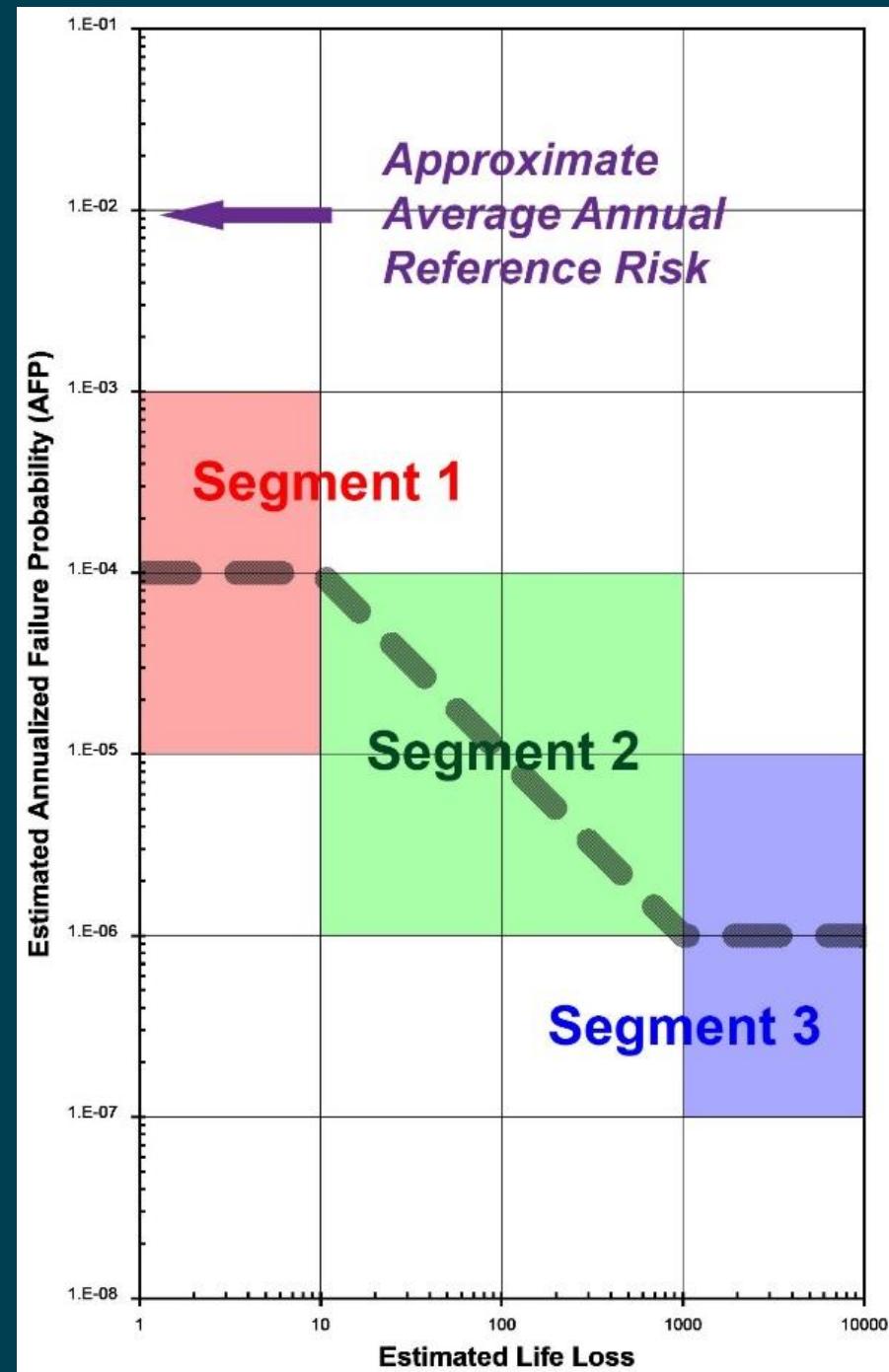


B.F. Sisk Dam Modification

- Largest Dam Safety Project, \$1.1 billion
- 5.6 Kilometer Dam, 116 meters high, 2.4 km^3
- Peak Ground Acceleration 1.2g



- Annualized Failure Probability
 - Seismic Loading
 - Reservoir Loading
 - Conditional Probability (response)

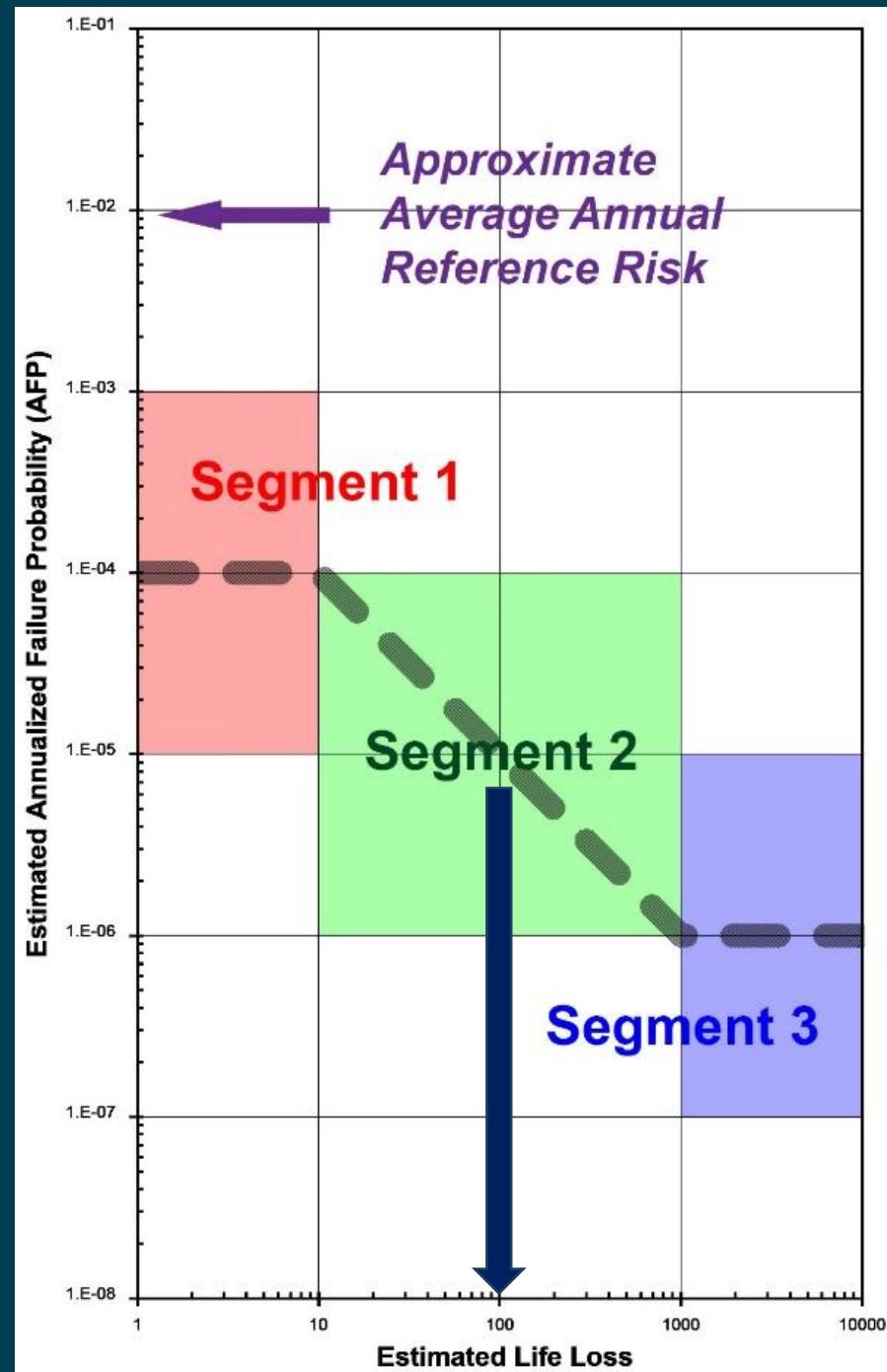


- Public Protection Guidelines

www.usbr.gov/dam/safety/references



- Annualized Failure Probability
 - Seismic Loading
 - Reservoir Loading
 - Conditional Probability (response)



- Public Protection Guidelines

www.usbr.gov/dam/safety/references



Question 1?

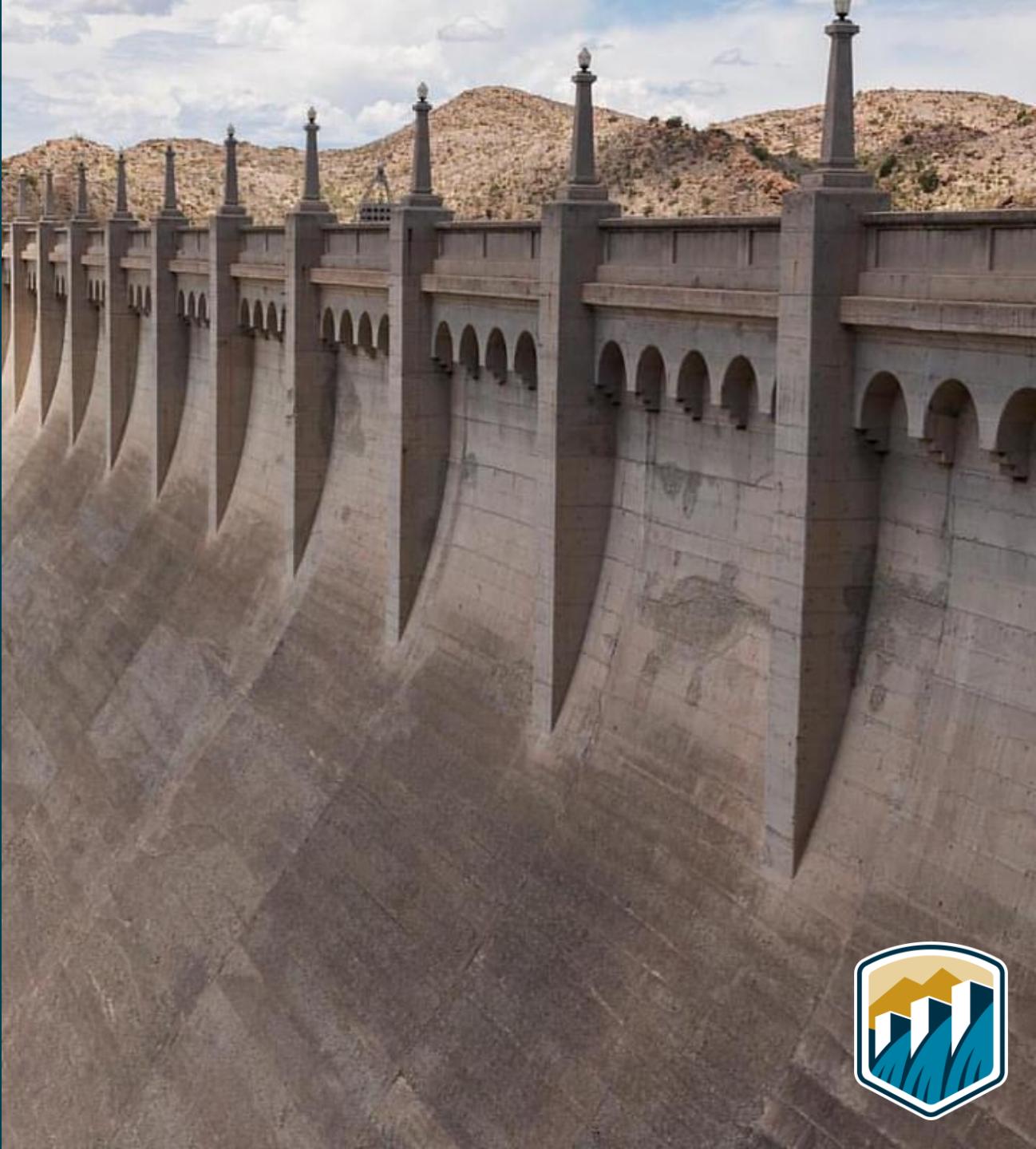
- At what threshold, either in terms of loading frequency or modification cost, does the level of uncertainty in the seismic risk model, including seismic hazard and structural response, support the decision to modify a dam to improve its seismic resilience?





Question 2?

- Is Reclamation's approach leading to decisions consistent with other dam owners and infrastructure?





Miguel Rocha
mrocha@usbr.gov



— BUREAU OF —
RECLAMATION



Non-linear seismic analysis of a concrete gravity dam using time domain spectral finite element method

Avirup Sarkar ¹, Ashutosh Bagchi ¹

¹ Concordia University, Montreal, Canada

Contents

- ✓ Introduction
- ✓ Problem Statement
- ✓ Time domain spectral FEM: main features
- ✓ Time domain spectral FEM: Matrix formulations
- ✓ Non-linear time history analysis details
- ✓ Comparison of computation time: FEM and TDSFEM
- ✓ Results of horizontal crest displacement (different cases)
- ✓ Stress plots showing potential failure zones
- ✓ Conclusions

Introduction

- ✓ Finite element method: most common analysis tool, has certain disadvantages for dynamic analysis of large structures
- ✓ Many number of elements required for accuracy
- ✓ Even for a uniform rod, many elements are necessary for dynamic analysis
- ✓ Requires huge computational time and space for large structures
- ✓ Alternate computationally efficient analysis tools: Spectral FEMs
- ✓ Spectral FEMs: Frequency domain based (FDSFEM), Time domain based (TDSFEM)
- ✓ FDSFEM: highly computationally efficient, not applicable for complex 2D geometry

Problem Statement

- ✓ To develop alternate computationally efficient technique for analysis of large structures like concrete gravity dams
- ✓ To demonstrate the computational efficiency of TDSFEM based procedure for non-linear seismic analysis of dams

Time domain based Spectral FEM: Main Features

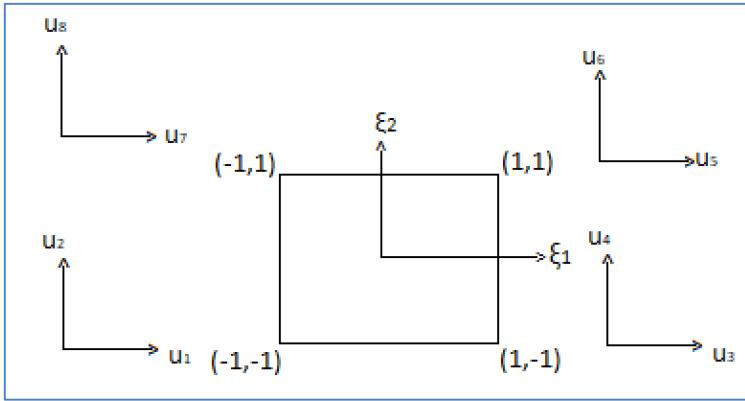
- ✓ It is similar to p-type FEM
- ✓ Instead of Gauss quadrature used in FEM, it uses Gauss-Legendre-Lobatto (GLL) quadrature
- ✓ This causes the mass matrix to be diagonal
- ✓ Leads to reduction of computation time compared to conventional FEM for same accuracy

Time domain based Spectral FEM: Matrix formulations

$$(1 - \xi^2) \frac{dP^{M-1}(\xi)}{d\xi} = 0, M \leftarrow m_1, m_2$$

$$w = \frac{2}{M(M-1)(P^{M-1}(\xi))^2}, M \leftarrow m_1, m_2$$

$$P^M(\xi) = \frac{1}{2^M M!} \frac{d^M}{d\xi^M} [(\xi^2 - 1)^M], \xi \leftarrow \xi^1, \xi^2$$

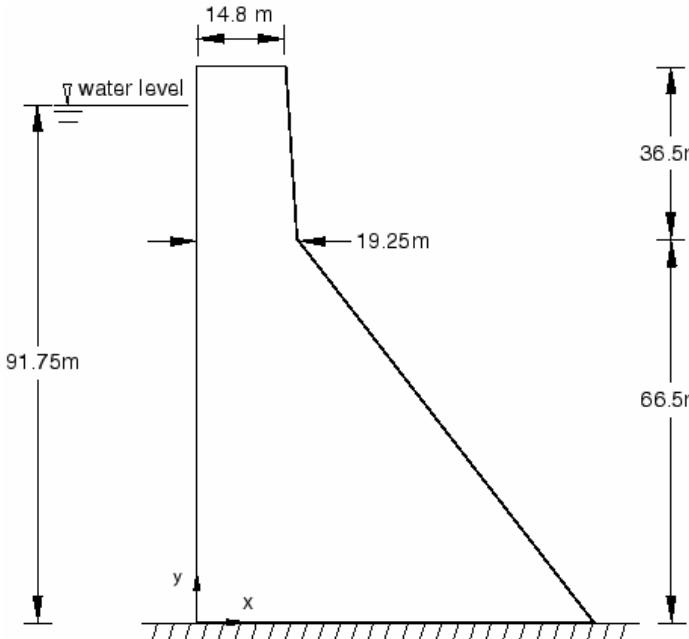


$$M_{(e)} = \int_{-1}^1 N_{(e)}^T(\xi) \mu N_{(e)}(\xi) j(\xi) d\xi \approx \sum_{p=1}^{n_p} w_p N_{(e)}^T(\xi_p) \mu N_{(e)}(\xi_p) j(\xi_p)$$

$$K_{(e)} = \int_{-1}^1 B_{(e)}^T(\xi) E B_{(e)}(\xi) j(\xi) d\xi \approx \sum_{p=1}^{n_p} w_p B_{(e)}^T(\xi_p) E B_{(e)}(\xi_p) j(\xi_p)$$

$$f_{(e)} = \int_{-1}^1 N_{(e)}^T(\xi) f_{(e)}(\xi) j(\xi) d\xi \approx \sum_{p=1}^{n_p} w_p N_{(e)}^T(\xi_p) f_{(e)}(\xi_p) j(\xi_p)$$

Non-linear dynamic time history analysis



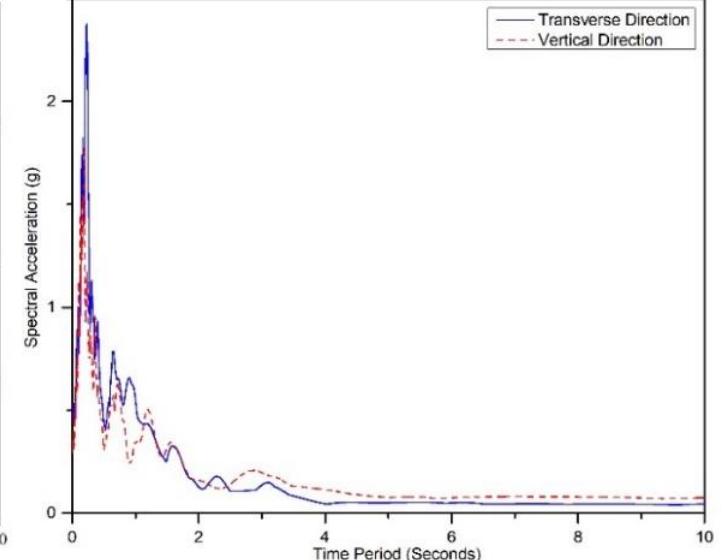
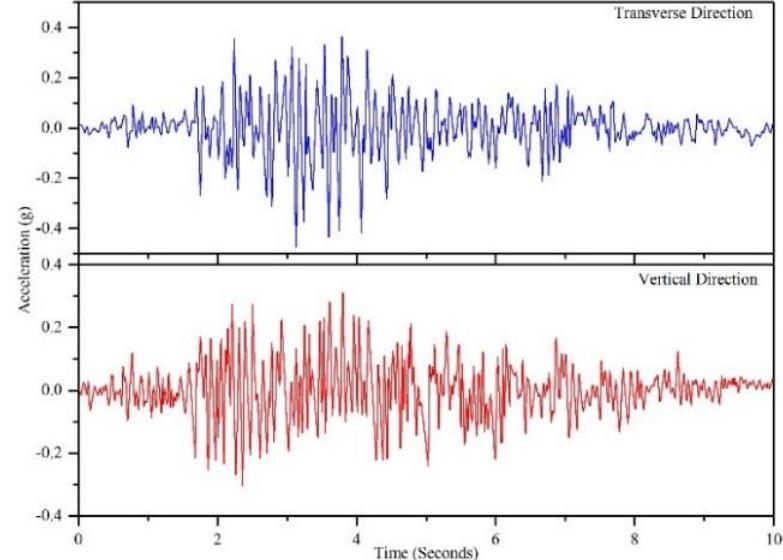
Material Properties of the Dam

Young's Modulus: 31027 MPa

Poisson's Ratio: 0.15

Density: 2643 kg/m³

Considered ground motions and response spectrum



(a)

(b)

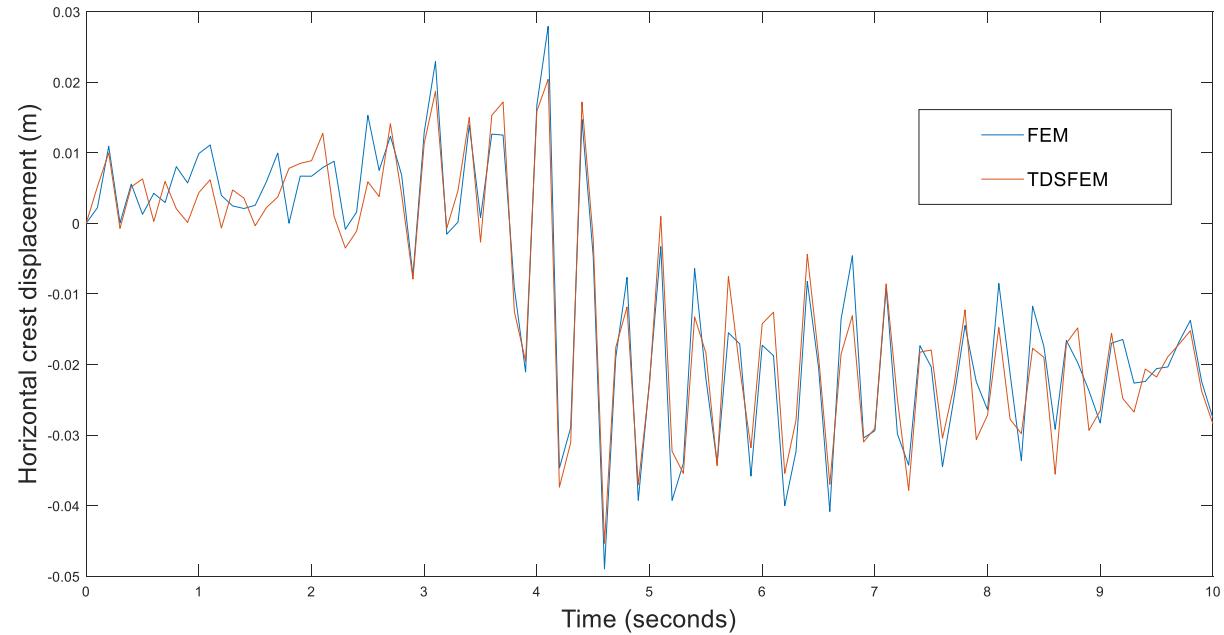
Damping Considered: Rayleigh's Proportional damping

Critical Damping Ratio: 0.03

Based on 1st modal frequency and Critical damping ratio=0.03,
 β value considered=0.00323

Material nonlinear model: Concrete damaged plasticity by Lee & Fenves (1998)

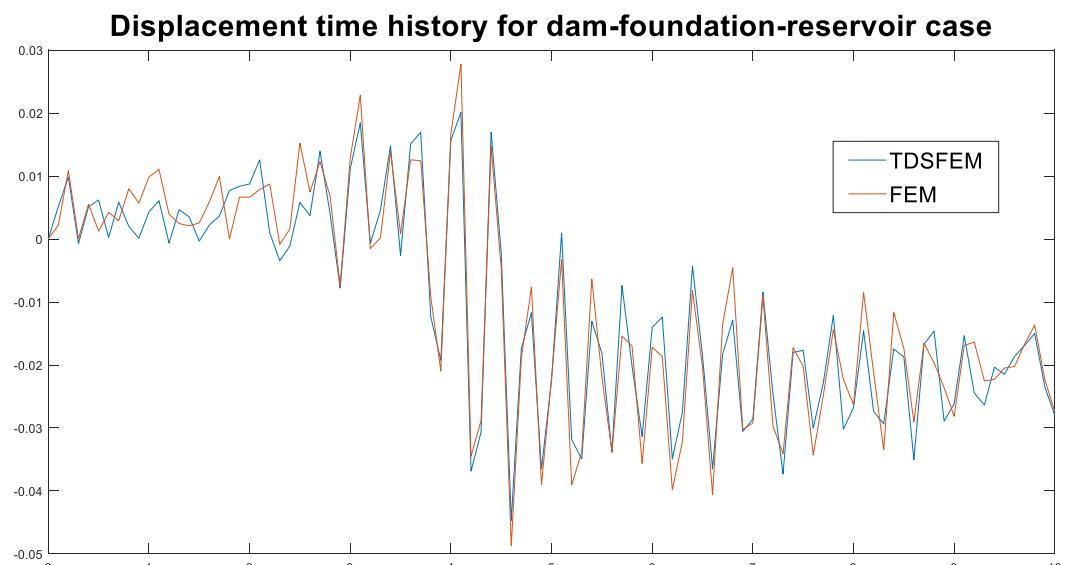
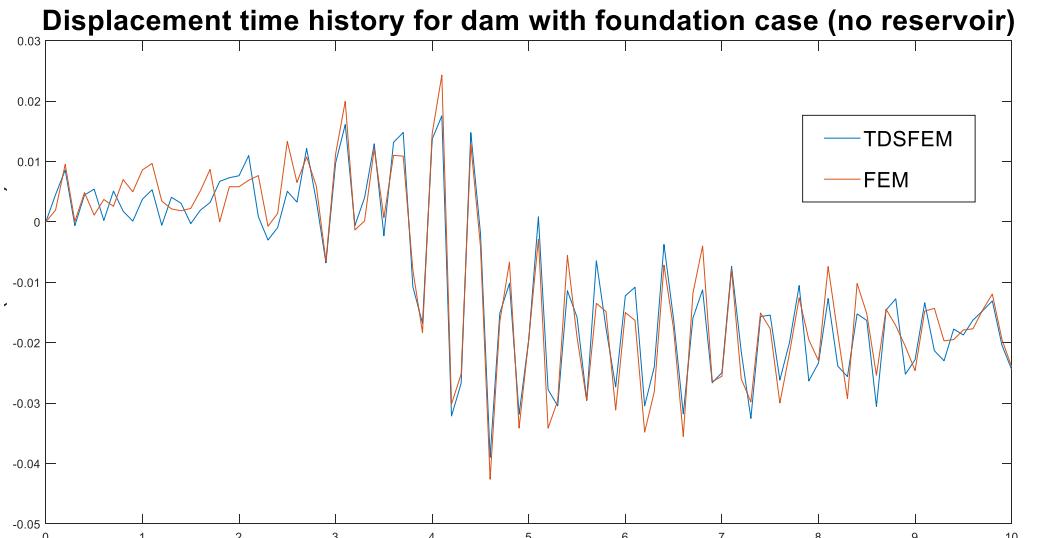
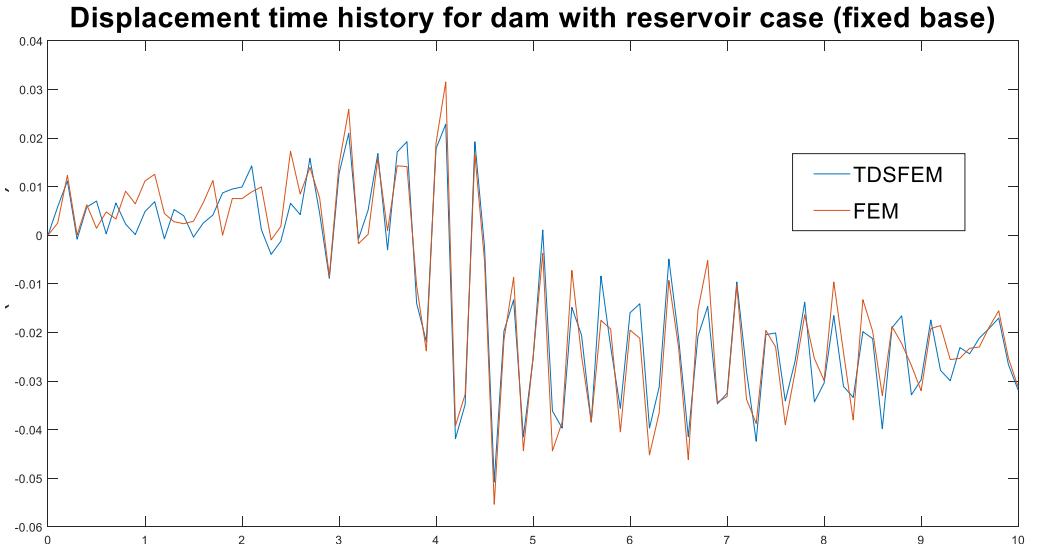
Comparison of results (FEM and TDSFEM)



Dam only case (fixed base)

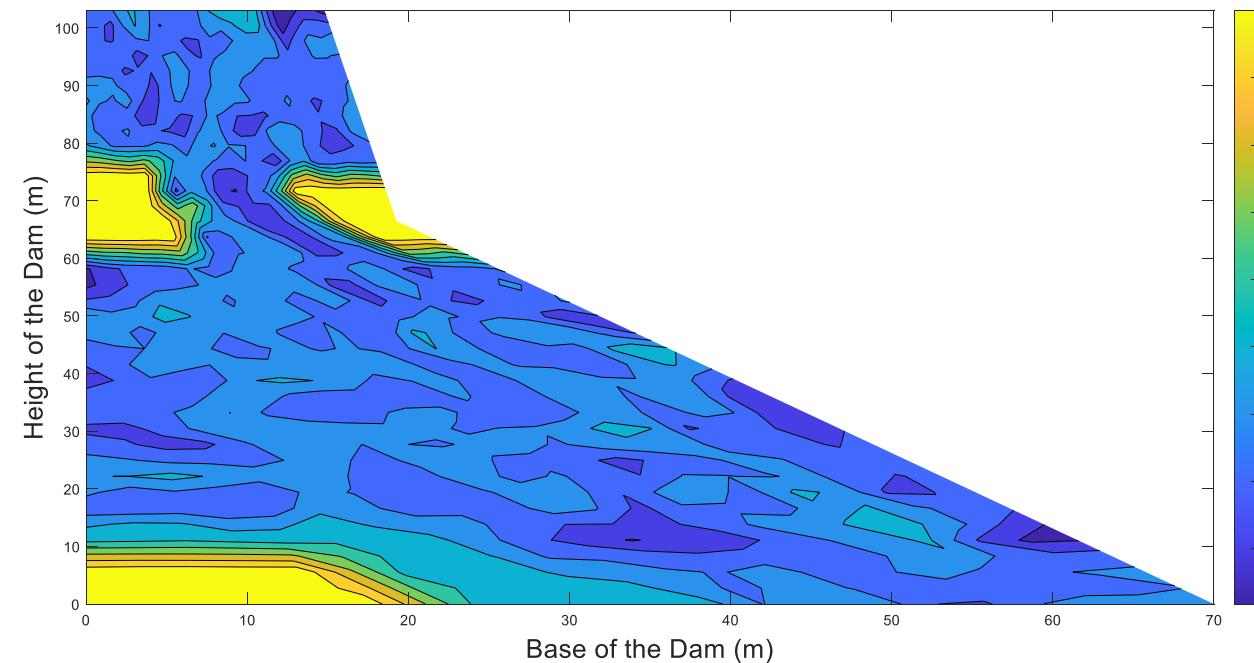
Case	Computation time FEM (seconds)	Computation time TDSFEM (seconds)
D	9357	4024
DR	9481	4211
DF	20017	8954
DFR	20238	9180

Results of horizontal crest displacement: other cases

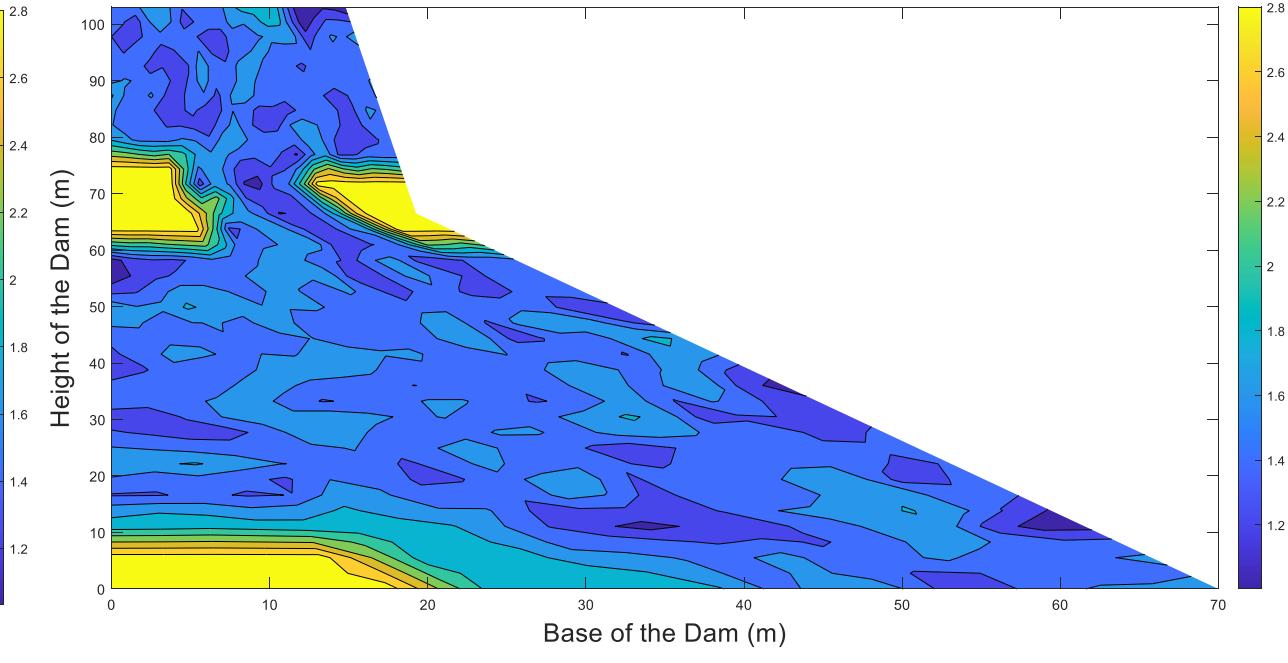


Stress plots showing failure zone(FEM vs TDSFEM)

Plot of Maximum Principal Stress (Dam-Foundation-Reservoir case) in MPa units



FEM



TDSFEM

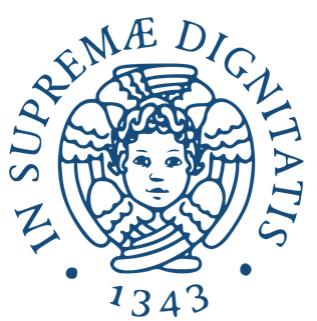
Conclusions

- 1) TDSFEM consumes much less amount of time for the analysis and provides reasonable accuracy.
- 2) The time of computation is reduced by 60 percent in case of TDFSEM in comparison to conventional FEM.
- 3) The computational efficiency of TDSFEM is also demonstrated when the whole dam-foundation-reservoir model is considered for dynamic analysis.
- 4) Due to the global matrices sizes getting bigger in this case, the advantage of computational time saving is even better realized in case of DFR (Dam-foundation-reservoir) system.
- 5) The results of non-linear dynamic analysis when subjected to seismic ground motion present the actual stress levels of the dam and failure zones are identified.
- 6) In case of non-linear analysis, the system of equations need iterations to be performed while solving, thus the time of computation becomes even more critical and TDSFEM provides saving in computation time in each step.
- 7) The results of dynamic analysis using material non-linear behavior show the potential permanent lateral displacement of the dam body subjected to seismic ground motion.



Thank you!

Any questions?



AON

Application of ground motion-compatible intensifying artificial acceleration in dams

G. Sevieri¹, M.A. Hariri-Ardebili², C. Resta³, A. De Falco⁴

¹ Aon Reinsurance Solutions, Milan, Italy

² University of Maryland, College Park, MD, USA

³ University of Pisa, Dept. of Energy, Systems, Territory and Construction, Pisa, Italy

⁴ University of Pisa, Dept. of Civil and Industrial Engineering, Pisa, Italy

Summary

Research objectives:

- Comparing the performance of the Endurance Time Analysis (ETA) with ground motion compatible Intensifying Artificial Acceleration (IAA) against IDA.
- Highlighting pros and cons of IAA, balancing the solution accuracy and the computational cost.



ETA is a time history-based dynamic pushover procedure that employs an intensifying artificial acceleration (IAA) input to analyse the structural behaviour.

With a single dynamic analysis, the ETA captures the structural behaviour of the system across different states up to the failure, for a wide range of seismic intensity levels (SILs).

Introduction: Derivation of numerical fragility curves

Analysis methods:

- Seismic Coefficient Method
- Equivalent Lateral Force Method
- Response Spectrum Modal Analysis Method
- Time History Modal Analysis Method
- Time History-Time Integration (THTI) procedure

Probabilistic approaches for the propagation of RTR uncertainties:

- Incremental dynamic analysis
- Cloud analysis
- Multiple-stripe analysis
- **Endurance time analysis with ground motion-based IAA**

Uncertainties must be properly modelled in the simulation of a complex system such as the dam-soil-basin interaction, under a seismic motion, while approaching the structural collapse.

Proxy models, machine and deep learning approaches can be successfully used to reduce the computational cost of the overall process.

Ground motion-compatible IAA

IAA is generated in a way that induces a seismic demand compatible with an actual ground motion record. This requires the unconstrained nonlinear optimization of the following objective function:

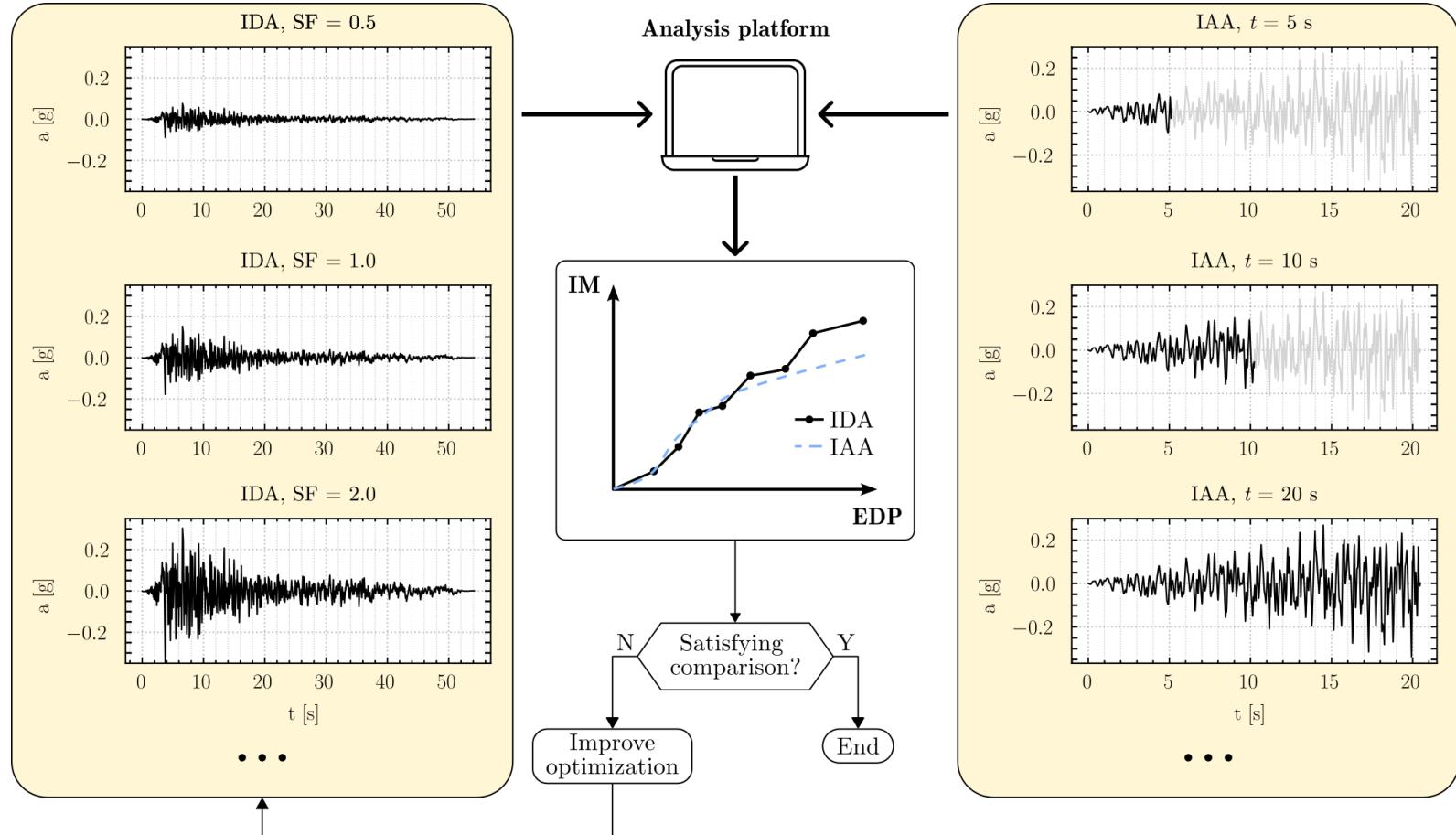
$$\begin{aligned}
 F_{IAA}(\ddot{u}_g) = & \int_{T=0}^{T_{max}} \int_{t=0}^{t_{max}} [S_a(t, T) - S_a^*(t, T)]^2 dt dT \\
 & + \int_{\mu=1}^{\mu_{max}} \int_{T=0}^{T_{max}} \int_{t=0}^{t_{max}} \left\{ \alpha_{u_m} [u_m(t, T, \mu) - u_m^*(t, T, \mu)] \right. \\
 & \quad \left. + \alpha_{E_H} [E_H(t, T, \mu) - E_H^*(t, T, \mu)] \right\} dt dT d\mu
 \end{aligned}$$

Hariri-Ardebili et al., 2023.

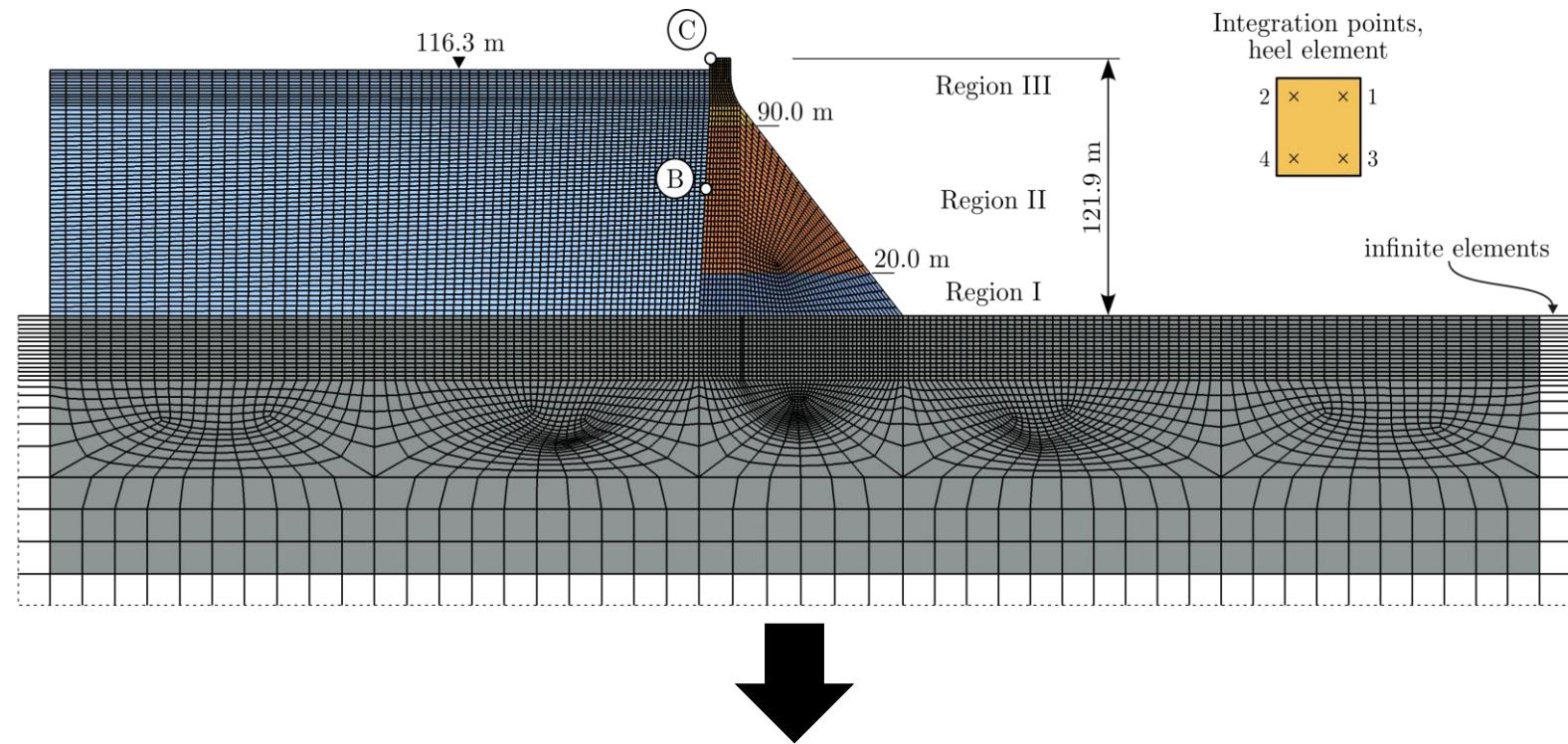
- $\ddot{u}_g(t)$ ground motion record
- $S_a(t, T)$ IAA acceleration spectra
- $u_m(t, T, \mu)$ IAA non-linear displacement
- $E_H(t, T, \mu)$ IAA hysteretic energy
- $S_a^*(t, T)$ target acceleration spectra
- $u_m^*(t, T, \mu)$ target non-linear displacement
- $E_H^*(t, T, \mu)$ target hysteretic energy
- α_{E_H} α_{u_m} optimization coefficients

A framework for validating IAA vs single-record IDA

Single-record IDA are used as benchmark for the validation of IAA curves.



Case study: the Pine Flat Dam

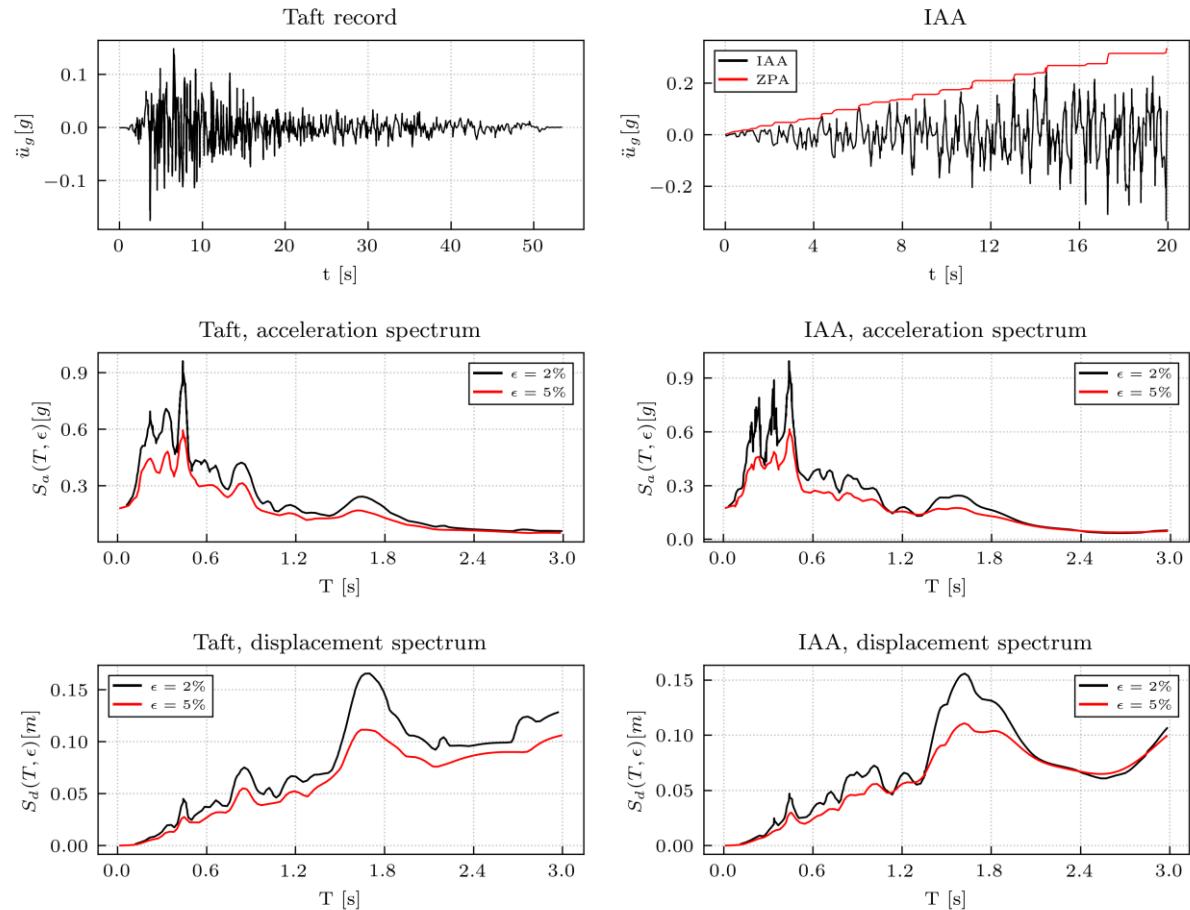


- a linear elastic system with massless foundation;
- a linear elastic system with massed foundation;
- a nonlinear, damaging system with massless foundation;
- a nonlinear, damaging system with massed foundation.

Case study: the Pine Flat Dam

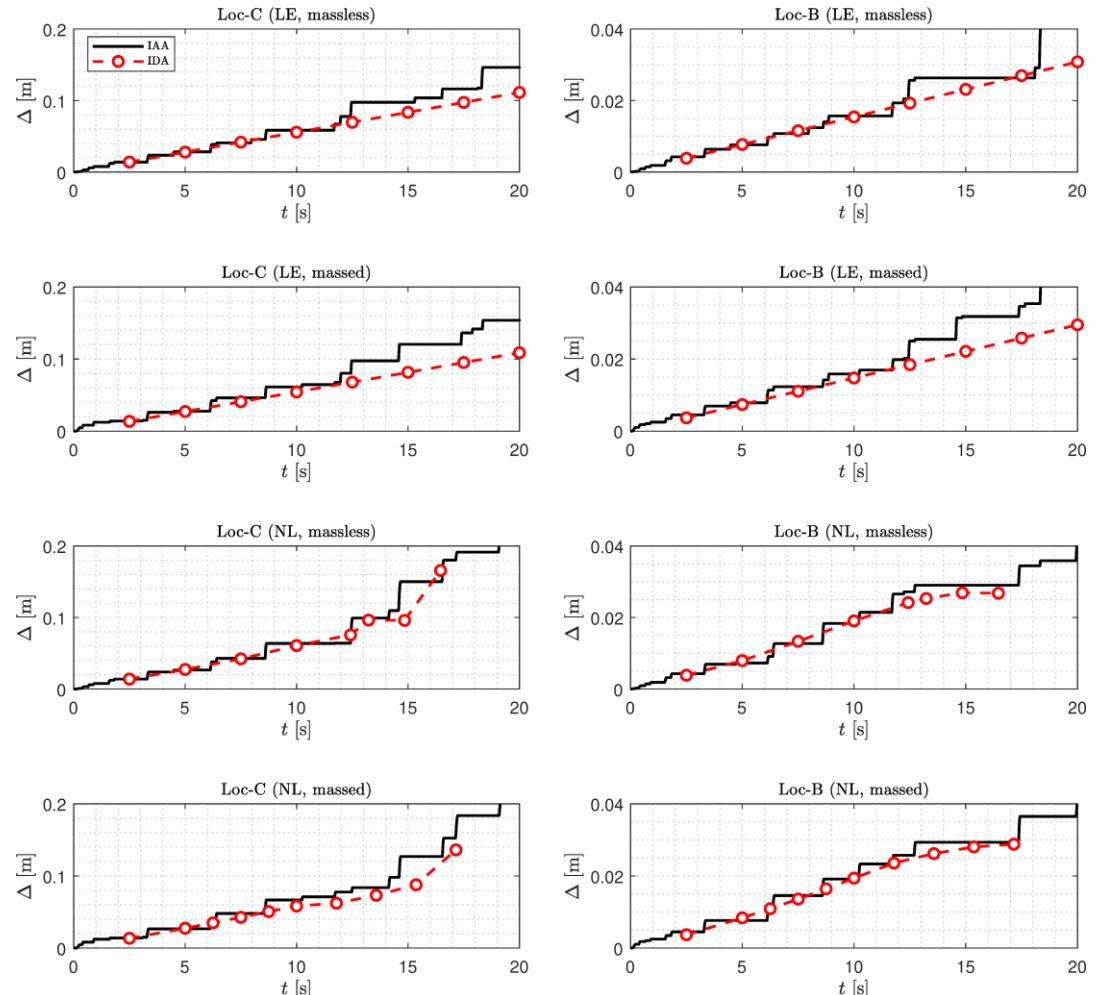
Target ground motion record vs IAA

Response spectra for IAA is plotted at the target time of 10 s.



IAA vs IDA displacements

C – crest and B - upstream mid-height.



Conclusion

- IAA-based capacity function can estimate both global (e.g., displacement) and local (e.g., stress and cracks) engineering demand parameters.
- While the cumulative inelastic duration in real ground motion may differ from IAA, the damage response remains consistent. The development of cracks is sensitive to slight variations in input excitation, with the most significant discrepancies observed in the upper region adjacent to the neck, while damage indices in lower parts remain nearly identical.
- The strong alignment between IAA and single-record IDA results highlights the computational advantages of the proposed framework.



Thank you!

Any questions?





METU



Comparison of damage predictions for concrete dams, finite elements with smeared crack vs. discrete element models

B.F. Soysal ¹, Y. Arici ²

¹ Cankaya University, Ankara, Turkey

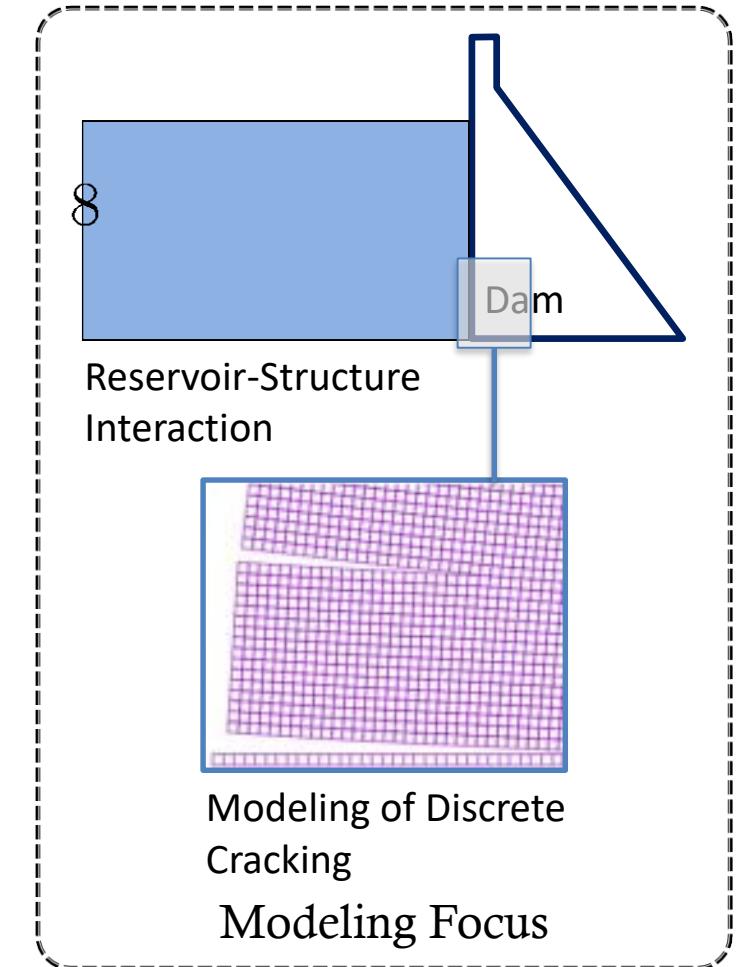
² Middle East Technical University, Ankara, Turkey

INTRODUCTION

The seismic response of concrete gravity dams is now investigated in the performance based framework with quantification of damage, in line with seismic practice.

The task is more challenging for massive plain concrete systems as both the soil-structure and reservoir-structure interaction has to be taken into account while conducting demanding nonlinear analysis.

This work is on combining a discrete element framework with rigorous reservoir modeling, with validation in frequency domain in elastic range and simulation of discrete cracking in high damage scenarios.



PROBLEM STATEMENT

Cracking, the main damage pattern for concrete gravity dams, is predicted with finite element models combined with smeared crack models.

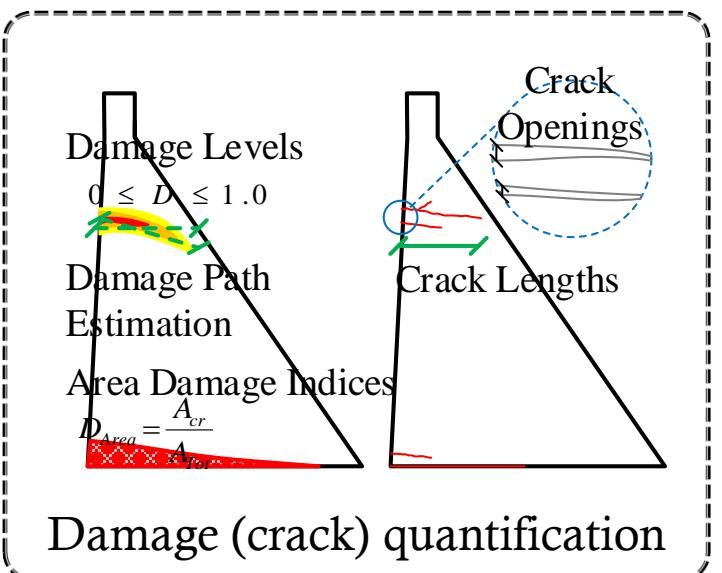
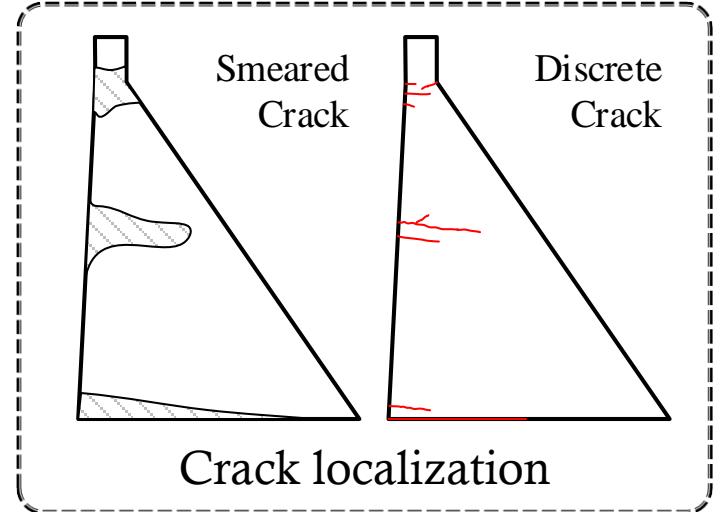
Finite element models based on continuum modeling:

Theoretical limitation: Plain concrete modeling with continuum representation of localized discrete crack,

Practical limitation: Defining and quantifying discrete cracks impeding damage rating of these systems.

(Araci and Soysal, 2022)

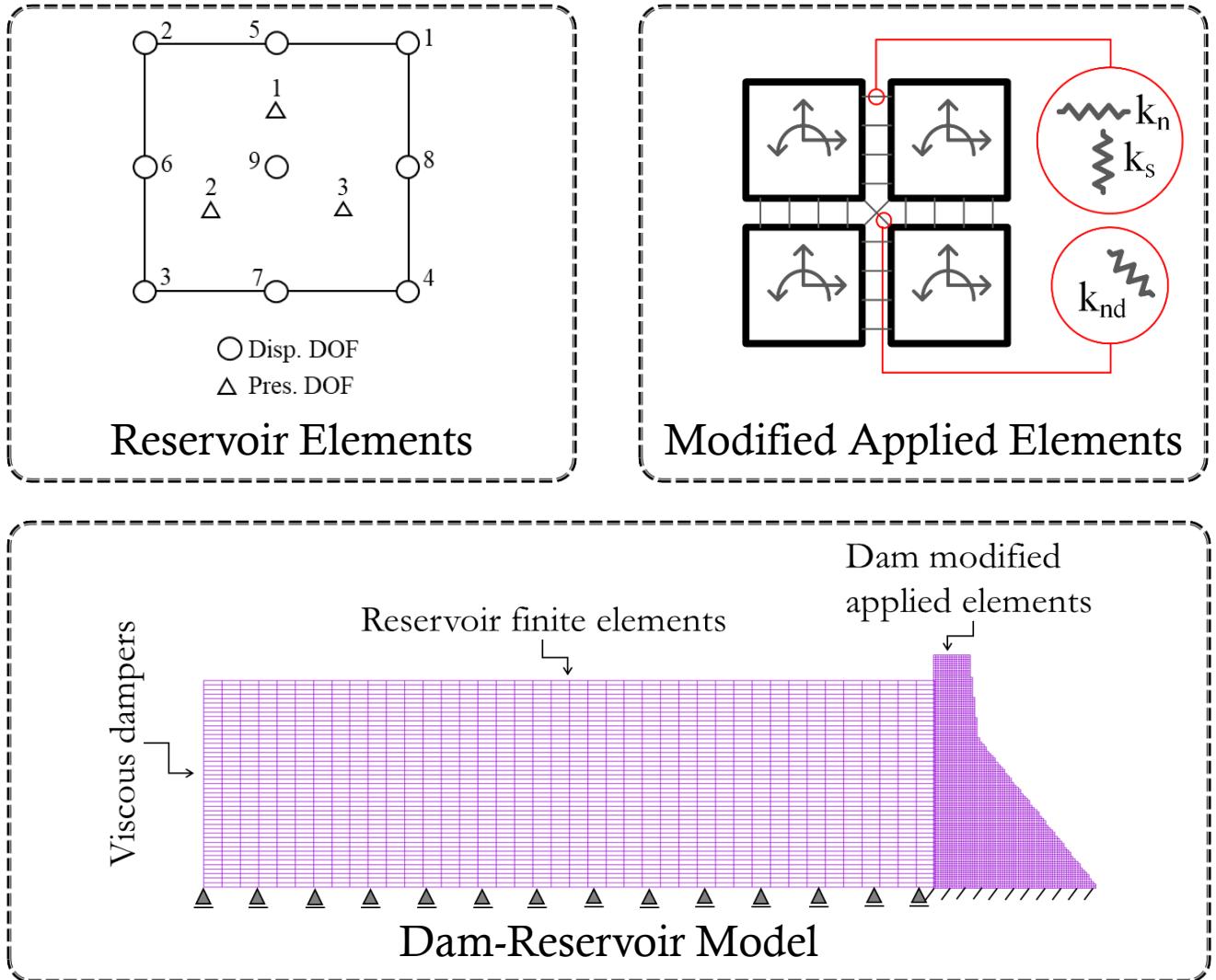
Discrete element models incorporating separation of elements offer alternatives for these brittle systems.



Modeling for the Prediction of Nonlinear Response

A new, discrete element based model has been developed to predict the cracking on concrete gravity dams. The model uses:

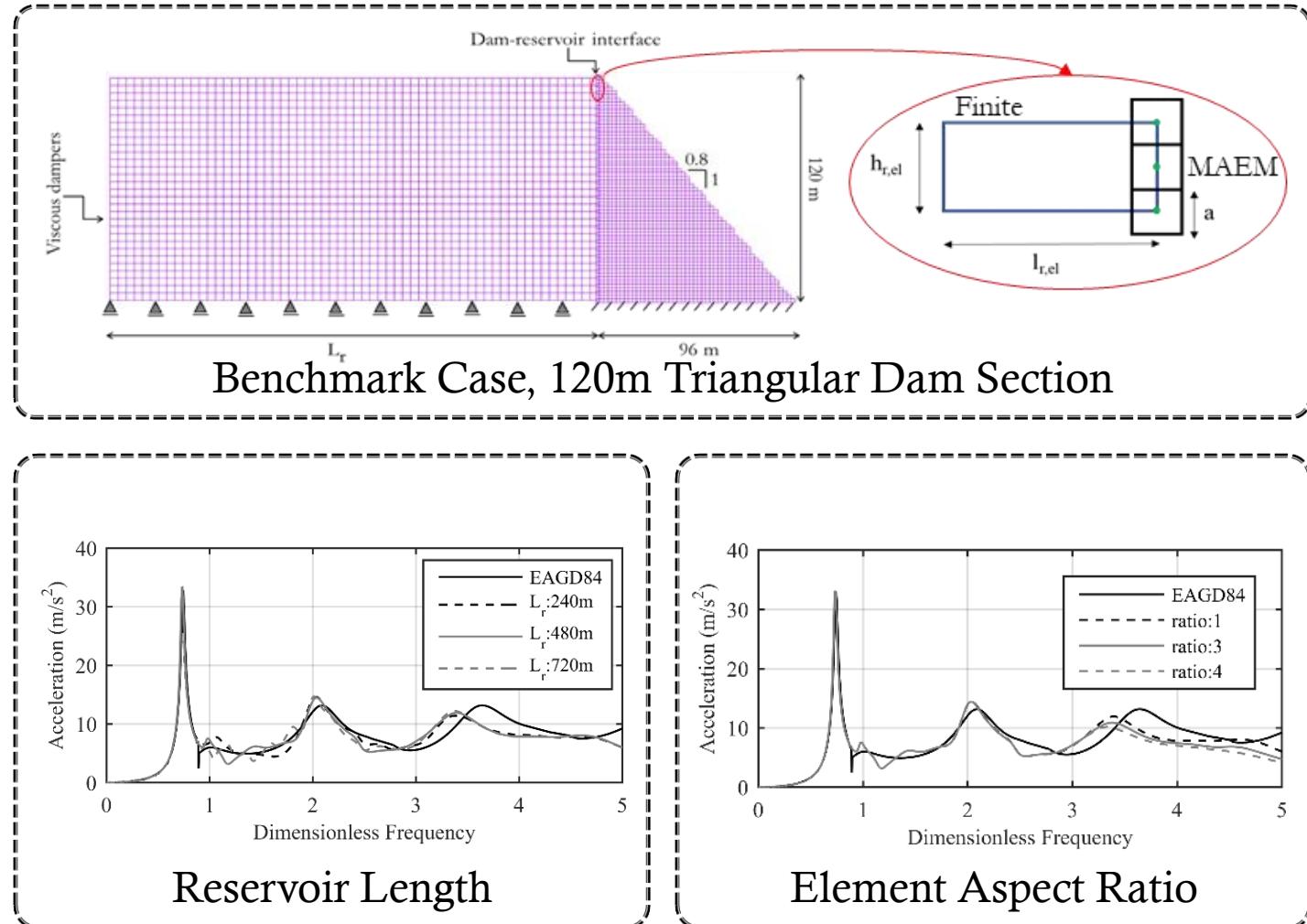
- Modified applied elements incorporating Poisson effect for accurate stress transfer,
- Mixed pressure-displacement elements for the reservoir simulating the reservoir-dam interaction accurately,
- Explicit time stepping.



Validation Studies for Dam-Reservoir Coupling

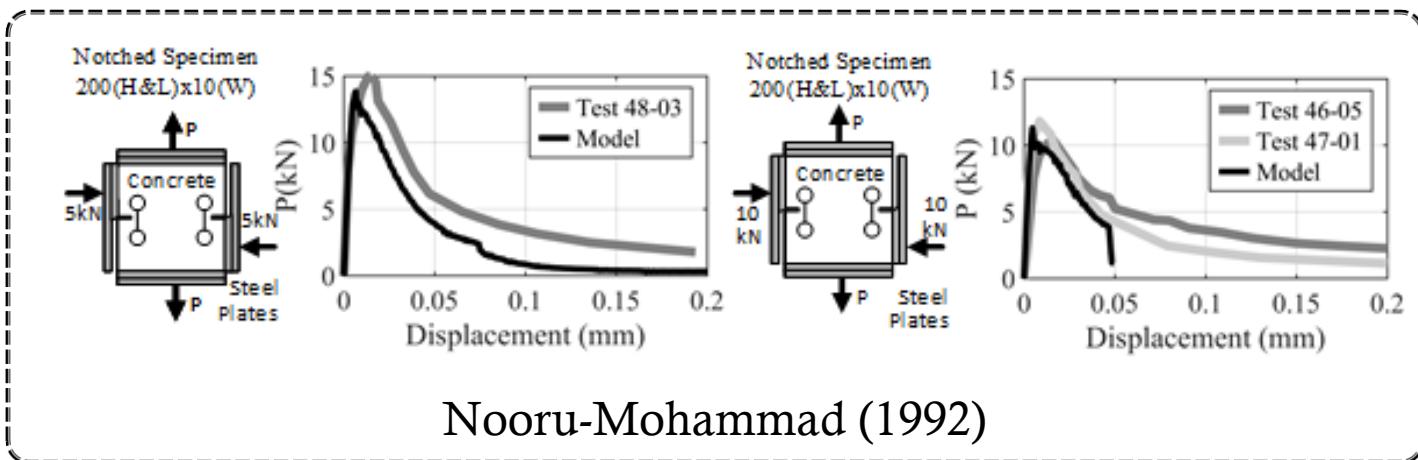
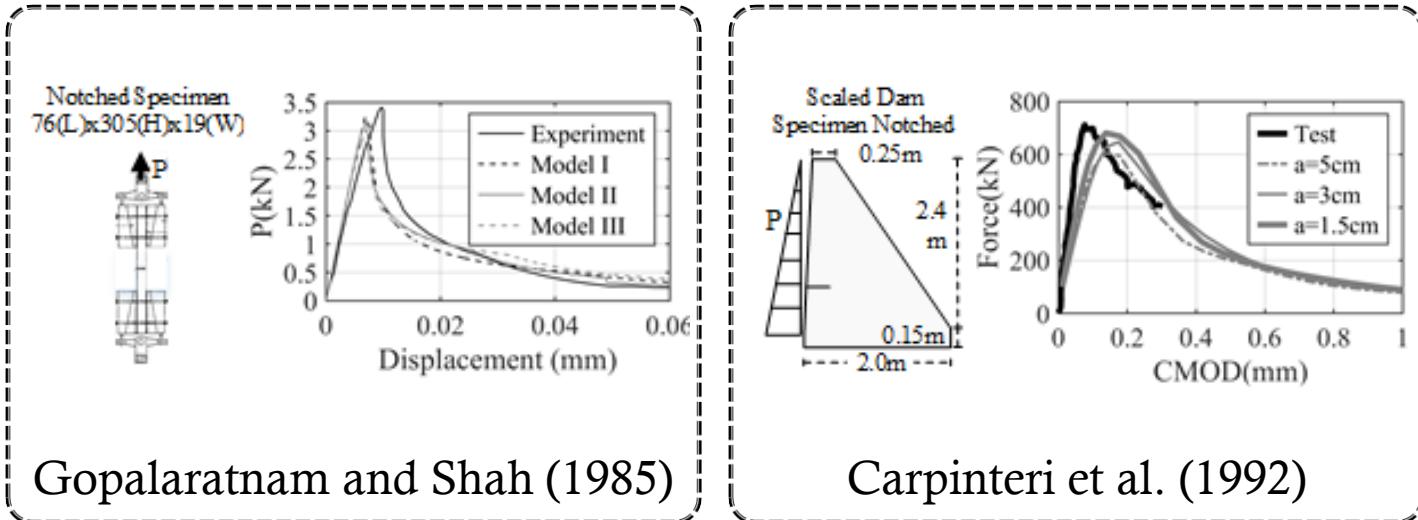
The reservoir-dam coupling has been investigated by comparison to the benchmark case from Fenves and Chopra (1984).

- Frequency response at the crest compared to benchmark for different reservoir lengths and element aspect ratios.
- The model works well even with limited reservoir length.
- The model works well with relatively high aspect ratios.



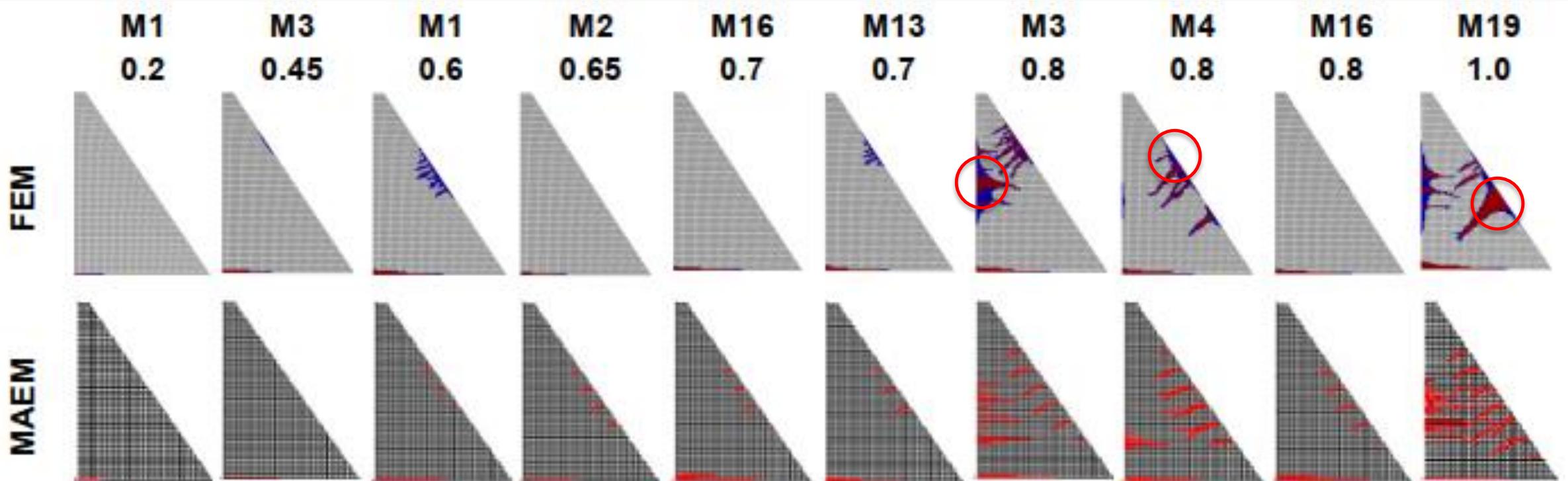
Validation Studies for Nonlinear Modeling

- The model addresses mesh bias issue with normalization using fracture energy at spring level,
- Softening has been modeled using the Maekawa model with history dependency,
- Extensively validated for a number of cases including, tensile mode I, combined tensile/bending and tensile/shear failure scenarios.



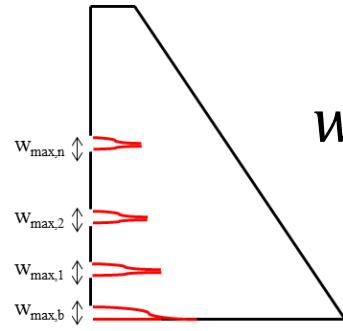
Comparison of Cracking, FEM vs. MAEM Models

- Initiation of cracking similar for both models,
- High damage cases – significant differences can be observed. Concentrations of cracked elements near the initiation point, typical for smeared crack models affects the results.



Crack Distribution on the U/S Face

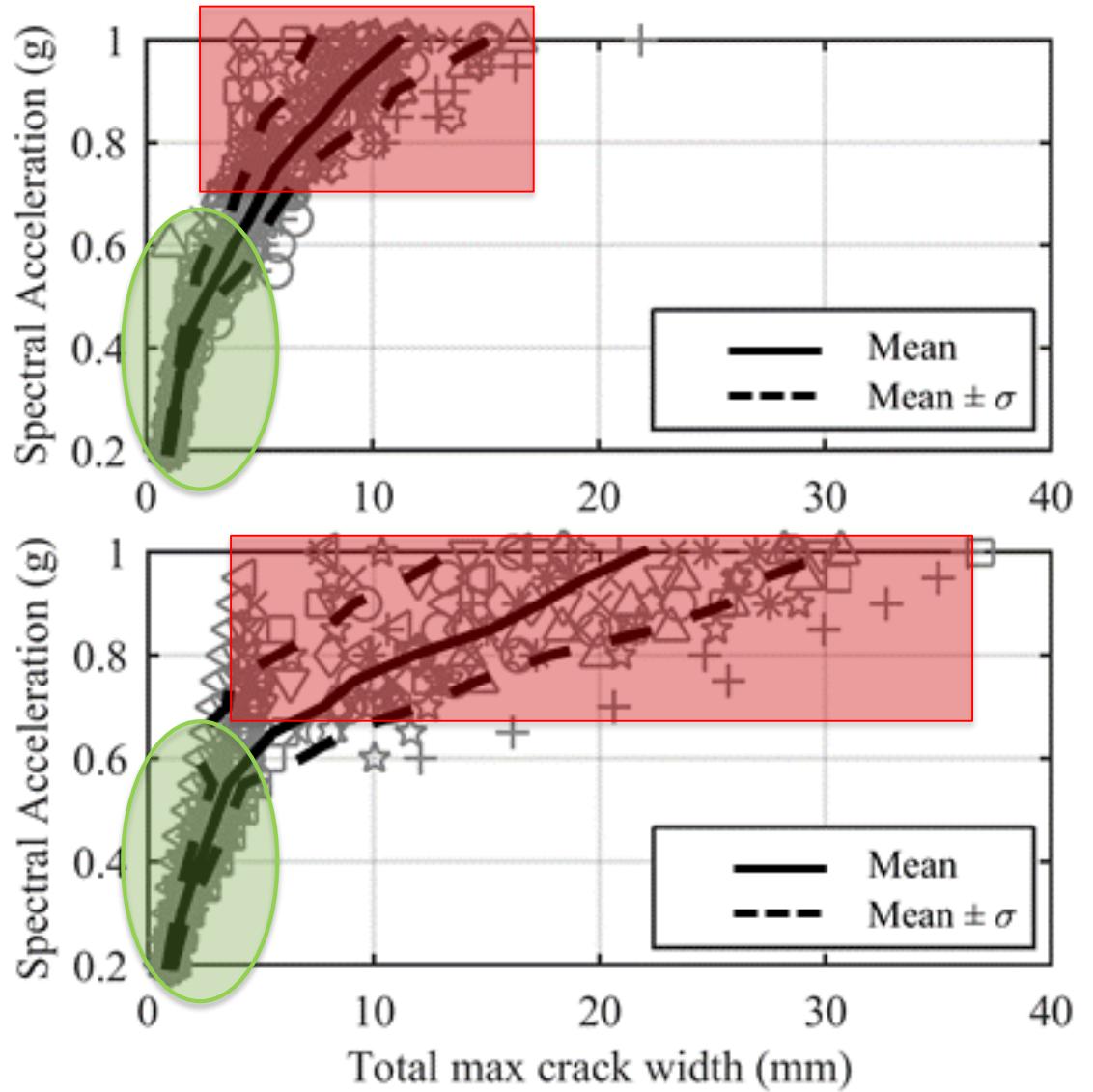
But the real difference is obtained on the crack widths on the U/S surface of the dam,



$$w_{\max \text{ total}} = w_{\max,b} + w_{\max,1} + \dots + w_{\max,n}$$

For low to medium shaking levels, the total width of cracks on the U/S surface similar.
 (shown in green in the figures)

For high shaking levels, significantly larger cracking levels are seen in the MAEM model
 (shown in red in the figures)



Conclusions

Performance based assessment of concrete gravity dams for seismic loads requires the evaluation of cracking which is discrete in nature. A discrete element based model was developed and compared to the FE solutions with smeared crack in this study.

- The developed model was combined with robust reservoir elements capturing the reservoir-structure interaction from theoretical benchmarks well.
- The framework was validated for benchmark tests including direct tensile, bending, shear and combined failure cases with the goal of capturing crack propagation.
- The outcome of compared models were similar for low and medium shaking levels. The results were different for larger shaking – spreading of cracking around the initiation point appears to significantly bias the results for the finite element solution.
- The developed framework, modeling separation, leads to more clear-cut demand parameters and less interpretation compared to the smeared crack+FE combination.



Thank you!

Any questions?



Centrifuge model tests and numerical simulations of irrigation dams during earthquake

K. Fukuda¹, S.S. Suzuki¹, H. Ishikawa², N. Takahashi¹

¹ R&D centre, Nippon Koei, Co., Ltd., Tokyo, Japan

² Sapporo Branch office, Nippon Koei, Co., Ltd., Hokkaido, Japan

Contents

- Background and Objective
- Centrifuge
- Centrifuge Model Tests
- Test Results
- Numerical Simulations
- Analysis Results
- Conclusions

Background and Objective

- The 2011 earthquake off the Pacific coast of Tohoku caused considerable damage to irrigation dams. There are approximately 0.15 million irrigation dams in Japan, and most of which were designed and **constructed before aseismic design was established**.
- Next great earthquake such as **Nankai Trough Earthquake** could happen soon, so we need **some methods to evaluate the seismic behavior of irrigation dams**.
- This study aimed to obtain the fundamental data to develop a seismic assessment method of irrigation dams with **centrifuge model tests** and **numerical simulations**.

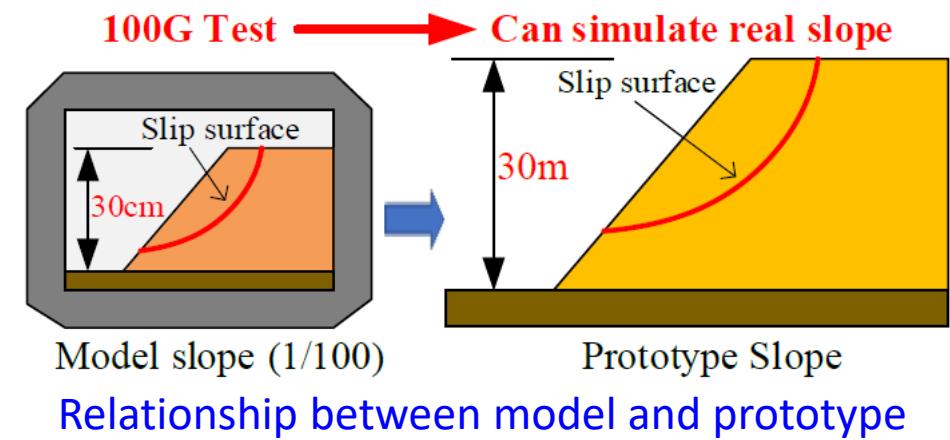


Centrifuge

- Centrifuge model test is a powerful experimental technique used in geotechnical engineering.
- It can be used to **simulate the real phenomena of related geotechnical structures** (such as slopes, embankments, foundations, and retaining walls) and verify practical designs or numerical analyses.
- For example, as shown in the bottom right figure, if **a 30 cm-high slope model** is used to conduct the model test at 100G (G is the centrifugal acceleration), then the size of the slope will be 100 times of the model slope; thus, **a 30 m-high prototype slope was simulated**.



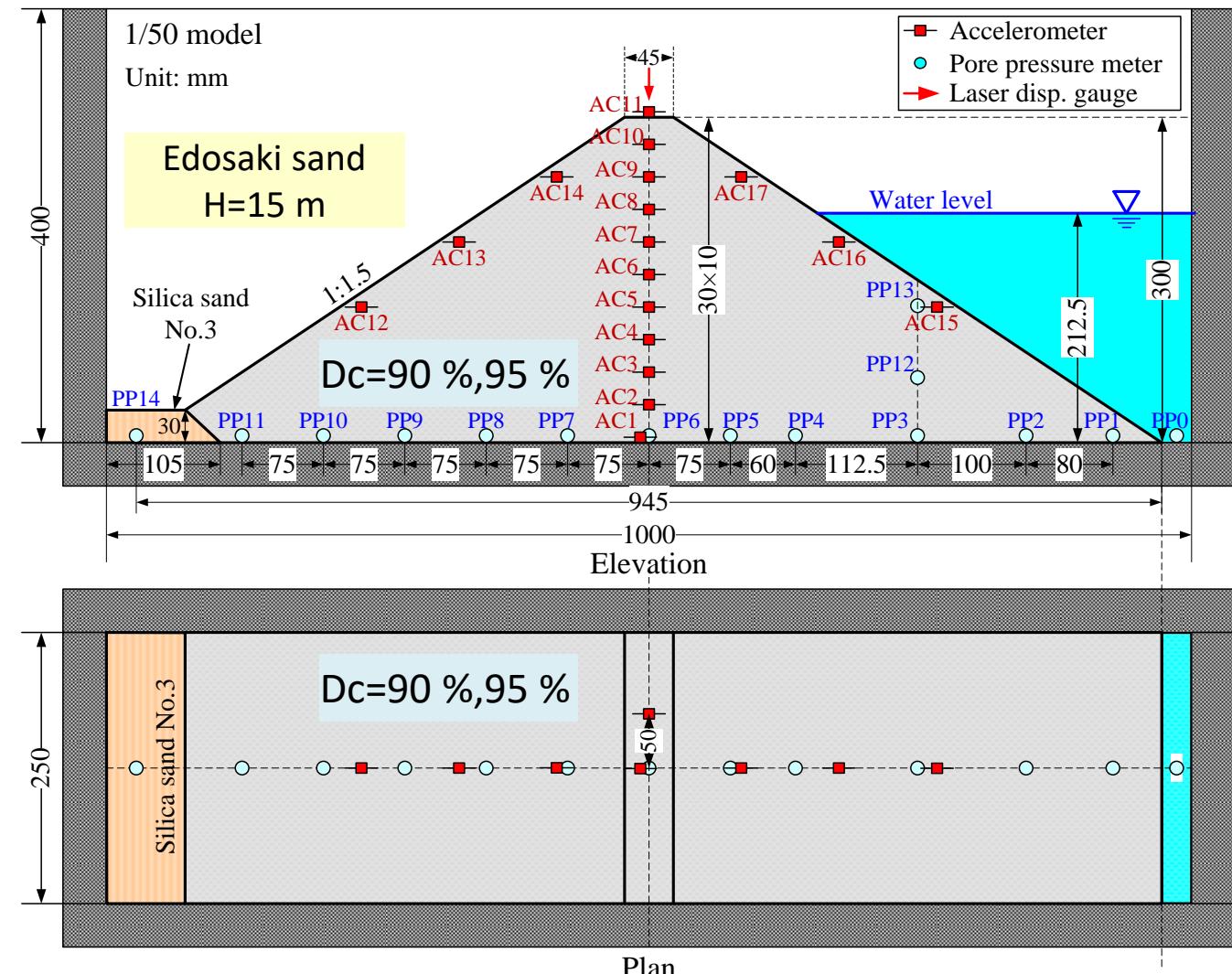
Centrifuge of Nippon Koei



Centrifuge Model Tests

- Centrifugal force field: 50G
- “Edosaki sand” sampled from Ibaraki Prefecture, Japan
- Model preparation: by compaction method with $D_c=90\%$ (Case 1) and $D_c=95\%$ (Case 2)
- Pore fluid: methylcellulose solution (metolose) fluid
- Dam height: 15 m (prototype)

D_c : degree of compaction(ratio of dry density to maximum dry density obtained from compaction test results)

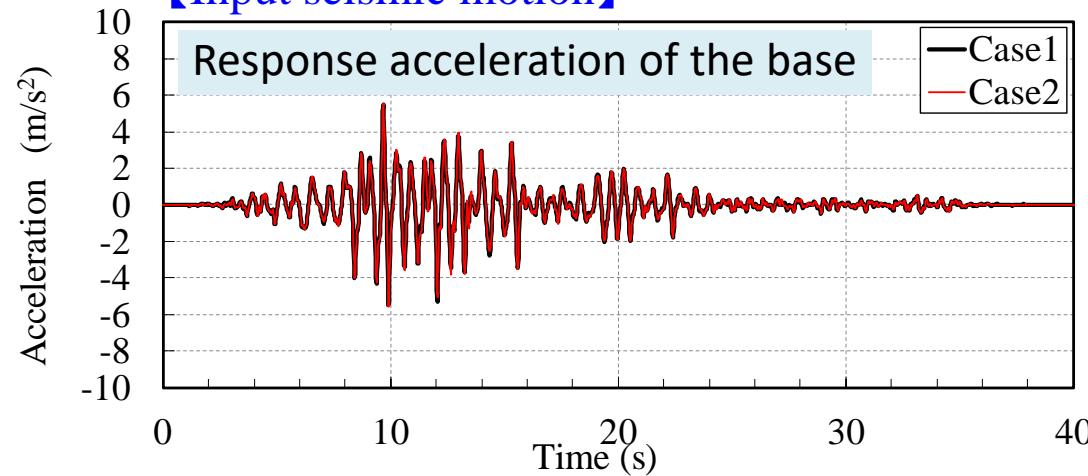


Centrifuge Model Tests

【Test cases】

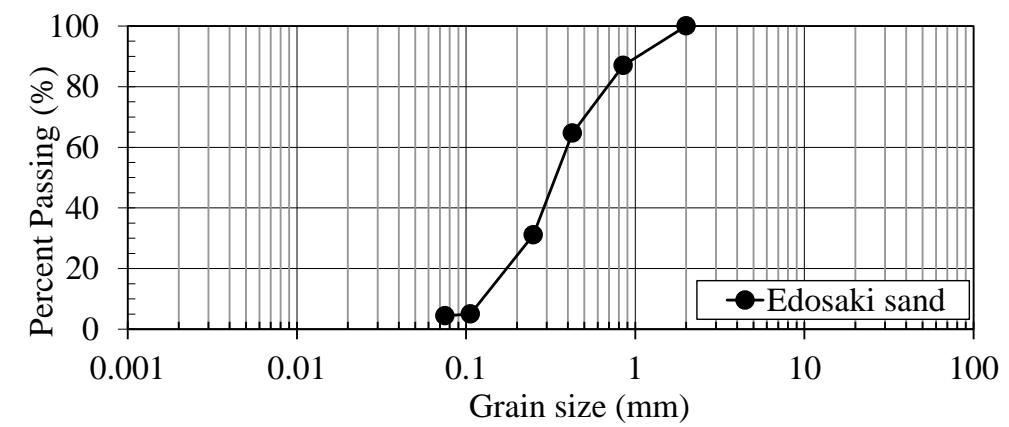
Case	Degree of Compaction (Dc)	Dam height	Water Level
Case 1	90 % ($\rho_d=1.536 \text{ g/cm}^3$, $w=15.0 \%$)	15 m	10.625 m
Case 2	95 % ($\rho_d=1.622 \text{ g/cm}^3$, $w=15.0 \%$)	(prototype)	(prototype)

【Input seismic motion】



A recorded wave (NS component) of JMA Kobe Kaiyo station of the 1995 Hyogoken-Nanbu earthquake by adjusting the wave amplitude to a maximum acceleration of approximately 6 m/s^2

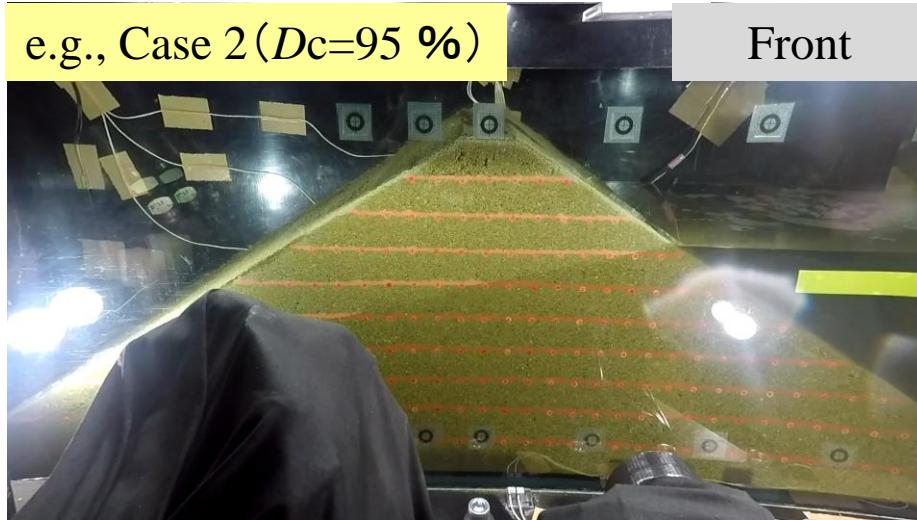
【Grain size distribution】



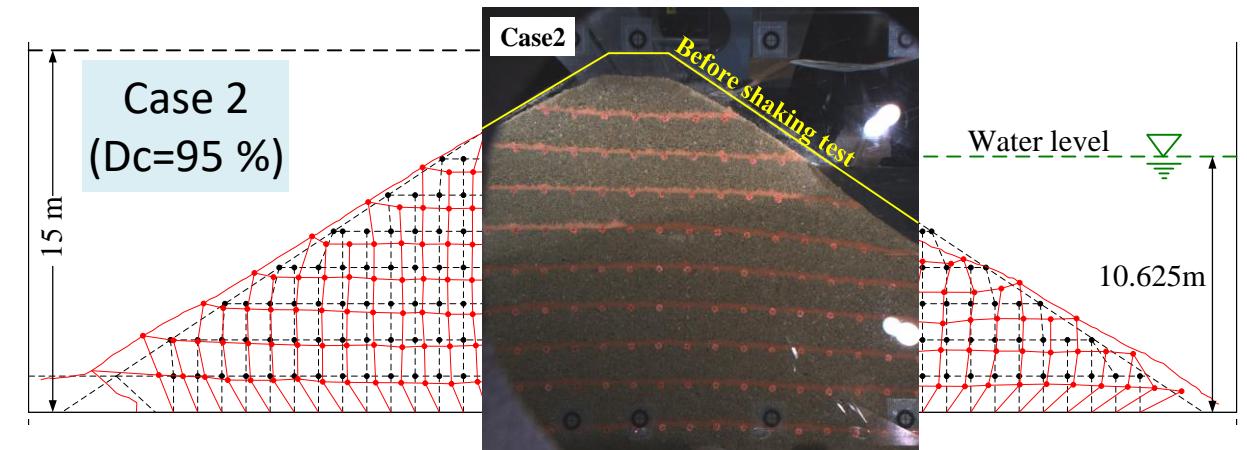
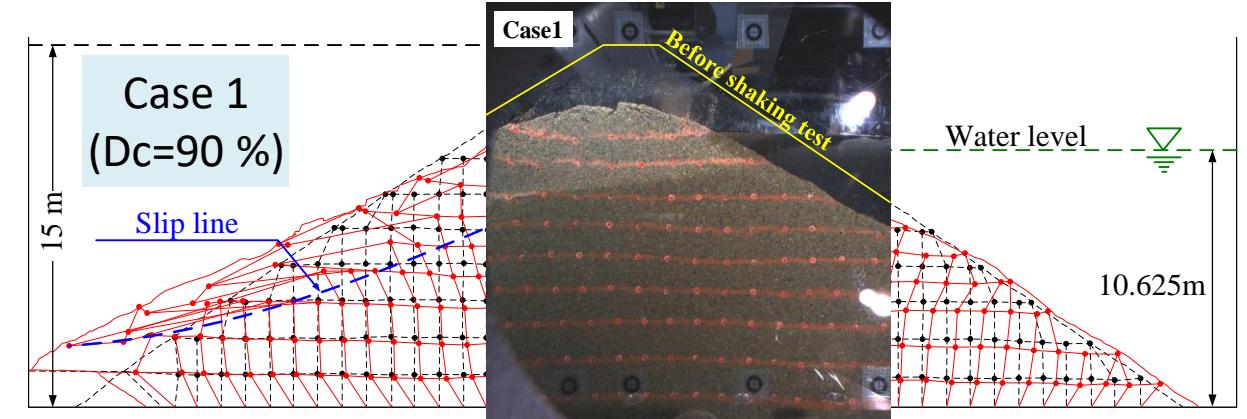
【Material properties of Edosaki sand】

D_{\max}	= 2.0 mm	D_{50}	= 0.335 mm
U_c	= 2.56	U_c'	= 1.00
F_c	= 4.4 %	ρ_s	= 2.681 g/cm^3
$\rho_{d\max}$	= 1.707 g/cm^3	w_{opt}	= 15.0 %

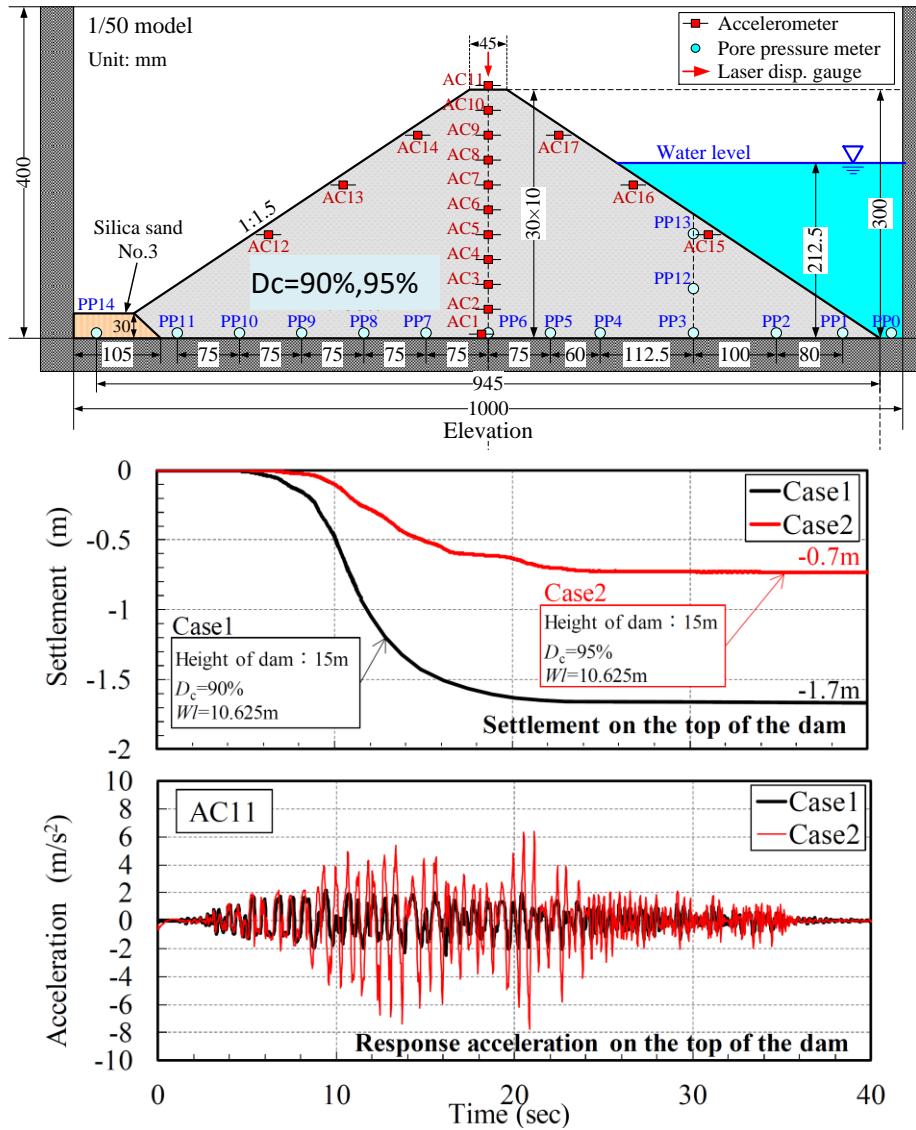
Test results (Shaking)



Deformation sketch of target markers

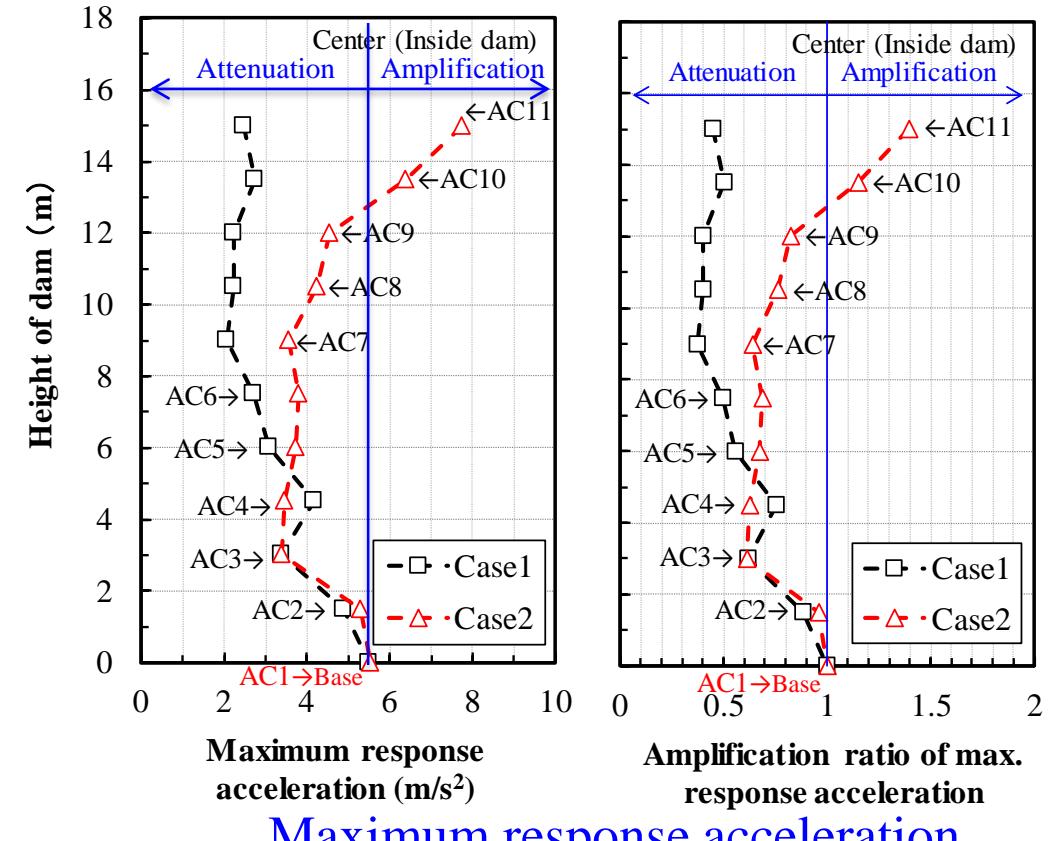


Dashed line: Before shaking, Solid line: After shaking



Settlement and response acceleration on the top of the dam

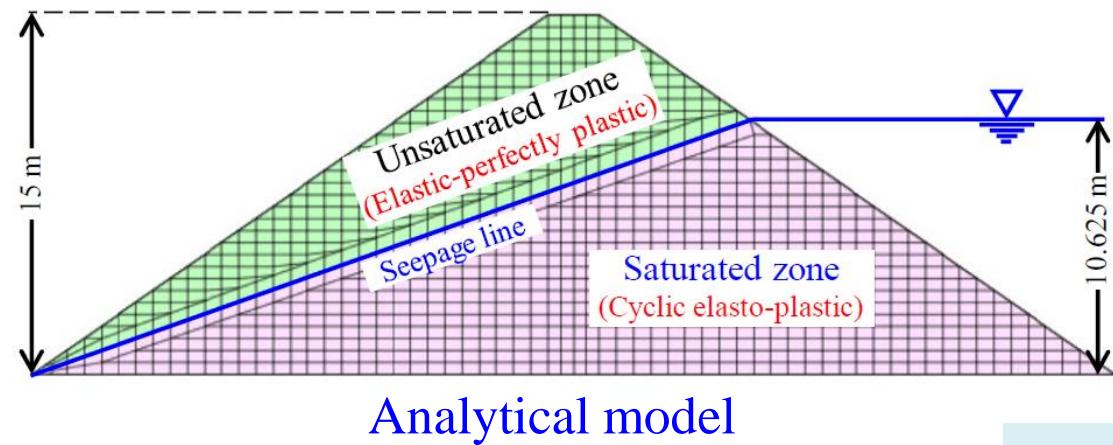
Test results



- Settlement of Case 1 was smaller than Case 2.
- Case 1 shows the attenuation at a point close to 4 m above the height of the dam.

Numerical Simulations

- The LIQCA (Oka et al. 1991*) was used to numerically simulate the test results. It is a fully coupled FEM for liquefaction analysis.



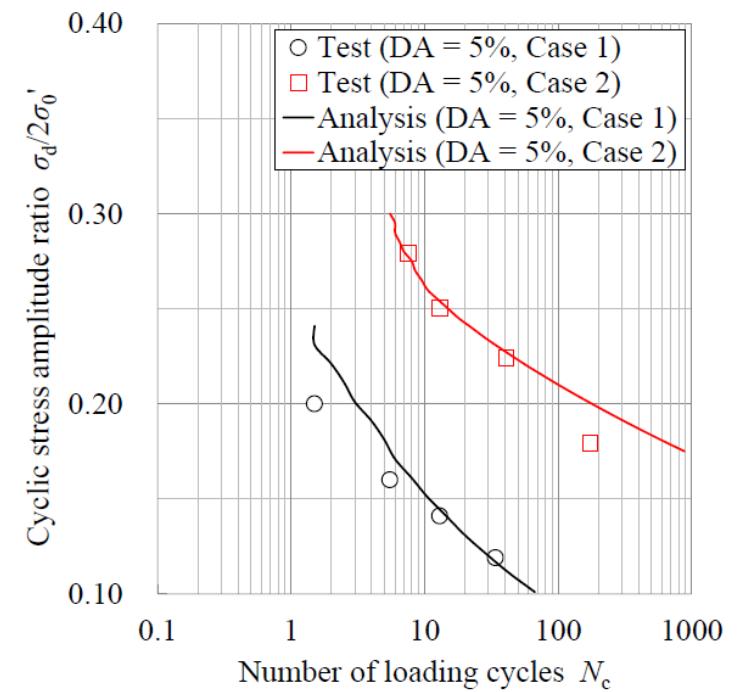
Case1

Parameters of elastic-perfectly plastic model

Young's Modulus, E_0 (kN/m ²)	Poisson ratio, ν	Density, ρ (g/cm ³)	Internal friction angle, ϕ' (rad)	Cohesion, c (kN/m ²)
93,394	0.333	1.763	0.585	1.25

Parameters of cyclic elasto-plastic model

ρ	e_0	λ	κ	$G_0/\sigma'm_0$	k/γ_w	M^*_m	M^*_f	K_f
1.963	0.746	0.018	0.0055	351.7	2.48×10^{-5}	0.870	1.105	2×10^6
B^*_0	B^*_1	C_f	C_d	OCR^*	D^*_0	n	γ^{P*}_r	γ^{E*}_r
2000	50	0.0	2000	1.0	13.0	3.0	0.0004	0.001



Simulation utilities for cyclic triaxial test

Case2

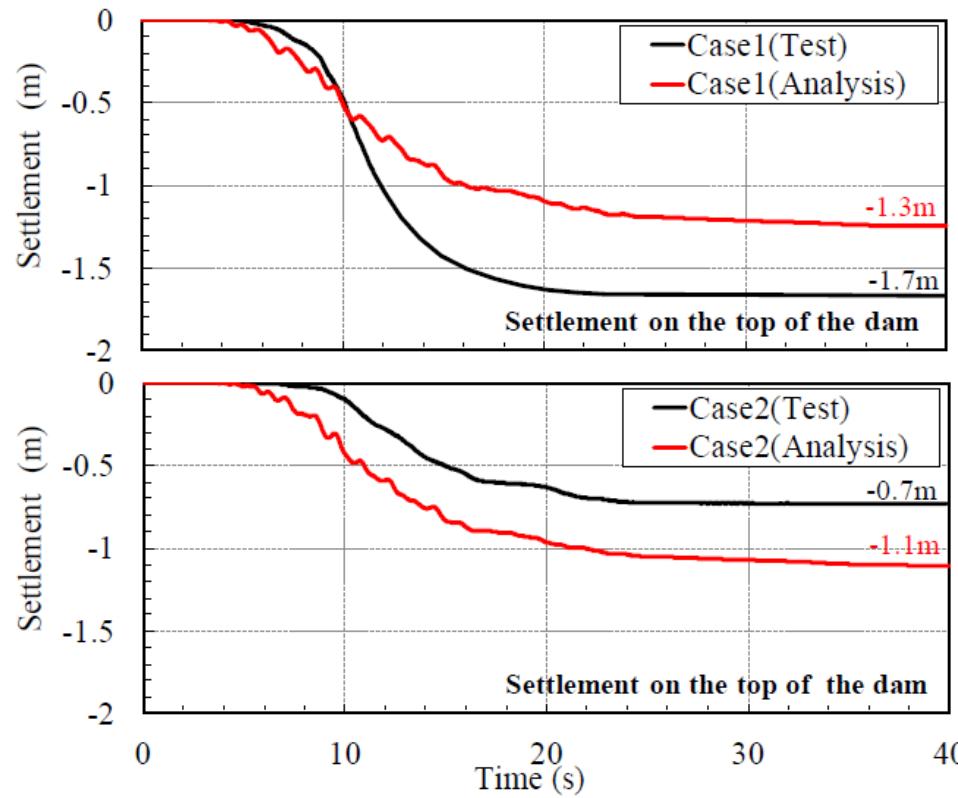
Parameters of elastic-perfectly plastic model

Young's Modulus, E_0 (kN/m ²)	Poisson ratio, ν	Density, ρ (g/cm ³)	Internal friction angle, ϕ' (rad)	Cohesion, c (kN/m ²)
121,742	0.333	1.866	0.586	18.7

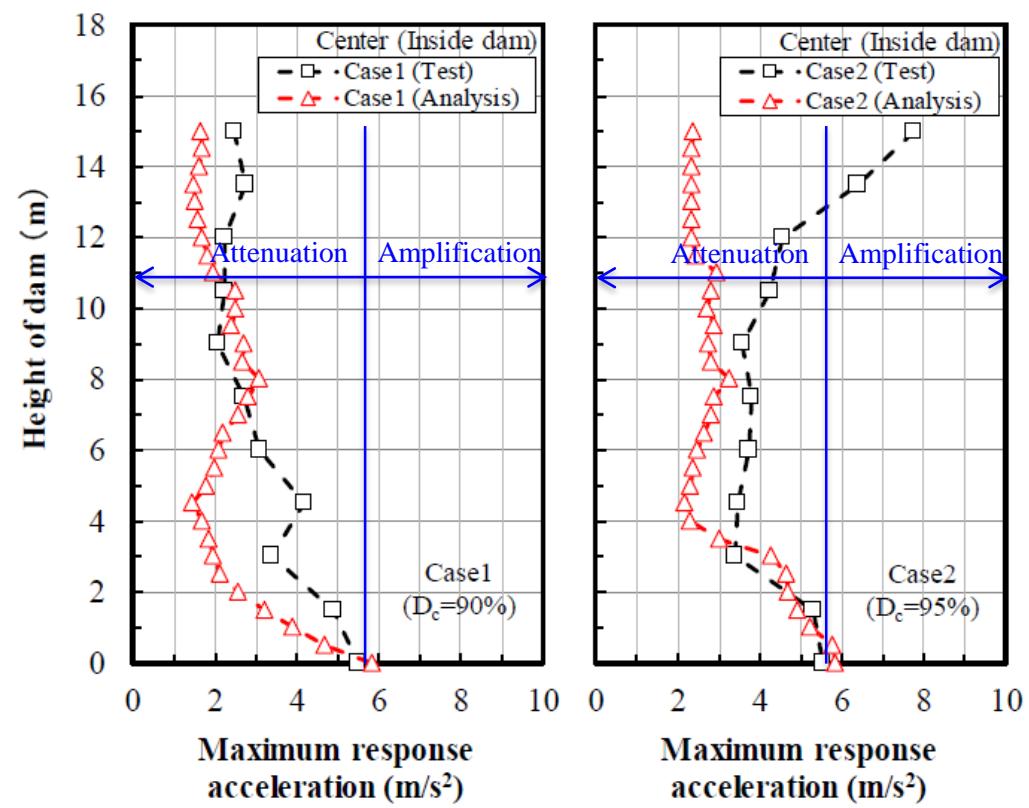
Parameters of cyclic elasto-plastic model

ρ	e_0	λ	κ	$G_0/\sigma'm_0$	k/γ_w	M^*_m	M^*_f	K_f
2.018	0.652	0.018	0.0055	408.0	9.56×10^{-6}	0.821	1.108	2×10^6
B^*_0	B^*_1	C_f	C_d	OCR^*	D^*_0	n	γ^{P*}_r	γ^{E*}_r
6000	60	0.0	2000	1.0	3.0	10.0	0.0005	0.010

Analysis results



Comparison of settlement on the top of the dam

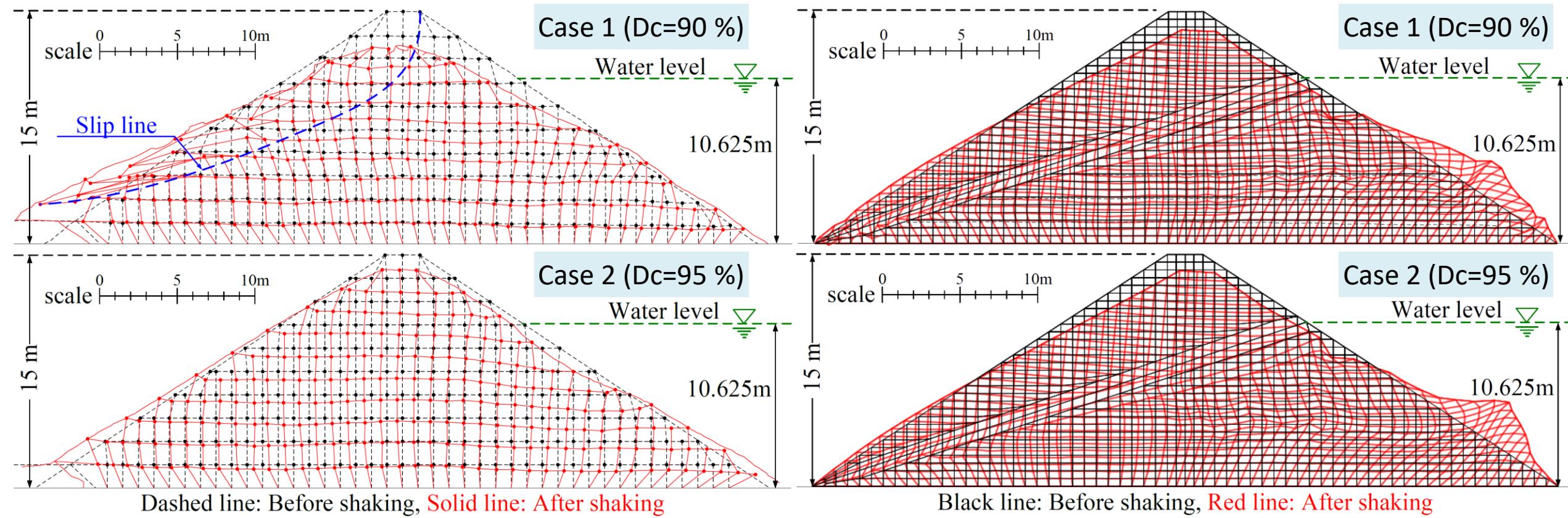


Comparison of maximum response acceleration

- Settlement; The difference between test and analysis results was 40cm. Overall, the test results were approximately simulated by LIQCA.
- Maximum response acceleration; In Case 1, analysis results was similar to test results. (attenuation) In Case 2, the difference of both results was large. (Analysis: attenuation, Test: amplification)

This may be due to the fact that the soil parameters of shear stiffness of Case 2 used in LIQCA were lower than the actual shear stiffness.

Analysis results



- Test**
- The analysis result shows that a slip line didn't occur on the non-submerged side slope, but large deformation was observed on the submerged side slope. The large deformation is due to **the occurrence of liquefaction phenomenon** caused by the increase of excess pore water pressure during shaking.
 - Overall, **the deformation characteristics were similar** between tests and analyses, but for future study, **it is necessary to verify the validity of the constitutive model and the soil parameters** in each zone.
- Analysis**

Conclusions

Two cases ($D_c = 90\%$ and $D_c = 95\%$) of dynamic centrifuge model tests of irrigation dams and their numerical simulations were conducted. The results of this study are summarized as follows:

- (1) Important fundamental data of the dynamic behavior of the dams were obtained from the centrifuge model tests and their numerical simulations.
- (2) In the test case of $D_c = 90\%$ (Case 1), the slip line occurred due to the shaking. The amount of settlement on the top of the dam increased significantly due to the slip.
- (3) In the test case of $D_c = 95\%$ (Case 2), the slip line did not occur, and a small deformation occurred on the non-submerged side slope during shaking, and a protrusion occurred near the toe of the slope on the submerged side slope. The amount of settlement on the top of the dam was significantly small.
- (4) The deformation characteristics in each test case were almost the same on the submerged side regardless of the degree of compaction.
- (5) An effective stress analysis program using cyclic elasto-plastic model called LIQCA was used to simulate the results of the centrifuge model tests. Overall, the test results were approximately simulated by the numerical simulations using the LIQCA program. However, since the response acceleration obtained from the analysis tended to be small in Case 2 and the deformation on the submerged side slope was extremely large in both cases, it is necessary to verify the validity of the constitutive model and the soil parameters.
- (6) For future study, tests and numerical simulations under different conditions should be conducted to investigate the dynamic behavior of the irrigation dam.



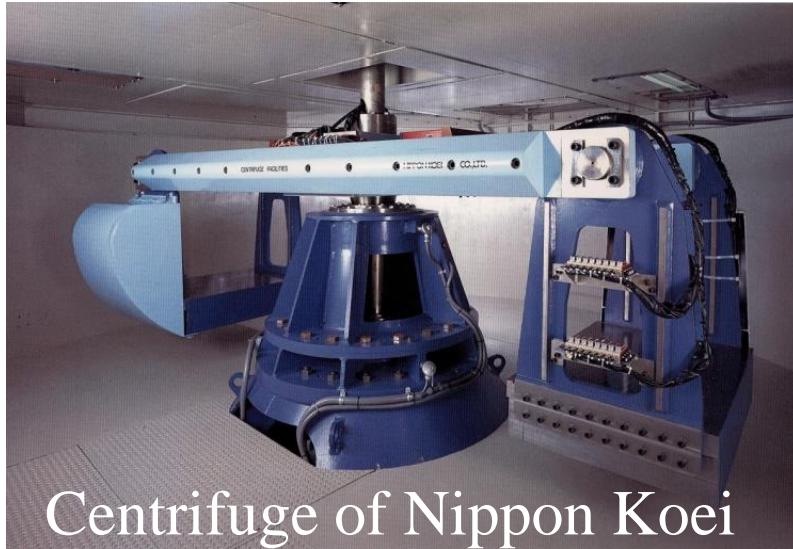
Thank you!

Any questions?



References

Centrifuge of Nippon Koei



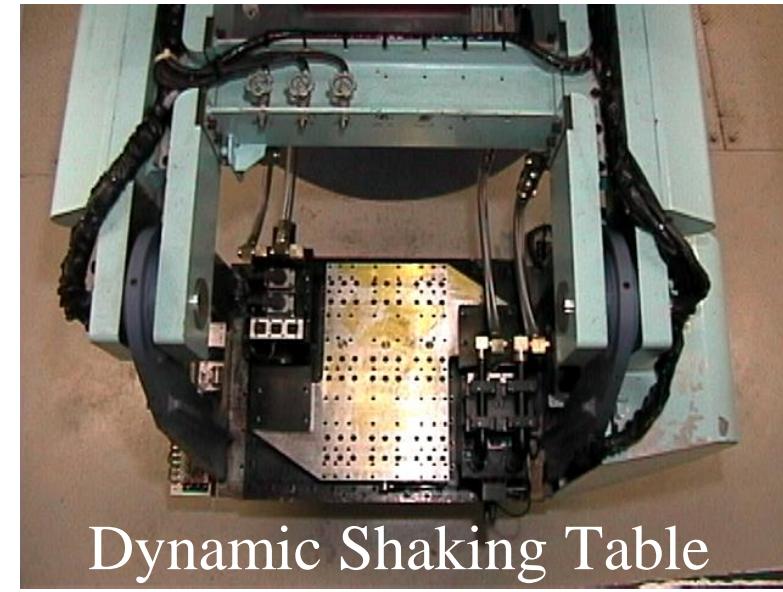
Centrifuge of Nippon Koei

Specifications of Centrifuge

Effective Radius:**2.60m**

Max. Acceleration (dynamic): **100g**

Max. Payload:**1,000kgf**



Dynamic Shaking Table

Specifications of Shaking Table

Shaking Control System: Electrohydraulic Servo Control

Max. Centrifugal Acceleration: 100 g

Max. Shaking Acceleration: 25 G (1/30 model 818gal)

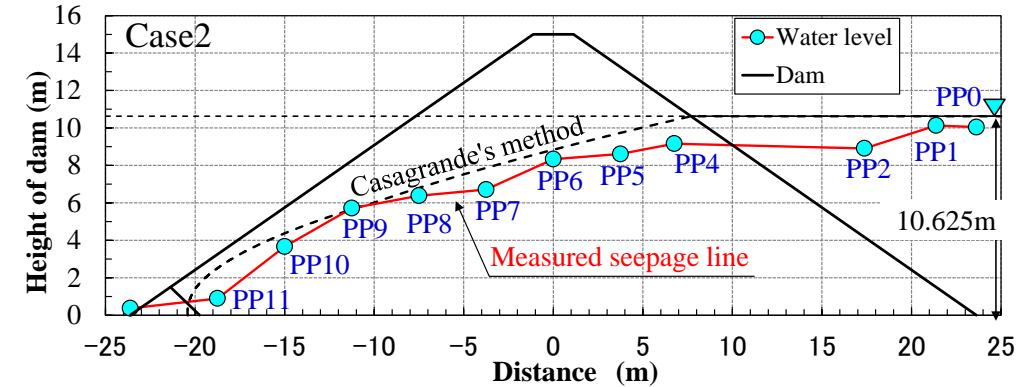
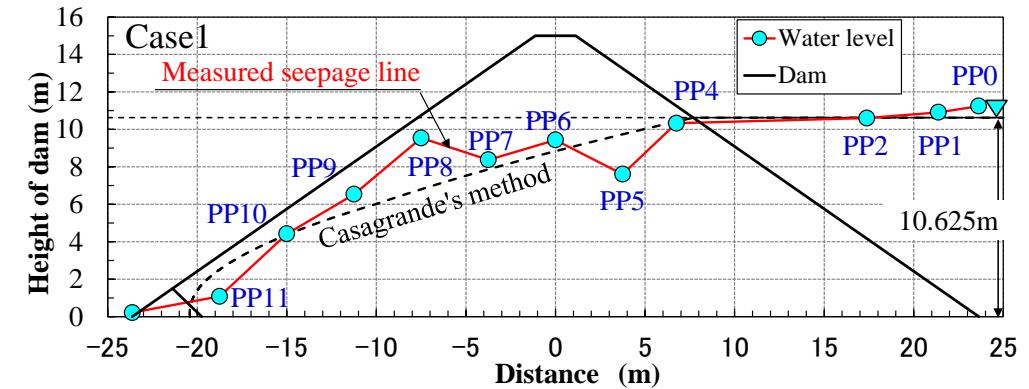
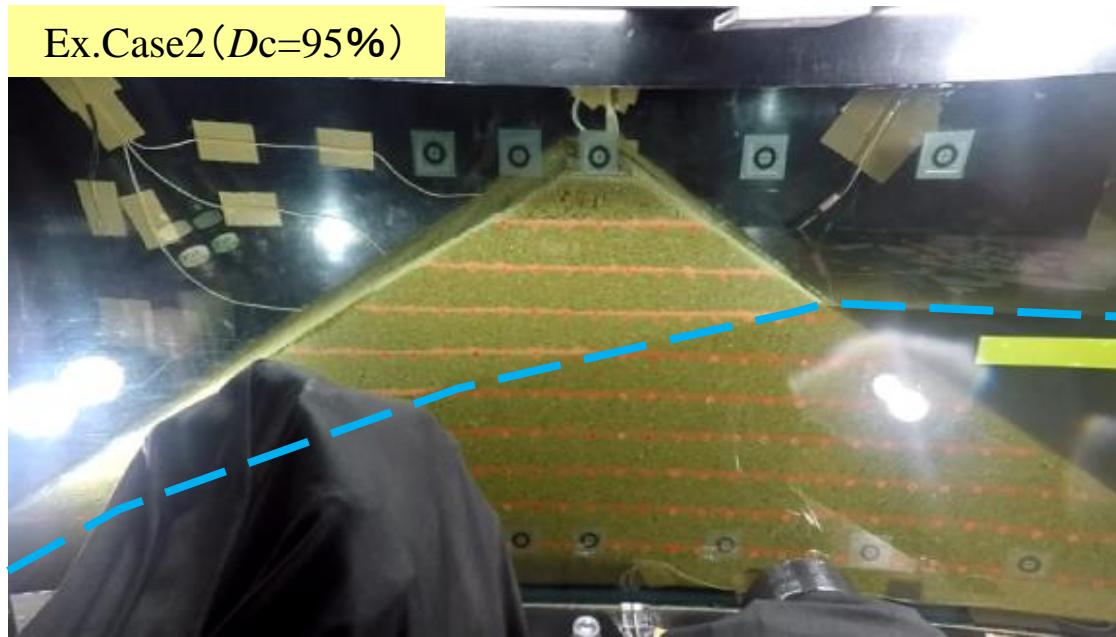
Max. Payload: 250kg

Max. Displacement: $\pm 3.0\text{mm}$

Frequency Range: 10 - 400Hz

Max Velocity: 40 cm/s

Test results (Seepage line)



Control water level and seepage line become constant in 50G

The seepage line observed from the piezometer partially agreed well with theoretical line of the Casagrande's method.

In Case1, it was significantly higher than the theoretical line, resulting in the partial destabilization of the non-submerged side.



Impacts of the February 06, 2023, Türkiye earthquake sequence on risk assessment of embankment dams

H. Tosun ¹, M.A. Hariri-Ardebili ²

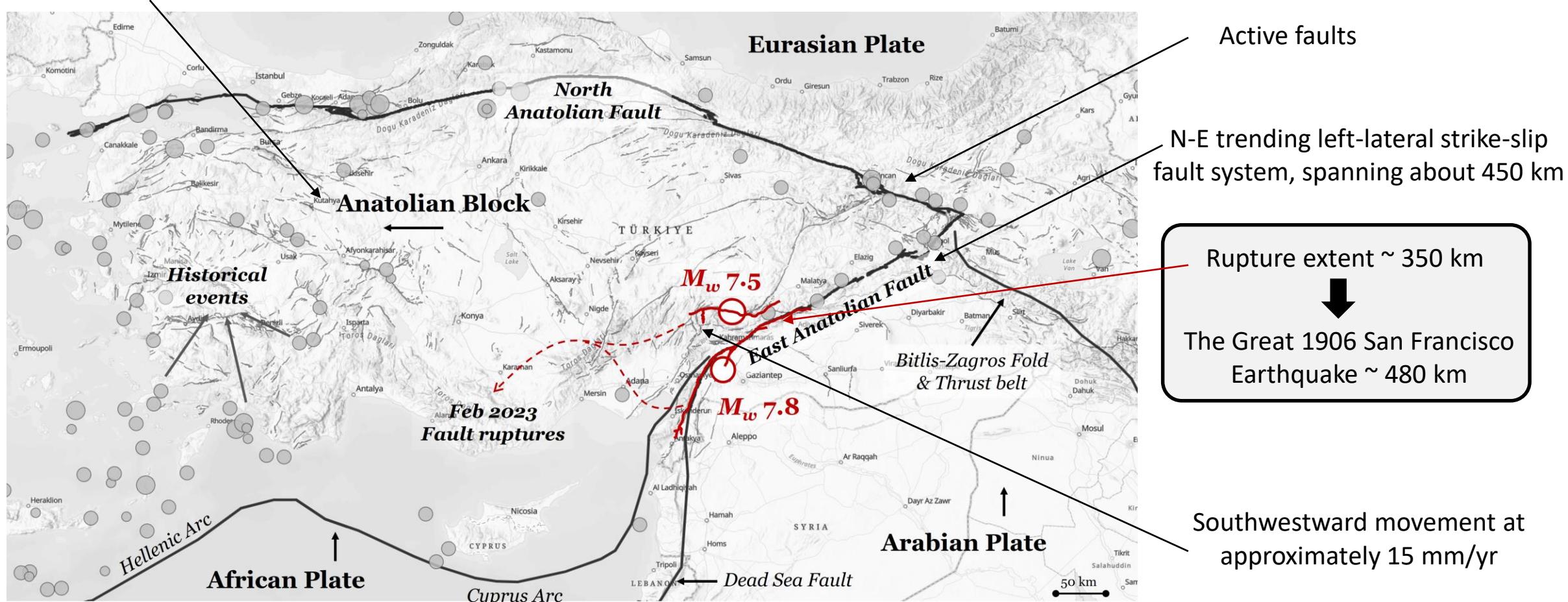
¹ Mudanya University, Bursa, Turkey

² University of Maryland, College Park, USA

Techtronic Plates and Fault Rupture

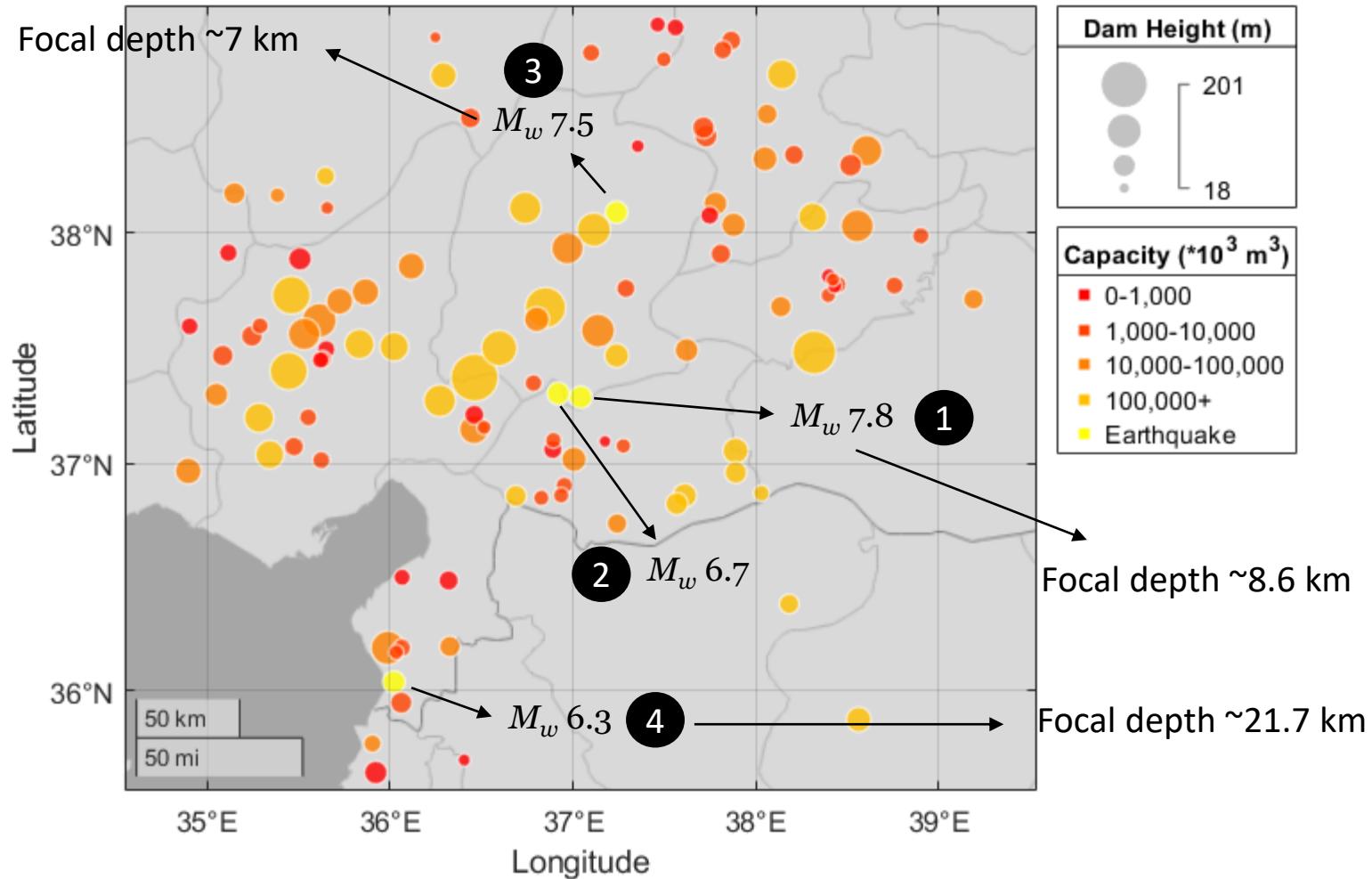
Westward movement at an approximate speed of 25 mm/yr

Source: USGS (2023)



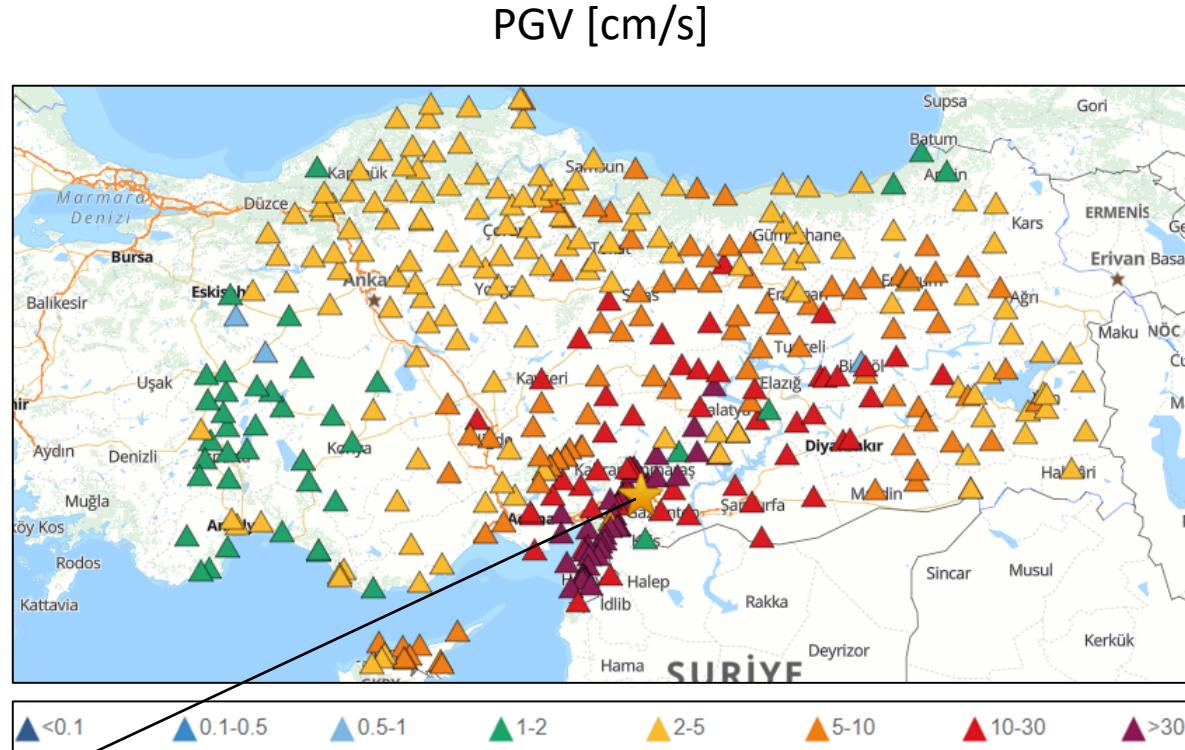
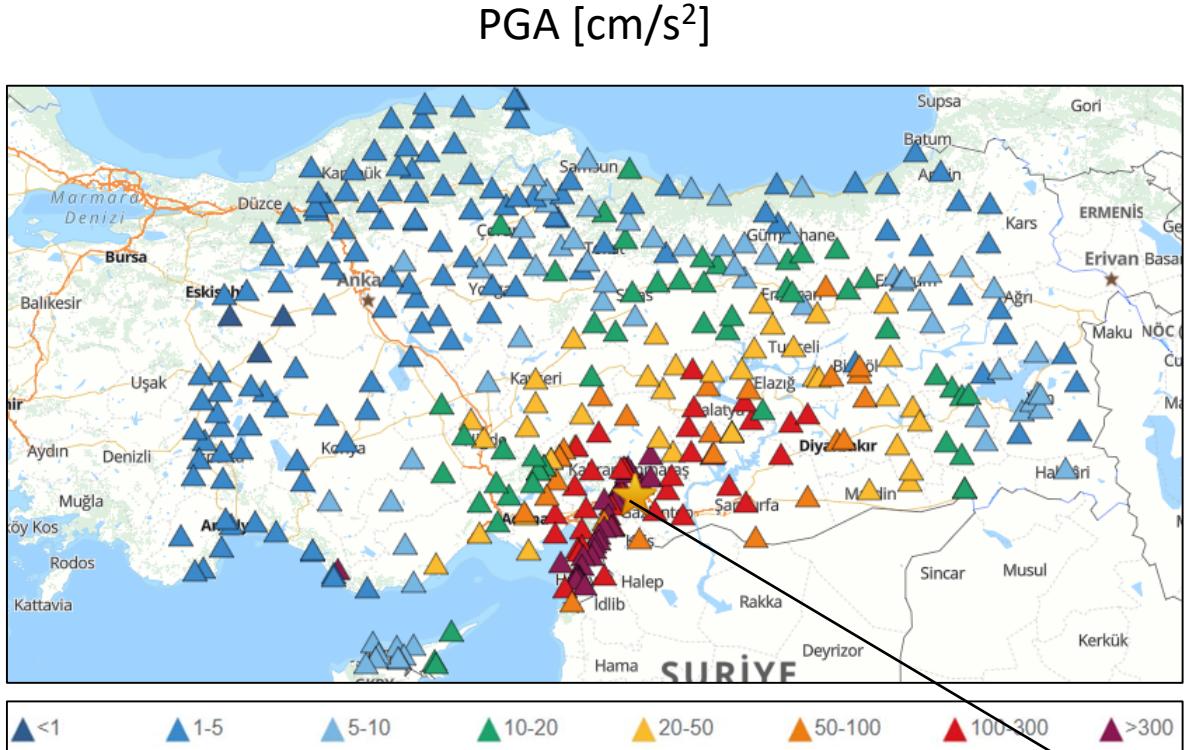
February 2023 Earthquake Sequence & Dams

- At 04:17 a.m. on Feb 6, 2023, a M_w 7.8 shook the EAF zone at Pazarcık.
- ~10 minutes later, M_w 6.7 shook Nurdagi.
- ~9 hours later, M_w 7.5 shook Elbistan.
- Feb 20, a M_w 6.3 shook Hatay.
- These are based on USGS's initial assessment.
- AFAD reported 7.7(1), 6.6(2), 7.6(3), 6.4(4)
- In the fortnight after the Feb 6 earthquake sequence, ~7500 aftershocks were recorded
- Geographic distribution of 110+ dams in the proximity of the Feb 2023 earthquakes



Source/dams: ICOLD (2023)

Recordings (reported from AFAD)

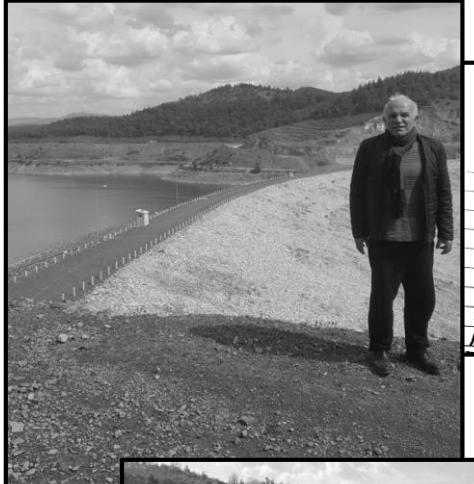


PGA, PGV, and PGD are available from AFAD. Example for M_w 7.8 event.

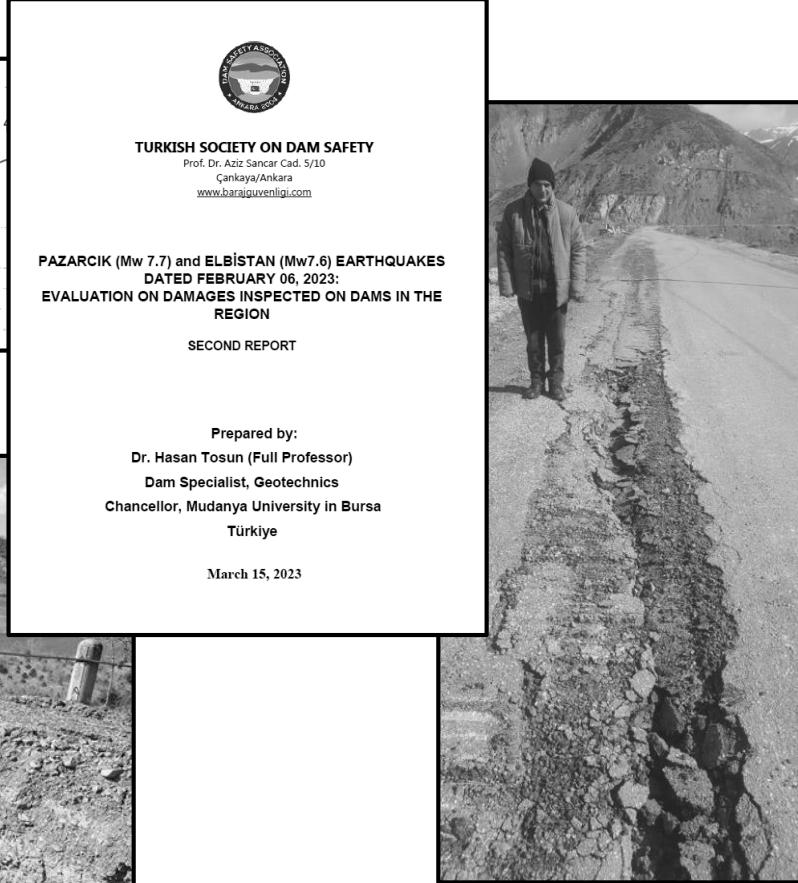
Source: AFAD (2023)

Reconnaissance Missions

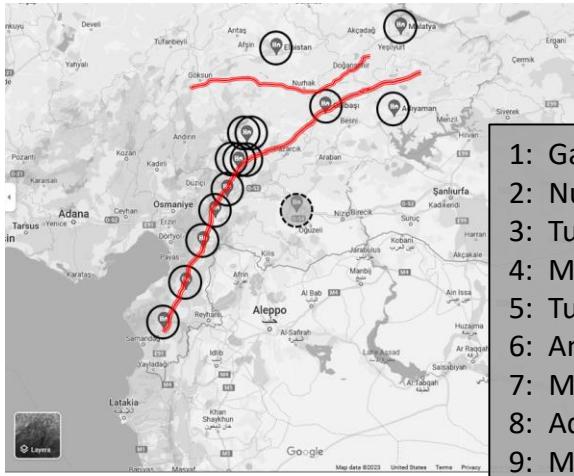
In person and virtual (Turkish Society of Dam Safety)



KSB 6	
Kolek	+ 38.958319 / 40.058964
Kigi	+ 39.369559 / 40.349669
Konaktepe	+ 39.2912 / 39.4726 ?
Oslue	+ 39.42968 / 40.08774
Fembelik	+ 39.06499 / 39.894977
Sapriktepe	+ 39.02462 / 39.891595
Tisan	+ 39.81234 / 39.817570
Thunayr	+ 38.981860 / 39.730121
Kebir	+ 38.901308 / 39.777095
Koktepe	

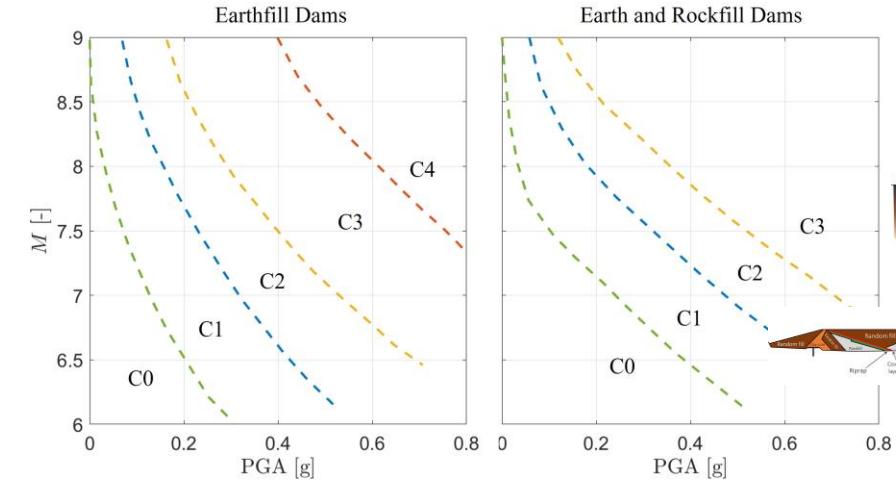


In person (ACI Committee 133)



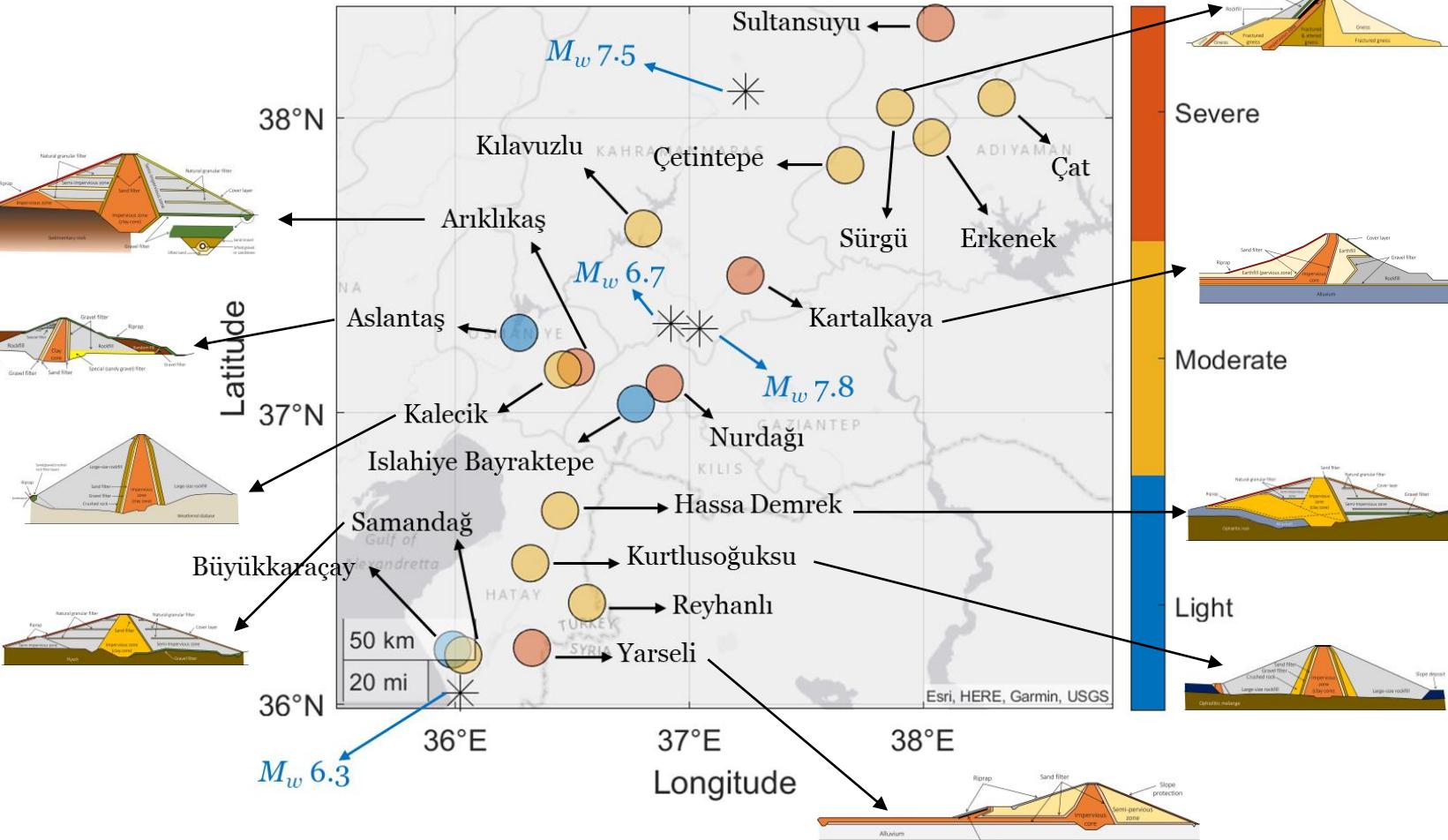
- 1: Gaziantep
- 2: Nurdagi
- 3: Turkoglu
- 4: Maras
- 5: Turkoglu
- 6: Antakya
- 7: Marash
- 8: Adiyaman
- 9: Malatya, Golbasi
- 10: Turkoglu, Islahiye
- 11: Hassa, Kirkhan
- 12: Elbistan

Distribution of Damaged Dams



Damage classification system (Pells and Fell, 2002)

Class	Description	Max longitudinal crack width [mm]	Max crest settlement [%]
C0	No	< 10	< 0.03
C1	Minor	10–30	0.03–0.20
C2	Moderate	30–80	0.20–0.50
C3	Major	80–150	0.50–1.50
C4	Severe	150–500	1.50–5.00
C5	Collapse	> 500	> 5.00

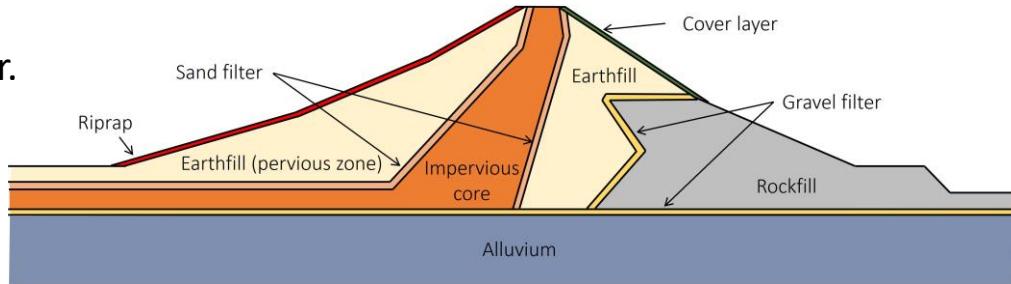


Detailed Characteristics of Damaged Dams

Dam	City	Basin	Height [m]	Crest Length [m]	Function	Dam Type	Body Volume [Mm³]	Construction Period [Year]	Reservoir Capacity [hm³]	Irrigated Area [ha]	Damage Status	Latitude	Longitude	Nearest Station Code (TK)	Distance from Nearest Station [km]
Ariklikas	Osmaniye	Ceyhan	33	355	I	Earthfill	0.62	1994-1998	2.2	268	Severe	37.156	36.514	'8002'	5.8
Kalecik	Osmaniye	Ceyhan	80	194	I	Concrete Faced Rockfill	0.84	1978-1985	32.8	4890	Moderate	37.148	36.459	'8002'	10.3
Aslantaş	Osmaniye	Ceyhan	95	566	I+E+F	Zoned Earthfill	8.49	-1984	1928		Light	37.273	36.272	'8004'	19.5
Kartalkaya	Kahramanmaraş	Ceyhan	57	205	I+DW	Zoned Earthfill	1.45	1965-1972	195	22810	Severe	37.467	37.239	'4614'	5.6
Kılavuzlu	Kahramanmaraş	Ceyhan	61	556	E	Earth Core Sand Gravel	3.8	-2014	74		Moderate	37.626	36.802	'4617'	5.2
Çat	Adiyaman	Euraphates	78	267	I	Rockfill	2.5	1985-1996	240	22091	Moderate	38.068	38.313	'0214'	8.8
Çetintepe	Adiyaman	Euraphates	116	780	I	Earth Core Rockfill	12.7	-2022	460		Moderate	37.840	37.666	'0208'	6.0
Sürgü	Malatya	Euraphates	55	736	I+DW	Earth Core Rockfill	1.22	1965-1969	70.9	10090	Moderate	38.035	37.879	'4408'	6.8
Sultansuyu	Malatya	Euraphates	60	721	I	Earth Core Sand Gravel	3.2	1986-1992	53.3	17614	Severe	38.319	38.052	'4406'	7.3
Büyükkaraçay	Hatay	Rebel	105	415	DW	Concrete Faced Rockfill	2.5	2009-2019	53.7	3736	Light	36.188	35.988	'3140'	12.3
Hassa-Demrek	Hatay	Rebel	30	503	I	Earthfill	0.36	1997-2006	2	276	Moderate	36.666	36.447	'3145'	4.2
İslahiye-Bayraktepe	Gaziantep	Rebel	41	233	I	Earth Core Sand Gravel	0.69	2015-2017	2.8	612	Light	37.031	36.771	'2718'	13.1
Kırıkhan-Kutlusoguksu	Hatay	Rebel	40	419	I	Earth Core Rockfill	0.36	2007-2017	0.75	92	Moderate	36.485	36.320	'3142'	4.4
Nurdağı-Hamidiye	Gaziantep	Rebel	29	182	I	Earth Core Rockfill	0.15	2015-2018	1.9	274	Severe	37.100	36.893	'2712'	17.0
Reyhanlı-Samandağı-Karamanlı	Hatay	Rebel	30	9271	I	Earthfill	20.73	2010-2020	480	58460	Moderate	36.349	36.562	'3133'	11.8
Yarseli	Hatay	Rebel	26	406	I	Earthfill	0.36	2001-2005	2	222	Moderate	36.169	36.033	'3129'	9.4
			45	960	I	Earth Core Sand Gravel	3	1985-1992	5	8343	Severe	36.194	36.327	'3136'	11.2

● Kartalkaya Dam

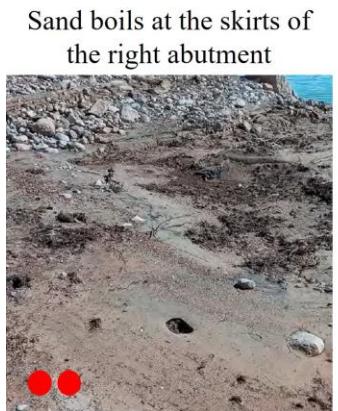
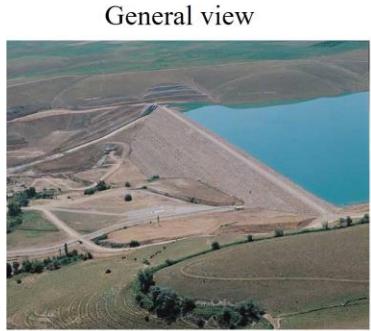
- Kartalkaya Dam serves the dual purpose of supplying drinking and irrigation water.
- $H = 56 \text{ m}$, $L = 205 \text{ m}$, zoned rock-fill dam, 52 yrs old
- Recorded $PGA (M_w 7.8)$ at the nearest station (R of 5.6 km) is $\sim 2 \text{ g}$.
- Estimated $PGA (M_w 7.8)$ with V_{S30} of 440 m/s is $\sim 1.2 \text{ g}$ (PGV is 116 cm/s).



- Reservoir was at a low pool due to drought.
- Significant damage, including large cracks in the dam body, slips on the upstream left bank, and settlement approximately 1.0 m to the left.
- The security cabin on the crest was destroyed.
- Vertical ground movement in the bedrock on the upstream right bank caused damage to the rock fill's bank + large rock falls obstructing roads.
- Crest cracks range from 15 to 80 cm in width and 20-90 cm in depth.
- No damage was observed on the US/DS faces.
- No leakage occurred at the downstream toe.
- Outlet structure remained unchanged, with superficial damage to the wingwalls.

● Sultansuyu Dam

- Sultansuyu Dam was designed for irrigation purposes.
- $H = 52$ m from rive basin (60 total), $L = 721$ m, earthfill dam, 32 yrs old.
- Recorded PGA (M_w 7.8) at the nearest station (R of 7.3 km) is ~ 0.14 g.
- Estimated PGA (M_w 7.8) with V_{S30} of 400 m/s is ~ 0.16 g (PGV is 40 cm/s).



- Estimated PGA_{max} is ~ 0.48 g (PGV_{max} is 70 cm/s).
- Dam mainly responds to an earthquake at its T_1 :
 S_a ($T = 0.1$ s) = ~ 1.2 g
 S_a ($T = 0.3$ s) = ~ 1.0 g
- The foundation comprises claystone-sandstone.
- Maximum water level was 10 m below the crest.
- Large cracks emerged in the embankment, leading to controlled discharge of water.
- Cracks width $\sim 0.8\text{-}1.0$ m.
- Crack depth reached 4.0 m ten days later.
- Lateral separation in the form of slides was observed, including general slips in the protective rock fill layer on the upstream slope and tension cracks in the middle height of the fill.
- Dam experienced lateral movement toward the US.
- **Maximum settlement of 80 cm was reported.**
- Differential movements were observed in several locations. No transverse cracks were found.
- **Liquefaction was reported in the form of sand boils.**

Source: ● adiyamannews.com & ●● EERI/GEER (2023)

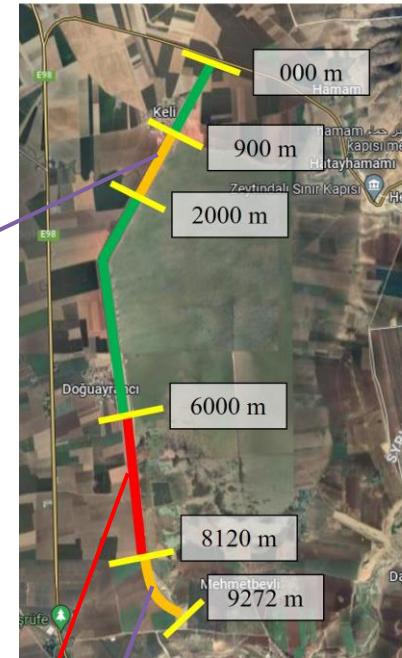
Reyhanlı Dam

- Reyhanlı Dam was designed for irrigation and flood protection.
- $H = 28 \text{ m}$, $L = 9,271 \text{ m}$, earth-fill dam, 4 yrs old.
- Recorded PGA (M_w 7.8) at the nearest station (R of 11.7 km) is $\sim 0.23 \text{ g}$.
- Estimated PGA (M_w 7.8) with V_{S30} of 210 m/s is $\sim 0.25 \text{ g}$ (PGV is 53 cm/s).

Lateral separations exceeding 1.0 m in this section, with variable crack depths in the crest, reaching up to 1.2 m.

- The dam is composed of two different sections, i.e., homogeneous and clay core earth dams.
- Substantial damages on the crest and both US/DS slopes.
- Damage varied across different regions (color-coded):
 - Green (no damage)
 - Orange (crack width around 30 cm and settlement of 5-10 cm)
 - Red (crack width over 1.0 m and crest settlement of 15-80 cm)
- While no soil liquefaction or leakage was observed, we cannot rule out the possibility of liquefaction in the red zone.

General view and damage classification



Red area; lateral deformation & settlement



Orange area; cracking & tilted bolts



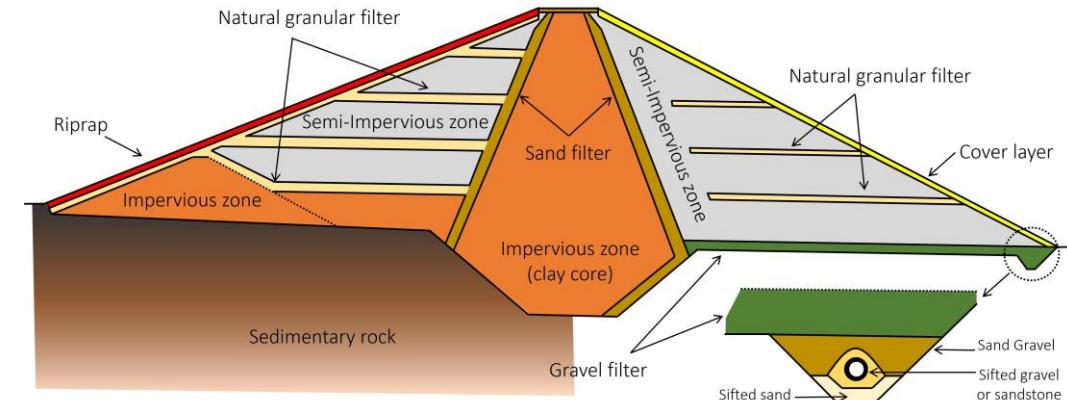
Lateral separations reached 1.5 m, and crack depths reached 3.5 m. Settlements approaching 50 cm in the US/DS direction. Damages were attributed to proceeding circular slip surfaces formed in the US and DS directions.

● Arıklikas Dam

- Arıklikas Dam serves irrigation purposes.
- $H = 33$ m (25 rive basin), $L = 355$ m, homogeneous earth-fill, 26 yrs old.
- Recorded PGA (M_w 7.8) at the nearest station (R of 5.7 km) is ~ 0.27 g.
- Estimated PGA (M_w 7.8) with V_{S30} of 480 m/s is ~ 0.30 g (PGV is 48 cm/s).



● Source: EERI/GEER (2023)



- Significant damages on the crest and US face of the fill.
- Lateral displacements exceeding 5.0 m in the embankment due to sliding movements.
- Tensile cracks reaching up to 4.0 m, and horizontal movement in the US direction up to a maximum of 1.2 m.
- The dam's abutments exhibited no significant cracking.
- The spillway and outlet structures remained undamaged.
- **Sand boils towards the toe were also observed.**

According to local observers, the dam sustained damage in the initial M_w 7.8 event, with further damages occurring in after-shocks (M_w 6+).

Çat Dam

- Çat Dam serves irrigation purposes.
- The side slopes are 3H:1V (US), 2.5H:1V (DS).
- $H = 78 \text{ m}$, $L = 267 \text{ m}$, rockfill dam, 30 yrs old.
- Recorded PGA ($M_w 7.8$) at the nearest station (R of 8.7 km) is $\sim 0.06 \text{ g}$.
- Estimated PGA ($M_w 7.8$) with V_{S30} of 540 m/s is $\sim 0.44 \text{ g}$ (PGV is 120 cm/s).

General view



Cracks at embankment-spillway junction



Cracks at the crest



Slip surface movements



Rockfalls at the spillway site



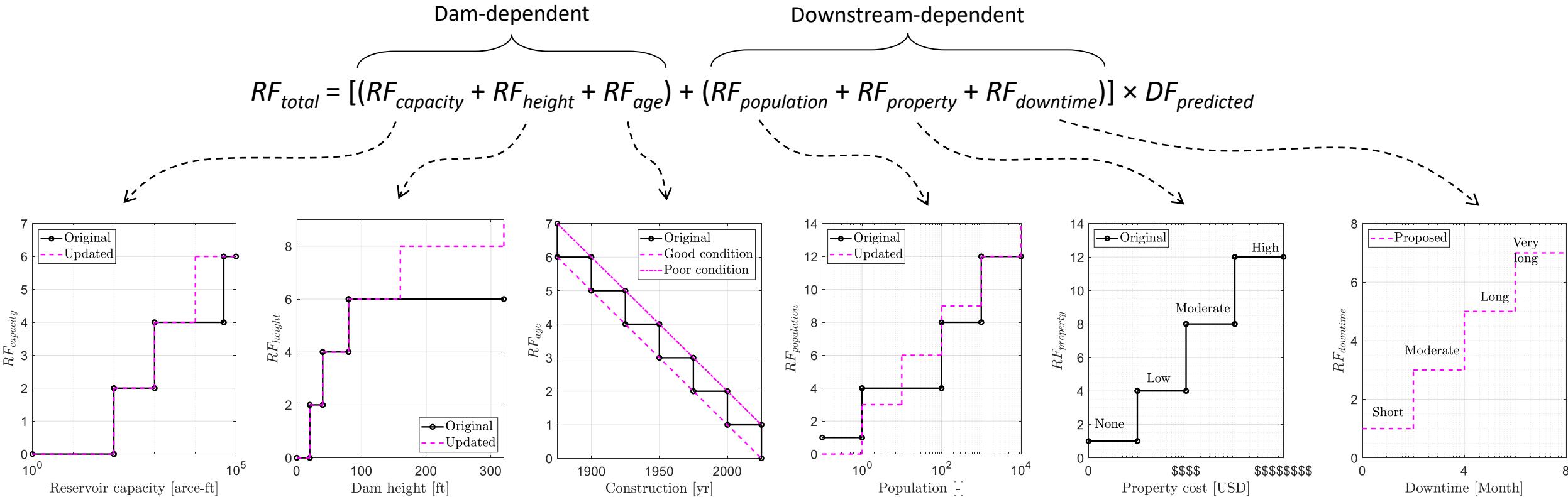
Differential settlement



- Cracks within the soil-rock fill, separations in building joints, and the development of slip planes in various areas.
- Rockfalls were observed in the spillway area, accompanied by cracks in the dam body in both US and DS directions.
- Tension cracks at the embankment crest exhibited separations up to 25-30 cm.
- Sliding along rotational slip planes occurred in parts of the embankment, generating surface cracks in the middle of the fill.
- Separations at the dam fill and spillway concrete junction, with observed differential settlements.
- Settlements up to 40 cm were identified in the spillway structure-embankment junction.
- Slipping and flowing events on the left side of the spillway caused partial damage to the walls.

Semi-Quantitative Risk Ranking

- A semi-quantitative (empirical) method was developed by Bureauand and Ballentine (2002).
- A total risk factor (RF) depends on (1) dam type, (2) dam age, (3) dam size, (4) downstream risk potential, and (5) dam's vulnerability.



Source: Hariri and Nuss (2018)

Risk Assessment of Dams in Türkiye

- Total risk analyses for the selective dams. M_{max} : Maximum earthquake magnitude; R_{min} : Minimum distance to fault segment
- PGA_{50%}: Mean PGA at the 50th percentile; PGA_{84%}: Mean PGA at the 84th percentile
- OBE: Operational Based Earthquake; MDE: Maximum Design Earthquake; SEE: Safety Evaluation Earthquake

	Dam	Arıklaş	Kalecik	Kartalkaya	Çat	Sürgü	Sultansuyu	Reyhanlı	Yarseli
Dam	City	Osmaniye	Osmaniye	K.maraş	Adiyaman	Malatya	Malatya	Hatay	Hatay
information	Height (m)	33	85	57	78	57	60	30	45
	Type	EF	RF	EF	RF	RF	EF	EF	EF
	Body volume (Mm ³)	0.62	0.84	1.45	2.5	1.2	3.2	20.8	3
	Reservoir capacity (hm ³)	2.2	32.8	195	240	70.9	53.3	480	5
Deterministic method	M_{max}	7	7.7	7.6	7.4	7.4	7.6	7.3	7.1
	R_{min} (km)	7.6	5.7	7.5	2.8	1.2	8.5	3.2	3.4
	PGA _{50%} (g)	0.311	0.363	0.354	0.471	0.463	0.351	0.453	0.397
	PGA _{84%} (g)	0.505	0.591	0.569	0.762	0.761	0.563	0.733	0.643
Probabilistic method	OBE (g)	0.304	0.379	0.228	0.322	0.369	0.162	0.31	0.342
	MDE (g)	0.407	0.525	0.331	0.434	0.52	0.239	0.423	0.462
	SEE (g)	0.562	0.591	0.497	0.607	0.766	0.37	0.597	0.643
Hazard analysis	Class	IV	IV	IV	IV	IV	IV	IV	IV
	Hazard ratio	Very high	Very high	Very high	Very high	Very high	Very high	Very high	Very high
Total risk	Risk factor	28	34	34	36	34	34	32	32
	Risk class	IV	IV	IV	IV	IV	IV	IV	IV
	Risk ratio	Very high	Very high	Very high	Very high	Very high	Very high	Very high	Very high

Connection!

- This presentation covered the damaged dams in Türkiye and their associated risk analysis.
- In the Monitor session, a complementary presentation is provided for another series of dams in Türkiye that were not damaged and have a monitoring system in place.



Thank you!

Any questions?



Monitoring and simulated response of dams to the February 2023 Türkiye earthquake sequence

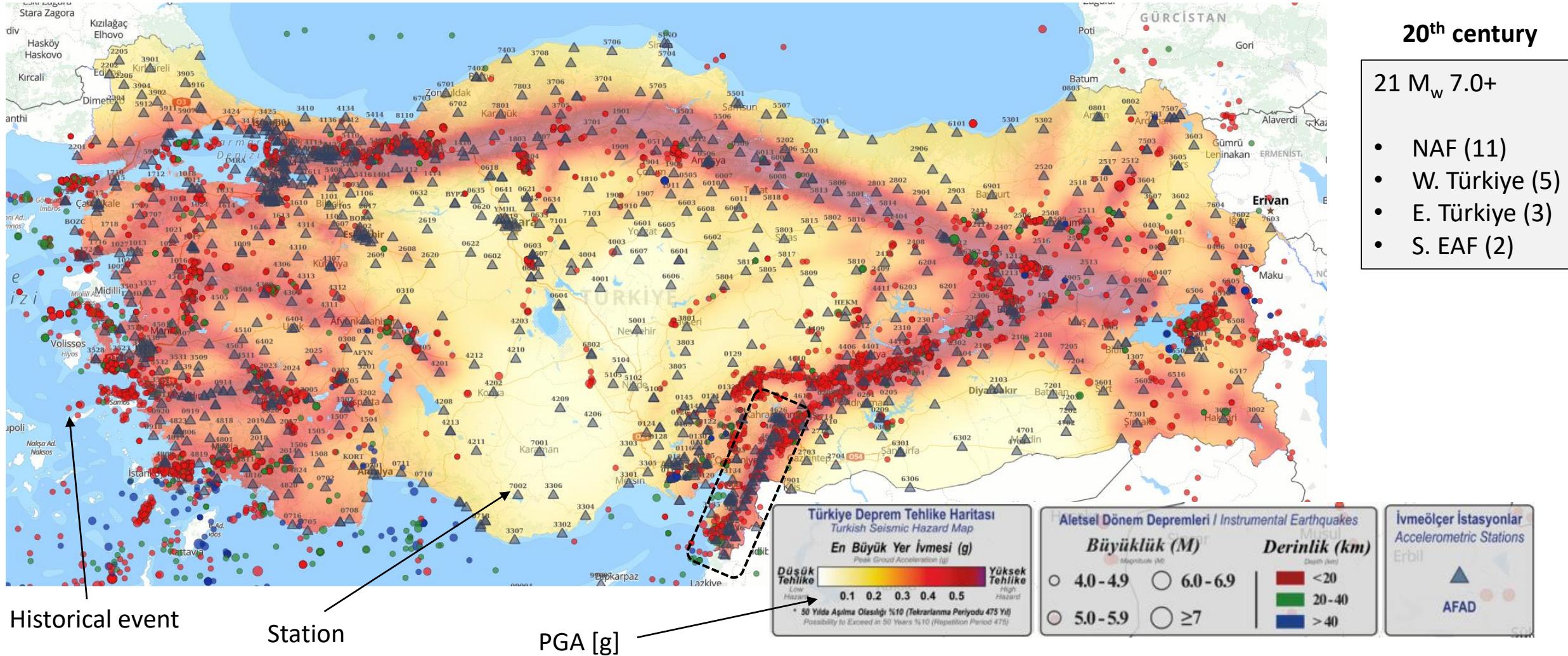
M.A. Hariri-Ardebili ¹, H. Tosun ²

¹ University of Maryland, College Park, USA

² Mudanya University, Bursa, Türkiye

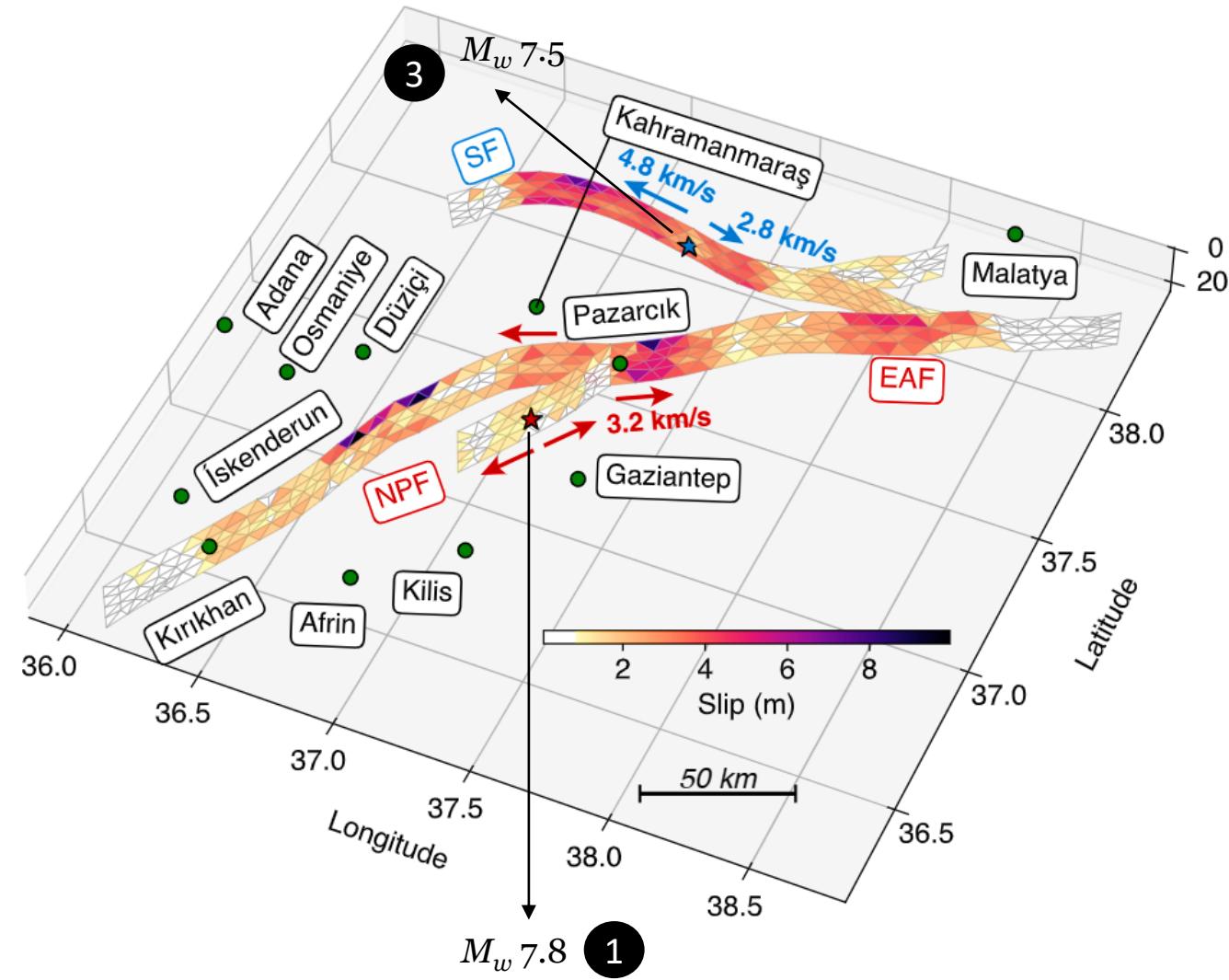
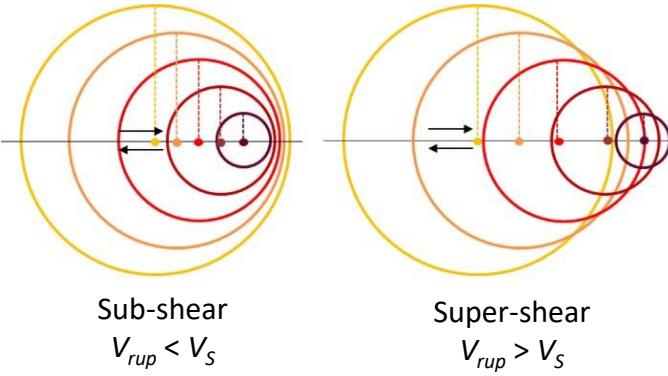
Seismic Hazard Map and Historical Events

Source: AFAD (2023) => Ministry of Interior Disaster and Emergency Management Presidency



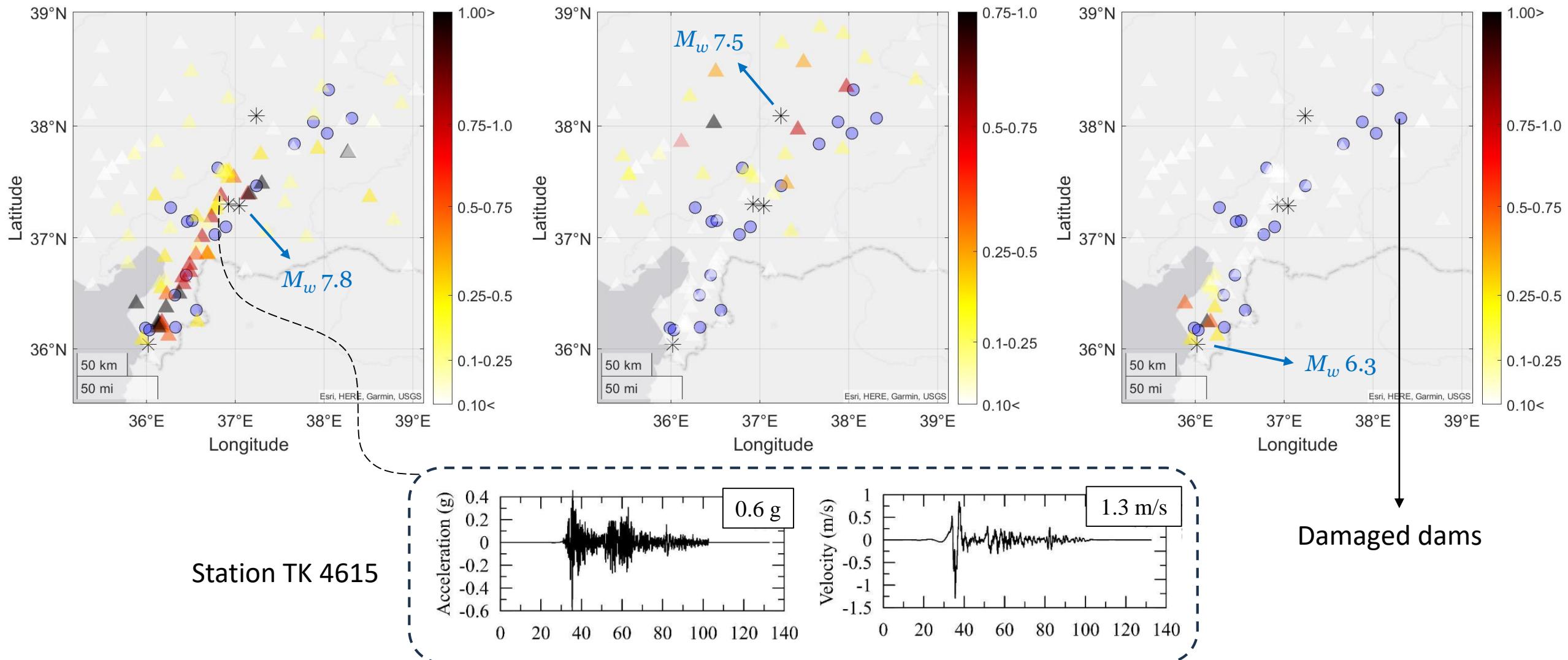
Seismology of the Earthquake Sequence

- The M_w 7.8 earthquake released left-lateral strike-slip motion and ruptured bilaterally from the epicenter.
- The fault segments along the EAF broke in two parts. At first, it travelled N-E, and then to the S-W at speeds of ~ 3.2 km/s, for a total duration of 80-117 seconds.
- Statistically there was a 7% chance that a mainshock will trigger a subsequent earthquake of a similar magnitude.
- The M_w 7.5 earthquake, first ruptured westwards at extremely fast (super-shear) speeds of 4.8 km/s for up to 17 seconds. Then, the earthquake rupture continued to the east for a further 14 seconds at 2.8 km/s (sub-shear).



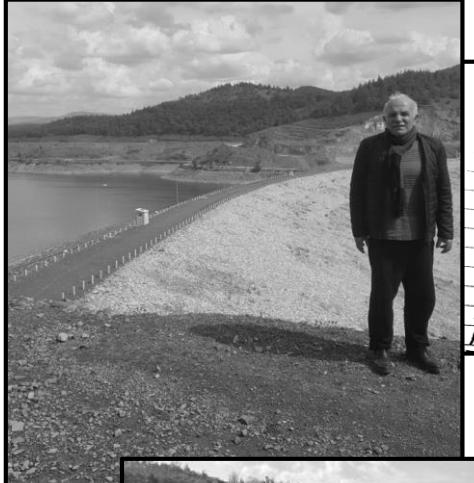
Source: Melgar et al. (2023)

Total Horizontal PGA [g] at Stations (triangular)



Reconnaissance Trips

In person and virtual (Turkish Society of Dam Safety)



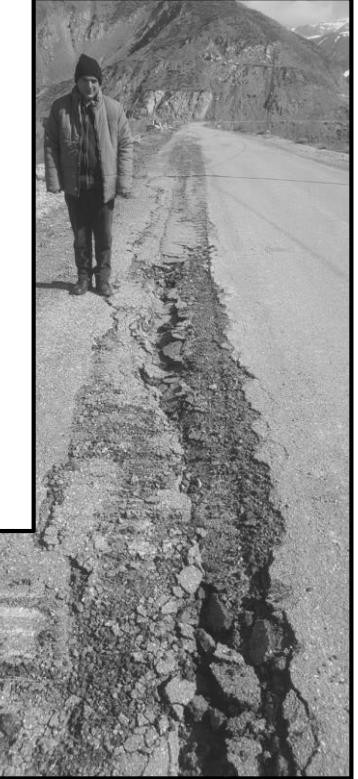
KSB 6.	
Kolek	+ 38.958319 / 40.058964
Kigi	+ 39.369559 / 40.349669
Konaktepe	+ 39.2912 / 39.4726 ?
Oslue	+ 39.42968 / 40.08774
Fembelik	+ 39.06499 / 39.894977
Saprintepe	+ 39.02462 / 39.891595
Tisan	+ 39.812334 / 39.817570
Thunayr	+ 38.981860 / 39.730121
Kebir	Koktepe
	+ 38.901308 / 39.777095



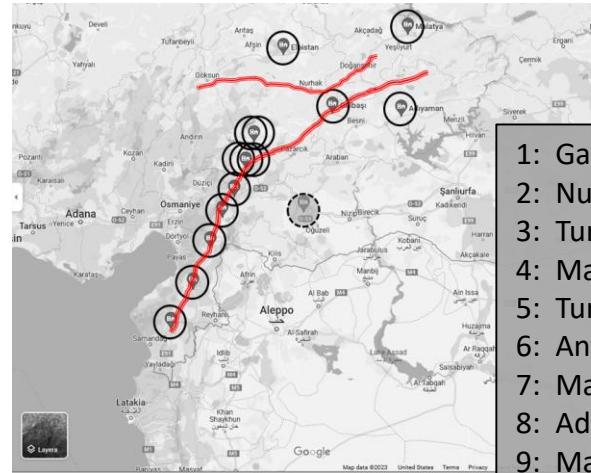

TURKISH SOCIETY ON DAM SAFETY
 Prof. Dr. Aziz Sancar Cad. 5/10
 Çankaya/Ankara
www.barsiguvendili.com

PAZARCIK (Mw 7.7) and ELBİSTAN (Mw 7.6) EARTHQUAKES
DATED FEBRUARY 06, 2023:
EVALUATION ON DAMAGES INSPECTED ON DAMS IN THE REGION
SECOND REPORT

Prepared by:
Dr. Hasan Tosun (Full Professor)
Dam Specialist, Geotechnics
Chancellor, Mudanya University in Bursa
Türkiye
March 15, 2023

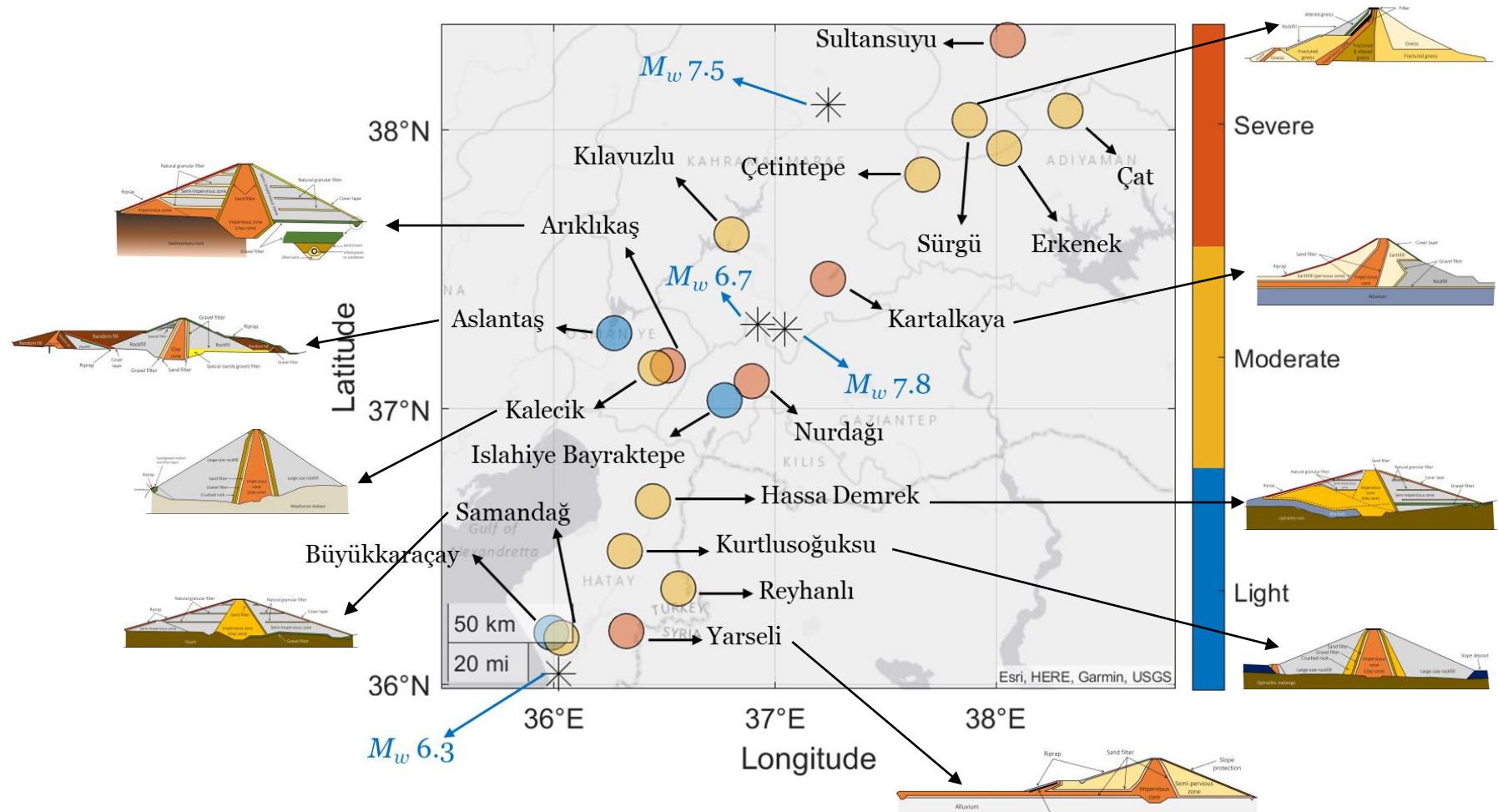


In person (ACI Committee 133)



- 1: Gaziantep
- 2: Nurdagi
- 3: Turkoglu
- 4: Maras
- 5: Turkoglu
- 6: Antakya
- 7: Marash
- 8: Adiyaman
- 9: Malatya, Golbasi
- 10: Turkoglu, Islahiye
- 11: Hassa, Kirkhan
- 12: Elbistan

Damaged Dams (Covered previously)



Source: Hariri and Tosun (2024)

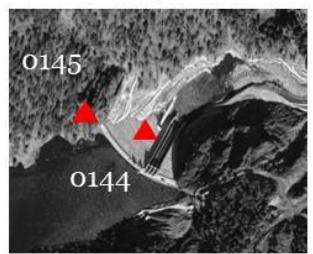
Instrumented dams (no damage!)

- Eleven dams in the region equipped with accelerometers. No damage has been reported in these dams.

Karaaisalı Karaguz



Göktaş HES



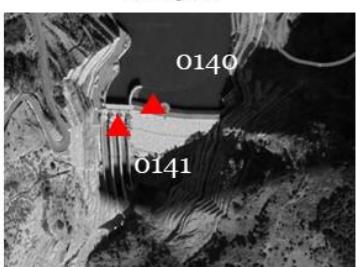
Yamanlı



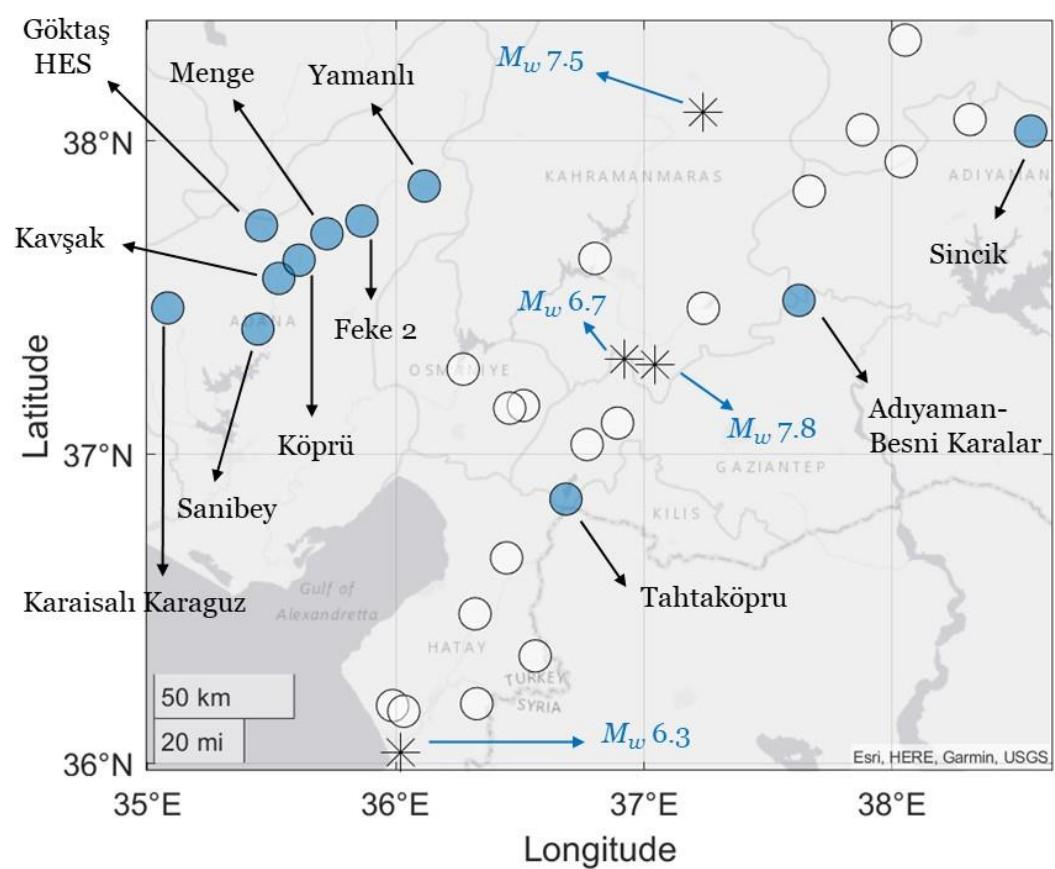
Sanibey



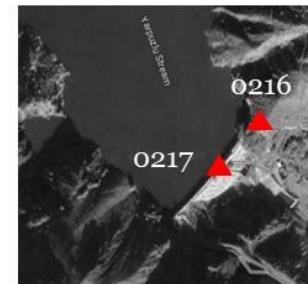
Kavşak



Köprü



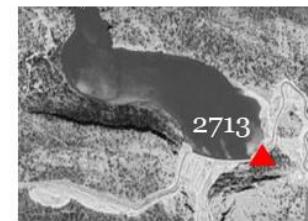
Sincik



Menge



Adiyaman-Besni Karalar

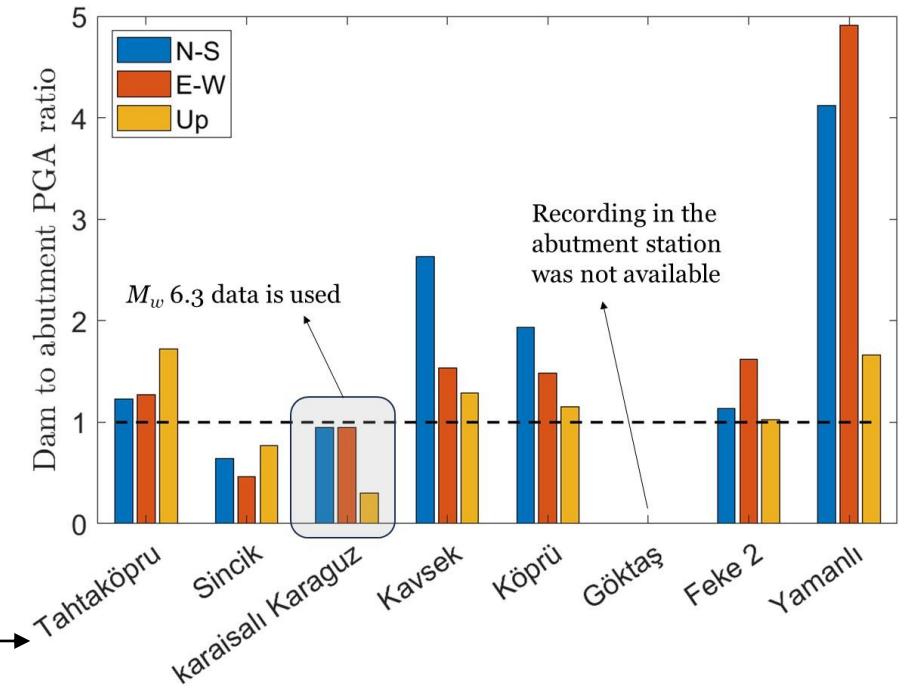
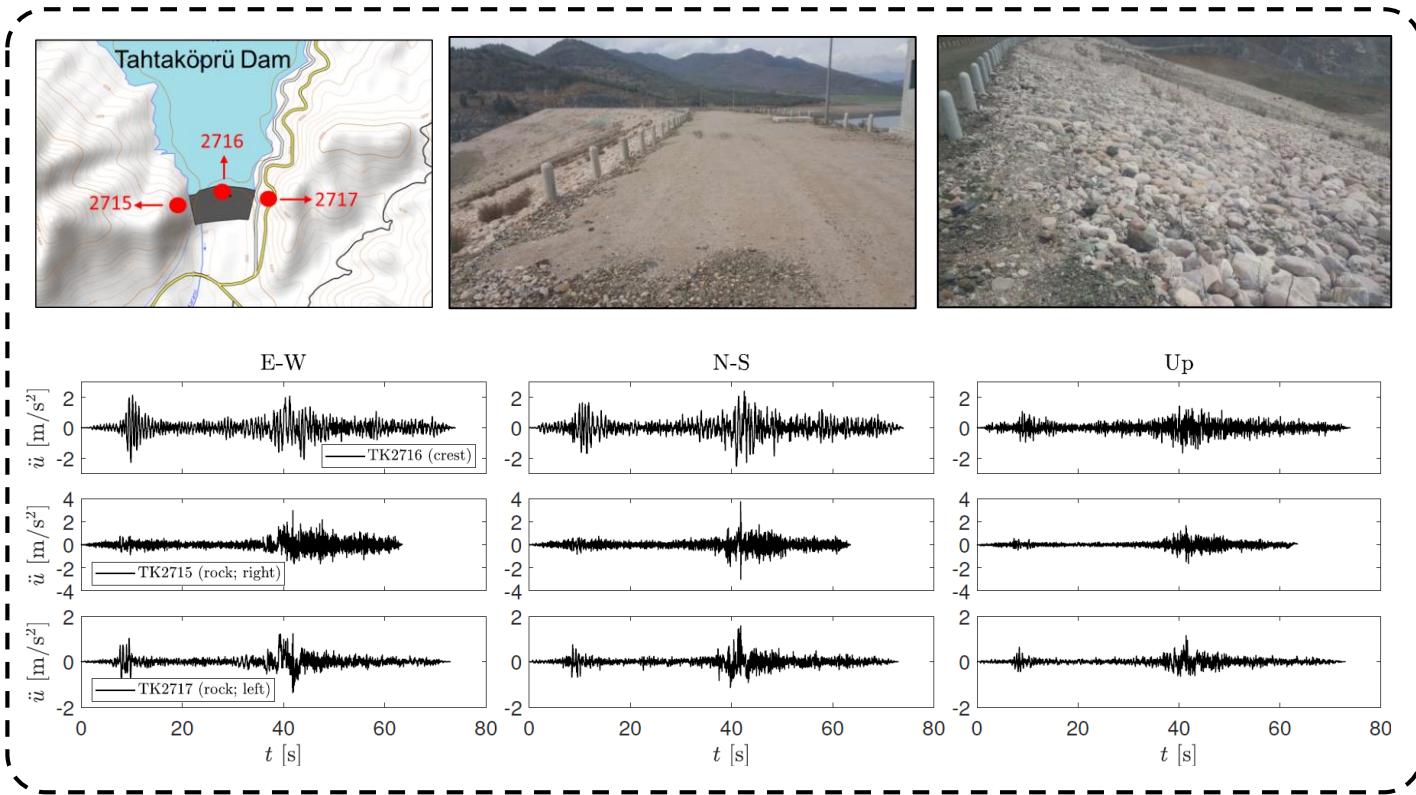


Feke 2

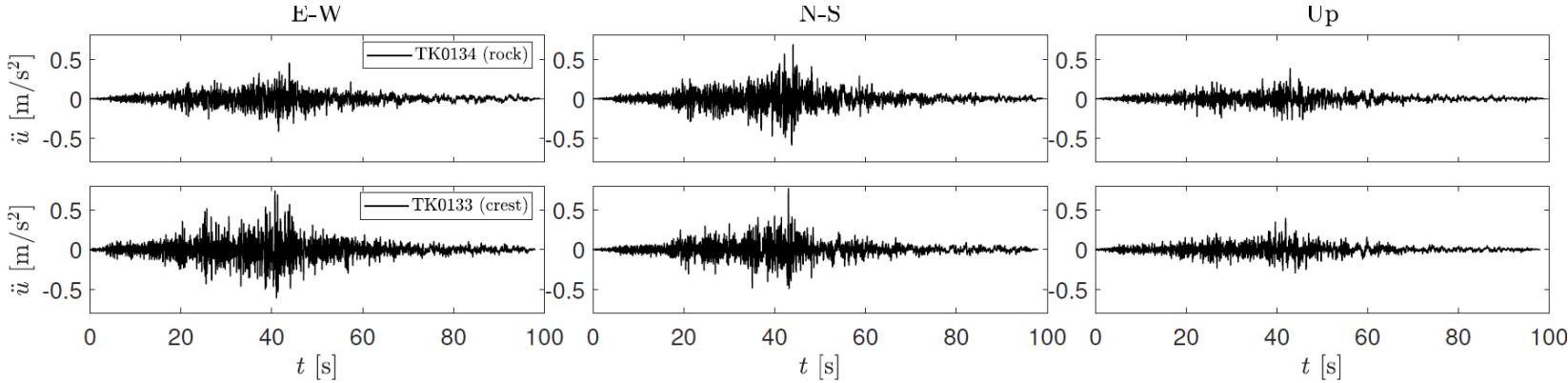
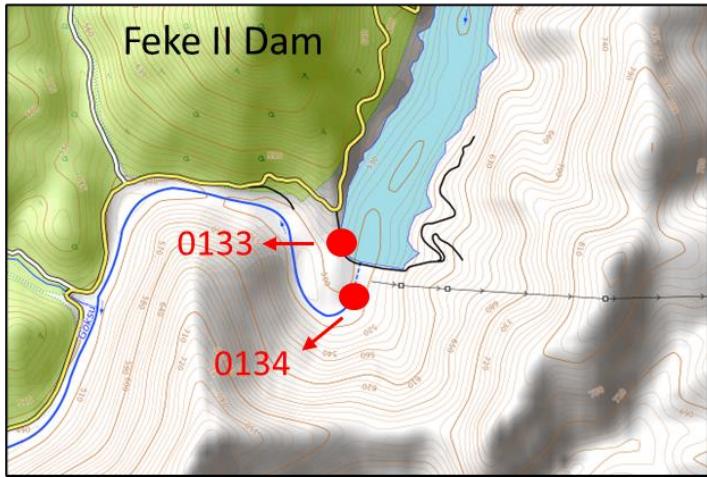


Processing of the Recordings

- Most of these dams feature at least two accelerometers (one on the dam and another on the abutment or downstream rock).
- AceBox sensors are commonly used. → An advanced accelerograph, employs three Force Balance Accelerometers to record seismic signals with high resolution (up to 100 Hz frequency), storing the data on embedded USB memory.



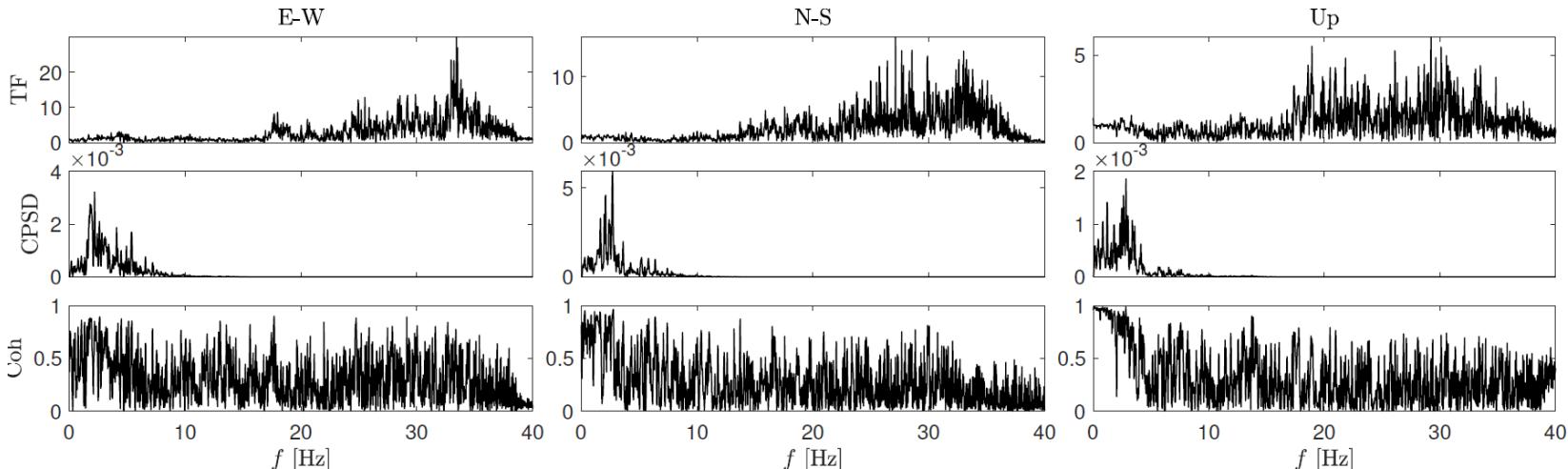
System Identification



Ratio of Fourier amplitude (transfer func.)
 $TF_{2,1} = S_2 / S_1$

Cross power spectral density function
 $CPSD_{2,1} = S_2 \times S_1$

Coherency function (0-1)
 $C^2_{2,1} = |CPSD_{2,1}^2| / (CPSD_{2,2} CPSD_{1,1})$



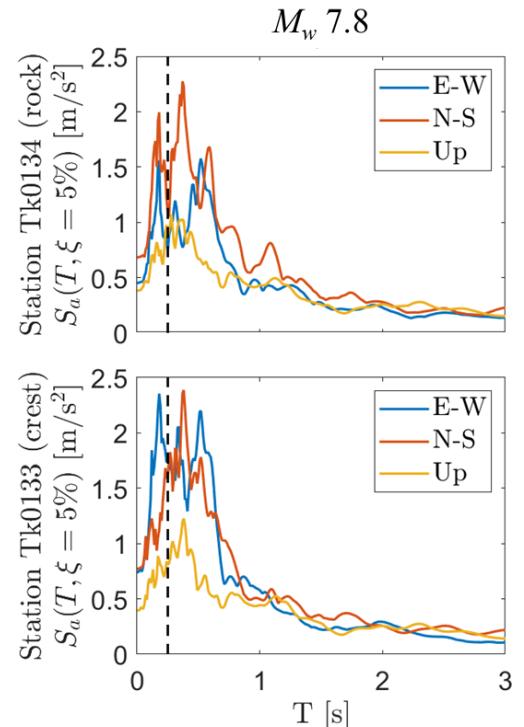
Feke II RCC dam (Instrumented, No damage)

- Feke II Dam is an RCC dam constructed in 2011 ($H = 70$ m, $L = 256$ m). The upstream and downstream slopes are 1:0.07 and 1:0.80.
- The volume of RCC and the total dam volume are 194,000 and 227,000 m³, respectively.
- Concrete placement occurred in layers of 0.3 m.
- The mix design comprises 60 kg/m³ of cement and 50-60 kg/m³ pozzolan (Low-lime fly ash - ASTM Class F).
- Assumed concrete properties: $E_c = 20$ GPa and, $\rho_c = 2,400$ kg/m³. An overall damping of 3% was used.

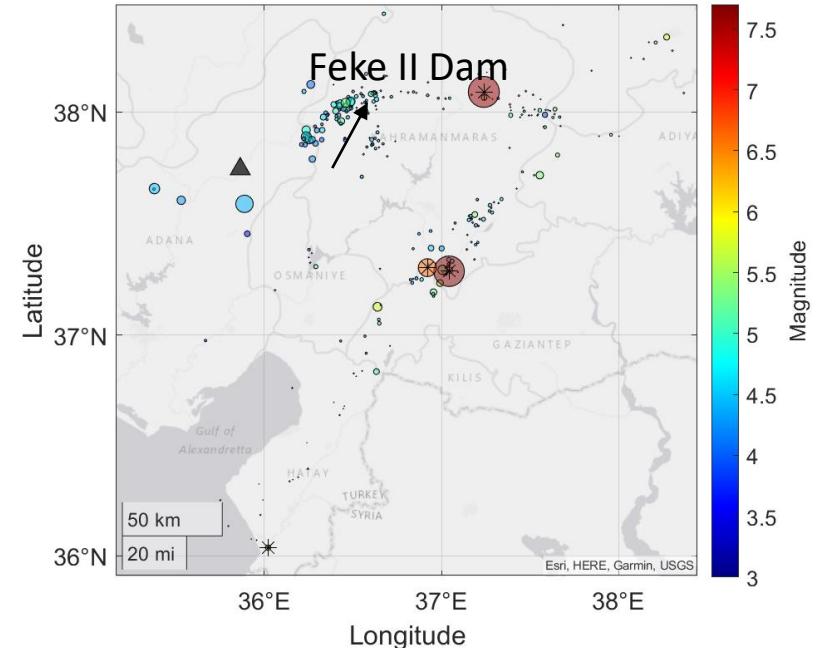


A downstream view;

Source: rccdams.co.uk/dams/feke-ii/



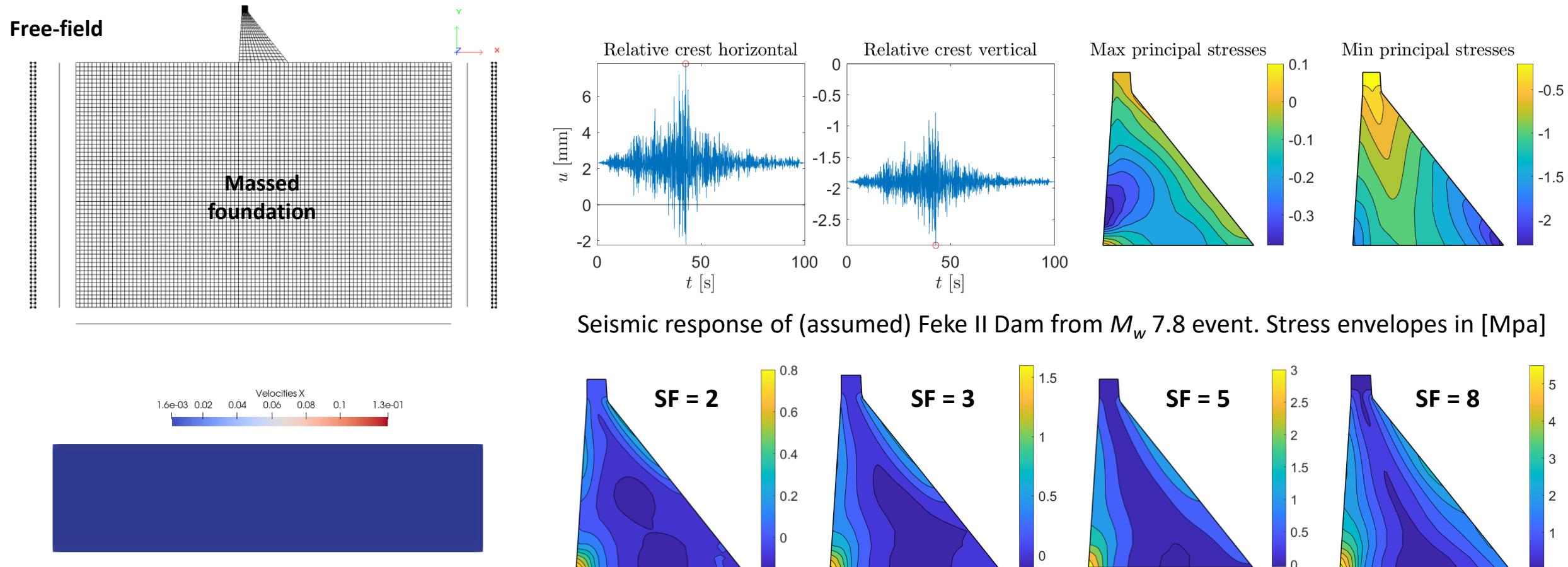
Acceleration response spectra at two stations



280+ events have been recorded in TK0133 station during February to October 2023

Finite Element Simulations

- A linear elastic model is developed in Merlin with free-field boundary condition for massed foundation.
- Reservoir is modelled using approximate formulation.



Tensile stress distribution [MPa] from the M_w 7.8 event with N-S and Up components

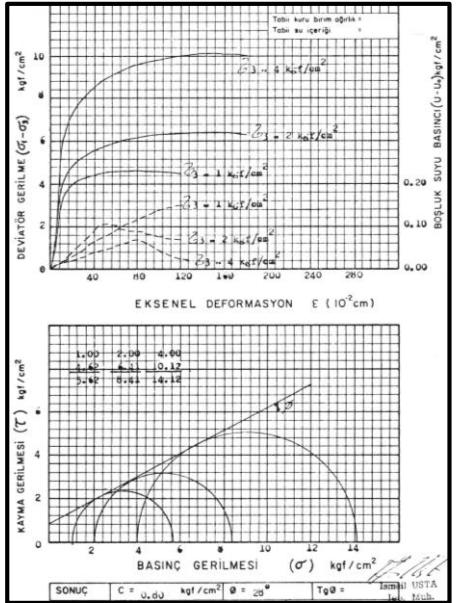
Arıklıkaş Dam (Not instrumented, Damaged)



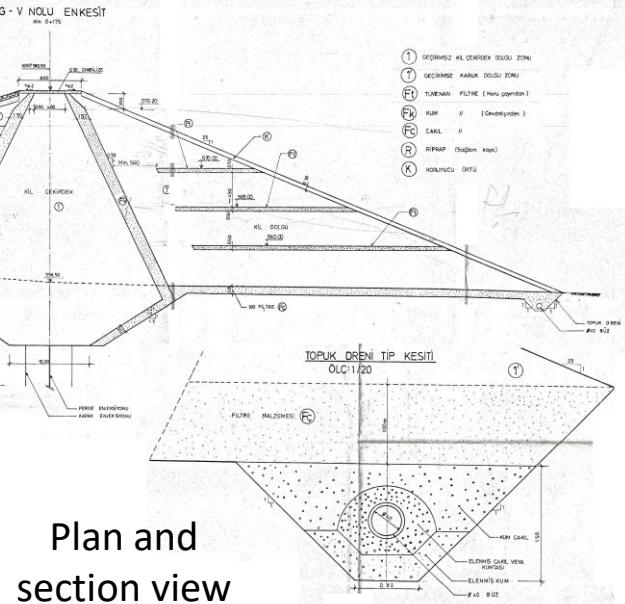
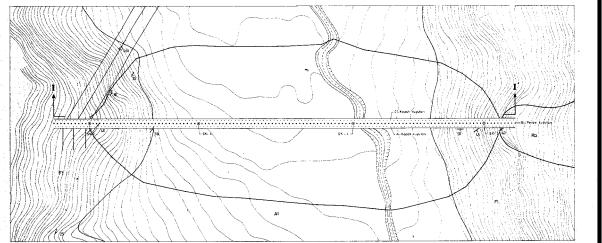
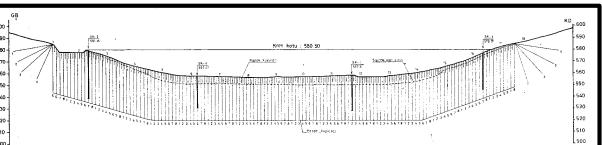
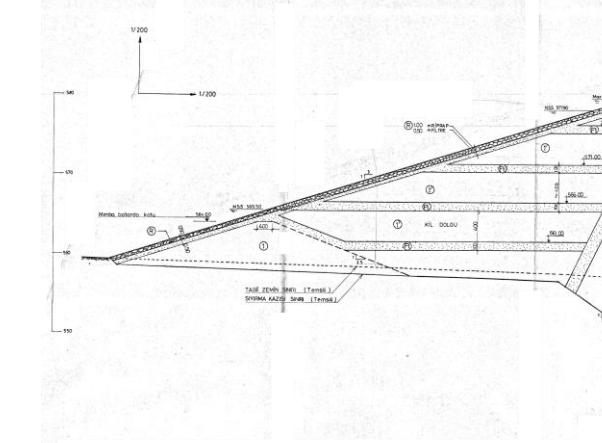
Downstream view



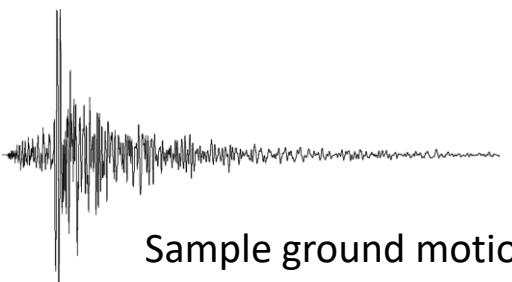
Upstream view



Samples of available data



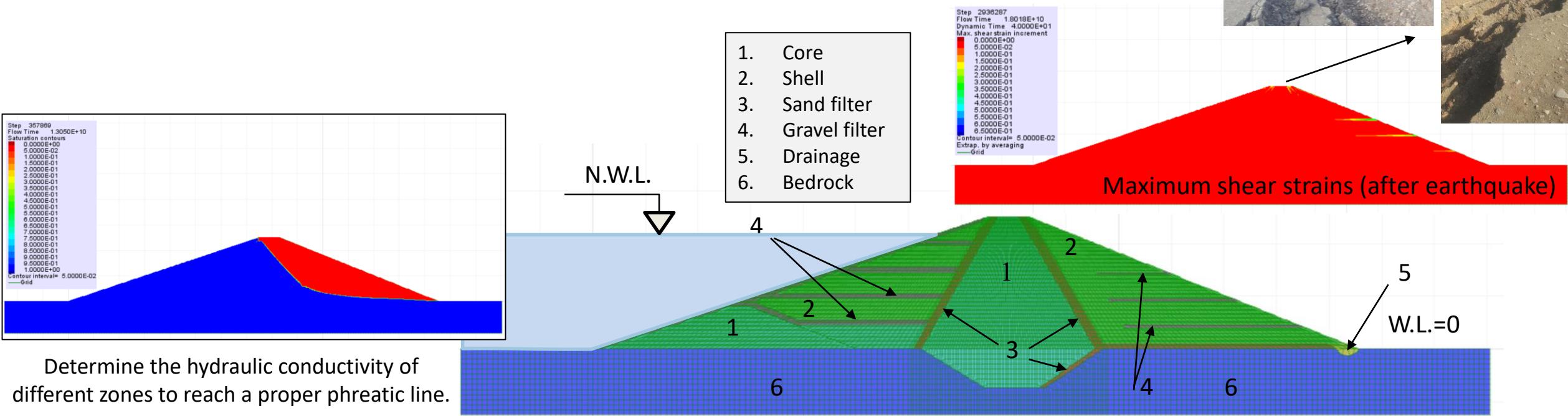
Plan and section view



Sample ground motion (PGA ~ 0.4 g)

Preliminary FE model (25% progress)

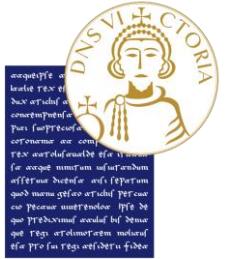
- Arıklıtaş Dam is a homogeneous earth-fill structure and is founded on low-plasticity clay.
- Bedrock consists of a sedimentary rock, including layers of claystone, siltstone, sandstone, marl, and limestone.
- H = 33 m (25 rive basin), L = 355 m. Body volume is ~0.62 Mm³. Reservoir capacity is ~2.2 hm³.
- FLAC2D is used to develop the finite element model (reservoir impoundment and seismic analyses).
- Free-field B.C. is used for seismic analyses (FLAC built-in model) including deconvolution of seismic waves.
- Drucker-Prager yield criterion (or Finn model).





Thank you!

Any questions?



Seismic performance of an earth dam with strong motion input signals selected with different criteria

M. Tretola¹, G. Fiorentino², F. Sabetta², S. Sica¹

¹ **University of Sannio, Benevento, ITALY**

² Roma Tre University, Rome, ITALY

OUTLINE OF THE PRESENTATION

1

Introduction

2

Seismotectonic of the dam site

3

Input motion

4

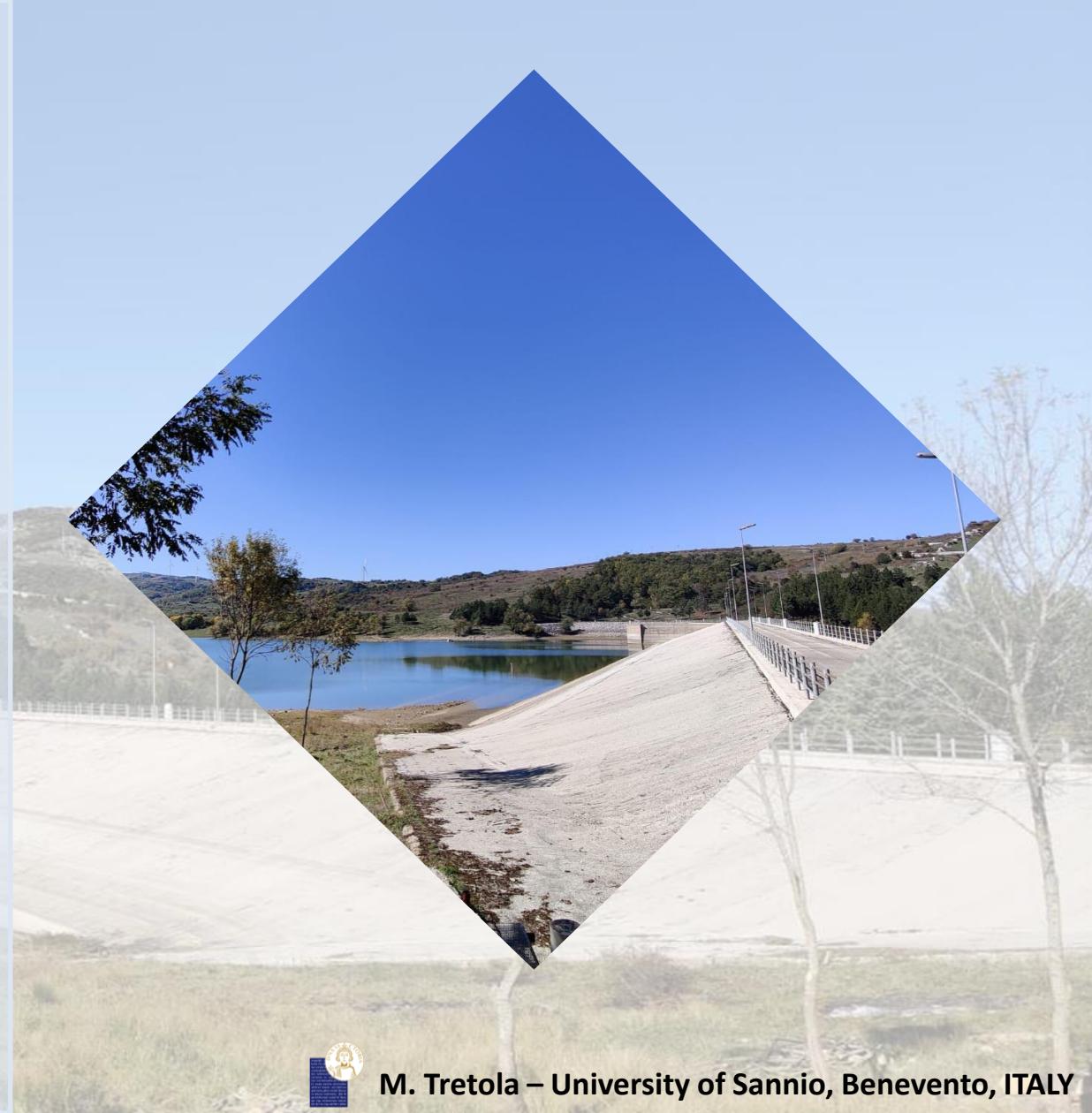
Case study: description and numerical approach

5

Results

6

Conclusions



INTRODUCTION

The most advanced technical codes and standards prescribe **nonlinear time-history analyses** to assess the seismic performance of earth dams.



The analysis results may be **highly sensitive** to the acceleration time-histories adopted to represent the reference seismic motion.



The selection of proper natural accelerograms suffers from the limited availability of recordings consistent with the expected earthquake scenarios and the local features of the dam site.

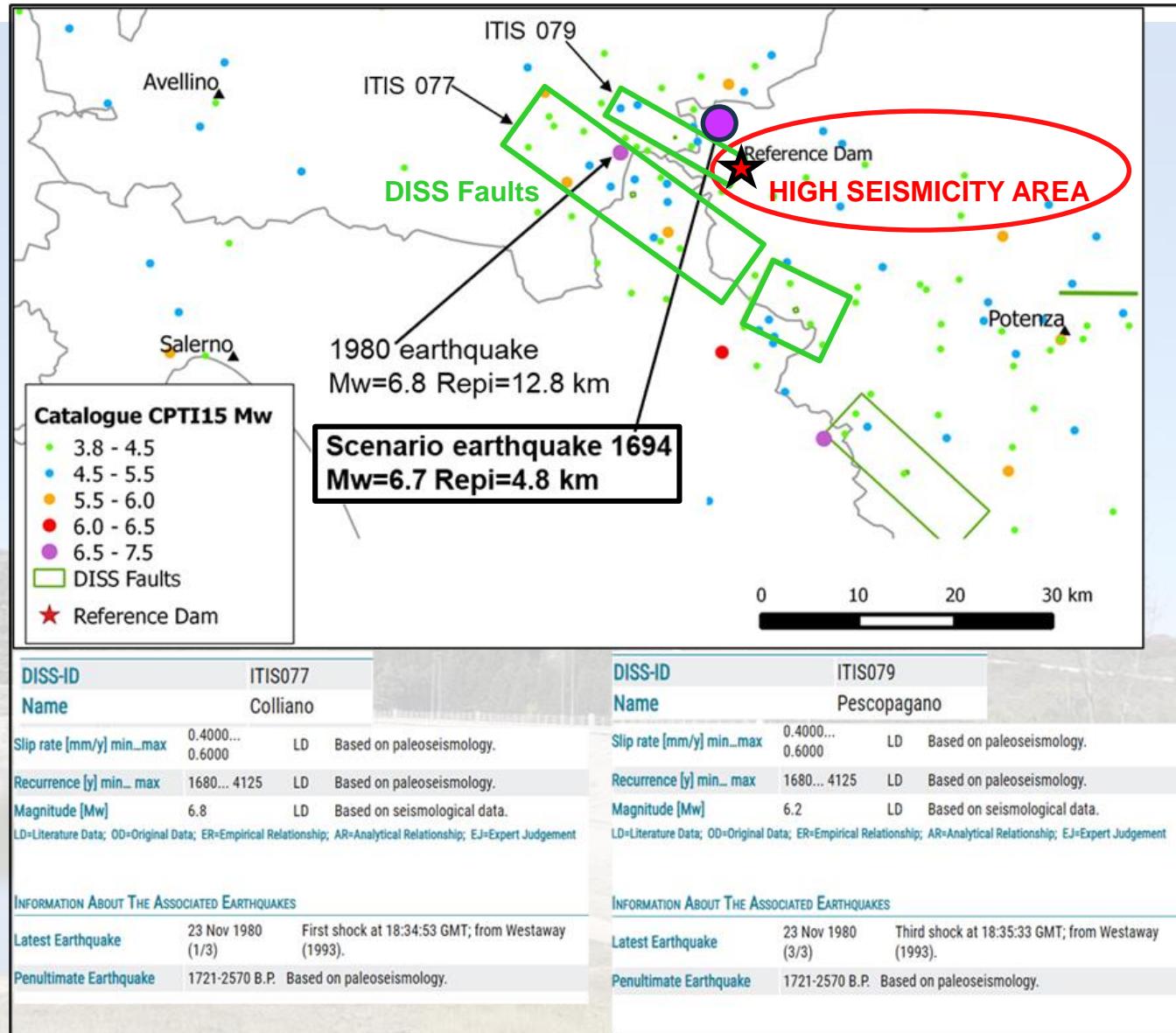


Spectrum-compatibility is usually invoked by the most advanced technical codes and standards. In Italy a **scale factor in the range 0.5÷2 should be respected**, condition difficult to be fulfilled especially for the higher return periods relevant to the ultimate limit states of a dam.

Simulated signals can be particularly helpful by overcoming these limitations.

 The goal of this study is to detect how the performance of an existing earth dam could be affected by a different choice of the spectrum-compatible input accelerations.

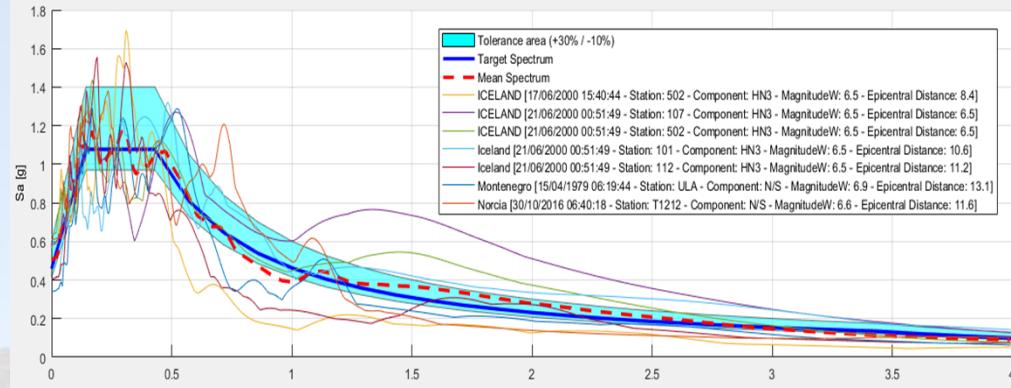
SEISMOTECTONIC OF THE DAM SITE



INPUT MOTIONS

RECORDED ACCELEROGRAMS

ENGINEERING STRONG-MOTION DATABASE (ESM)

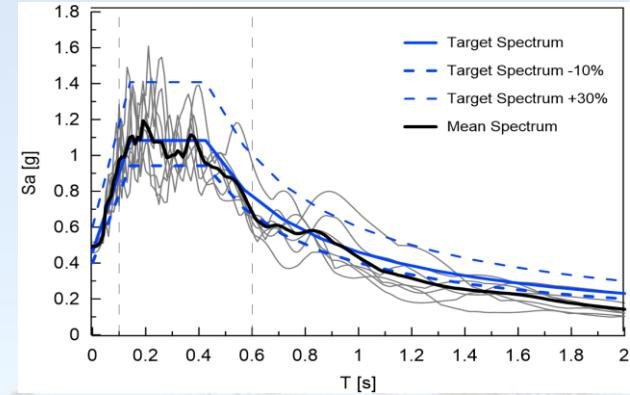


#	nation	station	PGA (g)	PGD (cm)	Arias (cm/s)	scale factor	δ
1	Italy	T1212	0.610	28.0	339.8	2.19	0.211
2	Montenegro	ULA	0.341	10.1	231.2	1.94	0.155
3	Iceland	101	0.408	28.2	208.2	3.40	0.197
4	Iceland	112	0.406	19.4	181.6	3.59	0.261
5	Iceland	107	0.586	37.1	172.2	1.06	0.212
6	Iceland	502	0.570	12.8	158.7	0.78	0.289
7	Iceland	502	0.633	18.3	156.1	1.08	0.156

DYNAMIC ANALYSES

SIMULATED ACCELEROGRAMS

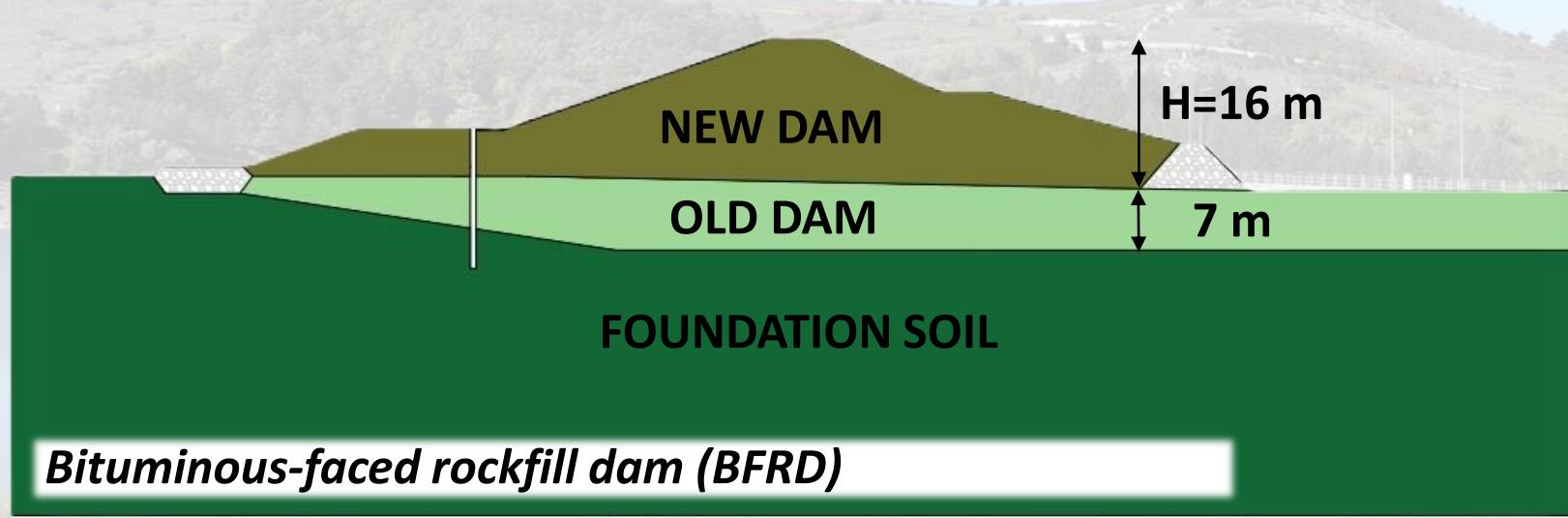
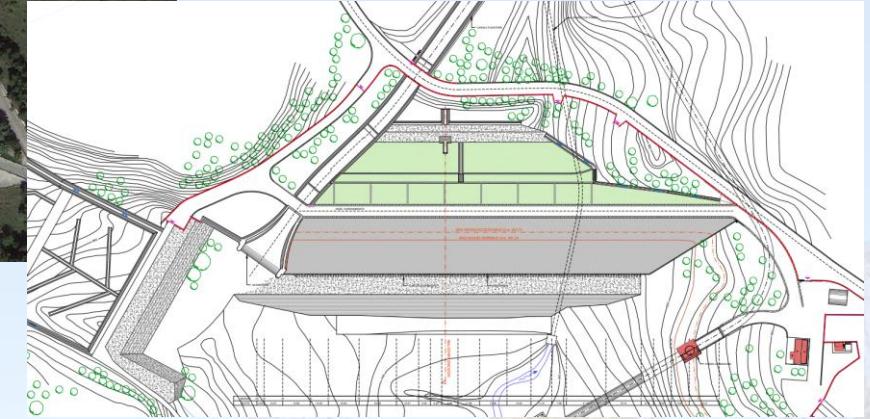
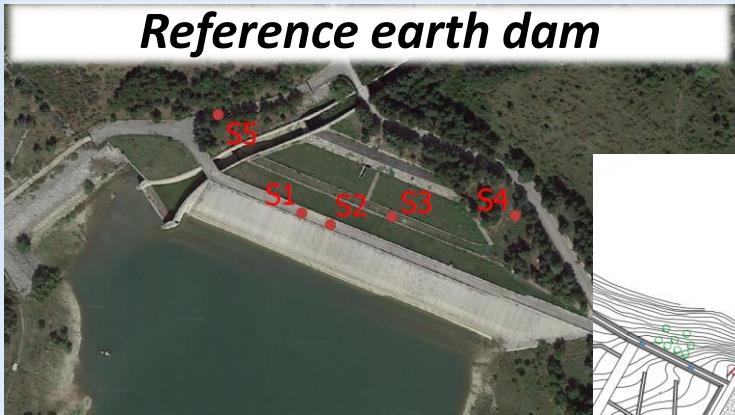
SIGMA CODE (Fiorentino, 2022)



#	Mw	R _{epi} (km)	V _{S30} (m/s)	PGA (cm/s ²)	PGD (cm)	Arias (cm/s)	Duration (s)	Scale factor	δ
60	7.0	1.1	806	485	10.1	223	9.6	1.08	0.171
210	7.0	5.0	840	490	7.5	221	8.6	0.95	0.173
26	6.9	0.0	867	506	7.3	217	8.5	1.01	0.199
178	7.0	4.9	833	480	10.4	203	9.4	0.99	0.202
19	6.8	0.0	803	493	7.4	200	7.3	1.04	0.202
87	6.9	2.2	835	474	7.3	192	11.0	1.03	0.206
24	6.9	0.0	867	449	7.8	151	10.1	1.11	0.211

CASE STUDY – REFERENCE DAM

- **1930** – construction of a homogeneous dam
- **1980** – old dam demolished and reconstructed with coarse grained soil materials – bituminous-faced rockfill dam

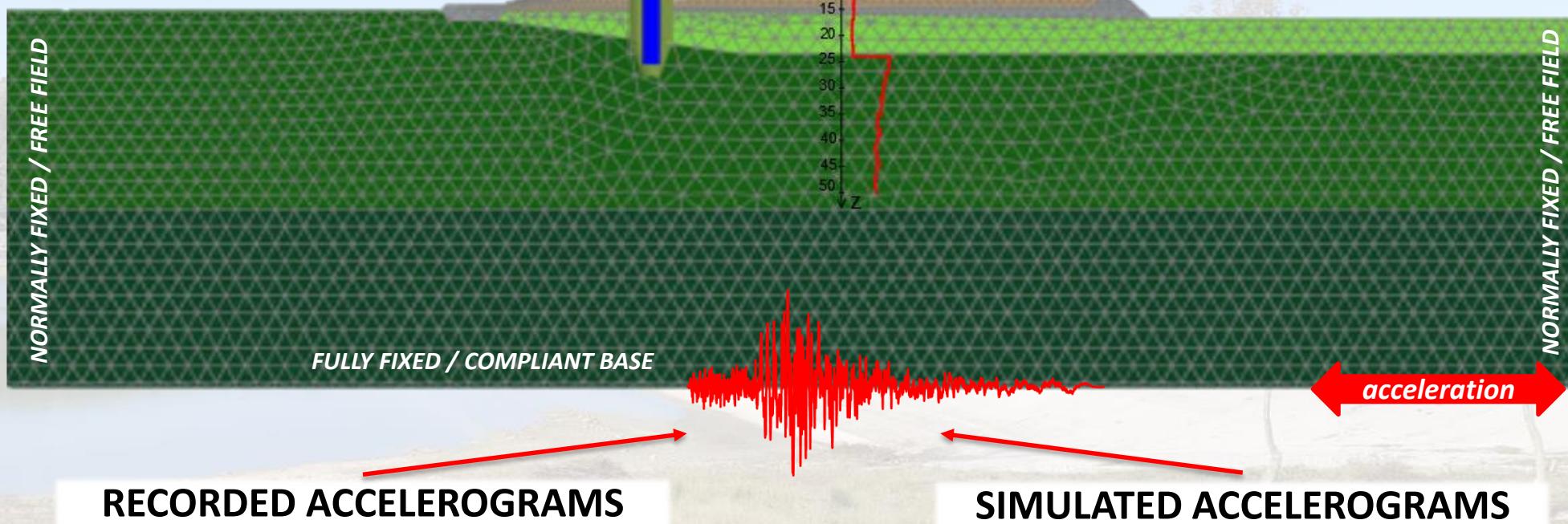


CASE STUDY – NUMERICAL APPROACH

ADVANCED DYNAMIC ANALYSIS

PLAXIS 2D

- NEW DAM BODY
- OLD DAM BODY
- FOUNDATION CLAY 1
- FOUNDATION CLAY 2

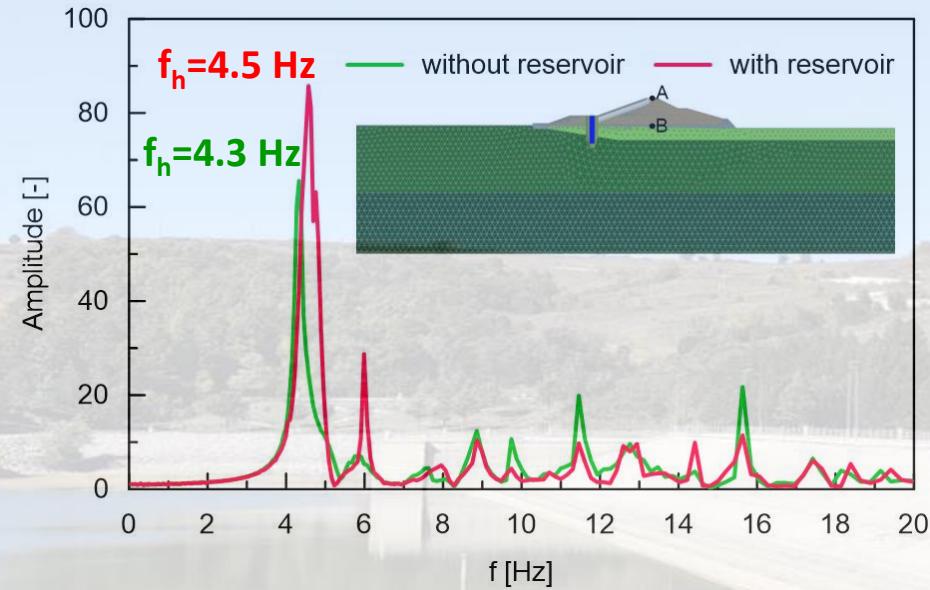


RESULTS - Natural vibration frequencies of the dam

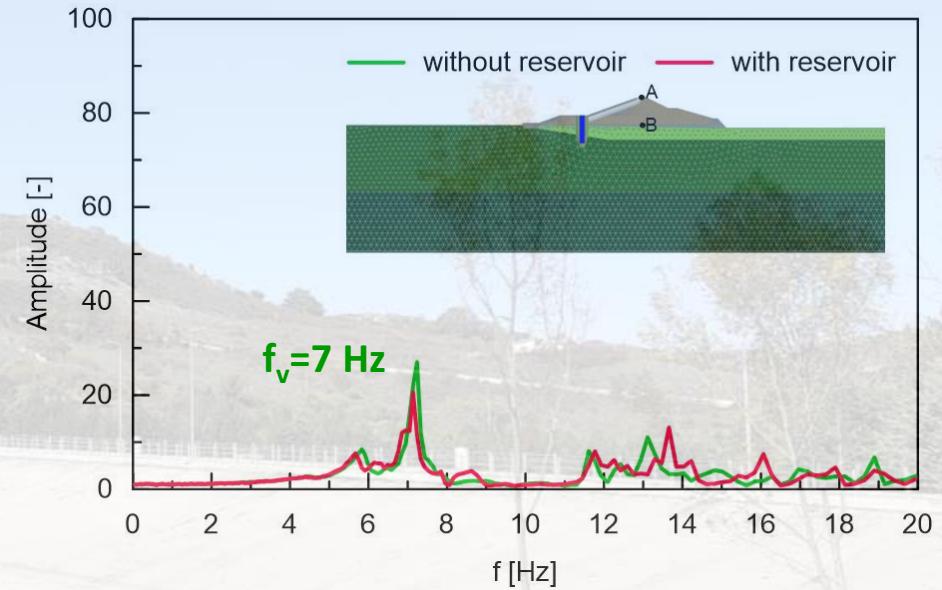
 FULL RESERVOIR

 EMPTY RESERVOIR

HORIZONTAL FUNDAMENTAL FREQUENCY



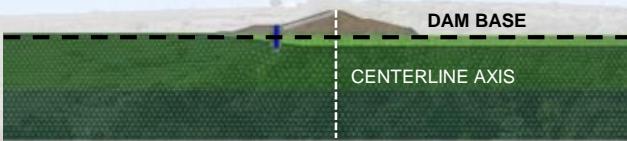
VERTICAL FUNDAMENTAL FREQUENCY



RESULTS - Recorded vs simulated displacements

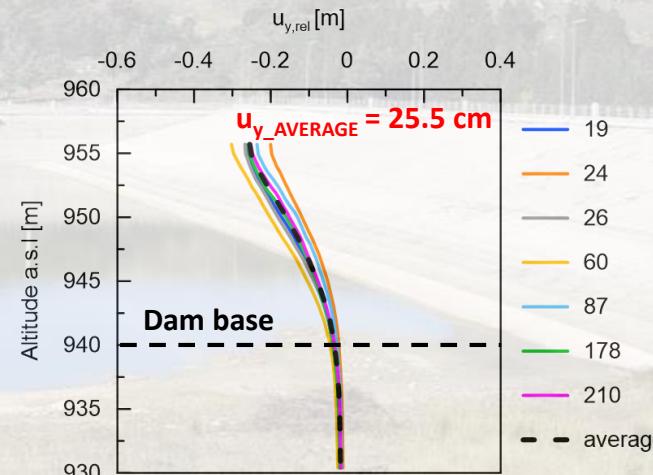
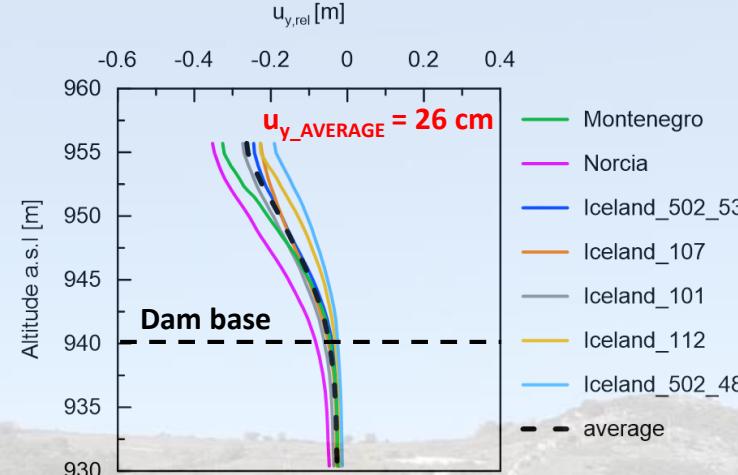
COLLAPSE LIMIT STATE
 $(T_R=1950 \text{ years})$

RECORDED INPUT SIGNALS

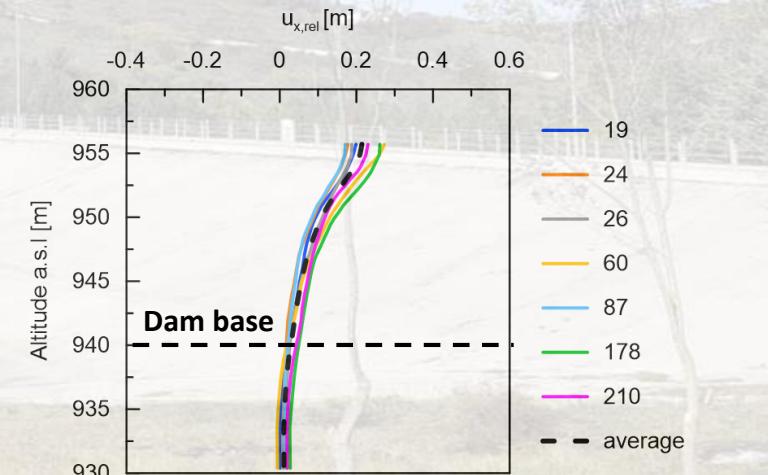
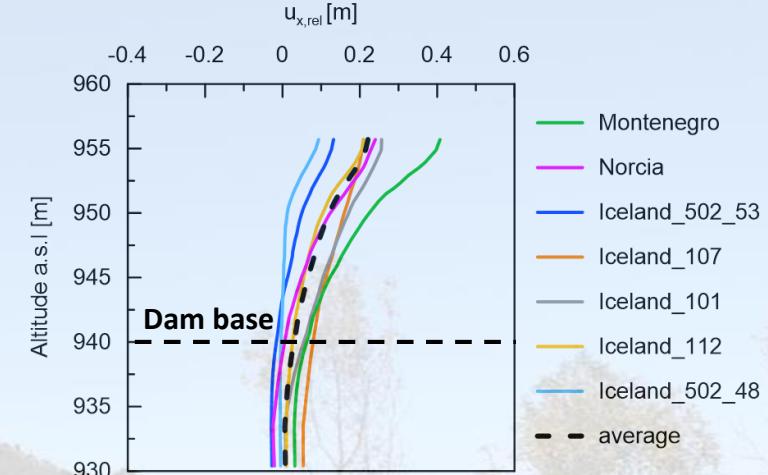


SIMULATED INPUT SIGNALS

SEISMIC-INDUCED VERTICAL DISPLACEMENTS



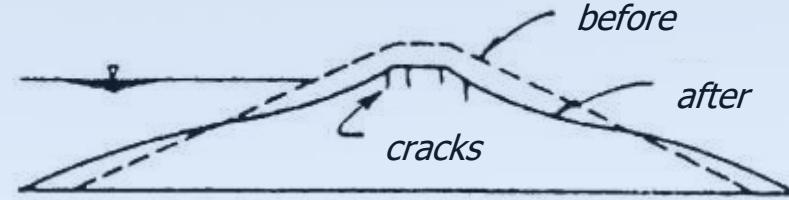
SEISMIC-INDUCED HORIZONTAL DISPLACEMENTS



RESULTS - Recorded vs simulated displacements

COLLAPSE LIMIT STATE
 $(T_R=1950 \text{ years})$

FREEBOARD LOSS DAMAGE



$$w/H = 1.4\%$$

RECORDED ACCELEROMETERS

SIMULATED ACCELEROMETERS

Damage class		Max longitudinal crack width (mm)	Max relative settlement at the crest (%)
#	Description		
0	None	< 10	<0.03
1	Slight	10-30	0.03-0.2
2	Moderate	30-80	0.2-0.5
3	Significant	80-150	0.5-1.5
4	Severe	150-550	1.5-5
5	Collapse	>500	>5



(Pells and Fell, 2003; Swaisgood, 1995 - 1998)

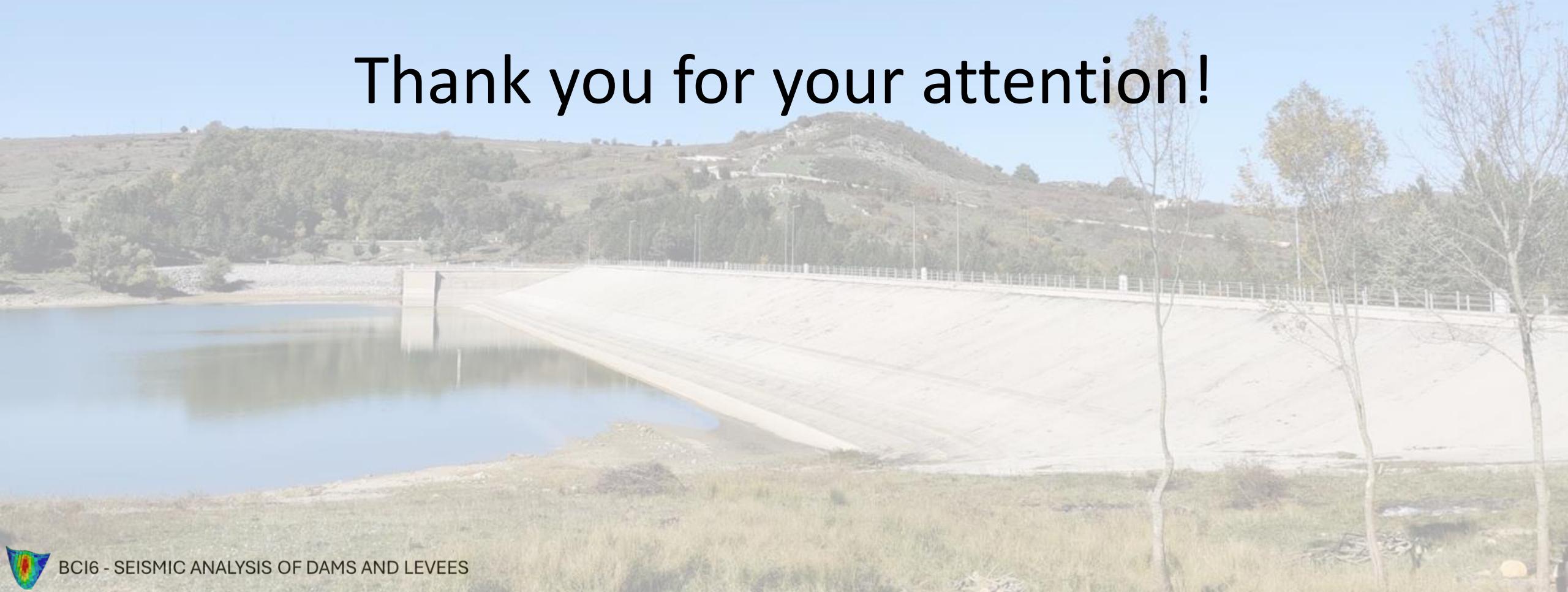
CONCLUSIONS

- A sensitivity analysis was carried out to ascertain how different selection criteria of the input acceleration time-histories could impact the seismic performance of **an existing earth dam**.
- Finding natural recordings satisfying all the requirements of seismic compatibility can be challenging, especially for very high return periods. **Simulated accelerograms** can be particularly helpful by overcoming these limitations.
- The results show that the two sets of input signals, selected through different criteria, do not significantly affect typical damage indicators for earth dams, such as the freeboard loss.
- When it is difficult to find natural accelerograms consistent with the seismic scenario at the dam site, the use of simulated input signals (e.g. SIGMA CODE) could be promising.
- As a perspective of this study, additional dynamic analyses accounting for the vertical component of the input motions (neglected) and Uniform Hazard Spectrum compatibility will be implemented.





Thank you for your attention!





EFFECT OF INTERNAL STRUCTURE OF LEVEES ON THE SEISMIC AND SEEPAGE BEHAVIOR

Ryosuke Uzuoka ¹, Shogo Yamada ¹, Kyohei Ueda ¹

¹ Disaster Prevention Research Institute, Kyoto University, Japan

Damage of river levee during earthquake

Deformation form of damaged levee depends on the internal structure.

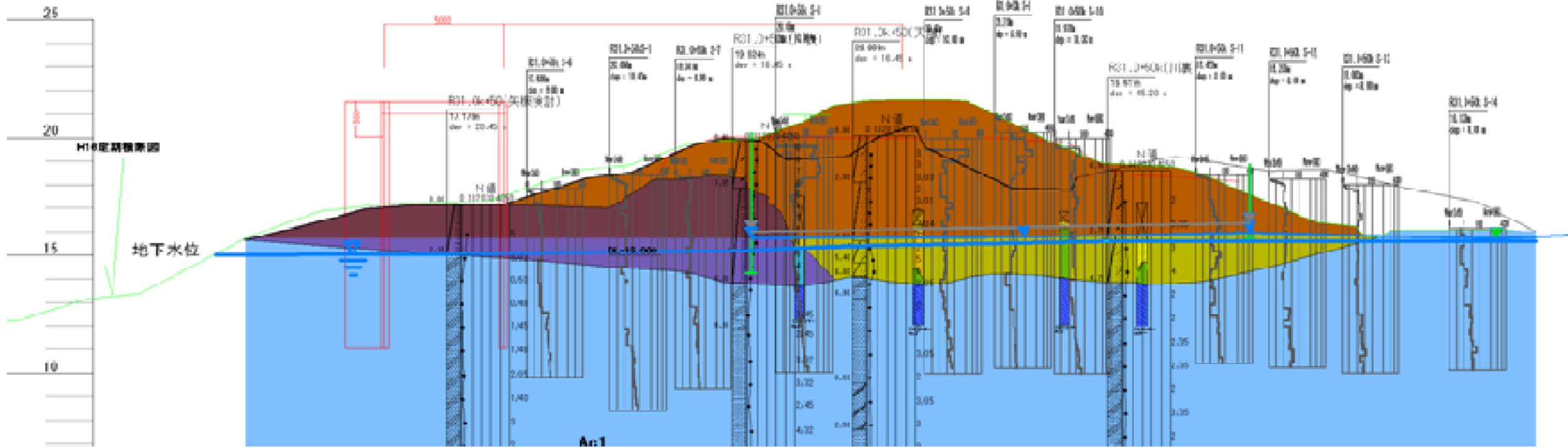


Figure 2. Open-cut survey of Abukuma River levee after the 2011 off the Pacific coast of Tohoku Earthquake (MLIT, 2011). (yellow: sand, brown: sand and gravel, blue: clay, violet: silt)

Damage of river levee during post-earthquake rainfall

Heavy rainfall in June 2016 caused cascading disaster after the Kumamoto Earthquake in April 2016.



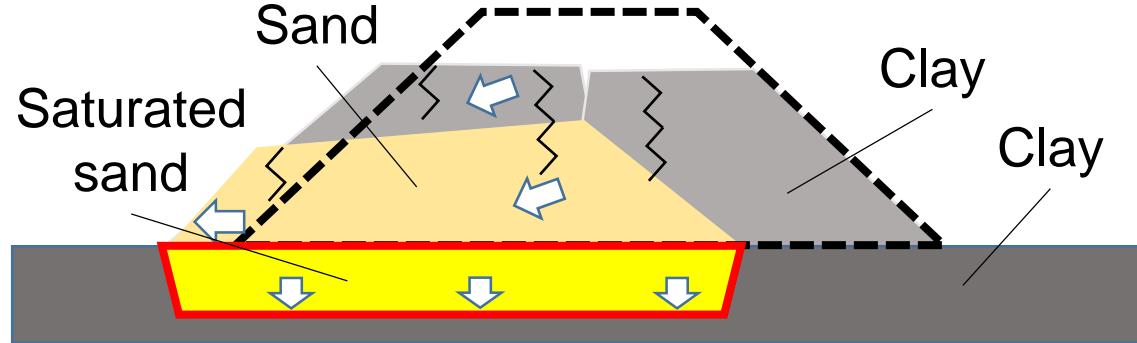
Objectives

We examined the effects of the internal structure of river levees on seismic deformation during shaking and post-shaking seepage performance.

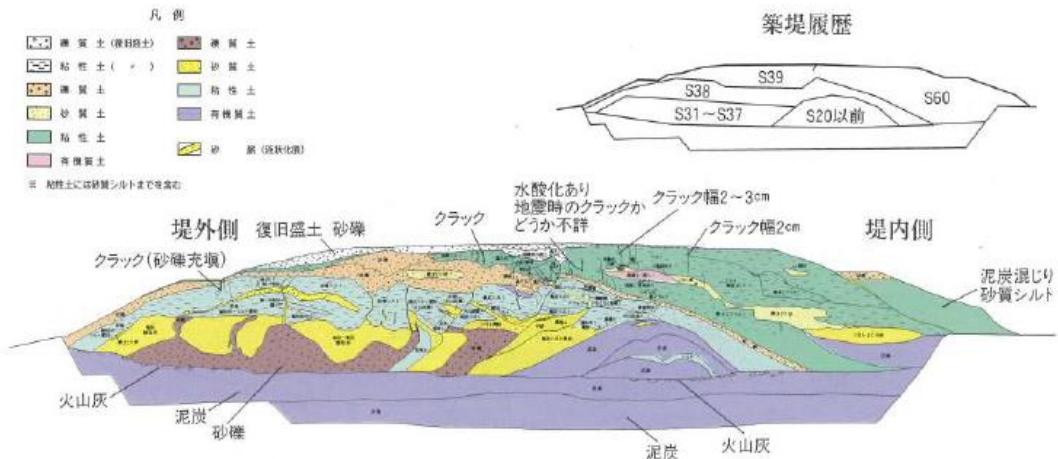
1. By interpreting the open-cut survey results of past damaged river levees and classifying them according to the internal structure, we summarized the failure types and deformation forms induced by earthquake with different internal structures.
2. We investigated seismic behavior during shaking and post-shaking seepage behavior of embankments with different internal structures using dynamic centrifugal model tests.

Classification of failure types (eight) in damage cases

Type: C-1

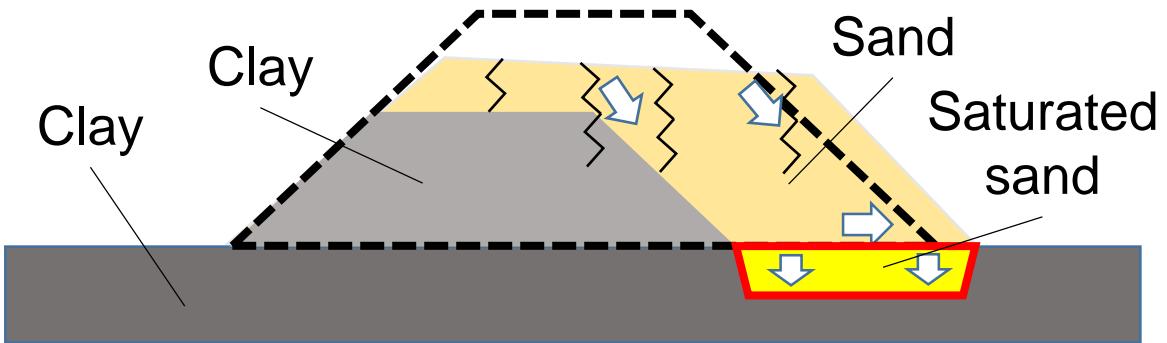


Internal structure and deformation form

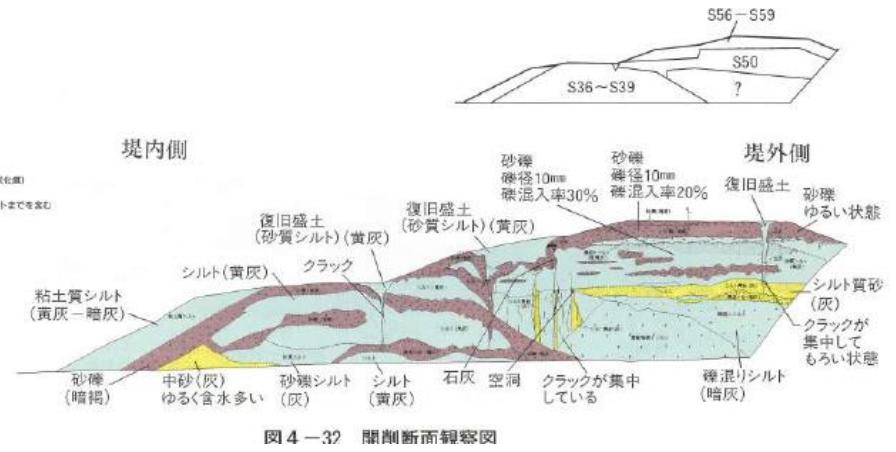


Typical damage case

Type: D-1



Internal structure and deformation form

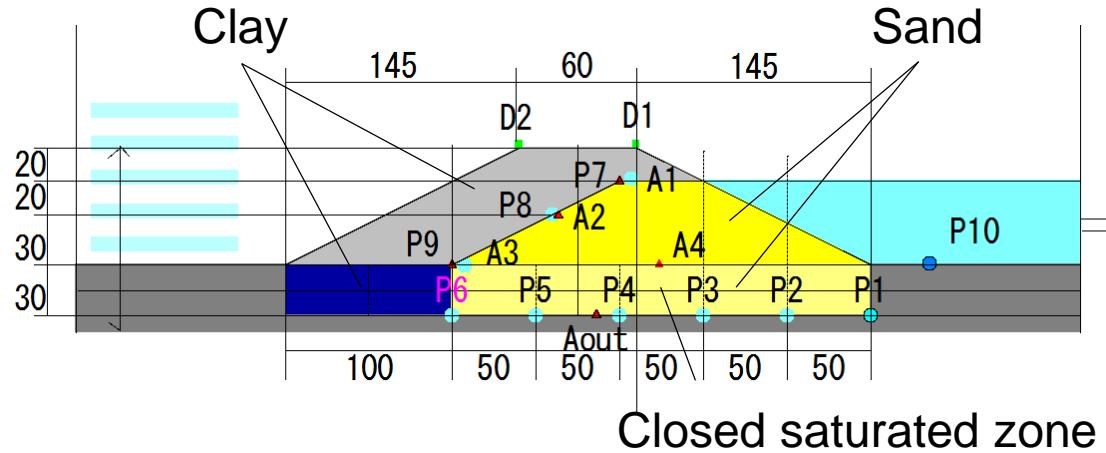


Typical damage case

Centrifuge experiments (50G)

Type: C-1

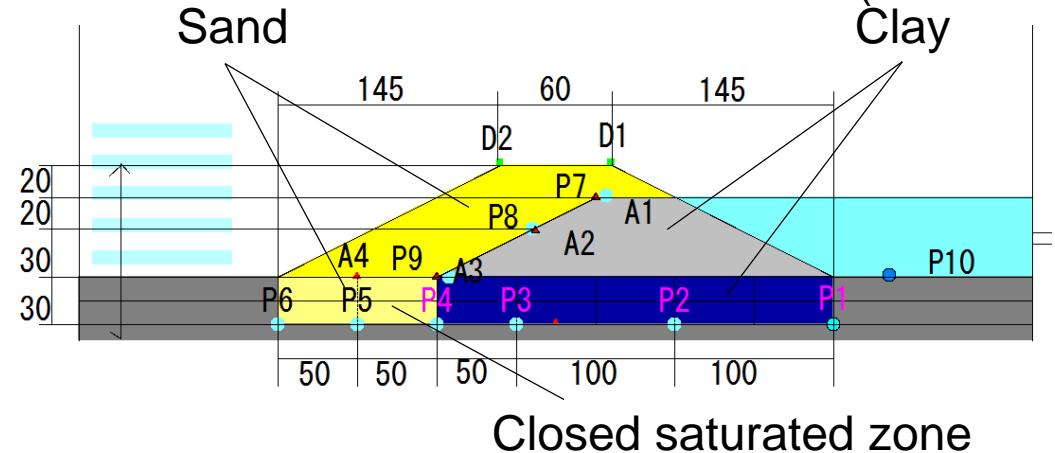
Case 1, 2, 3



Type: D-1

Case 4, 5, 6

Model scale (unit: mm)



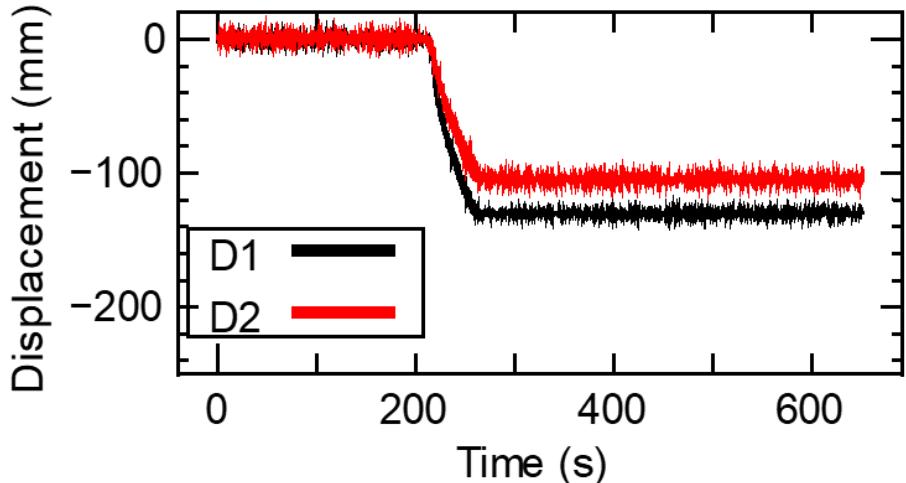
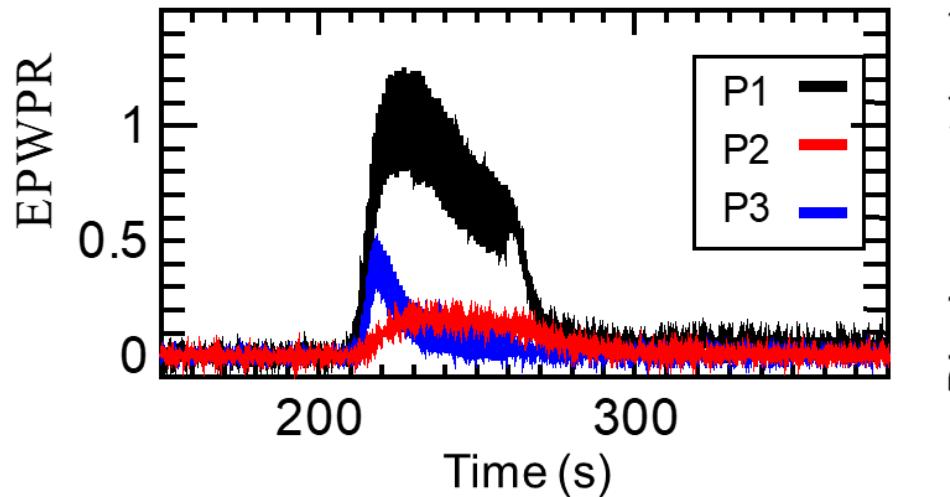
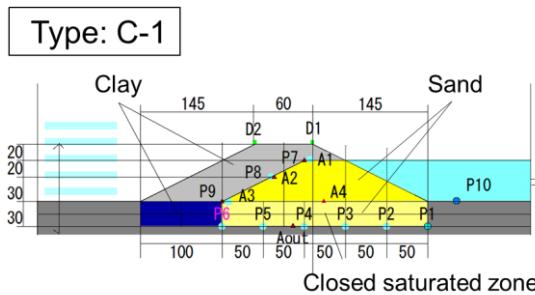
Case	Old embankment body	New embankment body	Shaking
Case 1	Sandy soil	Clayey soil	None
Case 2	Sandy soil	Clayey soil	Weak (2 m/s^2 with 20 cycles)
Case 3	Sandy soil	Clayey soil	Strong (3 m/s^2 with 40 cycles)
Case 4	Clayey soil	Sandy soil	None
Case 5	Clayey soil	Sandy soil	Weak (2 m/s^2 with 20 cycles)
Case 6	Clayey soil	Sandy soil	Strong (3 m/s^2 with 40 cycles)

Water level was raised to 1.35 m, 2.70 m and to the embankment top with 3.5 m in prototype scale after the shaking.

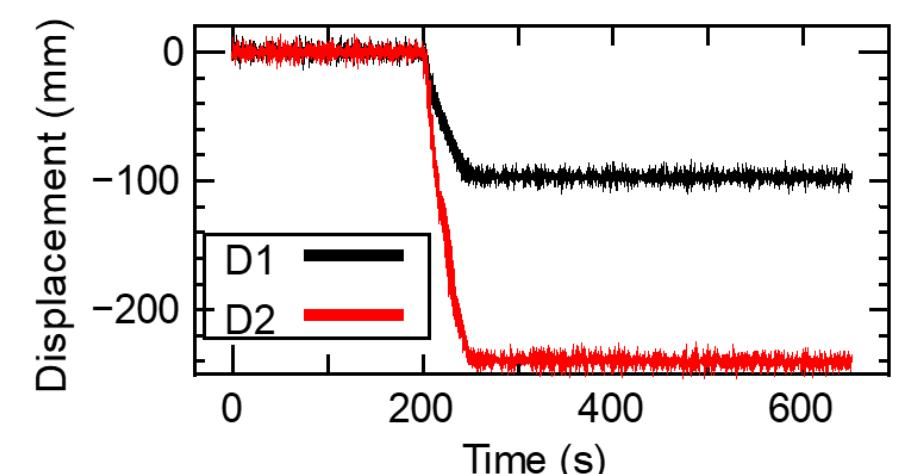
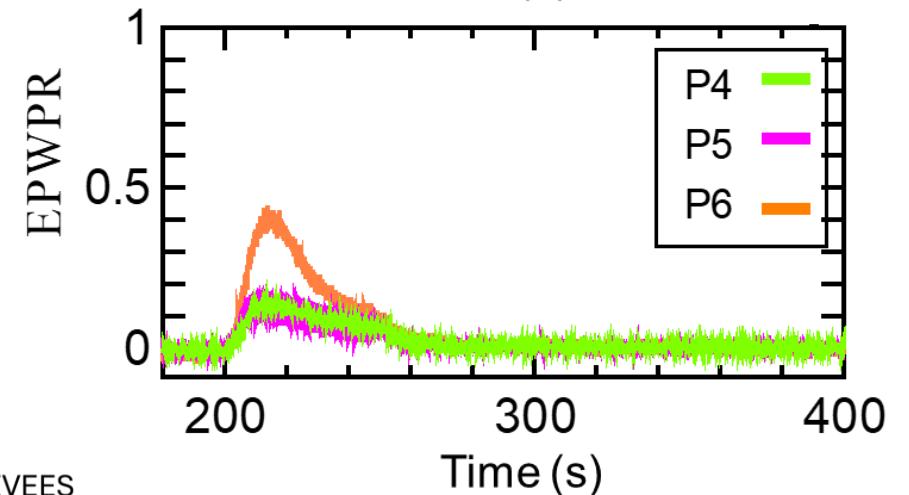
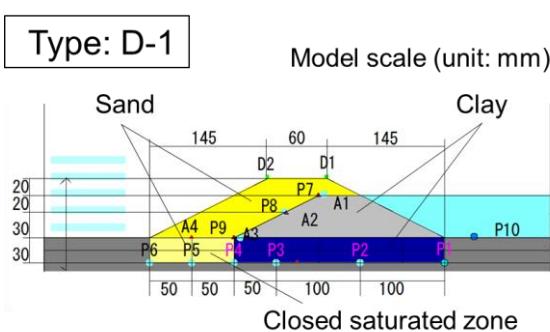
Seismic behavior during shaking

The results of seismic deformation showed the similar tendency as the past damage cases.

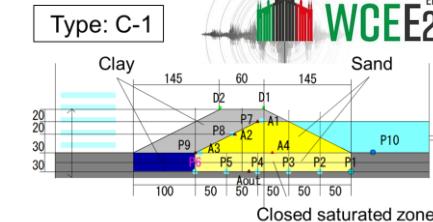
Case 3



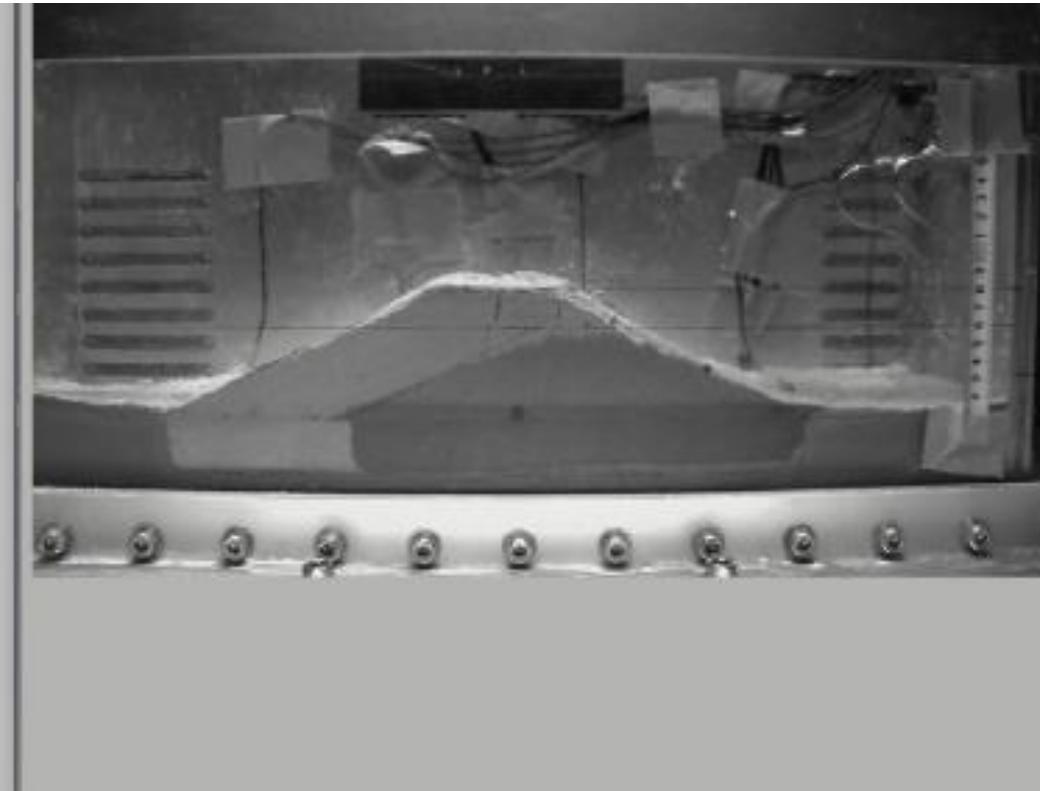
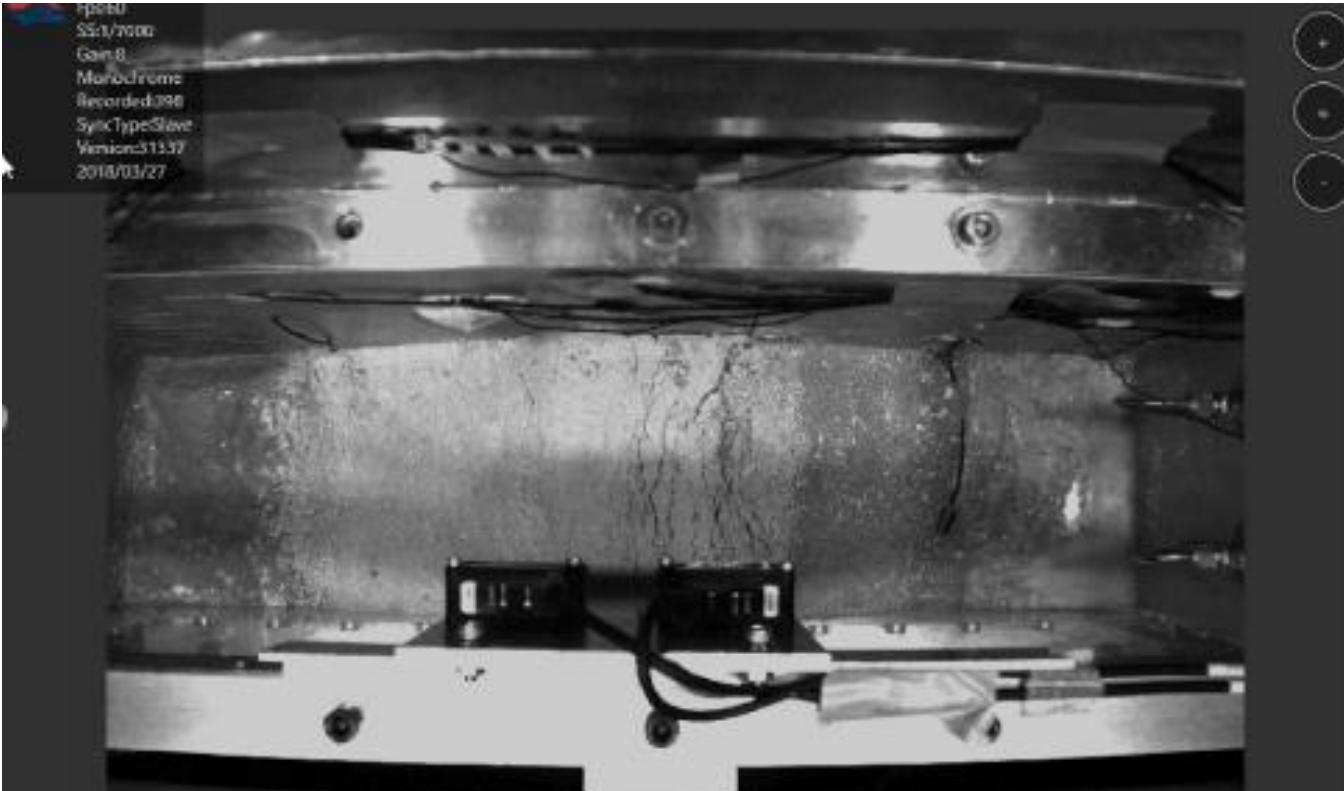
Case 6



Post-shaking seepage behavior (Case 3)

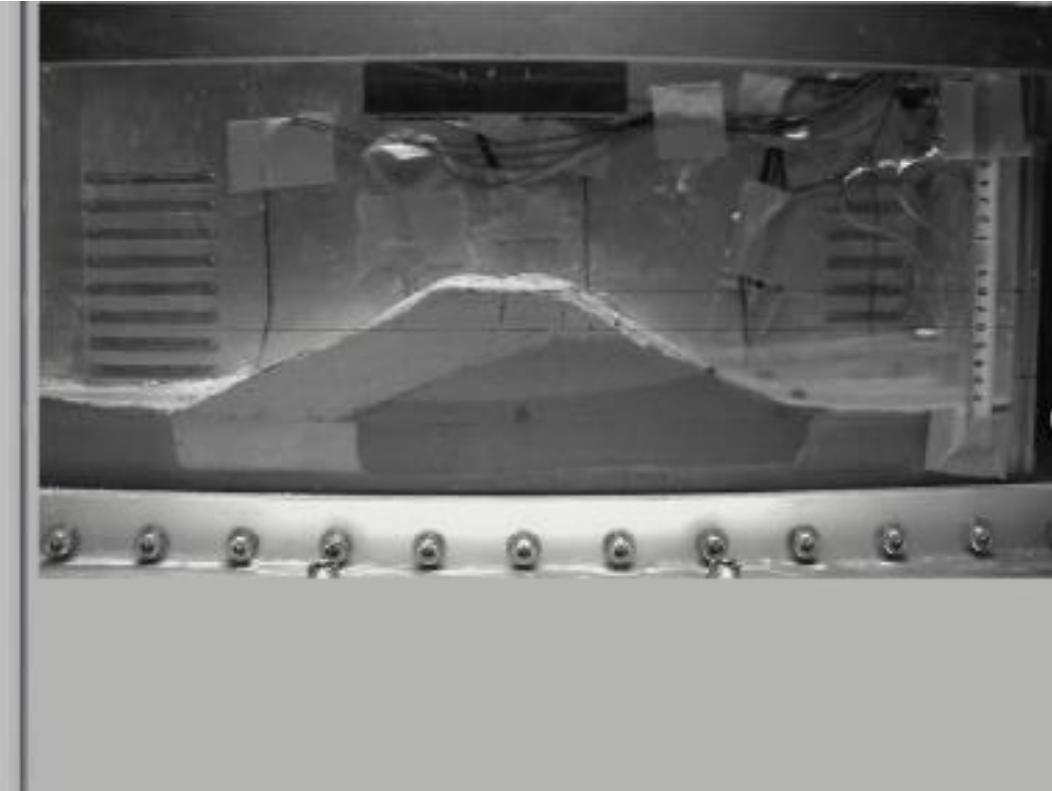


Cracks induced by shaking expanded as water level rose. Seepage failure occurred near the foot of the slope.

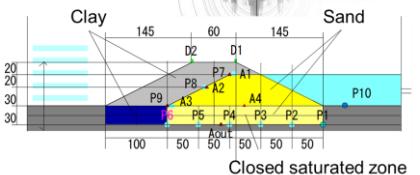


Post-shaking seepage behavior (Case 3)

Cracks induced by shaking expanded as water level rose. Seepage failure occurred near the foot of the slope.

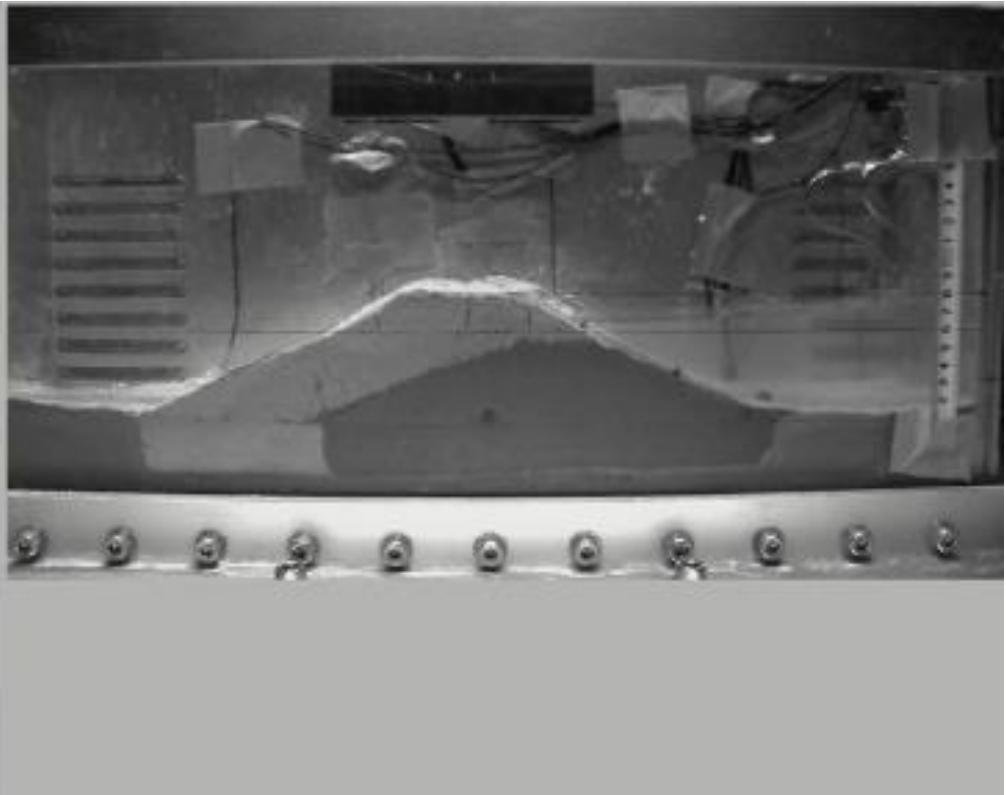
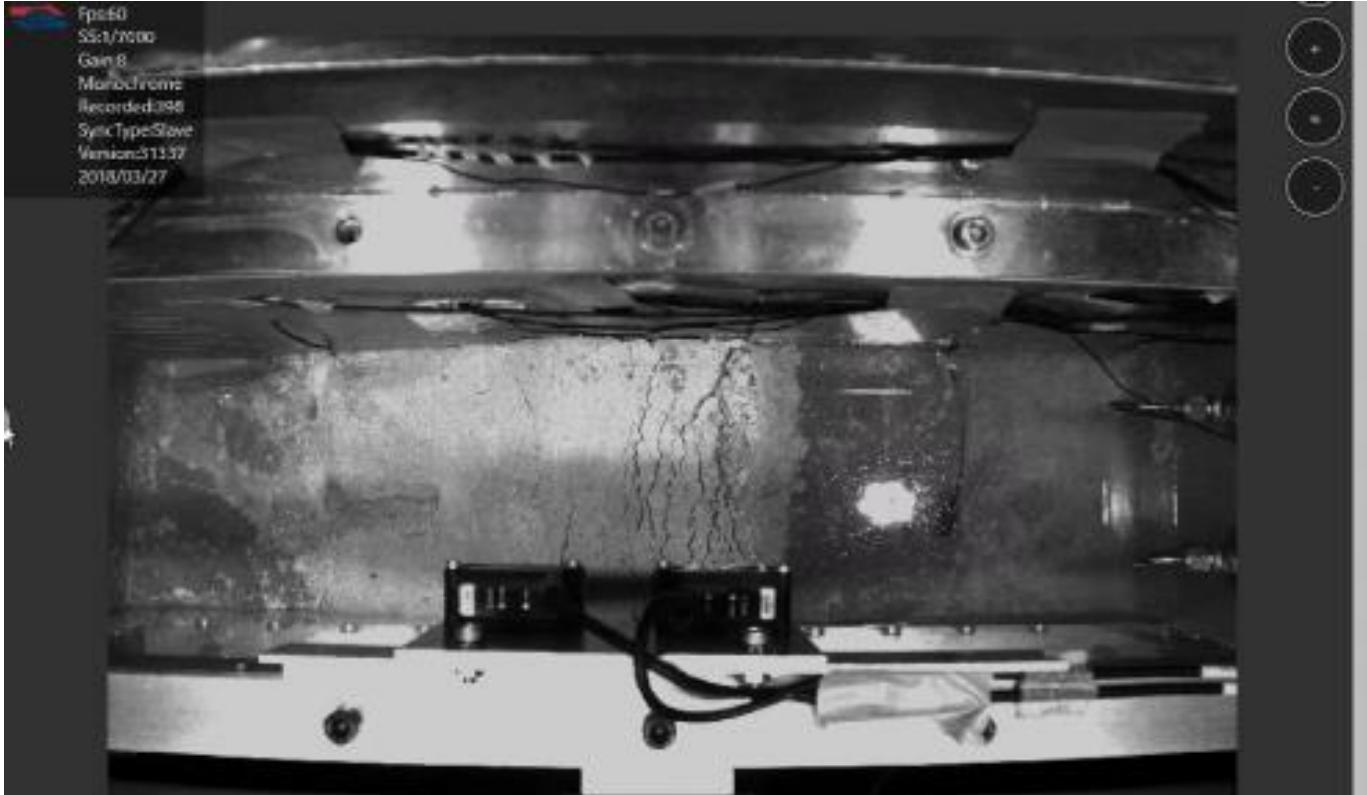


Type: C-1

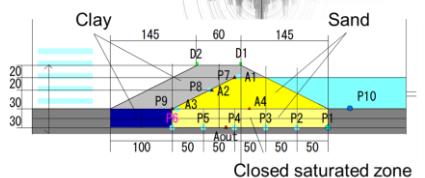


Post-shaking seepage behavior (Case 3)

Cracks induced by shaking expanded as water level rose. Seepage failure occurred near the foot of the slope.



Type: C-1

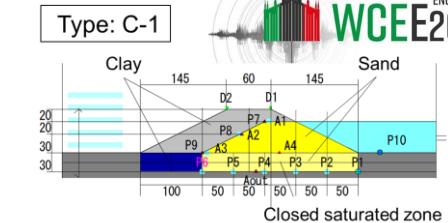


Post-shaking seepage behavior (Case 3)

Cracks induced by shaking expanded as water level rose. Seepage failure occurred near the foot of the slope.



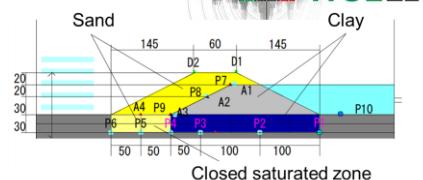
Post-shaking seepage behavior (Case 3)



Cracks induced by shaking expanded as water level rose. Seepage failure occurred near the foot of the slope.

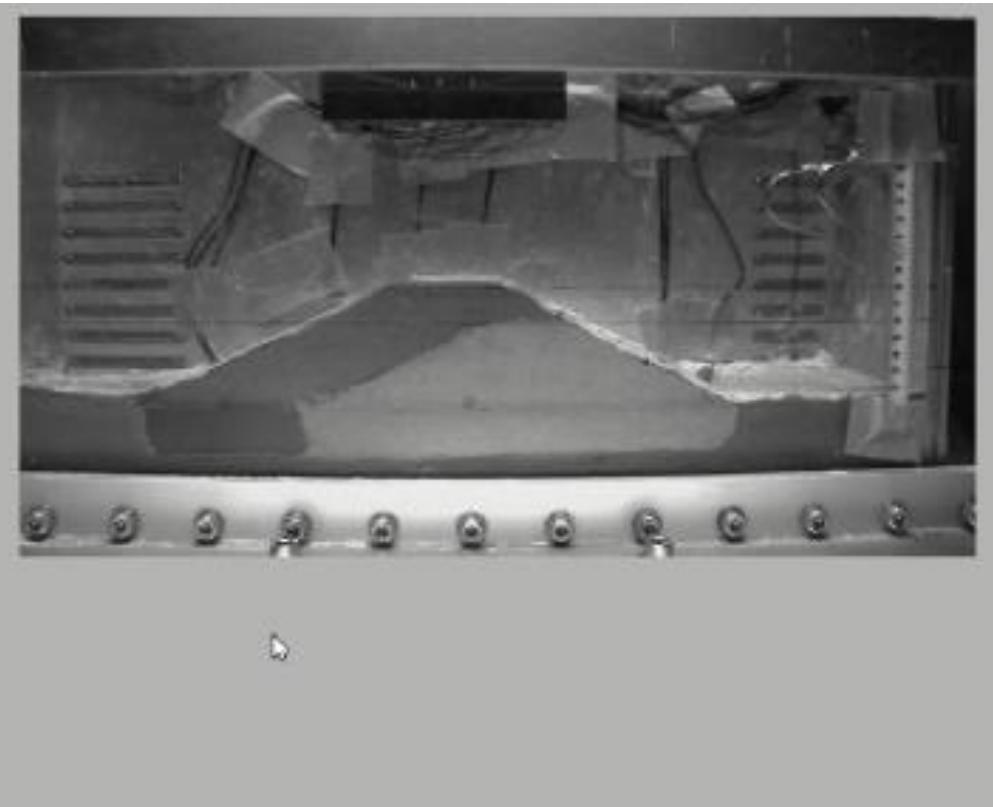
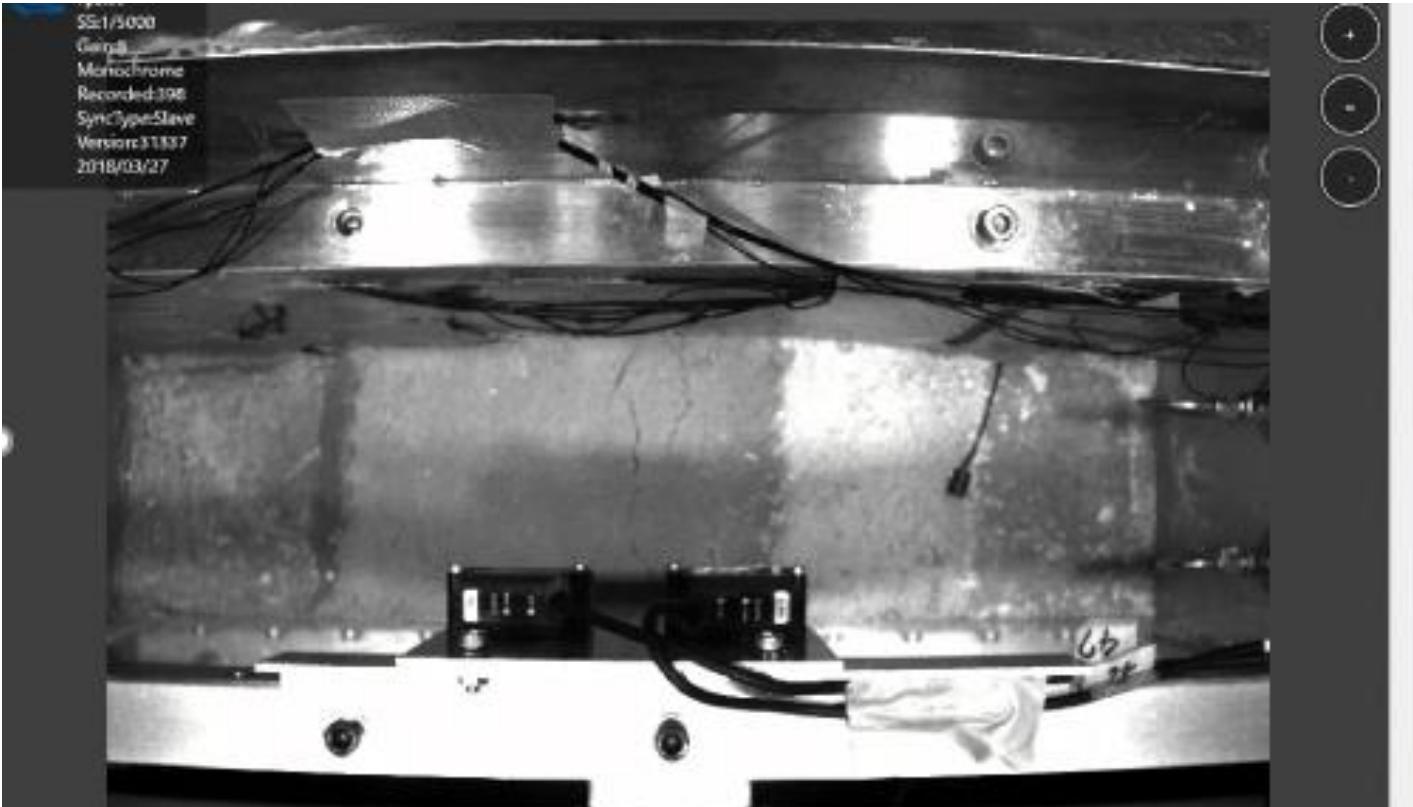


Type: D-1

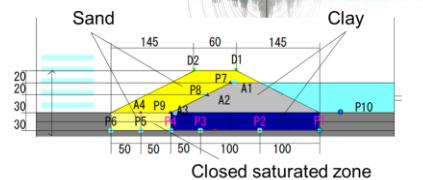


Post-shaking seepage behavior (Case 6)

Cracks at the top increased as water level rose, and overflow occurred when the water level reached near the top.

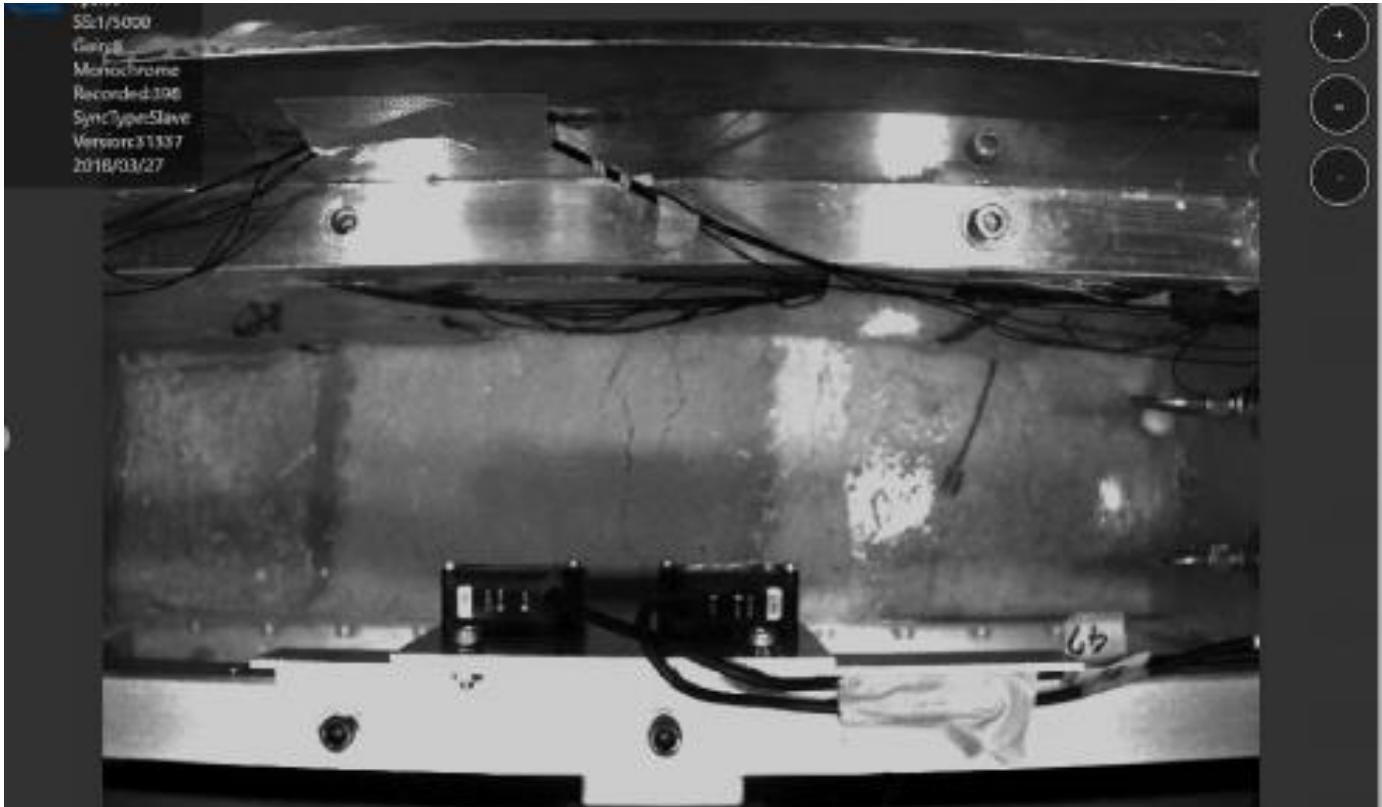


Type: D-1

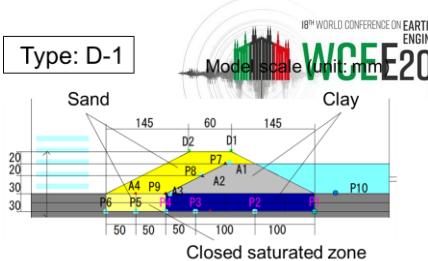


Post-shaking seepage behavior (Case 6)

Cracks at the top increased as water level rose, and overflow occurred when the water level reached near the top.

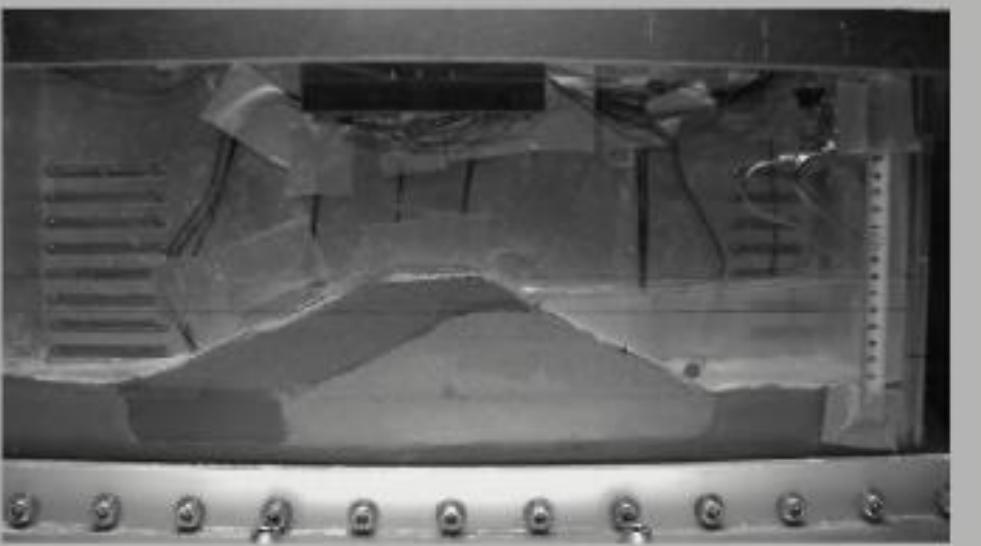
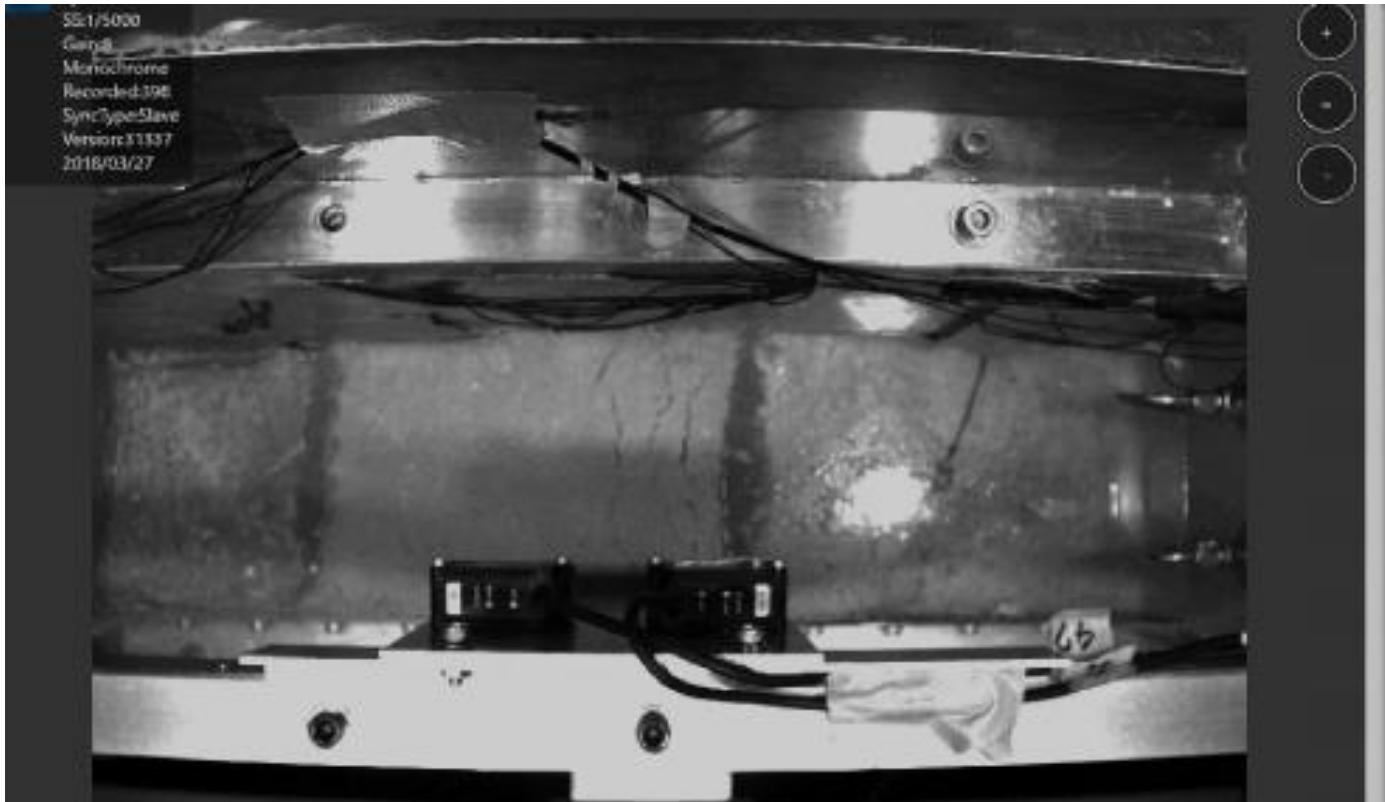


Type: D-1

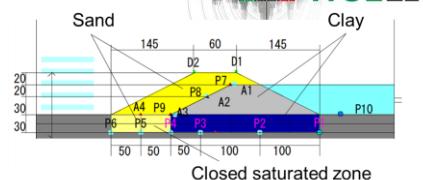


Post-shaking seepage behavior (Case 6)

Cracks at the top increased as water level rose, and overflow occurred when the water level reached near the top.

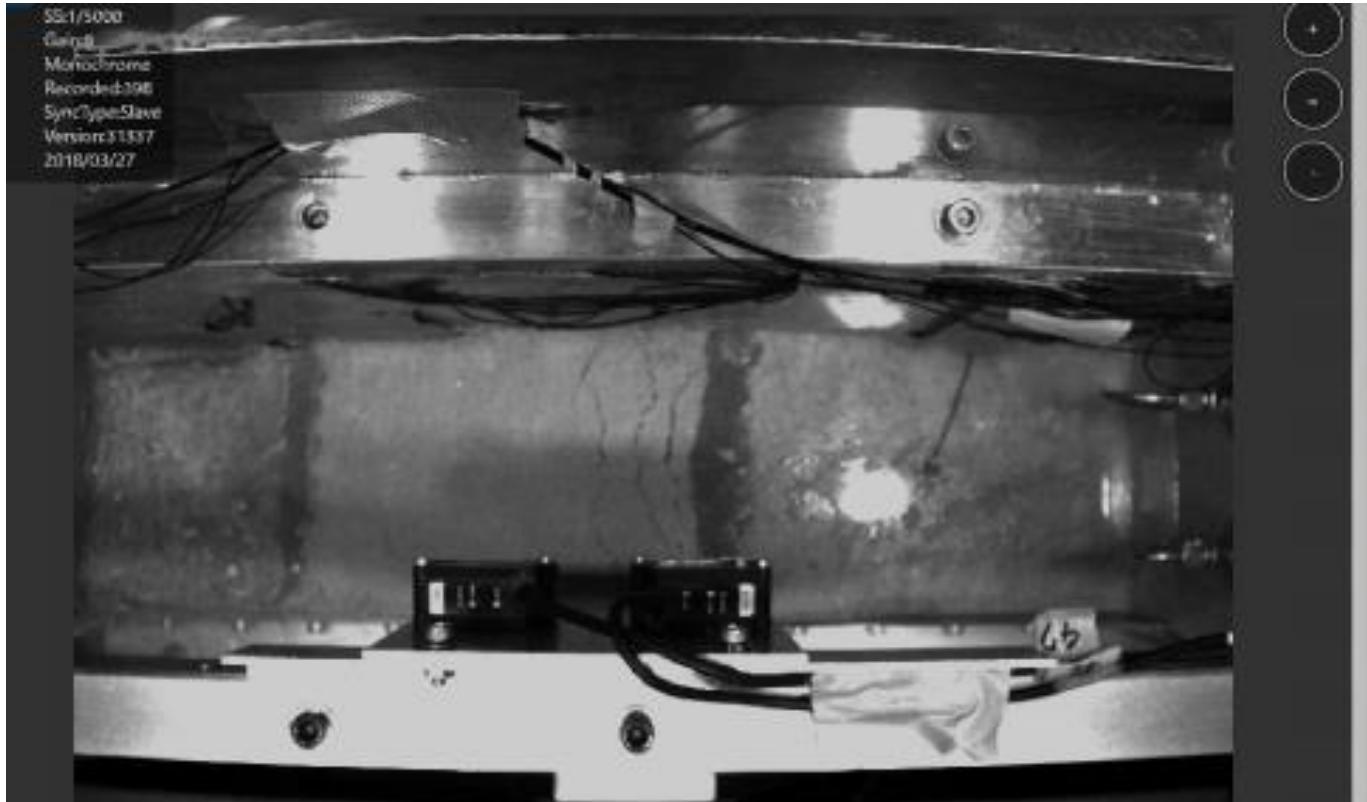


Type: D-1

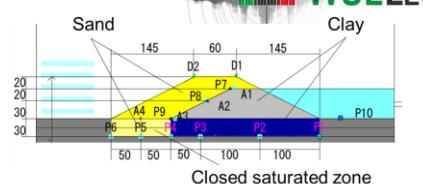


Post-shaking seepage behavior (Case 6)

Cracks at the top increased as water level rose, and overflow occurred when the water level reached near the top.

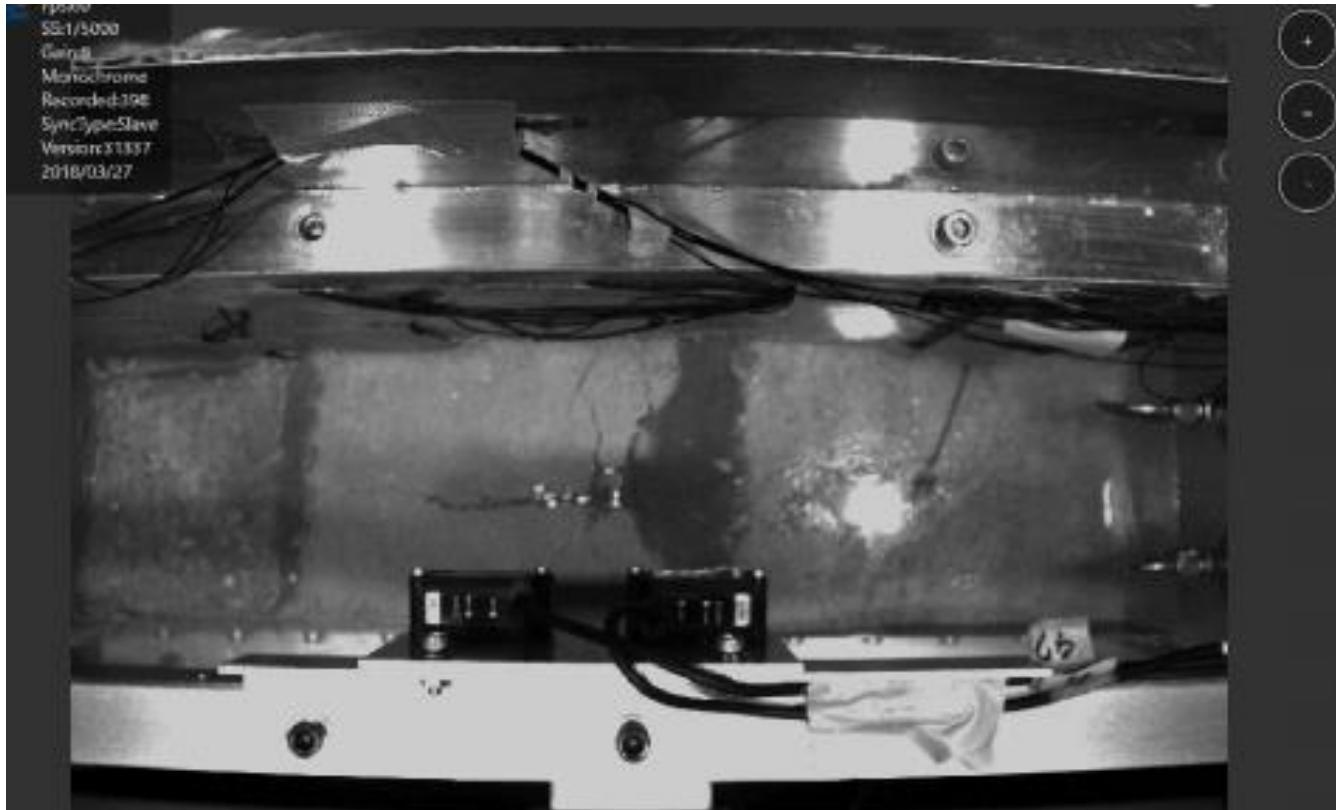


Type: D-1



Post-shaking seepage behavior (Case 6)

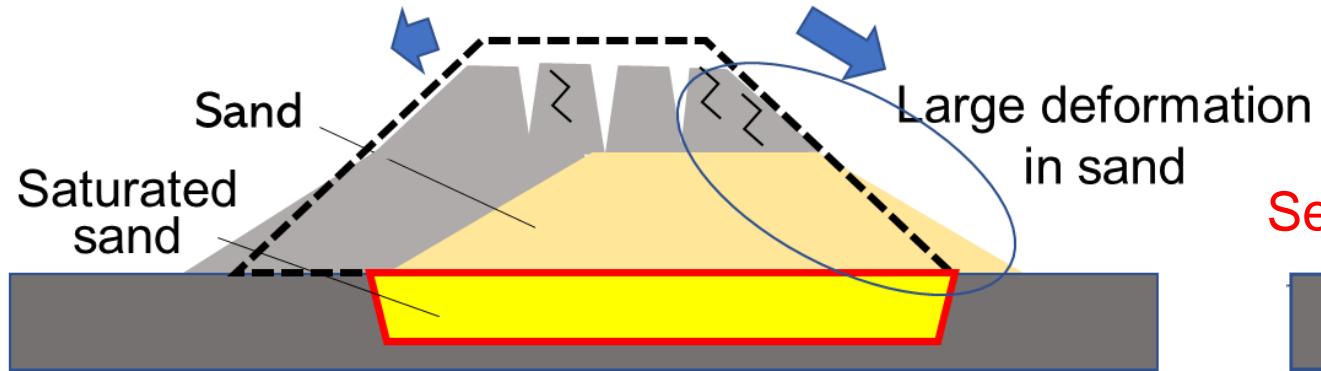
Cracks at the top increased as water level rose, and overflow occurred when the water level reached near the top.



Conclusions of the centrifuge experiments

Case 1, 2, 3

Shaking



Post-shaking seepage

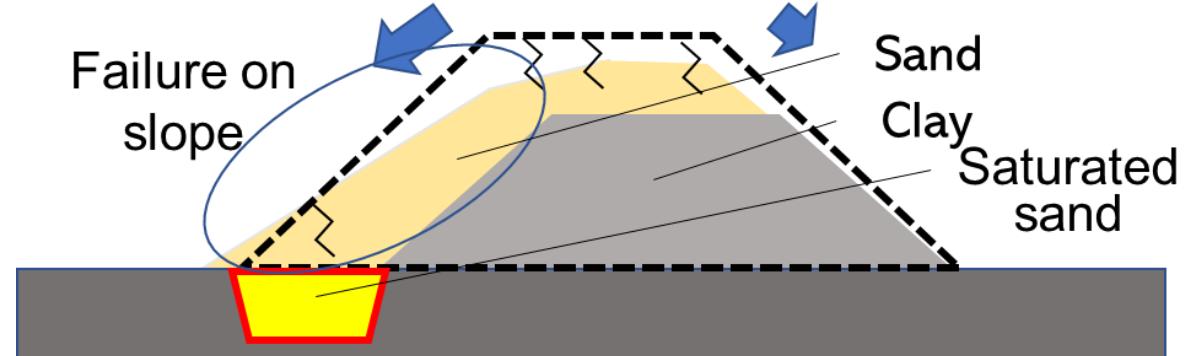
Cracks expand

Seepage failure



Case 4, 5, 6

Shaking

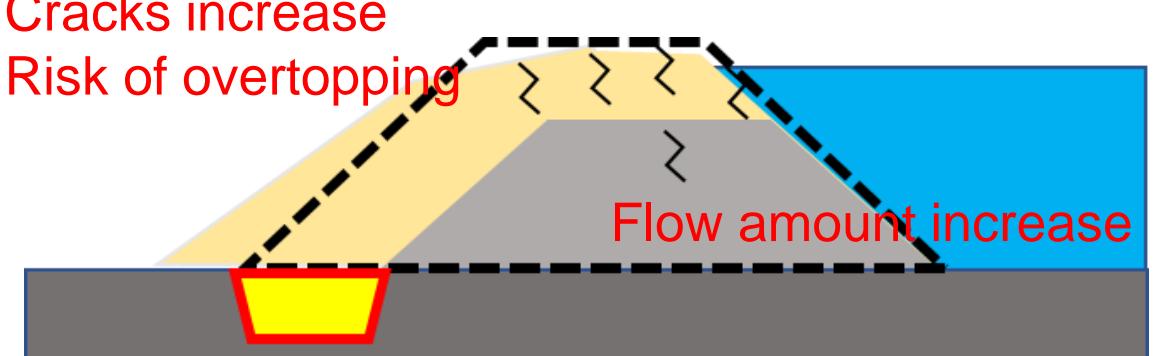


Post-shaking seepage

Cracks increase

Risk of overtopping

Flow amount increase



Conclusions

- By interpreting the open-cut survey results of past damaged river levees and classifying them according to the internal structure, we summarized the failure types and deformation forms induced by earthquake with different internal structures.
- We investigated seismic behavior during shaking and post-shaking seepage behavior of embankments with different internal structures using dynamic centrifugal model tests.
- The seismic deformation of levee in the model test showed the similar tendency as observed in the past damaged cases.
- The difference in the internal structure caused different seismic behavior during shaking and different post-shaking seepage behavior.



Thank you!

Any questions?



Seismic Assessment of the Garcia Dam

Presenting:

Eng. Roberta Vincifora

Technical Specialist, Harpaceas

Structural and Geotechnical Engineering Department

Authors:

Eng. Roberta Vincifora, Eng. Giuseppe Amato, Eng. Marco Filippo Ferotto, Eng. Salvatore Pagnotta, Eng. Alphonso Cusmano, Eng. Salvatore Volo

Seismic Assessment of the Garcia Dam



The Garcia Dam, located in the Belice Valley of Sicily (Italy), is a **critical infrastructure** that provides water for irrigation to the surrounding agricultural areas, allowing for continuity in the valley agri-food production.

The Dam was designed and built before the introduction of the current seismic hazard classification of the Italian territory, which made it necessary to provide a **seismic assessment** of the Dam in order to guarantee the safety of the areas located on the downstream side.

Seismic Hazard and Dam Safety



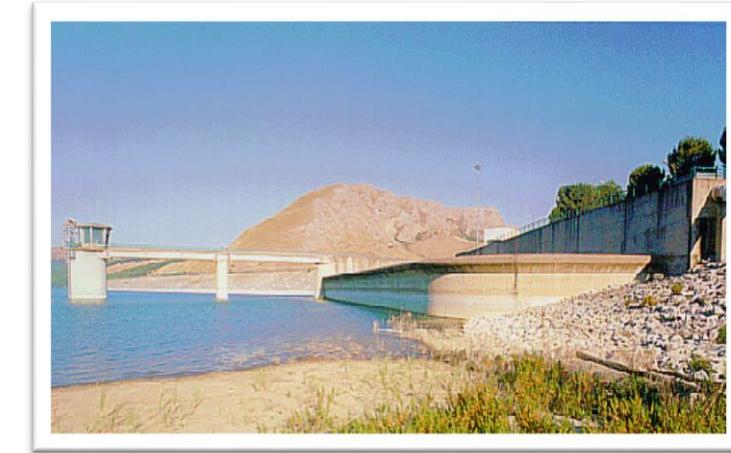
Seismic Hazard in Italy

Many dams in Italy, including the Garcia Dam, are located in areas prone to severe earthquakes, but were designed and built before the introduction of the current seismic hazard classification of the Italian territory.



Importance of Dam Safety

The safety of these dams is crucial for the areas located on the downstream side, as their failure could result in the uncontrolled release of retained water, endangering the surrounding communities and environment.

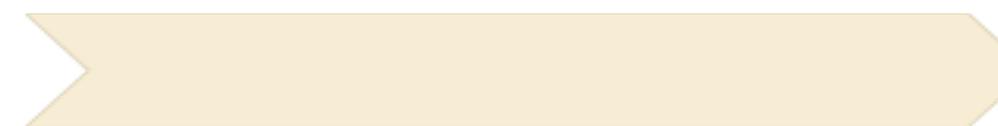


Seismic Assessment of Existing Dams

The Italian Government has promoted the seismic assessment of existing dams, with the aim of verifying their seismic capacity and eventually retrofitting them to ensure their safety.

Collaboration and Expertise

In this context, in 2021, the **Bonification Consortium 2 Palermo** entrusted the company **Volo Engineering and Consulting s.r.l.** with the task of preparing the "Certificate of Structural Suitability for Reinforced Concrete Structures and Seismic Checks on the Garcia Dam".



Volo Engineering and Consulting

The company responsible for the seismic assessment of the Garcia Dam, led by Eng. Salvatore Volo Ph.D.

Work Group:

Eng. Salvatore Volo Ph.D

Eng. Alessandra Amato

Dott. Geol. Gianvito Graziano

Eng. Giuseppe Amato

Eng. Marco Filippo Ferrotto Ph.D

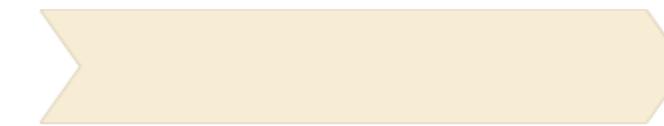
Eng. Salvatore Pagnotta Ph.D.

Specialist collaboration was provided by Eng. Alphonso Cusmano, Geotechnical Engineer.



Geolab s.r.l.

The company that carried out the in-situ/laboratory structural and geotechnical investigations.



Harpaceas s.r.l.

The company that provided technical support for the use of Flac2D, through Eng. Samuele Perni and Eng. Roberta Vincifora.

Geographical Context

The Belice River Basin

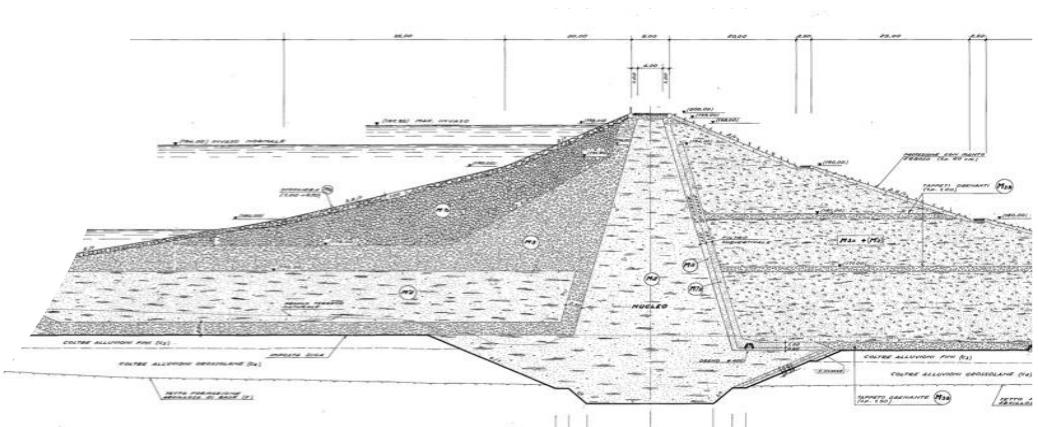
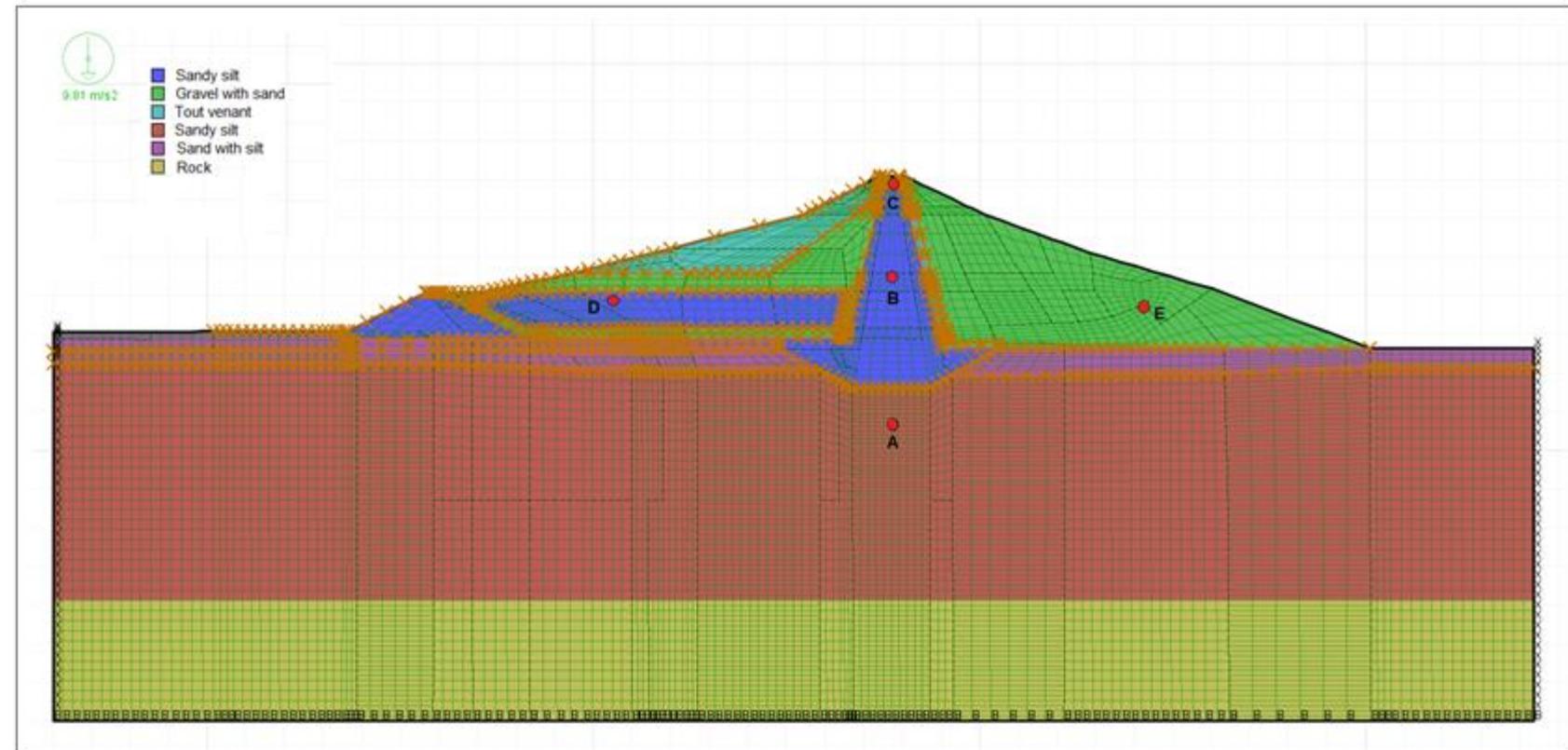
The Garcia Dam is located in the Belice River Basin, which spans the territories of Palermo, Trapani and Agrigento in Sicily.

The basin covers nearly 1.000 km² and is bordered by various mountain ranges, with the Belice River extending over 100 km from the mountains to the Mediterranean Sea.



Modeling the Garcia Dam

The Dam was modelled through Flac2D in order to predict in a very precise way its response to seismic excitation according to the seismic demand of the site of interest.



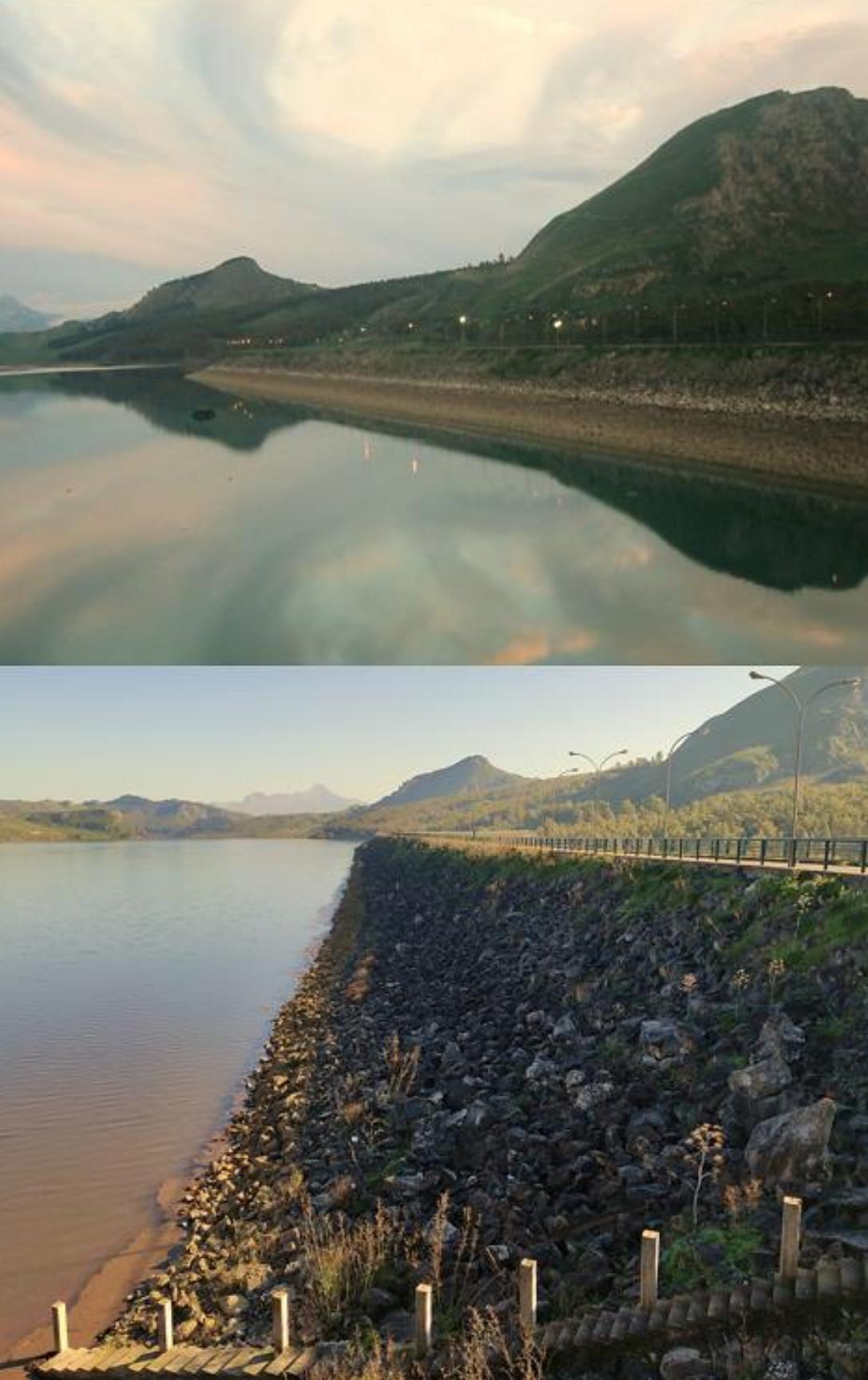
Explicit Dynamics



Non-Linear Analysis

The software works in explicit dynamics, on the basis of the finite difference method, allowing for the precise simulation of the seismic phenomenon according to the **theory of wave propagation**.

The software performs non-linear time history analyses, taking into account the **non-linear behavior** of the soil based on the assumed constitutive model.



Modeling the Garcia Dam

1

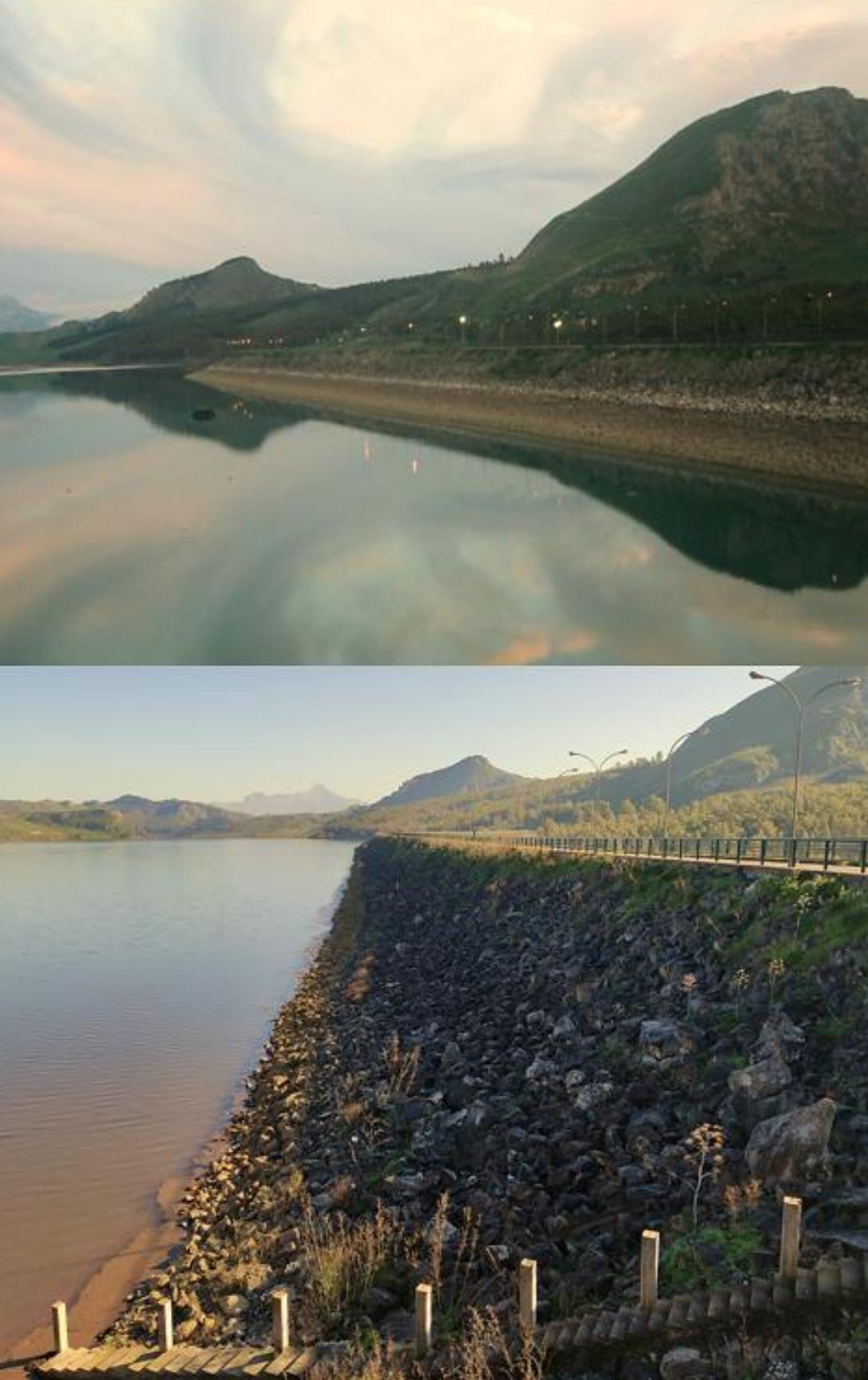
Soil Characterization – Back Analysis

The Dam was modeled characterizing each zone (upstream shell, downstream shell, core, and foundation) by its stiffness and strength parameters.

The Mohr-Coulomb constitutive model was chosen.

The resistance parameters were evaluated on the basis of the **design values** and the **tests** made during the construction stages.

For the stiffness parameters there was lower availability of data, reason why a **back analysis** was performed to estimate the Young modulus best fitting monitored subsidence values: for each attempt value of the Young modulus, a static analysis in long-term drained conditions was performed, by considering a water height 8 meters lower than full reservoir.



Modeling the Garcia Dam

2

Full Reservoir – Static Analysis

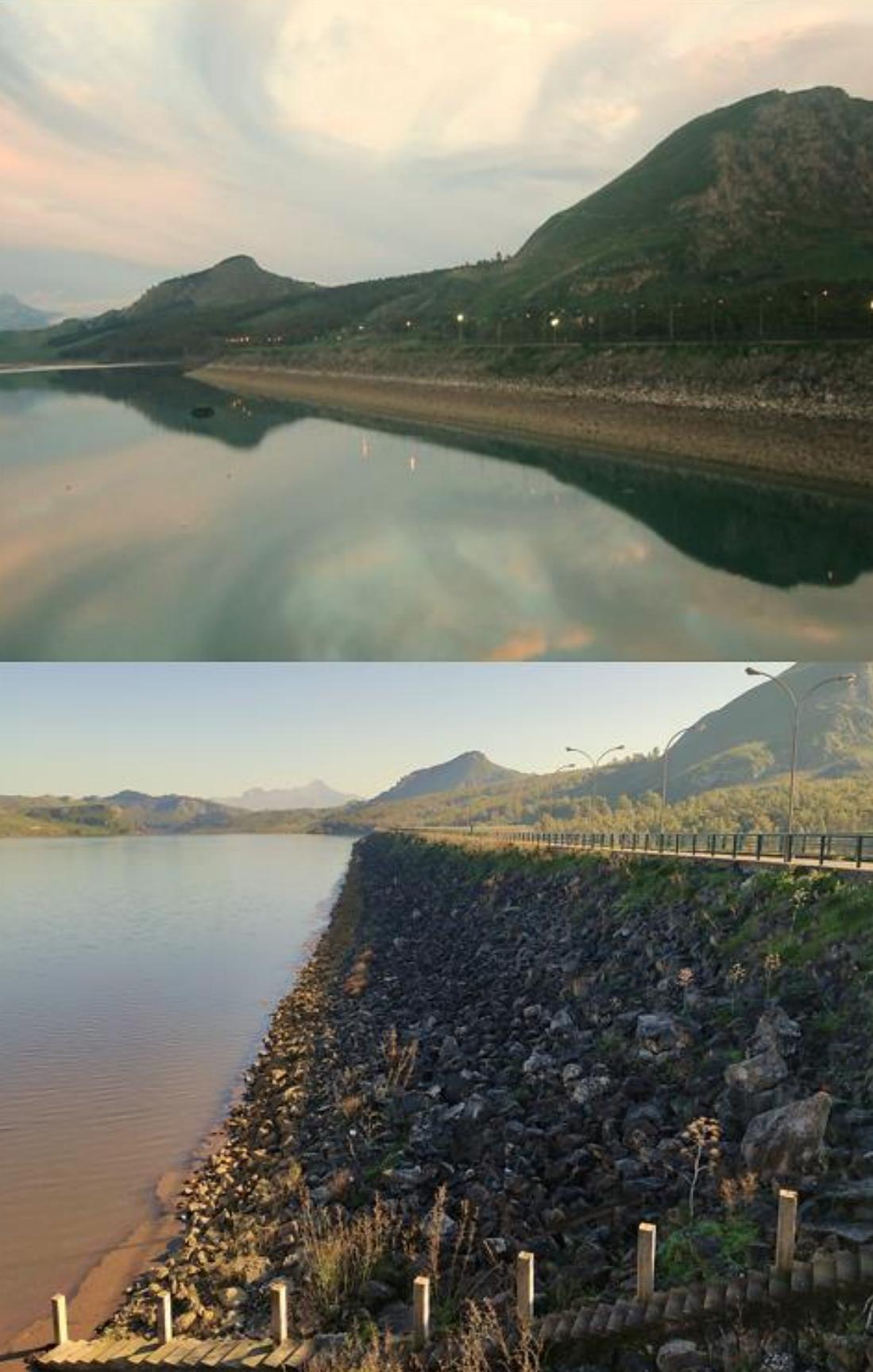
A further static analysis was carried out considering the full reservoir condition.

The analysis was carried out by performing a **hydraulic analysis** followed by a **mechanical analysis**.

Thus, the effective stress state and filtration through the dam under steady-state conditions were determined.

Then **the factor of safety** in static conditions was computed according to the **strength reduction method**.

This is the method assumed by the software to compute the FoS by progressively reducing the strength parameters until the first unstable condition is found.



Modeling the Garcia Dam

3

Seismic Event – Dynamic Analysis

The seismic analysis was performed assuming, **for each Limit State considered (DLS – LSLS - CLS)**, a set of seven spectrum-compatible real accelerograms selected from the European strong-motion database referred to the soil according to the Italian Code.

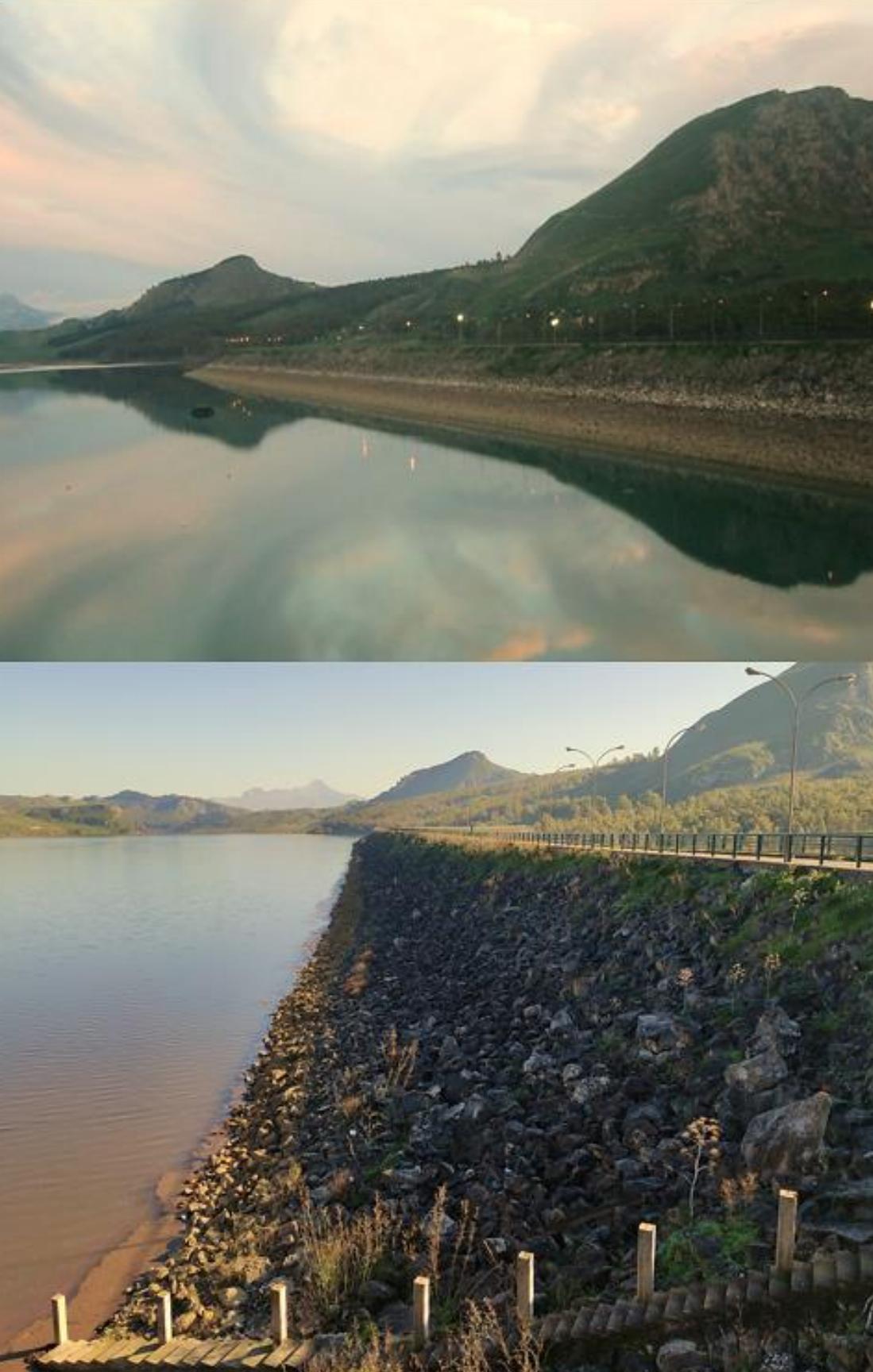
The dynamic boundary conditions were inserted in the model as follows:

- **quiet boundary** conditions were assumed for the model base
- **free field** boundary conditions were assumed for the lateral edges of the model.

The presence of quiet boundary conditions at the model base made it necessary to insert the seismic excitation in terms of **shear stresses applied at the bedrock level**: $\tau(t) = -2 \rho c_s v_s(t)$

The dynamic analyses were performed by assuming **undrained behavior** to simulate the short-term condition characterizing the seismic event.

Then **the factor of safety** was computed by the **strength reduction method**.



Modeling the Garcia Dam

4

Post Seismic Phase

It was necessary to analyze the phase immediately following the earthquake: the dissipation of overpressures can lead to excessive **subsidence**, causing internal erosion (fracturing) or external erosion (overtopping).

The phase of consolidation following the earthquake was evaluated by performing an **analysis under drained conditions**.

The acceptability of subsidence was evaluated using an empirical criterion available in literature and developed by **Swaisgood** (1998, 2003). The criterion allows four damage classes to be defined on the basis of the Peak Ground Acceleration and the following ratio:

$$\% \text{ } Stlmt = \Delta \cdot 100 / (DH + AT)$$

- Δ = subsidence
- DH = 55m = dam height
- AT=45m = height of deformable layer on which the dam rests.

Results

At the DLS, the average subsidence recorded at the Dam crest is equal to 0.111 m.

Such value falls within the “minor damage” interval according to Swaisgood criterion, so these results do not give rise to any concern for the water tightness capacity or against overflow.

At the LSLS and CLS, the average subsidence recorded at the Dam crest is much higher, equal to 0.615 m and 1.029 m, but not leading to the dam collapse. These values fall across the intervals “moderate damage” and “serious damage” according to Swaisgood criterion.

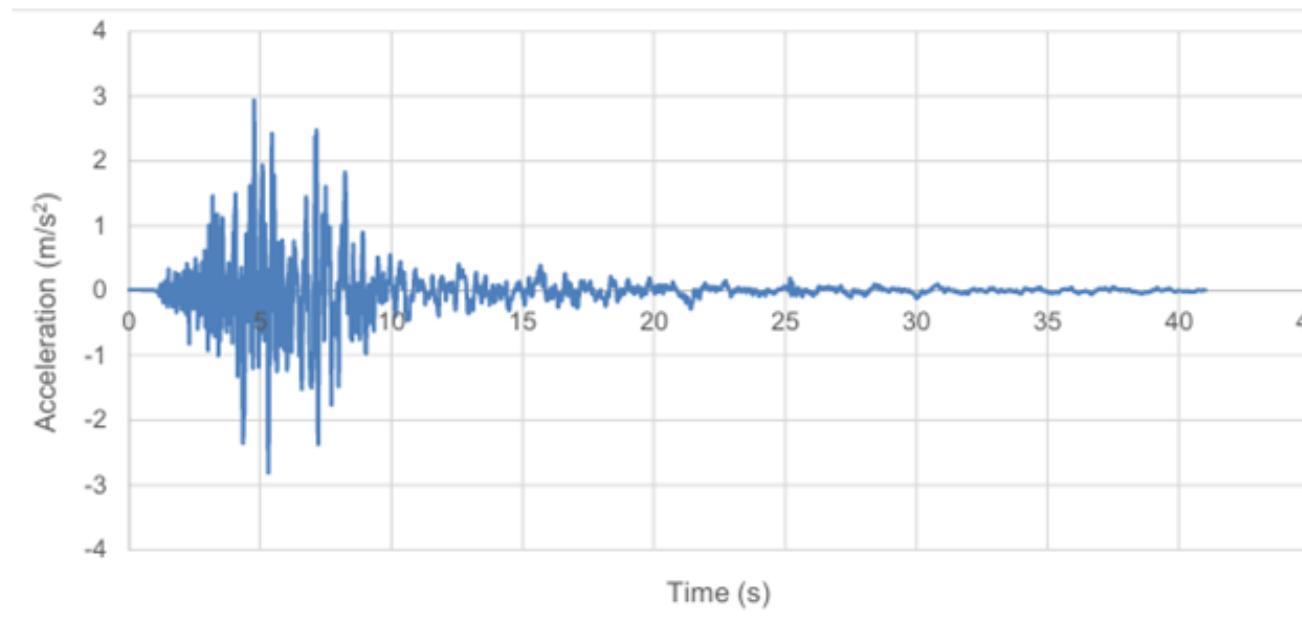
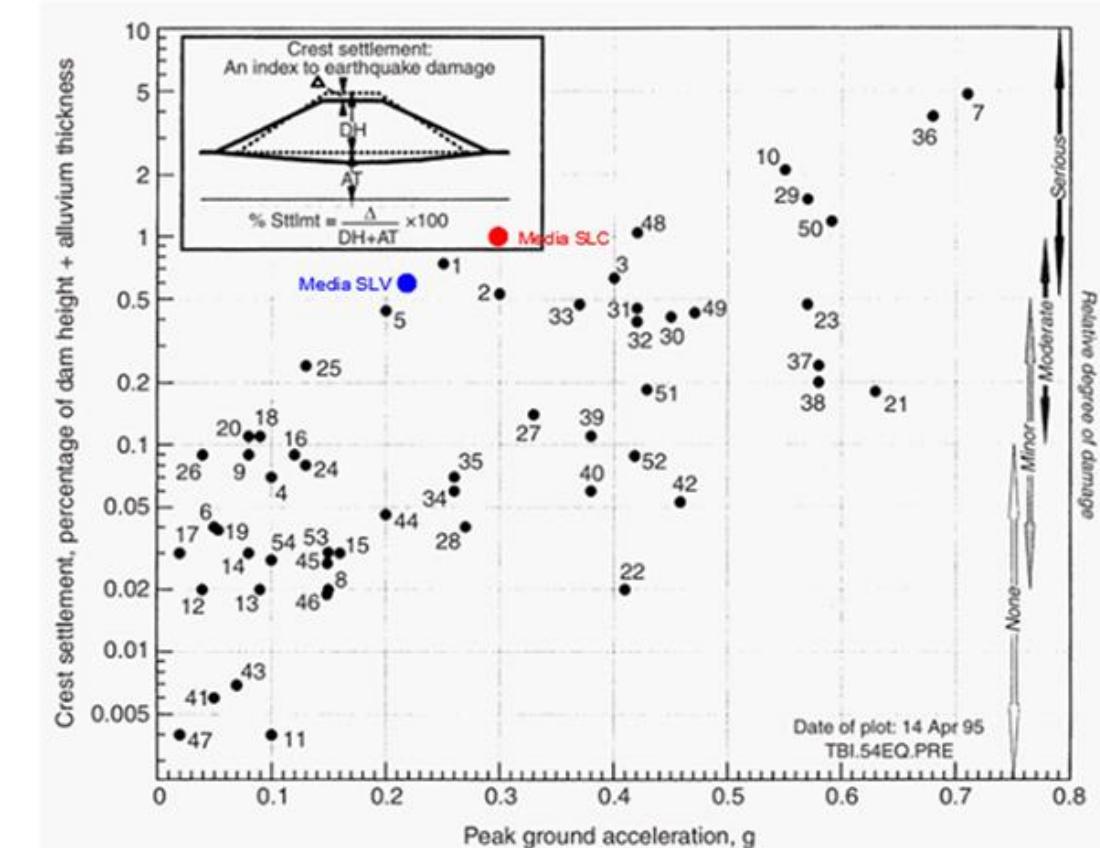


Figure . Collapse limit state accelerogram associated to a PGA=2.94 m/s².



Results

Regarding the instability checks of the Dam, for all the accelerograms considered, the factor of safety computed after the dynamic analysis was much greater than one, which made it possible to exclude instability problems associated to the seismic event.

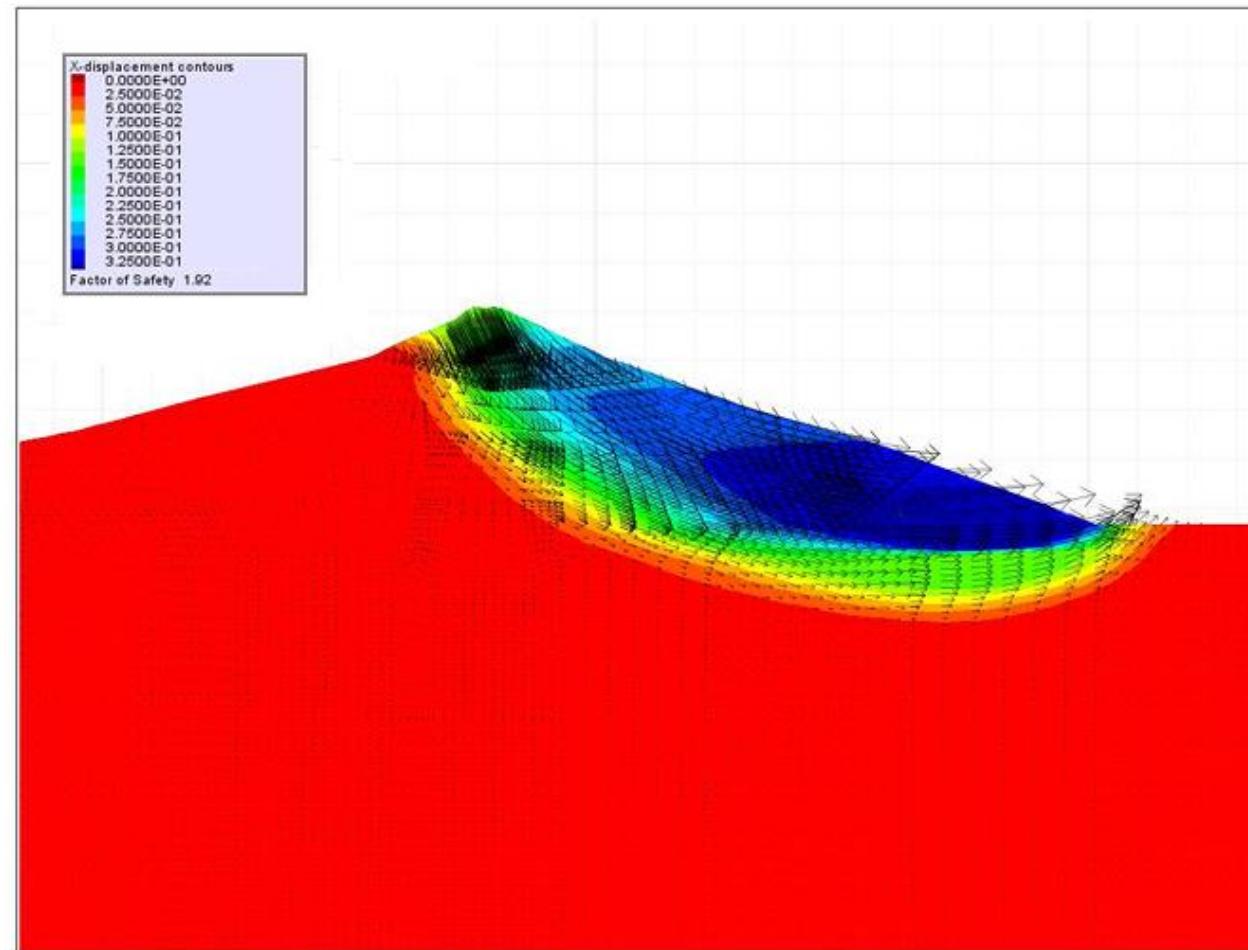


Figure . Factor of safety after the seismic event and associated mechanism.

Conclusions

Geotechnical Modeling

The use of Flac2D allowed for the creation of a detailed geotechnical model of the Garcia Dam, considering the various soil zones and their respective properties.

Seismic Assessment

The seismic assessment was carried out using the non-linear time history analysis method, considering three limit states as per the Italian National Code.

Satisfactory Results

The results of the study have demonstrated that the Garcia Dam does not exhibit seismic issues and can be considered seismically adequate in accordance with current regulations.

A thought and, in some cases a memory, is expressed towards the Designers Eng. Franco Bigalli, Eng. Alessandro De Boni, Eng. Giovanni Sallusto, Eng. Giancarlo Madoni (all members of the S.I.A. in Milan), the General Consultant in the Course of the Work Prof. Eng. Ruggiero Jappelli, the Works Director (as well as Site Laboratory Director and Collaborator of the General Consultant in the Course of the Work) Eng. Gianni Cusmano and the Specialist Geologist Lorenzo Veronese.

Thanks for your attention!





Comparisons between two reinforcement methods for a high embankment dam on thick alluvial deposit

Zhao Wang¹, Rui Wang¹, Jian-Min Zhang¹

¹ Tsinghua University, Beijing, China



1 Introduction

2 Numerical model and material properties

3 Results and discussions

4 Conclusions

Introduction



清华大学
Tsinghua University



- West China is rich in hydropower resources, but also characterized by high seismic intensity and widespread thick layered deposits. (*Li et al., 2018*).
- Therefore, it is of great importance to investigate seismic reinforcement methods for such hydropower projects.
- Traditional alluvial removal approach are unfeasible for very thick deposit.



Changhe Dam
(a 240m-high dam on 50m-thick deposit)



Yele Dam
(a 124.5m-high dam on 420m-thick deposit)



Suwalong Dam
(a 110m-high dam on 79.3m-thick deposit)

Introduction

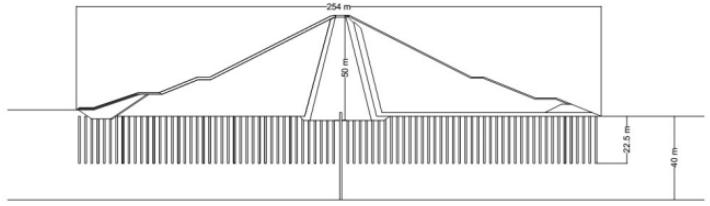


清华大学
Tsinghua University

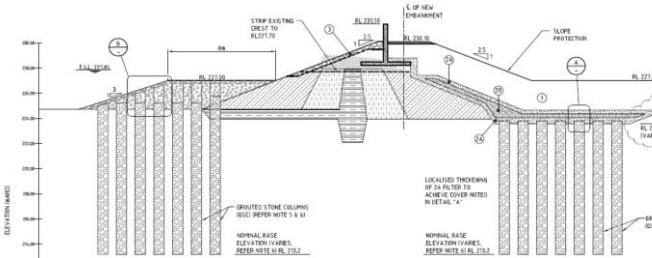


Gravel columns

- A mitigation strategy to increase stability and prevent liquefaction
- Densification effect, drainage effect and shear reinforcement enhancement



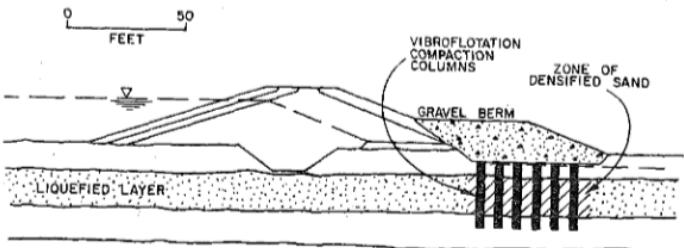
Kissir Dam (Karech et al., 2017)



Toorourrong Reservoir (Avalle et al., 2012)

Berms

- Improve slope stability



Thermalito Afterbay Dam (Haider et al., 1984)



The study focuses on ...

- A high embankment dam on thick deposit reinforced with gravel columns and berms
- Investigate the mitigation mechanism of gravel columns and berms
- Practice parameter sensitivity analysis of gravel columns and berms



1 Introduction

2 Numerical model and material properties

3 Results and discussions

4 Conclusions

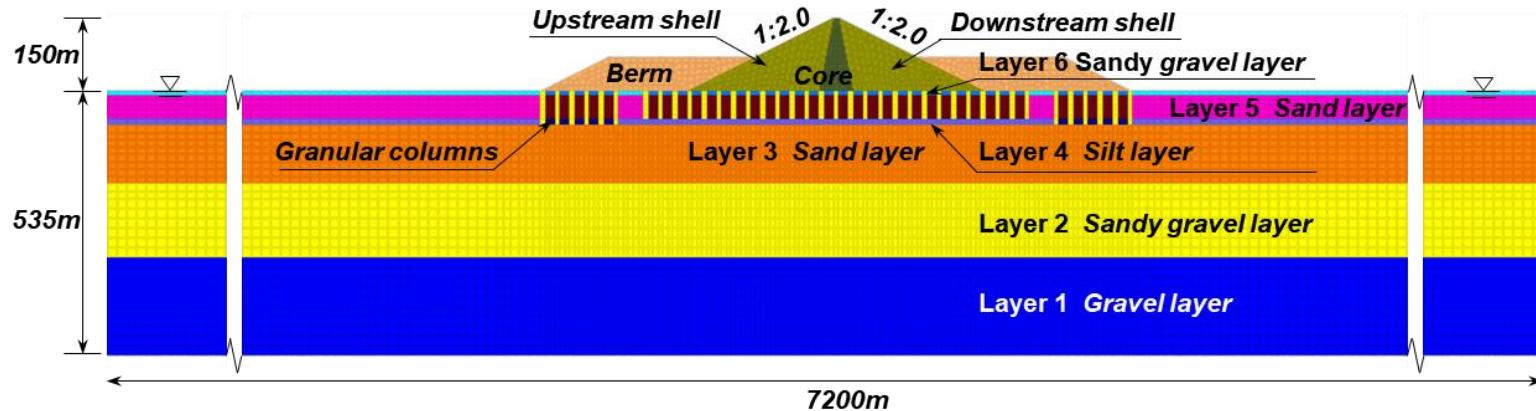
Numerical model and material properties



清华大学
Tsinghua University



Model description Simulation process



Properties of the embankment dam and deposit

	Sand	ρ (kg/m ³)	k (m/s)	e		Sand	ρ (kg/m ³)	k (m/s)	e
Layer 6	Sand gravel	2400	7.50E-05	0.4	Gravel columns	/	2400	7.50E-04	0.4
Layer 5	Sand	2000	3.00E-05	0.55	Core	/	1709	/	0.7
Layer 4	Silt	1900	1.50E-07	0.7	Rockfill	/	1800	/	0.4
Layer 3	Sand	2100	7.50E-06	0.5	Berm	/	1800	/	0.2
Layer 2	Sand gravel	2400	6.00E-06	0.2					
Layer 1	gravel	2400	1.00E-06	0.2					

Model 0 (BS): Baseline

Model 1 (GC): Gravel columns

Model 2 (BM): Berms

Model 3 (BM-GC): Berms and
gravel columns

Numerical model and material properties



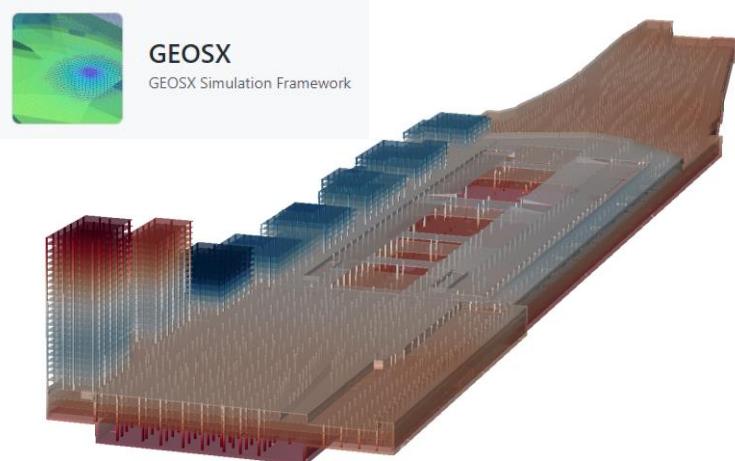
清华大学
Tsinghua University



Model description

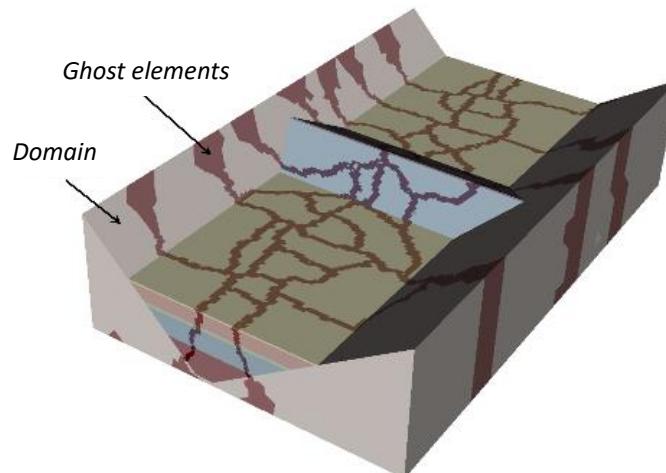
Simulation process

- GEOSX: an open-source, multiphysics simulator (Fu et al., 2013; Settgast et al., 2016)
- High-performance solid-fluid coupled framework (Wang, 2020; Yu et al., 2023)



GEOSX
GEOSX Simulation Framework

GEOSX



Parallel domain partition

Numerical model and material properties



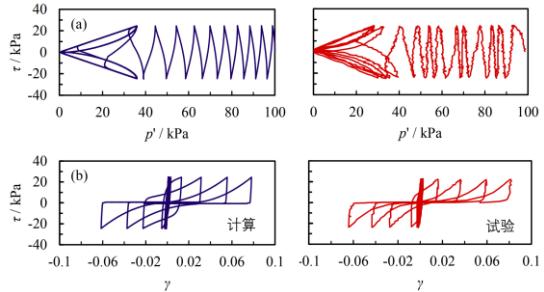
清华大学
Tsinghua University



Model description

Simulation process

- CycLiq: a plasticity constitutive model for large post-liquefaction deformation of sand (Wang et al., 2014, Zhang, 1997)



Simulation of undrained cyclic torsional shear tests with CycLiq
(Wang et al., 2014)

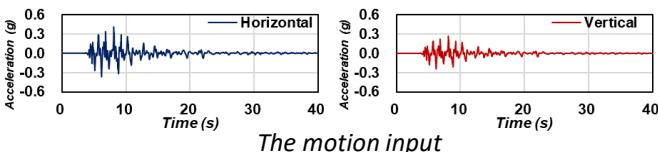
Parameter	Description
G_0, κ	Elastic modulus
h, n^p	Plastic modulus
M, e_o, λ_o, ξ	Critical state
$d_{re,1}, d_{re,2}, n^d$	Reversible dilatancy
$d_{ir}, \alpha, \gamma_{dr}$	Irreversible dilatancy

Model parameters description of CycLiq

Model parameters of the dam and deposit

(Choi., 2004, Zou et al., 2019, He et al., 2020)

	G_0	κ	h	M	$d_{re,1}$	$d_{re,2}$	d_{ir}	α	γ_{dr}	n^p	n^d	λ_c	e_o	ξ
Layer 6	360	0.003	2.8	2	0.55	38	0.95	30	0.05	0.5	18	0.018	0.85	0.7
Layer 5	300	0.007	1.3	1.4	1.4	30	1.4	30	0.05	2.2	6	0.0112	0.85	0.7
Layer 4	200	0.018	1.8	1.35	1.4	30	0.2	30	0.05	2.2	6	0.019	0.95	0.7
Layer 3	250	0.006	1.1	1.4	1.4	30	1.4	30	0.05	2.2	6	0.0112	0.75	0.7
Layer 2	330	0.005	3.8	1.8	0.55	30	0.95	30	0.05	0.5	18	0.018	0.9	0.7
Layer 1	360	0.005	3.8	2	0.55	30	0.95	30	0.05	0.5	18	0.018	0.9	0.7
Gravel column	360	0.003	2.8	2	0.55	38	0.95	30	0.05	0.5	18	0.018	0.9	0.7
Core	200	0.02	1.8	1.5	1.4	30	0.2	30	0.05	2.2	6	0.019	0.95	0.7
Rockfill	360	0.003	2.8	2	0.55	38	0.95	30	0.05	0.5	18	0.018	0.85	0.7
Berm	300	0.01	2.8	1.7	0.55	30	0.95	30	0.05	0.5	18	0.018	0.7	0.7



The motion input





1 Introduction

2 Numerical model and material properties

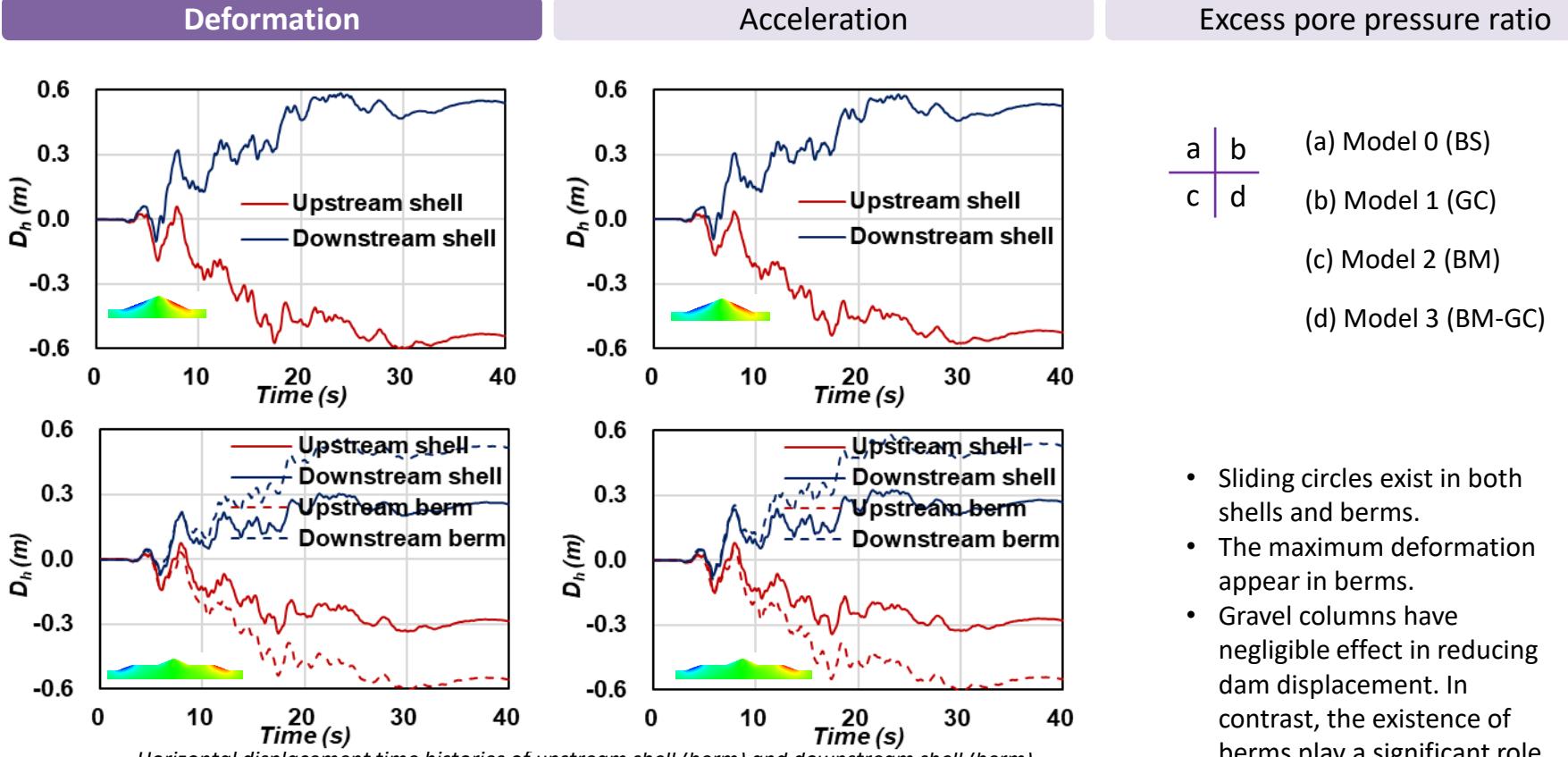
3 Results and discussions

4 Conclusions

Results and discussions



清华大学
Tsinghua University



- Sliding circles exist in both shells and berms.
- The maximum deformation appear in berms.
- Gravel columns have negligible effect in reducing dam displacement. In contrast, the existence of berms play a significant role.

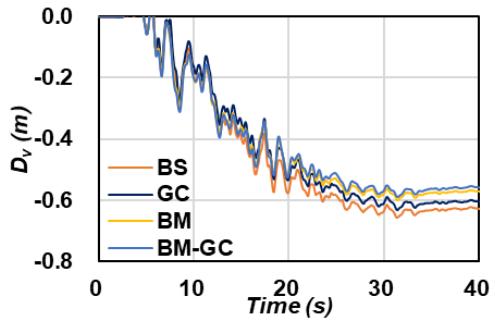
Results and discussions



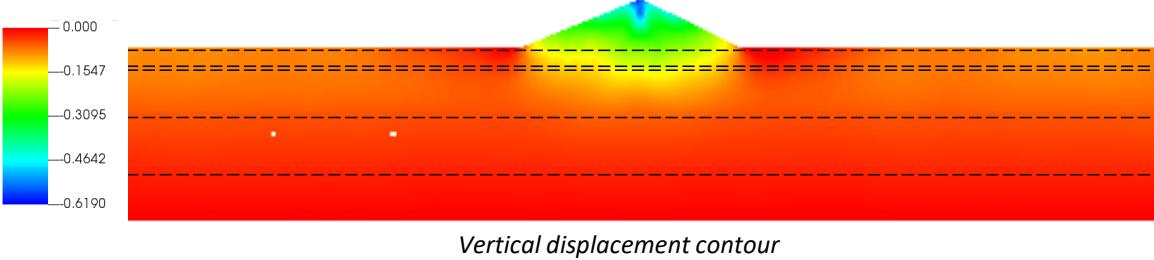
清华大学
Tsinghua University



Deformation Acceleration Excess pore pressure ratio



Vertical displacement time histories at the crest of the dam



Vertical displacement contour

Vertical displacement time histories in different layers

	BS		GC		BM		BM-GC	
	Dv (m)	Proportion	Dv (m)	Proportion	Dv (m)	Proportion	Dv (m)	Proportion
Dam	0.359	56.7%	0.345	56.5%	0.337	58.6%	0.329	58.3%
Layer 6	0.004	0.6%	0.007	1.1%	0.004	0.7%	0.003	0.5%
Layer 5	0.060	9.5%	0.055	9.0%	0.040	7.0%	0.038	6.7%
Layer 4	0.016	2.5%	0.014	2.3%	0.011	1.9%	0.013	2.3%
Layer 3	0.108	17.1%	0.106	17.3%	0.105	18.3%	0.104	18.4%
Layer 2	0.053	8.4%	0.048	7.9%	0.044	7.7%	0.043	7.6%
Layer 1	0.033	5.2%	0.036	5.9%	0.034	5.9%	0.034	6.0%

- The application of berms is clearly more effective in controlling settlement than gravel columns.
- The reduction is limited and nonessential because the settlement of layer 5 only accounts for around 9%.

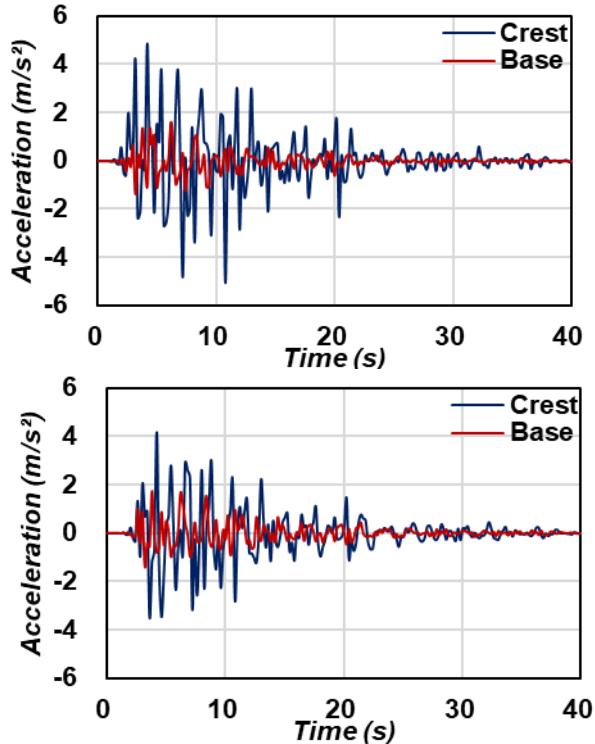
Results and discussions



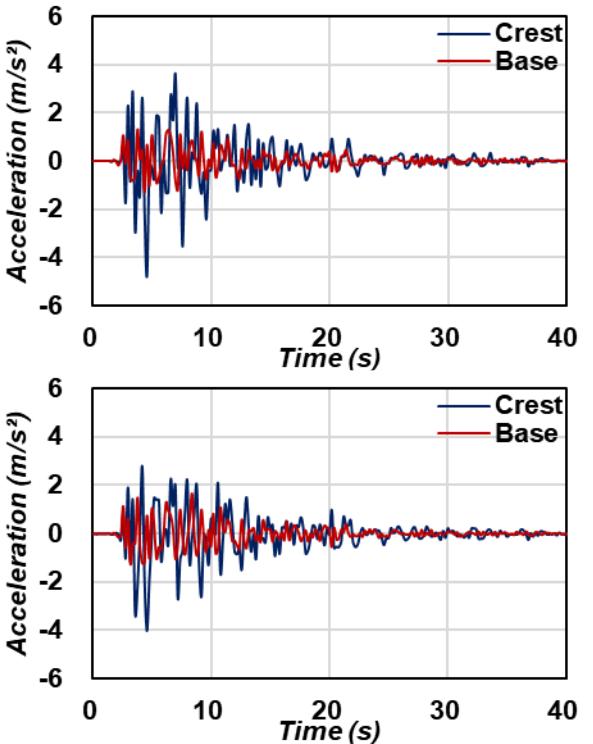
清华大学
Tsinghua University



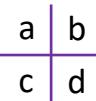
Deformation



Acceleration



Excess pore pressure ratio



- (a) Model 0 (BS)
- (b) Model 1 (GC)
- (c) Model 2 (BM)
- (d) Model 3 (BM-GC)

- The amplification ratio of Model BS, GC, BM, and BM-GC are 3.00, 3.04, 2.53, and 2.43, showing that berms can significantly reduce the acceleration of the dam.

Acceleration response at the crest and base of the dam along the dam axis



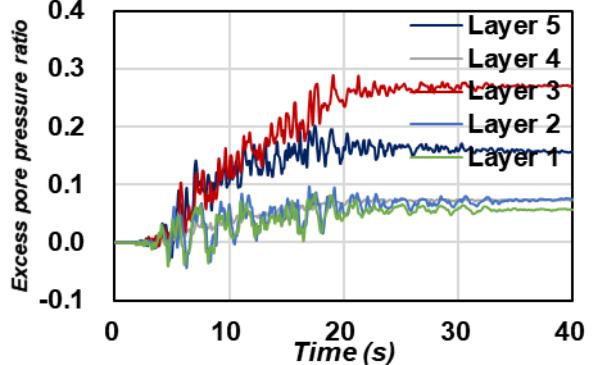
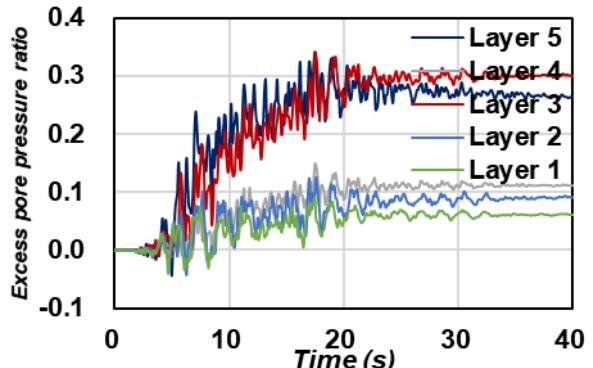
Results and discussions



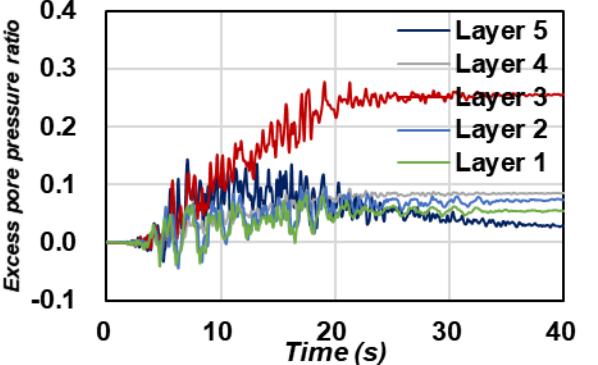
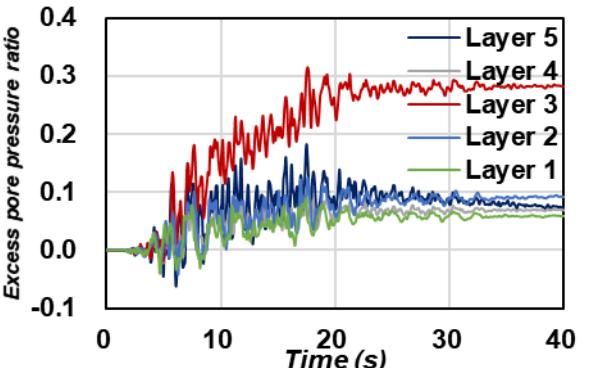
清华大学
Tsinghua University



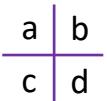
Deformation



Acceleration



Excess pore pressure ratio



(a) Model 0 (BS)

(b) Model 1 (GC)

(c) Model 2 (BM)

(d) Model 3 (BM-GC)

- The drainage effect of gravel columns plays a role in suppressing the excess pore pressure ratio in layer 5 via increased permeability.
- Berms also help decrease due to its effect in increasing confining stress, especially in layer 5.
- The excess pore pressure ratio in the deep Layers 1 and 2 reach only approximately 0.1 and are not significantly affected by the reinforcement methods.

Excess pore pressure ratio time histories in different layers along the dam axis



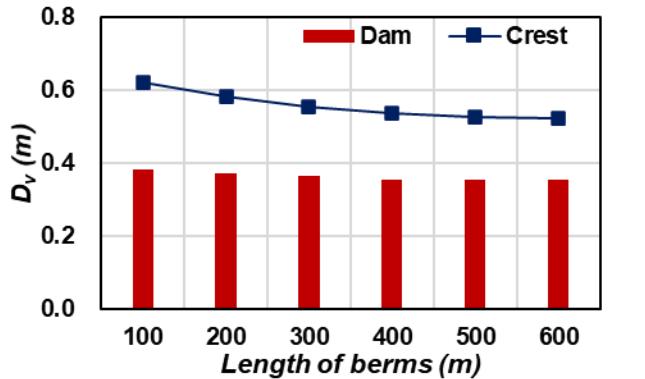
Results and discussions



清华大学
Tsinghua University



Parametric study of berms



Parametric study of gravel columns

Horizontal displacements of the dam treated by berms

Length of berms (m)		100	200	300	400	500	600
Upstream Dh(m)	Berm	-0.541	-0.577	-0.570	-0.539	-0.540	-0.556
	Dam	-0.383	-0.292	-0.274	-0.259	-0.247	-0.241
Downstream Dh(m)	Berm	0.519	0.552	0.532	0.520	0.510	0.520
	Dam	0.336	0.254	0.229	0.222	0.219	0.213

- Sensitivity analysis reveals that the most effective length is 400m to reach a minimum deformation. Further increases in the length of berms yield marginal additional improvements.

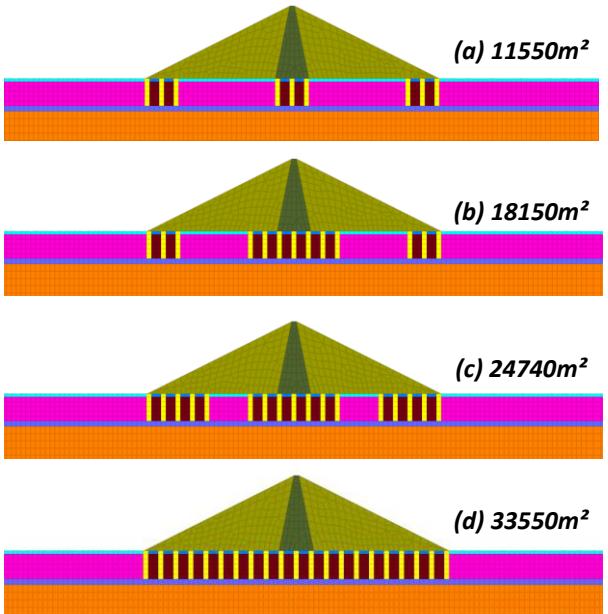
Results and discussions



清华大学
Tsinghua University

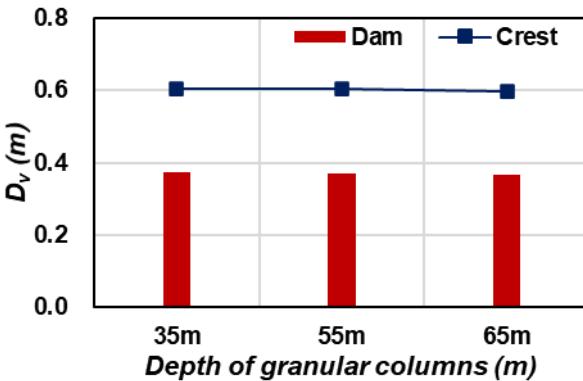
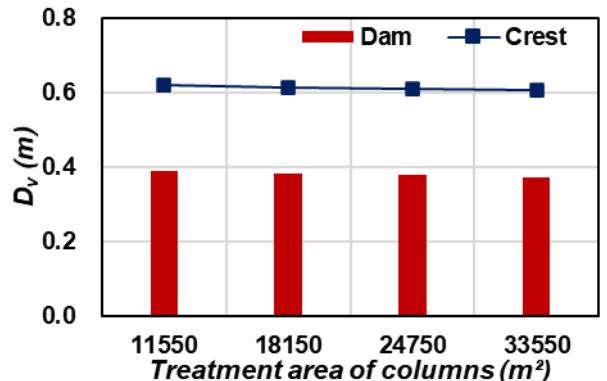


Parametric study of berms



Local geometries of models treated with different treatment areas of columns

Parametric study of gravel columns



Vertical displacements of the dam treated by gravel columns

Horizontal displacements of the dam treated by granular columns with different treatment area

Treatment area of columns (m^2)	11550	18150	24740	33550
Upstream Dh(m)	-0.536	-0.533	-0.532	-0.531
Downstream Dh(m)	0.530	0.530	0.523	0.519

Horizontal displacements of the dam treated by granular columns with different depths

Depth of granular columns (m)	35	55	65
Upstream Dh(m)	-0.536	-0.531	-0.529
Downstream Dh(m)	0.522	0.519	0.516

- Varying treatment depths and areas of gravel columns make negligible difference in dam displacements and deformations.



- 1 Introduction
- 2 Numerical model and material properties
- 3 Results and discussions
- 4 Conclusions

Conclusions



清华大学
Tsinghua University



- Berms demonstrate a substantial effect to reduce dam settlement and suppress the accumulation of excess pore pressure ratio within the sand layer.
- The displacement the dam decreases with the extension of berms. The most effective berm length is found to be 400m. Further lengthening of berms is unlikely to produce significant additional improvements.
- Gravel columns show limited effect in suppressing deformations and settlements, but provides noteworthy enhancement in drainage.
- Changes in treatment depths and areas of gravel columns do not lead to substantial improvements in dam deformation.



清华大学
Tsinghua University



Thank you!

Any questions?

Predictive model for seismic displacements of a general flexible sliding block in near-fault region

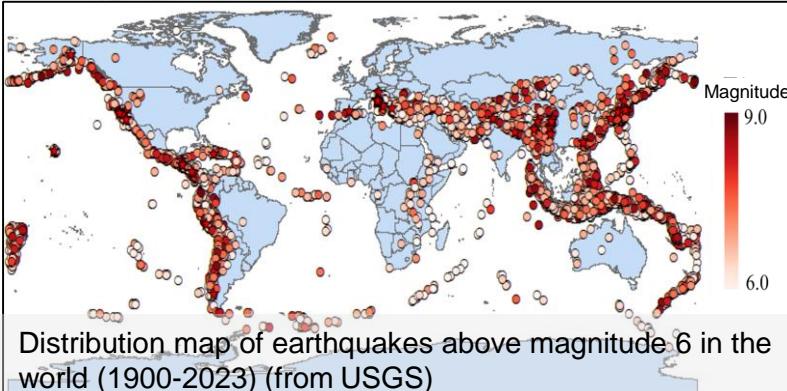
Xiang Chenlin¹, Huang Dongliang², Zhang Yingbin¹, Zhao Lianheng²

¹ School of Civil Engineering, Southwest Jiaotong University

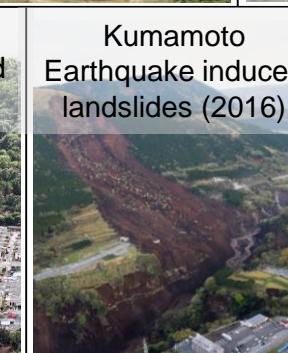
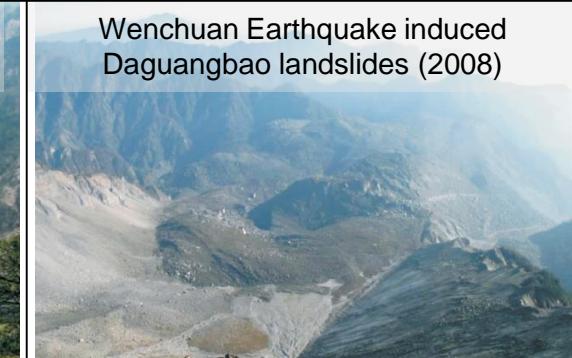
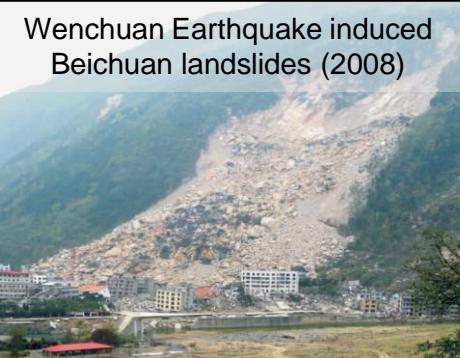
² School of Civil Engineering, Central South University

1. Background of research
2. Objective
3. Ground Motion Database
4. Methodology
5. Prediction Model for Permanent Displacement
6. Discussion
7. Application
8. Conclusion

Background of research



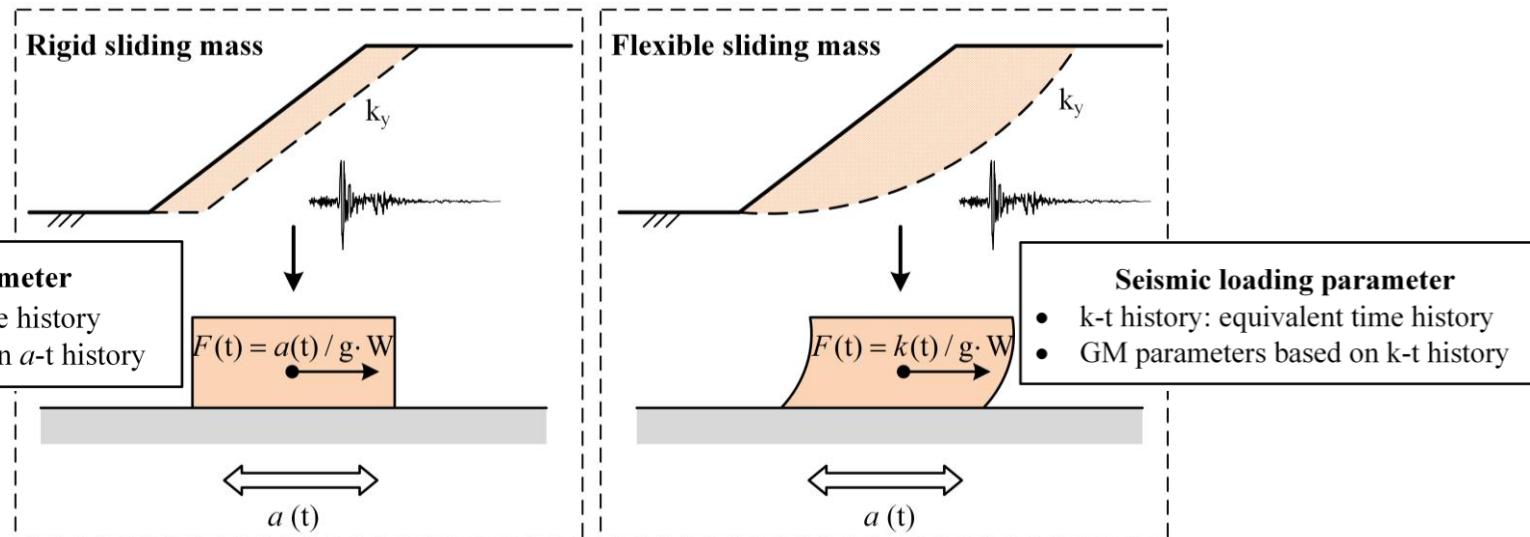
Since this century, more than **1.23 million** people have died in earthquakes around the world. The life and property loss caused by earthquake-induced landslides exceed **50%** of the total losses caused by earthquake.



Earthquake-induced landslide is the most common and most destructive secondary disaster of earthquake.

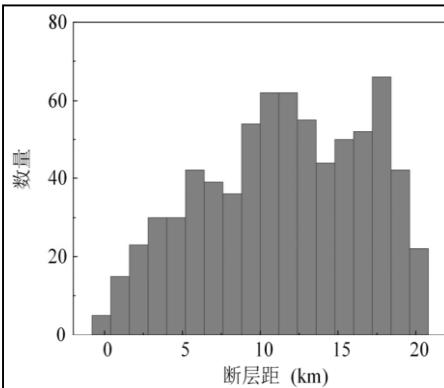
Background of research

Permanent displacement is an index for evaluating the stability of slope when considering earthquakes. It is mainly divided into **rigid sliding block**, **decoupled** and **coupled analysis**. In this study, **a general flexible sliding model was proposed to consider the vertical ground motion in near fault area.**

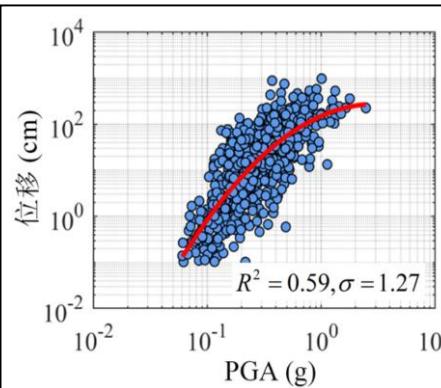


Objective

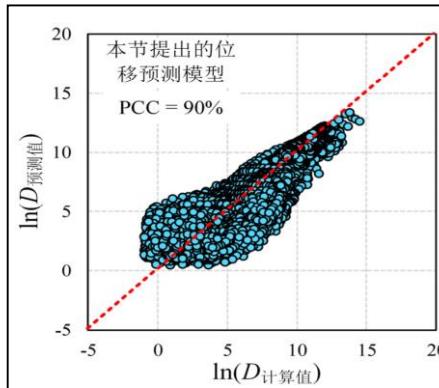
The objective is to establish the predictive model based on proposed sliding model. Then, using the displacement model to identify the hazard of earthquake-induced landslides.



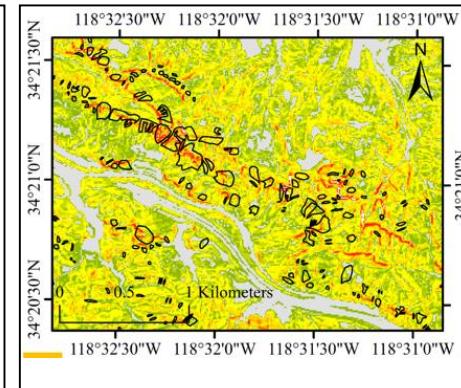
GMs Database



Parameter correlation



Predictive model



Application

Step 1

Step 2

Step 3

Step 4

Ground Motion Database

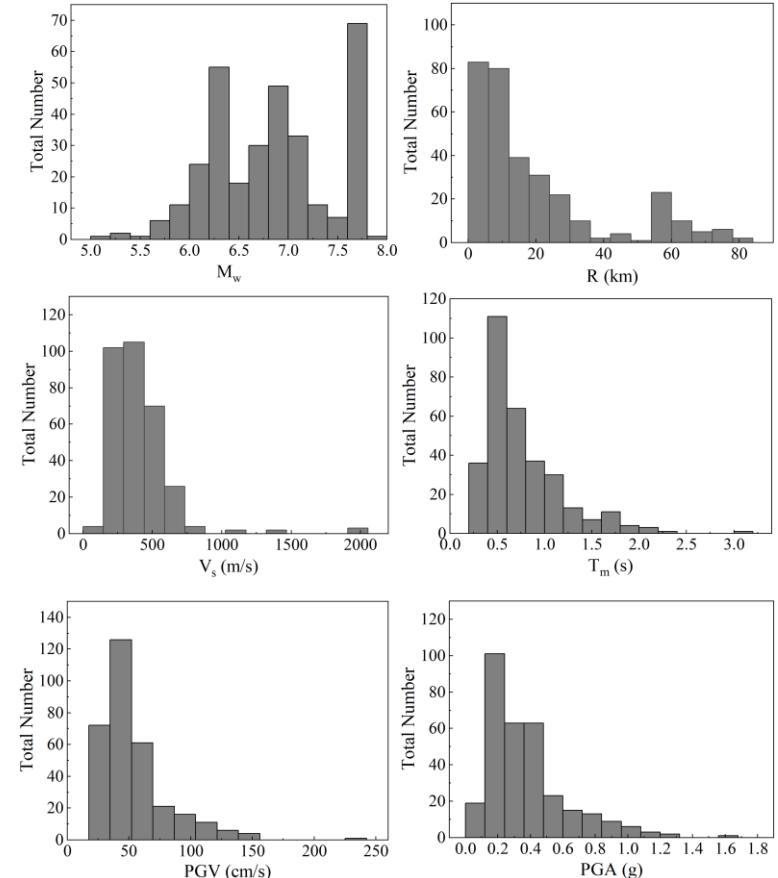
In this study, the Chang's algorithm (2016) was used to identify the pulse-like ground motions.

It mainly includes two criteria:

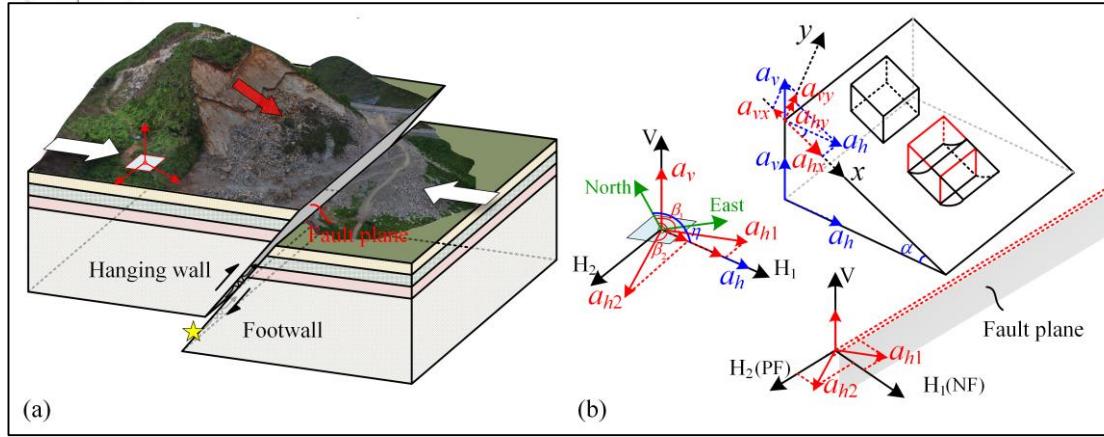
- (1) the PGV greater than 30 cm/s
- (2) pulse indicator (E_p) of ground motion > 0.34

318 pulse-like ground motions were classified as pulse-like from ground motion database.

As pulse-like ground motions could be observed within a certain range of orientation, all of the ground motions were rotated to the orientation with the largest E_p . The distribution of pulse-like ground motions is shown in the Fig.



Methodology



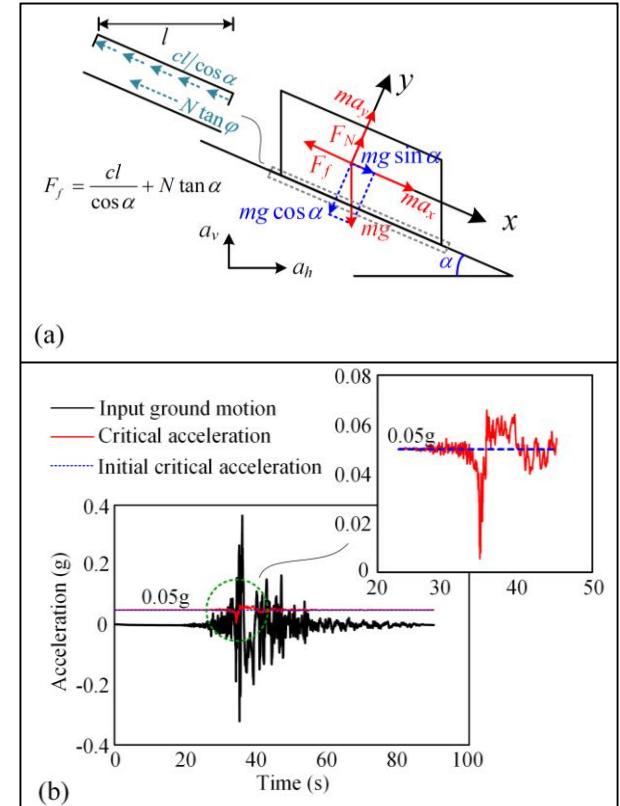
Yield acceleration

$$k_y = \tan(\varphi - \alpha) + a_v \tan(\varphi - \alpha) + \frac{c}{\gamma H (\cos^2 \alpha + \sin \alpha \cos \alpha \tan \varphi)}$$

$k_y = 0.02, 0.05, 0.1, 0.2, 0.3,$ and $0.4g$

$T_s = 0, 0.5, 1, 1.5, 2, 2.5, 3, 3.5, 4, 4.5, 5, 5.5,$ and $6s$

A total of **9508** effective displacements were used to establish the displacement model.



Prediction Model for Permanent Displacement

Based on previous study, comparing the distributions of correlation coefficient between different parameters and permanent displacement, the optimal parameter was selected.

In order to better predict permanent displacement, the period ratios were divided into 25 subclasses, with a period ratio interval of 0.3.

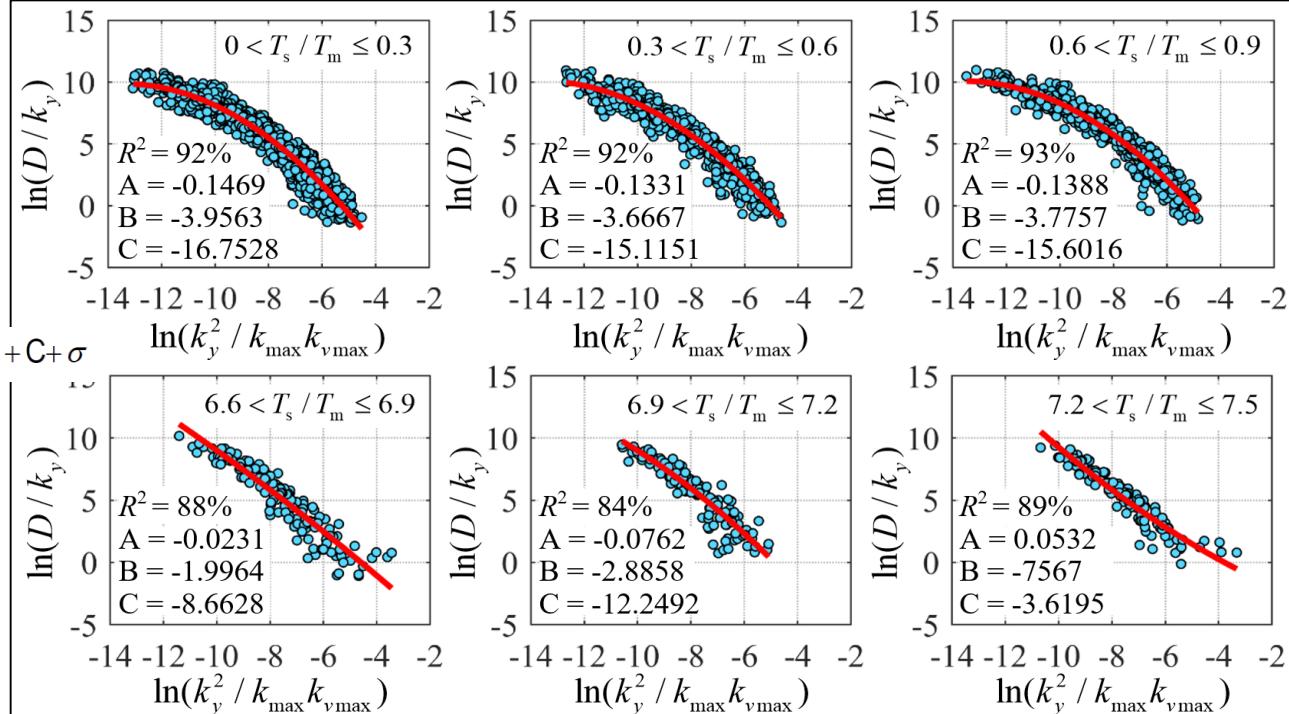
$$\ln(D/k_y) = A \ln(k_y^2 / k_{\max} k_{v\max})^2 + B \ln(k_y^2 / k_{\max} k_{v\max}) + C + \sigma$$

The coefficients (A, B and C) are calculated as follows:

$$A = A_{01}(T_s/T_m)^2 + A_{02}(T_s/T_m) + A_{03}$$

$$B = B_{01}(T_s/T_m)^2 + B_{02}(T_s/T_m) + B_{03}$$

$$C = C_{01}(T_s/T_m)^2 + C_{02}(T_s/T_m) + C_{03}$$



Prediction Model for Permanent Displacement

There're some prediction models of the dynamic response using ground motion intensity measures. In this study, a new predictive dynamic response model was established.

In order to predict dynamic response parameter, the period ratios were divided into 25 subclasses.

$$\ln(k_y^2 / k_{\max} k_{v,\max}) = a \cdot \ln(k_y^2 / \text{PGAPGV}) + b + \sigma$$

$0 < T_s / T_m \leq 2.4$

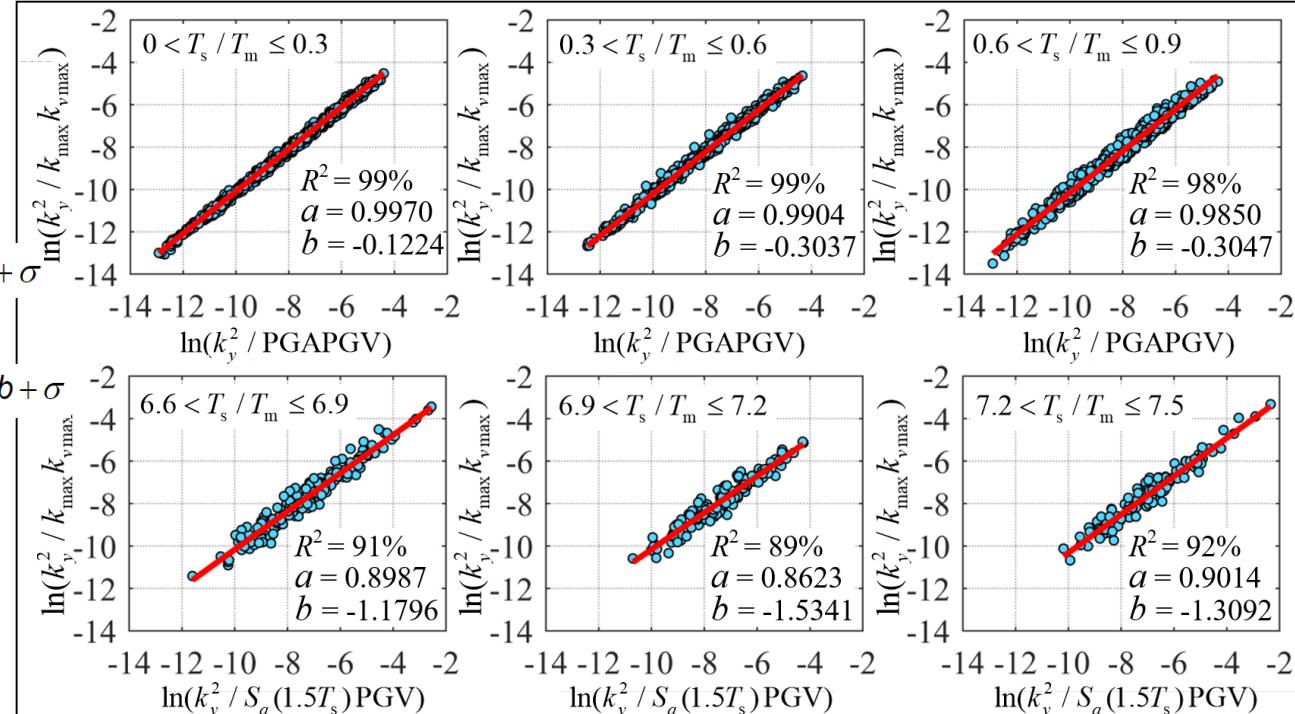
$$\ln(k_y^2 / k_{\max} k_{v,\max}) = a \ln(k_y^2 / S_a(1.5T_s) \text{PGV}) + b + \sigma$$

$2.4 < T_s / T_m \leq 7.5$

The coefficients (a and b) are calculated as follows:

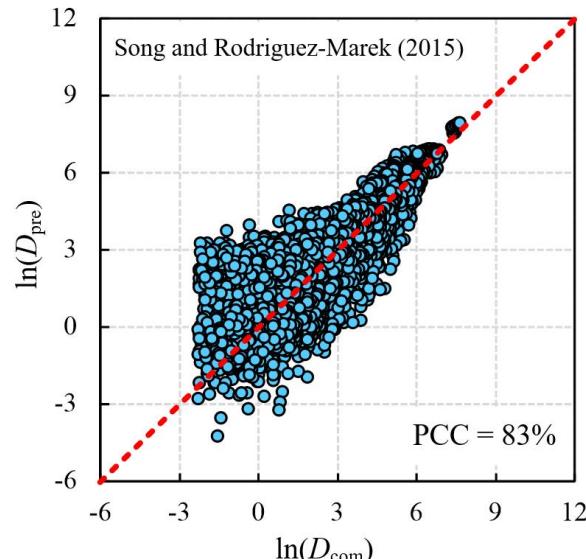
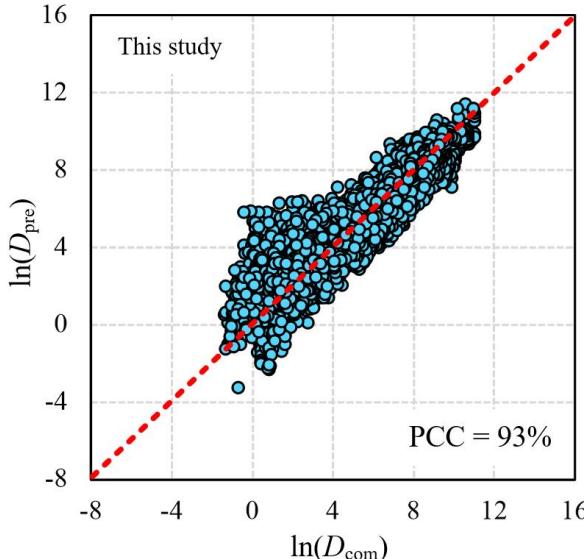
$$a = a_{01}(T_s / T_m)^2 + a_{02}(T_s / T_m) + a_{03}$$

$$b = b_{01}(T_s / T_m)^2 + b_{02}(T_s / T_m) + b_{03}$$



Discussion

To further verify the validity of the predictive model in considering vertical ground motions, the predicted permanent displacements and the displacements calculated using proposed sliding model are compared.

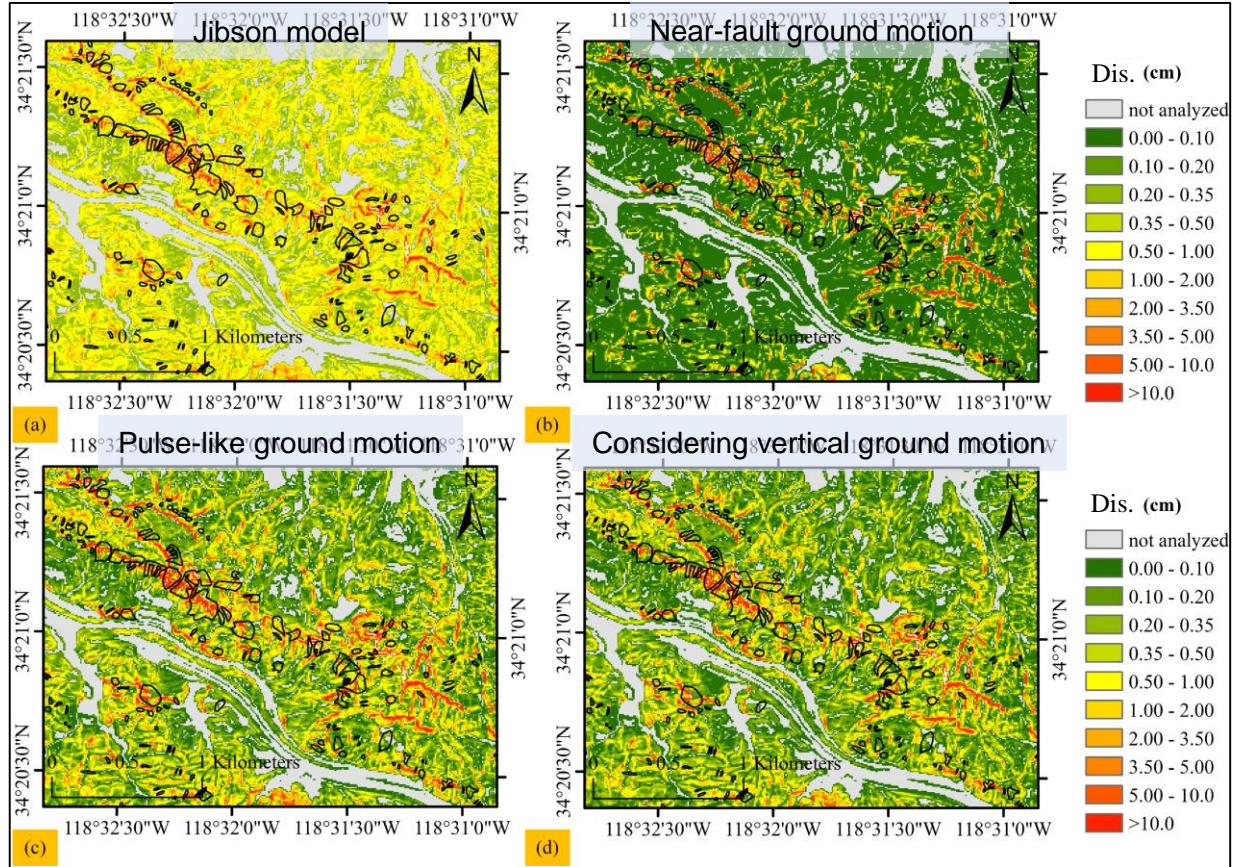
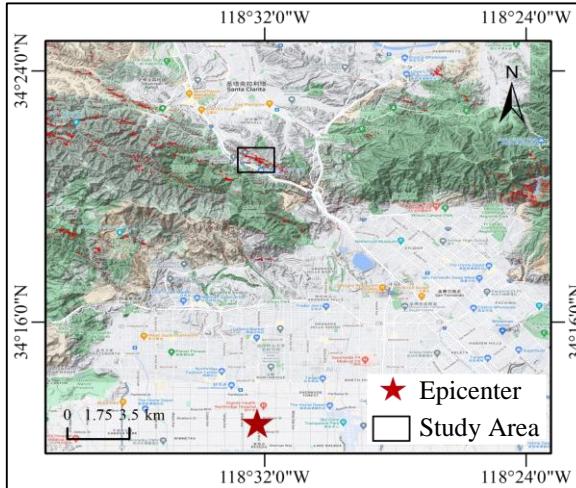


The red dashed line represents the predicted permanent displacement, which is the same as the displacement calculated using the sliding system method. The distance of between the blue data points and the red dashed line is more smaller, the more accurate the prediction.

The vertical ground motions **has effect** on the permanent displacement. This means when assess the stability of slope in near fault area, **the vertical ground motion** need to be considered.

Application

The Northridge earthquake is the first earthquake for which we have all of the data sets needed to conduct a detailed regional analysis of factors related to triggered landslides.



Application

Landslide hazard class	Dis.	Jibson model	D_r Near-fault ground motion	Pulse-like ground motion	Pulse-like ground motion considering vertical motion
Low	0-0.5 cm	0.6058	0.7850	0.7025	0.6757
Median	0.5-5 cm	1.2063	2.3113	1.6271	1.4395
High	5-50 cm	4.1227	4.1837	4.1169	3.8026
Very High	>50 cm	4.8497	4.5562	4.4477	4.6132
Quality sum Q_s	—	0.3213	0.4613	0.4689	0.4769
Low	0-1 cm	0.7283	0.8286	0.7674	0.7388
Median	1-5 cm	1.8938	2.6529	2.1135	1.8324
High	5-15 cm	3.8532	3.8246	3.8495	3.5820
Very High	>15 cm	4.8466	4.7425	4.6188	4.4161
Quality sum Q_s	—	0.4260	0.4343	0.4872	0.4977

It means when identify the hazard of earthquake-induced landslides in fault area, the vertical ground motion need to be considered.

Conclusion

- At a small period ratio ($0 < T_s \leq 2.4$), the dynamic response parameters ($k_y^2/k_{\max} k_{v-\max}$) can be replaced by PGA and PGV.
- When the period ratio exceed 2.4, the parameter ($k_y^2/S_a(1.5 T_s)PGV$) has a high correlation with the dynamic response parameters ($k_y^2/k_{\max} k_{v-\max}$) compared with the parameter($k_y^2 /PGAPGV$).
- It is necessary to consider the vertical ground motion when identify the hazard of earthquake-induced landslides in fault area.

Thanks for listening!

Xiang Chenlin, Huang Dongliang, Zhang Yingbin, Zhao Lianheng

School of Civil Engineering, Southwest Jiaotong University

School of Civil Engineering, Central South University

If you are interested in the research or have any questions, welcome to contact us.

E-mail: xiangchenlin@my.swjtu.edu.cn



Instituto de Investigaciones
Antisísmicas
UNIVERSIDAD NACIONAL DE SAN JUAN



DYNAMIC RESPONSE OF THE PUNTA NEGRA DAM UNDER THE 2021 SAN JUAN EARTHQUAKE

F. Zabala , N.G. Sánchez N. & G.S. Zabala

Earthquake Engineering Research Institute
National University of San Juan, Argentina

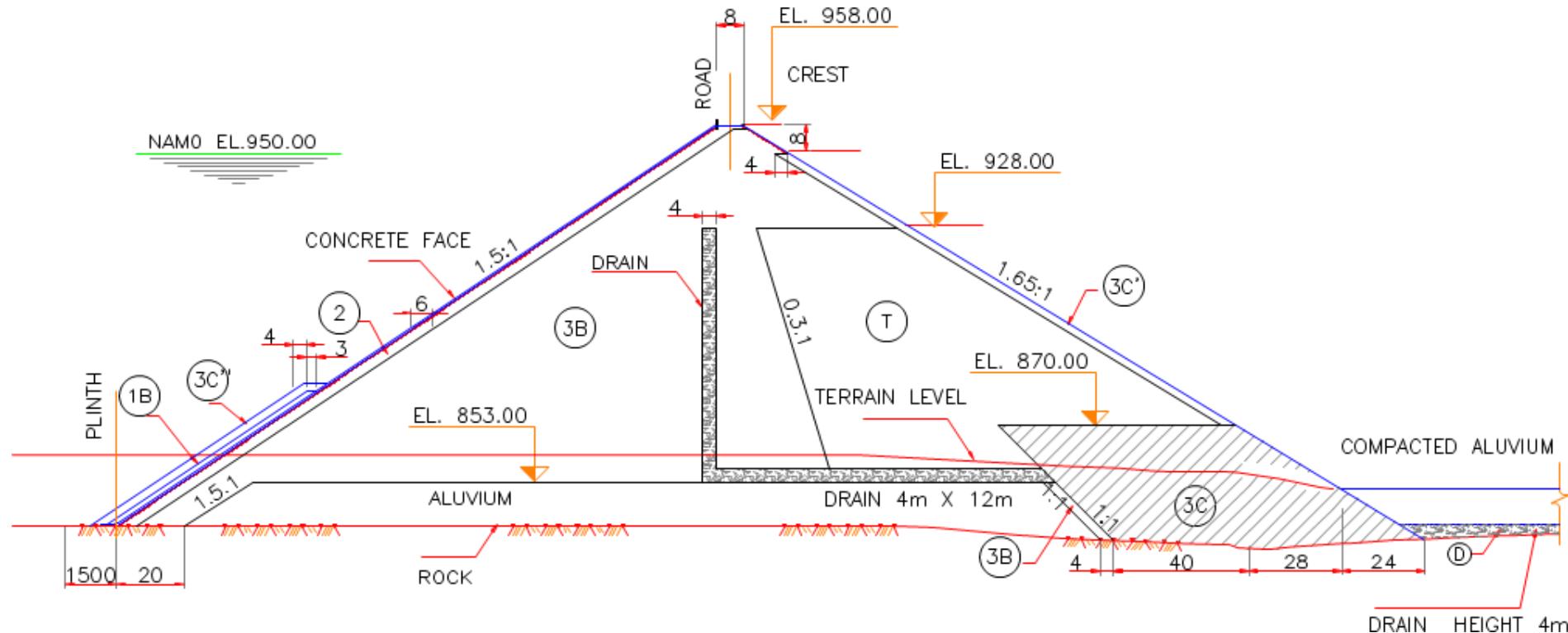
Punta Negra dam and the city of San Juan, Argentina



Location of accelerometers in Punta Negra dam

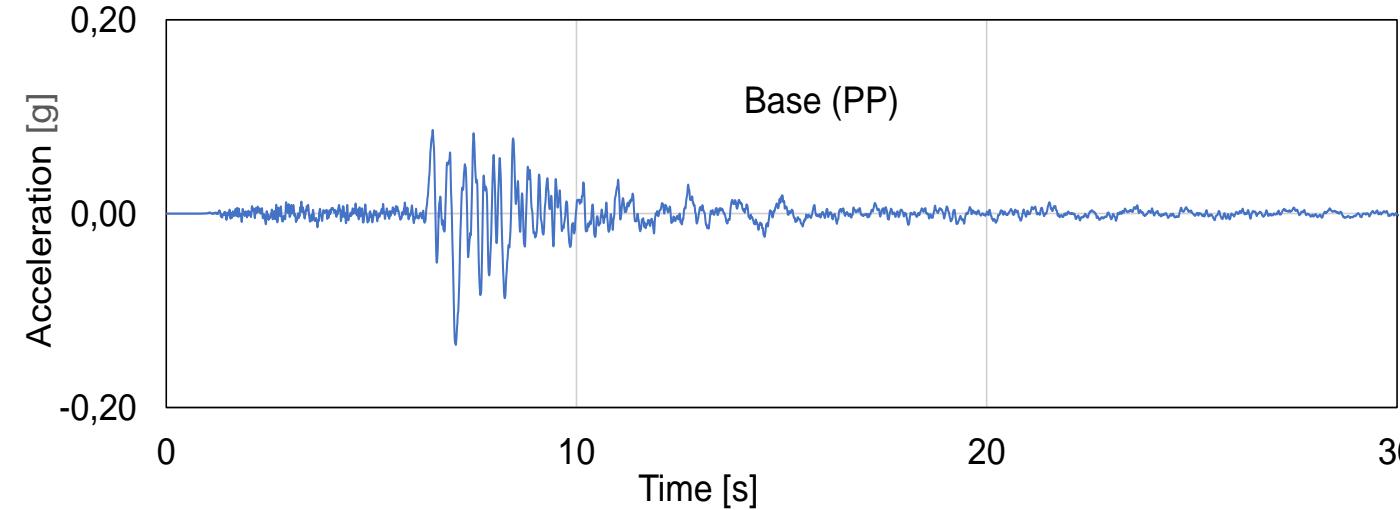


Dam (CFRD) highest section



Very well graded gravel
Height of 118 meters
Concrete face plinth in rock

Acceleration records of the 2021 San Juan earthquake at the Punta Negra dam

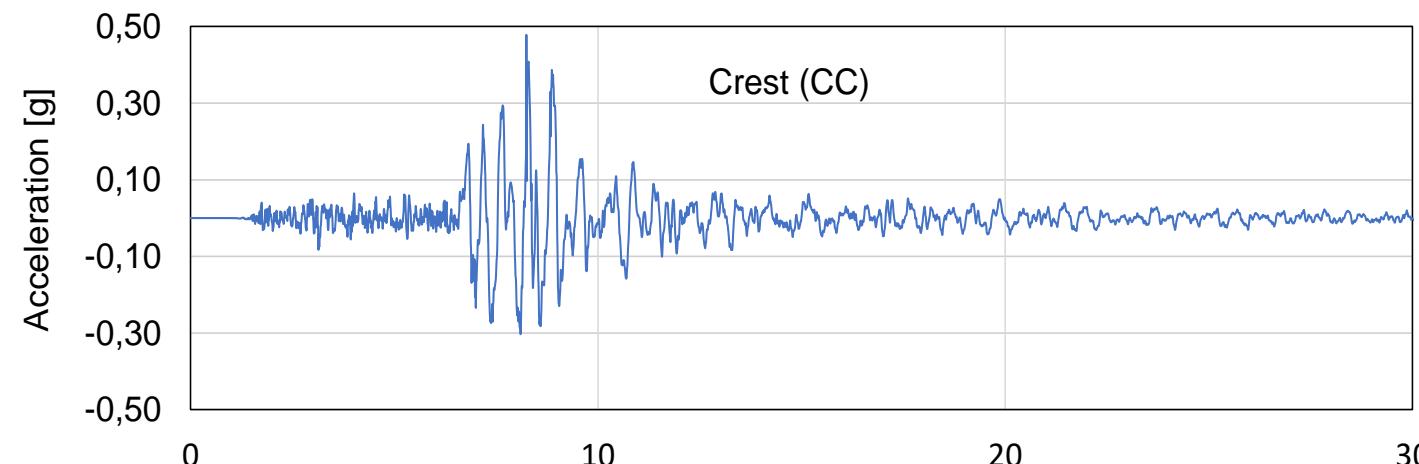


$M_w=6.4$

Epicenter distance=
39km

Depth = 8 km
Base peak

acceleration= **0.14 g**

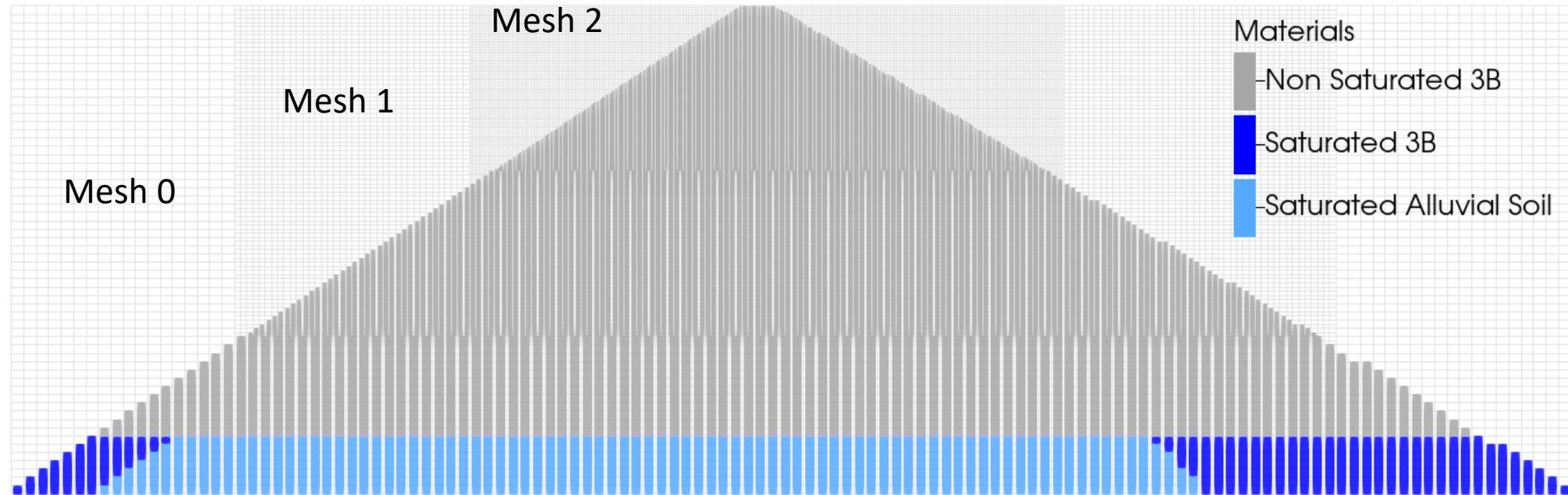


Crest peak

acceleration = **0.47 g**

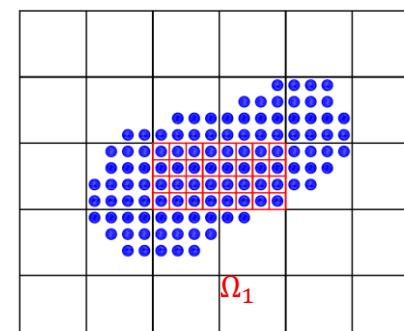
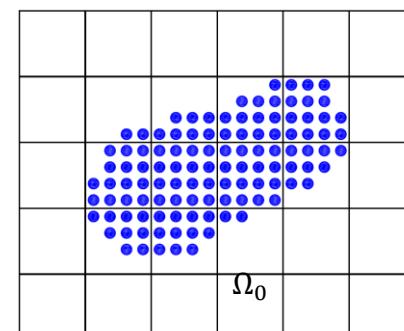
Amplification= **3.35**

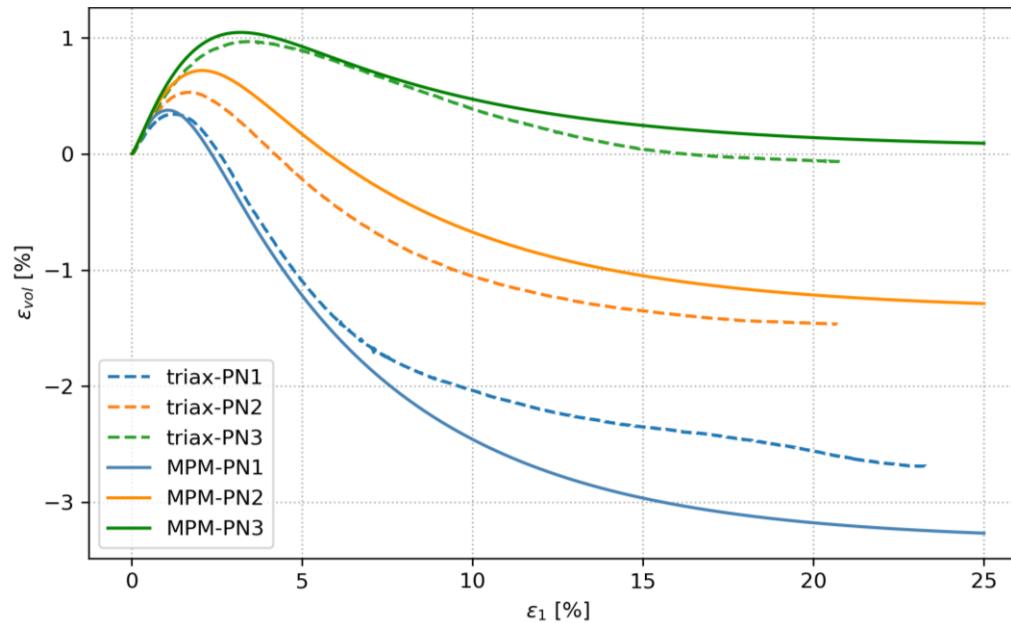
Material Point Method (MPM) model



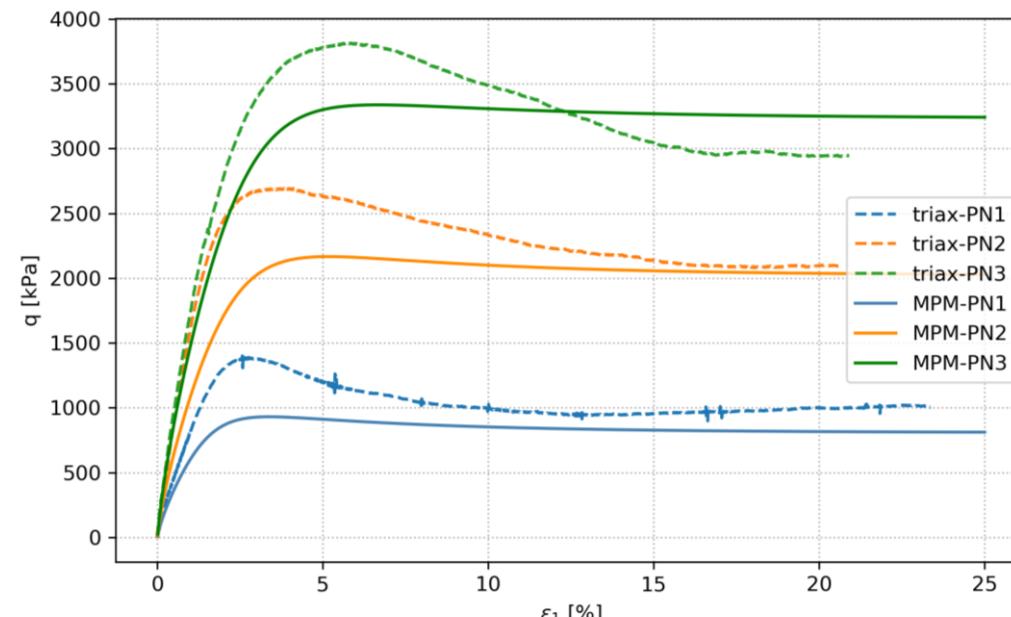
Moving Material Points:
Lagrangian Particles

Eulerian Fixed hierarchical
meshes



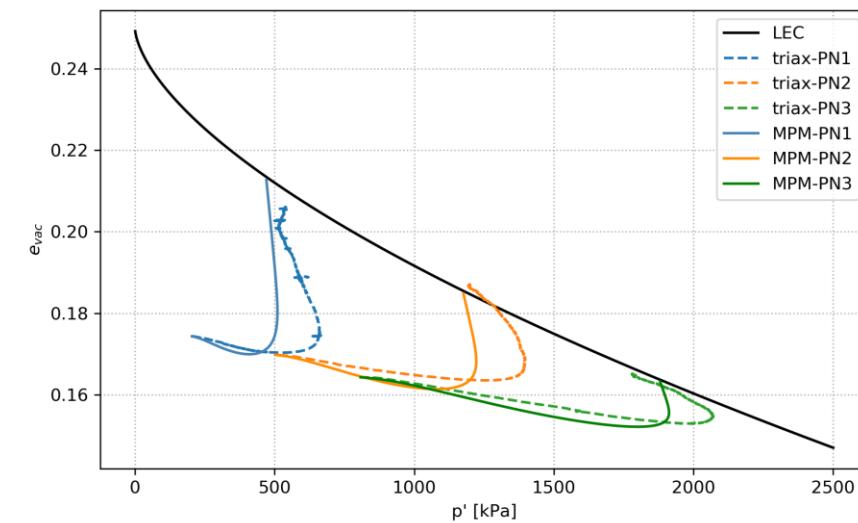


Volumetric vs axial strains



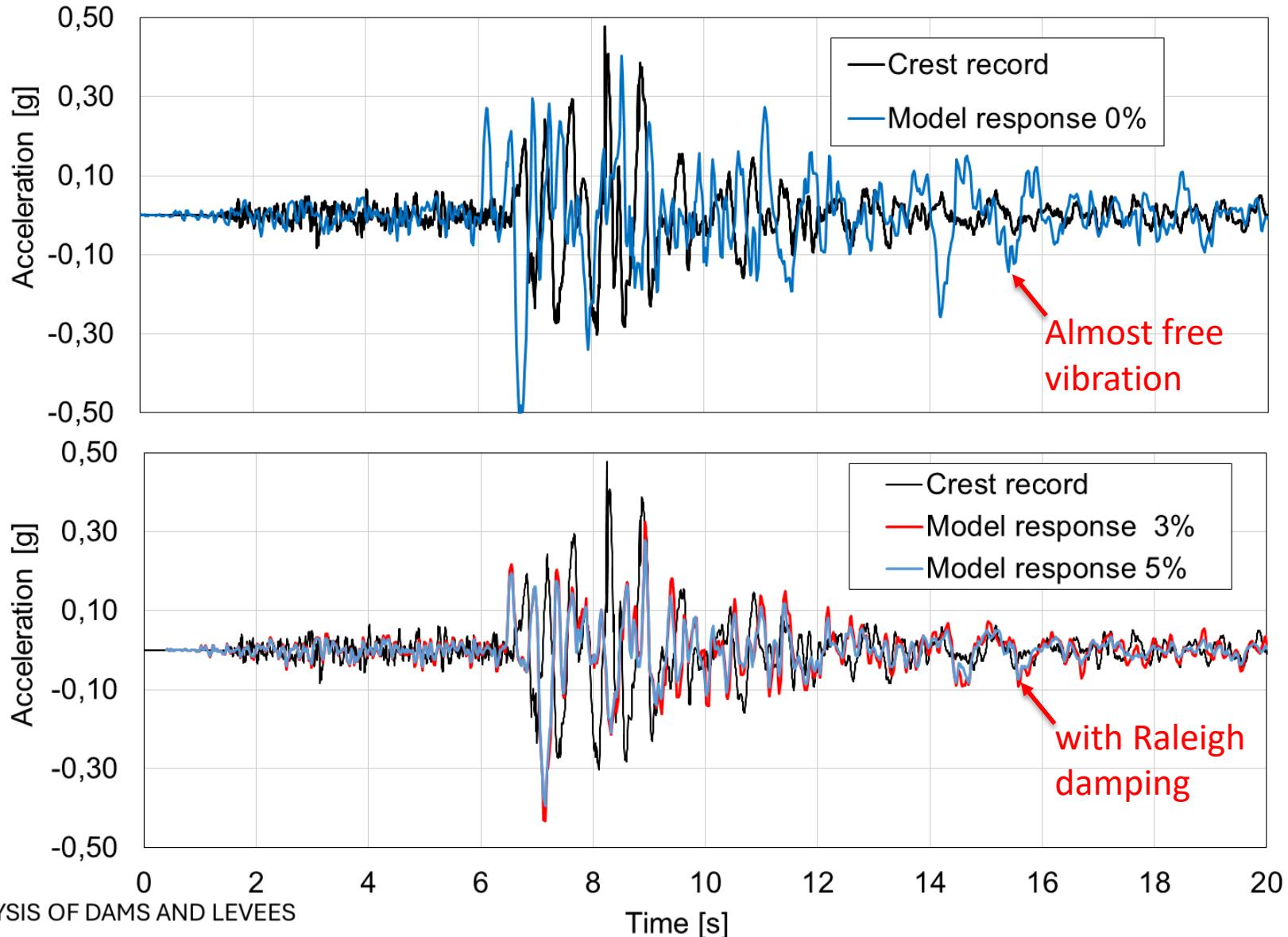
Deviator stress vs axial strain

Dafalias-Manzari (SANISAND) constitutive model: parameter calibration by triaxial testing

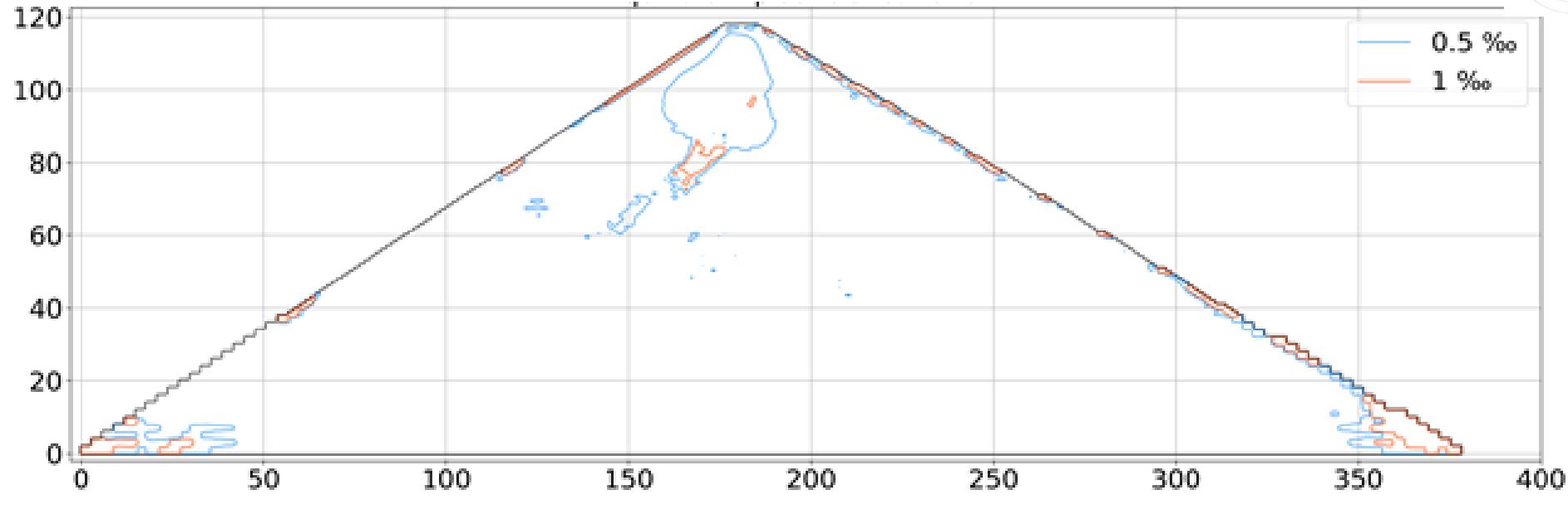


Void ratio vs effective pressure

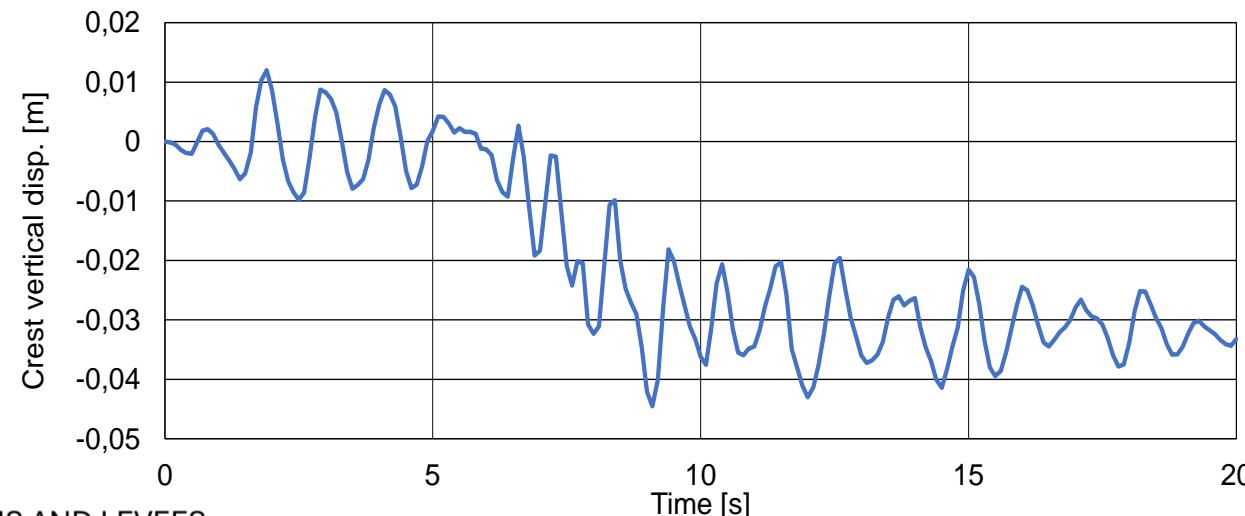
Crest record vs. model response



Other model results

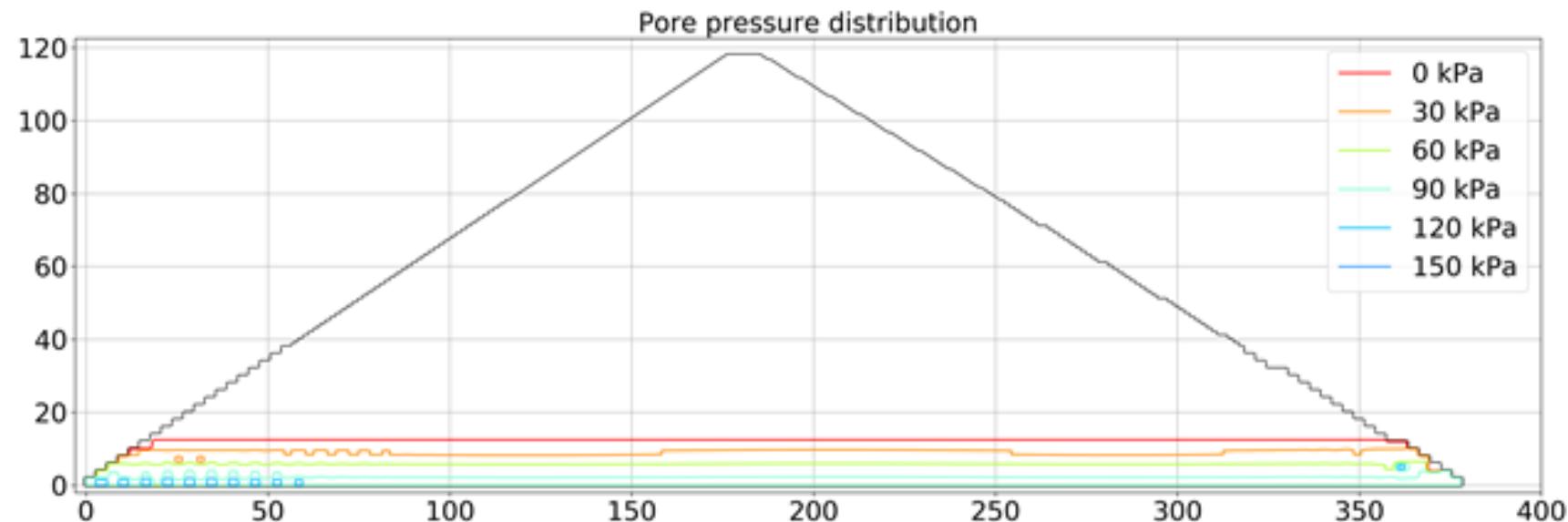


Equivalent plastic shear strains



Crest vertical displacement

Other model results: Foundation Pore Pressure



Conclusions

- The acceleration records of the Punta Negra dam have allowed the feeding of a multi-mesh MPM model of the dam. The model is able to reproduce well the magnitude of the response accelerations.
- The SANISAND constitutive model, calibrated with triaxial tests, appears to correctly represent the overall stiffness of the dam.
- The model response after the intense part of the earthquake has rather large long period oscillations. The addition of a small amount of mass-proportional damping improved the model response.
- The largest estimated plastic strains are relatively small compared to the strains corresponding to the peak strengths of the materials. These strains occur in the zone near the dam crest. In addition, the calculated ratio of pore pressure increase in the foundation is also small.



Thank you!

Any questions?



BCI6 - SEISMIC ANALYSIS OF DAMS AND LEVEES



Seismic response analysis of water-sediment-foundation-arch dam system

J. Zhang ¹, S. L. Chen ¹

¹ College of Aerospace Engineering, Nanjing University of Aeronautics and Astronautics, Nanjing, China

hydropower resources: renewable + clean + mature technology +low cost ...

Xiao-Wan Hydropower Station and complex river valleys

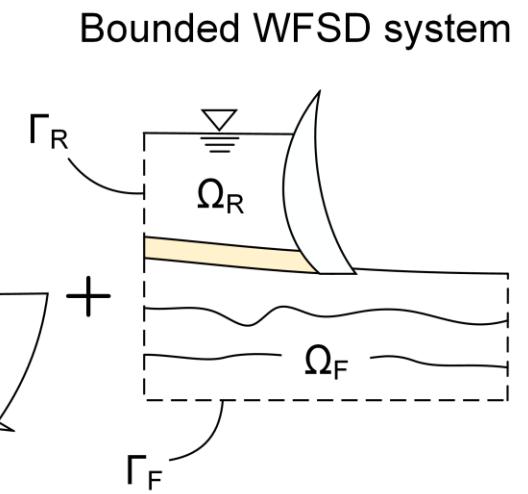
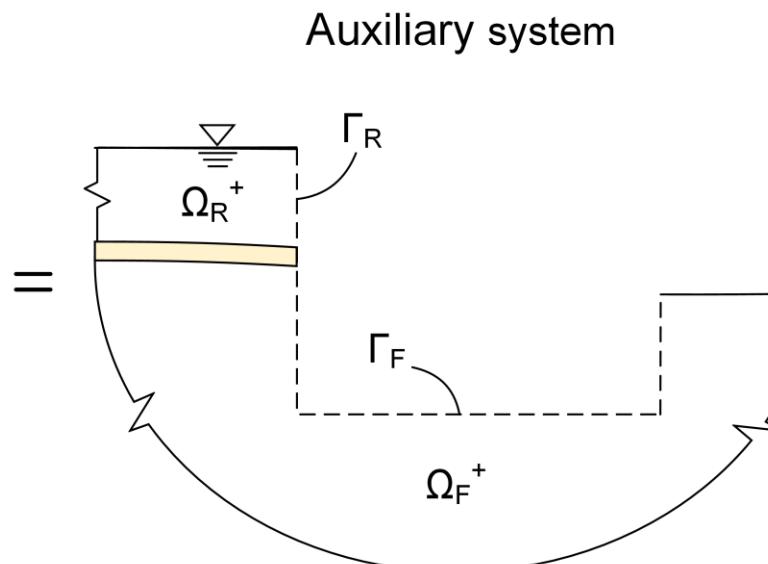
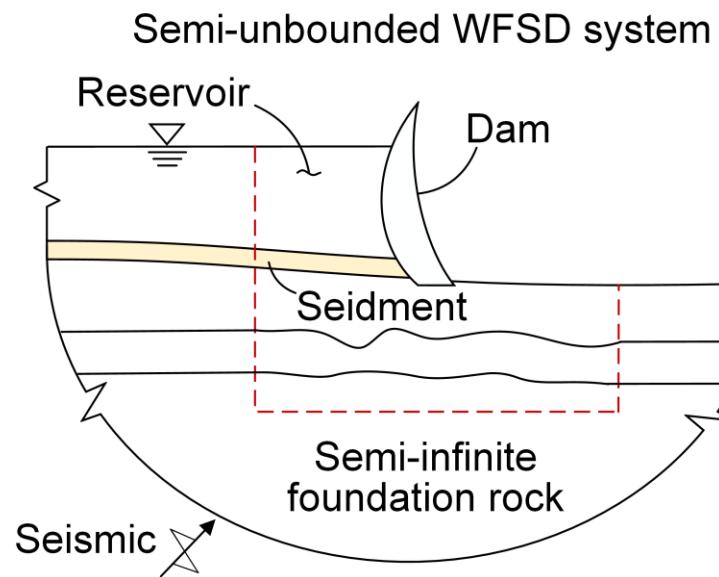


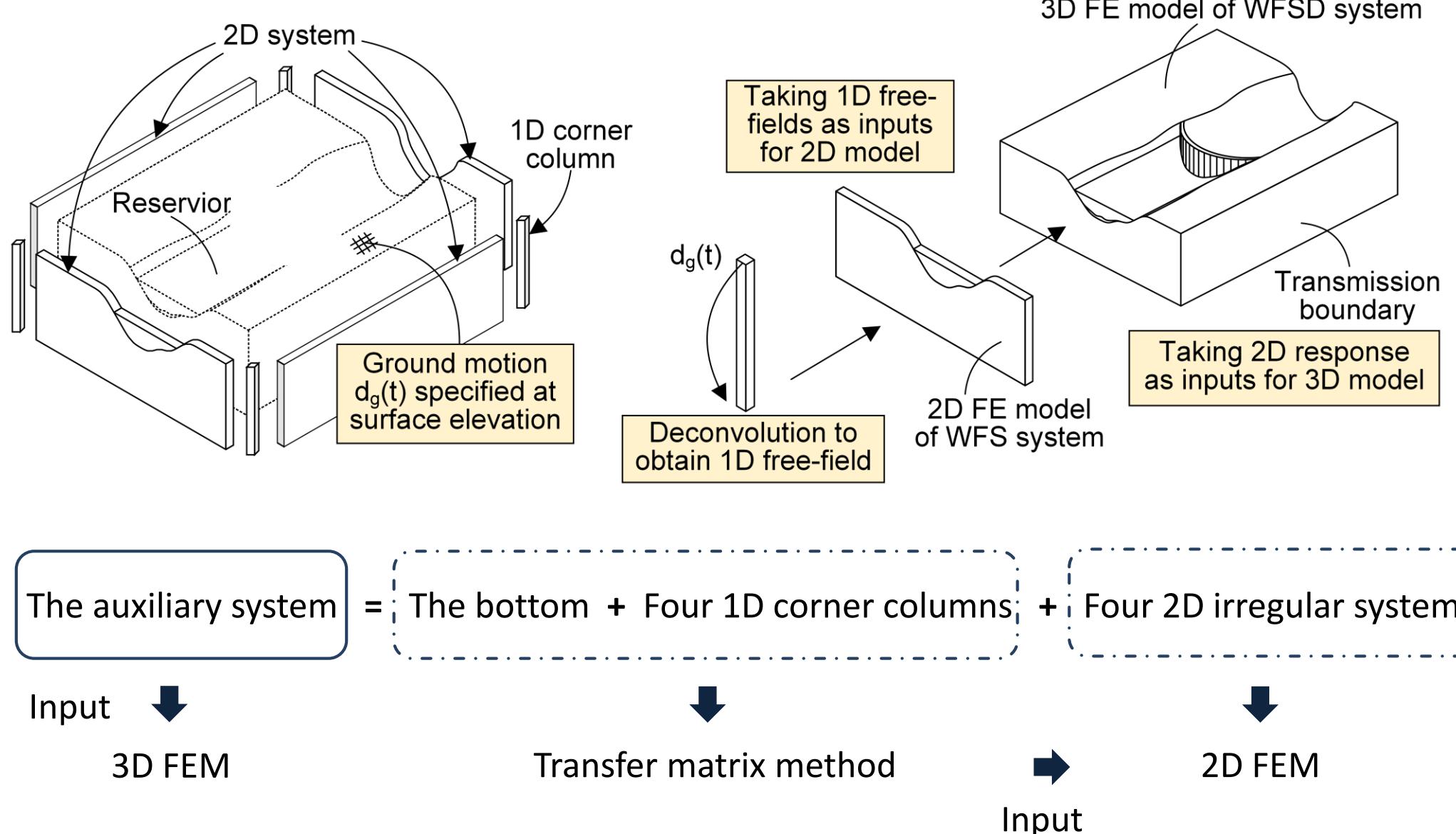
The seismic response analysis should include these factors:

- ★ Radiation damping associated with the semi-unbounded extent of the fluid and foundation
- ★ Dynamic pressure and compressibility of reservoir water
- ★ Wave absorption of the sediments at the reservoir bottom
- ★ Water–foundation-sediment-dam interaction (the WSFD system)

The uniform channel with linear fluid and sediment Ω_R^+
 The semi-unbounded, regular, linear foundation Ω_F^+

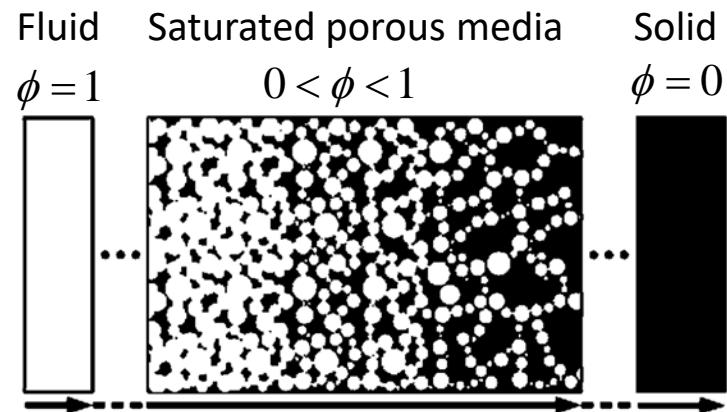
The dam and the irregular nonlinear parts of foundation Ω_F and fluid Ω_R





2D/3D FEM

The unified solver
 (generalized saturated porous media)



Internal node

Explicit solution strategy (central difference method and single difference method)

$$\mathbf{u}_i^{p+1} = 2\mathbf{u}_i^p - \mathbf{u}_i^{p-1} - (\Delta t)^2 (\mathbf{F}_{si}^p + \mathbf{T}_{si}^p - \mathbf{S}_{si}^p) / m_{si}$$

$$\mathbf{U}_i^{p+1} = 2\mathbf{U}_i^p - \mathbf{U}_i^{p-1} - (\Delta t)^2 (\mathbf{F}_{wi}^p + \mathbf{T}_{wi}^p - \mathbf{S}_{wi}^p) / m_{wi}$$

Interface node

The continuity conditions of force and displacement

$$\mathbf{u}_i - \mathbf{u}_k = 0 \quad (\mathbf{n}^T \phi (\mathbf{U} - \mathbf{u}))^i + (\mathbf{n}^T \phi (\mathbf{U} - \mathbf{u}))^k = 0$$

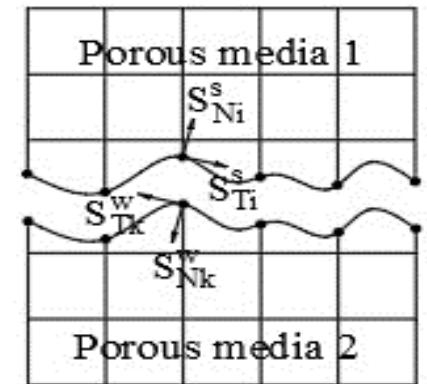
$$\pi_i - \pi_k = 0 \quad ((1-\phi) \mathbf{S}^s + \phi \mathbf{S}^f)^i + ((1-\phi) \mathbf{S}^s + \phi \mathbf{S}^f)^k = 0$$

Boundary node

Multi-transmitting formula (MTF)

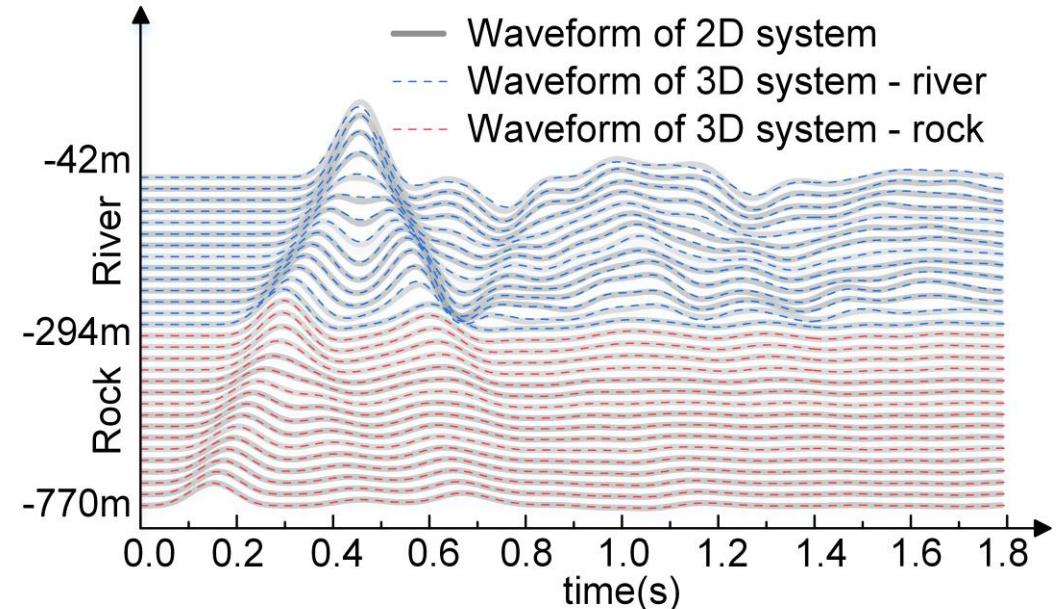
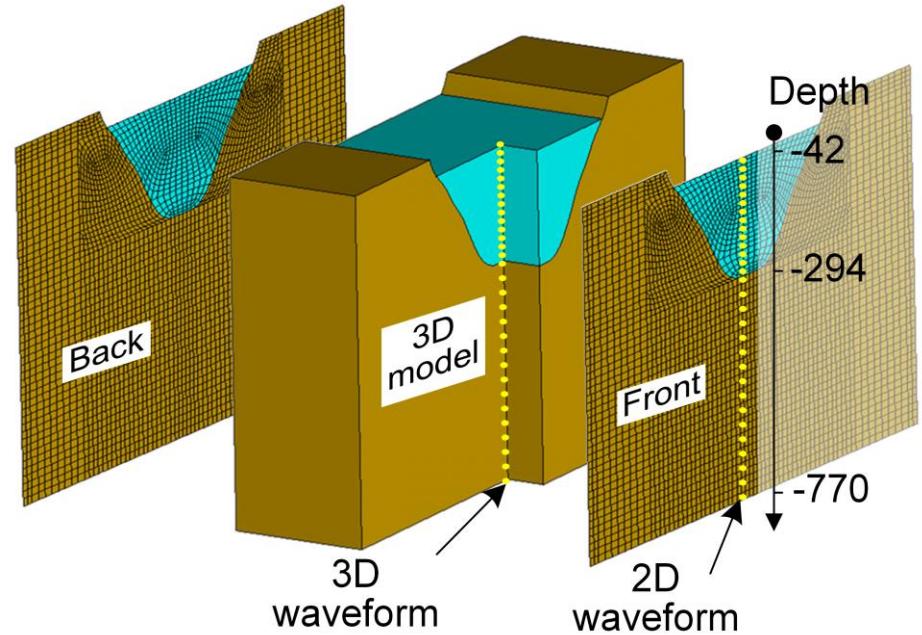
$$\mathbf{W}^{p+1} = \mathbf{W}_s^{p+1} + \mathbf{W}_f^{p+1}$$

$$\mathbf{W}_s^{p+1} = \sum_{j=1}^N (-1)^{j+1} C_N^j \left(\mathbf{W}_j^{p+1-j} - \mathbf{W}_{sj}^{p+1-j} \right) + \mathbf{W}_{fj}^{p+1-j}$$



VALIDATION

The uniform valley model with linear river

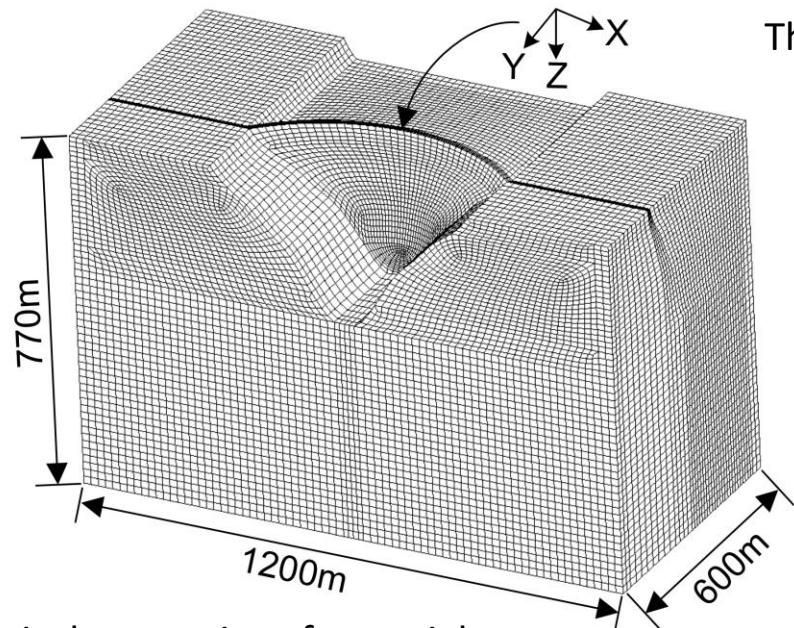


The effectiveness of the free-field computing method for the irregular site

The accuracy of the seismic analysis technique for the coupled system

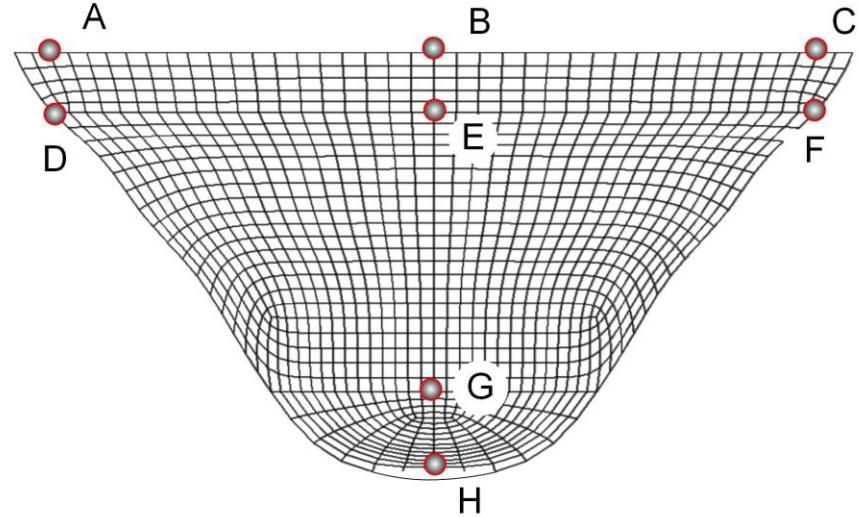
APPLICATION

The FE model of WSFD system of Xiao-Wan Dam



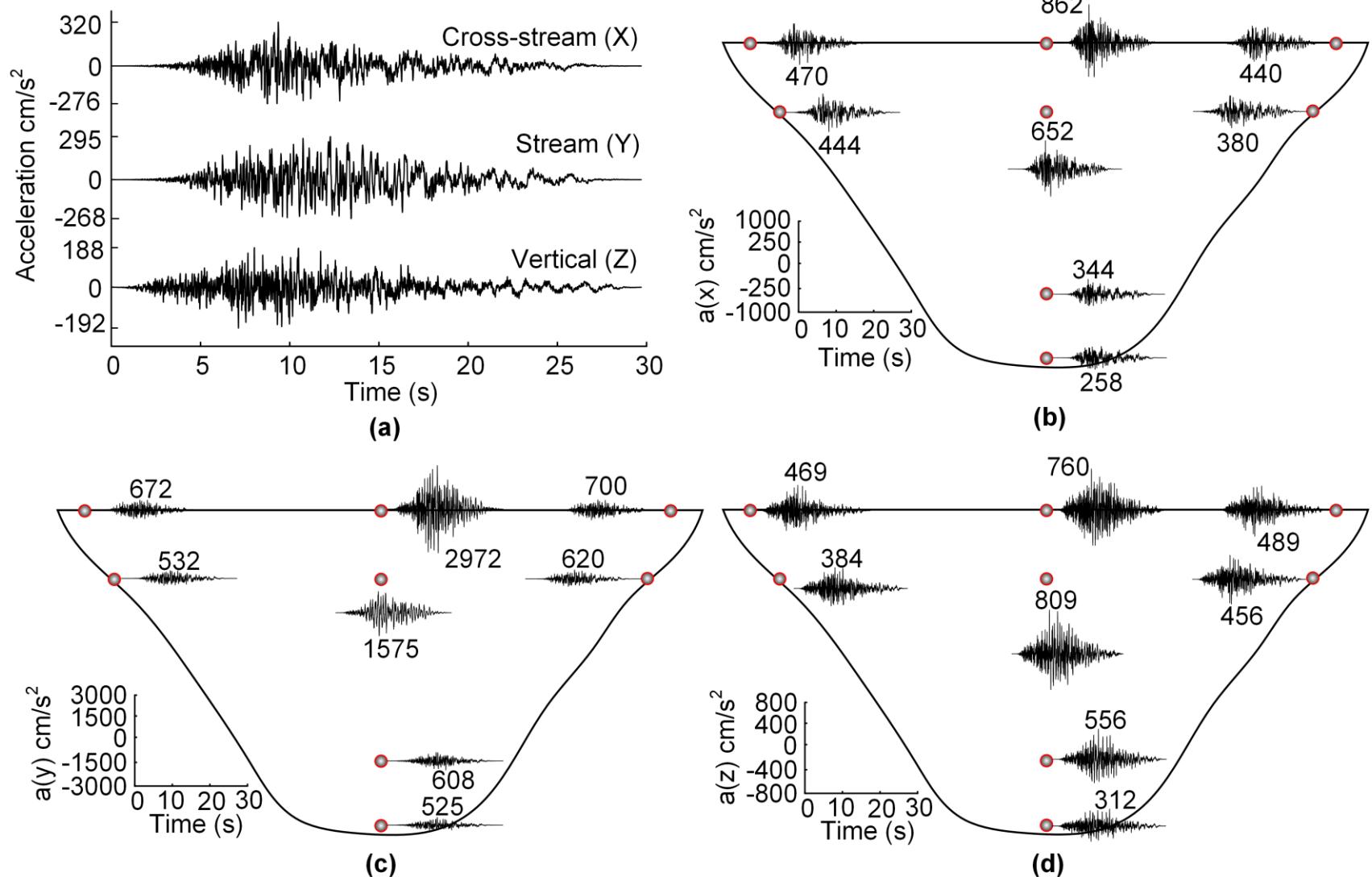
Parameters of mechanical properties of materials

The monitoring points at the upstream surface of the dam



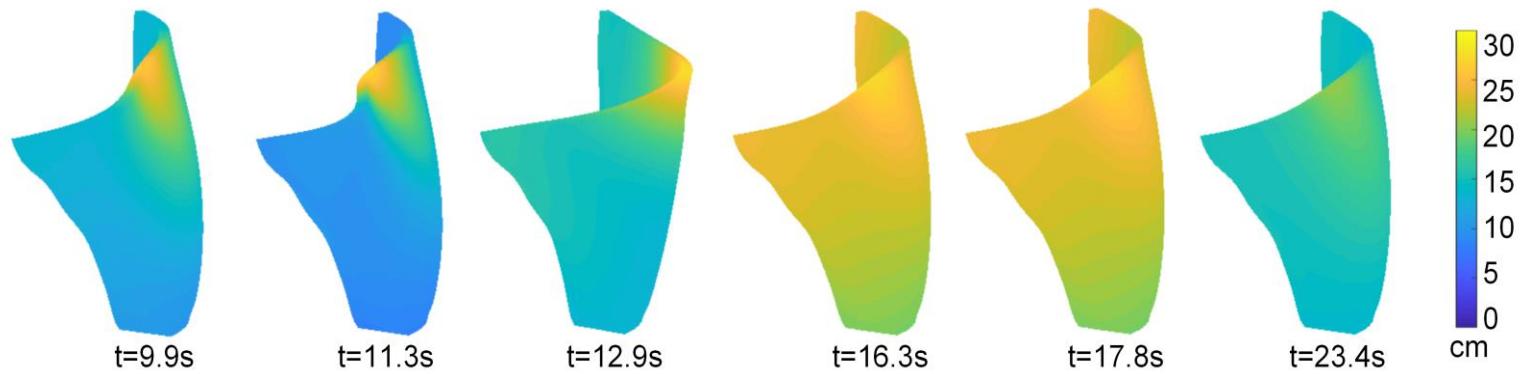
Components	ρ_s (kg/m^3)	ρ_w (kg/m^3)	ν	ξ	E (GPa)	V_p (m/s)	V_s (m/s)
Water	-	1000	0.49	0.005	-	1500	-
Dam	2400	-	0.20	0.033	28.6	3638	2228
Foundation	2630	-	0.27	0.020	21.0	3158	1773
Sediment	2083	1000	0.35	0.035	0.77	2582	754

Acceleration response

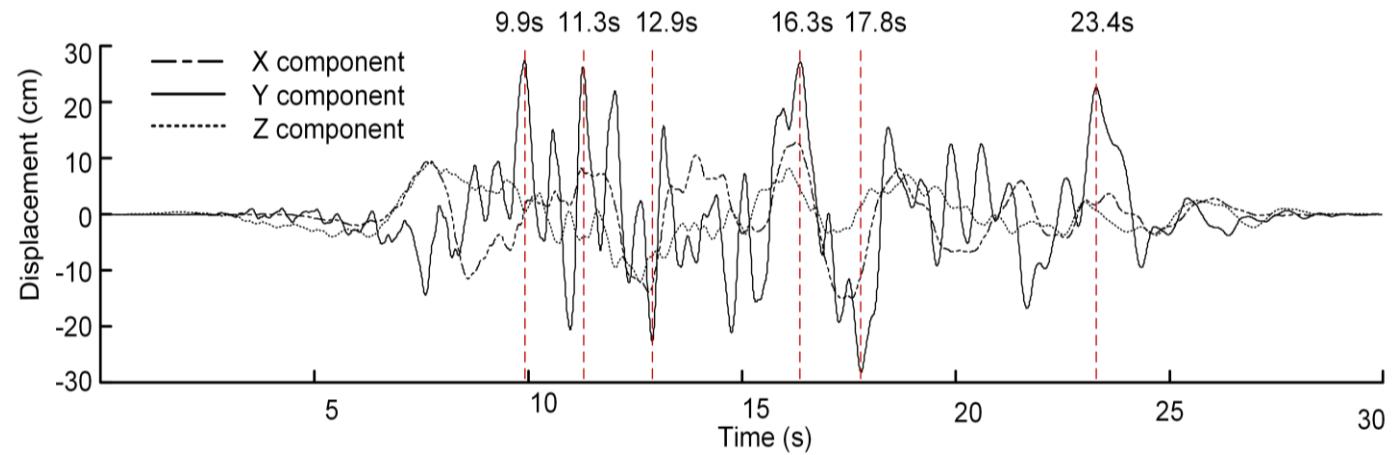


(a) The acceleration history of Iwate-Japan record;
(b-d) The acceleration histories of the dam in X, Y, and Z direction, respectively

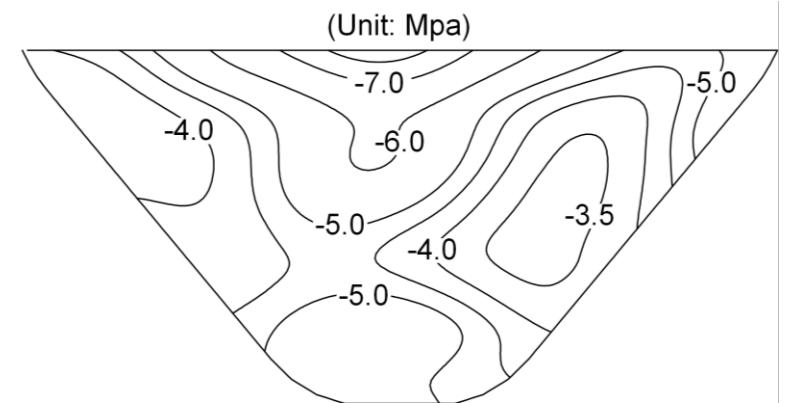
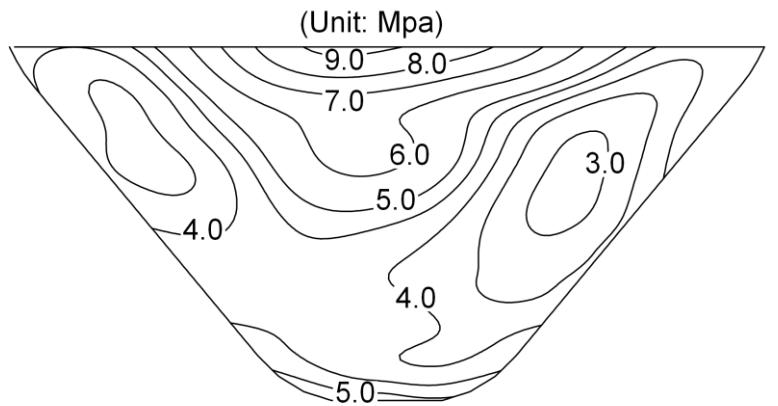
Displacement response



Deformation of the dam at different times (magnification 300X)



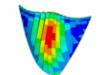
Stress response





Thank you!

Any questions?



BCI6 - SEISMIC ANALYSIS OF DAMS AND LEVEES

